Zhiqun Lin
Yingkui Yang
Aiqing Zhang *Editors*

Polymer-Engineered Nanostructures for Advanced Energy Applications

Springer

Engineering Materials and Processes

Series editor

Brian Derby, Manchester, UK

More information about this series at http://www.springer.com/series/4604

Zhiqun Lin · Yingkui Yang · Aiqing Zhang
Editors

Polymer-Engineered Nanostructures for Advanced Energy Applications

Springer

Editors
Zhiqun Lin
School of Materials Science and Engineering
Georgia Institute of Technology
Atlanta, GA
USA

Aiqing Zhang
School of Chemistry and Materials Science
South-Central University for Nationalities
Wuhan, Hubei
China

Yingkui Yang
School of Chemistry and Materials Science
South-Central University for Nationalities
Wuhan, Hubei
China

Preface

Nanostructured materials lie at the heart of fundamental advances in modern science and engineering, and hold the key to the next generation of energy conversion and storage devices. An enormous variety of nanostructures and the resulting materials have been successfully developed by a tremendous amount of techniques in the face of limited fossil fuels and ever-increasing energy requirements. The past decades have witnessed considerable progress in the field of nanostructured materials for advanced energy applications. Polymers, in particular, have the ability to produce nanostructures by self-assembly, assisted organization, templated growth, in-situ hybridization, and/or ex-situ recombination strategies which enable the rational design and optimal fabrication of nanostructured polymers, nanoarchitectured inorganics, and organic-inorganic nanocomposites.

With contributions from 50 internationally renowned experts with interdisciplinary and broad perspectives, this book is likely one of the most authoritative references ever published that focuses solely on the state-of-the-art knowledge of polymer-engineered nanostructures, their unique properties, and the new cutting edge, breakthroughs, future horizons, and insights into such functional materials for energy applications. With over 2500 references, 370 figures, and 14 tables included, this book attempts to offer a highly valuable source for scientists, students, and engineers working in the field of photovoltaics, fuel cells, thermoelectrics, piezo-electrics, ferroelectrics, batteries, supercapacitors, and photocatalysis. Based on the above topics, this book contains the following three parts and 18 chapters.

Part I includes six chapters, which outline the recent advancements of engineering nanostructures with polymers and polymer processing techniques.

Chapter 1 reports on the preparation of nanostructured ceramic fibers with tailored morphologies and hierarchical architectures through polymer-mediated electrospinning and the energy-related applications of the as-fabricated fibers.

Chapter 2 provides an overview on the design and fabrication of various metal, semiconductor, and polymer nanostructures using polymer microbeads and adjusting processing parameters.

Chapter 3 illustrates the top-down technique strategies for the fabrication of metal-containing polymers with well-defined nanostructures.

Chapter 4 summarizes the recent development of porous polymer materials, including covalent organic frameworks, hyper-crosslinked polymers, conjugated microporous polymers, macroporous polymers, and their synthetic methods as well as potential applications.

Chapter 5 discusses the fabrication strategies and formation mechanisms of structure-tailored polymer photonic crystals and their responsive characteristics under various external stimuli.

Chapter 6 describes the design and synthesis methods of nanostructured polymeric materials with diverse stimuli-responsive features and their multifunctional smart applications.

Part II includes six chapters which are focused on the energy storage applications of polymer-engineered nanostructures.

Chapter 7 introduces the fabrication of polymer nanofibers and their derived carbon-based nanofibers with a particular focus on their applications in rechargeable batteries and supercapacitors.

Chapter 8 reviews recent studies on the synthesis of graphene/conducting polymer composites and their supercapacitor applications.

Chapter 9 presents the recent development of conducting polymer/inorganic nanohybrids as electrodes for rechargeable batteries, fuel cells, and supercapacitors.

Chapter 10 introduces general strategies for constructing polymer-derived carbon/inorganic composites and the rational design of electrode materials for high-performance batteries and electrocatalytic hydrogen evolution.

Chapter 11 reports on the formulation, design, and performance tailoring of polymer-based electrolytes by incorporating nanoparticles and/or by adding organic solvents or ionic liquids for electrochemical energy applications.

Chapter 12 introduces theoretical considerations for concomitantly increasing the dielectric permittivity and breakdown strength of polymer nanocomposites. Recent studies on core-shell structured and dielectric anisotropy polymer nanocomposites for high energy density were further reviewed.

Part III includes six chapters which are focused on the energy conversion applications of polymer-engineered nanostructures.

Chapter 13 describes the latest developments of flexible piezoelectric and pyroelectric polymers and their nanocomposites for energy harvesting.

Chapter 14 focuses on the recent progress of nanostructured polymers and polymer/inorganic nanocomposites with multidimensional nanostructures for thermoelectric applications.

Chapter 15 deals with the use of polymer/inorganic nanocomposite materials in various categories of polymer electrolyte membrane fuel cells.

Chapter 16 summarizes the influence of chemical structures on the orientation of semiconducting polymer backbones and the device performances.

Chapter 17 focuses on the recent work in the design, fabrication, and surface modification of metal oxide semiconductors to improve the performance of excitonic solar cells.

Chapter 18 provides an overview on the development of nanostructured porous polymers for metal-free photocatalysis.

Atlanta, USA   Zhiqun Lin
Wuhan, China   Yingkui Yang
Wuhan, China   Aiqing Zhang

Acknowledgements

Contents

Editors and Contributors

About the Editors

Dr. Zhiqun Lin is currently Professor of Materials Science and Engineering at the Georgia Institute of Technology. He received his Ph.D. in Polymer Science and Engineering from University of Massachusetts, Amherst in 2002. He did his postdoctoral research at University of Illinois at Urbana-Champaign. He joined the Department of Materials Science and Engineering at the Iowa State University as an Assistant Professor in 2004 and was promoted to Associate Professor in 2010. He moved to Georgia Institute of Technology in 2011, and became a Professor in 2014. His research interests include polymer-based nanocomposites, block copolymers, polymer blends, conjugated polymers, functional nanocrystals of different architectures, solar cells (in particular perovskite solar cells, organic–inorganic hybrid solar cells, and dye-sensitized solar cells), lithium ion batteries, hydrogen generation, hierarchically structured and assembled materials, and surface and interfacial properties. Currently, he serves as an Associate Editor for *Journal of Materials Chemistry A* and an editorial advisory board member for *Nanoscale*.

Dr. Yingkui Yang is currently Professor in the School of Chemistry and Materials Science at South-Central University for Nationalities, China. He completed his Ph.D. degree in Polymer Chemistry and Physics at Huazhong University of Science and Technology in 2007. He has worked as Research Fellow, Postdoctoral Fellow, and Visiting Professor at City University of Hong Kong and Hong Kong Polytechnic University over the past decade. He has also served as a Visiting Scholar at the University of Sydney (2010–2011) and Georgia Institute of Technology (2014–2015). He joined the School of Materials Science and Engineering at Hubei University in 2007 and was promoted to Full Professor in 2013. He then moved to South-Central University for Nationalities in 2016. His current research interests include surface/interface engineering of nanostructures, polymer-templated nanostructures, polymer-based nanocomposites, graphitic nanocarbons (in particular graphene and carbon nanotubes) and their nanohybrids for actuators, electrochemical energy, electronics, environmental materials, and dielectric applications.

Dr. Aiqing Zhang is currently working as Professor and Dean of the School of Chemistry and Materials Science at South-Central University for Nationalities, China. He obtained his B.Sc. (1983), M.Sc. (1990), and Ph.D. (1998) from Huazhong University of Science and Technology, China. He served as a Postdoctoral Fellow (2000–2001) at Chonbuk National University, Korea. He has ever worked at Shanxi Mining Institute (currently merged into Taiyuan University of Technology) during 1983–1987 and Wuhan Automotive Polytechnic University (currently merged into Wuhan University of Technology) during 1990–1994, respectively. He then moved to

South-Central University for Nationalities in 1998 while became a full professor. His scientific interests particularly focus on the rational design and optimal synthesis of functional polymer materials for photosensitive, low-dielectric, and catalytic applications.

Contributors

Paschalis Alexandridis Department of Chemical and Biological Engineering, University at Buffalo, The State University of New York (SUNY), Buffalo, NY, USA

Avinash Baji Engineering Product Development (EPD) Pillar, Singapore University of Technology and Design (SUTD), Singapore, Singapore

Dmitry Bedrov Department of Materials Science and Engineering, University of Utah, Salt Lake City, UT, USA

Yajnaseni Biswas Polymer Science Unit, Indian Association for the Cultivation of Science, Jadavpur, Kolkata, India

Christopher Rhys Bowen Department of Mechanical Engineering, Materials and Structures Centre, University of Bath, Bath, UK

Guozhong Cao Department of Materials Science and Engineering, University of Washington, Seattle, WA, USA

Madhab Dule Polymer Science Unit, Indian Association for the Cultivation of Science, Jadavpur, Kolkata, India

Kingshuk Dutta Department of Chemical Engineering, Indian Institute of Technology, Kharagpur, India

Cheng Fang Global Centre for Environmental Remediation (GCER), University of Newcastle, Newcastle, NSW, Australia

Qingsheng Gao Department of Chemistry, Jinan University, Guangzhou, China

Alexandra Ho Department of Chemistry, University of Liverpool, Liverpool, UK; Institute of Materials Research and Engineering (IMRE), Agency for Science, Technology and Research (A*STAR), Singapore, Singapore

Cheuk-Lam Ho Institute of Molecular Functional Materials, Department of Chemistry and Institute of Advanced Materials, Hong Kong Baptist University, Kowloon Tong, Hong Kong, China

Wei Huang Max Planck Institute for Polymer Research, Mainz, Germany

Somdeb Jana Polymer Science Unit, Indian Association for the Cultivation of Science, Jadavpur, Kolkata, India

Xiaolu Jia Key Laboratory of Materials Chemistry for Energy Conversion and Storage of Ministry of Education, School of Chemistry and Chemical Engineering, Huazhong University of Science and Technology, Wuhan, China

Qingyin Li School of Chemistry and Chemical Engineering, Huazhong University of Science and Technology, Wuhan, China

Run Li Max Planck Institute for Polymer Research, Mainz, Germany

Xu Li Institute of Materials Research and Engineering (IMRE), Agency for Science, Technology and Research (A*STAR), Singapore, Singapore

Yuanhua Lin School of Materials Science and Engineering, Tsinghua University, Beijing, China

Zongqiong Lin School of Materials Science and Engineering, Nanyang Technological University, Singapore, Singapore; Key Laboratory of Flexible Electronics (KLOFE) and Institute of Advanced Materials (IAM), Jiangsu National Synergetic Innovation Center for Advanced Materials (SICAM), Nanjing Tech University (NanjingTech), Nanjing, China

Yuchen Liu Department of Industrial and Systems Engineering, Texas A&M University, College Station, TX, USA

Yunfei Liu School of Chemistry and Chemical Engineering, Huazhong University of Science and Technology, Wuhan, China

Beatriz Chiyin Ma Max Planck Institute for Polymer Research, Mainz, Germany

Yiu-Wing Mai Centre for Advanced Materials Technology (CAMT), School of Aerospace, Mechanical and Mechatronic Engineering, The University of Sydney, Sydney, NSW, Australia

Tarun K. Mandal Polymer Science Unit, Indian Association for the Cultivation of Science, Jadavpur, Kolkata, India

Tsuyoshi Michinobu Department of Organic and Polymeric Materials, Tokyo Institute of Technology, Tokyo, Japan

Ce-Wen Nan School of Materials Science and Engineering, Tsinghua University, Beijing, China

Prakash Sengodu Department of Chemistry, National Taiwan Normal University, Taipei, Taiwan

Yang Shen School of Materials Science and Engineering, Tsinghua University, Beijing, China

Bien Tan School of Chemistry and Chemical Engineering, Huazhong University of Science and Technology, Wuhan, China

Haiying Tan Key Laboratory of Materials Chemistry for Energy Conversion and Storage of Ministry of Education, School of Chemistry and Chemical Engineering, Huazhong University of Science and Technology, Wuhan, China

Liangxiao Tan School of Chemistry and Chemical Engineering, Huazhong University of Science and Technology, Wuhan, China

Youhong Tang School of Computer Science Engineering and Mathematics, Centre for Nanoscale Science and Technology, Flinders University, Adelaide, SA, Australia

Jianjun Tian Institute of Advanced Materials and Technology, University of Science and Technology Beijing, Beijing, China

Chaoying Wan Warwick Manufacturing Group, International Institute for Nanocomposites Manufacturing (IINM), University of Warwick, Coventry, UK

Kewei Wang School of Chemistry and Chemical Engineering, Huazhong University of Science and Technology, Wuhan, China

Shiren Wang Department of Industrial and Systems Engineering, Texas A&M University, College Station, TX, USA

Shixun Wang Institute of Advanced Materials and Technology, University of Science and Technology Beijing, Beijing, China

Suxi Wang Institute of Materials Research and Engineering (IMRE), Agency for Science, Technology and Research (A*STAR), Singapore, Singapore

Wei Wang Department of Chemical and Biological Engineering, University at Buffalo, The State University of New York (SUNY), Buffalo, NY, USA

Yang Wang Department of Organic and Polymeric Materials, Tokyo Institute of Technology, Tokyo, Japan

Wai-Yeung Wong Institute of Molecular Functional Materials, Department of Chemistry and Institute of Advanced Materials, Hong Kong Baptist University, Kowloon Tong, Hong Kong, China; Department of Applied Biology and Chemical Technology, The Hong Kong Polytechnic University, Hung Hom, Hong Kong, China

Lichun Yang School of Materials Science and Engineering, South China University of Technology, Guangzhou, China

Yuwan Yang School of Chemistry and Chemical Engineering, Huazhong University of Science and Technology, Wuhan, China

Sze-Chun Yiu Institute of Molecular Functional Materials, Department of Chemistry and Institute of Advanced Materials, Hong Kong Baptist University, Kowloon Tong, Hong Kong, China

Haifei Zhang Department of Chemistry, University of Liverpool, Liverpool, UK

Kai A.I. Zhang Max Planck Institute for Polymer Research, Mainz, Germany

Qichun Zhang School of Materials Science and Engineering, Nanyang Technological University, Singapore, Singapore; Division of Chemistry and Biological Chemistry, School of Physical and Mathematical Sciences, Nanyang Technological University, Singapore, Singapore

Xin Zhang School of Materials Science and Engineering, Tsinghua University, Beijing, China

Jintao Zhu Key Laboratory of Materials Chemistry for Energy Conversion and Storage of Ministry of Education, School of Chemistry and Chemical Engineering, Huazhong University of Science and Technology, Wuhan, China

Abbreviations

4-AP	4-Aminephenol
4B-TEMPO	4-Benzoyloxy-2,2,6,6-tetramethyl-piperidine-1-oxyl
4-NP	4-Nitropheno
4-VP	4-Vinylpyridine
AAc	Acrylic acid
AAO	Anodic aluminum oxide
ABF	Angular bright field
ABL	Anode buffer layer
ADA	Adamantane
ADMET	Acyclic diene metathesis
AFM	Atomic force microscopy
ALD	Atomic layer deposition
APS	Ammonium persulfate
ARLIB	Aqueous rechargeable lithium ion battery
ATRP	Atom transfer radical polymerization
BA	Benzyl alcohol
BBT	Benzobisthiadiazole
BCB	Bis(benzocyclobutene)
BCMA	Bis(chloromethyl) anthracene
BCMBP	Bis(chloromethyl)biphenyl
BCP	Block copolymer
BDBA	1,4-Benzenediboronic acid
BDF	Benzodifuran
BDM	1,4-Benzenedimethanol
BET	Brunauer-Emmett-Teller
BF	Benzofuran
BHJ	Bulk heterojunction
BIEE	1,2-Bis-(2-iodoethoxy)ethane
BNNSs	Boron nitride nanosheets
BOPP	Biaxially oriented polypropylene

BPO	Benzoyl peroxide
BTDADA	Benzothiadiazole diboronic acid
CAC	Critical aggregate concentration
CBL	Cathode buffer layer
CD	Cyclodextrin
CLSM	Confocal laser scanning microscopy
CMP	Conjugated microporous polymer
CNFs	Carbon nanofibers
CNTs	Carbon nanotubes
COF	Covalent organic framework
CPE	Composite polymer electrolyte
CPM	Complex polymeric micelle
CTA	Chain transfer agent
CTAB	Cetyltrimethylammonium bromide
CTF	Covalent triazine framework
CTFE	Chlorotrifluoroethylene
CVD	Chemical vapor deposition
D-A	Donor–acceptor
DADMAC	N,N'-Diallyl-N,N'-dimethylammoniumchloride
DAMAB	4-(N,N'-Diallyl-N-methylammonio)-butanoate
DBF	Dibenzofuran
DBT	Dibenzothiophene
DCX	Dichloroxylene
DDT	1-Dodecanethiol
DEGMMA	Di(ethylene glycol) methyl ether methacrylate
DFT	Density function theory
DHBC	Double hydrophilic block copolymers
DLS	Dynamic light scattering measurements
DMAc	N,N'-Dimethylacetamide
DMAEMA	N,N'-Dimethylaminoethyl methacrylate
DMF	N,N'-Dimethylformamide
DMFC	Direct methanol fuel cell
DMO	Degree of molecular orientation
DMSO	Dimethyl sulfoxide
DNQ	2-Diazo-1,2-napthoquinone
DOAC	N,N'-Dimethyloctadeyl allyl ammonium chloride
DOP	Dioctyl phthalate
DOX	Doxorubicin
DSDMA	Disulphide dimethacrylate
DSSC	Dye-sensitized solar cell
DTPA	N,N,N',N'-Tetraphenylbiphenyl-4,4′-diamine
DTT	Dithiothreitol
EBL	Electron-beam lithography
EC	Ethylene carbonate
EDLC	Electrical double layer capacitance

EES	Electrochemical energy systems
EIS	Electrochemical impedance spectroscopy
EP	Electropolymerization
EQE	External quantum efficiency
ESC	Excitonic solar cell
ESR	Equivalent series resistance
EV	Electric vehicle
FFES	Far-field electrospinning
FTO	F-doped tin oxide
GCE	Glassy carbon electrode
GIXD	Grazing incidence X-ray diffraction
GO	Graphene oxide
GPC	Gel permeation chromatography
GPE	Gel polymer electrolyte
GPTMS	3-Glycidoxypropyl trimethoxysilane
GTP	Group transfer polymerization
HATN	Hexaazatrinapthylene
h-BN	Hexagonal boron nitride
HCF	Hexacyanoferrate
HCP	Hyper-crosslinked polymer
HEMA	2-Hydroxyethyl methacrylate
HER	Hydrogen evolution reaction
HHTP	2,3,6,7,10,11-Hexahydroxytriphenylene
HIPE	High internal phase emulsion
HLB	Hydrophilic lyophilic balance
HMOC	Hollow microporous organic capsule
HOMO	Highest occupied molecular orbital
HPB	Hexaphenylbenzene
IPCE	Incident photon-to-current conversion efficiency
Irgacure 2959	2-Hydroxy-1-[4-(hydroxyethoxy)phenyl]-2-methyl-1-propanone
ITO	Indium tin oxide
LCD	Liquid crystal display
LCP	Liquid crystalline polymer
LIB	Lithium ion battery
LSG	Laser-scribed graphene
LUMO	Lowest unoccupied molecular orbital
MAO	Methylaluminoxane
MCDE	Monochlorodimethyl ether
MD	Molecular dynamics
MDR	Multidrug resistance
MEA	Membrane electrode assemble

MEG	Multiple exciton generation
MFC	Microbial fuel cell
MFM	Magnetic force microscope
MMA	Methyl methacrylate
MMT	Montmorillonite
MOF	Metal organic framework
MON	Microporous organic network
MOP	Microporous organic polymer
MPGMA	Macroporous (glycidylmethacrylate)
MPTMS	3-Mercaptopropyl-trimethoxysilane
MWCNT	Multiwalled carbon nanotube
NBE	*o*-Nitrobenzyl ester
NCP	Nanostructured conducting polymer
NDT	Naphthodithiophene
NFES	Near-field electrospinning
NIL	Nanoimprint lithography
NIR	Near infrared
NMP	*N*-Methyl-2-pyrrolidinone
NP	Nanoparticle
NSL	Nanosphere lithography
NW	Nanowire
O/IL	Oil-in-ionic liquid
O/O	Oil-in-oil
O/W	Oil-in-water
OD	Octyldodecyl
OEG	Oligo ethyleneglycol
OFET	Organic field-effect transistor
OHP	Outer Helmoholtz plane
OLED	Organic light-emitting diode
OPV	Organic photovoltaic
ORR	Oxygen reduction reaction
P(NIPAAm-*co*-NHMAAm)	Poly(*N*-isopropylacrylamide-*co*-*N*-hydroxymethylacrylamide)
P(NVP-*co*-PBA)	Poly(*N*-vinyl-2-pyrrolidone)-*co*-poly(phenylboronic acid)
P(*o*-NBMA-*co*-MMA-*co*-EGMA)	Poly(*o*-nitrobenzyl methacrylate-*co*-methyl methacrylate-*co*-(ethylene glycol) methacrylate)
P(VDF-CTFE)	Poly(vinyl idene fluoride-chlorotrifluoroethylene)
P(VDF-HFP)	Poly(vinyl idene fluoride-hexafluoropropylene)
P(VDF-TrFE)	Poly(vinyl idene fluoride-trifluoroethylene)
P3HT	Poly(3-hexylthiophene)
P4VP	Poly(4-vinyl pyridine)
PA	Polyacetylene
PAA	Poly(acrylic acid)

PAA-*b*-PS	Poly(acrylic acid)-*b*-polystyrene precursor copolymers
PAA-*co*-PDMAEMA	Poly(acrylic acid)-*co*-poly((*N*,*N*-dimethylamino) ethylmethacrylate)
PAA-*co*-PVP	Poly(acrylic acid)-*co*-poly(vinylpyridine)
PAF	Porous aromatic framework
PAM	Poly(acrylamide)
PAMT	Poly(2-amino-5-mercapto-1,3,4-thiadiazole)
PAN	Poly(acrylonitrile)
PANI	Polyaniline
PBA	Phenylboronic acid
PBI	Polybenzimidazole
PBS	Phosphate-buffered saline
PBTTT	Poly(2,5-bis(3-alkylthiophen-2-yl)thieno[3,2-b] thiophene)
PC	Photonic crystals
PCBMAA-1T	Poly(2-((2-hydroxyethyl)(2-methacrylamidoethyl) ammonio)acetate)
PCE	Power conversion efficiency
PDA	Polydopamine
PDBA	Pyrene-2,7-diboronic acid
PDEA	Poly(2-(diethyl amino)ethyl methacrylate)
PDEAEMA	Poly(*N*,*N*-dimethyl amino ethyl methacrylate)
PDMA-*b*-PAPBA	Poly(*N*,*N*-dimethyl acrylamide)-*b*-poly (3-acrylamidophenylboronic acid)
PDMAEMA-*b*-PMA	Poly(2-(dimethyl amino)ethyl methacrylate)-*b*-(methacrylic acid))
PDMAEMA-*b*-PMMA-*b*-PMA	Poly(2-(dimethyl amino)ethyl methacrylate)-*b*-(methyl methacrylate)-*b*-(methacrylic acid))
PDMAEMA-*b*-PTHPMA	Poly(2-(dimethyl amino)ethyl methacrylate-*b*-2-tetrahydropyranyl methacrylate)
PDMAEMA-*co*-PAzM	Poly(2-(dimethyl amino) ethyl methacrylate-*co*-poly (azo-methacrylate)
PDMNBA-*b*-PS	Poly(4,5-dimethoxy-2-nitrobenzyl acrylate)-*b*-polystyrene
PDMS	Poly(dimethyl siloxane)
PDPA	Poly(2-(diisopropylamino)ethyl methacrylate)
PDPB	Poly(diphenyl butadiene)
PEDOT	Poly(3,4-ethylenedioxy-thiophene)
PEDOT:PSS	Poly(3,4-ethylenedioxy thiophene:poly(styrene sulfonate)
PEEK	Poly(ether ether ketone)
PEEP	Poly(ethyl ethylene phosphate)
PEG	Poly(ethylene glycol)

PEG-*b*-(PAA-*co*-PAAPBA)	Poly(ethyleneglycol)-*b*-poly(acrylic acid-*co*-acryla-midophenylboronic acid)
PEG-*b*-PnBMA-*b*-PDMAEMA	Poly(ethylene glycol)-*b*-poly(n-butylmethacrylate)-*b*-poly(*N*,*N*′-dimethylamino ethyl methacrylate)
PEG-*b*-PPBDEMA	Poly(ethylene glycol)-*b*-poly [(2-phenylboronicester-1,3-dioxane-5-ethyl) methylacrylate]
PEGDME	Poly(ethylene glycol) dimethyl ether
PEI	Poly(ethylene imine)
PEM	Polymer electrolyte membrane
PEMFC	Polymer electrolyte membrane fuel cell
PEO	Poly(ethylene oxide)
PEO-*b*-P(BMA-*co*-CMA)	Poly(ethylene oxide)-*b*-poly(*n*-butyl methacrylate-*co*-4-methyl-[7-(methacryloyl)-oxyethyloxy] coumarin)
PEO-*b*-P(ETEGA-*co*-NBA)	Poly(ethylene oxide)-*b*-poly(ethoxytri(ethylene glycol) acrylate-*co*-*o*-nitrobenzyl acrylate)
PEO-*b*-PAA	Poly(ethylene oxide)-*b*-poly(acrylic acid)
PEO-*b*-PAD	Poly(ethylene oxide)-*b*-poly((*N*-amidino)dodecyl acrylamide)
PEO-*b*-PDEACMM	Poly(ethylene oxide)-*b*-poly([7-(diethylamino) coumarin-4-yl] methyl methacrylate)
PEO-*b*-PMAA	Poly(ethylene oxide)-*b*-poly(methacrylic acid)
PES	Poly(ether sulfone)
PEtO-*b*-PNBA	Poly(2-ethyl-2-oxazoline)-*b*-poly(2-nitrobenzyl acrylate)
PFDTS	Perfluorodecyltriethoxysilane
PFPE	Perfluoropolyether
PFS	Polyferrocenylsilanes
PI	Polyimide
PLAM	Poly(ε-ʟ-lysinyl acrylamide)
Pluronic F68	Poly(ethylene glycol)-*b*-poly(propylene glycol)-*b*-poly(ethylene glycol)
PMMA	Poly(methyl methacrylate)
PNBMA	Poly(2-nitrobenzylmethyl methacrylate)
PNIPAm	Poly(*N*-isopropylacrylamide)
PNIPAM-*b*-PAzoM	Poly(*N*-isopropylacrylamide)-*b*-poly{6-[4-(4-methylphenyl-Azo) phenoxy] hexylacrylate}
POSS	Polyhedral oligomeric silsesquioxane
PP	Polypropylene
PPFPA	Poly(pentafluorophenyl acrylate)
PPP	Polyparaphenylene)
PPy	Polypyrrole
PPyMA	Poly(1-pyrenylmethyl methacrylate)
PQT-12	Poly(3,3′-didodecylquaterthiophene)

PS	Polystyrene
PSA	Poly(L-serinyl acrylate)
PS-*b*-P4VP	Polystyrene-*b*-polyvinylpyridine
PS-*b*-PEO	Polystyrene-*b*-poly(ethylene oxide)
PS-*b*-PSVBC	Polystyrene-*b*-poly(styrene-*co*-vinylbenzylchloride)
PS-*b*-QP2VP	Polystyrene-*b*-quaternized poly(2-vinyl pyridine)
PSC	Perovskites solar cell
PSC	Polymer solar cell
PSPMA-*b*-PDEGMMA	Poly(spiropyranmethacrylate)-*b*-poly((diethylene glycol) methyl ether methacrylate)
PSS	Poly(styrene sulfonate)
PtBA	Poly(tertbutyl acrylate)
PTh	Polythiophene
PTIIG-Np	Poly(thienoisoindigo-*alt*-naphthalene)
PTMSP	Poly(1-(trimethylsilyl)-1-propyne)
PU	Polyurethane
PVA	Poly(vinyl alcohol)
PVAc	Poly(vinyl acetate)
PVB	Poly(vinyl butyral)
PVC	Polyvinyl chloride
PVDF	Poly(vinyl idene fluoride)
PVFc-*b*-PMMA	Poly(vinyl ferrocene)-*b*-poly(methyl methacrylate)
PVK	Poly(*N*-vinyl carbazole)
PWA	Phosphotungstic acid
PXRD	Powder X-ray diffraction
PZS	Poly(cyclotriphosphazene-4,4′-sulfonyldiphenol)
PZT	Zirconium titanate
QD	Quantum dot
QDSC	Quantum dot-sensitized solar cell
RAFT	Reversible addition-fragmentation chain transfer polymerization
RGO	Reduced graphene oxide
RIE	Reactive ion etching
ROMP	Ring-opening metathesis polymerization
ROP	Ring-opening polymerization
RPAE	Reducible poly(β-amino ester)s
SEM	Scanning electron microscopy
SERS	Surface-enhanced Raman scattering
SKPM	Scanning kelvin probe force microscopy
SPAEK	Sulfonated poly(arylene ether ketone)
SPE	Solid polymer electrolyte
STM	Scanning tunneling microscopy
SWCNT	Single-walled carbon nanotube
TBAC	Tetrabutylammonium chloride
TBPM	Tetra(4-dihydroxyborylphenyl)methane

TBPS	Tetra(4-dihydroxyborylphenyl)silane
TEM	Transmission electron microscopy
TEOS	Tetraethylorthosilicate
TfOH	Trifluoromethanesulfonic acid
TFSI	Trifluoromethyl sulfonyl imide
TGA	Thermogravimetric analysis
TGTG	Trans-gauche-trans-gauche
TMICl	1-Methyl-3-[(triethoxysilyl)propyl]imidazolium chloride
TNT	2,4,6-Trinitrotoluene
TP	1,3,5-Triformylphloroglucinol
TPD	1,1,2,2-Tetraphenylethane-1,2-diol
TPE	Tetraphenylethylene
TrFE	Trifluoroethylene
TzTz	Thiazolothiazole
UV	Ultraviolet
VB	Valance band
VC	Vinylene carbonate
VDF	Vinylidene fluoride
VPP	Vapor phase polymerization
VSM	Vibrating sample magnetometer
W/CO_2	Water-in-CO_2
W/O	Water-in-oil
ZnO	Zinc oxide
ZrO_2	Zirconium oxide

Part I
Engineering Nanostructures with Polymers

Chapter 1
Engineering Ceramic Fiber Nanostructures Through Polymer-Mediated Electrospinning

Avinash Baji and Yiu-Wing Mai

Abstract Electrospinning is increasingly used as a simple and straightforward technique to fabricate one-dimensional fibers from both organic and inorganic materials. These one-dimensional fibers with controlled sizes possess some unique features such as large surface area to volume ratio, high porosity, and low density. Compared to other conventional materials, these features make them attractive for applications such as energy harvesting, energy storage, super-hydrophobic membranes, and sensors. This chapter provides an overview on the synthesis of inorganic fibers through polymer-mediated electrospinning. Some of the common techniques employed by many researchers, such as solgel combined with electrospinning, emulsion electrospinning, and electrospinning combined with solid–gas reaction, to fabricate metal oxide fibers are discussed. In addition, techniques to fabricate ceramic and metal oxide fibers having different morphologies and hierarchical structures are described. Recent applications of electrospun metal oxide fibers are finally highlighted with a focus on filtration, sensors, photocatalysis, and energy.

1.1 Introduction

The interest in nanostructured materials has grown tremendously in the last few years mainly due to the development in techniques that enable us to fabricate structures with controlled geometry and dimensions [1–7]. These nanostructures with controlled size and geometry display some unique characteristics and functions

A. Baji (✉)
Engineering Product Development (EPD) Pillar, Singapore University
of Technology and Design (SUTD), Singapore 487372, Singapore
e-mail: avinash_baji@sutd.edu.sg

Y.-W. Mai (✉)
Centre for Advanced Materials Technology (CAMT), School of Aerospace,
Mechanical and Mechatronic Engineering, The University of Sydney,
Sydney, NSW 2006, Australia
e-mail: yiu-wing.mai@sydney.edu.au

that are important for the design and development of advanced devices and systems [4, 5, 7]. In particular, the one-dimensional structures such as fibers and wires due to their large aspect ratio and surface area have attracted great attentions of researchers and are being considered as building blocks for nanoscale electronics and electrochemical devices [8–10]. The geometry and size of these nanostructured fibers ensure that the fibers display enhanced electrical conductivity and thermal transport characteristics. The nanostructured fibers also show good interaction with surrounding matrix and therefore are used to enhance its mechanical stiffness and strength [6, 10–12].

Among all the fabrication techniques used to produce one-dimensional fibers and wires, electrospinning is regarded as a simple and efficient technique to produce continuous fibers with controlled dimensions from a range of organic and inorganic materials [13–15]. Also, electrospinning can be used to obtain fibers with various structures and morphologies [16–18]. For example, modifying the conventional electrospinning setup and using a coaxial spinneret can yield core–shell or hollow fibers [19, 20]. Similarly, modifying the collector used in conventional electro-spinning can lead to the collection of yarns or aligned fibers [15, 21]. Fibers with unique surface structures can also be obtained by decorating the surface of the fibers with nanoparticles or by introducing substructures on the surface of the fibers [22, 23]. Introduction of such nanoscale features on the surface of the fibers can greatly impact the surface properties of the fibers, which can expand their applications. In particular, inorganic metal oxide fibers obtained using electrospinning of precursor metal oxide salts followed by thermal annealing display some unique morphology on the fiber surfaces [13, 24]. Such fibers with high surface area and interconnected porosity are technologically important materials for various functional applications. For example, it is reported that the charge transport in metal oxide fibers can be a few orders of magnitude higher than that in their counterparts which are based on nanoparticles [8, 11]. Similarly, metal oxide fibers have been actively investigated for novel electrode materials for electrochemical storage devices [12, 25]. Thus, metal oxide fibers have found applications in nanoelectronics, sensors, fuel cells, solar cells, catalysis, hydrogen storage batteries, etc. [26–31].

Since the first report published in 2002–2003 on fabrication of metal oxide fibers using electrospinning combined with solgel technique [32, 33], many researchers have adopted this polymer-mediated electrospinning technique to produce a variety of ceramic and metal oxide fibers [13, 20, 24, 34, 35]. They have gone even further to fabricate hybrid and hierarchical ceramic and metal oxide fibers [18, 36], hollow and core–shell ceramic fibers [7, 37], porous ceramic fibers, and carbon nanotube-filled ceramic fibers [38]. Recently, some researchers have also fabricated hierarchical fibers by growing substructures on the surface of inorganic fibers. For example, electrospinning and hydrothermal treatment have been applied to grow ZnO nanostructures on the surface of Co_3O_4 fibers [39]. In a similar way, Ostermann et al. [36] fabricated nanorod-on-fiber structures by growing V_2O_5 nanorods on the surface of TiO_2 fibers.

We acknowledge that there are many articles in the literature on electrospinning which have extensively reviewed the electrospinning mechanisms and applications of electrospun fibers in the areas of tissue engineering and biomedical engineering. We will not duplicate the existing work here. Hence, in this chapter, we will review some of common electrospinning setups and techniques used to fabricate ceramic and metal oxide fibers. We will show how the fiber size and morphology can be controlled because they are important factors in engineering these complex structures for use in different advanced and novel applications. We will also present the use of electrospinning to fabricate hybrid and hierarchical fibers based on ceramics. Some recent applications of these inorganic fibers are given.

1.2   Electrospinning: Fabrication of Inorganic Fibers

Ceramic or metal oxide fibers have captured wide interest as promising candidates for electrodes in lithium-ion batteries due to their high-energy densities [1, 7, 10, 29]. Although there are various methods such as electrodeposition, lithography, and electron beam to produce such one-dimensional ceramic fibers [8, 40–42], most of them are cumbersome and expensive. By contrast, polymer-mediated electrospinning offers an attractive alternative route to produce one-dimensional (1D) ceramic fibers in large quantities. Below, we present some common electrospinning techniques used to produce 1D ceramic and metal oxide fibers.

1.2.1   Solgel Method

Electrospinning combined with solgel approach is often used to obtain inorganic fibers [13, 32, 34, 43]. This method is particularly efficient and useful as the metal oxides produced using this method are typically pure and the method enables us to obtain the ceramic or metal oxide from molecular precursors [29]. The process can be controlled, and hence, 'tailor-made' materials can be obtained using this method. Typically, two different processing techniques are used in the preparation of the sol solution. The first approach is based on hydroxylation and condensation of molecular precursors [44]. Here, the metal precursor salts are hydrolyzed in alcohol or water. Following this, the hydrolyzed precursor salts are condensed in organic acid. This leads to the formation of metal-oxo or metal-hydroxo polymeric gels that are spinnable.

The second approach is a common technique that is used to fabricate ceramic or metal oxide fibers. Typically, to obtain such inorganic fibers, metal salt precursors are dispersed homogeneously in a solvent [34, 42, 44]. Then, a suitable polymer is dissolved in this solvent to prepare the solution for electrospinning. Electrospinning this solution with metal salts and polymer leads to polymer fibers with well-dispersed metal oxide precursor, which can be thermally annealed to reduce

the precursor to ceramic or metal oxide. Finally, the polymer is removed to obtain neat metal oxide or ceramic fibers. To obtain continuous and uniform ceramic fibers, it is essential that the weight ratio of the precursor to polymer in electrospinning be between 50 and 80%. As an example, this approach is used to fabricate bismuth ferrite fibers [34]. Here, $Bi(NO_3)_{3.5}H_2O$ and $Fe(NO_3)_{3.9}H_2O$ are chosen as the precursor salts which are dispersed in a solution mixture of 2-methoxyethanol and glacial acetic acid. Polyvinylpyrrolidone (PVP) is dissolved in a dimethylformamide/ethanol solution mixture. Finally, the precursor solution mixture and the PVP solution are blended and electrospun to obtain homogenous precursor fibers. Thermal annealing of these fibers produces neat $BiFeO_3$ fibers. We have also used this method to fabricate barium titanate ($BaTiO_3$) fibers [27]. A solgel solution is first prepared by adding known quantities of barium acetate, titanium isopropoxide, and acetic acid. This solution is then added into a PVP–ethanol solution and electrospun to obtain the precursor fibers. Figure 1.1a shows the scanning electron microscopy (SEM) image of precursor fibers. The fibers are thermally annealed to obtain $BaTiO_3$ fibers. Figure 1.1b, c shows the SEM and
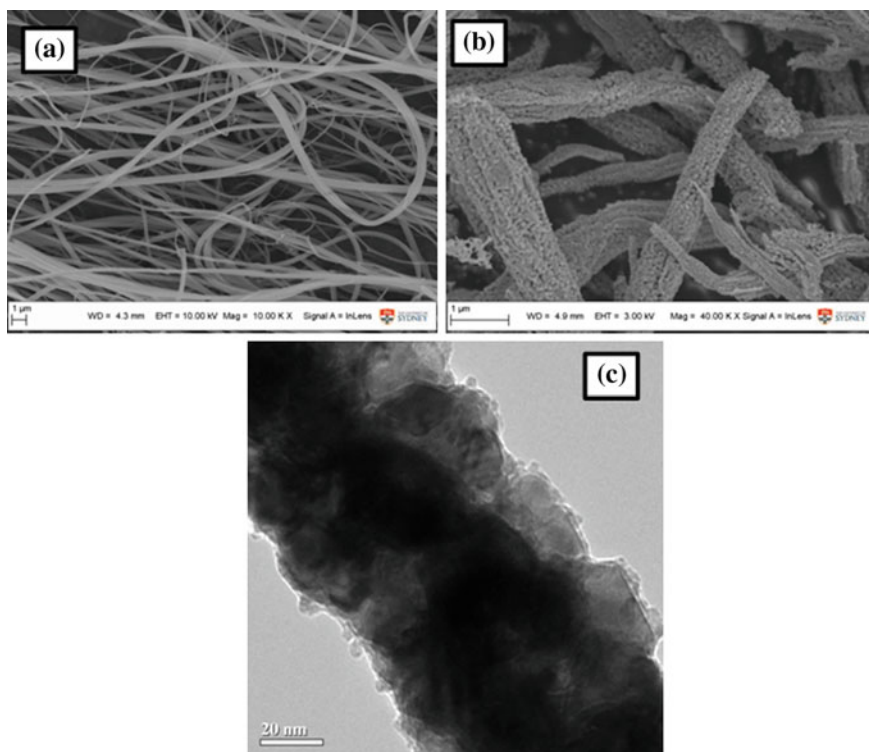
Fig. 1.1 **a** SEM image of PVP fibers with $BaTiO_3$ precursors, **b** SEM image of $BaTiO_3$ fibers obtained after thermal annealing, and **c** TEM image of $BaTiO_3$ fibers (reproduced from Ref. [27] with kind permission of © 2011 Elsevier)

transmission electron microscopy (TEM) images of the obtained fibers. It is evident from Fig. 1.1b, c that $BaTiO_3$ fibers are made of many fine-grained structures [27].

The size of the fibers can be determined by controlling the electrospinning processing variables, the annealing temperature and annealing time [15]. During annealing, the organic polymer phase is selectively burnt off while the inorganic phase is evolved to a polycrystalline phase. For example, TiO_2 precursor with polyvinyl pyrrolidone (PVP) polymer is electrospun and thermally annealed to obtain TiO_2 fibers. It is shown that during annealing, the polymer is removed and the size of the fibers is reduced [38, 45, 46]. Polycrystalline TiO_2 fibers are obtained after the thermal annealing stage, and the crystalline phase formation is determined by the annealing temperature used. TiO_2 fibers with anatase phase are obtained when the annealing temperature is 510 °C. This anatase phase is converted to a rutile phase if 800 °C for 3 h is used for annealing [47]. Similar observations are noted for WO_3 fibers [48, 49]. Either tetragonal or orthorhombic phases are obtained that depend on the temperature used for annealing.

1.2.2 Dispersion of Metal Oxide Particles

Electrospinning combined with solgel has been used to fabricate a wide range of ceramic and metal oxide fibers. However, when this technique is used, the fiber diameter varies with the hydrolyzing time [50]. Furthermore, the solution can be electrospun only during, but not before or after, the solgel reaction. A more direct and straightforward technique to produce inorganic fibers relies on dispersing the nanoparticles of the metal or metal oxides of known concentration directly into a polymer solution [51–53] which can be electrospun to obtain polymer fibers filled with nanoparticles. Then, the fibers are thermally treated to sinter the nanoparticles. During thermal treatment, the polymer matrix is burnt off leaving behind neat sintered particles in the form of fibers.

Ding et al. [53] used this technique to fabricate porous silica fibrous structures and showed that the porosity could be controlled by adjusting the concentration of silica added into the electrospinning solution. By using this approach, the variability that is associated with solgel hydrolyzing time can be avoided. However, with this technique, it is crucial to disperse the nanoparticles uniformly in the polymer solution such that polymer fibers with uniformly filled particles can be obtained. Studies also report that the size of nanoparticles used influences their aggregation in the polymer fibers [54]. For homogenous particle dispersion, it is important that the particles and the polymer share a common solvent [52]. For example, silica nanoparticles can be dispersed homogeneously in water-soluble polymers [52]. However, the fibers obtained using water-soluble polymers are often cross-linked to expand their applications that involve the use of water. Newsome et al. [52] dispersed silica nanoparticles in water-soluble PVP and cross-linked the polymer by heating the fibers at 200 °C. The polymer was later burnt off to sinter the nanoparticles and obtain fibers composed of pure silica nanoparticles.

1.2.3 Gas–Solid Reaction

The method of dispersing metal oxide particles in the electrospinning solution to obtain metal oxide fibers is a convenient and straightforward method. However, the particles tend to aggregate and cannot be homogeneously dispersed in the electrospinning solution, making it difficult to obtain uniform fibrous structures after the sintering process. Similar to the method of dispersing nanoparticles in the polymer solution, inorganic fibers fabricated using gas–solid reaction method are obtained by first dissolving the doped precursor particles of metal or metal oxide into the electrospinning polymer solution [42]. Then, gas–solid reaction treatment is applied to the fibers to synthesize metal or metal oxide particles within the polymer fibrous matrix. The polymer matrix can then be removed to obtain neat metal or metal oxide particles as fibers. Lu et al. [55] dispersed lead acetate in PVP polymer solution and electrospun to obtain PVP/lead acetate fibers. These fibers are then exposed to H_2S gas to convert lead acetate to PbS. Thus, after gas treatment, PbS nanoparticles dispersed in PVP are obtained. In a similar study [56], a solution consisting of polyacrylonitrile (PAN) and silver nitrate ($AgNO_3$) is prepared and electrospun to obtain $AgNO_3$–PAN fibers and exposed to HCl gas. The exposure to HCl synthesized AgCl particles and led to the collection of PAN fibers filled with AgCl particles with uniform size. It is further shown that the size and density of the particles with in the PAN fibers can be controlled by adjusting the $AgNO_3$ concentration within the electrospinning solution. Other researchers have used this gas–solid reaction method to obtain neat metallic or metal oxide fibers. Hence, Bognitzki et al. [57] dispersed copper nitrate in a poly(vinyl butyral) (PVB) solution that was electrospun to obtain copper nitrate–PVB fibers. These fibers are then thermally treated to remove the polymer and subsequently annealed in hydrogen atmosphere at 300 °C to obtain neat copper fibers.

1.2.4 Emulsion Electrospinning

Recently, emulsion electrospinning has been increasingly used to fabricate inorganic fibers [23, 42, 58]. This technique is similar to conventional electrospinning; however, a water-in-oil emulsion is used instead of a solution. Electrospinning this emulsion results in the separation of the phases within the fibers. Hence, this technique is useful to obtain highly porous fibers or hollow tubes. It eliminates the need of a complex coaxial spinneret to obtain core–shell fibers. With this technique, two different polymer solutions are first prepared and mixed to form an emulsion, followed by electrospinning to obtain fibers with two separated polymer phases. Lu et al. [23] used emulsion electrospinning to prepare highly porous TiO_2 nanotubes that are decorated with WO_3 nanoparticles on the internal and external sidewalls of the nanotubes. In their study, a solution consisting of titanium acetate and PVP solution is prepared. To this viscous gel, known quantity of viscous oil is added to

prepare the emulsion. This emulsion is then electrospun into fibers that are thermally treated to obtain porous TiO_2 nanotubes. Typically, in this process, oil along with the solvent evaporates from the surface of the fibers once the jet is ejected from the electrospinning nozzle. This produces a region near the surface of the fibers that is rich in PVP and precursor salts. The residual oil gathers at the inner regions of the fiber to obtain core–shell fibers. When the fibers are thermally annealed, the oil present in the core region of the fibers is removed and hollow nanotubes are obtained. Following this step, Lu et al. [23] used a thermal evaporation method to deposit tungsten carbide nanoparticles on the inside as well as outside walls of the hollow fibers. The fibers are then thermally treated in air to convert tungsten carbide particles to WO_3 particles. This has led to the synthesis of TiO_2 nanotubes decorated with WO_3 nanoparticles. A similar fabrication technique is used in another study [58] to obtain porous TiO_2 fibers.

1.3 Ceramic and Metal Oxide Fibers with Controlled Structures

The use of electrospinning to fabricate ceramic or metal oxide fibers has many advantages as the morphology and the structure of the fibers can be easily controlled. Some of the techniques that are used to control the morphology as well as the structure of the fibers are discussed in this section.

1.3.1 Unique Fiber Structures

The fiber morphology can be controlled by adjusting the electrospinning processing variables or the temperature and/or time during the annealing stage [59]. For example, ultra-thin zinc oxide fibers can be fabricated using a combined solgel and electrospinning technique. Zinc acetate, a precursor for zinc oxide, is added to the polyvinyl alcohol (PVA) solution and electrospun to fibers that are thermally annealed to obtain zinc oxide fibers. SEM and TEM images are used to show that zinc oxide particles are self-assembled and arranged to yield zinc oxide fibers [59, 60]. Similar results are observed when fabricating $BaTiO_3$ fibers whose SEM image in Fig. 1.2 shows that the fibers comprise $BaTiO_3$ particles. These particles are self-arranged and organized to obtain fibrous structures.

Research demonstrates that the size of the fiber can be controlled by adjusting the PVA concentration within the electrospinning solution and the morphology of the fiber can be varied by adjusting the thermal annealing temperature and/or annealing time. Apart from tailoring the electrospinning variables, the morphologies of ceramic fibers which are obtained using the solgel route are also influenced by the heating rate, cooling rate, and the atmosphere in which the sample is
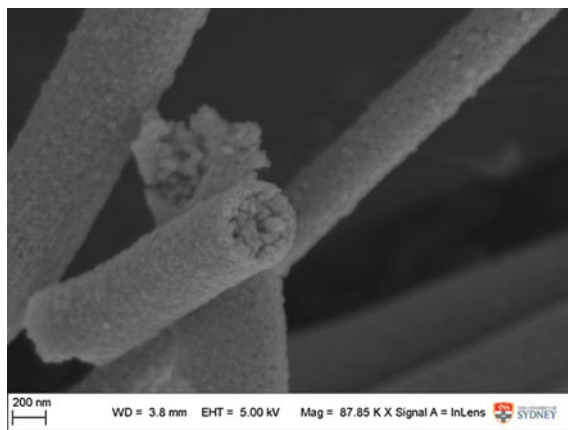
Fig. 1.2 SEM image of BaTiO$_3$ fibers demonstrating self-assembly and organization of BaTiO$_3$ particles (reproduced from Ref. [59] with kind permission of © 2013 Elsevier)

annealed. Fibers consisting of multi-grain structures can be developed by controlling the annealing temperature. It is reported that the size of the particles increases with annealing temperature. Hence, the use of high temperature causes crystallization and allows the grains to coalesce. For example, Xia et al. [61] investigated the effect of thermal annealing temperature on the morphology of SrTiO$_3$ fibers. Their results demonstrate that when the precursor fibers are thermally annealed at 800 °C, the morphology of the fibers is smooth and homogeneous. However, when the thermal annealing temperature is increased to 900 or 1000 °C, coarse fibers are obtained due to the irregular growth of the particles within the fibers. Figure 1.3 shows a BaTiO$_3$ coarse fiber obtained by controlling the annealing temperature. When 750 °C is used for annealing, the fibers have a continuous surface structure
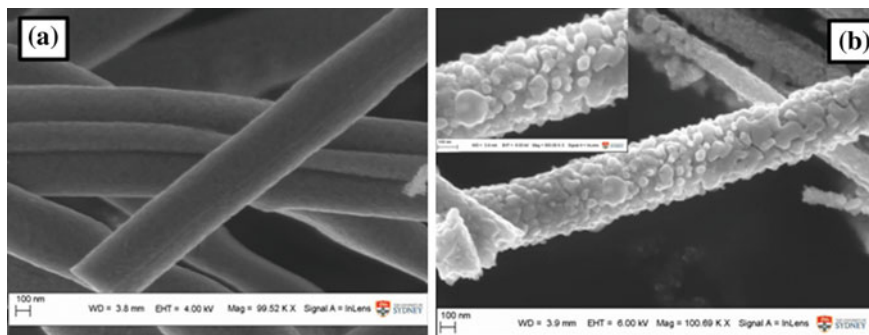
Fig. 1.3 SEM images of BaTiO$_3$ fibers obtained by thermally annealing the precursor fibers at **a** 750 °C and **b** 1000 °C. The *inset* shows the magnified image of the fiber (reproduced from Ref. [61] with kind permission of © 2015 Elsevier)

(see Fig. 1.3a). However, coarse fibers are obtained when the annealing temperature is increased.

In an another study, Anjusree et al. [45] showed that when PVP was used as the polymer along with a TiO$_2$ precursor, the fibers obtained were continuous and uniform. However, when polyvinyl acetate (PVAc) was used in the electrospinning solution instead of PVP, rice-shaped fibers were obtained. They also showed that leaf-like TiO$_2$ fibers could be obtained when both PVAc and PVP were used as the polymer in the electrospinning solution. They argued that the chemical nature of the polymer used in the electrospinning solution and the interactions between the polymer and the inorganic precursor defined the morphology of the ceramic fibers. For example, the hydrolysis of precursor metal oxide occurs when it is dissolved in polar PVP in a solvent. The hydroxyl groups of the precursor metal salts interact with PVP via hydrogen bonding. This suggests that the precursor metal oxide is attached to PVP, and hence, it assumes the shape of the fibers. Therefore, after thermal annealing treatment, the metal oxide retains the uniform and continuous shape. Rice-shaped fibers (Fig. 1.4) are obtained when PVP is replaced by PVAc. These unique shaped structures are caused by the reduced chemical interaction of the metal oxide precursor with PVAc. Microscale phase separation happens when the fibers are annealed. One phase is rich in metal oxide domains while the other phase is predominantly PVAc domains. The coexistence of these two phases within the fiber prolongs these domains during annealing, leading to the formation of rice-like structures of the metal oxide. Lastly, leaf-shaped structures can be obtained when a mixture of PVP and PVAc is used to electrospin TiO$_2$ fibers. The metal oxide precursor interacts with both PVP and PVAc at the same time. Thus, when these fibers are thermally annealed, the anisotropy in TiO$_2$ morphology leads to the formation of the leaf-like structures. Similar results are reported by Jo et al. [24] in their study which investigated the effect of polymer type used in the solgel solution that was used to prepare the inorganic fibers. The miscibility of the polymer with the precursor solgel and its interaction with the precursor metal oxide define the morphology of the fibers.

Rice-shaped TiO$_2$

1μm
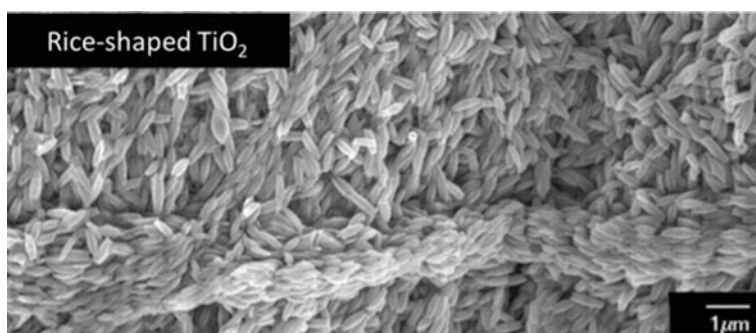
Fig. 1.4 SEM image of rice-shaped TiO$_2$ fibers obtained via electrospinning technique (reproduced from Ref. [45] with kind permission of © 2013 Royal Society of Chemistry)

1.3.2 Porous Fibrous Structures

It is desirable to fabricate inorganic porous fibers with high specific surface area for functional applications as the functionality of these fibers can be optimized. For example, these porous fibrous structures show tremendous potential as electroactive materials for energy harvesting applications [29, 31]. These structures are capable of demonstrating considerable improvement in power and energy density when compared to electrodes that are made using bulk materials [29, 31]. The one-dimensional structure of the fiber enables efficient transport of electrons along the fiber axis direction. The large surface area afforded by these porous fibers also promotes quick lithium-ion transfer. Thus, the charge transport can be orders of magnitude higher than the bulk counterparts.

Porous inorganic fibers can be easily obtained using electrospinning by controlling the concentrations of the polymer and the inorganic precursor in the electrospinning solution. Pores are formed when the metal salts and the polymer in the fibers are decomposed during thermal annealing [20, 60]. Kumar et al. [16] showed that porous fibers could be obtained by controlling the annealing temperature used to obtain the inorganic fibers and that the pores were formed when the polymer phase was removed from the fibers during the annealing process. Figure 1.5 shows an example of porous fibers obtained in the laboratory by controlling the concentration of polymer in the electrospinning solution.

Recently, emulsion electrospinning is an efficient tool to fabricate highly porous ceramic or metal oxide fibers [46, 58]. It can be used to produce fibers with high surface area to volume ratio compared to fibers prepared using the conventional electrospinning approach. In this approach, the emulsion solution used to prepare the fibers is the key factor that controls the fiber porosity. Lu et al. [58] used this method to prepare highly porous TiO_2 fibers. First, PVP–titanium acetate solution is prepared that forms a viscous gel. Then, a homogeneous and stable gel is prepared by adding a known quantity of mineral oil to the PVP–titanium acetate gel solution

Fig. 1.5 SEM image of porous $BaTiO_3$ fibers obtained by controlling the concentration of polymer in the electrospinning solution (reproduced from Ref. [16] with kind permission of © 2011 Royal Society of Chemistry)
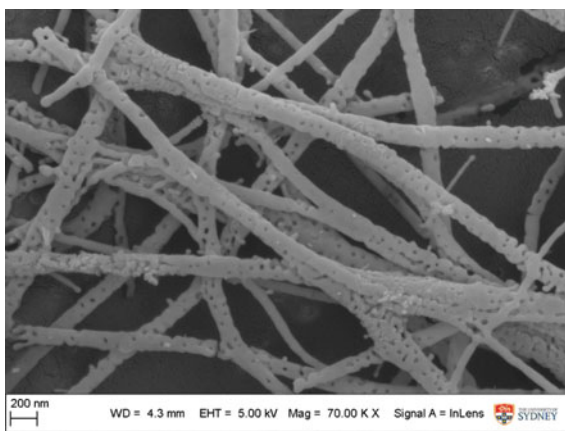
which can be used for electrospinning. When the fibers are ejected from the nozzle, the oil present on the fiber surface and the solvent evaporates. The evaporation of the solvent from the fiber surface ensures that the surface comprises PVP and precursor of the metal oxide. This leads to the formation of core–shell fibers with oil present in the core region of the fiber, while the outer shell consists of PVP and metal oxide precursor. When the oil from the inner core is evaporated, PVP hollow tubes and metal oxides are deposited on the collector. Finally, TiO_2 nanotubes are produced when the obtained fibers are annealed. Porous nanotubes are obtained during this process because the residual oil present in the shell region of the fiber is evaporated during thermal treatment. Uniformly distributed pores with 12 nm diameter are found on the surface of the fiber. A similar approach is used by Liu et al. [62] to produce porous TiO_2 fibers. They argue that the presence of tiny droplets of mineral oil in the surface region of the fibers is responsible for the porosity. Similarly, Chen et al. [46] prepared porous TiO_2 fibers using microemulsion combined with electrospinning. PVP and metal oxide precursor are first dissolved in a solvent solution to which paraffin oil is added to prepare the microemulsion mixture. The solution is then electrospun to obtain the precursor fibers. Paraffin oil is dispersed within the fibers and serves as the pore-forming agent. Metal oxide precursors are the matrix phase. During subsequent annealing, paraffin oil is removed and pores are formed. They explained that the multi-scale porous structures are obtained because paraffin oil droplets merge during electrospinning to form different sizes of the droplets. Thus, multi-scale porous structures are obtained when the fibers are thermally annealed.

1.3.3 Hollow Fibers

Electrospinning has also been used as a processing technique to fabricate ceramic fibers with complex architectures such as hollow fibers or coaxial fibers. Such hollow or tubular ceramic fibers have found applications in a wide variety of fields including gas storage, energy harvesting, catalysis, gas and chemical sensors, dye-sensitized solar cells, and electrodes for supercapacitors [4, 11, 20, 23, 34]. These hollow metal oxide fibers have captured the interest of researchers due to their unique catalytic, electrical, sensing, and electrochemical properties. The high surface to volume ratio and unique transport properties that arise owing to the fiber geometry and confinement effects can be attributed to the properties of the hollow ceramic fibers. Two separate fabrication techniques based on electrospinning are widely employed to obtain hollow ceramic fibers.

One of the fabrication techniques relies on using sacrificial templates for obtaining hollow fibers [63–65]. Here, the fabrication of polymer fibrous membrane using electrospinning is first effected. These polymer fibers are used as templates. Precursors of the inorganic materials are then coated on the surface of these fibers. Following this step, the polymer core is selectively removed or etched away to obtain hollow ceramic or metal oxide fibers. Choi et al. [63], in their study, used

this approach to fabricate hollow fibers with several centimeters in length and submicron diameters. The wall thickness of the hollow fibers is several tens of nanometers. Briefly, electrospinning is used in the first step to obtain polyvinyl acetate (PVAc) fibers that serve as sacrificial templates. Then, precursor materials of inorganic zinc oxide (ZnO) are used to coat the fibers by physical vapor deposition. Finally, the fibers are thermally treated to decompose the PVAc core and obtain inorganic ZnO as the shell.

The second technique used to produce hollow fibers is based on coaxial electrospinning [64]. This straightforward approach uses a coaxial spinneret to produce core–shell fibers. Here, two immiscible solutions are fed independently into the core and shell capillaries of the coaxial spinneret. It is critical that the core and shell solutions are immiscible to obtain well-defined coaxial fibers. Typically, the precursor for the inorganic material is fed into the shell capillary and mineral oil into the core capillary of the coaxial setup. The fiber formation mechanism is similar to that of conventional electrospinning. When a voltage is applied, the solution ejected from the spinneret is electrically charged and the electrostatic forces stretch the jet to form the fibers. The solution emanating from the inner capillary of the spinneret is stretched due to the shear stresses developed from stretching of the shell solution. Once the fibers are formed, they are heat treated to remove the mineral oil from the core region of the fiber and obtain the inorganic shell phase. Li et al. [33] used this method to produce hollow TiO_2 fibers. Figure 1.6 shows the SEM image of the hollow fibers obtained using this technique.

The size of the fibers can be tailored by controlling the feeding rate of the core and the shell solutions. A higher feeding rate of the mineral oil results in hollow fibers with thin walls. However, only some segments of the fibers are seen to be hollow when the feeding rate of the mineral oil is low. Zhang et al. [66] used this approach to fabricate hollow TiO_2 fibers. Briefly, the precursor material consisting of titanium isopropoxide and polyvinylpyrrolidone (PVP) is dissolved in a solvent. This solution is fed to the shell capillary, while heavy mineral oil is fed to the inner

Fig. 1.6 SEM image of hollow TiO_2 fibers obtained using core–shell electrospinning (reproduced from Ref. [33] with kind permission of © 2003 American Chemical Society)
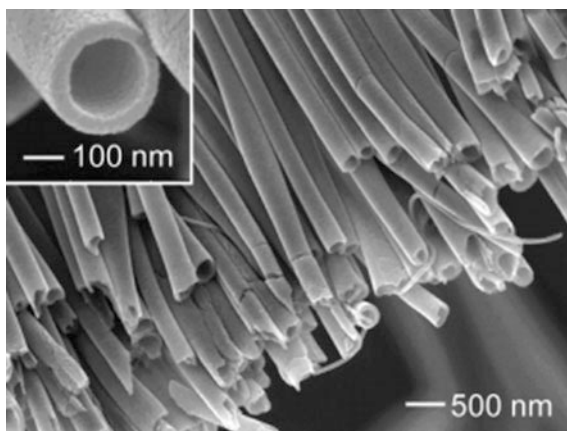
core capillary. The as-spun fibers are immersed in octane for 12 h to remove the heavy mineral oil. Following this, the fibers are thermally treated to obtain crystalline hollow TiO_2 fibers whose diameter is determined by the concentration of PVP used in the precursor solution. Researchers have also demonstrated that hollow inorganic fibers can be obtained using conventional single spinneret electrospinning. In this process, the inorganic precursor solution is mixed with two different polymer solutions. For this purpose, immiscible polymers are chosen such that they phase separate during electrospinning. Thus, Zhang et al. [67] prepared a solution consisting of polyacrylonitrile (PAN), PVP, and zinc acetate. Fibers are then formed using conventional electrospinning. Their results indicate that due to phase separation, PAN forms the core of the fiber, while PVP and zinc acetate constitute the fiber shell. Hollow zinc oxide (ZnO) fibers are obtained after thermal treatment and after the polymer phases are burnt off.

1.3.4 Controlled Assembly

Electrospinning setup can be modified to collect controlled assembly of fibers such as aligned and ordered structures. It has been shown that such aligned fibers can have tremendous potential for device applications including electrical and photonic devices. Also, anisotropic properties are displayed when the fibers are aligned. Li et al. [68] show that aligned arrays of SnO_2 fibers have anisotropic properties. Aligned SnO_2 fibers have 15 times higher electrical conductivity along the fiber axis compared to that transverse to the fiber axis. Similarly, other studies have demonstrated that the energy generation efficiency can be improved by aligning the fibers [69].

Typically, the setup for conventional electrospinning can be changed to collect aligned array of metal oxide fibers [15, 21, 70]. The electrospinning solution is prepared in a similar manner as for conventional electrospinning for obtaining aligned array of metal oxide fibers. The precursor of the inorganic material is dispersed in a polymer solution and electrospun using a modified electrospinning setup to collect the aligned fibers. Example of one such modified setup that is commonly used to collect aligned fibers is based on parallel plates. Aligned fibers are collected using grounded parallel plates as these grounded electrodes affect the electric field near the collecting area [15, 70]. The electrostatically charged electrospinning jet is sensitive to the electric field created by the grounded collector causing the fibers to deposit transverse to the plates and across the air gap between them. This results in deposition of an aligned array of fibers.

It is argued that the electrical conductivity of the electrospinning solution must be within a critical range to enable deposition of the fibers across the parallel plates. When the solutions with a low electrical conductivity are electrospun, the electrostatic forces are insufficient to pull the fiber across the air gap, and hence, the parallel plate method is ineffective to collect aligned array of fibers. Conversely, when the solutions with high electrical conductivity are electrospun, the jet motion

is dominated by the random whipping instabilities and aligning the fibers becomes difficult. Hence, the electrical conductivity of the solution and applied voltage should be carefully controlled when using the parallel plate method for collecting aligned array of fibers.

Wu et al. [71] in their study modified the conventional electrospinning setup in order to fabricate aligned inorganic fibers. In their approach, the fibers are collected between the electrodes. Briefly, a metallic triangular tip with 60° apex angle is the spinneret. The triangular shape of the tip helps establish the Taylor cone during electrospinning. The counter electrode has a grounded coin placed 3 cm away from the tip which, in turn, is dipped into the electrospinning solution such that a small droplet sits on the surface of the tip. When a high voltage is applied, bundles of aligned fibers are formed between the tip and the grounded electrode. The jet ejected from the Taylor cone is pulled toward the ground electrode without any bending. The jet is stretched between the tip and the grounded collector. As the solvent evaporates, the dried and stretched jet forms bundles of aligned fiber arrays between the tip and the collector. The fibers are later transferred onto silicon wafer and thermally annealed to obtain aligned inorganic fibers.

1.3.5 Composite Fibers

The potential of using one-dimensional structures such as fibers, tubes, whiskers, and needles for functional applications is well established and proven by several groups [5, 8, 9, 13, 27, 33, 34, 72–74]. The high surface area and aspect ratio of these 1D structures are known to greatly influence their mechanical, electrical, and thermal transport characteristics. Hence, researchers have identified them as the building blocks for nanoscale/microscale devices. Electrospinning not only enables the control of fiber assembly, fiber size, and geometry but also increases the structural complexity of fiber composites.

One-dimensional composite structures in the form of fibers are fabricated by combining two or more materials with an aim of improving the functionality and material properties of the matrix material. As an example, carbon nanotubes (CNTs) are often incorporated within the inorganic matrix to improve the mechanical strength, stiffness, and resistance to corrosion of the composite [35, 38]. A straightforward technique to produce composite fibers is based on incorporating inorganic fillers into the solgel solution prior to electrospinning. The fibers with inorganic fillers are then thermally annealed to obtain hybrid fibers.

Wen et al. [43] dispersed SiO_2 nanoparticles within the precursor solgel solution of SiO_2. Hybrid fibers are obtained after electrospinning and thermal treatment. In a similar study, Aryal et al. [38] dispersed multi-walled carbon nanotubes (MWCNT) in the precursor solgel solution of TiO_2. The solution mixture is electrospun, and the fibers are thermally annealed to obtain MWCNT-reinforced TiO_2 fibers. Zhu et al. [75] used the same method to prepare CNT-reinforced TiO_2 fibers for

lithium-ion battery applications. They showed that these composites displayed improvement in capacity retention.

The solgel and electrospinning technique that is used for fabrication of single-phase ceramic fibers can also be extended to process composite ceramic fibers. In this approach, precursor solutions of two different materials are separately prepared and added into a polymer solution, which is electrospun to obtain the precursor fibers. These fibers are then annealed to yield the composite ceramic fibers [18, 38, 76].

Zhang et al. [76] used this technique to produce CeO_2–ZrO_2 composite fibers. Briefly, precursors of CeO_2 and ZrO_2 are separately dissolved in solvents. The polymer solution is prepared by dissolving PVP in ethanol. Then, both solutions with precursors are mixed in the polymer solution. This composite solution is electrospun, and the fibers are subsequently annealed to obtain composite ceramic fibers. In our recent study [13], we also used this approach to prepare $BaTiO_3$/$CoFe_2O_4$ composite fibers.

Figure 1.7 shows TEM images of $BaTiO_3$/$CoFe_2O_4$ composite fibers which display magnetoelectric properties. Li et al. [72] used coaxial electrospinning to prepare porous TiO_2–carbon nanofibers and used these fibers as anode materials in Li-ion batteries. Briefly, poly(methyl methacrylate) (PMMA) solution is fed into the core capillary of the spinneret, while polystyrene (PS) along with TiO_2 precursors is fed into the shell capillary of the spinneret. The PMMA phase within the core–shell fibers served as the sacrificial component and played a role in producing the pores, while PS in the fiber served as the carbon source. Thus, porous TiO_2–carbon fibers are produced after thermally annealing the precursor fibers. These porous TiO_2–carbon fibers exhibit excellent electrochemical performance.
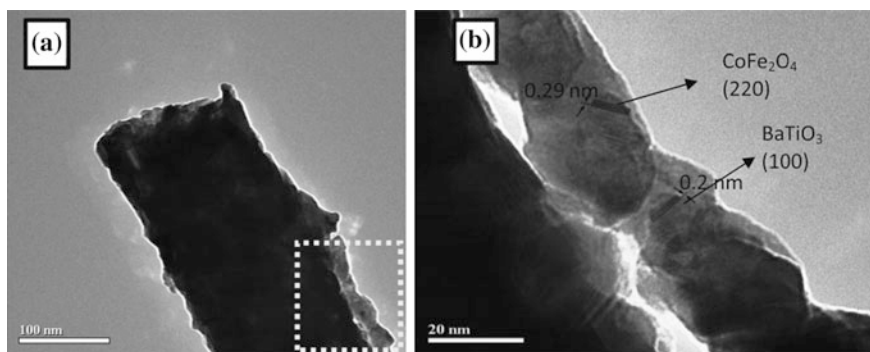
Fig. 1.7 **a** TEM image of $BaTiO_3$/$CoFe_2O_4$ composite fiber and **b** high magnification TEM image of a selected region (reproduced from Ref. [13] with kind permission of © 2014 Royal Society of Chemistry)

1.3.6 Hierarchical Structures Based on Ceramic Fibers

Recently, researchers have focused their interests on fabricating inorganic fibers based on complex architectures as these fibers are capable of demonstrating improved functionality [39]. For example, hierarchical structures based on inorganic ceramic or metal oxide fibers give superior photoelectrochemical performance, optical and electrical properties compared to their bulk counterparts and neat fibers [16, 39, 43]. In general, electrospinning can be used in two different ways to fabricate hybrid fibers or hierarchical structures based on ceramic fibers. In one technique, nanostructures grown on the fiber surface rely on hydrothermal treatment of the inorganic fibers in an aqueous solution.

Kanjwal et al. [39] dispersed ZnO nanoparticles in a precursor Co_3O_4 solgel solution. This colloidal solution is electrospun and then thermally annealed to obtain Co_3O_4 fibers dispersed with ZnO particles. An aqueous solution containing bis-hexamethylene triamine and zinc nitrate hexahydrate is prepared, and the annealed fibers are hydrothermally treated in this solution to grow ZnO nanostructures. Figure 1.8 shows the SEM image of Co_3O_4 fibers with ZnO nanostructures uniformly deposited on its surface.

Similar technique is used by Dai et al. [22] to grow K_xMnO_2 nanoplates on the surface of TiO_2 fibers. In their study, porous TiO_2 nanofibers using solgel combined with electrospinning technique are first prepared. Following this, the porous TiO_2 fibers are immersed in sulfuric acid with $KMnO_4$. This leads to the deposition of K_xMnO_2 plates on the surface of the fibers. It is further shown that the density can be controlled by adjusting the concentration of $KMnO_4$ in sulfuric acid and by adjusting the soaking time. Athauda et al. [77] used a similar approach to fabricate TiO_2 fibers. Dense ZnO nanorods are then grown on the surface of TiO_2 fibers by hydrothermal methods. First, TiO_2 fibers are dipped in ZnO seed solution, and then dip coated in a growth solution consisting of zinc nitrate hexahydrate and hexamethylenetetramine. The SEM image of the fabricated hybrid fibers is shown in Fig. 1.9.

Fig. 1.8 SEM image of Co_3O_4 fibers with ZnO nanostructures deposited on its surface (reproduced from Ref. [39] with kind permission of © 2011 Elsevier.)
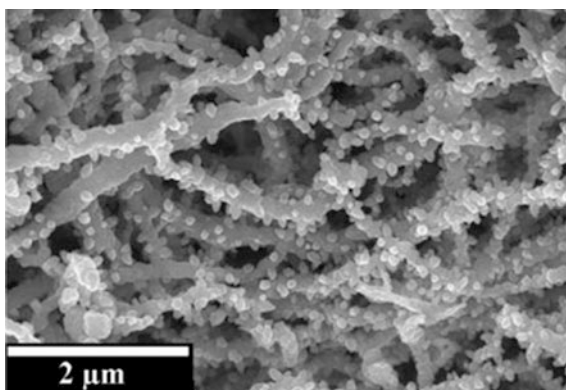
Fig. 1.9 SEM image of TiO$_2$–ZnO hierarchical structures. ZnO nanorods are grown on the surface of TiO$_2$ fibers (reproduced from Ref. [77] with kind permission of © 2012 American Chemical Society)
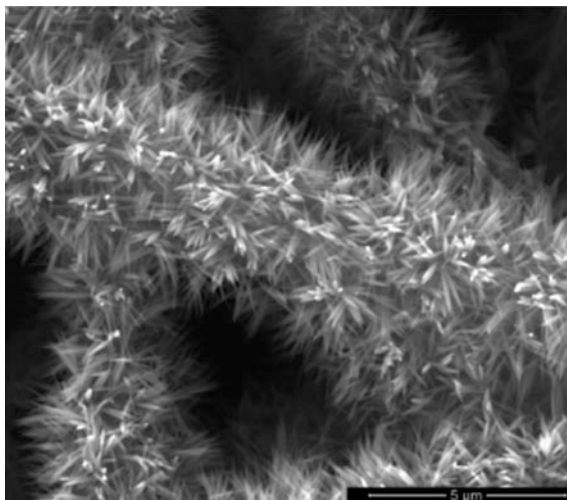
Another technique to fabricate hierarchical structures depends on the generation of nanostructures on the surface of the inorganic fibers. Here, desired metal salts can be introduced directly into the solgel solution and electrospun to obtain composite fibers. Following this step, the composite fibers can be thermally treated to grow metallic nanostructures on the surface of the fibers. Ostermann et al. [36] showed that electrospinning polymer solution containing a mixture of precursors led to the formation of composite metal oxide fibers. By controlling the annealing temperature and time, V$_2$O$_5$ nanorods can be grown on the surface of TiO$_2$ fibers. In the first step, the precursors of both V$_2$O$_5$ and TiO$_2$ are mixed in PVP solution. This solution is then electrospun to obtain PVP fibers with precursors of V$_2$O$_5$ and TiO$_2$. During annealing, both V$_2$O$_5$ and TiO$_2$ phases begin to crystallize. But their difference in crystallization results in phase separation, forming a unique morphology [36] which can be tailored by controlling the concentration of TiO$_2$ precursor in the electrospinning solution and annealing temperature. Thinner and more uniform V$_2$O$_5$ nanorods are grown on TiO$_2$ fiber surface when a lower annealing temperature is used.

In another study, Zhang et al. [78] produced hierarchical structures by first fabricating carbon fibers produced by electrospinning poly(amic acid) fibers which are thermally imidized and carbonized in a tube furnace. Then, a low-temperature chemical bath deposition process is utilized to grow Ni(OH)$_2$ nanoplatelets on the surface of the fibers. Ni(NO$_3$)$_2$·6H$_2$O and small quantity of urea are dissolved in deionized water and ethyl alcohol solution. The carbon fibers are treated in this solution to grow Ni(OH)$_2$ nanoplatelets on their surfaces. Figure 1.10 shows a SEM image of the obtained carbon fibers with Ni(OH)$_2$ nanoplatelets.

Recent studies have also demonstrated the use of electrospinning as a straightforward technique to produce carbon fibers that are decorated with metal oxide particles [35]. Lee et al. [35] showed that single nozzle electrospinning could be

Fig. 1.10 SEM image of carbon fibers/Ni(OH)$_2$ hybrid fibers (reproduced from Ref. [78] with kind permission of © 2015 American Chemical Society)
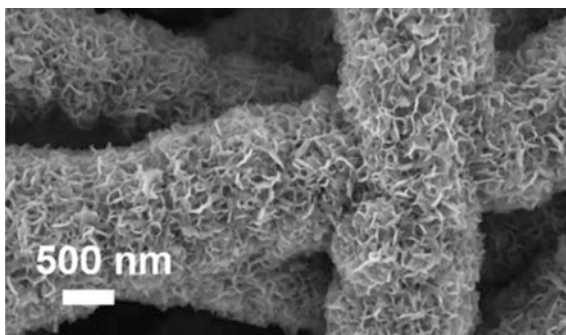
used to produce such hybrid fibers. The electrospinning solution prepared consisted of 4 components, viz. polyacrylonitrile (PAN), PVP, precursor solution of ZnAc$_2$, and precursor solution of SnCl$_4$. Due to the differences in the viscosities of PAN and PVP, and their immiscibility, the lower viscosity of PVP forms the continuous phase while the higher viscosity solution of PAN forms the droplets, which leads to the formation of core–shell fibers [35]. When this solution is electrospun, electrical forces act on the outer continuous phase while the inner phase only experiences shear force that is applied on its surface due to the flow of the outer continuous phase. Figure 1.11 shows the TEM image of the PAN–PVP core–shell fibers. Inorganic precursors along with PVP formed the shell and the PAN formed the core in the core–shell structures. Thermally annealing these fibers carbonized the PAN in the core region and led to the formation of ZnO and SnO$_2$ nanoparticles on the surface of the fibers. It is further shown that the concentration of the nanoparticles

Fig. 1.11 TEM image of PAN–PVP core–shell fiber (reproduced from Ref. [35] with kind permission of © 2011 American Chemical Society)
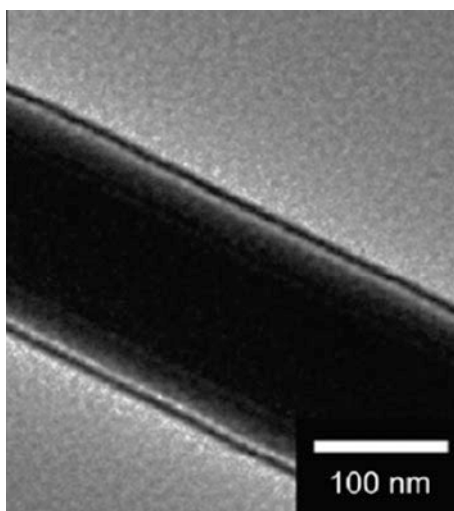
on the surface of the fibers can be controlled by adjusting the concentration of the precursors in the initial solgel solutions.

1.4 Applications of Inorganic Fibers

Electrospinning is a simple straightforward fabrication technique that can be used to produce inorganic nanofibers with controlled size and structures. Therefore, these electrospun inorganic fibers have found applications in many fields including energy harvesting, filtration, sensors, electrocatalysis, super-hydrophobic and super-hydrophilic surfaces, and biomedical fields. Some common applications of these metal oxide fibers are discussed in this section.

1.4.1 Filtration

Recent interest among researchers is to develop membranes to filter specific molecules and a wide range of contaminants from aqueous solutions or from air medium [31, 79–81]. Electrospun fibrous membranes are most sought after because of their efficient filtration performance, high surface area to volume ratio, and their superior ability to trap contaminants. The function of these membranes is to allow only certain specific molecules to pass through it and block others including the contaminants. Dai et al. [22] fabricated hierarchical structures using electrospinning and demonstrated their use for water filtration applications. In their study, TiO_2 nanofibrous membranes are first fabricated and then K_xMnO_2 nanoplatelets grown on the surface of the fibers. These hierarchical structures are shown to remove Congo red molecules efficiently from an aqueous medium. The mechanical integrity and stability of the membranes are also proven since shear flow of solution has not damaged the K_xMnO_2 nanoplatelets on the surface of the fibers [22].

Electrospun membranes are also widely used for air filtration and personal healthcare applications. Membranes based on nanofibers have shown some promising applications as filters that are capable of intercepting Escherichia coli, severe acute respiratory syndrome (SARS) virus, and influenza A (H1N1) virus [82–84]. The membranes based on fibers can also be used as N95 respirator mask if the channels and the size of the structural elements match the size of the particulates that are to be captured [85]. The efficiency of the filter can be improved if the size of the fibers within the membranes is reduced to nanoscale dimensions. It is argued that fibers of finer diameters have better filtration performance with no change in permeability compared to micron size fibers [85]. The membrane based on electrospun fibers not only has high permeability but also is capable of capturing dust particles due to its small pore size. The dust particles can later be removed by reversing the air flow through it or by other mechanical methods. Although electrospun membranes based on polymers are widely used for air filtration

applications, their applications are limited due to the low thermal stability of the polymers. Hence, they cannot be used as high-temperature filter membranes. However, membranes based on inorganic materials owing to their chemical and thermal stability can function at high temperatures and are being increasingly used for such filtration applications. The functionality of the inorganic membranes can be further improved by addressing their brittleness.

Mao et al. [79] used a solgel combined with electrospinning technique to fabricate a new class of flexible silica fibrous membranes that can be used at high temperatures. The thermal stability of these membranes is demonstrated using thermogravimetric analysis. Their results show no weight loss of the inorganic membrane in the range 100–900 °C. They also studied the effect of annealing temperature on the mechanical strength and flexibility. The results show that membranes obtained using lower annealing temperatures have better flexibility compared to those fabricated at higher annealing temperatures. The formation of quartz crystals is attributed to the better flexibility seen for the membranes that are fabricated at lower annealing temperatures [79]. The filtration efficiency of these membranes is tested by feeding neutralized NaCl aerosol through the filters and is over 99.7%. The working principle is by trapping the NaCl aerosol particles in the top layers of the membranes.

In a similar study, Yang et al. [81] fabricated flexible inorganic membranes based on silica nanofibers using solgel combined with electrospinning. Following this, polymerized fluorinated polybenzoxazine layer is incorporated on the surface of the fabricated silica membranes by dipping the membranes in solvent containing the monomers. They showed that these membranes are highly flexible and can potentially be used for high-temperature filtration applications. In another study [80], Wang et al. used electrospinning to fabricate flexible alumina fibers and demonstrated its ability for filtration applications. The filtration efficiency is tested by passing neutrally charged dioctyl phthalate (DOP) aerosols through the membrane and noting the concentration of the aerosol before and after filtration. These membranes have filtration efficiency of 99.8%.

1.4.2   Sensors

Semiconducting metal oxides such as SnO_2, In_2O_3, ZnO, and TiO_2 have been frequently used as gas sensors due to their ability to detect molecules of gases [17, 35, 60, 86]. Typically, a mesoporous layer of 1–10 μm thickness acts as an active sensing layer. This layer consists of sintered and interconnected nanometer-sized particles. The sensing mechanisms are based on the diffusion-reaction mechanisms. The gas molecules diffuse into the layer and interact with some of the pre-adsorbed O-adions that are present on the surface of the nanoparticles. This is known to affect the charge transfer interaction between nanoparticles and the gas adsorbates, which in turn affects the electrical resistance of the sensing layer. By monitoring the electrical resistance, the changes in the surrounding gas composition can be traced.

Thus, having a porous sensing layer improves the sensitivity as it enables gas penetration and exchange. Conventional techniques used to prepare the porous layers limit their gas sensing abilities due to the difficulty for the gas to diffuse into the inner regions of the layers.

Electrospinning is extensively explored to develop novel structures and fibers that can be used as sensors. One-dimensional structures, e.g., fibers, wires, rods, and tubes, which are obtained using electrospinning, are shown to have distinct properties compared to their bulk counterparts [17, 35, 60, 86]. These 1D fibers are shown to demonstrate improved chemical sensing behavior compared to the conventional thin-film sensors. This is attributed to the large surface to volume ratio of the 1D structures. Due to its high sensing abilities, they are capable of sensing very low concentration of gases such as NO_x and Cl_2. Lim et al. [17] used solgel combined with electrospinning technique to fabricate mesoporous indium acetate (In_2O_3) fibers and demonstrated its ability to detect CO in air. The high surface area of the fibers presented large quantity of sites on its surface for CO adsorption and reaction.

Similarly, other studies [12, 86, 87] have developed electrospun nanofiber membranes based on TiO_2 and SnO_2 for gas sensing applications. In these studies, when the sensing membranes are exposed to traces of gases in air, their electrical resistance is seen to change. This resistance is monitored to detect any changes in gases. The usual practice is to evaluate the sensitivity of the fabricated materials at elevated temperatures. Heating the material thermally activates the process on the surface region of the material to quicken the response and recovery. Lee et al. [35] in their study fabricated hybrid fibers by depositing metal oxides on the surface of the carbon fibers. They showed that these metal oxides decorated carbon fibers that can be used as chemical sensors. These materials demonstrated excellent sensitivity and are reported to be 10–100 times more sensitive compared to carbon nanotubes. This is attributed to the presence of metal oxide nanoparticles present on the surface of the fibers that help increase the surface area of the material.

1.4.3 Photocatalysis

n-type semiconducting metal oxides are widely used as photocatalyst because of their excellent catalytic properties and abilities to remove pollutants from aqueous solutions or gases. Water purification using such materials relies on a photon-assisted oxidation process. This method abates and mineralizes the organic pollutants with the help of highly reactive hydroxyl radicals. When the semiconducting metal oxides are exposed to photons that have energies similar to or greater than the energy associated with its band gap energy, the electrons from the valence bands jump to the conduction band. This process results in a hole generated at the valence band [88]. The electrons generated by the photon energy and the holes can recombine to release energy. Alternatively, the electrons and holes can interact with electron donors or acceptors that are adsorbed on the surface of the semiconducting

metal oxides. The electrons can react with O_2 molecules that are adsorbed on the surface of the semiconducting metal oxides and reduce them to radical O_2^- anions. By contrast, the holes possessing positive charge can interact with hydroxyl or water molecules to oxidize them into hydroxyl radicals. It is these radicals that act on the organic compounds by decomposing them [88].

It is well established that nanostructures of metal oxides demonstrate superior catalytic properties compared to their bulk counterparts due to the huge surface area associated with the nanostructured materials. Hence, electrospun metal oxide fibers have found great potential for water treatment. These metal oxide fibers can help to degrade the organic pollutants present in the aqueous solutions. Lu et al. [58] used emulsion electrospinning to fabricate porous TiO_2 nanofibers and showed their use for water treatment. The porous TiO_2 fibers have large surface area and a combination of anatase and rutile crystal phases which can improve the efficiency of the photocatalysis due to efficient separation of mixed electrons and holes. Zhan et al. [37] used the core–shell electrospinning setup to produce hollow TiO_2 fibers. Mesopores on the fibers are introduced with the help of pore-directing agent. They showed that these mesoporous TiO_2 fibers exhibited higher photocatalytic behavior toward methylene blue degradation compared to commercial TiO_2 nanoparticles and mesoporous TiO_2 powders. The increased photocatalytic behavior of the mesoporous hollow TiO_2 fibers is attributed to increased surface area. In yet another study, electrospun ZnO nanofibers are shown to degrade polycyclic aromatic hydrocarbons and naphthalene in the presence of UV radiation [59]. Methods to further improve the photocatalytic activities of electrospun metal oxide fibers have been investigated. Typically, the photocatalytic activity can be reduced due to rapid recombination rate of the holes and the excited electrons. This issue can be resolved by doping the metal oxides with other transition metals. The dopants reduce the recombination rate of holes and excited electrons and increase the surface area.

1.4.4 Energy

Nanofibers fabricated using electrospinning owing to their geometry and associated properties have been the focus of interest for applications related to energy storage and energy devices [8, 11, 29]. The high surface area and porous structures of the fibers have been found to be beneficial for energy storage and conversion [31, 42]. Electrospinning is increasingly investigated for fabrication of fibers for energy conservation applications such as fuel cells and solar cells as well as for energy storage applications such as supercapacitors. Electrospun fibers have been used in dye-sensitized solar cells (DSSCs) to enable conversion of light to electricity [24, 46, 89]. Porous metal oxide fibers are deposited on a transparent conducting glass to serve as the photoanodes in DSSCs. A photosensitizing dye is adsorbed on these semiconducting metal oxide fibers. Hence, when the dye absorbs the photons in these solar cells, the photoelectrons move into the conduction band of the

semiconducting metal oxide fibers. These photoelectrons are collected on the photoanode and transferred to the counter electrode via an external circuit. The flow of electrons through the external circuit produces current. Studies demonstrate that the one-dimensional geometry of the fiber increases the energy efficiency due to better charge conduction [8, 29]. Porous metal oxide fibers such as TiO_2 are widely investigated for photoanodes as the high surface area ensures that a larger amount of photosensitizing dye is absorbed.

Further, one-dimensional fibrous structures obtained using electrospinning have fewer grain boundaries compared to sintered nanoparticles, which improves charge conduction and reduces recombination of the charge carriers. Nair et al. [89] fabricated porous TiO_2 fibers using electrospinning and developed DSSCs based on TiO_2 fibers as photoanodes. This DSSC shows an efficiency of $\sim 4.2\%$ and incident photon to electron conversion efficiency of $\sim 50\%$. The DSSC gives a current density of 8 mA/cm^2 and an open-circuit voltage of 0.81 V.

Fuel cell is another area in which electrospun fibers are used to convert chemical energy into electrical energy. Among all types of fuel cells, direct methanol fuel cells (DMFCs) are widely investigated due to their low operating temperature and high power density [11, 26, 28]. Within these fuel cells, catalysts of platinum nanoparticles are loaded onto the supporting material. Studies demonstrate that the type of supporting material used has a great influence on the catalytic activity of the platinum nanoparticles. The criterion for selecting the supporting material for DMFCs is that the supporting material should have large surface area, stable, and electrically conductive. Electrospinning has been widely used to fabricate fibers as supporting materials in DMFCs. The 1D geometry of the fibers ensures the stability of the supporting material and plays a role in improving the performance of the resulting electrodes. Electrospun fibers based on carbon materials due to their ease in fabrication, low cost, and good electrical conductivity are used as catalyst support in DMFCs.

Li et al. [25] have used electrospinning to produce polyacrylonitrile (PAN) fibers which are thermally treated to convert to carbon fibrous mats. Then, a multi-cycle CV method is employed to deposit platinum clusters onto these mats. These platinum-loaded carbon fibrous mats are used in DMFC and shown to improve the catalytic peak current to 420 mA/mg. Thus, 1D carbon fibrous mats improve the performance of the catalyst.

1.5   Conclusions and Future Perspective

Development of novel materials with controlled structures and geometries is shown to be the candidate of choice for applications such as energy devices, sensors, filtration, and photocatalysis. One-dimensional structures in the form of fibers have immense significance in these applications. Of all the fabrication techniques,

electrospinning is attractive for fabrication of 1D fibers and provides the flexibility to control the compositions of the fibers. This technique can also be used to fabricate ceramic or metal oxide fibers from precursor polymers and affords an opportunity to fabricate binary and multi-component ceramic oxide fibers.

In this chapter, we review the various techniques based on electrospinning to fabricate ceramic or metal oxide nanofibers with various morphologies, structures, and geometries. Typically, the ceramic or metal oxide fibers obtained using electrospinning are polycrystalline. This is in contrast to the inorganic fibers fabricated using conventional techniques such as CVD where the material can be grown to consist of one single crystalline phase. The domain size in electrospinning can in some cases match the size of the fibers. This can provide additional functionality to the fibers as they demonstrate improved sensitivity. Hollow or porous fibers obtained using electrospinning have been widely used as electrodes in solar cells. It is also shown that the energy conversion efficiency of these fibers is significantly higher compared to other nanomaterials.

Similarly, ceramic and metal oxide fibers obtained using electrospinning are also shown to have better photocatalytic performance compared to other nanostructures produced using conventional techniques. It is illustrated that the geometry and morphology of obtained fibers can be tailored by controlling the processing variables. Thus, the performance of inorganic fibers can be easily altered based on the processing conditions. Modification of these one-dimensional inorganic fibers into hybrid or hierarchical fibrous structures can further improve its application in energy devices. The hybrid or hierarchical fibrous structures can improve light absorbance and carrier collection efficiency compared to neat ceramic or metal oxide fibers. Such fibers can be assembled and potentially important for future smart nanoscale electronic devices.

Although these inorganic fibers have many proven functional applications, their brittleness is one technical issue that must be resolved. Obtaining flexible ceramic or metal oxide fibers can improve their applications in filtration where the filters should possess high mechanical robustness. Recent studies have successfully fabricated hybrid inorganic fibers and demonstrated the membranes to be flexible. Other studies have shown that by adding polymer to ceramic or metal oxide particles as a binder, the resulting membrane can be dimensionally stable and flexible. This approach can be extended to electrospinning. Polymer-ceramic core–shell fibers can be fabricated by coaxial electrospinning, and these fibers can be used for photocatalytic applications.

References

1. Liu SX, Hu LF, Xu XJ et al (2015) Nickel cobaltite nanostructures for photoelectric and catalytic applications. Small 11(34):4267–4283
2. Sharma J, Imae T (2009) Recent advances in fabrication of anisotropic metallic nanostructures. J Nanosci Nanotechnol 9(1):19–40
3. Ye XZ, Qi LM (2011) Two-dimensionally patterned nanostructures based on monolayer colloidal crystals: controllable fabrication, assembly, and applications. Nano Today 6(6):608–631
4. Cozzoli PD, Pellegrino T, Manna L (2006) Synthesis, properties and perspectives of hybrid nanocrystal structures. Chem Soc Rev 35(11):1195–1208
5. Law M, Goldberger J, Yang PD (2004) Semiconductor nanowires and nanotubes. Annu Rev Mater Res 34:83–122
6. Moriarty P (2001) Nanostructured materials. Rep Prog Phys 64(3):297–381
7. Wang ZY, Zhou L, Lou XW (2012) Metal oxide hollow nanostructures for lithium-ion batteries. Adv Mater 24(14):1903–1911
8. Barth S, Hernandez-Ramirez F, Holmes JD et al (2010) Synthesis and applications of one-dimensional semiconductors. Prog Mater Sci 55(6):563–627
9. Kim FS, Ren GQ, Jenekhe SA (2011) One-dimensional nanostructures of pi-conjugated molecular systems: assembly, properties, and applications from photovoltaics, sensors, and nanophotonics to nanoelectronics. Chem Mater 23(3):682–732
10. Kim Y, Shanmugam S (2013) Polyoxometalate-reduced graphene oxide hybrid catalyst: synthesis, structure, and electrochemical properties. ACS Appl Mater Interfaces 5(22):12197–12204
11. Dong ZX, Kennedy SJ, Wu YQ (2011) Electrospinning materials for energy-related applications and devices. J Power Sources 196(11):4886–4904
12. Kim ID, Jeon EK, Choi SH et al (2010) Electrospun SnO_2 nanofiber mats with thermo-compression step for gas sensing applications. J Electroceram 25(2–4):159–167
13. Baji A, Mai Y-W, Yimnirun R et al (2014) Electrospun barium titanate/cobalt ferrite composite fibers with improved magnetoelectric performance. RSC Adv 4(98):55217–55223
14. Baji A, Mai Y-W, Li Q et al (2011) Electrospinning induced ferroelectricity in poly (vinylidene fluoride) fibers. Nanoscale 3(8):3068–3071
15. Baji A, Mai Y-W, Wong SC et al (2010) Electrospinning of polymer nanofibers: effects on oriented morphology, structures and tensile properties. Compos Sci Technol 70(5):703–718
16. Kumar PS, Nizar SAS, Sundaramurthy J et al (2011) Tunable hierarchical TiO_2 nanostructures by controlled annealing of electrospun fibers: formation mechanism, morphology, crystallographic phase and photoelectrochemical performance analysis. J Mater Chem 21 (26):9784–9790
17. Lim SK, Hwang SH, Chang D et al (2010) Preparation of mesoporous In_2O_3 nanofibers by electrospinning and their application as a CO gas sensor. Sens Actuators, B 149(1):28–33
18. Wang Y, Huang HB, Gao JX et al (2014) TiO_2–SiO_2 composite fibers with tunable interconnected porous hierarchy fabricated by single-spinneret electrospinning toward enhanced photocatalytic activity. J Mater Chem A 2(31):12442–12448
19. Baji A, Zhou LM, Mai Y-W et al (2015) On the Adhesion performance of a single electrospun fiber. Appl Phys A-Mater 118(1):51–56
20. Li CR, Zhang XQ, Dong WJ et al (2012) High photocatalytic activity material based on high-porosity ZnO/CeO_2 nanofibers. Mater Lett 80:145–147
21. Baji A, Mai Y-W, Du XS et al (2012) Improved tensile strength and ferroelectric phase content of self-assembled polyvinylidene fluoride fiber yarns. Macromol Mater Eng 297 (3):209–213
22. Dai YQ, Lu XF, McKiernan M et al (2010) Hierarchical nanostructures of K-birnessite nanoplates on anatase nanofibers and their application for decoloration of dye solution. J Mater Chem 20(16):3157–3162

23. Lu BA, Li XD, Wang TH et al (2013) WO$_3$ nanoparticles decorated on both sidewalls of highly porous TiO$_2$ nanotubes to improve UV and visible-light photocatalysis. J Mater Chem A 1(12):3900–3906

24. Jo SM, Song MY, Ahn YR et al (2005) Nanofibril formation of electrospun TiO$_2$ fibers and its application to dye-sensitized solar cells. J Macromol Sci Pure 42(11):1529–1540

25. Li MY, Han GY, Yang BS (2008) Fabrication of the catalytic electrodes for methanol oxidation on electrospinning-derived carbon fibrous mats. Electrochem Commun 10(6):880–883

26. Agarwal S, Greiner A, Wendorff JH (2013) Functional materials by electrospinning of polymers. Prog Polym Sci 38(6):963–991

27. Baji A, Mai Y-W, Li Q et al (2011) Nanoscale investigation of ferroelectric properties in electrospun barium titanate/polyvinylidene fluoride composite fibers using piezoresponse force microscopy. Compos Sci Technol 71(11):1435–1440

28. Wang XH, Richey FW, Wujcik KH et al (2014) Ultra-low platinum loadings in polymer electrolyte membrane fuel cell electrodes fabricated via simultaneous electrospinning/electrospraying method. J Power Sources 264:42–48

29. Cavaliere S, Subianto S, Savych I et al (2011) Electrospinning: designed architectures for energy conversion and storage devices. Energy Environ Sci 4(12):4761–4785

30. Sahay R, Kumar PS, Sridhar R et al (2012) Electrospun composite nanofibers and their multifaceted applications. J Mater Chem 22(26):12953–12971

31. Thavasi V, Singh G, Ramakrishna S (2008) Electrospun nanofibers in energy and environmental applications. Energy Environ Sci 1(2):205–221

32. Larsen G, Velarde-Ortiz R, Minchow K et al (2003) A method for making inorganic and hybrid (organic/inorganic) fibers and vesicles with diameters in the submicrometer and micrometer range via sol-gel chemistry and electrically forced liquid jets. J Am Chem Soc 125(5):1154–1155

33. Li D, Xia YN (2003) Fabrication of titania nanofibers by electrospinning. Nano Lett 3(4):555–560

34. Baji A, Mai YW, Li QA et al (2011) One-dimensional multiferroic bismuth ferrite fibers obtained by electrospinning techniques. Nanotechnology 22(23):235702

35. Lee JS, Kwon OS, Park SJ et al (2011) Fabrication of ultrafine metal-oxide-decorated carbon nanofibers for DMMP sensor application. ACS Nano 5(10):7992–8001

36. Ostermann R, Li D, Yin YD et al (2006) V$_2$O$_5$ nanorods on TiO$_2$ nanofibers: a new class of hierarchical nanostructures enabled by electrospinning and calcination. Nano Lett 6(6):1297–1302

37. Zhan SH, Chen DR, Jiao XL et al (2006) Long TiO$_2$ hollow fibers with mesoporous walls: sol–gel combined electrospun fabrication and photocatalytic properties. J Phys Chem B 110(23):11199–11204

38. Aryal S, Kim CK, Kim KW et al (2008) Multi-walled carbon nanotubes/TiO$_2$ composite nanofiber by electrospinning. Mater Sci Eng, C 28(1):75–79

39. Kanjwal MA, Sheikh FA, Barakat NAM et al (2011) Co$_3$O$_4$–ZnO hierarchical nanostructures by electrospinning and hydrothermal methods. Appl Surf Sci 257(18):7975–7981

40. Isobe T, Kameshima Y, Nakajima A et al (2006) Extrusion method using nylon 66 fibers for the preparation of porous alumina ceramics with oriented pores. J Eur Ceram Soc 26(12):2213–2217

41. Jang YS, Jank M, Maier V et al (2010) SiC ceramic micropatterns from polycarbosilanes. J Eur Ceram Soc 30(13):2773–2779

42. Lu XF, Wang C, Wei Y (2009) One-dimensional composite nanomaterials: synthesis by electrospinning and their applications. Small 5(21):2349–2370

43. Wen SP, Liu L, Zhang LF et al (2010) Hierarchical electrospun SiO$_2$ nanofibers containing SiO$_2$ nanoparticles with controllable surface-roughness and/or porosity. Mater Lett 64(13):1517–1520

44. Danks AE, Hall SR, Schnepp Z (2016) The evolution of 'sol-gel' chemistry as a technique for materials synthesis. Mater Horiz 3(2):91–112

45. Anjusree GS, Bhupathi A, Balakrishnan A et al (2013) Fabricating fiber, rice and leaf-shaped TiO$_2$ by tuning the chemistry between TiO$_2$ and the polymer during electrospinning. RSC Adv 3(37):16720–16727

46. Chen HY, Zhang TL, Fan J et al (2013) Electrospun hierarchical TiO$_2$ nanorods with high porosity for efficient dye-sensitized solar cells. ACS Appl Mater Interfaces 5(18):9205–9211

47. Nuansing W, Ninmuang S, Jarernboon W et al (2006) Structural characterization and morphology of electrospun TiO$_2$ nanofibers. Mater Sci Eng, B 131(1–3):147–155

48. He ZY, Liu Q, Hou HL et al (2015) Tailored electrospinning of WO$_3$ nanobelts as efficient ultraviolet photodetectors with photo-dark current ratios up to 1000. ACS Appl Mater Interfaces 7(20):10878–10885

49. Leng JY, Xu XJ, Lv N et al (2011) Synthesis and gas-sensing characteristics of WO$_3$ nanofibers via electrospinning. J Colloid Interface Sci 356(1):54–57

50. Chen ZX, Zhang Z, Tsai CC et al (2015) Electrospun mullite fibers from the sol-gel precursor. J Sol–Gel Sci Technol 74(1):208–219

51. Guo AR, Liu JC, Dong X et al (2013) Preparation of porous silica ceramics from silica spinning solution and introduced silica particles by electrospinning. Mater Lett 95:74–77

52. Newsome TE, Olesik SV (2014) Electrospinning silica/polyvinylpyrrolidone composite nanofibers. J Appl Poly Sci 131(21)

53. Ding T, Tian Y, Liang K et al (2011) Anisotropic oxygen plasma etching of colloidal particles in electrospun fibers. Chem Commun 47(8):2429–2431

54. Zhang CL, Yu SH (2014) Nanoparticles meet electrospinning: recent advances and future prospects. Chem Soc Rev 43(13):4423–4448

55. Lu XF, Zhao YY, Wang C (2005) Fabrication of PbS nanoparticles in polymer-fiber matrices by electrospinning. Adv Mater 17(20):2485–2488

56. Bai J, Li YX, Yang ST et al (2007) Synthesis of AgCl/PAN composite nanofibres using an electrospinning method. Nanotechnology 18(30):305601

57. Bognitzki M, Becker M, Graeser M et al (2006) Preparation of sub-micrometer copper fibers via electrospinning. Adv Mater 18(18):2384–2386

58. Lu BA, Zhu CQ, Zhang ZX et al (2012) Preparation of highly porous TiO$_2$ nanotubes and their catalytic applications. J Mater Chem 22(4):1375–1379

59. Singh P, Mondal K, Sharma A (2013) Reusable electrospun mesoporous ZnO nanofiber mats for photocatalytic degradation of polycyclic aromatic hydrocarbon dyes in wastewater. J Colloid Interface Sci 394:208–215

60. Wang PP, Qi Q, Xuan RF et al (2013) A facile method for enhancing the sensing performance of zinc oxide nanofibers gas sensors. RSC Adv 3(43):19853–19856

61. Xia YJ, Song JL, Yuan DN et al (2015) Synthesis and characterization of one-dimensional metal oxides: TiO$_2$, CeO$_2$, Y$_2$O$_3$-stabilized ZrO$_2$ and SrTiO$_3$. Ceram Int 41(1):533–545

62. Liu BT, Peng LL (2013) Facile formation of mixed phase porous TiO$_2$ nanotubes and enhanced visible-light photocatalytic activity. J Alloy Compd 571:145–152

63. Choi SH, Ankonina G, Youn DY et al (2009) Hollow ZnO nanofibers fabricated using electrospun polymer templates and their electronic transport properties. ACS Nano 3 (9):2623–2631

64. Choi SJ, Chattopadhyay S, Kim JJ et al (2016) Coaxial electrospinning of WO$_3$ nanotubes functionalized with bio-inspired Pd catalysts and their superior hydrogen sensing performance. Nanoscale 8(17):9159–9166

65. Liu RL, Liu HQ, Liu JS et al (2012) Fabrication of patterned inorganic nanofibers by electrospinning. Prog Chem 24(8):1484–1496

66. Zhang J, Choi SW, Kim SS (2011) Micro- and nano-scale hollow TiO$_2$ fibers by coaxial electrospinning: preparation and gas sensing. J Solid State Chem 184(11):3008–3013

67. Zhang ZY, Li XH, Wang CH et al (2009) ZnO hollow nanofibers: fabrication from facile single capillary electrospinning and applications in gas sensors. J Phys Chem C 113 (45):19397–19403

68. Li D, Wang YL, Xia YN (2003) Electrospinning of polymeric and ceramic nanofibers as uniaxially aligned arrays. Nano Lett 3(8):1167–1171

69. Chang JY, Domnner M, Chang C et al (2012) Piezoelectric nanofibers for energy scavenging applications. Nano Energy 1(3):356–371
70. Baji A, Mai Y-W, Wong SC (2011) Effect of fiber diameter on the deformation behavior of self-assembled carbon nanotube reinforced electrospun polyamide 6,6 fibers. Mater Sci Eng, A 528(21):6565–6572
71. Wu H, Lin DD, Zhang R et al (2007) Oriented nanofibers by a newly modified electrospinning method. J Am Ceram Soc 90(2):632–634
72. Li XY, Chen YM, Zhou LM et al (2014) Exceptional electrochemical performance of porous TiO_2-carbon nanofibers for lithium ion battery anodes. J Mater Chem A 2(11):3875–3880
73. Li XY, Chen YM, Wang HT et al (2016) Inserting sn nanoparticles into the pores of TiO_2-x-c nanofibers by lithiation. Adv Funct Mater 26(3):376–383
74. Li XY, Chen YM, Huang HT et al (2016) Electrospun carbon-based nanostructured electrodes for advanced energy storage-A review. Energy Storage Mater 5:58–92
75. Zhu PN, Wu YZ, Reddy MV et al (2012) Long term cycling studies of electrospun TiO_2 nanostructures and their composites with MWCNTs for rechargeable Li-ion batteries. RSC Adv 2(2):531–537
76. Zhang YF, Li JY, Li Q et al (2007) Preparation of CeO_2–ZrO_2 ceramic fibers by electrospinning. J Colloid Interface Sci 307(2):567–571
77. Athauda TJ, Neff JG, Sutherlin L et al (2012) Systematic study of the structure-property relationships of branched hierarchical TiO_2/ZnO nanostructures. ACS Appl Mater Interfaces 4 (12):6916–6925
78. Zhang LS, Ding QW, Huang YP et al (2015) Flexible hybrid membranes with $Ni(OH)_2$ nanoplatelets vertically grown on electrospun carbon nanofibers for high-performance supercapacitors. ACS Appl Mater Interfaces 7(40):22669–22677
79. Mao X, Si Y, Chen YC et al (2012) Silica nanofibrous membranes with robust flexibility and thermal stability for high-efficiency fine particulate filtration. RSC Adv 2(32):12216–12223
80. Wang Y, Li W, Xia YG et al (2014) Electrospun flexible self-standing gamma-alumina fibrous membranes and their potential as high-efficiency fine particulate filtration media. J Mater Chem A 2(36):15124–15131
81. Yang LP, Raza A, Si Y et al (2012) Synthesis of superhydrophobic silica nanofibrous membranes with robust thermal stability and flexibility via in situ polymerization. Nanoscale 4(20):6581–6587
82. Yoon K, Hsiao BS, Chu B (2008) Functional nanofibers for environmental applications. J Mater Chem 18(44):5326–5334
83. Ding B, Wang MR, Wang XF et al (2010) Electrospun nanomaterials for ultrasensitive sensors. Mater Today 13(11):16–27
84. Hung CH, Leung WWF (2011) Filtration of nano-aerosol using nanofiber filter under low Peclet number and transitional flow regime. Sep Purif Technol 79(1):34–42
85. Wang XF, Ding B, Sun G et al (2013) Electro-spinning/netting: a strategy for the fabrication of three-dimensional polymer nano-fiber/nets. Prog Mater Sci 58(8):1173–1243
86. Landau O, Rothschild A, Zussman E (2009) Processing-microstructure-properties correlation of ultrasensitive gas sensors produced by electrospinning. Chem Mater 21(1):9–11
87. Kim ID, Rothschild A, Lee BH et al (2006) Ultrasensitive chemiresistors based on electrospun TiO_2 nanofibers. Nano Lett 6(9):2009–2013
88. Malwal D, Gopinath P (2016) Fabrication and applications of ceramic nanofibers in water remediation: a review. Crit Rev Env Sci Technol 46(5):500–534
89. Nair AS, Jose R, Shengyuan Y et al (2011) A simple recipe for an efficient TiO_2 nanofiber-based dye-sensitized solar cell. J Colloid Interface Sci 353(1):39–45

Chapter 2
Polymer Microbead-Templated Nanostructures

Cheng Fang and Youhong Tang

Abstract In this chapter, nanostructures templated by polymer microbead, which is usually made of polystyrene with a diameter range of 300 nm–1 µm, are reviewed. We first focus on formation of the microbead monolayer in terms of the driving force for self-assembly, the junction among the neighbouring microbeads and the uniformity of microbead monolayer. Then, we discuss applications of microbead monolayer as a template for nanostructure fabrication. Because the assembled monolayer features an ordered structure scaling up to centimetre (cm) size, microbead-templated nanostructures also show an ordered arrangement in cm size, which is attractively simple and can be achieved in common laboratories. From the microbead monolayer template, the subsequent fabrication approaches include electrochemical deposition, sputter coating deposition, plasma etching, annealing, wet etching and dry etching as well. The templating targets include metals, semiconductors, polymers, and nano-moieties such as nanobeads and nanocubes. Various types of nanostructure have been fabricated using these approaches individually or by combining them to increase the flexibility of fabrication. Controllable and ordered nanostructures have been achieved by adjusting the fabrication parameters. Finally, we review the application of nanostructures templated by the polymer microbeads, particularly as surface-enhanced Raman scattering (SERS) substrates. We demonstrate approaches for identifying the position of the hot spot and how to achieve single-molecule detection.

C. Fang (✉)
Global Centre for Environmental Remediation (GCER),
University of Newcastle, Newcastle, NSW 2308, Australia
e-mail: cheng.fang@newcastle.edu.au

Y. Tang
School of Computer Science Engineering and Mathematics, Centre for Nanoscale Science
and Technology, Flinders University, Adelaide, SA 5042, Australia
e-mail: youhong.tang@flinders.edu.au

2.1   Introduction

Polymer microbeads have been studied for decades, focusing on self-assembly into monolayers and then used as templates for the fabrication of nanostructures [1, 2]. The technique of nanosphere lithography (NSL) is economic and simple, which enables general laboratories to fabricate nanostructures without clean room support. The self-assembly of polymer microbeads means that an ordered structure can be generated. Consequently, the fabricated nanostructures are ordered, not random. Furthermore, from the ordered templates, many versatile nanostructures can be fabricated by fine-tuning the subsequent fabrication approach, using means such as deposition, etching and annealing. Basically, imagination need not be restricted, and newly fabricated nanostructures are frequently reported.

Fabricated nanostructures have demonstrated surprising properties that cannot be expected from macro-structures or bulk. Besides their large surface area, nanostructures display nanosize-related enhancements resulting in catalytic activity, as well as quantum and plasmonic resonance effects. Here, we also discuss the applications as surface-enhanced Raman scattering (SERS) substrates.

2.2   Microbead Monolayer

2.2.1   Polymer Microbeads and Silica Microbeads

Polymer microbeads are usually made of polystyrene (PS), which differ from silica microbeads. Silica is an inorganic material and is therefore more stable than PS, chemically and thermally. When used as a sensor, such as a SERS substrate, the silica itself might feature a background cleaner than that of PS, except for the two main peaks positioned around 519 and 900–1100 cm^{-1} [3]. However, the stable property of silica microbeads might restrict their flexibility for the fabrication of nanostructures. For example, when thermal annealing is selected to follow the microbead templating, a PS microbead template could be easily burnt off and removed due to organic components, whereas this did not occur with silica [4]. However, we recognise the similarity between polymer and silica microbeads in terms of microsphere lithography templating nanostructures. In this chapter, we focus our discussion on polymer microbeads.

### 2.2.2   Microbead Monolayer and Multilayers

Generally, a monolayer of microbeads is used as a template for the fabrication of a nanostructure, although a multilayer might also be useful [5, 6]. However, the forming conditions of microbead multilayers are difficult to control and relevant

research has been rarely reported. In this chapter, we focus our discussion on the monolayer template. A schematic drawing of a microbead monolayer is presented in Fig. 2.1a, b. Figure 2.1c shows the templated bottom structure after removal of the microbead monolayer. The inset in Fig. 2.1c is a cross-sectional view with a tilt angle of $\sim 30°$.

There are several types of driving force that induce microbeads to self-assemble into a dense monolayer [7]: capillary force when the solvent is evaporating; flux of the solvent, i.e., hydrodynamic steering during the evaporation process; increased Van der Waals force between neighbouring microbeads due to their high energy surface. The main contribution comes from the capillary force, as shown in Fig. 2.2 [6]. The capillary force or surface tension can be enhanced by adding surfactants into the colloid solution prior to the monolayer formation. For example, Triton-X-100, a typical surfactant, is generally used as an ingredient for dense packing of a microbead monolayer [8, 9]. The other contributors for the assembling driving force are discussed below.

The driving force is so strong that the monolayer can extend to centimetre (cm) size, as shown in Fig. 2.3. Due to the diffraction of light, a blue–purple colour is observed from the formed monolayer when the mean diameter of the microbeads is ~ 500 nm, which can be used as pre-screening to judge the success of a monolayer assembly [10].

Here, the monolayer deposition was conducted using spinning coating at 800 rpm on a silicon surface. The PS microbeads with a mean diameter of 500 nm were used directly without dilution ($\sim 10\%$ w/w in aqueous solution). Defects along the assembly domain boundaries (Fig. 2.3c) and within a domain (Fig. 2.3d) mainly originate from the non-uniformity of the microbead diameters, particularly considering the accumulation effect from sub-micrometre to centimetre during the monolayer formatting process. This hypothesis can be evidenced in Fig. 2.4, where the imaging position was kept unchanged while images were repeatedly collected every 5 min. We can see the movement of the microbeads in the marked areas, which is likely due to the static–electric interaction among the neighbouring microbeads resulting from the charging e-beam under the SEM operation. Therefore, the non-uniform diameters of microbeads are the main reason for
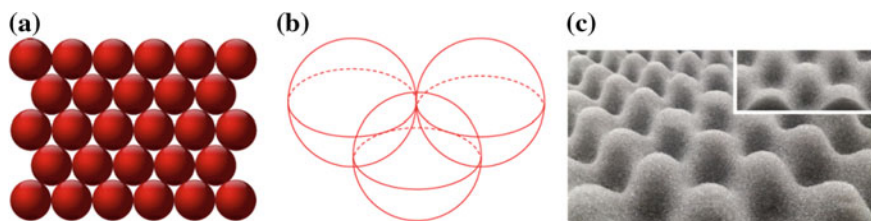
Fig. 2.1 **a** Schematic drawing of a microbead monolayer, **b** three neighbouring microbeads and **c** a photo-image of a templated bottom with a tilt angle of $\sim 30°$. The *inset* is a cross-sectional view
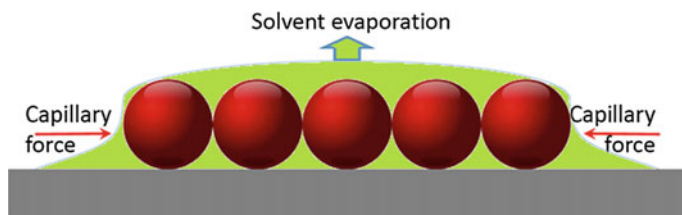
Fig. 2.2 Schematic drawing of the capillary force for a monolayer assembly
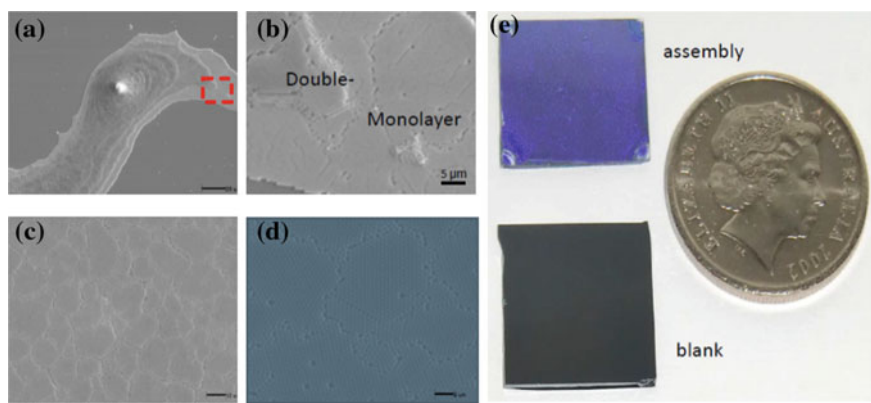
Fig. 2.3 **a–d** SEM images and **e** a photo-image of polymer microbead monolayers. **a** a Stacked multilayer, **b** a double layer and a monolayer, zoomed in from the marked area in **a**, **c** and **d** zoomed in monolayers, including boundaries and densely packed monolayer domains, and **e** an assembled monolayer with a bright *blue–purple* colour (*top*), which can be easily distinguished from the blank silicon wafer used for the assembly support (*bottom*). A *coin* is shown on the *right* to demonstrate the size of the monolayer assembly (Color figure online)
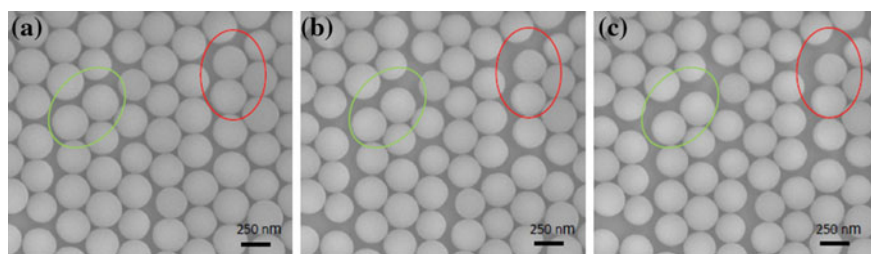
Fig. 2.4 SEM images at the same areas (*red* and *light green) ellipses* showing the movement of microbeads under the e-beam due to charging effects. The assembly conditions were the same as those in Fig. 2.3 except for the microbeads with a mean diameter of ∼330 nm (Color figure online)
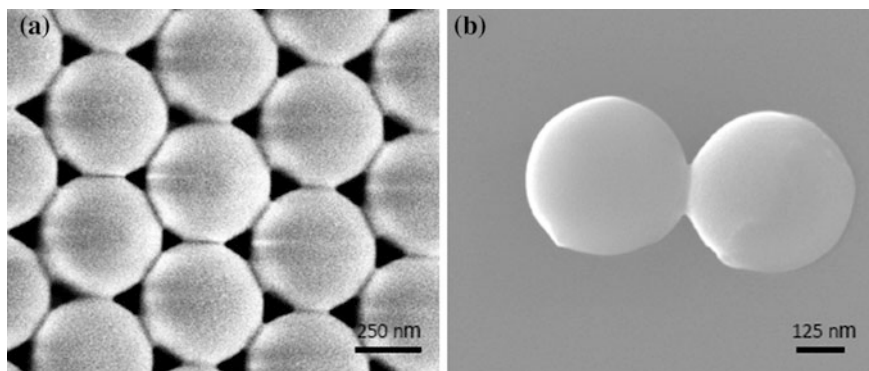
Fig. 2.5 SEM images of neighbouring microbeads. The deposition conditions were the same as those in Fig. 2.4

assembling defects and restriction into a dense monolayer scaling up to millimetre or even centimetre.

The high surface energy of polymer microbeads leads easily to the conjunction of neighbouring microbeads [11]. However, with respect of the conjunction, important contributing factors are the conditions of the assembly, such as solvent types, added surfactants, temperatures, ageing periods and aftermath treatment, as shown in Fig. 2.5. Fortunately, the junction has a limited effect on the subsequent templating process to fabricate nanostructures [12].

2.3 Fabricated Nanostructures

2.3.1 Templated Deposition

A simple method of fabrication of a nanostructure is the employment of microbeads as a template for deposition. Because the monolayer does not completely cover the support surface, leaving some voids, as shown in Fig. 2.1a, b, the deposition can occur on top of the monolayer microbeads and on the bottom of the monolayer. In the latter case, the deposition occurs directly on the monolayer support's surface through the voids, as shown in Fig. 2.1c. Deposition methods include electrochemical deposition [13, 14] and sputtering coating [3], as shown in Fig. 2.6. In the former case (electrochemical deposition), the template of the microbead monolayer should be kept stable in the deposition solution for the subsequent electrochemical reaction, and thus an annealing process is employed to plasticine the monolayer. After the annealing process, the polymer beads are connected (conjunction) due to their high surface energy. The plastic temperature might be significantly different from the bulk melting temperature, as discussed in the following.
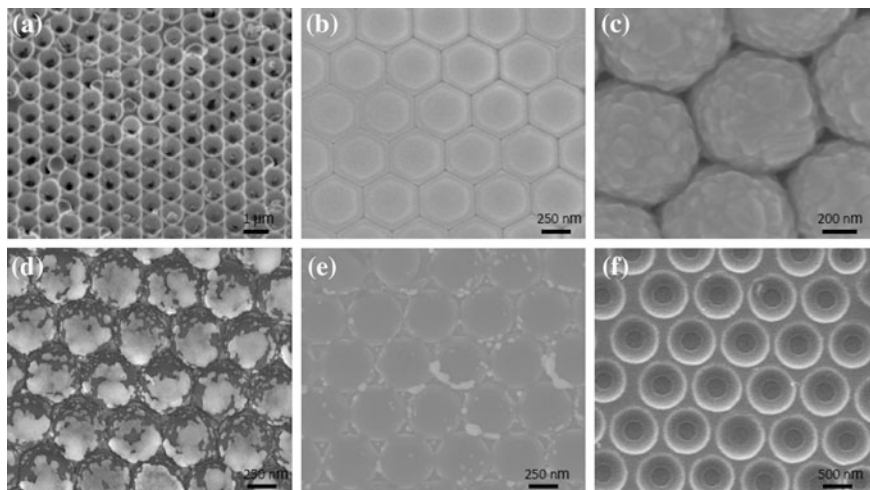
Fig. 2.6 SEM images of structures templated by polymer microbead monolayers. **a** Electrodeposited gold after lifting-off a microbead template (Reproduced from Ref. [14] with kind permission of © 2004 Wiley-VCH); **b** Microbead monolayer after sputter coating on the surface (as *ceiling*), and **c** Detailed morphology; **d**, **e** *Bottom* structure after lifting-off the monolayer template, **f** Templated PS by sinking of a monolayer assembly of silica. For the structures in **b–e**, the monolayer template was prepared according to Fig. 2.3. The deposited metals were ∼30 nm titanium and ∼300 nm silver. The subsequent washing off was carried out in toluene solution to lift-off the PS microbeads; **f** Porous PS preparation protocols are listed in main text

The advantage of electrochemical deposition is that the set-up is simple, and only an electrochemical workstation is required. However, selection of the deposition target is limited, as only materials that can easily be oxidised, electropolymerised, or reduced by the electrochemical system, can be deposited. The substrate/support for the monolayer template also needs to be conductive for electrochemistry, such as indium tin oxide (ITO). A representative structure is shown in Fig. 2.6a. In that case, deposition cannot occur on the top of the monolayer because the microbeads are not conductive.

In contrast, the sputtering coating process is more flexible. Some materials, such as carbon or aluminium that cannot be used in the electrochemical system, can be deposited using this approach. Furthermore, the monolayer's substrate/support can be glass/silicon because the conductivity of the substrate is not compulsory for the sputtering coating. Typical structures are shown in Fig. 2.6b, c before lift-off. After lifting off the microbead monolayer template, the bottom structures are shown in Fig. 2.6d, e. The difference between them lies in the extent of the lift-off. In Fig. 2.6d, the deposited shields/ceilings partly remain on top of the microbeads. In Fig. 2.6e, only the bottom is retained, while the top ceiling on the monolayer assembly has been completely removed.

A similar approach can be extended to the fabrication of polymer structures, such as the porous PS shown in Fig. 2.6f. The protocol is listed as follows:

(i) PS was dissolved into 1:4 toluene and spin coated on a silicon wafer surface to obtain a thin film of ~400 nm thickness; (ii) a silica monolayer template of microbeads with 500 nm diameter was deposited using the approach detailed above; (iii) incubation was carried out in toluene vapour for ~10 min to sink the silica monolayer into the polystyrene layer; and (iv) silica microbeads were removed by washing with hydrogen fluoride (HF, ~20%, w/w, ~5 min).

This is a bottom-up approach, i.e., the bulk structure was sunk/coined by a microbead monolayer template, not a top-down approach in which the deposition was templated by a microbead monolayer. With this method, we expanded the materials for nano-fabrication from electrochemically active materials such as gold, and sputter coating materials such as silver, gold, aluminium, carbon and titanium, to polymers in general.

Sometimes, microbeads need to be shrunk in an attempt to fine-tune the deposited nanostructure, as shown in Fig. 2.7. The shrinking might be conducted using argon or oxygen plasma. From Fig. 2.7a–c, the diameter of the beads has been gradually shrunk. Their templated and deposited nanostructures are shown in Fig. 2.7d–f. The deposited metal islands increase in size, when the diameter of the microbeads shrinks.

Not only have metal and polymer been deposited and templated by the microbead monolayers, but extra microbeads can also be templated. The extra microbeads are usually smaller than the primary beads, as shown in Fig. 2.8 [5, 6].
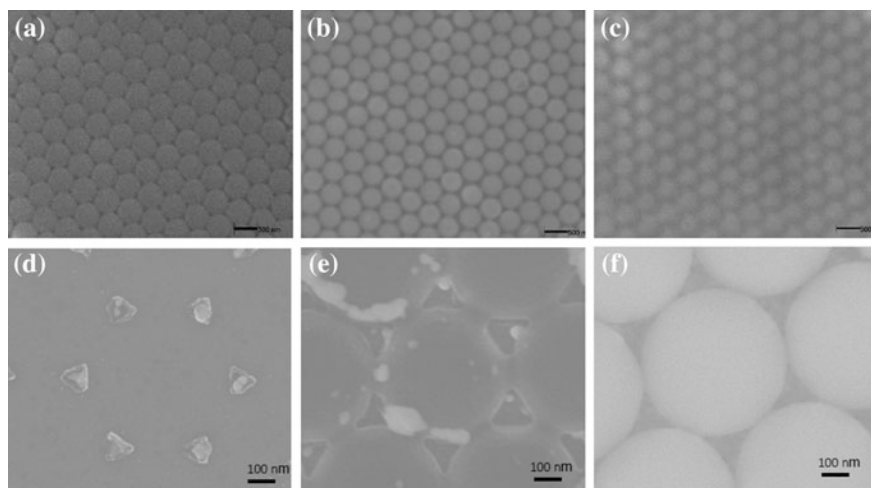
Fig. 2.7 SEM images of controllable nanostructures templated by microbead monolayers. The microbead monolayer was prepared according to Fig. 2.3. Oxygen plasma etching was carried out for different periods (**a**) 0 min, (**b**) 2 min and (**c**) 5 min. Their corresponding templated nanostructures are shown in **d**, **e** and **f**

Fig. 2.8 SEM images showing binary microbead monolayers (Reproduced from Ref. [5] with kind permission of © 2003 Wiley-VCH)
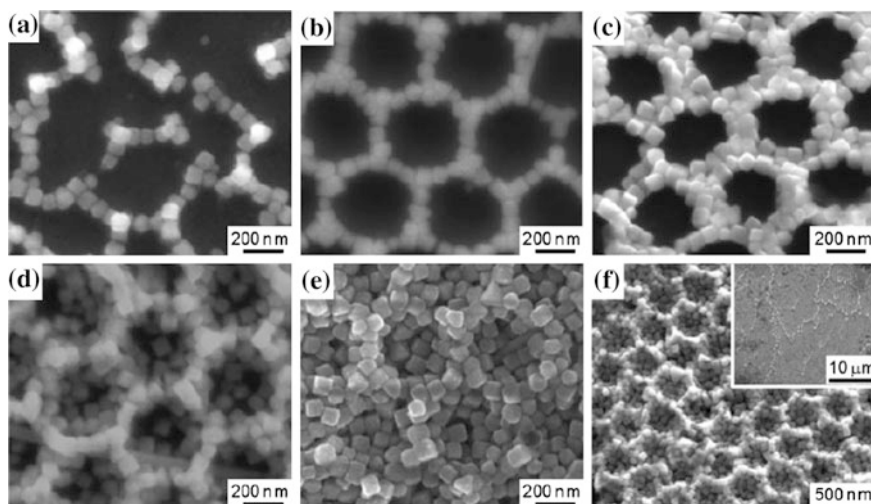
Fig. 2.9 SEM images of templated silver nanocubes. The polymer microbead monolayer was prepared according to Fig. 2.3. The deposition of nanocubes was carried out by dropping different concentrations of solution containing nanocubes and drying in air. Toluene was used to wash off the microbeads (Reused from Ref. [7] with kind permission of © 2013 Royal Society of Chemistry)

The driving force for the crystallisation structure was supposed to be the capillary force, as mentioned before.

Interestingly, the extra moieties can also be nanocubes, as shown in Fig. 2.9 [7]. We used this approach to build a high density of coupled nanocubes. The primary monolayer of microbeads works as islands to break the colloid liquid (containing nanocubes) into small areas as shown in Fig. 2.1a, b, with void areas less than μm^2. Within these small areas, the driving force for self-assembly from the capillary force of solvent evaporation is more efficient for arranging the nanocubes towards assembly. This assembly process within a small area (less than μm^2 rather than greater than cm^2) offers the possibility of densely packing the nano-moieties. That is, the monolayer template divides/grids the thin layer of solution containing

nanocubes into small areas, as shown in Fig. 2.2. Under the monolayer template, the void is small and the number of nanocubes is significantly reduced. Consequently, the assembly in this tiny void area is more operative than that in a large area without the monolayer template.

2.3.2 Combination with Annealing

To remove the polymer microbead monolayer template, in addition to the wash-off process with solvents, thermal annealing or de-wetting can also be used to remove the template by burning the polymer microbeads off. Annealing thus adds flexibility towards the nanostructure fabrication [4]. In terms of deposited silver, the annealing temperature is usually ~500–700 °C, which is lower than its bulk melting point (961.8 °C). The reason is due to the high surface energy of the nanostructure [15]. It has been reported that the surface atoms on the nanostructure, particularly at the tips or corners, look like liquid rather than solid [11]. This is because the nano surface means that the number of neighbouring atoms is much less than that in the bulk. The crystal grid is thus full of defects. Consequently, the surface atoms face less restriction than those in the bulk. The annealing approach and results are shown in Fig. 2.10. Basically, the silver ceiling on the top of the monolayer template or PS nanosphere mask shrinks into a nanoparticle, the size of which is dependent on the amount of deposited silver or the deposition thickness. Meanwhile, the silver
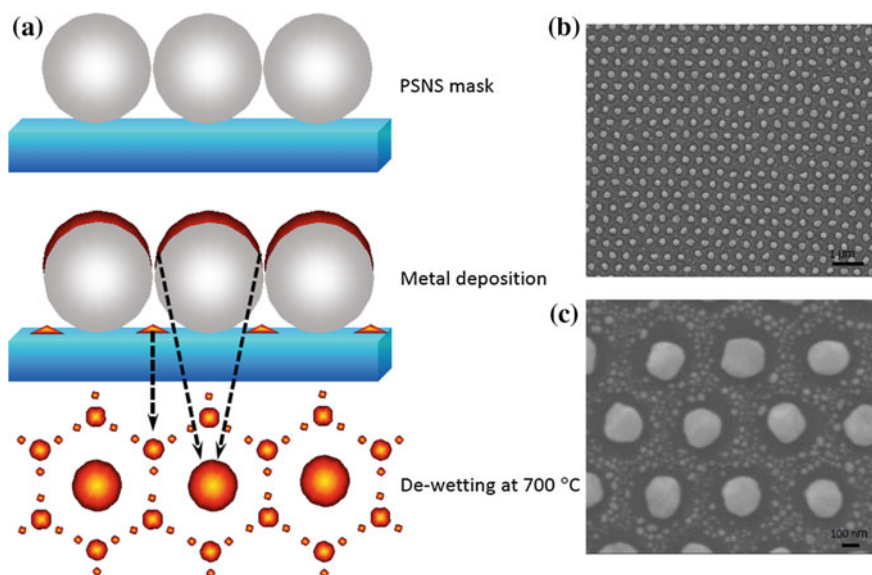
Fig. 2.10 a Schematic drawing and **b**. **c** SEM images of annealing results under different magnifications

deposited on the bottom void under the monolayer template shrinks into smaller nanoparticles to surround the central nanoparticles that stem from the ceiling shrinking.

For vertical deposition, different nanostructures can be fabricated by adjusting the annealing process, as shown in Fig. 2.11b, c. In removal of the template monolayer prior to the annealing process, the central nanoparticle is avoided and only the satellite nanoparticles remain. On the other hand, the tilting angle for the metal deposition also makes a significant difference [4], because it determines the deposition direction and the amount of metal for the subsequent annealing, as shown in Fig. 2.11. In Fig. 2.11d–e, with regard to the tilting deposition, it can be seen that the subsequent annealing leads to the appearance of the central nanoparticles without the surrounding satellite nanoparticles, which is contrary to the vertical deposition. In the meantime, by controlling the deposition amount, the size of the nanoparticles is also adjustable.

Annealing temperature and speed are other factors that should be considered, such as the melting point for bulk gold is 1064 °C vs. that of silver which is 961.8 °C. However, the annealing approach of gold is usually kept the same as the silver annealing profile since no obvious difference has been observed [4].

2.3.3   Combination with Etching

As known, metal can catalyse the etching reaction on silicon [4]. The underlying process is not fully understood but an electrochemical cell should be involved, which includes an anode for oxidisation of silicon and a cathode for reduction of oxidant or water, i.e., emission of hydrogen. Because polymer microbeads can feature a metal template of an ordered pattern on the silicon surface (discussed above), the subsequent catalysis etching fabricates an ordered nanostructure including female pores and male pillars, as shown in Fig. 2.12.

The sinking of a metal template into the silicon bulk can be evidenced from the etched structure in Fig. 2.12a. Basically, from the template fabricated from Fig. 2.7c, the deposited silver is treated by the toluene wash-off process to remove the polymer microbead monolayer. A porous silver film, akin to a net, remains on the silicon surface, as shown in Figs. 2.7f, 2.12a (inset). The silver net acts as a catalysis centre when silver-silicon is dipped into HF solution. Meanwhile, the void area without silver remains almost unchanged. The area covered with bulk silver film (not porous) is also maintained because it is shielded from the HF. Consequently, the array structure of the microbead monolayer is coined and sunk into the depth of silicon, as shown in Fig. 2.12a, b.

In Fig. 2.12a, along the boundary of the microbead monolayer domain, the etching morphology is different from that in the other parts. On the left of that boundary (dashed line), the etching is not obvious because the silicon/HF has been shielded by the silver film. On its right, when the silver template sinks into the silicon depth due to the etching, the silver net is stretched. Consequently, it does not
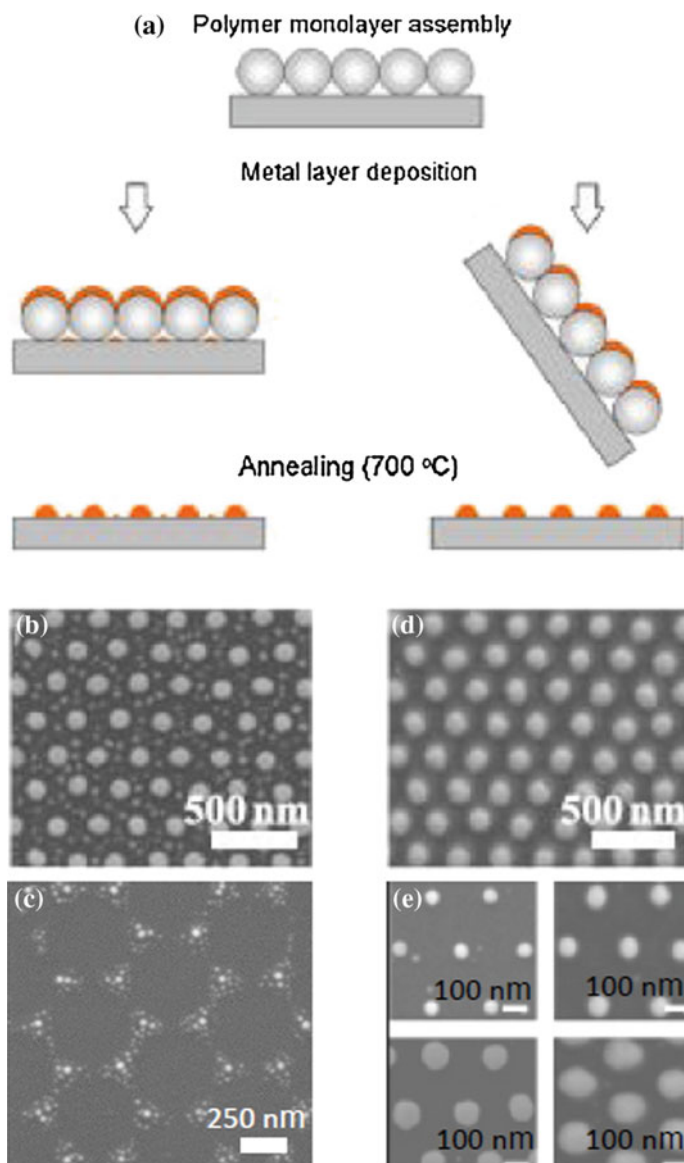
Fig. 2.11 Effect of deposition direction and amount. The microbead monolayer was prepared according to Fig. 2.3. **a** Schematic demonstration of a metal deposition and a subsequent annealing process; The vertically deposited ceiling layer of metal is kept (**b**) or removed (**c**) by using a solvent wash-off process prior to an annealing process; and **d**, **e** show the tilted deposition amount of the metal controlling the size of the annealed nanoparticles (Reproduced from Ref. [4] with kind permission of © 2013 Springer)
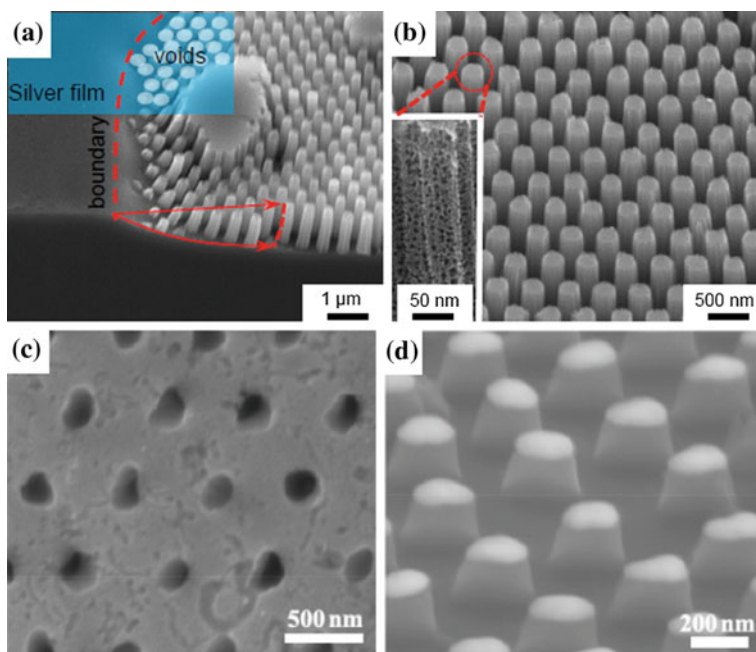
Fig. 2.12 SEM images of nanostructures of **a**–**c** wet etching and **d** dry etching. The polymer microbead monolayer was prepared according to Fig. 2.3. Then plasma etching occurred as illustrated in Fig. 2.7c, followed by metal deposition, toluene wash off and wet etching by dipping into a solution of 1:5:10 of HF–H_2O_2–H_2O (v/v) to obtain Fig. 2.12**a**, **b** structures. The *inset* in **a** schematically shows a metal template for the etching, and the *inset* in **b** shows the detailed structure. The metal nanoparticle array was prepared according to Fig. 2.11**d** and then followed by **c** wet etching or **d** dry etching (Reproduced from Ref. [4] with kind permission of © 2013 Springer)

sink directly and vertically into the bulk, rather than with an arc, as indicated by the arrow in Fig. 2.12a. Therefore, the pillar is not vertical to the etching surface but in the shape of an arc. Depending on the etching condition, the pillar left behind can also be porous, as shown in Fig. 2.12b (inset) [16–18].

In Fig. 2.12c, the female holes in the silicon were etched in a solution of HF–H_2O_2–H_2O with ratio of 1:5:10 (v/v) by the deposited metal's catalysis from the metal template as shown in Fig. 2.11d, a process which is called wet etching. Dry etching, on the other hand, features different structures, as shown in Fig. 2.12d. Dry etching is usually conducted using a plasma of reactive gases such as fluorocarbons [4]. It can effectively etch silicon, while the deposited metal can persist. Thus, metal (platinum) can shield and protect the silicon below to fabricate male pillars, as shown in Fig. 2.12d.

2.4 Applications

2.4.1 Surface Plasmon of Templated Nanostructures

Ordered structures have received increased attention recently due to their unique properties that cannot be expected in random structures. For example, an anisotropic nanostructure means that its surface plasmon will feature an anisotropic field, specifically an electric–magnetic field. When used as a SERS substrate, the enhancement will be anisotropic because the enhancement of the Raman signal stems mainly from the electric–magnetic field within the nanostructures, which usually are called as hot spots. If the arrangement of nanostructures such as nanocube assembly can be controlled, the distribution of hot spots on the SERS substrate surface can thus be controlled. In this case, the ordered structure means an ordered rather than random arrangement of hot spots. The resulting distribution of Raman intensity is uniform, as shown in Fig. 2.13 [7].
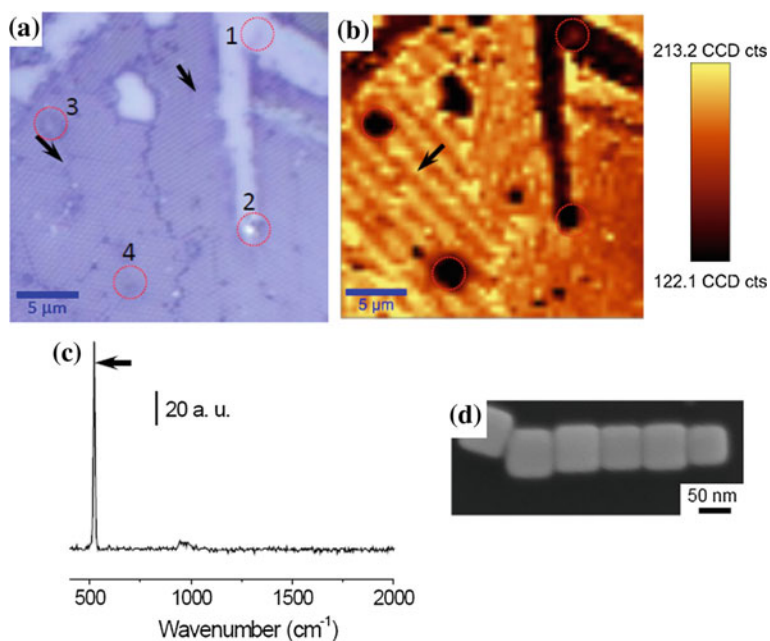
Fig. 2.13 **a** Silver nanocubes templated by a polymer microbead monolayer, **b** Raman mapping image based on **c** the silicon peak and **d** the coupled silver nanocubes. The preparation conditions of the nanocube pattern using polymer microbeads were given in Fig. 2.9**b** [4]. In Fig. 2.13**a, b**, the *marked areas* indicate (*1*) the non-ordered monolayer, (*2*) the stacked microbeads and (*3, 4*) defects. The *arrow* directions in **a** and **b** are different due to the different signal collecting approaches, namely, (**a**) a photo-image and (**b**) a Raman mapping image (Reused from Ref. [7] with kind permission of © 2013 Royal Society of Chemistry)

Figure 2.13a shows a photo picture collected under microscopy. The domains of the microbead monolayer and their boundaries can be seen. These polymer microbeads were supported by the bottom silicon. The silicon's Raman peak at 519 cm^{-1} (shown in Fig. 2.13c) was collected to map its image, as presented in Fig. 2.13b. The similarity between the photo-image in Fig. 2.13a and the nanostructure distribution in Fig. 2.13b can be identified, confirming that the Raman enhancement originated from the nanostructure (hot spot), as shown in Fig. 2.13d. The uniformity of the enhanced Raman signal in the ordered nanostructure area can be seen in Fig. 2.13b, supporting the above hypothesis about the anisotropic field.

There are two important issues to be identified about hot spots, namely, the position of the hot spot and the electric–magnetic field intensity within the hot spot [2, 19, 20]. The former determines the robustness of the Raman signal (distribution and density), and the latter controls the intensity of the signal, the sensitivity and the limit of detection.

2.4.2 Identification of Hot spot Position

Simulation and calculation have suggested that there is a much higher electric–magnetic field around the corners of a nanocube than in the other areas [21–23]. Experimental proof was lacking, however, until a recent report [7]. One approach is demonstrated in Fig. 2.14 [7]. Basically, a self-assembled monolayer (SAM) of thio was used to cap a silver nanocube (AgNC) surface [24]. It has been reported that a SAM is always accompanied by defects/pinholes [25, 26]. In the primary SAM (A, 1-dodecanethiol, or DDT) formed on silver nanocubes ($\sim$50 nm), the defects/pinholes are most likely to be located on the corner. Therefore, the attacking position for the secondary thio (B, 2-mercaptopyridine, or MPy) occurs at the corner. Consequently, a mixture of SAM (A + B) is obtained with B on the corners, as shown in Fig. 2.14a–c with a pure SAM (B) shown in Fig. 2.14d for comparison. Using a microbead monolayer as a template, silver nanocubes were patterned as a SERS substrate with high enhancement (Fig. 2.14e). It can be found that Raman scattering intensity of molecule B is almost the same, regardless of from SAM (A + B) (MPy-DDT_AgNC) or from SAM (B) (MPY_AgNC), as shown in Fig. 2.14f, with peak heights marked by black lines. Therefore, the dominating position for SERS is on the corner, i.e., the hot spot position is on the corner.

Another approach is shown in Fig. 2.15 [27]. The gold nanocube surface, Fig. 2.15a, was capped and coated with a layer of silica, which was formed by dipping in a solution of tetraethylorthosilicate (TEOS). The corresponding structure is shown in Fig. 2.15b. Then the capped nanocube's coating was etched using NaOH. By carefully controlling the etching process, the corners were exposed while the other positions were still coated, as shown in Fig. 2.15c. A Raman probe of 1,4-benzenedithiol was then loaded onto the exposed gold corners due to the strong Au-S bonds, which could not be applied on the silica coating surface.
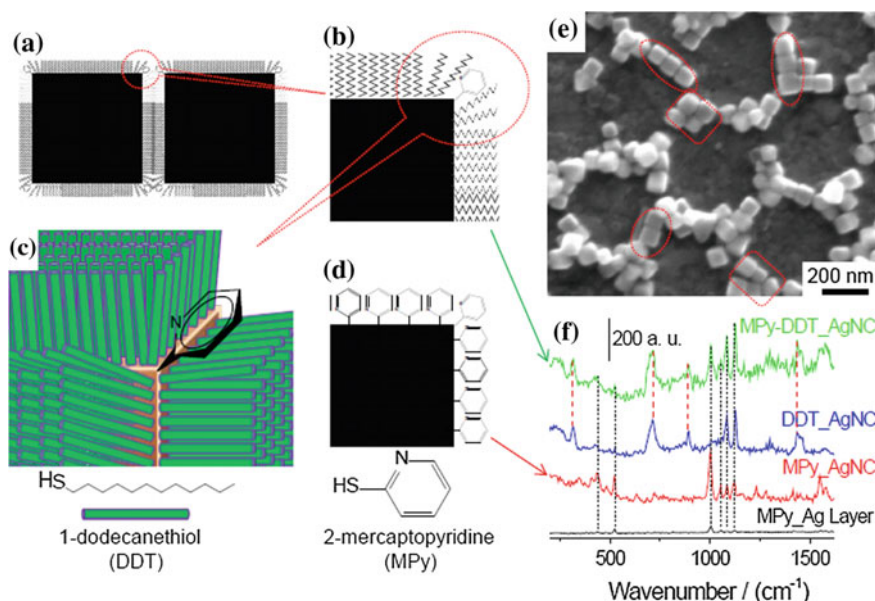
Fig. 2.14 a–d Schematic drawings of SAMs and **e** a SEM image of patterned silver nanocubes and **f** the Raman signals. The preparation conditions were described in Fig. 2.9c. Then the substrate was incubated in an ethanol solution containing 1-dodecanethiol (DDT) (0.1%, v/v) for 2 h (DDT_AgNC). After being washed off with ethanol and dried under a stream of nitrogen gas, the substrate was further incubated in an aqueous solution containing 2-mercaptopyridine (MPy) (10 µM) for 1 h (MPy-DDT_AgNC). Another substrate was prepared by directly incubating it in the MPy solution for 1 h (MPy_AgNC) [4]. For comparison, MPy standard Raman signals were collected from a silver film surface and presented (Reused from Ref. [7] with kind permission of © 2013 Royal Society of Chemistry)
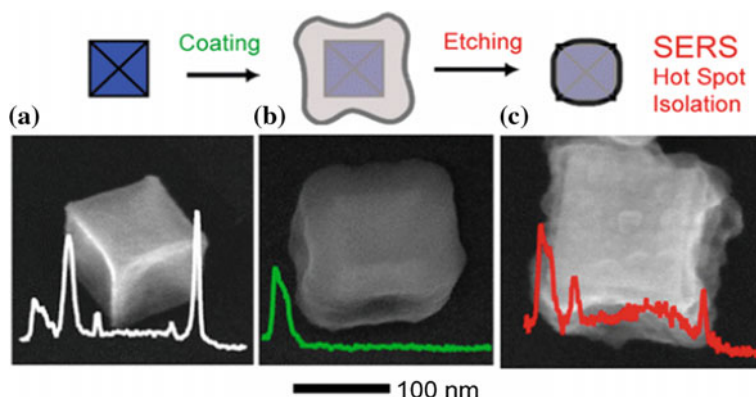
Fig. 2.15 Schematic drawing (*upper*) of the coating and etching approach and (*lower*) the corresponding results (Reproduced from Ref. [27] with kind permission of © 2012 American Chemical Society)

With the above process, the hot spots were chemically isolated and confirmed on
the corner of the nanocube, as shown.

2.4.3 Single Molecule Detection

It is well known that SERS can reach single molecule detection [28, 29]. Here,
another approach has been developed recently by us to demonstrate this single
molecule detection [3, 7, 30, 31]. Two types of molecule have been selected here. In
this bi-analysis approach, these two molecules (A and B) behave similarly in terms
of loading affinity onto a SERS substrate, Raman activities, etc. Their concentra-
tions are diluted (to the limit of detection) for single molecule loading, and their
Raman signals have been mapped using their characteristic peaks and the results are
shown in Fig. 2.16.
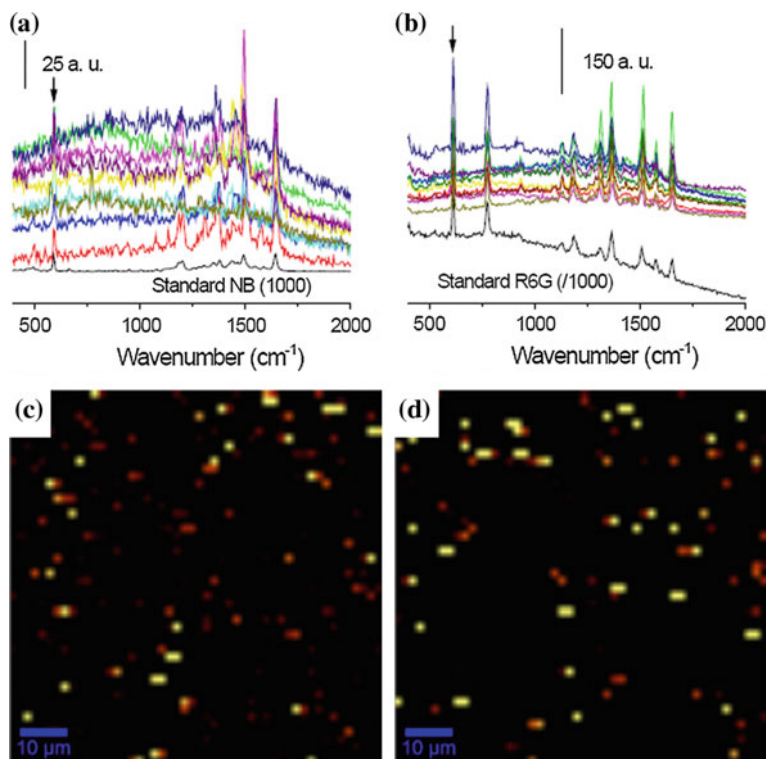
Fig. 2.16 Typical Raman spectra of **a** Nile blue (NB), **b** Rhodamine 6G (R6G) and **c**, **d** their
corresponding mapping images. The Raman spectra in **a** and **b** were randomly collected at the
bright spots in **c** and **d**, respectively. Their characteristic peaks are marked for the mapping
(Reused from Ref. [7] with kind permission of © 2013 Royal Society of Chemistry)

Statistically, if a hot spot can be occupied by only one molecule, there are two possibilities, that it is occupied by A or by B, individually, not simultaneously, with similar possibility ($\sim$50% vs. $\sim$50%). During the mapping process, the high-intensity Raman signals, corresponding to the bright dots in the mapping images, should originate from hot spots occupied by A or B individually, not simultaneously. Consequently, the bright spots in mapping image of A do not overlap on the bright spots in mapping image of B. Furthermore, the density of the bright spots in mapping images of A and B should be similar ($\sim$50% vs. $\sim$50%). However, if a hot spot can contain two molecules, there are four possibilities, i.e. AA ($\sim$25%), AB ($\sim$25%), BA ($\sim$25%) or BB ($\sim$25%). In this case, there will be a $\sim$25% chance of collecting pure A Raman signals from AA, another $\sim$25% possibility of collecting pure B signals from BB, individually, not simultaneously. Meanwhile, we have a $\sim$50% chance of collecting mixed signals from AB/BA, which maps as A, and also as B, simultaneously. Therefore, for the mapping images of A and B, we see that $\sim$50% of bright spots will overlap. The map will feature an even higher overlapping percentage if a hot spot can contain three ($\sim$75%) or four molecules ($\sim$87.5%). Considering the variation of statistics, we believe that single molecule detection has been achieved when the overlapping percentage is less than 5%.

As mentioned, to reach the single molecule detection level or for a hot spot to catch only one molecule, the concentration must be low. That is, the solution needs to be diluted gradually for the individual Raman probe to be loaded on the SERS substrate surface, until we have <5% overlap from the collectable signals' mapping images. This concentration for a single molecule loading and detection is significantly dependent on the loading affinity of the Raman probe or the target molecule [3]. In other words, there are three main factors that should be considered for high-sensitivity SERS analysis: enhancement factor from the substrate, Raman activity and loading affinity. For example, we adjusted the concentration of Nile blue (NB) (10 nM) and Rhodamine 6G (R6G) (2 nM) in a bi-analysis solution (not the same), to reach the single molecule detection and balance their Raman signals [32], which has been echoed recently [33].

During the mapping process, the laser spot is around μm in size or smaller, depending on the focusing lens and the laser wavelength. The size of a hot spot, however, is in the nm range. Therefore, one laser spot could cover several hot spots, depending on the hot spot density on the SERS substrate surface. That is, a bright spot in the mapping image can be linked with one or more hot spots, as shown in Fig. 2.17. This complicates the statistical estimation of single molecule detection. On the other hand, the electric–magnetic field is high in the hot spot and the laser used for Raman excitation is intensive. As a consequence, during the signal collection process, there is a possibility that the molecule within a hot spot does not contribute to the Raman signal due to the shielding effect from laser excitation or from Raman scattering as marked with a red cross in Fig. 2.17, or from the photo-degradation (bleaching) of a Raman probe.

Fig. 2.17 Schematic drawing
of Raman signal collection
process
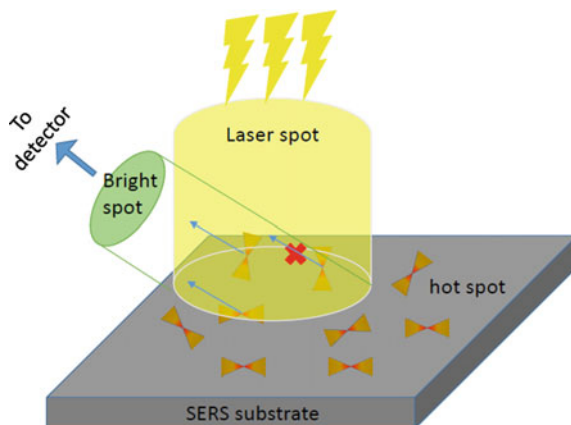
2.5   Summary

Polymer microbeads can be easily assembled into a monolayer for lithography to
fabricate nanostructures via deposition, etching, annealing, etc. The templating
targets include metals, semiconductors, polymers, nanobeads and nanocubes.
Added together, there are many possibilities and much flexibility to fabricate various nanostructures. Fabricated nanostructures have various applications, such as
SERS substrates to enhance Raman signals.

References

1. Haynes CL, Van Duyne RP (2001) Nanosphere lithography: a versatile nanofabrication tool
   for studies of size-dependent nanoparticle optics. J Phys Chem B 105(24):5599–5611
2. Jones MR, Osberg KD, Macfarlane RJ et al (2011) Templated techniques for the synthesis
   and assembly of plasmonic nanostructures. Chem Rev 111(6):3736–3827
3. Fang C, Bandaru NM, Ellis AV et al (2013) Beta-cyclodextrin decorated nanostructured
   SERS substrates facilitate selective detection of endocrine disruptor chemicals. Biosens
   Bioelectron 42:632–639
4. Brodoceanu D, Fang C, Voelcker N et al (2013) Fabrication of metal nanoparticle arrays by
   controlled decomposition of polymer particles. Nanotechnology 24(8):085304
5. Kitaev V, Ozin GA (2003) Self-assembled surface patterns of binary colloidal crystals. Adv
   Mater 15(1):75–78

6. Velikov KP, Christova CG, Dullens RPA et al (2002) Layer-by-layer growth of binary colloidal crystals. Science 296(5565):106–109
7. Fang C, Brodoceanu D, Kraus T et al (2013) Templated silver nanocube arrays for single-molecule SERS detection. RSC Adv 3(13):4288–4293
8. Cheung CL, Nikolić RJ, Reinhardt CE et al (2006) Fabrication of nanopillars by nanosphere lithography. Nanotechnology 17(5):1339
9. Lipson AL, Comstock DJ, Hersam MC (2009) Nanoporous templates and membranes formed by nanosphere lithography and aluminum anodization. Small 5(24):2807–2811
10. Fudouzi H, Xia Y (2003) Photonic papers and inks: color writing with colorless materials. Adv Mater 15(11):892–896
11. Roduner E (2006) Size matters: why nanomaterials are different. Chem Soc Rev 35(7):583–592
12. Mitsui T, Onodera T, Wakayama Y et al (2011) Influence of micro-joints formed between spheres in coupled-resonator optical waveguide. Opt Express 19(22):22258–22267
13. Sun F, Cai W, Li Y et al (2004) Morphology-controlled growth of large-area two-dimensional ordered pore arrays. Adv Funct Mater 14(3):283–288
14. Sun F, Cai WP, Li Y et al (2004) Morphology control and transferability of ordered through-pore arrays based on the electrodeposition of a colloidal monolayer. Adv Mater 16(13):1116–1121
15. Moon K-S, Dong H, Maric R et al (2005) Thermal behavior of silver nanoparticles for low-temperature interconnect applications. J Electron Mater 34(2):168–175
16. Li X (2012) Metal assisted chemical etching for high aspect ratio nanostructures: a review of characteristics and applications in photovoltaics. Curr Opin Solid State Mater Sci 16(2):71–81
17. S-w Chang, Chuang VP, Boles ST et al (2010) Metal-catalyzed etching of vertically aligned polysilicon and amorphous silicon nanowire arrays by etching direction confinement. Adv Funct Mater 20(24):4364–4370
18. Chiappini C, Liu X, Fakhoury JR et al (2010) Biodegradable porous silicon barcode nanowires with defined geometry. Adv Funct Mater 20(14):2231–2239
19. Halvorson RA, Vikesland PJ (2010) Surface-enhanced raman spectroscopy (SERS) for environmental analyses. Environ Sci Technol 44(20):7749–7755
20. Haynes CL, McFarland AD, Duyne RPV (2005) Surface-enhanced raman spectroscopy. Anal Chem 77(17):338A–346A
21. Lee SY, Hung L, Lang GS et al (2010) Dispersion in the SERS enhancement with silver nanocube dimers. ACS Nano 4(10):5763–5772
22. McLellan JM, Li Z-Y, Siekkinen AR et al (2007) The SERS activity of a supported Ag nanocube strongly depends on its orientation relative to laser polarization. Nano Lett 7(4):1013–1017
23. Wu H-L, Tsai H-R, Hung Y-T et al (2011) A comparative study of gold nanocubes, octahedra, and rhombic dodecahedra as highly sensitive SERS substrates. Inorg Chem 50(17):8106–8111
24. Ulman A (1996) Formation and structure of self-assembled monolayers. Chem Rev 96(4):1533–1554
25. Hakkinen H (2012) The gold-sulfur interface at the nanoscale. Nat Chem 4(6):443–455
26. Palmer RE, Robinson APG, Guo Q (2013) How nanoscience translates into technology: the case of self-assembled monolayers, electron-beam writing, and carbon nanomembranes. ACS Nano 7(8):6416–6421
27. Rycenga M, Langille MR, Personick ML et al (2012) Chemically isolating hot spots on concave nanocubes. Nano Lett 12(12):6218–6222
28. Bohn JE, Le Ru EC, Etchegoin PG (2009) A statistical criterion for evaluating the single-molecule character of sers signals. J Phys Chem C 114(16):7330–7335
29. Le Ru EC, Meyer M, Etchegoin PG (2006) Proof of single-molecule sensitivity in surface enhanced raman scattering (SERS) by means of a two-analyte technique. J Phys Chem B 110(4):1944–1948

30. Fang C, Xie Y, Johnston MR et al (2015) SERS and NMR studies of typical aggregation-induced emission molecules. J Phys Chem A 119(29):8049–8054
31. Fang C, Ellis AV, Voelcker NH (2012) Electrochemical synthesis of silver oxide nanowires, microplatelets and application as SERS substrate precursors. Electrochim Acta 59:346–353
32. Fang C, Shapter JG, Voelcker NH et al (2014) Electrochemically prepared nanoporous gold as a SERS substrate with high enhancement. RSC Adv 4(37):19502–19506
33. Zrimsek AB, Wong NL, Van Duyne RP (2016) Single molecule surface-enhanced raman spectroscopy: a critical analysis of the bianalyte versus isotopologue proof. J Phys Chem C 120(9):5133–5142

Chapter 3
Nanopatterning of Functional Metallopolymers via Top-Down Approach

Sze-Chun Yiu, Cheuk-Lam Ho and Wai-Yeung Wong

Abstract Putting metal into macromolecules has drawn immense attention in materials science due to the tunable features and large spectrum of potential applications of these metallopolymers. However, a precise control in metallopolymer nanostructure is always required for tailoring the final application. A variety of nanopatterning methods has been reported in recent years and can be simply classified into either bottom-up or top-down approaches. This chapter will be focused on the general strategy for the fabrication of well-defined nanostructures of metal-containing polymers by using top-down techniques with selected examples.

3.1 Introduction

Metallopolymers (or metal-containing polymers) have been introduced to the family of polymers for more than half a century, but their rapid blossoms have just happened over the last two decades due to the advance in synthetic methodology and adequate characterization [1–8]. Apart from the good processibility advantage of polymer itself, the incorporation of metal center expands the scope of functionalities of the polymer due to the special features arising from the metal ions. By different combination of metal ions and functional ligands, access to a wide range of desired functions was provided, from electroluminescent and photovoltaic devices

S.-C. Yiu · C.-L. Ho (✉) · W.-Y. Wong (✉)
Institute of Molecular Functional Materials, Department of Chemistry and Institute of Advanced Materials, Hong Kong Baptist University, Kowloon Tong, Hong Kong, China
e-mail: clamho@hkbu.edu.hk

W.-Y. Wong
e-mail: wai-yeung.wong@polyu.edu.hk

W.-Y. Wong
Department of Applied Biology and Chemical Technology, The Hong Kong Polytechnic University, Hung Hom, Hong Kong, China

[9–11], catalysis, and stimuli-responsive materials [12] to biomedical and nanoscience applications [13–17]. These functional metal-containing polymeric materials can also be fabricated into patterns in large scale at low cost.

From the structural aspect, metal center could be selectively added in the main chain, side chain, or as a terminal group in the polymer. Because of the complicated electron configuration, multiple coordination number, and different geometry of metal center, a diverse spectrum of chain architectures, such as linear, hyper-branched dendritic, star, and even cyclic structure, can be obtained. In addition, because of the variant binding modes (covalent, coordination, and ionic bond) between metal and organic parts, this would further make metallopolymers distinct from their organic counterparts. By modulating the binding strength of metal ions, structures from dynamic to static mode can be easily achieved, which opens up a new avenue in materials science to mimic complex protein structure in nature. On the other hand, metallo-supramolecular polymer is a class of switchable materials, which has been extensively studied as self-healing materials [18, 19].

Metallopolymers have been widely studied in the past two decades, and their rapid growth is also partly driven by the demand in nanoscience and nanomaterials research. The two main size-dependent effects, surface and quantum effects, have pushed materials scientists in studying the size and shape of the solid-state matter in nanoscale toward potential applications [20, 21]. Furthermore, the gain in controlling the periodicity and long-range order in the nanostructure of metallopolymer is an important issue that needs to be figured out as the nanostructure of the end product eventually determines its functionality. Therefore, much research effort has been devoted to the development of the process in metallopolymer patterning, in which the patterning methods can be classified simply by the direction of strategies: top-down and bottom-up. The former relies on the use of masked or molded stamps to transfer specific pattern to metallopolymer with regard to the corresponding application, such as photolithography and nanoimprint lithography (NIL). The latter one depends on the self-assembling abilities of the metal-containing polymers in order to generate different hierarchical architectures. Block copolymer (BCP) lithography is one of the promising candidates for bottom-up method. In this chapter, the top-down approach toward patterning of metallopolymers will be discussed.

3.2   Top-Down Approaches

There are three main top-down approaches in the metallopolymer patterning. The first approach involves the usage of porous media, such as porous anodic alumina or mesoporous silica (e.g., MSM-41) [22–24], to provide ordered channels to accommodate the metallopolymers, which can be further pyrolyzed to give nanocomposite with great control over particle-size distribution. Generally, the monomer of metallopolymer is first infiltrated into the channels with various loading, followed by polymerization. Taking the porous media of anodic aluminum

oxide (AAO) as an example, the dimensions and patterns of the AAO templates can be simply tuned by the electrochemical parameters during its fabrication, and then, the monomer of metallopolymer can be embedded into the AAO porous before polymerization. Apart from the infiltration of monomer, the template formed by the porous media can also be used as a mold to imprint its porous pattern to the polymer thin film [25].

The second top-down approach that is commonly used is carried out by some conventional lithography, such as electron-beam lithography (EBL), ion-beam lithography, UV-photolithography, or X-ray lithography. Among them, EBL [26–30] and UV [31, 32] lithographic techniques have been widely investigated for metallopolymer patterning. The former one can generate relatively small-sized pattern features but perform in slow speed, whereas the latter one can produce relatively large features and is capable of performing fast processing. In both cases, metallopolymers act as negative resists, which allow pattern to receive directly or transfer to the underlying materials.

Mechanical patterning techniques, including nanosphere lithography (NSL) [33–35], microcontact printing [36], and NIL [37], are another approach for top-down patterning. These techniques are attractive due to their high-throughput and low processing cost, which is suitable for large-area, parallel lithography. Metallopolymers here are employed as printing ink, in which patterns were received from elastic stamps, such as polydimethylsiloxane (PDMS). In the following sections, we are going to discuss different top-down approaches as a tool for metallopolymer patterning by using direct-write EBL, UV-photolithography, NSL, and NIL with selected examples.

3.2.1 Direct-Write Electron-Beam Lithography (EBL)

Direct-write EBL has been used to fabricate mask for the lithography industry and for small-scale device with fine-structure fabrication. In spite of its high processing cost, it is still widely implemented for nanopatterning due to its high feature resolution and high accuracy in pattern positioning. Recently, its resolution capability down to sub-10 nm was revealed [38, 39], which is small enough to meet the demanding feature size targeted in the roadmap of semiconductor industry nowadays. In principle, EBL makes use of high-energy-focused electron beam to create shapes on the electron-sensitive resist surface [40, 41] (Fig. 3.1a). After exposure, either exposed or non-exposed region is selectively removed by solvent due to the change in solubility during patterning formation. The created pattern can then be transferred to the underlying materials via chemical etching or deposition, followed by mask removal.

In the view of metallopolymer, polymer itself can act as a negative-tone resist and allows the direct-write EBL to happen. This process enables us to eliminate several intermediate steps of pattern transfer, so that the overall cost and time required can be reduced (Fig. 3.1b). For example, the mask used in EBL sometimes
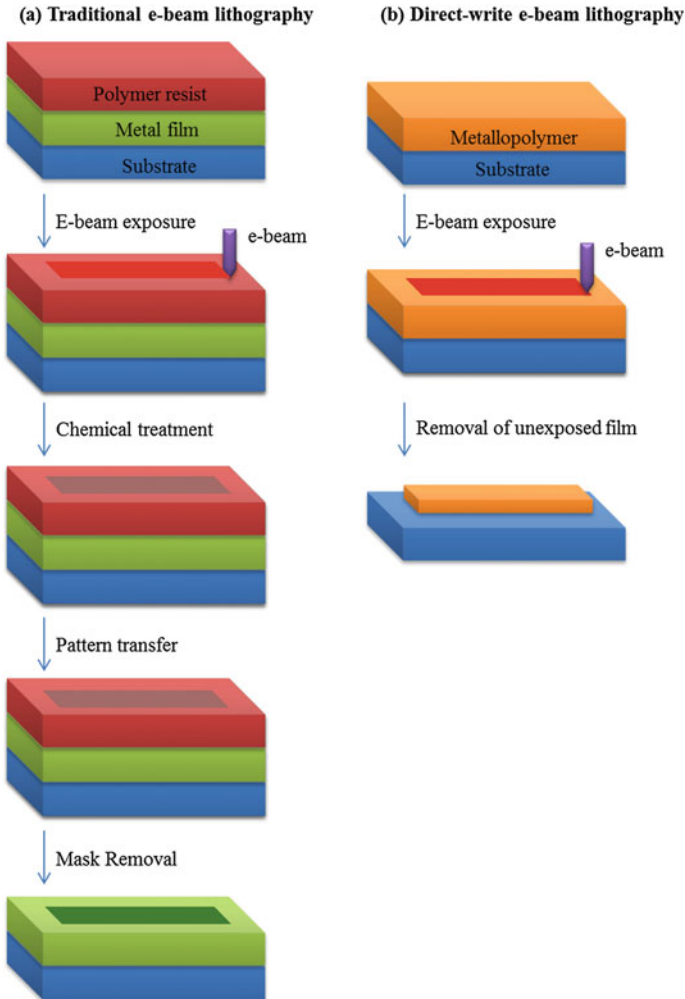
Fig. 3.1 Comparison of **a** traditional EBL versus **b** direct-write EBL. Reproduced from Ref. [42] with kind permission of © 2013 Elsevier

limits the resolution and requires strict control to minimize errors in chemical processing, so direct-write patterning on functional metallopolymer would allow us to have sufficient control over the whole process. During the direct-writing process, metallopolymers are exposed to e-beam for pattern transfer and the exposed region would become insoluble [42]. It is believed that the electron beam would induce the homolytic cleavage of σ-bond and radical dimerization, which results in polymer chain cross-linking and makes the polymer to be insoluble [30]. In 2000, Johnson et al. have reported the use of ruthenium-containing cluster polymer as the negative resist for the fabrication of nanowire with 100 nm thick in width [43]. After that, Ruda and Manners reported the patterning of cobalt, molybdenum, and nickel
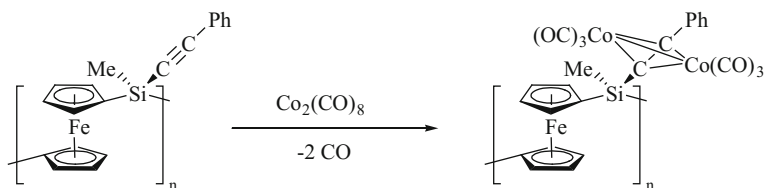
Fig. 3.2 Structure of Co-containing PFS. Reproduced from Ref. [26] with kind permission of © 2004 Wiley-VCH

clustered polyferrocenylsilane (PFS) with the assistance of EBL for their potential use as magnetic materials or catalysts [26–28].

In the system of Co-containing PFS (Fig. 3.2), the polymer solution in toluene was spin-coated ($\sim$200 nm in thickness) on the silicon substrates and then exposed to an e-beam with a dose of 25 mC cm^{-2} and a current of 6 nA. After removal of the unexposed polymers, 0.5 μm × 4.0 μm arrays of bars were left. More than 99% of these bars remained intact by the analysis of scanning electron microscopy (SEM). Pyrolysis of the bars under a nitrogen atmosphere at 900 °C yielded the metallic nanoclusters. After pyrolysis, shape retention of the bars was achieved, but a decrease in height from 210 ± 1 to 74 ± 2 nm was detected under atomic force microscopy (AFM) (Fig. 3.3). In comparison with the hysteresis loops of pyrolyzed bars before and after e-beam patterning, there was a significant increase in coercivity from 42 kA m^{-1} in the unpatterned features to 110 kA m^{-1} in the patterned rectangular bars. On the contrary, the squareness of the loop was reduced after patterning. The authors suggested that the squareness reduction may be the result of the broader distribution of crystallites in the patterned samples. These results showed that EBL can be used for the fabrication of nanoscale magnetic ceramics, which are potentially useful in the fabrication of spintronics and logic circuits.

Few years later, Manners and Wong et al. demonstrated the use of direct-write EBL for the synthesis of FePt alloy nanoparticle (NP) patterns from the bimetallic
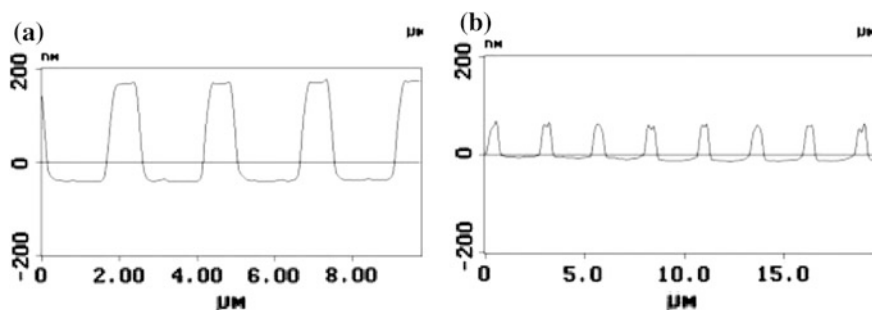
Fig. 3.3 Average sectional analysis images of tapping mode AFM images of patterned bars **a** prior to pyrolysis and **b** following pyrolysis. Reproduced from Ref. [26] with kind permission of © 2004 Wiley-VCH
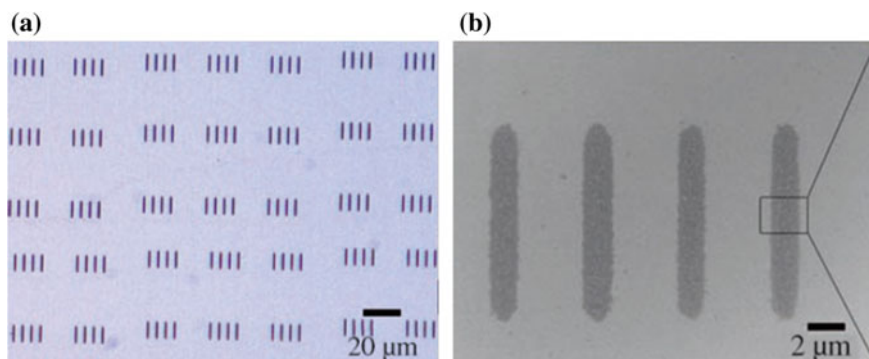
Fig. 3.4 a Optical micrograph of FePt bimetallic metallopolyyne microbars formed by EBL and **b** SEM image of microbars pyrolyzed at 500 °C under nitrogen. Reproduced from Ref. [29] with kind permission of © 2008 Wiley-VCH

metallopolyyne precursor [29]. In this study, a readily solution-processed film-forming bimetallic metallopolyyne precursor was utilized and drop-casted directly on silicon substrate which was then exposed to an e-beam with a dose of 2.5 mC cm^{-2}. After development in dichloromethane, unexposed polymer was removed and an array of microbars (ca. 1.0×10 μm^2) was observed under optical microscope (Fig. 3.4). Pyrolysis of the patterned sample at 500 °C under a nitrogen atmosphere showed randomly oriented magnetic dipoles in heterogeneous ferromagnetic FePt NPs. In addition, the shape of microbars was retained and densely covered by FePt NPs with an average size of 9 nm under SEM.

3.2.2 UV-Photolithography

Unlike the serial writing with EBL or ion-beam lithography, UV-photolithography provides high throughput and is therefore suitable for large-area, parallel fabrication. Similar to the EBL, a photosensitive material is exposed to electromagnetic radiation in order to change the solubility of the material, which is followed by immersing it in an appropriate solvent to either remove the unexposed (negative photoresist) or exposed area (positive photoresist) [40]. As a result, the pattern can be controlled by the photoexposure. In the semiconductor industry, the use of 193-nm laser with immersion lithography or double patterning is commonly employed to produce the node feature size down to 22 nm [44].

In 2004, Manners et al. proposed the use of UV-photolithography for patterning a cobalt-containing PFS [31], in which this polymer was used as a negative photoresist to create micron-size magnetic patterns. The polymer contains both carbonyl and pendent acetylene moieties which was considered to be an excellent candidate as a resist material under UV exposure. The acetylene moieties attached

on PFS were responsible for the thermal cross-linking by cyclotrimerization and coupling reaction between acetylene in the adjacent chains [45]. In addition, the presence of metal carbonyls has proved to have a catalytic effect on the photoin-duced polymerization of acetylene [46–49]. By covering the polymer film with a shadow mask with feature size between 50 and 500 µm followed by the exposure to UV radiation at λ of 350–400 nm with 450 W, a well-defined pattern was observed under optical microscope after development in THF. Further pyrolysis under a nitrogen atmosphere at 900 °C for 5 h yielded Co/Fe alloy magnetic ceramic lines with good shape retention. From both AFM and magnetic force microscope (MFM) images, island morphology was revealed with the height ranging from 5 to 87 nm (Fig. 3.5).

Manners et al. have further extended the usage of UV-photolithography to molybdenum-containing and nickel-containing PFS [28]. Using a mask with 20 µm or above, line patterns were found with a nice shape retention for the molybdenum-containing PFS sample (Fig. 3.6). Interestingly, the nickel-containing PFS was found to give no pattern after UV exposure, which is mainly due to the lack of decarbonylation process in the polymer chains (Fig. 3.7).
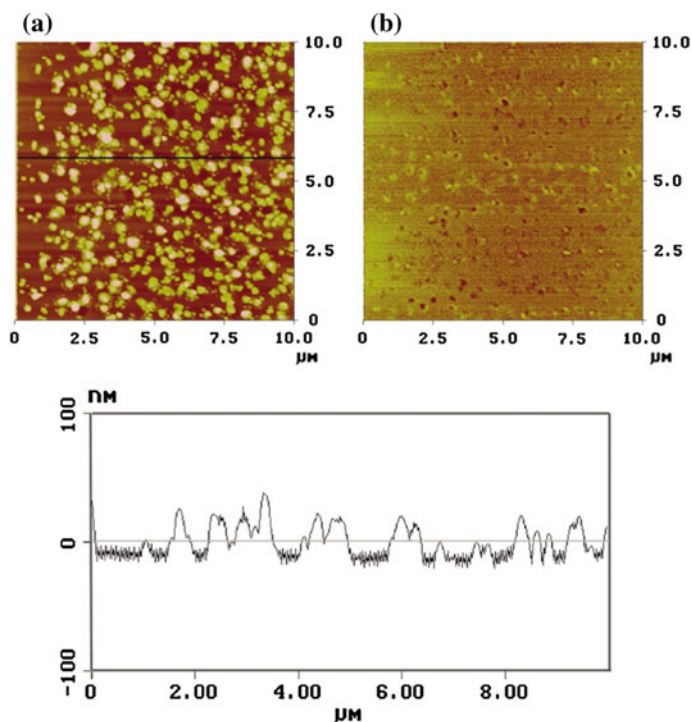
Fig. 3.5 **a** AFM image of a region on a pyrolyzed pattern with (*bottom*) cross-sectional height profile of ceramic islands. **b** MFM image of the same region. Reproduced from Ref. [31] with kind permission of © 2004 Royal Society of Chemistry
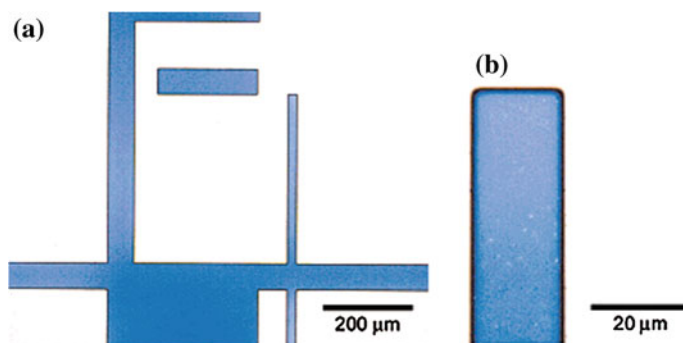
Fig. 3.6 a Bright field optical micrographs of a pattern of Mo-PFS fabricated with UV-photolithography using a chrome contact mask and **b** the smallest line in **a** at higher magnification. Reproduced from Ref. [28] with kind permission of © 2005 American Chemical Society
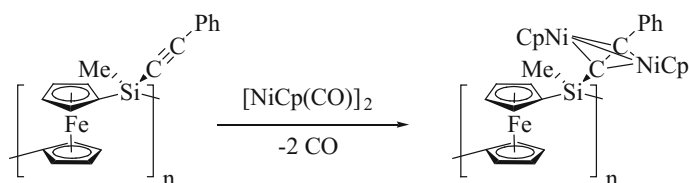
Fig. 3.7 Structure of Ni-containing PFS. Reproduced from Ref. [28] with kind permission of © 2005 American Chemical Society

With the UV-photolithography, the bimetallic alloy NPs are believed to be directly formed from metallopolymers with specific functionalities which have been found to be useful in catalysis and spintronic devices with desired nanostructures.

3.2.3 Nanosphere Lithography (NSL)

Although the radiation-based lithography has been extensively investigated and commercially used in semiconducting industries for more than a few decades, the limited resolution by the wavelength of light in UV-photolithographic approach and high processing cost in EBL partially prohibited these advanced top-down techniques for practical use, especially in the large-size pattern fabrication. In addition, these conventional techniques usually require strict processing environment, such as clean room, because the contaminant in atmosphere would destroy the well-defined pattern fabrication by creating some undesired spots on the pattern.

Alternatively, mechanical patterning may provide a more forgiving approach by the use of a soft mask which may trap the dirt during the compression of mask and
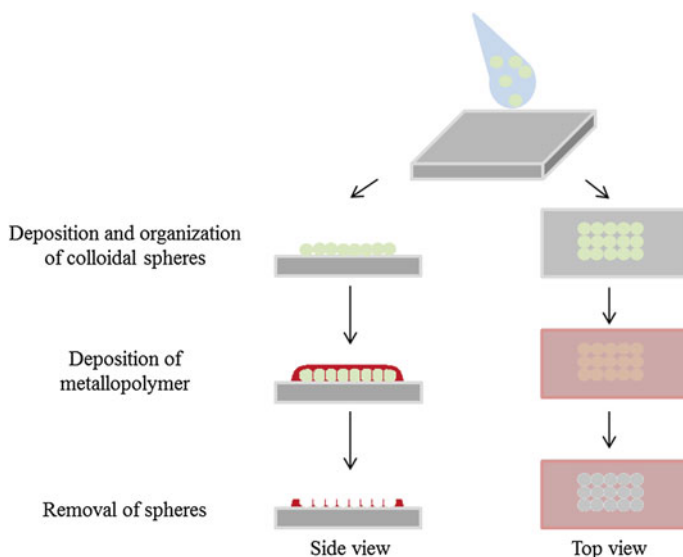
Fig. 3.8 Schematic diagram of NSL process. Reproduced from Ref. [50] with kind permission of © 2013 Hindawi Publishing Corporation

produce the pattern correctly. NSL is one of the promising candidates using homogeneous and ordered arrays of colloidal spheres to pattern the substrates underneath. In general, two steps are included, namely mask preparation and liftoff of mask (Fig. 3.8) [50].

In the first stage, the monodisperse colloidal spheres (e.g., polystyrene or silica beads) are spread on a flat substrate by physical methods, such as dip-coating [51, 52], spin-coating [53, 54], self-assembly in-between two interfaces [55–57], and electrophoretic deposition [58, 59]. Among them, spin-coating potentially provides possibilities of mass production and scaling up by an easy, time-saving implementation with large-area processing ability. Based on the evaporation of solvent with a good control on the spinning condition, defect-free and highly ordered spherical colloids are formed on the substrate surface. After the self-organization, additional materials are being deposited into the small gaps among the spherical bead in order to transfer the pattern from nanospheres to either the additional material or the underlying substrates. Finally, the spheres are being removed by washing with solvent or reactive-ion etching (RIE).

In 2009, Huskens and Vancso et al. reported the use of iron-containing homopolymer, poly(ferrocenylmethylphenylsilane) (PFMPS), as an etch mask material to obtain freestanding porous polyethersulfone membrane (PES) on a silicon substrate via NSL [33]. Membrane material is widely studied with a wide range of applications, e.g., in pharmaceutical industry, water purification, and energy sustainability [60]. Traditional fabrication methods are limited by the narrow range of pore diameters, low porosity, and randomly distributed pores. With the use

of NSL, ordered and hexagonal-packed cylindrical pores can be made. Additional rigidity is provided to the pattern transfer process when metallopolymer is used as an etch mask between the PES and spherical colloids. Instead of the formation of volatile compounds in organic domain after RIE, the formation of metal oxide surface acts as a protective layer to preserve the pattern and allows further pattern transfer directly to the underlying materials [61].

In their study, the silica colloidal particles (∼300 nm in diameter) were spread through the whole surface of mild-oxidized PES on the silicon substrates via capillary-assisted deposition. The PFMPS polymer was then spin-coated on the colloidal layer. After that, argon ion sputtering and aqueous hydrogen fluoride were used to remove the top layer of PFMPS and silica particles, respectively. Further treatment with oxygen plasma and aqueous nitric acid was used to remove unprotected PES area and PFMPS residue. The AFM analysis of the sample surface showed that the original height of particle array was approximately 60 nm, which decreased to 40 nm after infiltration of 80-nm PFS layer (Fig. 3.9). Such decrease was suggested to be the occupation of triangular voids among the spheres by PFMPS. After the exposure to argon ion sputtering, hexagonal-packed circle-shaped spheres were revealed under AFM. Because of the different sputtering rate on silica materials, the diameter of the spheres was found to be smaller than that of the original spheres. After removal of the unpatterned residue, the highly ordered PES membrane was released by dissolving the sacrificial layer (i.e., cellulose acetate) between PES and silicon substrate. The intact and highly porous membrane was found to be 500 nm in thickness and 230 nm in pore size, which was able to be picked up by tweezers and transferred to another substrate (Fig. 3.10). In this demonstration, the metal-containing polymer acted as the etch mask material and protective layer to retain the underneath materials during RIE. As a result, pores were formed in the PES membrane during pattern transfer.

Extension of the usage of PFMPS with silica colloidal particle having different sizes to fabricate both freestanding PES membrane and patterned silicon substrate was carried out by the same research group [34]. For the PES membrane fabrication, 150-, 300-, and 500-nm silica particles were employed to generate negative replica array in PES layers in a similar manner aforementioned (Fig. 3.11a). In the case of patterned silicon substrate, silica particles with diameters of 60, 300, and 500 nm were used to cover the silicon substrate surface. With subsequent infiltration of PFMPS and a series of etching and washing steps, a silica mold was formed for further NIL on another silicon substrate spin-coated with poly(methyl methacrylate) (PMMA) (Fig. 3.11b). The authors first demonstrated the effect of particle sizes on patterned silicon substrate. By varying the size of silica particles employed, both pores' size and periodicity can be controlled. The larger the silica particle size, the larger the feature size on the silicon substrate. However, the quality of the pattern can be greatly affected by the size distribution of colloidal particles. In addition, the hexagonal pores may somehow vary in shape from hexagonal to spherical.
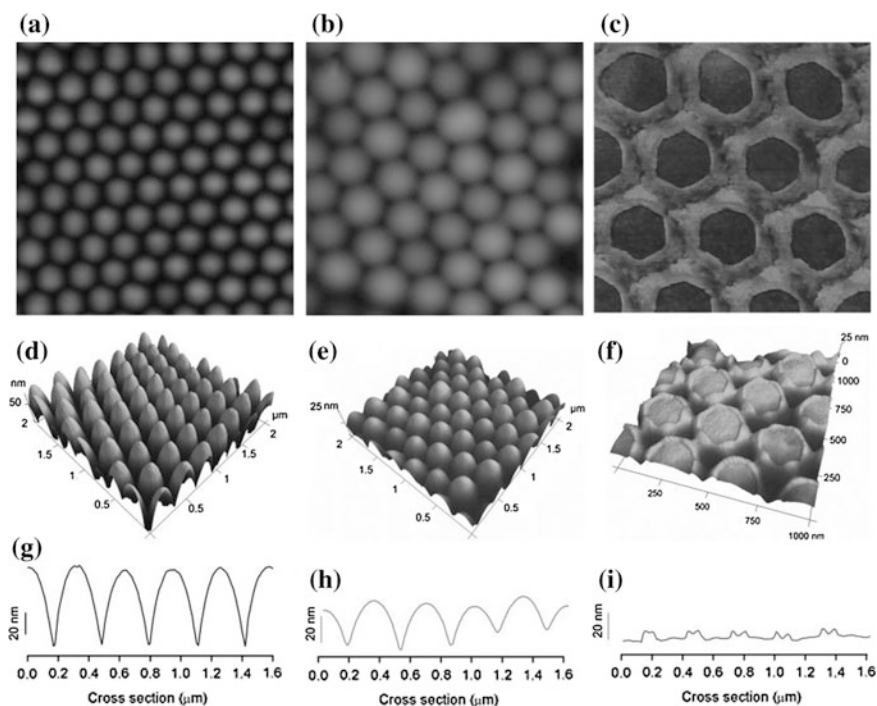
Fig. 3.9 AFM height images of **a** 300-nm colloidal sphere array, **b** array infiltrated with PFMPS, and **c** array after argon ion sputtering; **d–f** are the corresponding 3D AFM images for **a–c,** and **g–i** are the corresponding cross-sectional height profile. Reproduced from Ref. [33] with kind permission of © 2009 Wiley-VCH
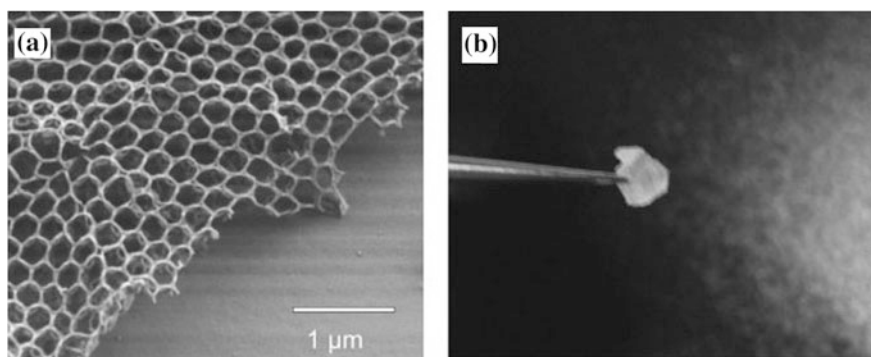
Fig. 3.10 **a** SEM image of PES membrane was being peeled off and transferred to a substrate. **b** Optical photograph of a piece of PES membrane picked up by tweezers. Reproduced from Ref. [33] with kind permission of © 2009 Wiley-VCH
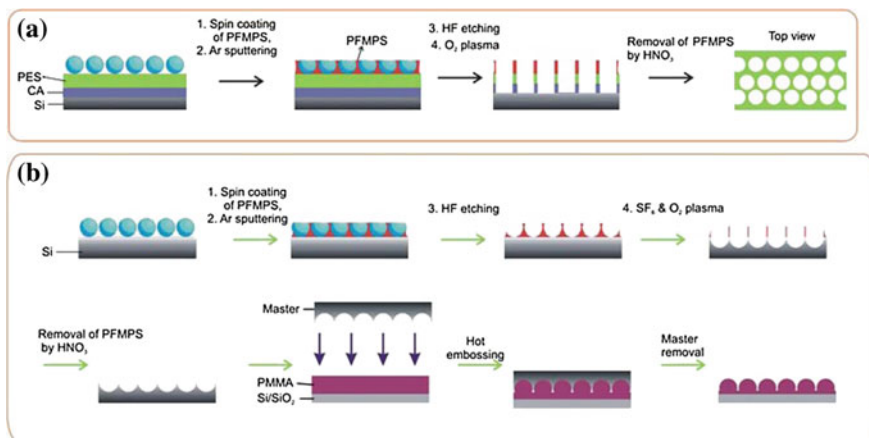
Fig. 3.11 Schematic diagrams of **a** negative replication, for the formation of freestanding PES membrane, and **b** positive replication, for the formation of patterned silicon substrate. Reproduced from Ref. [34] with kind permission of © 2010 Royal Society of Chemistry

Fig. 3.12 SEM images of silicon mold surface after SF_6/O_2 etching treatment for **a** 10 s, **b** 30 s, and **c** 60 s. **d** Plot of the feature size against etching duration. Reproduced from Ref. [34] with kind permission of © 2010 Royal Society of Chemistry
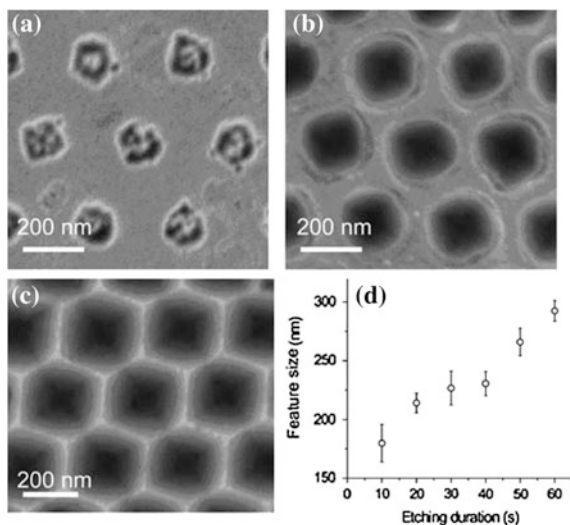
Alternatively, the time of RIE treatment with SF_6/O_2 (sulfur hexafluoride/oxygen) can also alter the pore size of hole created. It was found that the longer the etching duration was used, the larger the feature size was obtained (Fig. 3.12). To imprint the PMMA, the mold was covered with a layer of 1H, 1H, 2H, 2H-perfluorodecyltriethoxysilane (PFDTS) first and was then pressed against the PMMA to yield complementary patterns with similar shape and height
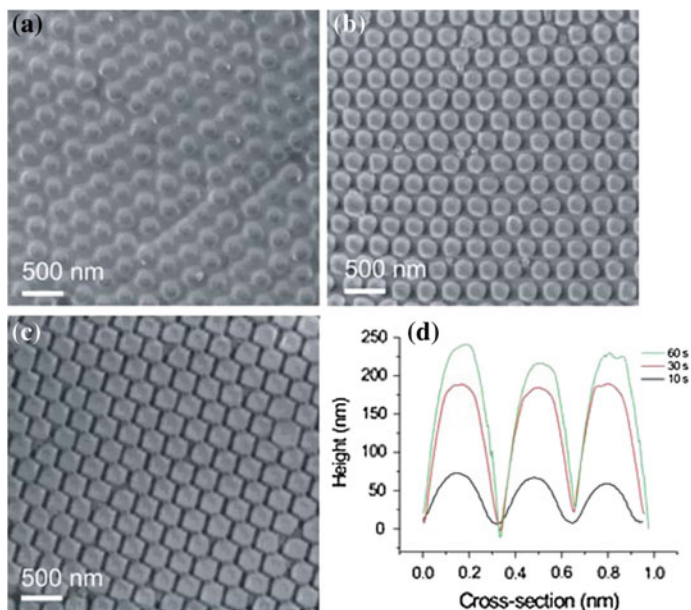
Fig. 3.13 SEM images of imprinted PMMA with silicon mold with SF_6/O_2 etching treatment for **a** 10 s, **b** 30 s, and **c** 60 s, and **d** AFM height profile of imprinted PMMA with different etching duration. Reproduced from Ref. [34] with kind permission of © 2010 Royal Society of Chemistry

(Fig. 3.13). From the SEM and AFM images, the replicated PMMA structures were proved to be almost the same in pattern and size as the mold.

With the use of metallopolymer in NSL, silica particles were used as an inversion mask rather than etch mask, which can provide a simple and rapid approach to pattern membrane materials and generate patterned silicon substrates for NIL use. Taking the high etching resistance advantage of organometallic macromolecules, polymeric patterns obtained by NSL can be directly transferred to the underlying substrates in a single step. It further eliminates the complicated process in metal evaporation and liftoff process. As a result, regular and periodic structures can be easily fabricated over a large area.

In another example, Cosnier et al. have reported the use of NSL together with electropolymerization to nanopattern an electrogenerated photosensitive ruthenium-containing polymer [35]. The electrochemical and photoelectrochemical properties of the metallopolymer have been studied, and the improved photoelectrochemical properties stemming from varying the nanostructure were demonstrated.

3.2.4 Nanoimprint Lithography (NIL)

Apart from NSL, NIL is a mechanical patterning technique to make use of a mechanical mold (e.g., PDMS) to shape the materials into certain features, which potentially provides high resolution in large-area fabrication with a low processing cost [62]. Thus, NIL has been regarded as one of the next-generation cost-effective methods for semiconductors manufacturing and magnetic storage disks fabrication [63]. During the NIL process, the imprinted materials were physically deformed under a mold and regular pattern was formed according to the pattern on the mold. The material underneath can be further cured by UV light or high temperature [37, 64] to obtain an intact structure. In contrast to photolithography, the resolution is not limited by the wave diffraction or scattering or interference in a resist [65], but by the ability of making ultra-small features on the mold by some other techniques. During the nanopatterning of metallopolymers, polymers imprinted were used as both imprint resists and functional materials [66]. This reduced the etching or liftoff process so as to minimize the defects in pattern transfer.

Wong and co-workers have demonstrated the use of NIL to pattern a polyferroplatinyne polymer, followed by pyrolysis to generate FePt NPs for the potential use as bit-patterned media (BPM) in magnetic data storage devices [67] (Fig. 3.14). In contrary to the traditional imprinting process, the metal-containing polymer was directly imprinted in its liquid phase through dropwise addition onto the substrate, without any spinning and patterning of photoresist or subsequent etching/liftoff of the polymer film (Fig. 3.15). This makes the single-step fabrication possible. In this study, the PDMS mold with either line array (740-nm periodicity and 350-nm feature size) or dot array (500-nm periodicity and 250-nm feature size) pattern was used to pattern the casting polyferroplatinyne solution on the silicon substrate, and UV light was subsequently exposed onto the patterned substrate to transform the polymers into some higher molecular weight materials by cross-linking in the solid state.

The SEM analysis illustrated the imprinted dot arrays of the FePt-containing metallopolymer with similar diameter and periodicity (Fig. 3.16a). Finally, the

Fig. 3.14 Solution processable FePt-containing metallopolymer. Reproduced from Ref. [67] with kind permission of © 2012 Wiley-VCH
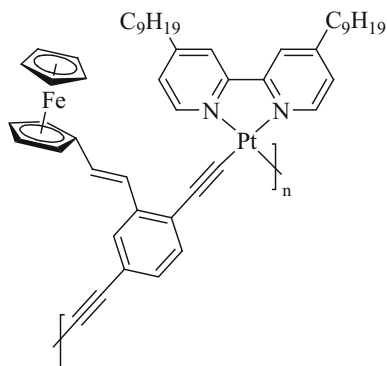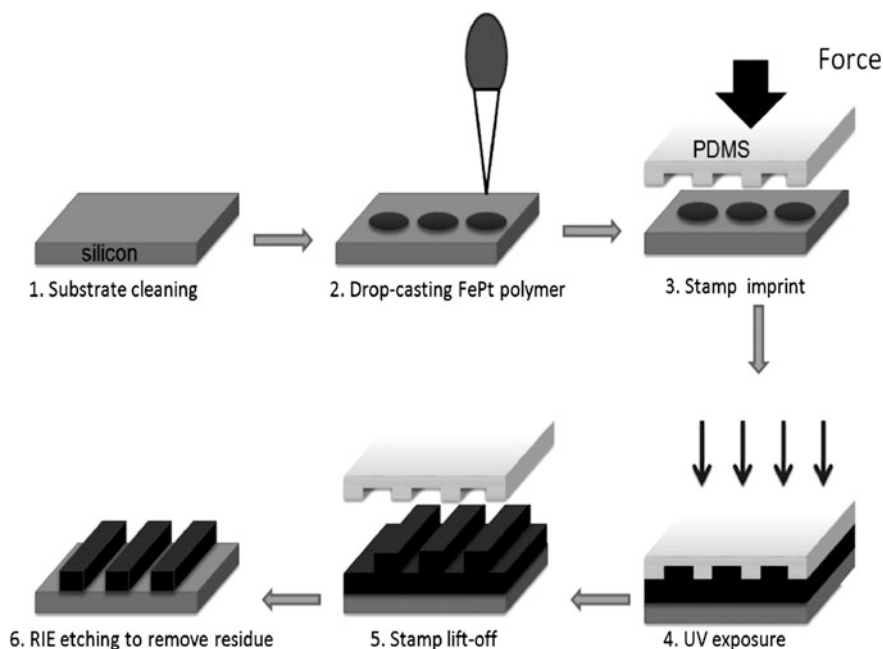
Fig. 3.15 Schematic illustration of the fabrication of large-area nanostructures from the FePt-based bimetallic metallopolymer by NIL. Reproduced from Ref. [67] with kind permission of © 2012 Wiley-VCH

mold was lifted off, and the patterned film was annealed at 800 °C under argon to generate the desired $L1_0$ phase FePt NPs. The line array pattern was preserved after the high-temperature annealing, whereas the height of dot array was between 5 and 8 nm (Fig. 3.16b), which is comparatively small to the original mold with a height of 80 nm. The authors suggested that this may be due to the collapse of materials after pyrolysis. From the bulk pyrolysis, it was confirmed that the average size of FePt NPs formed was about 4.6 ± 1.2 nm with a narrow standard deviation. The magnetic property of the patterned sample was investigated by vibrating sample magnetometer (VSM). The coercivity measured at room temperature was about 1.4 T for the dot patterns (Fig. 3.16c) which was comparable to that in the magnetic data storage media used at that moment.

To further demonstrate the external field writing of patterned FePt NPs, field annealing in the −Z direction was demonstrated with an external magnetic field of 1 T at the same annealing temperature for 1 h. To switch the Z direction to the opposite side, an external magnetic field of 1.8 T was applied at room temperature. The corresponding 3D MFM images were taken to show the magnetic signal over the sample with area of 5×5 μm (Fig. 3.17). Both images showed the same periodicity of dot array pattern but in opposite Z direction. This prototype provided an areal density of 2.58 Gb in^{-2}, which can offer BPM with a storage density
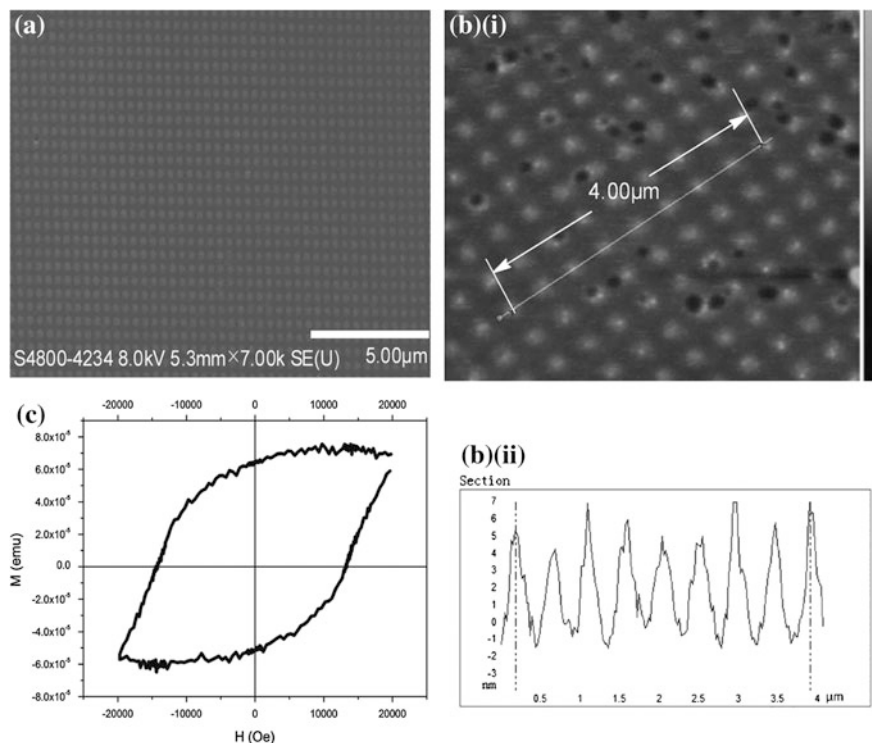
Fig. 3.16 **a** SEM image of the nanoimprinted dot array pattern of FePt-containing metallopolymer. **b** *I* AFM image of nanoimprinted dot array FePt NPs after pyrolysis. *II* Cross-sectional analysis of the measured distance as indicated in **b**(*I*). **c** Hysteresis loop measurement by VSM at room temperature in the out-of-plane direction of the nanoimprinted dot array pattern of FePt NPs after pyrolysis. Reproduced from Ref. [67] with kind permission of © 2012 Wiley-VCH

beyond 1 Tb in^{-2} without the use of sophisticated technologies. Recently, the same groups further demonstrated the generation of $L1_0$ FePt NPs by nanoimprinting the blend of iron- and platinum-containing homopolymers [68] and the synthesis of $L1_0$ CoPt NPs by imprinting cobalt-/platinum-containing bimetallic polymer for the ferromagnetic applications [69]. This rapid nanoimprinting method is not just limited in patterning magnetic NPs, but also for the surface patterning in photovoltaic, light-emitting, and biochemical sensing application.

3.3 Conclusions

In this chapter, different top-down approaches for the nanofabrication of metal-containing polymers have been illustrated and selected examples have been presented. In the top-down approach, the sophisticated EBL, well-developed
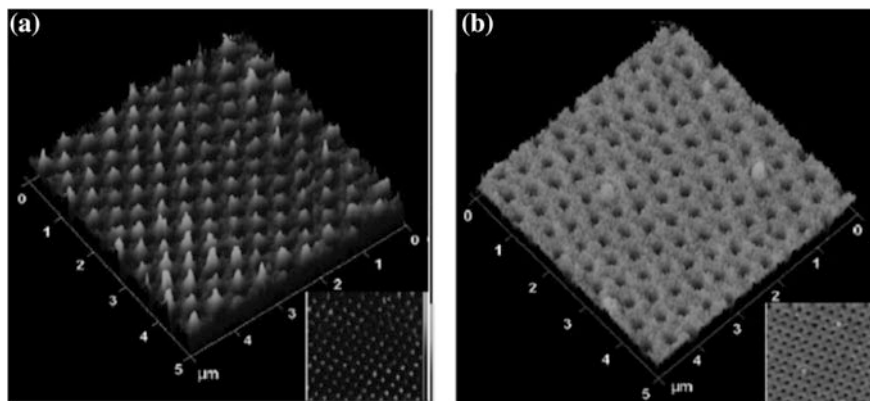
Fig. 3.17 **a** MFM images of the imprinted dot array pattern of FePt NPs field-annealed in the −Z direction and **b** +Z direction. Reproduced from Ref. [67] with kind permission of © 2012 Wiley-VCH

UV-photolithography, easily processed NSL, and NIL have provided the direct way to transfer pattern to metallopolymer through focused electron beam, UV light, colloidal spheres, and mechanical mold, respectively. They are particularly useful for the patterning of homopolymers or random copolymers due to the lack of microphase separation in the polymer. These fabrication techniques are believed to be promising for metallopolymer patterning and important for their use in different applications.

References

1. Arimoto FS, Haven AC (1955) Derivatives of dicyclopentadienyliron. J Am Chem Soc 77 (23):6295–6297
2. Pittman CU, Lai JC, Vanderpool DP et al (1970) Polymerization of ferrocenylmethyl acrylate and ferrocenylmethyl methacrylate. Characterization of their polymers and their polymeric ferricinium salts. Extension to poly(ferrocenylethylene). Macromolecules 3(6):746–754
3. Takahashi S, Murata E, Kariya M et al (1979) A new liquid-crystalline material. Transition metal-poly(yne) polymers. Macromolecules 12(5):1016–1018
4. Abd-El-Aziz AS, Manners I (2007) Frontiers in transition metal-containing polymers. John Wiley & Sons, Hoboken
5. Whittell GR, Manners I (2007) Metallopolymers: new multifunctional materials. Adv Mater 19(21):3439–3468

6. Abd-El-Aziz AS, Shipman PO, Boden BN et al (2010) Synthetic methodologies and properties of organometallic and coordination macromolecules. Prog Polym Sci 35:714–836

7. Hardy CG, Zhang J, Yan Y et al (2014) Metallopolymers with transition metals in the side-chain by living and controlled polymerization techniques. Prog Polym Sci 39(10):1742–1796

8. Zhou J, Whittell GR, Manners I (2014) Metalloblock copolymers: new functional nanomaterials. Macromolecules 47(11):3529–3543

9. Ho C-L, Wong W-Y (2011) Metal-containing polymers: facile tuning of photophysical traits and emerging applications in organic electronics and photonics. Coord Chem Rev 255(21–22):2469–2502

10. Happ B, Winter A, Hager MD et al (2012) Photogenerated avenues in macromolecules containing Re(I), Ru(II), Os(II), and Ir(III) metal complexes of pyridine-based ligands. Chem Soc Rev 41(6):2222–2255

11. Xiang J, Ho C-L, Wong W-Y (2015) Metallopolymers for energy production, storage and conservation. Polym Chem 6(39):6905–6930

12. Feng X, Zhang K, Hempenius MA et al (2015) Organometallic polymers for electrode decoration in sensing applications. RSC Adv 5(129):106355–106376

13. MacLachlan MJ, Ginzburg M, Coombs N et al (2000) Shaped ceramics with tunable magnetic properties from metal-containing polymers. Science 287(5457):1460–1463

14. Cheng JY, Ross CA, Chan VZH et al (2001) Formation of a cobalt magnetic dot array via block copolymer lithography. Adv Mater 13(15):1174–1178

15. Whittell GR, Hager MD, Schubert US et al (2011) Functional soft materials from metallopolymers and metallosupramolecular polymers. Nat Mater 10(3):176–188

16. Al-Badri ZM, Maddikeri RR, Zha Y et al (2011) Room temperature magnetic materials from nanostructured diblock copolymers. Nat Commun 2:482

17. Yan Y, Zhang J, Ren L et al (2016) Metal-containing and related polymers for biomedical applications. Chem Soc Rev 45:5232

18. Bode S, Zedler L, Schacher FH et al (2013) Self-healing polymer coatings based on crosslinked metallosupramolecular copolymers. Adv Mater 25(11):1634–1638

19. Sandmann B, Happ B, Kupfer S et al (2015) The self-healing potential of triazole–pyridine-based metallopolymers. Macromol Rapid Commun 36(7):604–609

20. Roduner E (2006) Size matters: why nanomaterials are different. Chem Soc Rev 35(7):583–592

21. Ramanathan M, Darling SB (2013) Nanofabrication with metallopolymers-recent developments and future perspectives. Polym Int 62(8):1123–1134

22. MacLachlan MJ, Aroca P, Coombs N et al (1998) Ring-opening polymerization of a [1] silaferrocenophane within the channels of mesoporous silica: Poly(ferrocenylsilane)-MCM-41 precursors to magnetic iron nanostructures. Adv Mater 10(2):144–149

23. MacLachlan MJ, Ginzburg M, Coombs N et al (2000) Superparamagnetic ceramic nanocomposites: synthesis and pyrolysis of ring-opened poly(ferrocenylsilanes) inside periodic mesoporous silica. J Am Chem Soc 122(16):3878–3891

24. Ginzburg-Margau M, Fournier-Bidoz S, Coombs N et al (2002) Formation of organometallic polymer nanorods using a nanoporous alumina template and the conversion to magnetic ceramic nanorods. Chem Commun 24:3022–3023

25. Liu K, Fournier-Bidoz S, Ozin GA et al (2009) Highly ordered magnetic ceramic nanorod arrays from a polyferrocenylsilane by nanoimprint lithography with anodic aluminum oxide templates. Chem Mater 21(9):1781–1783

26. Clendenning SB, Aouba S, Rayat MS et al (2004) Direct writing of patterned ceramics using electron-beam lithography and metallopolymer resists. Adv Mater 16(3):215–219

27. Greenberg S, Clendenning SB, Liu K et al (2005) Synthesis and lithographic patterning of polycarbosilanes with pendant cobalt carbonyl clusters. Macromolecules 38(6):2023–2026

28. Chan WY, Clendenning SB, Berenbaum A et al (2005) Highly metallized polymers: synthesis, characterization, and lithographic patterning of polyferrocenylsilanes with pendant cobalt, molybdenum, and nickel cluster substituents. J Am Chem Soc 127(6):1765–1772

29. Liu K, Ho C-L, Aouba S et al (2008) Synthesis and lithographic patterning of FePt nanoparticles using a bimetallic metallopolyyne precursor. Angew Chem Int Ed 47(7): 1255–1259

30. Cha S-H, Huh G, Lee J-C (2014) Preparation of copper containing methacrylic polymers and their application for the copper patterns. J Ind Eng Chem 20(2):682–688

31. Cheng AY, Clendenning SB, Yang G et al (2004) UV photopatterning of a highly metallized, cluster-containing poly(ferrocenylsilane). Chem Commun 7:780–781

32. Satyanarayana VSV, Singh V, Kalyani V et al (2014) A hybrid polymeric material bearing a ferrocene-based pendant organometallic functionality: synthesis and applications in nanopatterning using EUV lithography. RSC Adv 4(104):59817–59820

33. Acikgoz C, Ling XY, Phang IY et al (2009) Fabrication of freestanding nanoporous polyethersulfone membranes using organometallic polymer resists patterned by nanosphere lithography. Adv Mater 21(20):2064–2067

34. Ling XY, Acikgoz C, Phang IY et al (2010) 3D ordered nanostructures fabricated by nanosphere lithography using an organometallic etch mask. Nanoscale 2(8):1455–1460

35. Fritea L, Haddache F, Reuillard B et al (2014) Electrochemical nanopatterning of an electrogenerated photosensitive poly-[trisbipyridinyl-pyrrole ruthenium(II)] metallopolymer by nanosphere lithography. Electrochem Commun 46:75–78

36. Ginzburg M, MacLachlan MJ, Yang SM et al (2002) Genesis of nanostructured, magnetically tunable ceramics from the pyrolysis of cross-linked polyferrocenylsilane networks and formation of shaped macroscopic objects and micron scale patterns by micromolding inside silicon wafers. J Am Chem Soc 124(11):2625–2639

37. Acikgoz C, Vratzov B, Hempenius MA et al (2009) Nanoscale patterning by UV nanoimprint lithography using an organometallic resist. ACS Appl Mater Interfaces 1(11):2645–2650

38. Hu W, Sarveswaran K, Lieberman M et al (2004) Sub-10 nm electron beam lithography using cold development of poly(methylacrylate). J Vac Sci Technol B 22(4):1711–1716

39. Manfrinato VR, Zhang L, Su D et al (2013) Resolution limits of electron-beam lithography toward the atomic scale. Nano Lett 13(4):1555–1558

40. Acikgoz C, Hempenius MA, Huskens J et al (2011) Polymers in conventional and alternative lithography for the fabrication of nanostructures. Eur Polym J 47(11):2033–2052

41. Chen Y (2015) Nanofabication by electron beam lithography and its applications: a review. Microelectron Eng 135:57–72

42. Lee SW, Sankaran RM (2013) Direct writing via electron-driven reactions. Mater Today 16 (4):117–122

43. Johnson BFG, Sanderson KM, Shephard DS et al (2000) Electron-beam induced formation of nanoparticle chains and wires from a ruthenium cluster polymer. Chem Commun 14: 1317–1318

44. Pease RF, Chou SY (2008) Lithography and other patterning techniques for future electronics. Proc IEEE 96(2):248–270

45. Swanson SA, Fleming WW, Hofer DC (1992) Acetylene-terminated polyimide cure studies using carbon-13 magic-angle spinning NMR on isotopically labeled samples. Macromolecules 25(2):582–588

46. Masuda T, Kuwane Y, Yamamoto K et al (1980) Polymerization of acetylene derivatives induced by UV irradiation via metal carbonyls. Polym Bull 2(12):823–827

47. Masuda T, Yamamoto K, Higashimura T (1982) Polymerization of phenylacetylene induced by uv irradiation of group 6 transition metal carbonyls. Polymer 23(11):1663–1666

48. Landon SJ, Shulman PM, Geoffroy GL (1985) Photoassisted polymerization of terminal alkynes by $W(CO)_6$ involving catalyst generation by an alkyne to vinylidene ligand rearrangement. J Am Chem Soc 107(23):6739–6740

49. Badarau C, Wang ZY (2003) Photoinitiated cross-linking of acetylene-containing polymers in the presence of tungsten hexacarbonyl. Macromolecules 36(19):6959–6961

50. Colson P, Henrist C, Cloots R (2013) Nanosphere lithography: a powerful method for the controlled manufacturing of nanomaterials. J Nanomater 2013:19

51. Dimitrov AS, Nagayama K (1996) Continuous convective assembling of fine particles into two-dimensional arrays on solid surfaces. Langmuir 12(5):1303–1311
52. Nagao D, Kameyama R, Kobayashi Y et al (2007) Multiformity of particle arrays assembled with a simple dip-coating. Colloids Surf A 311(1–3):26–31
53. Deckman HW, Dunsmuir JH (1982) Natural lithography. Appl Phys Lett 41(4):377–379
54. Hulteen JC, Van Duyne RP (1995) Nanosphere lithography: a materials general fabrication process for periodic particle array surfaces. J Vac Sci Technol A 13(3):1553–1558
55. Rybczynski J, Ebels U, Giersig M (2003) Large-scale, 2D arrays of magnetic nanoparticles. Colloids Surf A 219(1–3):1–6
56. Ruan W-D, Lü Z-C, Ji N et al (2007) Facile fabrication of large area polystyrene colloidal crystal monolayer via surfactant-free Langmuir–Blodgett technique. Chem Res Chin U 23 (6):712–714
57. Goldenberg LM, Wagner J, Stumpe J et al (2002) Simple method for the preparation of colloidal particle monolayers at the water/alkane interface. Langmuir 18(14):5627–5629
58. Giersig M, Mulvaney P (1993) Preparation of ordered colloid monolayers by electrophoretic deposition. Langmuir 9(12):3408–3413
59. Rogach AL, Kotov NA, Koktysh DS et al (2000) Electrophoretic deposition of latex-based 3D colloidal photonic crystals: a technique for rapid production of high-quality opals. Chem Mater 12(9):2721–2726
60. Le NL, Nunes SP (2016) Materials and membrane technologies for water and energy sustainability. Sustain Mater Technol 7:1–28
61. Lammertink RGH, Hempenius MA, Chan VZH et al (2001) Poly(ferrocenyldimethylsilanes) for reactive ion etch barrier applications. Chem Mater 13(2):429–434
62. Xin JZ, Lee FK, Li SYW et al (2011) Transfer imprint lithography using a soft mold. Microelectron Eng 88(8):2632–2635
63. Chou SY, Krauss PR, Renstrom PJ (1995) Imprint of sub-25 nm vias and trenches in polymers. Appl Phys Lett 67(21):3114–3116
64. Kooy N, Mohamed K, Pin LT et al (2014) A review of roll-to-roll nanoimprint lithography. Nanoscale Res Lett 9(1):1–13
65. Dauksher WJ, Le NV, Ainley ES et al (2006) Nano-imprint lithography: templates, imprinting and wafer pattern transfer. Microelectron Eng 83(4–9):929–932
66. Li G, Dong Q, Xin J et al (2013) Patterning micro- and nano-structured FePt by direct imprint lithography. Microelectron Eng 110:192–197
67. Dong Q, Li G, Ho C-L et al (2012) A polyferroplatinyne precursor for the rapid fabrication of L10-FePt-type bit patterned media by nanoimprint lithography. Adv Mater 24(8):1034–1040
68. Dong Q, Li G, Ho C-L et al (2014) Facile generation of $L1_0$-FePt nanodot arrays from a nanopatterned metallopolymer blend of iron and platinum homopolymers. Adv Funct Mater 24(6):857–862
69. Dong Q, Qu W, Liang W et al (2016) Metallopolymer precursors to $L1_0$-CoPt nanoparticles: synthesis, characterization, nanopatterning and potential application. Nanoscale 8(13): 7068–7074

Chapter 4
Organic Porous Polymer Materials: Design, Preparation, and Applications

Liangxiao Tan, Kewei Wang, Qingyin Li, Yuwan Yang, Yunfei Liu and Bien Tan

Abstract The synthesis of porous organic polymer materials with nanoscale range has long been an important science subject and received an increasing level of research interest owing to their essential properties merging both of the porous materials and polymers such as low skeleton density, processability, easy functionality, and diverse synthetic methods. In this chapter, several porous polymer materials including covalent organic frameworks (COFs), hypercrosslinked polymers (HCPs), conjugated microporous polymers (CMPs), polymers of intrinsic microporosity (PIMs), and macroporous polymers from high internal phase emulsions (HIPEs) will be introduced as well as their diversiform synthetic methods and potential applications including gas storage, carbon capture, separation, catalysis, sensing, energy storage and conversion.

4.1 Introduction

Design, construction, and utilization of advanced functional materials with special porous architectures in micro- and nanoscale range have long been an important science subject. Porous polymers especially have attracted a large amount of research attention owing to their unique characteristics that combine both porous materials and polymers [1]. First of all, porous polymers are able to be designed and prepared with high surface area and well-controlled pore structure [2–4]. Secondly, porous polymers are processable due to their polymer chain essence. For instance, they can be easily synthesized with various micromorphology such as hollow nanosphere [5–7], thin film [8–10], and monolithic form [11–15]. Some kinds of porous polymers may even be dissolved in common organic solvents for further solvent-based process technology, however, without losing their porosity [16–18].

L. Tan · K. Wang · Q. Li · Y. Yang · Y. Liu · B. Tan (✉)
School of Chemistry and Chemical Engineering, Huazhong University of Science
and Technology, Wuhan 430074, China
e-mail: bien.tan@mail.hust.edu.cn

Furthermore, a wide range of optional organic building blocks as well as multitudinous synthesis methods enable the resulting porous polymers facile to incorporate multiple chemical functionalities within networks or pore surface which is far different from inorganic porous materials such as zeolite, carbon, and silica [4, 19–22]. Besides, porous polymer frameworks are composed of light elements which provide a weight advantage in many applications.

For the porous polymers, surface area and pore size are the two most important factors that affect their performance. According to the IUPAC recommendation, pores can be divided into the following three species: micropores with pore size less than 2 nm; mesopores with pore size between 2 and 50 nm; and macropores with pore size larger than 50 nm [23]. Usually, smaller pore size contributes larger adsorption amount of sorbate molecules at lower pressures which results in a higher surface area [24]. To introduce micropore into the polymer matrix, rigid aromatic building blocks are necessary to be adopted directly linking together or by other rigid groups such as alkynes [25] or alkenes [26] in order to construct a fixed rigid structure which prevent the polymer chains from collapsing. After the removal of solvent, the space that solvent filled previously will be permanent pore [27].

According to the synthetic methods and the chemical structure, microporous organic polymers (MOPs) can be roughly classified as covalent organic frameworks (COFs) [3, 28], hypercrosslinked polymers (HCPs) [29, 30], conjugated microporous polymers (CMPs) [31, 32], polymers of intrinsic microporosity (PIMs) [33, 34], covalent triazine-based frameworks (CTFs) [35, 36], porous aromatic frameworks (PAFs) [2, 37], and so on. Among them, COFs are a class of crystalline networks with well-ordered structures and uniform pore size that related to their monomers. COFs are usually formed via reversible bond-forming chemistry such as boronic acids' self-condensation or with diols to form bromine rings by which the most thermodynamically stable structure can exist [27].

Some other polymers possess rather amorphous networks with disordered structure and normally a wider pore size range [38]. Amorphous networks always require metal-catalyzed high-yielding reactions to achieve entire condensation as possible. For example, Lewis acid catalytic Friedel–Crafts alkylation reaction is usually for HCPs synthesis [29], and CMPs are prepared by noble metal catalytic Sonographer–Ghaghara coupling, Yamamoto coupling, Suzuki coupling reactions, and so on [32].

In this chapter, we mainly discuss the following microporous organic polymers including covalent organic frameworks, hypercrosslinked polymers, conjugated microporous polymers and polymers of intrinsic microporosity as well as some macroporous polymers based on polymerization of high internal phase emulsions (polyHIPEs). Not only the design and synthetic strategies, but also the potential applications of these porous polymers will be introduced in detail including gas storage, carbon capture, separation, catalysis, sensing, energy storage, and conversion.

4.2 Covalent Organic Frameworks

Covalent organic frameworks are a new class of porous covalent crystalline organic networks based on dynamic covalent chemistry which leads to the process of forming, broking, and reforming covalent bonds [39]. Generally, linking organic molecules by covalent bonds into extended networks typically generates amorphous, disordered solid materials. The ability to develop strategies for obtaining crystals of such solids is of interest because it opens the way for precise control of the geometry and functionality of the extended structure, and the stereochemical orientation of its constituents. The attainment of crystals is done by several techniques in which a balance is struck between the thermodynamic reversibility of the linking reactions and their kinetics. This success has led to the expansion of COFs including organic units linked by these strong covalent bonds: B–O, C–N, B–N, and B–O–Si. Compared to the amorphous porous organic polymers (PIMs, CMPs, and HCPs), COFs have permanent geometry, and it is possible to predict the structures of the resulting COFs using powder X-ray diffraction (PXRD) techniques. For this advantage, it can be directed to the synthesis of COFs structures by design and for their formation with desired composition, pore size, and aperture, which make COFs an attractive class of new porous materials. In 2005, Yaghi and co-workers demonstrated the utilization of the topological design principle in their synthesis of covalent-linked crystalline porous organic frameworks [28]. Since this seminal work, the chemical synthesis of COFs has progressed significantly, and been used in gas storage, solid supports for catalysis, and optoelectronic devices. In this account, we outline how this chemistry was used to prepare crystalline COFs and highlight their synthesis, characterization, and applications.

4.2.1 Design and Synthesis

The synthesis of COFs could be designed through the principles of reticular chemistry [40–44]. Normally, the basic concerns for design mainly focus on the porosity and the structural regularity. In this regard, much experience has been obtained from the synthesis of metal-organic frameworks (MOFs). However, the crystalline framework of MOFs via the coordination bonds is much easier formed than to fabricate crystalline COFs via the covalent bonds. In order to form the crystalline solid, the formation of linkages should be well reversible and the reaction rate must be on a timescale that allows for self-correction of defects [45].

4.2.1.1 Design Principles

Crystalline COFs are synthesized in condensation reactions of organic building blocks, with geometry shape. The structure of the building blocks must meet two
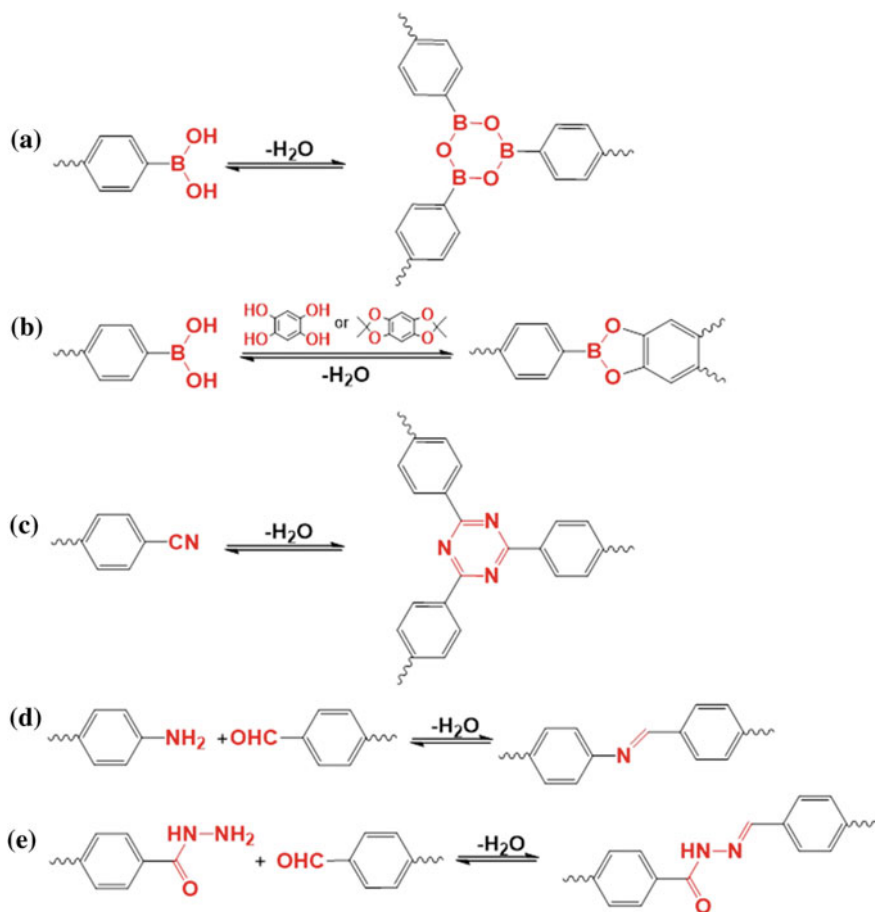
Fig. 4.1 Reversible reactions that have been successfully developed for the construction of COFs [36, 47–49, 70]

requirements: (1) the formation reaction should be reversible, and (2) the geometry of the building blocks should be well preserved in the COFs [46]. Figure 4.1 summarizes the synthetic reactions successfully applied for the COFs synthesis. The reaction A is based on the reversible formation of boronate anhydride from the dehydration of boronic acid. The synthesis of COF-1 was led by Yaghi and co-workers via this reaction [47]. An analogous dehydration reaction (reaction B) between boronic acid and (acetonide-protected) catechol results in the reversible formation of boronate esters by which a series of boron-containing COFs have been successfully obtained [47, 48]. The synthesis of triazine-based frameworks has been prepared via the nitrile cyclotrimerization under ionothermal condition, which represents a unique method (reaction C) [36, 49]. CTFs simultaneously provide high thermal, chemical, and mechanical stabilities along with a high degree of

conjugation; however, they typically possess low crystallinity as a result of the poor reversibility of the trimerization reaction. The reactions D and E are based on the imine bonds structure (–C=N–), by which several COFs have been synthesized with the new networks. The dehydration of aldehyde and amine gives rise to the Schiff base-type linkage (reaction D), while the reaction E between aldehyde and hydrazide affords the hydrazine structure.

As mentioned above, the rigid conformation of the building blocks enables the topological design of the COFs. Figure 4.2 summarizes the building units used, the general features of which are rigid in structure and symmetric multiconnective so as to meet the requirement for constructing the regular pores of COFs. For clarity, these building blocks are classified based on functional groups such as (–B(OH)$_2$, –OH, –CHO, –NH$_2$, and –CN). The synthetic strategies for COFs are based on diversity of building blocks, which endows the COFs with high flexibility in their molecular design.
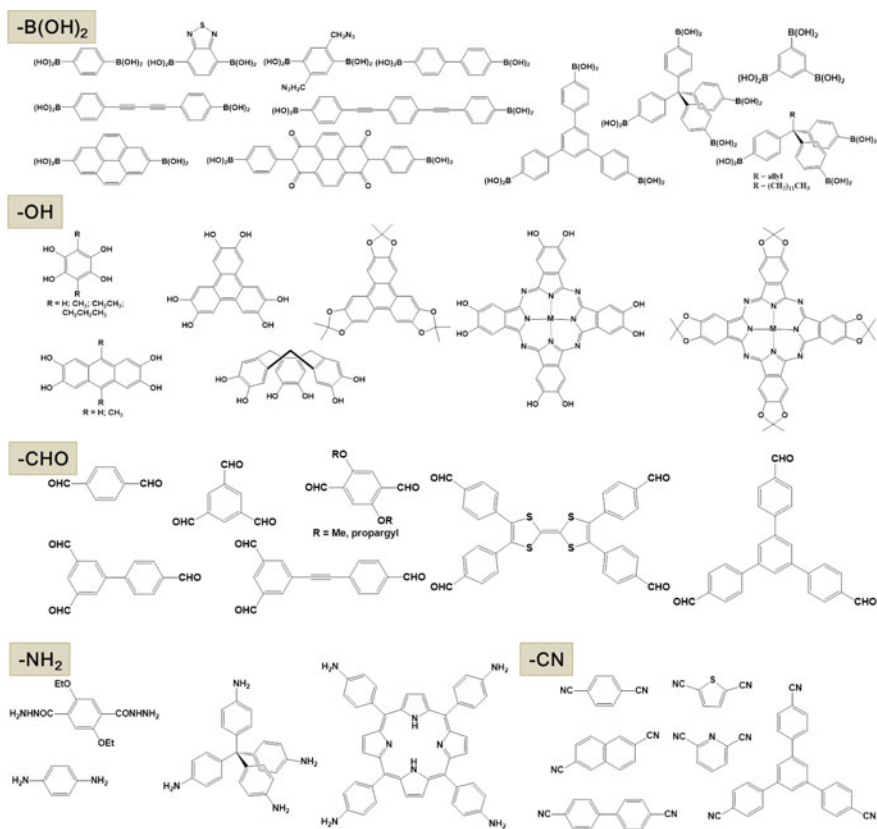
Fig. 4.2 Building units that have been successfully utilized for the synthesis of COFs [36, 47–49, 70]

4.2.1.2 Synthetic Methods

Since Yaghi and co-works exploited the solvothermal method to achieve the first successful COF-1 in order to construct the skeleton of COFs, many research groups have attempted to expand the synthetic possibility in different ways. We summarize the solvothermal, ionothermal, and microwave methods applied for the COFs synthesis below. Compared to bulky methods, surface or film COFs have been developed via reactions on substrates, such as metal surface and graphene sheet.

Solvothermal Synthesis

Initial studies were carried out in Pyrex tube via the solvothermal synthesis method which was degassed using several freeze–pump–thaw cycles, sealed, and heated to a desired temperature for 2–9 days. The precipitate was obtained, washed with suitable solvents, and dried under vacuum to yield the COFs powder. Issues such as the solubility, reaction pressure, crystal growth rate, and reversibility are the important points to be considered when selecting the reaction media and conditions. For example, whether fully soluble or completely insoluble building blocks can lead to the synthesis of COFs needs further experimental investigations [50, 51].

Moreover, solvent combination and ratio are the important factors for the highly crystalline COFs synthesis. As an example, Jiang and co-workers discussed the influence of solvents on the crystallinity of COFs [51]. When the ratio of mesitylene and dioxane is 19/1 or 9/1(v/v), COFs with high crystallinity could be obtained. At the same time, a suitable temperature and optimal inside pressure ensure the reversibility of the reaction. Generally, COFs have been prepared at temperatures ranging from 85 to 120 °C which is dependent on the chemical reactivity of the building blocks.

Microwave Synthesis

Microware-assisted reactions have been widely adopted in chemistry and material synthesis [52, 53]. 2D COF-5 and 3D COF-102 were obtained via the microwave heating by Cooper and co-workers [54, 55]. Compared to the solvothermal methods, microwave synthesis provides several advantages, such as rapid reaction, without sealed vessel, and more efficient.

Ionothermal Synthesis

Thomas and co-workers exploited the ionothermal synthesis method to produce crystalline porous CTFs [36]. Cyclotrimerization of nitrile building units in molten $ZnCl_2$ at 400 °C affords crystalline CTFs. The molten $ZnCl_2$ plays important roles in this system, not only as the solvent and catalyst but also as the template for the reversible cyclotrimerization and crystallization. However, most synthesized CTFs are amorphous materials, a probable reason is that this method seems to be partially reversible [46].

Synthesis of Monolayer COFs on Substrates

Forming the monolayer COFs on surface takes a further step for real applications. So far, Ag, highly ordered pyrolytic graphite (HOPG), and graphene have been used to prepare monolayer COFs. Condensation of the building blocks onto a metal surface formed monolayer of COF-1 and COF-5 [5]. The molecular arrays were obtained by the sublimation of 1,4-benzenediboronic acid (BDBA) and 2,3,6,7,10,11-hexahydroxytriphenylene (HHTP) under ultrahigh vacuum (UHV) from two heated molybdenum crucible evaporators onto a clean Ag(111) surface. Images of molecular layers were conducted using scanning tunneling microscopy (STM) at room temperature [56] (Fig. 4.3). The preparation of defect-free monolayer may require fine-tuning reaction conditions, highly purified building blocks, and employing a suitable single-crystal metal substrate to direct the building block alignment.

Subsequently, a HOPG surface was adopted instead of a metal surface to prepare monolayer COFs [57]. In this experiment, biphenyldiboronic acid, 1,4-benzenediboronic acid, and 9,9-dihexylfluorene-2,7-diboronic acid were deposited onto a HOPG surface from their THF solutions, and $CuSO_4·5H_2O$ as a water "reservoir," followed by heating in a sealed autoclave at 150 °C for 1 h to form COFs monolayer. Structural analysis of the network showed a uniform pore spacing of 2.3 nm, which was in excellent agreement with the 2.27 nm size predicted by density functional theory (DFT) calculations and thus confirming the covalent formation of boroxine-linked SCOF-1. To achieve the reliable interface of electrodes or incorporate into real devices, Dichtel and co-workers reported the synthesis and characterizations of layered oriented COF-5 films onto single-layer graphene (SLG on SiO_2) surface (Fig. 4.4) [58–60]. Then, TP-COF, NiPc-COF, HHTP-DPB-COF, and ZnPc-PPE-COF were successfully prepared on graphene surfaces, and their thicknesses can be tuned by controlling the reaction time.

Fig. 4.3 STM image of the near-complete monolayer of SCOF-1 film synthesized from the deposition of 1 on Ag (111). The inset shows the proposed chemical structure for SCOF-1. Reproduced from Ref. [56] with kind permission of © 2008 American Chemical Society
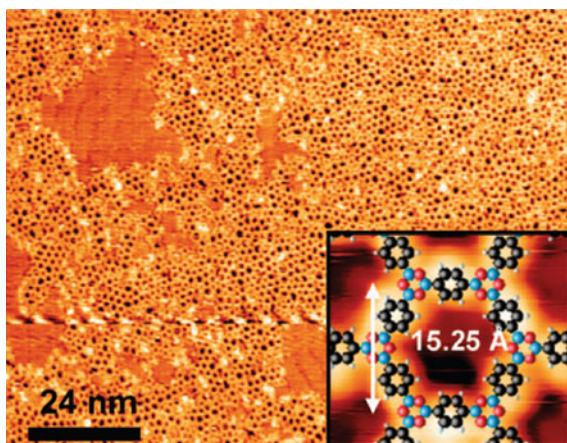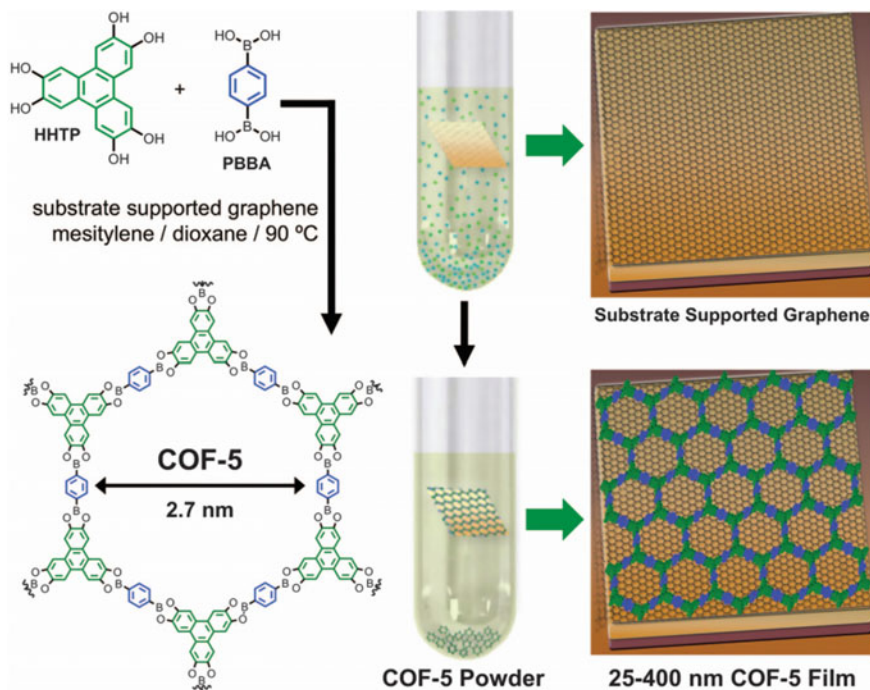
Fig. 4.4 Solvothermal synthesis of HHTP and PBBA on a single-layer graphene surface, affording COF-5 as the film on the graphene surface and as the powder precipitated around the bottom of the tube. Reproduced from Ref. [58] with kind permission of © 2011 The American Association for the Advancement of Science

4.2.1.3 Structural Studies

Due to the highly crystalline structure, COFs with special architecture can be characterized by PXRD techniques. The structural simulation provides an important tool in revealing COFs' stacking structures. Besides, the structural regularity, composition, and atomic linkage of the COFs can be characterized by infrared spectroscopy, solid-state NMR spectroscopy, elemental analysis, and X-ray photoelectron spectroscopy. In molecular perspective, COFs can be classified into three categories: boron-containing, triazine-based, and imine-based COFs.

Boron-containing COFs

In 2006, COF-1 was synthesized as a crystalline material by the self-condensation of 1,4-phenylenediboronic acid (BDBA) which resulted in a structure consisting of extended layers stacked in staggered form and gave hexagonal pores with 1.5 nm diameter and BET surface area of 711 $m^2\ g^{-1}$. It has also been applied for the synthesis of three-dimensional COFs by condensation of molecules with tetrahedral structure, such as tetra(4-dihydroxyborylphenyl)methane (TBPM) and tetra

(4-dihydroxyborylphenyl)silane (TBPS) [3]. Subsequently, Lackinger and co-workers used para-diboronic acids, in which the size of the organic backbone varied from phenyl to quaterphenyl incrementally, to synthesize a series of isoreticular 2D COFs [61]. These networks ranged from 1.5 to 3.8 nm, and the corresponding pore sizes increased from 1.0 to 3.2 nm. Scanning tunneling microscopy was employed for structural characterization of the covalent networks as well as non-covalent self-assembled structures that were formed on the surface prior to the thermally activated polycondensation reaction. Recently, Fischer and co-workers developed a novel synthesis strategy for COF-1 at room temperature which was suitable for multigram scale synthesis [62]. This methodology shifts COF synthetic chemistry from sealed tubes to open beakers.

In addition to self-condensation, boronic acids can also react with catechols to form five-membered C_2O_2B boronate esters. And the mechanistic studies of COF-5 formation have been done from initial homogenous conditions (Fig. 4.5) [63]. The obvious advantage of this co-condensation strategy is the diverse combination of boronic acids and diols as building units, by which a series of COFs could be constructed with different properties and functionalities. For example, via the co-condensation of monomers 2,3,6,7,10,11-hexahydroxytriphenylene (HHTP) and pyrene-2,7-diboronic acid (PDBA), a 2D COF material (TP-COF) was successfully obtained [64]. TP-COF is a highly blue luminescent and electrical conductive material. Moreover, the functionality of COFs could be tailored with more versatile building units. For instance, via the co-condensation of donor and acceptor monomers, COFs with segregated donor–acceptor heterojunctions were synthesized [59, 65, 66]. Meanwhile, photoresponsive structurally dynamic COFs [67], polygonal shape-persistent macrocycles COFs [68], and star-shaped COFs [69] were also successfully synthesized using this strategy.
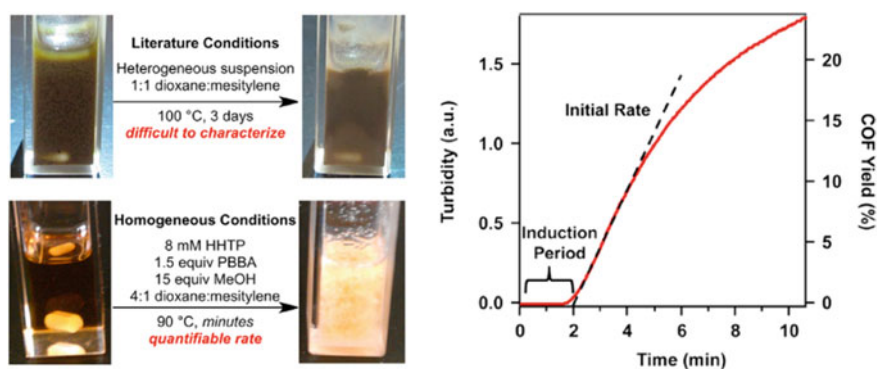
Fig. 4.5 A comparison of heterogeneous and homogeneous growth conditions for COF-5 and turbidity measurement of COF-5 formation as a function of time (8 mM HHTP, 1.5 equiv of PBBA, 15 equiv of MeOH, 4:1 dioxane/mesitylene, 90 °C). Reproduced from Ref. [63] with kind permission of © 2014 American Chemical Society

Based on the methods above, three-dimensional COFs were synthesized by condensation or co-condensation of molecules with tetrahedral geometry, such as TBPM or TBPS, TBPM, and HHTP [3].

Imine-based COFs

Similarly, C=N bond formation reaction has been applied to synthesize COFs with imine linkages [70]. One category is the "Schiff base"-type COFs formed via the co-condensation of aldehydes and amines (reaction D in Fig. 4.1). The first imine-based COF (COF-300) was synthesized via the dehydration reaction of tetra-(4-anily)methane and terephthaldehyde [70]. Subsequently, many scientists involved in this field. Jiang [71–76] and Rahul [77–81] are the best of them. Jiang and co-workers used this method mainly to focus on porphyrin-containing COFs synthesis [71, 73, 76]. By tuning the size and length and by introducing specific functional groups of the building blocks, photochemical active COFs [73], chiral COF catalysts, [75], adsorbents [73, 76], and chemical probe [82] can be produced. Rahul and co-workers designed a series of COFs based on the 1,3,5-triformylphloroglucinol (TP) units [77, 79–81, 83]. More recently, 3D imine-based COFs were synthesized via the Knoevenagel condensation reaction, showing excellent catalytic activity [84]; the other one was 3D pyrene-based COF, which was constructed through [4+4] imine condensation reactions. The novel 2D COFs with two different pores were recently developed.

Zhao and co-workers designed a dual-pore COF, which possessed both mico-pores and mesopores (7.1 and 26.9 Å) (Fig. 4.6a) [85]. Zhang and co-workers successfully synthesized two COFs with heterogeneous pore structures through the desymmetrized vertex design strategy [86]. Pore size distribution analysis revealed that two types of micropores (1.06 and 1.96 nm) were incorporated into the resulting COFs (Fig. 4.6b).
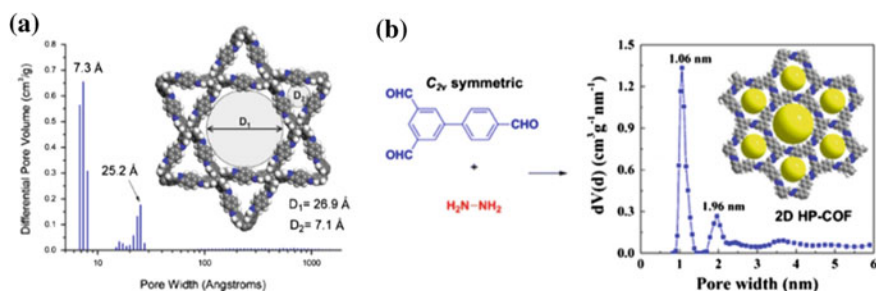
Fig. 4.6 a Schematic representation for the synthesis of TpBDH and TfpBDH [one unit of a space filling model of TpBDH and TfpBDH is shown in the inset of the chemical drawing model]; **b** syntheses of HP-COF-1 and PSDs of HP-COF-1. Reproduced from Ref. [85] with kind permission of © 2014 American Chemical Society, Reproduced from Ref. [86] with kind permission of © 2015 American Chemical Society
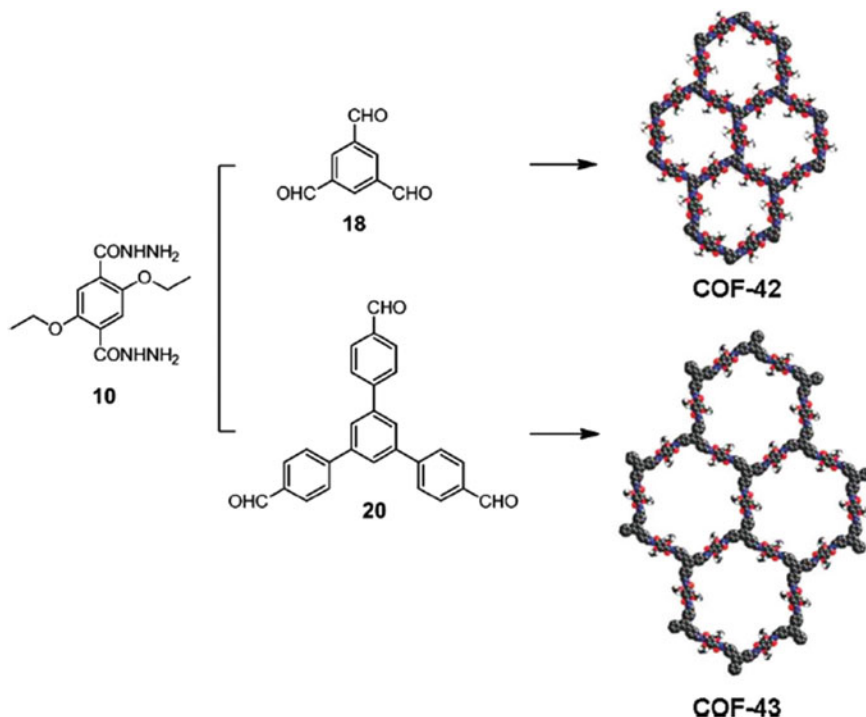
Fig. 4.7 Building units and the extended structures of COF-42 and COF-43. Reproduced from Ref. [87] with kind permission of © 2011 American Chemical Society

Another type of imine-based COFs is hydrazone-linked COFs synthesized by pioneer Yaghi and co-workers via the co-condensation reaction of aldehydes and hydrazides (Fig. 4.7). By employing 2,5-diethoxyterephthalohydrazide and 1,3,5-triformylbenzene or 1,3,5-tris(4-formylphenyl)benzene as the building units, COF-42 and COF-43 were successfully synthesized [87]. The existence of abundant hydrogen bonds within the hydrazone units is beneficial for the formation of the eclipsed structure. More recently, Wang and co-workers designed fluorescent COFs (COF-LZU8) by introducing the thioether groups into COF-42 for efficient detection and removal of Hg^{2+} ions [88].

Triazine-based COFs

Covalent triazine-based frameworks were firstly developed by Thomas and co-workers [36]. The CTFs synthesis was based on cyclotrimerization of aromatic nitrile building units in molten $ZnCl_2$ at 400 °C (reaction C in Fig. 4.1). Interestingly, the ratio of $ZnCl_2$ to monomer is the key to the CTFs synthesis. The higher ratio (10:1) would lead to an amorphous polymer but with higher surface area (1123 $m^2 g^{-1}$). Compared to the two types of materials above, the CTFs are

usually of lower crystallinity. The reaction for CTFs is partially reversible reaction. To date, only two crystalline CTFs have been successfully synthesized [36, 49].

Other COFs

Polyimide-COFs (PI-COFs) were designed by Yan and co-workers using the imidization reaction. The resulting PI-COFs possessed large pore sizes that can be tuned by extending the building units, and in particular, PI-COF-3 displayed the largest size (5.3 nm) among the results reported to date [89]. Subsequently, 3D porous PI-COFs with non- or fourfold-interpenetrated diamond networks were synthesized which represented the first kind of COFs ever to be employed in controlled drug delivery with high loading and good release control [90]. Novel COFs with two types of covalent bonds have been developed using orthogonal reactions. This strategy can be adapted not only in binary systems but also in more complicated systems. For example, the first multiple-component NTU-COF-2 showed both high BET surface area and large H_2 uptake capacity [91].

4.2.2 Application Exploration

The applications of COFs are derived from their porosity and functional unit skeleton. With tunable porous architecture, these COFs are new candidates for further applications, such as gas storage, catalyst, and photoelectric device.

4.2.2.1 Gas Storage

Hydrogen Storage

Fossil fuels such as oil, natural gas, and coal contain carbon and produce CO_2, CO gases including a higher ratio of nitrogen oxides (NO_x) and sulfur dioxide (SO_2) which lead to pollution and global warming. Moreover, coal and fuel oil are available in limited supply. However, hydrogen is a clean, highly abundant, and non-toxic renewable fuel, and it is viewed as a promising clean fuel in the future which only generates water vapor after burning. The major problem with this fuel is its storage since it needs to be stored like other compressed gases. Hydrogen is usually stored in three different ways, viz. compression, liquefaction, and in a solid material [92, 93]. COFs have generated much interest in the study of the hydrogen storage materials.

Normally, COFs with larger surface areas possess higher hydrogen uptake capacities under the same condition. For example, 3D COF-102 with a higher BET surface area of 3620 m^2 g^{-1} showed the highest hydrogen uptake up to 7.2 wt% at 1 bar and 77 K [94]. This capacity is comparable to that of MOF-177 (7.5 wt%, S_{BET}: 4500 m^2 g^{-1}) [95], MOF-5 (7.6 wt%, S_{BET}: 3800 m^2 g^{-1}) [96], and PAF-1

(7.5 wt%, S_{BET}: 5600 m^2 g^{-1}) [2]. For 2D COFs, COF-10 (S_{BET}: 1760 m^2 g^{-1}) showed the highest hydrogen uptake of 3.92 wt% at 1 bar and 77 K compared to the other 2D COFs [94]. Recently, Zhao and co-workers developed a high BET surface area (1619 m^2 g^{-1}) NTU-COF-2, with two types of covalent bonds using orthogonal reaction. Its hydrogen uptake is 1.55 wt% at 1.0 bar and 77 K [91]. However, the exceptional COF-11 Å with the lower BET surface area (105 m^2 g^{-1}) showed hydrogen uptake of 1.22 wt% at 1.0 bar and 77 K [94]. The DOE road map target for hydrogen storage is set to be 9 wt% and 81 kg H$_2$ m^{-3} at 253–323 K with a pressure of 100 atm by the year 2015. Rooting on this purpose, the practical employment of COFs toward hydrogen uptake seems remoted.

Carbon Dioxide Storage

The emission of CO$_2$ due to the combustion of fossil fuels is one of the major sources for the accumulation of CO$_2$ in the atmosphere. To stabilize atmospheric CO$_2$ level, it is necessary to develop CO$_2$ capture and storage/sequestration technologies [94]. The storage of CO$_2$ has been extensively studied using a wide range of porous materials, for example, porous carbons, silicas, and MOFs [42, 97, 98]. Yaghi and co-workers achieved a very high CO$_2$ uptake of COF-102 reaching 120 wt% at 55 bar and 298 K [94]. However, COF-102 showed higher adsorption at low pressures than COF-108 because of their compact atomic packing; on the contrary, at high pressures, higher CO$_2$ uptake value (422.4 wt%) was obtained for COF-108. Compared with other porous materials (for example, ZIFs) [43, 99], COFs via reasonable design might become good candidates for CO$_2$ storage.

Methane Storage

Natural gas has been demonstrated to be potential as an alternative fuel for vehicular application due to its abundance and low price. Much effort has been focused on reaching the DOE target (180 cm^3) of storing methane at 35 bar, because this is the pressure in natural gas pipelines. Similar to the cases of hydrogen storage, the capability of methane storage is based on surface areas of COFs. The adsorption capacity of methane at 35 bar and 298 K in 3D COF-102 (18.7 wt%, 3620 m^2 g^{-1}) is higher than that of 3D COF-103 (17.5 wt%, 3530 m^2 g^{-1}) [94]. For 2D COFs, COF-5 has a lower value (8.9 wt%). Although the capacities of methane storage are similar in some COFs, decreasing the costs and efforts in synthesizing COFs still remain a big challenge toward the practical employment.

Ammonia Storage

Boron-containing COFs with abundant boron element (electron-deficient element) are useful for adsorbing ammonia. Among the series of boron-containing COFs, COF-10 has the highest ammonia uptake (15 mol kg^{-1}) at 1 bar and 298 K [100]. Moreover, COF-10 has a good circulation property. However, the stability of boron-containing COFs restrains their application.

4.2.2.2 Heterogeneous Catalysis

Organocatalysis in homogeneous systems is problematic because of the difficulty of separating expensive catalysts for repeated use [101–103]. Most heterogeneous organocatalysts are based on linear polymer supports; however, such catalysts exhibit low activity owing to the inefficient access to the catalytic sites. To overcome this issue, crystalline MOF-based organocatalysts have been developed. However, their stability, enantioselectivity, and diastereoselectivity need to be improved [75]. Imine-based COFs, due to containing abundant C=N (basic group), are useful for organic catalysis. Jiang and co-workers developed π-electronic COFs as a new type of metal-free heterogeneous catalyst, which enabled the high-performance catalysis of Diels–Alder reactions in neat water and ambient condition. Meanwhile, they prepared the mesoporous COFs with two distinct chiral segments by post-synthetic functionalization. The resulting crystalline metal-free catalysts displayed high activity, enantioselectivity, and recyclability for Michael reactions. On the other hand, imine-based COFs can incorporate metal ions into its pores via the coordination reaction with nitrogen atoms in the COFs. In 2011, Wang and co-workers realized the first application of metal COFs (Pd/COF-LZU1) for highly efficient Suzuki-Miyaure coupling catalysis reaction [104]. Recently, Vaidhyanathan and co-workers reported an amphiphilic triazine COF and the facile single-step loading of Pd(0) nanoparticles. The 18–20% of nano-Pd loading gave highly active composite working in open air at low concentrations (Conc. Pd (0) < 0.05 mol%, average TON 1500) catalyzing simultaneous multiple site Heck couplings and C–C couplings using "non-boronic acid" substrates, and exhibited good recyclability with no sign of catalyst leaching [105].

4.2.2.3 Photoelectric Applications

COFs with the photoelectric performance (PPy-COF) were firstly synthesized via the self-condensation of PDBA under solvothermal condition by Jiang and co-workers [106]. Remarkably, PPy-COF possessed 2D eclipsed structures with a higher BET surface area of 868 $m^2 g^{-1}$, and showed a fluorescence shift compared to its monomer PDBA. PPy-COF is electrically conductive, displaying photoconductivity with a quick response to light irradiation, and is capable of repetitive on–off photocurrent switching with a large on–off ratio (Fig. 4.8).

   Phthalocyanines (Pcs) have received considerable attentions due to their unique optical and electronic properties which give rise to the application of Pcs in various domains, such as organic field-effect transistor, optical information storage, organic solar cell, photodynamic therapy, and nonlinear optical material. Phthalocyanine-based polymers combine the excellent physical and chemical properties of Pcs as well as good solubility and processability, which are becoming one of the research hot spots. Spitler and Dichtel synthesized an eclipsed 2D COF (PC-PBBA-COF) containing metal-free phthalocyanine groups using phthalocyanine tetra(acetonide) and BDBA [48]. At the same time, Jiang and co-workers synthesized nickel
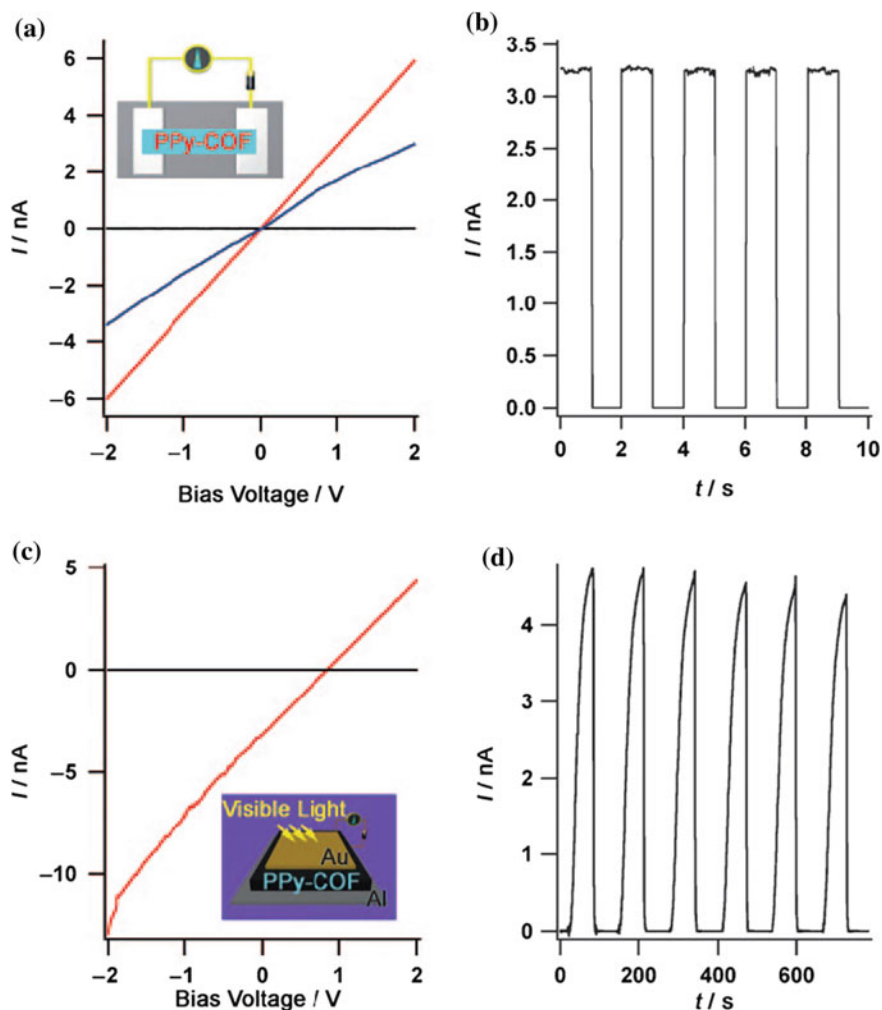
Fig. 4.8 **a** I–V profile of PPy-COF between two Pt electrodes 10 mm apart (*black curve*: without PPy-COF; *blue curve* with PPy-COF; *red curve* with iodine-doped PPy-COF). **b** Electric current when the 2 V bias voltage was turned on or off. **c** I–V profile of PPy-COF between sandwich-type Al/Au electrodes (*black curve* without light irradiation; *red curve* upon light irradiation). **d** Photocurrent when the light was turned on or off. Reproduced from Ref. [106] with kind permission of © 2009 Wiley-VCH (color figure online)

phthalocyanine-based COFs (NiPc COF and 2D-NiPc-BTDA COF) via the boronate esterification reaction of (2,3,9,10,16,17,23,24-octahydroxyphthalocyaninato) nickel(II) with BDBA or benzothiadiazole diboronic acid (BTDADA) [50, 51]. Both NiPc COF and 2D-NiPc-BTDA COF possessed eclipsed structures with BET surface areas of 624 and 877 m^2 g^{-1}, respectively. Due to 2D eclipsed structure,

NiPc COF showed an enhanced light-harvesting capability in the visible and near-infrared regions. And NiPc COF revealed highly photoconductive property, exhibiting a panchromatic light response and exceptional sensitivity to visible and near-infrared photons. Subsequently, they synthesized 2D tetragonal metalloph-thalocyanine by introducing electron-withdrawing blocks at the edges of n-channel 2D COFs. 2D-NiPc-BTDA COF turned to be an n-type semiconductor and exhibited great changes in the carrier transport mode with a broad and enhanced absorbance of light up to 1000 nm. Moreover, this COF exhibited panchromatic photoconductivity and was highly sensitive to near-infrared lights. Recently, they developed a new donor–acceptor strategy to construct COFs with various skeletons and pore for charge separation and photoenergy conversion. For example, using a three-component topological design diagram in conjunction with click chemistry, they developed a method for converting the open lattice of COFs into photoelectric structures. Most recently, they reported the design and synthesis of a photore-sponsive COF with anthracene units as the photoresponsive π-building blocks. The COF is switchable upon photoirradiation to yield a concavo-convex polygon skeleton through the interlayer[4p+4p] cycloaddition of anthracene units stacked in the π-columns [67].

Porphyrins possess extensive π-conjugated systems which contribute to electron transfer from donor unit to acceptor unit, and high molar absorption coefficient in light absorption, and their properties can be easily tuned via synthetic modifications for the periphery or by metal insertion into the cavity of porphyrin. In recent years, porphyrins have been applied in the synthesis of porous materials such as MOFs [47, 107, 108], CMPs [109], and COFs [76]. Jiang and co-workers reported the porphyrin-based COF (ZnP-COF) constructed via the boronate esterification reac-tion of zinc(II) 5,10,15,20-tetrakis(4-(dihydroxyboryl)phenyl) porphyrin and 1,2,4,5-tetra-hydroxybenzene. ZnP-COF revealed a tetragonal 2D eclipsed structure with a large BET surface area of 1742 $m^2 \ g^{-1}$ and an average pore size of 2.5 nm. Subsequently, the photoelectronic properties of ZnP-COF and other two porphyrin-based COFs (H_2-COF and CuP-COF) have been studied [46]. Compared to H_2-COF, ZnP-COF and CuP-COF showed high-rate ambipolar and electron conduction, respectively. CuP-COFs have been investigated in a recent work, in which fluoro-substituted and non-substituted arenes at different molar ratios were integrated into the edge units that stack to trigger self-complementary π-electronic interactions in the COFs. These interactions also showed a prominent effect on changing the π-electron distribution in the framework and lowering the HOMO-LUMO gap (Fig. 4.9) [71].

4.2.3   Summary

COFs have emerged as an important class of materials because their backbone is built entirely from light elements (thus far, C, N, O, B, Si) held together by strong covalent bonds (B–O, C–N, B–N, and B–O–Si) to make robust porous materials
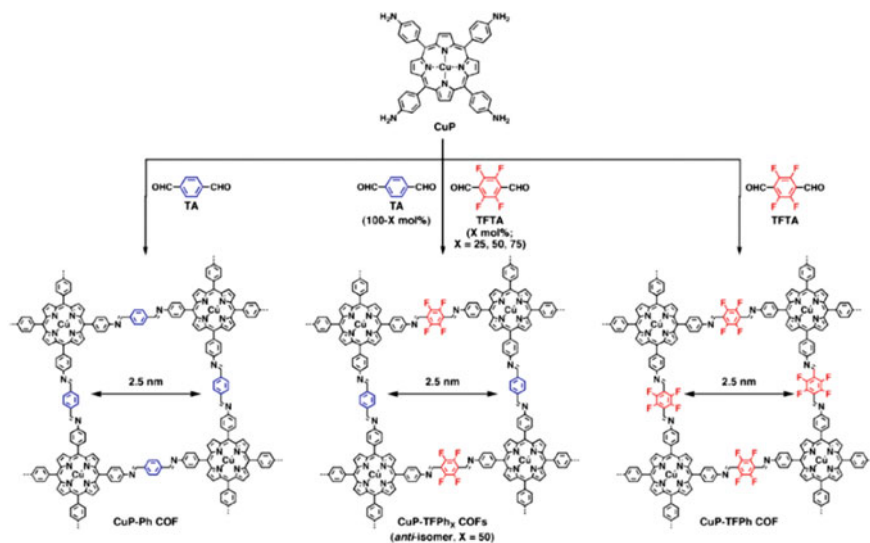
Fig. 4.9 Schematic representation of the synthesis of COFs integrated with self-complementary π-electronic interactions (CuP-TFPh$_X$, X = 25, 50, and 75 mol%) and the CuP-Ph and CuP-TFPh Controls. Reproduced from Ref. [71] with kind permission of © 2013 American Chemical Society

including the advantages of predictable structures and tunable pore functionality and metrics. The crystallization problem has been overcome in COF chemistry except CTFs, and a large variety of COF structures have been made and will continue to evolve in their diversity and complexity. However, the development of new synthetic methods is the key to broaden the COFs family. Formability is another important issue for the practical application of COFs. Finally, both the introduction of functional groups and post-modification are the critical subjects according to the practical application of COFs.

4.3 Hypercrosslinked Polymers

Hypercrosslinked polymers represent a novel class of porous polymer materials containing abundant microporous structure [29, 30]. These polymers are mainly prepared by the Friedel–Crafts chemistry and developed by taking the concepts of "crosslinking" which, however, is further extended [110]. The obtained polymer networks are usually cross-linked with highly rigidity linkages which prevent the polymer chains from collapsing. Therefore, these resulting polymer materials contain permanent micropore, high surface area, and large pore volume. According to the difference between the synthetic methods, hypercrosslinked polymers are mainly prepared by the following three approaches: (1) post-crosslinking polymer precursors, (2) direct one-step polycondensation of functional monomers, and

(3) knitting rigid aromatic building blocks with external crosslinker. In this part, we will introduce the development of hypercrosslinked polymers in detail as well as compare the merits between various synthetic methods. Networks with specific functionalities and controlled micromorphology which can be applied in broad practical and potential applications such as gas storage, adsorption, separation, catalysis, sensing are also discussed.

4.3.1 Post-crosslinking Procedure

"Davankov-type" resins are commonly regarded as the first category of hyper-crosslinked polymers which were initially discovered and investigated in the early 1970s [111]. These hypercrosslinked polymeric networks can be generated by further crosslinking of either dissolved linear polystyrene or swollen gel-type styrene-divinylbenzene copolymer precursors [112]. The representative reaction scheme is provided in Fig. 4.10. The polymer precursors are dissolved or swollen in solvents which separate the polymer chains, and then, a crosslinking step was carried out immediately to lock these chains forming a rigid intensive network. After removing the solvent, the rigid linkage units prevent the chains from collapsing thus resulting in interconnected pores in the polymer matrix [113].

As pioneers in this field, Davankov with his colleagues has done a large amount of research in preparing various kinds of hypercrosslinked materials as well as exploring the reaction conditions [110, 112, 114–116]. An intermolecular hyper-crosslinked soluble material was obtained from the linear polystyrene using monochlorodimethyl ether (MCDE) as the crosslinking agent in the presence of $SnCl_4$ catalyst [114]. A series of surface areas up to 680–1000 $m^2 \, g^{-1}$ can be obtained with materials showing potential applications in chromatography, separation of contaminants from liquid solutions, and adsorption of organic vapors.
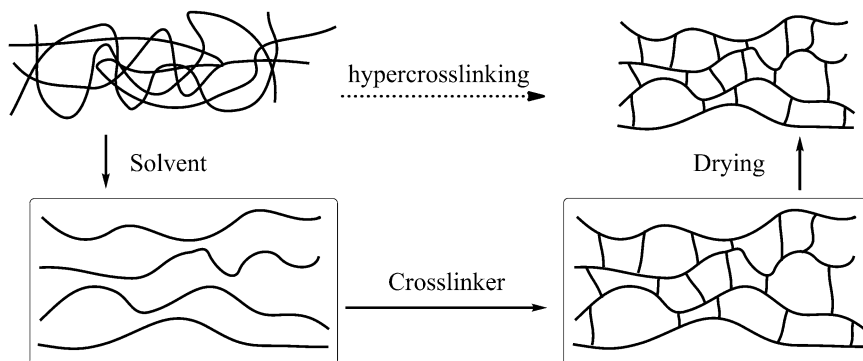
Fig. 4.10 Scheme of the representative hypercrosslinking reaction. Reproduced from Ref. [113] with kind permission of © 2007 Royal Society of Chemistry

Low-cost CCl$_4$ is a good crosslinker with less toxicity compared with mono-chlorodimethyl ether. By post-crosslinking styrene-divinylbenzene copolymer precursors, a series of 1000 m^2 g^{-1} surface area hypercrosslinked resins were produced via Friedel–Crafts reaction with CCl$_4$ as the crosslinker as well as aluminum or ferric chloride as the catalyst [117].

With similar linear structure as polystyrene, polyDVB-VBC (which is short for polydivinylbenzene-co-vinylbenzyl chloride) can be efficient precursors for hypercrosslinking which convert the chloromethyl groups into methylene bridges thus creating stronger crosslinking linkages (Fig. 4.11) [118, 119]. Sherrington and co-workers [119] synthesized a variety of hypercrosslinked polymers based on polyDVB-VBC precursors and investigated the porosity discrepancy affected by different synthetic conditions including the monomer ratio, solvent, catalyst, and reaction time. The resulting surface areas ranged from 300 to 2000 m^2 g^{-1} of different precursors with tiny structure variation using Lewis acid catalysts. For example, a gel-type precursor containing 2 mol% DVB yielded a surface area of ~1200 m^2 g^{-1} within only 15 min initiating crosslinking which rose steadily to 2090 m^2 g^{-1} after 18 h.

Despite various synthetic strategies, hypercrosslinked polymers with controllable pore size and size distribution were also studied. Tan group [120] chose the typical poly(DVB-VBC) copolymer as the precursor to investigate the influence of the precursor structure on porosity. By increasing the DVB content, the pore size of the obtained hypercrosslinked poly(divinylbenzene-co-vinylbenzyl chloride) (HCP-DVB-VBC) can be efficiently adjusted from macropore to micropore size showing a more uniform and narrower microporous structure. When the DVB concentration is higher than 7%, a typical type I nitrogen adsorption/desorption isotherm was observed indicating a pure microporous polymer network. Gas adsorption properties of these materials were also investigated indicating that the smaller micropore size and higher microporous volume are beneficial for H$_2$ and CO$_2$ uptakes.

Recently, polystyrene-base block copolymers exhibited attractive advantages in designing microporous materials with hollow structure [121, 122]. By adopting the self-assembly of PMMA-b-PS copolymer, Wu et al. [122] synthesized uniform
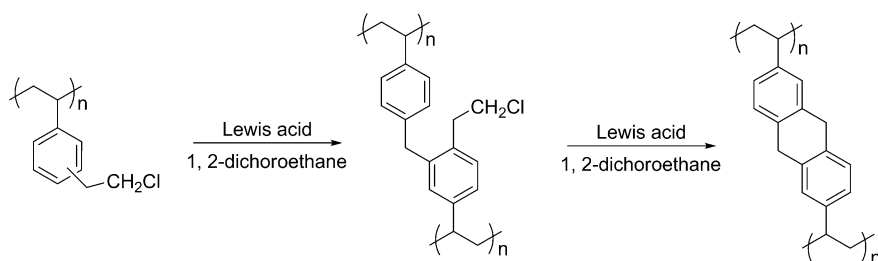
Fig. 4.11 Post-hypercrosslinking of DVB-VBC polymer precursors. Reproduced from Ref. [119] with kind permission of © 2006 American Chemical Society

PMMA@PS core–shell micelles in a selected mixed solvents, followed by hyper-crosslinking to produce microporous hollow spheres. Precise control over the nanostructures can be achieved by the variation of the molecular composition of PMMA-b-PS. After carbonization into carbon hollow spheres, these as-prepared nanoscale materials showed good CO_2 capture and supercapacitance properties.

4.3.2 Direct One-Step Self-polycondensation

In recent years, "Davankov-type" resins displayed a rapid development in the synthetic strategies. However, their post-crosslinking essences resulted in limited applications because of the tedious reaction process as well as restricted optional precursors. What if hypercrosslinked polymer synthesized directly from small molecule monomers which contain functional groups such as chloromethyl group? Early researches were started by Cooper and co-workers [123]. Via a simple one-step condensation polymerization process, three kinds of bis(chloromethyl) aromatic monomers (Fig. 4.12) including dichloroxylene (DCX), bis(chloromethyl) biphenyl (BCMBP), and bis(chloromethyl) anthracene (BCMA) linked together with the elimination of functional groups and formed a highly crosslinked network. By changing the monomer ratio among the monomers as well as Lewis acid catalyst amount, surface area and porous structure of the resulting materials can be easily tuned. According to the N_2 adsorption/desorption analysis, these materials were predominantly microporous and exhibited apparent highest BET surface areas of up to 1904 m^2 g^{-1}. Owing to their high surface area and permanent microporosity, these materials also showed outstanding performance in hydrogen adsorption [123], methane storage [13], and CO_2 capture [124] indicating their potential applications in energy and environment field.

This one-step condensation polymerization of small monomers highly extended the range of optional building blocks. Moreover, multifunctional polymer materials can be easily obtained by a simple copolymerization with other functional monomers.
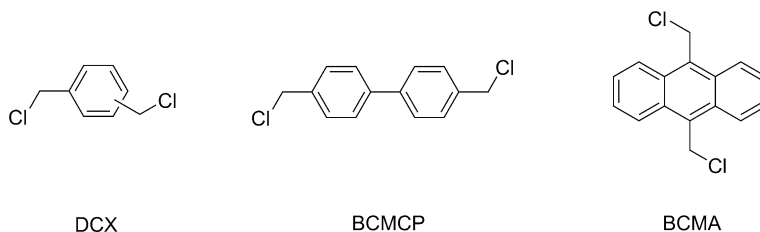
Fig. 4.12 Three typical monomers used in self-condensation polymerization. Reproduced from Ref. [123] with kind permission of © 2007 American Chemical Society

Yang et al. [125] synthesized a series of microporous copolymers from triphenylamine and p-DCX using $FeCl_3$- promoted oxidative polymerization and Friedel–Crafts alkylation. The BET specific surface areas ranging from 318 to 1530 $m^2 g^{-1}$ were obtained with the increasing content of p-DCX. These nitrogen-functionalized materials exhibited an enhanced CO_2 uptake of 4.60 mmol g^{-1}, which was comparable with the best reported results for MOPs, activated carbon, and MOFs under the same conditions. Following investigation about hydrocarbons/water separation properties was also made using BCMCP as the crosslinker [126]. By changing the monomer ratio, hypercrosslinked polymers with apparent BET surface areas of 1362 and 1338 $m^2 g^{-1}$ were obtained which showed benzene/water vapor selectivity as high as 53.5 and 63.6, respectively. Moreover, a monolithic polymer was also prepared to show potential application in oil spill cleanup.

Except for the traditional chloromethyl groups, Tan group [127] has explored two kinds of aromatic hydroxymethyl monomers such as 1,4-benzenedimethanol (BDM) and benzyl alcohol (BA) that can also be prepared into self-condensation microporous polymers (Fig. 4.13). N_2 adsorption/desorption isotherms of the polymers indicated a predominantly microporous network with high surface areas of up to 847 and 742 $m^2 g^{-1}$, respectively. Polymer networks based on BA monomers can store a significant amount of CO_2 up to 8.46 wt% at 273 K/1 bar and H_2 up to 0.97 wt% at 77.3 K/1 bar. This research has enlarged the optional building blocks that even monofunctional compounds can be involved in the construction of hypercrosslinked polymers.

Following this study, Tan group [21] has recently demonstrated that rigid aromatic monomers and derivatives can also be utilized for a novel one-step self-polycondensation reaction (Fig. 4.14). This strategy is based on the Lewis acid catalytic Scholl reaction [128], which involves the elimination of aryl-bound hydrogen atoms accompanied by the formation of new aryl-aryl bonds. Due to the universality of this strategy, a wide variety of monomers are suitable including monomers with both high or low electron density, acidic or alkaline functional group containing monomers, aryl or fused ring-based monomers, as well as heterocyclic ring containing monomers. A series of microporous organic polymers with surface areas ranging from 636 to 1421 $m^2 g^{-1}$ were synthesized according to the N_2 sorption analysis. Moreover, the porous structure and functionalities of the resulting networks can be easily modulated by adopting different functional building blocks indicating potential applications in gas storage, catalyst, optoelectronic sensing, and semi-conducting.

Zhu group [129] introduced several three-dimensional monomers such as triphenylamine, tetraphenylmethane, tetraphenylsilane, and tetraphenylgermane for the construction of spatial hypercrossslinked networks via the Scholl coupling reaction. With moderate surface areas reaching up to 1119 $m^2 g^{-1}$, the resulting polymer networks exhibited relatively high CH_4 and CO_2 sorption capacity of 1.04 and 3.52 mmol g^{-1}, respectively (at 273 K/1.13 bar).
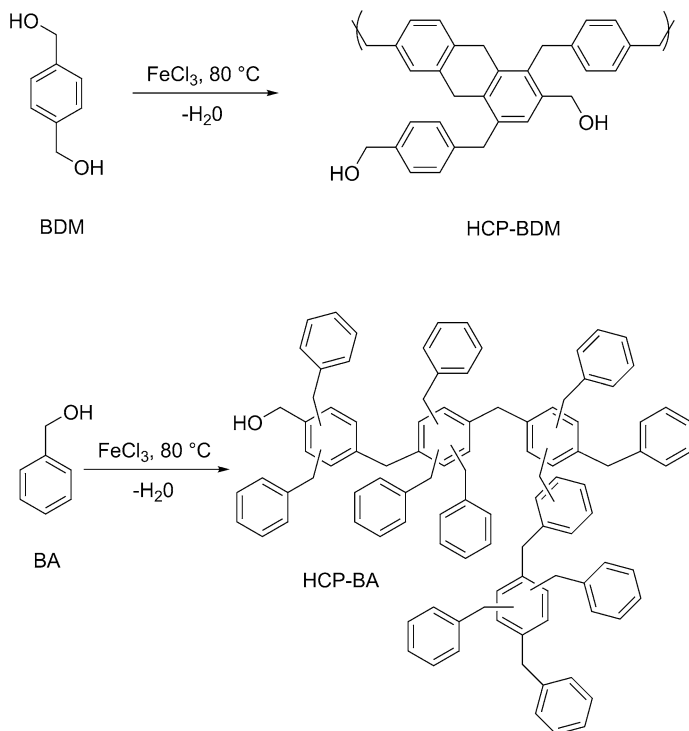
Fig. 4.13 Synthesis route of HCP-BDM and HCP-BA. Reproduced from Ref. [127] with kind permission of © 2013 American Chemical Society

4.3.3 External Crosslinking Strategy

Although this one-step self-polycondensation strategy has extended the optional building blocks boundary, there are still limitations for the synthetic routes. For example, the preparation of functional group containing monomers like chloromethyl group or hydroxymethyl group is difficult and is of high cost. Moreover, the hydrogen chloride generated from chloromethyl group also will do damage to fabrication facilities in large-scale industrial production and the environmental issues also need to be considered.

Considering these problems, a new strategy was proposed by Tan group [130] that using formaldehyde dimethyl acetal (FDA) external crosslinker to knit low functionality rigid aromatics via a simple Friedel–Crafts reaction in which anhydrous $FeCl_3$ acts as catalyst. This strategy is gentle, facile, flexible, and is of low cost that a wide variety of building blocks can be involved resulting in materials with predominantly microporous structure and high surface area (Fig. 4.15). By adjusting the ratio of monomer and the crosslinker, surface areas as well as the porous structure of the resulting networks can be roughly controlled and a high
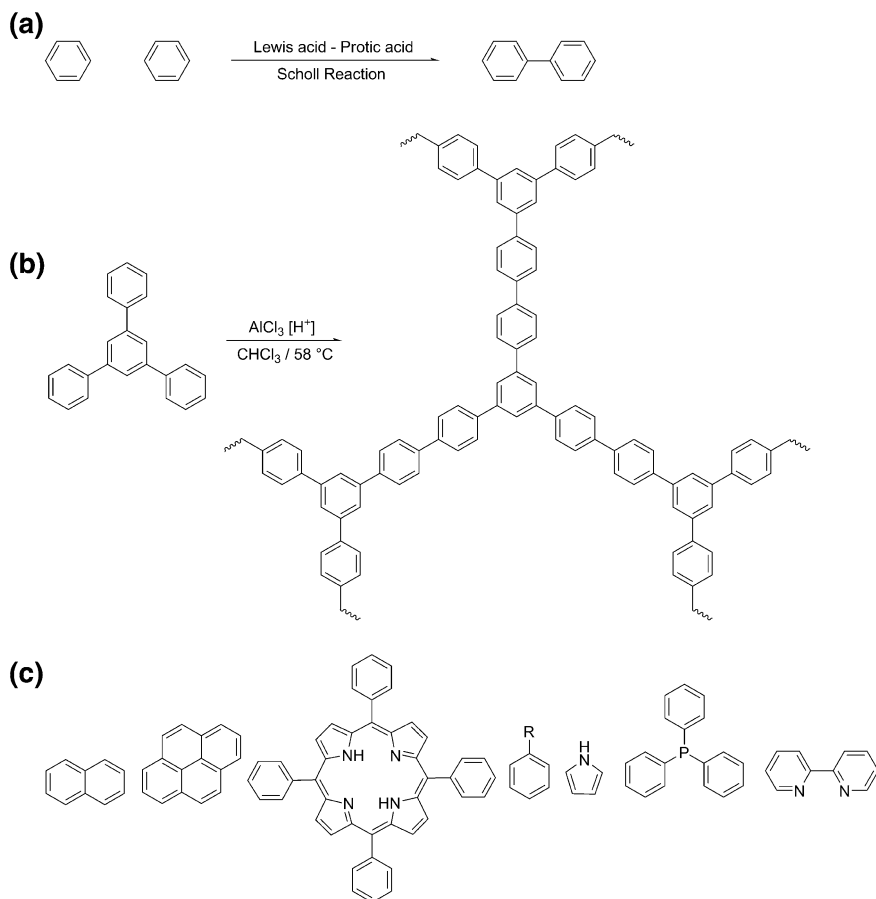
Fig. 4.14 a Typical Scholl reaction, **b** polymer networks form 1,3,5-triphenyl benzene, **c** other monomers. Reproduced from Ref. [21] with kind permission of © 2014 Royal Society of Chemistry

BET surface area of 1391 m^2 g^{-1} was obtained for benzene-based network. In addition, the functionality of the polymer networks can be easily modulated by introducing functional monomers. This knitting strategy demonstrated evident advantages compared with previous methods: (1) a large amount of monomers can be adopted even without specific functional groups, (2) facile synthesis conditions and low cost are easy to scale up, (3) result in materials with abundant microporosity and high surface area, and (4) modulation of microporous structure and functionality networks is simple, thus providing a novel pathway for the construction of functional polymers or materials with unique micromorphology.

The environmental issues are always the human concerns. The change in a global climate caused by excessive CO_2 emissions has attracted widespread public attention in recent years [131]. CO_2 capture and storage (CCS) technology is a
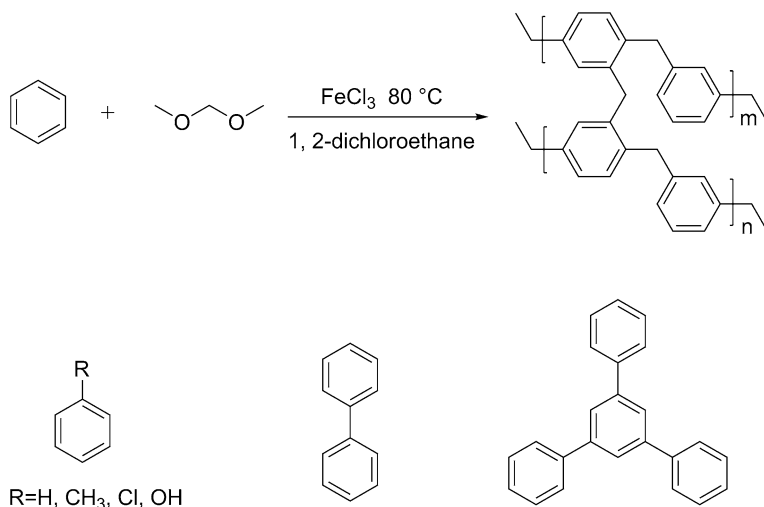
Fig. 4.15 Knitting rigid aromatic building blocks with FDA crosslinker. Reproduced from Ref. [130] with kind permission of © 2011 American Chemical Society

promising method using MOPs as physical adsorption material in which high adsorption capacity should be the key factor [132]. Enormous research has shown that the introduction of functional groups such as carboxyl and amine may enhance the CO_2 adsorption and selectivity for CO_2/N_2 by increasing the interactions between adsorbent and adsorbate [133–135].

Prof. Cooper thought highly of this strategy which extended the approach to a wide range of low functionality aromatic monomers, and these materials possessed more promising CO_2 uptakes at the higher pressures that are relevant to precombustion CCS [136]. By employing this knitting method, firstly they successfully synthesized a series of amino group containing polymer networks by the copolymerization of aniline and benzene [137]. Varying the monomer ratio leaded to a highest BET surface area of up to 1100 m^2 g^{-1} as well as an improved CO_2/N_2 selectivity up to 49.2; however, the entire benzene network only showed a CO_2/N_2 selectivity of 15.9. Polymerization of alcohol-containing monomers using knitting process produced microporous networks with surface areas of up to 1015 m^2 g^{-1} [138]. Moreover, synthesis of chiral networks without any complex monomer involvement is also successful. The investigation of CO_2 adsorption performance for these materials in "wet" condition showed that hydrophobicity endures a much smaller drop in CO_2 capacity which could be an important point to consider in the future design of sorbents for CO_2 capture. To move forward one step, they tested the CO_2 adsorption behaviors for several different kinds of microporous materials including carbon, zeolite 13x, ZIF-8, HKUST-1, and FDA knitting polymers [136]. The results showed that unlike other polar adsorbents, the hydrophobic FDA knitting polymers are hardly affected by the water vapors and adsorb CO_2 in a different way by physical swelling thus giving rise to a higher CO_2 capacity and

much better CO_2 selectivity. As a result, these knitting polymers have superior function as a selective gas adsorbent as would be required for materials preparation on the large industrial scale required for carbon capture.

By adopting this knitting method, some other researches focus on the development of constructing polymer networks using novel building blocks with special functional groups such as amino, hydroxyl, carbazole, and triptycene.

Zhu group [139] successfully prepared highly porous materials derived from amino and hydroxyl containing tetrahedral monomers with apparent surface areas up to 1230 and 1608 $m^2 g^{-1}$, respectively. According to their functionality, the corresponding polymer networks revealed enhanced CO_2 adsorption capacities and higher heats of adsorption than the non-functionalized materials.

Dai and co-workers produced triazine- and carbazole-bifunctionalized task-specific porous polymers via the Friedel–Crafts reaction with surface areas of 563 and 913 $m^2 g^{-1}$, respectively [22]. The resultant porous framework exhibits a comparable 18 wt% CO_2 uptake (273 K, 1 bar) and 38 selectivity for CO_2 over N_2. In addition, a series of novel carbohydrate-based microporous polymers were synthesized by knitting various hydroxyl-functionalized carbohydrate monomers [140]. BET surface areas around 800 $m^2 g^{-1}$ were obtained as well as a considerable amount of CO_2 adsorption of 12 wt% with a 42 CO_2/N_2 selectivity at 273 K. Several factors including the quantity and reactivity of hydroxyl groups and the structure of the carbohydrate monomers that contributed to CO_2 adsorption were discussed indicating these microporous polymers' promising applications in carbon capture.

Han group [141] also selected two carbazole-based building blocks for constructing knitting porous materials via $FeCl_3$-promoted one-step oxidative coupling and Friedel–Crafts reaction. N_2 adsorption analysis confirmed that these networks were permanently microporous with BET specific surface areas around 1190 $m^2 g^{-1}$. Besides the H_2 and CO_2 storage, these microporous networks also exhibited potential application in eliminating harmful small molecules from the environment such as toluene and formaldehyde.

Jiang group reported several kinds of knitting microporous organic polymers synthesized from a series of functional monomers containing hydroxyl, carbazole, and silole. The polymer networks based on tetraphenylethylene (TPE) and/or 1,1,2,2-tetraphenylethane-1,2-diol (TPD) [20] displayed surface areas ranging from 1980 to 618 $m^2 g^{-1}$ with a decrease in CO_2 adsorption capacities. However, the CO_2/N_2 selectivity enhanced to the highest 119 with the TPD content increase. The carbazole-based knitting polymers [142] showed a comparatively performance in CO_2 storage and separation with 1845 $m^2 g^{-1}$ high surface area. Novel silole-containing monomers were also used for building knitting aromatic polymers with similar surface areas around 1200 $m^2 g^{-1}$ [143]. The introduction of silicon atom enhanced the binding affinity between the adsorbent and CO_2 molecules, thus resulting in a slight higher CO_2/N_2 selectivity compared with other non-functionalized MOPs. The activated carbon materials with high surface area of 2065 $m^2 g^{-1}$ were obtained directly by potassium hydroxide-activated carbonization of a nitrogen-rich knitting polymer based on *N,N,N′,N′*-

tetraphenylbiphenyl-4,4′-diamine (DTPA) monomer [144]. An extreme high CO_2 uptake up to 6.51 mmolg^{-1} (1.13 bar/273 K) was obtained with a comparable 57 CO_2/N_2 selectivity. Considering the high surface area and good gas sorption performance, these knitting polymers are promising for CO_2 capture industrial applications.

Triptycene and its derivatives have earned a large amount of attention in supramolecular chemistry and materials science fields due to their specific three-dimensional rigid structure and easy functionalization. Zhang group has synthesized two series of triptycene-based knitting microporous polymers from hexaphenylbenzene-based triptycene [145] and tricarbazolyltriptycene building blocks [146]. According to the N_2 adsorption/desorption analysis, the obtained surface areas were 569 and 893 m^2 g^{-1}, respectively. With high thermal stability and comparable high surface area, these porous polymers are promising candidates for H_2 storage and carbon capture. In addition, triptycene monomer can be knitted with FDA crosslinker directly which resulted in high surface area reaching 1426 m^2 g^{-1} [147]. With hierarchical porosity, this kind of knitting polymer could be used as adsorbent for organic solvents and dyes in water treatment application.

The knitting strategy can also be directly used for crosslinking heterocyclic aromatic building blocks. Tan group [148] synthesized heteroatom-decorated knitting polymers using three typical heterocyclic molecules pyrrole, thiophene, and furan as monomers (Fig. 4.16). The BET surface areas were about 437–726 m^2 g^{-1} which were much lower compared to the benzene-knitted polymer network. However, the introduced heteroatoms provided excess lone electron pairs on the network skeleton which enhanced the binding affinity to CO_2 molecules by dipole–dipole interaction. As a result, Py-1 shows an extraordinarily high selectivity of CO_2/N_2 about 117 at 273 K which was the highest among all the microporous materials reported at that time.

Saleh et al. [149] explored more heterocyclic monomers including indole (IN), benzothiophene (BT), benzofuran (BF), carbazole (CBZ), dibenzofuran (DBF), and dibenzothiophene (DBT) for the construction of heteroatom-functionalized knitting polymers. Based on the N_2 sorption analysis, the synthesized polymer networks showed diversified surface areas in the range of 391–1022 m^2 g^{-1}. By attributing to
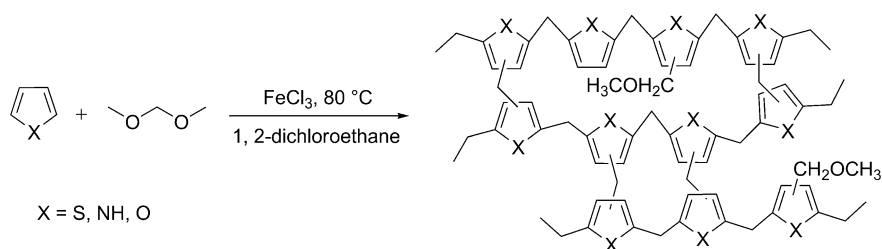
Fig. 4.16 Synthesis of aromatic heterocyclic microporous polymers via the knitting strategy. Reproduced from Ref. [148] with kind permission of © 2012 Wiley-VCH

their electron-rich electronic essence, these materials not only displayed high selective adsorption of CO_2/N_2 but also exhibited stable selective adsorption of CO_2/CH_4.

For organic chemistry field, the cheap and renewable CO_2 is an ideal carbon source. As a result, the incorporation of CO_2 capture and storage as well as the CO_2 utilization is an attractive potential application. In this respect, functionalized porous materials with both adsorption property and catalytic sites for CO_2 conversion could be promising materials.

Zhang et al. [150] developed a novel series of knitting porous polymers with phosphonium salt incorporated into the networks. By copolymerization triphenylphosphane (PPh_3) salts with benzene monomer, high surface area of 1168 m^2 g^{-1} was obtained with a moderate CO_2 uptake. These knitting microporous polymers can be used as catalysts for the conversion of CO_2 with propylene oxide into propylene carbonate which revealed a higher catalytic activity than the PS-supported phosphonium catalyst.

As is mentioned above, this knitting strategy via the Friedel–Crafts alkylation reaction proposed a simple and efficient synthetic route forming cost-effective porous materials with special functionality which can be promising solid sorbents for practical application in CCS technologies.

Moreover, the knitting strategy was also adopted for the preparation of heterogeneous catalyst [151–155]. Tan group [154] synthesized a phosphorus-decorated knitting polymers by crosslinking PPh_3 with benzene and then Pd was banded with PPh_3 groups to form KAPs(Ph–PPh_3)–Pd catalyst. The BET surface area was found to be 1036 m^2 g^{-1} for the knitting polymer network, which however showed no obvious decrease after binding with Pd (1025 m^2 g^{-1}). The resulting networks showed a uniform dispersion of Pd nanoparticle owing to their refined microporous structure, and the heterogeneous nature improved the reactant diffusion of small molecules. As a result, the KAPs (Ph–PPh_3)–Pd exhibited excellent activity and selectivity for the Suzuki-Miyaura cross-coupling reaction of aryl chlorides in an aqueous ethanol solution under mild conditions. Following this study, three N-heterocyclic carbenes were successfully integrated into the skeleton of the knitting polymer for Pd loading [155]. BET surface area as high as 1229 m^2 g^{-1} was achieved. Due to the substantial porosity and individual pore structure, the catalyst afforded rapid conversion for the Suzuki-Miyaura cross-coupling reactions including various aryl halides and arylboronic acids in aqueous media. In particular, it can be used for 5 times without obvious inactivation.

The knitting methods can also be used for the synthesis of metal-free heterogeneous photocatalysts which contain photoactive-conjugated organic semiconductor units such as 4,7-diphenylbenzo [1, 2, 5] and thiadiazole (BT-Ph$_2$) [156]. The resulting photocatalysts were directly employed for a visible light-promoted, highly selective bromination reaction using HBr as a bromine source and molecular oxygen as a clean oxidant, however, without transition metal. High catalytic efficiency and good reusability were observed within the materials. The utilization of the simply prepared knitting microporous polymer photocatalyst opens new opportunities toward a sustainable and efficient material design.

The knitting microporous polymers were also prepared into electron sensor devices. Zhang et al. [157, 158] investigated the humidity sensing properties of the 3-hydroxybenzoic acid monomer-based knitting porous polymers. After loading LiCl salt [157], the sensors revealed good humidity sensing properties that the impedances dropped with the increase of relative humidity which is attributed to the interaction between the loaded LiCl and water molecules. In addition, the enhanced humidity sensing properties can be obtained when the knitting materials were loaded with lithium hydroxide [158]. Therefore, the lithium-modified knitting polymers could be a new category of humidity-sensitive materials.

In general, the utilization of this simple and efficient knitting strategy has greatly expanded the variety of hypercrosslinked polymers as well as application range by incorporating different functional monomers. In addition, this strategy was also adopted for the preparation of microporous materials with precisely controlled micromorphology such as nanoparticles [159], hollow microcapsules [5–7], two-dimensional polymeric membranes [8, 9, 160], and monolithic blocks [14, 15].

Hollow microporous organic capsules (HMOCs) combining the advantages of microporosity and nanocapsule were fabricated via the hard templating methods in which nano-SiO_2 was used as core template (Fig. 4.17) [7]. SiO_2@PS-DVB precursors with core–shell structure were prepared via a simple traditional emulsion polymerization process. After the knitting and etching approach, the HMOCs were obtained with specific hollow morphology and high surface areas up to 1129 m^2 g^{-1}. By adjusting the DVB concentration, the resulting surface areas can be easily controlled which revealed a decreasing trend with the increasing DVB content. With hollow cavity inside, these HOMCs showed a much higher ibuprofen adsorption compared with the solid nanoparticles. Moreover, the controlled microporous structure made HOMCs to possess zero-order drug release kinetics demonstrating their attractive applications in medical field.

Compared to hollow capsule model, two-dimensional polymeric membranes have greater superiority for molecular level separation applications in industrial-scale chemistry, energy, and environment fields. Dai and co-workers [9] developed a facile one-pot approach for the synthesis of polymeric molecular sieve membranes by using non-porous polystyrene membrane as precursor via an in situ knitting process (Fig. 4.18). The resulting knitting polymeric membrane showed a sandwich porous structure comprising a dense microporous layer with an inner
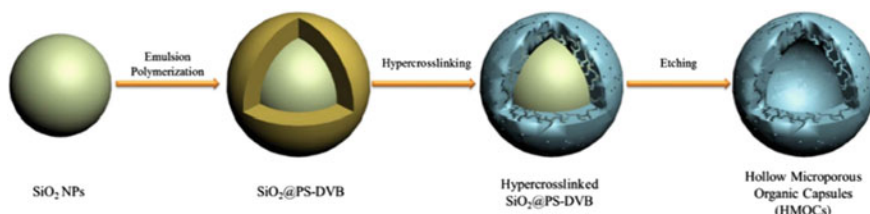
Fig. 4.17 Preparation of hollow microporous organic capsules. Reproduced from Ref. [7] with kind permission of © 2013 Macmillan Publishers Limited
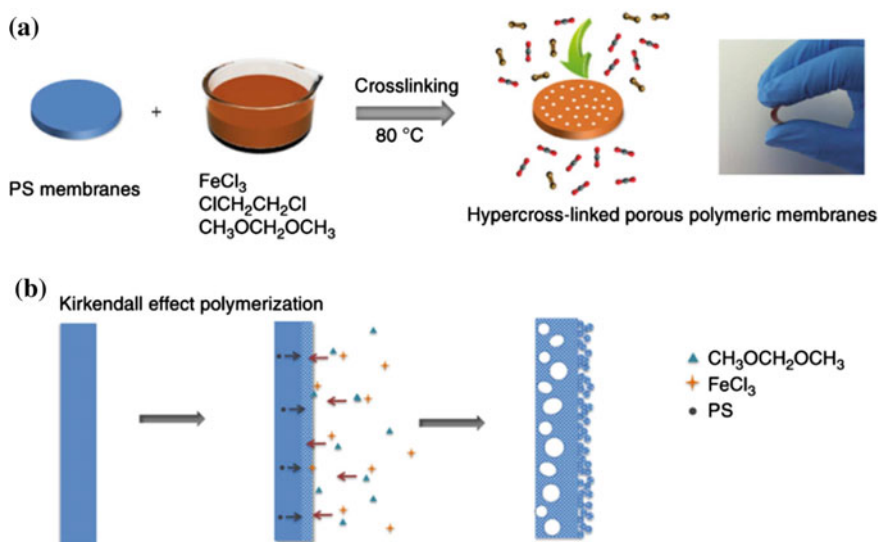
Fig. 4.18 a Synthesis of knitting microporous polystyrene membranes, **b** Mechanism for the formation of hierarchical porous structure. Reproduced from Ref. [9] with kind permission of © 2014 Macmillan Publishers Limited

macroporous core and outer mesoporous surface formed by small polymer particles. N_2 sorption analysis demonstrated the hierarchical porous structure showing type 1 reversible sorption isotherms with a slight hysteresis loop at relative high pressures. The BET surface areas varied from 218 to 618 $m^2 g^{-1}$ with the crosslinking time increasing, while the CO_2 permeability increased from 222.2 to 5261 barrer. On the contrary, the CO_2/N_2 selectivity decreased to 18.5 from 30. The high permeability and good selectivity indicated the promising potential applications in gas separation.

Based on this novel in situ concept, Kim et al. synthesized the knitting microporous polystyrene ionic liquid membranes via an in situ crosslinking of polystyrene membrane precursors [8, 160]. The 1-allyl-3-methylpyridinium bromide ionic liquid was incorporated into polymer matrix directly by dissolving in DMF solvent with polystyrene. Followed by a casting process, the polystyrene ionic liquid membranes were obtained. After coordinating with ferric [8] and nickel salts [160], these membranes were applied for the catalysis of H_2 generation from sodium borohydride and 4-nitrophenol reduction, respectively.

Compared with other specific micromorphology, three-dimensional macroscopic hierarchical porous monolith forms have attracted significant attention due to the rapid mass transport driven by convection through the internal connecting pores. Svec and co-workers reported the preparation of porous polymer monoliths by knitting styrene-type polymers involving three external crosslinkers BCMBP, DCX, and FDA [15]. Polymeric monoliths with surface areas reaching up to 900 $m^2 g^{-1}$ were obtained using BCMBP as crosslinker in only 2.5 h knitting

process. Owing to the high surface area and interconnecting hierarchical porous structure, the monoliths as the stationary phase for liquid chromatography delivered a significant improvement in efficiency in the reversed phase separation of small molecules. Tan group [14] also synthesized hierarchical porous polystyrene monoliths by knitting poly(styrene-divinylbenzene) high internal phase emulsions. BET surface areas of 196–595 $m^2 g^{-1}$ were obtained by N_2 sorption analysis with interconnecting well-defined macroporous, mesoporous, and permanent microporous structure. Owing to the interconnected cellular structure as well as the hydrophobicity in the skeleton, these monoliths exhibited a fast equilibrium and high adsorption capacity for organic solvents.

In summary, the knitting strategy using FDA as external crosslinker has become a very practical method for the preparation of hypercrosslinked polymer with multifunctionality and special micromorphology, while the surge to expand the synthesis strategy never stops.

4.3.4 Summary

Hypercrosslinked polymers have experienced an extended exploration in the design, synthetic strategy and potential applications since the discovery by Davankov. According to the development, there are mainly three synthetic routes: (1) post-crosslinking polymer precursors, (2) direct one-step polycondensation of functional monomers, and (3) knitting rigid aromatic building blocks with external crosslinker. Among them, the external knitting strategy has been proved to be a facile and efficient method and widely adopted for the synthesis of functional polymers or materials with unique micromorphology.

Even though, there also exists some challenges for developing HCPs. For example, the polymer networks of HCPs are highly irregular due to their fast dynamical character of the Lewis acid catalytic reaction. The huge amount heats generated by hypercrosslinking and hydrogen chloride released from unavoidable catalyst hydrolysis are also intractable problems for large-scale industrial production. Looking for new synthetic approaches for higher surface area HCPs which can be more than 3000 $m^2 g^{-1}$ is always highly desired. HCPs with controllable structure and new function will be a prolonged research hot spot with broad applications in photoelectricity, sensors, and semi-conducting devices.

4.4 Conjugated Microporous Polymers

CMPs, firstly reported in 2007 [25], are a class of microporous organic polymers consisting of π-conjugated segments totally bonded by covalent bonds, which inherently combine π-conjugated skeleton with microporous structure.

Porous architecture of CMPs can be controlled by molecular design, for instance, the surface areas and pore volumes can be easily tuned by using different monomers with various molecular lengths. Moreover, employment of diverse functional modules is feasible to construct CMPs. By selecting proper monomers, CMPs usually can be synthesized by conventional metal-catalyzed reactions, such as Sonogashira–Hagihara coupling [161], Suzuki coupling [162], Yamamoto couplings [163], oxidative polymerizations [164], and Schiff base reaction [165]. CMPs materials are always prepared by irreversible reactions, so they are usually amorphous and show short range of structural order. The pores are accessible to various guest molecules and metal ions, which allow the construction of supramolecular structures and organic–inorganic hybrids. Compared with crystalline COFs and MOFs, amorphous CMPs can be synthesized more easily by linking the appropriate organic building units to achieve functionalization and the functional groups can be fully exposed. The incorporation of new functional groups into CMPs has generated numerous new functional materials.

Although most of the works focus on developing new strategies, tuning the pore size distribution and surface area of CMPs, some efforts have already been made to control morphology, such as quasi-zero-dimensional (0D) microspheres [162], one-dimensional (1D) nanofibers and nanotubes [166], two-dimensional (2D) nanosheet structures [167], as well as three-dimensional (3D) monoliths [168]. What's more, the development of soluble CMPs also remains to be well explored [169].

CMPs have attracted tremendous attention and become one of the fastest developing types of porous materials. These kinds of material allow the complementary utilization of π-conjugation and porosity, which are unique and usually not available in other porous materials. Such structural features bring CMPs a large number of exciting properties and potential applications, such as gas storage [170], catalysis [171], sensors [163], and anode materials [172].

4.4.1 Synthesis and Modification

Typically, linear polymers are created with two end groups monomers ($A_2 + B_2$). As for three-dimensional CMPs, one or more monomers with more than two end groups ($A_x + B_y$, $x > 2$, $y > 2$) are needed.

4.4.1.1 Synthesis Method

Laybourn et al. [173] studied the framework formation mechanism of CMPs. The results showed that monomer concentration, solvent, temperature, and building block structure would affect the network formation in complex situations (Fig. 4.19). Firstly, oligomers are formed in solution, which resulted in clusters. And then, these clusters precipitate from solution and continue to react in solid state
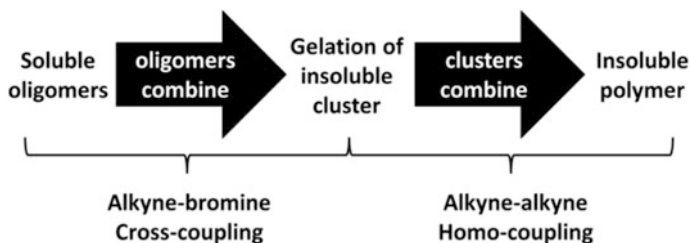
Fig. 4.19 Proposed reaction mechanism for the formation of CMP networks. Reproduced from Ref. [173] with kind permission of © 2014 American Chemical Society

by crosslinking, which lead to the formation of CMPs frameworks at last. The initial precipitated material exhibits a low degree of microporosity and significant interparticulate mesoporosity; true microporous materials are only formed at longer time upon fusion of the clusters and further crosslinking within the particles. Xu et al. [174] disclosed that the linkage geometry plays a vital role in the control over the porosity, gas adsorption, π-conjugation, exciton migration, and luminescence of CMPs. Works from Dawson et al. [175] and Tan et al. [176] showed that the choice of the reaction solvent is also important.

Many CMPs have been synthesized with miscellaneous polymerization, including Suzuki coupling reactions [177], Sonogashira coupling [25], Yamamoto coupling reaction [178], oxidative coupling polymerization [179], Schiff base chemistry [180], and electropolymerization (EP) [181] etc.

Suzuki cross-coupling reaction is one of the most powerful one-step pathways for the formation of carbon-carbon bonds [162] (Fig. 4.20a). Typically, Suzuki coupling reactions are performed under homogeneous conditions using a variety of phosphine ligand/palladium catalytic complexes. However, oxygen will cause the formation of homocoupling and deboronation by-products. Consequently, the Suzuki reaction often needs to be performed under highly oxygen free condition. Sonogashira coupling reaction which introduces acetylenyl groups in CMP frameworks is one of the most studied reactions among all the synthetic methods for the fabrication of CMPs [161] (Fig. 4.20b). Moreover, triple bonds may lead to a more rigid and extended network structure and can be used to adjust the porosity [182], and pore size and surface area [183]. At the same time, the final properties of CMPs can also be affected by the reaction conditions. Yamamoto coupling reaction is a C–C coupling of aryl-halogenide compounds mediated by transition metal complexes [163] (Fig. 4.20c). Only halogen-functionalized monomers are involved, while on the other hand, stoichiometric quantities of the nickel complexes are also important. Oxidative coupling polymerization has cost-effective advantages in the preparation of CMPs. CMPs materials can be prepared in large scales by oxidative coupling polymerization which shows advantages of adopting cheap catalyst, with low room temperature and only need single monomers [164] (Fig. 4.20d). Catalyst can be completely removed by easy purification [184]. Schiff base chemistry is a novel synthetic strategy for CMPs, which is a catalyst-free and
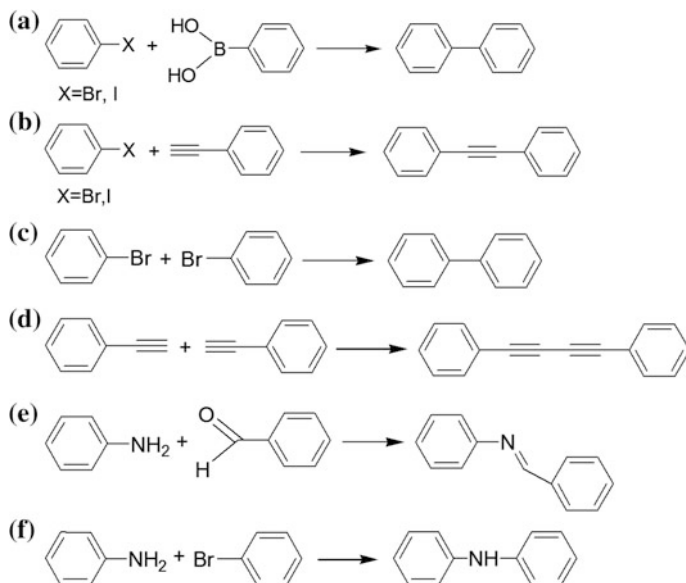
Fig. 4.20 Reactions have been successfully used for the construction of CMPs [161–165, 185]

one-pot reaction. Schiff base chemistry can build nitrogen-rich CMPs networks with high surface areas [165] (Fig. 4.20e). Buchwald–Hartwig (BH) coupling is utilized for the generation of C–N bonds via the palladium-catalyzed cross-coupling of amines with aryl halides [185] (Fig. 4.20f). The BH coupling approach allows the expansion of repertoire of possible C–N bond formation through the facile synthesis of aromatic amines. This useful method also provides a simple route to nitrogen-containing redox-active systems.

Direct arylation polymerization is a new method for synthesizing CMPs [186]. However, CMPs synthesized by direct arylation polycondensation are only limited to monomers containing two-arm fluoroarenes and nitrogen-free tri- or tetra-bromoarenes (Fig. 4.21).

Electropolymerization has been proven to be a useful method for fabricating electroactive CMPs films, which is an in situ polymerization of CMPs precursors or monomers [197]. The precursors are dissolved at first, and then, the coupling reaction occurs on the electrode surface. At last, the CMPs films depose on the electrode (Fig. 4.22). This strategy is of low cost, without catalyst, and controlled thickness of the film can be obtained.

4.4.1.2 Modification

The incorporation of metal sites into CMPs opens up the second-generation porous materials. Porphyrin which possesses macrocyclic cavity basic pyrroles is widely
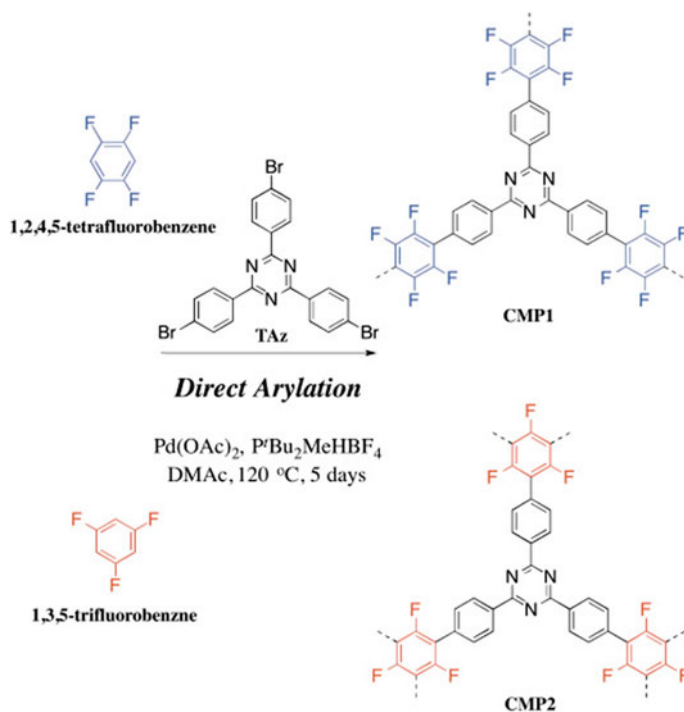
Fig. 4.21 Direct arylation polycondensation of fluoroarene monomers with TAz into CMPs. Reproduced from Ref. [186] with kind permission of © 2016 Elsevier

Fig. 4.22 Setup of the three-electrode electrochemical cell for the polymerization of monomers and the deposition of CMPs films on ITO. Reproduced from Ref. [197] with kind permission of © 2015 Wiley-VCH
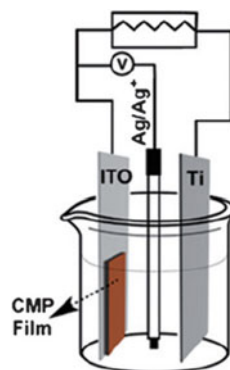
used in CMPs to form modified CMPs. Some metal-porphyrin CMPs using metal-porphyrin (metal: Zn, Co, Cu, Fe, Ni, etc.) as monomer have shown combined chemical and physical properties for applications in catalysis [187–190], supercapacitor [191], photosensitizer [192], and adsorption [89]. Metal ions (Fe and Al) can also be introduced into porphyrin-based CMPs and show good performance

in adsorption [184] and CO_2 capture [193]. Some other methods are also used to introduce metals into CMPs framework. Jiang et al. [194] prepared MO-CMP by two methods: post-treating bipyridine-functionalized CMPs with metal complexes (Re, Rh, and Ir) and the direct Sonogashira–Hagihara cross-coupling of halogenated metal-organic monomers. Fischer et al. [195] copolymerized $Li[B(C_6F_4Br)_4]$ with 1,3,5-triethynylbenzene using Sonogashira coupling $[Mn^{II}(bpy)]^{2+}$ complex and then immobilized in the CMP networks which is a promising catalyst for the aerobic oxidation of alkenes. Xie et al. [196] reported a class of Co/Al-coordinated CMPs which exhibit outstanding CO_2 capture comparable to MOFs.

Lee et al. [198] prepared CMPs by Sonogashira coupling and then prepared CMP-Co_3O_4 composites via organometallic complexation of cobalt carbonyl with microporous organic networks (MONs) and the successive oxidation. The materials showed the enhanced stability as anode materials.

Some organic molecules are also used as modifiers. For example, thiolyne can be introduced into CMPs networks [199–201]. Ratvijitvech et al. [202] reported the post-synthetic modification of amine-functionalized CMPs by anhydrides to build a series of amide-functionalized networks.

4.4.2 Control of Morphology

Morphology is an important factor in CMPs properties. Many efforts have been focused on the morphology control. Normally, template strategy and stepwise method have been used to control CMPs morphology.

4.4.2.1 Template Strategy

Template strategy is a straightforward method to build CMPs with specific morphology similar to the template. Zhuang et al. [203] reported a graphene-inspired synthetic approach for the preparation of sandwich-like CMP. Furthermore, they demonstrated a series of heterostructures CMPs with 0D, 1D, or 2D morphology, by using bromo-functionalized carbon nanospheres (0D CSs), single-walled carbon nanotubes (1D SWNTs), and reduced graphene oxide (2D RGO) as templates. The resulting CMPs showed nanosphere, nanotube, and nanosheet morphologies, and then carbonized. They found that the performance of these nanocarbon-based zinc-air batteries using nanocarbon as air electrode was affected by morphology (2D > 1D > 0D) [204]. Son group studied the synthesis of new functional MONs based on Sonogashira coupling by template strategy. SiO_2 [205, 206], Fe_3O_4 [187, 207], zeolites [208], and MOF [209] were used as templates, and the resulting materials showed good performances as catalysts [187, 206], precursor of inorganic materials [205, 207], and adsorbents [208, 209]. Tan et al. [210] reported a one-step synthesis of nanoscale CMP (NCMP) capsules by using PMAA microspheres as

self-sacrificial templates. The morphology, nanostructure, and shell thickness can be precisely controlled.

4.4.2.2 Stepwise Method

By controlling reaction conditions, CMPs with different morphology can be obtained. Tan et al. [176, 211] found that reaction solvents and the structure of monomers would influence the morphologies of the polymers (sphere, tubular, and plate). Ma et al. [212] illustrated the design principle and the synthesis of CMPs nanoparticle (Fig. 4.23).

Chun et al. [166] studied the mechanism of the formation for tubular CMPs synthesized by Sonogashira coupling (Fig. 4.24). Briefly, the formation of three types of structures (1D connection, interconnection of 1D chains to 2D networks, and 3D networking) occurred at the same time in which competition happened among them. The kinetic differences in these competitions may lead to morphology anisotropy. At last, tubular CMPs were formed. In order to optimize CMPs performance, thin films play a crucial role. The method to fabricate CMPs films mainly focuses on surface-initiated [167], layer-by-layer crosslinking [213, 214], casting soluble CMPs [169, 215], and electropolymerization [181, 191, 197, 216, 217]. First investigated by Cooper's group [169], efforts have been focused on the solubility of CMPs (SCMP). Hu's group demonstrated a "catalyst@pore" method to synthesize SCMPs by utilizing a well-defined silica-supported carbon nanomembranes as the nanoreactors by which the SCMPs particle size can be controlled by tuning the pore size of the nanoreactor [218, 219].

Up to now, the development of general and effective methods for the preparation of high-performance CMPs monolithic materials is still remained a huge challenge. Du et al. [220] reported CMPs aerogels derived from drying the gel matrix (Fig. 4.25). At the same time, high internal phase emulsion (HIPE) polymerization has been proved to be an efficient technique in building CMPs monolithic materials [221].

Fig. 4.23 Synthetic route to CMP NPs via (A_3 + B_2)-type Suzuki-Miyaura or Sonogashira–Hagihara cross-coupling polycondensation reactions in an oil-in-water miniemulsion system. Reproduced from Ref. [212] with kind permission of © 2015 Royal Society of Chemistry
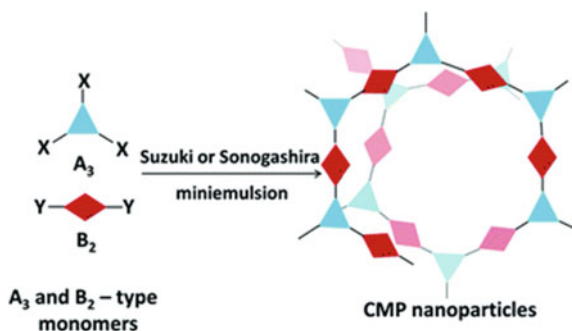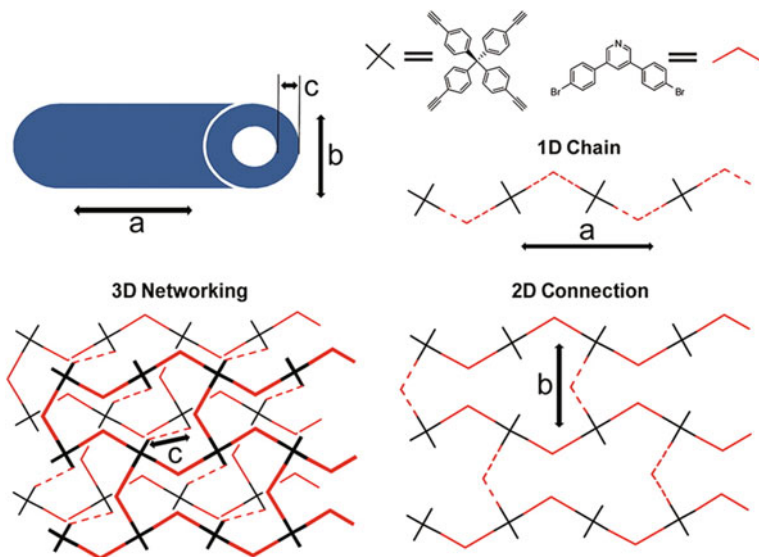
Fig. 4.24 Suggested mechanistic aspects of tubular CMPs. Reproduced from Ref. [166] with kind permission of © 2012 American Chemical Society

Fig. 4.25 Schematic illustration of the structure and preparation procedures for the PTEB aerogel and xerogel. Reproduced from Ref. [220] with kind permission of © 2014 Wiley-VCH
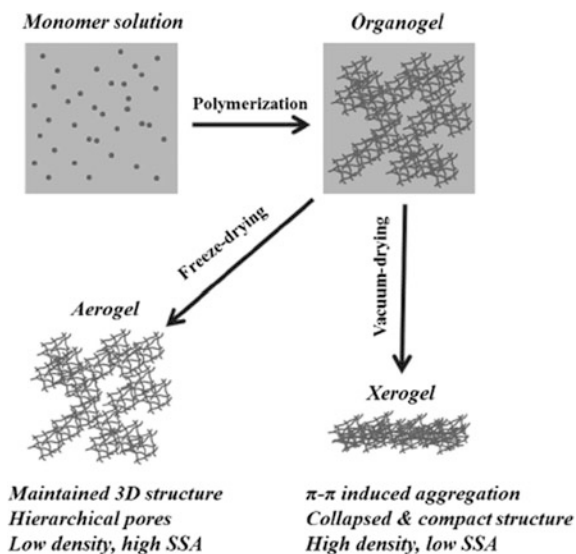
4.4.3 Application

4.4.3.1 Absorbent and Gas Storage

CMPs with structural tunability and high porosity have great potential to be developed as efficient absorbents. In the past few years, most studies have focused on the synthesis of CMPs with specific chemical and physical properties for chemical capture, sequestration, and separation. CMPs have been provided as efficient absorbents absorbing toxic chemicals such as amines [208, 222], iodine [89, 223], toluene [184, 209], benzene [224], and oil [168, 225].

CMPs possess π-conjugation along the main chain, which provides CMPs the potential in gas storage. It is known that gas adsorption performances of CMP materials depend on the character of building blocks. By introducing N, S, O elements into CMPs structure, CO_2 adsorption performance will be improved due to the strong interactions with CO_2 molecules [164, 182, 226–229]. What's more, Fischer et al. [230] fabricated CMPs with weak coordinating cations in their backbone. The material presented a CO_2 uptake of 2.49 mmol g^{-1} at 273 K and 1 bar and 2.85 mmol g^{-1} after ion exchange with chloride. A class of Co/Al-coordinated CMPs reported by Xie et al. [196] exhibited outstanding CO_2 capture comparable to metal-organic frameworks.

4.4.3.2 Battery and Supercapacitors

Considering environmental problem, clean and sustainable energy systems have been investigated. With a high degree of π-conjunction, homogeneous microporous structure, high surface area, and flexibility in the molecular design, CMPs have enormous potential as electrode materials for energy storage devices. Lee et al. [198] reported MON-Co_3O_4 composites and studied its applications as anode materials in lithium-ion batteries. Zhang et al. [231] synthesized CMPs from 4,7-dicarbazyl-[2,1,3]-benzothiadiazole (PDCzBT) by $FeCl_3$ oxidation coupling polymerization which exhibited excellent electrochemical performance for Li and Na storage including high specific capacity, outstanding cycle stability, and superior rate performance.

As material with 2D morphology can be benefit for energy storage, CMPs films now are studied as potential electrode materials in supercapacitors [191, 232, 233]. The reported materials all had high specific capacity, superior cycle stability, and remarkable rate capability. What's more, CMPs also can be carbonized as efficient supercapacitor materials due to its conjugated structure [204, 207, 234].

4.4.3.3 Catalyst

CMPs, combining the photoactive π-electron backbone and porous surface properties, have been recently introduced as stable heterogeneous photocatalysts for organic synthesis [235], such as oxidative coupling [206, 212, 236, 237], and oxidative hydroxylation of arylboronic acid [238]. Metal CMPs possess catalytic activities to reactions including carbene insertion into N–H bonds [187], carbon dioxide conversion to cyclic carbonates [190], Suzuki coupling reactions [239], and oxygen reduction reaction [189].

Furthermore, Zhang et al. [164] synthesized carbazole-based multifunctional CMPs which act as an efficient heterogeneous organocatalyst for Knoevenagel condensation with high activity, wide substrate adaptability, and good recyclability. Wang et al. [240] envisioned that chiral organometallic catalysts could be introduced into the structure of CMPs for the first time.

4.4.3.4 Fluorescence Property and Sensor

Large surface areas of CMPs provide a broad interface for interaction between analyte and sensor materials. Liu et al. [163] reported the first example of a chemosensing CMPs, which allow the material to achieve rapid responses and dramatically enhanced detection sensitivities. In sensing applications, solution-processible fluorescent porous materials based on CMPs are useful. Wu et al. [241] succeeded in developing solution-dispersible CMPs which exhibited a selective and sensitive fluorescence quenching response to 2,4,6-trinitrotoluene (TNT). Up to date, attentions have been paid to prepare fluorescence films. CMPs are possible to tune their electronic and photophysical properties by modifying the optical band gap. Cooper's group introduced different comonomers and varied the monomer distribution to tuned CMPs photophysical properties by controlling optical band gaps in CMPs [242, 243]. Ma et al. [244] obtained dendrimer films by EP method, which were verified to be rapid response, highly sensitive, and excellent reusable fluorescence probes for TNT vapor, Fe^{3+}, and benzene vapor.

4.4.3.5 Others

Jin et al. [245] studied the entrapment and release behavior of hollow CMPs spheres toward guest molecules, which can be controlled by media. At the same time, by using an appropriate solvent, guests could be entrapped into the cavity of the hollow structure. Based on the controlled release behavior of the guest-entrapped CMPs materials, a fluorescent alert system for organic solvent existence in water can be developed.

Tan et al. [210] synthesized nanoscale CMPs capsules by using PMAA microspheres as self-sacrificial templates. The resulting material showed a tunable absorption ability and shape-dependent photothermal conversion efficiency. Upon

exposure to 808 nm light, these materials rapidly generated heat and caused thermal ablation of HeLa cells with less than 10% viability.

4.4.4 Summary

CMPs are a class of MOPs that combine π-conjugation structure with porosity. A wide variety of chemical reactions are used to build CMPs with different structures and functionalities. The flexibility of molecular design and the tunable structure make CMPs extensive applications in various fields. However, the synthesis of CMPs with controlled morphologies and functionalities is still a challenge.

4.5 Polymers of Intrinsic Microporosity

Over a long period of time, tremendous efforts of porous materials have been devoted to the research of macroporosity and mesoporosity [246, 247]. However, it was largely unexplored for preparing pure organic microporous networks within polymeric materials [248]. It has been known that active carbon is used in various aspects as adsorbents, catalyst supports, and deodorizers [249, 250]. Considering its vast commercial value while with the limited quantities for systematic chemical and structural modification, researchers were inspired to imitate the structure of active carbon, and thus, a wide range of PIMs were developed.

The main chains of PIMs are constructed with rigid and contorted molecular structures, which cannot fill space efficiently [16]. Unlike conventional microporous materials, PIMs are soluble and can be processed readily for enormous applications. It is worth noting that microporous structure of PIMs will maintain either in solid state or in liquid state, which offers wide applications in gas separation, heterogeneous catalysis, hydrogen storage, and so on.

4.5.1 Preparation of Polymers of Intrinsic Microporosity

Initially, the Pc macrocycle was selected as the basic unit by Mckeown and co-workers owing to its extended planarity and unique property [251]. The structural diversity of Pc-containing polymers and their optical and electronic properties made them suitable for a wide range of applications. However, due to strong non-covalent interactions (predominantly π–π interactions), the prepared Pc-containing polymers showed a strong tendency that the aromatic units tend to aggregate into columnar stacks, leading to non-porous solids, which failed to form microporous architecture. Hence, it is essential to introduce a highly rigid and nonlinear linking group between the phthalocyanine subunits to ensure the

space-inefficient packing, thus avoiding structural relaxation and consequent loss of microporosity. To fulfill these requirements, they introduced microporous structure into phthalocyanine subunits, and obtained the first Pc-containing PIMs in the later 2002 [252]. A nonlinear linking group derived from the commercially available 5,5′,6,6′-tetra-hydroxy-3,3,3′,3′-tetramethyl-1,1′-spirobisindane (**A1**) was designed to connect phthalocyanine subunits and provided the nonlinear shape by means of efficient dioxane-forming reaction between **A1** and 4,5-dichlorophthalonitrile (**B1**), to produce a rigid phthalocyanine microporous polymer network (Fig. 4.26). They also confirmed that the spirocyclic crosslinking prevents a compact packing of the phthalocyanine components, which resulted in an amorphous microporous structure. Nitrogen adsorption measurements showed that the materials possessed high surface areas in the range of 450–950 $m^2\ g^{-1}$, with significant adsorption at low relative pressure ($p/p_0 < 0.01$) indicating microporosity.

Following on the progress of these phthalocyanine-based polymers of intrinsic microporosity (Pc-network-PIMs), other rigid structures are also investigated to determine whether they are suitable components for constructing microporous organic materials. Due to the potential heterogeneous catalysis properties, metal-containing porphyrins are treated as desirable components of microporous organic materials. Nevertheless, the preparation of porphyrins is a low-yielding process, which is unsuitable for polymer network assembly. To conquer this difficulty, rigid spirocyclic linking groups were introduced directly into preformed porphyrin subunits by means of the efficient dioxane-forming reaction between the mesotetrakis(pentafluorophenyl) porphyrin (monomer **B2**) and the monomer **A1** [253]. A number of useful applications were obtained for heterogeneous catalysis by supporting porphyrins within or on the surface of materials matrix. A synthetic strategy based on the reaction of preformed porphyrin **1** was devised. For the
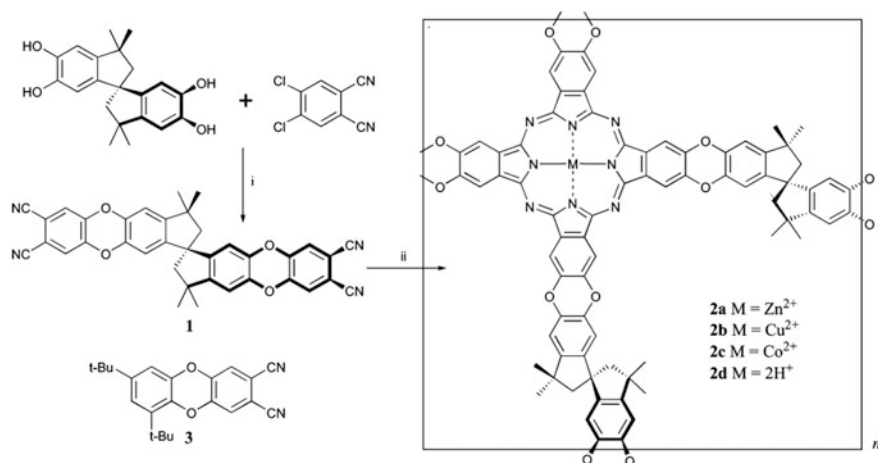
Fig. 4.26 Synthetic route of Pc-network-PIMs. Reproduced from Ref. [252] with kind permission of © 2002 Royal Society of Chemistry

preparation of the bis(phthalonitrile) precursor into the phthalocyanine network polymers, a facile reaction between 5,5′,6,6′-tetrahydroxy-3,3,3′,3′-tetramethyl-1,1′-spirobisindane **2** and 4,5-dichlorophthalonitrile was used. Porphyrin network polymers were directly prepared from **1** and **2** via dibenzodioxane formation, and the resulting porphyrin-network-PIM demonstrated to show high surface areas around 1000 $m^2\ g^{-1}$.

It offers a general reaction from the formation of Pc-network-PIMs and Porphyrin-network-PIMs by dioxane formation reaction which links planar aromatic macrocycles with a rigid spirocyclic spacer [33]. It can be concluded that for microporosity, at least one of the monomers must contain rigid contorted structure, which may be a spirocentre (e.g., **A1** and **B8**), a non-planar rigid skeleton (e.g., **A2**, **A4**, and **A6**), or a single covalent bond around which rotation is hindered (e.g., **A7**, **B1** and **B7**). If reaction occurs between two planar monomers (e.g., **A5** with **B4**), the non-porous material will be formed finally (Fig. 4.27).

It has been described in 2003 by Tattershall and co-workers for the earliest synthesis of a nanoporous network polymer incorporating 5,6,11,12,17,18-hexaazatrinapthylene (HATN) rigid functional units through the efficient dibenzodioxane forming reaction [254]. The described HATN-network-PIM, derived from the spiro-monomer **A1** and HATN **B2**, exhibited high surface areas in the range of 750–850 $m^2\ g^{-1}$ and was suitable as catalytic support which provided a high loading of accessible active sites. It also indicated a potential application as adsorbents for the removal of toxic organic compounds such as phenols from water or gas streams.

Of particular interest is the potential to tune the microporous structure by choosing different monomer precursors, and one of the examples is the utilization of monomers that contain preformed cavities to provide sites of an appropriate small size for hydrogen adsorption. In 2007, a novel triptycene-based PIM (Trip-PIM)
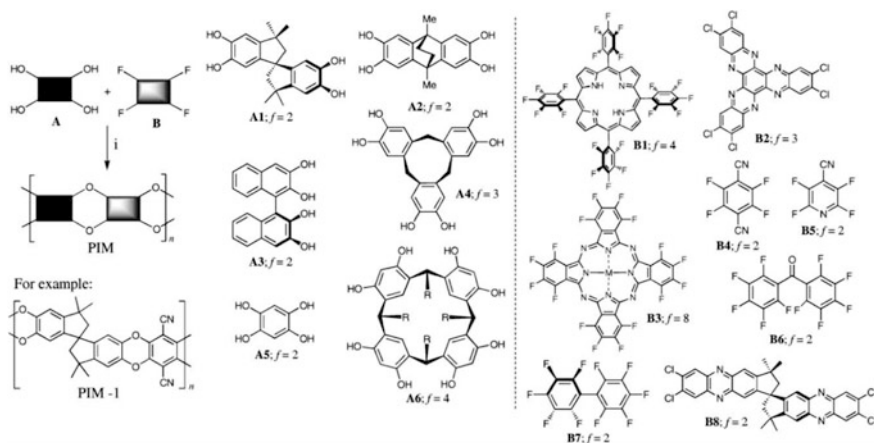
Fig. 4.27 Synthesis and properties of PIMs. Reproduced from Ref. [33] with kind permission of © 2006 Royal Society of Chemistry

was developed and displayed enhanced surface area of 1065 $m^2 g^{-1}$, and reversibly adsorbed 2.71% hydrogen by mass at 10 bar/77 K [255]. The effective blocking of close, face-to-face association between these fused-ring struts may be helpful to further frustrate space-efficient packing of the macromolecules leading to larger microporosity. Following this work, in 2010, Mckeown et al. reported the synthesis of network-PIMs derived from triptycene monomers containing alkyl groups attached to their bridgehead positions [256]. Gas adsorption can be controlled by varying the alkyl chains, and the apparent BET surface area of the materials was within the range of 618–1760 $m^2 g^{-1}$. Shorter alkyl chains or chains with branched structure provided the materials with larger microporosity, while longer alkyl chains appear to block the microporosity created by the rigid organic framework.

Since some of network-PIMs displayed swelling property in the presence of an adsorbate, researchers have sorted for new types of intrinsic microporosity which could be obtained from a linear polymer without a network structure. As can be seen from the previous results, insoluble network-PIMs possess both high surface areas and hydrogen storage which may be attributed to highly covalent connected network structure resulting in larger microporous volume. The microporosity within network-PIMs is maintained by a robust network of covalent bonds. It is reasonable to anticipate that above a certain amount of free volume, the voids would be interconnected, and therefore, the polymer will behave as a conventional microporous material despite the lack of a network structure. Such a material could be soluble and would facilitate solution-based processing, which provides advantages over other microporous materials.

In 2004, Budd et al. demonstrated that a network of covalent bonds is not an essential aspect for microporous organic materials. A family of non-network polymers was described which formed microporous solids simply because their highly rigid and contorted molecular structure cannot fill space efficiently. Under this guidance, they successfully synthesized the first soluble PIM using the same dioxane-forming polymerization reaction between the aromatic tetrol monomers **A1–A3** with the appropriate fluorine-containing compounds **B1–B3**, in which microporosity arises simply from a polymer whose molecular structure is highly rigid and contorted so that space-efficient packing in the solid state is frustrated [16]. The lack of rotation freedom along the polymer backbone ensures that the macromolecules cannot rearrange their conformation to collapse the open structure of the material. Consequently, the polymer molecular structure remains intact which maintains the microporosity. PIM-1 showed highest surface area among PIM 1–6 up to 850 $m^2 g^{-1}$. Nitrogen sorption analysis indicated a significant proportion of micropores with dimensions in the range of 0.4–0.8 nm. There was also evidence of some mesoporosity that the marked hysteresis at low pressures may be attributed to pore network effects.

For the purpose of enhancing hydrogen adsorption, Mckeown et al. incorporated the bowl-shaped receptor monomer, cyclotricatechylene (CTC), within a network-PIM by using benzodioxane-forming reaction via CTC and tetra-flurotere-phthalonitrile [257]. The hydrogen adsorption property of CTC-network-PIM (0.56 wt%) is much higher than that of PIM-1 (0.5 wt%) and

HATN-network-PIM (0.43 wt%), which suggests that the greater predominance of ultramicropores resulting from the bowl-shaped CTC subunits enhances hydrogen adsorption.

In 2007, Thomas and co-workers expanded the concept of dibenzodioxane-based, soluble, ladder-type polymers to more common polymers of higher commercial interest, such as polyamides (PA) or polyimides (PI) [18]. They used 9,9′-spirobifluorene as the structure-directing motif since it can be easily modified to give 2,2′-dicarboxy-9,9′-spirobifluorene or 2,2′-diamino-9,9′-spirobi-fluorene compounds, and formed aromatic polyamides, polyimides, or poly(benz-imidazole)s (PBI) PIM-P4. They showed intrinsic microporosity and consequently high surface areas of 550 m^2 g^{-1}. Before this work, the synthesis of polyimides based on a spirobifluorene monomer has already been reported, but no attention was paid to the investigation of microporosity. Compared to linear PI, these polymers showed superior properties in terms of solubility and processability.

In the later 2008, Ghanem et al. prepared novel PIMs via bis(phenazyl) monomers derived from readily available bis(catechol)s [17]. They described the simple synthesis of suitable reactive tetrachloride monomers 4 and 5 based on phenazine units. PIMs 7–9 are soluble in several organic solvents (especially $CHCl_3$), but PIM-10 is soluble only in m-cresol and concentrated H_2SO_4, and the films from PIM-7 are particularly flexible and robust. Nitrogen sorption analysis provides an apparent surface area of 680 m^2 g^{-1} for PIM-7. The promising gas permeability data for PIM-7 confirms that PIMs are excellent for designing highly rigid but solution-processible polymers, which combine high selectivity with high permeability as required for the fabrication of efficient gas separation membranes.

In 2009, Yampolskii et al. reported a series of PIM-PIs prepared by reacting with various aromatic diamines of bis(carboxylic anhydride) containing spirocenters [258]. Membranes were directly prepared by casting from chloroform solution. In comparison with other polyimides, these novel groups of PIM-PIs showed espe-cially good results for the separation of the mixtures CO_2/CH_4 and CO_2/N_2. The gas separation properties exceeded most of the permeable conventional polyimides.

In 2011, Mckeown et al. introduced a rigid and propeller-like shape unit, hexaphenylbenzene (HPB) into polymers, resulting in HPB-PIM-1 and HPB-PIM-2 derived from 1,2- and 1,4-di(3′,4′-dihydroxyphenyl)tetraphenylbenzene monomers, respectively [259]. The inefficient molecular packing of benzene rings led to intrinsic microporosity. HPB-PIM-2 showed significantly lower permeability sim-ilar to PIM-1 but enhanced selectivity ($CO_2/N_2 = 26$), which can be attributed both to lower diffusivity due to lower intrinsic microporosity and lower solubility due to a smaller concentration of polar groups such as ether and nitrile. Owing to the advantages of these aspects, HPB-PIM-2 was still attractive for gas separation.

In general, improving carbon dioxide capture by introducing functional groups often results in the loss of the accessible pores and surface area. While in the year 2012, Yavuz and co-workers reported the first noninvasive functionalization of the
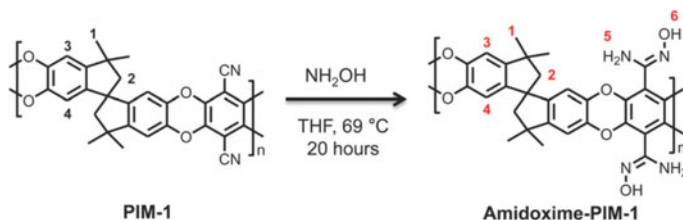
Fig. 4.28 Synthetic pathway of amidoxime-PIM-1. Reproduced from Ref. [260] with kind permission of © 2012 Royal Society of Chemistry
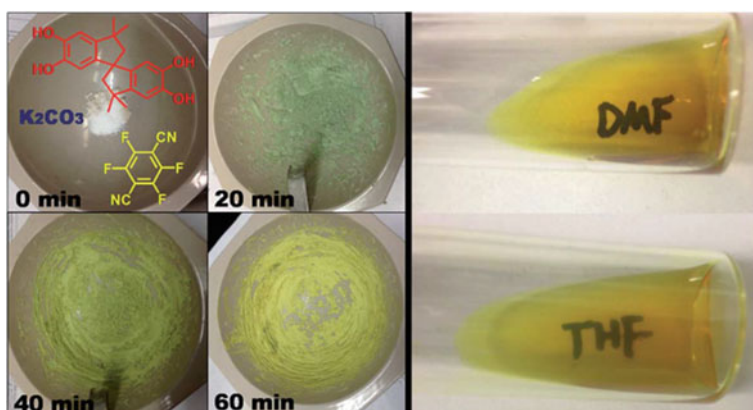
Fig. 4.29 Preparation of PIM-1-MS and 1 wt% solution in different solvents. The big difference between PIMs and common polymers arouses great interest of researchers. Reproduced from Ref. [261] with kind permission of © 2015 Royal Society of Chemistry

PIMs by introducing the amidoxime groups in PIM-1 (Fig. 4.28) without adversely affecting physicochemical properties [260]. Incorporating amidoxime group increased a carbon dioxide adsorption capacity up to 17 wt%, and the amidoxime-based PIM-1 still exhibited good processability without losing the film-forming ability.

In 2015, Dai et al. reported a solvent-free mechanochemical approach to construct PIM-1-MS and PIM-4-MS polymers with high molecular weight and low polydispersity by solid grinding [261]. Both the number average molar mass (M_n) and weight average molar mass (M_w) were much higher than PIM-1 and PIM-4 polymers, while the value of M_n/M_w and surface area was much lower (Fig. 4.29).

4.5.2 Applications

4.5.2.1 Gas Permeability and Separations

Due to the wide applications for commercial, it has been a hot topic to explore polymeric membranes with both high gas permeability and separation. Before the appearance of PIMs, polymers with high permeability, like poly[1-(trimethylsilyl)-1-propyne] (PTMSP), often revealed low selectivity [262]. As well, polymers with high selectivity usually met with low permeability. As to microporous polymer materials, membranes made from PIM-1 and PIM-7 show higher selectivity compared with polymers which have similar permeability [263]. At the same time, the selectivity of CO_2/CH_4, H_2/N_2, and H_2/CH_4 is all relatively high, which indicates the superior performance of PIMs.

In terms of the separation of O_2 and N_2, the key factor is the mobility selectivity. PIMs are more likely to adsorb smaller oxygen molecule (diameter = 0.346 nm), rather than the larger nitrogen molecule (diameter = 0.364 nm). For microporous polymers, it initially depended on the micropores size distribution, while PIM-1 and PIM-7 have rather smaller pore size.

Regarding how to improve the performance of gas permeability and selectivity of PIMs membranes, researchers have also carried out a large amount of researches and achieved some progress. In 2013, Mckeown et al. used the Tröger's base (TB) polymerization reaction to prepare ethanoanthracene-based TB polymer and spirobisindane-based TB polymer, which extended the polymerization types of PIMs (Fig. 4.30) [264]. BET surface areas of 1028 m^2 g^{-1} for PIM-EA-TB and 745 m^2 g^{-1} for PIM-SBI-TB are obtained, respectively, and theses PIMs were proved to be highly soluble in chloroform and can be prepared into thin films readily.

In 2014, Jansen and co-workers used borane complexes to reduce nitrile groups in PIM-1 forming the amine-PIM-1 [265]. The incorporation of primary amine decreased the CO_2 diffusion coefficient and permeability, while enhanced the
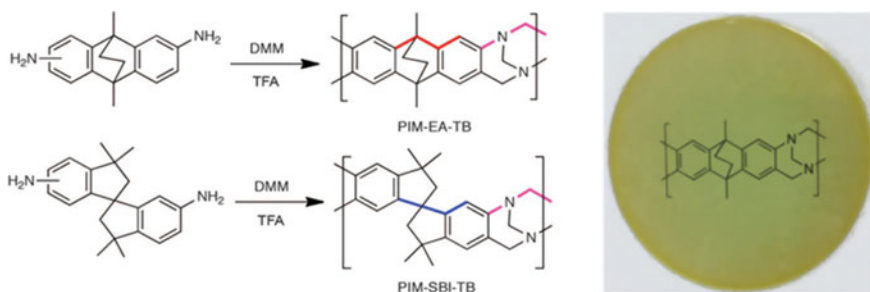
Fig. 4.30 Synthesis and molecular structures of PIM-EA-TB and PIM-SBI-TB (*left*). A solvent cast film (10 cm in diameter) of PIM-EA-TB (*right*). Reproduced from Ref. [264] with kind permission of © 2013 The American Association for the Advancement of Science

banding affinity for CO_2 and the sorption selectivity of CO_2/N_2 and CO_2/CH_4. Colina et al. reported a functionalized PIM with carboxylate backbone [266]. It was found that the enthalpy of CO_2 adsorption and adsorption capacity increased, which can be attributed to the increasing concentration of ions. Meanwhile, the selectivity of CO_2/N_2 and CO_2/N_2 enhanced in accordance with the increasing ion content.

Shamsipur and co-workers prepared a hydroxyl-functionalized polyimides using 2,2-bis(3-amino-4-hydroxyphenyl)hexafluoropropane and 4,6-diamino-resorcinol monomers, which was followed by a thermal treatment at 450 °C under N_2 for 1 h yielding the polybenzoxazole polymers (Fig. 4.31) [267]. This conversion increased membrane gas permeability and CO_2/N_2 selectivity, and also enhanced solvent resistance. Although the microporous structure and chemical functionalities enable PIMs with high gas uptake, permeability and selectivity, and solvent-resistant nanofiltration properties [268–271]. One major obstacle to the commercialization of glassy amorphous PIMs for membrane application is physical aging and the ensuing instability of their permeation property over time. In 2015, Pinnau et al. investigated the effect that relatively extreme intra-chain rigidity and high ultramicroporosity in some of the most permeable and selective PIMs potentially alleviate long-term physical aging and plasticization [272]. Through this work, they found this physical aging occurs in all PIMs despite their high interchain rigidity. Meanwhile, the inherent chain architecture plays an important role in physical aging. And finally, higher interchain rigidity does not prevent plasticization.

Various approaches have been made to avoid physical aging including copolymerization [273], crosslinking [274], and surface plasma treatment [275]. In 2014, Sivaniah and co-workers reported thermo-oxidative crosslinking of PIM-1 by heating in a suitable temperature window (350–450 °C) in the presence of trace amount of oxygen [276]. The pore size distribution, structure of channel and pore can be successfully tailored and subsequently increase the selectivity. The thermal-oxidative crosslinked PIM-1 (termed as TOX-PIM-1) polymer exhibited
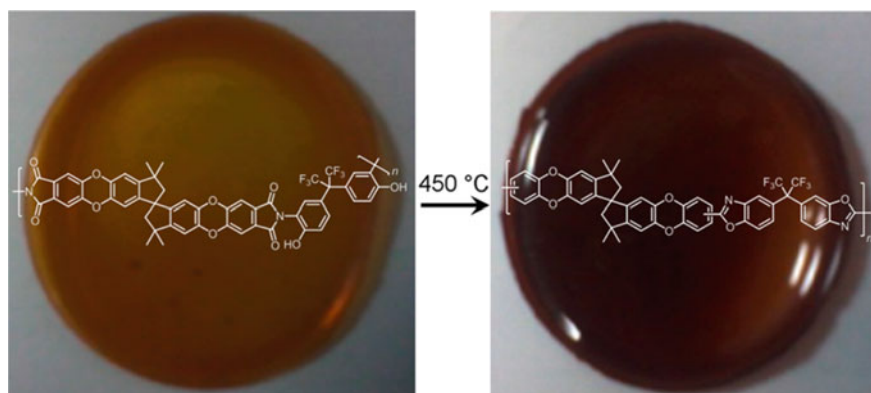
Fig. 4.31 PIM-PBO membrane derived from PIM-PI-OH membrane. Reproduced from Ref. [267] with kind permission of © 2014 American Chemical Society

decreased solubility compared with PIM-1 (Fig. 4.32). After crosslinking at 385 °
C, the CO_2/CH_4 selectivity of TOX-PIM-1 membrane increased up to 70, along
with a high CO_2 permeability of 1100 barrer. In 2015, the Sivaniah and co-workers
incorporated nanofillers into TOX-PIM-1 polymer which combined the covalent
crosslinking of microporous polymers [277]. This thermal oxidative crosslinking of
the PIM-1 polymer improved the gas selectivity of nanocomposites; meanwhile, the
gas permeability remained at a remarkably high level. After aging for two years,
they tested the gas separation properties again and demonstrated a higher
selectivity.

   Although these methods can successfully reduce aging, there still exists a big
challenge for the performance loss in permeability. One efficient method to over-
come this challenge is incorporating a secondary phase to form a mixed matrix
membrane. In 2016, Casiraghi and co-workers combined PIMs with graphene, and
formed PIM-1/graphene (PIM-1/Gr) composites [278]. The presence of PIM-1
enhanced the direct exfoliation of graphene in chloroform, and the graphene con-
centration played an important role in the efficiency of the process and stability of
the resulting dispersion. It has been proved that there is strong re-stacking of
initially exfoliated graphene in solution when forming the composites, which is
expected to produce strong promotion in mechanical properties and physical aging
of the membranes.
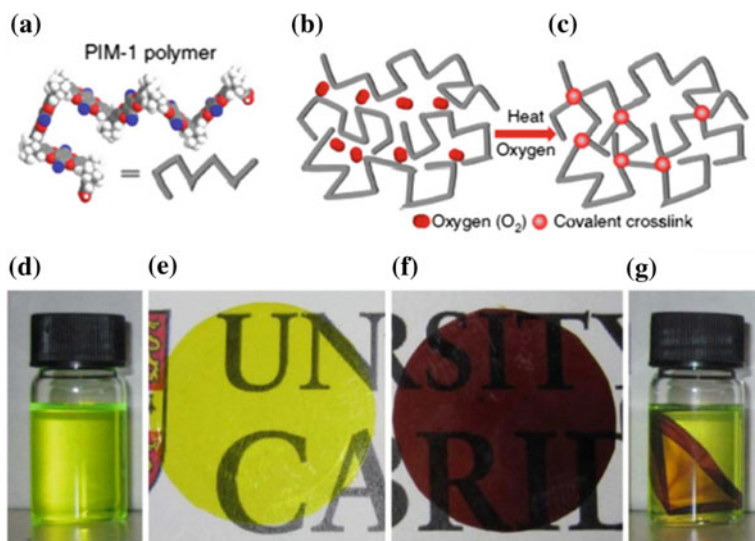
Fig. 4.32 a An ideal molecular model of PIM-1 polymer chain segment. **b**, **c** Two-dimensional
schematic illustration of thermal oxidative crosslinking. **d** Photograph of PIM-1 polymer solution
in chloroform. **e** Photograph of as-prepared PIM-1 membrane. **f** Photograph of TOX-PIM-1
membrane. **g** Solubility test of TOX-PIM-1 membrane in chloroform. Reproduced from Ref. [276]
with kind permission of © 2014 Macmillan Publishers Limited

Fig. 4.33 Molecular structure of PIM-1 and the hypercrosslinked polymer used as the filler (*top*). Schematic illustration of effect of filler on the performance of MMMs. Reproduced from Ref. [279] with kind permission of © 2016 Royal Society of Chemistry
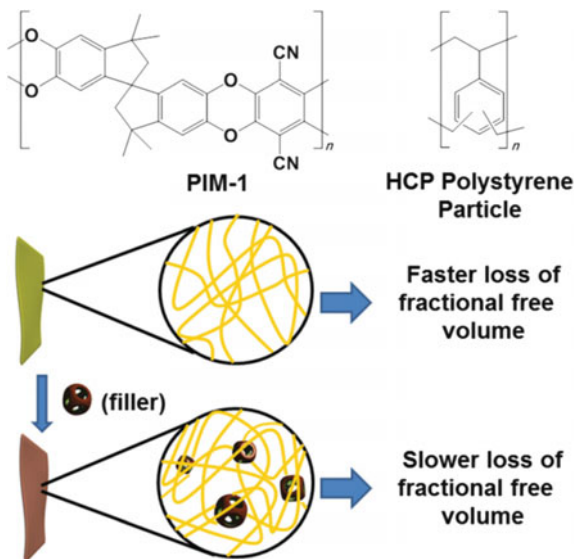
The free volume in PIMs will diminish over time, thus limiting the real application. Besides the nanofillers mentioned above, other new types of fillers are also selected to enhance the properties of PIMs. Cooper et al. reported a mixed matrix membrane by adding hypercrosslinked polystyrene as a filler into PIM-1 [279]. Since hypercrosslinked polymers possess water- and acid-tolerant properties, these mixed matrix membranes not only resulted in higher permeability but also alleviated polymer aging and permeability loss (Fig. 4.33).

4.5.2.2 Heterogeneous Catalysis

Usually, PIMs network containing porphyrin, phthalocyanine, or hexaazatrinaphthylene subunits could be used for catalysis by incorporating appropriate transition metal ions. For example, PcCo-network-PIM could be used for the degradation of hydrogen peroxide and showed a great enhanced rate compared to a non-porous microcrystalline model compound. In addition, this network-PIM is efficient for the catalysis of the oxidation of cyclohexene to 2-cyclohexene-1-one (78% yield after 48 h) which was comparable to the cobalt phthalocyanine-based homogeneous catalysts. The HATN subunits are well-established ligands capable of forming a complex with up to three transition metal ions. By exposing the orange HATN-network-PIM to a chloroform solution containing bis(benzonitrile) palladium(II) dichloride, the resulting material catalyzed a model Suzuki aryl-aryl coupling reaction with high efficiency, however that around 20% of the metal leached from the PIMs.

Similar palladium-containing materials with even higher specific surface area can be derived from PIM-7 by exploiting the ability of its phenazine subunits which act as ligands for metal ion coordination. This material contained over 20% by mass Pd^{2+} and showed a surface area of 650 $m^2 g^{-1}$. It can be deduced that the Pd^{2+} ions act as bridges between the PIM macromolecules to result in a network. Of great interest, a solvent cast film of PIM-7, swollen in methanol, can also be linked by Pd^{2+} to give an insoluble network.

In 2014, Mckeown and co-workers synthesized PIM-TB-Trip microporous polymer networks, which were assembled from triamino-triptycene monomers using Tröger's base forming polymerization reaction [280]. BET surface areas up to 1035 $m^2 g^{-1}$ for PIM-TB-Trip-1 and 752 $m^2 g^{-1}$ for PIM-TB-Trip-2 can be obtained, respectively. These materials possess high catalytic efficiency for Knoevenagel condensation reaction between benzaldehyde and malononitrile compounds.

In 2016, Marken and co-workers developed a composite film electrode by incorporating traditional carbon microparticles into PIM-EA-TB with a BET surface area of 1027 $m^2 g^{-1}$, then immobilized the free radical 4-benzoyloxy-2,2,6,6-tetramethyl-piperidine-1-oxyl (4B-TEMPO) on the surface of electrode [281]. Good access of solvent, substrate to catalyst site through rigid pores, and stabilization toward corrosion allow the porous PIM-EA-TB polymer to act as a host matrix for embedding free radical catalyst, thus improving the catalytic process for primary alcohols oxidation in a carbonate buffer at pH 10.3 (Fig. 4.34).

4.5.2.3 Hydrogen Storage

Under the condition of 77 K/1 bar, three PIMs (PIM-1, HATN-network, and CTC-network) are measured for their hydrogen adsorption properties with efficient H_2 uptake of 0.56 wt% for CTC-network, 0.43 wt% for HATN-network, and
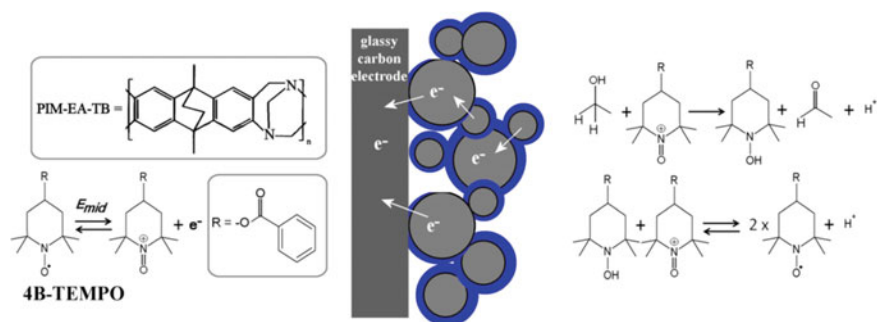
Fig. 4.34 Structure of the PIM-EA-TB polymer and 4B-TEMPO (*left*). Scheme showing the composite film with electrocatalyst embedded in PIM-EA-TB on carbon microparticles (*right*). Reproduced from Ref. [281] with kind permission of © 2016 Springer

0.5 wt% for PIM-1, respectively [257]. The bowl-shaped CTC subunits showed enhanced H_2 adsorption due to the greater predominance of ultramicropores. These results indicate that PIMs adsorb comparable amounts of H_2 to that of the best examples for zeolites and MOFs. Moreover, unlike all other types of microporous materials, the structures of PIMs are not necessarily constrained by a fixed network structure and may be dissolved in suitable solvents and swollen by several non-solvents. In order to achieve practical hydrogen storage materials from PIMs, it will be necessary to explore examples with higher surface areas (>2000 m^2 g^{-1}) while maintain the predominately ultramicroporous structure which is necessary to retain the beneficial multiwall interactions with H_2 molecules.

4.5.2.4 Other Applications

Except for the wide applications in gas separation and adsorption, heterogeneous catalysis, and hydrogen storage, PIMs have been employed in some of the unexplored fields. In 2015, chiral PIMs have been developed for selective membrane permeation of enantiomers by Shea and co-workers [282]. They reported the synthesis of chiral ladder polymers, (+)-PIM-CN and (+)-PIM-COOH, by using 5,5′,6,6′-tetrahydroxy-3,3,3′,3′-tetramethyl-1,1′-spirobisindan building blocks. The as-prepared chiral polymers were found to be strongly effective in the selection of a range of enantiomers. Marken et al. discussed the vacuum carbonization of PIM-EA-TB in generating a novel type of microporous heterocarbon materials in 2015 [283]. Compared to traditional organic precursors which usually causes tremendous structural damage and vanish of morphology under vacuum carbonization, the rigid molecular backbone of PIM-EA-TB was retained even carbonized under 500 °C in vacuum. Although the BET surface area decreased drastically from 1027 to 242 m^2 g^{-1}, microporosity increased considerably. Further study showed an interesting switch of electrochemical properties to higher pH-dependent capacitance from ca. 33 Fg^{-1} (oxidized) to ca. 147 Fg^{-1} (reduced), without significant electron transfer reactivity toward oxygen and toward hydrogen peroxide, and conductivity of approximately 40 MΩ/square for a ca. 1–2-μm-thick film.

4.5.3 Limitation and Challenge of Development

Compared with other MOPs materials, PIMs have advantages which can be listed as follows: Linear PIMs can be easily dissolved in suitable organic solvents, which makes it possible to test molecular weight by using gel permeation chromatography (GPC). This parameter provides information for controlling the reaction conditions. Furthermore, membranes with microporous structure can be obtained by casting, and then applied to gas separation and adsorption, and even the selectivity of CO_2, H_2, CH_4, and so on. Moreover, PIMs show great potential in hydrogen storage and gas adsorption. The main problem for the development of PIMs is that surface areas

cannot achieve very high value as well as the limited contorted structure and toneless types of polymerization. In addition, how to enhance the gas permeability and separation property also needs further discussion.

4.6   Macroporous Polymers

Porous polymers which are normally quiet low in density and very high in porosity have gained considerable attention and research. And when there are interconnected pore canals in polymer framework, high permeability and large effective surface area can be achieved [284, 285]. The different kinds of porous polymers with appropriate pore structure show potential applications in catalysts [102, 286–288], waste oil and wastewater treatment [14, 289–291], tissue engineering scaffolds [292–296], and separation [276, 297]. To satisfy the various application requirements, macroporous polymers are always designed with an adjustable pore structure and a high porosity. Compared to the microporous and mesoporous materials, macroporous materials have obvious advantages of fast mass transfer and simple separation [14, 293, 294]. The complex macrostructures can be achieved either by the incorporation of a functional comonomer into the HIPE [289, 298], or via a post-polymerization functionalization approach [14, 299] as well as the use of 3D printing [300, 301]. At present, macroporous materials prepared by feasible HIPE templates exhibit advantages in controllable pore size as well as inherent high porosity by varying the volume ratio of dispersed phase and continue phase.

HIPEs are defined as the untraditional emulsions which are highly viscous, paste-like emulsions with the internal volume ratio above 74% [285]. At present, polyHIPEs from water-in-oil (W/O) HIPEs and oil-in-water (O/W) HIPEs are becoming more and more common. The investigation range of HIPEs has been expanded a lot including supercritical CO_2-in-water (CO_2/W) HIPEs, non-aqueous oil-in-oil (O/O) HIPEs, and oil-in-ionic liquid (O/IL) HIPEs. In addition, the use of ionic liquids can extend the range of synthesis temperatures, which has been limited by the presence of water, to above 100 °C [302]. In recent work, the ionic liquid-in-oil (IL/O) HIPEs have been synthesized of which the external phase (20%) was lauryl methacrylateand and the internal phase (80%) was a 1.15 wt% solution of bis(trifluoromethane) sulfonimide lithium salt in 1-ethyl-3-methylimidazolium bis(trifluoromethylsulfonyl)imide. The ability to synthesize water-free polyHIPEs could have a major impact upon polyHIPEs development, expanding the types of polymerization reactions that are sensitive to the presence of water (step growth polymerizations, anionic, cationic, or metathesis chain growth polymerizations) [303].

A typical polyHIPEs porous structure with voids and interconnecting holes can be achieved once the appropriate surfactant concentration is determined. Internal phase contents of over 74% can be reached for monodispersed droplets through their deformation into polyhedral. Meanwhile, the internal phase can also be obtained through the formation of a polydisperse droplet size distribution.
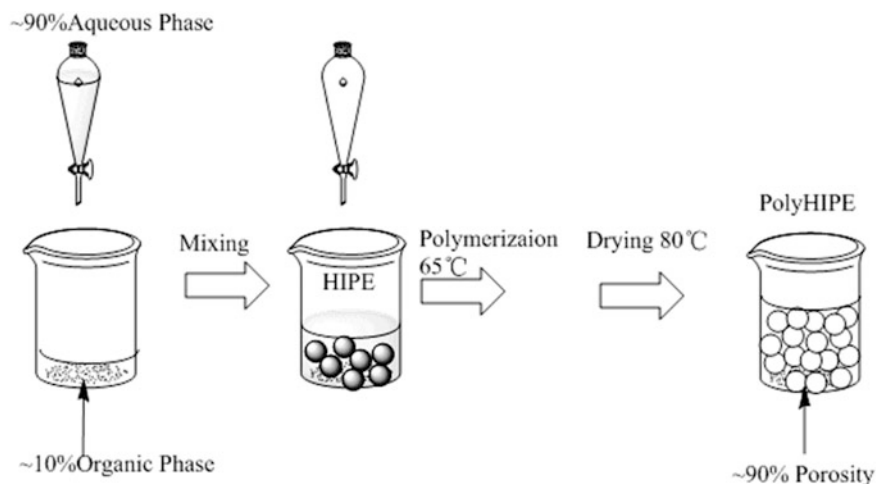
Fig. 4.35 Schematic illustration of HIPE formation and polyHIPEs synthesis in a W/O HIPE that contains an aqueous internal phase dispersed in a hydrophobic monomer external phase. Reproduced from Ref. [285] with kind permission of © 2014 Elsevier

Theoretical analysis has shown that the formation of polyhedral from monodispersed droplets should be favored over the formation of a polydisperse droplet size distribution [284, 285]. The conventional HIPEs are based on amphiphilic surfactants, such as sorbitan monooleate (Span 80), cetyltrimethylammonium bromide (CTAB), amphiphilic block polymers, and amphiphilic solid particles. Upon adding surfactants with the amount up to 5–50% into the continuous phase, a stable HIPE can be achieved. In a traditional polyHIPEs, the monomers are only dissolved in a continuous external phase, which surround the dispersed droplets of the internal phase. The formation of a typical W/O HIPEs (an aqueous internal phase dispersed within the hydrophobic monomers in the external phase) and the synthesis of a typical polyHIPE are illustrated schematically in Fig. 4.35.

A "typical" polyHIPE porous structure with voids and interconnecting holes is seen. In the traditional thermally initiated free radical polymerization process, droplet coalescence, volume shrinkage of monomer, and Ostwald ripening occur during polymerization, especially when the elevated temperatures are used for polymerization which enhance diffusion and interfacial destabilization. The widespread formation of such holes transforms the discrete droplets of the HIPE's internal phase into a continuous interconnected phase in the polyHIPEs. Removal of the internal phase, which now becomes continuous, yields voids in place of the internal phase droplets and results in a highly interconnected, open-cell, emulsion-templated porous structure [285, 304, 305]. Recent work on polyHIPEs with tunable void sizes and narrow void size distributions has been carried out for developing theoretical models to describe the relationships between the void size and the mechanical behavior. The formation of open pores can be contributed to

several factors, such as partial coalescence between neighboring droplets, phase separation at surfactant rich phase and polymer rich phase, and volume contraction in the process of conversion from monomer to polymer [305].

The types of polyHIPEs systems developed including copolymers, interpenetrating polymer networks, biodegradable polymers, bicontinuous polymers, organic–inorganic hybrids, porous inorganics, and nanocomposites. PolyHIPEs have also been developed for applications such as chemical synthesis, chromatography, ion exchange, separation, sensing, tissue engineering, and controlled drug delivery. The recent surge in publications on polyHIPE systems mirrors that for porous polymers, the results of a relatively restrictive literature search for articles that contain "polyHIPEs." This part is a brief review and survey of recent advances made in macroporous materials synthesis, structure, and application by polyHIPEs.

4.6.1   Macroporous Polymer Synthesis in PolyHIPEs of W/O

Traditionally, the polymeric surfactants suitable for HIPE preparation have been limited to several kinds of polyethylene oxide (PEO)-based copolymers, such as Pluronic and Hypermer. Recently, more and more efforts have been directed for the design of amphiphilic block copolymers that can be used for the stabilization of HIPEs, which can provide a one-step route for the surface functionalization of the 3D matrix [306]. Wang et al. disclosed a facile and rapid route for tailoring the polymer amphiphilicity, which can enable systematic investigation of the influence of polymer amphiphilicity on the phase behaviors of high internal phase emulsions [307]. A commercial polystyrene-b-polyvinylpyridine (PS-b-P4VP; Mn = 8800 Da; PDI = 1.15) was applied as the surfactant with a water contact angle of 95° which can be obtained by recombining trifluoroacetic acid (CF_3COOH) to adjust the hydrophilization of the P4VP segment. So, it is worth mentioning that this method for tailoring the amphiphilicity of PS-b-P4VP is rather facile and controllable by quaternization reaction. The surfactant with a molar ratio of 1:0.2 of the pyridine rings to carboxyl groups possessed a more extraordinary gel-like property of thixotropic non-Newtonian fluids even if the vial was placed upside down for two weeks and the highest internal phase volume of 95% was achieved with adding 40 mg mL^{-1} of the amphiphilic mixture [307]. Due to its relative low specific surface area, the adsorption capacity of macroporous materials is much smaller that limits their practical applications in treatment of water contamination. Thus, assembling the macroporous materials with nanoscale mesoporous particles could be an ideal solution to overcome these drawbacks, because hierarchical macro- and mesoporous adsorbents will have both of their advantages [14]. Pan et al. [308] fabricated a new hierarchical porous foam with macroporous and mesoporous structure. The macroporous (glycidylmethacrylate) (MPGMA) foams were synthesized by W/O HIPEs template. Then, carboxylated mesoporous silica nanoparticles (CMSNs) were grafted onto the interface of macroporous foams via the chemical bond (Fig. 4.36). Large amounts of carboxyl groups which were
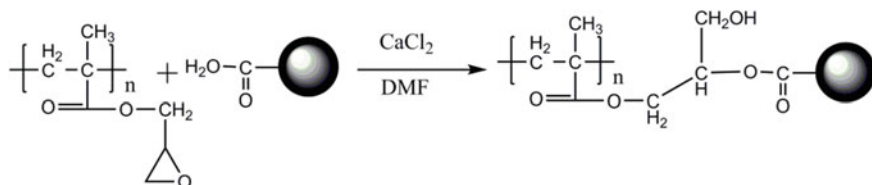
Fig. 4.36 Schematic illustration for the reaction of the MPGMA's epoxy groups with CMSN's carboxyl groups. Reproduced from Ref. [308] with kind permission of © 2016 Elsevier

Fig. 4.37 Schematic illustration for the preparation and application of chiral helical macroporous materials. Reproduced from Ref. [298] with kind permission of © 2015 American Chemical Society
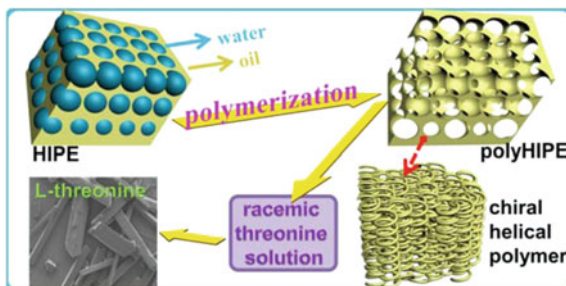
introduced into the as-prepared hierarchical porous foams could be benefited for the rapid capture of pollutants. The maximum adsorption capacity of HPFs for λ-cyhalothrin and Cu(II) was 80.11 and 21.79 mg g^{-1} at 288 K, respectively. And the excellent adsorption ability provides more potential opportunities for the HIPEs to be applied in the field of simultaneous removal of λ-cyhalothrin and Cu (II) [308].

A variety of achiral advanced materials have been fabricated through HIPEs and exhibit potential applications such as biomaterials and separation materials. Chiral porous materials combine two special properties, chirality and porosity, which can render the material with smartness by certain stimulation, e.g., optical, PH, and force. However, for chiral porous organic polymers, there have been only a few reports [309]. Meanwhile, the open pore structure in polyHIPEs has a positive effect on the sufficient contact between racemates and polyHIPEs and the bulk polyHIPEs are extremely easily recyclable compared with the other types of induced crystal. Deng group combined the HIPEs approach with chiral acetylenic monomers for preparing a novel, unique type of chiral porous material. The novel macroporous materials consisting of chiral helical polymer by coordination polymerization or free radical polymerization (Fig. 4.37) demonstrated their significant applications as chiral inducers for enantioselective crystallization. The high *cis* content with the max ratio of 90% by measuring the UV–Vis absorption and Raman spectra endowed the polyHIPEs to possess optical activity and exhibited promising application in chiral resolution. Enantioselective L-threonine and L-alanine were successfully induced to crystals from respective racemic solution. For a series of crystallization of racemic threonine, the max enantiomeric excess (ee) was about 74% [298].

4.6.2   HIPE of O/W

Conventional O/W HIPEs are stabilized by surfactants, such as polyethylene glycol tert-octylphenyl ether (Triton X-405), polyethylene glycol dodecyl ether (Brij 35), and poly(ethylene glycol)-block-poly(propylene glycol)-block-poly(ethylene glycol) (Pluronic F68). However, large amounts of expensive surfactants are required to stabilize HIPEs at the concentration of 5–50% with respect to the continuous phase [284, 285]. In recent work, macroporous materials have been used as biomaterials and tissue engineering materials. Pores with size in the range of 25–300 μm in macroporous polymer are required so as to be larger than the dimensions of mammalian cells, which are typically around 20–30 μm. And it is desirable for scaffolds to possess high surface areas (>500 m^2 g^{-1}), high porosities (>90%), and a high degree of pore interconnectivity to facilitate transport of nutrients and oxygen as well as cell migration and cell attachment [310]. Nevertheless, it has been found that the optimal pore size for tissue engineering scaffolds is in the range of 50–300 μm depending on the cell type. Cells are mostly shown to be spreading on the outer surface of the scaffold and have rather limited cell penetration into the scaffolds due to small pore throat in the range of 5–20 μm of hydrophilic polyHIPEs [295]. Then this system allows the injection of cell-laden hydrogel scaffold, which offers significant advantages over other types of rigid scaffolds that require open surgery for their implantation by eliminating possible complications that may accompany invasive surgery or a potential misfit of the scaffold in the defect site because of its ability to construct into a potential defect site.

Bismarck group designed a biocompatible amphiphilic copolymer, specifically gelatin-graft-poly (N-isopropylacrylamide) (GN) (Fig. 4.38a), as surfactant to construct high internal phase emulsion templates, thus proposing an effective and versatile route to create remarkably high porosity and interconnected macroporous foams, which are also biocompatible and suitable as cell carriers. The amphiphilic copolymer without any cytotoxic can stabilize oil phase (p-xylene) in water phase (Fig. 4.38b), which can produce the resultant hydrogel scaffold as biocompatibility
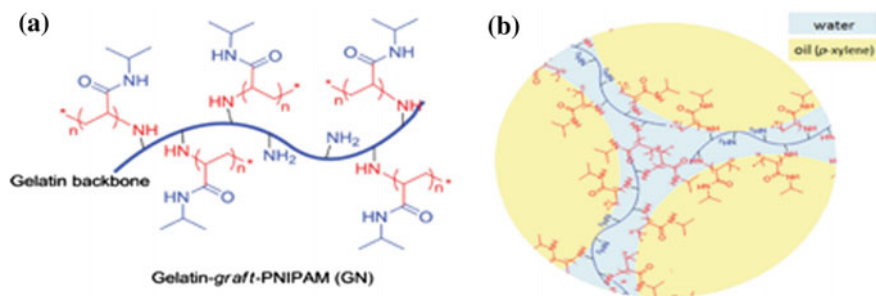
Fig. 4.38 **a** Molecular structure of gelatin-graft-PNIPAM; **b** schematic of the oil (p-xylene)/water interface of HIPE stabilized by GN. Reproduced from Ref. [311] with kind permission of © 2015 Wiley-VCH

materials. In this work, human skin fibroblast cells with large amount of proliferation colonized the bulk surface of the foams, spreading extensively and extending into the scaffold along the pore throats [311]. Due to the dual temperature sensitivity of polyHIPE hydrogel, the cells break the associations between gelatin chains, widen the pores, and loosen the hydrogel network for the cells to penetrate deeper into the scaffold in warm culture medium.

4.6.3 HIPE of CO_2/Water

In order to facilitate the template removal and to avoid the contamination of the porous structure by residual traces of organic solvents, the high internal phase CO_2/W emulsion templating technique was developed [285]. Supercritical carbon dioxide ($ScCO_2$) is a nontoxic, nonflammable, non-expensive, natural solvent and can be used as an alternative to conventional organic solvents for the preparation of high internal phase CO_2/W emulsions [312]. Above 70 bar, the decrease in surface tension (γ) was smaller as CO_2 is less compressible at higher pressures. In this range of higher pressures, the value of the W/CO_2 interfacial tension was close to 20 mNm^{-1}. The requirements for surfactants for lowering the interfacial tension are less stringent than for microemulsions. A potential solution to this problem is to prepare CO_2/W emulsion templates. These are composed of an ionic or neutral hydrophilic head associated with a CO_2-philic tail consisting of fluorinated or branched aliphatic sequences, polysiloxanes or polyvinyl esters [313]. With the exception of fluorinated and silicone-based polymers, CO_2 lacks the solvent power to solvate macromolecules easily. Although these fluorinated or silicone-based materials have been studied as steric stabilizers in dispersion polymerization and as surfactants in preparing CO_2/W or water-in-CO_2 (W/CO_2) emulsions or microemulsions, the associated cost and poor environmental degradability may prohibit their industrial-scale applications. CO_2 is a naturally abundant alternative to the organic solvents, which can be readily removed from a polyHIPEs scaffold simply by depressuring the system as shown in Fig. 4.39. The materials with well-defined porous structures without using any volatile organic solvents, only water and CO_2, are used [314].

In earlier work, Butler et al. used perfluoropolyether (PFPE) surfactants and poly (vinyl alcohol) (PVA) as a co-surfactant to stabilize CO_2/W emulsions of acrylamide polymers [315]. Palocci et al. reported the preparation of dextran-based macroporous materials using supercritical CO_2 as the internal phase and ammonium salt of perfluoropolyether (PFPE, Mw = 550 g/mol) carboxylic acid as the surfactant [316]. Debuigne et al. used sugar-based fluorinated compound as emulsifiers and PVA as co-stabilizer (5% w/v based on water) at 60 °C and 250 bar to prepare highly interconnected macroporous poly(acrylamide) and poly(vinylimidazolium) porous monoliths [314]. Macroporous PAM was a brittle porous sample with the size of large pores (18 μm and cells 30–100 μm). The better performance of the fluorinated surfactant **40b** over the aliphatic **40a** for the polyHIPE synthesis is in agreement with the higher CO_2/W surface activity recorded for **b** compared to **a** as
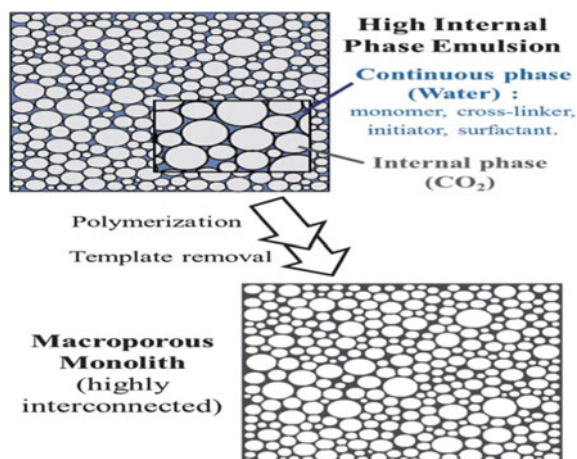
Fig. 4.39 Schematic representation for the fabrication of polyHIPEs. Reproduced from Ref. [314] with kind permission of © 2013 Royal Society of Chemistry
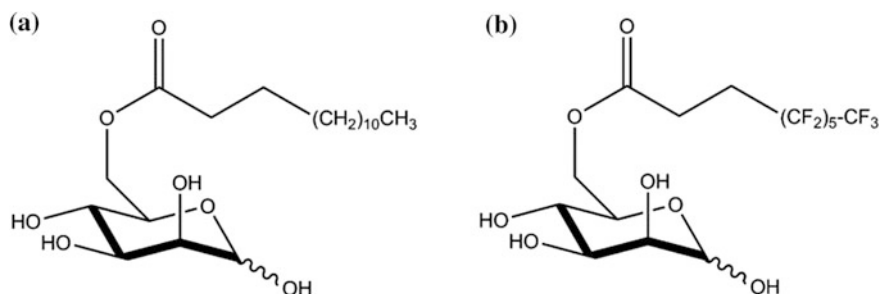
Fig. 4.40 Chemo-enzymatic syntheses of the sugar-based surfactants considered in this study. Reproduced from Ref. [314] with kind permission of © 2013 Royal Society of Chemistry

shown in Fig. 4.40. The beneficial effect of the fluorinated tail on the stabilization of the CO_2/W emulsion and the preparation of PAM polyHIPE was further confirmed when using a surfactant with a longer fluorinated chain.

However, synthesis of these fluorinate polymers and siloxane-based polymers which cannot be degraded in the nature will lead to big environment problems. Considering the principles of green chemistry, the non-fluorous and non-siloxane hydrocarbon is necessary in the $ScCO_2$ application. HIPEs prepared with non-fluorinated surfactants at lower pressures (<120 bar) can also be accessed [312]. In previous work, Da Rocha et al. studied the behavior of poly(propylene oxide)-b-poly(ethylene oxide)-b-poly(propylene oxide) (Fig. 4.41a) at the W/CO_2 interface as a function of their Mw and hydrophilic/CO_2-philic balance (HCB) [317]. A symmetric triblock copolymer comprising 30 propylene oxide units and 26 ethylene oxide has the lowest γ with a slightly turbid W/CO_2 emulsion for

over 10 min using 0.1 wt% of surfactant/CO_2 and less than 1 w/w% of water. Sarbu et al. [312] designed the new non-fluorous $(CHOCO_2)_n$–$(EO)_m$–$(CHOCO_2)_m$ poly(ether-carbonate) (Fig. 4.41b) that can be dissolved in CO_2 by optimizing the balance between enthalpy and entropy of solute–copolymer and copolymer–copolymer interaction. $CHO–CO_2)_{25}$–$(EO)_7$–$(CHO–CO_2)_{25}$ is soluble in CO_2 at lower pressures than 15 MPa, and when added 1.8 mM polymer to a mixture of water and CO_2, it forms an emulsion upon stirring which is stable for hours. Meanwhile, the emulsion is more stable at pressures between 170 and 350 bar than at pressures above 400 bar.

However, these CO_2-soluble hydrocarbon surfactants are applied in high internal water-CO_2 emulsion. Later on, stable CO_2/W HIPEs were formulated with amphiphilic poly(vinyl acetate)/poly(ethylene glycol) (PVAc-b-PEO, Fig. 4.41c1) block copolymers and cured for polymerization of acrylamide. Then, Tan et al. [318] prepared the diblock copolymer oligo (vinyl acetate) as surfactant to synthesize the porous, crosslinked poly(acrylamide) (PAM) materials (bulk density
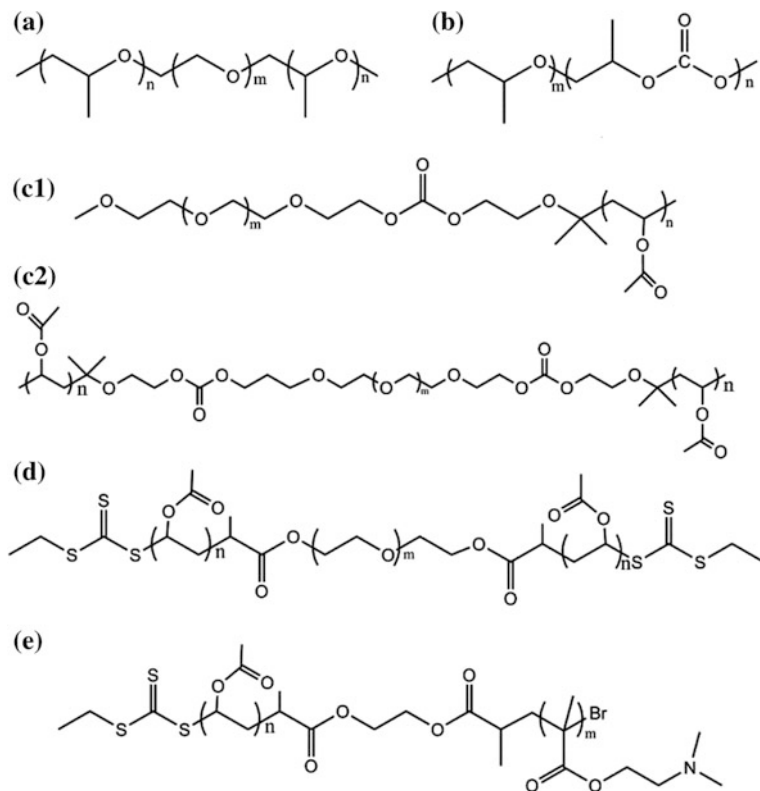
Fig. 4.41 Molecular structures of **a** PPO-b-PEO-b-PPO, **b** poly(ether-carbonate) $(CHO–CO_2)_n$–$(EO)_m$–$(CHO–CO_2)_n$, **c1** PVAc-b-PEO, **c2** PVAc-b-PEO-b-PVAc, **d** X-OVAc-b-PEG-b-OVAc-X, **e** PVAc-b-PDMAEMA [294, 312, 317–319]

0.057 g/cm^3, median pore diameter 10.85 μm) by emulsion-templated material via polymerization of a CO_2/W emulsion (90% v/v CO_2). And the triblock polymer PVAc-b-PEG-b-PVAc surfactant (Fig. 4.41c2, $m = 60$, $n = 30$) was found to emulsify up to 97% v/v CO_2 in water and form a uniform, opaque emulsion which can be stable for at least 48 h.

Following, Tan group adjusted the hydrophic-CO_2 philic balance of X-OVAc-b-PEG-b-OVAc-X (Fig. 4.41d) copolymer surfactants in the water-CO_2 emulsion to prepare the macroporous materials (pore size in the range of 3.2–10.0 μm, the intrusion volume in the range of 4.66–7.82 cm^3/g) under lower pressures which were achieved using a low-temperature redox-initiated polymerization of acrylamide-based HIPEs [319]. The influence of the surfactant concentration and molecular weight of OVAc block on the morphology of the porous structures was also investigated.

Then, Zhang et al. [294] designed and grafted the ionic component polydimethyl-aminoethyl methacrylate (PDMAEMA) to PVAc-b-PDMAEMA (Fig. 4.41e) which contains pendant tertiary amines that are easily protonated below their pKa (7.5) and demonstrate a strong hydrophilic character. By adjusting the appropriate hydrophilic/CO_2-philic ratio of PVAc-b-PDMAEMA, the $(PVAc)_{16}$-b-$(PDMAEMA)_{17}$ with best hydrophilic/CO_2-philic balance ratio can stable the emulsion for 12 h under static conditions. Moreover, the HIPE is still formed when the concentration of surfactant decreases to 0.16% (w/v), and remains stable for at least 1.5 h. When the concentration of $(PVAc)_{16}$-b-$(PDMAEMA)_{17}$ is 1.0%, the pore size of the PAM materials is mostly below 10 μm (taking up 81% volume), and the percentage of macropores (>19 μm) is very low (<4%) (Fig. 4.42) [294].

Compared with other high internal phase emulsions, CO_2/W adopts different stabilizers. Tan et al. [292] reported a method to stable CO_2/W emulsions using only partially hydrolyzed PVA solutions without the addition of any surfactants PVA (25% w/v solution in H_2O) and crosslinker (glutaraldehyde 20% w/w based on PVA) which formed the milky white CO_2/W emulsions under 8 °C and proved to be stable for at least 12 h without the phenomenon of phase separation
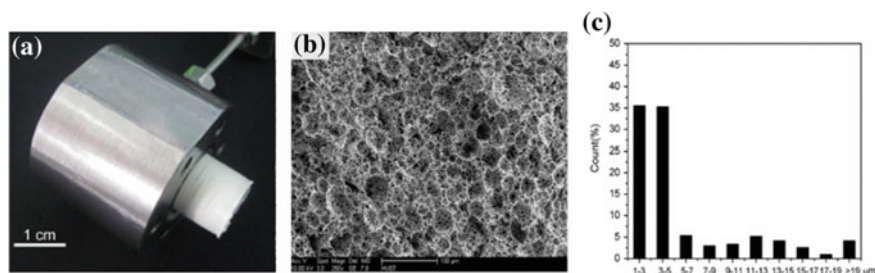
Fig. 4.42 **a** Photographs of low-density C/W emulsion-templated PAM-based materials. **b** SEM analysis of PAM-based macroporous materials and their pore size distributions prepared by C/W emulsion templating polymerization with various concentrations of the $(PVAc)_{16}$-b-$(PDMAEMA)_{17}$ surfactant (w/v) 1.0%. Reproduced from Ref. [294] with kind permission of © 2014 American Chemical Society
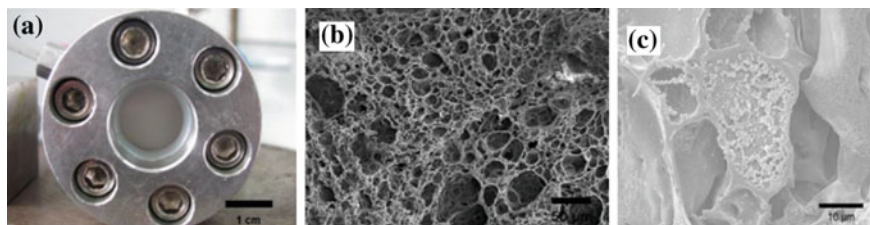
Fig. 4.43 **a** Photographs of a PVA hydrogel formed by gelation of a C/W emulsion, **b** SEM image of hydrogels at a constant ratio of V_{CO2}/V_{H2O} (8/2), 16.8% w/v PVA (88% hydrolyzed, Mw: 22,000 g/mol) based on aqueous phase, **c** SEM images of fibroblast cells attached to PVA hydrogels. Reproduced from Ref. [292] with kind permission of © 2015 Elsevier

(Fig. 4.43a). In this work, it is mentioned that PVA solution with a high viscosity can increase the stable concentrated CO_2/W emulsions owing to the high viscosity of PVA solution and higher solubility of PVA in CO_2 under lower temperature.

As shown in Fig. 4.43b, the hydrogels have an open porous structure (the average pore size of PVA (10.18 ± 3.28 μm), cavities of which are interconnected by a series of channels enable rapid nutrient and oxygen transfer through a polyHIPE material, which is important for cell culture. Due to using biodegradable surfactants, human embryonic lung diploid fibroblast cells' cellular growth and proliferation in PVA hydrogels were examined by SEM in Fig. 4.43c to demonstrate the feasibility of using the processed PVA hydrogels for tissue engineering applications. And the commercial partially hydrolyzed PVA (80% hydrolyzed, Mw 10,000) as surfactant was used to prepare the macroporous PAM (the size range of 13.18–26.67 μm) in high internal emulsion CO_2/W. The H9c2 cardiac muscle cells can grow and proliferate on the surface of these porous PAM scaffolds demonstrating their applications to produce organs by 3D printing technology [292].

4.6.4 HIPE of Pickering Emulsion

The relative large amounts of surfactant are needed for HIPE stabilization reflecting the instability inherent in dispersing the major internal phase within the minor external phase. Residual surfactants can affect the structure, properties, and applications of the resulting polyHIPEs materials. And some short-chain surfactants are leachable contaminants especially in biotechnology application. These surfactants can be difficult and expensive to remove. Some organic–inorganic hybrid polyHIPEs materials synthesized by the post-process of polymer would waste large amount of solvent which cause serious environmental problem. Unlike short-chain surfactants, particles can irreversibly adsorb on the interface of emulsions because of their appropriate wettability and high energy of attachment, which makes them good emulsifiers (Fig. 4.44) [327].
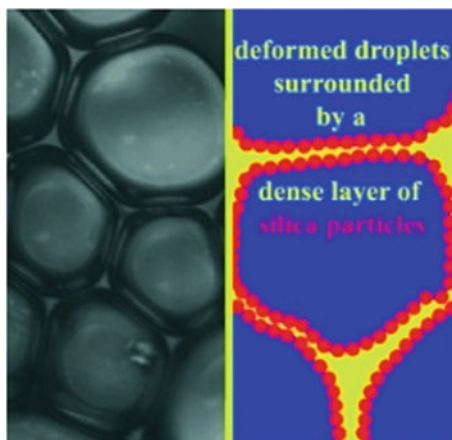
It has been proved that many solid particles, such as silica particles, titania particles [320], iron oxide nanoparticles [321], polymer, and graphene oxide flakes [322], can also be used to stabilize HIPEs, which is named as the Pickering HIPEs. Some specific approaches have also been developed to open pores of poly-Pickering HIPEs, including the use of a particular poly(urethane urea) stabilizer, an amphiphilic monomer to costabilize HIPEs, or a reactive lignin stabilizer [323]. The larger droplets of Pickering emulsions lead to thicker monomer layer between droplets. The particle geometry and dimension should also be well regulated in order to avoid the instability caused by gravity and Brownian motion. Meanwhile, these nanoparticles, quasi-irreversibly anchored at the oil–water interface, form dense interfacial barriers that resist coalescence. These solid shells could protect the emulsion droplets against any structural imperfection during polymerization, including coalescence and film rupture. Therefore, closed pores solid particles adsorbed firmly on the oil–water interface can act as steric barriers to hinder the formation of pore throats. The excellent barrier effect of solid particles is dominant in most cases unfortunately, leading to a closed-cell structure [324].

PolyHIPEs synthesized from Pickering HIPEs can be stabilized by relatively low loadings (compared to typical surfactant contents) of nanoparticles specially carbon nanotubes. For example, Noa et al. [325] prepared the organic–inorganic hybrid macroporous material by PS-based CNT-filled HIPEs. The CNTs which migrated from the HIPE's aqueous phase droplets into the HIPE's organic phase formed interconnected bundles within the polyHIPEs walls, act as "bridges," that enhanced the connection between existing conductive pathways. The surfaces of the polyHIPEs are covered with spherical particles whose diameters range from around 300 to 1000 nm. There are no changes to the nanoparticles or to the porous structure on sulfonation that could be discerned using SEM (Fig. 4.45).

Furthermore, the incorporation of inorganic solid particles into the organic framework in poly-Pickering HIPEs can endow porous polymers with functional particles decorated pore walls exhibiting additional properties, such as magnetism,
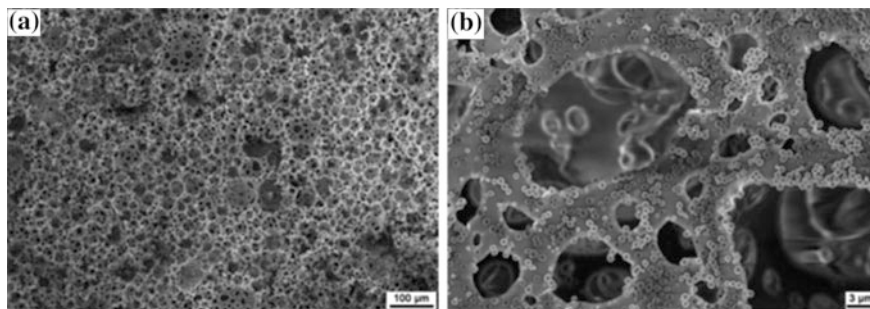
Fig. 4.45 Polymer-nanoparticles-covered polyHIPEs from W/O HIPEs containing surfactant-stabilized CNTs in the aqueous internal phase (SEM). A **a**, **b** typical porous polyHIPE structure with polymer nanoparticles on the void surfaces (SEM). Reproduced from Ref. [325] with kind permission of © 2013 Royal Society of Chemistry

electrical, or thermal conductivity. The use of magnetic, electrical, or thermal conductive particles can also introduce corresponding properties to materials. For example, Mert et al. [326] prepared the macroporous polymers with magnetic response by the removal of the internal phase after the curing of emulsions at 80 °C. The porosity and pore morphology of the macroporous polymers were characterized by nitrogen sorption analysis, the specific surface area and average pore size of the magnetic polyHIPEs with 5 wt% Fe_3O_4@ Humic acid is 36.48 m^2 g^{-1} and 2.7 nm responsively. The M–H curves of all samples display no hysteresis. Meanwhile, the value of magnetization sharply increases with the applied magnetic field even if it does not attain saturation in the presence of a relatively strong magnetic field of even 20 kOe for the sample MP3.

4.6.5 Conclusions

This review has focused upon recent advances in macroporous polymer by different high internal emulsion polymerization types (O/W, W/O, CO_2/W, and Pickering emulsion). The traditional W/O HIPEs will focus on more new composite materials with more applications (photoelectricity, heterogeneous catalysis, high strength modulus materials, and tissue engineering). A large fraction of contemporary polyHIPEs research and development has focused on expanding the library of novel monomers that can be used for polyHIPEs synthesis. And the synthesis of macroporous materials by HIPEs will become more and more environmental benign and low cost by CO_2/W and IL/W. This way will make the tissue engineering become reality due to the rapid expansion of green chemistry. Then, the hybrid of inorganic and organic, or organic and organic macroporous material by high internal phase Pickering emulsion can endow one composite material with

multifunctional materials for various applications. In a word, the development of polyHIPEs with new synthesis chemistries, material component, and porous structures has clearly established their potential for numerous applications and this is now driving the continuing expansion and intensification of polyHIPEs research.

4.7 Outlook and Perspective

The introduction of porous architecture into traditional non-porous polymers has been a successful innovation in materials science and showed dramatic expansion over the last decades. Owing to the fast development of modern organic synthesis and polymer chemistry, a wide range of optional building blocks as well as numerous synthetic strategies are available for the design and construction of MOPs with well-controlled porous structures. Moreover, diverse chemical functionalities can be easily incorporated into the polymer networks with functional monomers or by post-modification methods which are hardly to be achieved for inorganic porous materials. These remarkable advantages ensure MOPs with additional interesting properties, thus creating more advanced application fields in energy, environment, and health. For example,

Gas storage—HCPs as absorbents for hydrogen, for methane storage and for CO_2 capture and storage; COFs for ammonia storage
Separation—PIM membranes for CO_2 separation; hierarchical porous monoliths for liquid chromatography separation of small molecules and as absorbents for oil spill cleaning
Catalysis—MOPs as platform for heterogeneous catalysis; BT-Ph$_2$-based knitting polymers as photocatalysts
Sensors—CMPs as fluorescence probes for TNT, Fe^{3+}, and benzene sensing; lithium-modified knitting polymers as humidity-sensitive materials; COFs as repetitive on–off photocurrent switcher
Energy devices—CMPs as electrode materials for energy storage devices and supercapacitors
Drug delivery—HMOCs as drug nanocarriers for controlled release; COFs for drug release
Thermal therapy—CMPs capsules with tunable NIR absorption ability for thermal ablation of HeLa cells

In spite of these outstanding achievements, a number of challenges are also needed to be addressed. For instance, COFs are usually synthesized with consuming period and difficult to scale up; the cost of CMPs is extremely high due to their noble metal catalysis and special monomers; HCPs are highly irregular networks which limit the real applications in advanced fields such as photoelectric devices; PIMs can be soluble in organic solvents while thier surface areas are relatively low. These challenges, which are also generated along with the evolution

of MOPs, will always inspire scientists and researchers to develop new routes for novel materials' invention as a result of encouraging collaboration with researchers in related disciplines and creating new applications.

References

1. Wu D, Xu F, Sun B et al (2012) Design and preparation of porous polymers. Chem Rev 112 (7):3959–4015
2. Ben T, Ren H, Ma S et al (2009) Targeted synthesis of a porous aromatic framework with high stability and exceptionally high surface area. Angew Chem Int Ed 48(50):9457–9460
3. El-Kaderi HM, Hunt JR, Mendoza-Cortés JL et al (2007) Designed synthesis of 3d covalent organic frameworks. Science 316(5822):268–272
4. Jiang J-X, Trewin A, Su F et al (2009) Microporous poly(tri(4-ethynylphenyl)amine) networks: synthesis, properties, and atomistic simulation. Macromolecules 42(7):2658–2666
5. Shi S, Chen C, Wang M et al (2014) Designing a yolk-shell type porous organic network using a phenyl modified template. Chem Commun 50(65):9079–9082
6. Yang X, Song K, Tan L et al (2014) Hollow microporous organic capsules loaded with highly dispersed Pt nanoparticles for catalytic applications. Macromol Chem Phys 215 (12):1257–1263
7. Li B, Yang X, Xia L et al (2013) Hollow microporous organic capsules. Sci Rep 3:2128
8. Chinnappan A, Chung W-J, Kim H (2015) Hypercross-linked microporous polymeric ionic liquid membranes: synthesis, properties and their application in H_2 generation. J Mater Chem A 3(45):22960–22968
9. Qiao Z, Chai S, Nelson K et al (2014) Polymeric molecular sieve membranes via in situ crosslinking of non-porous polymer membrane templates. Nat Commun 5:3705
10. Kim JK, Yang SY, Lee Y et al (2010) Functional nanomaterials based on block copolymer self-assembly. Prog Polym Sci 35(11):1325–1349
11. Beiler B, Vincze Á, Svec F et al (2007) Poly(2-hydroxyethyl acrylate-co-ethyleneglycol dimethacrylate) monoliths synthesized by radiation polymerization in a mold. Polymer 48 (11):3033–3040
12. Svec F (2010) Porous polymer monoliths: amazingly wide variety of techniques enabling their preparation. J Chromatogr A 1217(6):902–924
13. Wood CD, Tan B, Trewin A et al (2008) Microporous organic polymers for methane storage. Adv Mater 20(10):1916–1921
14. Yang X, Tan L, Xia L et al (2015) Hierarchical porous polystyrene monoliths from polyHIPE. Macromol Rapid Commun 36(17):1553–1558
15. Maya F, Svec F (2014) A new approach to the preparation of large surface area poly (styrene-co-divinylbenzene) monoliths via knitting of loose chains using external crosslinkers and application of these monolithic columns for separation of small molecules. Polymer 55(1):340–346
16. Budd PM, Ghanem BS, Makhseed S et al (2004) Polymers of intrinsic microporosity (PIMs): robust, solution-processable, organic nanoporous materials. Chem Commun 2:230–231
17. Ghanem BS, McKeown NB, Budd PM et al (2008) Polymers of intrinsic microporosity derived from bis(phenazyl) monomers. Macromolecules 41(5):1640–1646

18. Weber J, Su Q, Antonietti M et al (2007) Exploring polymers of intrinsic microporosity—microporous, soluble polyamide and polyimide. Macromol Rapid Commun 28(18–19):1871–1876

19. Du N, Robertson GP, Song J et al (2008) Polymers of intrinsic microporosity containing trifluoromethyl and phenylsulfone groups as materials for membrane gas separation. Macromolecules 41(24):9656–9662

20. Yao S, Yang X, Yu M et al (2014) High surface area hypercrosslinked microporous organic polymer networks based on tetraphenylethylene for CO_2 capture. J Mater Chem A 2 (21):8054–8059

21. Li B, Guan Z, Yang X et al (2014) Multifunctional microporous organic polymers. J Mater Chem A 2(30):11930–11939

22. Zhu X, Mahurin SM, An S-H et al (2014) Efficient CO_2 capture by a task-specific porous organic polymer bifunctionalized with carbazole and triazine groups. Chem Commun 50 (59):7933–7936

23. Sing KSW, Everett DH, Haul RAW et al (1985) Reporting physisorption data for gas/solid systems with special reference to the determination of surface area and porosity (recommendations 1984). Pure Appl Chem 57(4):603–619

24. Germain J, Fréchet JMJ, Svec F (2009) Nanoporous polymers for hydrogen storage. Small 5 (10):1098–1111

25. Jiang J-X, Su F, Trewin A et al (2007) Conjugated microporous poly (aryleneethynylene) networks. Angew Chem Int Ed 46(45):8574–8578

26. Dawson R, Su F, Niu H et al (2008) Mesoporous poly(phenylenevinylene) networks. Macromolecules 41(5):1591–1593

27. Dawson R, Cooper AI, Adams DJ (2012) Nanoporous organic polymer networks. Prog Polym Sci 37(4):530–563

28. Côté AP, Benin AI, Ockwig NW et al (2005) Porous, crystalline, covalent organic frameworks. Science 310(5751):1166–1170

29. Xu S, Luo Y, Tan B (2013) Recent development of hypercrosslinked microporous organic polymers. Macromol Rapid Commun 34(6):471–484

30. Tan L, Tan B (2015) Research progress in hypercrosslinked microporous organic polymers. Acta Chim Sinica 73(6):530–540

31. Cooper AI (2009) Conjugated microporous polymers. Adv Mater 21(12):1291–1295

32. Xu Y, Jin S, Xu H et al (2013) Conjugated microporous polymers: design, synthesis and application. Chem Soc Rev 42(20):8012–8031

33. McKeown NB, Budd PM (2006) Polymers of intrinsic microporosity (PIMs): organic materials for membrane separations, heterogeneous catalysis and hydrogen storage. Chem Soc Rev 35(8):675–683

34. McKeown NB, Budd PM (2010) Exploitation of intrinsic microporosity in polymer-based materials. Macromolecules 43(12):5163–5176

35. Ren S, Bojdys MJ, Dawson R et al (2012) Porous, fluorescent, covalent triazine-based frameworks via room-temperature and microwave-assisted synthesis. Adv Mater 24 (17):2357–2361

36. Kuhn P, Antonietti M, Thomas A (2008) Porous, covalent triazine-based frameworks prepared by ionothermal synthesis. Angew Chem Int Ed 47(18):3450–3453

37. Ben T, Qiu S (2013) Porous aromatic frameworks: synthesis, structure and functions. Cryst Eng Comm 15(1):17–26

38. Stockel E, Wu X, Trewin A et al (2009) High surface area amorphous microporous poly (aryleneethynylene) networks using tetrahedral carbon- and silicon-centred monomers. Chem Commun 2:212–214

39. Rowan SJ, Cantrill SJ, Cousins GRL et al (2002) Dynamic covalent chemistry. Angew Chem Int Ed 41(6):898–952

40. O'Keeffe M (2009) Design of MOFs and intellectual content in reticular chemistry: a personal view. Chem Soc Rev 38(5):1215–1217

41. O'Keeffe M, Yaghi OM (2012) Deconstructing the crystal structures of metal-organic frameworks and related materials into their underlying nets. Chem Rev 112(2):675–702

42. D'Alessandro DM, Smit B, Long JR (2010) Carbon dioxide capture: prospects for new materials. Angew Chem Int Ed 49(35):6058–6082

43. Banerjee R, Furukawa H, Britt D et al (2009) Control of pore size and functionality in isoreticular zeolitic imidazolate frameworks and their carbon dioxide selective capture properties. J Am Chem Soc 131(11):3875–3877

44. Tranchemontagne DJ, Mendoza-Cortes JL, O'Keeffe M et al (2009) Secondary building units, nets and bonding in the chemistry of metal-organic frameworks. Chem Soc Rev 38 (5):1257–1283

45. Waller PJ, Gandara F, Yaghi OM (2015) Chemistry of covalent organic frameworks. Acc Chem Res 48(12):3053–3063

46. Feng X, Liu L, Honsho Y et al (2012) High-rate charge-carrier transport in porphyrin covalent organic frameworks: switching from hole to electron to ambipolar conduction. Angew Chem Int Ed 51(11):2618–2622

47. Beletskaya I, Tyurin VS, Tsivadze AY et al (2009) Supramolecular chemistry of metalloporphyrins. Chem Rev 109(5):1659–1713

48. Spitler EL, Dichtel WR (2010) Lewis acid-catalysed formation of two-dimensional phthalocyanine covalent organic frameworks. Nat Chem 2(8):672–677

49. Bojdys MJ, Jeromenok J, Thomas A et al (2010) Rational extension of the family of layered, covalent, triazine-based frameworks with regular porosity. Adv Mater 22(19):2202–2205

50. Ding X, Guo J, Feng X et al (2011) Synthesis of metallophthalocyanine covalent organic frameworks that exhibit high carrier mobility and photoconductivity. Angew Chem Int Ed 50(6):1289–1293

51. Ding X, Chen L, Honsho Y et al (2011) An n-channel two-dimensional covalent organic framework. J Am Chem Soc 133(37):14510–14513

52. Kappe CO (2004) Controlled microwave heating in modern organic synthesis. Angew Chem Int Ed 43(46):6250–6284

53. Kappe CO, Dallinger D (2009) Controlled microwave heating in modern organic synthesis: highlights from the 2004–2008 literature. Mol Divers 13(2):71–193

54. Makhseed S, Samuel J (2008) Hydrogen adsorption in microporous organic framework polymer. Chem Commun 36:4342–4344

55. Ritchie LK, Trewin A, Reguera-Galan A et al (2010) Synthesis of COF-5 using microwave irradiation and conventional solvothermal routes. Microporous Mesoporous Mater 132(1–2):132–136

56. Zwaneveld NAA, Pawlak R, Abel M et al (2008) Organized formation of 2D extended covalent organic frameworks at surfaces. J Am Chem Soc 130(21):6678–6679

57. Guan CZ, Wang D, Wan LJ (2012) Construction and repair of highly ordered 2D covalent networks by chemical equilibrium regulation. Chem Commun 48(24):2943–2945

58. Colson JW, Woll AR, Mukherjee A et al (2011) Oriented 2D covalent organic framework thin films on single-layer graphene. Science 332(6026):228–231

59. Spitler EL, Colson JW, Uribe-Romo FJ et al (2012) Lattice expansion of highly oriented 2D phthalocyanine covalent organic framework films. Angew Chem Int Ed 51(11):2623–2627

60. Spitler EL, Koo BT, Novotney JL et al (2011) A 2D covalent organic framework with 47-nm pores and insight into its interlayer stacking. J Am Chem Soc 133(48):19416–19421

61. Dienstmaier JF, Medina DD, Dogru M et al (2012) Isoreticular two-dimensional covalent organic frameworks synthesized by on-surface condensation of diboronic acids. ACS Nano 6(8):7234–7242

62. Kalidindi SB, Wiktor C, Ramakrishnan A et al (2013) Lewis base mediated efficient synthesis and solvation-like host-guest chemistry of covalent organic framework-1. Chem Commun 49(5):463–465

63. Smith BJ, Dichtel WR (2014) Mechanistic studies of two-dimensional covalent organic frameworks rapidly polymerized from initially homogenous conditions. J Am Chem Soc 136 (24):8783–8789

64. Wan S, Guo J, Kim J et al (2008) A belt-shaped, blue luminescent, and semiconducting covalent organic framework. Angew Chem Int Ed 47(46):8826–8830

65. Chen L, Furukawa K, Gao J et al (2014) Photoelectric covalent organic frameworks: converting open lattices into ordered donor-acceptor heterojunctions. J Am Chem Soc 136 (28):9806–9809

66. Xu F, Jin S, Zhong H et al (2015) Electrochemically active, crystalline, mesoporous covalent organic frameworks on carbon nanotubes for synergistic lithium-ion battery energy storage. Sci Rep 5:8225

67. Huang N, Ding X, Kim J et al (2015) A photoresponsive smart covalent organic framework. Angew Chem Int Ed 54(30):8704–8707

68. Yang H, Du Y, Wan S et al (2015) Mesoporous 2D covalent organic frameworks based on shape-persistent arylene-ethynylene macrocycles. Chem Sci 6(7):4049–4053

69. Feng X, Dong Y, Jiang D (2013) Star-shaped two-dimensional covalent organic frameworks. Cryst Eng Comm 15(8):1508–1511

70. Uribe-Romo FJ, Hunt JR, Furukawa H et al (2009) A crystalline imine-linked 3-D porous covalent organic framework. J Am Chem Soc 131(13):4570–4571

71. Chen X, Addicoat M, Irle S et al (2013) Control of crystallinity and porosity of covalent organic frameworks by managing interlayer interactions based on self-complementary pi-electronic force. J Am Chem Soc 135(2):546–549

72. Xu H, Jiang D (2014) Covalent organic frameworks: crossing the channel. Nat Chem 6 (7):564–566

73. Chen X, Addicoat M, Jin E et al (2015) Locking covalent organic frameworks with hydrogen bonds: general and remarkable effects on crystalline structure, physical properties, and photochemical activity. J Am Chem Soc 137(9):3241–3247

74. Dalapati S, Addicoat M, Jin S et al (2015) Rational design of crystalline supermicroporous covalent organic frameworks with triangular topologies. Nat Commun 6:7786

75. Xu H, Gao J, Jiang D (2015) Stable, crystalline, porous, covalent organic frameworks as a platform for chiral organocatalysts. Nat Chem 7(11):905–912

76. Huang N, Krishna R, Jiang D (2015) Tailor-made pore surface engineering in covalent organic frameworks: systematic functionalization for performance screening. J Am Chem Soc 137(22):7079–7082

77. Kandambeth S, Mallick A, Lukose B et al (2012) Construction of crystalline 2D covalent organic frameworks with remarkable chemical (acid/base) stability via a combined reversible and irreversible route. J Am Chem Soc 134(48):19524–19527

78. Biswal BP, Chandra S, Kandambeth S et al (2013) Mechanochemical synthesis of chemically stable isoreticular covalent organic frameworks. J Am Chem Soc 135(14): 5328–5331

79. Chandra S, Kandambeth S, Biswal BP et al (2013) Chemically stable multilayered covalent organic nanosheets from covalent organic frameworks via mechanical delamination. J Am Chem Soc 135(47):17853–17861

80. Chandra S, Kundu T, Kandambeth S et al (2014) Phosphoric acid loaded azo (–N horizontal line N–) based covalent organic framework for proton conduction. J Am Chem Soc 136 (18):6570–6573

81. Das G, Biswal BP, Kandambeth S et al (2015) Chemical sensing in two dimensional porous covalent organic nanosheets. Chem Sci 6(7):3931–3939

82. Chen X, Huang N, Gao J et al (2014) Towards covalent organic frameworks with predesignable and aligned open docking sites. Chem Commun 50(46):6161–6163

83. Das G, Balaji Shinde D, Kandambeth S et al (2014) Mechanosynthesis of imine, beta-ketoenamine, and hydrogen-bonded imine-linked covalent organic frameworks using liquid-assisted grinding. Chem Commun 50(84):12615–12618

84. Fang Q, Gu S, Zheng J et al (2014) 3D microporous base-functionalized covalent organic frameworks for size-selective catalysis. Angew Chem Int Ed 53(11):2878–2882

85. Zhou TY, Xu SQ, Wen Q et al (2014) One-step construction of two different kinds of pores in a 2D covalent organic framework. J Am Chem Soc 136(45):15885–15888

86. Zhu Y, Wan S, Jin Y et al (2015) Desymmetrized vertex design for the synthesis of covalent organic frameworks with periodically heterogeneous pore structures. J Am Chem Soc 137 (43):13772–13775
87. Uribe-Romo FJ, Doonan CJ, Furukawa H et al (2011) Crystalline covalent organic frameworks with hydrazone linkages. J Am Chem Soc 133(30):11478–11481
88. Ding SY, Dong M, Wang YW et al (2016) Thioether-based fluorescent covalent organic framework for selective detection and facile removal of mercury(II). J Am Chem Soc 138 (9):3031–3037
89. Fang Q, Zhuang Z, Gu S et al (2014) Designed synthesis of large-pore crystalline polyimide covalent organic frameworks. Nat Commun 5:4503
90. Fang Q, Wang J, Gu S et al (2015) 3D porous crystalline polyimide covalent organic frameworks for drug delivery. J Am Chem Soc 137(26):8352–8355
91. Zeng Y, Zou R, Luo Z et al (2015) Covalent organic frameworks formed with two types of covalent bonds based on orthogonal reactions. J Am Chem Soc 137(3):1020–1023
92. Zuttel A (2004) Hydrogen storage methods. Naturwissenschaften 91(4):157–172
93. Fichtner M (2005) Nanotechnological aspects in materials for hydrogen storage. Adv Eng Mater 7(6):443–455
94. Furukawa H, Yaghi OM (2009) Storage of hydrogen, methane, and carbon dioxide in highly porous covalent organic frameworks for clean energy applications. J Am Chem Soc 131 (25):8875–8883
95. Furukawa H, Miller MA, Yaghi OM (2007) Independent verification of the saturation hydrogen uptake in MOF-177 and establishment of a benchmark for hydrogen adsorption in metal-organic frameworks. J Mater Chem 17(30):3197–3204
96. Kaye SS, Dailly A, Yaghi OM et al (2007) Impact of preparation and handling on the hydrogen storage properties of $Zn_4O(1,4$-benzenedicarboxylate$)_3$ (MOF-5). J Am Chem Soc 129(46):14176–14177
97. Haszeldine RS (2009) Carbon capture and storage: how green can black be? Science 325 (5948):1647–1652
98. Xu X, Song C, Andrésen JM et al (2003) Preparation and characterization of novel CO_2 "molecular basket" adsorbents based on polymer-modified mesoporous molecular sieve MCM-41. Microporous Mesoporous Mater 62(1–2):29–45
99. Phan A, Doonan CJ, Uribe-Romo FJ et al (2010) Synthesis, structure, and carbon dioxide capture properties of zeolitic imidazolate frameworks. Acc Chem Res 43(1):58–67
100. Doonan CJ, Tranchemontagne DJ, Glover TG et al (2010) Exceptional ammonia uptake by a covalent organic framework. Nat Chem 2(3):235–238
101. MacMillan DW (2008) The advent and development of organocatalysis. Nature 455 (7211):304–308
102. Yoon M, Srirambalaji R, Kim K (2012) Homochiral metal-organic frameworks for asymmetric heterogeneous catalysis. Chem Rev 112(2):1196–1231
103. Lee J, Farha OK, Roberts J et al (2009) Metal-organic framework materials as catalysts. Chem Soc Rev 38(5):1450–1459
104. Ding SY, Gao J, Wang Q et al (2011) Construction of covalent organic framework for catalysis: Pd/COF-LZU1 in Suzuki-Miyaura coupling reaction. J Am Chem Soc 133 (49):19816–19822
105. Mullangi D, Nandi S, Shalini S et al (2015) Pd loaded amphiphilic COF as catalyst for multi-fold Heck reactions, C–C couplings and CO oxidation. Sci Rep 5:10876
106. Wan S, Guo J, Kim J et al (2009) A photoconductive covalent organic framework: self-condensed arene cubes composed of eclipsed 2D polypyrene sheets for photocurrent generation. Angew Chem Int Ed 48(30):5439–5442
107. Shultz AM, Farha OK, Hupp JT et al (2009) A catalytically active, permanently microporous MOF with metalloporphyrin struts. J Am Chem Soc 131(12):4204–4205
108. Drain CM, Varotto A, Radivojevic I (2009) Self-organized porphyrinic materials. Chem Rev 109(5):1630–1658

109. Chen L, Yang Y, Jiang D (2010) CMPs as scaffolds for constructing porous catalytic frameworks: a built-in heterogeneous catalyst with high activity and selectivity based on nanoporous metalloporphyrin polymers. J Am Chem Soc 132(26):9138–9143

110. Tsyurupa MP, Davankov VA (2002) Hypercrosslinked polymers: basic principle of preparing the new class of polymeric materials. React Funct Polym 53(2–3):193–203

111. Davankov VA, Rogozhin SV, Tsyurupa MP (1971) US Patent 3729457

112. Tsyurupa MP, Davankov VA (2006) Porous structure of hypercrosslinked polystyrene: State-of-the-art mini-review. React Funct Polym 66(7):768–779

113. Germain J, Fréchet JMJ, Svec F (2007) Hypercrosslinked polyanilines with nanoporous structure and high surface area: potential adsorbents for hydrogen storage. J Mater Chem 17(47):4989

114. Davankov VA, Ilyin MM, Tsyurupa MP et al (1996) From a dissolved polystyrene coil to an intramolecularly-hyper-cross-linked "nanosponge". Macromolecules 29(26):8398–8403

115. Davankov V, Tsyurupa M, Ilyin M et al (2002) Hypercross-linked polystyrene and its potentials for liquid chromatography: a mini-review. J Chromatogr A 965(1–2):65–73

116. Tsyurupa MP, Blinnikova ZK, Borisov YA et al (2014) Physicochemical and adsorption properties of hypercross-linked polystyrene with ultimate crosslinking density. J Sep Sci 37(7):803–810

117. Hradil J, Králová E (1998) Styrene-divinylbenzene copolymers post-crosslinked with tetrachloromethane. Polymer 39(24):6041–6048

118. Veverka P, Jeřábek K (1999) Mechanism of hypercrosslinking of chloromethylated styrene-divinylbenzene copolymers. React Funct Polym 41(1–3):21–25

119. Ahn J-H, Jang J-E, Oh C-G et al (2006) Rapid generation and control of microporosity, bimodal pore size distribution, and surface area in davankov-type hyper-cross-linked resins. Macromolecules 39(2):627–632

120. Li B, Gong R, Luo Y et al (2011) Tailoring the pore size of hypercrosslinked polymers. Soft Matter 7(22):10910–10916

121. Seo M, Kim S, Oh J et al (2015) Hierarchically porous polymers from hyper-cross-linked block polymer precursors. J Am Chem Soc 137(2):600–603

122. Li Z, Wu D, Huang X et al (2014) Fabrication of novel polymeric and carbonaceous nanoscale networks by the union of self-assembly and hypercrosslinking. Energy Environ Sci 7(9):3006–3012

123. Wood CD, Tan B, Trewin A et al (2007) Hydrogen storage in microporous hypercrosslinked organic polymer networks. Chem Mater 19(8):2034–2048

124. Martín CF, Stöckel E, Clowes R et al (2011) Hypercrosslinked organic polymer networks as potential adsorbents for pre-combustion CO_2 capture. J Mater Chem 21(14):5475–5483

125. Yang Y, Zhang Q, Zhang S et al (2013) Synthesis and characterization of triphenylamine-containing microporous organic copolymers for carbon dioxide uptake. Polymer 54(21):5698–5702

126. Yang Y, Zhang Q, Zhang S et al (2014) Triphenylamine-containing microporous organic copolymers for hydrocarbons/water separation. RSC Adv 4(11):5568–5574

127. Luo Y, Zhang S, Ma Y et al (2013) Microporous organic polymers synthesized by self-condensation of aromatic hydroxymethyl monomers. Polym Chem 4(4):1126–1131

128. Grzybowski M, Skonieczny K, Butenschön H et al (2013) Comparison of oxidative aromatic coupling and the scholl reaction. Angew Chem Int Ed 52(38):9900–9930

129. Li L, Ren H, Yuan Y et al (2014) Construction and adsorption properties of porous aromatic frameworks via $AlCl_3$-triggered coupling polymerization. J Mater Chem A 2(29):11091–11098

130. Li B, Gong R, Wang W et al (2011) A new strategy to microporous polymers: knitting rigid aromatic building blocks by external cross-linker. Macromolecules 44(8):2410–2414

131. Dawson R, Stoeckel E, Holst JR et al (2011) Microporous organic polymers for carbon dioxide capture. Energy Environ Sci 4(10):4239–4245

132. Nielsen CJ, Herrmann H, Weller C (2012) Atmospheric chemistry and environmental impact of the use of amines in carbon capture and storage (CCS). Chem Soc Rev 41(19):6684–6704

133. Chen S, Zhang J, Wu T et al (2009) Multiroute synthesis of porous anionic frameworks and size-tunable extraframework organic cation-controlled gas sorption properties. J Am Chem Soc 131(44):16027–16029
134. Couck S, Denayer JFM, Baron GV et al (2009) An Amine-Functionalized MIL-53 metal-organic framework with large separation power for CO_2 and CH_4. J Am Chem Soc 131(18):6326–6327
135. Farha OK, Spokoyny AM, Hauser BG et al (2009) Synthesis, properties, and gas separation studies of a robust diimide-based microporous organic polymer. Chem Mater 21(14): 3033–3035
136. Woodward RT, Stevens LA, Dawson R et al (2014) Swellable, water- and acid-tolerant polymer sponges for chemoselective carbon dioxide capture. J Am Chem Soc 136 (25):9028–9035
137. Dawson R, Ratvijitvech T, Corker M et al (2012) Microporous copolymers for increased gas selectivity. Polym Chem 3(8):2034–2038
138. Dawson R, Stevens LA, Drage TC et al (2012) Impact of water coadsorption for carbon dioxide capture in microporous polymer sorbents. J Am Chem Soc 134(26):10741–10744
139. Jing X, Zou D, Cui P et al (2013) Facile synthesis of cost-effective porous aromatic materials with enhanced carbon dioxide uptake. J Mater Chem A 1(44):13926–13931
140. Li H, Meng B, Mahurin SM et al (2015) Carbohydrate based hyper-crosslinked organic polymers with –OH functional groups for CO_2 separation. J Mater Chem A 3(42): 20913–20918
141. Zhu J-H, Chen Q, Sui Z-Y et al (2014) Preparation and adsorption performance of cross-linked porous polycarbazoles. J Mater Chem A 2(38):16181–16189
142. Yang X, Yu M, Zhao Y et al (2014) Hypercrosslinked microporous polymers based on carbazole for gas storage and separation. RSC Adv 4(105):61051–61055
143. Zhang Y, Li Y, Wang F et al (2014) Hypercrosslinked microporous organic polymer networks derived from silole-containing building blocks. Polymer 55(22):5746–5750
144. Yang X, Yu M, Zhao Y et al (2014) Remarkable gas adsorption by carbonized nitrogen-rich hypercrosslinked porous organic polymers. J Mater Chem A 2(36):15139–15145
145. Zhai T-L, Tan L, Luo Y et al (2016) Microporous polymers from a carbazole-based triptycene monomer: synthesis and their applications for gas uptake. Chem-Asian J 11 (2):294–298
146. Zhang C, Zhu P-C, Tan L et al (2016) Synthesis and properties of organic microporous polymers from the monomer of hexaphenylbenzene based triptycene. Polymer 82:100–104
147. Zhang C, Zhu P-C, Tan L et al (2015) Triptycene-based hyper-cross-linked polymer sponge for gas storage and water treatment. Macromolecules 48(23):8509–8514
148. Luo Y, Li B, Wang W et al (2012) Hypercrosslinked aromatic heterocyclic microporous polymers: a new class of highly selective CO_2 capturing materials. Adv Mater 24(42): 5703–5707
149. Saleh M, Lee HM, Kemp KC et al (2014) Highly stable CO_2/N_2 and CO_2/CH_4 selectivity in hyper-cross-linked heterocyclic porous polymers. ACS Appl Mater Interfaces 6(10): 7325–7333
150. Wang J, Yang JGW, Yi G et al (2015) Phosphonium salt incorporated hypercrosslinked porous polymers for CO_2 capture and conversion. Chem Commun 51(86):15708–15711
151. Guan Z, Li B, Hai G et al (2014) A highly efficient catalyst for Suzuki-Miyaura coupling reaction of benzyl chloride under mild conditions. RSC Adv 4(69):36437–36443
152. Song K, Liu P, Wang J et al (2015) Controlled synthesis of uniform palladium nanoparticles on novel micro-porous carbon as a recyclable heterogeneous catalyst for the Heck reaction. Dalton Trans 44(31):13906–13913
153. Song K, Zou Z, Wang D et al (2016) Microporous organic polymers derived microporous carbon supported pd catalysts for oxygen reduction reaction: impact of framework and heteroatom. J Phys Chem C 120(4):2187–2197

154. Li B, Guan Z, Wang W et al (2012) Highly dispersed Pd catalyst locked in knitting aryl network polymers for Suzuki-Miyaura coupling reactions of aryl chlorides in aqueous media. Adv Mater 24(25):3390–3395

155. Xu S, Song K, Li T et al (2015) Palladium catalyst coordinated in knitting N-heterocyclic carbene porous polymers for efficient Suzuki-Miyaura coupling reactions. J Mater Chem A 3 (3):1272–1278

156. Li R, Wang ZJ, Wang L et al (2016) Photocatalytic selective bromination of electron-rich aromatic compounds using microporous organic polymers with visible light. ACS Catal 6 (2):1113–1121

157. Jiang K, Fei T, Zhang T (2014) Humidity sensing properties of LiCl-loaded porous polymers with good stability and rapid response and recovery. Sens Actuators, B 199:1–6

158. Jiang K, Kuang D, Fei T et al (2014) Preparation of lithium-modified porous polymer for enhanced humidity sensitive properties. Sens Actuators, B 203:752–758

159. Yang X, Li B, Majeed I et al (2013) Magnetic microporous polymer nanoparticles. Polym Chem 4(5):1425–1429

160. Chinnappan A, Tamboli AH, Chung W-J et al (2016) Green synthesis, characterization and catalytic efficiency of hypercross-linked porous polymeric ionic liquid networks towards 4-nitrophenol reduction. Chem Eng J 285:554–561

161. Ji G, Yang Z, Zhao Y et al (2015) Synthesis of metalloporphyrin-based conjugated microporous polymer spheres directed by bipyridine-type ligands. Chem Commun 51 (34):7352–7355

162. Xu Y, Nagai A, Jiang D (2013) Core-shell conjugated microporous polymers: a new strategy for exploring color-tunable and -controllable light emissions. Chem Commun 49(16): 1591–1593

163. Liu X, Xu Y, Jiang D (2012) Conjugated microporous polymers as molecular sensing devices: microporous architecture enables rapid response and enhances sensitivity in fluorescence-on and fluorescence-off sensing. J Am Chem Soc 134(21):8738–8741

164. Zhang Y, Sigen A, Zou Y et al (2014) Gas uptake, molecular sensing and organocatalytic performances of a multifunctional carbazole-based conjugated microporous polymer. J Mater Chem A 2(33):13422–13430

165. Ding X, Han BH (2015) Copper phthalocyanine-based CMPs with various internal structures and functionalities. Chem Commun 51(64):12783–12786

166. Chun J, Park JH, Kim J et al (2012) Tubular-shape evolution of microporous organic networks. Chem Mater 24(17):3458–3463

167. Senkovskyy V, Senkovska I, Kiriy A (2012) Surface-initiated synthesis of conjugated microporous polymers: chain-growth Kumada catalyst-transfer polycondensation at work. ACS Macro Lett 1(4):494–498

168. Yang RX, Wang TT, Deng WQ (2015) Extraordinary capability for water treatment achieved by a perfluorous conjugated microporous polymer. Sci Rep 5:10155

169. Cheng G, Hasell T, Trewin A et al (2012) Soluble conjugated microporous polymers. Angew Chem Int Ed 51(51):12727–12731

170. Chen Q, Luo M, Hammershoj P et al (2012) Microporous polycarbazole with high specific surface area for gas storage and separation. J Am Chem Soc 134(14):6084–6087

171. Cho HC, Lee HS, Chun J et al (2011) Tubular microporous organic networks bearing imidazolium salts and their catalytic CO_2 conversion to cyclic carbonates. Chem Commun 47(3):917–919

172. Kang N, Park JH, Choi J et al (2012) Nanoparticulate iron oxide tubes from microporous organic nanotubes as stable anode materials for lithium ion batteries. Angew Chem Int Ed 51(27):6626–6630

173. Laybourn A, Dawson R, Clowes R et al (2014) Network formation mechanisms in conjugated microporous polymers. Polym Chem 5(21):6325–6333

174. Xu Y, Jiang D (2014) Structural insights into the functional origin of conjugated microporous polymers: geometry-management of porosity and electronic properties. Chem Commun 50(21):2781–2783

175. Dawson R, Laybourn A, Khimyak YZ et al (2010) High surface area conjugated microporous polymers: the importance of reaction solvent choice. Macromolecules 43(20):8524–8530
176. Tan D, Fan W, Xiong W et al (2012) Study on the morphologies of covalent organic microporous polymers: the role of reaction solvents. Macromol Chem Phys 213(14): 1435–1440
177. Schmidt J, Weber J, Epping JD et al (2009) Microporous conjugated poly(thienylene arylene) networks. Adv Mater 21(6):702–705
178. Schmidt J, Werner M, Thomas A (2009) Conjugated microporous polymer networks via yamamoto polymerization. Macromolecules 42(13):4426–4429
179. Jiang J-X, Su F, Niu H et al (2008) Conjugated microporous poly(phenylene butadiynylene) s. Chem Commun 4:486–488
180. Schwab MG, Fassbender B, Spiess HW et al (2009) Catalyst-free preparation of melamine-based microporous polymer networks through schiff base chemistry. J Am Chem Soc 131(21):7216–7217
181. Gu C, Chen Y, Zhang Z et al (2013) Electrochemical route to fabricate film-like conjugated microporous polymers and application for organic electronics. Adv Mater 25(25):3443–3448
182. Wang X, Zhao Y, Wei L et al (2015) Nitrogen-rich conjugated microporous polymers: impact of building blocks on porosity and gas adsorption. J Mater Chem A 3(42): 21185–21193
183. Jiang J-X, Su F, Trewin A et al (2008) Synthetic control of the pore dimension and surface area in conjugated microporous polymer and copolymer networks. J Am Chem Soc 130 (24):7710–7720
184. Feng L-J, Chen Q, Zhu J-H et al (2014) Adsorption performance and catalytic activity of porous conjugated polyporphyrins via carbazole-based oxidative coupling polymerization. Polym Chem 5(8):3081–3088
185. Liao Y, Weber J, Faul CFJ (2014) Conjugated microporous polytriphenylamine networks. Chem Commun 50(59):8002–8005
186. Hayashi S, Togawa Y, Ashida J et al (2016) Synthesis of π-conjugated porous polymers via direct arylation of fluoroarenes with three-arm triazine. Polymer 90:187–192
187. Yoo J, Park N, Park JH et al (2015) Magnetically separable microporous fe-porphyrin networks for catalytic carbene insertion into N–H bonds. ACS Catal 5(1):350–355
188. Xiao Z, Zhou Y, Xin X et al (2015) Iron(III) Porphyrin-based porous material as photocatalyst for highly efficient and selective degradation of congo red. Macromol Chem Phys 217(4):599–604
189. Lu G, Yang H, Zhu Y et al (2015) Synthesis of a conjugated porous Co(ii) porphyrinylene-ethynylene framework through alkyne metathesis and its catalytic activity study. J Mater Chem A 3(9):4954–4959
190. Chun J, Kang S, Kang N et al (2013) Microporous organic networks bearing metal-salen species for mild CO_2 fixation to cyclic carbonates. J Mater Chem A 1(18):5517–5523
191. Zhang H, Zhang Y, Gu C et al (2015) Electropolymerized conjugated microporous poly (zinc-porphyrin) films as potential electrode materials in supercapacitors. Adv Energy Mater 5(10):1402175
192. Ding X, Han BH (2015) Metallophthalocyanine-based conjugated microporous polymers as highly efficient photosensitizers for singlet oxygen generation. Angew Chem Int Ed 54 (22):6536–6539
193. Sheng X, Guo H, Qin Y et al (2015) A novel metalloporphyrin-based conjugated microporous polymer for capture and conversion of CO_2. RSC Adv 5(40):31664–31669
194. Jiang J-X, Wang C, Laybourn A et al (2011) Metal-organic conjugated microporous polymers. Angew Chem Int Ed 123(5):1104–1107
195. Fischer S, Schmidt J, Strauch P et al (2013) An anionic microporous polymer network prepared by the polymerization of weakly coordinating anions. Angew Chem Int Ed 52 (46):12174–12178

196. Xie Y, Wang TT, Liu XH et al (2013) Capture and conversion of CO_2 at ambient conditions by a conjugated microporous polymer. Nat Commun 4:1960

197. Gu C, Huang N, Chen Y et al (2015) Pi-conjugated microporous polymer films: designed synthesis, conducting properties, and photoenergy conversions. Angew Chem Int Ed 54 (46):13594–13598

198. Lee HS, Choi J, Jin J et al (2012) An organometallic approach for microporous organic network (MON)–Co_3O_4 composites: enhanced stability as anode materials for lithium ion batteries. Chem Commun 48(1):94–96

199. Lindemann P, Schade A, Monnereau L et al (2016) Surface functionalization of conjugated microporous polymer thin films and nanomembranes using orthogonal chemistries. J Mater Chem A 4(18):6815–6818

200. Liu J, Tobin JM, Xu Z et al (2015) Facile synthesis of a conjugated microporous polymeric monolith via copper-free Sonogashira-Hagihara cross-coupling in water under aerobic conditions. Polym Chem 6(41):7251–7255

201. Urakami H, Zhang K, Vilela F (2013) Modification of conjugated microporous poly-benzothiadiazole for photosensitized singlet oxygen generation in water. Chem Commun 49(23):2353–2355

202. Ratvijitvech T, Dawson R, Laybourn A et al (2014) Post-synthetic modification of conjugated microporous polymers. Polymer 55(1):321–325

203. Zhuang X, Zhang F, Wu D et al (2013) Two-dimensional sandwich-type, graphene-based conjugated microporous polymers. Angew Chem Int Ed 52(37):9668–9672

204. Zhuang X, Gehrig D, Forler N et al (2015) Conjugated microporous polymers with dimensionality-controlled heterostructures for green energy devices. Adv Mater 27(25):3789–3796

205. Kang N, Park JH, Jin M et al (2013) Microporous organic network hollow spheres: useful templates for nanoparticulate CO_3O_4 hollow oxidation catalysts. J Am Chem Soc 135(51):19115–19118

206. Ko JH, Kang N, Park N et al (2015) Hollow microporous organic networks bearing triphenylamines and anthraquinones: diffusion pathway effect in visible light-driven oxidative coupling of benzylamines. ACS Macro Lett 4(7):669–672

207. Lim B, Jin J, Yoo J et al (2014) Fe_3O_4 nanosphere@microporous organic networks: enhanced anode performances in lithium ion batteries through carbonization. Chem Commun 50(57):7723–7726

208. Kang S, Chun J, Park N et al (2015) Hydrophobic zeolites coated with microporous organic polymers: adsorption behavior of ammonia under humid conditions. Chem Commun 51(59):11814–11817

209. Chun J, Kang S, Park N et al (2014) Metal-organic framework@microporous organic network: hydrophobic adsorbents with a crystalline inner porosity. J Am Chem Soc 136(19):6786–6789

210. Tan J, Wan J, Guo J et al (2015) Self-sacrificial template-induced modulation of conjugated microporous polymer microcapsules and shape-dependent enhanced photothermal efficiency for ablation of cancer cells. Chem Commun 51(98):17394–17397

211. Zhang SC, Luo YL, Yang HW et al (2013) Functional oligo(vinyl acetate) bearing bipyridine moieties by RAFT polymerization and extraction of metal ions in supercritical carbon dioxide. Polym Chem 4(12):3507–3513

212. Ma BC, Ghasimi S, Landfester K et al (2015) Conjugated microporous polymer nanoparticles with enhanced dispersibility and water compatibility for photocatalytic applications. J Mater Chem A 3(31):16064–16071

213. Kim M, Byeon M, Bae J-S et al (2011) Preparation of ultrathin films of molecular networks through layer-by-layer crosslinking polymerization of tetrafunctional monomers. Macromolecules 44(18):7092–7095

214. Lindemann P, Tsotsalas M, Shishatskiy S et al (2014) Preparation of freestanding conjugated microporous polymer nanomembranes for gas separation. Chem Mater 26(24):7189–7193

215. Wu X, Li H, Xu Y et al (2014) Thin film fabricated from solution-dispersible porous hyperbranched conjugated polymer nanoparticles without surfactants. Nanoscale 6(4): 2375–2380
216. Gu C, Chen Y, Zhang Z et al (2014) Achieving high efficiency of PTB7-based polymer solar cells via integrated optimization of both anode and cathode interlayers. Adv Energy Mater 4(8):1301771
217. Gu C, Huang N, Gao J et al (2014) Controlled synthesis of conjugated microporous polymer films: versatile platforms for highly sensitive and label-free chemo- and biosensing. Angew Chem Int Ed 53(19):4850–4855
218. Deng S, Zhi J, Zhang X et al (2014) Size-controlled synthesis of conjugated polymer nanoparticles in confined nanoreactors. Angew Chem Int Ed 53(51):14144–14148
219. Huang B, Zhao P, Dai Y et al (2016) Size-controlled synthesis of soluble-conjugated microporous polymer nanoparticles through sonogashira polycondensation in confined nanoreactors. J Polym Sci Pol Chem 54(15):2285–2290
220. Du R, Zhang N, Xu H et al (2014) CMP aerogels: ultrahigh-surface-area carbon-based monolithic materials with superb sorption performance. Adv Mater 26(47):8053–8058
221. Wang ZJ, Landfester K, Zhang KAI (2014) Hierarchically porous π-conjugated polyHIPE as a heterogeneous photoinitiator for free radical polymerization under visible light. Polym Chem 5(11):3559–3562
222. Liu X, Xu Y, Guo Z et al (2013) Super absorbent conjugated microporous polymers: a synergistic structural effect on the exceptional uptake of amines. Chem Commun 49(31):3233–3235
223. Chen Y, Sun H, Yang R et al (2015) Synthesis of conjugated microporous polymer nanotubes with large surface areas as absorbents for iodine and CO_2 uptake. J Mater Chem A 3(1):87–91
224. Wang J, Wang G, Wang W et al (2014) Hydrophobic conjugated microporous polymer as a novel adsorbent for removal of volatile organic compounds. J Mater Chem A 2(34): 14028–14037
225. Du R, Zheng Z, Mao N et al (2015) Fluorosurfactants-directed preparation of homogeneous and hierarchical-porosity CMP aerogels for gas sorption and oil cleanup. Adv Sci 2(1–2):1400006
226. Chen Q, Liu DP, Luo M et al (2014) Nitrogen-containing microporous conjugated polymers via carbazole-based oxidative coupling polymerization: preparation, porosity, and gas uptake. Small 10(2):308–315
227. Wang J, Senkovska I, Oschatz M et al (2013) Highly porous nitrogen-doped polyimine-based carbons with adjustable microstructures for CO_2 capture. J Mater Chem A 1(36):10951–10961
228. Song W-C, Xu X-K, Chen Q et al (2013) Nitrogen-rich diaminotriazine-based porous organic polymers for small gas storage and selective uptake. Polym Chem 4(17):4690–4696
229. Qiao S, Wang T, Huang W et al (2016) Dendrimer-like conjugated microporous polymers. Polym Chem 7(6):1281–1289
230. Fischer S, Schimanowitz A, Dawson R et al (2014) Cationic microporous polymer networks by polymerisation of weakly coordinating cations with CO_2-storage ability. J Mater Chem A 2(30):11825–11829
231. Zhang S, Huang W, Hu P et al (2015) Conjugated microporous polymers with excellent electrochemical performance for lithium and sodium storage. J Mater Chem A 3(5): 1896–1901
232. Xu F, Chen X, Tang Z et al (2014) Redox-active conjugated microporous polymers: a new organic platform for highly efficient energy storage. Chem Commun 50(37):4788–4790
233. Yuan K, Guo-Wang P, Hu T et al (2015) Nanofibrous and graphene-templated conjugated microporous polymer materials for flexible chemosensors and supercapacitors. Chem Mater 27(21):7403–7411
234. To JWF, Chen Z, Yao H et al (2015) Ultrahigh surface area three-dimensional porous graphitic carbon from conjugated polymeric molecular framework. ACS Cent Sci 1(2):68–76

235. Zhang K, Kopetzki D, Seeberger PH et al (2013) Surface area control and photocatalytic activity of conjugated microporous poly(benzothiadiazole) networks. Angew Chem Int Ed 52(5):1432–1436
236. Wang ZJ, Ghasimi S, Landfester K et al (2015) Molecular structural design of conjugated microporous poly(benzooxadiazole) networks for enhanced photocatalytic activity with visible light. Adv Mater 27(40):6265–6270
237. Wang ZJ, Ghasimi S, Landfester K et al (2014) Highly porous conjugated polymers for selective oxidation of organic sulfides under visible light. Chem Commun 50(60): 8177–8180
238. Luo J, Zhang X, Zhang J (2015) Carbazolic porous organic framework as an efficient, metal-free visible-light photocatalyst for organic synthesis. ACS Catal 5(4):2250–2254
239. Wang ZJ, Ghasimi S, Landfester K et al (2015) Photocatalytic suzuki coupling reaction using conjugated microporous polymer with immobilized palladium nanoparticles under visible light. Chem Mater 27(6):1921–1924
240. Wang X, S-m Lu, Li J et al (2015) Conjugated microporous polymers with chiral BINAP ligand built-in as efficient catalysts for asymmetric hydrogenation. Catal Sci Technol 5 (5):2585–2589
241. Wu X, Li H, Xu B et al (2014) Solution-dispersed porous hyperbranched conjugated polymer nanoparticles for fluorescent sensing of TNT with enhanced sensitivity. Polym Chem 5(15):4521–4525
242. Bonillo B, Sprick RS, Cooper AI (2016) Tuning photophysical properties in conjugated microporous polymers by co-monomer doping strategies. Chem Mater 28(10):3469–3480
243. Jiang J-X, Trewin A, Adams DJ et al (2011) Band gap engineering in fluorescent conjugated microporous polymers. Chem Sci 2(9):1777–1781
244. Ma H, Li F, Li P et al (2016) A dendrimer-based electropolymerized microporous film: multifunctional, reversible, and highly sensitive fluorescent probe. Adv Funct Mater 26 (12):2025–2031
245. Jin J, Kim B, Park N et al (2014) Porphyrin entrapment and release behavior of microporous organic hollow spheres: fluorescent alerting systems for existence of organic solvents in water. Chem Commun 50(94):14885–14888
246. Okay O (2000) Macroporous copolymer networks. Prog Polym Sci 25(6):711–779
247. Cameron NR, Sherrington DC (1996) High internal phase emulsions (HIPEs)-structure, properties and use in polymer preparation. Biopolymers liquid crystalline polymers phase emulsion. Springer Berlin Heidelberg, pp 163–214
248. McKeown NB, Budd PM, Msayib KJ et al (2005) Polymers of intrinsic microporosity (PIMs): bridging the void between microporous and polymeric materials. Chem Eur J 11(9):2610–2620
249. Patrick J, WaIker A (eds) (1995) Porosity in carbons. Edward Arnold, London
250. Kaneko K, Ishii C, Ruike M et al (1992) Origin of superhigh surface area and microcrystalline graphitic structures of activated carbons. Carbon 30(7):1075–1088
251. McKeown NB (2000) Phthalocyanine-containing polymers. J Mater Chem 10(9):1979–1995
252. McKeown NB, Makhseed S, Budd PM (2002) Phthalocyanine-based nanoporous network polymers. Chem Commun 23:2780–2781
253. McKeown NB, Hanif S, Msayib K et al (2002) Porphyrin-based nanoporous network polymers. Chem Commun 23:2782–2783
254. Budd PM, Ghanem B, Msayib K et al (2003) A nanoporous network polymer derived from hexaazatrinaphthylene with potential as an adsorbent and catalyst support. J Mater Chem 13(11):2721–2726
255. Ghanem BS, Msayib KJ, McKeown NB et al (2007) A triptycene-based polymer of intrinsic microposity that displays enhanced surface area and hydrogen adsorption. Chem Commun 1:67–69
256. Ghanem BS, Hashem M, Harris KDM et al (2010) Triptycene-based polymers of intrinsic microporosity: organic materials that can be tailored for gas adsorption. Macromolecules 43(12):5287–5294

257. McKeown NB, Gahnem B, Msayib KJ et al (2006) Towards polymer-based hydrogen storage materials: engineering ultramicroporous cavities within polymers of intrinsic microporosity. Angew Chem Int Ed 45(11):1804–1807

258. Ghanem BS, McKeown NB, Budd PM et al (2009) Synthesis, characterization, and gas permeation properties of a novel group of polymers with intrinsic microporosity: PIM-polyimides. Macromolecules 42(20):7881–7888

259. Short R, Carta M, Bezzu CG et al (2011) Hexaphenylbenzene-based polymers of intrinsic microporosity. Chem Commun 47(24):6822–6824

260. Patel HA, Yavuz CT (2012) Noninvasive functionalization of polymers of intrinsic microporosity for enhanced CO_2 capture. Chem Commun 48(80):9989–9991

261. Zhang P, Jiang X, Wan S et al (2015) Advancing polymers of intrinsic microporosity by mechanochemistry. J Mater Chem A 3(13):6739–6741

262. Nagai K, Masuda T, Nakagawa T et al (2001) Poly[1-(trimethylsilyl)-1-propyne] and related polymers: synthesis, properties and functions. Prog Polym Sci 26(5):721–798

263. Budd PM, McKeown NB, Fritsch D (2005) Free volume and intrinsic microporosity in polymers. J Mater Chem 15(20):1977–1986

264. Carta M, Malpass-Evans R, Croad M et al (2013) An efficient polymer molecular sieve for membrane gas separations. Science 339(6117):303–307

265. Mason CR, Maynard-Atem L, Heard KWJ et al (2014) Enhancement of CO_2 affinity in a polymer of intrinsic microporosity by amine modification. Macromolecules 47(3): 1021–1029

266. Hart KE, Colina CM (2014) Ionomers of intrinsic microporosity: in silico development of ionic-functionalized gas-separation membranes. Langmuir 30(40):12039–12048

267. Shamsipur H, Dawood BA, Budd PM et al (2014) Thermally rearrangeable PIM-polyimides for gas separation membranes. Macromolecules 47(16):5595–5606

268. Bernardo P, Drioli E, Golemme G (2009) Membrane gas separation: a review/state of the art. Ind Eng Chem Res 48(10):4638–4663

269. Fang W, Zhang L, Jiang J (2010) Polymers of intrinsic microporosity for gas permeation: a molecular simulation study. Mol Simul 36(12):992–1003

270. Fritsch D, Merten P, Heinrich K et al (2012) High performance organic solvent nanofiltration membranes: Development and thorough testing of thin film composite membranes made of polymers of intrinsic microporosity (PIMs). J Membr Sci 401:222–231

271. Anokhina T, Yushkin A, Budd P et al (2015) Application of PIM-1 for solvent swing adsorption and solvent recovery by nanofiltration. Sep Purif Technol 156:683–690

272. Swaidan R, Ghanem B, Litwiller E et al (2015) Physical aging, plasticization and their effects on gas permeation in "rigid" polymers of intrinsic microporosity. Macromolecules 48(18):6553–6561

273. Kelman SD, Rowe BW, Bielawski CW et al (2008) Crosslinking poly[1-(trimethylsilyl)-1-propyne] and its effect on physical stability. J Membr Sci 320(1–2):123–134

274. Li FY, Xiao Y, Chung T-S et al (2012) High-performance thermally self-cross-linked polymer of intrinsic microporosity (PIM-1) membranes for energy development. Macromolecules 45(3):1427–1437

275. Shao L, Samseth J, Hägg MB (2007) Effect of plasma treatment on the gas permeability of poly (4-methyl-2-pentyne) membranes. Plasma Processes Polym 4(9):823–831

276. Song Q, Cao S, Pritchard RH et al (2014) Controlled thermal oxidative crosslinking of polymers of intrinsic microporosity towards tunable molecular sieve membranes. Nat Commun 5:4813

277. Song Q, Cao S, Pritchard RH et al (2016) Nanofiller-tuned microporous polymer molecular sieves for energy and environmental processes. J Mater Chem A 4(1):270–279

278. Shin Y, Prestat E, Zhou K-G et al (2016) Synthesis and characterization of composite membranes made of graphene and polymers of intrinsic microporosity. Carbon 102:357–366

279. Mitra T, Bhavsar RS, Adams DJ et al (2016) PIM-1 mixed matrix membranes for gas separations using cost-effective hypercrosslinked nanoparticle fillers. Chem Commun 52(32):5581–5584

280. Carta M, Croad M, Bugler K et al (2014) Heterogeneous organocatalysts composed of microporous polymer networks assembled by Troger's base formation. Polym Chem 5(18):5262–5266
281. Ahn SD, Kolodziej A, Malpass-Evans R et al (2016) Polymer of intrinsic microporosity induces host-guest substrate selectivity in heterogeneous 4-benzoyloxy-TEMPO-catalysed alcohol oxidations. Electrocatalysis 7(1):70–78
282. Weng X, Baez JE, Khiterer M et al (2015) Chiral polymers of intrinsic microporosity: selective membrane permeation of enantiomers. Angew Chem Int Ed 54(38):11214–11218
283. Rong Y, He D, Sanchez-Fernandez A et al (2015) Intrinsically microporous polymer retains porosity in vacuum thermolysis to electroactive heterocarbon. Langmuir 31(44): 12300–12306
284. Silverstein MS (2014) Emulsion-templated porous polymers: a retrospective perspective. Polymer 55(1):304–320
285. Silverstein MS (2014) PolyHIPEs: recent advances in emulsion-templated porous polymers. Prog Polym Sci 39(1):199–234
286. Herbst A, Khutia A, Janiak C (2014) Brønsted instead of lewis acidity in functionalized MIL-101Cr MOFs for efficient heterogeneous (nano-MOF) catalysis in the condensation reaction of aldehydes with alcohols. Inorg Chem 53(14):7319–7333
287. Wickenheisser M, Janiak C (2015) Hierarchical embedding of micro-mesoporous MIL-101 (Cr) in macroporous poly(2-hydroxyethyl methacrylate) high internal phase emulsions with monolithic shape for vapor adsorption applications. Microporous Mesoporous Mater 204:242–250
288. Zhu Y, Hua Y, Zhang S et al (2015) Open-cell macroporous bead: a novel polymeric support for heterogeneous photocatalytic reactions. J Polym Res 22(4):1–6
289. Wickenheisser M, Paul T, Janiak C (2016) Prospects of monolithic MIL-MOF@poly (NIPAM)HIPE composites as water sorption materials. Microporous Mesoporous Mater 220:258–269
290. Yu S, Tan H, Wang J et al (2015) High porosity supermacroporous polystyrene materials with excellent oil-water separation and gas permeability properties. ACS Appl Mater Interfaces 7(12):6745–6753
291. Tebboth M, Kogelbauer A, Bismarck A (2015) Liquid-liquid extraction within emulsion templated macroporous polymers. Ind Eng Chem Res 54(29):7284–7291
292. Luo W, Zhang S, Li P et al (2015) Surfactant-free CO_2-in-water emulsion-templated poly (vinyl alcohol) (PVA) hydrogels. Polymer 61:183–191
293. Luo W, Xu R, Liu Y et al (2015) Emulsion-templated poly(acrylamide)s by using polyvinyl alcohol (PVA) stabilized CO_2-in-water emulsions and their applications in tissue engineering scaffolds. RSC Adv 5(112):92017–92024
294. Zhang S, Luo W, Yan W et al (2014) Synthesis of a CO_2-philic poly(vinyl acetate)-based cationic amphiphilic surfactant by RAFT/ATRP and its application in preparing monolithic materials. Green Chem 16(9):4408–4416
295. Hayward AS, Sano N, Przyborski SA et al (2013) Acrylic-acid-functionalized polyHIPE scaffolds for use in 3D cell culture. Macromol Rapid Commun 34(23–24):1844–1849
296. Prieto EM, Page JM, Harmata AJ et al (2014) Injectable foams for regenerative medicine. Wiley Interdiscip Rev Nanomed Nanobiotechnol 6(2):136–154
297. Qu Q, Pan J, Yin Y et al (2015) Synthesis of macroporous polymer foams via pickering high internal phase emulsions for highly efficient 2,4,5-trichlorophenol removal. J Appl Polym Sci 132(6):41430
298. Liang J, Wu Y, Deng X et al (2015) Optically active porous materials constructed by chirally helical substituted polyacetylene through a high internal phase emulsion approach and the application in enantioselective crystallization. ACS Macro Lett 4(10):1179–1183
299. Sevsek U, Brus J, Jerabek K et al (2014) Post polymerisation hypercrosslinking of styrene/divinylbenzene poly(HIPE)s: Creating micropores within macroporous polymer. Polymer 55(1):410–415

300. Liliang O, Rui Y, Xi C et al (2015) 3D printing of HEK 293FT cell-laden hydrogel into macroporous constructs with high cell viability and normal biological functions. Biofabrication 7(1):015010
301. Wu Z, Su X, Xu Y et al (2016) Bioprinting three-dimensional cell-laden tissue constructs with controllable degradation. Sci Rep 6:24474
302. Perez-Garcia MG, Carranza A, Puig JE et al (2015) Porous monoliths synthesized via polymerization of styrene and divinyl benzene in nonaqueous deep-eutectic solvent-based HIPEs. RSC Adv 5(30):23255–23260
303. Carranza A, Pojman JA, Mota-Morales JD (2014) Deep-eutectic solvents as a support in the nonaqueous synthesis of macroporous poly(HIPEs). RSC Adv 4(78):41584–41587
304. Tebboth M, Kogelbauer A, Bismarck A (2015) Highly permeable macroporous polymers via controlled agitation of emulsion templates. Chem Eng Sci 137:786–795
305. Menner A, Bismarck A (2006) New evidence for the Mechanism of the pore formation in polymerising high internal phase emulsions or why polyHIPEs have an interconnected pore network structure. Macromol Symp 242(1):19–24
306. Mathieu K, Jerome C, Debuigne A (2015) Influence of the macromolecular surfactant features and reactivity on morphology and surface properties of emulsion-templated porous polymers. Macromolecules 48(18):6489–6498
307. Huang X, Yang Y, Shi J et al (2015) High-internal-phase emulsion tailoring polymer amphiphilicity towards an efficient NIR-sensitive bacteria filter. Small 11(37):4876–4883
308. Pan J, Zeng J, Cao Q et al (2016) Hierarchical macro and mesoporous foams synthesized by HIPEs template and interface grafted route for simultaneous removal of lambda-cyhalothrin and copper ions. Chem Eng J 284:1361–1372
309. Qiu H, Che S (2011) Chiral mesoporous silica: chiral construction and imprinting via cooperative self-assembly of amphiphiles and silica precursors. Chem Soc Rev 40(3):1259–1268
310. Hayward AS, Eissa AM, Maltman DJ et al (2013) Galactose-functionalized polyHIPE scaffolds for use in routine three dimensional culture of mammalian hepatocytes. Biomacromol 14(12):4271–4277
311. Oh BHL, Bismarck A, Chan-Park MB (2015) Injectable, interconnected, high-porosity macroporous biocompatible gelatin scaffolds made by surfactant-free emulsion templating. Macromol Rapid Commun 36(4):364–372
312. Sarbu T, Styranec T, Beckman EJ (2000) Non-fluorous polymers with very high solubility in supercritical CO_2 down to low pressures. Nature 405(6783):165–168
313. Eastoe J, Paul A, Nave S et al (2001) Micellization of hydrocarbon surfactants in supercritical carbon dioxide. J Am Chem Soc 123(5):988–989
314. Boyère C, Favrelle A, Léonard AF et al (2013) Macroporous poly (ionic liquid) and poly (acrylamide) monoliths from CO_2-in-water emulsion templates stabilized by sugar-based surfactants. J Mater Chem A 1(29):8479–8487
315. Butler R, Davies CM, Cooper AI (2001) Emulsion templating using high internal phase supercritical fluid emulsions. Adv Mater 13(19):1459–1463
316. Palocci C, Barbetta A, La Grotta A et al (2007) Porous biomaterials obtained using supercritical CO_2-water emulsions. Langmuir 23(15):8243–8251
317. da Rocha SRP, Harrison KL, Johnston KP (1999) Effect of surfactants on the interfacial tension and emulsion formation between water and carbon dioxide. Langmuir 15(2):419–428
318. Tan B, Cooper AI (2005) Functional Oligo(vinyl acetate) CO_2-philes for solubilization and emulsification. J Am Chem Soc 127(25):8938–8939
319. Chen K, Grant N, Liang L et al (2010) Synthesis of CO_2-philic Xanthate-Oligo(vinyl acetate)-based hydrocarbon surfactants by RAFT polymerization and their applications on preparation of emulsion-templated materials. Macromolecules 43(22):9355–9364
320. Li X, Sun G, Li Y et al (2014) Porous TiO_2 materials through pickering high-internal-phase emulsion templating. Langmuir 30(10):2676–2683

321. Kovacic S, Matsko NB, Ferk G et al (2013) Macroporous poly(dicyclopentadiene) gamma Fe_2O_3/Fe_3O_4 nanocomposite foams by high internal phase emulsion templating. J Mater Chem A 1(27):7971–7978
322. Yi W, Wu H, Wang H et al (2016) Interconnectivity of macroporous hydrogels prepared via graphene oxide-stabilized pickering high internal phase emulsions. Langmuir 32(4):982–990
323. Yang Y, Wei Z, Wang C et al (2013) Lignin-based pickering HIPEs for macroporous foams and their enhanced adsorption of copper(II) ions. Chem Commun 49(64):7144–7146
324. Horozov TS, Binks BP (2006) Particle-stabilized emulsions: a bilayer or a bridging monolayer? Angew Chem Int Ed 45(5):773–776
325. Cohen N, Samoocha DC, David D et al (2013) Carbon nanotubes in emulsion-templated porous polymers: polymer nanoparticles, sulfonation, and conductivity. J Polym Sci Pol Chem 51(20):4369–4377
326. Mert EH, Yildirim H, Uzumcu AT et al (2013) Synthesis and characterization of magnetic polyHIPEs with humic acid surface modified magnetic iron oxide nanoparticles. React Funct Polym 73(1):175–181
327. Ikem VO, Menner A, Bismarck A (2008) High internal phase emulsions stabilized solely by functionalized silica particles. Angew Chem Int Ed 47(43):8277–8279

Chapter 5
Responsive Photonic Crystals with Tunable Structural Color

Xiaolu Jia, Haiying Tan and Jintao Zhu

Abstract Since colorimetric sensors can respond to environmental stimulus by the color change, they are widely concerned because of their low cost and low power consumed. A new material in colorimetric sensors called photonic crystals (PCs) was fabricated for sensing the external stimulus. PCs are composed of periodic ordered dielectrics nanostructures with photonic band gap. Different from dye, PCs can exhibit vivid structural color, which can be tailored by lattice spacing variation under the external stimulus. The PCs materials have important applications in the fields of display, sensors, anti-counterfeiting, and others. In this chapter, we will discuss strategies and mechanism for the fabrication of responsive PCs. Moreover, PCs materials demonstrate response characteristic under external stimuli, such as mechanical force, temperature, pH, ionic species, solvents, biomolecules, light, electrical or magnetic fields, and others. Challenge and perspective of this emerging area will also be discussed at the end of this chapter.

5.1   Introduction

Photonic crystals (PCs) materials consist of a periodicity in dielectric constant, which exhibit vivid structural color existing in nature for billions of years [1–7]. The concept of PCs was first proposed in 1987, and then extensive attention was paid on it [8, 9]. Photonic band gap is the major characteristic of PCs, giving rise to the certain wavelengths where light cannot spread in the PCs [10]. As the photonic band gap locates in the visible light region, PCs show structural color due to the Bragg diffraction. According to different distributions of the refractive index in space, PCs can be divided into three types: one-dimensional (1D), 2D, and 3D PCs (Fig. 5.1). Based on the distinct feature of manipulating light, PCs can be applied

X. Jia · H. Tan · J. Zhu (✉)
Key Laboratory of Materials Chemistry for Energy Conversion and Storage of Ministry of Education, School of Chemistry and Chemical Engineering, Huazhong University of Science and Technology, Wuhan 430074, China
e-mail: jtzhu@mail.hust.edu.cn
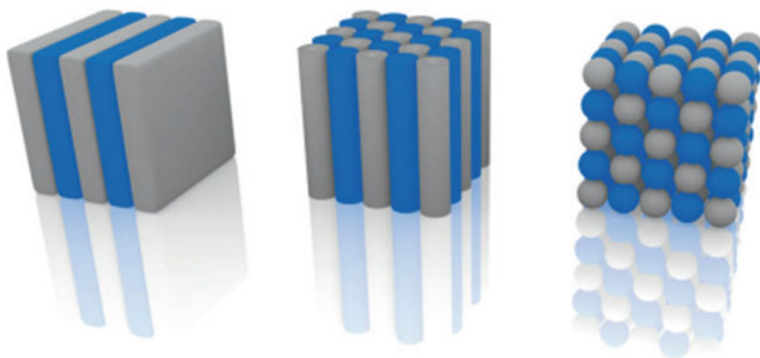
Fig. 5.1 Schematic illustration of 1D, 2D, and 3D PCs. The different colors are showed for distinguishing different dielectric constants (reproduced from Ref. [11] with kind permission of © 2014 Wiley-VCH) (Color figure online)

for high-efficient reflector, optical fibers, sensors, and color display devices, among others [7, 12].

When the ordered nanostructures and responsive polymers meet together, responsive PCs are generated. In general, responsive PCs are the material whose lattice constant can be tuned by external stimuli, such as solvents, temperature, ionic strength, pH, biomolecules, mechanical force, light, and electrical and magnetic fields [13]. Compared with traditional sensing materials, PC sensors had attracted great attention because of their low cost and easy processing ability. The responsive mechanism for this sensor is that the lattice constant of PCs materials can be tuned under external stimulus, leading to the variation of structural color. Therefore, the structural color offers an easy and efficient means to indicate the lattice structure of PCs, and the change of structural color can be visually identified by the naked eyes. The structural color appearances of PCs can be ascribed to the interference and reflection of light, which can be described by the Bragg's law:

$$\lambda_{\max} = 2n_{\mathrm{eff}}d \tag{5.1}$$

where λ is the diffraction wavelength, n is the effective refractive index of the material, and d is the center-to-center space of colloidal particles. Therefore, the diffraction wavelength and the resulting structural color can be tailored by manipulating the lattice spacing of the nanoparticles (NPs) in the PCs.

In this chapter, we will highlight recent advances in responsive PCs for sensing external stimuli. The objectives of this chapter are as follows: (1) summarization of fabrication strategies and mechanism of the responsive PCs; (2) providing an overview of the responsiveness of PCs under different external stimuli; (3) discussion of the challenge and perspective of this emerging research area.

5.2 Fabrication of Responsive PCs

The fabrication strategies of PCs materials can be divided into two main groups: top–down and bottom–up approach. The top–down methods often use traditional microfabrication methods to produce responsive PCs, such as photolithography and etching techniques to produce microstructures with desired shape, size, and order from bulk materials [14–18]. The disadvantages of top–down method are high cost and complicated preparation process. Compared with top–down method, the bottom–up method is a low-cost and efficient approach to fabricate ordered structures through the self-assembly route.

5.2.1 Fabrication of 1D Responsive PCs

5.2.1.1 Fabrication of 1D Responsive PCs by Spin-Coating

One-dimensional PCs with structure of multilayer stacks can be fabricated by alternating high and low refractive indices through spin-coating method. In general, as shown in Fig. 5.2, the multilayer stacks can be prepared by spin-coating the titania suspension of high refractive indices and inorganic NPs suspension of low
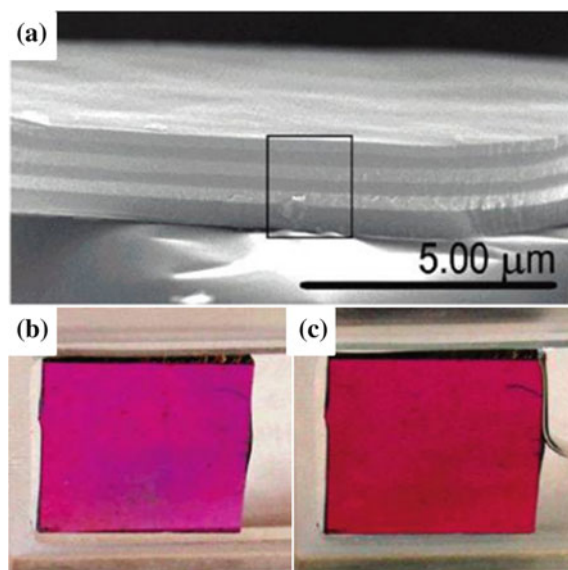
Fig. 5.2 a Scanning electron microscopy (SEM) images of Bragg stack composed of six alternating composition layers of TiO_2 and SiO_2. **b** Photograph of PCs film in air or (**c**) in ethanol (reproduced from Ref. [19] with kind permission of © 2006 American Chemical Society)

refractive indices [19]. A new layer was prepared by baking and removing the solvent with heating processing. Due to the large refractive index difference, the structural color and stopband position of PCs were controlled by changing the thickness of the layer. Moreover, the responsive 1D PCs with structure of multilayer stacks were designed by spin-coating the titania suspension of high refractive indices and responsive polymer materials of low refractive indices. The lattice distance and structural color can be tuned under external stimulus [20, 21].

5.2.1.2 Fabrication of 1D Responsive PCs by Self-assembly of Block Copolymers (BCPs)

In general, symmetry BCPs could form 1D periodic lamellar structure [22–24]. Typically, as shown in Fig. 5.3, the lamellar BCP PCs hydrogel can be fabricated by self-assembly of polystyrene-*b*-quaternized poly(2-vinyl pyridine) (PS-*b*-QP2VP) diblock copolymer in the following four steps: [24] (a) the BCPs was dispersed in propylene glycol monomethyl ether acetate; (b) the polymer solution was spin-coated onto a substrate; (c) the film was annealed under chloroform atmosphere to form the lamellar structure; (d) P2VP in the film was then quaternized and cross-linked through reacting with the mixtures of 1-bromoethane and 1,4-dibromobutane. Formation mechanism of the lamellar PCs films is that microphase separation occurs in BCPs under the driving force of positive enthalpy of mixing and low mixing entropy.

5.2.1.3 Fabrication of 1D Responsive PCs by Self-assembly of Magnetic NPs

Adding magnetic components to the colloidal building blocks provides an opportunity for convenient and precise control of the properties of PCs through an external magnetic field. Superparamagnetic colloids in solution can form particular arrangement under magnetic field. In other words, incorporation of magnetic NPs into the colloidal building blocks will provide opportunities for convenient and precise control of the properties of PCs. For example, Fe_3O_4 can assemble into a long 1D chain structure in solution under magnetic field when a balance is reached between magnetic and electrostatic repulsive forces [25, 26]. Compared with charged PS or silica (SiO_2) NPs, Fe_3O_4 NPs suspension can display brilliant structural color within 1s under the magnetic field (see Fig. 5.4), and the ordered structure cannot be destroyed by less ionic impurities [25]. Moreover, the structural color and reflection spectra of Fe_3O_4 NPs suspension can also be tuned by varying magnetic field intensity.
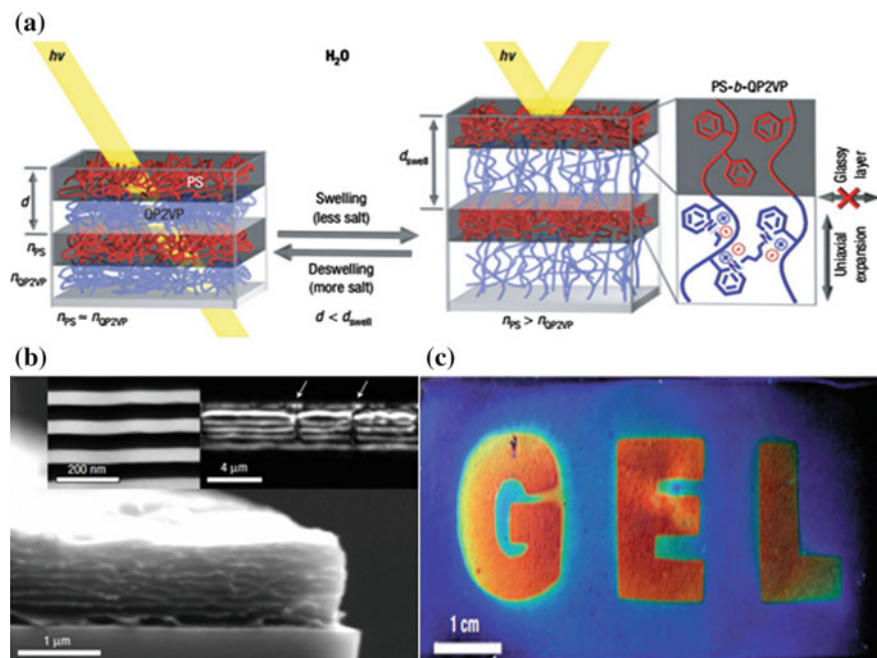
Fig. 5.3 **a** Schematic illustration showing PCs film and the structural color variation mechanism. The PCs film was fabricated by self-assembly of PS-*b*-QP2VP diblock copolymer. The lattice spacing of PCs can be tuned by aqueous solution. **b** SEM images of a dried lamellar PCs film. The film was prepared on a silicon wafer by fracturing after freezing in liquid nitrogen. The *left* transmission electron microscopy (TEM) *inset* image was stained with I_2 vapor (*dark* domains were QP2VP domains). The *upper right inset* image is a reflection-mode laser-scanning confocal microscope image (xz scan) of a swollen film showing defect channels (marked by *arrows*) across the layers. **c** Photograph of the PCs film based on different cross-linking densities in different regions. As the cross-linking density of PCs in the region 'GEL' is lower than the other region of the initial film, the pattern shows *red* on a *blue* background (reproduced from Ref. [24] with kind permission of © 2007 Nature) (Color figure online)

5.2.2 Fabrication of 2D Responsive PCs

Two-dimensional responsive PCs can be fabricated by the 2D template [27–29]. As shown in Fig. 5.5, ordered 2D close-packed array of PS NPs can firstly be formed by dropping PS NPs in aqueous propanol on the Hg surface. Because the suspension has moderate surface tension, PS suspension can spread rapidly on the surface of Hg. Monolayer of 2D PS NPs with closely packed structure was formed after the solvent evaporation. Second, the monomer solution containing cross-linker and initiator was dropped onto the 2D array on Hg, and 2D responsive PCs can be prepared after UV polymerization [29]. This synthesis strategy is facile and effective to produce responsive PCs with high quality. Yet, the high toxicity of mercury limits the practical application of this method.

Fig. 5.4 **a** TEM image and **b** schematic illustration of poly(acrylate) capped-Fe_3O_4 NPs. **c** Photographs of Fe_3O_4 colloidal crystals formed under external magnetic field; the magnetic field intensity decreases gradually from *right* to *left* by tuning distance between the magnet and sample (reproduced from Ref. [25] with kind permission of © 2007 Wiley-VCH)
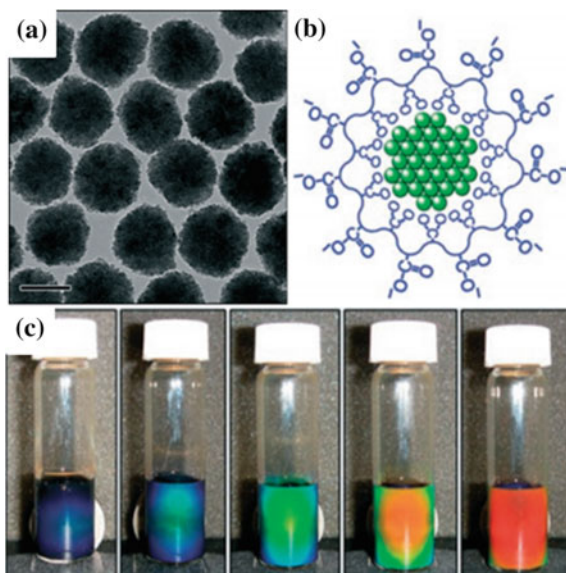
Fig. 5.5 **a** Schematic illustration showing the fabrication of a 2D PCs hydrogel. **b** SEM images of a 2D PS colloidal crystals. **c** Photograph of 2D PCs hydrogel containing COOH groups at pH 3.2 and 7.2 (reproduced from Ref. [29] with kind permission of © 2011 American Chemical Society)
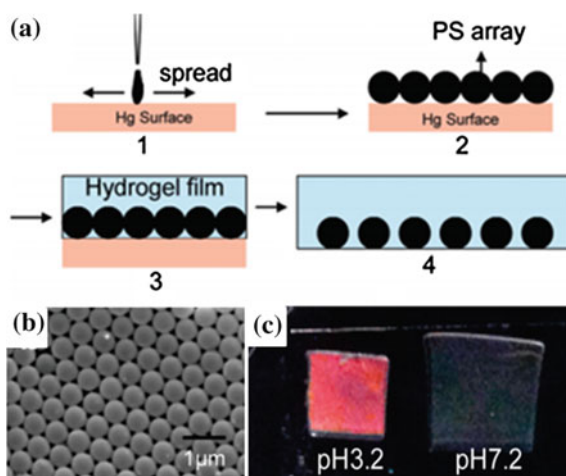
5.2.3 Fabrication of 3D Responsive PCs

5.2.3.1 Fabrication of Non-closely Packed 3D Responsive PCs

Charged colloidal NPs can form non-closely packed structure by electrostatic repulsion between monodisperse colloidal NPs [30]. Due to the minimum energy configuration, the colloidal NPs can self-assemble into non-closely packed body-centered cubic or face-centered cubic colloidal crystal array structure.

However, the 3D ordered structure of charged colloidal NPs can easily be destroyed by ionic impurities. Three-dimensional responsive PCs can be fabricated by fixing the charged colloidal NPs in the responsive hydrogel network or polymerizing the responsive monomer which is embedded in the crystalline colloidal arrays. The stopband and structural color could be tuned by the variation of the lattice spacing under external stimulus [31, 32].

5.2.3.2 Fabrication of Inverse Opal 3D Responsive PCs

Inverse opal 3D responsive PCs can be prepared based on the closely packed colloidal crystal templates [33, 34]. Closely packed templates can be fabricated by solvent evaporation. Then, a monomer solution is infiltrated into the closely packed colloidal crystal templates with subsequent polymerization. Subsequently, the inverse opal PCs film can be prepared after removal of the templates. Due to the porous structure of PCs, the stopband of the inverse opal PCs changed rapidly with environmental variation [34]. Moreover, compared with the non-closely packed colloidal crystal array, the ionic monomer can be infiltrated into the templates without destroying the 3D ordered structure.

5.3 Sensing Applications of the Responsive PCs

5.3.1 Pressure Sensors

PCs-based pressure sensors were prepared by immobilizing colloidal crystals in the mechanically responsive polymers [35–44]. The lattice constants and the corresponding structural color of pressure sensors are changed by deformation of elastomeric polymers under pressure stimulus. Moreover, polymerized crystalline colloidal arrays can prevent the ordered structure of NPs to be destroyed by ionic impurities. Asher et al. first reported N-vinylpyrrolidone/acrylamide-based mechanically responsive film by fixing colloidal crystals arrays [35]. As the lattice distance of (111) planes was decreased under tension, the diffraction peak shifted from 573 to 538 nm. Meanwhile, Ozin group fabricated highly sensitive elastomeric PCs of inverse opal structure by the template method [36]. Due to the low-pressure threshold, the diffraction peak of PCs film had a blue-shift (~ 60 nm) under 15 kPa and can be used for displaying fingerprints with high accuracy. Yet, the shift range of diffraction peak was not stable after 10 compression–decompression cycles.

In order to improve the optical manipulation range and simplify the preparation process, Ge and coworkers fabricated responsive mechanochromic photonic gel by fixing metastable SiO_2 colloidal crystalline arrays [40]. The preparation route of metastable SiO_2 colloidal crystalline arrays dramatically improved the production

efficiency. The structural color of photonic gel can be tuned from red to blue, and the reflection wavelength had a totally 150-nm blue-shift due to the increased elasticity of photonic hydrogel with the incorporation of ethylene glycol. Moreover, the photonic hydrogel had a stable and reversible mechanochromic response in compression–decompression investigation. Recently, our group prepared poly (acrylamide)-based photonic hydrogel for compression sensing by self-assembly of monodisperse carbon-encapsulated Fe_3O_4 NPs (Fig. 5.6) [37]. Due to the large volume swelling of photonic hydrogel after polymerization, the large reflection peak shift (4.3 kPa and 200 nm) was observed within 1 s under pressure. When 0.2 kPa compression was applied on the photonic hydrogel, reflection peak showed 37-nm blue-shift. Moreover, the sensitivity of mechanochromic photonic hydrogel can be adjusted by manipulating the concentration of monomers. The detection range of compression sensor can increase from 0–4.3 to 0–130.6 kPa.

On the other hand, 1D mechanochromic PCs can be prepared by self-assembly of a diblock copolymer. For example, Stafford et al. fabricated lamellar mechanochromic PCs by self-assembly of PS-b-P2VP [44]. The ordering of the structure can be improved by solvent (e.g., chloroform) annealing. Moreover, the elasticity of PCs and lattice spacing can be varied by exposing this material to a mixture of acetic acid and water. The reflection peaks of lamellar PCs shifted from 760 to 520 nm obviously when the compressive strain increased from 10 to 30%. Meanwhile, Gong and colleagues fabricated mechanochromic PCs by introducing a second hydrogel into poly(dodecyl glyceryl itaconate)/polyacrylamide with bilayer structure [43]. Based on the double network strategy, a second polyacrylamide network can be prepared by introducing and fixing the acrylamide and

Fig. 5.6 a–e Photographs and f corresponding reflection spectra of the photonic hydrogel with 20 wt% monomer at a fixed detection angle (90) under different compressions: a 0 N, b 0.049 N, c 0.196 N, d 0.392 N, and e 0.980 N (reproduced from Ref. [37] with kind permission of © 2015 American Chemical Society)
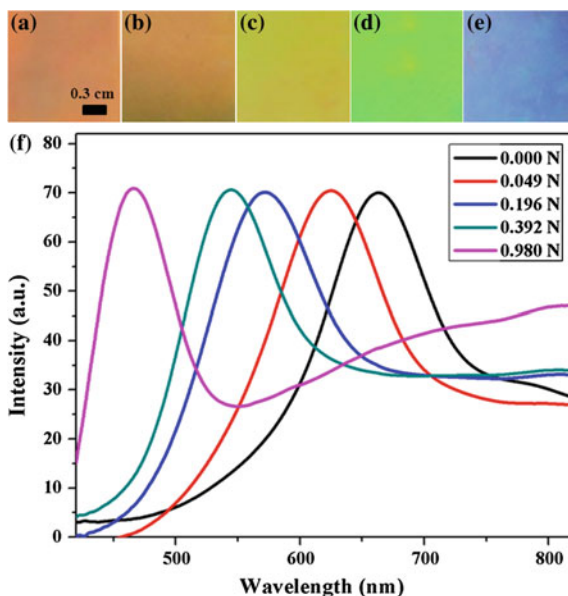
2-oxoglutaric acid into the polyacrylamide layers of PCs. The reflection peak shifted from 715 to 385 nm by applying compression strain. Though the shift range of stopband is large and covers all the colors, it takes few seconds ($\sim$15 s) for the mechanochromic PCs to return to the original structural color after removal of the compressive strain.

In order to improve the pressure response rate, Gong et al. fabricated mechanochromic PCs with an ultrafast response (Fig. 5.7). The amide groups in the polyacrylamide layers can be changed to carboxyl groups by a hydrolysis reaction. The increased charges in the hydrogel lead to the swelling of the hydrogel, and the PCs demonstrate the ultrafast response. Moreover, the PCs have excellent mechanical stability and the structural color can be reversibly switched after 10,000 times compression–decompression cycles without degradation [42].

5.3.2 Temperature Sensors

Generally, temperature sensors can be fabricated by introducing thermo-sensitive hydrogel [45–51]. Asher group first prepared the temperature sensors based on thermo-sensitive poly(N-isopropylacrylamide) (PNIPAm) [45]. PNIPAm is a kind of thermo-sensitive polymer and has the lower critical solution temperature (32 °C), which can be tuned between a hydrated state and a dehydrated state. As the temperature increases, the PNIPAm hydrogel expels water, thus the distance between NPs decreased. Depending on the reversible swelling and shrinking of the PNIPAm hydrogel, temperature can be detected.

Porous PCs hydrogel was synthesized by Takeoka et al. using closely packed SiO_2 colloidal crystal as template [46]. The porous structure of PCs hydrogel made it respond quickly to temperature with the volume variation of the hydrogels. Moreover, high cross-linking degree would limit the swelling ratio of the PCs hydrogel, thus the shift range of diffracted wavelength increased with the decrease of cross-linking degree.

Takeoka et al. [47] fabricated the interconnected and trapped thermo-sensitive opal-structured hydrogel by filling NIPAm monomer into PS template of inverse opal structure. Since the lattice constant decreased with the shrinking of PCs hydrogel volume, the reflected wavelength of the interconnected opal-structured PC hydrogel had a blue-shift as the temperature increased. The trapped opal-structured PCs hydrogel did not exhibit the change of reflected peak position, while the intensity of reflection spectra decreased with the increase of temperature. The reason can be ascribed to that the PNIPAm NPs adhere to PS template as the temperature increased, resulting in destruction of the ordered array of the PNIPAm NPs.
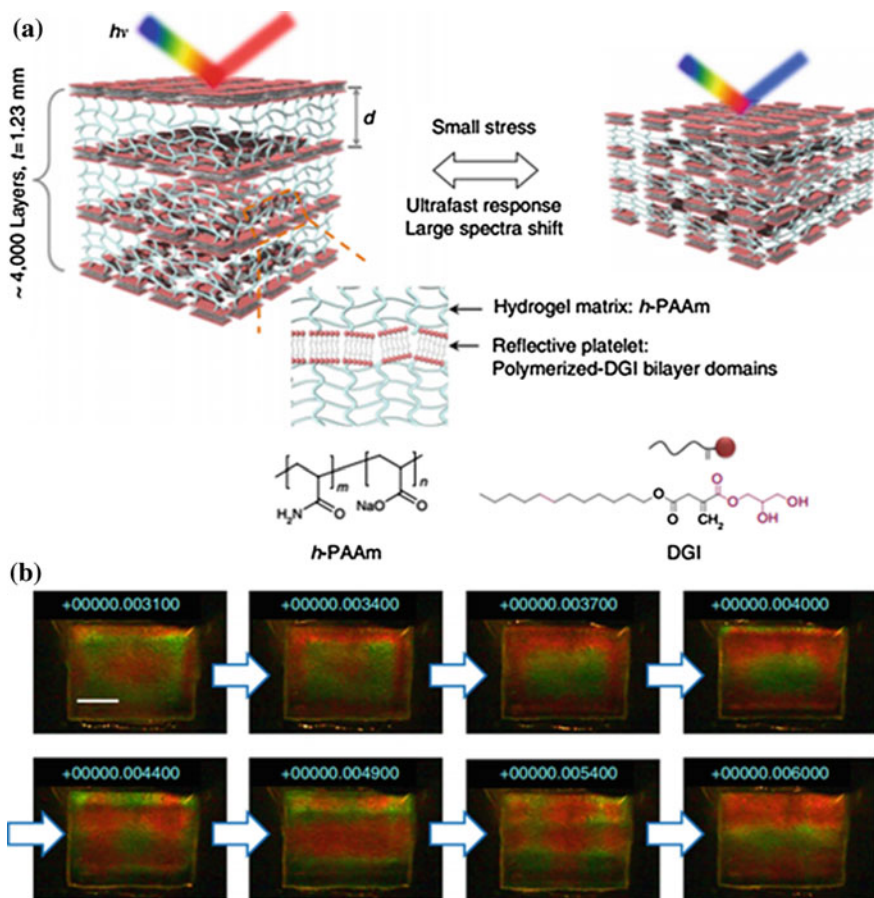
Fig. 5.7 a Schematic illustration showing PCs hydrogel which consist of hydrolyzed poly (dodecyl glycerylitaconate)/polyacrylamide. Because hydrolyzed polyacrylamide layers are quasi-elastic and compressed rapidly under pressure stimulus. Thus, the PCs hydrogel exhibits a fast response time, full-color tunability, low actuating stress, and good mechanical stability. **b** Photographs of PCs film under high-speed plastic spheres stimulus. The time can be recorded by a high-speed camera (10,000 fps). The time interval between the neighboring images was 0.3–0.6 ms (reproduced from Ref. [42] with kind permission of © 2014 Nature)

Interestingly, Hayward group fabricated 1D poly(*para*-methyl styrene)/PNIPAm multilayer thermo-sensitive sensors by spin-coating and photo-cross-linking ways [48]. The benzophenone in the polymer is photo-active units that can be cross-linked under irradiation of 365-nm UV light with the wavelength at 365 nm. This approach is more simple and efficient for fabricating 1D thermo-sensitive PCs than self-assembly of BCPs.

5.3.3 Organic Solvent Sensors

Organic solvents are harmful to human kidneys, lungs, and immune and nervous systems under the long-time contact [52]. Since certain polymers have the ability to swell or shrink under the treatment of organic solvent, responsive PCs materials with desirable polymers can be used for detecting organic solvent by naked eyes [24, 52–55]. Takeoka and coworkers fabricated polyacrylamide-based PCs hydrogel to detect the content of acetone [52]. When the content of acetone increased, the lattice constant of PCs hydrogel decreased and the structural color changed from red to blue. As shown in Fig. 5.8, Gao et al. synthesized polyacrylamide inverse opal hydrogel in response to alcohols based on the colloidal crystal template [54]. Compared with the above mentioned PCs hydrogels, inverse opal hydrogel has interconnecting porous structure. The organic solvent can diffuse into the hydrogel and lead to the quick variation of the structural color.

Based on the solvent-responsive property, photonic paper can be prepared for pattern display. Xia and Fudouzi developed the photonic paper/ink system by encapsulating PS colloidal crystal in the poly(dimethylsiloxane) (PDMS) [55]. As the ink (silicone fluid) was written on the PCs film, PDMS was swelled, the structural color showed a red-shift. Based on the different structural colors in different regions, the generated pattern can be distinguished by naked eyes, and the structural colors can return to the original state after removal of all the silicone fluid. Thomas et al. fabricated 1D lamellar PCs gel through the self-assembly of PS-*b*-QP2VP within two steps: [24] first, PS-*b*-P2VP films were formed by spin-casting, followed by annealing the film under chloroform atmosphere. Then, P2VP blocks were quaternized and cross-linked after treating the P2VP blocks with 1-bromoethane and 1,4-dibromobutane. The lattice constant and structural colors of PCs gels can be manipulated by swelling the hydrophilic polymer with water.
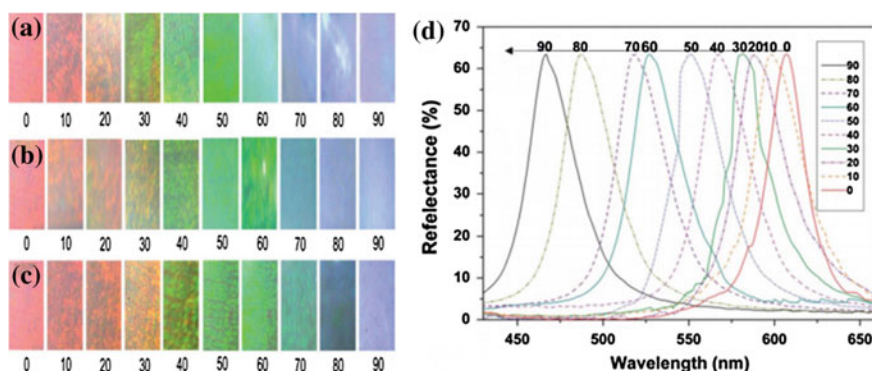
Fig. 5.8 **a–c** Optical photographs and of PCs hydrogel in binary mixture of alcohol and water with varied alcohol content: **a** methanol, **b** ethanol, and **c** isopropanol. **d** Reflection spectra of PCs hydrogel in the in binary mixture of methanol and water with varied methanol content (reproduced from Ref. [54] with kind permission of © 2012 Royal Society of Chemistry)

The structural color patterns can be formed by both coating and cross-linking of the films. First, a high cross-linking degree of PCs film was prepared by coating and quaternization. Second, the letters 'GEL' with low cross-linking degree formed by spraying the BCP solution through a mask and cross-linking. Because the cross-linking degree of the pattern 'GEL' was lower than the initial substrate, the pattern turned to red on a blue substrate. The film had no structural colors after drying because the stopband location was not located in the visible area, and the pattern display can be repeated over 100 times with stable optical properties.

5.3.4 pH and Ionic Sensors

The hydrogel with ion-responsive groups can display volume change as the osmotic pressure of hydrogel is varied by ions [29, 56–70]. When the colloidal crystals were encapsulated in these hydrogel with ion-responsive groups, their stopbands of PCs hydrogel can be tuned under the ions stimulus. Asher et al. fabricated photonic hydrogel with polymerized crystalline colloidal array for pH and ionic strength sensing [56]. As pH value in the solution increased, carboxyl groups in the hydrogel deprotonated, leading to the increase of Donnan potential and swell of the hydrogel. The diffracted wavelengths of PCs hydrogel showed a red-shift as pH increased. Due to the formation of metal complex in the hydrogel networks, the degree of cross-linking in the hydrogel increased, the volume of the photonic hydrogel shrunk, and the reflection peak shifted to the blue range with the ionic strength increasing. Asher and colleagues prepared PCs hydrogel for Pb^{2+} or K^+ sensing by introducing the molecular-recognition group 18-crown-6 in the hydrogel [57]. Due to the selective binding of metal ions Pb^{2+} or K^+ with the crown ether, Donnan osmotic pressure of the hydrogel increased, resulting in the swelling of the hydrogel and of red-shift of the diffraction peak. On the other hand, Thomas et al. fabricated lamellar photonic hydrogels by self-assembly of BCPs and then quaternization with full-color tunability by direct exchange of counteranions [58]. Due to the different hydration strengths between QP2VP units and counteranions, the stopband of the PCs hydrogel can be easily tuned by directly changing the counteranions with different hydration characteristics (Fig. 5.9). Because $CH_3CO_2^-$ anions possess high hydration strength, the PCs hydrogel can demonstrate red color. When the $CH_3CO_2^-$ anions were replaced by the other anions with lower hydration strength (e.g., Br^-, I^-, NO_3^-), the structural color showed a blue-shift.

5.3.5 Electric Field Sensor

Electric fields represent a kind of convenient and efficient method among external stimulus, so electrically responsive PCs attracted extensive attention [71–75].

Fig. 5.9 **a** Schematic illustration showing the mechanism for structural color change of PS-*b*-QP2VP lamellar PCs by a direct exchange of counterions. **b** Optical photographs and **c** corresponding reflection spectra of the lamellar PCs with direct exchange of counteranions (reproduced from Ref. [58] with kind permission of © 2012 American Chemical Society)
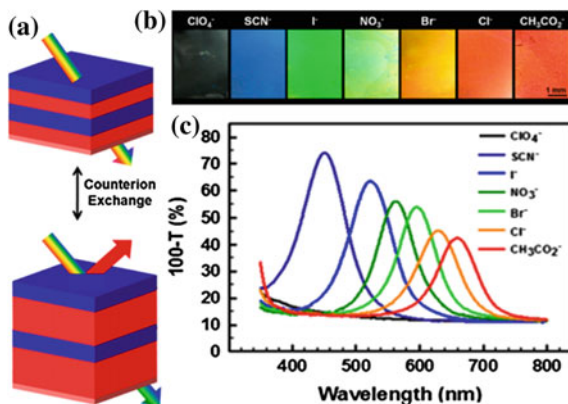
Ozin and coworkers fabricated electrically responsive PCs films by fixing colloidal crystal in the redox-active polymers [71]. The PCs film consists of poly(ferrocenylsilane), such as poly(ferrocenylmethylvinylsilane) and poly(ferrocenyldivinylsilane), which was sandwiched between indium tin oxide (ITO) glass slides. Poly(ferrocenylsilane) showed reversible electrochemical reduction and oxidation of the partial electronic delocalization, leading to a different degree of oxidation. The lattice spacing of the silica NPs can be tuned with the volume change of cross-linked polymer under electric fields. If oxidative potential is applied to the PCs film, electrons are extracted from the iron atoms in the polymer and anions in the electrolyte transfer to the polymers to neutralize its positive charges. The movement of ions and solvent leads to the swelling of the polymers and red-shift of the diffraction wavelength. On the contrary, if reducing potential is applied to the PCs film, electrons are injected to the iron atoms in the polymer and anions in the electrolyte are expelled from the polymer due to the repulsion force between charges. The movement of ions and solvent leads to the shrink of the polymer volume and blue-shift of the diffraction wavelength. The PCs materials have good stability after 100 times oxidation–reduction cycles. Because the electrolyte or electron permeated into the polymerized crystalline colloidal arrays in the different ways, the structural color of the PCs films changed within several seconds under electric fields. Yet, in this case, the switching speed of PCs film was still slow, and higher drive voltage was usually needed.

To solve this problem, Ozin et al. [72] fabricated inverse opal PCs films in which electrolyte and electron can infuse the porous film quickly. The inverse opal PCs film consists of redox-active poly(ferrocenylmethylvinylsilane) and poly(ferrocenyldivinylsilane). The inverse opal PCs film showed different structural colors in the entire visible light range under 1.2–2.8 V voltages. The stopband range of the inverse polymer-gel opal (cross-linker degree 10 mol%) was about 240 nm under 2.4 V. The stopband range of the inverse polymer-gel opal was larger than the non-closely packed colloidal crystal films under the condition of the same cross-linker degree and voltage. However, the manipulation range of the

non-closely packed colloidal crystal films (cross-linker degree 10 mol%) was ~100 nm under 2.4 V.

Compared with the long response time (several seconds) of redox-active PCs films, Yang et al. fabricated electrically responsive crystalline colloidal arrays with fast response and low threshold voltage speed by self-assembly of highly charged PS NPs [73]. The sulfonated PS suspension was infiltrated through two ITO glass plates. The charged colloidal NPs showed electrophoretic movement toward oppositely charged electrode induced by the coulombic force under the uniform electric field, leading to the decrement of lattice spacing. Because the electrokinetic force and repulsive force between NPs reach a balance, the lattice spacing depends on the electric field intensity. The structural color of the crystalline colloidal arrays changed from red to blue under the electric field. As electric field intensity increased from 0 to −1.8 V, the reflection peak of the colloidal crystalline arrays showed ~100-nm blue-shift, covering all colors in visible light range. The reflection peaks of colloidal crystalline arrays shifted within a second under the DC field stimulus. Moreover, the pattern with the reflection color can be displayed in a desired area by using patterned electrode.

5.3.6 Magnetic Field Sensor

Different from other crystalline colloidal arrays, superparamagnetic colloidal particles could form 1D ordered structure under external magnetic field [76–82]. The lattice spacing of these superparamagnetic colloidal NPs can be tuned by magnetic fields. Bibette and coworkers first reported magnetically responsive colloidal PCs formed from emulsion droplets containing Fe_2O_3 NPs [76]. Yet, the colloidal particles were not stable in water. Asher et al. fabricated superparamagnetic PCs by the self-assembly of highly charged, monodispersed PS/iron oxide composite colloidal NPs [77]. Due to the electrostatic repulsive force between NPs, the colloidal particles assembled into 3D ordered structure in the medium. When the magnetic and electrostatic repulsive forces between Fe_3O_4 NPs reach a balance, the NPs formed a 1D ordered structure along the direction of magnetic field. As a magnetic field was applied to the colloidal crystalline arrays, the lattice spacing of colloidal crystalline arrays decreased due to magnetic field force. Generally, the diffraction wavelength had a blue-shift (~100 nm) as the magnetic field increased. Though the highly charged NPs were more stable than Fe_2O_3 NPs in water, the low content of magnetic components in PS NPs led to a small shift range of diffraction peak.

In order to increase the loading of magnetic materials, Yin and coworkers prepared polyacrylate-capped superparamagnetic colloidal particles with relatively narrow size distributions. The Fe_3O_4 NPs assembled quickly in water under external magnetic field, and the structural color could be manipulated by varying the strength of magnetic field. The diffraction wavelength shifted from 730 to 450 nm as the strength of magnetic field increased from 87.8 to 352 Gauss. If the superparamagnetic colloidal particles were encapsulated in the polymer, the 1D

ordered structure was stable. Yin et al. demonstrated a kind of clear and polychrome pattern within seconds by controlling the magnetic field and maskless lithography system (Fig. 5.10) [78]. Without external magnetic field, the superparamagnetic colloidal particles were dispersed in photo-curable resin and showed an intrinsic brown color. Under an external magnetic field, the superparamagnetic colloidal particles formed 1D chain structures along the magnetic field lines. The distance of NPs can be tuned by the intensity of applied magnetic field; meanwhile, the colloidal particles show different structural colors. When the pattern with desired structural color was tuned under the external magnetic field, it could be maintained by solidifying the photo-curable resin through a maskless lithography system under UV light. Then, the structural color of unsolidified location could be tuned by changing the strength of magnetic field. The other structural colored pattern can be obtained at a different location under UV light.

Therefore, the polychrome pattern was produced by repeating this tuning and fixing process without moving the substrate or the mask. Chen and colleagues developed a novel and simple method for fabricating the PCs [79]. The structural color (purple, yellow, and cyan) can be formed by mixing carbon-capped
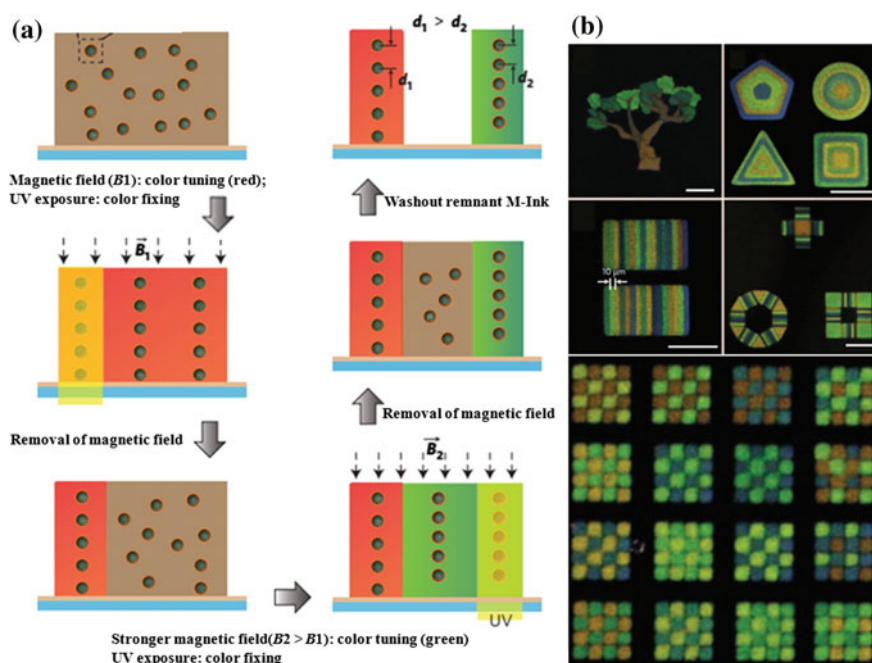
Fig. 5.10 **a** Schematic representation of multicolor patterning of structural color by the sequential steps of tuning magnetic field intensity and photo-polymerization. The structural color can be tuned by changing the strength of the magnetic fields. Then, the ordered structure in the desired region can be fixed by patterned UV light. **b** Optical photographs of high-resolution multiple structural color patterns (reproduced from Ref. [78] with kind permission of © 2009 Nature)

superparamagnetic colloidal NPs with different sizes. The different NPs could self-assemble into double photonic band gap structure under the magnetic field. Moreover, the mixed superparamagnetic colloidal NPs could be used to form photonic anti-counterfeiting label.

5.3.7   Optical Sensor

Light is a simple and effective stimulus to tune the structural color of PCs containing photo-sensitive molecules [83–86]. Sato and coworkers fabricated optically responsive PCs by infiltrating reversibly photo-response dyes into opal crystal. Two kinds of dyes, 1,3-dihydro-1,3,3-trimethylspiro-[2H-indol-2,3'-[3H]-naphth[2,1-b] [1, 4]oxazine] (SP) and cis-1,2-dicyano-1,2-bis(2,4,5-trimethyl-3-thienyl) ethane (CMTE), were used [86]. The initial state of the SP dye in the PCs was the ring-close form, which could transfer into ring-open form under UV light. The reflection peak was, thus, shifted from 723 to 738 nm, and the intensity of reflection peak increased simultaneously. Different from SP, the initial state of CMTE in the PCs was the mixture of both the ring-open and ring-close. This CMTE dyes transfer into the ring-close form under UV light. The shift range of reflection peak ($\sim$3 nm) was smaller than that of PCs containing SP dye.

Moreover, the intensity of reflection peak was smaller than that of PCs containing SP dye. The shift of reflection peak could be ascribed to the change of refractive index under UV light. The intensity change of reflection peak resulted from the phase transition from order to disorder. Meanwhile, Asher group fabricated optically responsive PCs containing azobenzene groups for recordable and erasable memories or display devices [83]. Information or patterns are easily recorded and erased by irradiating the PCs with UV light or visible light. The azobenzene group is trans-structure in the dark, while the *trans*-structure can be transformed into *cis*-structure under UV light. Due to the increase of free energy of hydrogel containing azobenzene group under UV light irradiation, the volume of PCs swelled and the corresponding reflection peak shifted from 530 to 580 nm. Moreover, the structural color and reflection peak could return to its original state after 1 min under visible light irradiation.

5.3.8   Biomolecule Sensors

Biomolecule diagnostics is an important field based on specific sensors. In particular, there is an increasing demand for biomolecule analysis by naked eyes [87–96]. One of the most important PCs sensors in biomedical fields is glucose sensing. Asher group fabricated PCs films for glucose and galactose sensing based on glucose oxidase as the recognition group [87]. When the glucose sensor was introduced into a glucose solution, the glucose can be converted to gluconic acid

under the catalysis of glucose oxidase in the PCs hydrogel. The gluconic acid led to the PCs hydrogel swelling. The glucose can be detected in the concentration range 0.1–0.5 mM in the presence of oxygen. However, several problems still existed when the PCs sensors were used for glucose sensing. First, the glucose oxidase will be destroyed in the process of storage and usage. Moreover, the glucose response depended on the concentration of oxygen in the solution. In order to solve these problems, PCs containing phenylboronic acid were fabricated based on the fact that phenylboronic acid can combine with glucose reversibly. Takeoka et al. developed a glucose sensor with porous structure for monitoring glucose by naked eyes [88]. There was an equilibrium between the undissociated and the dissociated states of phenylboronic acid in alkalescent aqueous solutions. The undissociated state of phenylboronic acid transferred into dissociated state when phenylboronic acid combined with glucose. Thus, the charged compound was increased by the addition of glucose due to the increase of osmotic pressure in the hydrogel, which will induce the volume increase of the PCs hydrogel. The PCs hydrogel can detect the glucose concentrations between 5 and 20 mM.

The detection of DNA hybridization had very important applications in the field of disease diagnosis, food or environmental analysis, and others. Gu group fabricated PCs hydrogel for label-free DNA detection by using DNA as cross-linker [89]. The hydrogel was composed of acrylamide, *N,N*-methylenebisacrylamide, and acryloyl-modified DNA. The target DNA can specifically combine with the cross-linked probe ssDNA in the PCs hydrogel; then, the double-stranded DNA forms. The lattice distance of the PCs hydrogel was decreased, and diffraction peak had a blue-shift due to the formation of the DNA double helix structure in the process of multiplex label-free DNA detection. The PCs hydrogel can detect the DNA concentrations between 1 nM and 1 mM. The largest shift of the diffraction peak reached 23-nm blue-shift when the concentration of target DNA was 1 mM.

The identification of specific marker proteins often required in the field of disease diagnosis. Asher and colleagues fabricated 2D PCs hydrogel for detecting the protein avidin [90]. The biotin can bind with the protein avidin strongly, which leads to the increase of degree of cross-linking of the PCs hydrogel and shrinking of the PCs hydrogel volumes. The lattice spacing of PCs hydrogel, thus, decreased, leading to the blue-shift of diffraction peak. The diffraction light shifted from 617 to 550 nm, while the structural color was tuned from red to yellow as the concentration of avidin increased from 0 to 1 mg/mL.

5.4 Summary and Outlook

In this chapter, we have demonstrated the recent advances in responsive PCs and applications of PCs materials as sensors. The PCs structure, preparation methods, and response mechanism are discussed in detail. The structural color of PCs depends on variations of lattice spacing, and the structural color variation can be identified by naked eyes without expensive apparatuses. Therefore, the shift range

of diffraction peak is an important property, and the large shift range in the visible region can be easily identified by naked eyes. Nowadays, many responsive PCs are fabricated by fixing the colloidal crystalline arrays in the hydrogel. The ordered structure of colloidal crystalline arrays can be destroyed as the hydrogel is completely dry. Therefore, it will be significance to fabricate responsive composite PCs using a new matrix material instead of hydrogels.

On the other hand, the responsive PCs have been reported for sensing pressure, solvent, temperature, pH, biomolecule, and others factors, and the structural colors of the responsive PCs can be tuned by several external stimulus. However, this principle, based on the structural color, makes it more challenging to specifically detect only one stimulus. Thus, one of the challenges in this field is prevalent in structural color sensors for both physical and chemical stimuli. In order to have industrial application, the responsive PCs need to have good specificity for analytes. Recently, several efforts have been explored to improve the specificity of the structural color-based colorimetric detection, such as lock-and-key detection (highly specific ligand binding or molecular imprinting) and combinatorial response of sensor arrays where each has weak specificity individually. It is, thus, necessary to consider whether the sensitivity, response rate, and durability of the responsive PCs can satisfy the practical requirements. Moreover, the sensing style of the responsive PCs is still limited, and it is very necessary to fabricate the new kind of responsive PCs to meet the broad requirement of applications.

References

1. Whitney HM, Kolle M, Andrew P (2009) Floral iridescence, produced by diffractive optics, acts as a cue for animal pollinators. Science 323:130–133
2. Noyes JA, Vukusic P, Hooper IR (2007) Experimental method for reliably establishing the refractive index of buprestid beetle exocuticle. Opt Express 15:4351–4358
3. Kinoshita S, Yoshioka S, Fujii Y et al (2002) Photophysics of structural color in the morpho butterflies. Forma 17:103–121
4. Gao XF, Yan X, Yao X et al (2007) The dry-style antifogging properties of mosquito compound eyes and artificial analogues prepared by soft lithography. Adv Mater 19:2213–2217
5. Parker AR, McPhedran RC, McKenzie DR et al (2001) Photonic engineering. aphrodite's iridescence. Nature 409:36–37
6. Parker AR, Welch VL, Driver D et al (2003) Structural colour: opal analogue discovered in a weevil. Nature 426:786–787
7. Zhao YJ, Xie ZY, Gu HC et al (2012) Bio-inspired variable structural color materials. Chem Soc Rev 41:3297–3317
8. John S (1987) Strong localization of photons in certain disordered dielectric superlattices. Phys Rev Lett 58:2486–2489

9. Yablonovitch E (1987) Inhibited spontaneous emission in solid-state physics and electronics. Phys Rev Lett 58:2059–2062

10. Huang Y, Zhou JM, Su B et al (2012) Colloidal photonic crystals with narrow stopbands assembled from low-adhesive superhydrophobic substrates. J Am Chem Soc 134:17053–17058

11. Fenzl C, Hirsch T, Wolfbeis OS (2014) Photonic crystals for chemical sensing and biosensing. Angew Chem Int Ed 53:3318–3335

12. Ge JP, Yin YD (2011) Responsive photonic crystals. Angew Chem In Ed 50:1492–1522

13. Aguirre CI, Reguera E, Stein A (2010) Tunable colors in opals and inverse opal photonic crystals. Adv Funct Mater 20:2565–2578

14. Yablonovitch E, Gmitter TJ, Leung KM (1991) Photonic band structure: the face-centered-cubic case employing nonspherical atoms. Phys Rev Lett 67:2295–2298

15. Tondiglia VP, Natarajan LV, Sutherland RL et al (2002) Holographic formation of electro-optical polymer–liquid crystal photonic crystals. Adv Mater 14:187–191

16. Mizeikisa V, Juodkazisa S, Marcinkevi A et al (2001) Tailoring and characterization of photonic crystals. J Photoch Photobio C 2:35–69

17. Liu Y, Liu S, Zhang XS (2006) Fabrication of three-dimensional photonic crystals with two-beam holographic lithography. Appl Optics 45:480–483

18. Lehmann V, Föll H (1990) Formation mechanism and properties of electrochemically etched trenches in n-type silicon. J Electrochem Soc 137:653–659

19. Choi SY, Mamak M, Freymann GV et al (2006) Mesoporous bragg stack color tunable sensors. Nano Lett 6:2456–2461

20. Lotsch BV, Knobbe CB, Ozin GA (2009) A Step Towards optically encoded silver release in 1D photonic crystals. Small 5:1498–1503

21. Wang ZY, Zhang JH, Wang ZH et al (2013) Biochemical-to-optical signal transduction by pH sensitive organic–inorganic hybrid Bragg stacks with a full color display. J Mater Chem C 1:977–983

22. Fan Y, Walish JJ, Tang SC et al (2014) Defects, solvent quality, and photonic response in lamellar block copolymer gels. Macromolecules 47:1130–1136

23. Lee W, Yoon J, Thomas EL et al (2013) Dynamic changes in structural color of a lamellar block copolymer photonic gel during solvent evaporation. Macromolecules 46:6528–6532

24. Kang Y, Walish JJ, Gorishnyy T et al (2007) Broad-wavelength-range chemically tunable block-copolymer photonic gels. Nat Mater 6:957–960

25. Ge JP, Hu YX, Yin YD (2007) Highly tunable superparamagnetic colloidal photonic crystals. Angew Chem Int Ed 46:7428–7431

26. Lee H, Kim J, Kim H et al (2010) Colour-barcoded magnetic microparticles for multiplexed bioassays. Nat Mater 5:745–749

27. Zhang JT, Smith N, Asher SA (2012) Two-dimensional photonic crystal surfactant detection. Anal Chem 84:6416–6420

28. Zhang JT, Wang LL, Chao X et al (2013) Vertical spreading of two-dimensional crystalline colloidal arrays. J Mater Chem C 1:6099–6102

29. Zhang JT, Wang LL, Luo J et al (2011) 2-D array photonic crystal sensing motif. J Am Chem Soc 133:9152–9155

30. Asher SA, Peteu SF, Reese CE et al (2002) Polymerized crystalline colloidal array chemical-sensing materials for detection of lead in body fluids. Anal Bioanal Chem 373:632–638

31. Kanai T, Lee D, Shum HC et al (2010) Fabrication of tunable spherical colloidal crystals immobilized in soft hydrogels. Small 6:807–810

32. Kamenjicki M, Asher SA (2005) Epoxide functionalized polymerized crystalline colloidal arrays. Sens Actuators, B Chem 106:373–377

33. Ye BF, Rong F, Gu HC et al (2013) Bioinspired angle-independent photonic crystal colorimetric sensing. Chem Commun 49:5331–5333

34. Zhao YJ, Zhao XW, Hu J et al (2009) Encoded porous beads for label-free multiplex detection of tumor markers. Adv Mater 21:569–572

35. Asher SA, Holtz J, Liu L et al (1994) Self-assembly motif for creating submicron periodic materials. Polymerized crystalline colloidal arrays. J Am Chem Soc 116:4997–4998
36. Arsenault A, Clark TJ, Wang RZ et al (2006) From colour fingerprinting to the control of photoluminescence in elastic photonic crystals. Nat Mater 5:179–184
37. Jia XL, Wang JY, Wang K et al (2015) Highly sensitive mechanochromic photonic hydrogels with fast reversibility and mechanical stability. Langmuir 31:8732–8737
38. Foulger SH, Jiang P, Ying Y et al (2001) Photonic bandgap composites. Adv Mater 13:1898–1901
39. Fudouzi H, Sawada T (2006) Photonic rubber sheets with tunable color by elastic deformation. Langmuir 22:1365–1368
40. Yang DP, Ye SY, Ge JP (2014) From metastable colloidal crystalline arrays to fast responsive mechanochromic photonic gels: an organic gel for deformation-based display panels. Adv Funct Mater 24:3197–3205
41. Wang XQ, Wang CF, Zhou ZF et al (2014) Robust mechanochromic elastic one-dimensional photonic hydrogels for touch sensing and flexible displays. Adv Optical Mater 2:652–662
42. Yue Y, Kurokawa T, Nonoyama T et al (2014) Mechano-actuated ultrafast full-colour switching in layered photonic hydrogels. Nat Commun 5:4659
43. Haque MA, Kurokawa T, Kamita G et al (2011) Rapid and reversible tuning of structural color of a hydrogel over the entire visible spectrum by mechanical stimulation. Chem Mater 23:5200–5207
44. Chan EP, Walish JJ, Thomas EL et al (2011) Block copolymer photonic gel for mechanochromic sensing. Adv Mater 23:4702–4706
45. Weissman JM, Sunkara HB, Tse AS et al (1996) Thermally switchable periodicities and diffraction from mesoscopically ordered materials. Science 274:959–960
46. Matsubara K, Watanabe M, Takeoka Y (2007) A thermally adjustable multicolor photochromic hydrogel. Angew Chem Int Ed 46:1688–1692
47. Kumoda M, Watanabe M, Takeoka Y (2006) Preparations and optical properties of ordered arrays of submicron gel particles: interconnected state and trapped state. Langmuir 22:4403–4407
48. Chiappelli MC, Hayward RC (2012) Photonic multilayer sensors from photo-crosslinkable polymer films. Adv Mater 24:6100–6104
49. Takeoka Y, Watanabe M (2003) An electro and thermochromic hydrogel as a full-color indicator Langmuir 19:9104–9106
50. Ma HR, Zhu MX, Luo W et al (2015) Free-standing, flexible thermochromic films based on one-dimensional magnetic photonic crystals. J Mater Chem C 3:2848–2855
51. Tsuji S, Kawaguchi H (2005) Colored thin films prepared from hydrogel microspheres. Langmuir 21:8439–8442
52. Zhang YQ, Qiu JH, Hu RR et al (2015) A visual and organic vapor sensitive photonic crystal sensor consisting of polymer-infiltrated SiO_2 inverse opal. Phys Chem Chem Phys 17:9651–9658
53. Takeoka Y, Watanabe M (2003) Controlled multistructural color of a gel membrane. Langmuir 19:9554–9557
54. Pan Z, Ma JK, Yan J et al (2012) Response of inverse-opal hydrogels to alcohols. J Mater Chem 22:2018–2025
55. Fudouzi H, Xia YN (2003) Photonic papers and inks: color writing with colorless materials. Adv Mater 15:892–896
56. Lee K, Asher SA (2000) Photonic crystal chemical sensors: pH and ionic strength. J Am Chem Soc 122:9534–9537
57. Holtz JH, Asher SA (1997) Polymerized colloidal crystal hydrogel films as intelligent chemical sensing materials. Nature 389:829–832
58. Lim HS, Lee J, Walish JJ et al (2012) Dynamic swelling of tunable full-color block copolymer photonic gels via counterion exchange. ACS Nano 6:8933–8939
59. Xu XL, Goponenko AV, Asher SA (2008) Polymerized polyhema photonic crystals: pH and ethanol sensor materials. J Am Chem Soc 130:3113–3119

60. Cui QZ, Wang W, Gu BH et al (2012) A combined physical–chemical polymerization process for fabrication of nanoparticle—hydrogel sensing materials. Macromolecules 45:8382–8386
61. Zhang ML, Feng J, Zheng ML et al (2014) Inverse opal hydrogel sensor for the detection of pH and mercury ions. RSC Adv 4:20567–20572
62. Lee YJ, Braun PV (2003) Tunable inverse opal hydrogel pH sensors. Adv Mater 15:563–566
63. Xue F, Meng ZH, Qi FL et al (2014) Two-dimensional inverse opal hydrogel for pH sensing. Analyst 139:6192–6196
64. Xia HW, Zhao JP, Meng C et al (2011) Amphoteric polymeric photonic crystal with U-shaped pH response developed by intercalation polymerization. Soft Matter 7:4156–4159
65. Shin J, Braun PV, Lee W (2010) Fast response photonic crystal pH sensor based on templated photo-polymerized hydrogel inverse opal. Sens Actuators B Chem 150:183–190
66. Yetisen AK, Butt H, Vasconcellos F et al (2014) Light-directed writing of chemically tunable narrow-band holographic sensors. Adv Optical Mater 2:250–254
67. Jiang HL, Zhu YH, Chen C et al (2012) Photonic crystal pH and metal cation sensors based on poly(vinyl alcohol) hydrogel. New J Chem 36:1051–1056
68. Griffete N, Frederich H, Maitre A et al (2011) Photonic crystal pH sensor containing a planar defect for fast and enhanced response. J Mater Chem 21:13052–13055
69. Li C, Lotsch BV (2012) Stimuli-responsive 2D polyelectrolyte photonic crystals for optically encoded pH sensing. Chem Commun 48:6169–6171
70. Fenzl C, Wilhelm S, Hirsch T et al (2013) Optical sensing of the ionic strength using photonic crystals in a hydrogel matrix. ACS Appl Mater Interfaces 5:173–178
71. Arsenault AC, Puzzo DP, Manners I et al (2007) Photonic-crystal full-colour displays. Nat Photonics 1:468–472
72. Puzzo DP, Arsenault AC, Manners I et al (2009) Electroactive inverse opal: a single material for all colors. Angew Chem Int Ed 48:943–947
73. Shim TS, Kim SH, Sim JY et al (2010) Dynamic modulation of photonic bandgaps in crystalline colloidal arrays under electric field. Adv Mater 22:4494–4498
74. Walish JJ, Kang YJ, Mickiewicz RA et al (2009) Bioinspired electrochemically tunable block copolymer full color pixels. Adv Mater 21:3078–3081
75. Lu YJ, Xia HW, Zhang GZ et al (2009) Electrically tunable block copolymer photonic crystals with a full color display. J Mater Chem 19:5952–5955
76. Bibette J (1993) Monodisperse ferrofluid emulsions. J Magn Magn Mater 122:37–41
77. Xu XL, Friedman G, Humfeld KD et al (2001) Superparamagnetic photonic crystals. Adv Mater 13:1681–1684
78. Kim H, Ge JP, Kim J et al (2009) Structural colour printing using a magnetically tunable and lithographically fixable photonic crystal. Nat Photonics 3:534–540
79. Hu HB, Chen QW, Tang J et al (2012) Photonic anti-counterfeiting using structural colors derived from magneticresponsive photonic crystals with double photonic bandgap heterostructures. J Mater Chem 22:11048–11053
80. Ge JP, He L, Goebl J et al (2009) Assembly of magnetically tunable photonic crystals in nonpolar solvents. J Am Chem Soc 131:3484–3486
81. Ge JP, Hu YX, Zhang TR et al (2008) Self-assembly and field-responsive optical diffractions of superparamagnetic colloids. Langmuir 24:3671–3680
82. Kim J, Song Y, He L et al (2011) Real-time optofluidic synthesis of magnetochromatic microspheres for reversible structural color patterning. Small 7:1163–1168
83. Kamenjicki M, Lednev IK, Mikhonin A et al (2003) Photochemically controlled photonic crystals. Adv Funct Mater 13:774–780
84. Gu ZZ, Hayami S, Meng QB et al (2000) Control of photonic band structure by molecular aggregates. J Am Chem Soc 122:10730–10731
85. Kamenjicki M, Lednev IK, Asher SA (2004) Photoresponsive azobenzene photonic crystals. J Phys Chem B 108:12637–12639
86. Gu ZZ, Iyoda T, Fujishima A et al (2001) Photo-reversible regulation of optical stop bands. Adv Mater 13:1295–1298

87. Holtz JH, Holtz JS, Munro CH et al (1998) Intelligent polymerized crystalline colloidal arrays: novel chemical sensor materials. Anal Chem 70:780–791
88. Nakayama D, Takeoka Y, Watanabe M et al (2003) Simple and precise preparation of a porous gel for a colorimetric glucose sensor by a templating technique. Angew Chem Int Ed 42:4197–4200
89. Zhao YJ, Zhao XW, Tang BC et al (2010) Quantum-dot-tagged bioresponsive hydrogel suspension array for multiplex label-free dna detection. Adv Funct Mater 20:976–982
90. Zhang JT, Chao X, Liu XY et al (2013) Two-dimensional array Debye ring diffraction protein recognition sensing. Chem Commun 49:6337–6339
91. Liu M, Yu LP (2013) A novel platform for sensing an amino acid by integrating hydrogel photonic crystals with ternary complexes. Analyst 138:3376–3379
92. Liu Y, Zhang YJ, Guan Y (2009) New polymerized crystalline colloidal array for glucose sensing. Chem Commun 1:1867–1869
93. Kabilan S, Blyth J, Lee MC et al (2004) Glucose-sensitive holographic sensors. J Mol Recognit 17:162–166
94. Hong XD, Peng Y, Bai JL et al (2013) A novel opal closest-packing photonic crystal for naked-eye glucose detection. Small 10:1308–1313
95. Yang ZK, Shi DJ, Chen MQ et al (2015) Free-standing molecularly imprinted photonic hydrogels based on b-cyclodextrin for the visual detection of L-tryptophan. Anal Methods 7:8352–8359
96. MacConaghy KI, Chadly DM, Stoykovich MP et al (2015) Label-free detection of missense mutations and methylation differences in the p53 gene using optically diffracting hydrogels. Analyst 140:6354–6362

Chapter 6
Responsive Polymer Nanostructures

Yajnaseni Biswas, Somdeb Jana, Madhab Dule and Tarun K. Mandal

Abstract Here in this review, we describe recent advances and challenges toward the design and development of stimuli-responsive polymeric materials that are self-assembled to from nanostructured building blocks. A short introduction describing non-materials in general along with the different synthetic methodologies for making polymeric materials that are responsive toward several physical, chemical, or biochemical stimuli such as temperature, light, pH, redox reaction, ionic strength, glucose, CO_2, enzyme. A general discussion on the cause of thermoresponsivenes in polymers having either lower critical solution temperature (LCST) or upper critical solution temperature (USCT) transition is described. This followed by the detailed description of the nanostructured polymer materials, which are responsive to temperature. pH-responsive polymers are important materials in terms of their diverse range of applications, such as drug delivery, diagnostics. Thus, we describe the details of synthesis of different polymer and copolymer systems and their pH-responsive assembly into several types of nanostructures such as micelles, vesicles followed by their pH-triggered disassembly in aqueous solution. The polymeric nanomaterials responsive to light in particular has attracted much attention since light can be localized in time and space and can be applied from outside of the system. Therefore, it is indeed important to discuss the nanostructured polymer materials that are responsive to light followed by their potential applications. Polymeric nanomaterials that are responsive to other different stimuli such as redox reaction, CO_2, sugar are also described in this review. Finally, we also describe different multi-stimuli-responsive nanostructured polymer systems. The main goal of this chapter is to serve as a guideline to inspire future researchers toward the design and synthesis of stimuli-responsive materials so that novel applications and new generations of smart materials can be realized.

---

[*]These authors contributed equally to this chapter.

Y. Biswas[*] · S. Jana[*] · M. Dule · T.K. Mandal (✉)
Polymer Science Unit, Indian Association for the Cultivation of Science,
Jadavpur, Kolkata 700032, India
e-mail: psutkm@iacs.res.in

6.1 Introduction

Nanostructures are defined as having at least one dimension is in the size range of 1–100 nm. A great number of articles, reviews, and books about polymer nanostructures and their applications are available in the literature. Polymer nanostructures of different morphology (micelle, vesicle, cylindrical, worm-like micelle etc.) have been received great interest due to their wide range of potential applications such as encapsulates for drug [1], gene [2], enzyme [1], protein [3], catalyst [4] as dielectrics for electronics [5], as absorbent materials for sound and microwave [6], as nanocarrier for fabrication of nanodevices [7], and as label free chip sensor [8]. Among them, stimuli-responsive polymer nanostructures have attracted growing interest for their potential use in medicine, especially as drug delivery system and potential platform to mimic organelles as biological nanoreactors [9–11].

Over the past 25 years, responsive polymer-based nanostructured soft materials such as micelles, vesicles, polymersomes have gained increasing attention to the polymer research community because of the broad opportunities of these systems in vivo applications [12–16]. Responsive polymer nanostructured materials (Fig. 6.1) can also refer to as "environmentally sensitive" [17], "smart" [18], or "intelligent" [19] polymer materials that undergoes conformational and chemical
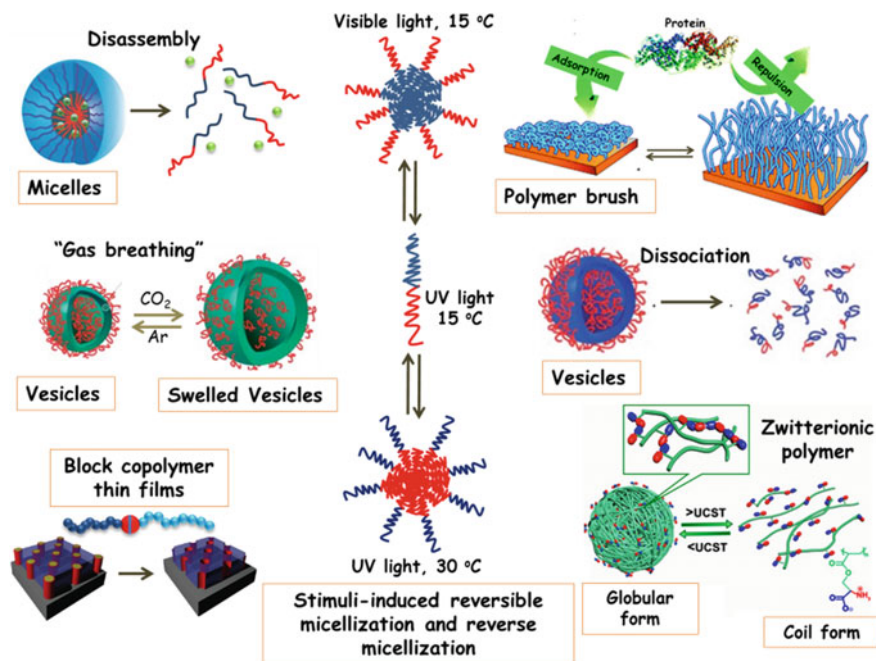
Fig. 6.1 Schematic representation of different types of stimuli-responsive polymer nanostructured materials

changes on receiving an external signal [20] and made this class of materials very promising in the field of nanotechnology, nanoscience, and nanomedicine [21]. Mother Nature exhibits plentiful instances of responsive materials. Examples of such systems include sea cucumbers that change their stiffness by several orders of magnitude in the face of danger; the leaves of *Mimosa Pudica* collapse immediately upon touching; chameleons change their skin color according to their environment. The responsive materials present in these living systems are either biomacro-molecules or biopolymers. Thus, researchers paid more attention toward the design and synthesis of responsive polymer materials to mimic the functions of several macromolecular organisms in living systems.

These responsive materials are generally derived from polymers and are proven its robustness in wide range of applications such as responsive biointerfaces that are mimic to natural surfaces [22], controlled delivery of drugs and its release to the desired site [23–25], tissue engineering [26, 27], "smart" optical systems [28], biosensors [29, 30], coatings [31, 32]. Responsive polymers mainly contain reactive functionalities that can show sharp responses to changes in external stimuli. Upon small changes in the environmental conditions, these materials can significantly change their properties such as shape, mechanical properties, phase separation, surface, permeability, optical properties, electrical, and chemical properties [33]. It is also known that different functional groups respond to different stimuli. The most common and frequently utilized stimuli are temperature [20, 34, 35], pH [36, 37], light [38–40], redox reaction [41], ionic strength [42] glucose [43], and carbon dioxide (CO_2) [44]. The pH, ionic strength, redox reactions can be categorized as chemical stimuli and temperature; light is indeed very important and promising physical stimuli in the responsive systems. However, biochemical stimuli can also be considered as another important category of stimuli that involve responses to enzymes, antigens, and other biochemical agents [20].

A detailed survey of the literature clearly tells that the number of scientific con-tributions to synthetic polymers with stimuli-responsive properties is increased epi-demically in the last few decades [45, 46]. This is mainly ascribable to the fact that several new methods for the polymerization of various functional monomers are developed in last two decades. In this context, various controlled radical polymer-ization techniques such as the atom transfer radical polymerization (ATRP) [47], the reversible addition-fragmentation chain transfer (RAFT) [48], nitroxide-mediated polymerization (NMP) [49], ring-opening polymerization (ROP) [50], techniques have been used intensively to synthesize different stimuli-responsive polymers. Indeed, these polymerization methods show a high tolerance toward functional monomeric groups while providing the benefit to result in polymers and block copolymers with a narrow molecular weight distribution and well-defined end-groups. In addition, another new synthetic approach in polymer chemistry namely post-polymerization modifications [51] of polymeric precursors via "click" chemistry [52] is also found to be a very highly appealing tool to introduce responsive functional moieties into the polymer backbone. Thus, different stimuli-responsive polymeric materials with a variety of functionalities can be designed and prepared easily by using the above-mentioned polymerization techniques.

Smart macromolecular nanostructures are designated by their stimuli-responsive behavior, which is basically controlled by the presence of functional moieties within or on a polymer chain. Different functionalities respond to different stimuli and a broad library of such functionalities has been studied. Recently, synthetic smart polymeric materials may also respond to more than one or two stimuli [53, 54]. These materials are generally known as dual or multistimuli-responsive polymer systems and can be prepared by the successive introduction of different stimuli-responsive functional groups into one polymer chain. It is worth noting that these materials attracted significant and increasing attention toward academia as well as in industry because of not only their tunable physical and chemical properties but also their emerging potentiality toward biological application such as controlled release of drugs, tissue engineering, and responsive coatings.

This chapter is intended to present the recent developments as well as fabrication strategies of stimulus active polymer-based soft nanomaterials that are sensitive to heat, pH, redox, light, glucose, CO_2 etc. This chapter also deals with various methods and recent advancement toward dual as well as multistimuli-responsive polymers, bearing more than one or two responsive functional groups in one polymer chain. The breadth/target of this chapter is to demonstrate the current possibilities and chances as well as challenges toward the development of new generation of "smart" nanomaterials by comprehensively summarizing related interesting examples in this field, which have been published recently. Finally, wide applications and future perspective of these "smart" materials are summarized. We expect that this chapter will not only help the interdisciplinary readers to understand the recent stage of this area but also shed some light on future research directions in this important field.

6.2 Thermoresponsive Polymer Nanostructures

Thermoresponsive polymers are a class of "smart" materials that have the ability to respond to a change in temperature. Among all the studied responsive systems, thermoresponsive polymers are widely investigated because temperature stimulus can easily be tuned from outside, and it is easy to monitor the change in different properties, especially the change of solution properties and the adopted nanostructures morphologies (e.g., micelles, vesicles) of polymers with temperature. Thermoresponsive behaviors of polymers and biopolymers can be induced in a variety of settings, including in vivo [20, 35, 55], and potential benefits have been envisioned for a range of biologically relevant applications, including controlled drug delivery [56–58], bioseparations, [59, 60], filtration [61–63], making smart surfaces [64–66], and regulating enzyme activity [67].

Temperature-responsive polymers exhibit a volume phase transition at a certain temperature, which causes a sudden change in the solvation state. Polymers, which become insoluble upon heating, have a so-called LCST (Lower Critical Solution Temperature)-type transition and which become soluble upon heating have an

UCST (upper critical solution temperature)-type transition. Polymers exhibiting LCST-type behavior were soluble in solution due to extensive hydrogen bonding interactions with the surrounding solvent molecules (such as water) and restricted intra- and inter-molecular hydrogen bonding between polymer chains. At LCST, upon heating, hydrogen bonding with solvent molecule is disrupted, and intra- and inter-molecular hydrogen bonding/hydrophobic interactions dominate, which results in the polymer to phase-separate from solution due to a molecular transition from a coiled, enthalpically favored structure to a dense globular, entropically favored structure (Fig. 6.2) [68]. This process will minimize the free energy of the system considerably.

Following this principle, the solution macroscopically starts to become turbid due to the phase separation of the polymer while heating [69]. Among different LCST non-ionic polymers, poly(N-isopropylacrylamide) (PNIPAAm) is indeed one of the most investigated LCST polymers in aqueous solution, as the phase transition temperature, which is also known as cloud point temperature of PNIPAAm (32 °C) is close to physiological temperature [35]. Other important classes of synthetic thermoresponsive non-ionic polymers featuring a LCST in aqueous solution includes poly(acrylamides), poly(vinyl methyl ether) (PVME) [70–73], polyoxazolines [26, 74, 75], as well as poly(oligoethylenenoxide)methacrylates [76–79]. Polymers with different cloud points have been summarized in Table 6.1. The LCST is further dependent on different parameters such as polymer chain length [80, 81] tacticity [82], and incorporation of comonomers [83], pressure [84], or even the chemical nature of the end group [85, 86].

Compared with polymers having LCST in aqueous media, polymers with UCST are relatively uncommon. A polymeric system comprising of poly(acrylic acid) (PAA)/poly(acrylamide) (PAm) is well-studied showing UCST-type of transition in
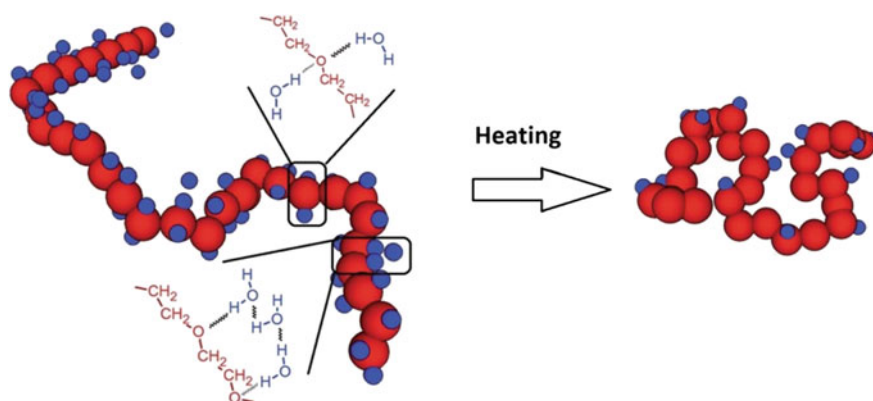
Fig. 6.2 Schematic representation of the conformational change of poly(ethylene oxide) (PEO) from a hydrated coil to a dehydrated collapsed globule at LCST. *Red balls* correspond to ethylene oxide units and *blue balls* to water molecules (reproduced from Ref. [68] with kind permission of © 2013 Royal Society of Chemistry) (color figure online)

Table 6.1 The chemical structures and transition temperatures of various temperature-responsive polymers in water

Thermoresponsivepolymers	Cloud point temperature (°C)	LCST/UCST	References
Poly(N-isopropylacrylamide) (PNIPAAm)	32	LCST	[35]
Poly(N-n-propylacrylamide) (PNNPAAm)	10	LCST	[108]
Poly(N-cyclopropylacrylamide) (PNCPAAm)	53	LCST	[109]
Poly(N,N-diethylacrylamide) (PDEAAm)	33	LCST	[110]
Poly(N-(N-isobutylcarbamido)propyl methacrylamide) (PiBuCPMAAm)	13	LCST	[111]
Poly(N-(N-ethylcarbamido)propyl methacrylamide)	49.5–56.5	LCST	[111]
Poly(N-(1-hydroxymethyl) propylmethacrylamide) (PHMPMAAm)	30 (L-isomer) 34 (DL-mixture)	LCST	[112–114]
Poly[N-(2,2-dimethyl-1,3-dioxolane)methyl] acrylamide (PDMDOMAAm)	23	LCST	[115]
Poly([N-(2,2-dimethyl-1,3-dioxolane)methyl] acrylamide-co-[N-(2,3-dihydroxyl-n-propyl)] acrylamide)	23–49	LCST	[115]
Poly(N-(2-methoxy-1,3-dioxan-5-yl) methacrylamide) (PNMMAm)	22	LCST	[116]
Poly(N-(2-ethoxy-1,3-dioxan-5-yl) methacrylamide)	52	LCST	[116]
Poly(N-(2,2-di-methyl-1,3-dioxan-5-yl) methacrylamide) (PNDMMAm)	15.3	LCST	[117]
Poly(N-(2,2-di-methyl-1,3-dioxan-5-yl) acrylamide)	17.8	LCST	[117]
Poly(N-vinylisobutyramide) (PNVIBAm)	39	LCST	[118]
Poly(ethylene oxide) (PEO) Poly(ethylene glycol) (PEG)	85	LCST	[56]
Poly(propylene oxide) (PPO) Poly(propylene glycol) (PPG)	0–50	LCST	[119]
Poly(2-(2-methoxyethoxy)ethyl methacrylate) (PMEO₂MA)	26	LCST	[120]
Poly(oligo(ethylene glycol) methacrylate (POEGMA)	60–90	LCST	[77, 121]
Poly(2-ethyl-2-oxazoline) (PEtOx)	62–65	LCST	[122]
Poly(2-isopropyl-2-oxazoline) (PiPOx)	36	LCST	[123, 124]
Poly(2-n-propyl-2-oxazoline) (PnPOx)	36	LCST	[125]
Poly([oligo(2-ethyl-2-oxazoline) methacrylate]-co-(methyl methacrylate))	35–80	LCST	[126]
Poly(N-vinylcaprolactam) (PVCL)	32	LCST	[127, 128]
Poly(N-vinylpyrrolidone) (PVPy)	30 (1.5 M KF)	LCST	[129]
Poly[N-(2-methacryloyloxyethyl) pyrrolidone] (PNMP)	51.9	LCST	[130]

(continued)

Table 6.1 (continued)

Thermoresponsive polymers	Cloud point temperature (°C)	LCST/UCST	References
Poly(*N*-ethylpyrrolidine methacrylate) (PEPyM)	15	LCST	[131]
Poly(*N*-acryloylpyrrolidine) (PAPR)	51	LCST	[121]
Poly(dimethylaminoethyl methacrylate) (PDMAEMA)	14–50	LCST	[132, 133]
Poly(*N*-isopropylacrylamide)-b-poly[3-(*N*-(3-methacrylamidopropyl)-*N*,*N*-dimethyl) ammoniopropane sulfonate] (PNIPAAm-b-PSPP)	8.6–19	UCST	[134]
Poly(*N*-acryloylglycinamide) (PNAGA)	22–23	UCST	[88, 135, 136]
Poly(acrylonitrile-co-acrylamide) (P (An-co-AM))	6–60	UCST	[136]
Poly(methacrylamide) (PMAAm)	57	UCST	[136]
Poly(*N*-acryloylasparaginamide) (PNAAAM)	4–28	UCST	[137]

water [87]. Later on, non-ionic poly(*N*-acryloylglutamineamide) (PNAGA) was found to be exhibit UCST-type of transition [88] in water. There are also many other polymers such as poly(sulfobetaine)s [89, 90], poly(6-(acryloxyloxy-methyl) uracil) [91], and ureido-derivatized polymers [92] that exhibits UCST-type transition. These polymers usually have a pair of interactive sites that cause the polymers to be insoluble at lower temperature due to intra-molecular and inter-molecular interactions(such as hydrogen bonding and electrostatic attraction) among polymer chains, which can be disrupted at higher temperature due to intensified molecular motion within the polymer chains, resulting in a hydrated polymer [93]. Since we are concerned here about the polymer nanostructures driven by external stimuli, we mainly focused here the self-assembly of amphiphilic block copolymers into various nanostructures, ranging from spheres, worms, to vesicles, and structures kinetically trapped as intermediate morphologies in solution.

"Living" radical polymerization (LRP) allows a wide variety of amphiphilic block copolymers to be synthesized in bulk or solution with excellent control over the block lengths and chemical compositions [48, 94–96]. It has been demonstrated that the presence of a thermoresponsive block in a di or tri block copolymers results in the rapid assembly into 3D structures upon heating a homogeneous polymer/water solution above its LCST [97, 98]. The assemblies form varieties of 3D nanostructures of different shapes and sizes depending upon the ratio of the hydrophilic to hydrophobic block lengths. These nanostructures are fully reversible in terms of morphology upon cooling [99, 100], unless crosslinked at temperatures above the LCST [98, 101–107]. For the sake of completeness, it should be mentioned that beside the solution state thermoresponsive phase behavior of polymers in solid-state film also exists as well that we are not going to review in this chapter.

For a better understanding of the reader, we purposefully divided the thermoresponsive polymer into non-ionic and ionic categories.

6.2.1 Non-ionic Polymer Nanostructures

6.2.1.1 LCST-Type Polymer Nanostructures

Poly(*N*-substituted (meth)acrylamide)-Based Nanostructures

Poly(*N*-isopropylacrylamide) (PNIPAAm) was the first polymer showing LCST in aqueous solution, which was an important member of poly(*N*-(meth)acrylamide) polymer family [138]. The homopolymers and copolymers of PNIPAAm have gained significant attention [19, 20, 35, 56, 139–144] due to the sharp phase transition (soluble one phase to turbid two phase) around 32 °C (near room and body temperatures). However, the incorporation of comonomers containing hydrophilic groups makes PNIPAAm—copolymers of easily tunable LCST near body temperature, which promotes them as prominent candidates in biomedical applications [35, 69]. Above LCST, the unperturbed coil PNIPAAm chains turn into partially dehydrated globules. In this collapsed state, the amide groups of PNIPAAm lead to the formation of intra-molecular and inter-molecular NH···O=C hydrogen bonding interactions [145]. Hence, during the cooling process, the rehydration of PNIPAAm is hindered by these additional interactions, leading to a broad hysteresis during the cooling process.

It is known that the amphiphilic copolymers, synthesized by controlled polymerization techniques, have enabled the formation of a variety of nanostructures due the self-assembly among the copolymer chains. Incorporation of a polymer block into amphiphilic block copolymer that has stimuli-dependent miscibility and immiscibility in a given solvent provides a powerful method for reversibly changing the size and structure of the resulting assemblies. For example, thermomorphic PNIPAAm, which exhibit a LCST in water below which chains are miscible and above which chains are immiscible. This property has been utilized by many researchers to prepare thermoresponsive polymer nanostructures. For example, Convertine et al. have reported a series of thermally responsive di(AB)- and tri(ABA) block copolymers containing hydrophilic poly(*N*,*N*-dimethylacrylamide) (PDMAM) block of constant lengths and PNIPAAm blocks of variable lengths using room temperature RAFT polymerization to systematically study the temperature-dependent micellization behavior of these systems [146]. They demonstrate that these block copolymers are indeed capable of reversibly forming micelles in response to changes in solution temperature, and the micellar size and transition temperature are dependent on both the PNIPAAm block length and the polymer architecture (diblock vs triblock). In this context, it should be mentioned that not only amphiphilic block copolymers but also some double-hydrophilic block copolymers (DHBC)s having a thermoresponsive block (undergoes a transition

from soluble to insoluble in water) shows various aggregated nanostructures [147]. Typically, most reports on such systems exploit the wide-spread occurrence of a LCST of non-ionic polymers in water. However, for DHBCs above the critical temperature, one of the hydrophilic blocks collapses, generating hydrophobic microdomain, which eventually aggregated into micro/nanostructure of various morphologies. Such aggregated micro/nanostructures are reversibly dissociated into unperturbed chain structure by lowering the temperature below a critical value. This strategy can be used to trigger the release of encapsulated materials, e.g., for controlled drug delivery [148].

A number of research groups have enhanced these pioneering examples of polymer systems that undergo stimulus-driven transitions between assemblies with well-defined structures. Grubbs and coworkers have been designed several ABC-type triblock copolymers that respond to a stimulus by transforming from one stable assembled form to another [100]. The triblock copolymer, PEO-*b*-PNIPAAm-*b*-poly(isoprene), comprised of hydrophilic end block, a thermally responsive central block, and a hydrophobic end block have been synthesized using the sequential nitroxide-mediated polymerization. They are designed to be largely hydrophilic at room temperature and largely hydrophobic above the LCST of PNIPAAm, thus forming small assemblies (spherical micelles) with a highly curved assembly-water interface at lower temperatures and larger assemblies (vesicles) with a less-curved interface at higher temperatures (Fig. 6.3) [100]. They have shown by transmission electron microscope (TEM) and dynamic light scattering (DLS) analysis the formation of large spherical micelles ($D \sim 9$ nm) at room temperature and formation of large vesicular assemblies with a mean radius greater than 100 nm after heating at 65 °C for 4 weeks.
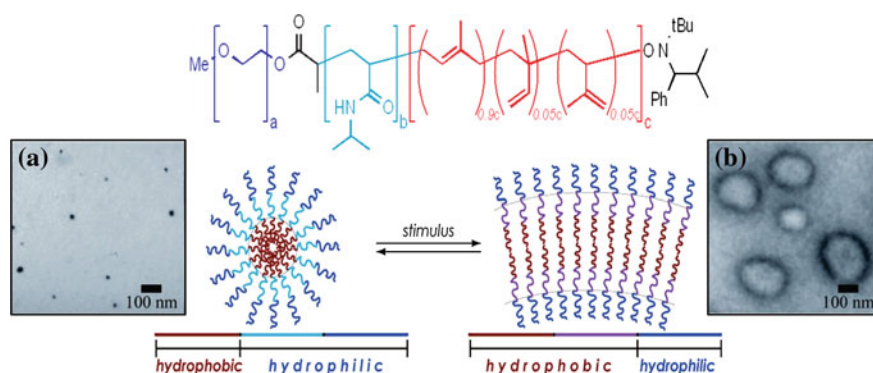
Fig. 6.3 Schematic illustration of the expected change in amphiphilic balance for ABC triblock copolymer chain with a stimulus-responsive B block and interfacial curvature for assemblies of these triblock copolymers in water upon passage through the LCST of the B block. TEM images of copolymer **a** as drop-cast from aqueous solution at room temperature (OsO₄ stain) and **b** as drop-cast from aqueous solution heated at 65 °C for 4 weeks (OsO₄ stain) (reproduced from Ref. [100] with kind permission of © 2008 American Chemical Society)

A number of other examples of polymers that exhibit similar behavior, which are discussed in more detail below, have also been recently described in the literature. Zhou et al. [149] reported a triblock copolymer, poly(ethylene propylene)-*b*-poly (ethylene oxide)-*b*-PNIPAAm, in which the hydrophilic block occupies the central position and the responsive block a terminal position (PEP_{45}-*b*-PEO_{565}-*b*-$PNIPAAm_z$, where $z = 33, 83, 187$), which assemble to form micelles having a PEP core with PEO and PNIPAAm blocks in the corona at room temperature in water. However, above the LCST of PNIPAAm, the outermost part of the corona became much less hydrophilic and the micelles are reorganizing, but under the experimental condition, it appears to be more favorable for micelles to aggregate through association of PNIPAM domains than to reorganize into other micellar forms. Further, Qiao et al. [150] synthesized a thermalresponsive fluorescent block copolymer comprised of temperature-responsive PNIPAAm unit, hydrophilic poly(maleic anhydride) (PMAn) unit, and fluorescent7-amino-4-methylcoumarin (AMC) groups by RAFT polymerization method. According to them, with increasing temperature, PNIPAAm chains become collapsed making the block copolymer more hydrophobic above the LCST resulting in larger aggregates. Thus, a part of the fluorescent groups would be embedded inside the enlarged block copolymer micelles, resulting in lower fluorescence intensity (Fig. 6.4).

However, PNIPAAm possesses some inherent drawbacks, such as controversial biocompatibility, phase transition hysteresis, and a significant end group influence on phase transition behavior [151, 152]. Other members of this family that have also been investigated as thermoresponsive polymers are poly(*N-n*-propylacrylamide) (PNnPAAm) and poly(*N*-cyclopropylacrylamide) (PNCPAAm) having phase
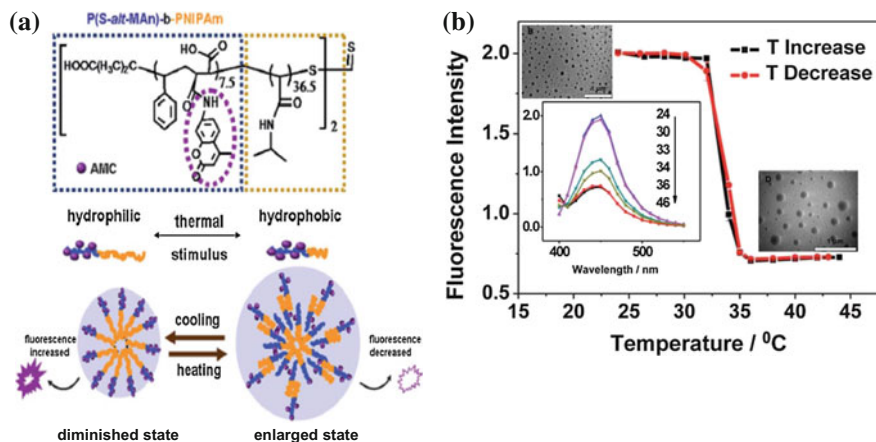
Fig. 6.4 **a** Schematic representation of fluorescence responses to temperature due to change in morphology of the block copolymer. **b** Fluorescence intensity versus temperature diagram of block copolymer in aqueous solution and the *inset* shows the TEM micrographs of micelles, at 24 °C; and at 44 °C respectively (reproduced from Ref. [150] with kind permission of © 2012 Royal Society of Chemistry)

transition behaviors significantly different from PNIPAAm, with LCST-type transition temperatures of 10 and 53 °C, respectively [108, 109, 153]. However, LCST transition of poly(N,N-diethylacrylamide) (PDEAAm) has been reported (~ 33 °C) near to that of PNIPAAm [110], though this value has been demonstrated to be tacticity-dependent [154]. In addition to the study of responsive behavior, several groups have reported applications of PDEAM that exploit its temperature-dependent solubility. For example, a well-defined amphiphilic poly-isobutylene-b-poly(N,N-diethylacrylamide) (PIB-b-PDEAAm) diblock copolymers of varying compositions were synthesized by sequential living carbocationic and RAFT polymerization techniques, which self-assembled into large compound micelles in aqueous media. These compound micelles responded sharply to temperature as examined by UV–Vis and DLS studies. Above LCST, the transmittance decreased remarkably while hydrodynamic diameter (D_h) increased acutely. LCSTs of PIB-b-PDEAAm diblock copolymers were in the range of 29.0–31.8 °C which rose with elongating the length of hydrophilic PDEAAm segment [155]. Angelopoulos et al. have been synthesized a triblock copolymer PDEAAm-b-poly (acrylic acid)-b-PDEAAm (PDEAAm-b-PAA-b-PDEAAm) by sequential anionic polymerization led to reversible gelators. At high pH and temperatures above the cloud point of PDEAAm end block, a sol–gel transition of PDEAAm-b-PAA-b-PDEAAm was observed due to the formation of a three-dimensional transient network comprised of a PDEAAm hydrophobic physical crosslink interconnected by negatively charged PAA chains [156].

Further, Lowe and coworkers have reported numerous examples of PDEAM-based thermoresponsive systems [157, 158]. Recently, a series of new thermoresponsive polymers based on poly(N-(N'-alkylcarbamido)propyl methacrylamide) analogs have also been reported [111]. For instance, poly(N-(N'-isobutylcarbamido)propyl methacrylamide) exhibited a LCST phase transition at 13 °C, whereas the transition temperature of poly(N-(N'-ethylcarbamido)propyl methacrylamide) was reported to be 49.5–56.5 °C. These polymers have demonstrated potential in temperature-dependent chromatographic separations of peptides and proteins from aqueous mobile phases [111] L- and DL-forms of poly(N-(1-hydroxymethyl)propylmethacrylamide) (PHMPMAAm) have also been reported to be temperature-responsive [112–114, 159]. Several other novel thermoresponsive poly(N-alkylacrylamide)s have also been studied, including poly[N-(2,2-dimethyl-1,3-dioxolane)-methyl] acrylamide (PDMDOMAAm) (Table 6.1) [115], which exhibited a cloud point around 23 °C in water. Interestingly, this transition temperature can be easily tuned within the temperature ranges of 23–49 °C by the controlled degree of cleavage of the pendant dioxalane groups to form hydrophilic diol monomer units (Table 6.1). More recently, the same group tried to control precisely the LCST of poly(N-alkylacrylamide)s-based homopolymers and block copolymers by using controlled radical polymerization techniques such as RAFT or ATRP which allow one to obtain nearly the same structure sequence and length for each chain in the polymer sample [146, 160]. For instance, a detailed study on poly(N-alkylacrylamide)s family by tuning the N-alkyl substitution group has been conducted by Cao et al. [160]. They showed that the bulkier the N-alkyl

substituent, the lower was the LCST, which can be understood by the enhancement of hydrophobic interactions between the polymer chains.

Poly(alkylene oxide)-Based Nanostructures

Poly(ethylene oxide) (PEO) is the most famous and widely studied members in poly (alkylene oxide) family, which is also known as poly(ethylene glycol) (PEG) for those of small molecular weights (below 10,000 Da). PEO is the simplest water soluble polymer. Its chemical structure $(CH_2CH_2O)_n$ contains the right balance between hydrophobic and hydrophilic moieties, which allows PEO chains to be soluble in water in awide range of temperature and concentration. The LCST of PEO is above 100 °C for low molecular weight chains, e.g., LCST of 2000 Da PEO being 170–180 °C; it decreases to 100 °C with the molecular weight of $M_n = 106$ Da [161]. Another important member of this family is poly(propylene oxide) (PPO) [or poly(propylene glycol) (PPG)] which is also a well-known for its thermoresponsive behavior [56, 162]. In fact, a variety of copolymers consisting of different PEG and PPO compositions are commercially available under the names Pluronics, Poloxamers, and Tetronics [163]. Thermoresponsive polymers with significant PEG content have gained attention particularly from a biomedical perspective, because of their low toxicity/immunogenicity and high biocompatibility.

A wide varieties of shell-crosslinked (SCL) micelles have been reported from various PEG and PPO-based block copolymers [164, 165]. Shell-crosslinked (SCL) micelles with hydroxy-functional coronas have also been constructed in aqueous solution by exploiting the micellar self-assembly behavior of a new thermoresponsive ABC-type triblock copolymer, PPO-*b*-poly(dimethyl amino ethyl methacrylate)-*b*-poly(glycerol monomethacrylate)(PPO-*b*-PDMAEMA-*b*-PGMA), prepared via ATRP. The PDMAEMA block was crosslinked using 1,2-bis (2-iodoethoxy)-ethane. To create the SCL micelles, the solutions were heated to above the thermal transition of PPO, followed by the crosslinking of the PDMAEMA block. The size of the resulting SCL micelles could be controlled by changing the temperatures at which crosslinking occurs [165]. Further, Li et al. [164] demonstrated the formation of SCL micelle fromPEG-*b*-poly[(*N,N*-dimethylacrylamide)-*stat*-(*N*-acryloxysuccinimide)]-*b*-PNIPAAm, [PEG-*b*-P(DMA-*stat*-NAS)-*b*-PNIPAM], where the NAS block was crosslinked using cystamine. They showed by DLS that the SCL micelles increased in size upon cooling due to the swelling of the PEG core (Fig. 6.5).

Furthermore, thermoresponsive polymer nanoshells were generated by shell-crosslinking of poly(ethylene oxide)-poly(propylene oxide)-poly(ethylene oxide) (PEO-PPO-PEO) dimethacrylate triblocks [166]. The PPO blocks aggregated, upon heating to 50 °C, leaving a methacrylate-functionalized PEG corona. Once cooled, the crosslinked triblock copolymers expanded to create a solvated nanoshell. Rank et al. have studied the formation of polymersomes made up of poly (2-vinylpyridine)-*b*-poly(ethylene oxide) (P2VP-*b*-PEO) block copolymer [167]. They reported that vesicles with a bilayer membrane of P2VP-*b*-PEO were formed
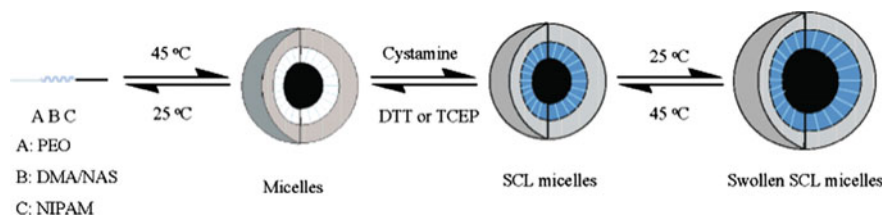
Fig. 6.5 Schematic illustration of the formation of reversible shell-crosslinked (SCL) micelles from triblock copolymers (reproduced from Ref. [164] with kind permission of © 2006 American Chemical Society)

spontaneously in aqueous solutions by polymer film hydration. Interestingly, the authors reported a cylinder to vesicle shape transition when the vesicles were subjected to a specific cooling/warming process. Upon cooling the vesicles to 4 °C, there was a transition from the vesicular structure to basket-like aggregates, which further disintegrate into worm-like micelles (Fig. 6.6). Warming back the suspension to 25 °C results in the recovery of unilamellar and almost monodisperse vesicles via intermediate discoid- and octopus-like structures. The reason for this thermoresponsive behavior lies in the temperature-dependent solubility of the PEO block. Upon warming, the solubility of PEO in water decreases and consequently the volume of the water-swollen PEO layer decreases. This reduces the interfacial area at the hydrophilic–hydrophobic interface.

In a pioneering work of Grubbs et al., an amphiphilic ABC triblock poly (ethylene oxide)-*b*-poly(ethylene oxide-*stat*-butylene oxide)-*b*-poly(isoprene) (E-BE-I) copolymers of varying compositions with narrow molecular weight distributions have been synthesized by the combination of sequential living anionic and controlled nitroxide-mediated radical polymerizations [168]. These block copolymers self-assembled into spherical micelles at room temperature which transformed to vesicles (polymersomes) at elevated temperatures as detected by them via DLS and TEM studies, for both with and without crosslinking of polymer assemblies (Fig. 6.7). The rate of transformation with E-BE-I systems is more rapid than that observed for poly(ethylene oxide)-*b*-poly(isoprene) assemblies reported earlier by the same group, suggesting that inter-chain hydrogen bonding of responsive blocks after dehydration plays an important role in the kinetics of aggregate rearrangement [169]. These results demonstrate that incorporation of a thermoresponsive block into an amphiphilic block copolymer results in discrete hydrophobic/hydrophilic volume ratios above and below the LCST of the thermoresponsive block, thus allowing the polymer assembly to be switched between large and small aggregates as a function of temperature.

"Schizophrenic" thermoresponsive copolymers are a special class polymer designed as double thermoresponsive polymers. Typically, one block possesses a LCST while the other displays an UCST. It has been reported that poly(acrylamide-*co*-acrylonitrile) poly(AAm-*co*-AN) block copolymer is one of the rare examples of uncharged polymers showing a UCST-type single phase transition in water and
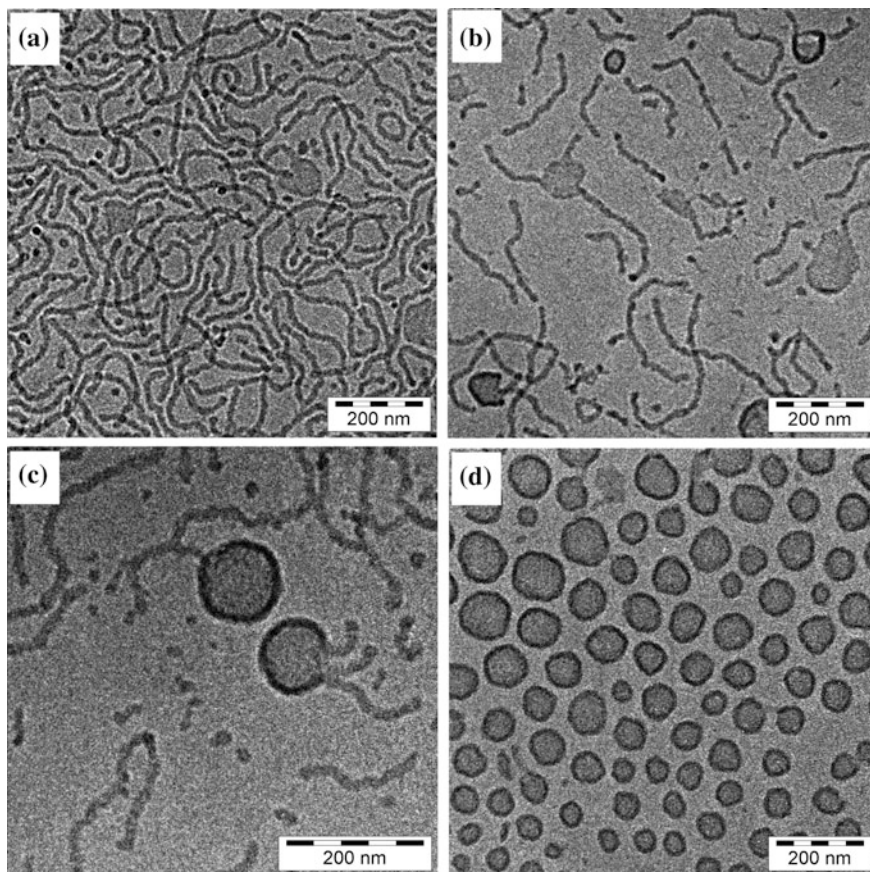
Fig. 6.6 Cyro-TEM of intermediate structures during warming up of P2VP$_{66}$-*b*-PEO$_{46}$ micelles **a** 1 h, **b** 2.5 h, or **c** 24 h after a temperature jump from 4 to 16 °C and **d** 1 h after a temperature jump from 16 to 25 °C (reproduced from Ref. [167] with kind permission of © 2009 American Chemical Society)

physiological medium, which was discussed later [136]. However, Agarwal et al. cleverly combined this poly(AAm-*co*-AN) block copolymer with PEG-based macro-azoinitiator to prepare a Schizophrenic" thermoresponsive copolymer using a simple conventional radical polymerization [170]. The copolymer showed dual thermoresponsivity of LCST- and UCST-type of transition in one system as investigated by turbidity and light scattering measurements in aqueous solution. The phase transition behavior and transition temperatures were found to depend on the PEG block length, polymer concentration, and ratio of AAm and AN mono-mers. The temperature-dependent change in the morphology from micelles to agglomerates and back to micelles was observed and correlating well with the phase transition behavior.
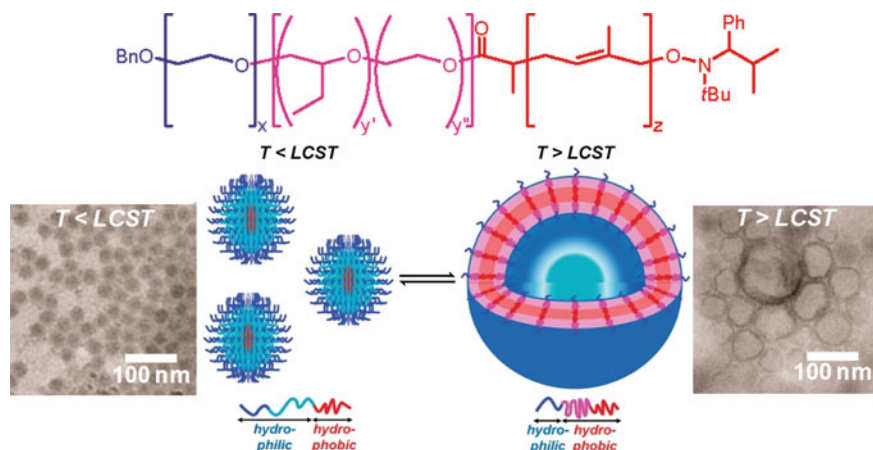
Fig. 6.7 Schematic illustration of the thermally induced size change of copolymer assemblies containing a thermoresponsive block. Below the LCST, the central block (*cyan*) is hydrophilic; above the LCST, the central block (*pink*) becomes hydrophobic (reproduced from Ref. [168] with kind permission of © 2010 American Chemical Society) (color figure online)
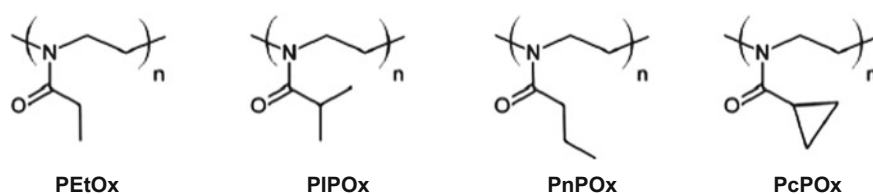
Fig. 6.8 Chemical structures of different poly(alkyl oxazoline)s

Poly(2-alklyl-2-oxazoline)- and Poly(2-oxazines)-Based Polymer Nanostructures

Poly(2-alkyl-2-oxazoline)s are another class of thermoresponsive polymers that are synthesized via living cationic ring-opening polymerization (CROP). Poly(alkyl oxazoline)s (PAOxs) (Fig. 6.8) are considered as pseudopolypepide and are being developed as alternatives to the famous water soluble thermosensitive polymers, PEG and PNIPAAm, for biological applications [80, 171]. The major disadvantage of PNIPAAm is the strong hysteresis during the thermal transition as discussed above, which makes PAOxs an interesting material for applications where the precipitation event is exploited [35]. In contrast, PAOxs show a LCST-type transition without hysteresis, which makes them more suitable for all applications (e.g., smart surfaces, thermoresponsive micelles) [80, 171]. Among the various PAOxs, poly(2-ethyl-2-oxazoline)(PEtOx) [122], poly(2-isopropyl-2-oxazoline) (PIPOx) [123, 124], and poly(2-n-propyl-2-oxazoline) (PnPOx) [125] are known to exhibit a thermal transitions in aqueous solution. PIPOx is another structural isomer of PNIPAM that exhibits a cloud point of approximately near 36 °C in aqueous

solution, and the transition can be tuned by the addition of sodium chloride or surfactant [123, 124]. In these reports, they have also compared the thermoresponsiveness of PIPOx with that of PNIPAAm [123] PEOx, an isomer of poly(*N,N*-dimethylacrylamide) (PDMAAm) [172], that showed a LCST-type phase behavior approximately at around 62–65 °C in aqueous solution [122] Schubert, Hoogenboom, and coworkers reported a series of PEtOx-based thermoresponsive comb- and graft-shaped polymers from poly[oligo(2-ethyl-2-oxazoline) methacrylate]s (POEtOxMA) [126]. First, they have synthesized well-defined OEtOxMA macromonomers via CROP and subsequently homopolymerized and copolymerized with methyl methacrylate using RAFT polymerization to make such comb and graft polymers. It was observed that the LCST behaviors of the aqueous solutions of these polymers was dependent on the copolymer composition and could be tuned by varying the PMMA block composition. Rueda et al. have developed a doubly thermoresponsive polymer system by grafting PEtOx from a modified PNIPAAm backbone [173].

As discussed above, there have been many reports of studies of thermoresponsive behaviors of PAOxs and its copolymers. However, there were only very few reports that dealt with the thermoresponsive nanostructures made up of PAOxs- and PAOxs-based copolymers. In early 2000, a novel series of temperature- and pH-sensitive hydrogels based on poly(2-ethyl-2-oxazoline) and three-arm poly(D,L-lactide) were reported by Wang et al. The gel polymeric networks were prepared via photocopolymerization of two types of macromonomers, namely poly (2-ethyl-2-oxazoline) dimethacrylate and three-arm poly(D,L-lactide) trimethacrylate. As analyzed through SEM, the porous hydrogel network was composed of interconnected nanosized gel particles resulting in a material of high water retention capacity and exhibited reversible swelling–shrinking behavior in response to temperature and pH variations. According to them, these PEtOx-containing hydrogels are biodegradable and can be used as a potential thermoresponsive biomaterial [174].

In another study, Halacheva et al. have prepared a series well-defined, sparsely grafted, comb-like linear poly(ethylene imine)/poly(2-ethyl-2-oxazoline) (LPEI-*comb*-PEtOx) polymers with various degrees of polymerization [175]. Their aqueous solution properties were investigated by means of dynamic light scattering (DLS) and small-angle neutron scattering (SANS) over a temperature range of 25–65 °C. It has shown that the LPEI-*comb*-PEtOx polymer formed particles with typically bimodal distributions and featured smoother temperature variations in aqueous solution. They have also studied the shape and structure evolution of the small LPEI-*comb*-PEtOx aggregates (average radius ∼ 6 nm) with temperature. A variety of structures such as elongated aggregates, spherical core–shell were observed, depending upon the polymer composition and grafting densities of PEtOx [175].

Lactam/Pyrrolidone/Pyrrolidine-Based Polymers

Poly(*N*-vinylcaprolactam) (PVCL), poly(*N*-vinylpyrrolidone) (PVPy), and poly (vinylpyrrolidine) (PNVP) are the another few important non-ionic polymers which

also exhibit thermoresponsiveness in aqueous solution. Therefore, it is important to include the discussion of their thermoresponsive properties in this chapter, although to the best of our knowledge there are no such reports formation of responsive nanostructures such as micelles based on these polymers. PVCL contains a seven-membered lactam ring with a repeat unit consisting of a hydrophilic heterocyclic amide ring, and it is water soluble and biocompatible exhibiting a LCST-type thermal transition around 32 °C as reported by Lau et al. and Tager et al. [127, 128]. PVCL. Apart from these properties, of potential interest for biomedical applications, PVCL offers benefits of low toxicity, water and organic solubility, high complexing ability, and good film-forming properties [129, 176–178]. A similar macromolecule, poly(N-vinylpyrrolidone) (PVPy), contains a five-membered lactam ring, as compared to PVCL seven-membered ring, it did not show any LCST in water. However, it exhibited LCST behavior in solutions containing a large amount of salt [129]. Maeda et al. found PVPy underwent a phase separation around 30 °C in aqueous 1.5 M potassium fluoride. Furthermore, poly[N-(2-methacryloyloxyethyl) pyrrolidone] (PNMP), a well-defined pyrrolidone-based polymer also exhibited a sharp LCST-type phase separation at 52 °C in water [130]. Poly(N-ethylpyrrolidinemethacrylate) (PEPyM), the pyrollidine analog of PNMP, exhibited a LCST-type cloud point in water at 15 °C [131]. They have shown that the LCST cloud point could be tuned up to 80 °C by copolymerizing PEPyM with a hydrophilic monomer, such as N,N-dimethylacrylamide (DMAM). Laschewsky and coworkers have synthesized thermoresponsive poly(N-acryloylpyrrolidine) (PAPR) via RAFT polymerization, with PAPR exhibiting a LCST-typecloud point at 51 °C [121].

Poly(aminoalkyl methacrylate)-Based Nanostructures

Poly(aminoalkyl methacrylate)s (see Table 6.1) represent a class of weak polybases, is another example of a temperature-responsive polymer, which has been studied extensively by many research groups recently [132, 133, 179–184]. One of the most renown members of this family is poly((N,N-dimethylamino)ethylmethacrylate) (PDMAEMA), which is also known for its LCST-type phase transition behavior in alkaline medium, since the tertiaryamine moieties can hydrogen-bond with water, while the gemini methyl groups exert hydrophobic effects. The amine functional group in the monomer is sensitive to pH and gets protonated below its pKa (between 7 and 10 depending on the substituents). This protonation, in turn, influences the polymer LCST: it delays the collapse of polymer chains during heating by increasing intra- and inter-chains repulsive electrostatic forces. As a consequence, a higher pH value promotes a lower cloud point. The reported cloud point of PDMAEMA ranges from 14 to 50 °C in pure water, depending on its molecular weight and other parameters [132, 133, 179–184].

Schubert and his coworkers utilized RAFT polymerization technique to prepare a series of statistical random copolymers of varying compositions by polymerizing N,N-(dimethylamino)ethyl methacrylate (DMAEMA) and poly(ethylene glycol)

methyl ether methacrylate (PEGMA) monomers at 70 °C. The phase behavior of the pH- and temperature-sensitive copolymers was studied in aqueous solution by measuring the LCST-type transition by UV/vis spectroscopy. The measurements were performed at three different pH values (4, 7, and 10). At pH 7 and pH 10, it has been observed that the LCST linearly increased with the wt% of PEGMA in the copolymer feed. On the contrary, at pH 4, the hydrophilicity of the P(DMAEMA-*stat*-PEGMA) copolymers is too high due to the protonation of the DMAEMA units. Thus, no LCST has been detected for most of them. By varying the pH and the composition of the P(DMAEMA-*stat*-PEGMA) copolymers, the LCST can be easily tuned between 34.7 and 82.0 °C [183].

In another work, poly[2-(dimethylamino)ethyl methacrylate]-*b*-poly(glutamic acid) (PDMAEMA-*b*-PGA) double-hydrophilic block copolymers (DHBCs) can be readily synthesized from poly(γ-benzyl-L-glutamate)-*b*-poly[2-(dimethylamino) ethyl methacrylate] amphiphilic block copolymer precursors through alkali hydrolysis. Self-assembly in water of these PDMAEMA-*b*-PGA (DHBCs) can be selectively triggered by a variation of either the pH or the temperature [185]. Such doubly responsive DHBCs self-assembled into nanostructures of either electrostatic polymersomes or spherical polymeric micelles, depending on the pH of the solution and temperature (Fig. 6.9). The resulting morphologies also depend on the overall composition of the DHBCs. According to them, for pH values below and above the isoelectric point (IEP), the DHBCs behave as unimers owing to the high solubility of the PDMAEMA block. Close to the IEP, direct or inverse electrostatic polymersomes were generated by electrostatic interactions developing between the two charged blocks driving the formation of the hydrophobic membrane of the polymersomes, which was stabilized in water by uncompensated charges. The thermosensitivity of the DHBCs relates to the LCST behavior of PDMAEMA around 40 °C. Thus, at pH = 11 and below the LCST of PDMAEMA, free chains of DHBC unimers are evidenced, while above the LCST, the hydrophobicity of PDMAEMA drives the self-assembly of the DHBCs in a reversible manner. In this case, spherical polymeric micelles or polymersomes were observed, depending on the PGA block length.

Muller and coworkers studied the aqueous solution phase behavior of both star-shaped and linear PDMAEMA and showed that the cloud point can be readily tuned by changing the pH of the solution, molecular weight, and the concentration of the polymer [133]. Furthermore, a dual thermo- and photoresponsive densely grafted molecular brushes have been prepared from DMAEMA monomer and trans-4-methacryloyloxyazobenzene (MOAB), a monomer containing a light-sensitive azobenzene group using successive ATRP technique. Incorporation of these two monomers allowed for control of the temperature-responsive behavior by photoirradiation [186]. The copolymer brush with *trans*-azobenzene units demonstrated LCST-type phase transition behavior, while the less hydrophobic *cis*-azobenzene isomer did not respond within the examined temperature range.

Since PDMAEMA itself could be deemed as a weak polyelectrolyte to a certain extent, the effect of pH and ionic strength of aqueous media may impose significant influence on the phase transition of its aqueous solution. Therefore, the aqueous
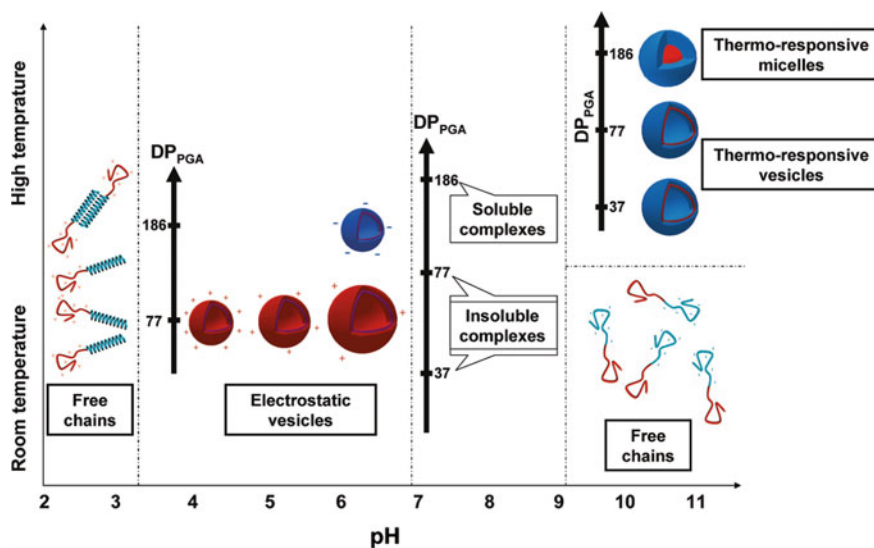
Fig. 6.9 Schematic representation of the various morphologies obtained from polypeptide-based PDMAEMA block copolymers at different temperature and pH (reproduced from Ref. [185] with kind permission of © 2010 American Chemical Society)

PDMAEMA systems might exhibit a multidimensional stimuli-responsive behavior. Moreover, the amines of PDMAEMA could undergo *N*-alkylation (quaternization or betainization), to result in cationic polyelectrolytes or zwitterionic polybetaines, respectively. The final ionic polymers also exhibited a different stimuli-responsive phase transition behavior which will be discussed later in the other Sect. 6.2.2.1 of this chapter.

POSS-Based Polymer Nanostructures

Polyhedral oligomeric silsesquioxane (POSS) has attracted a great deal of attention because of the unique nanoscale cage-shaped structure and good solubility in organic solvents [187]. Thus, POSS can be easily incorporated into polymeric matrices to prepare novel polymer hybrids by physical blending or chemical modification through copolymerization with POSS-based vinyl monomers or growing of polymer from POSSend-functionalized initiator [188–193]. Some novel POSS-containing polymers with well-defined structures have been synthesized using living/controlled radical polymerization techniques, and the self-assembly behavior of these hybrid polymers has also been attracted great attention. The self-assembly behavior of POSS-containing block copolymers is quite dependent on the rigidity of POSS blocks, strong intra-chain association, and their miscibility with organic sub-chains. Thus, the self-assembly behavior of POSS-containing hybrid block copolymers could be modulated by controlling the nature of the

inorganic sub-chains, the architecture of the block copolymers and the types of organic polymer blocks connected to the POSS block, which may create a variety of nanostructures. These POSS-based nanostructures can exhibit stimuli (temperature, pH, light, etc.)-responsiveness if some responsive functional groups are present in the organic polymer block.

For example, Zheng et al. have reported the synthesis of organic-inorganic, amphiphilic ABC–type triblock copolymer PEO-*b*-poly(MA-POSS)-*b*-PNIPAAm triblock copolymers via ATRP. The hybrid triblock copolymers PEO-*b*-P (MA-POSS)-*b*-PNIPAAm were composed of one highly hydrophobic mid block (i.e., P(MA-POSS)) and two water soluble end blocks (viz., PEO and PNIPAAm blocks). Furthermore, the PNIPAAm block is thermoresponsive and is capable of undergoing the coil-to-globule transition with a change in temperature. The hybrid triblock copolymers were microphase-separated above LCST. Both TEM and DLS showed that all the triblock copolymers can be self-organized into micellar aggregates in aqueous solutions. The sizes of the micellar aggregates can be modulated by changing the temperature [194].

Zhang et al. synthesized tadpole-shaped hybrid PNIPAAm using a POSS-containing RAFT agent [195]. The tadpole-shaped POSS-PNIPAAm hybrid self-assembled into core–shell nanostructured micelles with uniform diameter. Furthermore, an amphiphilic fluorescent polymer containing asymmetric perylenebisimide was designed and synthesized by combining reaction of perylene anhydride with amino functional POSS and ATRP of NIPAAm [196]. The self-assembly of this amphiphilic POSS-polymer hybrid into hybrid nanoparticles in aqueous solution was investigated by DLS and TEM. The hybrid nanoparticles exhibited attractive high red fluorescence at 645 nm due to the significant effect of the bulky POSS moieties. Moreover, based on the thermoresponsive PNIPAAm coronas, the fluorescence intensity of the self-assembled hybrid nanoparticles can be further enhanced and tuned by changing temperature (Fig. 6.10).

6.2.1.2 Non-ionic UCST-Type Polymers

Non-ionic polymers showing an upper critical solution temperature (UCST) in water are rare. Hence, it is really hard to find any nanostructures (e.g., miclelles, vesicles) made up of polymers that exhibit UCST-type thermoresponsiveness in aqueous solution. But, it is worthy to discuss the polymeric system that exhibits UCST-type transition as these UCST-type polymers exists as nanosized globules or nanogels in aqueous solution below a particular temperature. In this context, recently, the non-ionic homopolymer, poly(*N*-acryloyl glycinamide) (poly (NAGA)), has been shown to exhibit a sharp UCST-type transition in pure water as well as in electrolyte solution [136, 197]. Although, the polymer poly(NAGA) is known for decades and was first synthesized by Haas and Schuler in 1964 [198], but the UCST behavior had not been reported earlier. They only observed a gelatin-like thermoreversible gelation of concentrated aqueous solutions.
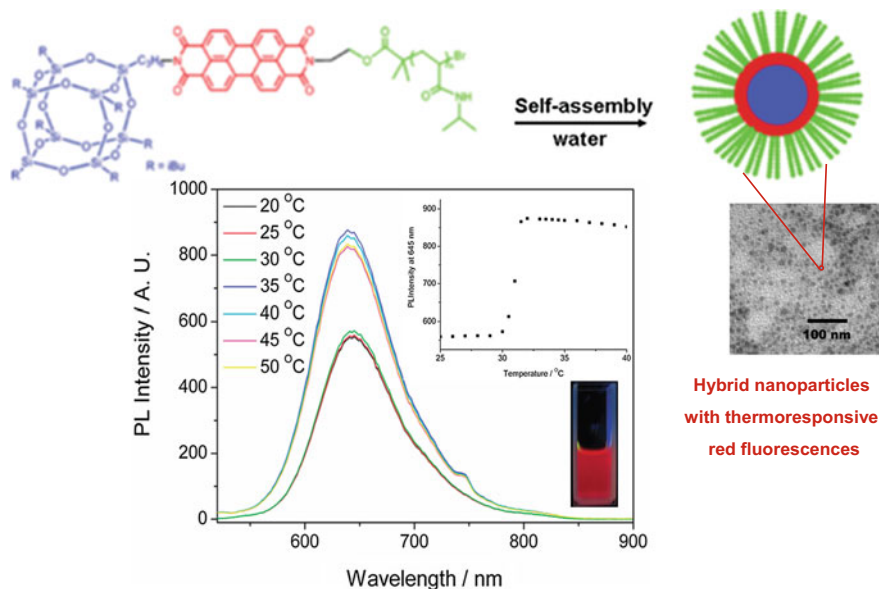
Fig. 6.10 Schematic representation of self-assembled thermoresponsive fluorescences nanostructure and TEM image obtained for hybrid nanoparticles self-assembled from 0.1 g/L aqueous solution of POSS-PBI-PNIPAAm$_{245}$ at 25 °C. Temperature-dependent fluorescence spectra obtained for 0.1 g/L aqueous solution of POSS-PBI-PNIPAAm$_{245}$ (λ_{ex} = 495 nm) *Inset* Picture of POSS-PBI-PNIPAM$_{245}$ hybrid nanoparticles in pure water (0.1 g/L) under a hand-held UV lamp ($\lambda_{ex.}$ = 365 nm) (reproduced from Ref. [196] with kind permission of © 2012 American Chemical Society)

In further studies, they concluded that the gelation is based on physical crosslinking by hydrogen bonding [199, 200]. However, in the aforementioned publications, no UCST behavior was reported until Agarwal et al. reported such property of this polymer in 2010 [88]. Failure to notice the UCST-type transition in the past by Hass et al. was because ionic groups have been introduced unintentionally by either acrylate impurities in the monomer, hydrolysis of the polymer side chains, and/or usage of ionic initiators or chain transfer agents. The presence of traces of ionic groups in the polymer prevented phase separation. The proof for these conclusions along with a procedure to obtain stable aqueous solutions of non-ionic poly(NAGA) so that the UCST behavior can be exploited in pure water as well as in physiological milieu was recently published by the same group [201]. The UCST phase transition temperature of a 1 wt% aqueous solution of poly(NAGA) is about 22 °C.

Not only poly(NAGA) homopolymer, but also its copolymer, poly(acrylamide-*co*-acrylonitrile), exhibited a UCST as demonstrated by Agarwal and coworkers [136]. Controlled increase of the UCST by copolymerization of acrylamide with varying amounts of acrylonitrile was shown, and it could be varied between 6 and 60 °C. The hysteresis between the cloud point upon cooling and heating was very

small with only 1–2 °C in most cases. The cloud points of these polymers in pure water were similar to that measured in phosphate buffered saline solution.

Maruyama et al. demonstrated that polymers with ureido groups undergo UCST-type phase transitions under physiologically relevant conditions [202]. Poly (allylurea) copolymers showed UCST-type behavior at pH 7.5 in 150 mM NaCl even at the low polymer concentration of 0.13 mg/mL. Their phase separation temperatures could be controlled up to 65 °C. Similar thermosensitivity was also observed by them with copolypeptides consisting of *L*-citrulline having an ureido group.

### 6.2.1.3 Polymer Nanostructures in Water-Alcohol Cosolvent System

Ethanol/water solvent mixtures are environmentally friendly solvents that exhibit interesting abnormal properties due to the presence of hydration shells around the ethanol molecules [203, 204]. The addition of cosolvent or co-nonsolvent also strongly influences the thermoresponsive behavior of a polymer. Here, we describe few polymeric system that exhibits some abnormal responsive behavior in cosolvent system, which has been recently reviewed by Zhang and Hoogenboom [205]. Poly(methyl methacrylate) (PMMA) is insoluble in both water and ethanol at ambient temperature, although a UCST-type transition was reported for PMMA in pure methanol as well as in pure ethanol at ~ 87 °C or above [206]. The polymer, however, showed a decreased in its UCST when adding water to the alcohol [207–211]. UCST behavior of PMMA in other lower aliphatic alcohols, e.g., methanol, 1-propanol, 2-propanol, and *t*-butanol has also been reported, exhibiting increased solubility, i.e., lower cloud point, with increasing size of the alkyl group [207, 208]. Due to the structural similarity of poly(methyl acrylate) (PMA) and PMMA, it is not surprising that PMA also exhibits a UCST transition in ethanol/water solvent mixtures [212]. Thermoresponsive micelles were then obtained in ethanol/water solvent mixtures for polystyrene-*b*-PMA (PS-*b*-PMA) block copolymers of various compositions above the UCST of PMA.

It was shown by DLS and TEM that these block copolymer micelles transformed into thermoresponsive micellar aggregates when the solution was cooled below the UCST transition temperature of the PMA block (Fig. 6.11a). But, the temperature above UCST, the micellar aggregates dissociated into unit micelles. It was further shown in another study that the double hydrophobic block copolymer, PS_{88}-*b*-$PMMA_{80}$ was self-assembled into micelle in an ethanol/water solvent mixture containing 80 vol% of ethanol [209]. At a polymer concentration below 0.2 wt%, spherical unit micelles were obtained from BCP with equal block sizes due to the relatively large radius of gyration (Rg) of the fully hydrated PMMA chains as shown by small-angle neutron scattering (SANS) study. A thermoresponsive micellar gel was formed by a polymer concentration of 1 wt%, ascribed to the large Rg of the PMMA block facilitating interactions between the formed unit micelles (Fig. 6.11b).
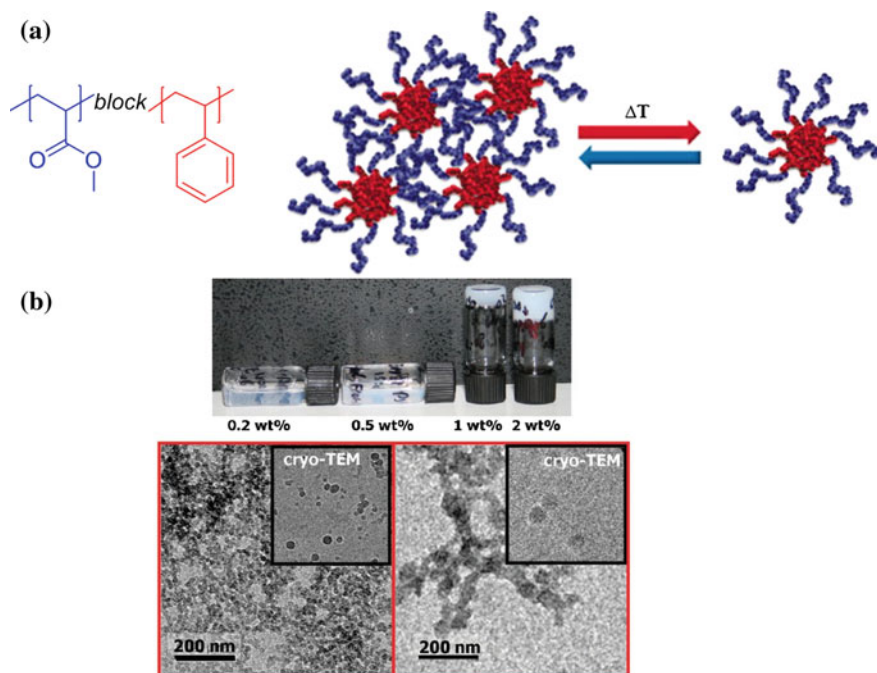
Fig. 6.11 **a** Chemical structure of PMA-*b*-PS block copolymer and schematic representation of thermoresponsive micellization process of the block copolymer (reproduced from Ref. [212] with kind permission of © 2011 Wiley-VCH), and **b** *top* pictures of the vial inversion test for micellar solutions of PS$_{88}$-*b*-PMMA$_{80}$ in an ethanol–water 80/20 wt% mixture with different polymer concentrations. *Bottom* TEM images of PS$_{88}$-*b*-PMMA$_{80}$ (*left*) and PS$_{112}$-*b*-PMMA$_{2800}$ (*right*) micelles at 0.2 wt% concentration. The *insets* show the corresponding cryo-TEM images (same scale) (reproduced from Ref. [209] with kind permission of © 2009 Royal Society of Chemistry)

Poly(2-alkyl/aryl-2-oxazoline)s (PAOx) having short side chains are either totally soluble or show LCST-type phase transition in pure water or in ethanol/water solvent mixtures. However, extending the hydrophobic side chain length to a butyl group induces UCST-type phase behavior depending on the content of ethanol in the mixture [213]. The amount of ethanol required to induce a UCST-type transition increased with increasing hydrophobicity of the polymer side chains. Furthermore, PAOx with aromatic substituents, PPhOx, and PBnOx also exhibited UCST-type behavior in ethanol/water mixture [213]. The higher hydrophobicity of the PBnOx is clearly evidenced by the higher UCST cloud points as well as a clear shift in the transition temperature with higher ethanol content. Solution phase behavior of the BCPs, PMeOx-*b*-PPhOx, and EtOx-*b*-PhOx showed that both of the two series of copolymers exhibit UCST behavior at high content of PPhOx block in ethanol/water mixture with high content of ethanol [214]. The solubility maxima of those copolymers occurred at an ethanol content of around 80 wt%. In addition, a remarkable observation was made for the PEtOx$_{50}$–PPhOx$_{50}$
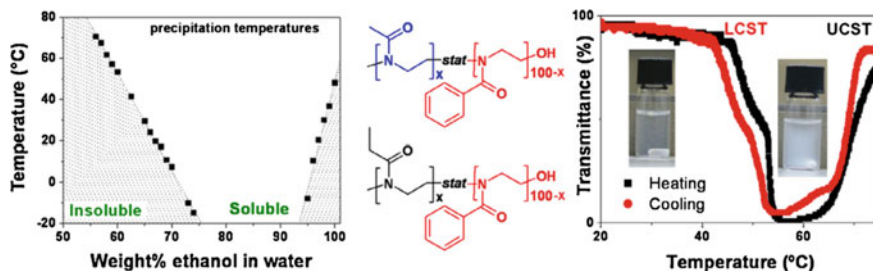
Fig. 6.12 Transmittance as a function of temperature for PEtOx$_{50}$–PPhOx$_{50}$ copolymer in 40 wt % ethanol in water demonstrating a LCST as well as an UCST transitions (reproduced from Ref. [214] with kind permission of © 2008 Royal Society of Chemistry)

copolymer in an aqueous solution with 40 wt% ethanol content showing both a LCST and a subsequent UCST, so-called closed-loop coexistence (Fig. 6.12).

Furthermore, Fustin et al. have been reported the pathway-dependent micellization behavior of tri- and tetra block copoly(2-oxazoline)s composed of solvophilic PEtOx and/or PMeOx blocks and a solvophobic poly(2-nonyl-2-oxazoline) (PNonOx) block, as well as a PPhOx block, of which the solubility can be switched from solvophilic in ethanol/water mixture with 60 wt% of ethanol to solvophobic in ethanol/water mixture with 40 wt% of ethanol [215]. They claimed that the size and morphology of the self-assembled nanostructures can be tuned depend on the solvophobic content of the copolymers and the block order as well as the solvent composition. In particular, triblock copolymer (MPN) containing PMeOx, PPhOx, and PNonOx blocks form spherical micelles together with larger, irregularly shaped, nanoaggregates in ethanol/water (60/40) mixture, while coexistence of spherical micelles and cylindrical micelles was observed in ethanol/water (40/60) mixture. Interestingly, dilution with water of the MPN micellar solution in ethanol/water (60/40) to (40/60) resulted in a collapse of the PPhOx block onto the PNonOx core leading to a core–shell structure indicating a pathway-dependent self-assembly behavior (Fig. 6.13).

6.2.2 Ionic Polymer Nanostructures

Not only non-ionic polymer but also some polymers carrying ionic functional groups, namely ionic polymers also shows response toward external stimuli such as temperature, pressure, ionic strength of solution, light, redox. Ionic water soluble polymers are a diverse class of polymers, ranging from biopolymers such as nucleic acids and proteins that mediate life processes to commercial polymers with applications in water remediation, drag reduction, and formulation of pharmaceutics, cosmetics, and coatings. Charged polymers can be arbitrarily divided into two classes: polyelectrolytes and polyzwitterions. The former have ionizable functional
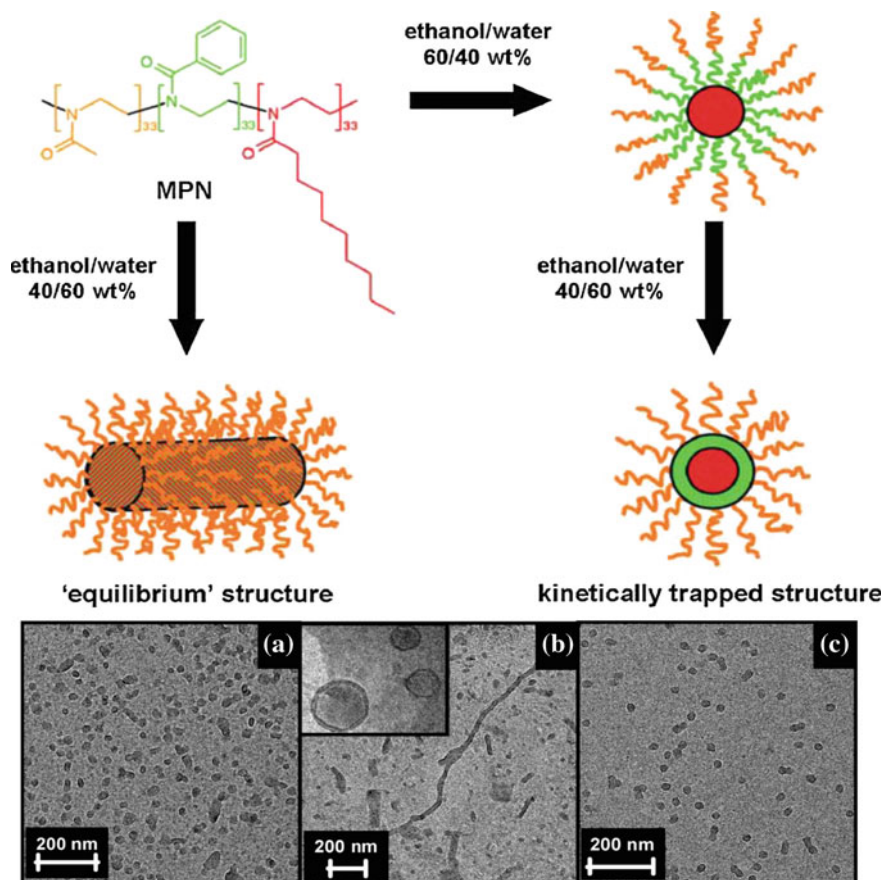
Fig. 6.13 *Top* Schematic representation of the micelles formed by the MPN triblock copolymer in ethanol/water (60/40) mixture and after addition of water to reach an ethanol/water 40/60 composition. *Below* TEM images of the MPN triblock copolymer in the EtOH/water (**a**) and 40/60 (**b**, **c**) mixtures, whereby sample **c** was prepared by diluting sample **a** with water. The *inset* of image **b** shows another area of the sample (same scale) (reproduced from Ref. [215] with kind permission of © 2010 Wiley-VCH)

groups that are either anionic or cationic in nature. The charges may be along or pendent to the macromolecular backbone, and charges are balanced by small counterions. Zwitterionic polymers have both cationic and anionic charges along or pendent to the backbone and they are charge-neutral. Polymers containing cationic and anionic functionality on different monomer units are designated as polyampholytes while those having both charges on a single monomer unit are called polybetaines [216]. Because of their zwitterionic character, these ionic polymers exhibit markedly different behavior than polyelectrolytes in aqueous solutions [217–219]. The charge–charge repulsions along the polyion backbone resulting

from counter ion mobility are responsible for chain extension and the large hydrodynamic volume of polyelectrolytes in water at low ionic strength.

However, polyelectrolytes usually exhibit decreases in the hydrodynamic volume and solution viscosity upon the addition of electrolytes such as inorganic salts. This polyelectrolytes effect is due to conformational changes that occur when the added electrolytes shield the electrostatic repulsions of like charges along the polymer chain, causing the polymer coils to contract [220]. On the other hand, polymers with charge balance, trend to adopt collapsed or globular conformations in salt-free solution because of the electrostatic attractions between opposite charges [219, 221, 222]. Indeed, the electrostatic associations are so strong among polyzwitterion molecules that it may phase-separate in solution even in the absence of low MW electrolytes such as inorganic salts. However, as simple electrolytes are added to polyzwitterions solution, the electrostatic interactions are shielded, and the polyzwitterions can adopt random-coil conformations, called the "antipolyelectrolyte effect." The globule-to-coil transition that occurs upon the addition of electrolytes results in increased polymer hydrodynamic volume and solution viscosity [219, 223, 224]. Many factors govern the solution properties of polyzwitterions, including the charge density, charge asymmetry (i.e., degree of charge imbalance), and chemical properties of the ionizable groups [219, 225, 226]. The polyzwitterions solubility and magnitude of the globule-to-coil transition (i.e., change in the hydrodynamic size) exhibited by polyzwitterions are typically determined by the charge density of the system. As the polyzwitterion charge density increases, greater concentrations of electrolytes are required to promote coil expansion and the relative increase in the hydrodynamic size upon electrolyte addition tends to be greater. Unbalanced polyzwitterions (i.e., polyzwitterions with a net charge) usually exhibit a combination of polyzwitterions and polyelectrolytes solution behavior according to the degree of charge imbalance. Polyzwitterions generally tend to exhibit behavior more characteristic of conventional polyelectrolytes with increasing charge asymmetry. For polyzwitterions bearing weakly acidic and/or weakly basic functional groups (i.e., carboxylic acids and/or tertiary amines), the charge density and charge asymmetry are dominated by the level of functional group incorporation and the solution pH. Thus, reversible transitions between polyelectrolytes and polyzwitterions behavior can be triggered by changes in the solution pH. Further, polybetaines have been classified as polycarboxybetaines, polyphosphobetaines and polysulfobetaines (Fig. 6.14).

Another important member in the family of ionic polymers is the poly(ionic liquid)s (PILs) or polymerized ionic liquids (ILs), which is referred to a subclass of polyelectrolytes that feature an IL species in each monomer repeating unit, connected through a polymeric backbone to form a macromolecular architecture. Some of the unique properties of ILs are incorporated into the polymer chains, giving rise to a new class of polymeric materials. PILs expand the properties and applications of ILs and common polyelectrolytes. As an emerging interdisciplinary topic among polymer chemistry and physics, materials science, catalysis, separation, analytical chemistry, and electrochemistry, PILs are attracting increasing interest among the scientific community [227].
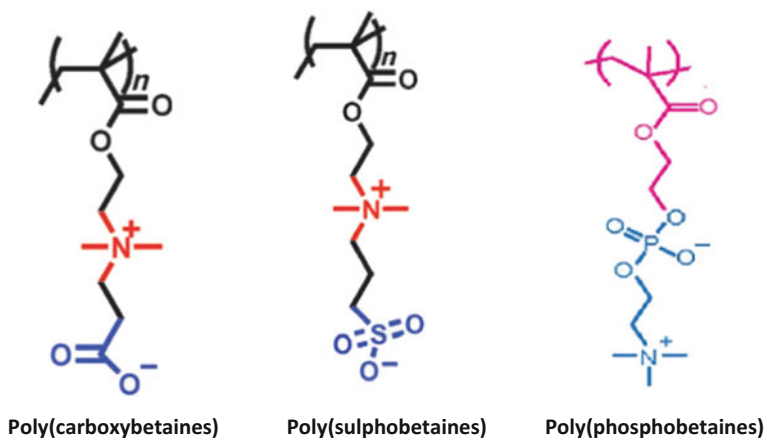
Poly(carboxybetaines)   **Poly(sulphobetaines)**   **Poly(phosphobetaines)**

Fig. 6.14 Chemical structures of different polybetaines

6.2.2.1 Zwitterionic Polymer Nanostructures

Zwitterionic polymers such as carboxybetaine methacrylate (CBMA), sulfobetaine methacrylate (SBMA), and phosphorylcholine-based polymers have been widely utilized as superhydrophilic and ultra-low fouling biomaterials [228, 229]. It is known that commercially available low fouling non-ionic PEG resists non-specific protein adsorption via hydration forces, which are formed via hydrogen bonding between water molecules and PEG [230]. Zwitterionic materials, with their strong intra- and inter-molecular electrostatic interactions, can bind water molecules strongly and form electrostatically induced hydration [231–233], which resists non-specific protein adsorption over a long period. Polyzwitterions, specifically polysulfobetaines usually exhibit a UCST-type phase transition, i.e., they are water-insoluble at lower temperature due to the electrostatic attraction. Zwitterionic moieties can form associations through the electrostatic interactions between the cationic and anionic groups. Heating promotes the water molecules to diffuse into the network, leading to the disruption of the network at a critical temperature. As a result, the solution undergoes an emulsion–dissolution phase transition. Chang and coworkers reported a detailed investigation of solution properties of zwitterionic poly(sulfobetaine methacrylate)s (polySBMAs) [234].

It has been reported that the aqueous solution of polySBMAs exhibited an UCST-type transition that is attributed to the charge–charge or dipole–dipole interactions among the zwitterionic sulfobetaine groups [89, 235, 236]. The insoluble–soluble phase transition of polySBMA in aqueous solution was due to inter-molecular associations and dissociation of polyzwitterion molecules, which depend strongly on the stimuli-responsive control of solution pH and ionic strength (Fig. 6.15). It has been found that polySBMAs of increasing molecular weights had enhanced mutual intra- and inter-chain associations of the sulfobetaine groups in
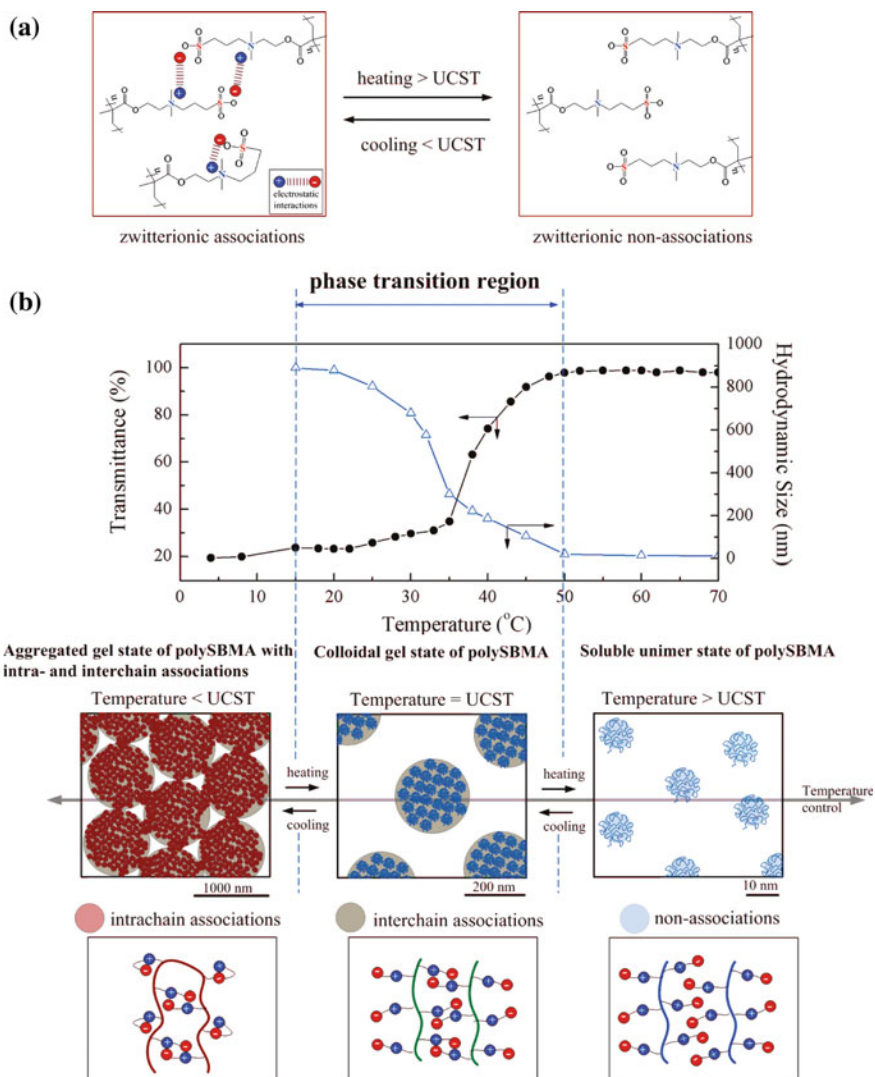
Fig. 6.15 a Chemical structures of associated and nonassociated polySBMA homopolymers; **b** temperature-dependent solubility of the zwitterionic polymer in aqueous solution. In phase transition region, there is a formation of colloidal gel state of polySBMA at cloud point temperature (reproduced from Ref. [234] with kind permission of © 2010 American Chemical Society)

aqueous solution, resulting in the increase of their UCST-type cloud point associated with the non-fouling nature of polySBMA's suspension.

Afterwards, Laschewsky and coworkers reported a block copolymer consisting two hydrophilic blocks, PNIPAAm, and the zwitterionic Poly
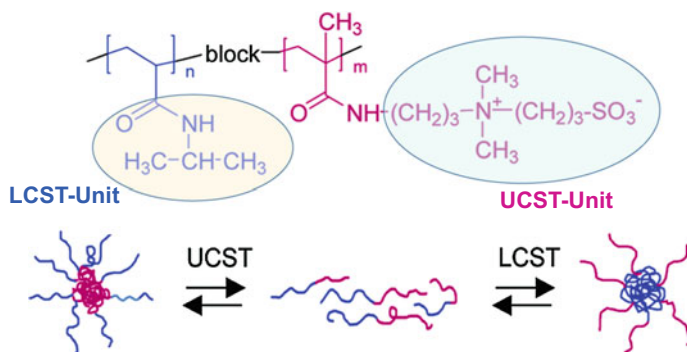
Fig. 6.16 Schematic representation of different types of association among poly(NIPAAm-*b*-SPP) block copolymer molecules with temperature (reproduced from Ref. [134] with kind permission of © 2002 American Chemical Society)

(3-[*N*-(3-methacrylamidopropyl)-*N*,*N* dimethyl] ammoniopropane sulfonate) (PSPP) exhibiting double thermoresponsive behavior in water. This BCP formed PNIPAAm-cored micelles above the LCST of PNIPAAm (29–35 °C) and PSPP-cored micelles below the UCST of PSPP (8–20 °C) (Fig. 6.16) [134].

Sulfobetaines derived from acrylamide and methacrylates are two of the prominently used monomers for making a wide variety of zwitterionic polymers [237, 238]. However, these monomers are hydrolytically unstable [239]. To overcome such difficulty, Vasantha et al. reported a hydrolytically stable vinyl benzene substituted imidazole-based sulfobetaine-type zwitterionic polymers. These imidazole-based polysulfobetaines exhibited many unusual solubility characteristics. Unlike the acrylate and acrylamide-derived polysulfobetaines which were soluble in water, the benzimidazole-based polysulfobetaines were only soluble in concentrated brine solution (22.6 wt% NaCl) and also swell in deionized water. Further, they exhibited reversible phase transitions due to the formation of expanded chains at elevated temperature and aggregates below the UCST cloud point as studied by DLS, turbidity, and viscosity measurements. The unique thermoreversible gelling properties as well as unusual solubility characteristics make them interesting materials for a wide range of applications.

Shao and coworkers compared thermo- and salt-responsive behaviors of sulfobetaine and carboxybetaine polymers by examining their rheological properties as a function of temperature and their hydrodynamic sizes as a function of salt concentration [240]. In this work, they investigated the structure and dynamics of associations among cationic and anionic groups present in these two zwitterionic polymers. Results showed that the difference in the charge density of cationic and anionic groups of zwitterionic moieties dictates associations among moieties: the less difference results in more and stronger associations. These different interaction behaviors lead to the diversified properties of zwitterionic materials. Thus, carboxybetaine polymers do not exhibit stimuli responses as expected from the antipolyelectrolyte behavior of zwitterionic polymers as observed in sulfobetaine polymers.

Zhao et al. [241] also observed similar phenomenon in their work. In their work, they copolymerized temperature-responsive NIPAAm monomer with zwitterionic monomers, carboxybetaine methacrylate (CBMA) and sulfobetaine methacrylate (SBMA), and synthesized the statistical copolymers, poly(NIPAAm-*co*-CBMA) and poly(NIPAAm-*co*-SBMA), respectively. Above the LCST of PNIPAAm, a clear sol–gel transition was observed, accompanied by an increase in the turbidity and elastic modulus of the copolymer solution. The hydrophilic sulfobetaine group present in the PSBMA block was strongly influenced by elevated temperatures, which counter affected the thermal properties in the pure PNIPAAm-based polymer at temperatures higher than its LCST. While the carboxybetaine group in PCBMA is weakly affected by temperatures, poly(NIPAAm-*co*-CBMA) solution is able to preserve its thermoresponsive nature. In addition, CBMA moiety acted as stronger ionic bridges in poly(NIPAAm-*co*-CBMA) to form reinforced elastic networks with superior recovery features when compared with poly(NIPAAm-*co*-SBMA). Thus, incorporation of PCBMA block with the thermoresponsive PNIPAAm provides a tractable and facile way to introduce non-fouling property with thermoresponsive characters, without compromising with the mechanical properties.

Further, zwitterionic polymers have been investigated as surface coating materials due to their low protein adsorption properties, which reduce immunogenicity, biofouling, and bacterial adsorption of coated materials. Most zwitterionic polymers, reported so far, are based on (meth)acrylate polymers which can induce toxicity by residual monomers or amines produced by degradation. Jeong et al. [242] demonstrated a zwitterionic polymer consisting of phosphorylcholine (PC) and biocompatible poly(propylene glycol) (PPG) blocks as a new thermogelling material. The aqueous solution of PC-PPG-PC BCP undergone unique multiple sol–gel transitions with increasing temperature. A heat-induced unimer-to-micelle transition, changes in ionic interactions, and dehydration of PPG block are involved in the sol–gel transitions (Fig. 6.17). Based on the broad gel window and low protein adsorption properties, the PC-PPG-PC thermogel can be utilized for sustained delivery of protein drugs and stem cells over 1 week. Further, a novel triblock copolymer based on PPO, poly(2-(methacryloyloxy)ethyl phosphorylcholine) (PMPC), and PNIPAAm have also been synthesized via ATRP [243]. Two architectures were created: an ABC triblock and an ABA triblock copolymer, with the A-block being PPO, the B block being PMPC, and the C block being PNIPAAm. At reduced temperatures, all three blocks are water soluble, while PPO became insoluble between 15 and 31 °C, and the PNIPAAm block became insoluble above 31 °C. Between 15 and 31 °C, the PPO blocks aggregated creating micelles, and above 31 °C the PNIPAAm blocks aggregated creating a gel.

6.2.2.2 Poly(Ionic Liquid) Nanostructures

Yuan and Men and coworkers were the first to report an anionic PIL, poly (4-tetrabutylphosphonium styrene sulfonate) (PTPSS) exhibiting an LCST-type phase transition in aqueous solution [244]. Very interestingly, the experiments
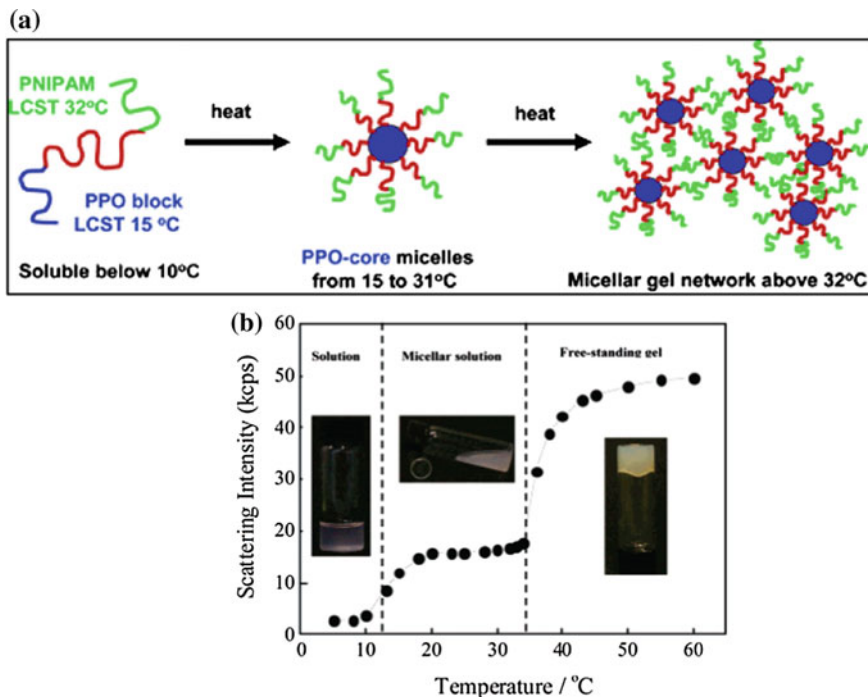
Fig. 6.17 a Schematic representation of the aqueous solution phase behavior of the PPO-PMPC-PNIPAM triblock copolymers: molecular dissolution at 5 °C, formation of PPO-core micelles between 10 and 20 °C temperature, and formation of a micellar gel network above 33 °C (which corresponds to the LCST of the outer PNIPAAm chains). **b** Temperature dependence of the scattered light intensity for PPO$_{43}$-PMPC$_{160}$-PNIPAAm$_{81}$ triblock copolymer solution in PBS buffer at pH 7.4. *Inset* shows photographs for the same copolymer dissolved at a much higher concentration (20 wt%) in PBS buffer: (*left*) a transparent free-flowing copolymer solution at 5 °C, (*middle*) a slightly turbid free-flowing micellar solution at 20 °C, and (*right*) the free-standing micellar gel formed at 37 °C (reproduced from Ref. [243] with kind permission of © 2005 American Chemical Society)

indicated that cloud point temperature can be shifted to either higher or lower temperature, depending on the type of the added foreign salts such as potassium bromide, tetrabutylphosphonium bromide (TPB), and the salt of TPSS monomer. This PIL also exhibited a very high stabilizing power for carbon nanostructures and can readily synthesize environment-sensitive graphene dispersion. The same group also discovered a new type of gemini PILs, poly[(1,8-octanediyl-bis (tri-n-butylphosphonium) 4-styrenesulfonate], synthesized via conventional free radical polymerization of a dicationic IL monomer in DMF [245]. This PIL presented a LCST-type phase transition in aqueous solution. Copolymerization of this gemini dicationic IL monomer with divinyl benzene crosslinker in water resulted in the formation of hydrogel, which exhibited a temperature-triggered volume change in water. Recently, the same group reported a cationic PIL, poly
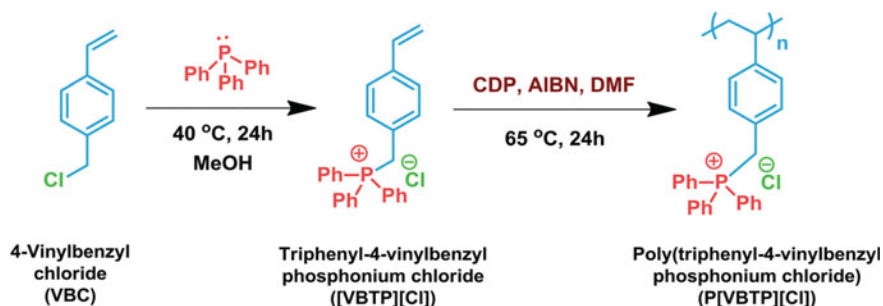
Fig. 6.18 Synthesis of [VBTP][Cl] monomer and P[VBTP][Cl] (reproduced from Ref. [247] with kind permission of © 2016 Royal Society of Chemistry)

(tributyl-4-vinylbenzylphosphonium pentanesulfonate) that showed a similar LCST-type transition in aqueous solution [246]. This phase transition occurred in a wide temperature range in terms of PIL concentration as well as type and concentration of externally added salts. According to them, anion exchange and salting out effects are responsible for the flexible phase transition temperatures.

Very recently, we have discovered a new cationic phosphonium PIL, poly (triphenyl-4-vinylbenzylphosphonium chloride) (P[VBTP][Cl]), exhibiting responsiveness in water [247] RAFT polymerization technique have been employed to synthesize (P[VBTP][Cl])s of varying and controllable molecular weights (Fig. 6.18), which exhibited an UCST-type phase transition in aqueous solution in the presence of externally added halide ions. The addition of halide ions transformed the transparent aqueous PIL solution into a turbid two-phase solution, forming insoluble microgel aggregates ($D = 2.5$ μm) owing to the screening of the positively charged phosphonium groups of PILs and eventually forms intra- and/or inter-chain crosslinking among the PIL chains through halide ion bridges.

Further, this turbid solution exhibits a distinct UCST-type phase transition and transformed into a one-phase transparent solution due to the disruption of ion bridges upon heating (Fig. 6.19). The rate of aggregation of P[VBTP][Cl] increased sharply with an increase of the size of the added halide ions in this order $I^- > Br^- > Cl^-$. The cloud point temperature increased linearly with increasing halide ion concentration as well as with increasing molecular weights of the PIL. The phase diagram of aqueous PIL solution shows the highest cloud point at 6 wt %. This PIL exhibits very good stabilizing ability for carbon nanotubes in water, whose dispersion state can be switched from dispersed to agglomerate and vice versa by adding halide ions and increasing the temperature, respectively. The crosslinked hydrogel of P[VBTP][Cl] also shows dual responsiveness toward both halide ions and temperature.

Tenhu and coworkers also observed UCST-type phase behaviors of imidazolium- and DMAEMA-based polycations in aqueous solution in the presence of both LiNTf$_2$ and NaCl salts [248]. Moreover, there are also some reports of amphiphilic block copolymers in the literature consisting of cationic/anionic
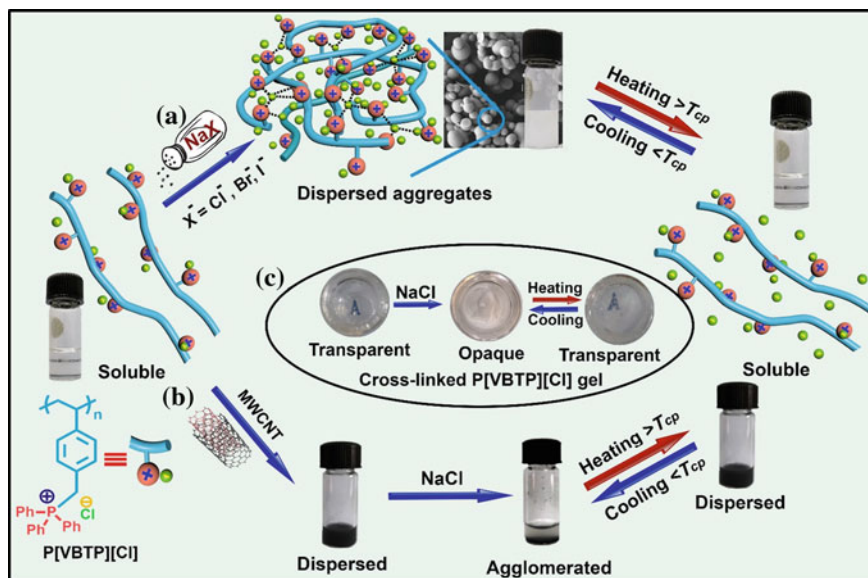
Fig. 6.19 Schematic representation of **a** of halide ion-induced soluble–insoluble and temperature-induced insoluble–soluble UCST-type phase transition of aqueous P[VBTP][Cl] solution. *Inset* show the FESEM image the aggregates of P[VBTP][Cl]. **b** Photographs of dual responsiveness of P[VBTP][Cl]-stabilized MWCNT dispersion in water. **c** Crosslinked hydrogel of P[VBTP][Cl]-40 K in H_2O demonstrating salt and temperature-induced deswelling and reswelling (reproduced from Ref. [247] with kind permission of © 2016 Royal Society of Chemistry)

polymer as one of the blocks. These block copolymers are able to self-assemble into a range of 3-dimensional morphologies in aqueous solution, whose characteristics and size can be readily tuned by the block copolymer's chemical composition and physical properties [249, 250].

O'Reilly and coworkers reported a BCP containing charged end group can undergo a relatively fast and fully reversible transition between micelle and vesicle morphologies (Fig. 6.20) [99]. Initially, the diblock copolymer PMA_{27}-*b*-$PNIPAAm_{47}$ synthesized using sequential RAFT polymerization techniques employing a "head-group" functionalized RAFT CTA. Here, the block copolymer system studied employed a chain end functional charged "head-group," to act as a permanently hydrophilic group to stabilize the structures when the block copolymer becomes completely hydrophobic above the LCST of the copolymer. Thus, at room temperature, the amphiphilic block copolymer formed micelle and above the LCST, vesicular morphology was created generating a tuneable and reversible morphology switching copolymer system.

Li et al. [251] explored the improved thermoresponsiveness of PNIPAAm hydrogels by using poly(sodium p-styrenesulfonate) (PSSNa), a strong anionic polyelectrolyte (i.e., a permanently water soluble polymer); PSSNa was incorporated into PNIPAAm network as the blocky sub-chains. To achieve this, a
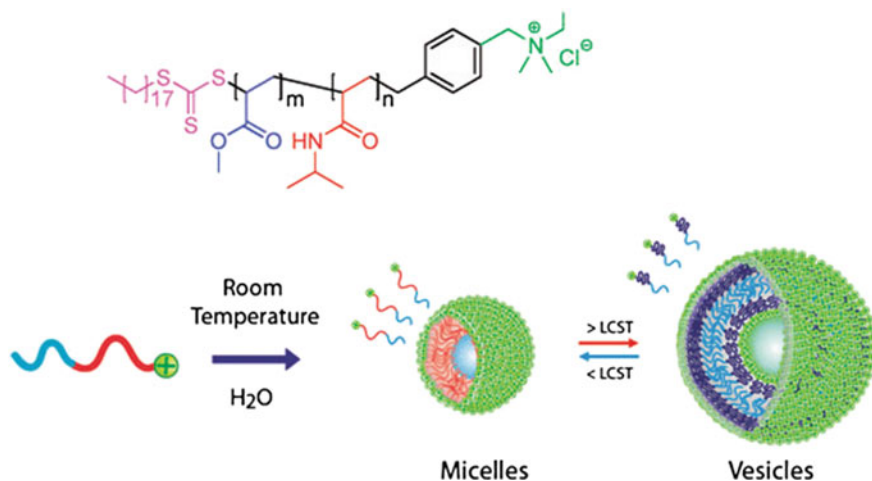
Fig. 6.20 Thermally induced reversible micelle–vesicle switching for a charged amphiphilic diblock copolymer (reproduced from Ref. [99] with kind permission of © 2011 Royal Society of Chemistry)

sequential RAFT polymerization approach was employed to access the blocked PNIPAM networks. The morphologies of BCP networks were studied by means of TEM and small-angle X-ray scattering (SAXS). The thermoresponsive properties of the hydrogels were examined in terms of swelling, deswelling, and reswelling tests. According to them, such improvement thermoresponse was attributable to the formation of the PSSNa nanophases, which promoted the transportation of water molecules into the crosslinked networks.

6.3   pH-Responsive Polymer Nanostructures

One other stimulus that has been explored extensively within the scientific community is the change of pH of the solution [36, 139, 252]. The incorporation of ionisable monomer units containing –COOH/–NH$_2$ into polymer backbones enables pH-dependent phase transitions and solubility changes. pH-responsive polymeric systems are polymers whose solubility, volume, configuration, and conformation can be reversibly manipulated by changes in external pH [253, 254]. The adjustment in pH alters the ionic interaction, hydrogen bonding, and hydrophobic interaction, resulting in a reversible microphase separation or self-organization phenomenon. pH-responsive polymers have drawn attention as an intelligent material, in drug delivery due to their abilities to sense changes and rapidly stimulate structural or morphological responses [139, 255]. Such pH-triggered delivery system could be achieved by the following: (a) incorporation of pH-responsive moiety to the polymer structure; (b) destabilization of

self-assembled polymeric aggregates; or (c) chemical conjugation of pH-liable linkage between polymers and drugs [256, 257]. Herein, we categorized our discussion into two parts that based on pH-responsive non-ionic and ionic polymers.

6.3.1 Non-ionic Polymer Nanostructures

It is known that amphiphilic block copolymers, consisting of at least one block that is hydrophilic and at least one block that is hydrophobic, undergo self-assembly into polymeric nanostructurs in aqueous media to minimize the unfavorable interactions between the hydrophobic block and the surrounding water. Introduction of a pH-responsive functionality into an amphiphilic BCP capable of generating polymer nanostructures responsive to pH. The core–shell pH-responsive microgel particles containing PMMA core and poly(methacrylic acid-co-ethyl acrylate) P(MAA-co-EA) shell crosslinked with di-allyl phthalate (DAP) have been synthesized [258]. PMMA core was first synthesized through conventional seeded emulsion polymerization, and the second pre-emulsified monomers and small amounts of initiator were introduced slowly under monomer-starved feeding conditions to grow the pH-responsive shell layer.

Other systems, such as those composed of poly(methacrylic acid) (PMAA) and poly(N,N-diethylaminoethyl methacrylate) (PDEAM) chains, have recently been reported [259]. In contrast to the PMAA or poly(acrylic acid) (PAA) based systems, such latex was swellable at low pH due to the protonation of amino segments of PDEAM. Polymer scaffolds bearing activated ester pentafluorophenylacrylate (PFPA) groups were successfully synthesized by Doncom et al. utilizing RAFT method [260]. The PFPA groups were easily substituted with N,N-diisopropylethylenediamine and the RAFT end group modified with either a charged tertiary amine acrylate or triethylene glycolmethyl ether acrylate, to achieve pH-responsive block copolymers with the same backbone but different end-groups. These polymers were self-assembled into vesicles at basic pH to and there was a morphology transition to a micelle upon lowering the solution pH (Fig. 6.21). The large block copolymers took longer to stabilize after a morphology switch than the smaller block copolymers. In addition, the encapsulation and control release of a hydrophilic dye, Rhodamine B, was demonstrated.

In another study, a series of pH-sensitive micelles were generated from poly[(ethylene oxide)-b-glycerolmonomethacrylate-b-2-(diethylamino) ethylmethacrylate] P(PEO–GMA–DEA) and poly[(ethylene oxide)-b-2-hydroxyethyl methacrylate-b-2-(diethylamino)ethylmethacrylate]   P(PEO–HEMA–DEA)   triblock copolymers [261]. These triblock copolymers were synthesized via ATRP of GMA or HEMA followed by DEA monomers using a PEO-based macroinitiator. These copolymers were totally soluble in water at low pH but deprotonation of the DEA layers above pH 8 led to the formation of the three-layer micelles. At pH 8, the micelle contained DEA cores with GMA or HEMA innershells and PEO chains as the outer surface layer (corona). Selective crosslinking of the hydroxy-functional
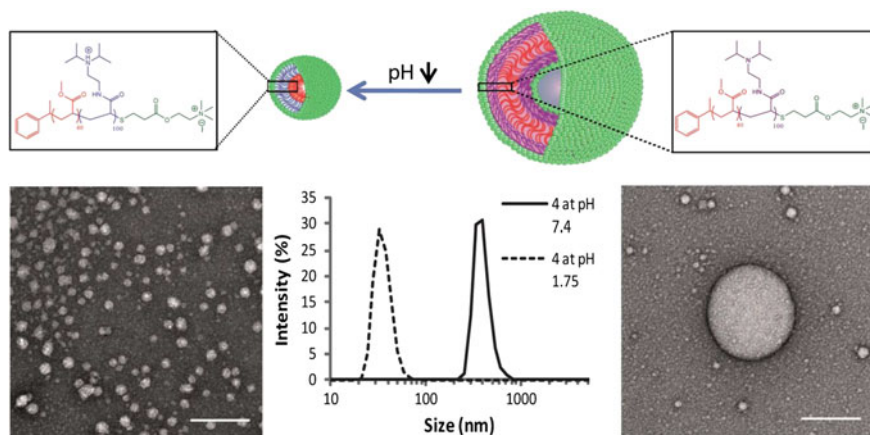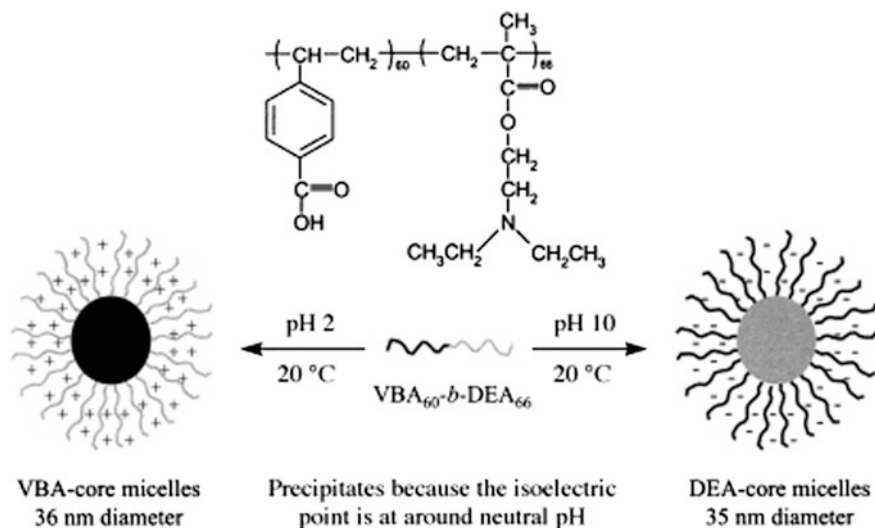
Fig. 6.21 (*Top*) Schematic representation of morphology change of the block copolymer with pH. (*Bottom left*) Representative TEM image of self-assembled block copolymer at pH 1.75, stained with uranyl acetate; (*middle*) DLS plot showing change in size with change in pH; (*right*) representative TEM image of self-assembled block copolymer at pH 7.4, stained with uranyl acetate (reproduced from Ref. [260] with kind permission of © 2012 Royal Society of Chemistry)

innershell was carried out with divinyl sulfone [DVS] under alkaline conditions retaining the DEA at the core of the micelle resulting in SCL micelles. These SCL micelles exhibited reversible pH-dependent swelling behavior upon protonation of the DEA cores at low pH.

The same group also prepared a series of pH-responsive "schizophrenic" AB-type diblock copolymers via ATRP that formed two types of micelles in aqueous solution depending on pH [262–264]. The first diblock copolymer, P (VBA-*b*-DEA), was comprising of 2-(diethylamino)ethyl methacrylate (DEA) and 4-vinyl benzoic acid (VBA) monomer unit [262]. They observed the formation of both conventional micelles and inverted micelles from P(VBA-*b*-DEA) in aqueous solution at ambient temperature, by controlling the solution pH (Fig. 6.22). According to them, at low pH, VBA-core micelles were formed, but at high pH DEA-core micelles were formed, and at neutral pH, the system precipitated from the solution. In another work, a similar type of diblock copolymer, poly [4-vinylbenzoic acid-*b*-2-*N*-(morpholino)ethyl methacrylate] P(VBA$_{63}$-*b*-MEMA$_{123}$), was synthesized via ATRP (Fig. 6.23) [263]. This copolymer also self-assembled into similar conventional micelles and inverted micelles at two different pHs (Figure). The key to this behavior was in choosing the correct polymer block, i.e., the use of PVBA (pKa $\sim$7.1) as one block and the other block, poly(2-*N*-(morpholino)ethylmethacrylate) (PMEMA) (pKa of the conjugate acid $\sim$4.9) ensured that precipitation did not occur during pH variation across the isoelectric point.

In the literature, there are several other examples of polymeric system that exhibits "schizophrenic" behaviors [56, 181, 265, 266]. One of such example

Fig. 6.22 Chemical structure of P(VBA$_{60}$-b-DEA$_{66}$) diblock copolymer and its pH-induced "schizophrenic" micellization behavior in aqueous solution (reproduced from Ref. [262] with kind permission of © 2002 Wiley-VCH)
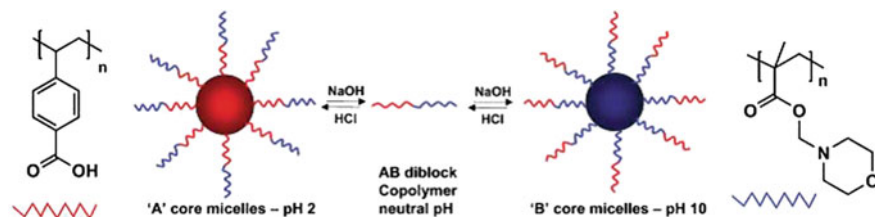
Fig. 6.23 Schematic representation and chemical structure of P(VBA$_{63}$-b-MEMA$_{123}$) diblock copolymer and its pH-induced "schizophrenic" micellization behavior in aqueous solution (reproduced from Ref. [263] with kind permission of © 2003 American Chemical Society)

involved poly(propylene oxide)-based (PPO) macroinitiator for the polymerization of 2-(diethylamino)ethyl methacrylate (DEA) by ATRP technique in alcoholic media at 55 °C [181]. The resulting P(PPO-b-DEA) diblock copolymer dissolved in cold water at pH 6.5. DEA-core micelles were formed at 5 °C in mildly alkaline solution (pH 8.5) and PPO-core micelles were obtained at pH 6.5 at elevated temperatures (40 ± 70 °C).

Zhang and coworkers have developed an efficient way to achieve nanoparticle-to-vesicle transition of an ABC-type triblock copolymer by in-to-out switch of the pH-sensitive core-forming C block [267]. A well-defined triblock copolymer, poly(N,N-dimethylacrylamide)-b-polystyrene-b-poly[N-(4-vinylbenzyl)-N,N-dibutylamine] (PDMA-b-PS-b-PVBA) was synthesized by seeded dispersion RAFT polymerization, which self-assembled into corona–shell–core nanoparticles at a particular pH.

They observed the nanoparticle-to-vesicle transition of this pH-sensitive ABC triblock copolymer to form unsymmetrical ABC triblock copolymer vesicles through the in-to-out switch of the pH-sensitive core-forming C block.

It was found that the length of the core-forming C block of PVBA greatly affects the morphology transition of the ABC triblock copolymer nanoparticles. The triblock copolymers of varying compositions, $PDMA_{38}$-b-PS_{167}-b-$PVBA_{19}$ and $PDMA_{38}$-b-PS_{167}-b-$PVBA_{37}$, containing a short core-forming PVBA block, formed nanoparticles with sizes 29 and 33 nm, respectively, whose sizes did not change upon changing the pH of the solution suggesting no morphology transition of the two triblock copolymers. Whereas, when the DP of the core-forming C block of PVBA increased to 76, the nanoparticle-to-vesicle transition occurred and 39 nm petal-like vesicles of $PDMA_{38}$-b-PS_{167}-b-$PVBA_{76}$ with an etched shell were formed. When the DP of the core-forming PVBA block increased to 114, the nanoparticle-to-toroid transition occurred and the $PDMA_{38}$-b-PS_{167}-b-$PVBA_{114}$ toroids with sizes ranging from 60 to 80 nm were observed. Interestingly, some of the ABC triblock copolymer toroids were disjointed into worm-like rods.

Yang et al. have designed a series of amphiphilic 4- and 6-armed star triblock copolymers based on poly(ε-caprolactone) (PCL), poly(2-(diethylamino)ethyl methacrylate) (PDEAEMA), and poly(poly(ethylene glycol) methyl ether methacrylate) (PPEGMA) blocks. The star-armed polymer has been synthesized by a combination of ROP and continuous activators regenerated by electron transfer ATRP (ARGET ATRP) [268]. The star copolymers self-assembled to form micelles in aqueous solution, which showed pH-responsive behavior owing to the tertiary amine groups of DEAEMA. Upon changing the pH, one can protonate or deprotonate DEAEMA groups that eventually induce the swell or shrink of the formed micelles (Fig. 6.24). As the pH decreased from 10 to 3, transmittance was almost unchanged at lower concentrations of 0.1 and 1 mg/mL, but sharply increased at concentrations of 10 mg/mL. The hydrodynamic diameter (D_h) and zeta potential exhibited almost the same tendency, which slightly increased with the concentration increased and increased rapidly as the pH decreased from 7 to 4 followed by a slight decrease at pH < 4.

A simple, new, two-step method was introduced for preparing hollow pH-responsive poly(methyl methacrylate-co-methacrylic acid) particles (Fig. 6.25). The hollow particles swelled at moderate pH values, formed gels in concentrated dispersions and can be disassembled by adding reducing agents. The pH-responsive particles have enabled preparation of space filling gels with microporous (inter-connected) porosity (Fig. 6.26). The main advantage is that these particles are prepared without the use of small molecule surfactants [269].

Zhang and coworker have been constructed pH-dependent flexible nanostructures by the self-assembly of two kinds of hyperbranched polymers and then validated its potency as the controllable siRNA/drug co-delivery vehicle for the combination of chemotherapy with RNA interfering (RNAi) therapy [270]. They have shown that pH-reversible phenyl boronate linking phenylboronic acid-tethered hyperbranched oligoethylenimine (OEI600-PBA) and1,3-diol-rich hyperbranched polyglycerol (HBPO) spontaneously interlinked together to form a core–corona
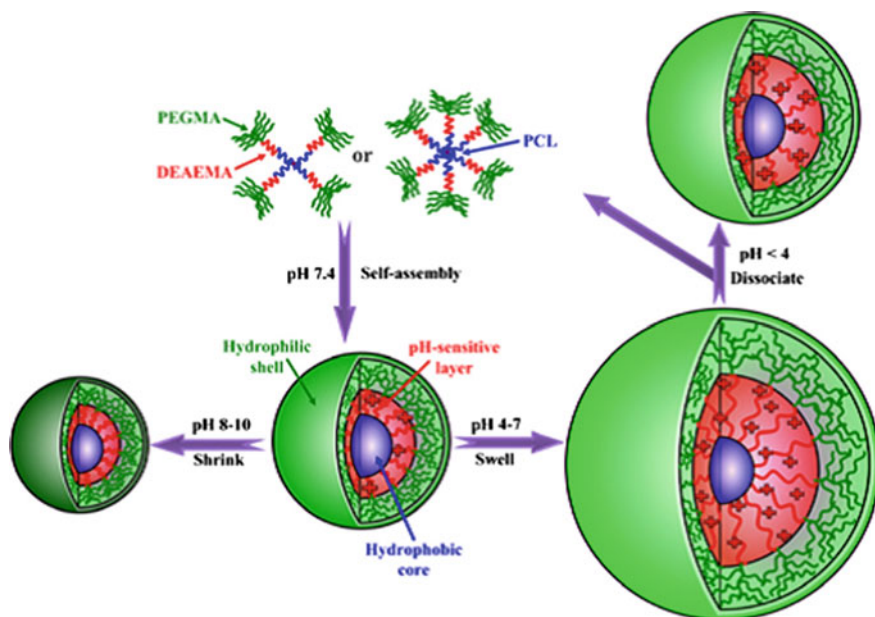
Fig. 6.24 Schematic representation of micellization of 4 or 6 armed SPCL-*b*-PDEAEMA-*b*-PPEGMA and pH-responsive behavior (reproduced from Ref. [268] with kind permission of © 2013 Springer)
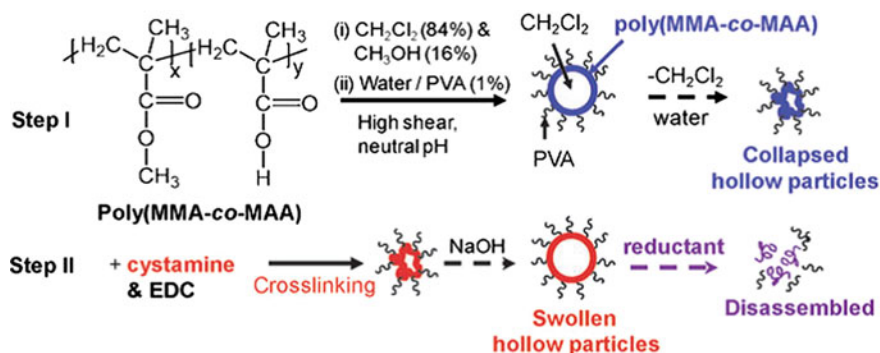
Fig. 6.25 Schematic representation of the two-step method used to prepare reversibly crosslinked hollow pH-responsive particles (reproduced from Ref. [269] with kind permission of © 2011 Royal Society of Chemistry)

nanostructure (Fig. 6.27). The special build-up of compactly clustering OEI600-PBA units around hydrophobic HBPO aggregate offered significant advantages over parent OEI600-PBA, including strengthened affinity to siRNA, ability of further loading anticancer drug, easier cellular transport, and acidity-responsive release of payloads. To evaluate the co-delivery capability,
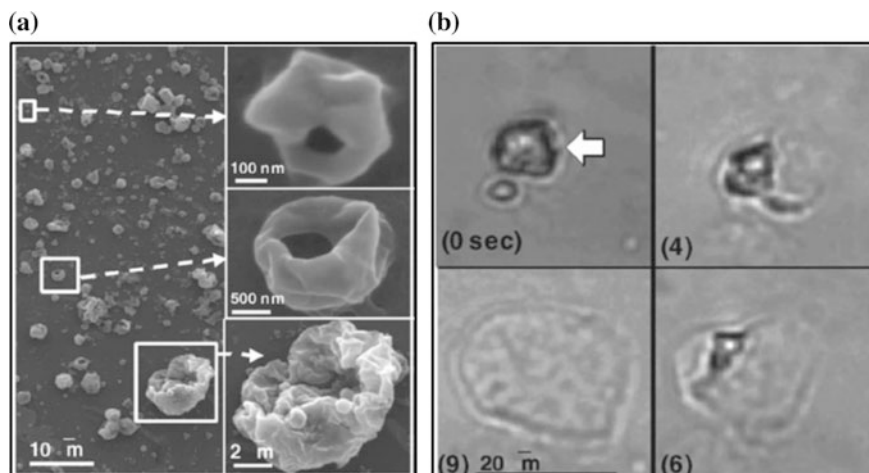
Fig. 6.26 a SEM images of reversibly crosslinked poly(MMA-*co*-MAA/Cyst) particles. **b** Swelling of a particle after exposure to high pH water (time shown in seconds) (Reproduced from Ref. [269] with kind permission of © 2011 Royal Society of Chemistry)
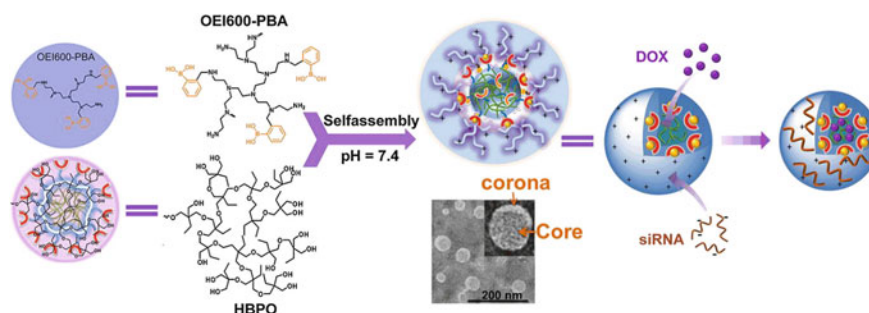
Fig. 6.27 Structural illustration of HBPO-(OEI600-PBA)$_{10}$ nanostructured assembly and its typical TEM image (reproduced from Ref. [270] with kind permission of © 2015 Elsevier)

Beclin1 siRNA and antitumor DOX were used as the therapeutic models in order to suppress the post-chemotherapy survival of tumor cells caused by drug-induced autophagy. The nanoassembly-mediated co-delivery of siRNA together with DOX can effectively silence Beclin1 gene, suppress DOX-induced autophagy, and consequently provide strong synergism with a significant enhancement of cell-killing effects in cultured cancerous cells. The in vivo combinational treatment was shown to make the tumor more sensitive to DOX chemotherapy while displaying substantially improved safety as compared with the monochemotherapy.

6.3.1.1 POSS-Based pH-Responsive Polymer Nanostructures

As we mentioned above in the section of *POSS-based thermoresponsive polymer*, the responsive nanostructures made up of inorganic/organic hybrid polymer containing POSS have gained lot of attention recently. Furthermore, responsive polymeric micelles have been widely studied because of their potential use in nanocontainers and nanocarriers. A tadpole-shaped inorganic/organic hybrid containing poly(tert-butyl acrylate) (P^{t}BA) was prepared by RAFT polymerization using a POSS-containing chain transfer agent (CTA) [271]. POSS-P^{t}BA was further hydrolyzed into amphiphilic, tadpole-shaped POSS-poly(acrylic acid) (POSS-PAA) hybrid nanostructures. The self-assembly of POSS-PAA in aqueous solution at pH 8.5 resulted in the formation of a simple core–shell micellar nanostructures with POSS molecules as the core and PAA as the shell (Fig. 6.28). Apparently, micellar aggregates were formed where the POSS moieties are dispersed in the particle. The aggregates were pH-responsive, and the size contraction occurred upon decreasing the pH from 8.5 to 4.

Ma et al. [272] have developed a POSS end-capped PDMAEMA (POSS-PDMAEMA) organic/inorganic hybrid polymer, a stimuli-responsive (both pH and salt) hybrid synthesized via ATRP technique. The POSS-PDMAEMA hybrid molecules self-assembled into a single unit micelles with the POSS molecules forming a crystal core and the PDMAEMA chains stretching as a corona in aqueous solution. The unit single micelles were then acting as building blocks to reversibly form a hierarchical micelle-on-micelle structure (complex micelle) under external stimuli (Fig. 6.28).

6.3.2 pH-Responsive Ionic Polymer Nanostructure

There are only very few recent reviews that discussed different aspects of pH-responsive ionic polymers [216, 273]. As mentioned above, ionic polymers can be classified as polyelectrolyte, polyzwitterions, poly(ionic liquid)s, etc. Thus, we have separately discussed these different types of ionic polymers in terms of their pH-responsive nanostructure formation in this chapter below.

6.3.2.1 Zwitterionic Polymer Nanostructures

As mentioned above, polyzwitterions can be categorized into two groups (a) polyampholytes and (b) polybetaines. In these types of polymers, the pH-responsiveness arises due to the presence of ionizable cationic or anionic functional groups of zwitterions.
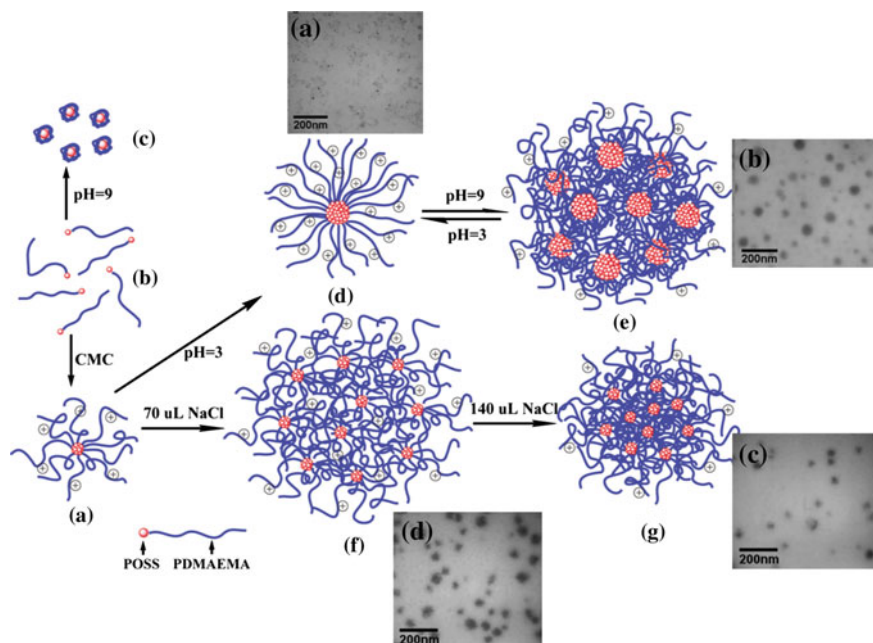
Fig. 6.28 Schematic representation of self-assembly of POSS-PDMAEMA hybrid molecules in aqueous solution at different pH and salt concentration. TEM images of self-assembled micelles of POSS-PDMAEMA in aqueous solution of varying pH values **a** pH 3.0 to **b** pH 9.0 and with **c** 140 and **d** 70 μL of 1 M NaCl in 2 mL of aqueous POSS-PDMAEMA solution (reproduced from Ref. [272] with kind permission of © 2011 American Chemical Society)

Polyampholytes

Polyampholytes, i.e., the copolymers of anionic and cationic monomers could form a homogeneous solution when dissolved in acidic or alkaline solution to achieve a high charge asymmetry, characteristic of common polyelectrolyte. However, the phase transition from a solution to an emulsion could be triggered by adjusting the pH around its isoelectric point (IEP), in which there is no net charge in polyampholytic chain [226, 274]. The typical polyampholytes, including poly(acrylic acid)-*co*-poly(vinylpyridine) (PAA-*co*-PVP) and poly(acrylic acid)-*co*-poly((*N*,*N*-dimethylamino)ethylmethacrylate) (PAA-*co*-PDMAEMA), have been intensively investigated for a detailed understanding on their phase transition behavior and conformational change in solution [226, 274–276]. Liu et al. [262] have demonstrated a new zwitterionic AB diblock copolymer that undergoes spontaneous self-assembly in aqueous solution at ambient temperature to form both micelles and reverse micelles, simply by switching the solution pH, which has been discussed above in detail in Sect. 6.3.1. It should be mentioned here that the P(VBA-*b*-DEA) diblock copolymer is a more hydrophobic analog of the extensively reported ampholytic poly(2-(dimethylamino)ethyl methacrylate)-*b*-(methacrylic acid))

(PDMAEMA-*b*-PMA) diblock and poly(2-(dimethylamino) ethyl methacrylate)-*b*-(methyl methacrylate)-*b*-(methacrylic acid)) (PDMAEMA-*b*-PMMA-*b*-PMA) triblock copolymers [277–286]. In these cases, a series of diblcok PDMAEMA-*b*-PMA and triblock PDMAEMA-*b*-PMMA-*b*-PMA copolymers of varying compositions have been synthesized by Patrickios et al. [285] via group transfer polymerization (GTP). These block polymers showed a strong tendency to precipitate near the isoelectric point. The presence of the hydrophobic block (PMMA) in the triblock copolymer resulted in formation of micelles in water.

Later on, Chen and coworkers reported that the structure of the micelles is such that the hydrophobic PMMA block is always in the center of the micelle, irrespective of the net charge born by the other ionic blocks in the triblock copolymer. Thus, if the PMMA block is between the acid and basic blocks, the micelle diameter is restricted to be about the copolymer contour length, while if the PMMA block is at the end of the molecule, the micelle radius is determined by the polymer contour length [277]. In this connection, it is worthy to mention that Armes and coworkers also synthesized zwitterionic poly(2-(dimethylamino)ethyl methacrylate-*b*-methacrylic acid) (PDMAEMA-*b*-PMAA) copolymers by group transfer polymerization [283, 284]. They further demonstrated that these copolymers underwent reversible micellization in aqueous media as examined through DLS and variable temperature ^{1}H NMR spectroscopy [283, 284].

In an another work, Armes and coworkers first synthesized poly(2-(dimethylamino)ethyl methacrylate-*b*-2-tetrahydropyranyl methacrylate) (PDMAEMA-*b*-PTHPMA) diblock copolymer precursor, which upon hydrolysis readily converted into ampholytic poly(2-(dimethylamino)ethyl methacrylate-*b*-methacrylic acid) (PDMAEMA-*b*-PMAA) block copolymer [287]. Depending on the reaction sequence, two types of zwitterionic SCL micelles were generated from the PDMAEMA-*b*-PTHPMA block copolymer precursors using the 1,2-bis-(2-iodoethoxy)ethane (BIEE) crosslinker (Fig. 6.29). For the synthesis of the Type-I SCL micelles, which have anionic PMAA cores and cationic PDMAEMA coronas, conventional micelles of the PDMAEMA-*b*-PTHPMA precursor were initially prepared in aqueous solution using 5 vol% THF followed by its hydrolysis with HCl. PDMAEMA-*b*-PMAA copolymer self-assembled into micelles with PDMAEMA cores and PMAA coronas, which upon crosslinking with BIEE produced Type-II SCL micelles (cationic cores and anionic coronas) [287]. In contrast, the P(VBA-*b*-DEA) diblock copolymer reported here to form compact, well-defined PVBA-core micelles at low pH and PDEA-core micelles at high pH [262].

Polyzwitterion

Among the different biomimetic zwitterionic groups, such as functional groups of phosphorylcholine (PC), sulfobetaine (SB), and carboxybetaine (CB), CB group is found to be pH-responsive due to the simultaneous presence of the positive quaternary amine group and the negatively charged carboxylate group in the each
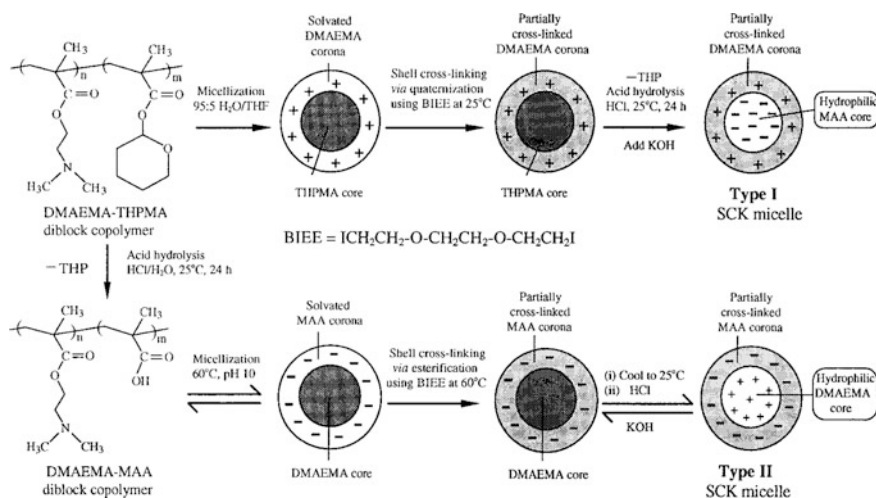
Fig. 6.29 Reaction scheme for the synthesis of Type-I and Type-II zwitterionic SCL micelles. The same block copolymer precursor and crosslinking reagent (BIEE) was used in each route (reproduced from Ref. [287] with kind permission of © 1999 American Chemical Society)

repeating unit. Zwitterionic polycarboxybetaine materials have attracted noticeable interest for biomedical applications, such as wound healing/tissue engineering [288, 289], medical implants [290], and biosensors [291, 292], due to their excellent antifouling properties and design flexibility. Antifouling materials with buffering capability are particularly useful for many biomedical applications.

A pH- and salt-responsive carboxybetaine monomer, 4-(N,N-diallyl-N-methyl-lammonio)-butanoate (DAMAB), was first prepared and then cyclocopolymerized with the cationic monomer N,N-diallyl-N,N dimethylammonium chloride (DADMAC) in 0.5 M NaCl aqueous solution (pH 7.0) using 2-hydroxy-1-[4-(hydroxyethoxy)phenyl]-2-methyl-1-propanone (Irgacure 2959) as the free radical photoinitiator [216]. As per their report, the formed copolymer, PDAMAB-co-PDADMAC with a large excess charge exhibited typical polyelectrolyte behavior, while those with balanced charge exhibit "antipolyelectrolyte" behavior reported for zwitterionic copolymers. Unlike solutions of sulfobetaine-containing polymers [293], PDAMAB-co-PDADMAC remains soluble in water at very low ionic strength even up to 100% incorporation of PDAMAB block. Additionally, the solution of PDAMAB-co-PDADMAC exhibited a pH-dependent viscosity. PDAMAB-co-PDADMAC copolymers with more than 28 mol% of PDAMAB block showed viscosity responsiveness between pH values of 2.5 and 4.5. The maximum pH response was achieved for the solution of PDAMAB-co-PDADMAC containing 37 and 56 mol% of the PDAMAB block containing carboxybetaine monomer.

Zhang et al. [294] prepared five different polycarboxybetaines brushes, including one polycarboxybetaine methacrylate (polyCBMA) and four polycarboxybetaine

acrylamides (polyCBAAs), with different spacer groups from gold surface covered with initiators using surface-initiated ATRP technique. This polymer-coated gold surface was then incubated with fibrinogen, and their adsorption was measured as a function of ionic strengths and pH values using surface plasmon resonance sensors. The responsive protein adsorption on four polyCBAAs brushes was mapped out. Their results showed that most of these surfaces exhibited high protein resistance in a wide range of ionic strengths and are more effective than zwitterionic self-assembled monolayers. Although the protein adsorption tends to increase at low ionic strength and low pH value, it is still very low for polycarboxybetaines with a methylene, an ethylene, or a propylene spacer group but is more evident for polyCBAA with a longer spacer group (i.e., a pentene group). The responses to ionic strengths and pH values can be attributed to the antipolyelectrolyte effect and protonation/deprotonation properties of polycarboxybetaines, respectively. It has been believed that since sulfonic acid is a strong acid, no hydrolysis or association occurs for aqueous polysulfobetaine systems. Consequently, pH-sensitive properties could only exist in aqueous polycarboxybetaines systems, and it was absent or rather weak at least, in aqueous polysulfobetaine systems [295, 296]. However, several research groups have systematically investigated the pH-sensitive properties of aqueous polysulfobetaine systems. It was revealed then that even aqueous polysulfobetaine systems can exhibit a series of pH-sensitive solution properties [286, 297].

In continuation with polycarboxybetaines, Thayumanavan et al. have been reported a one-pot synthesis of acrylamide-based zwitterionic amphiphilic homopolymers with hydrophilic and hydrophobic components placed orthogonally in every repeat unit (Fig. 6.30) [298]. Here, they have introduced glycinebetaines
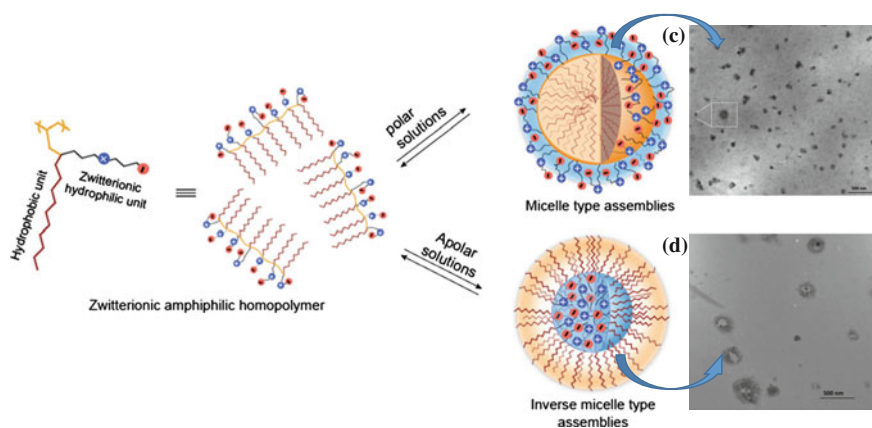

Fig. 6.30 Schematic representation of solvent dependent self-assembled aggregates formation of zwitterionic amphiphilic polymers. *Inset* shows the TEM images of the micellar and inverse micellar assemblies (reproduced from Ref. [298] with kind permission of © 2015 Royal Society of Chemistry)

unit as charge-neutral, zwitterionic, hydrophilic moieties in amphiphilic homopolymers. Due to the presence of zwitterionic hydrophilic glycinebetaines component in the polymer, it reversibly switched between cationic, zwitterionic, and anionic forms depending on the pH of the solution. These zwitterionic polymers spontaneously self-assembled into micelle-like and inverse micelle-like assemblies depending on the solvent environment and act as hydrophilic and hydrophobic nanocontainers in apolar and polar solvents, respectively (Fig. 6.30). Moreover, they have shown pH-responsive surface charge and size variations of the micelles.

Recently, Cheng and coworkers designed and synthesized an integrated zwitterionic polymeric material, poly(2-((2-hydroxyethyl)(2-methacrylamidoethyl)ammonio)acetate) (PCBMAA-1T), to investigate its many interesting properties such as antifouling, switchability, and buffering capability [299]. A tertiary amine was used to replace quaternary ammonium as the cation to endow the materials with buffering capability under neutral pH (Fig. 6.31). The tertiary amine cation does not compromise antifouling properties of zwitterionic materials. The amount of adsorbed proteins on PCBMAA-1T polymer brushes is less than 0.8 ng/cm^2 for fibrinogen and 0.3 ng/cm^2 (detection limit of the surface plasmon resonance sensor) for both undiluted blood plasma and serum. It was reported that the tertiary amine was favorable to obtain good lactone ring stability in switchable PCB materials. Titration study showed that PCBMAA-1T could resist pH changes under both acidic (pH 1–3) and neutral/basic (pH 7–9) conditions. To the best of our knowledge, such an all-in-one material has not been reported earlier. We believe this material can be potentially used for a variety of applications, including tissue engineering, chronic wound healing, and medical device coating.
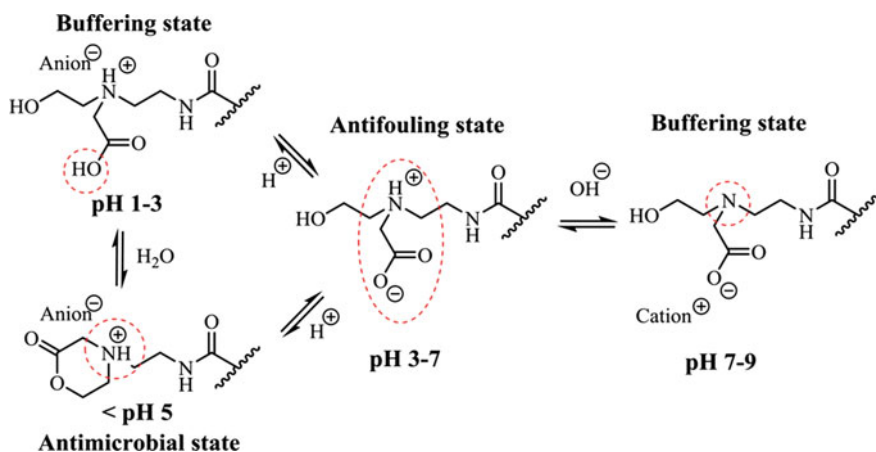

Fig. 6.31 Switchable charged state of CBTAA-1 in different conditions (reproduced from Ref. [299] with kind permission of © 2015 American Chemical Society)

Amino Acid-Based Zwitterionic Polymer

Incorporation of biologically active amino acid moieties into the polymer main chain or side chain induces better biocompatibility of the resulting biopolymers [300]. This has drawn to the focus of polymer scientists in recent times for synthesizing stimuli-responsive amino acid-based polymer architectures [301, 302]. In these cases, the pH-responsiveness arises due to the presence of ionisable zwitterionic functional groups (–COOH and –NH$_2$) of amino acids. Although, zwitterionic amino acid-based polymers are interesting, but are less investigated class of ionic polymers [303, 304]. There are some excellent recent reviews discussing the developments of amino acid-based polymers with stimuli-responsive properties [305–307]. Furthermore, several different zwitterionic polymers based on lysine, cysteine, ornithine, aspartic acid, and glutamic acid have been developed and investigated their potential protein and bacterial resistivity [303, 308–310].

Recently, Liu et al. [311] have reported synthesis of zwitterionic poly(serine methacrylate) brushes from gold surface via a surface-initiated photoiniferter-mediated polymerization with good antifouling property which has comparable protein resistivity with zwitterionic poly(sulfobetaine). Lu et al. [312] have designed a L-histidine-based zwitterionic polymer which exhibited soluble–insoluble phase transition depending upon pH of the solution in addition to its antiprotein-adsorptionability. Furthermore, there is another report of synthesis of two different types of methacrylic polybetaines bearing trans-4-hydroxy-L-proline connected via its hydroxyl group, one with an aliphatic spacer of 6 carbon atoms and the other without any spacer [313]. These two polyzwitterions showed pH sensitivity in aqueous media having an isoelectric point (IEP) close to 3. Swelling of networks prepared from these two monomers exhibited reversible pH sensitivity; the largest the pH distance from the IEP, the higher the net charge (positive or negative) and the higher the swelling. At basic pH and an ionic strength of 0.15, maximum swelling degrees of around 11 and 24 (water/gm of polymer) have been found for these systems with and without spacer, respectively [313].

Our group had reported a L-lysine-based zwitterionic polymer which showed Cu (II) ion-induced pH-responsive nanogel aggregate formation [314]. A convenient and water-based approach was described for the synthesis of an L-lysine-based zwitterionic polymer, poly(ε-L-lysinyl acrylamide) (PLAM), by conventional radical polymerization technique. PLAM contained both amine and carboxylic acid groups in each repeating unit, which can either be protonated or deprotonated just by altering the pH of the solution to obtain overall positive or negative charge in the polymer chain. PLAM is tested for its applicability as a zwitterionic polymeric buffer in water. Spherical nanogel aggregates were formed at pH 9.5 due to aggregation of PLAM through its complexation with Cu(II) ion. Spherical aggregates appeared to dissociate via breaking of the complexation at a pH < 5.5 resulting in molecular dissolution of PLAM. The aggregation process was pH-reversible. The Cu(II)–PLAM aggregates are used as a template for generations of CuO and CuS nanoparticles (Fig. 6.32) [314].
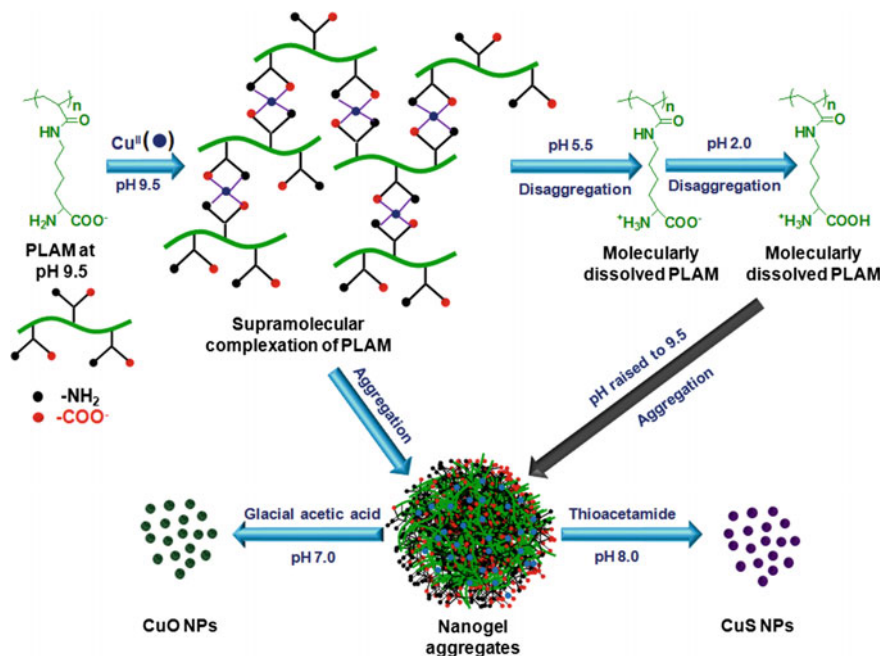
Fig. 6.32 Schematic illustration of Cu(II)-induced aggregation of PLAM into nanogel spheres at pH 9.5, its pH response and generation of CuO and CuS nanoparticles [PLAM] = 0.1 wt% (Reproduced from Ref. [314] with kind permission of © 2013 Wiley-VCH)

Furthermore, we have extended this approach to synthesize L-serine-based zwitterionic polymers, poly(L-serinyl acrylate)s, which exhibited an interesting dual-responsive behavior with respect to pH and temperature in aqueous solution [315]. The details of this responsive system will be discussed in the Sect. 6.10.1.

Poly(ionic liquid) Nanostructures

Another important class of ionic polymer is the PILs. Recently, our group has demonstrated pH-dependent self-aggregation behavior of an imidazolium-based PIL hybrids [316]. Here, we have synthesized semitelechelic POSS-poly(vinyl imidazole) (POSS-PVim) hybrid via simple radical polymerization technique using thiol-functionalized POSS as initiator as well as chain transfer agent (Fig. 6.33). Amphiphilic POSS-PVim hybrid molecules self-assembled into primary micelles in water as well as in DMF. These primary micelles further aggregated into hybrid nanospheres in an aqueous solution of pH 6. It was observed that there was a complete transformation of morphology from spherical aggregates to large cube, pyramid, and even chain-like aggregates composed of polygons with delicate variation of solution pH. It was proposed that such higher order aggregated
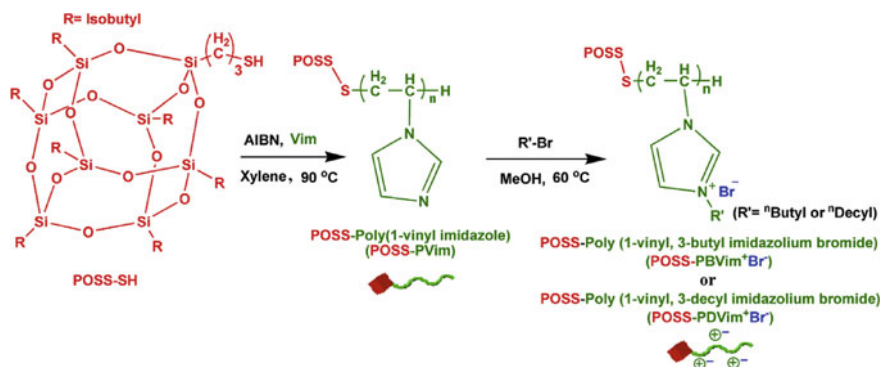
Fig. 6.33 Synthetic scheme for preparation of semitelechelic POSS-PVim hybrid and POSS-PIL hybrids (reproduced from Ref. [316] with kind permission of © 2015 Elsevier)
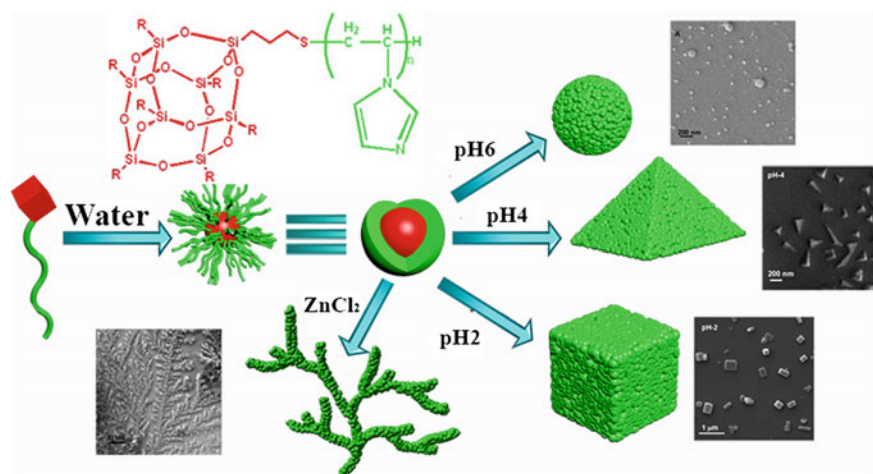
Fig. 6.34 Schematic representation of self-aggregation of semitelechelic POSS-PVim hybrid into nanostructures of different shapes under different conditions and their typical TEM images (reproduced from Ref. [316] with kind permission of © 2015 Elsevier)

structures were formed due to the ionic secondary interactions among the polymer in the outer layer of the spherical primary micelles. Surprisingly, it was also found that the addition of Zn(II) ion in the solution of POSS-PVim hybrid produced dendritic nanostructures composed of primary spherical micelles. Furthermore, two different POSS-PIL hybrids are prepared by post-modification of pendent imidazole groups of PVim block of POSS-PVim hybrid with different 1-bromoalkanes of varying chain lengths. POSS-PIL hybrid molecules also self-aggregated in water to generate cubic hybrid nanostructures (Fig. 6.34). The combined zeta potential and XRD analyses provided further evidence in favor of secondary aggregation of initially formed spherical primary micelles.
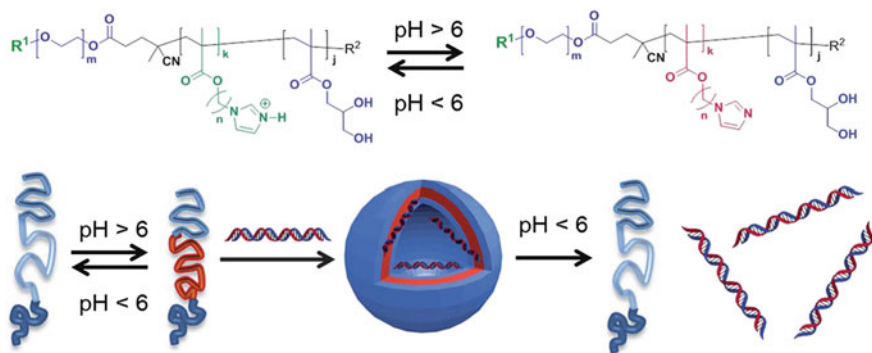
Fig. 6.35 Self-assembly of pH-responsive triblock copolymers. Deprotonation of the central imidazole-containing blocks above a critical pH ranges causes self-association of hydrophobic components and formation of polymer nanoparticles. Assembly of nanoparticles in the presence of short DNA strands results in encapsulation of nucleic acids, which can be released subsequently by a pH switch (reproduced from Ref. [317] with kind permission of © 2014 Royal Society of Chemistry)

Recently, a new pH-sensitive PIL has been designed by Matini and coworker [317], through incorporating pH-responsive imidazolic units at varying distance in a polymer backbone to generate materials that can be tuned to exploit specific local conditions for therapy. Variation in comonomer content, molar mass, and block ratios/compositions affected the pH-responsiveness of this PIL. As a result, the PIL molecules were undergone reversible self-assembly into either micelles and/or polymersomes (Fig. 6.35). These transitions can be tuned to achieve environmental responses in a pH range from 5 to 7, as shown by turbidimetric analysis, NMR, and dynamic light scattering measurements (DLS). Further characterization by TEM indicated that polymersomes with diameters of 100–200 nm can be formed under certain pH ranges where the weakly basic side-chains were deprotonated. The ability of the systems assembled with these polymers to act as pH-responsive containers was shown by DNA encapsulation and release studies, and their potential for application as vehicle for drug delivery was proved by cell metabolic activity and cell uptake measurements.

In another study, the hydrophobically associating cationic polyacrylamides (C-HAPAM), containing a major part of hydrophilic polyacrylamide backbones and a minor part of ionic hydrophobic groups, i.e., N,N'-dimethyloctadeyl allyl ammonium chloride (DOAC), were synthesized via free radical polymerization by Lu et al. [318]. They have investigated the self-assembling behaviors of the C-HAPAM molecules in water under different concentrations and pH values [318]. The critical aggregate concentration (CAC) for C-HAPAM was about 0.42 wt% and a solution-sol–gel transition has been observed for C-HAPAM aqueous solutions with increasing concentration. Rheological tests demonstrated a pH-reversible sol–gel transition when the pH was regulated from its original value of 7.45 to the weak alkaline value of 9.87 by adding NaOH and then switched back to 5.28 by

adding HCl. The sol–gel transition was actually attributed to the fiber-network aggregate structure transition as shown by SEM, AFM, and DLS analyses. The mechanism of above-mentioned pH-responsive self-assembling behavior was explained by the remarkable counter ion effect of OH^-. Specifically, they proposed that the OH^- ion was additionally capable of H-bonding with surrounding water molecules which promoted the solvation of C-HAPAM and induced thick hydration layer. The strong counterion effect of OH^- ion and the inter-molecular hydrophobic association interactions of C-HAPAM collectively triggered the formation of joints and hence the network structure transition, i.e., sol–gel transition.

6.4 Light-Responsive Polymer Nanostructures

The polymeric materials responsive to external stimuli such as light has attracted much attention since light can be localized in time and space and can be applied from outside of the system [144]. Indeed, photo processes usually start or stop when the light is switched on or off and generates only very limited amount of byproducts as there are no additional reactants [39]. In addition to this, a lot of parameters such as wavelength as well as intensity of light can also be tuned for achieving good control over the reaction. In these contexts, the wavelength of light ranging from hard UV right up to the deep infrared can be applied that allow a high diversity in tuning the light-responsive polymer system which cannot be offered by any other stimulus. The use of light as an external stimulus to control the properties of polymer nanostructures such as micelles, vesicles has started being mostly exploited since 2004. Developing polymer systems that can undergo micellization/demicellization upon light irradiation is an attractive idea that would allow external control of drug encapsulation and release.

Different kinds of photochromic units shown in Fig. 6.36 such as *o*-nitrobenzyl [319], azobenzene [320], coumarinyl [321], pyrenylmethyl [322], spiropyran [323] spirooxazine [324], and fulgide [53] can be introduced into the polymers or block copolymers of different amphiphilicity to make them photoresponsive. The first demonstration of photocontrollable nanostructured polymeric micelles was reported in 2004 by Zhao and coworkers [325]. Since then, there has been growing interest in designing and developing polymer nanomaterials whose aggregation states and functions can be controlled by light irradiation. Matyjaszewski and coworkers showed that the light can be employed as an effective tool to release encapsulated substance from light-responsive block copolymer micelles [326].

Zhao et al. [327] recently wrote an excellent review on different types photoresponsive polymer and block copolymer systems. As compare to other stimuli, light enables more temporal and positional control over photoprocess, and we can trigger the secondary structure formation, function, and properties of polymer systems simply by shining light from outside of the system; these materials have potential application in diverse field including light triggered controlled delivery of drugs, "smart" optical systems, biosensors, and responsive coatings. Here, we
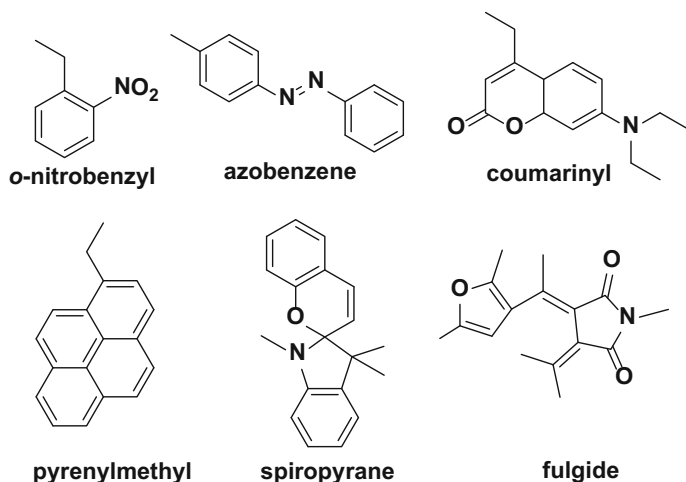
Fig. 6.36 Chemical structures of photoresponsive functional groups

should mention that even one light-responsive unit can be sufficient to influence the properties of the whole polymer chain within a light-responsive polymer system [328]. The summary of different photosensitive groups that have been incorporated so far into the polymer and block copolymer systems as well as their potential applications are discussed in the following section.

6.4.1   o-Nitrobenzyl Functional Group Containing Polymer Nanostructures

In this regard, *o*-nitrobenzyl ester (NBE) is a promising class of photoresponsive group and is used diversely in synthetic polymers or block copolymers to make them photosensitive. Photolysis of *o*-nitrobenzyl moieties proceeds irreversibly via Norrish II type intra-molecular rearrangement (Fig. 6.37) in the presence of UV light of wavelength 365 nm as well as near infrared light of wavelength 700 nm, and it does not require any solvents [329]. Zhao and coworkers are the first to describe how to obtain a photosensitive amphiphilic block copolymer containing *o*-nitrobenzyl ester (NBE) functionality [319]. They used ATRP technique to synthesize diblock copolymer with PEO as a hydrophilic block and a hydrophobic block of poly(2-nitrobenzylmethyl methacrylate) (PNBMA) (Fig. 6.38). As shown in Fig. 6.38, the block copolymer self-aggregated into well-dispersed spherical micelles in an aqueous medium. Upon UV irradiation ($\lambda = 350$ nm), the photocleavage of the PNBMA block of the PEO-*b*-PNBMA BCP takes place, and that leads to the formation of the doubly hydrophilic poly(ethylene oxide)-*b*-poly (acrylic acid) (PEO-*b*-PAA) BCP causing the rupture of core–shell micelles
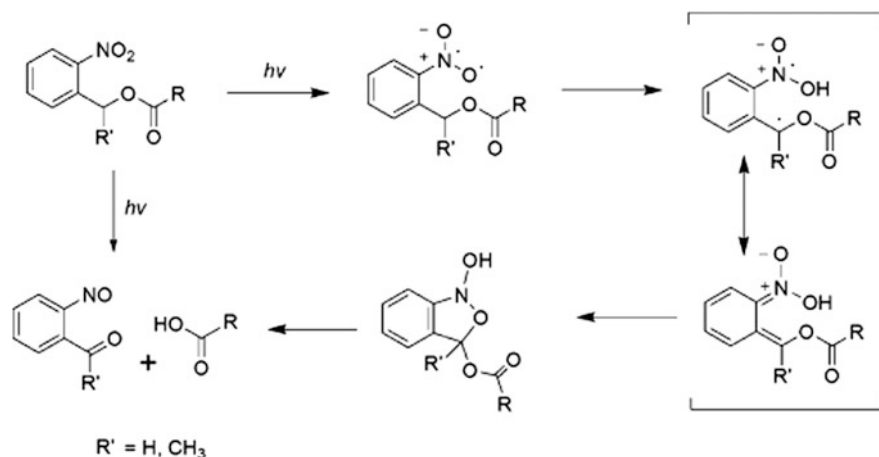
Fig. 6.37 Photoisomerization mechanism of *o*-nitrobenzyl alcohol derivatives into *o*-nitrosobenzaldehyde and carboxylic acid

(Fig. 6.38), and the release of the encapsulated guest molecules have been observed.

We have also involved in designing photoresponsive block copolymer. We have prepared a novel amphiphilic BCP namely poly(2-ethyl-2-oxazoline)-*b*-poly (2-nitrobenzyl acrylate) (PEtOx-*b*-PNBA) via combination of microwave-assisted cationic ring-opening polymerization CROP and ATRP [330]. The amphiphilic nature of this BCP causes them to self-assemble into primary micelles in THF/H$_2$O, which further undergo secondary aggregation into nanostructured micellar agglomerates (Fig. 6.39). Upon UV light (λ = 360 nm) irradiation, the photolysis reaction of 2-nitrobenzyl ester group takes place which results in the cleavage of 2-nitrosobenzaldehyde from the polymer, which transformed the hydrophobic PNBA into the hydrophilic poly(acrylic acid) (PAA) and triggered the micellar dissociation (Fig. 6.39). Photocontrolled release of a loaded hydrophobic dye, Nile Red (NR), from an aqueous micellar solution of PEtOx-*b*-PNBA upon UV light irradiation was investigated by monitoring the fluorescence emission of NR (Fig. 6.39). As a result of the photocleavage of NBE moiety of PNBA block upon UV irradiation, there was a disruption of NR-loaded BCP micelles/micellar agglomerates, consequently leading to the release of NR from hydrophobic micellar core to water medium outside the micelles. However, the NR is insoluble in water, which results in the decrease of the fluorescence intensity of NR present inside the micellar core with increasing UV irradiation time that, in turn, proves the release of NR dye (Fig. 6.39).

As mentioned above that even one light-responsive unit can be sufficient to influence the properties of the whole polymer chain. In this context, Kang and Moon described the synthesis of an easily cleavable polystyrene-*b*-poly(ethylene oxide) (PS-*ONB*-PEO) block copolymer by ATRP technique in which a
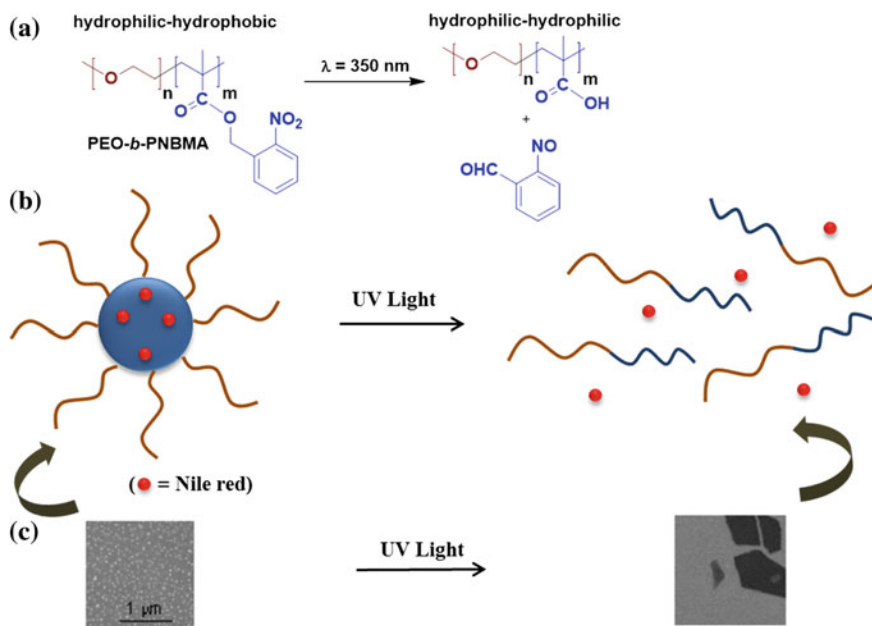
Fig. 6.38 Chemical structure and photocleavage reaction of *o*-nitrobenzyl group containing amphiphilic BCP (**a**); schematic representation of controlled release of an encapsulated guest molecule as a result of the photoinduced dissociation of the polymer micelle (**b**) and SEM images revealed the formation of core-shell micelles from aqueous BCP solution before irradiation and the disappearance of the micelles after 20 min of UV irradiation (**c**) (reproduced from Ref. [319] with kind permission of © 2006 American Chemical Society)

photochemically sensitive *o*-nitrobenzyl (ONB) group was installed as a linker (Fig. 6.40) [331]. According to their report, the BCP cleaved into individual PS block and PEO block upon exposure to UV light at 350 nm in solution (Fig. 6.40). Cleavage upon irradiation with UV light was also shown to be successful in solid state. The as-cast PS-*ONB*-PEO film showed vertically aligned cylindrical morphology which transformed completely into nanoporous structure after UV light irradiation followed by washing with MeOH/H$_2$O (Fig. 6.40).

Recently, Fustin and coworkers developed a more versatile synthetic route using one pot combined ATRP and "click" reaction techniques to prepare a series of BCPs such as PEO-*ONB*-PS, poly(ethylene oxide-*ONB*-poly(ᵗbutyl acrylate) (PEO-*ONB*-PᵗBA), and polystyrene-*ONB*-poly(methyl methacrylate) (PS-*ONB*-PMMA), with narrow dispersities containing a single photocleavable ONB junction (Fig. 6.41) [332]. Photocleavage of this diblock copolymer by UV light (λ = 300 nm) was demonstrated for PEO-*ONB*-PS in solution to be complete after 15 min, as proven by size-exclusion chromatography (SEC) and UV-visible spectroscopy (Fig. 6.41). Their synthetic procedure avoids the preparation of a macroinitiator (PEO-*ONB*-Br in Fig. 6.40), which is often more difficult to synthesize than small molecule initiators (Fig. 6.41).
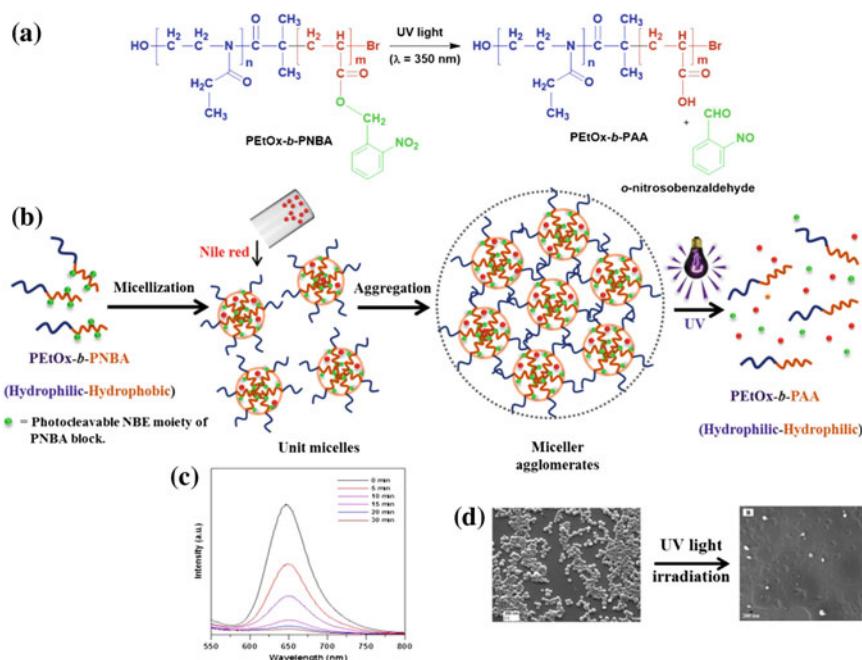
Fig. 6.39 Schematic representation of the photocleavage of *o*-nitrobenzyl group containing amphiphilic PEtOx-*b*-PNBA BCP (**a**); Schematic representation for self-aggregation of BCP into unit micelles/micellar agglomerates and its UV-induced disruption (**b**); Fluorescence emission spectra of NR encapsulated aqueous micellar solution of PEtOx-*b*-PNBA BCP upon UV light irradiation for different times. Fluorescence emission of NR gradually decreases due to the release of NR molecules from BCP micellar core into water (**c**) and FESEM image showing the self-assembly of PEtOx-*b*-PNBA BCP into micellar agglomerates before UV irradiation and disruption of micellar association after 45 min of UV irradiation in THF/H$_2$O mixture (**d**) (reproduced from Ref. [330] with kind permission of © 2016 American Chemical Society)

Coughlin and coworkers extended this synthetic strategy to prepare PS-*ONB*-PEO containing single photocleavable ONB junction (Fig. 6.42) by the combination of RAFT polymerization and a subsequent intermacromolecular azide-alkyne "click" reaction, providing more flexibility in synthesis of photocleavable block copolymers [333]. A highly ordered thin film was prepared from this photocleavable BCP and after photoetching the resulting nanoporous film was used to prepare highly ordered array of silica nanodots by the treatment of PDMS and oxygen plasma (Fig. 6.42). This was the first example of preparation of silica nanostructures from a photocleavable polymer template. Block copolymers having photocleavable junction recently attracted much attention toward research community to prepare nanoporous thin films for nanopatterning, separation membranes, and sensors.

Apart from the fabrication of well-ordered nanoporous thin film application, block copolymers with a ONB junction also have some use in the
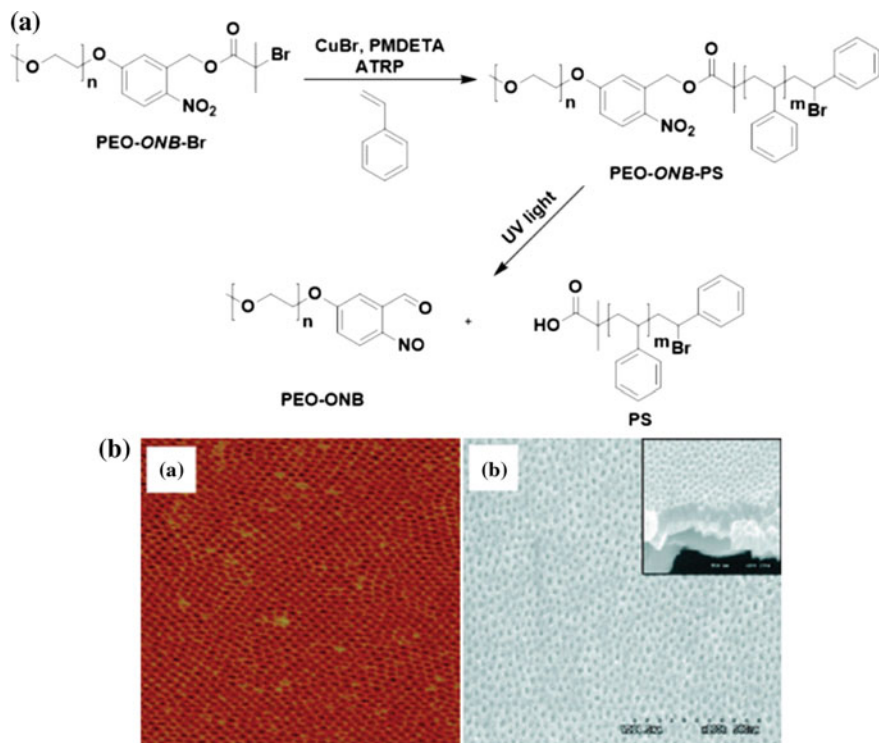
Fig. 6.40 Synthesis and photolysis of PS-*ONB*-PEO BCP by UV light irradiation (350 mn) (**a**); AFM image (*A*) of PS-*ONB*-PEO BCP (23.7-*b*-5.0 K) films (*thickness* = 43 nm) spin-coated onto silicon wafers and solvent annealed for 2 h in benzene/water mixed solvent and SEM image (*B*) of the nanoporous PS thin film resulting from photocleavage and selective solvent removal (methanol/water) of PEO phase. A side view (45°) is shown in the *inset* image of B (**b**) (reproduced from Ref. [331] with kind permission of © 2008 American Chemical Society)

encapsulation/release of guest molecules through, for example, a polymersome-micelle transition. In this regard, Meier and coworkers reported the synthesis of a new amphiphilic BCP, poly(γ-methyl-ε-caprolactone)-*ONB*-poly (acrylic acid) (P*m*CL-*ONB*-PAA), with a ONB junction by ring-opening polymerization and ATRP techniques [334]. Here, a dual initiator based on ONB was synthesized and used for the preparation of doubly hydrophobic poly(γ-methyl-ε-caprolactone)-*ONB*-poly(ᵗbutyl acrylate) (P*m*CL-*ONB*-PᵗBA) (by sequential ring-opening polymerization (ROP) of *m*CL and ATRP of ᵗBA (Fig. 6.43). Afterward, the PᵗBA block was hydrolyzed, resulting in the formation of amphiphilic diblock copolymer and P*m*CL-*ONB*-PAA (Fig. 6.43).

The amphiphilic BCPs were shown to self-assemble into different nanostructures including micelles and vesicles that can be degraded by light, as demonstrated by a decrease in the size of the aggregates after UV irradiation (Fig. 6.44). These BCP
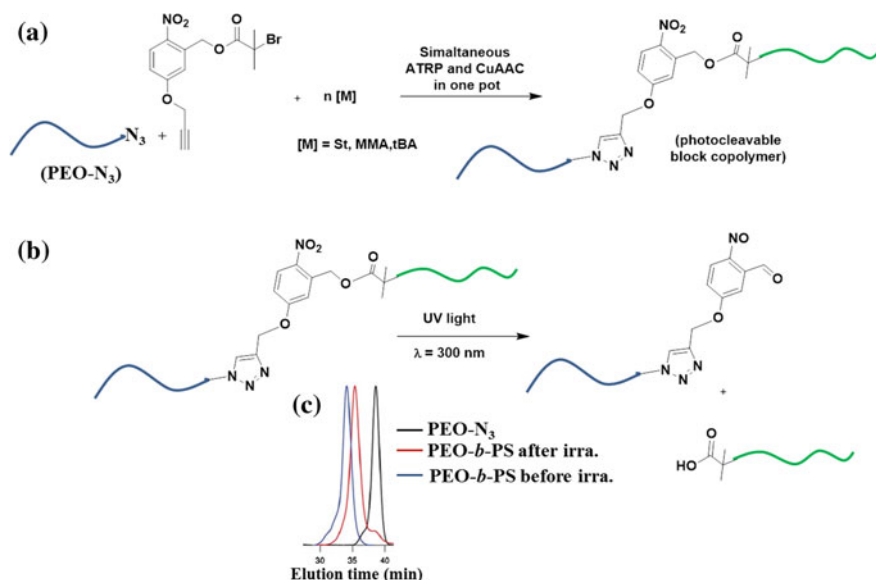
Fig. 6.41 Synthesis of block copolymers with a photocleavable junction between the blocks by one-pot simultaneous ATRP–CuAAC "click" reaction techniques (**a**); products obtained after photoirradiation of such block copolymers (**b**) and SEC traces of starting PEO-N₃ block, PEO-*ONB*-PS before UV irradiation and PEO-*ONB*-PS after UV irradiation (**c**). SEC traces of BCP shifted to the higher retention after UV irradiation indicating the occurrence of photocleavage (reproduced from Ref. [332] with kind permission of © 2010 Royal Society of Chemistry)

systems can be applied as efficient light-responsive nanocarriers for hydrophilic as well as hydrophobic guest molecules.

PCL-based BCP having an ONB photocleavable junction have also been investigated by Nojima et al. They synthesized a PS-*ONB*-PCL diblock copolymer with an ONB-based junction. They clearly showed that this synthesized BCP possesses a nanostructured cylindrical morphology and the crystallization behavior of the PCL chains behaves very differently before and after irradiation with UV light, as a result of the cleavage of the PCL chains [335]. An alternative synthetic strategy was reported by Zhao and his coworkers where they incorporated a photodegradable polyurethane block (PUNB) in the middle of an amphiphilic triblock copolymer, PEO-*b*-PUNB-*b*-PEO (Fig. 6.45) [336]. Here, the short polyurethane middle block was composed of multiple *ONB* units that allowed a fast photodegradation of the micelles in solution (Fig. 6.45). The release of a model hydrophobic guest, Nile red (NR) from aqueous BCP micellar solution upon photoinduced disintegration of the micelle core was also investigated in this study.

However, light-responsive BCP has been largely used for micelle disruption and drug release but only few examples of light-induced micellization have been reported [325, 326]. Gohy and his coworkers reported a different synthetic approach to synthesize *ONB* group containing BCP composed of a poly
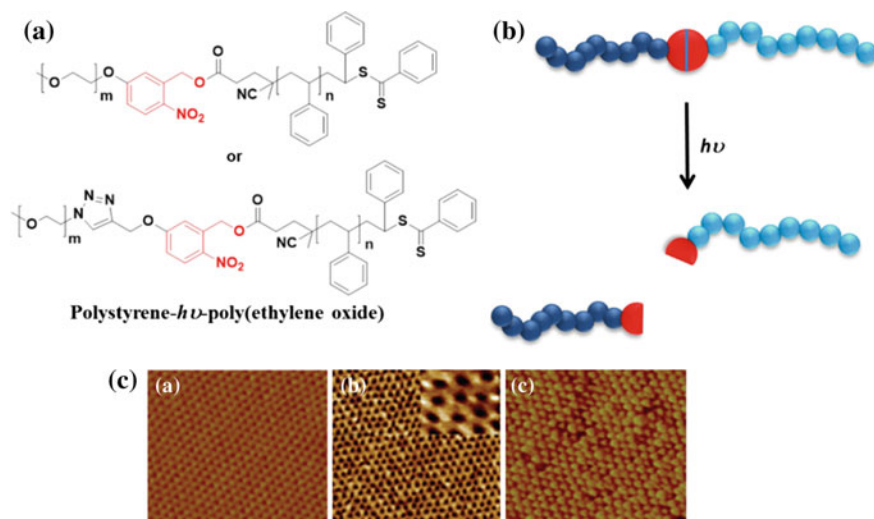
Fig. 6.42 Chemical structures PS-*b*-PEO BCP having photocleavable *ONB* junction prepared by RAFT polymerization (**a**); schematic illustration of photolysis of the PS-*ONB*-PEO BCP into two constituent block (**b**); AFM image (*A*) of solvent annealed thin film of PS-*ONB*-PEO containing photocleavable ONB junction before UV irradiation and AFM image (*B*) of the nanoporous PS film after UV light irradiation followed by rinsing with a solvent to selectively remove PEO domains and AFM image (*C*) of silica nanodots obtained from nanoporous film by the treatment of PDMS and oxygen plasma (**c**) (reproduced from Ref. [333] with kind permission of © 2011 American Chemical Society)

(4,5-dimethoxy-2-nitrobenzyl acrylate) block and of a polystyrene block (PDMNBA-*b*-PS) [337]. This BCP has been synthesized by grafting a derivative of 4,5-dimethoxy-2-nitrobenzyl onto poly(acrylic acid)-*b*-polystyrene precursor copolymers (PAA-*b*-PS) prepared by ATRP. Upon light illumination, cleavage of the side chromophores takes place, and consequently, PDMNBA block is turned into a fully hydrophilic PAA block which is insoluble in the chloroform) (Fig. 6.46). Self-assembly of PAA-*b*-PS thus takes place, forming micelles made of a PAA core and a PS corona (Fig. 6.46). In addition, they have also demonstrated the ability of their system to act as a trapping agent by the encapsulation of coumarin 343 into the micellar core produced during the irradiation of the block copolymers in solution (Fig. 6.46).

Light-induced micellization could be very promising in the field of encapsulation, notably because the trapping process can start whenever it is needed and have some robust application such as in situ product removal [338] or product separation by micellar extraction [339]. ONB side chain functional group can also be introduced into the polymer for thin film patterning application. Doh et al. designed a terpolymer poly(*o*-nitrobenzyl methacrylate-*co*-methyl methacrylate-*co*-(ethylene glycol) methacrylate) (P(*o*-NBMA-*co*-MMA-*co*-EGMA)) to prepare thin film patterns on the micrometer scale [340]. They showed that for a terpolymer with
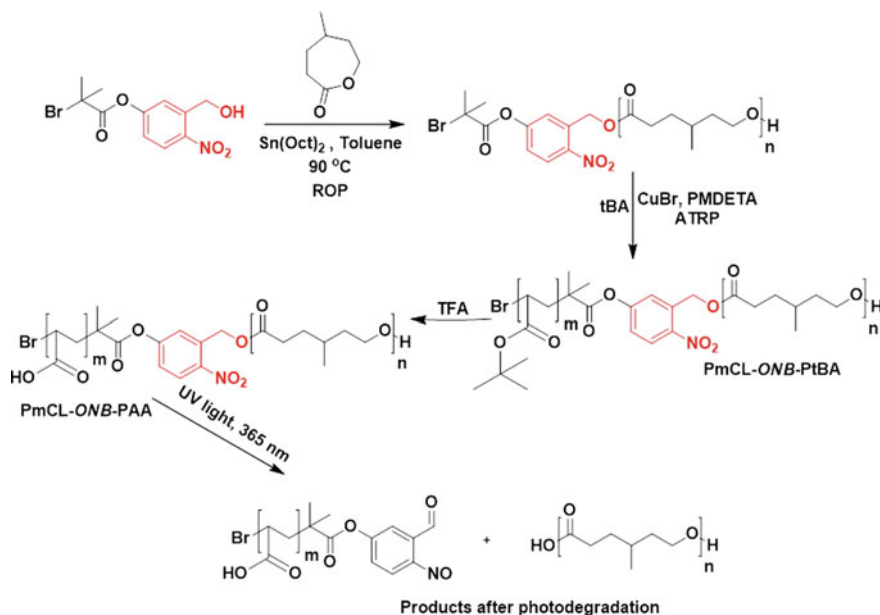
Fig. 6.43 Synthetic procedure for the preparation of PmCL-*ONB*-PAA diblock copolymers and their photodegradation (redrawn from Ref. [334] with kind permission of © 2010 Wiley-VCH)

composition of 43 wt% of *o*-NBMA, 38 wt% of MMA, and 19 wt% of EGMA, the exposed areas of a thin film could be dissolved by phosphate-buffered saline (PBS) after UV irradiation (Fig. 6.47). Bowman, Khire, and coworkers immobilized ONB acrylate functional moieties on the surface of silica nanoparticles simply by acid amine coupling and used them to grow linear polymers by thiolene "click" chemistry. Upon exposure to UV light, the graft copolymers are released and analyzed and they were found to be similar to polymers formed in bulk [341].

6.4.2 Azobenzene-Based Polymer Nanomaterials

Azobenzene containing polymers and block copolymers (BCPs) have attracted much attention in the active research field mainly because of the reversible *cis–trans* photoisomerization of azobenzene present in the system upon UV light irradiation [40]. In this process of photoisomerization, the apolar *trans*-isomer can be converted to the polar *cis*-isomer upon UV irradiation, and the process is reversible with respect to visible light irradiation. Indeed, morphology and related self-organized nanostructures of azobenzene containing BCPs can be easily tuned reversibly by simple exposure of UV light in solution. Previously, azobenzene containing polymers synthesized via anionic polymerization or post-functional
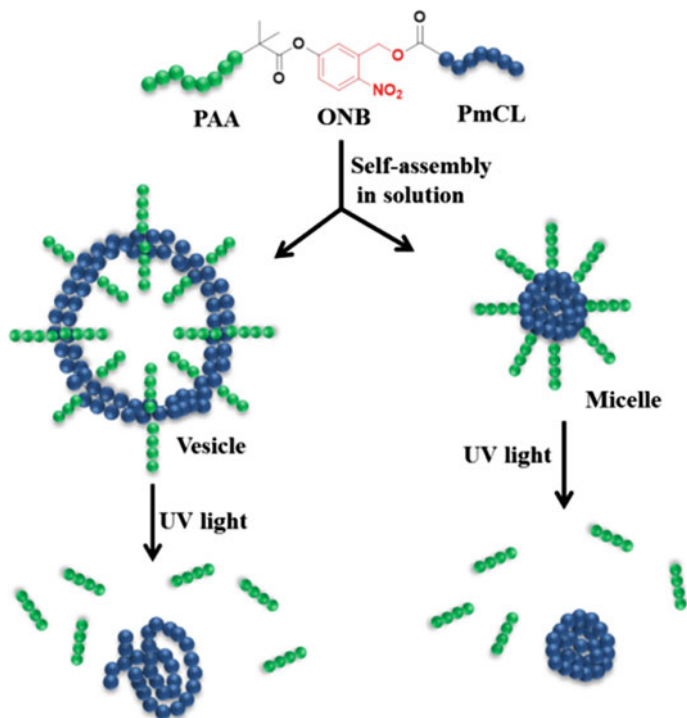
Fig. 6.44 Schematic representation of photocleavable nanocarriers (micelles, vesicles) formed by the self-assembly of PmCL-*ONB*-PAA BCP in solution (redrawn from Ref. [334] with kind permission of © 2010 Wiley-VCH)

modification was mainly used as a mesogen for liquid crystalline polymers (LCPs) [342–344]. In recent years, the interest in azo-BCPs has been stimulated by the accessibility of several controlled radical polymerizations techniques such as ATRP [47] and RAFT polymerization [345]. Thus, a growing number of studies on azobenzene containing BCPs have been reported by many researchers. It should be noted that *trans-cis* photoisomerization of Azo-BCPs may affect the nanostructure morphology of the system. Kadota et al. demonstrated a novel ABA-type triblock copolymer, where A and B correspond to azobenzene (Azo) containing poly (methacrylate) and PEO, respectively, was synthesized by ATRP [346]. Here, an Azo-containing methacrylate monomer was polymerized from both ends of a PEO-based ATRP macroinitiator using CuBr/HMTETA catalyst systems to synthesize the triblock copolymer (Fig. 6.48). The monolayer thin film on mica with *trans*-Azo groups displayed morphology with a mixture of dot- and rod-shaped microdomains of the Azo polymer block (Fig. 6.48). However, they observed morphology transformation to long stripes of the microdomains when the *trans*-Azo film was exposed with UV light irradiation due to conversion into its *cis*-isomer (Fig. 6.48).
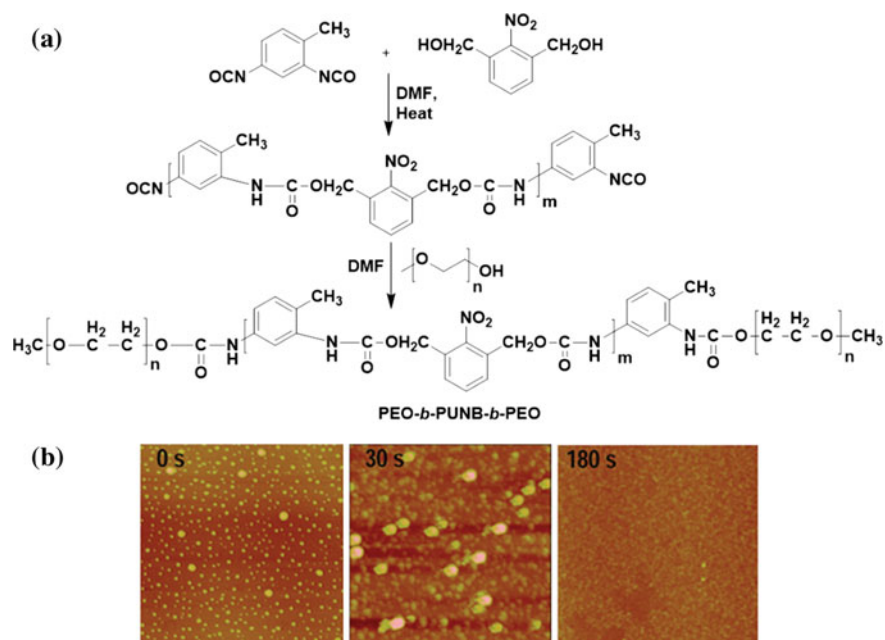
Fig. 6.45 Synthetic route to the triblock copolymer of PEO-*b*-PUNB-*b*-PEO (**a**); AFM height images of the micelle solution cast on mica before and after UV irradiation (30 and 180 s) (*image area*: 2 μm × 2 μm) (**b**). It clearly showed the complete disappearance of micellar aggregates after 3 min of UV irradiation (reproduced from Ref. [336] with kind permission of © 2011 American Chemical Society)

This photoinduced change of morphology from *trans* to *cis*-form was ascribed to an anisotropic expansion of the microdomains with Azo groups in the *cis*-form, as the more polar *cis*-isomer became in contact with the water surface. The microdomain expansion was also followed in reduction of the height difference from 1.70 ± 0.25 nm for the film with the *trans*-isomer to 1.05 ± 0.250 nm for the film with the *cis*-isomer. Reversible photoisomerization process of azo benzene system has also been utilized by Zhao and coworkers to design a micellar system that is disrupted upon UV irradiation and reforms itself when irradiated with visible light [325, 347]. They reported a diblock copolymer containing on one side a hydrophilic random poly(*t*butyl acrylate-co-acrylic acid) (P(*t*BA-*co*-AA)) block and on the other side a poly(methacrylate) bearing azobenzenes as pendent groups (PMAzo) (Fig. 6.49).

Spherical micelles and/or vesicles have been observed from this BCP when it is dissolved in a dioxane/water mixture depending on the amount of water content (Fig. 6.49). Upon UV light irradiation, the azobenzene side-chain groups in the apolar *trans*-form were converted into the polar *cis*-form resulting in an increase of polarity of the PAzoMA block followed by disruption of the micellar aggregates (Fig. 6.49). Afterwards, when the visible light was applied, azobenzene
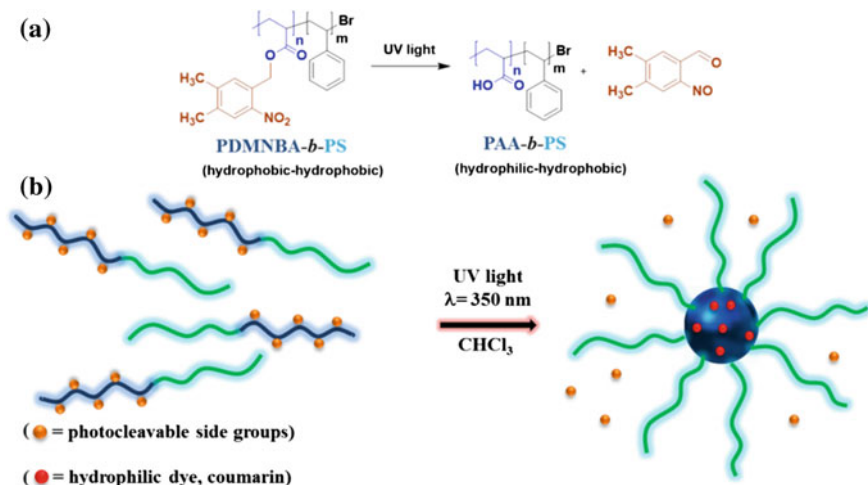
Fig. 6.46 Schematic representation for photosolvolysis of PDMNBA-*b*-PS BCP (**a**) and schematic illustration of light-induced micellization of the BCP followed by a dye (coumarin 343) encapsulation (**b**) (redrawn from Ref. [337] with kind permission of © 2011 Royal Society of Chemistry)
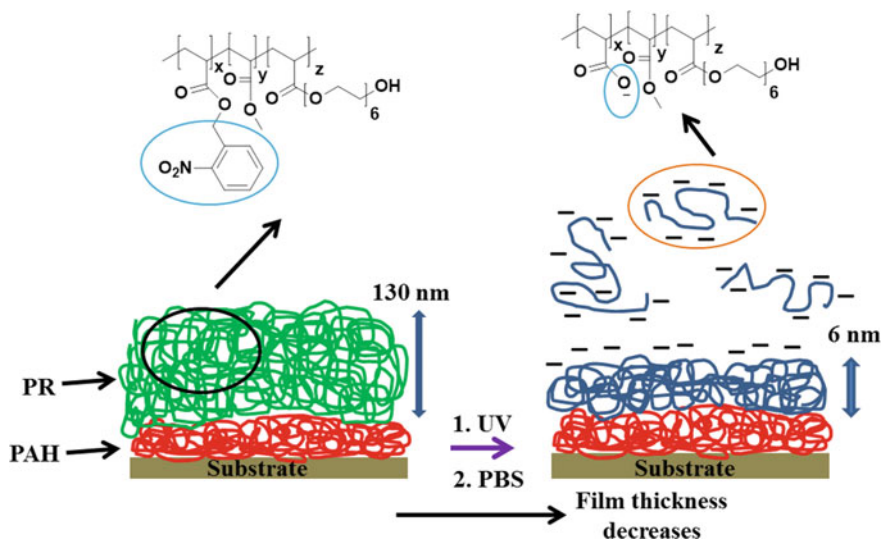
Fig. 6.47 Chemical structure of photoresists (PR) and its mechanism for in situ polyelectrolyte bilayer formation (redrawn from Ref. [340] with kind permission of © 2004 American Chemical Society)
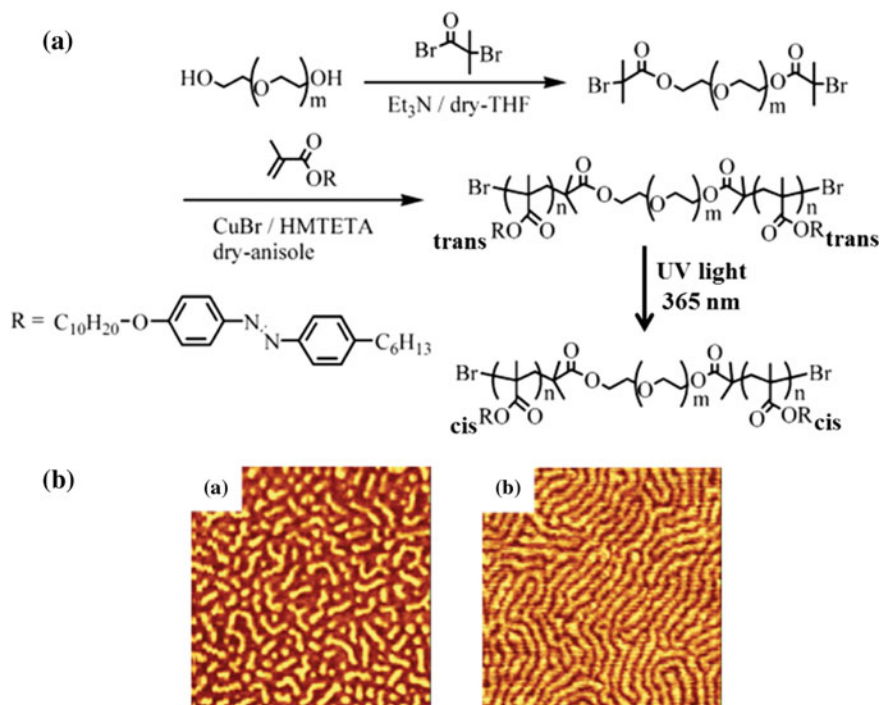
Fig. 6.48 Synthetic route to the formation of amphiphilic PAz-*b*-PEO-*b*-Paz triblock copolymer and its UV-induced photoisomerization (*A*), AFM height images of the Langmuir–Blodgett film made from the PAz-*b*-PEO-*b*-PAz triblock copolymer (1 μm^2) before (**a**) (*trans*-form) and after (**b**) (*cis*-form) UV light irradiation (**b**) (reproduced from Ref. [346] with kind permission of © 2005 American Chemical Society)

chromophores isomerized back into the *trans*-form and the micellar aggregates reformed (Fig. 6.49). In addition to the reversible micelle formation and disruption, azobenzene containing photoresponsive BCPs can also induce the morphological transitions for the irradiated micellar agglomerates [34, 348, 349]. For example, Li and coworkers reported a new BCP, poly(*N*-isopropylacrylamide)-*b*-poly{6-[4-(4-methylphenyl-Azo) phenoxy] hexylacrylate}(PNIPAM-*b*-PAzoM) synthesized by RAFT polymerization [350]. Amphiphilic PNIPAM-*b*-PAzoM is shown to be self-assembled into giant micro-vesicles (Fig. 6.50). Upon photoirradiation at 365 nm, fusion of the vesicles was taken place, as observed directly through optical microscope (Fig. 6.50). The associated surface expansion increases the surface-free energy and fusion of vesicles appears to be the most likely way to reduce that excess of free energy and thus stabilizes the objects.

A fascinating application of azobenzene-based photoresponsive BCP was reported by Hoffman and Stayton [351], where they synthesized a light-responsive BCP namely poly(*N*,*N*-dimethylacrylamide)-*b*-poly(*N*-4-phenylazophenyl acrylamide) (Fig. 6.51) by radical polymerization in the presence of a functional chain
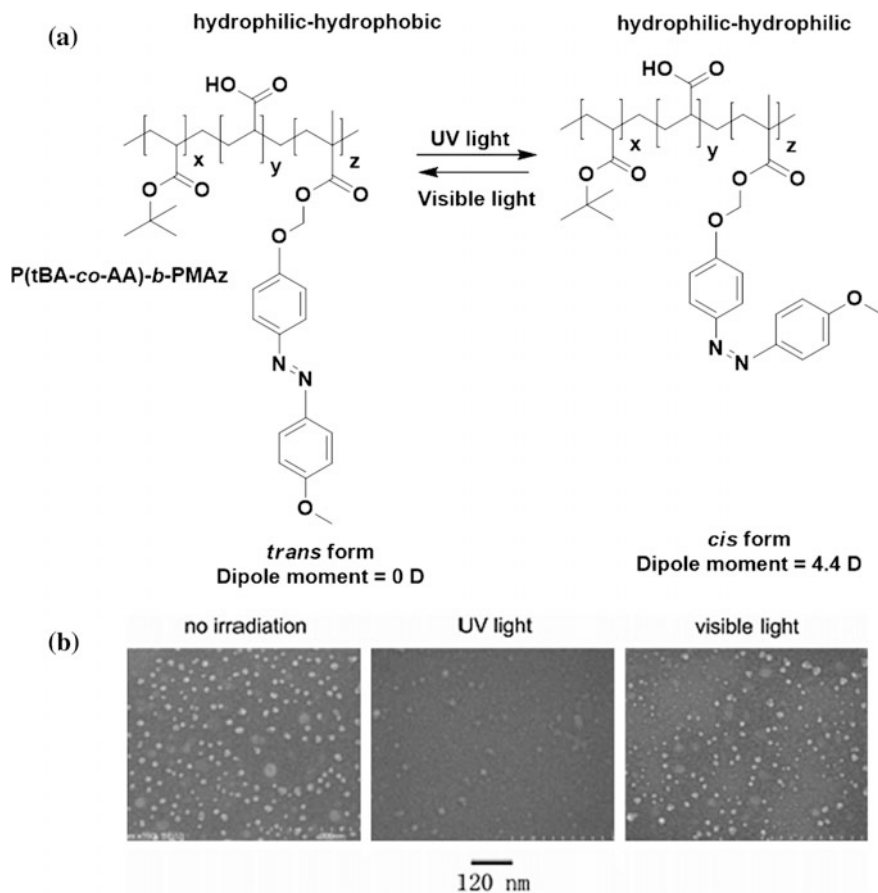
Fig. 6.49 Reversible change in the polarity of P(^{t}BA-*co*-AA)-*b*-PAzoMA BCP induced by photoisomerization of azobenzene moieties (redrawn after the ref) (**a**) and SEM images from the BCP (PAzoMA-*b*-PAA) solution before UV irradiation, after UV irradiation and after subsequent visible light irradiation confirms the reversible photocontrolled disaggregation and re-aggregation process (**b**) (reproduced from Ref. [325] with kind permission of © 2004 American Chemical Society)

transfer agent. They demonstrated that the photoinduced changes in the size and hydration of this BCP chain due to its transformation from coil to globule can be used to regulate substrate access and enzyme activity when conjugated to the enzyme at a specific point just outside the active site. The "smart" photoresponsive polymer can act as a molecular antenna and actuator to reversibly turn the enzyme endoglucanase 12A (EG 12A) activity on and off in response to distinct wavelengths of light (Fig. 6.51).

The above highlighted works on BCPs containing azobenzene moiety are good examples of generating specific functionality by making use of the
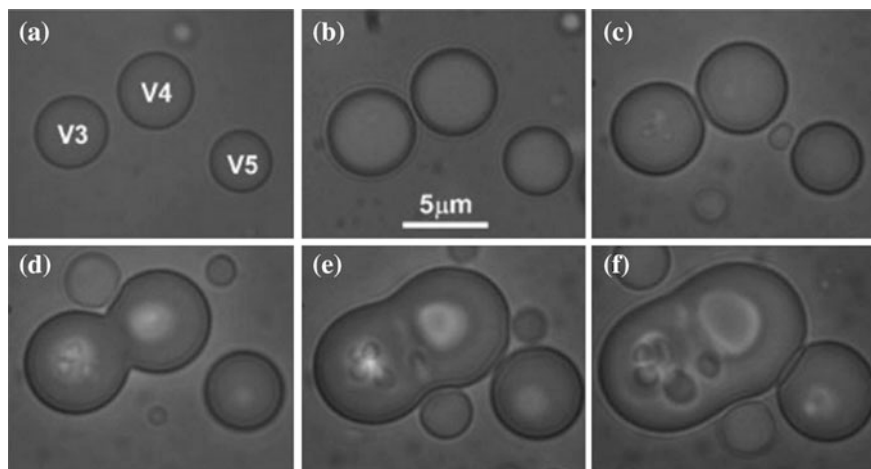
Fig. 6.50 Photoinduced fusion process of the PNIPAM-*b*-PAzoM vesicles. Initial vesicles (**a**) and vesicles observed after irradiation of 16 (**b**), 33 (**c**), 42 (**d**), 58 (**e**), and 80 (**f**) min (reproduced from Ref. [350] with kind permission of © 2007 Wiley-VCH)

photoisomerization of azobenzene. It should also be noted that azobenzene remains the chromophore of choice toward many polymer research community for the photocontrolled ordering of BCP nanostructures where an efficient and controllable photoinduced molecular orientation and/or motion is the key condition.

6.4.3 Pyrenylmethyl Polymer-Based Nanomaterials

Upon UV light irradiation, esters of pyrenylmethyl undergo a photolysis reaction requiring the presence of a protonic solvent such as H_2O (Fig. 6.52). In the pioneering work by Jiang et al. [322] ATRP was used to synthesize a novel amphiphilic BCP composed of hydrophilic PEO and a hydrophobic block of poly (1-pyrenylmethyl methacrylate) (PPyMA). Upon UV light irradiation on aqueous micellar solution of BCP (PEO-*b*-PPyMA), the photolysis of pyrenylmethyl esters takes place, which cleaves 1-pyrenemethanol from the polymer and, consequently, the hydrophobic PPyMA block of this BCP converts into hydrophilic PMA block as depicted in Fig. 6.52. They have shown by FESEM that core–shell micelles ($D = 15$ nm) obtained from aqueous solution of PEO_{47}-*b*-$PPyMA_{72}$ BCP were disappeared after 15 min of UV light irradiation ($\lambda = 365$ nm, Intensity ~ 2 W). They have also proposed that this BCP can be a good candidate for biological application especially in photoinduced drug delivery by demonstrating the photoinduced release of a model hydrophobic dye, Nile red (NR). NR dye was encapsulated into the micellar core of aqueous micellar solution formed by the BCP (PEO-*b*-PPyMA). Upon UV light irradiation, the photocleavage of pyrenylmethyl
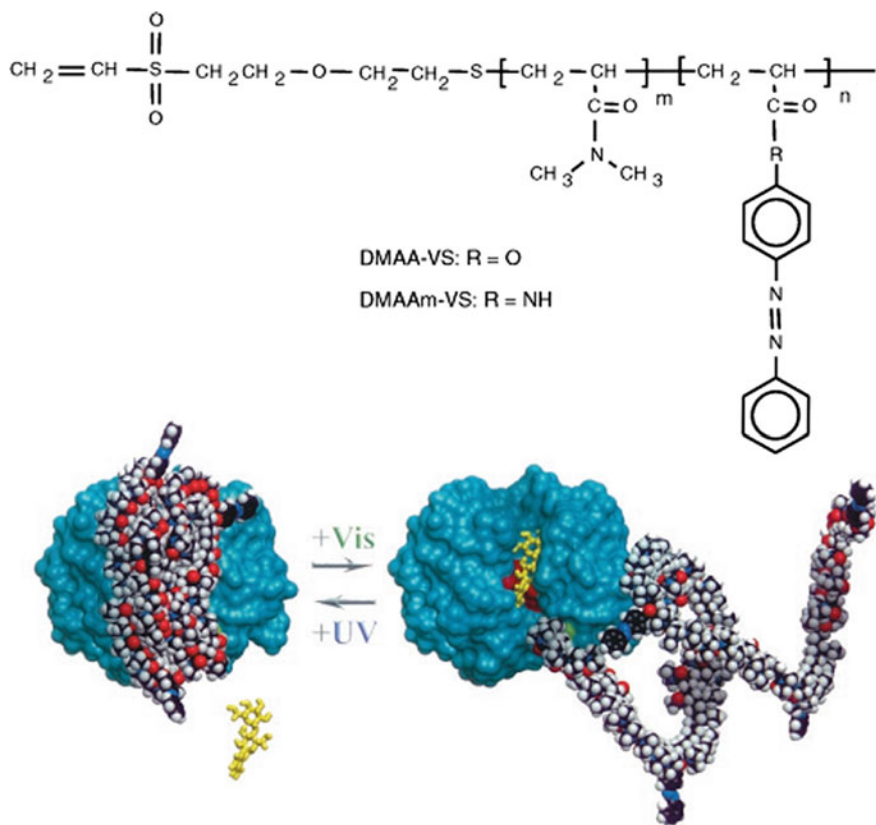
Fig. 6.51 Schematic model for the photoresponsive enzyme switch. The photoresponsive copolymer compositions are shown with the end-modified vinyl sulfone terminus for thiol-specific conjugations (reproduced from Ref. [351] with kind permission of © 2002 National Academy of Sciences)

groups disrupts the micellar association and, consequently, the release of encapsulated NR taken place as shown by fluorescence emission spectroscopy (Fig. 6.52).

6.4.4 Spiropyran Polymer-Based Nanomaterials

Photresponsive spiropyran moiety can respond to light and undergo a reversible isomerization between colorless spiropyron (SP) and colored mecrocyanine (ME) (Fig. 6.53) [352]. The reversible photochromic behavior of spiropyran polymer-based material has led to their consideration in several useful applications such as optical and electrical switching, [353] data recording [354], and
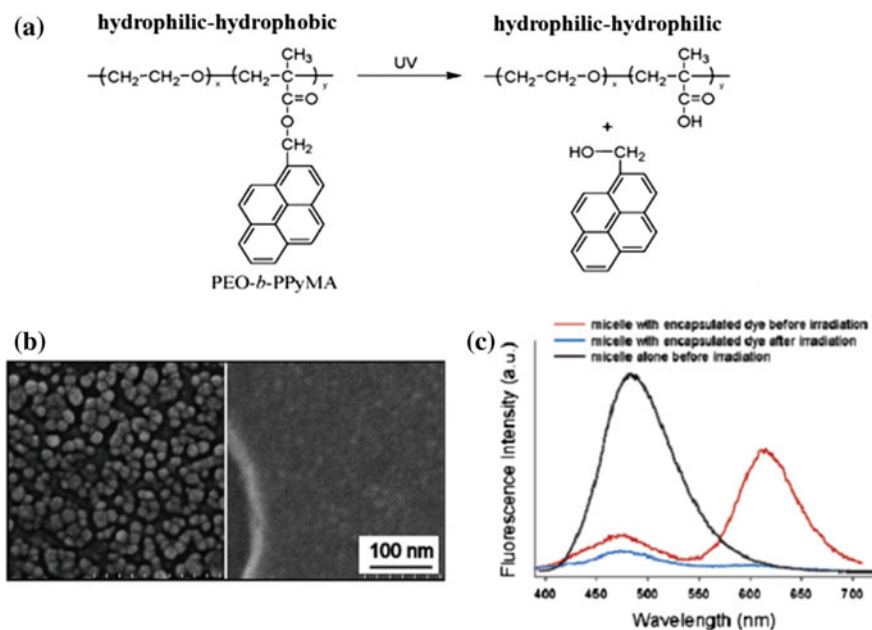
Fig. 6.52 Schematic representation of the photocleavage of pyrene containing amphiphilic BCP (PEO-*b*-PPyMA) (**a**); SEM images for a micellar solution cast on a silicon wafer: solution prior to UV irradiation (*left*) and the same solution after UV irradiation ($\lambda = 365$ nm) (*right*) (**b**) and fluorescence emission spectra of BCP micellar solution alone before irradiation, micelles with encapsulated dye (NR) before irradiation and micelles with encapsulated dye after irradiation (**c**) (reproduced from Ref. [322] with kind permission of © 2005 American Chemical Society)

light-actusted-nanovalves [355]. Matyjaszewski and coworkers proposed the use of photoresponsive spiropyran (SP) moieties toward reversible photoinduced micellar association-dissociation process [326]. They synthesized amphiphilic PEO-*b*-poly (spiropyran) (PEO-*b*-PSP) copolymer where methacrylate block bears spyropyran side chain functionality (Fig. 6.53).

This BCP self-assembled in aqueous solution to form micelles in which the hydrophobic spiropyran containing block forms the inner core and the hydrophilic PEO block forms the outer shell (Fig. 6.53). Irradiation with UV light ($\lambda = 365$ nm) led to the photoisomerization of hydrophobic spiropyran (SP) into hydrophilic zwitterionic mecrocyanine (ME) which completely disrupted the micelles due to the formation of doubly hydrophilic PEO-*b*-PME copolymer (Fig. 6.53). Reversible micellization was also triggered by photochemical inversion from ME to SP, which occurred as a result of visible light irradiation ($\lambda = 620$ nm) into the disrupted micellar solution (Fig. 6.53). They have also studied the encapsulation of coumarin 120 into the micellar solution formed by the BCP (PEO-*b*-PSP), and its photocontrolled release upon UV light irradiation was demonstrated by fluorescence emission measurements. Moreover, the authors described the
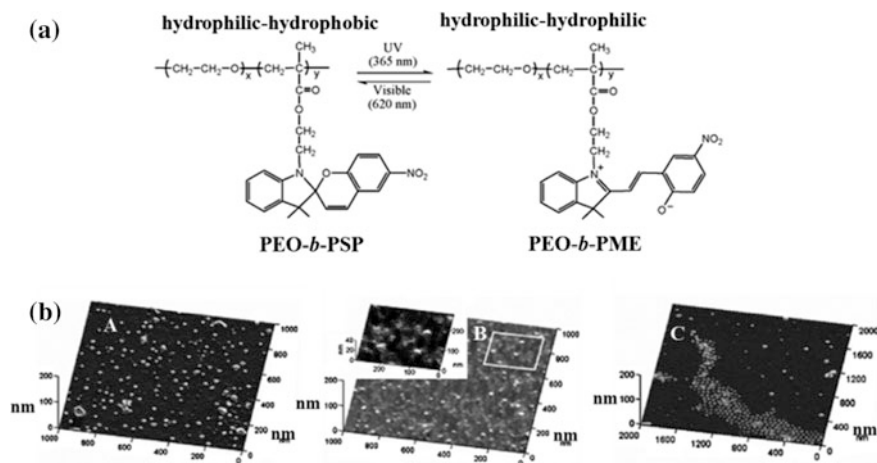
Fig. 6.53 Schematic representation of reversible photoreaction of a spiropyran (SP) containing amphiphilic PEO-*b*-PSP BCP (**a**); AFM height images of PEO-*b*-PSP solutions spin-coated on mica under various conditions (**b**): (*A*) PEO-*b*-PSP micelles; (*B*) PEO-*b*-PSP micelles after UV light (λ = 365 nm) exposure for 30 min; (*C*) PEO-*b*-PSP micelles after 365 nm UV light exposure for 30 min followed by 620 nm visible light exposure for 120 min (reproduced from Ref. [326] with kind permission of © 2007 Wiley-VCH)

partial re-encapsulation of the fluorescent dyes on regeneration of the micelles which can be achieved by visible light irradiation.

6.4.5 Coumarin Containing Polymer Nanomaterials

Another important class of photochromic group that can be introduced to design photoresponsive BCP material is coumarin. The beauty of coumarin is that it is sensitive toward UV and near-infra red (NIR) light equally and efficiently. The light-responsive BCP micelles that have been reported till now are mainly activated by UV and visible light. There is only one reported example where photocleavage of *o*-nitrobenzyl group containing BCP occurs upon NIR light irradiation at 700 nm, but the sensitivity was low because of inefficient two-photon absorption [319]. However, NIR light having the wavelength within the range of 700–1000 nm is more suitable for biomedical application compared to UV or visible light. The reason is that at this longer wavelength, the irradiation is less harmful to healthy cells. Therefore, the BCP micelles that are sensitive to NIR light are essentially more promising candidate toward biomedical applications.

Babin et al. [321] reported a novel coumarin chromophore-based amphiphilic BCP namely poly(ethylene oxide)-*b*-poly([7-(diethylamino)coumarin-4-yl]methyl methacrylate) (PEO-*b*-PDEACMM) whose micellar disruption can effectively be triggered by two-photon NIR absorption at 794 nm. According to them, upon NIR
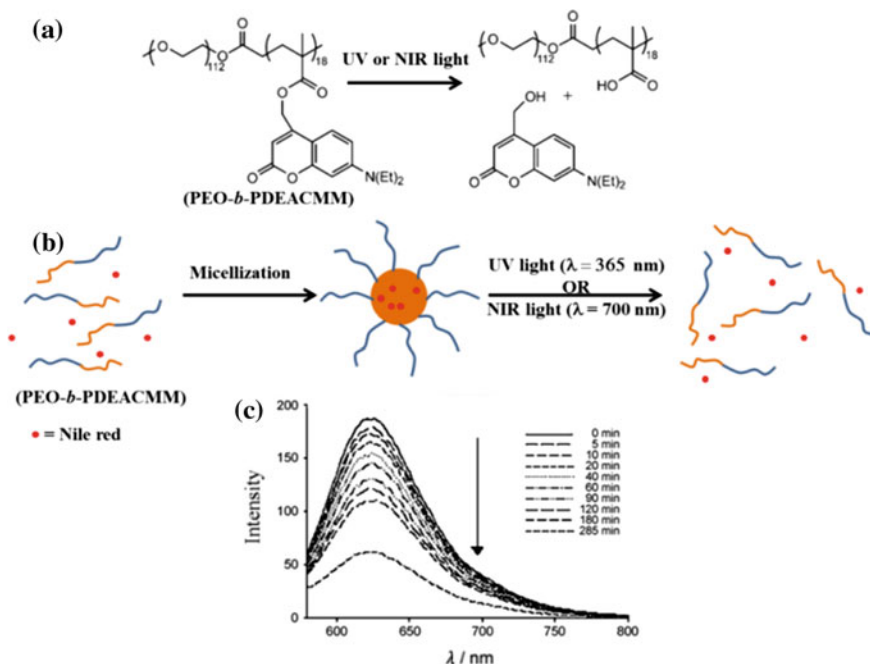
Fig. 6.54 Schematic representation of photolysis of the coumarin-based amphiphilic PEO-*b*-PDEACMM block copolymer; (**a**) schematic representation of encapsulation of Nile *red* (NR) within the hydrophobic core of PEO-*b*-PDEACMM BCP micelles during micellization as well as release of dye due to the disruption of micellar structure by UV/NIR light irradiation (**b**) and fluorescence emission intensity of NR encapsulated aqueous BCP (PEO-*b*-PDEACMM) micellar solution decreases with increasing UV irradiation time which indicates the photocontrolled release of guest molecules (**c**) (reproduced from Ref. [321] with kind permission of © 2009 Wiley-VCH) (color figure online)

or UV light irradiation, photosolvolysis of 7-(diethylamino)coumarin-4-yl]methyl ester moieties of the BCP was taken place which resulted in the cleavage of 7-(diethylamino)-4-(hydroxyethyl)coumarin from the polymer, and consequently, the hydrophobic PDEACMM block converted into hydrophilic PMA as presented in Fig. 6.54. Thus, photosolvolysis of the PEO-*b*-PDEACMM upon NIR or UV light irradiation leads to the formation of the doubly hydrophilic PEO-*b*-PMA BCP causing the rupture of initially formed micelles (Fig. 6.54). A hydrophobic dye, NR was also encapsulated, and its release upon UV or NIR light irradiation was monitored by fluorescence emission measurements (Fig. 6.54).

However, light-responsive BCP micelle-drug conjugates are highly unplumbed and may represent an exciting future research direction. Recently, an anticancer drug, 5-fluorouracil, was linked covalently to coumarin side group on the hydrophobic block of a diblock copolymer namely (poly(ethylene oxide)-*b*-poly(*n*-butyl methacrylate-*co*-4-methyl-[7-(methacryloyl)-oxyethyloxy]coumarin)) (PEO-*b*-P(BMA-*co*-CMA) through UV-induced cycloaddition at comparatively larger

wave length (>320 nm) and subsequent release from the micelles formed by the drug conjugated BCP under shorter wave length UV light (254 nm) [356].
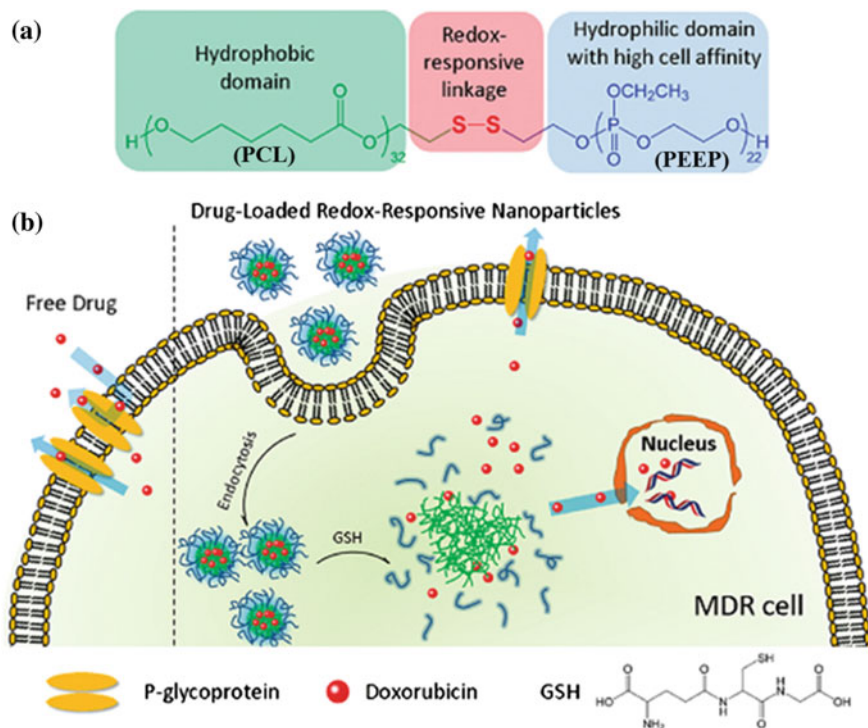
6.5 Redox-Responsive Polymer Nanostructures

Among the available chemical stimuli, redox reaction is one of the most popular stimuli employed to trigger sharp changes in the properties of a polymer material. Recently, the design and fabrication of redox-responsive polymeric drug delivery systems based on the tumor microenvironment have received immense attention. Redox reaction is particularly promising because the disulfide bonds can be cleaved to the corresponding thiol units in the presence of reducing agents [357]. In these aspects, glutathione (GSH) is a thiol-containing tripeptide which is capable of reducing disulfide bonds in the biological environment. The concentration of GSH in the cytoplasm (1–10 mM) is much higher than that in blood plasma (2 μM). Moreover, in vivo research has demonstrated that the concentration of GSH in the tumor tissue can be many-fold higher than that in normal tissue [358–360]. Therefore, this kind of dramatic concentration incline of GSH provides an opportunity for designing the redox-responsive drug delivery systems for cancer treatment.

Many research studies introduce polymeric drug delivery vehicles having GSH-responsive disulfide bonds into the backbones or side groups of the polymeric carriers where drugs are encapsulated or covalently conjugated with the polymer [361–363]. The polymeric drug delivery systems containing GSH-cleavable disulfide bonds are stable during the blood circulation, while they will disassemble rapidly and give burst drug release triggered by the intracellular redox stimuli at the tumor sites [364, 365]. Thus, it is noteworthy that drug delivery vehicles based on disulfide functionalities can potentially facilitate extracellular stability and intracellular release of the encapsulated drug molecules.

Recently, there was a report of a novel redox-responsive micellar drug nanocarrier formed by the self-assembly of single disulfide bond-bridged block polymer consisting of poly(ε-caprolactone) and poly(ethyl ethylene phosphate) (PCL-SS-PEEP) [366]. Such polymeric carriers can rapidly release the encapsulated doxorubicin (DOX) in response to the intracellular reductive environment and therefore significantly enhanced the cytotoxicity of DOX to multidrug resistance (MDR) cancer cells. Here, it should be mentioned that MDR is a major restriction to the success of cancer chemotherapy. The intracellular accumulation of drug and the intracellular release of drug molecules from the carrier could be the most important barriers for nanoscale carriers in overcoming MDR. Redox-responsive micellar nanoparticles based on PCL-SS-PEEP block polymer can act as a drug carrier and also can significantly overcome the two barriers in overcoming the MDR of cancer cells, thus reversing the multidrug resistance of cancer cells.

On the one hand, nanoparticles bearing PEEP shell exhibit a high affinity to cells and are more efficiently internalized by cells, which help the drug escape from the

Fig. 6.55 Chemical structure of disulfide-bridged PCL-SS-PEEP block copolymer (**a**) and schematic illustration of redox-responsive nanoparticles for overcoming multidrug resistance of cancer cells (**b**). (reproduced from Ref. [366] with kind permission of © 2011 American Chemical Society)

pump-off by P-glycoprotein (P-gp) and lead to high levels of cellular drug accumulation. On the other hand, it is known that MDR in cancer cells is often associated with an elevation in the concentration of reductive glutathione (GSH) [367]. Such shell-detachable nanoparticles are sensitive to the intracellular glutathione of MDR cancer cells, resulting in significantly enhanced intracellular drug release and rapid accumulation of free drug in MDR cancer cells (Fig. 6.55).

In biomedical applications, the thiol-disulfide exchange reaction [368] is exploited extensively for constructing redox-responsive gene and drug carriers [362, 369] For example, Meng and Zhong's group demonstrated a facile way to prepare the disulfide-linked dextran-*b*-PCL amphiphilic block copolymer using the thiol-disulfide exchange reaction between dextran orthopyridyl disulfide (Dex-SS-py, 6000 Da) and mercapto PCL (PCL-SH, 3100 Da) under mild conditions (Fig. 6.56) [370]. It was observed that the as-synthesized BCP self-assembled into micelles with an average size of 60 nm in phosphate buffer solution (Fig. 6.56) and, interestingly, these micelles formed large aggregates rapidly in response to 10 mM dithiothreitol (DTT), most likely due to shedding of the dextran shells
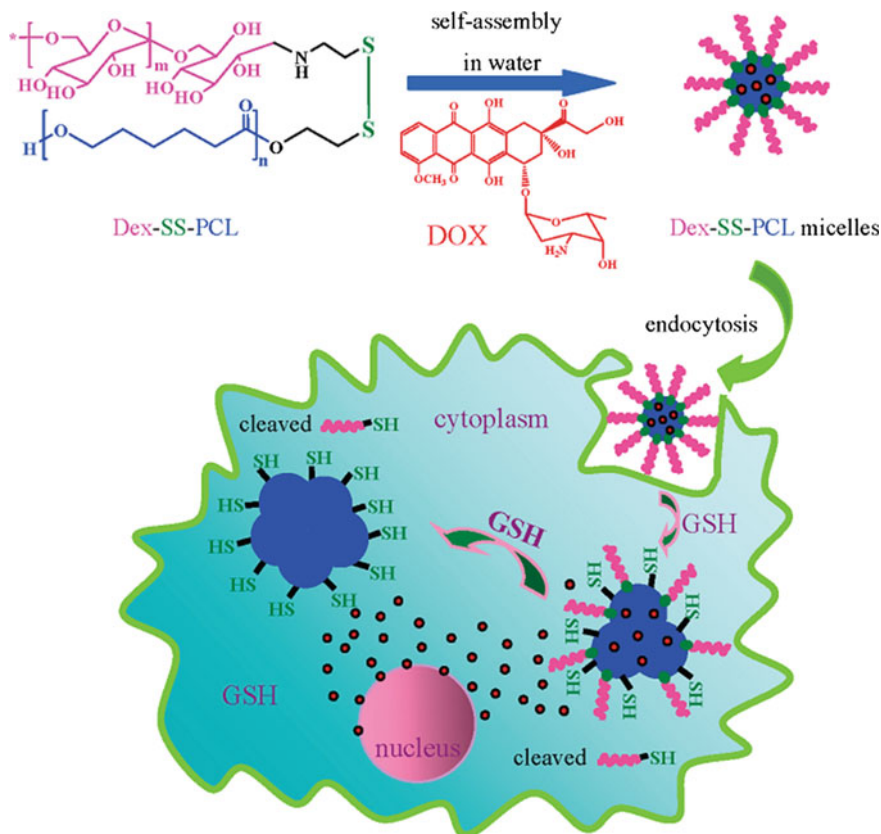
Fig. 6.56 Schematic illustration of redox-responsive Dex-SS-PCL micelles and the intracellular release of DOX where dextran shells of DOX-loaded Dex-SS-PCL micelles are shed off due to the cleavage of the intermediate disulfide bond triggered by GSH and resulting in the fast destabilization of micelles and quantitative release of DOX in the cytosol and into the cell nucleus (reproduced from Ref. [370] with kind permission of © 2010 American Chemical Society)

through reductive cleavage of the intermediate disulfide bonds. The effective shedding of dextran shells and almost zero-order release of DOX in response to 10 mM DTT, analogous to the intracellular redox potential, was observed. It was shown by confocal laser scanning microscopy (CLSM) that the DOX was rapidly released to the cytoplasm as well as to the cell nucleus. These redox-responsive biodegradable micelles have appeared highly promising for the targeted intracellular delivery of hydrophobic chemotherapeutics in cancer therapy (Fig. 6.56).

Not only disulfide linkage, many researchers introduced redox-sensitive inorganic metal-metal bond to design redox-responsive polymer materials. Selenium has similar kind of chemical properties like sulfer because they are present in the same group of the periodic table and also diselenide bond energy is very less (E_{Se-Se} = 172 kJ mol^{-1}). Therefore, researchers paid attention toward diselenide linkage
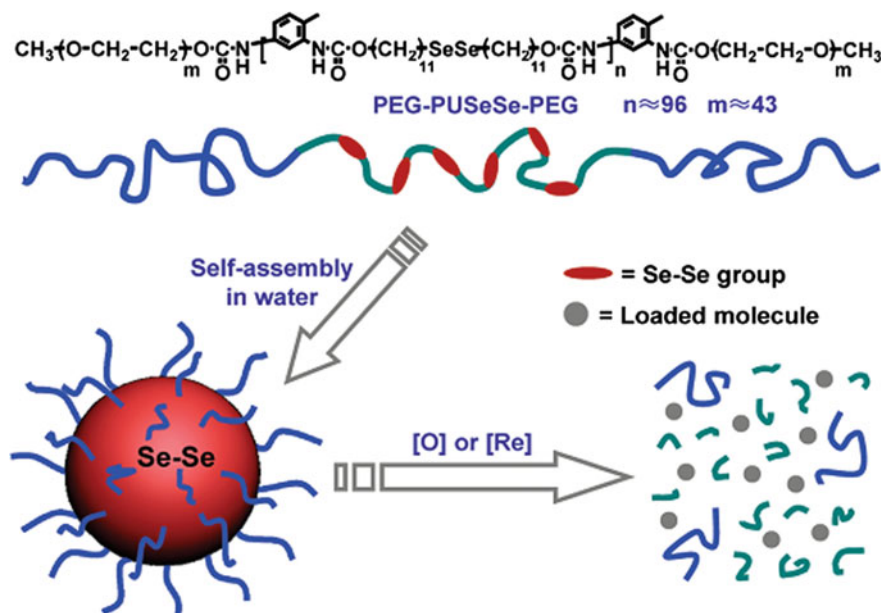
Fig. 6.57 Chemical Structure of PEG-PUSeSe-PEG amphiphilic triblock copolymer and schematic illustration of the dual redox-responsive disassembly of PEG-PUSeSe-PEG micelles (reproduced from Ref. [371] with kind permission of © 2010 American Chemical Society)

to fabricate redox-responsive polymeric nanostructures for controlled drug delivery. Normally, Se–Se bond can be cleaved and oxidized to seleninic acid in the presence of oxidants and reduced to selenol in a reducing environment. The selenium containing polymer was, however, still unexplored due to the lack of efficient synthetic methods to overcome its poor solubility. In 2010, Xu and Zhang's group reported a dual diselenide containing redox-responsive polyurethane (PU) triblock copolymer, PEG–PUSeSe–PEG, using toluene diisocyanate as the chain extension agent (Fig. 6.57) [371]. This amphiphilic triblock copolymer (PEG–PUSeSe–PEG) self-assembled into micellar structure in aqueous environment. They investigated that the redox-responsive PEG-PUSeSe-PEG micelles were quite stable under ambient conditions but disrupts very rapidly in the presence of external redox stimuli (oxidants or reductants) due to the destruction of Se–Se bonds (Fig. 6.57). The release of encapsulated Rhodamine B from the aqueous micellar solution of the following triblock copolymer (PEG–PUSeSe–PEG) upon addition of suitable oxidants (e.g., H_2O_2) or reductants (e.g., GSH) were also investigated and the results indicated that the diselenide was much more sensitive: Even under 0.01 mg mL^{-1} of GSH, the encapsulated Rhodamine B could still be released almost entirely in only 5 h, while they were stable without redox stimuli.

To confirm its use in drug delivery and tumor inhibition, Liu et al. introduced the diselenium bond into a hyperbranched structure and found that the hyperbranched
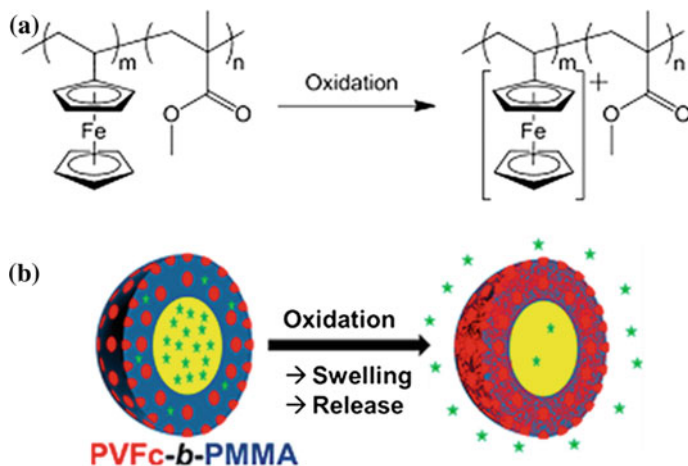
Fig. 6.58 Schematic representation of the oxidation of PVFc-*b*-PMMA BCP, (**a**) and schematic representation showing the oxidation-responsive release of the hydrophobic payload from the PVFc-*b*-PMMA patchy nanocapsules (**b**) (reproduced from Ref. [377] with kind permission of © 2012 American Chemical Society)

polydiselenide could not only be used as a biocompatible drug carrier but itself had the ability to inhibit tumor proliferation [372]. Another interesting redox-active couple in polymeric systems is the ferrocene/ferrocenium system. Ferrocene containing polymers are one of the well-studied oxidation-responsive polymers with promising applications ranging from biomedicine, biosensors, batteries, and liquid crystals to electronics and other related areas [373–376]. As per the position of ferrocene in the polymer, these polymers can be roughly classified into three categories: polymers with ferrocene in the backbone, polymers with ferrocene on the side chain, and polymers with ferrocene as the terminal group. Staff et al. successfully designed poly(vinylferrocene)-*b*-poly(methyl methacrylate) (PVFc-*b*-PMMA) nanocapsules with ferrocene on the side chain [377]. Microphase separation in the nanoparticles led to a patchy assembly, where PVFc patches are surrounded by the PMMA phase (Fig. 6.58). Furthermore, the PVFc nanopatches could be selectively oxidized into hydrophilic ferrocenium, thereby inducing a transition from a purely hydrophobic patchy object to a hydrophobic object with swollen hydrophilic nanopatches (Fig. 6.58). The hydrophobic to hydrophilic transition of the PVFc nanopatches was advantageously utilized to release a hydrophobic payload upon selective oxidation of the nanopatches. Polymers with terminal ferrocene group are usually used to construct more complex polymeric systems utilizing ferrocene related host-guest chemistry. Depending on the redox state of ferrocene, the inclusion complexation between ferrocene and cyclodextrin has already been established to associate and disassociate reversibly.

Yan, Yin, and coworkers synthesized a pseudo block copolymer via orthogonal assembly between cyclodextrin-modified poly(styrene) (*β*-CD-PS) and ferrocene
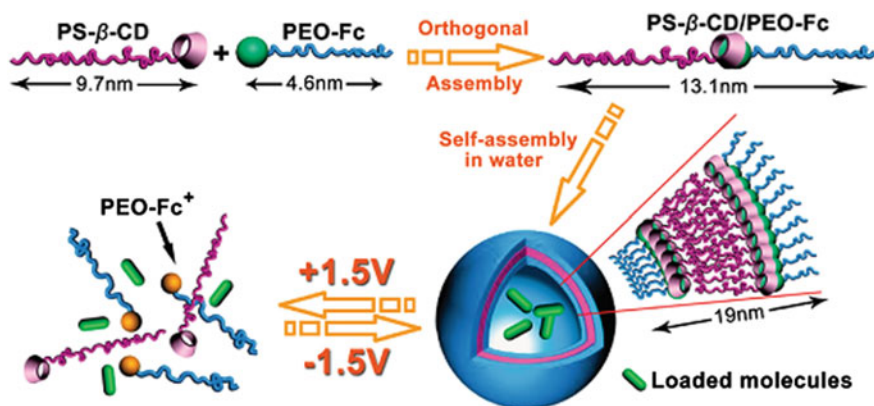
Fig. 6.59 Schematic illustration of voltage-responsive reversible assembly and disassembly of PS β-CD-PS/PEO-Fc supramolecular vesicles (reproduced from Ref. [378] with kind permission of © 2010 American Chemical Society)

end-functionalized poly(ethylene oxide) (PEO-Fc) in aqueous solution (Fig. 6.59) [378]. The following supramolecular block copolymer can self-assembled into vesicles with voltage-responsiveness. The association-dissociation balance of the supramolecular vesicles could be reversibly addressed by electro-stimuli. For example, upon application of +1.5 V voltage stimulus, the vesicles disassembled into small pieces in less than 5 h, while under a −1.5 V voltage, the fragments could reassemble into vesicles (Fig. 6.59). Additionally, from the controlled release experiments, they claimed that the release rate can be well-controlled by slightly tuning the voltage strength, exhibiting great potential in electrochemical therapeutic applications [379].

Further, Xiong et al. recently fabricated redox-responsive nanogels by radical copolymerization of an ionic liquid (IL)-based monomers, 1,n-butanediyl-3,30-bis-1-vinylimidazolium dibromide ($[C_nVIm]Br$, $n = 4$, 6), and disulfide dimethacrylate (DSDMA) monomer in selective solvents [380]. The sizes of PIL-based nanogel particles can be tuned by the feed ratio of the IL monomer and DSDMA. Moreover, the redox-response performances of these nanogels were evaluated through the size variation in the presence of dithiothreitol (DTT) and benzoyl peroxide (BPO). The capability of PIL-based nanogels for controlled release was also investigated by using rhodamine B (RhB) as prototype model drug. It was found that DTT-triggered release of RhB could be achieved. Only less than 50% RhB could be released in the absence of DTT, while over 80% RhB could be released with the addition of DTT. This high cargos release was attributed to the cleavage of disulfide bonds in reducing environments. Thus, the redox-responsive nanogel particles could selectively increase intracellular drug release and potentially used as controlled carrier in biological medicine [380].

6.6   Glucose-Responsive Polymer Nanostructures

Polymeric micelles (PMs) formed by the self-assembly of block copolymers have also attracted immense interests for their potentiality to control the release of insulin and fast response to glucose levels, as well as other advantages, such as small size and defined core–shell structures [381–383]. Phenylboronic acid-containing materials have been most widely studied and used in construction of glucose-responsive system. As shown in Fig. 6.60, phenylboronic acid (PBA) exists in equilibrium between the undissociated (neutral trigonal) and dissociated (charged tetrahedral) forms in an aqueous milieu. An increase in the glucose concentration induces a shift in the equilibrium, increasing the fraction of total borate anions (B and C) and decreasing the fraction of the uncharged form (A) [384]. This kind of shift in the direction of the charged phenylborates results in an increased hydrophilicity. Thus, the change in the glucose concentration should have a significant effect on the solubility of amphiphilic polymer strands having pendant phenylborate moieties [385].

Shi and his coworkers reported PBA-based polymer micelles formed through the self-assembly of poly(ethylene glycol)-*b*-poly(acrylic acid-*co*-acrylamidophenylboronic acid) (PEG-*b*-(PAA-*co*-PAAPBA)) BCP exhibiting glucose-responsive release of insulin under physiological conditions [386]. They claimed that these monodisperse micelles were sensitive to pH and glucose in aqueous solutions. The micelles swelled and dissociated in the presence of glucose at pH = 7.4 which was caused by the conjugation of PAAPBA segments with glucose unit and the resultant increases in hydrophilicity of the PAAPBA core (Fig. 6.61). They have also demonstrated that the insulin-loaded micelles disaggregated at a faster rate in the solution with higher concentration of glucose, and the cumulative amount of insulin released from the micelles gradually increased with time.
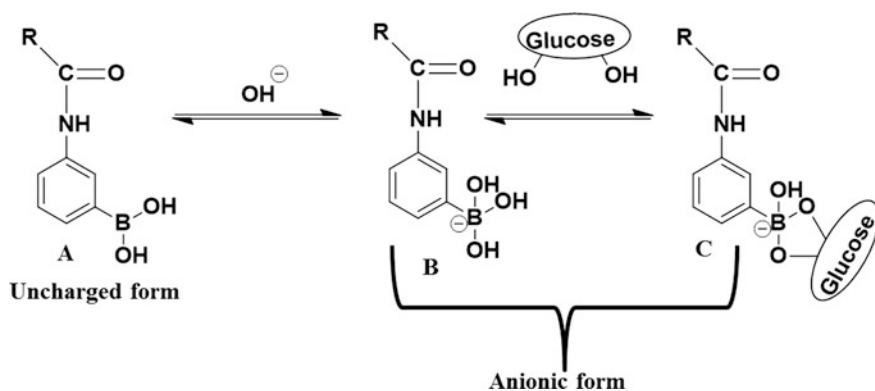
Fig. 6.60 Chemical equilibration of phenylboronic acid in between the uncharged form and the charged form
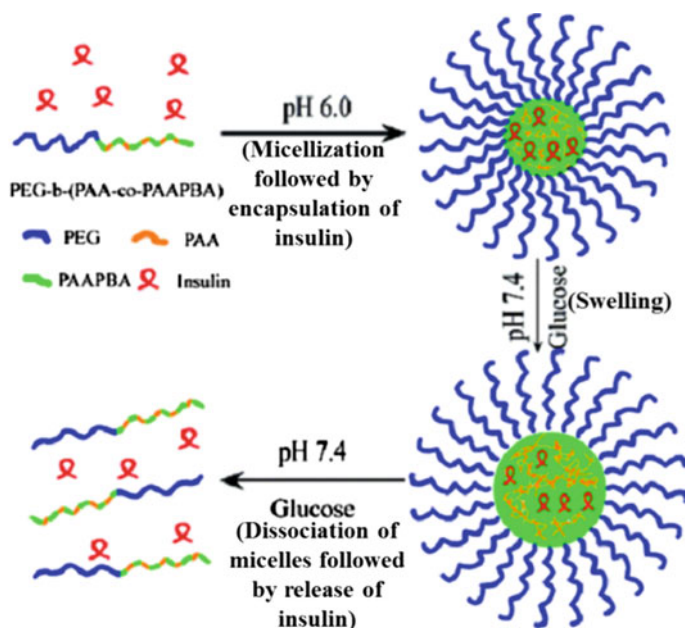
Fig. 6.61 Schematic illustration of glucose-induced swelling as well as disruption of micelles followed by the release of insulin (reproduced from Ref. [386] with kind permission of © 2009 American Chemical Society)

Kataoka and his coworkers have made excellent contributions to the synthesis and application of PBA-based glucose-responsive polymeric materials. Their magnificent work was the synthesis of a complex gel based on the reversible complexation between PBA moiety of poly(N-vinyl-2-pyrrolidone)-co-poly(phenylboronic acid) (P(NVP-co-PBA)) and diols moiety of poly(vinyl alcohol) (PVA) [387]. Afterwards, glucose-responsive release of insulin using this complex gel was established successfully [388].

Recently, Liu et al. [389] developed a glucose-responsive complex polymeric micelle (CPM) through the self-assembly of two types of diblock copolymers, poly (ethylene glycol)-b-poly(aspartic acid-co-aspartamidophenylboronic acid) (PEG-b-P(Asp-co-AspPBA)) and poly(N-isopropylacrylamide)-b-poly(aspartic acid-co-aspartamidophenylboronic acid) (PNIPAM-b-P(Asp-co-AspPBA)). The complex micelles had a common P(Asp-co-AspPBA) core and a mixed PEG/PNIPAM shell (Fig. 6.62). Upon increasing the temperature up to 37 °C, PNIPAM chains collapsed on the glucose-responsive P(Asp-co-AspPBA) core, forming a novel core–shell–corona structure (Fig. 6.62). The complex micelles exhibited a reversible swelling in response to changes in the glucose concentration, enabling the repeated on–off release of insulin regulated by the glucose level (Fig. 6.62). Additionally, the formation of a continuous PNIPAM shell (membrane) around the micellar core could provide fruitful insulin protection against protease degradation. This kind of
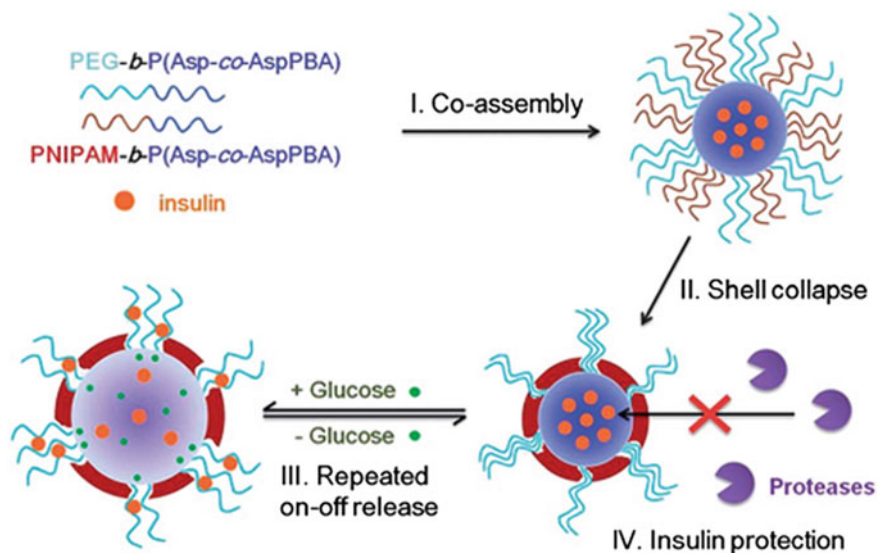
Fig. 6.62 Schematic illustration of glucose-responsive complex polymeric micelles (CPM) of two different diblock copolymers for repeated on-off release and insulin protection under physiological conditions (reproduced from Ref. [389] with kind permission of © 2013 Royal Society of Chemistry)

the biocompatible complex polymer micelle could be very effective for constructing self-regulated insulin delivery systems to control diabetes.

Sumerlin and his coworkers synthesized a BCP, namely poly(*N,N*-dimethyla-crylamide)-*b*-poly(3-acrylamidophenylboronic acid) (PDMA-*b*-PAPBA) by RAFT polymerization and elementarily investigated the sensitivity of PNIPAM-*b*-PBA micelles to pH and glucose [382]. It should be mentioned that the boronic acid-acyclic diol complexes are less stable and can easily dissociated in the presence of appropriate saccharide molecules because, the rigid *cis*-diols found in many saccharides generally exhibits higher binding affinities with organoboronic acid through reversible boronate ester formation [390]. However, this kind of competition mechanism between sugar molecule and acyclic diol toward organoboronic acid provides an excellent opportunity for unfolding/developing novel type of sugar-responsive macromolecules. Inspired by this competition concept, Yuan and his coworkers recently reported the synthesis of an amphiphilic BCP namely poly (ethylene glycol)-*b*-poly[(2-phenylboronic ester-1,3-dioxane-5-ethyl) methylacry-late] (PEG-*b*-PPBDEMA) which contains phenylborate ester as a leaving group in response to glucose in the hydrophobic block (Fig. 6.63) [391]. They showed that BCP self-assembled into core–shell micelles in aqueous solution with hydrophobic PPBDEMA segments as the core and hydrophilic PEG units as the shell (Fig. 6.63). Upon addition of sugar into aqueous micellar solution, the marked pinacol phenylboronate moieties present on the hydrophobic part of the BCP were
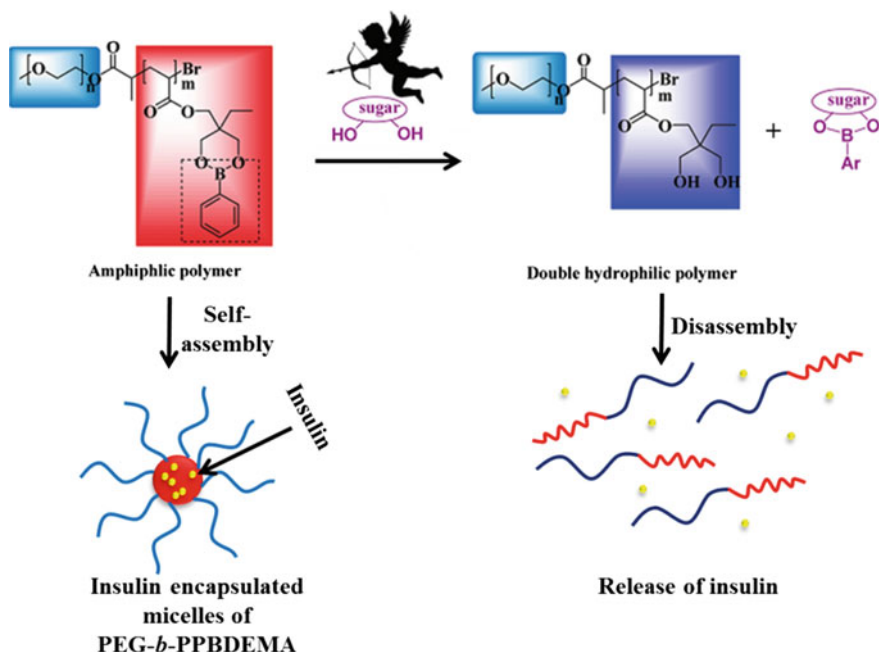
Fig. 6.63 Schematic representation of glucose-responsive polymeric micelles formed from PEG-*b*-PPBDEMA for the controlled release of insulin at neutral pH (reproduced from Ref. 391] with kind permission of © 2012 American Chemical Society)

combined with sugar molecules because of its predominant binding force with organoborane and resulting in the detachment of phenylborate ester from the BCP as phenylboronate-saccharide complex (Fig. 6.63). The detachment of phenylboronate groups from the BCP changes the polarity of the BCP from amphiphile to double hydrophile, and thus leading to the disruption of the initial nanoaggregates formed via self-assembly of the amphiphilic PEG-*b*-PPBDEMA BCP (Fig. 6.63). Additionally, glucose-responsive release of encapsulated insulin from these BCP micelles at neutral pH was also successfully investigated in this report (Fig. 6.63).

6.7 CO$_2$ Responsive Polymer Nanostructures

In recent years, majority of scientific reports on stimuli-responsive polymers have focused on some particular stimuli including pH, light, and temperature. However, pH, light, and temperature-responsive polymer systems have some kind of limitations. For example, repeated switchable cycles of pH-responsive polymer systems require repeated addition of acids and bases to the solution, which may contaminate the system and weaken the switch ability due to salt accumulation [392, 393]. On

the other hand, the light-responsive BCP micelles that have been reported till now are mainly activated by UV light. However, light and pH as stimuli are harmful to biological tissues in some cases and therefore not widely applicable. The penetration depth of UV light in tissue is very short because of its small wavelength, and extended irradiation of high-energy UV light can also lead to the damage of biological tissues [321]. Therefore, investigation of alternative stimuli is highly recommendable for the utilization of responsive polymers in biomedical applications. Carbon dioxide (CO_2) can be considered as a kind of "green trigger" and plays an important role as an endogenous metabolite [394]. In addition, CO_2 is a non-toxic, inexpensive, and abundant gas. It is, therefore, an attractive stimulus toward responsive polymeric systems in biological applications such as drug or gene delivery, tissue engineering. Furthermore, CO_2 can react with different responsive functional groups such as amines or amidines resulting in the generation of hydrophilic compounds [44]. We can also recover original compound upon removal of CO_2 simply by purging with inert gases or heating. Therefore, using CO_2 as a stimulus can lead to many switching cycles without the accumulation of any byproducts. Another appealing feature of CO_2-responsive polymeric materials is their ability to capture CO_2. The pathway to utilize and capture CO_2 is really a crucial issue to minimize the greenhouse gas [395, 396].

In the past years, there has been immense interest in possibilities to capture CO_2 from the atmosphere and ensure a safe storage. Recently, Yuan, Yan, and his coworkers designed amidine containing BCP to fabricate CO_2-responsive vesicles having biomimetic "breathing" feature [394]. Here, they have synthesized poly (ethylene oxide)-*b*-poly((*N*-amidino)dodecyl acrylamide) (PEO-*b*-PAD) amphiphilic BCP using PEO-based macroinitiator by ATRP (Fig. 6.64). Amidine can transform into a charged amidinium species upon reaction with CO_2, and this reaction is reversible upon exposure to argon (Fig. 6.64) [397]. The conductivity of the PEO-*b*-PAD solution rose dramatically from 3.4 to 26.9 μS cm^{-1} accompanied with a decrease of the pH value from approximately 6.94 to 5.68 was observed when CO_2 passed through the solution indicating that a number of protonated species formed in the BCP solution because of the formation of amidinium ion. However, the original low conductivity of this BCP solution was regained upon treatment with Ar gas owing to an opposite deprotonation effect. Due to its amphiphilic nature, this BCP can self-assemble into vesicles in aqueous solution (Fig. 6.64). The notable finding was that these vesicles can swell and expand its size when CO_2 is passed through the BCP solution (Fig. 6.64). It was noted that upon CO_2 treatment only 37% amidine side groups are protonated, this probably the reason behind why vesicles are still remaining in solution. Therefore, CO_2 can tune the size of these vesicles over a wide range by controlling the degree of protonation of amidine side chains of this BCP. They have also investigated that these vesicles can return to their initial size upon removal of CO_2 by bubbling Ar gas through the solution. This kind of reversible expansion and contraction phenomena of polymeric vesicles in response to CO_2 or Ar gas is called "breathing" vesicles. Based on
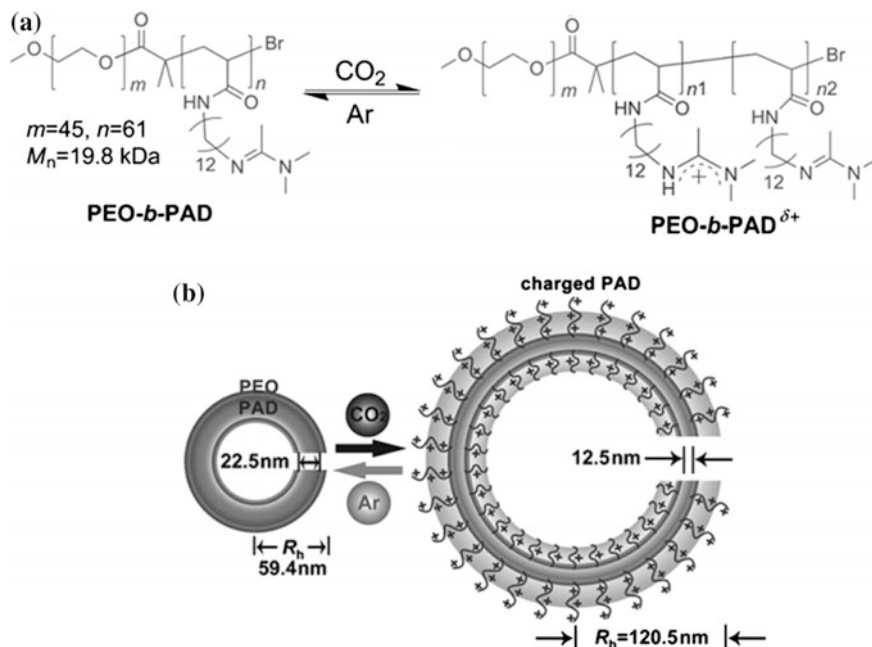
Fig. 6.64 Gas-switchable structure of amidine containing diblock copolymer PEO-*b*-PAD (**a**) and schematic representation of its self-assembly into vesicles and their reversible gas-responsive "breathing" in aqueous media (**b**) (reproduced from Ref. [394] with kind permission of © 2011 Wiley-VCH)

this "breathing" phenomenon, Yuan and his coworkers further extended their investigation toward membrane permeability of these vesicles [398].

First report on CO_2-responsive polymer brushes was highlighted in 2013 by Kumar, Zhao and his coworkers [399]. The brushes were prepared by grafting PDEAEMA from a surface under ATRP conditions. This polymer brushes can be switched between extended (hydrated) and collapsed (dehydrated) chain conformational states just by passing CO_2 gas and an inert gas like N_2 in solution, respectively. At room temperature, PDEAEMA chains are generally hydrophobic in nature at neutral pH, and therefore, the respective PDEAEMA brushes are insoluble in water and exist in the collapsed state (Fig. 6.65) under these conditions. Upon passing CO_2 through the solution, tertiary amine groups of PDEAEMA unit gets protonated to form charged ammonium bicarbonates (Fig. 6.65), and consequently, PDEAEMA brushes become hydrophilic and adopting the chain extended state (Fig. 6.65). However, the reverse process can also be achieved by the introduction of N_2 through the solution to remove CO_2. Under N_2 purging, PDEAEMA brushes became hydrophobic and insoluble in water and regained the collapsed state from the extended state due to deprotonation. This kind of CO_2 triggered expansion and collapsed state of polymer brushes has some promising application in
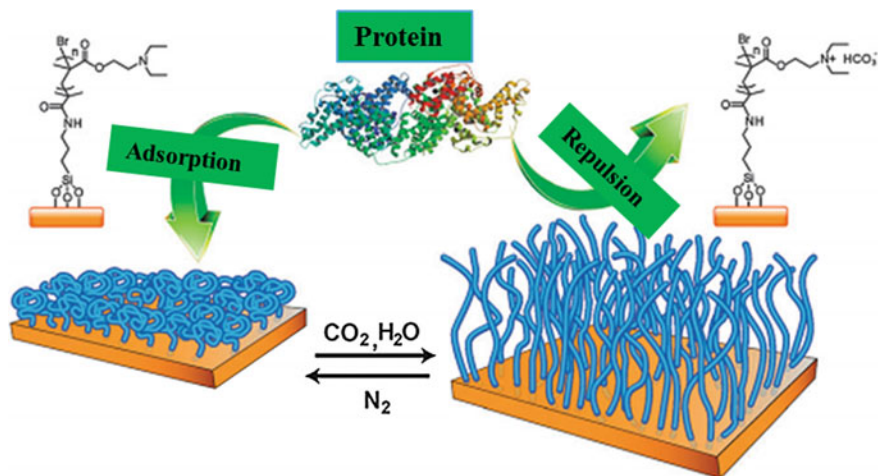
Fig. 6.65 Schematic illustration of protein capture and release using CO_2-responsive polymer (PDEAEMA) brushes. The chemical structure of CO_2-responsive brushes is also shown (reproduced from Ref. [399] with kind permission of © 2013 Royal Society of Chemistry)

gas-controlled reversible capture and release of protein where repeatable repelling and adsorption of protein occurred on the extended brush and the collapsed brush, respectively.

6.8 Cyclodextrin Inclusion Complexation-Based Responsive Polymer Nanostructures

Cyclodextrins (CDs) are a class of cyclic oligosaccharides that have molecular-compatible cavities. These semi-natural compounds commonly comprise several D-glucopyranoside units linked together by a 1,4-glycosidic bonds. The most common ones are α-, β- and γ-CDs, consisting of six, seven, and eight glucopyranose units, respectively. The exterior of the cavity is highly polar, because of the bristling hydroxy groups, while the interior is nonpolar. The inclusion complexation between CDs and various guests has been extensively investigated in supramolecular and polymer chemistry resulting in a broad scope of guest molecules available under different conditions [400] One of the most investigated pairs, i.e., the complexation between β-CD and adamantane (ADA) has been widely employed in macromolecular assembly as it has strong binding ability with an association constant around $1 \times 10^5 \, M^{-1}$ in water [400]. Many host-guest pairs with a binding ability that is adjustable to external environment, such as temperature, pH, light, and voltage, have drawn great attention, as they could be used in constructing stimuli-responsive assemblies. Furthermore, as the interaction strength

of different pairs covers a very broad range, and it provides a good opportunity to realize reversibility of self-assembly just by competition between different pairs. This includes amphiphilicity adjustment and various structures built by inclusion complexation. In this chapter, we focus on the stimuli-responsive polymer-based inclusion complex assemblies.

The use of amphiphilic macromolecules as building blocks has drawn increasing interest because of their controllable self-assembly, and the morphology transformation of the assemblies can be realized by tuning the amphiphilicity [401]. CDs are particularly valuable and extensively employed in tuning the amphiphilicity of macromolecules. Generally, once part of a macromolecule containing a guest moiety is connected to CDs via inclusion complexation, the part will become more hydrophilic, and thus, the amphiphilicity of the macromolecule as a whole is turned. For example, the block copolymer composed of two hydrophobic blocks, i.e., polystyrene and adamantyl polyphosphazene, could be converted to an amphiphilic copolymer when the adamant units enter the cavities of the added β-CDs. This resulted amphiphilic copolymer then self-assembled into micelles with polystyrene as the core and β-CD-modified polyphosphazene as the shell [402]. Kim et al. reported that a dendron amphiphile with a pyrene apex formed vesicles in aqueous solution. There is another example of nanostructure formation, where the amphiphilicity of the dendron was significantly altered by capping the dendron with β- or γ-CDs due to inclusion complexation between pyrene and CD, which made the vesicles convert into nanotubes [403]. However, when the binding ability of a host–guest pair is rather strong, it can be employed to link two linear polymers with respective host and guest groups at the chain ends into a pseudo block copolymer.

Shi et al. reported that ADA end-functioned PNIPAAm and β-CD end-functioned poly(4-vinylpyridine) (P4VP) formed a pseudo block copolymer via the ADA/b-CD interaction [404], which formed micelles in aqueous solution of pH 2.5 and at 60 °C, with a hydrophobic PNIPAAm core and a hydrophilic P4VP shell. When the condition was switched to pH 4.8 at 25 °C, PNIPAAm became hydrophilic and P4VP slightly hydrophilic, then vesicles with a radius around 80 nm were formed, in which a P4VP layer is sandwiched between the two PNIPAAm layers.

Following their systematic study on double-hydrophilic block copolymers (DHBC), Liu et al. achieved non-covalently linked DHBC containing β-CD terminated PNIPAAm and ADA-terminated poly(2-(diethylamino)ethyl methacrylate) (PDEA) [405]. At room temperature, the polymer pair molecularly dissolved at pH <6 but formed PDEA-core micelles at pH >8 with PNIPAAm as the hydrophilic outer layer of the micelles. In acidic media, above the LCST of PNIPAAm, vesicular nanostructures were formed with a PNIPAAm layer sandwiched by the hydrophilic PDEA layers.

Very recently, Zhang et al. [406] designed and synthesized a β-CD core four-arm PNIPAAm and functionalized PEGs with ADA groups at one or both of its ends. Thus, they obtained non-covalently linked block copolymers with different architectures by inclusion complexation (Fig. 6.66). They found that the thermosensitive behavior of the β-CD-core star PNIPAAm in the block copolymers was
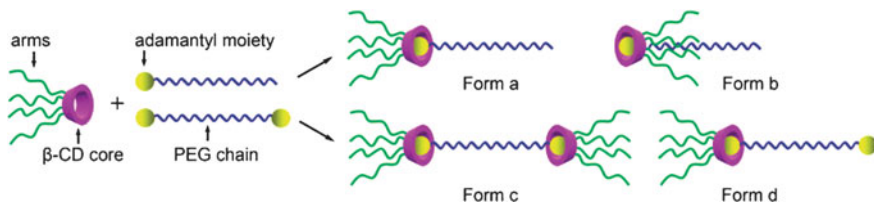
Fig. 6.66 Different chain architectures of pseudo block copolymers composed of β-CD-core star PNIPAM and PEG via inclusion complexation (reproduced from Ref. [406] with kind permission of © 2008 American Chemical Society)

changed significantly, i.e., LCST of these self-assembling systems was greatly increased depending on the ratio of ADA moiety to β-CD core and/or the length of the PEG blocks. When the PEG chain with ADA groups on both of its ends was used for complexation with β-CD-core star PNIPAAm, the LCST of linked block copolymer system reached to 39.2 °C. This method of combining short PEG chains to PNIPAAm by inclusion complexation provided an efficient way to control the LCST avoiding the conventional copolymerization of NIPAAm with hydrophilic monomers. So this supramolecular approach might be promising for the production of intelligent systems for biomedical and pharmaceutical applications.

Wang and Jiang used the concept of the inclusion complexation between β-CD and adamantyl group (ADA) as a driving force in constructing polymeric micelles [407, 408]. For this they have synthesized hydrophobic linear polymer PtBA-ADA and hydrophilic poly(glycidyl methylacrylate)) containing β-CD (PGMA-CD). The two polymers were dissolved in DMF, where their interaction was weak. Water was then added as a selective solvent, in which inclusion complexation came to dominate. Thus, micelles with PtBA-ADA as core and PGMA-CD polymer as shell were formed. The core and shell were non-covalently linked by inclusion complexation between β-CD and ADA. Moreover, when the shell was crosslinked and then the core was dissolved by switching the solvent from water to DMF, the micelles were converted into hollow spheres of PGMA-CD (Fig. 6.67) [407, 408].

Inclusion complexation could induce thermoresponsive assembly, because the binding ability of CD with different guests has its own entropy or enthalpy driven nature. Amphiphile containing a bipyridinium head and a bulky tail was taken to study the thermoresponsiveness of micelles [409]. The amphiphile formed a water soluble pseudorotaxane with α-CD below 60 °C. Since this structure is more entropy dependent, after heating, the amphiphile slid out of the α-CD cavities and formed micelles accommodating pyrene in the core. The whole process was fully thermoreversible accompanying the release or load of the pyrene moiety, which was monitored by the absorption spectra of pyrene. It was very interesting that in this system, if the ᵗBu group at the end was replaced by −OMe, α-CD was very stable on the chain of the amphiphile and could not be removed after heating. It is worth noting that this reversible thermoresponsiveness of the assembly is based on the thermal reversibility of inclusion complexation rather than the well-investigated
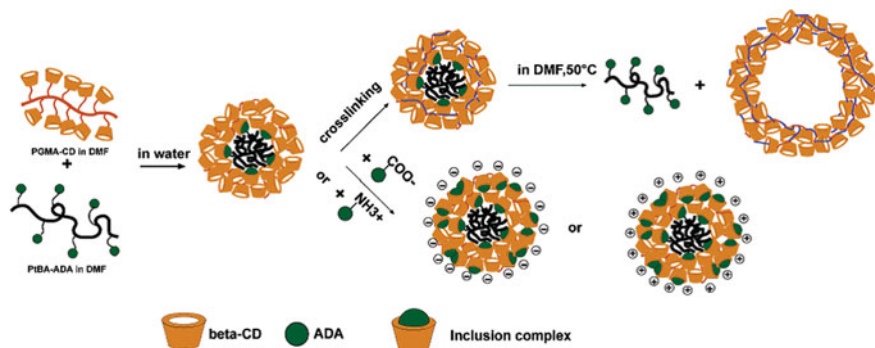
Fig. 6.67 Non-covalently connected micelles and the corresponding hollow sphere built by inclusion complexation (reproduced from Ref. [408] with kind permission of © 2006 American Chemical Society)

thermal behavior of polymers such as PNIPAAm chains. Further, Ritter et al. observed that PIL, poly[1-butyl-3-vinylimidazolium bis(trifluoromethanesulfonyl)-imide] showed a pseudo-LCST effect in aqueous solution in the presence of cyclodextrin due the temperature-sensitive formation/disruption of its inclusion complex [410].

AZO and Ferrocene (Fc) are the two most popular guests for reversible inclusion complexation with CDs. The *trans*-AZO binds strongly with α- or β-CD, while the binding capacities of *cis*-AZO with these CDs are very poor. With a few exceptions, CD normally binds to neutral or anionic compounds only. So the oxidized state of Fc binds very weakly to CDs because of its cationic nature, while the reduced state of neutral iron of Fc binds properly [378]. Recently, Wang et al. [411] reported the formation of micelles by inclusion complexation of two block copolymers. They synthesized two copolymers based on PEG-*b*-PAA with respective β-CD and AZO modifications on the PAA blocks, which were self-assembled into micelles driven by inclusion complexation between β-CD and AZO groups. After crosslinking, the assembly structure was capable of loading/unloading pyrene, which is photo-switchable by the inclusion complexation of CD/AZO. Further, Yuan et al. reported that β-CD end-capped PS(β-CD-PS) and Ferrocene (Fc) ended polyethylene oxide (PEO) (Fc-PEO) formed pseudo block copolymers of PS and PEO due to the inclusion complexation of β-CD and Fc [378]. The block copolymer formed stable vesicles in water. The vesicles were dismantled by positive electro-stimulation (+1.5 V) for 5 h, which oxidized Fc into Fc^+. This voltage-dissociated inclusion complexation was proved by a half-wave potential ($E_{1/2}$) decrease of 0.11 V accompanying an increase in the peak currents. Further negative electro-stimulation (−1.5 V) reassembled the vesicles by reduction of Fc^+ to Fc after 5 h (Fig. 6.68). Therefore, this work proved that voltage is also a good choice of clean stimuli for reversible association/disassociation based on inclusion complexation.

Further, a POSS-based supramolecular amphiphile prepared from the host–guest inclusion complexation between a mono adamantane-functionalized POSS
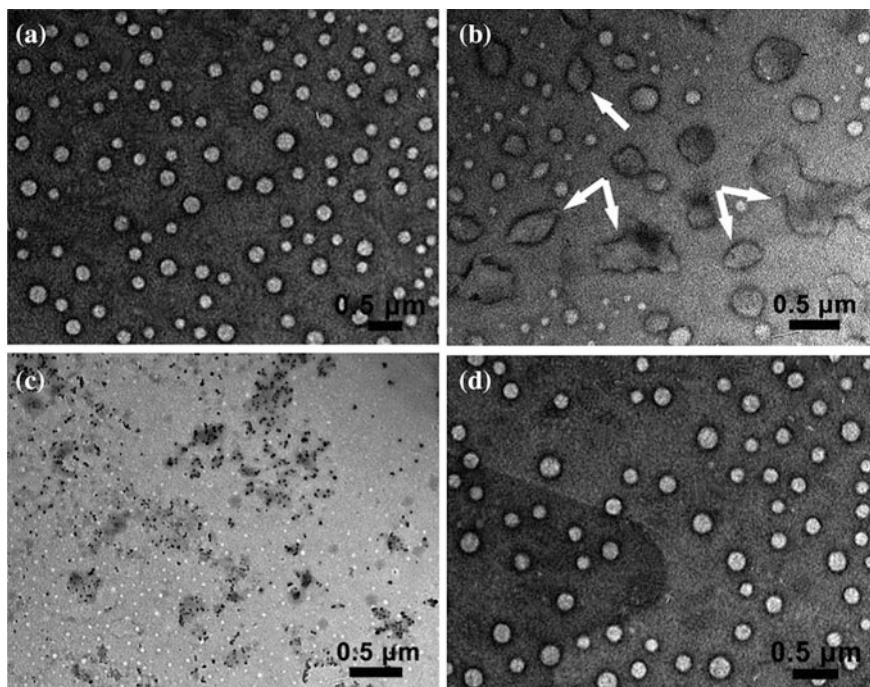
Fig. 6.68 TEM images of the reversible assembly/disassembly of the voltage-responsive β-CD-PS/Fc-PEO vesicles upon electric stimuli: **a** no external voltage, **b** +1.5 V (after 2 h), **c** +1.5 V (after 5 h), and **d** −1.5 V (after 5 h) (reproduced from Ref. [378] with kind permission of © 2010 American Chemical Society)

(AD-POSS) and a β-cyclodextrin oligomer [Poly(β-CD)] have been reported by Jiang et al. [412] (Fig. 6.69). Assisted by the interface of H$_2$O/toluene, the obtained supramolecular hybrids self-assembled into stable hollow nanospheres with thick walls. These hollow nanospheres aggregated together into a sphere layer through a spin coating technique, which then further transformed into a thin porous film containing nanometer-sized scaleholes.

6.9 Mechano-responsive Polymers

There is growing interest in the use of mechanical energy to alter the molecular and supramolecular structure of polymers to create stress-responsive materials [413, 414]. Chemical reactions that are accelerated by force remain poorly understood, and there is a need for the rapid discovery of new mechanophores (i.e., stress-sensitive units). Many specimens of chemically, thermally, electrically, optically, or otherwise responsive materials are known, but comparably few
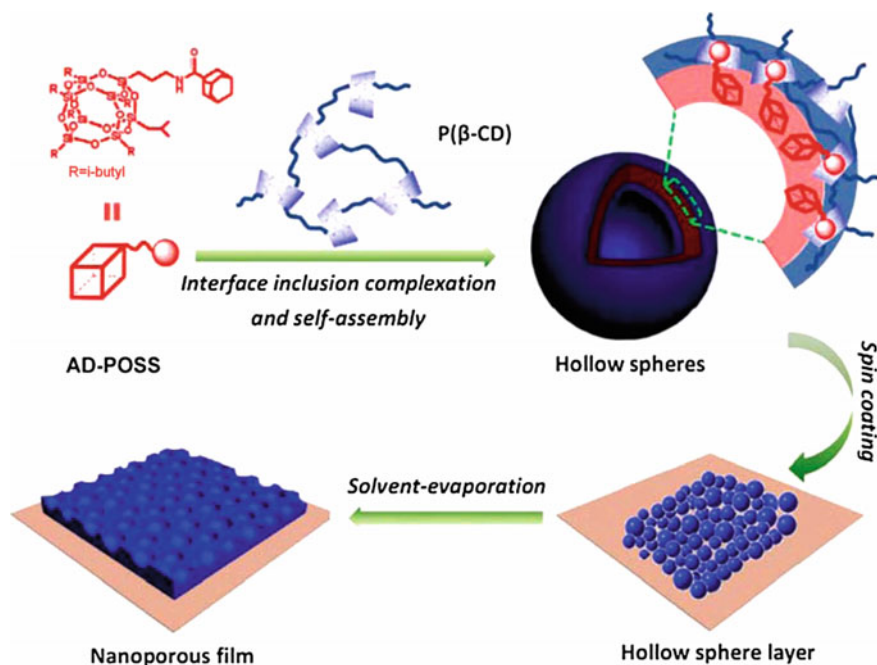
Fig. 6.69 Chemical structures of AD-POSS and P(β-CD) and schematic representation their hierarchical self-assembly into hollow spheres and thin nanoporous films (reproduced from Ref. [412] with kind permission of © 2012 Wiley-VCH)

materials have been studied, which respond in a useful and controlled manner to the exposure of mechanical stress. Therefore, a discussion regarding these types of mechano-reponsive polymer materials is highly important in the context of the present review, although, to the best of our knowledge there are no such reports formations of nanostructures such as micelles, vesicles that are responsive to mechanical energy.

In order to successfully design mechano-responsive materials, researchers are trying to draw inspiration from nature, especially biological systems, because most of them are mechano-responsive to their environment [415–417]. As for example, *titin*, (Fig. 6.70a) a giant protein in muscles, which own a remarkable combination of strength, toughness, and elasticity, is essential for the assembly and elasticity of the sarcomere. In other words, *titin* has good mechanical properties and is sensitive to mechano-stimulus. Generally, polymers do not have such a combination of properties.

However, Guan and coworkers described the synthesis of a *titin*'s prototype modular polymer by incorporating the quadruple hydrogen bonding 2-ureido-4 [1*H*]-pyrimidone (UPy) motif within a macrocycle that reveals a rare combination of high modulus, toughness, and elasticity, while demonstrating smart mechanical properties [417]. The target polymer (P1 in Fig. 6.70) (M_n = 18.0 kDa, PDI = 1.7)

was obtained by acyclic diene metathesis (ADMET) with a Grubbs Gen-2 catalyst, which did not aggregate in solution as shown by DLS. This polymeric material showed very intriguing mechanical properties. It is a relatively stiff kind of material with a Young's modulus of about 200 MPa and undergoes large deformation (maximal strain >100%) with a relatively small increase in stress, resulting in the absorption of a large amount of energy (Fig. 6.70b). The continuous unfolding of UPy dimer modules at the molecular level upon stretching bestows high toughness behavior on the material. In further studies, it was observed that the plastic deformation is not permanent and could gradually self-recover with time (>18 h) or upon heat treatment (about 30 s at 80 °C).

In addition to the self-healing process, the material also showed an interesting shape-memory behavior in spite of no permanent or physical crosslinks within
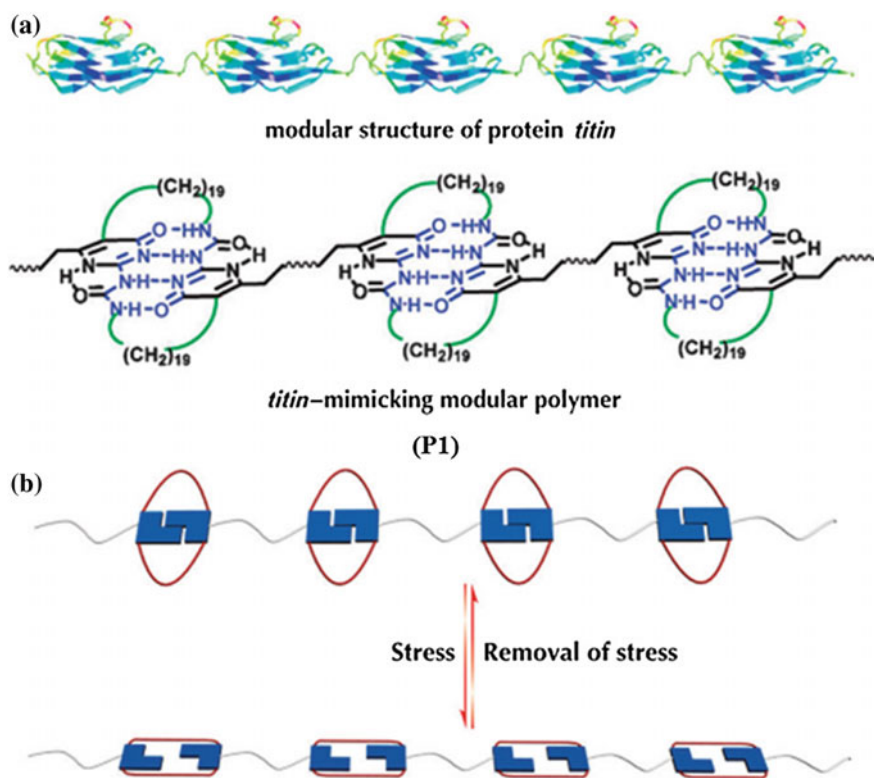
Fig. 6.70 Modular structure of *titin* protein and chemical structure of biomimetic linear modular polymer (P1), (**a**) and schematic illustration of the biomimetic polymer showing the stress effect on the molecular structure of P1 (**b**) (reproduced from Ref. [417] with kind permission of © 2009 American Chemical Society)
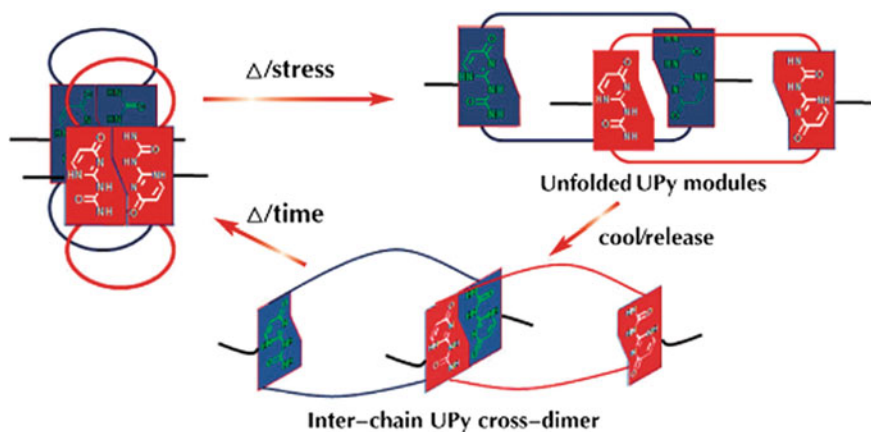
Fig. 6.71 The proposed molecular mechanism on the mechanical properties of the biomimetic modular polymer (P1) (reproduced from Ref. [417] with kind permission of © 2009 American Chemical Society)

the polymer. The unusual molecular topology can contribute to the formation of stable entanglements, thereby resulting in the shape-memory effect. Upon strain-induced breaking of the macrocyclic UPy dimer, inter-molecular UPy dimers form, fixing the material in a temporary state (Fig. 6.71). Once the UPy dimer reverts back to the preferred intra-macrocyclic dimer, the material recovers to its original state. The stress–strain behavior and the shape-memory effect show good mechanical properties found in *titin* and fascinating adaptive behavior. However, when the UPy units were protected to prevent dimer formation, the material was brittle and fractured at 7% strain, while lacking extensibility or any adaptive properties.

Ultrasonication has proven to be one of the most efficient mechanical stimuli to induce chain scission of polymers in solution [414, 418, 419]. Paulusse and his coworkers demonstrated an excellent example about sonication-induced reversible mechanochemistry of a Pd^{II} coordinated supramolecular polymer [414]. The following metallo-supramolecular polymer (P2 in Fig. 6.72, $M_w = 1.70 \times 10^5$) was developed by stirring a solution of diphenylphosphine-terminated poly(tetrahydrofuran) ($M_n = 7300$, PDI = 1.11) with a small excess of palladium dichloride (PdCl$_2$) in toluene for 2 days. After sonicating the polymer solution in the presence of toluene for 1 h, M_w of the as-synthesized polymer was shown to decrease from 1.70×10^5 to 1.02×10^5 while the original molecular weight of the polymer was recovered nearly quantitatively on removal of the sonication for 1 day (Fig. 6.72). The procedure was repeated five times without irreversible polymer abasement, showing that sonication-induced mechanical forces are highly selective for the metal-coordination bonds. Furthermore, it has been found that the sonication can
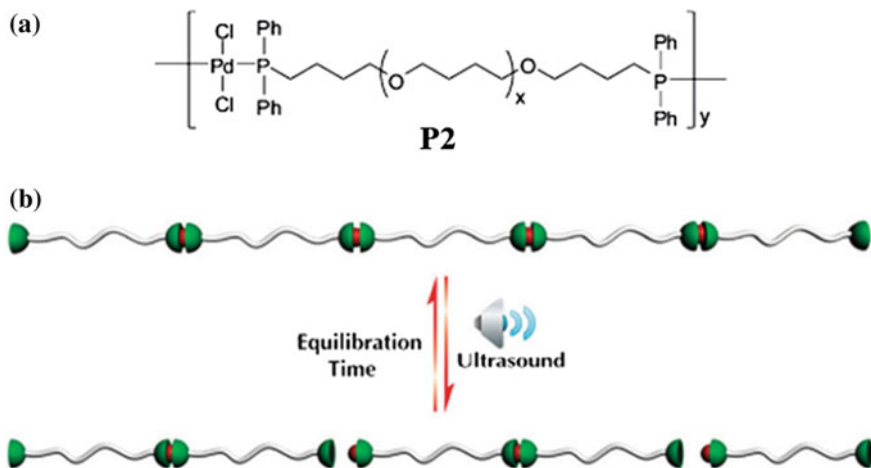
Fig. 6.72 Chemical structure of ultrasound-responsive metallo-supramolecular polymer (P2) (**a**) and schematic representation of its sonication-induced reversible mechanochemistry (**b**) (reproduced from Ref. [414] with kind permission of © 2004 Wiley-VCH)

also lead to an increase in polymeric material of a more specific length (after 5 min of sonication, the greatest increase was found at $M_w = 1.90 \times 10^5$) and ultrasonic chain scission is a non-random process that acts specially on longer chains. Afterwards, the same research group has also employed the similar technique to access an ultrasound-responsive metallo-supramolecular polymer gel [420] and moved on this concept to fabricate ultrasound-induced catalysis [421]. These valuable results and distinguished examples represent a novel methodology for exploring the reversible mechanochemistry of supramolecular polymer materials toward useful applications.

6.10 Dual Stimuli-Responsive Polymer Nanomaterials

In recent years, there have been lots of developments in the area of responsive polymers not only with respect to single stimulus but also show a responsive behavior to dual or multiple stimuli. Dual or multiresponsive polymer systems are of great interest and attracted notable attention in academia because of the possibility to tune their properties in multiple ways [320, 422–424]. For example, temperature-responsive polymers can be tagged with light-responsive chromophores to fabricate temperature and light-responsive polymers, and temperature-responsive polymers can be combined with pH-responsive functional group to build temperature- and pH-responsive polymers.

6.10.1   Temperature- and pH-Responsive Polymer Nanostructures

Temperature- and pH-responsive polymer nanomaterials have been extensively studied in drug delivery because these two parameters often differ from the normal value in diseased tissue [425–427]. Dual thermo- and pH-responsive polymers typically contain a PNIPAM or PEG unit as the thermoresponsive block and a polyamine or poly(carboxylic acid) unit as the pH-sensitive block. Hydrophilicities of both blocks undergo a substantial change in response to these stimuli and resulting in shifting of hydrophilic-lyophilic balance (HLB) of the polymer, and it can act as a driving force to umpire the assembly and disassembly process. Very recently, Liu, Chen, and his coworkers reported the self-assembly behavior of pH- and thermoresponsive hydrophilic ABCBA-type pentablock copolymer, consisting of PEG, PNIPAM, and poly(2-(diethylamino)ethyl methacrylate) (PDEA) [428]. This copolymer, PDEA-*b*-PNIPAM-*b*-PEG-*b*-PNIPAM-*b*-PDEA, was synthesized by consecutive RAFT polymerization technique. Solution properties of the copolymer (PDEA-*b*-PNIPAM-*b*-PEG-*b*-PNIPAM-*b*-PDEA) can be manipulated easily because of its multicomponent and multifunctional nature. For example, the copolymer was molecularly dissolved in acidic solution at room temperature because at this condition, pH of the solution is below the pK_a value of PDEA block and the temperature is below the LCST of PNIPAAm block (Fig. 6.73). However, in alkaline medium at room temperature, the copolymer can self-assembled into core–shell–corona micelles, with the hydrophobic PDEA block as the core, the thermoresponsive PNIPAAm block as the shell and the hydrophilic PEG block as the corona (Fig. 6.73). Upon increasing the temperature above the cloud point of PNIPAAm block in acidic medium, the copolymer self-assembled into hydrophobic PNIPAAm-core micelles with mixed hydrophilic PEG and pH-responsive PDEA coronas (Fig. 6.73). These properties of the thermo- and pH-responsive micelles open up new opportunities in the field of intelligent drug delivery systems.

We have also involved in the synthesis of amino acid-based dual thermo- and pH-responsive zwitterionic polymer. We have synthesized L-serine-based zwitterionic polymers (PSAs) of controllable molecular weights and low dispersities via RAFT polymerization technique in water (see Fig. 6.74) [315]. PSAs exhibited an isoelectric point at around pH 2.85 and within the pH range of 2.3–3.5, the aqueous PSA solution became a two-phase system due to the formation of insoluble aggregated structure of PSA through the electrostatic attraction between the pendent cationic ammonium and anionic carboxylate groups of PSA (Fig. 6.74). Furthermore, within this pH range of 2.3–3.5, the PSAs exhibited reversible UCST-type phase transition due to the formation of aggregated globular nanostructures below cloud point and transformed into soluble coils above the cloud point (Fig. 6.74). Finally, fluorescent labeling of PSA was carried out with FITC, and the final conjugate retained its dual-responsive nature (i.e., temperature and pH) for its future potential application in sensors and bioimaging. The work in this direction is currently underway in our laboratory.
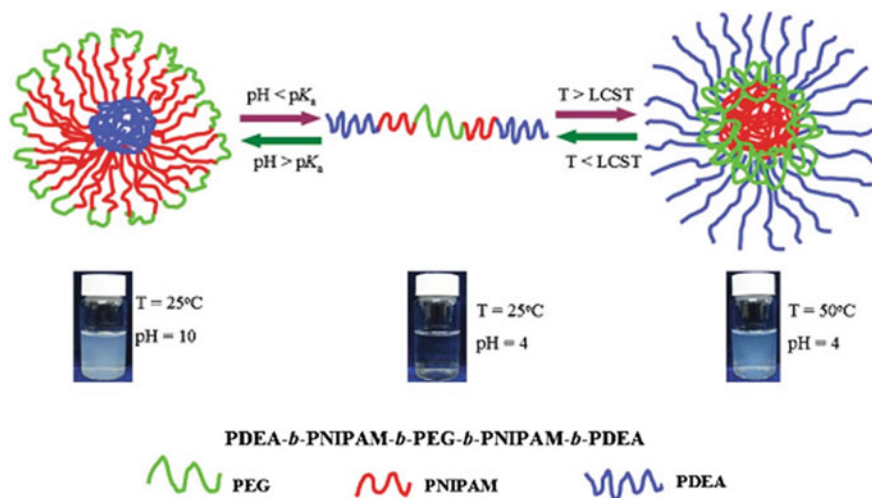
Fig. 6.73 Schematic representation of temperature- and pH-sensitive self-assembly behavior of the ABCBA-type pentablock copolymer (reproduced from Ref. [428] with kind permission of © 2013 Royal Society of Chemistry)
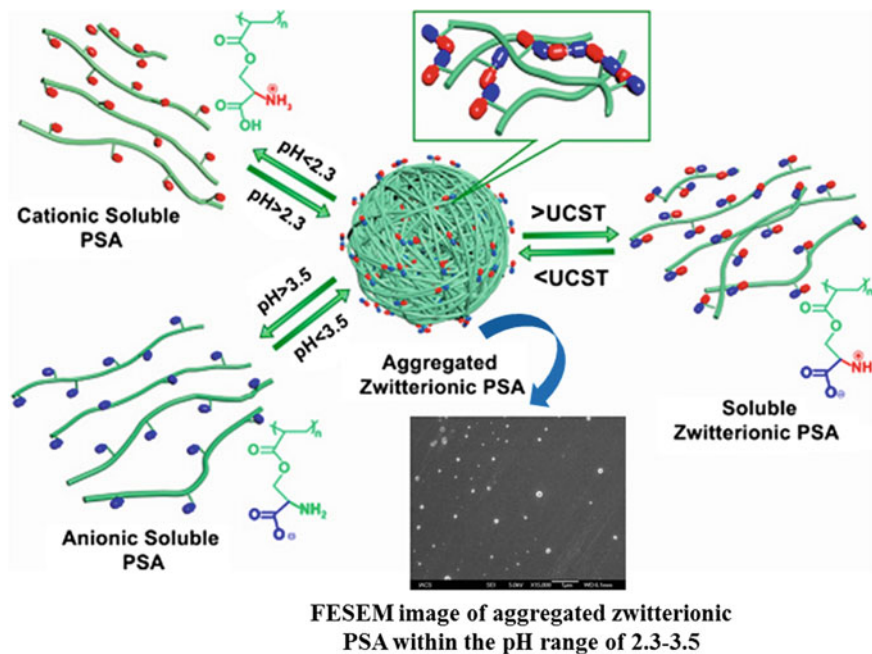
Fig. 6.74 Schematic illustration of temperature- and pH-induced phase transition of poly(L-serinyl acrylate) (PSA) (reproduced from Ref. [315] with kind permission of © 2015 American Chemical Society)
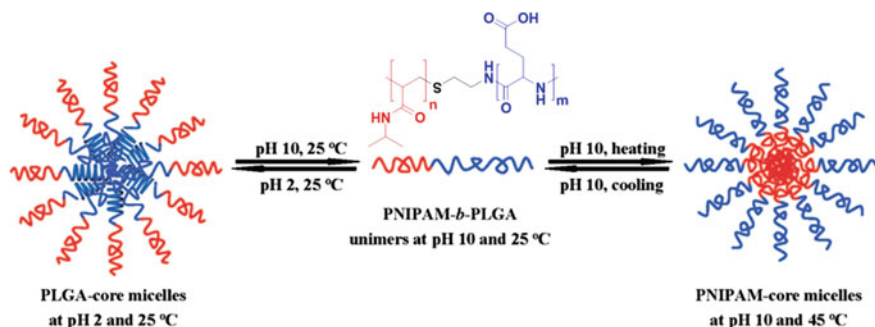
Fig. 6.75 Schematic representation of the thermo- and pH-sensitive micellization of PNIPAAm-*b*-PLGA associated with coil-to-helix transitions (reproduced from Ref. [429] with kind permission of © 2007 American Chemical Society)

Liu et al. reported a polypeptide hybrid double-hydrophilic poly(*N*-isopropylacrylamide)-*b*-poly(L-glutamic acid) (PNIPAAm-*b*-PLGA) BCP, which was synthesized via the ring-opening polymerization of γ-benzyl-L-glutamate *N*-carboxyanhydride using monoamino-terminated PNIPAAm as the macroinitiator [429]. It is noteworthy that the as-synthesized BCP contains a thermoresponsive PNIPAM block and pH-responsive PLGA block. However, the obtained polypeptide hybrid diblock copolymer molecularly dissolves (Fig. 6.75) in aqueous solution at alkaline pH, and at room temperature but supramolecularly self-assembled into PNIPAAm-core micelles (Fig. 6.75) at alkaline pH and at an elevated temperatures. Further at acidic pH and at room temperature, the PMIPAM-*b*-PLGA copolymer formed PLGA core micelles with coil-to-helix transition of the PLGA sequence.

A poly(ethylene glycol)-*b*-poly(n-butyl methacrylate)-*b*-poly(*N*,*N*′-dimethylamino ethyl methacrylate)(PEG-*b*-PnBMA-*b*-PDMAEMA) triblcok copolymer with a dual pH- and thermoresponsive PDMAEMA as end segment was developed via sequential RAFT polymerization [430]. The PEG-*b*-PnBMA-*b*-PDMAEMA triblock copolymer molecules self-assembled into spherical micelles in acidic solution but transformed into cylindrical micelles in alkaline solution. This pH-induced shape transformation was reversible. Moreover, this triblcok copolymer underwent a pathway-dependent re-assembly from cylinder to toroid or to vesicle upon programmed variation of solution pH and temperature in dilute aqueous solution. It was found that the re-assembly from cylinder to toroid or to vesicle was apparently irreversible as confirmed through DLS and cryogenic transmission electron microscopy (cryo-TEM).

Zhang et al. [431] have demonstrated a new approach based on using UCST polymers to develop assemblies that are able to undergo a solubility transition in aqueous solution at room or body temperature (37 °C) in response to a small pH change. Here, two copolymers, P(AAm-*co*-AN-*co*-AAc) or P(AAm-*co*-AN-*co*-4VP)), were synthesized by incorporating either acrylic acid (AAc) or 4-vinylpyridine (4VP) comonomer units in the random copolymer of acrylamide

and acrylonitrile, P(AAm-*co*-AN) through RAFT technique. As mentioned above that this random copolymer, P(AAm-*co*-AN)), exhibited an UCST-type phase transition [136]. The pH-induced shift of UCST cloud point was investigated by them by monitoring the solution cloud point. Their results revealed an unusually large shift of the cloud point upon pH variation over a small range.

In particular, one P(AAm-*co*-AN-*co*-4VP) sample exhibited a cloud point drop from 72 °C at pH 4.75–15 °C at pH 4.50, and its transition from soluble to insoluble state at room temperature was visually observable over a pH change as little as 0.05 unit. Using P(AAm-*co*-AN-*co*-4VP) as macromolecular chain transfer agent to polymerize dimethylacrylamide (DMAAm) through RAFT, an ABA-type triblock copolymer of P(AAm-*co*-AN-*co*-4VP)-*b*-PDMAAm-*b*-P(AAm-*co*-AN-*co*-4VP) was prepared, which showed an even larger cloud point switch from 71 to 10 °C with pH decreasing from 4.75 to 4.50. Consequently, the micelle formed by this block copolymer was stable at 37 °C with pH from 7.00 down to 4.75 but abruptly dissolved at pH 4.50 due to the water solubility switch [431]. This study demonstrated a new UCST polymer-based approach to polymer assemblies that can sense a very small pH change by undergoing straightforward water solubility switch.

In another example, an ionically assembled nanoparticles (INPs) have been prepared from poly(ionic liquid-*co*-*N*-isopropylacrylamide) composed of poly (ethylated 4-vinylpyridine) and PNIPAAm with deoxycholic acid through electrostatic interaction (Fig. 6.76) [432]. The assembled complex nanoparticles were disrupted under acidic conditions, where DA is protonated leading to a decrease in electrostatic interactions which are the driving force for the assembly. Appreciable release of guest molecules was observed at pH 5.2 at 37 °C, elevating the temperature enhanced the release percentage at the same pH. When heated above the LCST at pH 7.4, PNIPAAm presumably became less hydrophilic causing inter-particle aggregation, which likely caused the guest molecules to be squeezed out [432].

Zuo et al. [433] have been demonstrated a facile strategy for the preparation of thermo- and pH-responsive nanogels particles through RAFT crosslinking copolymerization of ionic liquid-based monomers. The use of chain transfer agents (CTAs) containing carboxyl group in the RAFT polymerizations is the key to producing highly thermoresponsive nanogel particles. It was demonstrated that the critical gelation temperature of the as-prepared nanogels can be tuned by adjusting the feed ratio of monomer and CTA. It was proposed based on the results of temperature-dependent FTIR and other control experiments that the hydrogen bonding interactions between the carboxyl groups of CTAs are responsible for the thermoresponsive behaviors of PIL-based nanogel nanoparticles. Furthermore, PIL-based nanogels are also found to be pH-sensitive and can be further decorated by PNIPAAm via surface-grafting polymerization. PNIPAAm-grafted nanogel aqueous suspensions can be reversibly transformed into macrogel particles upon a change in temperature [433]. A oral delivery copolymeric system consisting of thermoresponsive zwitterionic poly(sulfobetainemethacrylate) (polySBMA) and pH-responsive poly(2-(diisopropylamino)ethyl methacrylate) (PDPA) was
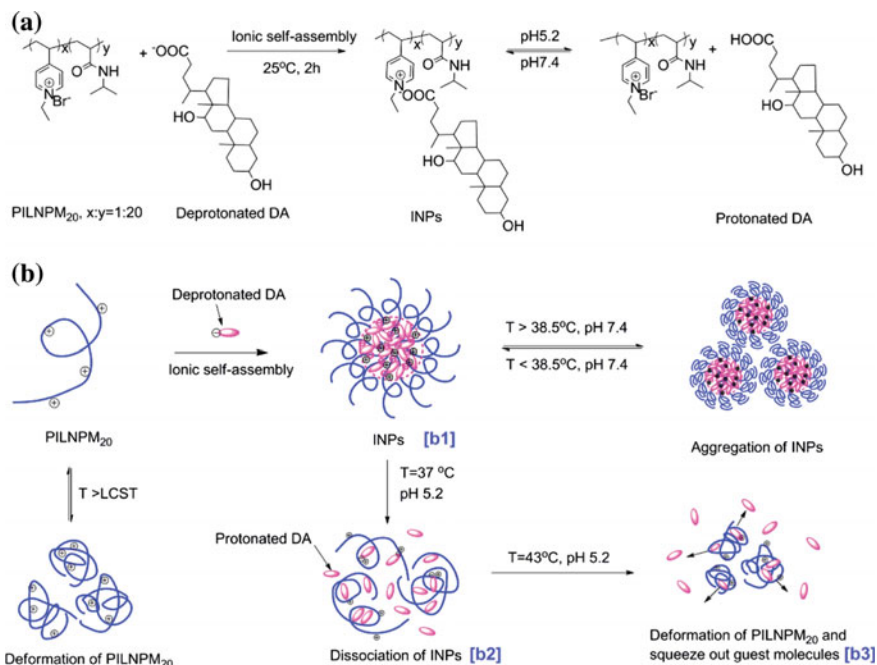
Fig. 6.76 a Preparation of INPs. **b** Temperature and pH mediated disassembly of electrostatically assembled nanoparticles (reproduced from Ref. [432] with kind permission of © 2012 American Chemical Society)

synthesized via free radical polymerization [434]. This copolymer self-aggregated into nanogel particles via electrostatic attraction between ammonium cation and sulfo-anion of poly(SBMA) and successfully encapsulate anticancer drug, curcumin. The stimuli-responsive phase transition behaviors of P(SBMA-*co*-DPA) copolymers at different pH buffer solution showed pH-dependent UCST-type transition attributed to the influence of protonation/deprotonation of the pH-responsive PDPA segments. Through the delicate adjustment of the poly (SBMA)/PDPA molar ratios, the stimuli-responsive phase transition could be adjusted to physiological environment [434].

6.10.2 Temperature- and Light-Responsive Polymer Nanostructures

There are several arresting reports that allow for a fine-tuning of the LCST/UCST-type cloud point of a polymer or block copolymer by light irradiation or enable the controlled formation of nanoaggregates by combining temperature and light. The first example of a temperature and light-responsive polymer system

was random copolymers of NIPAAm with *N*-(4-phenylazophenyl)acrylamide of varying compositions. The objective of their work was to control the phase transition temperature of aqueous solution of PNIPAAm by incorporating photochromic azobenzene moieties [435]. They have demonstrated that there was a clear shift in the LCST-type phase transition temperature from initially 21 to 27 °C after UV light irradiation ($\lambda = 360$ nm) was observed for the copolymer system containing 2.7 mol% of azobenzene group. This change was explained by the change in the dipole moment due to the *trans*-to-*cis* isomerisation of the azobenzene moieties upon UV light irradiation. As mentioned above that the isomerization of azobenzene upon UV/visible light irradiation is accompanied by a strong polarity change. This polarity change is a direct consequence of the change in the dipole moment from 0 Debye for the *trans*-isomer to 3 Debye for the *cis*-isomer [435]. However, the initial phase transition temperature of 21 °C was re-obtained after visible light ($\lambda = 440$ nm) exposure because at this wavelength, *cis*-form re-isomerizes into *trans*-form.

Another report based on thermo- and light-responsive copolymers was the work of Ravi and his coworkers [424]. The authors synthesized a copolymer, poly(2-(dimethylamino)ethyl methacrylate-*co*-poly(azo-methacrylate) (PDMAEMA-*co*-PAzM), via ATRP in which the PDMAEMA block exhibits a LCST behavior (Fig. 6.77). LCST of the PDMAEMA-*co*-PAzM BCP increased upon UV irradiation from 41 °C for the *trans*-form to 44 °C for the *cis*-form (Fig. 6.77). The LCST of the copolymer (PDMAEMA-*co*-PAzM) increased upon irradiation by UV light due to the *cis* conformers being more hydrophilic. In addition to this, the following copolymer (PDMAEMA-*co*-PAzM) can self-assembled into core–shell micelle as evident from TEM image (Fig. 6.77).

Another synthetic illustration of thermo-and light-responsive BCP was described by Kakuchi and his coworkers with the combination of ATRP and "click" chemistry. In this context, an azide terminated PNIPAM was conjugated to an alkyne terminated poly(6-[4-(4-methoxyphenylazo)phenoxy]hexyl methacrylate) by CUAAc technique, resulting in the formation of BCP consisting of one thermoresponsive block and one photoresponsive block [436]. They observed that upon UV light irradiation, LCST-type cloud point of the BCP increases up to 4.1 °C from *trans*- to *cis*-form of the BCP containing only 1.4 mol% of azobenzene. Another pioneering work in this area was on the synthesis of thermo- and light-sensitive BCP namely poly(ethylene oxide)-*b*-poly(ethoxytri(ethylene glycol) acrylate-*co*-*o*-nitrobenzyl acrylate) (PEO-*b*-P(ETEGA-*co*-NBA)) (Fig. 6.78) via ATRP and the investigation of the micellization/dissociation transitions in water in response to temperature changes and UV light irradiation [437]. The PETEGA sequence confers the thermosensitivity into the BCP, (PEO-*b*-P(ETEGA-*co*-NBA)) which displays a cloud point at around 25 °C (LCST$_1$). Upon UV light irradiation, the irreversible photocleavage of *o*-nitrobenzyl ester moieties into carboxylic acid increases the hydrophilicity of the BCP and consequently, increases the cloud point by more than 10 °C (LCST$_2$ = 36 °C). The PEO-*b*-P(ETEGA-*co*-NBA) BCP was molecularly dissolved in water at low temperature. But at higher temperature above LCST$_1$, the BCP can self-assemble into polymer micelles where the
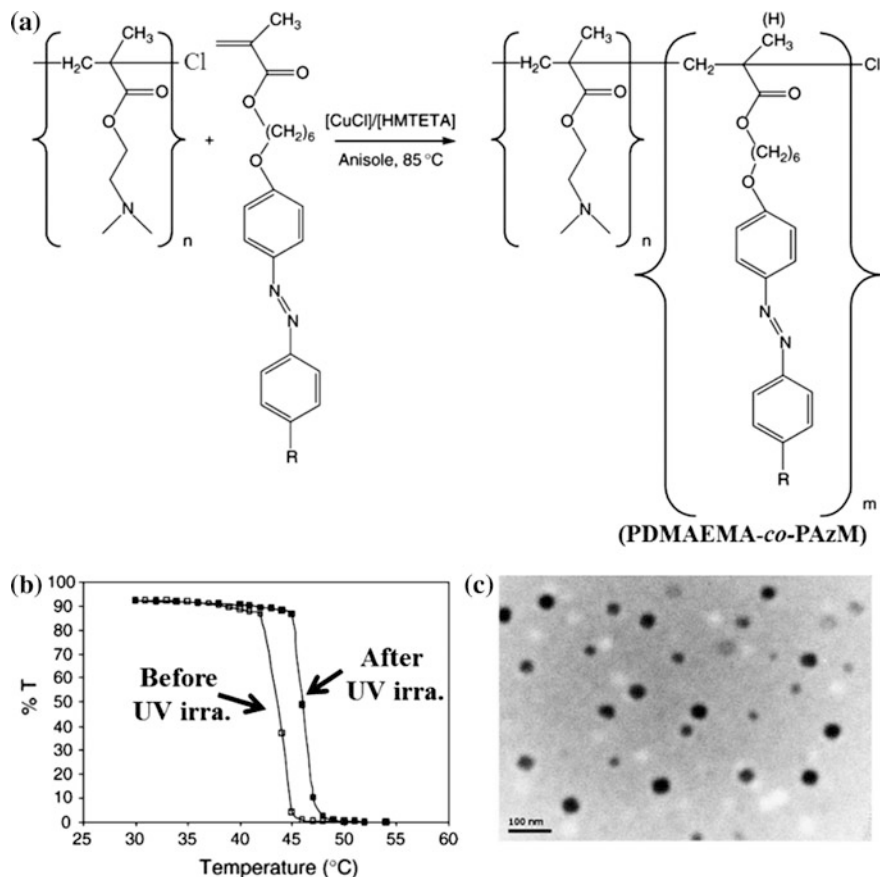
Fig. 6.77 Synthetic route to the formation of amphiphilic PDMAEMA-*co*-PAzM copolymer by ATRP; (**a**) %T at 600 nm of 0.7 wt% aqueous solutions of PDMAEMA-*co*-PAzM before and after UV light irradiation at different temperature (**b**) and TEM micrograph of micelles formed by the self-assembly of PDMAEMA-*co*-PAzM copolymer in water (**c**) (reproduced from Ref. [424] with kind permission of © 2005 American Chemical Society)

thermoresponsive PETEGA block forms the core and PEO block forms the corona (Fig. 6.78). Upon UV light irradiation, photolysis of *o*-nitrobenzyl ester units taken place and therefore, cloud point of thermosensitive block (PETEGA) was increased, causing the dissociation of micelles into unimers (Fig. 6.78), leading to the release of encapsulated fluorescent dye NR into water. However, further increase in the temperature above $LCST_2$ induced the reformation of micelles (Fig. 6.78) and re-encapsulation of NR. Here, the thermo-induced formation and dissociation of micelles were reversible.

In 2010, Jian et al. [438] developed spiropyran-based novel thermo- and light-responsive BCP to fabricate micelles and reverse micelles in aqueous solution. The BCP namely poly(spiropyranmethacrylate)-*b*-poly((diethylene glycol) methyl
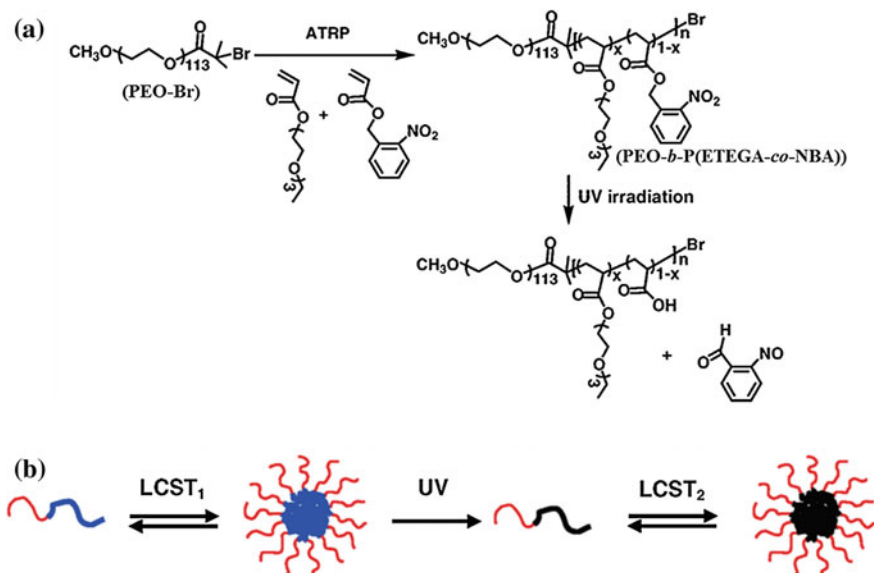
Fig. 6.78 Synthetic procedure of thermo- and light-responsive PEO-*b*-P(ETEGA-*co*-NBA) BCP through ATRP and cleavage of *o*-nitrobenzyl group by UV light irradiation; (**a**) multiple micellization and dissociation transitions of thermo- and light-sensitive PEO-*b*-P(ETEGA-*co*-NBA) in water in response to temperature changes and UV light irradiation (**b**) (reproduced from Ref. [437] with kind permission of © 2008 American Chemical Society)

ether methacrylate) (PSPMA-*b*-PDEGMMA) was synthesized by ATRP of spiropyran containing methylacrylate (SPMA) with di(ethylene glycol) methyl ether methacrylate (DEGMMA). At 15 °C and under visible light, the molecularly dissolved PSPMA-*b*-PDEGMMA in water was transforming into core–shell micelles (*D* = 80 nm) where photosensitive and hydrophobic PSPMA block was in the core and hydrophilic PDEGMMA formed the corona (Fig. 6.79).

Upon irradiation with UV light, spiropyran moiety changed from its nonpolar spiropyran to polar mecrocyanine form and resulting in the isothermal disruption of micelles (Fig. 6.79), and the process is fully reversible. Upon visible light exposure, mecrocyanine isomerized back into less polar spiropyran form and the micells are regenerated (Figure 6.79). However, further irradiation with UV light followed by heating resulted in the formation of reverse micelles having hydrodynamic diameter of 24 nm (Fig. 6.79). In this case, at higher temperature, thermosensitive PDEGMMA block forms the core and more polar mecrocyanine unit forms the corona (Fig. 6.79). This study represents a fascinating contribution to applying light and temperature independently in order to control the morphology of nanoaggregates in solution and can be used as "smart" polymer nanocarriers for controlled encapsulation, triggered release and re-encapsulation of model drug coumarin 102.
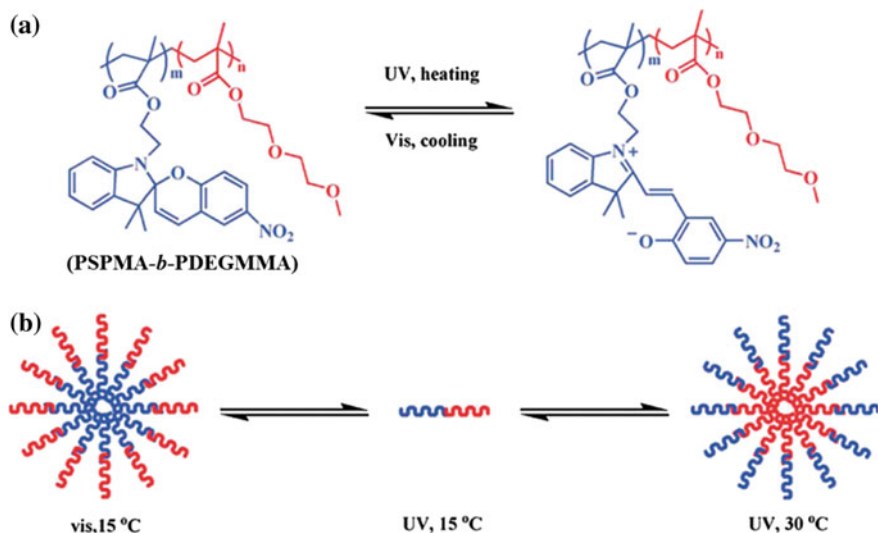
Fig. 6.79 Schematic representation of reversible photoreaction of a spiropyran (SP) containing amphiphilic PSPMA-*b*-PDEGMMA BCP; (**a**) Schematic representation of double-responsive micellization of PSPMA-*b*-PDEGMMA BCP in aqueous solution (**b**) (reproduced from Ref. [438] with kind permission of © 2010 Wiley-VCH)

6.10.3   Redox- and pH-Responsive Polymer Nanostructures

Among the so-called chemically responsive drug delivery systems composed of polymeric materials, pH and redox are two popular stimuli employed to instigate sharp changes in the properties of polymer materials. These are the major chemical stimuli to trigger the drug release from cargos. Polymer nanocarrier that is designed to respond separately toward single pH or redox stimulus has been extensively investigated. However, polymer nanocarriers that can respond to both pH and redox stimuli are rare and still not investigated in detail [36].

A recent report described the formation of dual pH and redox sensitive micelles from a novel copolymer-based on PEG and reducible poly(β-amino ester)s (RPAE) containing disulfide bonds in the backbone and studied the intracellular release of doxorubicin (DOX) from these micelles (Fig. 6.80) [439]. According to them, these sub-100 nm micelles represented core–shell morphology with the RPAE constituting the core and the PEG as the shell and were stable under physiological conditions (pH > 7.0) (Fig. 6.80). At pH < 6.5, the protonation of tertiary amine of RPAE unit of the copolymer disrupts the hydrophilic-lyophilic balance in the micelles resulting in the dissociation of micelles (Fig. 6.80). In addition, dithiothreitol (DTT) triggered dissociation of RPAE-PEG micelles was also demonstrated due to the degradation of disulfide bonds present in the RPAE backbone (Fig. 6.80). They further showed that the encapsulated anticancer drug DOX can be released from RPAE-PEG micelles either in acidic pH (6.5) or upon treatment with
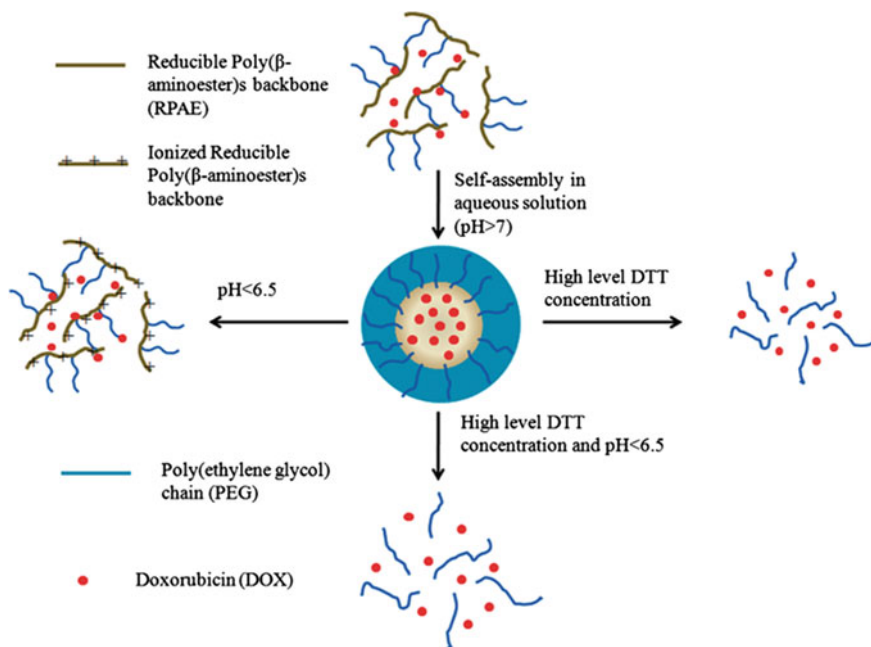
Fig. 6.80 Schematic representation of DOX-loaded RPAE-PEG copolymer micelles dissociation and release of DOX upon changes of pH, reducing agent concentration or both of them (Reproduced from Ref. [439] with kind permission of © 2011 American Chemical Society)

concentrated DTT solution (Fig. 6.80). The most important advantage of this design is that the highest rate of DOX release from the copolymer (RPAE-PEG) micelles was observed in an environment at a low pH value and with a high concentration of reductive agent (Fig. 6.80).

Another exciting example of dual pH- and redox-responsive polymer architecture is a core crosslinked micelle which was reported by Wang and his coworkers [440]. They designed the polymer on the concept of "AND" logic gate for intracellular drug delivery, since drug can only be released when both pH and redox stimuli are present. In this pioneering work, a drug molecule, adriamycin (ADR) was first attached to a hydrazine functionalized poly(ethylene oxide)-*b*-poly (methacrylic acid) (PEO-*b*-PMAA) BCP via the formation of hydrazone. The ADR-conjugated PEO-*b*-P(MAA-Hyd) can be self-assembled to form stable micelle which was further crosslinked in the presence of dithiodiethanoic acid. No remarkable ADR release was found under reducing conditions at neutral pH, due to the intact hydrazone linkage, even though the micelles were uncrosslinked due to the reduction of disulfides (Fig. 6.81). ADR was also not released upon treatment of the crosslinked micelles in an acidic pH. However, ADR was cleaved from the
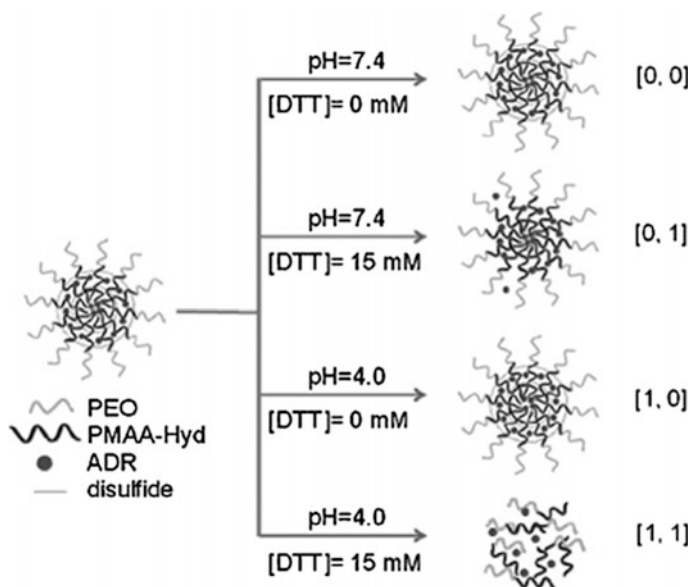
Fig. 6.81 "AND" logic gate for the release of adriamycin (ADR) from the crosslinked micelles of PEO-*b*-P(MAA-Hyd) using pH and DTT as input stimuli (reproduced from Ref. [440] with kind permission of © 2011 Wiley-VCH)

polymer backbone in acidic condition but it was trapped within the crosslinked micelles, and therefore, no effective release was observed (Fig. 6.81). The effective release of ADR could only be observed by simultaneous treatment at low pH and reducing reagents (Fig. 6.81). This smart device is therefore equipped with two triggers, pH, and redox with the "AND" logic gate for the releasing action, which is favorable for more complicated physiological conditions because the "ON" state is only realized under the simultaneous presence of the both the stimuli.

6.11 Multiple Stimuli-Responsive Polymer Nanostructures

Multiple stimuli-responsive polymer nanomaterials are responsive to more than two stimuli, are materially interesting, and are comparatively less investigated. However, recent research activities toward triple responsive polymer systems have gained propulsion. It is worth mentioning that effect of more than two stimuli on polymer system is highly advantageous because it will not only increase the degree of precision but also enlarge the switching window to play with its properties more sophisticatedly because of the higher level of complexity of the polymer.

6.11.1 Temperature-, pH- and Light-Responsive Polymer Nanostructures

Temperature-, pH-, and light-responsive polymer systems can only be obtained by the combination of building blocks that contain all pH-, thermo-, and photoresponsive moieties. In this direction, Zhou, Tang, and his coworkers reported the synthesis of temperature-, pH-, and light-responsive water soluble N,N-dimethylaminoethyl methacrylate (DMAEMA) homopolymers containing an azobenzene moiety as the terminal group by ATRP (Fig. 6.82) [54]. Indeed, the as-synthesized homopolymer exhibited a LCST-type transition that can be altered reversibly in response to pH and photoisomerization of the terminal azobenzene moiety. In an acidic pH (pH = 4), the DMAEMA units are fully protonated, resulting in increase in polarity and hence no LCST was observed. However, upon increase in pH, the LCST cloud point was lowered to 68 °C at pH = 7–30 °C at pH = 11 because of the continuous deprotonation of dimethyl amino groups. Additionally, upon UV light irradiation, the *trans*-to-*cis* photoisomerization of the azobenzene moiety increases the hydrophilicity of the polymer which leads to increase in cloud point. This kind of polymer systems is highly interesting for a variety of potential applications such as controlled drug delivery, intelligent materials because of their multistimuli-responsive property.

Another thermo-, pH-, and light-responsive polymer system was reported by Shinbo, Sumaru, and coworkers where they synthesized PNIPAAm functionalized with spirobenzopyran (SP) [441]. They investigated that the phase transition properties of aqueous solution of this copolymer exhibited a logic gate response with respect to light irradiation and in increase in temperature. It is worth mentioning that the PNIPAAm part in the polymer is responsible thermoresponsive behavior while light and pH-responsiveness is provided by the spirobenzopyran (SP) unit (Fig. 6.83). Similarly, Achilleos and Vamvakaki described synthesis of
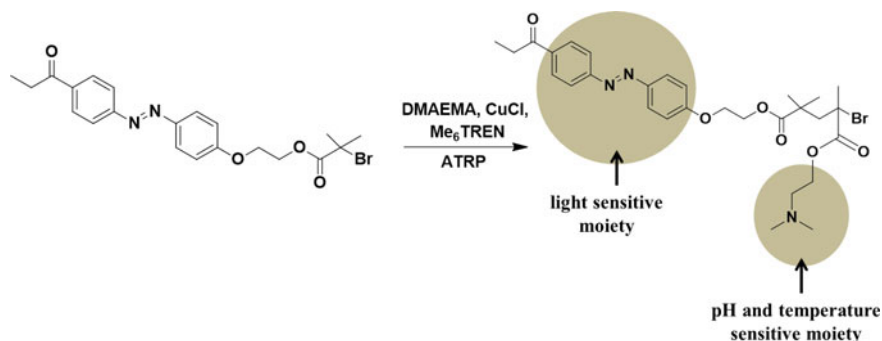
Fig. 6.82 Synthesis of triple-sensitive azobenzene-end functional PDMAEMA polymer system toward light, temperature and pH value (redrawn From Ref. [54] with kind permission of © 2010 Wiley-VCH)
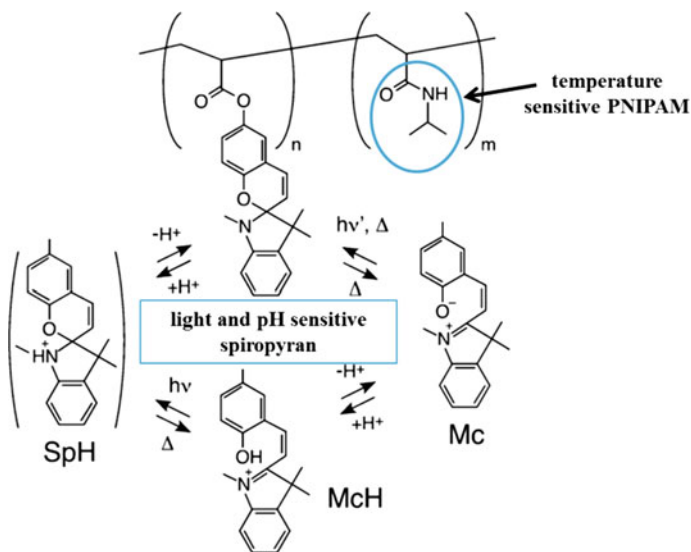
Fig. 6.83 Triple responsive polymer system based on dual-responsive (pH and light) spiropyran unit and thermoresponsive PNIPAAm unit (reproduced from Ref. [441] with kind permission of © 2004 American Chemical Society)

statistical copolymers comprising of a DMAEMA unit and a polymer block containing spiropyran unit [442]. In this case, not only the dimethylamino functionality acted as a pH-responsive unit, but also the spiropyran unit was able to respond to changes in pH along with the photoisomerization between the spiropyran and merocyanine isomers. Here, both the functional groups (DMAEMA and spiropyran) have dual-responsive property. DMAEMA moiety is sensitive toward both pH and temperature while spiropyran unit is sensitive toward pH and light.

Another triple-stimuli (thermo/pH/light)-responsive copolymer system was reported by Wang and coworkers [443]. In this report, poly(*N*-isopropylacrylamide-*co-N*-hydroxymethylacrylamide) P(NIPAAm-*co*-NHMAAm) was first synthesized by free radical polymerization method. Afterwards, photosensitive 2-diazo-1, 2-napthoquinone (DNQ) was partially grafted onto P(NIPAAm-*co*-NHMAAm) backbone through esterification to obtain triple-stimuli (thermo/pH/light)-responsive copolymer P(NIPAAm-*co*-NHMAAm-*co*-DNQMA) (Fig. 6.84). The NIPAM and NHMA moieties of the copolymer P(NIPAAm-*co*-NHMAAm-*co*-DNQMA) are considered to be thermo- and pH-responsive, respectively, while DNQ was designated as photoresponsive unit (Fig. 6.84). Upon UV light irradiation, hydrophobic DNQ moiety of the copolymer can undergo "Wolff" rearrangement irreversibly and converted into hydrophilic 3-indenecarboxylic acid derivative (Fig. 6.84). Photoirradiation increases the polarity and resulting in the change of hydrophilic-hydrophobic balance of the entire polymer. Indeed, they showed that
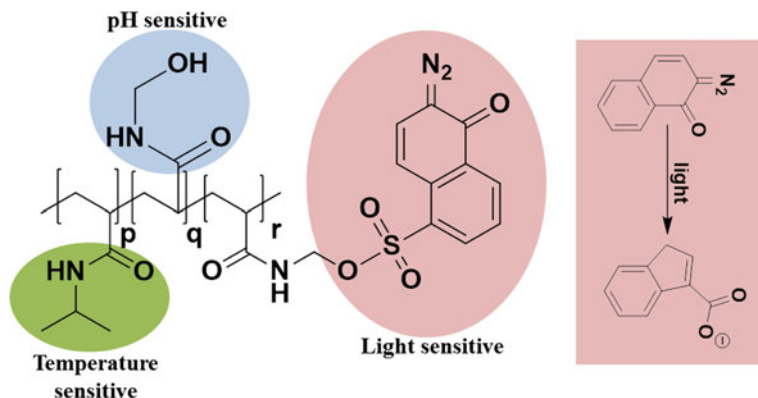
Fig. 6.84 Triple sensitive block copolymer system, P(NIPAAm-*co*-NHMAAm-*co*-DNQMA) containing temperature, light and pH-sensitive functional moieties (redrawn from Ref. [443] with kind permission of © 2009 Wiley-VCH)

the phase transition profile of P(NIPAAm-*co*-NHMAAm-*co*-DNQMA) copolymer can be tailored easily by pH variation as well as by UV light irradiation.

An interesting example of triple-stimuli (thermo/pH/light)-sensitive polymeric micelles for controlled release application was reported in 2013 by Dong and his coworkers [444]. To achieve the triple-stimuli sensitivity, they first synthesized hydrophilic pH/thermo-sensitive poly(*N,N*-dimethylaminoethyl methacrylate) (PDEAEMA). Afterwards, 14 mol% of dimethylamioethyl functionality of PDMAEMA block was quaternized by light-responsive 1-(bromomethyl)pyrene to introduce hydrophobicity into polymer system (Fig. 6.85). The BCP self-assembled into core–shell micelles in aqueous medium where the hydrophobic pyrene moieties constitute the core and the dimethylaminoethyl (DMAE) moieties forming the shell (Fig. 6.85). Above the LCST, PDMAEMA block becomes hydrophobic which resulted in shrinking of the micellar size (Fig. 6.85). However, upon UV light irradiation below LCST, photosolvolysis of pyrenylmethyl groups from the quaternized amine increases the hydrophilicity of the whole block polymer resulting in the complete disruption of micelles (Fig. 6.85). In addition, the micelles are collapsed to a complex micelle at high pH and swollen/dissociated at low pH (Fig. 6.85). It should be mentioned that the pH and the temperature-responsive behavior of this polymer were totally reversible while light-responsive behavior is fully irreversible because after light irradiation, the disrupted micelles never regain its initial form. These multistimuli-responsive polymer micelles have great potentiality to act as a sensitive nanocarrier for controlled release under the stimuli of UV light, temperature, and pH, especially under UV light and low pH where all the loaded guest molecules such as NR could be released completely.
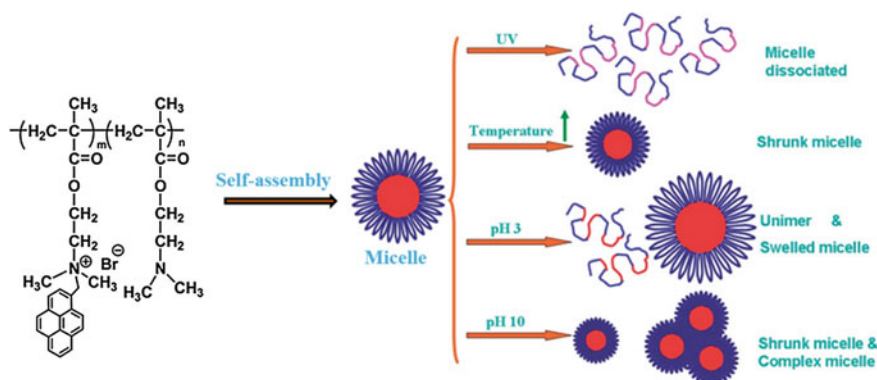
Fig. 6.85 Schematic representation of the structural changes of micelle under the stimuli of UV light, temperature, and pH (reproduced from Ref. [444] with kind permission of © 2009 Wiley-VCH)

6.11.2 Light-, Redox-, and Temperature-Responsive Polymer Nanostructures

Light-, redox-, and temperature-responsive polymer systems are also very interesting because of their unprecedented precision and versatility. However, this type of triple (light/redox/temperature)-responsive polymer systems are rare and less investigated. Theato et al. reported the synthesis of triple (light/redox/temperature)-responsive PNIPAM-based copolymers containing azobenzene and TEMPO moieties by post-polymerization modification strategy utilizing well-defined poly (pentafluorophenyl acrylate) (PPFPA) (Fig. 6.86) [445]. Here, TEMPO moiety is redox-responsive and can be reduced as well as re-oxidized in a reversible fashion by using ascorbic acid as a reducing agent and red prussiate as an oxidizing agent, respectively. The reduction of the TEMPO moiety to the corresponding hydroxylamine enhanced the hydrophilicity of the entire copolymer and resulting in the increase of LCST-type cloud point. However, oxidation of the hydroxylamine moiety back to the TEMPO radical was achieved directly by addition of red prussiate which led to a significant decrease of the cloud point. It is worth mentioning that the LCST-type cloud point of the copolymer can be fine-tuned simply by changing the degree of reduction of the TEMPO moieties. Additionally, upon UV light irradiation, the *trans*-to-*cis* photoisomerization of the azobenzene moiety increases the polarity of the entire polymer which also leads to increase in LCST-type transition.

One interesting example of multistimuli (light/redox/temperature)-sensitive amphiphilic BCP micelles was reported by Thayumanavan and his coworkers [446]. The synthesized BCP consists of an acid-sensitive tetrahydropyran-protected poly(hydroxylethyl methacrylate) (PHEMA) as the hydrophobic part and a temperature-sensitive PNIPAAm as the hydrophilic part with an intervening
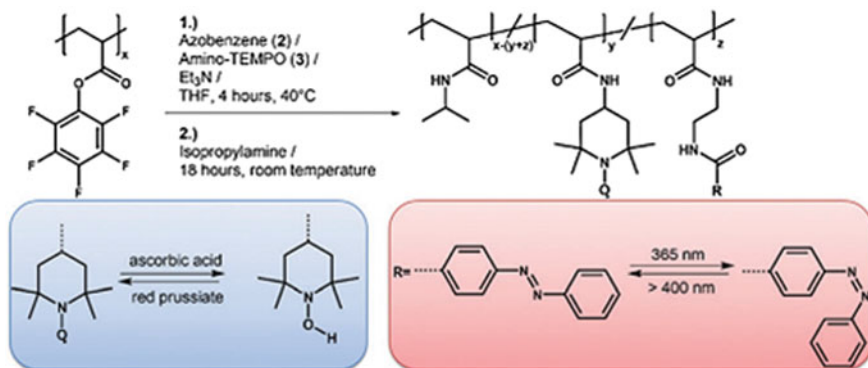
Fig. 6.86 Synthesis of triple (redox, pH, and light) responsive PNIPAAm-based copolymer containing azobenzene and TEMPO moieties by post-polymerization modification of PPFPA (reproduced from Ref. [445] with kind permission of © 2011 Royal Society of Chemistry)

disulfide bond which is designated as redox-sensitive unit (Fig. 6.87). The BCP exhibited LCST-type cloud point which can be tuned under wide range of temperature upon pH variation and redox reagent treatment. They have also investigated the micelle formation, and its disruption in response to different stimuli (Fig. 6.87). Upon mild acidic condition (pH = 4), deprotection of PHEMA takes place and consequently, the PHEMA block becomes hydrophilic which causes the disruption of BCP micelle due to the dramatic change in the hydrophilic/lipophilic balance (Fig. 6.87). On the other hand, above the LCST point, the hydrophilic thermoresponsive PNIPAAm block was converted to hydrophobic block, rendering the polymer insoluble in water which does not maintain its micellar structure any longer (Fig. 6.87). Finally, the addition of DTT triggers the reductive cleavage of disulfide linkage resulting in the separation of BCP into two distinct blocks, the hydrophobic PHEMA block precipitates while the hydrophilic PNIPAAm stays in solution and hence no assembly. They investigated the release kinetics of encapsulated guest molecule and showed that the application of just single stimulus leads to a very slow or incomplete release kinetic, but the combination of two stimuli accelerates the release of the encapsulated guest molecules, making drug delivery much more efficient.

6.11.3 Temperature-, Enzyme-, and pH-Responsive Polymer Nanostructures

Thayumanavan and his coworkers also reported a series of amphiphilic oligomers that exhibits sensitivity toward temperature, enzymatic reaction, and pH [447]. The amphiphiles composed of a penta(ethylene glycol) and alkyl moiety attached to the meta-positions of a benzoyl building block, which were then attached to oligoamine
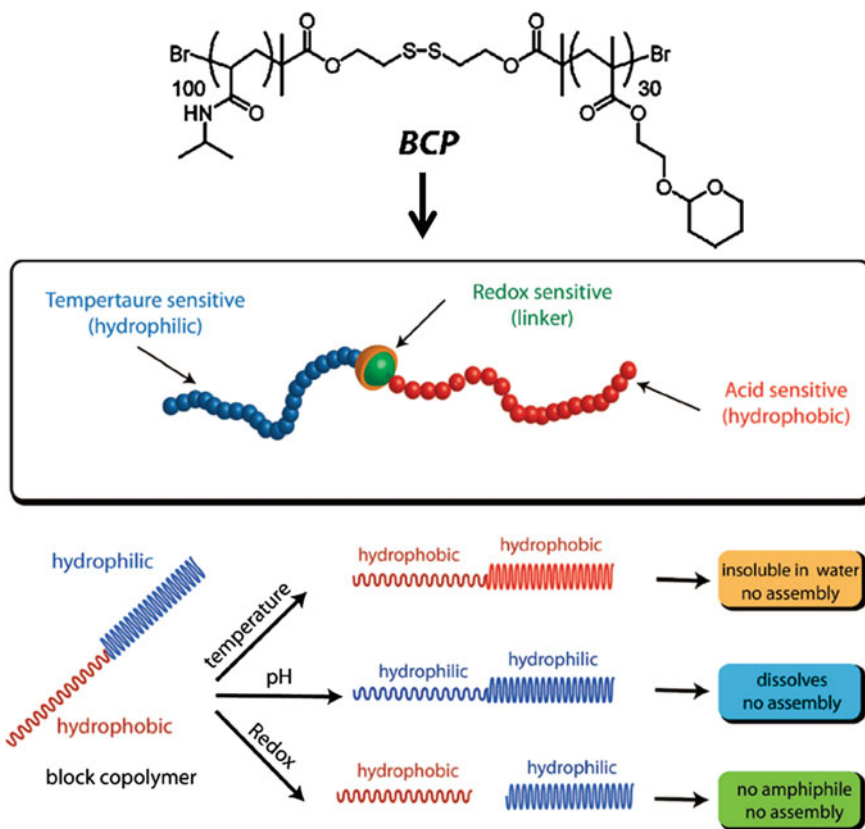
Fig. 6.87 Schematic illustration of amphiphilic block copolymer which can be respond to pH, temperature, and redox (reproduced from Ref. [446] with kind permission of © 2009 American Chemical Society)

scaffolds to yield monomeric to hexameric oligomers. Temperature sensitivity of oligomers was assessed by turbidity measurements using the high-tension voltage response of the photomultiplier on a CD spectrometer keeping the concentration of oligo ethyleneglycol (OEG) unit constant. The LCSTs of these oligomers showed increasingly sharp transitions with increasing numbers of OEG functional groups, indicating enhanced cooperativity in dehydration of the OEG moieties when they are covalently attached. Additionally, the oligomers are also esterase enzyme sensitive because the alkyl moiety is terminated with an ester. After the treatment of the oligomer with esterase, the final product was a pH-sensitive carboxylic acid which can upshot the hydrophilic-lyophilic balance as well as LCST cloud point of the oligomer.

6.12   Responsive Polymer Materials in Advanced Energy Applications

Stimuli-responsive polymer-engineered nanomaterials are not much explored as advanced energy materials. However, among the different categories of stimuli-responsive polymers, redox-responsive polymers are important materials in fabricating devices toward various advanced energy applications. Redox-responsive polymers are electroactive macromolecules containing functional groups that can be reversibly oxidized and reduced. Redox reactions can take place in a polymer side-chain, as in the case of a polymer carrying ferrocene functional group or in the polymer main chain, as in the case of conjugated electrically conducting polymers, such as polyaniline [448]. Due to the reversibility and easy external control of any redox process, these polymers are interesting materials for different applications including design of a number of electrochemical devices such as batteries, super-capacitors, electrochromic devices, thermoelectric cells, optoelectronic devices, biofuel cells.

As mentioned above, redox polymers are important materials for the biofuel cell, which is a simple electrochemical device that converts chemical into electrical energy using enzymes as catalysts where glucose is used as fuel. In order to convert energy efficiently, in a biofuel cell, the effective immobilization of enzymes is required. This can be done by immobilization of enzyme in redox-active polymer hydrogel network associated with electrodes [449]. For example, redox polymers were used for the electrical contacting of oxidases and dehydrogenases with electrodes acting as anodes of biofuel cells, and for the electrical wiring of bilirubin oxidase, cytochrome oxidase, and laccase with electrodes, that yield the cathode units of the biofuel cells [450]. Osmium-based redox polymers have shown to be the most promising candidates to act as mediators in cathodes of membrane-less biofuel cell [451]. In a study, oxygen-reducing enzyme electrodes were first prepared from laccase of Trametes versicolor and a series of osmium-based redox polymer as mediators covering a range of redox potentials from 0.11 to 0.85 V, which was used as an electrode for a biofuel cell.

A microstructured redox hydrogel was reported by photochemical approach and enzymes are immobilized inside the gel and evaluated with respect to its potential in biosensor and biofuel cell applications. For this, poly(dimethylacrylamide) polymers with both electroactive ferrocene groups and photoreactive benzophenone groups are synthesized and deposited as thin films on electrode surfaces [452]. Upon UV light irradiation, glucose oxidase containing polymer layer cross links and becomes firmly adhered to the glassy carbon electrodes. They obtained the glucose-oxidizing electrodes with very high catalytic current responses.

Among the other electrochemical energy storage systems, supercapacitors are a particular type of systems where the energy is stored through Faradic mechanism, a redox reaction, taking place at the electrode and the electric charge is stored electrostatically. Supercapacitors are able to charge/discharge at high rates containing high power density compared with batteries. There several reports of

Pseudocapacitor electrodes that are made up of polymer composites with metal oxides [453] or carbons [454], polymer-coated carbons [455] or conducting polymers such as polyaniline [456], polypyrrole [457], polythiophene [458], and their derivatives. Conducting polymers are suitable electrode materials as they are able to storage charges in their doped state. For this reason, several different strategies of fabricating composite electrode materials, nanostructured conducting polymers such as nanorods, nanofibers, nanowires, and nanotubes [459] or using carbons as negative electrodes have been investigated. Polyaniline was used as supercapacitor electrode material due to its high electroactivity, stability, and specific capacitance [460]. Composite electrodes of graphene and polyaniline also studied to get good cycle stability and high specific capacitance [461].

Cong et al. [462] presented the fabrication of a flexible graphene–polyaniline composite paper by in situ electropolymerization of polyaniline nanorods on the graphene paper with a specific capacitance of 763 F g^{-1} at a discharge current of 1 A g^{-1} and a good cycling stability with 82% of capacity retention after 1000 cycles. In recent years, nanostructured polypyrrole materials have been developed as more powerful supercapacitors [463]. For example, Huang et al. reported the synthesis of length controllable and well-oriented polypyrrole nanowire arrays with a capacitance of 566 F g^{-1} and retention of 70% after hundreds of charge/discharge cycles [464]. In another report, polypyrrole was used together with carbon materials to design a positive electrode material [465].

Recently, dye sensitized solar cells (DSSC) are very promising and can be readily achieved with certain level of efficiencies [466]. It is also considered as the next-generation photovoltaic devices. In this type of DSSC, the key component is a triiodide/iodide redox couple usually dissolved in an organic liquid electrolyte. This DSSC technology faces high-temperature stability issues to pass standardized packaging durability tests of solar cells. One of the solutions is its solidification [467] using a number of redox-responsive polymers [467]. Among all the different strategies, one of the important strategies includes the incorporation of iodide redox couple in poly(vinyl imidazolium) iodide polymeric ionic liquids. In another interesting strategy, PEDOT was successfully proposed due to its redox properties as a solid substitute of the iodine liquid electrolytes [468]. As per their report, the best performances of these solid solar cells are still low (aprox. 7%) but the advantages are considerable because they can be processed easily.

In general metal alloys are generally used as thermoelectric materials that generate electricity directly from heat. However, recently it has been suggested that organic semiconductors could offer cost-effective alternatives, made from solution that could open up new possibilities, including harvesting energy over large areas. This requires thermoelectric materials that are readily synthesized, air stable, environmentally friendly, and solution processable to create patterns on large areas [469]. There are very few conducting polymers that have been explored as thermoelectric materials [470]. However, research in this area is still not progressed much and extensive efforts are required to understand and utilize polymers. Crispin and coworkers showed that the PEDOT can be used as thermoelectric materials with its low intrinsic thermal conductivity ($\lambda = 0.37$ W m^{-1} K^{-1}) leaded to a

record thermoelectric figure of merit (Seebeck coefficient) ZT = 0.25 at room temperature. This value was slightly lower than the values required for efficient devices [469]. According to their report, the thermoelectric properties of PEDOT were mostly associated to its thermal and electrical conductivity, it is worth to remark that those properties and its doping level are directly linked to its redox properties [469].

6.13 Conclusions and Outlook

In the present century, the major focus of materials research is to develop "smart" responsive materials, mostly based on polymers that can be triggered by the stimuli present in living cells without causing any toxicity or inauspicious effects. Here, we have emphasized some recent developments in polymer and material science that covered the stimuli-responsive polymer nanomaterials. Various design strategies for the development of various stimuli-responsive polymer nanomaterials were systemically described with an aim to their potential applications. However, many challenges still need to be addressed, especially as far as applications of those systems are concerned. Now it is time to extend their use to biocompatible and biodegradable nanostructured polymer materials since, as mentioned earlier, the key interest of this type of nanomaterials is to develop a "smart" method for controlled drug delivery applications.

A straightforward perspective to prepare biocompatible and biodegradable stimuli-responsive block copolymer (BCP) micelles/vesicles probably is to combine the hydrophilic biocompatible polymers (such as PEO or poly(2-oxazoline)) with different functionalized hydrophobic polypeptide such as poly(glutamic acid), poly (aspartic acid), poly(lysine) by applying the established methodologies as discussed above. As for example, for photocontrolled drug delivery, one needs to develop biocompatible BCP nanomaterials that have some essential characteristics such as low cytotoxicity, can contain larger amount of payloads, stable inside the blood stream for a long circulation time, can selectively accumulate in the diseased cells or tissues and then, can be disrupted by NIR light in a controlled manner.

However, much advance research remains to be done to achieve this level of functions and controls. It is also important to control the size and shape of the nanostructured-responsive polymeric materials when someone thinks about the making of real and efficient and triggered drug delivery systems. For stimuli-responsive polymers and BCPs, it may also be interesting to start exploring some possible applications in other areas such as cosmetics, agricultural industries, optical devices, responsive coatings. Finally, the design, synthesis, and development presented in this chapter will surely be helpful for introduction of new concepts in stimuli-responsive polymer materials which may be beneficial for many new applications in future.

References

1. Mu B, Shen R, Liu P (2009) Facile preparation of crosslinked polymeric nanocapsules via combination of surface-initiated atom transfer radical polymerization and ultraviolet irradiated crosslinking techniques. Nanoscale Res Lett 4(7):773–777
2. Kolishetti N, Faust R (2007) Relative reactivity of cationic monomers isobutylene, styrene and ring substituted styrenes. Polym Prepr (Am Chem Soc, Div Polym Chem) 48:221–222
3. Lee JCM, Bermudez H, Discher BM et al (2001) Preparation, stability, and in vitro performance of vesicles made with diblock copolymers. Biotechnol Bioeng 73(2):135–145
4. Morris CA, Anderson ML, Stroud RM et al (1999) Silica sol as a nanoglue: flexible synthesis of composite aerogels. Science 284(5414):622–624
5. Fu GD, Shang Z, Hong L et al (2005) Nanoporous, ultralow-dielectric-constant fluoropolymer films from agglomerated and crosslinked hollow nanospheres of poly (pentafluorostyrene)-block-poly (divinylbenzene). Adv Mater 17(21):2622–2626
6. Wan M, Li J, Li S (2001) Microtubules of polyaniline as new microwave absorbent materials. Polym Adv Technol 12(11–12):651–657
7. Lu Y, Proch S, Schrinner M et al (2009) Thermosensitive core-shell microgel as a "nanoreactor" for catalytic active metal nanoparticles. J Mater Chem 19(23):3955–3961
8. Ahn DJ, Kim JM (2008) Fluorogenic polydiacetylene supramolecules: immobilization, micropatterning, and application to label-free chemosensors. Acc Chem Res 41(7):805–816
9. Gaitzsch J, Appelhans D, Wang L et al (2012) Synthetic bio-nanoreactor: mechanical and chemical control of polymersome membrane permeability. Angew Chem Int Ed 51 (18):4448–4451
10. Lomas H, Canton I, MacNeil S et al (2007) Biomimetic pH sensitive polymersomes for efficient DNA encapsulation and delivery. Adv Mater 19(23):4238–4243
11. Onaca O, Enea R, Hughes DW et al (2009) Stimuli-responsive polymersomes as nanocarriers for drug and gene delivery. Macromol Biosci 9(2):129–139
12. Stuart MAC, Huck WTS, Genzer J et al (2010) Emerging applications of stimuli-responsive polymer materials. Nat Mater 9(2):101–113
13. Skirtach AG, Munoz Javier A, Kreft O et al (2006) Laser-induced release of encapsulated materials inside living cells. Angew Chem Int Ed 45(28):4612–4617
14. Kreft O, Javier AM, Sukhorukov GB et al (2007) Polymer microcapsules as mobile local pH-sensors. J Mater Chem 17(42):4471–4476
15. Kakizawa Y, Kataoka K (2002) Block copolymer micelles for delivery of gene and related compounds. Adv Drug Deliv Rev 54(2):203–222
16. Oishi M, Hayashi H, Iijima M et al (2007) Endosomal release and intracellular delivery of anticancer drugs using pH-sensitive PEGylated nanogels. J Mater Chem 17(35):3720–3725
17. Qiu Y, Park K (2001) Environment-sensitive hydrogels for drug delivery. Adv Drug Deliv Rev 53(3):321–339
18. Hoffman AS, Stayton PS, Bulmus V et al (2000) Really smart bioconjugates of smart polymers and receptor proteins. J Biomed Mater Res 52(4):577–586
19. Kikuchi A, Okano T (2002) Intelligent thermoresponsive polymeric stationary phases for aqueous chromatography of biological compounds. Prog Polym Sci 27(6):1165–1193
20. Gil ES, Hudson SM (2004) Stimuli-reponsive polymers and their bioconjugates. Prog Polym Sci 29(12):1173–1222
21. Stayton PS, Shimoboji T, Long C et al (1995) Control of protein-ligand recognition using a stimuli-responsive polymer. Nature 378:472–474

22. Senaratne W, Andruzzi L, Ober CK (2005) Self-assembled monolayers and polymer brushes in biotechnology: current applications and future perspectives. Biomacromol 6(5):2427–2448

23. Jhaveri SJ, Hynd MR, Dowell-Mesfin N et al (2009) Release of nerve growth factor from HEMA hydrogel-coated substrates and its effect on the differentiation of neural cells. Biomacromol 10(1):174–183

24. Hoffman AS (2008) The origins and evolution of "controlled" drug delivery systems. J Control Release 132(3):153–163

25. Bayer CL, Peppas NA (2008) Advances in recognitive, conductive and responsive delivery systems. J Control Release 132(3):216–221

26. Zhang N, Luxenhofer R, Jordan R (2012) Thermoresponsive poly (2-oxazoline) molecular brushes by living ionic polymerization: kinetic investigations of pendant chain grafting and cloud point modulation by backbone and side chain length variation. Macromol Chem Phys 213(9):973–981

27. Ding Z, Chen G, Hoffman AS (1998) Unusual properties of thermally sensitive oligomer-enzyme conjugates of poly(N-isopropylacrylamide)-trypsin. J Biomed Mater Res 39(3):498–505

28. Wang S, Choi M-S, Kim S-H (2008) Bistable photoswitching in poly(N-isopropylacrylamide) with spironaphthoxazine hydrogel for optical data storage. J Photochem Photobiol A 198:150–155

29. Anker JN, Hall WP, Lyandres O et al (2008) Biosensing with plasmonic nanosensors. Nat Mater 7(6):442–453

30. Tokarev I, Minko S (2009) Stimuli-responsive hydrogel thin films. Soft Matter 5(3):511–524

31. Mendes PM (2008) Stimuli-responsive surfaces for bio-applications. Chem Soc Rev 37(11):2512–2529

32. Motornov M, Minko S, Eichhorn K-J et al (2003) Reversible tuning of wetting behavior of polymer surface with responsive polymer brushes. Langmuir 19(19):8077–8085

33. Meng H, Li G (2013) A review of stimuli-responsive shape memory polymer composites. Polymer 54(9):2199–2221

34. Dimitrov I, Trzebicka B, Muller AHE et al (2007) Thermosensitive water-soluble copolymers with doubly responsive reversibly interacting entities. Prog Polym Sci 32(11):1275–1343

35. Schild HG (1992) Poly(N-isopropylacrylamide): experiment, theory and application. Prog Polym Sci 17(2):163–249

36. Dai S, Ravi P, Tam KC (2008) pH-Responsive polymers: synthesis, properties and applications. Soft Matter 4(3):435–449

37. Murthy N, Campbell J, Fausto N et al (2003) Bioinspired pH-responsive polymers for the intracellular delivery of biomolecular drugs. Bioconjugate Chem 14(2):412–419

38. Ercole F, Davis TP, Evans RA (2010) Photo-responsive systems and biomaterials: photochromic polymers, light-triggered self-assembly, surface modification, fluorescence modulation and beyond. Polym Chem 1(1):37–54

39. Schumers J-M, Fustin C-A, Gohy J-F (2010) Light-responsive block copolymers. Macromol Rapid Commun 31(18):1588–1607

40. Zhao Y (2009) Photocontrollable block copolymer micelles: what can we control? J Mater Chem 19(28):4887–4895

41. Akhoury A, Bromberg L, Hatton TA (2011) Redox-responsive gels with tunable hydrophobicity for controlled solubilization and release of organics. ACS Appl Mater Interfaces 3(4):1167–1174

42. Magnusson JP, Khan A, Pasparakis G et al (2008) Ion-sensitive "isothermal" responsive polymers prepared in water. J Am Chem Soc 130(33):10852–10853

43. Ma R, Shi L (2014) Phenylboronic acid-based glucose-responsive polymeric nanoparticles: synthesis and applications in drug delivery. Polym Chem 5(5):1503–1518

44. Lin S, Theato P (2013) CO_2-Responsive polymers. Macromol Rapid Commun 34(14):1118–1133

45. Pasparakis G, Vamvakaki M (2011) Multiresponsive polymers: nano-sized assemblies, stimuli-sensitive gels and smart surfaces. Polym Chem 2(6):1234–1248
46. Urban MW (2011) Handbook of stimuli-responsive materials. Wiley-VCH, Weinheim
47. Matyjaszewski K, Xia J (2001) Atom transfer radical polymerization. Chem Rev 101 (9):2921–2990
48. Moad G, Rizzardo E, Thang SH (2008) Radical addition-fragmentation chemistry in polymer synthesis. Polymer 49(5):1079–1131
49. Hawker CJ (1994) Molecular weight control by a "living" free-radical polymerization process. J Am Chem Soc 116(24):11185–11186
50. Nuyken O, Pask SD (2013) Ring-opening polymerization-an introductory review. Polymers 5(2):361–403
51. Gauthier MA, Gibson MI, Klok H-A (2009) Synthesis of functional polymers by post-polymerization modification. Angew Chem Int Ed 48(1):48–58
52. Kolb HC, Finn MG, Sharpless KB (2001) Click chemistry: diverse chemical function from a few good reactions. Angew Chem Int Ed 40(11):2004–2021
53. Jochum FD, Forst FR, Theato P (2010) PNIPAM copolymers containing light-responsive chromophores: a method toward molecular logic gates. Macromol Rapid Commun 31 (16):1456–1461
54. Tang X, Liang X, Gao L et al (2010) Water-soluble triply-responsive homopolymers of N,N-dimethylaminoethyl methacrylate with a terminal azobenzene moiety. J Polym Sci Part A: Polym Chem 48(12):2564–2570
55. Scarpa JS, Mueller DD, Klotz IM (1967) Slow hydrogen-deuterium exchange in a non-.alpha.-helical polyamide. J Am Chem Soc 89(24):6024–6030
56. Alarcon DLHC, Pennadam S, Alexander C (2005) Stimuli responsive polymers for biomedical applications. Chem Soc Rev 34(3):276–285
57. Nakayama M, Okano T, Miyazaki T et al (2006) Molecular design of biodegradable polymeric micelles for temperature-responsive drug release. J Control Release 115(1):46–56
58. Bajpai A, Shukla SK, Bhanu S et al (2008) Responsive polymers in controlled drug delivery. Prog Polym Sci 33(11):1088–1118
59. Takei YG, Aoki T, Sanui K et al (1993) Temperature-responsive bioconjugates. 2. Molecular design for temperature-modulated bioseparations. Bioconjug Chem 4(5):341–346
60. Hoffman AS, Stayton PS (2007) Conjugates of stimuli-responsive polymers and proteins. Prog Polym Sci 32(8):922–932
61. Wu G, Li Y, Han M et al (2006) Novel thermo-sensitive membranes prepared by rapid bulk photo-grafting polymerization of N,N-diethylacrylamide onto the microfiltration membranes Nylon. J Membr Sci 283(1):13–20
62. Kanazawa H (2007) Thermally responsive chromatographic materials using functional polymers. J Sep Sci 30(11):1646–1656
63. Lokuge I, Wang X, Bohn PW (2007) Temperature-controlled flow switching in nanocapillary array membranes mediated by poly(N-isopropylacrylamide) polymer brushes grafted by atom transfer radical polymerization. Langmuir 23(1):305–311
64. Nath N, Chilkoti A (2002) Creating "smart" surfaces using stimuli responsive polymers. Adv Mater 14(17):1243–1247
65. Nagase K, Kobayashi J, Okano T (2009) Temperature-responsive intelligent interfaces for biomolecular separation and cell sheet engineering. J R Soc Interface 6(Suppl 3):S293–S309
66. Crespy D, Rossi RM (2007) Temperature-responsive polymers with LCST in the physiological range and their applications in textiles. Polym Int 56(12):1461–1468
67. Shimoboji T, Larenas E, Fowler T et al (2003) Temperature-induced switching of enzyme activity with smart polymer-enzyme conjugates. Bioconju Chem 14(3):517–525
68. Hocine S, Li M-H (2013) Thermoresponsive self-assembled polymer colloids in water. Soft Matter 9(25):5839–5861
69. Fujishige S, Kubota K, Ando I (1989) Phase transition of aqueous solutions of poly(N-isopropylacrylamide) and poly(N-isopropylmethacrylamide). J Phys Chem 93(8):3311–3313

70. Bhattacharjee RR, Chakraborty M, Mandal TK (2006) Reversible association of thermoresponsive gold nanoparticles: polyelectrolyte effect on the lower critical solution temperature of poly(vinyl methyl ether). J Phys Chem B 110(13):6768–6775

71. Confortini O, Du Prez FE (2007) Functionalized thermo-responsive poly (vinyl ether) by living cationic random copolymerization of methyl vinyl ether and 2-chloroethyl vinyl ether. Macromol Chem Phys 208(17):1871–1882

72. Spevacek J, Hanykova L, Labuta J (2011) Behavior of water during temperature-induced phase separation in poly(vinyl methyl ether) aqueous solutions. NMR and optical microscopy study. Macromolecules 44(7):2149–2153

73. Van Durme K, Van Assche G, Rahier H et al (2009) LCST demixing in poly(vinyl methyl ether)/water studied by means of a high resolution ultrasonic resonator. J Thermal Anal Calorimetry 98(2):495–505

74. Hoogenboom R (2009) Poly (2-oxazoline) s: a polymer class with numerous potential applications. Angew Chem Int Ed 48(43):7978–7994

75. Diehl C, Schlaad H (2009) Thermo-responsive polyoxazolines with widely tuneable LCST. Macromol Biosci 9(2):157–161

76. Shahidan NN, Liu R, Cellesi F et al (2011) Thermally triggered assembly of cationic graft copolymers containing 2-(2-methoxyethoxy) ethyl methacrylate side chains. Langmuir 27 (22):13868–13878

77. Lutz JF (2008) Polymerization of oligo (ethylene glycol)(meth) acrylates: toward new generations of smart biocompatible materials. J Polym Sci Part A Polym Chem 46 (11):3459–3470

78. Saeed AO, Magnusson JP, Moradi E et al (2011) Modular construction of multifunctional bioresponsive cell-targeted nanoparticles for gene delivery. Bioconjug Chem 22(2):156–168

79. Pasparakis G, Alexander C (2008) Sweet talking double hydrophilic block copolymer vesicles. Angew Chem Int Ed 47(26):4847–4850

80. Hoogenboom R, Thijs HML, Jochems MJHC et al (2008) Tuning the LCST of poly (2-oxazoline)s by varying composition and molecular weight: alternatives to poly(N-isopropylacrylamide)? Chem Commun 44:5758–5760

81. Plunkett KN, Zhu X, Moore JS et al (2006) PNIPAM chain collapse depends on the molecular weight and grafting density. Langmuir 22(9):4259–4266

82. Katsumoto Y, Kubosaki N (2008) Tacticity effects on the phase diagram for poly(N-isopropylacrylamide) in water. Macromolecules 41(15):5955–5956

83. Feil H, Bae YH, Feijen J et al (1993) Effect of comonomer hydrophilicity and ionization on the lower critical solution temperature of N-isopropylacrylamide copolymers. Macromolecules 26(10):2496–2500

84. Meersman F, Wang J, Wu Y et al (2005) Pressure effect on the hydration properties of poly (N-isopropylacrylamide) in aqueous solution studied by FTIR spectroscopy. Macromolecules 38(21):8923–8928

85. Furyk S, Zhang Y, Ortiz-Acosta D et al (2006) Effects of end group polarity and molecular weight on the lower critical solution temperature of poly(N-isopropylacrylamide). J Polym Sci Part A Polym Chem 44(4):1492–1501

86. Roth PJ, Jochum FD, Forst FR et al (2010) Influence of end groups on the stimulus-responsive behavior of poly [oligo (ethylene glycol) methacrylate] in water. Macromolecules 43(10):4638–4645

87. Ito D, Kubota K (1997) Solution properties and thermal behavior of poly(N-n-propylacrylamide) in water. Macromolecules 30(25):7828–7834

88. Maeda Y, Nakamura T, Ikeda I (2001) Changes in the hydration states of poly(N-alkylacrylamide)s during their phase transitions in water observed by FTIR spectroscopy. Macromolecules 34(5):1391–1399

89. Idziak I, Avoce D, Lessard D et al (1999) Thermosensitivity of aqueous solutions of poly(N, N-diethylacrylamide). Macromolecules 32(4):1260–1263

90. Akiyama Y, Shinohara Y, Hasegawa Y et al (2008) Preparation of novel acrylamide-based thermoresponsive polymer analogues and their application as thermoresponsive chromatographic matrices. J Polym Sci Part A Polym Chem 46(16):5471–5482

91. Aoki T, Muramatsu M, Nishina A et al (2004) Thermosensitivity of optically active hydrogels constructed with N-(L)-(1-hydroxymethyl) propylmethacrylamide. Macromol Biosci 4(10):943–949

92. Liu F, Urban MW (2008) 3D directional temperature responsive (N-(DL)-(1-hydroxymethyl) propylmethacrylamide-co-n-butyl acrylate) colloids and their coalescence. Macromolecules 41(2):352–360

93. Seto Y, Aoki T, Kunugi S (2005) Temperature-and pressure-responsive properties of l-and dl-forms of poly(N-(1-hydroxymethyl) propylmethacrylamide) in aqueous solutions. Colloid Polym Sci 283(10):1137–1142

94. Zou Y, Brooks DE, Kizhakkedathu JN (2008) A novel functional polymer with tunable LCST. Macromolecules 41(14):5393–5405

95. Huang X, Du F, Ju R et al (2007) Novel acid-labile, thermoresponsive poly(methacrylamide) s with pendent ortho ester moieties. Macromol Rapid Commun 28(5):597–603

96. Huang XN, Du FS, Zhang B et al (2008) Acid-labile, thermoresponsive (meth) acrylamide polymers with pendant cyclic acetal moieties. J Polym Sci Part A: Polym Chem 46 (13):4332–4343

97. Suwa K, Wada Y, Kikunaga Y et al (1997) Synthesis and functionalities of poly(N-vinylalkylamide). IV. Synthesis and free radical polymerization of N-vinylisobutyramide and thermosensitive properties of the polymer. J Polym Sci Part A Polym Chem 35(9): 1763–1768

98. Crespo CA, Cancho MS, Rubio GR et al (1999) Equation of state of aqueous polymer systems: poly(propylene glycol) + water. Phys Chem Chem Phys 1(2):319–322

99. Han S, Hagiwara M, Ishizone T (2003) Synthesis of thermally sensitive water-soluble polymethacrylates by living anionic polymerizations of oligo (ethylene glycol) methyl ether methacrylates. Macromolecules 36(22):8312–8319

100. Mertoglu M, Garnier S, Laschewsky A et al (2005) Stimuli responsive amphiphilic block copolymers for aqueous media synthesised via reversible addition fragmentation chain transfer polymerisation (RAFT). Polymer 46(18):7726–7740

101. Christova D, Velichkova R, Loos W et al (2003) New thermo-responsive polymer materials based on poly(2-ethyl-2-oxazoline) segments. Polymer 44(8):2255–2261

102. Diab C, Akiyama Y, Kataoka K et al (2004) Microcalorimetric study of the temperature-induced phase separation in aqueous solutions of poly(2-isopropyl-2-oxazolines). Macromolecules 37(7): 2556–2562

103. Uyama H, Kobayashi S (1992) A novel thermo-sensitive polymer poly(2-iso-propyl-2-oxazoline). Chem Lett 9:1643–1646

104. Boerman MA, Van der Laan HL, Bender JCME et al (2016) Synthesis of pH- and thermoresponsive poly(2-n-propyl-2-oxazoline) based copolymers. J Polym Sci Part A: Polym Chem 54(11):1573–1582

105. Weber C, Becer CR, Hoogenboom R et al (2009) Lower critical solution temperature behavior of comb and graft shaped poly[oligo(2-ethyl-2-oxazoline)methacrylate]s. Macromolecules 42(8):2965–2971

106. Lau AC, Wu C (1999) Thermally sensitive and biocompatible poly(N-vinylcaprolactam): synthesis and characterization of high molar mass linear chains. Macromolecules 32(3): 581–584

107. Tager A, Safronov A, Berezyuk E et al (1994) Lower critical solution temperature and hydrophobic hydration in aqueous polymer solutions. Colloid Polym Sci 272(10): 1234–1239

108. Maeda Y, Nakamura T, Ikeda I (2002) Hydration and phase behavior of poly(N-vinylcaprolactam) and poly(N-vinylpyrrolidone) in water. Macromolecules 35(1):217–222

109. Deng J, Shi Y, Jiang W et al (2008) Facile synthesis and thermoresponsive behaviors of a well-defined pyrrolidone based hydrophilic polymer. Macromolecules 41(9):3007–3014

110. Gonzalez N, Elvira C, Román JS (2005) Novel dual-stimuli-responsive polymers derived from ethylpyrrolidine. Macromolecules 38(22):9298–9303

111. Okubo M, Ahmad H, Suzuki T (1998) Synthesis of temperature-sensitive micron-sized monodispersed composite polymer particles and its application as a carrier for biomolecules. Colloid Polym Sci 276(6):470–475

112. Plamper FA, Ruppel M, Schmalz A et al (2007) Tuning the thermoresponsive properties of weak polyelectrolytes: aqueous solutions of star-shaped and linear poly(N,N-dimethylaminoethyl methacrylate). Macromolecules 40(23):8361–8366

113. Arotcarena M, Heise B, Ishaya S et al (2002) Switching the inside and the outside of aggregates of water-soluble block copolymers with double thermoresponsivity. J Am Chem Soc 124(14):3787–3793

114. Liu F, Seuring J, Agarwal S (2012) Controlled radical polymerizatiion of N-acryloylglycinamide and UCST-type phase transition of the polymers. J Polym Sci Part A: Polym Chem 50(23):4920–4928

115. Seuring J, Agarwal S (2010) Non-ionic homo-and copolymers with H-donor and H-acceptor units with an UCST in water. Macromol Chem Phys 211(19):2109–2117

116. Seuring J, Agarwal S (2012) First example of a universal and cost-effective approach: polymers with tunable upper critical solution temperature in water and electrolyte solution. Macromolecules 45(9):3910–3918

117. Glatzel S, Laschewsky A, Lutz JF (2010) Well-defined uncharged polymers with a sharp UCST in water and in physiological milieu. Macromolecules 44(2):413–415

118. Klenina O, Fain E (1981) Phase separation in the system polyacrylic acid-polycrylamide-water. Polym Sci USSR 23(6):1439–1446

119. Schulz D, Peiffer D, Agarwal P et al (1986) Phase behaviour and solution properties of sulphobetaine polymers. Polymer 27(11):1734–1742

120. Huglin MB, Radwan MA (1991) Unperturbed dimensions of a zwitterionic polymethacrylate. Polym Int 26(2):97–104

121. Aoki T, Nakamura K, Sanui K et al (1999) Adenosine-induced changes of the phase transition of poly(6-(acryloyloxymethyl)uracil) aqueous solution. Polym J 31:1185–1188

122. Mishra V, Jung S-H, Jeong HM et al (2014) Thermoresponsive ureido-derivatized polymers: the effect of quaternization on UCST properties. Polym Chem 5(7):2411–2416

123. Cai X, Zhong L, Su Y et al (2015) Novel pH-tunable thermoresponsive polymers displaying lower and upper critical solution temperatures. Polym Chem 6(20):3875–3884

124. Hawker CJ, Bosman AW, Harth E (2001) New polymer synthesis by nitroxide mediated living radical polymerizations. Chem Rev 101(12):3661–3688

125. Rosen BM, Percec V (2009) Single-electron transfer and single-electron transfer degenerative chain transfer living radical polymerization. Chem Rev 109(11):5069–5119

126. Matyjaszewski K, Tsarevsky NV (2009) Nanostructured functional materials prepared by atom transfer radical polymerization. Nat Chem 1(4):276–288

127. Smith AE, Xu X, Kirkland-York SE et al (2010) "Schizophrenic" self-assembly of block copolymers synthesized via aqueous RAFT polymerization: from micelles to vesicles†† Paper number 143 in a series on water-soluble polymers. Macromolecules 43(3):1210–1217

128. Li Y, Lokitz BS, McCormick CL (2006) RAFT synthesis of a thermally responsive ABC triblock copolymer incorporating N-acryloxysuccinimide for facile in situ formation of shell cross-linked micelles in aqueous media. Macromolecules 39(1):81–89

129. Moughton AO, Patterson JP, O'Reilly RK (2011) Reversible morphological switching of nanostructures in solution. Chem Commun 47(1):355–357

130. Sundararaman A, Stephan T, Grubbs RB (2008) Reversible restructuring of aqueous block copolymer assemblies through stimulus-induced changes in amphiphilicity. J Am Chem Soc 130(37):12264–12265

131. Zhang L, Yu K, Eisenberg A (1996) Ion-induced morphological changes in "crew-cut" aggregates of amphiphilic block copolymers. Science 272(5269):1777

132. Zhang L, Eisenberg A (1995) Multiple morphologies of "crew-cut" aggregates of polystyrene-b-poly (acrylic acid) block copolymers. Science 268(5218):1728–1731

133. Discher DE, Eisenberg A (2002) Polymer vesicles. Science 297(5583):967–973
134. Whittaker MR, Monteiro MJ (2006) Synthesis and aggregation behavior of four-arm star amphiphilic block copolymers in water. Langmuir 22(23):9746–9752
135. Lonsdale DE, Whittaker MR, Monteiro MJ (2009) Self-assembly of well-defined amphiphilic polymeric miktoarm stars, dendrons, and dendrimers in water: the effect of architecture. J Polym Sci Part A: Polym Chem 47(22):6292–6303
136. Lonsdale DE, Monteiro MJ (2011) Synthesis and self-assembly of amphiphilic macrocyclic block copolymer topologies. J Polym Sci Part A: Polym Chem 49(21):4603–4612
137. Jia Z, Xu X, Fu Q et al (2006) Synthesis and self-assembly morphologies of amphiphilic multiblock copolymers [poly(ethylene oxide)-*b*-polystyrene] n via trithiocarbonate-embedded PEO macro-RAFT agent. J Polym Sci Part A Polym Chem 44(20):6071–6082
138. Heskins M, Guillet JE (1968) Solution properties of poly(*N*-isopropylacrylamide). J Macromol Sci Chem 2(8):1441–1455
139. Schmaljohann D (2006) Thermo-and pH-responsive polymers in drug delivery. Adv Drug Delivery Rev 58(15):1655–1670
140. De P, Gondi SR, Sumerlin BS (2008) Folate-conjugated thermoresponsive block copolymers: highly efficient conjugation and solution self-assembly. Biomacromol 9(3):1064–1070
141. Roy D, Cambre JN, Sumerlin BS (2009) Triply-responsive boronic acidblock copolymers: solution self-assembly induced by changes in temperature, pH, or sugar concentration. Chem Commun 16:2106–2108
142. De P, Li M, Gondi SR et al (2008) Temperature-regulated activity of responsive polymer-protein conjugates prepared by grafting-from via RAFT polymerization. J Am Chem Soc 130(34):11288–11289
143. Vogt AP, Sumerlin BS (2008) Tuning the temperature response of branched poly(*N*-isopropylacrylamide) prepared by RAFT polymerization. Macromolecules 41(20):7368–7373
144. Dai S, Ravi P, Tam KC (2009) Thermo- and photo-responsive polymeric systems. Soft Matter 5(13):2513–2533
145. Kendhale A, Gonnade R, Rajamohanan PR et al (2006) Isotactic *N*-alkyl acrylamide oligomers assume self-assembled sheet structure: first unequivocal evidence from crystal structures. Chem Commun 26:2756–2758
146. Convertine AJ, Lokitz BS, Vasileva Y et al (2006) Direct synthesis of thermally responsive DMA/NIPAM diblock and DMA/NIPAM/DMA triblock copolymers via aqueous, room temperature RAFT polymerization. Macromolecules 39(5):1724–1730
147. Gohy J-F, Varshney SK, Jérôme R (2001) Water-soluble complexes formed by poly (2-vinylpyridinium)-block-poly(ethylene oxide) and poly(sodium methacrylate)-block-poly (ethylene oxide) copolymers. Macromolecules 34(10):3361–3366
148. Okano T (1993) Molecular design of temperature-responsive polymers as intelligent materials. Responsive gels: volume transitions II. Springer, pp 179–197
149. Zhou C, Hillmyer MA, Lodge TP (2011) Micellization and micellar aggregation of poly (ethylene-alt-propylene)-*b*-poly(ethylene oxide)-*b*-poly(*N*-isopropylacrylamide) triblock terpolymers in water. Macromolecules 44(6):1635–1641
150. Qiao J, Qi L, Shen Y et al (2012) Thermal responsive fluorescent block copolymer for intracellular temperature sensing. J Mater Chem 22(23):11543–11549
151. Xia Y, Burke NA, Stöver HD (2006) End group effect on the thermal response of narrow-disperse poly(*N*-isopropylacrylamide) prepared by atom transfer radical polymerization. Macromolecules 39(6):2275–2283
152. Wang X, Qiu X, Wu C (1998) Comparison of the coil-to-globule and the globule-to-coil transitions of a single poly(*N*-isopropylacrylamide) homopolymer chain in water. Macromolecules 31(9):2972–2976
153. Inomata H, Goto S, Saito S (1990) Phase transition of *N*-substituted acrylamide gels. Macromolecules 23(22):4887–4888

154. Kobayashi M, Ishizone T, Nakahama S (2000) Synthesis of highly isotactic poly(*N*,*N*-diethylacrylamide) by anionic polymerization with grignard reagents and diethylzinc. J Polym Sci Part A Polym Chem 38(S1):4677–4685
155. Ren C, Liu X, Jiang X et al (2015) Polyisobutylene-*b*-poly(*N*,*N*-diethylacrylamide) well-defined amphiphilic diblock copolymer: synthesis and thermo-responsive phase behavior. J Polym Sci Part A Polym Chem 53(9):1143–1150
156. Angelopoulos SA, Tsitsilianis C (2006) Thermo-reversible hydrogels based on poly(*N*,*N*-diethylacrylamide)-block-poly(acrylic acid)-block-poly(*N*,*N*-diethylacrylamide) double hydrophilic triblock copolymer. Macromol Chem Phys 207(23):2188–2194
157. Chan JW, Yu B, Hoyle CE et al (2009) The nucleophilic, phosphine-catalyzed thiol-ene click reaction and convergent star synthesis with RAFT-prepared homopolymers. Polymer 50(14):3158–3168
158. Li H, Yu B, Matsushima H et al (2009) The thiol-isocyanate click reaction: facile and quantitative access to ω-end-functional poly(*N*,*N*-diethylacrylamide) synthesized by RAFT radical polymerization. Macromolecules 42(17):6537–6542
159. Aoki T, Muramatsu M, Torii T et al (2001) Thermosensitive phase transition of an optically active polymer in aqueous milieu. Macromolecules 34(10):3118–3119
160. Cao Y, Zhu X, Luo J et al (2007) Effects of substitution groups on the RAFT polymerization of *N*-alkylacrylamides in the preparation of thermosensitive block copolymers. Macromolecules 40(18):6481–6488
161. Saeki S, Kuwahara N, Nakata M et al (1976) Upper and lower critical solution temperatures in poly(ethylene glycol) solutions. Polymer 17(8):685–689
162. Fusco S, Borzacchiello A, Netti P (2006) Perspectives on: PEO-PPO-PEO triblock copolymers and their biomedical applications. J Bioact Compat Polym 21(2):149–164
163. Alexandridis P, Holzwarth JF, Hatton TA (1994) Micellization of poly(ethylene oxide)-poly (propylene oxide)-poly(ethylene oxide) triblock copolymers in aqueous solutions: thermodynamics of copolymer association. Macromolecules 27(9):2414–2425
164. Li Y, Lokitz BS, Armes SP et al (2006) Synthesis of reversible shell cross-linked micelles for controlled release of bioactive agents†. Macromolecules 39(8):2726–2728
165. Pilon LN, Armes SP, Findlay P et al (2005) Synthesis and characterization of shell cross-linked micelles with hydroxy-functional coronas: a pragmatic alternative to dendrimers? Langmuir 21(9):3808–3813
166. Niu G, Djaoui AB, Cohn D (2011) Crosslinkable PEO-PPO-PEO triblocks as building blocks of thermo-responsive nanoshells. Polymer 52(12):2524–2530
167. Rank A, Hauschild S, Förster S et al (2009) Preparation of monodisperse block copolymer vesicles via a thermotropic cylinder-vesicle transition. Langmuir 25(3):1337–1344
168. Cai Y, Aubrecht KB, Grubbs RB (2010) Thermally induced changes in amphiphilicity drive reversible restructuring of assemblies of ABC triblock copolymers with statistical polyether blocks. J Am Chem Soc 133(4):1058–1065
169. Wegrzyn JK, Stephan T, Lau R et al (2005) Preparation of poly(ethylene oxide)-block-poly (isoprene) by nitroxide-mediated free radical polymerization from PEO macroinitiators. J Polym Sci Part A Polym Chem 43(14):2977–2984
170. Kafer F, Liu F, Stahlschmidt U et al (2015) LCST and UCST in one: double thermoresponsive behavior of block copolymers of poly (ethylene glycol) and poly (acrylamide-*co*-acrylonitrile). Langmuir 31(32):8940–8946
171. Park J-S, Kataoka K (2006) Precise control of lower critical solution temperature of thermosensitive poly(2-isopropyl-2-oxazoline) via gradient copolymerization with 2-ethyl-2-oxazoline as a hydrophilic comonomer. Macromolecules 39(19):6622–6630
172. Lin P, Clash C, Pearce EM et al (1988) Solubility and miscibility of poly(ethyl oxazoline). J Polym Sci Part B Polym Phys 26(3):603–619
173. Rueda J, Zschoche S, Komber H et al (2005) Synthesis and characterization of thermoresponsive graft copolymers of NIPAAm and 2-alkyl-2-oxazolines by the "grafting from" method. Macromolecules 38(17):7330–7336

174. Wang CH, Hsiue GH (2002) Synthesis and characterization of temperature-and pH-sensitive hydrogels based on poly(2-ethyl-2-oxazoline) and poly(D,L-lactide). J Polym Sci Part A Polym Chem 40(8):1112–1121
175. Halacheva S, Price GJ, Garamus VM (2011) Effects of temperature and polymer composition upon the aqueous solution properties of comblike linear poly(ethylene imine)/poly(2-ethyl-2-oxazoline)-based polymers. Macromolecules 44(18):7394–7404
176. Alzari V, Monticelli O, Nuvoli D et al (2009) Stimuli responsive hydrogels prepared by frontal polymerization. Biomacromol 10(9):2672–2677
177. Laukkanen A, Valtola L, Winnik FM et al (2004) Formation of colloidally stable phase separated poly(N-vinylcaprolactam) in water: a study by dynamic light scattering, microcalorimetry, and pressure perturbation calorimetry. Macromolecules 37(6):2268–2274
178. Makhaeva EE, Tenhu H, Khokhlov AR (1998) Conformational changes of poly (vinylcaprolactam) macromolecules and their complexes with ionic surfactants in aqueous solution. Macromolecules 31(18):6112–6118
179. Burillo G, Bucio E, Arenas E et al (2007) Temperature and pH-sensitive swelling behavior of binary DMAEMA/4VP grafts on poly(propylene) films. Macromol Mater Eng 292 (2):214–219
180. Butun V, Armes S, Billingham N (2001) Synthesis and aqueous solution properties of near-monodisperse tertiary amine methacrylate homopolymers and diblock copolymers. Polymer 42(14):5993–6008
181. Butun V, Armes SP, Billingham NC et al (2001) The remarkable "flip-flop" self-assembly of a diblock copolymer in aqueous solution. Macromolecules 34(5):1503–1511
182. Cho SH, Jhon MS, Yuk SH et al (1997) Temperature-induced phase transition of poly(N,N-dimethylaminoethyl methacrylate-co-acrylamide). J Polym Sci Part B Polym Phys 35 (4):595–598
183. Fournier D, Hoogenboom R, Thijs HM et al (2007) Tunable pH-and temperature-sensitive copolymer libraries by reversible addition-fragmentation chain transfer copolymerizations of methacrylates. Macromolecules 40(4):915–920
184. Liu Q, Yu Z, Ni P (2004) Micellization and applications of narrow-distribution poly[2-(dimethylamino) ethyl methacrylate]. Colloid Polym Sci 282(4):387–393
185. Agut W, Brulet A, Schatz C et al (2010) pH and temperature responsive polymeric micelles and polymersomes by self-assembly of poly[2-(dimethylamino) ethyl methacrylate]-b-poly (glutamic acid) double hydrophilic block copolymers. Langmuir 26(13):10546–10554
186. Hl Lee, Pietrasik J, Matyjaszewski K (2006) Phototunable temperature-responsive molecular brushes prepared by ATRP. Macromolecules 39(11):3914–3920
187. Cordes DB, Lickiss PD, Rataboul F (2010) Recent developments in the chemistry of cubic polyhedral oligosilsesquioxanes. Chem Rev 110(4):2081–2173
188. Hottle JR, Deng J, Kim HJ et al (2005) Blends of amphiphilic poly(dimethylsiloxane) and nonamphiphilic octaisobutyl-POSS at the air/water interface. Langmuir 21(6):2250–2259
189. Knight PT, Lee KM, Qin H et al (2008) Biodegradable thermoplastic polyurethanes incorporating polyhedral oligosilsesquioxane. Biomacromol 9(9):2458–2467
190. Mabry JM, Vij A, Iacono ST et al (2008) Fluorinated polyhedral oligomeric silsesquioxanes (F-POSS). Angew Chem Int Ed 120(22):4205–4208
191. Markovic E, Matisons J, Hussain M et al (2007) Poly(ethylene glycol) octafunctionalized polyhedral oligomeric silsesquioxane: WAXD and rheological studies. Macromolecules 40 (13):4530–4534
192. Su X, Guang S, Xu H et al (2009) Controllable preparation and optical limiting properties of POSS-based functional hybrid nanocomposites with different molecular architectures. Macromolecules 42(22):8969–8976
193. Xu H, Kuo S-W, Lee J-S et al (2002) Preparations, thermal properties, and Tg increase mechanism of inorganic/organic hybrid polymers based on polyhedral oligomeric silsesquioxanes. Macromolecules 35(23):8788–8793

194. Zheng Y, Wang L, Yu R et al (2012) Synthesis and self-assembly behavior of organic-inorganic poly(ethylene oxide)-block-poly (MA POSS)-block-poly(*N*-isopropylacrylamide) triblock copolymers. Macromol Chem Phys 213(4):458–469

195. Zhang W, Liu L, Zhuang X et al (2008) Synthesis and self-assembly of tadpole-shaped organic/inorganic hybrid poly(*N*-isopropylacrylamide) containing polyhedral oligomeric silsesquioxane via RAFT polymerization. J Polym Sci Part A Polym Chem 46(21): 7049–7061

196. Du F, Tian J, Wang H et al (2012) Synthesis and luminescence of POSS-containing perylene bisimide-bridged amphiphilic polymers. Macromolecules 45(7):3086–3093

197. Seuring J, Bayer FM, Huber K et al (2011) Upper critical solution temperature of poly(*N*-acryloyl glycinamide) in water: a concealed property. Macromolecules 45(1):374–384

198. Haas HC, Schuler NW (1964) Thermally reversible homopolymer gel systems. J Polym Sci Part B Polym Lett 2(12P):1095–1096

199. Haas HC, Moreau RD, Schuler NW (1967) Synthetic thermally reversible gel systems. II. J Polym Sci Part A-2: Polym Phys 5(5):915–927

200. Haas HC, Chiklis CK, Moreau RD (1970) Synthetic thermally reversible gel systems. III. J Polym Sci Part A-1: Polym Chem 8(5):1131–1145

201. Seuring J, Bayer FM, Huber K et al (2012) Upper critical solution temperature of poly (*N*-acryloyl glycinamide) in water: a concealed property. Macromolecules 45(1):374–384

202. Shimada N, Ino H, Maie K et al (2011) Ureido-derivatized polymers based on both poly (allylurea) and poly(L-citrulline) exhibit UCST-type phase transition behavior under physiologically relevant conditions. Biomacromol 12(10):3418–3422

203. Franks FT, Ives D (1966) The structural properties of alcohol-water mixtures. Chem Soc Rev 20(1):1–44

204. Noskov SY, Lamoureux G, Roux B (2005) Molecular dynamics study of hydration in ethanol–water mixtures using a polarizable force field. J Phys Chem B 109(14):6705–6713

205. Zhang Q, Hoogenboom R (2015) Polymers with upper critical solution temperature behavior in alcohol/water solvent mixtures. Prog Polym Sci 48:122–142

206. Cowie JM, McEwen I, Garay M (1986) Polymer-cosolvent systems: synergism and antisynergism of solvent mixtures for poly(methyl methacrylate). Polym Commun 27(5): 122–124

207. Cowie JMG, Mohsin MA, McEwen IJ (1987) Alcohol–water cosolvent systems for poly (methyl methacrylate). Polymer 28(9):1569–1572

208. Hoogenboom R, Becer CR, Guerrero-Sanchez C et al (2010) Solubility and thermoresponsiveness of PMMA in alcohol–water solvent mixtures. Aust J Chem 63(8):1173–1178

209. Hoogenboom R, Rogers S, Can A et al (2009) Self-assembly of double hydrophobic block copolymers in water–ethanol mixtures: from micelles to thermoresponsive micellar gels. Chem Commun 37:5582–5584

210. Piccarolo S, Titomanlio G (1982) Synergism in the swelling and solubility of poly(methyl methacrylate) in presence of ethanol/water mixtures. Macromol Rapid Commun 3(6): 383–387

211. Zhang Q, Schattling P, Theato P et al (2012) Tuning the upper critical solution temperature behavior of poly(methyl methacrylate) in aqueous ethanol by modification of an activated ester comonomer. Polym Chem 3(6):1418–1426

212. Can A, Hoeppener S, Guillet P et al (2011) Upper critical solution temperature switchable micelles based on polystyrene-block-poly(methyl acrylate) block copolymers. J Polym Sci Part A Polym Chem 49(17):3681–3687

213. Lambermont-Thijs HML, Van Kuringen HPC, van der Put JPW et al (2010) Temperature induced solubility transitions of various poly(2-oxazoline) s in ethanol–water solvent mixtures. Polymer 2(3):188–199

214. Hoogenboom R, Thijs HML, Wouters D et al (2008) Tuning solution polymer properties by binary water–ethanol solvent mixtures. Soft Matter 4(1):103–107

215. Fustin CA, Thijs-Lambermont HML, Hoeppener S et al (2010) Multiple micellar morphologies from tri- and tetrablock copoly(2-oxazoline)s in binary water–ethanol mixtures. J Polym Sci Part A Polym Chem 48(14):3095–3102
216. Thomas DB, Vasilieva YA, Armentrout RS et al (2003) Synthesis, characterization, and aqueous solution behavior of electrolyte-and pH-responsive carboxybetaine-containing cyclocopolymers. Macromolecules 36(26):9710–9715
217. Bekturov EA, Kudaibergenov SE, Rafikov SR (1990) Synthetic polymeric ampholytes in solution. J Macromol Sci Rev Macromol Chem Phys 30(2):233–303
218. Candau F, Joanny J (1996) Polymeric materials encyclopedia. In: Salomone JC (ed) CRC, vol 7, Boca Raton, FL, pp 5476–5488
219. Higgs PG, Joanny JF (1991) Theory of polyampholyte solutions. J Chem Phys 94(2):1543–1554
220. Fevola MJ, Bridges JK, Kellum MG et al (2004) pH-responsive polyzwitterions: a comparative study of acrylamide-based polyampholyte terpolymers and polybetaine copolymers. J Appl Polym Sci 94(1):24–39
221. Dobrynin AV, Erukhimovich IY (1995) Fluctuation theory of random copolymers. J Phys II 5(3):365–378
222. Kantor Y, Li H, Kardar M (1992) Conformations of polyampholytes. Phys Rev Lett 69(1):61
223. Corpart JM, Candau F (1993) Aqueous solution properties of ampholytic copolymers prepared in microemulsions. Macromolecules 26(6):1333–1343
224. Nisato G, Munch J, Candau S (1999) Swelling, structure, and elasticity of polyampholyte hydrogels. Langmuir 15(12):4236–4244
225. Dobrynin AV, Colby RH, Rubinstein M (1995) Scaling theory of polyelectrolyte solutions. Macromolecules 28(6):1859–1871
226. Lowe AB, McCormick CL (2002) Synthesis and solution properties of zwitterionic polymers. Chem Rev 102(11):4177–4190
227. Yuan J, Mecerreyes D, Antonietti M (2013) Poly (ionic liquid) s: an update. Prog Polym Sci 38(7):1009–1036
228. Chang Y, Chen S, Yu Q et al (2007) Development of biocompatible interpenetrating polymer networks containing a sulfobetaine-based polymer and a segmented polyurethane for protein resistance. Biomacromol 8(1):122–127
229. Zhang Z, Chao T, Chen S et al (2006) Superlow fouling sulfobetaine and carboxybetaine polymers on glass slides. Langmuir 22(24):10072–10077
230. Keefe AJ, Brault ND, Jiang S (2012) Suppressing surface reconstruction of superhydrophobic PDMS using a superhydrophilic zwitterionic polymer. Biomacromol 13(5):1683–1687
231. Gaberc-Porekar V, Zore I, Podobnik B et al (2008) Obstacles and pitfalls in the PEGylation of therapeutic proteins. Curr Opin Drug Discovery Dev 11(2):242
232. Herold DA, Keil K, Bruns DE (1989) Oxidation of polyethylene glycols by alcohol dehydrogenase. Biochem Pharmacol 38(1):73–76
233. Shen M, Martinson L, Wagner MS et al (2002) PEO-like plasma polymerized tetraglyme surface interactions with leukocytes and proteins: in vitro and in vivo studies. J Biomater Sci Polym Ed 13(4):367–390
234. Shih YJ, Chang Y (2010) Tunable blood compatibility of polysulfobetaine from controllable molecular-weight dependence of zwitterionic nonfouling nature in aqueous solution. Langmuir 26(22):17286–17294
235. Chang Y, Chen WY, Yandi W et al (2009) Dual-thermoresponsive phase behavior of blood compatible zwitterionic copolymers containing nonionic poly(N-isopropyl acrylamide). Biomacromol 10(8):2092–2100
236. Mary P, Bendejacq DD, Labeau MP et al (2007) Reconciling low-and high-salt solution behavior of sulfobetaine polyzwitterions. J Phys Chem B 111(27):7767–7777
237. McCormick CL, Salazar LC (1992) Water soluble copolymers: 46. Hydrophilic sulphobetaine copolymers of acrylamide and 3-(2-acrylamido-2-methylpropanedimethylammonio)-1-propanesulphonate. Polymer 33(21):4617–4624

238. Nguyen AT, Baggerman J, Paulusse JMJ et al (2011) Stable protein-repellent zwitterionic polymer brushes grafted from silicon nitride. Langmuir 27(6):2587–2594
239. Vasantha VA, Jana S, Parthiban A et al (2014) Water swelling, brine soluble imidazole based zwitterionic polymers-synthesis and study of reversible UCST behaviour and gel-sol transitions. Chem Commun 50(1):46–48
240. Shao Q, Mi L, Han X et al (2014) Differences in cationic and anionic charge densities dictate zwitterionic associations and stimuli responses. J Phys Chem B 118(24):6956–6962
241. Zhao Y, Bai T, Shao Q et al (2015) Thermoresponsive self-assembled NiPAm-zwitterion copolymers. Polym Chem 6(7):1066–1077
242. Ko DY, Patel M, Jung BK et al (2015) Phosphorylcholine-based zwitterionic biocompatible thermogel. Biomacromol 16(12):3853–3862
243. Li C, Buurma NJ, Haq I et al (2005) Synthesis and characterization of biocompatible, thermoresponsive ABC and ABA triblock copolymer gelators. Langmuir 21(24): 11026–11033
244. Men Y, Li XH, Antonietti M et al (2012) Poly(tetrabutylphosphonium 4-styrenesulfonate): a poly(ionic liquid) stabilizer for graphene being multi-responsive. Polym Chem 3(4):871–873
245. Men Y, Schlaad H, Voelkel A et al (2014) Thermoresponsive polymerized gemini dicationic ionic liquid. Polym Chem 5(11):3719–3724
246. Men Y, Schlaad H, Yuan J (2013) Cationic poly(ionic liquid) with tunable lower critical solution temperature-type phase transition. ACS Macro Lett 2(5):456–459
247. Biswas Y, Maji T, Dule M et al (2016) Tunable doubly responsive UCST-type phosphonium poly(ionic liquid): a thermosensitive dispersant for carbon nanotubes. Polym Chem 7(4): 867–877
248. Karjalainen E, Aseyev V, Tenhu H (2014) Counterion-Induced UCST for Polycations. Macromolecules 47(21):7581–7587
249. Blanazs A, Armes SP, Ryan AJ (2009) Self-assembled block copolymer aggregates: from micelles to vesicles and their biological applications. Macromol Rapid Commun 30(4–5): 267–277
250. Nystrom AM, Bartels JW, Du W et al (2009) Perfluorocarbon-loaded shell crosslinked knedel-like nanoparticles: lessons regarding polymer mobility and self-assembly. J Polym Sci Part A Polym Chem 47(4):1023–1037
251. Li J, Cong H, Li L et al (2014) Thermoresponse improvement of poly(N-isopropylacrylamide) hydrogels via formation of poly (sodium p-styrenesulfonate) nanophases. ACS Appl Mater Interface 6(16):13677–13687
252. Theato P, Sumerlin BS, O'Reilly RK et al (2013) Stimuli responsive materials. Chem Soc Rev 42(17):7055–7056
253. Park K (1997) Controlled drug delivery: challenges and strategies. American Chemical Society, Washington DC
254. Roy I, Gupta MN (2003) Smart polymeric materials: emerging biochemical applications. Chem Biol 10(12):1161–1171
255. Griffith L (2000) Polymeric biomaterials. Acta Mater 48(1):263–277
256. Na K, Lee KH, Bae YH (2004) pH-sensitivity and pH-dependent interior structural change of self-assembled hydrogel nanoparticles of pullulan acetate/oligo-sulfonamide conjugate. J Control Release 97(3):513–525
257. Oh KT, Yin H, Lee ES et al (2007) Polymeric nanovehicles for anticancer drugs with triggering release mechanisms. J Mater Chem 17(38):3987–4001
258. Tan B, Tam K, Lam Y et al (2005) Microstructure and rheological properties of pH-responsive core-shell particles. Polymer 46(23):10066–10076
259. Tan BH, Ravi P, Tam KC (2006) Synthesis and characterization of novel pH-responsive polyampholyte microgels. Macromol Rapid Commun 27(7):522–528
260. Doncom KE, Hansell CF, Theato P et al (2012) pH-switchable polymer nanostructures for controlled release. Polym Chem 3(10):3007–3015

261. Liu S, Weaver JV, Save M et al (2002) Synthesis of pH-responsive shell cross-linked micelles and their use as nanoreactors for the preparation of gold nanoparticles. Langmuir 18 (22):8350–8357

262. Liu S, Armes SP (2002) Polymeric surfactants for the new millennium: a pH-responsive, zwitterionic, schizophrenic diblock copolymer. Angew Chem Int Ed 41(8):1413–1416

263. Liu S, Armes SP (2003) Synthesis and aqueous solution behavior of a pH-responsive schizophrenic diblock copolymer. Langmuir 19(10):4432–4438

264. Weaver J, Armes S, Butun V (2002) Synthesis and aqueous solution properties of a well-defined thermo-responsive schizophrenic diblock copolymer. Chem Commun 18:2122–2123

265. Butun V, Billingham N, Armes S (1998) Unusual aggregation behavior of a novel tertiary amine methacrylate-based diblock copolymer: formation of micelles and reverse micelles in aqueous solution. J Am Chem Soc 120(45):11818–11819

266. Liu S, Billingham NC, Armes SP (2001) A schizophrenic water-soluble diblock copolymer. Angew Chem Int Ed 40(12):2328–2331

267. Xiao X, He S, Dan M et al (2014) Nanoparticle-to-vesicle and nanoparticle-to-toroid transitions of pH-sensitive ABC triblock copolymers by in-to-out switch. Chem Commun 50 (30):3969–3972

268. Yang YQ, Lin WJ, Zhang LJ et al (2013) Synthesis, characterization and pH-responsive self-assembly behavior of amphiphilic multiarm star triblock copolymers based on PCL, PDEAEMA, and PEG. Macromol Res 21(9):1011–1020

269. Bird R, Freemont TJ, Saunders BR (2011) Hollow polymer particles that are pH-responsive and redox sensitive: two simple steps to triggered particle swelling, gelation and disassembly. Chem Commun 47(5):1443–1445

270. Jia HZ, Zhang W, Zhu JY et al (2015) Hyperbranched-hyperbranched polymeric nanoassembly to mediate controllable co-delivery of siRNA and drug for synergistic tumor therapy. J Control Release 216:9–17

271. Zhang W, Fang B, Walther A et al (2009) Synthesis via RAFT polymerization of tadpole-shaped organic/inorganic hybrid poly(acrylic acid) containing polyhedral oligomeric silsesquioxane (POSS) and their self-assembly in water. Macromolecules 42(7):2563–2569

272. Ma L, Geng H, Song J et al (2011) Hierarchical self-assembly of polyhedral oligomeric silsesquioxane end-capped stimuli-responsive polymer: from single micelle to complex micelle. J Phys Chem B 115(36):10586–10591

273. Alvarez-Lorenzo C, Blanco-Fernandez B, Puga AM et al (2013) Crosslinked ionic polysaccharides for stimuli-sensitive drug delivery. Adv Drug Delivery Rev 65(9): 1148–1171

274. Kudaibergenov SE (1999) Recent advances in the study of synthetic polyampholytes in solutions. In: Polymer latexes-epoxide resins-polyampholytes. Springer, Berlin, pp 115–197

275. Dobrynin AV, Colby RH, Rubinstein M (2004) Polyampholytes. J Polym Sci Part B: Polym Phys 42(19):3513–3538

276. Sfika V, Tsitsilianis C (2003) Association phenomena of poly(acrylic acid)-b-poly (2-vinylpyridine)-b-poly(acrylic acid) triblock polyampholyte in aqueous solutions: from transient network to compact micelles. Macromolecules 36(13):4983–4988

277. Chen WY, Alexandridis P, Su CK et al (1995) Effect of block size and sequence on the micellization of ABC triblock methacrylic polyampholytes. Macromolecules 28(25): 8604–8611

278. Creutz S, Jerome R (1999) Effectiveness of poly(vinylpyridine) block copolymers as stabilizers of aqueous titanium dioxide dispersions of a high solid content. Langmuir 15(21): 7145–7156

279. Creutz S, van Stam J, Antoun S et al (1997) Exchange of polymer molecules between block copolymer micelles studied by emission spectroscopy. A method for the quantification of unimer exchange rates. Macromolecules 30(14):4078–4083

280. Creutz S, Van Stam J, De Schryver FC et al (1998) Dynamics of poly((dimethylamino) alkyl methacrylate-block-sodium methacrylate) micelles. Influence of hydrophobicity and

molecular architecture on the exchange rate of copolymer molecules. Macromolecules 31(3): 681–689

281. Gohy J-F, Creutz S, Garcia M et al (2000) Aggregates formed by amphoteric diblock copolymers in water. Macromolecules 33(17):6378–6387

282. Goloub T, de Keizer A, Cohen Stuart MA (1999) Association behavior of ampholytic diblock copolymers. Macromolecules 32(25):8441–8446

283. Lowe A, Billingham N, Armes S (1997) Synthesis and aqueous solution properties of novel zwitterionic block copolymers. Chem Commun 11:1035–1036

284. Lowe A, Billingham N, Armes S (1998) Synthesis and characterization of zwitterionic block copolymers. Macromolecules 31(18):5991–5998

285. Patrickios C, Hertler W, Abbott N et al (1994) Diblock, ABC triblock, and random methacrylic polyampholytes: synthesis by group transfer polymerization and solution behavior. Macromolecules 27(4):930–937

286. Patrickios CS, Sharma LR, Armes SP et al (1999) Precipitation of a water-soluble ABC triblock methacrylic polyampholyte: effects of time, pH, polymer concentration, salt type and concentration, and presence of a protein. Langmuir 15(5):1613–1620

287. Butun V, Lowe A, Billingham N et al (1999) Synthesis of zwitterionic shell cross-linked micelles. J Am Chem Soc 121(17):4288–4289

288. Chien H-W, Tsai W-B, Jiang S (2012) Direct cell encapsulation in biodegradable and functionalizable carboxybetaine hydrogels. Biomaterials 33(23):5706–5712

289. Zhang L, Cao Z, Bai T et al (2013) Zwitterionic hydrogels implanted in mice resist the foreign-body reaction. Nat Bitechnol 31(6):553–556

290. Cao B, Li L, Tang Q et al (2013) The impact of structure on elasticity, switchability, stability and functionality of an all-in-one carboxybetaine elastomer. Biomaterials 34(31):7592–7600

291. Yang W, Bai T, Carr LR et al (2012) The effect of lightly crosslinked poly(carboxybetaine) hydrogel coating on the performance of sensors in whole blood. Biomaterials 33(32): 7945–7951

292. Yang W, Xue H, Carr LR et al (2011) Zwitterionic poly(carboxybetaine) hydrogels for glucose biosensors in complex media. Biosens Bioelectron 26(5):2454–2459

293. Armentrout RS, McCormick CL (2000) Water soluble polymers. 76. Electrolyte responsive cyclocopolymers with sulfobetaine units exhibiting polyelectrolyte or polyampholyte behavior in aqueous media. Macromolecules 33(2):419–424

294. Zhang Z, Vaisocherova H, Cheng G et al (2008) Nonfouling behavior of polycarboxybetaine-grafted surfaces: structural and environmental effects. Biomacromol 9(10):2686–2692

295. Galin J (1996) In: Polyzwitterions (Overview) in polymeric materials encyclopedia, vol 4. In: Salamone JC (ed) Vol 4. CRC Press, Boca Raton, FL, pp 7189

296. Liaw DJ, Huang CC (1997) Dilute solution properties of poly(3-dimethyl acryloyloxyethyl ammonium propiolactone). Polymer 38(26):6355–6362

297. Lowe AB, McCormick CL (2002) Homogeneous controlled free radical polymerization in aqueous media. Aust J Chem 55(7):367–379

298. Ramireddy RR, Prasad P, Finne A et al (2015) Zwitterionic amphiphilic homopolymer assemblies. Polym Chem 6(33):6083–6087

299. Lee CJ, Wu H, Tang Q et al (2015) Structure-function relationships of a tertiary amine-based polycarboxybetaine. Langmuir 31(36):9965–9972

300. Li W, Liu Q, Liu L (2014) Amino acid-based zwitterionic polymers: antifouling properties and low cytotoxicity. J Biomater Sci Polym Ed 25(14–15):1730–1742

301. Li J, Wang T, Wu D et al (2008) Stimuli-responsive zwitterionic block copolypeptides: poly(N-isopropylacrylamide)-block-poly(lysine-co-glutamic acid). Biomacromol 9(10): 2670–2676

302. Wada T, Kano A, Shimada N et al (2012) α-Amino acid pendant polymers as endosomal pH-responsive gene carriers. Macromol Res 20(3):302–308

303. Alswieleh AM, Cheng N, Canton I et al (2014) Zwitterionic poly(amino acid methacrylate) brushes. J Am Chem Soc 136(26):9404–9413

304. Calvo A, Yameen B, Williams FJ et al (2009) Mesoporous films and polymer brushes helping each other to modulate ionic transport in nanoconfined environments. An interesting example of synergism in functional hybrid assemblies. J Am Chem Soc 131(31):10866–10868

305. Evans AC, Skey J, Wright M et al (2009) Functional and tuneable amino acid polymers prepared by RAFT polymerization. J Polym Sci Part A Polym Chem 47(24):6814–6826

306. Mori H, Endo T (2012) Amino-acid-based block copolymers by RAFT polymerization. Macromol Rapid Commun 33(13):1090–1107

307. Roy SG, De P (2014) pH responsive polymers with amino acids in the side chains and their potential applications. J Appl Polym Sci 131(20)

308. Li WC, Liu QS, Liu LY (2014) Amino acid-based zwitterionic polymers: antifouling properties and low cytotoxicity. J Biomater Sci Polym Ed 25(14–15):1730–1742

309. Wang X, Wu G, Lu C et al (2011) Synthesis of a novel zwitterionic biodegradable poly (alpha, beta-l-aspartic acid) derivative with some l-histidine side-residues and its resistance to non-specific protein adsorption. Colloids and Surf B 86(1):237–241

310. Weller D, Medina-Oliva A, Claus H et al (2013) Solution properties and potential biological applications of zwitterionic poly(ε-N-methacryloyl-L-lysine). Macromolecules 46(21):8519–8527

311. Liu Q, Singh A, Liu L (2012) Amino acid-based zwitterionic poly(serine methacrylate) as an antifouling material. Biomacromol 14(1):226–231

312. Lu C, Zhao D, Wang S et al (2014) Synthesis and characterization of zwitterionic peptides derived from natural amino acids and their resistance to protein adsorption. RSC Adv 4 (40):20665–20672

313. Doyaguez EG, Parra F, Corrales G et al (2009) New hydroxyproline based methacrylic polybetaines: synthesis, pH sensitivity and catalytic activity. Polymer 50(19):4438–4446

314. Banerjee S, Maji T, Paira TK et al (2013) Amino-acid-based zwitterionic polymer and its cu (II)-induced aggregation into nanostructures: a template for CuS and CuO nanoparticles. Macromol Rapid Commun 34(18):1480–1486

315. Maji T, Banerjee S, Biswas Y et al (2015) Dual-stimuli-responsive l-serine-based zwitterionic UCST-type polymer with tunable thermosensitivity. Macromolecules 48 (14):4957–4966

316. Dule M, Biswas M, Paira TK et al (2015) Hierarchical nanostructures of tunable shapes through self-aggregation of POSS end-functional polymer and poly(ionic liquid) hybrids. Polymer 77:32–41

317. Matini T, Francini N, Battocchio A et al (2014) Synthesis and characterization of variable conformation pH responsive block co-polymers for nucleic acid delivery and targeted cell entry. Polym Chem 5(5):1626–1636

318. Lu H, Liu Y, Wang B et al (2016) Self-assembling transition behavior of a hydrophobic associative polymer based on counterion and pH effects. Coll Surfaces A Physicochem Eng Aspects 490:1–8

319. Jiang J, Tong X, Morris D et al (2006) Toward photocontrolled release using light-dissociable block copolymer micelles. Macromolecules 39(13):4633–4640

320. Jochum FD, Theato P (2009) Temperature-and light-responsive polyacrylamides prepared by a double polymer analogous reaction of activated ester polymers. Macromolecules 42 (16):5941–5945

321. Babin J, Pelletier M, Lepage M et al (2009) A new two-photon sensitive block copolymer nanocarrier. Angew Chem Int Ed 48(18):3329–3332

322. Jiang J, Tong X, Zhao Y (2005) A new design for light-breakable polymer micelles. J Am Chem Soc 127(23):8290–8291

323. Pietsch C, Schubert US, Hoogenboom R (2011) Aqueous polymeric sensors based on temperature-induced polymer phase transitions and solvatochromic dyes. Chem Commun 47 (31):8750–8765

324. Chibisov AK, Görner H (2001) Photochromism of spirobenzopyranindolines and spiron-aphthopyranindolines. Phys Chem Chem Phys 3(3):424–431

325. Wang G, Tong X, Zhao Y (2004) Preparation of azobenzene-containing amphiphilic diblock copolymers for light-responsive micellar aggregates. Macromolecules 37(24):8911–8917

326. Lee Hi WuW, Oh JK et al (2007) Light-induced reversible formation of polymeric micelles. Angew Chem Int Ed 119(14):2505–2509

327. Zhao Y (2012) Light-responsive block copolymer micelles. Macromolecules 45(9): 3647–3657

328. Theato P (2011) One is enough: influencing polymer properties with a single chromophoric unit. Angew Chem Int Ed 50(26):5804–5806

329. Gohy JF, Zhao Y (2013) Photo-responsive block copolymer micelles: design and behavior. Chem Soc Rev 42(17):7117–7129

330. Jana S, Saha A, Paira TK et al (2016) Synthesis and self-aggregation of poly (2-ethyl-2-oxazoline)-based photocleavable block copolymer: micelle, compound micelle, reverse micelle, and dye encapsulation/release. J Phys Chem B 120(4):813–824

331. Kang M, Moon B (2008) Synthesis of photocleavable poly(styrene-block-ethylene oxide) and its self-assembly into nanoporous thin films. Macromolecules 42(1):455–458

332. Schumers JM, Gohy JF, Fustin CA (2010) A versatile strategy for the synthesis of block copolymers bearing a photocleavable junction. Polym Chem 1(2):161–163

333. Zhao H, Gu W, Sterner E et al (2011) Highly ordered nanoporous thin films from photocleavable block copolymers. Macromolecules 44(16):6433–6440

334. Cabane E, Malinova V, Meier W (2010) Synthesis of photocleavable amphiphilic block copolymers: toward the design of photosensitive nanocarriers. Macro Chem Phys 211 (17):1847–1856

335. Nojima S, Ohguma Y, Kadena KI et al (2010) Crystal orientation of poly(ε-caprolactone) homopolymers confined in cylindrical nanodomains. Macromolecules 43(8):3916–3923

336. Han D, Tong X, Zhao Y (2011) Fast photodegradable block copolymer micelles for burst release. Macromolecules 44(3):437–439

337. Bertrand O, Schumers JM, Kuppan C et al (2011) Photo-induced micellization of block copolymers bearing 4,5-dimethoxy-2-nitrobenzyl side groups. Soft Matter 7(15):6891–6896

338. Heerema L, Cakali D, Roelands M et al (2010) Micellar solutions of PEO-PPO-PEO block copolymers for in situ phenol removal from fermentation broth. Sep Purif Technol 73(2): 319–326

339. Huddleston JG, Willauer HD, Griffin ST et al (1999) Aqueous polymeric solutions as environmentally benign liquid/liquid extraction media. Ind Eng Chem Res 38(7):2523–2539

340. Doh J, Irvine DJ (2004) Photogenerated polyelectrolyte bilayers from an aqueous-processible photoresist for multicomponent protein patterning. J Am Chem Soc 126(30): 9170–9171

341. Khire VS, Kloxin AM, Couch CL et al (2008) Synthesis, characterization and cleavage of linear polymers attached to silica nanoparticles formed using thiol-acrylate conjugate addition reactions. J Polym Sci Part A Polym Chem 46(20):6896–6906

342. Tang X, Gao L, Fan X et al (2007) ABA-type amphiphilic triblock copolymers containing p-ethoxy azobenzene via atom transfer radical polymerization: synthesis, characterization, and properties. J Polym Sci Part A Polym Chem 45(11):2225–2234

343. Bohnert R, Finkelmann H (1994) Liquid-crystalline side-chain AB block copolymers by direct anionic polymerization of a mesogenic methacrylate. Macromol Chem Phys 195(2): 689–700

344. Walther M, Faulhammer H, Finkelmann H (1998) On the thread-like morphology of LC/I block copolymers in nematic solvents. Macromol Chem Phys 199(2):223–237

345. Chiefari J, Chong Y, Ercole F et al (1998) Living free-radical polymerization by reversible addition-fragmentation chain transfer: the RAFT process. Macromolecules 31(16):5559–5562

346. Kadota S, Aoki K, Nagano S et al (2005) Photocontrolled microphase separation of block copolymers in two dimensions. J Am Chem Soc 127(23):8266–8267

347. Tong X, Wang G, Soldera A et al (2005) How can azobenzene block copolymer vesicles be dissociated and reformed by light? J Phys Chem B 109(43):20281–20287

348. Han K, Su W, Zhong M et al (2008) Reversible photocontrolled swelling-shrinking behavior of micron vesicles self-assembled from azopyridine-containing diblock copolymer. Macromol Rapid Commun 29(23):1866–1870

349. Wang D, Ye G, Wang X (2007) Synthesis of aminoazobenzene-containing diblock copolymer and photoinduced deformation behavior of its micelle-like aggregates. Macromol Rapid Commun 28(23):2237–2243

350. Su W, Luo Y, Yan Q et al (2007) Photoinduced fusion of micro-vesicles self-assembled from azobenzene-containing amphiphilic diblock copolymers. Macromol Rapid Commun 28 (11):1251–1256

351. Shimoboji T, Larenas E, Fowler T et al (2002) Photoresponsive polymer-enzyme switches. Proc Natl Acad Sci 99(26):16592–16596

352. Berkovic G, Krongauz V, Weiss V (2000) Spiropyrans and spirooxazines for memories and switches. Chem Rev 100(5):1741–1754

353. Guo X, Zhang D, Zhou Y et al (2003) Synthesis and spectral investigations of a new dyad with spiropyran and fluorescein units: toward information processing at the single molecular level. J Org Chem 68(14):5681–5687

354. Parthenopoulos DA, Rentzepis PM (1989) Three-dimensional optical storage memory. Science 245(4920):843–845

355. Kocer A, Walko M, Meijberg W et al (2005) A light-actuated nanovalve derived from a channel protein. Science 309(5735):755–758

356. Jin Q, Mitschang F, Agarwal S (2011) Biocompatible drug delivery system for photo-triggered controlled release of 5-fluorouracil. Biomacromol 12(10):3684–3691

357. Khorsand B, Lapointe G, Brett C et al (2013) Intracellular drug delivery nanocarriers of glutathione-responsive degradable block copolymers having pendant disulfide linkages. Biomacromol 14(6):2103–2111

358. Hassan SSM, Rechnitz GA (1982) Determination of glutathione and glutathione reductase with a silver sulfide membrane electrode. Anal Chem 54(12):1972–1976

359. Ren T, Wu W, Jia M et al (2013) Reduction-cleavable polymeric vesicles with efficient glutathione-mediated drug release behavior for reversing drug resistance. ACS Appl Mater Interfaces 5(21):10721–10730

360. Saito G, Swanson JA, Lee K-D (2003) Drug delivery strategy utilizing conjugation via reversible disulfide linkages: role and site of cellular reducing activities. Adv Drug Deliv Rev 55(2):199–215

361. Ganta S, Devalapally H, Shahiwala A et al (2008) A review of stimuli-responsive nanocarriers for drug and gene delivery. J Control Release 126(3):187–204

362. Meng F, Hennink WE, Zhong Z (2009) Reduction-sensitive polymers and bioconjugates for biomedical applications. Biomaterials 30(12):2180–2198

363. Thambi T, Yoon HY, Kim K et al (2011) Bioreducible block copolymers based on poly (ethylene glycol) and poly(γ-benzyl $_L$-glutamate) for intracellular delivery of camptothecin. Bioconjugate Chem 22(10):1924–1931

364. Bauhuber S, Hozsa C, Breunig M et al (2009) Delivery of nucleic acids via disulfide-based carrier systems. Adv Mater 21:3286–3306

365. Wang H, Tang L, Tu C et al (2013) Redox-responsive, core-cross-linked micelles capable of on-demand, concurrent drug release and structure disassembly. Biomacromol 14(10): 3706–3712

366. Wang YC, Wang F, Sun TM et al (2011) Redox-responsive nanoparticles from the single disulfide bond-bridged block copolymer as drug carriers for overcoming multidrug resistance in cancer cells. Bioconjugate Chem 22(10):1939–1945

367. Balendiran GK, Dabur R, Fraser D (2004) The role of glutathione in cancer. Cell Biochem Funct 22(6):343–352

368. Gilbert HF (1982) Biological disulfides: the third messenger? Modulation of phosphofructokinase activity by thiol/disulfide exchange. J Biol Chem 257(20):12086–12091

369. Van Der Vlies AJ, Hasegawa U, Hubbell JA (2012) Reduction-sensitive tioguanine prodrug micelles. Mol Pharm 9(10):2812–2818

370. Sun H, Guo B, Li X et al (2010) Shell-sheddable micelles based on dextran-SS-poly (caprolactone) diblock copolymer for efficient intracellular release of doxorubicin. Biomacromol 11(4):848–854
371. Ma N, Li Y, Xu H et al (2010) Dual redox responsive assemblies formed from diselenide block copolymers. J Am Chem Soc 132(2):442–443
372. Liu J, Pang Y, Chen J et al (2012) Hyperbranched polydiselenide as a self assembling broad spectrum anticancer agent. Biomaterials 33(31):7765–7774
373. Ma Y, Dong WF, Hempenius MA et al (2006) Redox-controlled molecular permeability of composite-wall microcapsules. Nat Mater 5(9):724–729
374. Nakahata M, Takashima Y, Hashidzume A et al (2013) Redox-generated mechanical motion of a supramolecular polymeric actuator based on host-guest interactions. Angew Chem Int Ed 52(22):5731–5735
375. Nakahata M, Takashima Y, Yamaguchi H et al (2011) Redox-responsive self-healing materials formed from host-guest polymers. Nat Commun 2:511
376. Sui X, Feng X, Di Luca A et al (2013) Poly(N-isopropylacrylamide)-poly(ferrocenylsilane) dual-responsive hydrogels: synthesis, characterization and antimicrobial applications. Polym Chem 4(2):337–342
377. Staff RH, Gallei M, Mazurowski M et al (2012) Patchy nanocapsules of poly(vinylferrocene)-based block copolymers for redox-responsive release. ACS Nano 6(10):9042–9049
378. Qiu L, Yang X, Gou X et al (2010) Dispersing carbon nanotubes with graphene oxide in water and synergistic effects between graphene derivatives. Chemistry 16(35):10653–10658
379. Peng L, Feng A, Zhang H et al (2014) Voltage-responsive micelles based on the assembly of two biocompatible homopolymers. Polym Chem 5(5):1751–1759
380. Miao C, Li F, Zuo Y et al (2016) Novel redox-responsive nanogels based on poly(ionic liquid) s for the triggered loading and release of cargos. RSC Adv 6(4):3013–3019
381. Kim KT, Cornelissen JJ, Nolte RJ et al (2009) Polymeric monosaccharide receptors responsive at neutral pH. J Am Chem Soc 131(39):13908–13909
382. Roy D, Cambre JN, Sumerlin BS (2008) Sugar-responsive block copolymers by direct RAFT polymerization of unprotected boronic acid monomers. Chem Commun 21:2477–2479
383. Yao Y, Wang X, Tan T et al (2011) A facile strategy for polymers to achieve glucose-responsive behavior at neutral pH. Soft Matter 7(18):7948–7951
384. Matsumoto A, Ikeda S, Harada A et al (2003) Glucose-responsive polymer bearing a novel phenylborate derivative as a glucose-sensing moiety operating at physiological pH conditions. Biomacromol 4(5):1410–1416
385. Kataoka K, Miyazaki H, Okano T et al (1994) Sensitive glucose-induced change of the lower critical solution temperature of poly[N,N-(dimethylacrylamide)-co-3-(acrylamido)-phenylboronic acid] in physiological saline. Macromolecules 27(4):1061–1062
386. Wang B, Ma R, Liu G et al (2009) Glucose-responsive micelles from self-assembly of poly (ethylene glycol)-b-poly(acrylic acid-co-acrylamidophenylboronic acid) and the controlled release of insulin. Langmuir 25(21):12522–12528
387. Kitano S, Kataoka K, Koyama Y et al (1991) Glucose-responsive complex formation between poly(vinyl alcohol) and poly(N-vinyl-2-pyrrolidone) with pendent phenylboronic acid moieties. Macromol Rapid Commun 12(4):227–233
388. Kitano S, Koyama Y, Kataoka K et al (1992) A novel drug delivery system utilizing a glucose responsive polymer complex between poly(vinyl alcohol) and poly(N-vinyl-2-pyrrolidone) with a phenylboronic acid moiety. J Control Release 19(1–3):161–170
389. Liu G, Ma R, Ren J et al (2013) A glucose-responsive complex polymeric micelle enabling repeated on-off release and insulin protection. Soft Matter 9(5):1636–1644
390. Lorand JP, Edwards JO (1959) Polyol complexes and structure of the benzeneboronate ion. J Org Chem 24(6):769–774
391. Yao Y, Zhao L, Yang J et al (2012) Glucose-responsive vehicles containing phenylborate ester for controlled insulin release at neutral pH. Biomacromol 13(6):1837–1844

392. Motornov M, Sheparovych R, Katz E et al (2007) Chemical gating with nanostructured responsive polymer brushes: mixed brush versus homopolymer brush. ACS Nano 2(1): 41–52

393. Fielding LA, Edmondson S, Armes SP (2011) Synthesis of pH-responsive tertiary amine methacrylate polymer brushes and their response to acidic vapour. J Mater Chem 21 (32):11773–11780

394. Yan Q, Zhou R, Fu C et al (2011) CO_2-responsive polymeric vesicles that breathe. Angew Chem Int Ed 123(21):5025–5029

395. Jacobson MZ (2009) Review of solutions to global warming, air pollution, and energy security. Energy Environ Sci 2(2):148–173

396. Rochelle GT (2009) Amine scrubbing for CO_2 capture. Science 325(5948):1652–1654

397. Jessop PG, Phan L, Carrier A et al (2010) A solvent having switchable hydrophilicity. Green Chem 12(5):809–814

398. Yan Q, Wang J, Yin Y et al (2013) Breathing polymersomes: CO_2-tuning membrane permeability for size-selective release, separation, and reaction. Angew Chem Int Ed 52 (19):5070–5073

399. Kumar S, Tong X, Dory YL et al (2013) A CO_2-switchable polymer brush for reversible capture and release of proteins. Chem Commun 49(1):90–92

400. Chen G, Jiang M (2011) Cyclodextrin-based inclusion complexation bridging supramolecular chemistry and macromolecular self-assembly. Chem Soc Rev 40(5):2254–2266

401. Wang Y, Xu H, Zhang X (2009) Tuning the amphiphilicity of building blocks: controlled self-assembly and disassembly for functional supramolecular materials. Adv Mater 21 (28):2849–2864

402. Cho SY, Allcock HR (2009) Synthesis of adamantyl polyphosphazene-polystyrene block copolymers, and β-cyclodextrin-adamantyl side group complexation. Macromolecules 42(13): 4484–4490

403. Park C, Lee IH, Lee S et al (2006) Cyclodextrin-covered organic nanotubes derived from self-assembly of dendrons and their supramolecular transformation. Proc Natl Acad Sci 103 (5):1199–1203

404. Zeng J, Shi K, Zhang Y et al (2008) Construction and micellization of a noncovalent double hydrophilic block copolymer. Chem Commun 32:3753–3755

405. Liu H, Zhang Y, Hu J et al (2009) Multi-responsive supramolecular double hydrophilic diblock copolymer driven by host-guest inclusion complexation between β-cyclodextrin and adamantyl moieties. Macromol Chem Phys 210(24):2125–2137

406. Zhang ZX, Liu X, Xu FJ et al (2008) Pseudo-block copolymer based on star-shaped poly(*N*-isopropylacrylamide) with a β-cyclodextrin core and guest-bearing PEG: controlling thermoresponsivity through supramolecular self-assembly. Macromolecules 41(16): 5967–5970

407. Guo M, Jiang M (2009) Non-covalently connected micelles (NCCMs): the origins and development of a new concept. Soft Matter 5(3):495–500

408. Wang J, Jiang M (2006) Polymeric self-assembly into micelles and hollow spheres with multiscale cavities driven by inclusion complexation. J Am Chem Soc 128(11):3703–3708

409. Suzaki Y, Taira T, Takeuchi D et al (2007) Competing supramolecular assembly of amphiphiles to form micelles or pseudorotaxanes. Org Lett 9(5):887–890

410. Amajjahe S, Ritter H (2008) Supramolecular controlled pseudo-LCST effects of cyclodextrin-complexed poly (ionic liquids). Macromolecules 41(9):3250–3253

411. Wang Y, Zhang M, Moers C et al (2009) Block copolymer aggregates with photo-responsive switches: towards a controllable supramolecular container. Polymer 50(20):4821–4828

412. Jiang B, Tao W, Lu X et al (2012) A POSS-based supramolecular amphiphile and its hierarchical self-assembly behaviors. Macromol Rapid Commun 33(9):767–772

413. Hickenbooth CR, Moore JS, White SR et al (2007) Biasing reaction pathways with mechanical force. Nature 446(7134):423–427

414. Paulusse JMJ, Sijbesma RP (2004) Reversible mechanochemistry of a PdII coordination polymer. Angew Chem Int Ed 116(34):4560–4562

415. Chen Y, Guan Z (2010) Bioinspired modular synthesis of elastin-mimic polymers to probe the mechanism of elastin elasticity. J Am Chem Soc 132(13):4577–4579
416. Kushner AM, Gabuchian V, Johnson EG et al (2007) Biomimetic design of reversibly unfolding cross-linker to enhance mechanical properties of 3D network polymers. J Am Chem Soc 129(46):14110–14111
417. Kushner AM, Vossler JD, Williams GA et al (2009) A biomimetic modular polymer with tough and adaptive properties. J Am Chem Soc 131(25):8766–8768
418. Paulusse JM, Sijbesma RP (2006) Ultrasound in polymer chemistry: revival of an established technique. J Polym Sci Part A Polym Chem 44(19):5445–5453
419. Brantley JN, Wiggins KM, Bielawski CW (2011) Unclicking the click: mechanically facilitated 1, 3-dipolar cycloreversions. Science 333(6049):1606–1609
420. Paulusse JM, Van Beek D, Sijbesma RP (2007) Reversible switching of the sol-gel transition with ultrasound in rhodium (I) and iridium (I) coordination networks. J Am Chem Soc 129(8):2392–2397
421. Piermattei A, Karthikeyan S, Sijbesma RP (2009) Activating catalysts with mechanical force. Nat Chem 1(2):133–137
422. Jochum FD, Theato P (2009) Temperature and light sensitive copolymers containing azobenzene moieties prepared via a polymer analogous reaction. Polymer 50(14):3079–3085
423. Jochum FD, Zur Borg L, Roth PJ et al (2009) Thermo-and light-responsive polymers containing photoswitchable azobenzene end groups. Macromolecules 42(20):7854–7862
424. Ravi P, Sin S, Gan L et al (2005) New water soluble azobenzene-containing diblock copolymers: synthesis and aggregation behavior. Polymer 46(1):137–146
425. Wei H, Zhang XZ, Cheng H et al (2006) Self-assembled thermo-and pH responsive micelles of poly (10-undecenoic acid-b-N-isopropylacrylamide) for drug delivery. J Control Release 116(3):266–274
426. Zhang K, Wu XY (2004) Temperature and pH-responsive polymeric composite membranes for controlled delivery of proteins and peptides. Biomaterials 25(22):5281–5291
427. Zhang L, Guo R, Yang M et al (2007) Thermo and pH dual-responsive nanoparticles for anti-cancer drug delivery. Adv Mater 19(19):2988–2992
428. Chen J, Liu M, Gao C et al (2013) Self-assembly behavior of pH-and thermo-responsive hydrophilic ABCBA-type pentablock copolymers synthesized by consecutive RAFT polymerization. RSC Adv 3(35):15085–15093
429. Rao J, Luo Z, Ge Z et al (2007) "Schizophrenic" micellization associated with coil-to-helix transitions based on polypeptide hybrid double hydrophilic rod-coil diblock copolymer. Biomacromol 8(12):3871–3878
430. Luo C, Liu Y, Li Z (2012) Pathway-dependent re-assembly of dual-responsive ABC terpolymer in water. Soft Matter 8(9):2618–2626
431. Zhang H, Guo S, Fan W et al (2016) Ultrasensitive pH-induced water solubility switch using UCST polymers. Macromolecules 49(4):1424–1433
432. Cui W, Lu X, Cui K et al (2012) Dual-responsive controlled drug delivery based on ionically assembled nanoparticles. Langmuir 28(25):9413–9420
433. Zuo Y, Guo N, Jiao Z et al (2016) Novel reversible thermoresponsive nanogel based on poly (ionic liquid) s prepared via RAFT crosslinking copolymerization. J Polym Sci Part A Polym Chem 54(1):169–178
434. Chen CY, Wang HL (2014) Dual Thermo-and pH-responsive zwitterionic sulfobataine copolymers for oral delivery system. Macromol Rapid Commun 35(17):1534–1540
435. Kungwatchakun D, Irie M (1988) Photoresponsive polymers. Photocontrol of the phase separation temperature of aqueous solutions of poly-[N-isopropylacrylamide-co-N-(4-phenylazophenyl) acrylamide]. Macromol Rapid Commun 9(4):243–246
436. Tao X, Gao Z, Satoh T et al (2011) Synthesis and characterization of well-defined thermo-and light-responsive diblock copolymers by atom transfer radical polymerization and click chemistry. Polym Chem 2(9):2068–2073

437. Jiang X, Lavender CA, Woodcock JW et al (2008) Multiple micellization and dissociation transitions of thermo-and light-sensitive poly(ethylene oxide)-*b*-poly(ethoxytri (ethylene glycol) acrylate-*co*-o-nitrobenzyl acrylate) in water. Macromolecules 41(7):2632–2643

438. Jin Q, Liu G, Ji J (2010) Micelles and reverse micelles with a photo and thermo double-responsive block copolymer. J Polym Sci Part A Polym Chem 48(13):2855–2861

439. Chen J, Qiu X, Ouyang J et al (2011) pH and reduction dual-sensitive copolymeric micelles for intracellular doxorubicin delivery. Biomacromol 12(10):3601–3611

440. Wei C, Guo J, Wang C (2011) Dual stimuli-responsive polymeric micelles exhibiting "and" logic gate for controlled release of adriamycin. Macromol Rapid Commun 32(5):451–455

441. Sumaru K, Kameda M, Kanamori T et al (2004) Characteristic phase transition of aqueous solution of poly(*N*-isopropylacrylamide) functionalized with spirobenzopyran. Macromolecules 37(13):4949–4955

442. Achilleos DS, Vamvakaki M (2010) Multiresponsive spiropyran-based copolymers synthesized by atom transfer radical polymerization. Macromolecules 43(17):7073–7081

443. Yu YY, Tian F, Wei C et al (2009) Facile synthesis of triple-stimuli (photo/pH/thermo) responsive copolymers of 2-diazo-1, 2-naphthoquinone-mediated poly(*N*-isopropylacrylamide-*co*-N-hydroxymethylacrylamide). J Polym Sci A Polym Chem 47(11):2763–2773

444. Dong J, Wang Y, Zhang J et al (2013) Multiple stimuli-responsive polymeric micelles for controlled release. Soft Matter 9(2):370–373

445. Schattling P, Jochum FD, Theato P (2011) Multi-responsive copolymers: using thermo-, light-and redox stimuli as three independent inputs towards polymeric information processing. Chem Commun 47(31):8859–8861

446. Klaikherd A, Nagamani C, Thayumanavan S (2009) Multi-stimuli sensitive amphiphilic block copolymer assemblies. J Am Chem Soc 131(13):4830–4838

447. Wang F, Klaikherd A, Thayumanavan S (2011) Temperature sensitivity trends and multi-stimuli sensitive behavior in amphiphilic oligomers. J Am Chem Soc 133(34):13496–13503

448. Casado N, Hernandez G, Sardon H et al (2016) Current trends in redox polymers for energy and medicine. Prog Polym Sci 52:107–135

449. Gallaway JW, Calabrese Barton SA (2008) Kinetics of redox polymer-mediated enzyme electrodes. J Am Chem Soc 130(26):8527–8536

450. Barriere F, Ferry Y, Rochefort D et al (2004) Targetting redox polymers as mediators for laccase oxygen reduction in a membrane-less biofuel cell. Electrochem Commun 6(3):237–241

451. Scodeller P, Carballo R, Szamocki R et al (2010) Layer-by-layer self-assembled osmium polymer-mediated laccase oxygen cathodes for biofuel cells: the role of hydrogen peroxide. J Am Chem Soc 132(32):11132–11140

452. Bunte C, Prucker O, Konig T et al (2009) Enzyme containing redox polymer networks for biosensors or biofuel cells: a photochemical approach. Langmuir 26(8):6019–6027

453. Sen P, De A, Chowdhury AD et al (2013) Conducting polymer based manganese dioxide nanocomposite as supercapacitor. Electrochim Acta 108:265–273

454. Frackowiak E, Khomenko V, Jurewicz K et al (2006) Supercapacitors based on conducting polymers/nanotubes composites. J Power Sources 153(2):413–418

455. Zhang LL, Li S, Zhang J et al (2010) Enhancement of electrochemical performance of macroporous carbon by surface coating of polyaniline. Chem Mater 22(3):1195–1202

456. Cho S, Shin K-H, Jang J (2013) Enhanced electrochemical performance of highly porous supercapacitor electrodes based on solution processed polyaniline thin films. ACS Appl Mater Interface 5(18):9186–9193

457. Sun W, Zheng R, Chen X (2010) Symmetric redox supercapacitor based on micro-fabrication with three-dimensional polypyrrole electrodes. J Power Sources 195(20):7120–7125

458. Laforgue A, Simon P, Fauvarque JF (2001) Chemical synthesis and characterization of fluorinated polyphenylthiophenes: application to energy storage. Synth Metal 123(2):311–319

459. Cho S, Lee SB (2008) Fast electrochemistry of conductive polymer nanotubes: synthesis, mechanism, and application. Acc Chem Res 41(6):699–707

460. Wu M, Snook GA, Gupta V et al (2005) Electrochemical fabrication and capacitance of composite films of carbon nanotubes and polyaniline. J Mater Chem 15(23):2297–2303

461. Xu J, Wang K, Zu SZ et al (2010) Hierarchical nanocomposites of polyaniline nanowire arrays on graphene oxide sheets with synergistic effect for energy storage. ACS Nano 4(9): 5019–5026

462. Cong HP, Ren XC, Wang P et al (2013) Flexible graphene-polyaniline composite paper for high-performance supercapacitor. Energy Environ Sci 6(4):1185–1191

463. Shi Y, Pan L, Liu B et al (2014) Nanostructured conductive polypyrrole hydrogels as high-performance, flexible supercapacitor electrodes. J Mater Chem A 2(17):6086–6091

464. Huang J, Wang K, Wei Z (2010) Conducting polymer nanowire arrays with enhanced electrochemical performance. J Mater Chem 20(6):1117–1121

465. Chen GZ, Shaffer MSP, Coleby D et al (2000) Carbon nanotube and polypyrrole composites: coating and doping. Adv Mater 12(7):522–526

466. Wang M, Gratzel C, Zakeeruddin SM et al (2012) Recent developments in redox electrolytes for dye-sensitized solar cells. Energy Environ Sci 5(11):9394–9405

467. Xia J, Masaki N, Lira-Cantu M et al (2008) Influence of doped anions on poly (3,4-ethylenedioxythiophene) as hole conductors for iodine-free solid-state dye-sensitized solar cells. J Am Chem Soc 130(4):1258–1263

468. Azaceta E, Marcilla R, Sanchez-Diaz A et al (2010) Synthesis and characterization of poly (1-vinyl-3-alkylimidazolium) iodide polymers for quasi-solid electrolytes in dye sensitized solar cells. Electroch Acta 56(1):42–46

469. Bubnova O, Khan ZU, Malti A et al (2011) Optimization of the thermoelectric figure of merit in the conducting polymer poly(3,4-ethylenedioxythiophene). Nat Mater 10(6): 429–433

470. Culebras M, Gomez C, Cantarero A (2014) Review on polymers for thermoelectric applications. Materials 7(9):6701

Part II
Nanostructured Materials for Energy Storage

Chapter 7
Polymer- and Carbon-Based Nanofibres for Energy Storage

Alexandra Ho, Suxi Wang, Xu Li and Haifei Zhang

Abstract There is ever-increasing demand for energy worldwide. The constant use of energy particularly in portable devices and vehicles has required highly efficient and high-capacity energy storage. Materials research is at the front of addressing the society's demand for energy storage. This chapter focuses on the fabrication and use of polymer and carbon-based nanofibers for energy storage. The widely used fabrication methods such as chemical vapour deposition, electrospinning and the recently developed methods including controlled freezing and gelation for nanofibers have been described. Upon the preparation of polymer nanofibers, carbon nanofibers can be produced by pyrolysis under inert atmosphere. We then review the applications of carbon-based nanofibers in different types of rechargeable batteries and supercapacitors. The chapter is completed with conclusion and outlook.

7.1 Introduction

With the increase in demand for energy, there must be a corresponding increase in energy production which in turn leads to issues in supply and demand. Renewable energy sources such as wind and solar light demonstrate a great potential for reducing the dependence on fossil fuels and thus the production of greenhouse gas emissions [1]. Energy requirements are variable throughout the day, and a balance must be achieved that avoids undersupply, but also prevents wasting through overproduction. As the world looks towards renewable energy sources, we need a reliable electricity

A. Ho · H. Zhang (✉)
Department of Chemistry, University of Liverpool, Oxford Street,
Liverpool L69 7ZD, UK
e-mail: zhanghf@liverpool.ac.uk

A. Ho · S. Wang · X. Li (✉)
Institute of Materials Research and Engineering (IMRE), Agency for Science,
Technology and Research (A*STAR), 2 Fusionopolis Way, Innovis, #08-03,
Singapore 138634, Singapore
e-mail: x-li@imre.a-star.edu.sg

supply for 24 h a day. Since solar power and wind power are intermittent sources, the solution to this problem lies with energy storage. By storing the energy produced at low demand in powerful and reliable batteries/supercapacitors, a constant electricity supply can be provided without reliance on fossil fuels.

Even through the burning of renewable fuel sources such as biomass, energy storage methods are a necessity since variation in electricity production with the variation in demand is not recommended as this decreases the efficiency in production. There have also been numerous studies that have determined that the use of variable generation resources will impact the stability of the grid unless storage is included [1].

Within the realm of energy storage, there are several methods available which all store energy in different forms. Chemical energy storage encompasses many fields including hydrogen storage [2] and methane storage [3]. Another way is the storage of mechanical energy using constructions such as flywheels which are capable of storing 1 kWh of useable energy [4, 5]. Carbon nanotubes (CNTs) are of particular interest in the development of strong materials for flywheels, and as such, CNT-reinforced nanocomposites have been developed [6, 7].

Another type of energy storage is electrochemical energy storage, of which batteries and fuel cells are prime examples. Electrochemical cells are capable of generating electrical energy from chemical reactions as such their voltage is dependent upon the electrode potentials of each of the half-cells in use. For example, rechargeable lithium cells can provide voltage of around 3 V with good cycling capability. Lithium-ion batteries use intercalated lithium compounds as the cathode material, while the anodic material is most commonly graphite, though there is research into alternative electrode materials due to its limited theoretical capacity that is unsuitable for high-energy applications [8–10].

There are many materials that are currently being researched for their potential energy storage applications. One such material would be conductive polymers which are organic polymers that demonstrate as semiconductors most of the time. Conducting polymers store and conduct charge through redox processes; i.e., when oxidation (doping) occurs, ions are transferred to the polymer backbone, and the reverse occurs with reduction (dedoping), wherein ions are released back into solution [11]. The bulk of the film is responsible for charging, and as such, conducting polymers present the opportunity for high levels of specific capacitance. While long-term stability is expected to be a problem due to swelling and shrinking, some research has demonstrated stability over thousands of cycles [12, 13].

A rapidly developing area of research is focussed on electrical energy storage through systems such as superconducting magnetic energy storage which involves storing electrical energy in the form of direct current (DC) electricity that is the source of a DC magnetic field and has been shown to be capable of storing 1–3 MJ of energy with power outputs of up to 2 MW [14]. The conductor operates at cryogenic temperatures where it has relatively no energy losses because the magnetic field is in the superconducting region [14].

The energy storage area in which carbon-based nanofibres have been most prevalent is supercapacitors which are currently used in applications that require

many rapid charge and discharge cycles. Supercapacitors are constructed with two metal foils that act as current collectors, coated with an electrode material such as activated carbon or carbon nanofibres which act as the power connection between the electrode material and the external terminals of the capacitor. These electrode materials must have very high surface areas which may be achieved by various methods such as templating or activation. The methods of storing energy within a supercapacitor fall in two categories: electrical double-layer capacitance (EDLC) and pseudocapacitance which will be discussed later [15, 16].

Carbon nanofiber (CNF) composites include combinations of CNFs with metals, metal oxides, or polymers, which can lead to favourable behaviour during energy storage since CNFs store charges using surface properties, while metal oxides and polymers store charges using the body of the material. Combining the two materials allows for EDLC and pseudocapacitance to be used simultaneously in both Faradaic and non-Faradaic processes to store charges [16, 17]. The performance of CNF/metal oxide/polymer composites is largely determined by the dispersion of the CNFs within the matrix. Therefore, the technique used to achieve uniform dispersion plays a key role in the synthesis of CNF composites. There are two main approaches to achieving the dispersion of CNFs within a metal oxide or polymer matrix, melt mixing, and sonication in low viscosity solutions [6, 18, 19].

Carbon-based materials have attracted a lot of attention due to promising properties in their basic forms, i.e. graphene [20, 21], carbon-based nanofibres [22–26], and hierarchically porous carbon materials [27, 28]. The carbon material that has received the most attention recently is graphene, a one-atom-thick sheet of sp^2-bonded carbon arranged in a hexagonal lattice [29]. Graphene is the thinnest known material in the world and can be considered as the basic starting point for building many other carbon materials [29].

Currently, the main commercially used material for anodes is graphite; however, the theoretical capacity of this is limited to 372 mAh g^{-1} which cannot meet the requirements for high energy capacity [8]. Due to this deficiency, researches into other carbonaceous materials such as carbon nanotubes (CNTs), carbon nanofibres (CNFs), ordered mesoporous carbon, and hierarchically porous carbon have been carried out to show much higher capacity. This chapter focuses on the fabrication of polymer nanofibers and carbon-based nanofibres and the use of such materials for energy storage.

7.2 Fabrication Methods for Carbon-Based Nanofibres

7.2.1 History and Properties of Carbon Nanofibres

The first-recorded publication surrounding carbon-based nanofibres is a patent submitted by Hughes and Chambers on the manufacturing of filaments [30]. However, the true significance of these structures was not fully appreciated until

their structure could be analysed through electron microscopy. The first electron microscopy images of carbon nanofibres were observed by Soviet scientists Radushkevich and Lukyanovich. Published in 1952, they showed multi-wall carbon filaments 50 nm in diameter formed by CO decomposition on an iron substrate [31]. Early research was motivated by the wish to limit their formation. Filamentous carbon or carbon filaments were considered a nuisance as they often grew and accumulated upon metallic catalysts used in petrochemical processing and the conversion of carbon-containing gases.

In 1985, Buckminsterfullerene, C_{60}, was observed by Kroto et al. and earned them the Nobel Prize in 1997 [32]. The discovery was followed by a demonstration by Iijima that carbon nanotubes were formed during arc-discharge synthesis of C_{60} [33, 34]. Two years later, Iijima and Ichihashi and Bethune et al. synthesized single-walled carbon nanotubes (SWCNTs) [33, 35]. It was initially suggested that the carbon nanofibres formed through the catalytic chemical vapour deposition method were comprised of a duplex structure, an inner core of amorphous carbon surrounded by graphitic platelets [36, 37]. More recently, it has been shown that the structural arrangement of CNFs can vary significantly when subjected to different reaction conditions including the chemical nature and structure of the catalyst and the composition of the reactants [38].

As the name suggests, CNFs are nanoscale with respect to their diameters. Their small scale provides a promising basis for research into their properties and any modifications that could result in porosity. While chemical vapour deposition (CVD) was the first process by which CNFs were produced, many processes have since been developed which allow for greater control over structure, morphology, and dopants, while also providing a potentially "greener" approach to production. These methods can include electrospinning [39–41], controlled freezing/freeze-drying [2, 42, 43], and nanofibrous gels and carbonization [22, 44].

7.2.2 Chemical Vapour Deposition

Chemical vapour deposition (CVD) process is often used to produce solid high-quality, high-performance materials. Typically, a substrate is exposed to volatile precursors which may react and/or decompose on or near to a heated substrate surface to produce the desired deposit. Atomistic deposition like this can provide highly pure materials and structural control at atomic or nanometre-scale level [45]. This process can be used to produce single-layer, multi-layer, composite, nanostructured, and functionally graded coating materials [45]. CVD has become one of the main methods for the deposition of thin films and coatings for a wide range of applications including semiconductors for microelectronics, optoelectronics, energy conversion devices, dielectrics for microelectronics, refractory ceramic materials used for hard coatings, protections against corrosion, oxidation or as diffusion barriers, metallic films for microelectronics and for protective coatings, fibre production, and fibre coating [45].
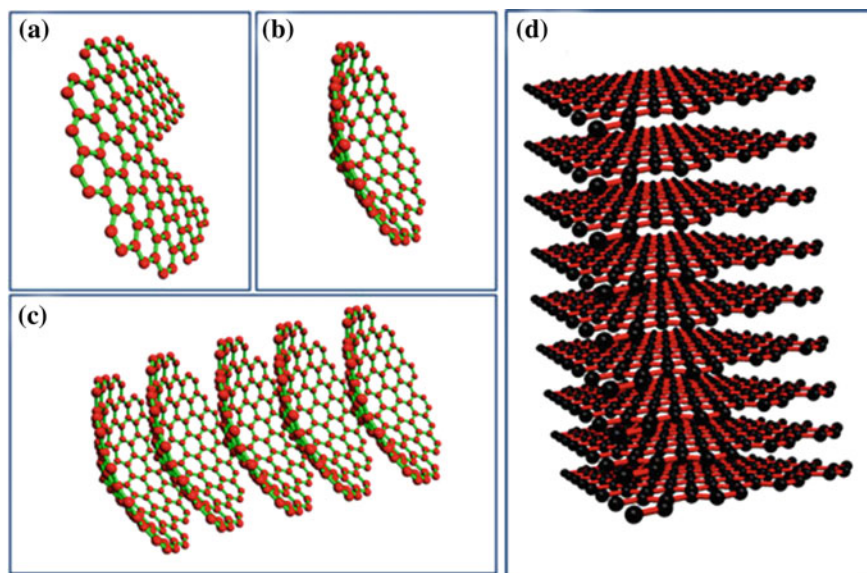
Fig. 7.1 Schematic demonstration of formation of cup-stacked CNF structure (**a–c**), and platelet CNF structure (**d**) (reproduced from Ref. [18] with kind permission of © 2014 Multidisciplinary Digital Publishing Institute)

As mentioned above, CNFs were first presented through a catalytic chemical vapour deposition method involving the iron-catalysed thermal decomposition of carbon monoxide [31]. Small organic molecules such as ethanol can be good precursors for CVD synthesis of CNFs and CNTs since they can decompose to simpler species such as methane, carbon monoxide, and hydrogen. The decomposition of a carbon source on a catalyst causes a solid solution of metal carbides to form, and then, excess carbon atoms in the metal carbide diffuse out from the catalyst to form CNFs. There are often volatile by-products produced through this method; however, these can usually be removed by gas flow through the reaction chamber.

Two types of CNFs can be prepared by CVD, cup-stacked CNFs, and platelet CNFs as shown in Fig. 7.1, [18]. Generally, the structures of CNFs formed are determined by the shapes of the catalytic nanosized metal particles. In a recent study, Lin et al. showed that the participation of chloroform, in a synthesis conducted through the pyrolysis of chloroform and ethanol in the presence of a nickel catalyst, led to Ni–Cl bonding on the surface of the catalyst resulting in a relatively poor crystalline layer and a course surface [46]. Low amounts of chlorine in the catalyst led to the formation of smaller catalyst particles with flat surfaces, causing graphene nanosheets to stack perpendicular to the fibre axis and became platelet graphite nanofibres. A high chlorine content, however, leads to aggregation of the catalyst and thus formation of large catalyst particles with rough surfaces. These rough surfaces resulted in the random stacking of graphene nanosheets which

became turbostratic carbon nanofibres, that is, the sheets of carbon atoms folded or crumpled together haphazardly [46].

7.2.3 Electrospinning

As mentioned above, electrospinning is a fibre production method which uses an electric potential to charge polymer solutions or melts and draws them into fibres. The fibres are usually of diameters from tens of nanometers to several microns. Electrospinning shares some characteristics of electrospraying, used in inkjet printing, and conventional dry spinning of fibres [47]. The origins of electrospinning can be dated back to 1934, where Formhals patented an invention relating to the process and producing artificial filaments through the application of 57 kV to a solution of cellulose [48].

When a sufficiently high voltage is applied to a liquid droplet, the body of the liquid becomes charged leading to electrostatic repulsion counteracting surface tension, and therefore, the droplet becomes stretched. At a critical point, a Taylor cone forms, which is the point at which a stream of liquid erupts from the surface of the droplet. A balance between molecular cohesion and conductivity must be achieved so that stream break-up does not occur and a charged jet can be formed [47, 49–52]. The jet dries in flight, and the charge migrates to the surface of the fibre; the mode of current flow changes from ohmic to convective.

Electrospinning is a highly versatile technique that has many variables that can be altered to change the structure of the fibres formed. The morphology of the structures is highly dependent on a combined effect of the electrostatic field and the material properties of the polymer. The charge transport due to the applied voltage is mainly because the polymer jet towards the collector and the variation in current are linked to the mass flow of the polymer from the nozzle tip [51]. For a poly (ethylene oxide)/water system, the fibre morphology changed from a defect-free fibre at the initiating voltage of 5.5 kV to a highly beaded structure at a voltage of 9.0, which was linked to a steep increase in the spinning current which controls bead formation in the electrospinning process [53].

The conductivity of the solution being electrospun is highly important. If the solution is completely insulating or the applied voltage is not high enough for the electrostatic force to overcome surface tension, no fibre can be produced [51]. The solution can be adjusted by adding salt to enhance the conductivity as demonstrated by Qin et al. [54] during their application of different salts to polyacrylonitrile (PAN) polymer solutions. Viscosity and shearing strength of electrospinning solutions are slightly affected by the addition of salts as well as the diameter of the nanofibres produced upon electrospinning, with a correlation being established between the size of the nanofibres formed and the size of the salts [54].

The distance between the nozzle and the collector can easily affect the morphology and structure of electrospun fibres due to the dependence on deposition time, evaporation rate, and whipping/instability interval [51]. A study by

Chang et al. [49] demonstrated the possibility for continuous near-field electrospinning in which solid nanofibres with orderly patterns were deposited over large areas. The needle to collector distance was fixed to 500 μm, while the jet initiation voltage was achieved at 1.5 kV [49]. The polymer concentration greatly affected the morphology of the electrospun nanofibres during this process. When poly (ethylene oxide) concentration was too low, there was insufficient viscoelasticity to suppress capillary break-up [49].

Electrospinning is not just limited to the production of purely polymeric fibres, and a benefit of this process is that solutions can be produced using a variety of materials as well as combinations of materials to produce fibres with unique properties. Combined with carbonization, it is possible to produce highly porous fibres through a number of routes that include spinning into a cryogenic liquid [55], mixing with metal oxide particles [56–59], and coaxial spinning [41, 57] where a material that conventionally would not spin may be encased in a polymer solution that can later be removed through carbonization.

Development of functional composite nanofibres by electrospinning has recently become a research area of intense interest for energy and environmental applications [60–62]. Electrospun nanofibres from polymers with high carbon yields (e.g. PAN in most cases, lignin, cellulose) can be converted to carbon nanofibres through subsequent high-temperature thermal treatment. This generally includes stabilization in air (which converts thermoplastic precursor fibres to highly condensed thermosetting fibres by complicated chemical reactions such as dehydrogenation, cyclization, and polymerization) and carbonization under noble gases. Sometimes, activation steps using steam, base, or acid as the activation agents [63], or hetero-atom doping during the heating treatment process [64], are needed to increase the specific surface area or electrical conductivity of the prepared carbon nanofibres. A unique feature of the electrospun carbon fibres for energy application is that they can form free-standing fibrous mats which can be directly employed as electrode materials for energy devices without using substrates or adding binders and conductive agents, thereby increasing the energy density and simplifying the fabrication process.

The most significant advantage of using electrospun carbon fibres for energy storage is the convenience to fabricate hybrid carbon fibre webs via incorporation of active components (e.g. metal precursors or nanoparticles) or electrically conductive materials (i.e. carbon nanotubes, graphene) to the precursor solutions to improve their electrochemical performance. Electrospinning also offers flexibility in controlling the morphology of prepared carbon nanofibres through variation of the electrospinning parameters (i.e. single or double nozzle, voltage, feeding rate, distance), thermal treatment conditions, as well as precursor compositions. Core–shell-structured electrospun carbon fibres can be created using either a coaxial spinneret [65], or a single spinneret based on the Kirkendall effect during the stabilization process [66, 67]. Hollow or highly porous carbon nanofibres [68–70] can be formed through decomposition or extraction of the incorporated pore-forming components, e.g. poly(methyl methacrylate) (PMMA), Pluronic F127

(a triblock copolymer), and mineral oil. It is also possible to obtain fused carbon fibrous mats by adding low-melting-point polymers in the precursor solutions [71].
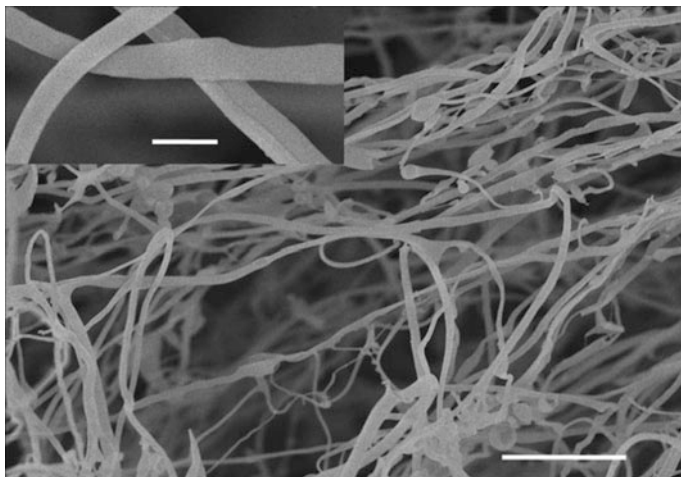
7.2.4 Controlled Freezing/Freeze-Drying

Compared to dry-processing routes, wet-shaping techniques are capable of producing materials with complex shapes that can satisfy a large range of applications through the fabrication of dense and porous materials [42]. Freeze-drying, also known as lyophilization, is an industrial dehydration process which works by freezing the material and reducing the surrounding pressure to allow any frozen water to sublimate and desorb under vacuum. The voids of ice crystals after sublimation generate porosity in the dried materials. This is how freeze-drying or more accurately ice templating can be used to produce a range of porous materials. The control of the freezing condition is the key to the tuning of pore morphology. For example, a directional freezing procedure may be employed, as illustrated in Fig. 7.2, allowing for the achievement of aligned microchanneled structures in the direction of freezing after removing the frozen solvent [72–75]. Importantly, the emulsion templating and ice templating can be combined to produce materials with systematically tuned porosity and provide an exciting route for the preparation of aqueous, organic, and poorly water-soluble drug nanoparticle suspensions [76–78].

With the ice-templating method, polymer solutions or colloidal suspensions are usually employed to produce a wide range of porous materials. However, when the
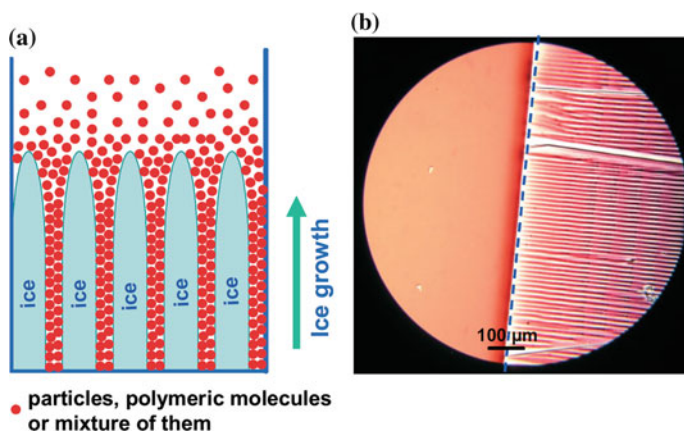
Fig. 7.2 **a** Schematic representation of the directional freezing process. As ice crystals grow in one direction, solutes such as particles and/or polymeric molecules are excluded and packed between the crystals. **b** An optical microscopic image showing the directional freezing of gold nanoparticle suspension. The *blue dashed line* indicates the freezing front, while the *red stripes* are concentrated gold nanoparticles excluded from the freezing front (reproduced from Ref. [74] with kind permission of © 2007 Wiley-VCH) (Color figure online)

Fig. 7.3 Sodium carboxymethyl cellulose (Mw 250 K) nanofibers prepared by controlled freezing and freeze-drying of its aqueous solution (0.02 wt%). *Scale bar* 5 μm and *inset* scale bar 600 nm (reproduced from Ref. [79] with kind permission of © 2009 Wiley-VCH)

concentrations of the polymers or colloids are very low, nanofibrous structures can be formed. For example, dilute aqueous polymer solutions were directionally frozen and freeze-dried to generate polymer nanofibres, as demonstrated with sodium carboxymethyl cellulose (shown in Fig. 7.3), poly(vinyl alcohol), and sodium alginate [79]. These polymer nanofibres could be further used as templates to prepare hollow titania microtubes and iron oxide nanofibres [79]. It was also possible to produce chitosan in porous and nanofibrous structures for the controlled release of bovine serum albumins [80] or chitosan/silica microsphere composite fibres for dual-controlled release drugs [81]. Dilute colloidal suspensions including metal, metal oxide, and polymers can be subjected to the directional freezing process, which allows the self-assembly of nanoparticles during freezing, and then produce colloids-composed nanofibres after freeze-drying [82–84]. Rather than using polymers or colloids, Mao et al. used the solution of the monomer, 2-hydroxyethyl methacrylate (HEMA), in tert-butyl alcohol. After being directionally frozen and polymerized by Υ-irradiation, at the temperature the solvent was still frozen, polyHEMA nanofibrous scaffolds were prepared and demonstrated as a highly active and recyclable catalyst support [85].

A general route for production of carbon materials is through the carbonization of polymers. However, to ensure a high carbon yield and maintenance of porous morphology, the polymer should have high carbon content and/or the carbonization procedures may be designed purposely. The controlled freezing-freeze-drying approach has been adopted for lignin solutions [86]. Excitingly, a device was developed to produce a large quantity of lignin nanofibres. The nanofibers were produced in thin films by delivering aqueous lignin solutions through a 0.254-mm aperture onto a liquid nitrogen-cooled drum collector. The resultant frozen ribbons

were then lyophilized to produce a templated lignin network which was then carbonized at 1000 °C to form CNFs [86]. The rapid freezing process described by Spender et al. resulted in elimination of larger lamellar spaces and macropores that had been observed in materials produced through the ice-segregation-induced self-assembly methodology [72, 86, 87].
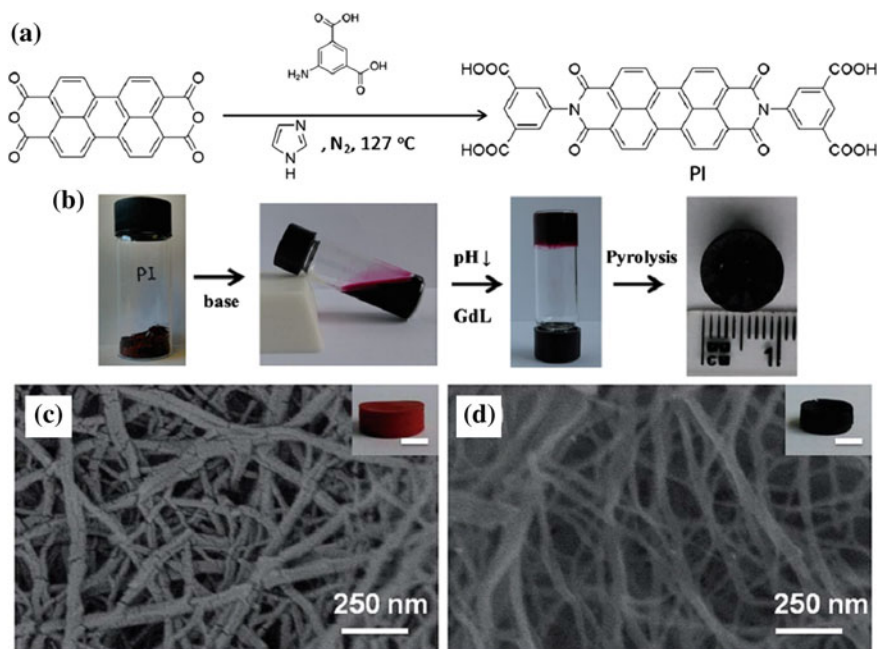
7.2.5 Nanofibrous Gels and Carbonization

Gels are defined as substantially dilute cross-linked systems which exhibit no flow when in the steady state [88]. The skeleton formed in such gels may be maintained by removing the solvent under supercritical condition since pores in the gels are free from capillary forces leaving behind porous, ultralight materials that have extremely low density and thermal conductivity. These aerogels can have high surface areas that could make them ideal as absorbents, catalyst supports, electrodes for electric double-layer capacitors, and materials for chromatographic separation [89].

If a nanofibrous gel can be formed, it is possible to produce a three-dimensional carbon nanofibrous monolith simply by carbonization. The prerequisites for this method are as follows: (1) a dry nanofibrous gel can be formed; (2) there is high carbon content in the gel material; and (3) the nanofibre morphology can be maintained after carbonization. Very often, one can observe the presence of nanofibres in gels, but that may be challenging for the whole gel to be nanofibrous. Perylene diimides are multi-aromatic molecules, with an extended quadrupolar π system, and are utilized in many fields, including biosensing, light-emitting diodes, and pigments. Due to their strong hydrophobicity, self-assembly of perylene diimides can form nanostructures in various organic solvents via π–π interaction/stacking and interaction of side chains.

Liu et al. reported the self-assembly of perylene diimide derivatives by pH-triggered gelation of aqueous solution at room temperature (Fig. 7.4) [22]. After washing with acetone and cyclohexane and then freeze-drying, 3D red porous scaffold consisting of entangled nanofibers with relatively uniform diameters (20–50 nm) was formed as either thin films or monoliths [22]. Upon carbonization, with little shrinkage, the replicated porous scaffolds with carbon nanofibres were successfully prepared (Fig. 7.4). It was very convenient to add different desirable compounds in the solution before gelation. For example, melamine and the surfactant Pluronic P123 could be added to produce N-doped mesoporous carbon nanofibres.

In a further development, nanofibrous microspheres were prepared by a water-in-oil emulsion formed with the aqueous perylene diimide derivative solution as the internal phase and o-xylene as the external phase [44]. Span 80 was used as the surfactant, and polystyrene (MW 192 K) was added to help stabilize the emulsion. Glucono-d-lactone (GdL) was added into the aqueous phase to initiate the gelation. GdL can be hydrolysed in water and render the solution acidic.

Fig. 7.4 **a** Synthesis and chemical structure of perylene diimide derivative (PI). **b** The procedure of preparing carbon via pH-triggered gelation, freeze-drying, and pyrolysis. **c** The nanofibrous gel structure after freeze-drying (*inset* showing the *red* monolith). **d** The carbon nanofibrous structure after pyrolysis (*inset* showing the *black* carbon monolith) (reproduced from Ref. [22] with kind permission of © 2015 Royal Society of Chemistry) (Color figure online)
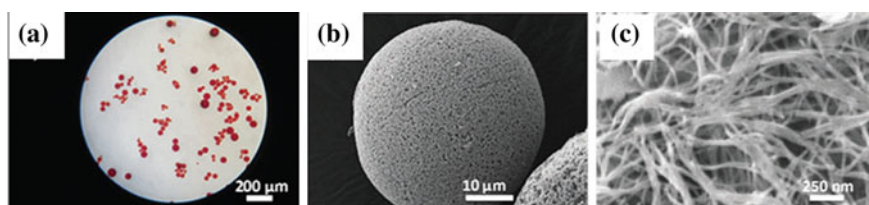
Fig. 7.5 **a** The *red* microspheres by optical microscopy. **b** The porous carbon microsphere. **c** The nanofibrous structure of the carbon microsphere (reproduced from Ref. [44] with kind permission of © 2015 Royal Society of Chemistry) (Color figure online)

The concentration of the GdL was key to producing discreet microspheres; i.e., the lowering pH induced by GdL hydrolysis should not initiate the gelation before a stable emulsion was formed. As shown in Fig. 7.5, porous red microspheres were formed. Upon carbonization, nanofibrous carbon microspheres were produced. This method is unique in that there are not many reports describing the preparation of nanofibrous microspheres. For example, the widely used CVD or electrospinning

would not be able to produce microspheres. Combining this gelation system with a droplet formation method can be a versatile way in preparing nanofibrous micro-spheres. Apart from the emulsion method, the microfluidic method may be employed to prepare such microspheres.

7.3 Energy Storage Applications

As the population and industrialization of the Earth has increased, so too have the energy demands, putting a great strain on the existing power infrastructure and posing serious implications for the future of a society so dependent on finite energy sources. Up to now, oil-based fuels have been largely used. However, with increasing limitations on the availability of such resources, a need for alternative energy sources has become apparent. New technologies have been developed which rely on sustainable energy forms such as wind energy, solar power, hydroelectricity, and geothermal energy. These methods of energy production provide some mea-sures of the solution needed. However, they are also unpredictable in their gener-ation since it is not always windy and sunny. Due to this inconsistency, renewable sources must be paired with a reliable form of energy storage which can store energy as mentioned above.

It is possible to store energy using several different methods which include chemical (e.g. hydrogen, liquid nitrogen, oxyhydrogen, and vanadium pentoxide), electrochemical (e.g. batteries and fuel cells), electrical (e.g. supercapacitors and superconducting magnetic energy storage), thermal, and mechanical energy. In this section, we will evaluate emerging technologies in the field of energy storage and how carbon-based nanofibres are proving to be useful materials in many applica-tions. Table 7.1 lists the energy storage applications where carbon-based nanofibers have been used.

7.3.1 Rechargeable Batteries

Rechargeable batteries, while initially costing more than the alternative primary batteries that can only be used until completely discharged and then must be dis-posed, cost much less over the lifetime of ownership in comparison. Their ability to cycle discharging and recharging makes them ideal for use in power stations that must vary their output as demand varies.

7.3.1.1 Li-Ion Batteries

Primary Li batteries were commercialized during the 1970s and involved using lithium metal electrodes. $Li–Li_xMnO_2$ was one of the systems developed by

Table 7.1 Carbon-based nanofibres for different energy storage systems and their capacities

Type of storage	Material	Capacity	Cycles
Lithium-ion batteries	Nitrogen-doped porous carbon nanofiber webs [90]	Specific: 943 mAh g^{-1} (max)	600
	Bubble-nanorod-structured Fe$_2$O$_3$- carbon nanofibres [91]	Reversible: 773 mAh g^{-1} (1.0 A g^{-1})	10
		Discharge: 812 mAh g^{-1} (1.0 A g^{-1})	300
Lithium-air batteries	Co$_3$O$_4$/carbon nanofibre composite [92]	Initial: 760 mAh g^{-1} (0.5 A g^{-1})	–
	Free-standing thin webs of activated carbon nanofibres [93]	Discharge: 6099 mAh g^{-1} (0.2 A g^{-1}) (Activation Temp: 1273 K)	–
Lithium-sulfur batteries	Coaxial graphene wrapping over sulfur-coated carbon nanofibres [71]	Initial: 745 mAh g^{-1}	–
		Reversible: 273 mAh g^{-1}	1500
	Free-standing carbon nanofibre interlayer—CO$_2$-activated CNFs [94]	Reversible: 1215 mAh g^{-1}	100
		Reversible: 910 mShg^{-1}	200
Sodium-ion batteries	Polyvinyl chloride nanofibres [95]	Initial: 178 mAh g^{-1} (1.2 A g^{-1})	–
		Reversible: 215 mAh g^{-1} (0.12 A g^{-1})	120
	MoS$_2$/carbon nanofibre membranes by electrospinning [56]	Charge: 283.9 mAh g^{-1} (0.1 mA g^{-1})	600
		Initial: 381.7 mAh g^{-1} (0.1 A g^{-1})	–
Electric double-layer capacitors	Porous nitrogen and phosphorus co-doped carbon nanofibre networks [96]	Specific: 280 F g^{-1} (1 A g^{-1})	–
		94% capacity retention	10,000
	Self-assembled perylene diimide derivatives [22]	Specific: 192 F g^{-1} (1 A g^{-1})	–
		Reversible: 226 F g^{-1} (4 A g^{-1})	1000
Pseudocapacitors	Carbon nanofibre/MnO$_2$ nanocables [57]	Specific: 311 F g^{-1}	Scan rate: 2 V s^{-1}
	Carbon nanofibres with encapsulated Co$_3$O$_4$ nanoparticles [97]	Specific: 586 F g^{-1} (1 A g^{-1})	–
		Reversible: 424 F g^{-1} (2 A g^{-1})	2000
Hybrid capacitors	Hierarchical porous V$_2$O$_5$ nanosheets on carbon nanofibres [98]	Specific: 408 F g^{-1} (1 A g^{-1}) 89.3%	–
		Capacity retention (1.2 A g^{-1})	10,000
	Ni-Al layered double-hydroxide nanosheets/carbon nanotubes [99]	Specific: 115 F g^{-1} (1 A g^{-1})	–
		57% Capacity retention (6 A g^{-1})	2000
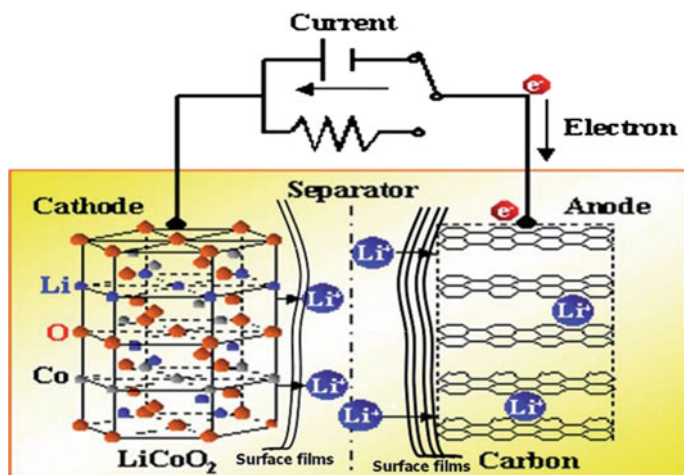
Fig. 7.6 A schematic presentation of the most commonly used Li-ion battery based on graphite anodes and LiCoO₂ cathodes (reproduced from Ref. [101] with kind permission of © 2011 Royal Society of Chemistry)

Tadiran, Inc., Israel, for use in mobile phones; however, it did not achieve widespread use due to safety problems [100]. Through further research into lithium as a power source, it became clear that lithium intercalated with transition metal oxides and sulphides could be used as reversible cathode materials for rechargeable Li batteries (Fig. 7.6) [101–103].

Lithium-ion batteries are most commonly found in portable electronic devices which require high cycling durability with a low power to weight ratio. These batteries can supply high energy density while showing small memory effect which can be found in nickel–cadmium batteries as well as some nickel-metal hydride batteries. Memory effect is the loss of charge capacity upon repeated partial charging and discharging. Applying lithium to develop high-performance batteries is motivated by its low standard reduction potential at −3.04 V (vs. the standard hydrogen electrode) as well as its low density, 0.53 g cm^{-3} [104].

During the charging process of Li-ion batteries, lithium ions are forced to leave the cathode material, which is usually lithium-containing metal oxides, under an external electric field and intercalate into a graphite lattice [104]. Bubble-nanorod-structured Fe_2O_3 carbon nanofibres were synthesized by Cho et al. presenting with a discharge capacity of 812 mAh g^{-1} upon its 300th cycle, in comparison with bare Fe_2O_3 nanofibres which showed a discharge capacity of 285 mAh g^{-1} at its 300th cycle with both measurements recorded at current density 1 A g^{-1} [91]. Qie et al. [90] presented porous, nitrogen-doped carbon nanofibre webs as anodes for Li-ion batteries with a higher specific capacity of 943 mAh g^{-1} even after 600 cycles at 2 A g^{-1}. While both processes show high capacities for use in Li-ion batteries, the novelty of the bubble-nanorod-structured Fe_2O_3 carbon

nanofibres presents the possibility of designing greater variations in the material that may present even more promising results.

7.3.1.2 Li-Air Batteries

Li-air batteries have not received much attention until recently due to the particular interest in its potential applications in transportation, where specific energy (energy per unit mass) and energy density (energy per unit volume) are most important [105]. In order to achieve efficiency and range equal to that provided by liquid fuels, a battery system with much higher specific energy and energy density is required. A Li-air battery has notably higher theoretical energy density because the anode metal possesses a high ratio of valence electrons to atomic nuclei and cathode oxygen is not stored in the cell [106]. This theoretical energy density is several times higher than that of state-of-the-art Li-ion battery technology and can even match that of 1700 Wh/kg provided by gasoline energy systems [107].

There are many possible reactions involving lithium and air. Depending on the chemical environment and mode of operation, several products may result from the reaction of Li and O_2 as shown in Scheme 7.1, [108]. There are four major types of Li-air battery systems: aqueous, aprotic/non-aqueous, all-solid-state, and hybrid. Each of these systems is classified by the type of electrolyte used. In particular, the non-aqueous system has attracted a lot of attention due to its potentially high energy density and rechargeability [107].

There is much research necessary for the development of practical Li-air batteries and commercialization. These include quantitatively demonstrating chemical reversibility of the electrochemical reactions (and their relationship to the discharge/charge currents) and understanding coulombic efficiency of the battery in cycling. Furthermore, the investigation of various functional materials has been highly active, covering oxidation-resistant electrodes and cost-effective catalysts (to reduce overpotentials for charge/discharge reactions where insoluble products are formed), new nanostructured air cathodes for optimal transport to active catalyst surfaces, and robust Li metal or composite electrode (capable of repeated cycling at high current densities). Also of great importance is the preparation of high-throughput air-breathing membranes that separate O_2 from ambient air (H_2O and CO_2 limit lifetime of Li-air batteries) and understanding and limiting of the origin of temperature dependences in Li-air batteries [109].

Recent work by Song et al. [92] on Li-air batteries has focussed on composites of Co_3O_4 and carbon nanofibres that were produced through the carbonization of Zeolitic Imidazolate Framework (ZIF)-9/PAN fibrous mats electrospun from dimethylformamide (DMF) solutions. The initial discharge capacity was presented

$$O_2 + 4Li^+ + 4e^- \leftrightarrow 2Li_2O \quad E_{rev} = 2.91 \text{ V}$$
$$O_2 + 2Li^+ + 2e^- \leftrightarrow 2Li_2O_2 \quad E_{rev} = 2.96 \text{ V}$$
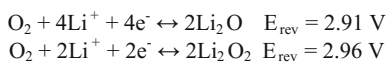
Scheme 7.1 Cell reactions of lithium and oxygen

at 760 mAh g^{-1} at a current density of 0.5 A g^{-1}, which retained 55% of its total capacity after 10 charge/discharge cycles [92]. This may be compared with an initial discharge capacity of CO_2-activated carbon nanofibres of 699 mAh g^{-1} presented by Nie et al. [93] at a current density of 0.2 A g^{-1}; however, it is worth noting that this cathode was not activated until reaching a temperature of 1273 K. The capacity of an electrode is also greatly dependent on the current density being used during measurements. A low current density will usually present with a greater capacity though this may not be suitable for real-life use.

7.3.1.3 Li-S Batteries

While Li-S and Li-air (referred to as Li–O_2 since O_2 is the fuel) share the same anode and have active cathode components (S and O_2) that are neighbours in group 16 of the periodic table, there are important differences regarding their chemistry and the states of their cathodes [110].

Advantages of lithium-sulphur batteries over other rechargeable battery systems include their high specific energy with low costs. Disadvantages, however, include poor electrochemical stability caused by diffusion of polysulphides from the cathode to the anode known as the shuttle effect. Solutions to preventing this migration and confining sulphur within the cathode region include the use of porous carbon structures [104, 111–113], inorganic oxides, and polymers.

Work by Ji et al. [114] pioneered developments of conductive mesoporous carbon frameworks to encapsulate sulphur nanofiller growth within its channels. The mesoporous structure allowed for access of Li$^+$ for reactivity with the sulphur while also inhibiting diffusion within the framework and the properties of the carbon helped in trapping polysulphides that are formed during redox. Reversible capacities of up to 730 mAh g^{-1} were obtained at C/5 rate after 150 cycles of charge/discharge after modifying the surface of hollow carbon nanofibres (as shown in Fig. 7.7) to prevent the detachment of Li$_x$S from the carbon surface and achieve specific capacities close to 1180 mAh g^{-1} with a capacity retention of 80% over 300 cycles [114–116].

7.3.1.4 Na-Ion Batteries

With the increase in portable electronics use, the prices of lithium-ion batteries have increased correspondingly. As more applications adopt lithium-ion batteries as power supplies, the strain on lithium sources is expected to increase to the point of running out and efforts to find new sources of the metal and recycle existing batteries will likely lag behind the current demands. An alternative to lithium lies in the development of sodium-ion batteries since it is possible for Na-ion batteries to be comparable if a cathode with 200 mAh g^{-1} capacity and a 500 mAh g^{-1} capacity anode can be discovered. Sodium is also the 4th most abundant element in the crust of the Earth making supply a much smaller issue [117].
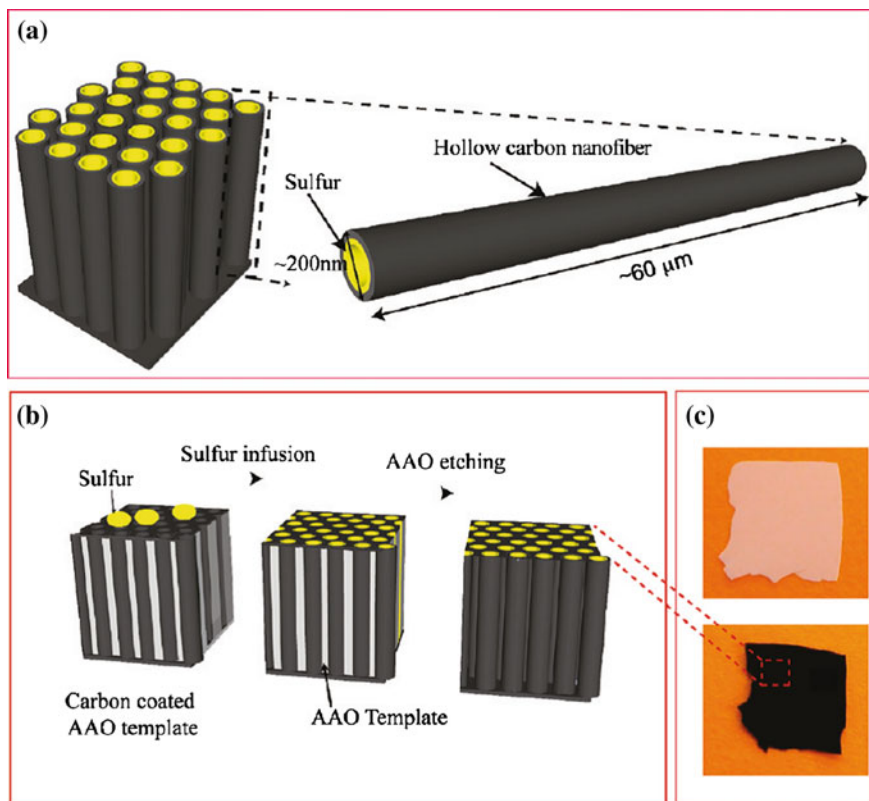
Fig. 7.7 Schematic design and fabrication process of hollow carbon nanofibres/sulfur composite structure. **a** Design principle showing the high aspect ratio of the CNF for effective trapping of polysulphides and **b** the fabrication process of carbon/sulfur cathode. **c** Digital camera images showing the contrast of AAO template before and after carbon coating and sulfur infusion (reproduced from Ref. [116] with kind permission of © 2011 American Chemical Society)

While sodium-ion devices are still in the early stages of development, they are promising for large-scale grid applications in spite of the high cost involved in production of sodium-containing precursors used to make components. To evaluate the potential of sodium-ion batteries as a replacement for lithium-ion, Ong et al. [118] provided a comparison between the two using similar materials operating in Li-ion and Na-ion systems. The larger mass and ionic radius of sodium to lithium as well as various thermodynamic parameters affect a ~ 300 mV higher standard reduction potential of sodium.

Doping nitrogen into the carbon-based anodes generated extrinsic defects which enhance reactivity and electronic conductivity. The sites at which nitrogen has been added can also adsorb lithium ions and improve lithium storage [90, 119]. This knowledge was used by Wang et al. [120] to improve the capacity of sodium-ion batteries using functionalized, interconnected carbon nanofibres doped with

nitrogen. The N-doped sites and functionalized groups were suggested as the cause for a high current density of 134 mAh g^{-1} after 200 cycles at 0.2 A g^{-1} due to their ability to capture sodium ions rapidly and reversible through surface adsorption and surface redox reactions [120].

Carbon materials with a large interlayer distance and disordered structure are of particular interest to the area surrounding sodium-ion batteries since these properties make them beneficial for Na^+ insertion/extraction [117]. In a study by Bai et al., polyvinyl chloride nanofibres were prepared though electrospinning and pyrolysis at increasing temperatures (600–800 °C) and used as anodic materials in a Na-ion cell, giving an initial reversible capacity of 271 mAh g^{-1} and retain 215 mAh g^{-1} after 120 cycles at 0.012 A g^{-1} [95]. While the current density affects the apparent capacity of the electrode material, further tests showed a reversible capacity of 147 mAh g^{-1} at 0.24 A g^{-1} [95].

7.3.2 Supercapacitors

A conventional capacitor stores energy in the form of electrical charge. Two conducting materials are separated by a dielectric. When an electric potential is applied across the conductors, electrons flow and charge accumulates on each conducting plate, which remain charged after the potential is removed until they are brought into contact again. The capacitance is a measure of the energy storage capability and is related to the amount of charge that can be stored at an applied potential.

The early patent surrounding electrochemical capacitors dates back to 1957 where a capacitor based on carbon with a high surface area was described [121]. Supercapacitors consist of two electrodes with extremely high surface areas kept separate by an ion-permeable membrane that is used as an insulator to protect the electrodes against short-circuiting. A liquid or viscous electrolyte that can be either organic or aqueous is added to the cell and enters the pores of the electrodes and serves as the conductive connection between electrodes across the insulator. These cells must be sealed to ensure stable behaviour over its lifetime [13, 122].

Supercapacitor is a colloquial name for capacitors which store energy within an electrochemical double layer at the electrode/electrolyte interface. Electrochemical double-layer capacitor (EDLC) is the name that best describes the storage principle; however, in general, there are contributions to the capacitance other than the double-layer effects. In addition to the capacitance that arises from the separation of charge in the double layer, reactions that occur on the surface of the electrode provide a contribution. The charge that is required to facilitate these reactions is dependent on the potential resulting in a Faradaic "pseudocapacitance" [13].

There are three types of supercapacitors: electrochemical double-layer capacitors, pseudocapacitors, and hybrid types formed by combining both EDLCs and pseudocapacitors.

7.3.2.1 Electric Double-Layer Capacitors (EDCLs)

Previously, all electrochemical capacitors were called double-layer capacitors; however, it became known that double-layer capacitors and pseudocapacitors were part of a new family of electrochemical capacitors. Double-layer capacitance is the electrostatic storage of electrical energy achieved through separation of charge in a Helmholtz double layer at the interface between the surface of a conductor electrode and an electrolytic solution electrolyte. The separation of charge in a double layer is a few angstroms (0.3–0.38 nm) and is static in origin [13]. Double-layer charge storage is a surface process, and as such, the surface characteristics of the electrode greatly influence the capacitance of the cell. Similarly, the connection between the electrode and the rest of the surface should be without the addition of other conductive or binding agents to reduce the mass of electrochemically inactive components present and sustaining a high specific capacitance with sufficiently high conductivity [123].

There are various models that have been developed over the years to explain the electrical processes that take place at the boundary between a solid conductor and an electrolyte. EDLCs have demonstrated good cycling stability as well as rate capability. However, they generally demonstrate low specific capacitance as well as low energy density [16, 17]. An electric double-layer capacitor is most simply made up of two electrodes immersed in an electrolyte yet kept separate by an ion-conduction but electron-insulating membrane [124]. Activated carbon with a large surface area provides a good platform material for double-layer formation since they allow the capture and release of the electrolyte with relatively decreased resistance, though this is dependent on the pore size and the solvated ion size of the electrolyte [125–127].

Work by Xu et al. [96] has shown the production of polyaniline nanofibre networks with a large specific capacitance of 280 F g^{-1} at a current density of 1 A g^{-1}. The polyaniline networks were co-doped with nitrogen and phosphorus since nitrogen doping can cause a shift of the Fermi level which facilitates electron transfer, while phosphorus doping can restrain the formation of unstable surface groups and also widen the potential window to increase the energy density of EDLCs [28, 96, 128–130]. Lu et al. demonstrate a method of producing porous nanofibres that exhibit a relatively high specific capacitance and may be easily scaled up to produce bulk amounts of material, since a drawback of the electrospinning process is a low production rate coupled with safety concerns and costs [123].

Nanofibrous gels formed using perylene diimide derivatives provided good electrode materials after freeze-drying and carbonization. Due to the formation of nanofibres during the self-assembly process, it is facile to incorporate other molecules into the CNFs. In the case of potassium stannate being used as a base to dissolve the perylene derivative, the preparation of Sn-incorporated CNFs was described [22]. This method yielded gels with higher capacities for those formed upon the incorporation of melamine into the gel, 115 F g^{-1} at a scan rate of 1 mVs^{-1}. When F-127 (a water-soluble triblock copolymer) was used as a

sacrificial template for CNFs during the carbonization process, higher surface area and more interconnected micropores/mesopores were achieved. This was believed to contribute positively towards an increased capacitance, 226 F g^{-1} at 4 A g^{-1} over 1000 cycles, through the improved movement of ions [22]. Nanofibrous microspheres produced by Liu et al., mentioned previously, also demonstrated good specific capacitance of 284 F g^{-1} at 1 A g^{-1}, with a 67% capacitance retention after 1000 cycles at a current density of 4 A g^{-1} [44].

7.3.2.2 Pseudocapacitors

Pseudocapacitance is named as such to differentiate it from electrostatic capacitance as it arises from reversible Faradaic reactions occurring at the electrode. The term "pseudo" arises in order to be able to differentiate it from electrostatic capacitance, since the charge transfer that occurs is voltage dependent and so a capacitive phenomenon occurs. There are two types of mechanisms that can cause such a phenomenon: redox reactions and the deposition of ions to form a monolayer.

Redox reactions occur at electrodes made from metal oxides or conducting polymers. In the case of ruthenium oxide, charging and discharging curves arise as a result of overlapping redox reactions as well as a significant double-layer capacitance due to the porous structure of the hydrous oxide [131]. Deposition of ions to form a monolayer on the electrode surface results in a Faradaic charge transfer. If the sites are occupied randomly in a fixed lattice, the Langmuir adsorption equation may be used to determine another equation, as shown in Scheme 7.2, which can be used to describe a pseudocapacitive relationship [132].

While "pure" CNF materials act as EDLCs, the intercalation of metal oxide nanoparticles results in pseudocapacitive action from the nanoparticles with the CNF acting as a conducting support. This makes CNFs particularly favourable as supports, since they can be easily intercalated with nanoparticles in layered structures which improve electronic conductivity while preventing active particles from detaching from the CNF [97]. Aboulali et al. demonstrated encapsulation of Co$_3$O$_4$ within electrospun carbon nanofibres producing materials that gave a capacitance of 586 F g^{-1} at a current density of 1 A g^{-1} and presented good cycling stability of 74% retention after 2000 cycles at 2 A g^{-1} [97]. The Co$_3$O$_4$ nanoparticles were securely dispersed within the CNF matrix, allowing for the pseudocapacitive action

$$C_\phi = \frac{q_1 F}{RT} \frac{Kc \pm \exp\left(\frac{-VF}{RT}\right)}{\left(1 + Kc \pm \exp\left(\frac{-VF}{RT}\right)\right)^2}$$

Scheme 7.2 Equation describing the pseudocapacitive relation caused by the adsorption/desorption of ions on the electrode surface where q_1 is the amount of charge required to form or disperse a complete monolayer, K is the electrochemical equilibrium constant, and V is the electrode potential [13, 131]

of the nanoparticles to occur without being hindered by separation and helped by the conductivity of the CNF matrix [97]. A similar principle was demonstrated by Wu et al. in their encapsulation of iron carbide nanoparticles within iron- and nitrogen-doped carbon nanofibres for use in electrocatalysis [133].

The pseudocapacitive ability of MnO_2 was shown by Zhi et al. when used as a coating for CNFs after carbonization of electrospun PAN fibres from DMF, giving an enhanced specific capacitance of 311 F g^{-1} for the whole electrode and showing remarkable stability in comparison with previously reported CNF/metal oxide coaxial electrodes [57, 134]. A drawback of this process would be the limited scalability of production due to the use of electrospinning which suffers from a low production rate.

7.3.2.3 Hybrid Capacitors (Asymmetric, Composite, Battery Type)

While supercapacitors have attracted an enormous amount of attention due to their various advantages including power density and fast charge/discharge capability, their energy densities are far behind batteries [135]. As such, it is necessary to explore opportunities to increase energy density while maintaining power delivery. Hybrid supercapacitors are typically made up of a carbon electrode from EDLC systems and a battery electrode. If an appropriate combination can be found, an increase in the cell voltage may be obtained, while a battery electrode material will deliver more specific capacitance when compared with activated carbons, thereby improving energy and power density [16].

Figure 7.8 shows the possible approaches to hybrid capacitors. Most hybrid electrochemical capacitors produced have used pseudocapacitive materials as the cathode, because they can accumulate charges through Faradaic processes which can increase the specific capacitance and extend the working voltage [136]. Hybrid capacitors can be assembled using hybrid materials such as mixed different metal oxides or doped conducting polymer materials [136–138].

Wang et al. demonstrated a high-performance asymmetric supercapacitor using carbon-MnO_2 nanofiber electrodes that showed only 6% loss in its initial capacitance after 5000 cycles at 4 A g^{-1} and excellent stability of the cell [135]. This can be compared to research by Li et al. who produced a nickel–aluminium layered double-hydroxide nanosheets/carbon nanotube composite which was then tested for both its electrochemical performance and also its possible application in an asymmetric capacitor [99]. Both electrode materials showed remarkable stability, ability to withstand repeated cycles at reasonable current densities, as well as being able to be easily integrated into a circuit given CNF capabilities to be used without binding agents.

Another example of hybrid capacitor electrode material was recently shown by Li et al. where hierarchical porous V_2O_5 nanosheets on carbon nanofibres were investigated. They demonstrated good electrochemical performance of 408 F g^{-1} at a current density of 1 A g^{-1}, as well as good cycling stability over 10,000 cycles, showing only 10.7% loss in specific capacity [98]. However, an advantage of this
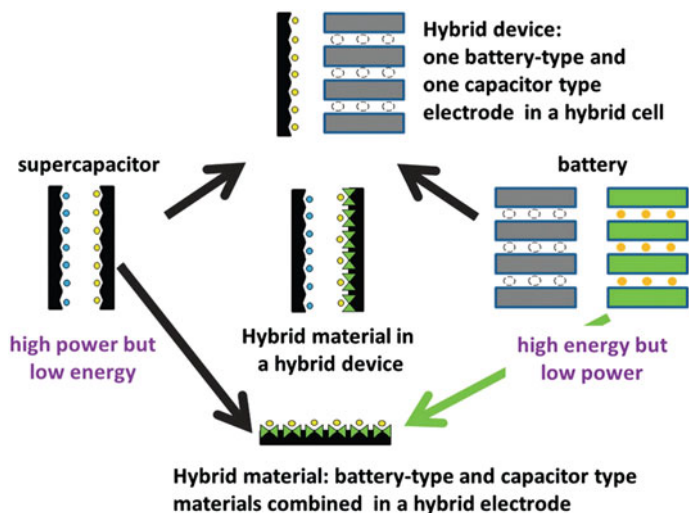
Fig. 7.8 Schematic representation of different hybridization approaches between supercapacitor and battery electrodes and materials (reproduced from Ref. [138] with kind permission of © 2015 Royal Society of Chemistry)

material would be its flexible nature and its ability to retain capacity after bending 200 times showing a robust nature suitable for practical application.

7.4 Conclusion and Outlook

There has been a global increase in demand for energy storage that can provide the high energy density requirements needed for a variety of applications. Carbon nanofibres have been shown to be promising in energy storage. Among the fabrication methods described in this chapter, electrospinning can form free-standing fibrous mats which, after carbonization, can be used without binders, substrates, or conducting agents, thereby increasing the energy density and making fabrication simpler by allowing the fibres to be directly employed as electrode materials. Through variation in feed rate, voltage, solution mix, and distance between the needle and collector, the morphology of fibres may be varied and thus their properties may change. Catalytic chemical vapour deposition is able to produce nanofibres rapidly, and the morphology of the fibres may be altered through the use of different starting materials. However, the instrument with high temperature and high vacuum is required for this technique. Two recently developed methods (controlled freezing and nanofibrous gelation) have been used to prepare polymer nanofibers, which can then be carbonized to produce carbon nanofibers. Polymers with high carbon content may have to be used. It is also more convenient to produce a large quantity of nanofibers with the latter two methods.

These carbon-based nanofibres have shown promising applications within the realm of rechargeable batteries, whether the cell be Li-ion, Li-air, Li-S, or Na-ion. Due to the interlayer spacing in CNFs, it is possible for metal ions to intercalate into a CNF-based anode during the charging process of the cell and be released later while showing relatively good cycling capability. Problems with batteries arise due to shortages of lithium as well as the "shuttle" effect that occurs in Li-S batteries and side reactions that occur in Li-air cells. While sodium is relatively abundant and inexpensive, achieving the appropriate capacity for use in transportation has been a problem, though Na-ion batteries have been shown to be good for use in grid applications. As electrode materials for supercapaitors, the carbon-based nanofibres have demonstrated high capacity and high recyclability. The porous CNFs, when co-doped with nitrogen and phosphorus, demonstrated an increase in energy density and facilitated electron transfer. The incorporation of metal oxides into the CNF matrix leads to an effective pseudocapacitive system due to redox reactions and/or the formation of a monolayer through deposition of ions. The use of CNF electrodes is also reported in hybrid capacitors.

However, to employ the carbon-based nanofibres for the perspective industrial energy storage applications, the materials need to be produced at a large scale with reproducible morphology and physical properties. The preparation conditions are required to be optimized with regard to control of the diameter, porosity, and doping composition of the nanofibers. The optimization of the procedures for preparing the electrodes and assembling the devices (e.g. batteries, supercapacitors) is equally important for safe and efficient use of this technology to meet the increasing energy demand.

References

1. Denholm P, Ela E, Kirby B et al (2010) The role of energy storage with renewable electricity generation (Technical Report). National Renewable Energy Laboratory, Golden, pp 1–61
2. Adeniran B, Mokaya R (2015) Low temperature synthesized carbon nanotube superstructures with superior CO_2 and hydrogen storage capacity. J Mater Chem A 3(9):5148–5161
3. Cao D, Zhang X, Chen J et al (2003) Optimization of single-walled carbon nanotube arrays for methane storage at room temperature. J Phys Chem B 107(48):13286–13292
4. Ahrens M, Kucera L, Larsonneur R (1996) Performance of a magnetically suspended flywheel energy storage device. IEEE T Contr Syst T 4(5):494–502
5. Bolund B, Bernhoff H, Leijon M (2007) Flywheel energy and power storage systems. Renew Sus Energy Rev 11(2):235–258
6. Cha SI, Kim KT, Arshad SN et al (2005) Extraordinary strengthening effect of carbon nanotubes in metal-matrix nanocomposites processed by molecular-level mixing. Adv Mater 17(11):1377–1381
7. Nayfeh TH (2010) High strength composite materials and related processes. US Patent Application 20100203351 A1

8. Winter M, Besenhard JO, Spahr ME et al (1998) Insertion electrode materials for rechargeable lithium batteries. Adv Mater 10(10):725–763
9. Linden D, Reddy TB (2002) Handbook of batteries, 3rd edn. McGraw-Hill, New York
10. Notten P, Bergveld H, Kruijt W (2002) Battery management systems: design by modeling. Kluwer Academic Publisher, Norwell
11. Skotheim TA (ed) (1997) Handbook of conducting polymers. CRC Press, Baco Raton
12. Mastragostino M, Arbizzani C, Soavi F (2001) Polymer-based supercapacitors. J Power Sources 97–98:812–815
13. Namisnyk AM (2003) A survey of electrochemical supercapacitor technology. University of Technology, Sydney
14. Buckles W, Hassenzahl WV (2000) Superconducting magnetic energy storage. IEEE Power Eng Rev 20(5):16–20
15. Zhang LL, Zhao XS (2009) Carbon-based materials as supercapacitor electrodes. Chem Soc Rev 38(9):2520–2531
16. Wang Y, Xia Y (2013) Recent progress in supercapacitors: from materials design to system construction. Adv Mater 25(37):5336–5342
17. Zhi M, Xiang C, Li J et al (2013) Nanostructured carbon-metal oxide composite electrodes for supercapacitors: a review. Nanoscale 5(1):72–88
18. Feng L, Xie N, Zhong J (2014) Carbon nanofibers and their composites: a review of synthesizing, properties and applications. Materials 7(5):3919–3945
19. Shokrieh MM, Esmkhani M, Haghighatkhah AR (2014) Flexural fatigue behaviour of carbon nanofiber/epoxy nanocomposites. Fatigue Fract Eng M 37(5):553–560
20. Cao J, Wang Y, Zhou Y et al (2013) High voltage asymmetric supercapacitor based on MnO_2 and graphene electrodes. J Electroanal Chem 689:201–206
21. Fan Z, Yan J, Wei T et al (2011) Asymmetric Supercapacitors Based on Graphene/MnO_2 and activated carbon nanofiber electrodes with high power and energy density. Adv Funct Mater 21(12):2366–2375
22. Liu X, Roberts A, Ahmed A et al (2015) Carbon nanofibers by pyrolysis of self-assembled perylene diimide derivative gels as supercapacitor electrode materials. J Mater Chem A 3(30):15513–15522
23. Śliwak A, Gryglewicz G (2014) High-voltage asymmetric supercapacitors based on carbon and manganese oxide/oxidized carbon nanofiber composite electrodes. Energy Technol 2(9–10):819–824
24. De Jong KP, Geus JW (2000) Carbon nanofibers: catalytic synthesis and applications. Catal Rev 42(4):481–510
25. Zhang L, Aboagye A, Kelkar A et al (2013) A review: carbon nanofibers from electrospun polyacrylonitrile and their applications. J Mater Sci 49(2):463–480
26. Li W, Zhang F, Dou Y et al (2011) A self-template strategy for the synthesis of mesoporous carbon nanofibers as advanced supercapacitor electrodes. Adv Energy Mater 1(3):382–386
27. Roberts AD, Wang S, Li X et al (2014) Hierarchical porous nitrogen-rich carbon monoliths via ice-templating: high capacity and high-rate performance as lithium-ion battery anode materials. J Mater Chem A 2(42):17787–17796
28. Xu G, Han J, Ding B et al (2015) Biomass-derived porous carbon materials with sulfur and nitrogen dual-doping for energy storage. Green Chem 17(3):1668–1674
29. Allen MJ, Tung VC, Kaner RB (2010) Honeycomb carbon: a review of graphene. Chem Rev 110(1):132–145
30. Hughes TYC, Chambers CR (1889) Manufacture of Carbon Filaments. US Patent 405480
31. Radushkevich LV, Lukyanovich VM (1952) O Strukture ugleroda, obrazujucegosja pri termiceskom razlozenii okisi ugleroda na zeleznom kontakte. Russ J Phys Chem 26:88–95
32. Kroto HW, Heath JR, O'Brien SC et al (1985) C 60: buckminsterfullerene. Nature 318 (6042):162–163
33. Iijima S, Ichihashi T (1993) Single-shell carbon nanotubes of 1-nm diameter. Nature 363 (6430):603–605
34. Iijima S (1991) Helical microtubules of graphitic carbon. Nature 354(6348):56–58

35. Bethune DS, Johnson RD, Salem JR et al (1993) Atoms in carbon cages: the structure and properties of endohedral fullerenes. Nature 366(6451):123–128
36. Baker RTK, Harris PS, Thomas RB et al (1973) Formation of filamentous carbon from iron, cobalt and chromium catalyzed decomposition of acetylene. J Catal 30(1):86–95
37. Baker RTK, Barber MA, Harris PS et al (1972) Nucleation and growth of carbon deposits from the nickel catalyzed decomposition of acetylene. J Catal 26(1):51–62
38. Melechko AV, Merkulov VI, McKnight TE et al (2005) Vertically aligned carbon nanofibers and related structures: controlled synthesis and directed assembly. J Appl Phys 97(4):041301
39. Faccini M, Borja G, Boerrigter M et al (2015) Electrospun carbon nanofiber membranes for filtration of nanoparticles from water. J Nanomater 2015:1–9
40. Aravindan V, Sundaramurthy J, Suresh Kumar P et al (2015) Electrospun nanofibers: a prospective electro-active material for constructing high performance Li-ion batteries. Chem Commun 51(12):2225–2234
41. Lee BS, Yang HS, Yu WR (2014) Fabrication of double-tubular carbon nanofibers using quadruple coaxial electrospinning. Nanotechnology 25(46):465602
42. Li WL, Lu K, Walz JY (2012) Freeze casting of porous materials: review of critical factors in microstructure evolution. Int Mater Rev 57(1):37–60
43. Samitsu S, Zhang R, Peng X et al (2013) Flash freezing route to mesoporous polymer nanofibre networks. Nat Commun 4:2653
44. Liu X, Ahmed A, Wang Z et al (2015) Nanofibrous microspheres via emulsion gelation and carbonization. Chem Commun 51(94):16864–16867
45. Choy KL (2003) Chemical vapour deposition of coatings. Prog Mater Sci 48(2):57–170
46. Wan Y, Yang Z, Xiong G et al (2015) Anchoring Fe_3O_4 nanoparticles on three-dimensional carbon nanofibers toward flexible high-performance anodes for lithium-ion batteries. J Power Sources 294:414–419
47. Bhardwaj N, Kundu SC (2010) Electrospinning: a fascinating fiber fabrication technique. Biotechnol Adv 28(3):325–347
48. Formhals A (1934) Process and apparatus for preparing artificial threads. US Patent 1975504A
49. Chang C, Limkrailassiri K, Lin L (2008) Continuous near-field electrospinning for large area deposition of orderly nanofiber patterns. Appl Phys Lett 93(12):123111
50. Li Z, Wang C (2013) Effects of working parameters on electrospinning. One-dimensional nanostructures. Springer, Berlin Heidelberg, pp 15–28
51. Subbiah T, Bhat GS, Tock RW et al (2005) Electrospinning of nanofibers. J Appl Polym Sci 96(2):557–569
52. Shin YM, Hohman MM, Brenner MP et al (2001) Experimental characterization of electrospinning: the electrically forced jet and instabilities. Polymer 42(25):09955–09967
53. Deitzel JM, Kleinmeyer J, Harris D et al (2001) The effect of processing variables on the morphology of electrospun nanofibers and textiles. Polymer 42(1):261–272
54. Qin X-H, Yang E-L, Li N et al (2007) Effect of different salts on electrospinning of polyacrylonitrile (PAN) polymer solution. J Appl Polym Sci 103(6):3865–3870
55. McCann JT, Marquez M, Xia Y (2006) Highly porous fibers by electrospinning into a cryogenic liquid. J Am Chem Soc 128(5):1436–1437
56. Xiong X, Luo W, Hu X et al (2015) Flexible membranes of MoS_2/C nanofibers by electrospinning as binder-free anodes for high-performance sodium-ion batteries. Sci Rep 5:9254
57. Zhi M, Manivannan A, Meng F et al (2012) Highly conductive electrospun carbon nanofiber/MnO_2 coaxial nano-cables for high energy and power density supercapacitors. J Power Sources 208:345–353
58. Liu H, Bai JIE, Wang QI et al (2014) Preparation and characterization of silver nanoparticles/carbon nanofibers via electrospinning with research on their catalytic properties. NANO 09(03):1450041

59. Savva I, Kalogirou AS, Chatzinicolaou A et al (2014) PVP-crosslinked electrospun membranes with embedded Pd and Cu$_2$O nanoparticles as effective heterogeneous catalytic supports. RSC Adv 4(85):44911–44921

60. Wang S-X, Yap CC, He J et al (2016) Electrospinning: a facile technique for fabricating functional nanofibers for environmental applications. Nanotechnol Rev 5(1):51–73

61. Cavaliere S, Subianto S, Savych I et al (2011) Electrospinning: designed architectures for energy conversion and storage devices. Energy Environ Sci 4(12):4761–4785

62. Mao X, Hatton TA, Rutledge GC (2013) A review of electrospun carbon fibers as electrode materials for energy storage. Curr Org Chem 17(13):1390–1401

63. Kim B-H, Bui N-N, Yang K-S et al (2009) Electrochemical properties of activated polyacrylonitrile/pitch carbon fibers produced using electrospinning. B Kor Chem Soc 30(9):1967–1972

64. Qiu Y, Yu J, Shi T et al (2011) Nitrogen-doped ultrathin carbon nanofibers derived from electrospinning: large-scale production, unique structure, and application as electrocatalysts for oxygen reduction. J Power Sources 196(23):9862–9867

65. Hwang TH, Lee YM, Kong B-S et al (2012) Electrospun core-shell fibers for robust silicon nanoparticle-based lithium ion battery anodes. Nano Lett 12(2):802–807

66. Kong J, Tan HR, Tan SY et al (2010) A generic approach for preparing core-shell carbon-metal oxide nanofibers: morphological evolution and its mechanism. Chem Commun 46(46):8773–8775

67. Kong J, Liu Z, Yang Z et al (2012) Carbon/SnO$_2$/carbon core/shell/shell hybrid nanofibers: tailored nanostructure for the anode of lithium ion batteries with high reversibility and rate capacity. Nanoscale 4(2):525–530

68. Park S-H, Kim B-K, Lee W-J (2013) Electrospun activated carbon nanofibers with hollow core/highly mesoporous shell structure as counter electrodes for dye-sensitized solar cells. J Power Sources 239:122–127

69. Yu Y, Gu L, Wang C et al (2009) Encapsulation of Sn@carbon nanoparticles in bamboo-like hollow carbon nanofibers as an anode material in lithium-based batteries. Angew Chem Int Ed 48(35):6485–6489

70. Wang H, Zhang C, Chen Z et al (2015) Large-scale synthesis of ordered mesoporous carbon fiber and its application as cathode material for lithium-sulfur batteries. Carbon 81:782–787

71. Wang S-X, Yang L, Stubbs LP et al (2013) Lignin-derived fused electrospun carbon fibrous mats as high performance anode materials for lithium ion batteries. ACS Appl Mater Interfaces 5(23):12275–12282

72. Gutiérrez MC, Ferrer ML, del Monte F (2008) Ice-templated materials: sophisticated structures exhibiting enhanced functionalities obtained after unidirectional freezing and ice-segregation-induced self-assembly. Chem Mater 20(3):634–648

73. Qian L, Zhang H (2011) Controlled freezing and freeze drying: a versatile route for porous and micro-/nano-structured materials. J Chem Technol Biotechnol 86(2):172–184

74. Zhang H, Cooper AI (2007) Aligned porous structures by directional freezing. Adv Mater 19(11):1529–1533

75. Zhang H, Hussain I, Brust M et al (2005) Aligned two-and three-dimensional structures by directional freezing of polymers and nanoparticles. Nat Mater 4(10):787–793

76. Wais U, Jackson AW, He T et al (2016) Nanoformulation and encapsulation approaches for poorly water-soluble drug nanoparticles. Nanoscale 8(4):1746–1769

77. Qian L, Ahmed A, Foster A et al (2009) Systematic tuning of pore morphologies and pore volumes in macroporous materials by freezing. J Mater Chem 19(29):5212–5219

78. Zhang H, Wang D, Butler R et al (2008) Formation and enhanced biocidal activity of water-dispersable organic nanoparticles. Nat Nanotechnol 3(8):506–511

79. Qian L, Willneff E, Zhang H (2009) A novel route to polymeric sub-micron fibers and their use as templates for inorganic structures. Chem Commun 26:3946–3948

80. Qian L, Zhang H (2010) Green synthesis of chitosan-based nanofibers and their applications. Green Chem 12(7):1207–1214

81. Ahmed A, Hearn J, Abdelmagid W et al (2012) Dual-tuned drug release by nanofibrous scaffolds of chitosan and mesoporous silica microspheres. J Mater Chem 22(48): 25027–25035

82. Zhang H, Lee JY, Ahmed A et al (2008) Freeze-align and heat-fuse: microwires and networks from nanoparticle suspensions. Angew Chem Int Ed 47(24):4573–4576

83. Shi Q, An Z, Tsung CK et al (2007) Ice-templating of core/shell microgel fibers through 'bricks-and-mortar' assembly. Adv Mater 19(24):4539–4543

84. Shi Q, Liang H, Feng D et al (2008) Porous carbon and carbon/metal oxide microfibers with well-controlled pore structure and interface. J Am Chem Soc 130(15):5034–5035

85. Mao Q, Shi S, Wang H (2015) Biomimetic nanowire structured hydrogels as highly active and recyclable catalyst carriers. ACS Sustain Chem Eng 3(9):1915–1924

86. Spender J, Demers AL, Xie X et al (2012) Method for production of polymer and carbon nanofibers from water-soluble polymers. Nano Lett 12(7):3857–3860

87. Sweetman LJ, Moulton SE, Wallace GG (2008) Characterisation of porous freeze dried conducting carbon nanotube-chitosan scaffolds. J Mater Chem 18(44):5417–5422

88. Ferry JD (1980) Viscoelastic properties of polymers, 3rd edn. Wiley, New York

89. Yamamoto T, Nishimura T, Suzuki T et al (2001) Control of mesoporosity of carbon gels prepared by sol-gel polycondensation and freeze drying. J Non-Cryst Solids 288(1–3):46–55

90. Qie L, Chen W-M, Wang Z-H et al (2012) Nitrogen-doped porous carbon nanofiber webs as anodes for lithium ion batteries with a superhigh capacity and rate capability. Adv Mater 24(15):2047–2050

91. Cho JS, Hong YJ, Kang YC (2015) Design and synthesis of bubble-nanorod-structured Fe_2O_3-carbon nanofibers as advanced anode material for Li-Ion batteries. ACS Nano 9(4): 4026–4035

92. Song MJ, Kim IT, Kim YB et al (2015) Self-standing, binder-free electrospun Co_3O_4/carbon nanofiber composites for non-aqueous Li-air batteries. Electrochim Acta 182:289–296

93. Nie H, Xu C, Zhou W et al (2016) Free-standing thin webs of activated carbon nanofibers by electrospinning for rechargeable $Li-O_2$ batteries. ACS Appl Mater Interfaces 8(3):1937–1942

94. Singhal R, Chung S-H, Manthiram A et al (2015) A free-standing carbon nanofiber interlayer for high-performance lithium-sulfur batteries. J Mater Chem A 3(8):4530–4538

95. Bai Y, Wang Z, Wu C et al (2015) Hard carbon originated from polyvinyl chloride nanofibers as high-performance anode material for Na-ion battery. ACS Appl Mater Interfaces 7(9):5598–5604

96. Xu G, Ding B, Pan J et al (2015) Porous nitrogen and phosphorus co-doped carbon nanofiber networks for high performance electrical double layer capacitors. J Mater Chem A 3(46):23268–23273

97. Abouali S, Akbari Garakani M, Zhang B et al (2015) Electrospun carbon nanofibers with in situ encapsulated Co_3O_4 nanoparticles as electrodes for high-performance supercapacitors. ACS Appl Mater Interfaces 7(24):13503–13511

98. Li L, Peng S, Wu HB et al (2015) A flexible quasi-solid-state asymmetric electrochemical capacitor based on hierarchical porous V_2O_5 nanosheets on carbon nanofibers. Adv Energy Mater 5(17):1500753

99. Li M, Liu F, Cheng JP et al (2015) Enhanced performance of nickel-aluminum layered double hydroxide nanosheets/carbon nanotubes composite for supercapacitor and asymmetric capacitor. J Alloys Comp 635:225–232

100. Dan P, Mengeritski E, Geronov Y et al (1995) Performances and safety behaviour of rechargeable AA-size Li/Li_xMnO_2 cell. J Power Sources 54(1):143–145

101. Etacheri V, Marom R, Elazari R et al (2011) Challenges in the development of advanced Li-ion batteries: a review. Energy Environ Sci 4(9):3243–3262

102. Gabano J-P (1983) Lithium batteries. Academic Press, London

103. Nazri G-A, Pistoia G (2008) Lithium batteries: science and technology. Springer Science & Business Media, Germany

104. Wu Y, Wang J, Jiang K et al (2013) Applications of carbon nanotubes in high performance lithium ion batteries. Front Phys 9(3):351–369
105. Christensen J, Albertus P, Sanchez-Carrera RS et al (2011) A critical review of li/air batteries. J Electrochem Soc 159(2):R1–R30
106. Peng B, Chen J (2009) Functional materials with high-efficiency energy storage and conversion for batteries and fuel cells. Coordin Chem Rev 253(23–24):2805–2813
107. Ma Z, Yuan X, Li L et al (2015) A review of cathode materials and structures for rechargeable lithium-air batteries. Energy Environ Sci 8(8):2144–2198
108. Yuan J, Yu J-S, Sundén B (2015) Review on mechanisms and continuum models of multi-phase transport phenomena in porous structures of non-aqueous Li-Air batteries. J Power Sources 278:352–369
109. Girishkumar G, McCloskey B, Luntz AC et al (2010) Lithium-air battery: promise and challenges. J Phys Chem Lett 1(14):2193–2203
110. Bruce PG, Freunberger SA, Hardwick LJ et al (2012) Li-O_2 and Li-S batteries with high energy storage. Nat Mater 11(1):19–29
111. Ye H, Yin Y-X, Xin S et al (2013) Tuning the porous structure of carbon hosts for loading sulfur toward long lifespan cathode materials for Li-S batteries. J Mater Chem A 1(22): 6602–6608
112. Chung S-H, Manthiram A (2014) Carbonized eggshell membrane as a natural polysulfide reservoir for highly reversible Li-S batteries. Adv Mater 26(9):1360–1365
113. Zhang Z, Wang G, Lai Y et al (2015) Nitrogen-doped porous hollow carbon sphere-decorated separators for advanced lithium-sulfur batteries. J Power Sources 300:157–163
114. Ji X, Lee KT, Nazar LF (2009) A highly ordered nanostructured carbon-sulphur cathode for lithium-sulphur batteries. Nat Mater 8(6):500–506
115. Zheng G, Zhang Q, Cha JJ et al (2013) Amphiphilic surface modification of hollow carbon nanofibers for improved cycle life of lithium sulfur batteries. Nano Lett 13(3):1265–1270
116. Zheng G, Yang Y, Cha JJ et al (2011) Hollow carbon nanofiber-encapsulated sulfur cathodes for high specific capacity rechargeable lithium batteries. Nano Lett 11(10):4462–4467
117. Slater MD, Kim D, Lee E et al (2013) Sodium-ion batteries. Adv Funct Mater 23(8): 947–958
118. Ong SP, Chevrier VL, Hautier G et al (2011) Voltage, stability and diffusion barrier differences between sodium-ion and lithium-ion intercalation materials. Energy Environ Sci 4(9):3680–3688
119. Zhou Z, Gao X, Yan J et al (2004) A first-principles study of lithium absorption in boron- or nitrogen-doped single-walled carbon nanotubes. Carbon 42(12–13):2677–2682
120. Wang Z, Qie L, Yuan L et al (2013) Functionalized N-doped interconnected carbon nanofibers as an anode material for sodium-ion storage with excellent performance. Carbon 55:328–334
121. Becker HI (1957) Low voltage electrolytic capacitor. US Patent 2800616A
122. Vangari Manisha, Pryor Tonya, Jiang L (2013) Supercapacitors: review of materials and fabrication methods. J Energy Eng 139(2):72–79
123. Lu Y, Fu K, Zhang S et al (2015) Centrifugal spinning: a novel approach to fabricate porous carbon fibers as binder-free electrodes for electric double-layer capacitors. J Power Sources 273:502–510
124. Choi N-S, Chen Z, Freunberger SA et al (2012) Challenges facing lithium batteries and electrical double-layer capacitors. Angew Chem Int Ed 51(40):9994–10024
125. Huang C-W, Hsu C-H, Kuo P-L et al (2011) Mesoporous carbon spheres grafted with carbon nanofibers for high-rate electric double layer capacitors. Carbon 49(3):895–903
126. Portet C, Yushin G, Gogotsi Y (2007) Electrochemical performance of carbon onions, nanodiamonds, carbon black and multiwalled nanotubes in electrical double layer capacitors. Carbon 45(13):2511–2518
127. Largeot C, Portet C, Chmiola J et al (2008) Relation between the ion size and pore size for an electric double-layer capacitor. J Am Chem Soc 130(9):2730–2731

128. Veerasamy VS, Yuan J, Amaratunga GAJ et al (1993) Nitrogen doping of highly tetrahedral amorphous carbon. Phys Rev B 48(24):17954–17959
129. Wang C, Zhou Y, Sun L et al (2013) Sustainable synthesis of phosphorus- and nitrogen-co-doped porous carbons with tunable surface properties for supercapacitors. J Power Sources 239:81–88
130. Hulicova-Jurcakova D, Puziy AM, Poddubnaya OI et al (2009) Highly stable performance of supercapacitors from phosphorus-enriched carbons. J Am Chem Soc 131(14):5026–5027
131. Conway BE, Birss V, Wojtowicz J (1997) The role and utilization of pseudocapacitance for energy storage by supercapacitors. J Power Sources 66(1–2):1–14
132. Langmuir I (1918) The adsorption of gases on plane surfaces of glass, mica and platinum. J Am Chem Soc 40(9):1361–1403
133. Wu Z-Y, Xu X-X, Hu B-C et al (2015) Iron carbide nanoparticles encapsulated in mesoporous Fe-N-doped carbon nanofibers for efficient electrocatalysis. Angew Chem Int Ed 54(28):8179–8183
134. Chen W, Rakhi RB, Hu L et al (2011) High-performance nanostructured supercapacitors on a sponge. Nano Lett 11(12):5165–5172
135. Wang J-G, Yang Y, Huang Z-H et al (2013) A high-performance asymmetric supercapacitor based on carbon and carbon-MnO_2 nanofiber electrodes. Carbon 61:190–199
136. Zhang Y, Feng H, Wu X et al (2009) Progress of electrochemical capacitor electrode materials: a review. Int J Hydrogen Energy 34(11):4889–4899
137. Wang H, Yoshio M, Thapa AK et al (2007) From symmetric AC/AC to asymmetric AC/graphite, a progress in electrochemical capacitors. J Power Sources 169(2):375–380
138. Dubal DP, Ayyad O, Ruiz V et al (2015) Hybrid energy storage: the merging of battery and supercapacitor chemistries. Chem Soc Rev 44(7):1777–1790

Chapter 8
Polymer/Graphene Composites for Energy Storage

Yuchen Liu and Shiren Wang

Abstract In recent years, tremendous research effort has been focused on novel supercapacitors because of their stable ultra-high power density, cycling life, and fast charging–discharging rate. These researches aimed at increasing the energy density of supercapacitors without sacrificing high power capability so that they reach the levels achieved in batteries and at lowering fabrication costs. For this purpose, conjugated polymers have been effectively integrated with graphene nanosheets for supercapacitor applications, which sparked great excitement in superior performance owing to their synergistic effects on charge absorption and transportation, and extraordinary characteristic of the reversible oxidation–reduction activity which enables a high energy density. In this chapter, simple pathways to tailor polymer/graphene composites architectures for improving supercapacitor performances were summarized. Further, a theoretical model has been established to quantify the influences of various factors on the supercapacitor behaviors. On this basis, challenges and perspectives in this exciting field are also discussed. These results not only provide fundamental insight into supercapacitors but also offer an important guideline for future design of advanced next-generation supercapacitors for industrial and consumer applications.

8.1 Introduction

With the rapid growth of hybrid vehicles and renewable energy systems, there is an urgent need for developing advanced electric energy storage with high-storage capacity and fast charge–discharge ability to meet practical application [1]. Among available energy storage devices, there are three typical traditional energy storage devices: fuel cells, batteries, and capacitors. Fuel cells have the largest energy density, while capacitors have the highest power density. The energy and power

Y. Liu · S. Wang (✉)
Department of Industrial and Systems Engineering, Texas A&M University,
College Station, TX 77843, USA
e-mail: S.Wang@tamu.edu

density of lithium batteries are between fuel cells and capacitors. Supercapacitors were invented in 1970s and quickly became one of the rising stars in the new century. Supercapacitors are a type of energy storage whose power density is extremely high compared with traditional batteries [2]. Physical, rather than chemical, energy storage makes it possible to operate safely and extend the life cycle. As the superior performance on the rate of charging and discharging, supercapacitor can be applied in electric vehicles (EV) [3]. From the comparison of all the devices presented above, the applications of supercapacitors are hindered by low energy density. Although supercapacitors have a much larger energy density than traditional capacitors, they have far less energy density than lithium batteries [4–6]. That is why supercapacitors are always installed with lithium batteries as a power device. In order to solve this challenge, high-performance supercapacitor with high energy density is needed to be developed. Graphene is selected as a promising material for various energy systems such as supercapacitors, solar cells, and fuel cells because of its reversible oxidation–reduction activity and the good conductivity of graphene. Hence, graphene materials are always composited with polymers which can promote the process ability and/or flexibility of graphene materials [7].

There are two types of supercapacitors according to the different charging–discharging mechanisms. The first one, performed from a double-layer capacitance, is called (electric or) electrochemical double-layer capacitor (EDLC). And the other one is so-called faradic pseudo-capacitor [8]. The definition of the capacitance of the ELDC is shown as below:

$$C_S = \frac{A\varepsilon_0\varepsilon_r}{d},\tag{8.1}$$

where C_s is the specific capacitance, ε_0 is the vacuum dielectric constant, and ε_r is the dielectric constant of electrolyte, A is the effective surface area, and d is the effective thickness of the electric double layer. This equation guides the direction of increasing the capacitance of EDLCs. EDLC materials always have a large effective surface area of the electrodes. Compared with the traditional physical capacitors, the thickness of the electric double layer (which refers as d in Eq. 8.1) varies within several nanometers, resulting in a larger specific capacitance.

The basic structure of an EDLC is shown in Fig. 8.1a. The membrane only allows ions to pass through in order to avoid the short circuit. During the charging process, the ions move to the opposite charged electrode and attach onto the electrode via electrostatic attraction. During the discharging process, the electrons travel through the external circuit, the ions leave the electrodes and consequently the system goes back to neutral. The structure of EDLC gives it huge power density because of extremely high-speed absorption/desorption process between thin electrochemical double layer and consequently resulting in the steady charge and discharge throughout a wide charge–discharge rate as shown in Fig. 8.1b.

On the other hand, the mechanism of the faradic pseudo-capacitor is more complicated than EDLC. Besides the huge surface area like that of EDLC, it also
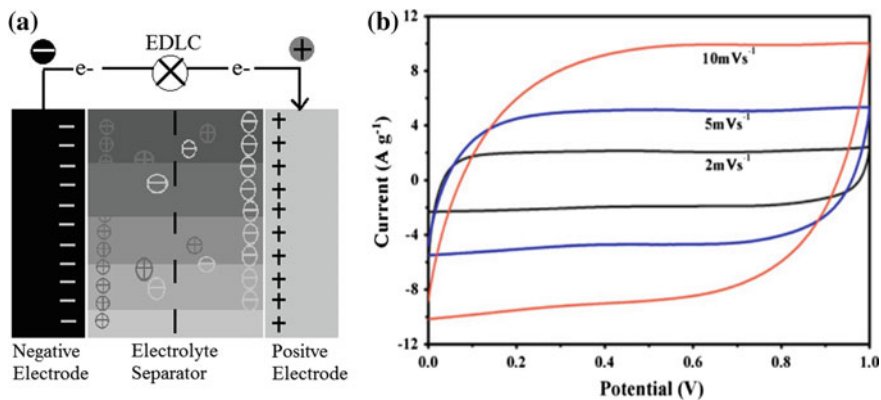
Fig. 8.1 Typical structure of EDLCs (**a**); representative cyclic voltagramm of EDLC (**b**) (Reproduced from Ref. [2] with kind permission of © 2004 American Chemical Society, and Ref. [5] with kind permission of © 2010 Springer)

involves the reversible electrochemical reactions. The definition of the capacitance of the pseudo-capacitor is shown as below:

$$i_p = an^{1.5}AD^{0.5}Cv^{0.5} \tag{8.2}$$

$$i = i_p \frac{nF}{RT}(E - E_{eq}) \tag{8.3}$$

$$C_S = \frac{\int i dt}{\Delta Vm}, \tag{8.4}$$

where i_p stands for peak current of electrode when electrochemical reactions occur, a is a constant number of 2.69×10^5, n is the number of electrons transferred in a specific electrochemical reaction, A is the effective surface area of electrode, D is the diffusion coefficient of electrolyte, v is the scan rate, C is the bulk concentration of electrolyte, t is the scanning time during the test, ΔV is the voltage difference between the beginning and of the end of scan, m is the mass of the electrode, i is the electrode current, F is the Faraday's constant, R is gas constant, T is thermodynamic temperature, E is the on-site potential, E_{eq} is the standard electrode potential for an electrode/electrolyte combination, and C_s is specific capacitance.

It is easy to realize that the specific capacitance of the pseudo-capacitor is determined by many variables. The peak value depends on the number of electrons transferred during the electrochemical reaction and the intrinsic property of the electrode material. The second most significant factor is the efficient surface area, and the third one is the diffusion coefficient of ions in the electrolyte. Hence, increasing the effective surface area, electrolyte concentration, and electrolyte diffusion coefficient is the key direction in enhancing the capacitance of pseudo-capacitor, after the electrode material is selected. The basic structure and
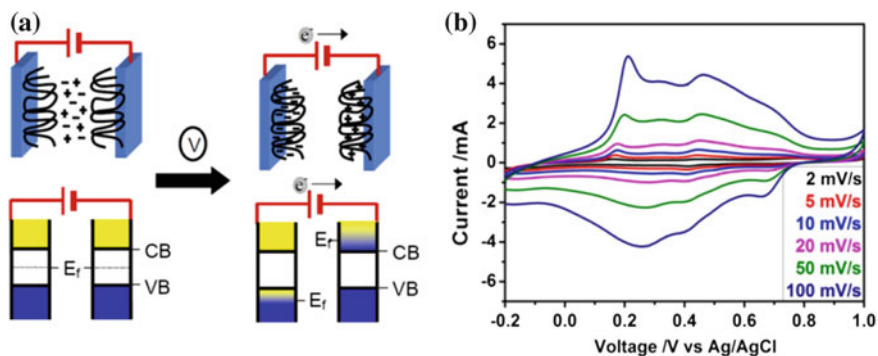
Fig. 8.2 Typical structure of pseudo-capacitor (**a**); representative cyclic votagramm of pseudo-capacitor (**b**) (Reproduced from Ref. [4] with kind permission of © 2004 SERDP)

cyclic voltammetry of pseudo-capacitors are presented in Fig. 8.2. The majority of difference between the EDLC and the pseudo-capacitor is that the materials of the pseudo-capacitor which have two or more reversible oxidation states (shown in Fig. 8.2a). During the charging process, the electrode received the charges from the ions and transferred to a higher oxidation state. The electric energy is transferred and stored as chemical energy. During the discharging process, the electrons move from the negative electrode to the positive one via the external loop, and electrode loses charges and goes back to the base state.

There are three main methods to determine the capacitance of conducting polymer materials, namely, constant current charge–discharge, cyclic voltammetry (CV), and electrochemical impedance spectroscopy (EIS). Theoretically, the charge–discharge curve for a capacitor should be linear with a slope equal to the current divided by the capacitance. Without the influence of redox processes, the cyclic voltammogram of a capacitor would be shaped as rectangular and the capacitance is equal to half the value of difference in plateau currents divided by the scan rate. The slope of the EIS data can represent the capacitance of a capacitor.

8.2 Polymer/Graphene Composite

8.2.1 Electrode Material Selection

8.2.1.1 Carbon-Based Materials

Most EDLC is based on the carbon materials which have huge surface areas and good electrical conductivity. In the ideal EDLCs, the only possible reaction which can reduce the life cycle of the materials is electrostatic attraction. High rate of charging–discharging in EDLC also refers to high power density. Hence, the main

research about EDLC focuses on improving the energy density and specific capacitance. In order to improve the capacitance, according to Eq. (8.1), it is effective to enlarge the effective surface area of electrode materials. Meryl D. Stoller et al., firstly, used chemically modified graphene (CMG) as the EDLC electrode material. The surface area measured by Brunauer–Emmett–Teller (BET) method was 705 m^2/g. And the specific capacitance was calculated as 135 and 99 F/g in aqueous and organic electrolyte, respectively, which are much lower than the theoretical value, 550 F/G [6]. Yoo et al. applied chemical vapor deposition to fabricate the ultrathin "planar graphene" and used a perpendicular electrode to avoid the agglomeration of graphene which commonly happened in the chemically prepared graphene. As a result, the surface area of planar graphene was significantly increased as high as 1310 m^2/g, and the specific capacitance can reach 247 F/g [9].

Kaner et al. employed laser scribed graphene (LSG) film as the electrode of supercapacitor. LSG can increase the surface area as 1520 m^2/g, and hence the capacitance can reach 276 F/g [10]. Another research reported by Zhu et al. increased the effective surface area of graphene up to 3100 m^2/g by via the chemical activation of microwave (or thermally)-exfoliated GO [11]. The recent trend focuses on PANI/graphene supercapacitor. Xie et al. demonstrated that the wavy-shaped PANI/graphene-based supercapacitor can reach 261 F/g capacitance and an energy density of 23.2 Wh/kg at a power density of 399 W/kg for a 0.8 V voltage window. Based on the above research, the theoretical capacitance of 550 F/g is difficult to achieve because the surface area of single-layer graphene is not fully used for charge transition at the electrochemical double layer. Although, it is hard to increase the specific capacitance of carbon-based materials, and the energy density is readily increased according to the equation:

$$E = \frac{1}{2} C_S V^2, \tag{8.5}$$

where E is energy density, C_s is the specific capacitance, and V is the voltage difference between the beginning and the end of discharging. Graphene is a relatively inert material even at high voltage. As a result, it is easy to increase energy density by adding the voltage. Water will electrolysis at 1.22 V, and it is easy to overcome this problem with replacing water by other organic electrolyte. $EMIMBF_4$ ionic liquid electrolyte can hold 4 V, which brought 16 times increments compared with water [3, 12]. Other organic systems were also studied, such as $TEABF_4/PC$, $TEABF_4/AN$ [6, 13, 14], NEt_4BF4-PC [15, 16], $LiClO_4/PC$ [17], and $BMIM$ BF_4/AN [11].

8.2.1.2 Conducting Polymer Materials

On the other hand, there are two main types of pseudo materials: metal oxides and conjugated polymers. The stored energy in these materials can be also classified into two types: direct electrostatic attraction and reversible chemical–electrical

energy conversions. Hence, a pseudo-capacitor can store much more energy and thus has a larger energy density at same voltage range. During charge–discharge process, negative ions can diffuse through the crystals of metal oxides and form metal complexes. Because of the robust structure of the crystal, the metal oxide to metal complex transition is highly reversible. This could result in long cycling life close to EDLCs. McKeown et al. used RuO_2 as pseudo materials which can make the specific capacitance reach the theoretical value 720 F/g.

Most recently, conjugated polymers have been investigated as electrode materials because of their fast kinetics of charge/discharge, high electrical conductivity, mechanical flexibility, and low cost [18]. Conducting polymers are easily to be manufactured as self-supporting, flexible thin film. These advantages attracted researchers as an ideal electrode material for flexible supercapacitor applications. However, the durability and electrochemical stability must be considered because of the stresses during charge/discharge process. Polyaniline (PANI), polypyrrole (PPy), polythiophene (PT), and PEDOT, and composites containing them are widely considered as electrode materials (Table 8.1).

Table 8.1 Specific capacitances of composite and treated materials [8]

Electrode material	Specific capacitance (F/g)	Electrolyte
PPy-SWNTs	144	Aqueous
PPy-funct-SWNTs	200	Aqueous
PEDOT-on-PPy	230	1 M $LiClO_4$ (aq)
PEDOT-on-PPy	290	1 M KCl (aq)
PPy-Fe_2O_3	420	$LiClO_4$ (aq)
PPy	78–137	PVDF-HFD gel electrolyte
PEDOT-MoO_3	300	Nonaqueous Li^+
Nonirradiated HCl-doped PANI	259	Gel polymer electrolyte
Nonirradiated HCl-doped PANI	210 (10,000 cycles)	Gel polymer electrolyte
Irradiated HCl-doped PANI	243	Gel polymer electrolyte
Irradiated HCl-doped PANI	220 (10,000 cycles)	Gel polymer electrolyte
RuOX-PEDOT-PSS	1409	
PPy-fast CV deposited	480	1 M KCl (aq)
ACP-PANI	273	1 M H_2SO_4
Non-treated PEDOT	72	1 M H_2SO_4
Ultrasonicated synthesis of PEDOT	100	1 M H_2SO_4
MWNT/PANI 20/80 wt%	360	
MWNT/PPy 20/80 wt%	190	
PANI coated CNF (20 nm)	264	
PEDOT/MSP-20	56 (1000 cycles)	Et_4NBF_4 in PC, $LiPF_6$ in EC/DMC

Polyaniline

PANI is considered one of the most promising supercapacitor or battery electrode material because of its low cost, ease of synthesis, high theoretical capacity, flexibility, high conductivity, good redox reversibility, and environmental stability [19–39]. The theoretical specific capacitance of PANI is 2000 F/g (if PANI is fully oxidized or reduced in charging–discharging process) [40]. However, a major constraint of PANI is that it needs a proton to be properly charged and discharged; as a result, a protic solvent, an acidic solution, or a protic ionic liquid is required [29]. The specific capacitance is higher for electrodeposited formed PANI than for chemically formed one. The capacity of PANI is varied from 44 to 270 mAh/g [19]. This variation comes from many factors, including synthetic route used, polymer morphology, the amount and type of binders and additives, and the thickness of the electrode. It is a good idea to use the method of design of experiment (DOE) to figure out the most significant factors.

To maximize capacitive behavior, the morphology of the PANI can be controlled on the nanoscale by forming nanowire or nanofibers. In the literature, Zhao et al. reported the highest specific capacitance as 1142 F/g when PANI nanowire was prepared by electrodeposition on an anodic aluminum oxide (AAO) template [41]. The fibrous PANIs were published owing higher effective surface area than those of non-fibrous PANI [42, 43]. The specific capacitance of thin nanofibrous PANI was 160 F/g, which is higher than that of thick nanofibrous PANI or that of spherical (non-fibrous) PANI for 120 and 90 F/g, respectively. The surface area measured by Brunauer–Emmett–Teller (BET) method was 70 m^2/g for the thin PANI nanofibers which is much larger for thick PANIs or spherical PANIs for 21 or 13 m^2/g, respectively.

Polypyrrole

PPy is another promising supercapacitor electrode material which offers a great degree of flexibility [44–67]. PPy is typically doped with single-charged anions such as Cl^-, ClO_4^-, and SO_3. But if doped with multiple-charged anions, e.g., SO_4^{2-}, physical cross-linking of the polymer occurs [68]. The theoretical specific capacitance of PPy is 620 F/g [69]. The supercapacitors which were assembled by poly-vinylidene fluoride co-hexafluoropropylene (PVDF-HFP)-based gel electrolytes sandwiched between PPy electrodes showed the specific capacitances about 78–138 F/g [70]. Other researchers demonstrated PPy-Nafion deposited on Pt or PPy modified composited membranes with good specific capacitance and cyclic stability for electrochemical applications [71, 72]. PPy/Nafion and PPy/paratoluene sulfonated, decomposited onto a gold-coated polyvinylidene difluoride (PVDF) membraned substrate, showed specific capacitances of 380 and 430 F/g, respectively. The PPy/Nafion electrode showed better properties on the cycling life and energy density than that of the PPy/paratoluene sulfonate electrode. In the CV curves, the capacitance of PPy/Nafion electrode was conserved up to 70% after 5000

cycles, whereas the capacitance of PPy/paratoluene sulfonate was only 12% remaining.

On the other hand, PPy nanospheres were able to be prepared in graphene layers to form a three-dimensional hierarchical cross-linking structure through simple hydrothermal method [73]. Gan et al. built a symmetric supercapacitor from the porous MnO_2/PPy nanocomposite yielded a specific capacitance of 142 F/g per mass of one electrode. The cycling life of this capacitor remained 93.2% capacitance retention after 1000 cycles [74].

Polythiophene

The electrical conductivity and the theoretical capacitance of polythiophene are estimated to be 300–400 S/cm and 485 F/g, respectively. In the literature, the specific capacitances of polythiophene derivatives showed as about 220 F/g [75]. Although this capacitance is lower than that of PANI and PPy, poly (3,4-ethylenedioxy-thiophene) (PEDOT) has advantages due to chemical and thermal stability in the oxidized form and fast electrochemical switching [76, 77]. PEDOT has many advantages such as good electrical conductivity, flexibility, low cost, and pseudo-capacitance. PEDOT was used as an active material in supercapacitors. In the recent research, the processing temperature of vapor phase polymerization (VPP) showed a significant effect on PEDOT morphology, the degree of orientation, and its electrical properties. By this effect, PEDOT-based composites show a specific capacitance up to 134 F/g with the polymerization temperature of 110 °C [78]. Zhao et al. used binder-free porous PEDOT electrodes for flexible capacitors. The specific capacitance, energy density, and coulombic efficiency of the PEDOT supercapacitor can reach 69 F/g, 24 Wh/kg, and 95% at a current density of 0.2 A/g, respectively. Also, PEDOT electrodes presented good cycling performance. The capacitance retention ratio is about ~72% after 1500 cycles. The results of PEDOT film from different current densities and scanning rates show the supercapacitors have better rate performances [79].

The use of PEDOT nanowires enables assembly of PEDOT mats which can be assembled into all-textile flexible supercapacitors using carbon cloth as the current collector. Electrospun polyacrylonitrile (PAN) nanofibrous membranes were used as the separator. Ionic liquid-impregnated PVDF-*co*-HFP was used as the solid electrolyte. The specific capacitance was shown about 20 F/g [80].

8.2.2 Electrolytes

In supercapacitor, the electrolytes are another significant part need to be considered. In common, the charges of a supercapacitor are carried by ions that travel through the electrolyte. Thus, the viscosity, ionic conductivity, and boiling points of

electrolytes are all key factors. Generally, electrolytes can be divided into three types: aqueous electrolyte, ionic liquid, and solid-state electrolyte.

8.2.2.1   Aqueous-Based Electrolytes

Aqueous-based electrolytes, which have low price, compatibility with most salts, and high ionic conductivity, are extensively investigated and widely used. The conductivity of aqueous electrolyte can be calculated in the following equation [81]:

$$\kappa = \sum C_i Z_i \lambda_i, \tag{8.6}$$

where C_i is the concentration of dissolved ion i, Z_i is the absolute value of the charge number of ion i, and λ_i is the equivalent ionic conductivity of ion i. The measured value of the ionic conductivity of 1 M HCl at room temperature is about 0.347 S/cm. As the HCl concentration and temperature increased, the conductivity increases, respectively [82]. The conductivity of Na_2SO_4 solution is higher than that of HCL, at 4.24 S/cm in 0.5 M at room temperature [83]. However, the application of aqueous electrolytes is limited since the water will be decomposed above 1.22 V. In the literature, the charge–discharge voltage of most aqueous-based supercapacitors is about 0.7–0.8 V. In this situation, the potential of electrodes is far from fully explored [84]. Wagner et al. showed that the equivalent conductivity of various aqueous-based electrolytes increases linearly as the temperature is increased between 0 and 100 °C, and the result can be seen in Fig. 8.3 [81]. As the saturated vapor pressure is relatively high (1 atm at 100 °C), it makes water easy to evaporate and even boil and consequently constraint the application of aqueous-based electrolytes.

Fig. 8.3 Conductivity–temperature dependence of various aqueous electrolytes (Reproduced from Ref. [81] with kind permission of © 2012 Research Gate)
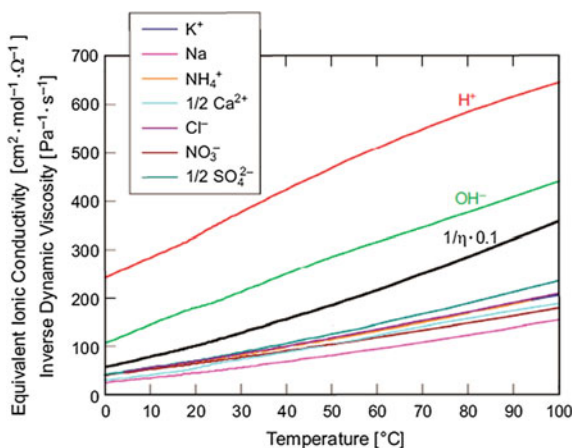
8.2.2.2 Ionic Liquid-Based Electrolytes

Ionic liquid is another major type of the electrolytes which attracted a huge amount of attention for several years. Typically, they kept in the liquid state and ionized organic salts at ambient temperature which results in showing a high ionic conductivity. The detailed chemical structures of cations and anions are presented in Fig. 8.4 [85]. Most of the cations are nitrogen-based hexagons and pentagons in a conjugated structure. As the molecules are stable of the rigid and conjugated structures, they are more stable in a wide temperature and voltage window, specifically up to 7 V and from −40 to 200 °C. In order to improve the specific capacitance, energy density and power density are directly correlated with charge–discharge voltage, and consequently it is significant to enhance the voltage of the electrochemical performance in a safe manner.

The low ionic conductivity is the key factor of ionic liquid, and it can be expressed by the equation [86]:

$$\Lambda = \frac{e^2 N_A}{k_B T}(D^+ + D^-),\tag{8.7}$$

where Λ is the conductivity at low ion concentration, N_A is Avogadro's number, e is the charge of one electron, k_B is Boltzmann's constant, and D^+ and D^- are the diffusion coefficients of cation and anion, respectively. The correlation between diffusion coefficient and viscosity is quantified by the Stokes–Einstein equation [87]:

$$D = \frac{k_B T}{6\pi \eta r},\tag{8.8}$$

where η is the viscosity of the ionic liquid and r is the radius of ions. The relationship between viscosity and temperature can be described by Vogel–Fulcher–Tamman equation as followed [88]:

$$\eta = \frac{\eta_0}{T^{\frac{1}{2}}} \exp\left(\frac{B}{T - T_0}\right),\tag{8.9}$$

where η_0 is a pre-exponential constant proportional to the viscosity coefficient, B is the pseudo-activation energy for viscous behavior, and T_0 is the ideal melting temperature of ionic liquid. From the equations, it can be seen that ionic liquids show better features at higher temperature with lower viscosity. On the other hand, a large ion radius results in a small diffusion coefficient and finally a low conductivity. This results in a smaller power density than that of aqueous electrolyte. Compared with other electrolytes, ionic liquids have high cost and lack of physical property and toxicity data which restricting the properly use as process chemicals and processing aids at current state [89]. In addition, as those ionic liquids are still

(a)

1-Alkyl-3-methylimidazolium
$[C_nC_1im]^+$

1-Alkylpyridinium
$[C_npyr]^+$

1-Alkyl-2,3-dimethylimidazolium
$[C_nC_1C_1im]^+$

1-Alkyl-1-methylpyrrolidinium
$[C_nC_1pyrr]^+$

1-Alkyl-1-methylpiperidinium
$[C_nC_1pip]^+$

Tetraalkylphosphonium
$[C_mC_mC_oC_pP]^+$

Tetraalkylammonium
$[C_mC_nC_oC_pN]^+$

Trialkylsulfonium
$[C_nC_mC_oS]^+$

(b)

Hexafluorophosphate
$[PF_6]^-$

Bis(trifluoromethyl-
sulfonyl)imide
$[NTf_2]^-$

Tetrafluoroborate
$[BF_4]^-$

Trifluoromethane-
sulfonate
$[OTf]^-$

Dicyanamide
$[N(CN)_2]^-$

Cl⁻, Br⁻, I⁻

Chloride, bromide, iodide

Methyl sulfate
$[MeSO_4]^-$

Dimethyl phosphate
$[Me_2PO_4]^-$

Acetate
$[MeCO_2]^-$

Fig. 8.4 Common ionic liquids: cations (**a**); anions (**b**) (Reproduced from Ref. [85] with kind permission of © 2012 Royal Society of Chemistry)

free to flow, a good container and good sealing is required when assembling the products which constrain their applications in flexible supercapacitors.

8.2.2.3 Solid-State Electrolytes

Modern electronics require not only higher and higher energy storage devices, but also other features, such as flexibility, smaller size, safety, and cheaper price. Solid-state electrolyte is the most outstanding candidate to meet all of the requirements. There are mainly two categories of solid-state electrolytes. The first type is glass and ceramics consist of mixture of lithium salts, such as lithium nitrides, sulfides, borates, phosphates, etc. [90–93]. However, most lithium salts are sensitive to moistures and no longer flexible after sintering. Another type of the solid-state electrolyte is the polymer-based solid-state electrolyte, which is prepared by doping proton acids or ionic liquids into polymer matrixes. Polyvinylidene fluoride (PVDF), polyethylene glycol (PEO or PEG), and polyvinyl alcohol (PVA) are the three most employed matrixes. PVDF matrix is coupled with ionic liquids and lithium salts by mixing in organic solvents [94]. PEG and PVA can be coupled with proton acids by dissolving in water making them more commonly used in both in research and applications. Capiglia et al. found that the ionic conductivity of the SiO_2-doped PEO_8–$LiClO_4$ was about 10^{-4} S/cm [95]. In Haijun Yu's study, the conductivity of KI-doped PVA–KOH can reach 10^{-2} S/cm [96]. The ionic conductivity of various solid-state electrolytes (and ionic liquids as well) is summarized in the Fig. 8.5 [97]. From the figure, it can be found that the ionic conductivity of PEO–$LiClO_4$ and $LiPF_6$/PVDF-HFP systems is only about 10^{-3} S/cm at room temperature. Although they can continuously increase as the increase of the temperature, respectively, their highest values are still only about 10^{-2} S/cm at 100 °C which is onefold lower than that of ionic liquid $LiBF_4$/$EMIBF_4$ (up to 10^{-1} S/cm), and twofolds lower than that of aqueous electrolytes. Hence, much lower power density could be expected according to $P = U/(4ESR^2)$. In this situation, low ionic conductivity is the major contributor of ESR.

Although the solid-state electrolytes are widely applied in electronics, the highest ionic conductivity is still lower than that of medium value in proton acids' aqueous electrolyte. Since there is no universal model to describe the conducting mechanism of solid-state electrolytes, the conducting behaviors of solid-state electrolytes can be approximately described by basic semiconductor equations as follows:

$$\sigma = qn\mu. \tag{8.10}$$

This is a universal equation to describe the conductivity of doped semiconductor, where σ is the conductivity, q is the charge of a carrier which is equal to Z^*
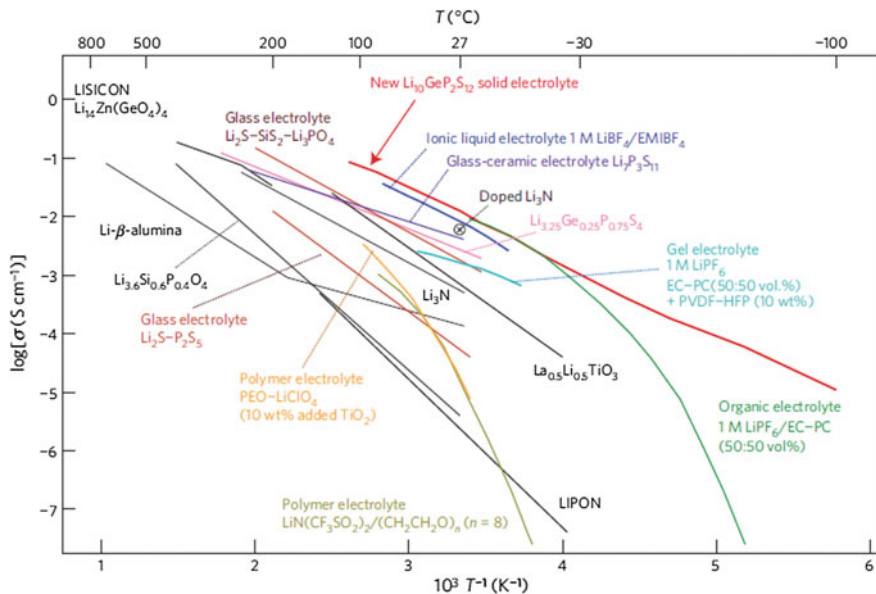
Fig. 8.5 Ionic conductivities of various solid state electrolytes (Reproduced from Ref. [97] with kind permission of © 2011 Macmillan Publishers Ltd)

1.602×10^{-19} C (when carrier is not electron), n is the carrier concentration, and μ is the carrier mobility. The carrier concentration and mobility have different formations depending on different materials.

In organic semiconductors, carrier mobility follows Langevin theory [98]:

$$\mu = \frac{eD}{k_B T}. \tag{8.11}$$

And the carrier concentration can be calculated by following equation [99]:

$$n^{+/-} = \frac{N_A}{1 + g \times \exp\left((E_A - E_F)\, kT\right)}, \tag{8.12}$$

where N_A is the nominal concentration of dopant, E_A is the ionization energy, E_F is the Fermi energy, g is the degeneracy factor for acceptor levels, and a value of 4 is commonly assigned to g.

It can be seen that the major variable affecting the carrier mobility is the diffusion coefficient. However, Eq. (8.8) is not applicable in the solid. Increasing the dopant concentration is the most direct approach to increase the carrier concentration.

8.3   Preparation of PANI Nanowires/Graphene Composites

In this chapter, three novel, facile, and scalable approaches are presented to control the geometries and structures of the graphene interlinked aligned PANI nanofibers to achieve optimal supercapacitive performance. By carefully selecting the synthesis approaches and parameters, PANI nanofibers with uniform alignment and narrow size distribution are realized. Also, a theoretical model has been established to quantify the electrode structures and performance relationship and to provide the guideline for the future fabrication and optimization. Thus, this chapter provided both experimental and theoretical approaches for constructing high energy density and high power density supercapacitors.

8.3.1   Melamine-Assisted Synthesis of PANI/Graphene Composites

Due to the strong π–π conjugation between the PANI hexagon ring and graphene, it is hard for the PANI to nucleate directly on graphene. Another problem is that graphene sheets and PANI nanowires are usually randomly dispersed and lacked of ordering and porous structure in the hybrids, which can significantly affect the performance of their supercapacitors. Thus, template-assisted nucleation is urgently needed for producing tailored PANI nanowire morphology to meet specified characteristics, such as orientation, size, and distribution. However, it is very challenging to apply a template to various graphene nanosheets randomly dispersed in the colloidal suspension.

In Wang's work [100], a small molecule is reported to generate heterogeneous nucleation of PANI on the graphene sheets to reduce the thickness of the PANI coating. Melamine is a conjugated small molecule, and its molecular structure is shown in Fig. 8.6. Because of the strong π–π conjugate between hexagonal rings, it can be strongly absorbed onto graphene by non-covalent interactions serving as nucleation sites for PANI nanowires. Along with the APS added, the amino groups are dissociated in the acidic solution and initialized the polymerization of PANI. The dilute ANI monomers are used to ensure the subsequent growth of PANI

Fig. 8.6 Structure of melamine
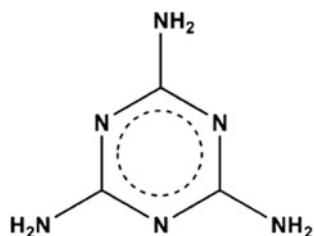
Fig. 8.7 Proposed mechanism of PANI nanowires: growth without melamine and heterogeneous nucleation and growth in bulk solution (Reproduced from Ref. [100] with kind permission of © 2013 Informa Group plc)
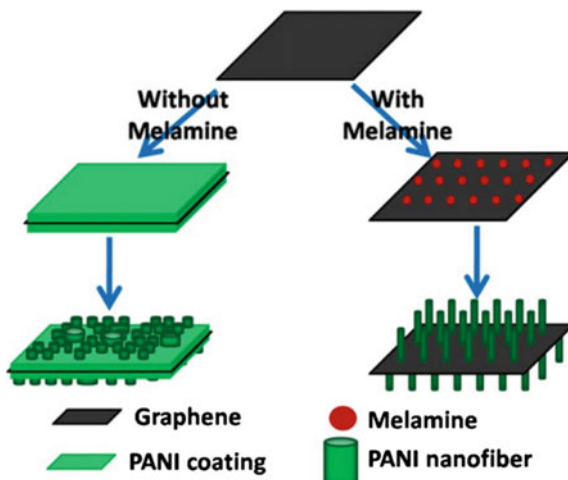
nanowires is vertically aligned. The relevant growth mechanism of PANI nanowires is described below (Fig. 8.7).

Simultaneously, melamine is further employed to tune the diameter and area density of PANI nanowires on both sides of graphene sheets by adjusting the concentrations of melamine and ANI. The smallest diameter and largest area density can be achieved when the concentration of melamine is 0.06 mM and ANI is 3 mM. The ordered porous network in the graphene/PANI nanowire hybrids can facilitate the ion diffusion, transportation, and exchange. These results suggest that melamine is promising to design and synthesize tunable nanostructures to meet the various needs.

8.3.2   Graphene Film Cross-Linked Ordered PANI

In Sect. 8.3.1, a soft template directed PANI/graphene hybrid is fabricated in the colloid. Despite its easy preparation and high yield, a lack of processability is the major challenge in the electrode applications. Also, additional conductive and adhesive materials have to be used to bind the PANI/graphene powders, which will reduce conductivity. To solve these problems, in situ synthesis of a PANI nanowires array on the conductive substrate is more attractive due to the low contact resistance between electrode and current collector. Moreover, the desired structure can be very stable (Fig. 8.8).

In this situation, a multilayered vertically aligned PANI nanowire arrays were prepared by using graphene film as an interlayer [101]. Specifically, the
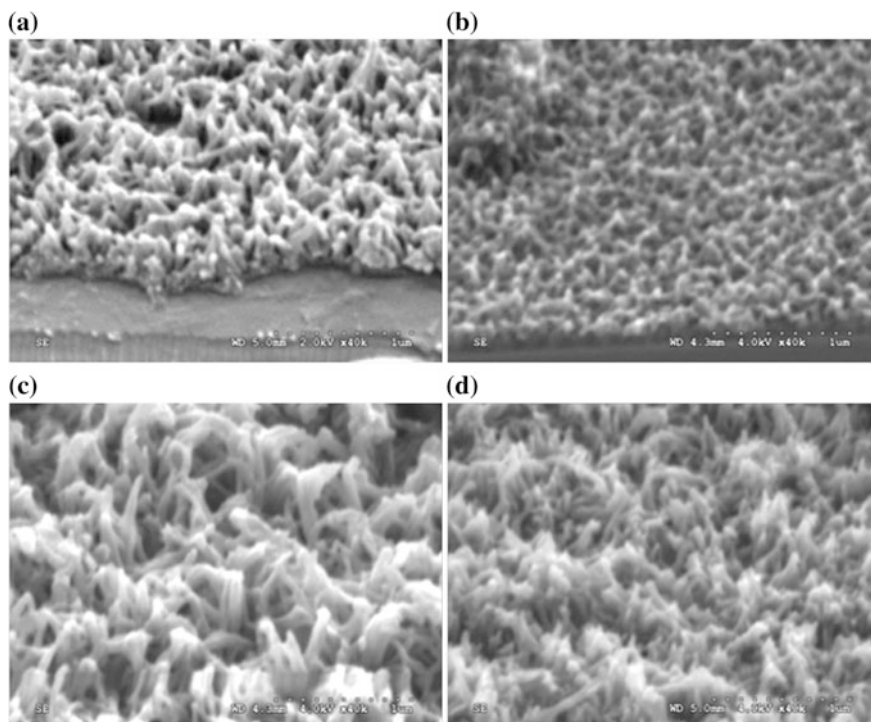
Fig. 8.8 SEM images of first layer of PANI array synthesized using different dopant: 1 M HCl (**a**); 2 M HCl (**b**); 1 M HClO$_4$ (**c**); and 2 M HClO$_4$ (Reproduced from Ref. [101] with kind permission of © 2013 Elsevier)

self-assemble molecule-induced dilute solution method was used for PANI arrays synthesis, then graphene paper was transferred onto it and a further PANI layer was also introduced on to graphene. In the process of synthesis, several different acids (HCl and HClO$_4$) were chosen as dopants. It turned out that using HClO$_4$ can help to achieve more favorable porous morphology and led to better electrochemical properties, which is owing to the dependence of PANI nanowire morphology on the size of dopants. At the beginning of synthesis, 4-ATP molecules were absorbed onto the gold foil and formed a soft template for ANI monomers to nucleate [102]. Subsequently, ANI monomers were in situ protonated, and the acidic radicals doped into the N atoms. Under such circumstances, the further growth can be approximately described by the dilute surfactant microcells mechanism proposed by Xia et al. [103]. Because ClO^{4-} is much larger than Cl$^-$ in size, it may generate greater steric hindrance, and thus lead to thinner nanowires. Obviously, the choice of acid in the synthesis process plays a critical role in the morphology of 3D network structures.

8.3.3   Monolayer Graphene Cross-Linked Ordered PANI

In the last synthesis method, a graphene film interconnected multilayered vertically aligned PANI nanowire array was studied. It was easy to tune the nanowire alignment and diameter to enhance the electrochemical performances by changing the dopants and their concentrations. However, two issues deteriorated their electrochemical performance more or less. First, the self-assembly small molecules between current collector and PANI hinder the charge transferring efficiency. Second, it was difficult to prepare a thin graphene interlayer by simply filtering. Hence, the densely packed graphene film significantly lowered the specific capacitance.

In the literature [104], the electrochemical deposition was employed to introduce monolayer graphene onto a PANI nanowire arrays with larger bonding strength for better charge transferring between PANI and current collector. The monolayer graphene can serve as both interlayer supporting skeleton and charge transferring media. Also, a two-step electrochemical method was used to fabricate a better aligned PANI nanowire array, in which $HClO_4$ was the dopant in the first step and HCl was the dopant in the second step. The role of the $HClO_4$ had been demonstrated to allow the PANI nucleation previously. As for HCl-doped PANI nanowires, monolayer GO can easily assembled onto the PANI nanowire array, which was proved in Fig. 8.9a, b. The whole process consists a series of intermediate reactions. First, the Cl^+ was attacked by acyl groups of carboxyl groups, and the resulted structure was an electron-defect compounds. This structure tended to bond with benzenoid amines by carbon side. Consequently, one electron was transferred from carbonyl group to acyl group, and the hypochlorite was removed from structure. Finally, the carbonyl group gave one proton away and the whole structure forms a stable amide bonding between PANI and GO.
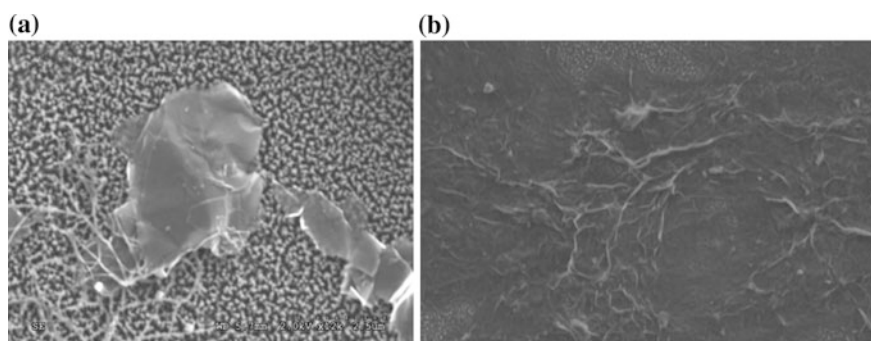
Fig. 8.9 Surface of PANI array after graphene oxide was electrochemically deposited. PANI array doped by $HClO_4$ (**a**); PANI array doped by HCl (**b**). Graphene oxide was deposited under 1.2 V, 5 μA for 0.5 h in both samples (Reproduced from Ref. [104] with kind permission of © 2013 Elsevier)
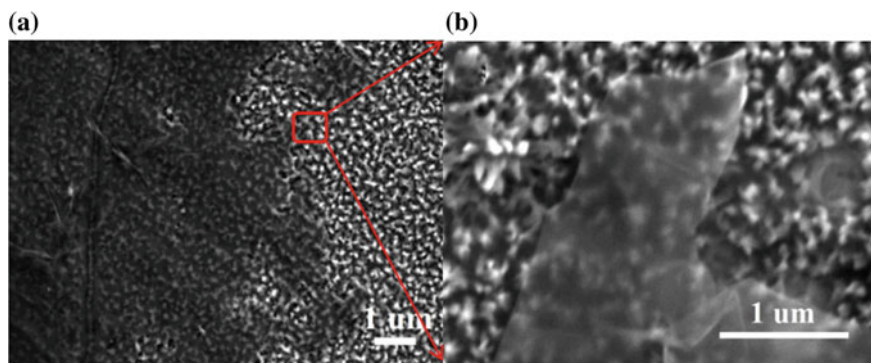
Fig. 8.10 SEM results of PANI nanowire array grown stepwise in 1 M $HClO_4$ for 1 h and 1 M HCl for 6 h at 2 $\mu A/cm^2$ current density, respectively. **a** Top view and **b** side view (Reproduced from Ref. [104] with kind permission of © 2013 Elsevier)

Therefore, a combined method was developed to produce well-aligned PANI nanowire array for readily assembly of monolayer GO. To be special, the synthesis was firstly carried out in the 1 M $HClO_4$ for 6 h, and then in 1 M HCl for another 1 h. Obviously, all the PANI nanowires were vertically aligned and diameter distribution was uniform, and a high coverage and continuous coating of GO was obtained and displayed in Fig. 8.10.

PANI nanowires with controlled diameter and length were vertically grown onto the GO surface while GO was in-situ reduced by an electrochemical method [105, 106]. The alternative growth of PANI nanowire array and assembly of monolayer GO was carried out for hierarchical 3D nanostructures, and the corresponding SEM results are shown in Fig. 8.11. This rationally designed architecture will be advantageous in boosting an optimal performance.

8.4 Electrochemical Performance of Polymer/Graphene Composites as Battery Electrodes

Several factors significantly affect the electrochemical performances of supercapacitor electrodes as summarized by Pandolfo and Hollenkamp in their review, such as structure of electroactive materials, electrical conductivity of electroactive materials, and the interface between electrode and electrolyte. In this chapter, hierarchical nanostructured materials consisting of stacked polymer nanowires forests interconnected by graphene sheets obtained through three synthetic methods mentioned in Sect. 8.2. After gradually improving synthetic parameter, growth of
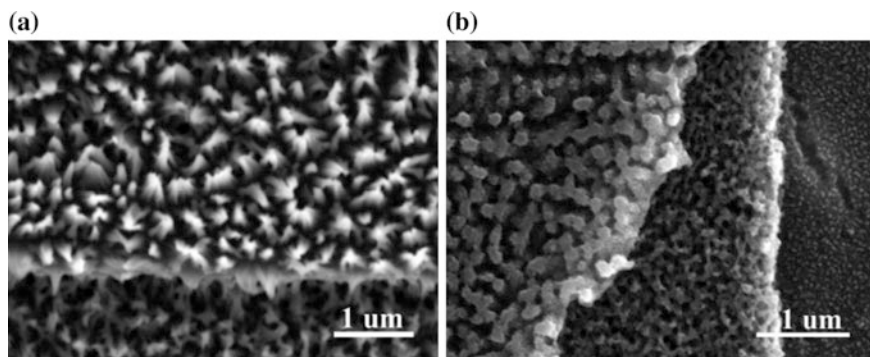
Fig. 8.11 a SEM image of two-stack 3D nanostructure; **b** three-stack 3D nanostructure (Reproduced from Ref. [104] with kind permission of © 2013 Elsevier)

PANI nanowire in $HClO_4$ and HCl stepwise is the best method for both good alignment and capability to be assembled with graphene. This structure not only can combine the high stability, high surface area, and conductivity of graphene with high capacitance of PANI. As a result, the synergistic effect between two components resulted in much superior performance. The highest specific capacitance in aqueous electrolyte was measured as 1443 F/g. Also, high energy and power density can be achieved simultaneously, specifically 100 Wh/kg at 63,534 W/kg [104].

The unique layer-dependent electrochemical performance was further investigated as shown in Fig. 8.6. For the cyclic voltammetry scanning, obvious oxidation and reduction were observed, indicating pseudo-capacitive behavior. The polarizing current increased linearly with the number of layers of the arrays. The equivalent series resistance (ESR) was less than 1.0 Ω and the shape of the curve clearly indicated finite-length porous electrodes. Proton (H^+) in acid solution could significantly dope PANI and make the PANI highly conductive, thus the charge transfer happened very quickly and electrochemical behavior was primarily dependent on the diffusion process. The diffusion resistance can be approximately calculated as 0.75 Ω by using equation:

$$R_{\Sigma} = 3\left(R_i - \text{ESR}\right) \tag{8.13}$$

where R_{Σ} is diffusion resistance and R_i is the intersection between high and low frequency. With the increasing number of PANI arrays, the diffusion would be more difficult because of the vertically diffusion path was blocked by GO, and thus the specific capacitance decreases slightly (Fig. 8.12).
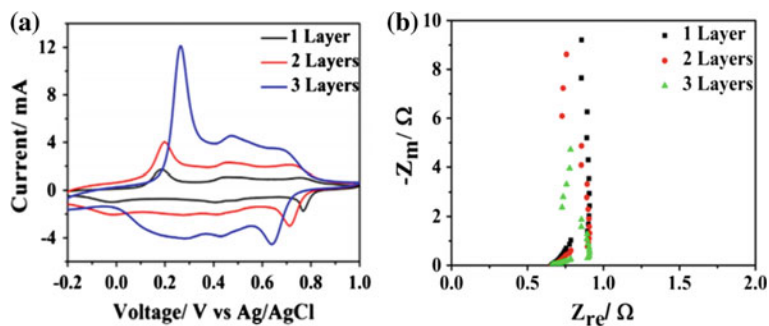
Fig. 8.12 Cyclic voltammetry of multilayered nanostructures scanned at 50 mV/s (**a**). Impedance test of 3D structured electrode in aqueous solutions (**b**) (Reproduced from Ref. [104] with kind permission of © 2013 Elsevier)

8.5   Influence of Electrolyte on Performance

Apart from advanced electrode materials, electrolyte is also a major parameter that is important in determining high-performance supercapacitors.

8.5.1   Organic Electrolytes

All the previous measurements (in Sect. 8.3) were carried out in aqueous solution. To further investigate the effect of organic electrolyte on the electrochemical behavior, the PANI/graphene composites were tested in TBAPF$_6$/acetonitrile electrolyte. There was no proton doping in the organic electrolyte and PANI was much less conductive, and thus charge transfer process dominates the whole electrochemical process. As shown in Fig. 8.13, the equivalent series resistance was as high as 28.1 Ω, indicating higher resistance of system. The original H$^+$ doping state in first PANI nanowire array was low, conductivity was low, and thus leads to low charge transfer rate. As GO was assembled and in situ reduced, the band gap of 3D nanostructured materials was lowered, and charge carriers density was increased. With more graphene layers were introduced into the 3D nanostructures, charge transfer capability was improved. The charge transfer resistance calculated as 2, 1.7, and 0.26 Ω for one-, two- and three-layer 3D nanostructured electrodes derived from the slope of low frequency region. This also agreed well with Wang's theoretical [107].
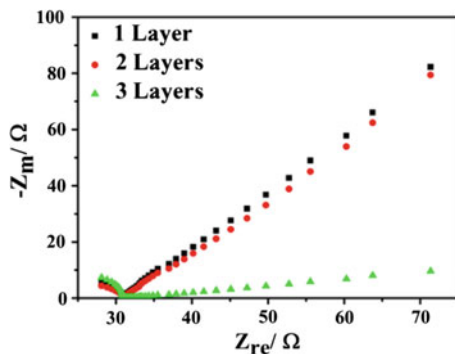
Fig. 8.13 Impedance test of 3D structured electrode in TBAPF$_6$/acetonitrile solutions (Reproduced from Ref. [107] with kind permission of © 2012 American Chemical Society)
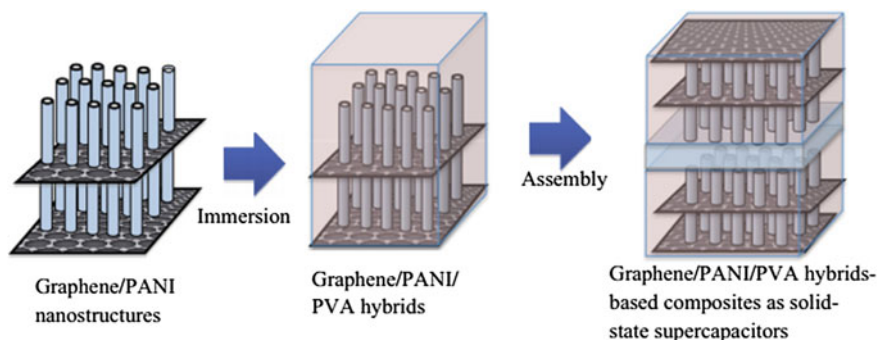
Fig. 8.14 Illustration of fabricating multiphase composites as solid-state supercapacitors. Graphene/PANI hybrid nanostructures were impregnated with PVA and assembled together to form ordered symmetrical solid-state supercapacitors (Reproduced from Ref. [108] with kind permission of © 2015 Elsevier)

8.5.2   Solid Electrolytes

Safety and relatively short cycling life are other two issues related to liquid electrolytes. Therefore, various solid-state electrolytes are suggested as promising alternatives because of their chemical and physical stability, leakage and maintenance requirements, and flexibility. Therefore, multilayered structured polyaniline (PANI) nanowire arrays linked by graphene, and then incorporated them into H$_3$PO$_4$–Nafion/PVA to form hybrid composites, which serve as solid-state supercapacitors. The relevant schematic can be seen in Fig. 8.14.

The specific capacitance was measured to be 83 F/g at 0.1 A/g, and it showed very less dependence on the current density. The hybrid composites also showed superior stability on the energy density in a big range of power density. When

power density ranged from 70 to 3600 W/kg, the energy density remained at 26.5 Wh/kg. The as-produced solid-state supercapacitors also demonstrated stable capacitance on both low frequency and high frequency, which may be due to the improved charge transporting of the solid-state electrolyte. The specific capacitance became quite stable after 13% drop in the first 400 cycles. These results indicated delicate PANI nanostructure and excellent charge transportation of the electrolyte play a critical role in the high-performance solid-state supercapacitors [108].

In order to obtain an insightful understanding of the relation between structure, electrolyte, and electrochemical performances, the electrochemical behavior was further theoretically investigated. In aqueous system, the diffusion was the dominating process since the electrochemical process was determined by the slowest step. Their electrochemical behavior can be described by the following equations [109]:

$$i_p = an^{1.5}AD^{0.5}Cv^{0.5} \tag{8.14}$$

$$i = i_p \frac{nF}{RT}(E - E_{eq}) \tag{8.15}$$

$$C_S = \frac{\int it}{\Delta Vm}, \tag{8.16}$$

where i_p stands for peak current, a is constant, 2.69×10^5, n is number of electrons transferred, A is surface area of electrode, D is diffusion coefficient of electrolyte, v is scan rate, C is bulk concentration of electrolyte, i is electrode current, F is Faraday constant, R is gas constant, T is thermodynamic temperature, E is electrode potential, E_{eq} is equilibrium potential, C_s is specific capacitance, t is scanning time, ΔV is the voltage difference between beginning and ending scan, and m is the mass of the PANI on the electrode. Combining them together results in a new equation as follows:

$$C_S = \frac{an^{1.5}AD^{0.5}Cv^{0.5}F \int (E - E_{eq})\,\mathrm{d}t}{RT\Delta vm}. \tag{8.17}$$

Obviously, the specific capacitance was a function of sophisticated competition among number of electrons transferred; electrode surface area and electrode mass. Since PANI was in the highest doping state in aqueous solution, the number of transferred electrons versus mass would not further increased in multiple-layered electrodes. In fact, it decreased because of the forming of big nanowires. The specific electrode surface area was deteriorated as well. As a result, the specific capacitance decreased as there were more PANI nanowire arrays. On the other hand, in organic system the original H$^+$ doping state was low and the charge transfer was the dominated step. The GO coating played a big role in the charge transferring after its deposition and in situ reduction. Reduced GO sheets interconnected with the neighbored PANI nanowire arrays and could also tune the PANI

carries concentration, and thus increased the number of transferred electrons with increasing the layer number of 3D structures. Therefore, the electrode behaves entirely different in organic electrolyte system.

8.6 Conclusions

In summary, this chapter summarized the high efficiency approaches and the new point of view on increasing both energy density and power density by tailoring the polymer/graphene electrode architecture. Also, a theoretical model has been established to quantify the electrode structures and performance relationship and to provide the guideline for the future fabrication and optimization. Thus, it provided both experimental and theoretical approaches for constructing high energy density and high power density supercapacitors based on polymer/graphene.

References

1. Zheng X, Yan X, Sun Y et al (2015) Au-embedded ZnO/NiO hybrid with excellent electrochemical performance as advanced electrode materials for supercapacitor. ACS Appl Mater Interfaces 7(4):2480–2485
2. Winter M, Brodd RJ (2004) What are batteries, fuel cells, and supercapacitors? Chem Rev 104(10):4245–4270
3. Liu C, Yu Z et al (2010) Graphene-based supercapacitor with an ultrahigh energy densiy. Nano Lett 10(12):4863–4868
4. Prokopuk N (2004) All organic supercapacitors as alternatives to lithium batteries. Report to SERDP
5. Li L, Qin Z, Wang L et al (2010) Anchoring alpha-manganese oxide nanocrystallites on multi-walled carbon nanotubes as electrode materials for supercapacitor. J Nanopart Res 12:2349–2353
6. Stoller M, Park S, Zhu Y et al (2008) Graphene-based ultracapacitors. Nano Lett 8:3498–3502
7. Sun Y, Shi G (2013) Graphene/polymer composites for energy applications. J Polym Sci Polym Phys 51(4):231–253
8. Graeme A, Pon K, Adam S (2011) Conducting-polymer-based supercapacitor devices and electrodes. J Power Sources 196(1):1–12
9. Yoo JJ, Balakrishnan K, Huang J et al (2011) Ultrathin planar graphene supercapacitors. Nano Lett 11(4):1423–1427
10. El-Kady MF, Strong V, Dubin S et al (2012) Laser scribing of high-performance and flexible graphene-based electrochemical capacitors. Science 335(6074):1326–1330
11. Zhu Y, Murali S, Stoller MD et al (2011) Carbon-based supercapacitors produced by activation of graphene. Science 332(6037):1537–1541
12. Rose M, Korenblit Y, Kockrick E et al (2011) Hierarchical micro and mesoporous carbide-derived carbon as a high-performance electrode material in supercapacitors. Small 7 (8):1108–1117
13. Izadi-Najafabadi A, Yamada T, Futaba DN et al (2011) High-power supercapacitor electrodes from single-walled carbon nanohorn/nanotube composite. ACS Nano 5(2):811–819

14. Korenblit Y, Kajdos A, West WC (2012) In situ studies of ion transport in microporous supercapacitor electrodes at ultralow temperatures. Adv Funct Mater 22(8):1655–1662

15. Pech D, Brunet M, Durou H et al (2010) Ultrahigh-power micrometre-sized supercapacitors based on onion-like carbon. Nat Nanotechnol 5(9):651–654

16. Liu H, Jin LH, He P et al (2009) Direct synthesis of mesoporous carbon nanowires in nanotubes using MnO_2 nanotubes as a template and their application in supercapacitors. Chem Commun 44:6813–6815

17. Chen Z, Augustyn V, Wen J et al (2011) High-performance supercapacitors based on intertwined CNT/V_2O_5 nanowire nanocomposites. Adv Mater 23(6):791–795

18. Heywang G, Jonas F (1992) Poly(alkylenedioxythiophene) s-new, very stable conducting polymers. Adv Mater 4(2):116–118

19. Sivakkumar SR, Saraswathi R (2004) Performance evaluation of poly(N-methylaniline) and polyisothianaphthene in charge-storage devices. J Power Sources 137(2):322–328

20. Ryu KS, Kim KM, Park NG et al (2002) Symmetric redox supercapacitor with conducting polyaniline electrodes. J Power Sources 103(2):305–309

21. Talbi H, Just PE, Dao LH (2003) Electropolymerization of aniline on carbonized polyacrylonitrile aerogel electrodes: applications for supercapacitors. J Appl Electrochem 33(6):465–473

22. Gómez-Romero P, Chojak M, Cuentas-Gallegos K et al (2003) Hybrid organic-inorganic nanocomposite materials for application in solid state electrochemical supercapacitors. Electrochem Commun 5(2):149–153

23. Kulesza PJ, Skunik M, Baranowska B et al (2006) Fabrication of network films of conducting polymer-linked polyoxometallate-stabilized carbon nanostructures. Electrochim Acta 51(11):2373–2379

24. Hussain AMP, Kumar A, Singh F et al (2006) Effects of 160 MeV Ni^{12+} ion irradiation on HCl doped polyaniline electrode. J Phys D Appl Phys 39(4):750

25. Ryu KS, Lee YG, Kim KM et al (2005) Electrochemical capacitor with chemically polymerized conducting polymer based on activated carbon as hybrid electrodes. Synth Met 153(1):89–92

26. Khomenko V, Frackowiak E, Beguin F (2005) Determination of the specific capacitance of conducting polymer/nanotubes composite electrodes using different cell configurations. Electrochim Acta 50(12):2499–2506

27. Jang J, Bae J, Choi M et al (2005) Fabrication and characterization of polyaniline coated carbon nanofiber for supercapacitor. Carbon 43(13):2730–2736

28. Zhang J, Shan D, Mu S (2006) A rechargeable Zn- poly(aniline-co-m-aminophenol) battery. J Power Sources 161(1):685–691

29. Wu M, Snook GA, Gupta V et al (2005) Electrochemical fabrication and capacitance of composite films of carbon nanotubes and polyaniline. J Mater Chem 15(23):2297–2303

30. Ryu KS, Lee Y, Han KS et al (2004) Electrochemical supercapacitor based on polyaniline doped with lithium salt and active carbon electrodes. Solid State Ionics 175(1):765–768

31. Neves S, Fonseca CP (2004) Mixed solid device based on conducting polymer composite and polymer electrolyte. J Braz Chem Soc 15(3):395–399

32. Karami H, Mousavi MF, Shamsipur M (2003) A new design for dry polyaniline rechargeable batteries. J Power Sources 117(1):255–259

33. Gurunathan K, Amalnerkar DP, Trivedi DC (2003) Synthesis and characterization of conducting polymer composite (PAn/TiO_2) for cathode material in rechargeable battery. Mater Lett 57(9):1642–1648

34. Ryu KS, Kim KM, Hong YS et al (2002) The polyaniline electrode doped with Li salt and protonic acid in lithium secondary battery. Bull Korean Chem Soc 23(8):1144–1148

35. Neves S, Fonseca CP (2002) Influence of template synthesis on the performance of polyaniline cathodes. J Power Sources 107(1):13–17

36. Oyama N, Hatozaki O (2000) Lithium polymer battery with high energy density. Macromol Symp Wiley-VCH 156(1):171–178

37. Oyama N, Hatozaki O (2000) New composite cathodes for lithium rechargeable batteries. Mol Cryst Liquid Crystals 349(1):329–334
38. Oyama N (2000) Development of polymer-based lithium secondary batery. Macromol Symp Wiley-VCH 159(1):221–228
39. Vol'fkovich YM, Bobe SL, Shlepakov AV et al (1993) Discharge macrokinetics of polyaniline electrode. Russ Electrochem 29(5):794–804
40. Li H, Wang J, Chu Q et al (2009) Theoretical and experimental specific capacitance of polyaniline in sulfuric acid. J Power Sources 190(2):578–586
41. Zhao GY, Li HL (2008) Preparation of polyaniline nanowire arrayed electrodes for electrochemical supercapacitors. Micropor Mesopor Mater 110(2):590–594
42. Wu Q, Xu Y, Yao Z et al (2010) Supercapacitors based on flexible graphene/polyaniline nanofiber composite films. ACS Nano 4(4):1963–1970
43. Hung PJ, Chang KH, Lee YF et al (2010) Ideal asymmetric supercapacitors consisting of polyaniline nanofibers and graphene nanosheets with proper complementary potential windows. Electrochim Acta 55(20):6015–6021
44. Snook GA, Chen GZ, Fray DJ et al (2004) Studies of deposition of and charge storage in polypyrrole-chloride and polypyrrole-carbon nanotube composites with an electrochemical quartz crystal microbalance. J Electroanal Chem 568:135–142
45. Snook GA, Chen GZ (2008) The measurement of specific capacitances of conducting polymers using the quartz crystal microbalance. J Electroanal Chem 612(1):140–146
46. Hashmi SA, Upadhyaya HM (2002) Polypyrrole and poly(3-methyl thiophene)-based solid state redox supercapacitors using ion conducting polymer electrolyte. Solid State Ionics 152:883–889
47. Wang J, Xu Y, Chen X et al (2007) Capacitance properties of single wall carbon nanotube/polypyrrole composite films. Compos Sci Technol 67(14):2981–2985
48. Wang J, Xu Y, Chen X et al (2007) Electrochemical supercapacitor electrode material based on poly(3,4-ethylenedioxythiophene)/polypyrrole composite. J Power Sources 163(2):1120–1125
49. Tripathi SK, Kumar A, Hashmi SA (2006) Electrochemical redox supercapacitors using PVdF-HFP based gel electrolytes and polypyrrole as conducting polymer electrode. Solid State Ionics 177(33):2979–2985
50. Hussain AMP, Saikia D, Singh F et al (2005) Effects of 160 MeV Ni^{12+} ion irradiation on polypyrrole conducting polymer electrode materials for all polymer redox supercapacitor. Nucl Instrum Meth B 240(4):834–841
51. Fan LZ, Maier J (2006) High-performance polypyrrole electrode materials for redox supercapacitors. Electrochem Commun 8(6):937–940
52. Boyano I, Bengoechea M, de Meatza I et al (2007) Improvement in the Ppy/V_2O_5 hybrid as a cathode material for Li ion batteries using PSA as an organic additive. J Power Sources 166(2):471–477
53. Boyano I, Bengoechea M, de Meatza I et al (2007) Influence of acids in the Ppy/V_2O_5 hybrid synthesis and performance as a cathode material. J Power Sources 174(2):1206–1211
54. Wang J, Wang CY, Too CO et al (2006) Highly-flexible fibre battery incorporating polypyrrole cathode and carbon nanotubes anode. J Power Sources 161(2):1458–1462
55. Wang CY, Ballantyne AM, Hall SB et al (2006) Functionalized polythiophene-coated textile: a new anode material for a flexible battery. J Power Sources 156(2):610–614
56. Sung JH, Kim SJ, Jeong SH et al (2006) Flexible micro-supercapacitors. J Power Sources 162(2):1467–1470
57. Hallik A, Alumaa A, Tamm J et al (2006) Analysis of electrochemical impedance of polypyrrole|sulfate and polypyrrole|perchlorate films. Synth Met 156(5):488–494
58. Wang J, Too CO, Zhou D et al (2005) Novel electrode substrates for rechargeable lithium/polypyrrole batteries. J Power Sources 140(1):162–167
59. Izadi-Najafabadi A, Tan DTH, Madden JD (2005) Towards high power polypyrrole/carbon capacitors. Synth Met 152(1):129–132

60. Yang J, Martin DC (2004) Microporous conducting polymers on neural microelectrode arrays: II. Physical characterization. Sensor Actuat A-Phys 113(2):204–211
61. Xiao Q, Zhou X (2003) The study of multiwalled carbon nanotube deposited with conducting polymer for supercapacitor. Electrochim Acta 48(5):575–580
62. Sung JH, Kim SJ, Lee KH (2003) Fabrication of microcapacitors using conducting polymer microelectrodes. J Power Sources 124(1):343–350
63. Iroh JO, Levine K (2003) Capacitance of the polypyrrole/polyimide composite by electrochemical impedance spectroscopy. J Power Sources 117(1):267–272
64. Park JH, Ko JM, Park OO et al (2002) Capacitance properties of graphite/polypyrrole composite electrode prepared by chemical polymerization of pyrrole on graphite fiber. J Power Sources 105(1):20–25
65. Garcia-Belmonte G, Bisquert J (2002) Impedance analysis of galvanostatically synthesized polypyrrole films. Correlation of ionic diffusion and capacitance parameters with the electrode morphology. Electrochim Acta 47(26):4263–4272
66. Amanokura J, Suzuki Y, Imabayashi S et al (2001) Polypyrrole/polymer electrolyte composites prepared by in situ electropolymerization of pyrrole as cathode/electrolyte material for facile electron transfer at the solid interface. J Electrochem Soc 148(4):D43–D48
67. Chen GZ, Shaffer MSP, Coleby D et al (2000) Carbon nanotube and polypyrrole composites: coating and doping. Adv Mater 12(7):522–526
68. Suematsu S, Oura Y, Tsujimoto H et al (2000) Conducting polymer films of cross-linked structure and their QCM analysis. Electrochim Acta 45(22):3813–3821
69. Lota K, Khomenko V, Frackowiak E (2004) Capacitance properties of poly (3,4-ethylenedioxythiophene)/carbon nanotubes composites. J Phys Chem Solids 65 (2):295–301
70. Wang J, Too CO, Wallace GG (2005) A highly flexible polymer fibre battery. J Power Sources 150:223–228
71. Park JH, Kim JH, Lee HK et al (2004) A novel direct deposition of Pt catalysts on Nafion impregnated with polypyrrole for PEMFC. Electrochim Acta 50(2):769–775
72. Kim BC, Ko JM, Wallace GG (2008) A novel capacitor material based on Nafion-doped polypyrrole. J Power Sources 177(2):665–668
73. Zhang LL, Li HH, Fan CY et al (2015) Polypyrrole nanosphere embedded in wrinkled graphene layers to obtain cross-linking network for high performance supercapacitors. Electrochim Acta 184:179–185
74. Gan JK, Lim YS, Huang NM et al (2015) Effect of pH on morphology and supercapacitive properties of manganese oxide/polypyrrole nanocomposite. Appl Surf Sci 357:479–486
75. Ru-Shi L (ed) (2012) Controlled nanofabrication: advances and applications. CRC Press, Boca Raton, p 508
76. Pettersson LAA, Carlsson F, Inganäs O et al (1998) Spectroscopic ellipsometry studies of the optical properties of doped poly(3,4-ethylenedioxythiophene): an anisotropic metal. Thin Solid Films 313:356–361
77. Czardybon A, Lapkowski M (2001) Synthesis and electropolymerisation of 3,4-ethylenedioxythiophene functionalised with alkoxy groups. Synth Met 119(1–3):161–162
78. Tong L, Skorenko KH, Faucett AC et al (2015) Vapor-phase polymerization of poly (3,4-ethylenedioxythiophene) (PEDOT) on commercial carbon coated aluminum foil as enhanced electrodes for supercapacitors. J Power Sources 297:195–201
79. Zhao Q, Wang G, Yan K et al (2015) Binder-free porous PEDOT electrodes for flexible supercapacitors. J Appl Polym Sci 132(41):9
80. Laforgue A (2011) All-textile flexible supercapacitors using electrospun poly (3,4-ethylenedioxythiophene) nanofibers. J Power Sources 196(1):559–564
81. Wagner H (2012) Influence of temperature on electrical conductivity of diluted aqueous solutions. Power Plant Chem 14(7):455–469

82. Usobiaga A, de Diego A, Madariaga JM (2000) Electrical conductivity of concentrated aqueous mixtures of HCl and KCl in a wide range of compositions and temperatures. J Chem Eng Data 45(1):23–28

83. Isono T (1984) Density, viscosity, and electrolytic conductivity of concentrated aqueous electrolyte solutions at several temperatures. Alkaline-earth chlorides, lanthanum chloride, sodium chloride, sodium nitrate, sodium bromide, potassium nitrate, potassium bromide, and cadmium nitrate. J Chem Eng Data 29(1):45–52

84. Wang H, Hao Q, Yang X et al (2010) Effect of graphene oxide on the properties of its composite with polyaniline. ACS Appl Mater Interf 2(3):821–828

85. Niedermeyer H, Hallett JP, Villar-Garcia IJ et al (2012) Mixtures of ionic liquids. Chem Soc Rev 41(23):7780–7802

86. MacFarlane DR, Forsyth M, Izgorodina EI et al (2009) On the concept of ionicity in ionic liquids. Phys Chem Chem Phys 11(25):4962–4967

87. Achuthan S, Chung BJ, Ghosh P et al (2011) A modified Stokes–Einstein equation for A β aggregation. BMC Bioinform 12(10):1

88. Seki S, Hayamizu K, Tsuzuki S et al (2009) Relationships between center atom species (N, P) and ionic conductivity, viscosity, density, self-diffusion coefficient of quaternary cation room-temperature ionic liquids. Phys Chem Chem Phys 11(18):3509–3514

89. Keskin S, Kayrak-Talay D, Akman U et al (2007) A review of ionic liquids towards supercritical fluid applications. J Supercrit Fluid 43(1):150–180

90. Francisco BE, Jones CM, Lee SH et al (2012) Nanostructured all-solid-state supercapacitor based on Li_2S-P_2S_5 glass-ceramic electrolyte. Appl Phys Lett 100(10):103902

91. Wang X, Hou Y, Zhu Y et al (2013) An aqueous rechargeable lithium battery using coated Li metal as anode. Sci Rep 3:1401

92. Chou SL, Wang YX, Xu J et al (2013) A hybrid electrolyte energy storage device with high energy and long life using lithium anode and MnO_2 nanoflake cathode. Electrochem Commun 31:35–38

93. Ohtomo T, Hayashi A, Tatsumisago M et al (2013) All-solid-state lithium secondary batteries using the $75Li_2$ S·$25P_2S_5$ glass and the $70Li_2S$·$30P_2S_5$ glass-ceramic as solid electrolytes. J Power Sources 233:231–235

94. Chen PC, Shen G, Sukcharoenchoke S et al (2009) Flexible and transparent supercapacitor based on In_2O_3 nanowire/carbon nanotube heterogeneous films. Appl Phys Lett 94 (4):043113

95. Capiglia C, Mustarelli P, Quartarone E et al (1999) Effects of nanoscale SiO_2 on the thermal and transport properties of solvent-free, poly(ethylene oxide)(PEO)-based polymer electrolytes. Solid State Ionics 118(1):73–79

96. Yu H, Wu J, Fan L et al (2011) Improvement of the performance for quasi-solid-state supercapacitor by using PVA–KOH–KI polymer gel electrolyte. Electrochim Acta 56 (20):6881–6886

97. Kamaya N, Homma K, Yamakawa Y et al (2011) A lithium superionic conductor. Nat Mater 10(9):682–686

98. Foertig A, Baumann A, Rauh D et al (2009) Charge carrier concentration and temperature dependent recombination in polymer-fullerene solar cells. Appl Phys Lett 95(5):052104

99. Sproul AB, Green MA (1993) Intrinsic carrier concentration and minority-carrier mobility of silicon from 77 to 300 K. J Appl Phys 73(3):1214–1225

100. Li L, Qiu J, Wang S (2013) Polyaniline nanowire-pillared graphene for supercapacitor electrode. Soft Mater 11:503–509

101. Li L, Qiu J, Wang S (2013) Three-dimensional ordered nanostructures for supercapacitor electrode. Electrochim Acta 99:278–284

102. Wu J, Tang Q, Li Q, Lin J (2008) Self-assembly growth of oriented polyaniline arrays: a morphology and structure study. Polymer 49:5262–5267

103. MacDiarmid A, Epstein A (1995) Secondary doping in polyaniline. Synth Met 69:85–92

104. Li L, Zhang X, Qiu J et al (2013) Reduced graphene oxide-linked stacked polymer forests for high energy-density supercapacitor. Nano Energy 2(5):628–635

105. Sheng K, Sun Y, Li C et al (2012) Ultrahigh-rate supercapacitors based on eletrochemically reduced graphene oxide for ac line-filtering. Sci Rep 2:247
106. Miller J, Outlaw R, Holloway B (2010) Graphene double-layer capacitor with ac line-filtering peformance. Science 329:1637–1639
107. Wang R, Huang L, Tian X (2012) Understanding the protonation of polyaniline and polyaniline–graphene interaction. J Phys Chem C 116:13120–13126
108. Li L, Wang S, Hui D et al (2015) Ordered multiphase polymer nanocomposites for high-performance solid-state supercapacitors. Compos Part B-Eng 71:40–44
109. Bard AJ, Faulkner LR, Leddy J et al (1980) Electrochemical methods: fundamentals and applications. Wiley, New York, pp 99–231

Chapter 9
Conducting Polymers/Inorganic Nanohybrids for Energy Applications

Prakash Sengodu

Abstract Conducting polymers/inorganic nanohybrids embrace the key to basic advances in electrical energy system, which are very important in order to meet the challenge of global warming and the finite nature of fossil fuels. This architecture has opened the possibility to combine in a single material both the attractive properties of a mechanically and thermally stable inorganic backbone and the specific chemical reactivity, dielectric, ductility, flexibility, and processability of the conducting polymer. Nanohybrids in particular offer combinations of properties as electrodes in a range of electrical energy devices. This chapter explains some recent developments in the discovery of electrodes for rechargeable batteries, fuel cells, and supercapacitors. The advantages and disadvantages of the conducting polymers/inorganic hybrid electrode design for such devices are also discussed.

9.1 Introduction

Electrochemical energy systems (EES) have concerned much attention as clean and safe energy sources due to their high conversion/storage efficiency and environmental compatibility. Recently, supercapacitors, rechargeable batteries, and fuel cells are attracting remarkable research interest among different EES [1]. For example, pumped hydro storage, thermal energy storage, compressed air energy storage, and flywheel energy storage [2] are due to their unique energy storage properties. The ability to deliver large amounts energy near instantaneously with a simple device that can last over millions of cycles is making EES one of the most attractive future options for large scale of them. The basic operation mechanism of the three different energy systems was presented in Fig. 9.1.

Supercapacitors is an electrical component capable of holding hundreds of times more electrical charge quantity than a standard capacitor and released at the interface of electrode and electrolyte. It covers short time (1–10 s), longer life

P. Sengodu (✉)
Department of Chemistry, National Taiwan Normal University, Taipei, Taiwan
e-mail: prakas.chemist@gmail.com
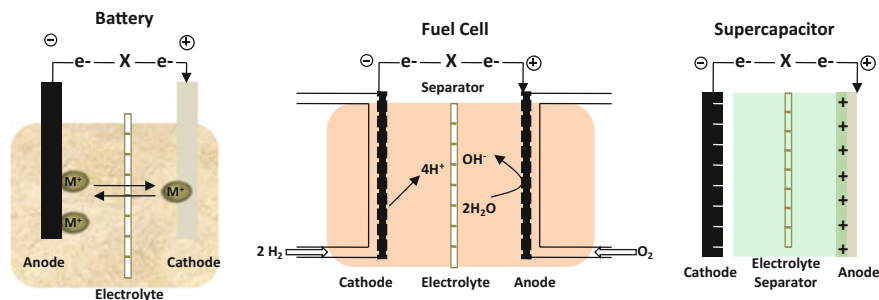
Fig. 9.1 Schematic diagram of a battery energy storage system operation, fuel cells, and supercapacitors (Reproduced from Ref. [1] with kind permission of © 2012 Elsevier and Reproduced from Ref. [4] with kind permission of © 2015 Royal Society of Chemistry)

Fig. 9.2 Ragone plots for batteries, fuel cells, electrochemical capacitors, and internal combustion (IC) engine (Reproduced from Ref. [2] with kind permission of © 2011 Elsevier)
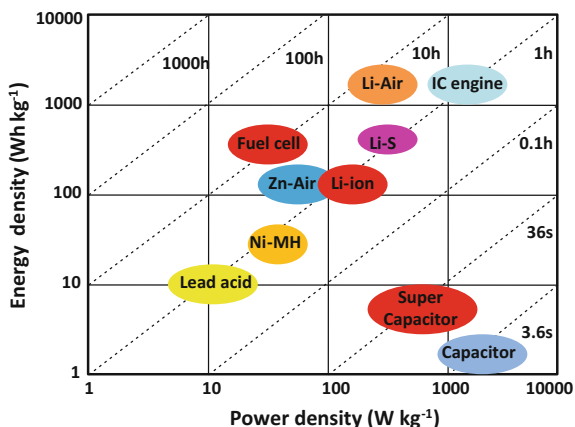
(1 million or 30,000 h), and high power (up to 10,000 W kg^{-1}). A rechargeable battery is an energy storage device that can be charged again after being discharged by applying DC current to its terminals. They are being of 10–60 min charge time, over 500 cycle life, and high specific energy 100–200 Wh/g. In contrast to battery' close systems, fuel cells are open systems where both electrodes are just charge transfer media and active materials undergoing redox reactions are delivered from outside. Electrodes and electrolytes are having the issues of poor stability and decomposition nature which leads to hurdle in practical applications in different EES. The performance of EES can be characterized by many key parameters such as specific capacity (mAh g^{-1}), coulombic efficiency (%), cycle life (maintain certain percentage of its initial capacity during cycles in batteries), specific energy density (Wh kg^{-1}), and specific power density (W Kg^{-1}). Last two parameters are significant key characteristics of EES are given as Ragone plots in Fig. 9.2.

Recent years, design and fabrication of electrodes have gained much interest in EES applications. The topic of electrode properties has also remained an important

area of research activity. With respect to EES, much emphasis has been placed on the fabrication and characterization of nanohybrids [3, 4]. They are also of great research interest as emerging electrode in academia and industry due to their structural diversity, flexibility, and tenability as well as high porosity, and, thus, a wide spectrum of applications toward sensors, solar energy, batteries, and supercapacitors have been investigated [5]. Interest in inorganic compounds is motivated by their potential applications to EES [6], due to their crystalline nature, electronic conductivity, and stability. Inorganic materials are also playing diversified roles in different systems [7]. In general, good crystalline, excellent conductivity, and redox properties make them suitable as "electrodes" (anode and cathode), and photo-catalysts (due to their nanometer size and structure) [8, 9].

The progress of conducting polymer-inorganic nanohybrid materials is special trendy in the past decade. This is indicated by the ever growing number of symposia, books, and particular journals that are devoted to this subject. They parallel the demanding research activity in complex systems at the atomic/molecular scale (nanometer scale) of polymer species of diverse functionality with inorganic entities, generally based on silica or silicates. Hybrid materials defined as solids resulting from the combination of two or more simple materials that develop a continuous phase (polymer, metal, ceramic, etc.), and a dispersed phase, such as glass fibers, carbon particles, silica powder, and clay minerals. They have essentially properties of different from the components taken separately. Within the huge collection of conducting polymer-inorganic composites, nanohybrids are an emerging group that received a great deal of attention not only because of their potential in industrial applications.

Conducting polymers (CPs) have not just used in the EES but also used to do so independent of form factor, and their mechanical properties are like to those of a plastic, allowing them to desire shapes [10–12]. CP electrodes possibly incorporated impeccably into conductive paper, textiles, data tattoos, structural panels, and the traditional prismatic or cylindrical cell [13–15]. Further, directly used in combine plastic power with polymer solar cells and light emitting diodes in a streamlined manufacturing process to produce cheap flexible devices [15, 16]. Many advantages of synthetic tailorability, cost, and processability make them ideal candidates for EES [17, 18]. Synthetic methods are effectively changed the properties of CPs [19]. Also the raw materials and methods are often cost-effective to make these CPs. Latest synthetic methods have improved processability by screen printing, doctor blading, or inkjet printing [20, 21].

Mainly, conducting polymers are perfect materials for nanohybrid in EES. The unique properties aroused from conducting backbone, electrical conductivity, and high molecular weight [15, 22–24]. Conductivity properties obtained from interchanging single and double carbon–carbon bonds with polymeric chains and can be assigned to reversible chemical, electrochemical, and physical properties controlled by a doping process. Particular interest of conducting polymer in EES has focused on the polyaniline (PANI), polypyrrole, and polythiophene (PT) and derivatives [25, 26] due to the presence of broad background research, the industrial user-friendliness of both monomers and polymers, and their ease of synthesis.

Inorganic materials have high surface area, as characterized by their clean and readily accessible surfaces, highly conductive open framework structure for easy transport of molecules and electrons and tunable surface chemistry, which are desired in fuel cells. With unique structures of inorganic material can serve as both supports of active materials, which benefits from good electron conductivity, electrolyte penetrability, and high energy density with power density can be received in supercapacitors and batteries. But, inorganic materials problems of cost, lack the conductivity, stability, and life cycles required for commercial application. In order to overcome this problem, conducting polymers can synergistically with inorganic materials through synthetic modification, processing option, and mechanical flexibility that can results in power sources, which can be designed to suited the electrical devices [27–29].

In this chapter, we have discussed the synthesis of conducting polymers/inorganic nanohybrids and their application for the performance of fuel cells, batteries, and supercapacitors. The chapter includes the brief literature surveys, properties, and electrochemical properties of various inorganic nanomaterials, nanofillers in polymer electrolytes and the conducting polymers. Furthermore, numerous recent advances in the field have made remarkable advance in addressing these issues and will be discussed.

9.2   Conducting Polymers

9.2.1   Activity of Conducting Polymers in EES

In fuel cells, CPs are typically used as a catalyst support to substitute or partially substitute both the generally used carbon support and the Nafion in the catalyst layer, and occasionally directly as metal-free catalysts. When CPs are used, a two-phase boundary in the catalyst layer is adequate for the electron and proton transport for the electrochemical reaction. As compared to the three-phase boundary while carbon is used as a catalyst support, because CPs are permeable to gases and water and exhibit both electronic and ionic conductivity [30]. CPs enabled removal of ionomers in a fuel cell catalyst layer could provide a new way for using low-Pt loading technology without suffering significant oxygen transport loss via ionomers, thus providing a major possibility for low-cost, commercially viable fuel cells. In rechargeable batteries, during the charge/discharge process, the anode materials undergoes large volume change (>300%). It causes vast damage in material and thus leads to cracking and crushing of particles. It gives poor reversible capacity and first cycle irreversible capacity loss. The secret is a tailored CP that conducts electricity and binds closely to Li/Na-storing particles along with advantages of low cost and compatibility. Even as they increase to more than three times their volume during charging, they shrink again during discharge. Also, some articles claimed CPs as anode for batteries based on their doped (oxidized or

reduced) state [31]. CP is a cathode also satisfactorily combined with inorganic redox oxides, giving systems suitable for electrochemical Li intercalation and improves performance. Polymers can decrease the polarization between the cathode particles and the electrolyte, promote electrolyte permeation into the surface of the active particles and hence enhance metal insertion-extraction during cycling process. There were many reports on the role of PANI in the cathode materials, such as improvement in the electrical conductivity, decrease in the polarization, and promoting the electrolyte [32–34].

Table 9.1 presents comparisons between commercial electrodes and conducting polymers [35–42]. CPs have mainly used as electrode in SC, due to their high redox-active capacitance, high conductivity, and, most importantly, high intrinsic flexibility, but relatively low mechanical stability and cycle life constraint their performances. Importantly, among the variety of the materials explored for SC applications, in the last years, CPs have drawn a greater deal of interest for flexible application, due to their inherent flexible polymeric nature, which is a crucial requirement for the portable flexible electronic. Table 9.2 showed the electrochemical properties of conducting polymers in compared with inorganic particles and carbon-based materials for supercapacitors [43].

9.2.2 Preparation of Conducting Polymers

Conductive polymers (CPs) defined as organic polymers that conduct electricity and may have metallic conductivity or can be semiconductors. Table 9.3 shows the conductivity of reported CPs [44, 45]. They have high electrical conductivity but poor mechanical properties compared to other commercially available polymers. The electrical properties can be changed by using the methods of organic synthesis and advanced dispersion techniques [46, 47]. Nobel laureates namely Heeger, MacDiarmid, and Shirakawa were discovered the metallic conductivity of polymer
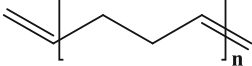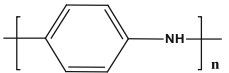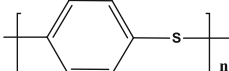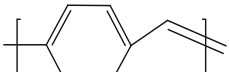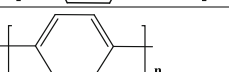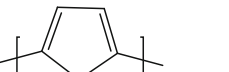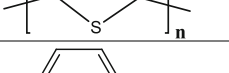
Table 9.1 Performance characteristics of conducting polymers as compared to current inorganic Li battery materials

Electrode	Voltage versus Li/Li$^+$	M_{wt} of repeating unit	Capacity (mAh g^{-1})		Energy density (mWh g^{-1})	Power density (mWh g^{-1})
			Theor.	Expt.		
Graphite [33]	∼0.1	12	372	360	372–744	–
LiCoO$_2$ [34]	∼3.8	97.9	274	135	30–144	100–1000
LiFePO$_4$ [35]	∼3.2	157.8	170	109	90–100	23–70
Polythiophene [36, 37]	3.1–4.0	82.1	326	82	93	89
Polypyrrole [38, 39]	3.0–4.0	65.1	412	82	60	10
PEDOT [40]	2.7–4.2	140.2	191	30–70	1–4	35–2500
Polyaniline [41]	3.0–4.0	91.1	294	100–147	300	100

Table 9.2 Physicochemical properties of the various supercapacitor materials

Physicochemical properties	Inorganic particles	Conducting polymers	Carbon materials
Conductivity	Low	Very high	Very high
Faradic capacitance	Very high	Very high	Very low
Non-faradic capacitance	Medium	Medium	Very high
Energy density	High	Medium	Low
Power density	Low	Medium	High
Price	High	Medium	Medium
Chemical stability	Low	High	Very high
Cycle life	Medium	Medium	Very high
Easy fabrication process	Low	High	Medium
Flexibility	Very low	High	Medium

Table 9.3 Some of the most important conducting polymers, conductivity, and type/doping

Polymer		Conductivity (S cm^{-1})	Type/ doping
Polyacetylene		200–1000	n, p
Polyaniline		1–100	p
Polyparaphenylene sulfide		3–300	p
Polyparaphenylenevinylene		1–1000	p
Polyparaphenylene		500	n, p
Polypyrrole		40–200	p
Polythiophene		10–100	p
Polyisothianaphthalene		1–50	p

in polyacetylene (PA) [48]. The main tasks of those synthetic procedures were to overcome their problem of its insolubility and unprocessability [49]. Some of synthetic methods represented innovative strategies in macromolecular synthesis and were responsible for the chemical evolution of the polymer field. In recent times, many methods have also been working for the synthesis of hybrid composites for different applications and presented in Table 9.4. Ziegler–Natta catalyst, Ti(OBu)$_4$/AlEt$_3$, and NaBH$_4$/Co(NO$_3$)$_2$.6H$_2$O catalysts have studied [50–52]. Physically blending method used for stable conducting polymers syntheses by conjugated polymers with certain non-conjugated macromolecules [53] and chemically synthesizing conducting polymer colloids [54] or conjugated oligomers [55].

Further, the soluble polymers were prepared by the random and alternating copolymerization, block and graft copolymerization, and substitution methods. Typically, the chemical properties of a polymer can changed by substitution of functional groups, polyacetylene grafted with methyl or phenyl side groups was reported [56], and poly(3-alkylthiophenes) meltable and soluble in most common organic solvents by 3-bromothiophene prepared (Scheme 9.1) [57]. Introducing alkyl side groups [58], and grafting with –SO$_3$H, –COOH, –OH groups onto pyrrole and aniline were synthesized for allowing the formation of water-soluble CPs [59]. Copolymerization of CPs with various soluble parts provides an alternative way to circumvent the intractability of polymers. The combination of optoelectronic properties characteristic of conjugated structures and the solubility of the polymeric segments into a single copolymer chain should, in principle, lead to a material with properties trait of both the constituent components. For highly soluble stilbenoid dendrimers, alkoxy chains group substituted at the peripheral benzene rings have synthesized (Scheme 9.2) [60].

For CPs film formation, they developed spin coating, precursor route, and electropolymerization methods. The spin coating method suggests excellent possibilities for advanced device fabrication, but the problems of the quality of polymer films, thus formed, such as possible weakening of the films mechanical properties by chemical modification of their structures, the reduction of device stability by trapped impurities, and complexity in choosing suitable solvent for preparing pinhole-free multi-layer polymer thin films. Thermal conversion of soluble non-conjugated precursor polymers has tried to avoid the intractability of formation of conjugated polymers. The ring-opening metathesis polymerization (ROMP) of cyclobutene derivatives, followed by thermal conversion into polyacetylene with the evolution of bis(trifluoromethyl)benzene reported by Edwards and Feast et al. (Scheme 9.3). The potentiostatic and potentiodynamic techniques have been used for electrochemical polymerization of electronically conducting polymers. Pyrrole can be polymerized onto electrode using a two-electrode electrochemical cell based on radical mechanism under potential or current (Scheme 9.4) [61]. Ammonium persulfate (chemical oxidant) is also used to offer the driving force for electrochemical synthesis of CPs to the surface of a submerged electrode [62]. As this type is carry out in an oxidizing environment, the ensuing polymers are formed in an already doped state. For instance, oxidative polymerization of aniline as emeraldine

Table 9.4 List of the synthesis methods of conducting polymer—inorganic hybrid composites and their merits and demerits

Methods	Advantages	Disadvantages
Ex situ methods	More suitable for large-scale industrial applications than the in situ method	The preparations of particles possess higher dispersibility in the polymer and have long-term stability against aggregation; in this process, the dispersion of the nanoparticles in polymer matrix is difficult
In situ methods	Prevents inorganic particle agglomeration while retain a good spatial distribution in the polymer matrix	The un-reacted products of the in situ reaction might influence the properties of the final materials
Mechanical methods	The cost of power and grinding medium is low, and it is suitable for both batch and continuous operation and for open with closed circuit grinding and is applicable for materials of all degrees of hardness	Contamination, long processing time, no control on particle morphology, agglomerates, and residual strain in the crystallized phase
Blending inorganic nanoparticles into polymer matrix	Reproducibly fabrication with controlled levels of electrical conductivity, and retaining the desired mechanical properties of the matrix, low-cost synthesis and avoid the oxidants or reductant chemicals	Difficulty in desired structure and properties, uniformless particles distribution
Nanostructured polymer with inorganic particles	Well-connected inorganic nanoparticles into polymers via chemical or physical bonding, soluble systems if they maintain solubility after nanoparticle formation are their potential use as thin film or free-standing films	Requiring the choice of the functional group have to introduce to polymers for interaction with inorganic particles
Sol–gel process	This method is good crystallinity, homogeneous mixing at the atomic or molecular level, low synthesis temperature, short heating time, good stoichiometric control, uniform particle size and small diameter, and down to nanometer level	High shrinkage, low yield, high precursor costs, acidic gases evolved during pyrolysis, and limited shelf life of sols
Surfactant-free solution processes	Simple physical attraction process without external surfactants	Relatively poor control of the uniformity of the shape and diameter
Layer-by-layer	Simple, cheap, and thin-film deposition method. Important quality of it is the high degree of control over thickness, which arises due to the linear growth of the films with the number of bilayers	Slow deposition, waste of materials, and small surface areas

Table 9.4 (continued)

Methods	Advantages	Disadvantages
Self-assembly	large variety of shapes and functions on many length scales can be obtained	more problematic due to many free parameters that require control
Microemulsion polymerization method	Enabling fast polymerization rates without loss of temperature control, the viscosity of the reaction medium remains close to that of water, and the final product can be used as is and does not generally need to be altered or processed	An unwanted product difficult to remove from final composite and water removal is an energy-intensive process for isolated the composites
Template method	Controllable length and diameter of nanotubes or wires	A post-synthesis is needed to remove the template
Ion exchange process	Reversible process and regenerated or loaded with desirable ions by washing with an excess of these ions	Dependent on the size of the ions, their charge, or their structure, final product can be formed

Scheme 9.1 Representation of the most common route to poly(3-alkylthiophenes)
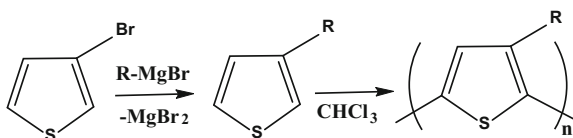
salt state of PANI and reductive polymerization of thiophene (n-type polymers) have been synthesized.

Nanostructured conducting polymers (NCPs) are synthesized by versatile methods for suitability in their applications. The detail discussion of NCPs synthetic method reported by Long et al. [63]. The hard template method has been reported to the aligned arrays of tubes and wires with controllable length and diameter, which problems of a need of post-synthesis process for template removal. For example, MnO_2/poly(3,4-ethylenedioxythiophene) (PEDOT) coaxial nanowires were prepared by co-electrodeposition in a porous alumina template. Soft template method is popular technique to produce CPs, but it is not uniform morphology oversamples, example of PANI micro/nanostructures. Beside, structure-directing molecules, surface micelles, surfactants, liquid crystalline, colloidal particles, phases, and aniline oligomers worked as soft templates have been developed: rapidly mixed reactions, reverse emulsion polymerization, template-free method, ultrasonic irradiation, interfacial polymerization, dilute polymerization, and radiolytic synthesis [64–71]. The interfacial polymerization process involves step polymerization of two monomers are dissolved, respectively, in two immiscible phases; thus, the reaction takes place at the interface between the two liquids. It is usually based on self-assembly mechanisms using hydrogen bonding, van der Waals forces, double bond stacking, and electrostatic interactions as driving forces [63, 64].
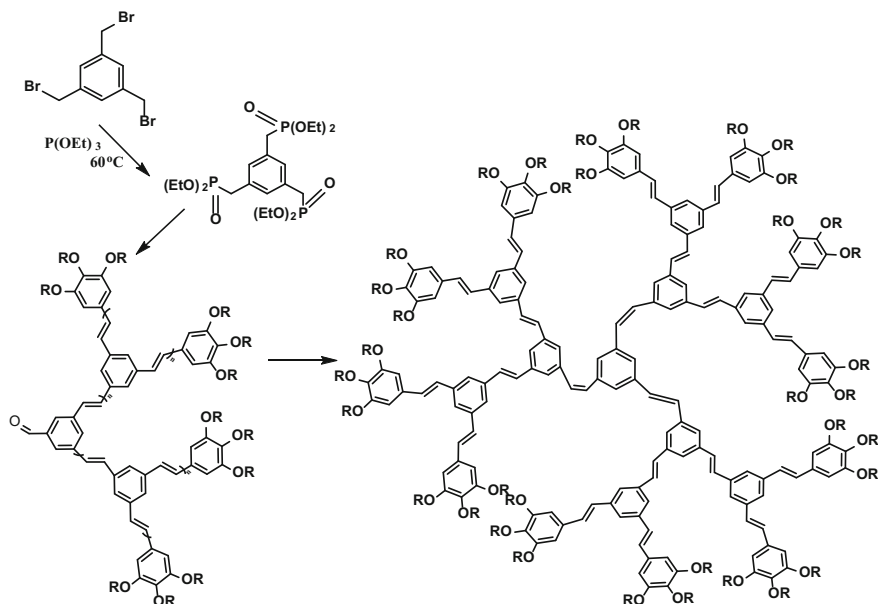
Scheme 9.2 Preparation of highly soluble stilbenoiddendrimers contains alkoxy chains substituted at the peripheral benzene rings
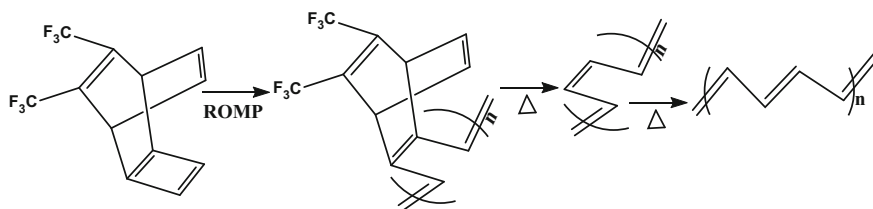
Scheme 9.3 Durham synthetic method to polyacetylene (PA)

The template-free method as simple self-assembly without an external template was proposed by Wan et al. PANI, and PPy nanostructures can be synthesized by in situ doping polymerization in the presence of dopants by controlling synthesis conditions, including temperature and molar ratio of monomer to dopant. In the self-assembled formation mechanism, the micelles formed by dopant and/or monomer dopant work as soft templates in the process of forming tubes/wires [66]. Up to now, different polyaniline micro/nanostructures were established.

Electrospun is an efficient approach to construct long polymer fibers with diameter from microns to nanoscale by using strong electrostatic forces [72, 73]. For example, micro/nanofibers of PANI/polyethylene oxide (PEO) have been prepared [74]. Soft lithography is a costless method to shape an initially flat polymer film by using a micromold in the presence of temperature or solvent
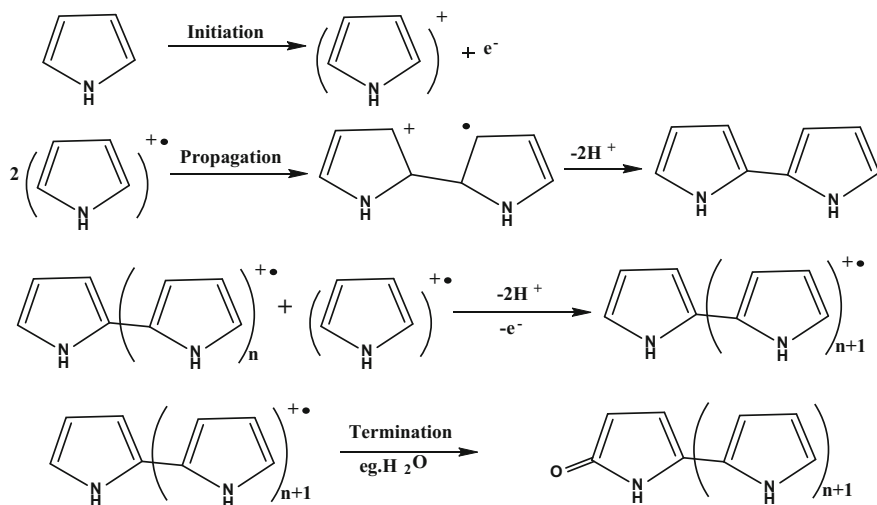
Scheme 9.4 Electrochemical synthesis mechanism of pyrrole and suitable for most of other conducting polymers

vapors. Recently, nanoimprint lithography and a lift-off process have been proposed for patterning of CPs [75]. In direct electrochemical nanowire assembly technique, CP wire is electrochemically polymerized and assembled onto two biased anode and cathode electrodes immersed in aqueous monomer solutions [76]. Nanolithography has used to the fabrication of luminescent nanostructures and controlled sized CP nanowires using dipper [77]. Recently, production of self-assembled CP nanofibers by a using anisotropic crystallization in a nematic liquid crystal, and obtain large-scale alignment of the nanofibers [78].

9.2.3 Intention of Conducting Polymer

To understand the function of conducting polymers (CPs) within the structure of an electrode, first we must judge the basic properties of CPs themselves. The conductivity and charge storage ability rely on electronic properties not possessed by aliphatic group of polymers and occur from the overlap of adjacent p-orbitals. Backbone and molecular orbitals of a conjugated polymer provide the band structure like to that observed in inorganic semiconductors [48]. The effective conjugation length is the point at which no extra monomer units added to the chain affect the electronic properties of the polymer [79]. Conduction band HOMO and LUMO values of polymers energy levels were caused stability, optical absorption wavelengths, and whether a polymer is more likely to be n-type or p-type [80]. The LUMO decreases and HOMO increases in energy with rising conjugation

length. Polymer is more susceptible to electrophiles due to its high HOMO level, i.e., more reactive.

They are two types of n-type and p-type polymers with counterions dopant. Owing to ability to stabilize a positive charge, the electron-rich polymers that have elevated HOMO levels formed p-type materials, to stabilize negative charges, the electron-poor polymers that have low-lying LUMO levels formed n-type materials [81]. p-doped polymers worked as cathodes and much work on them, but little reports on n-doped polymers as anodes [82]. Both electrodes have to be used in flexible EES applications and thus need to research new n-type electrode materials also. CPs can be doped by chemical and electrochemical process [83] as p- or n-doping process is presenting in Fig. 9.3. During doping process, create radical cations or anions (positive/negative polarons) and delocalized with the polymer backbone. This is proposed conductivity mechanism [4]. Charge delocalization is coupled to structural reform to quinoidal and changed fundamental molecular vibrations [84]. UV/vis and IR/Raman spectra can be used to look a new sub-gap energy states and formation of quinoidal structure [84]. Generally, in their native state having poor conductivities, on the order of 10^{-4}–10^{-9} S/cm, when doped, it can reach high conductivities [85]. Redox reactions coupled with polymer doping are concomitant with the movement of ions into and out of the polymer matrix for neutral balance [72]. However, oxidation generally results in anion movement within the film. Also cation movement occurs in certain conditions [86] and can occur for anions during polymer reduction. Raise the dense polymer films tends to
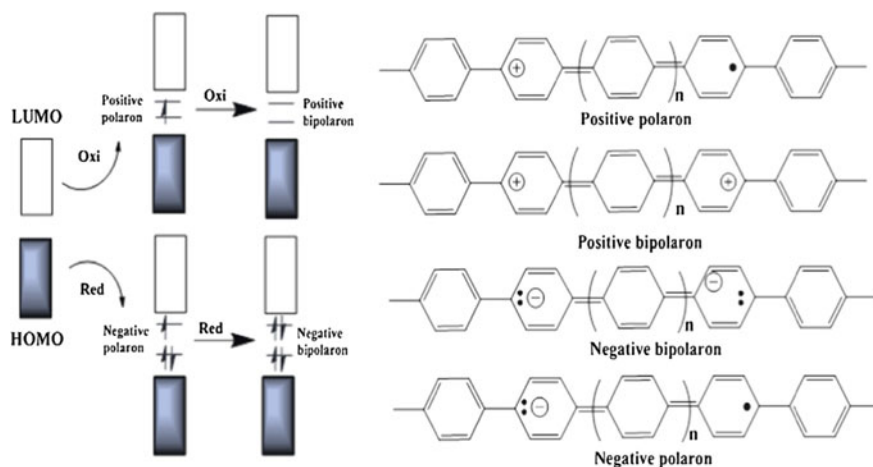
Fig. 9.3 Electronic and chemical structural change of polyphenelyene during oxidation (p-doping) and reduction (n-doping). A radical cation (positive polaron) formed from oxidation, and a radical anion (negative polaron) formed from reduction. High states of charging resulted to the creation of positive and negative bipolarons. Cations and anions counterbalance charges in the polymer chain (Reproduced from Ref. [4] with kind permission of © 2015 Royal Society of Chemistry)

react more slowly due to ion transport limitations and caused the lower capacities, lower energy, and power densities [86].

Nanostructured polymer such as nanowires, nanotubes, and nanoparticles can assist to improving the ion diffusion by increasing the surface area and porosity [87]. Further oxidative stability, ion diffusion also influences the electrodes performance. The specific capacity of the electrode determines by the number of monomer units over which a charge is delocalized. This amounts to one unit of charge for every two to three monomer units although higher levels of charging are likely for most polymers [72]. Higher levels of oxidation or reduction cause to higher specific capacity of polymers, but high levels of charging can lead to deterioration of the polymer matrix via useless interchain interactions or collapse of polymer chains [88]. Highly charged species are much more likely to react with common electrolytes and oxygen in the air, as well [101]. Low capacities can be alleviate to a limited extent by selection of dopant ion, electrolyte, or polymer structure [88]. There is evidence those strong interactions between the highly charged or doped polymers and a complementary polyion can serve to stabilize well-oxidized polymers [89]. Deficiencies associated with stability over many charge cycles have seen enhancements with select composite materials of carbon nanotubes or graphene [90].

9.2.4 Advantage and Disadvantage of Conducting Polymers

The majority research interests of conducting polymer are polyaniline (PANI), polypyrrole (PPy), and polythiophene (PT) due to their oxidative stability, relatively high theoretical capacity, simple synthesis, and electro-redox nature [36]. Other conducting polymer, i.e., polyphenylenes, polyacetylene, polyazule, polyindole, and polycarbazole also has been studied [91–96]. PANI electrodes construct use of the reversible reactions between fully reduced and partially oxidized salt state. Cycling stability can collapse as emeraldine salt irreversibly oxidizes to pernigraniline base due to their reaction pathway to pernigraniline salt is not favoured at higher potentials [97]. Stabilize the pernigraniline salt by et al. for the improved capacity and energy density [27]. However, there are problems of poor solubility, diffusion issues, and stability. Insolubility and intractability are habitually considered to be the main issues obstructing its usage in batteries [98]. To overcome it by traditionally been attended by dispersing the polymer in solutions using a series of steps intended to remove aggregates and ensure a stable suspension [99]. Doped the polyanions with nanofibers has permitted the suspension of PANI [99] and promote it mixed with carbon used to keep conductivity when PANI has conductive less state [98–100], but still has inferior capacity versus redox-active materials owing to the non-Faradaic nature of charge storage [101, 102]. To avoid the templates, additives, or difficulty techniques, PANI can also be made cheaply and quickly in solution [103], but its intractability issues as it is easily suspended in solution and stays thus for longtime periods [100]. As polymer hybrid composite shows

promising material in terms of higher conductivity for EES. Prakash et al. reported the good conductivity with even lower loadings of PANI/polyelectrolyte [poly (diallyldimethylammonium chloride)] as 4.5–42 mS cm^{-1} [11]. Because the two components work together synergistically to improve efficiency and charge transport, polymer composites have promise material for EES. Several ways have been developed to increase charge capacity without compromise polymer properties by including redox-active components in the polymer structure. Goodenough group worked in both high capacity and long-term cyclability of polypyrrole (PPy) via covalently anchoring ferrocene groups to the polymer [104], ferrocene-functionalized triphenylamine polymer, and a 2,2,6,6-tetramethylpiperidine-N-oxide-functionalized polythiophene (PT) [105, 106].

Also, some improvement was seen for PEDOT and PT [107] that since the Fermi level of cyanide anion was close to that of the polymers used in the study, the anion served as a mediator for charge transfer between them [63]. Tuned morphology of poly(3-alkylthiophenes) has been linked to better capacitance, conductivity, and stability [108]. A major issue is lack of reliable synthetic methods to make bulky quantities. Polyfluorene stabilizing silicon nanoparticles in a composite anode [29], and the better cycle life is ascribed to the polymer reversible lithium doping and the formation of an intimate composite. More, side-chain functionalization can be used to stabilize polythiophenes to n-doping [109]. One more concern, diffusion limitations are source of the poor response times at high current with small power efficiencies. Self-doped polymers have ionic side chains help to fast response times and improved processability, but problem of low conductivities [110, 111]. This can be improve by an extent with nanostructuring [111–113]. Diffusion limitations problem solved by the block copolymers of conducting PT and poly(ethylene oxide) was used to form films, and the resulting material was successfully employed in a solid-state battery [114, 115].

In another way, pyrrole, aniline, and thiophene are monomers of electronically conducting polymers; they have unique properties, such as good environmental stability, electroactivity, and unusual doping/de-doping chemistry, thus suitable for active electrode material usage in supercapacitors. While used as electrode materials, polymers have benefit over carbon-based materials because they have both electrochemical double-layer capacitance and pseudocapacitance arises mainly from the fast and reversible oxidation and reduction processes related to the π-conjugated polymer chain. But, CPs have problems of typical volumetric shrinkage during ions ejection (doped ions) and poor conductance at de-doped state. They would result in high ohmic polarization of supercapacitors. To overcome this problem, CPs were mixed with metal oxides to form nanocomposites and the synergistic effect of the polymer-metal oxide nanocomposites has been exploited. They were found to have the advantages of polymers such as flexibility, toughness, and coat-ability, and metal oxides such as hardness and durability. They also possess some synergetic properties which are different from that of parent materials.

Serious problem is in fuel cells to commercialization and how to reduce the cost of Pt catalysts by rising its catalytic efficiency and durability under the harsh working conditions [116]. The performance also depends on the properties of the

gas flow in the membrane electrode assembles (MEAs) [117] in which interfacial areas between the reactant, electrolyte, and catalyst itself (triple phase boundary) play important roles on the catalytic efficiency of Pt catalyst. To increase the electricity productivity of a PEMFC, the catalyst supporting material in the MEAs needs to own good conducting capability for both ion and electron except improving the Pt loading %.

In other words, we need lots of continuous pathways for the produced protons to pass through and then go into the electrolyte layer and also for the electrons to go into or out of the circuit. Subsequently, continuous catalyst supports with high porosity and conductivity was needed to allow the produced electrons, protons, and water to move faster. It can prepare conducting catalyst supports with nanoscaled pores to accept and disperse the implanted Pt [118]. Considering the continuous conducting pathway for electron transportation, conducting polymer is the only option because of their high surface area and porosity when they are directly electrochemically polymerized on the electrode in acidic media [119]. Functionalized Pt/PA-F composite demonstrated high performance in a single-cell testing developed [118]. To deposit Pt nanoparticles on PANI and single-walled carbon nanotubes (SWCNTs) by building up alternating layers of PANI-supported catalyst and high power densities was achieved [120]. The morphology-dependent electrochemical properties of catalyst supporter made of PANI micro/nanostructures in DMFC applications. Core–shell polyaniline/Vulcan carbon composite structures by in situ chemical polymerization to improve the CO anti-poisoning ability and catalytic efficiency of the Pt catalyst are reported. The preparing carbonization of nanostructured nitrogen-containing CPs has opened new perspectives in the preparation of nitrogen-containing conducting nanomaterial [121]. Prepare the nitrogen-containing nanotube/nanosheet of carbonized polyaniline as a new carbonaceous support for Pt nanoparticles, which demonstrated significant ORR in both acidic and alkaline media [122].

9.3 Conducting Polymers/Inorganic Nanohybrids for Electrical Energy Applications

Conducting polymers/inorganic nanohybrid electrodes are promising systems for EES applications owing to their remarkable combination of properties deriving from the different building blocks (Scheme 9.5). The flexibility and stability of composite electrodes derive from their polymer components and functionality. The general concept of designing composite starts from nanosized combination of polymers, metal particles, and functionality molecules. The composite materials are classified as based on their interaction: (a) functionalised polymer or metal precursor undergoes strong interaction by covalent and ionic bonds (amino-functionalised silicon nanoparticles and polymerized) [123], (b) inorganic nanopartilces embedded polymer (Physically or chemically attachment of iron

Scheme 9.5 General concept of conducting polymer/inorganic hybrid materials through physical and chemical interactions
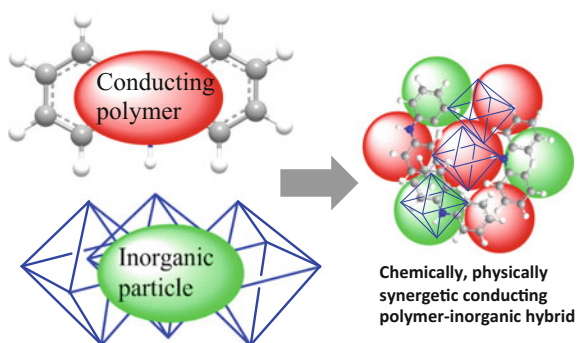
complex to the backbone of a conducting polymer leads to stabilization of the charge/discharge characteristics and higher electrode capacities of LiFePO$_4$) [105].

9.3.1 Nanosized Polymer-Inorganic Hybrid Synthesis

The preparing of hybrid is able to produce synergism from their chemical composition and physical structure for particular functional material application [105]. As a result of synergetic effect, they provide good catalytic, magnetic, semiconductor, and sensing properties depending on the kind of nanoparticles, polymer, and their characteristics, and also the effects of the electrolyte concentration besides the other reaction parameters on the final composite morphology/properties should be determined, controlled, improved, and characterized in a very precise and careful manner, during their synthesis reactions [5, 63]. Several methods have been also engaged for synthesis of hybrid composite for different applications. Including the simply conducting one-step, seeding template-assisted oxidative polymerization reactions with different oxidative agents, it is likely to generate core–shell or network-like composite structures that are composed of different morphology conducting polymers decorated with above mentioned inorganic nanoparticles [124–128]. As the supporting matrix, CPs used in different composites for intercalation of catalytically important nanoparticles thus that the catalytic activity can be reserved in the composite. Integrated Pt [129, 130] and PtO$_2$ [131] in a matrix of PPy and a poly(styrene sulfonate) (PSS) have been developed for oxygen reduction reaction (ORR) properties of the nanoparticles were prevailing though electrical conductivity suffered remarkably. It was overcome by using the PEDOT in the presence of NaPSS solution incorporated Pt nanoparticles with the good conductivity of 4 S cm^{-1}. The carboxylic acid groups of a conducting polymer anchored with AuNi dendrite have proposed for the catalysis of the ORR and H$_2$O$_2$ sensing. It showed enhancing performance of the catalyst because of an increase in the electrochemically active area by 12 times and a large shift toward more positive potential than the commercial Pt/C electrode [132]. PPy nanotubes decorated with

palladium, platinum, rhodium, or ruthenium nanoparticles were characterized by electron microscopy, conductivity, energy dispersive X-ray analysis, and FTIR and Raman spectroscopies. A typical metal content varied between 15 and 20 wt%. The catalytic activity of composites was illustrated on the reduction of 4-nitrophenol to 4-aminophenol. The carbonization of composites has been followed by thermogravimetric analysis in nitrogen atmosphere. The nanotubular morphology of polypyrrole was retained after carbonization up to 830 °C. The noble metal nanoparticles, nanometers in size, fused to clusters during this process, except for ruthenium. Polypyrrole nanotubes were converted to a nitrogen-containing carbon and platinum nanoparticles still preserved during carbonization at 400–500 °C.

Recently, Li-ion batteries are of great importance for fastest growing EES due to the high energy density, light-weight, and safety handle [133]. Conducting polymer-based nanohybrids are being appropriate materials for high performance of batteries electrodes due to their synergetic effects [134, 135]. With the advance properties of electrical conductivity, stress-buffer nature of polymer helps the transport of both electrons and ions as a result of the availability of short diffusion paths and good connectivity. Within 0-D to 3-D matrices of these composites electrode, considerable change in the shape, size, distribution, and connectivity of each phase during cycling may result in undesirable redistribution or segregation of phases, caused to electrical isolation of active electrode materials and thus capacity fading, deteriorating connectivity between carbon particles (increased resistance to current collection and charge transfer), and decline transport of electroactive reactants to (or products from) active sites (increased resistance to mass transfer and reduced rate of charge and discharge). For example, the morphology changes during charging and lithium dendrite formation may cause partial shorting of the two electrodes and eventually terrible failure of battery operation [136]. Some groups are proposing the synthesis of conducting polymers with silicon, tin, vanadium oxide nanoparticles, carbon, etc. The groups of Nazar [137] and Buttry [138] polymerized PANI in the presence of V_2O_5 to make inorganic/organic hybrid electrodes. The Li^+ ion diffusion coefficient for the PANI/V_2O_5 composite was 10 times that of V_2O_5, and the capacity was also superior than V_2O_5 xerogel. Cui et al. group, infusion of a PANI hydrogel into Si-based anodes: the hydrogel is polymerized in situ, resulting in a well-connected three-dimensional network structure consisting of SiNPs conformally coated by the PANI. With this anode, demonstrate a cycle life of 5000 cycles with over 90% capacity retention at 6.0 A g^{-1} current density [139]. SnNPs/PPy composite was prepared by chemically reducing and coating SnNPs onto the PPy surface. The composite shows a much higher surface area than the pure nanoSn reference sample, due to the porous higher surface area of PPy and the much smaller size of Sn in the nanoSn/PPy composite than in the pure tin nanoparticle sample [140]. Polyaniline (PANI)/multi-walled carbon nanotube (CNT) composite cathode was prepared by the in situ chemical polymerization of aniline in well-dispersed CNT solution. The cell delivered a maximum discharge capacity of 86 mAh g^{-1} at the 80th cycle with an average coulombic efficiency of 98% [141]. PANI-CNT nanoporous composite buffer layer-modified secondary lithium metal battery was fabricated for decreasing the safety risk of the

secondary Li metal battery in cycles of recharging processes and improves its cycle life in the future [142].

Supercapacitors are high energy storage devices compared to the conventional capacitors. Supercapacitors work on the simple phenomena of electrostatics and electrochemistry helping to harvest energy in a greener way. The combine into a conducting polymer matrix to form a hybrid material is an effective way to harness the electrochemical activity of nanosized oxide clusters. By anchoring them into CPs, the reversible redox chemistry of the otherwise soluble inorganic clusters can be combined with that of the CPs and be put to work in energy storage applications. Gomez et al. was presented the preliminary results that show how the resulting hybrid polymer displays the combined activity of its organic and inorganic components to store and release charge in a solid-state electrochemical capacitor device [143]. Internal pore volume over the total surface area in hybrid composite was responded to high specific capacitance of PEDOT–MnO_2 (315 F/g) and PANI–MnO_2 (221 F/g) than its constituent MnO_2 (158 F/g) [144].

Lee et al. developed a simple one-step way to synthesize the binary composites based on MnO_2–PEDOT coaxial nanowires by co-electrodeposition on a porous alumina template [145]. The core MnO_2 offers high energy storage capacity, as the highly conductive, porous, and flexible PEDOT shell facilitates the electron transport and ion diffusion into the core MnO_2 and considerably protects it from structurally collapsing and breaking. The coaxial nanowires exhibited high specific capacitance and good capacitance retention. The coaxial nanowires preserved 85% of their specific capacitance as the current density increases from 5 to 25 mA cm^2. Three-dimensional (3D) CoO–PPy composite electrodes exhibited very high capacitance and good rate capability. PPy was integrated into the nanowire array to improve the conductivity of the 3D electrode. The electrodes quietly maintain a good electrochemical reversibility of 99.86% even after 2000 cycles, and the asymmetric supercapacitors deliver a high energy density of 43.5 Wh kg^{-1} at a power density of 87.5 W kg^{-1} [146]. Further, developed a ternary MnO_2–CNT–PEDOT/PSS composite was used for high-performance EC electrodes. They found that the synergistic effects take place from the combination of MnO_2, and functionalized few-walled carbon nanotubes (fWNTs) and the commercial PEDOT/PSS conductive polymer could effectively utilize the full potential of all the desired functions of individual component. The ternary MnO_2–CNT-conductive polymer composite exhibited stable capacitance at high current density, but also showed great potential for use in power applications. Flexible solid-state SC device using PPy–Au as the electrode and a PVA/$HClO_4$ gel as the electrolyte and separator was developed by Meng et al. [147]. It achieves an excellent specific capacitance of 270 F g^{-1} at a low current density of 0.6 A g^{-1}. Fan and co-workers developed solid-state paper-like polymer supercapacitor based on the PANI–CNT composite film electrodes and showed a high specific capacitance of 31.4 F g^{-1} with excellent cycle stability [148]. PPy–MnO_2-carbon fiber composites as flexible supercapacitor showed a high specific capacitance of 69.3 F cm^3 at 0.1 A cm^{-3} current density and an energy density of 6.16 mW h cm^{-3} at a power density of 0.04 W cm^{-3}.

9.3.2 Ex Situ and In Situ Approaches

Most easiest and attractive routes to the fabrication of inorganic nanoparticle embedded polymer composite involve the following methods. In the ex situ approach, inorganic nanoparticles are first produced by soft chemistry routes and then dispersed into polymeric matrices and in situ approach; metals are generated inside a polymer matrix by decomposition (e.g., thermolysis, photolysis, radiolysis) or chemical reduction of a metallic precursor dissolved into the polymer. Hybrid composites were broadly studied for energy and electrical devices. The electrochemical deposition of Pd nanoparticles in poly(3,4-ethylenedioxythiophene) films gave evidence for three-dimensional growth of metal clusters at an initial stage [149]. The resulting nanocomposite shows a high electrocatalytic activity with respect to hydrogen adsorption. The $PtCl_4^{2-}$ anions have been trapped into a polypyrrole film during its electrochemical preparation, and, after solution exchange, these anions have been reduced cathodically to yield platinum metal particles of average size 10 nm, included in a 3D polypyrrole matrix [150]. The resulting composite film showed an electrocatalytic effect on the electrochemical methanol oxidation. Further, Pt nanoparticles have been incorporated into a polyaniline matrix, and the electrochemical process of hydrogen evolution has been studied at these composite electrodes [151]. Pt–Ru alloy-poly(vinylcarbazole) nanocomposite has been prepared electrochemically, and electrocatalytic activity of the resulting nanocomposites as regards anodic oxidation of methanol in an acidic solution has been shown [152]. Au $(ClO_4)^{4-}$ anion with a grain size less than 100 nm has been claimed to form during the ORR cycling of a Au electrode. Pyrrole has been found to autopolymerize on this roughened gold surface due to the electrochemical activity of the complexes, acting as an oxidant, resulting in a nanosized Au–PPy complex [153]. The ex situ approaches for PPy–$Cu_{1.4}Mn_{1.6}O_4$, with pzc at pH 2.6 composite electrodes having high electrocatalytic reactivity to the ORR and exhibiting a remarkable stability [154]. Cong et al. found that HO_2^- generation by the ORR inside PPy in a composite electrode GC/PPy/PPy(Ox)/PPy exhibited good stability and no loss of reactivity by chemical oxidation of the polymer [155]. For improving the electrocatalytic activity of Pt toward methanol oxidation, both the carbon paste electrode and poly(2-amino-5-mercapto-1,3,4-thiadiazole) (PAMT) were first used to deposit chestnut bur-like Pt particles. Resulted materials contribute to increase electrochemical active area of Pt catalyst and, therefore, have a positive effect on Pt's electrocatalytic activity [156].

In batteries, regulated porosity of polymers greatly affects stability of electrode. The porous polymer matrix has vacant space to permit for the large volume expansion and assist even cracked metal nanoparticles (MNPs) trapped into interconnected pore CPs, and high conductive coating helps to provide good electrical connection of MNPs during discharge/charge. To enhance the lithium storage capabilities of inorganic oxide-based anodes for LIBs, nanopainting with a thin layer of conducting polymer has been studied [157]. Typical layered transition metal sulfide (MoS_2) and same to graphite structure by S-Mo-S layer together with

van der Waals forces, which can facilitate to the Li^+ insertion/extraction. Poor conductivity between two adjacent sheets S–Mo–S can be improved by PANI via in situ method as anode materials presenting high capacity and good cyclability for Li-ion batteries [158]. $LiFePO_4$ particles are generally problem associated with slow diffusion of Li-ion across the two-phase boundary and/or low conductivity, which was overcoming by prepared composite by in situ polymerization restriction method. Fe^{3+} acts as precipitating agent for PO_4^{3-} and oxidant for aniline polymerization and then coated on graphite (1–2 nm). Their material offered good rate performance of 80 mAh g^{-1} at 60 C rate (Fig. 9.4) [159]. Ding et al. proposed new anode material of $CoCO_3$ with having two-step conversion reactions with a total theoretical value of 7 Li per $CoCO_3$. The 'first-order' reaction involves reduction of $CoCO_3$ to metallic Co and the formation of Li_2CO_3, and the second reaction involves the further reduction of Li_2CO_3 to Li_xC_2 ($x = 0, 1, 2$), along with the formation of Li_2O. The weakness of stability of the electrode enhanced by mixed with PPy to $CoCO_3$–PPy composite, which showed remarkable cycle stability and its reversibility, appearing to be a very promising anode material for LIBs (Fig. 9.4) [160].
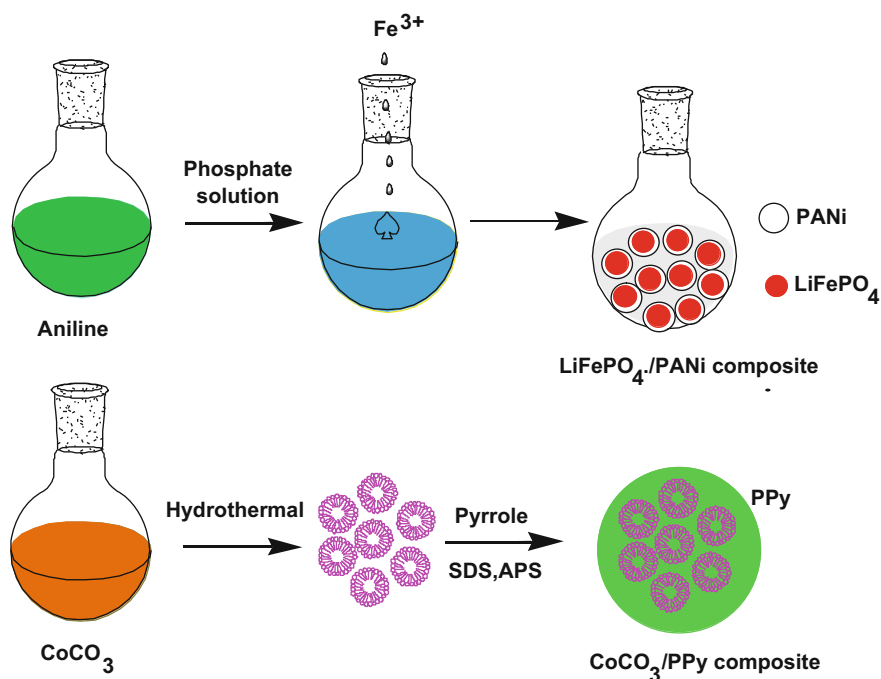
Fig. 9.4 Designed the $LiFePO_4$/carbon and $CoCO_3$/PPy composites including an in situ polymerization reaction and two typical restriction processes (Reproduced from Ref. [4] with kind permission of © 2015 Royal Society of Chemistry)

High capacity anode Si and Sn having huge volume expansion during cycling, which was controlled by PEDOT/PSS was embedded by an in situ polymerization of EDOT in PSS water solution with dispersed nanosize Si particles and subsequent carbonization of Si/PEDOT/PSS, which showed retaining a specific capacity of 768 mAh g^{-1} and a 99.2% CE after 80 cycles [161]. NanoSn–PPy composite with CMC as the binder had both superior capacity retention and good rate capability. It showed that both CMC and polypyrrole (PPy) can work as composite binders and prevent the formation of cracks in electrodes during the charge–discharge process, caused to good cycling stability, despite the big volume changes [140].

Generally, poor electronic conductivity of pristine anode and cathode materials is obstructed to the commercial applications. For improving the performance of electrode, conducting polymers are introduced by in situ/ex situ preparation method. Arbizzani et al. [41] introduce the PEDOT on the $Li_{1.03}Mn_{1.97}O_4$ by oxidation and subsequent polymerization of the EDOT on the $Li_{1.03}Mn_{1.97}O_4$ particles promoted by itself, due to its oxidative property. For improving the cycling process of $LiMn_2O_4/Li_xV_2O_5$ lithium-ion cell, coating with PPy on the surface of the anode was performed via in situ polymerization method [162]. PANI was intercalated into MnO_2, which has a swelled layered structure, with a uniform mesoporous structure, a typical nanosize, and a high surface area, resulting in a high electrochemical performance for Li-storage [163]. The enhanced electrochemical performance of β-$AgVO_3$/PANI triaxial nanowires was synthesized by in situ way [164]. A V_2O_5/PPy hybrid was prepared for improving the 20% of performance [165]. The basic routes of preparation of hybrid composite are in situ synthesis of MNPs, polymers, or both components simultaneously. Final or precursor mixed components can proceed. Ternary nanocomposite of graphene–Fe_2O_3–polyaniline (GFP) in which the PANI was synthesized via in situ polymerization of aniline with the well-dispersed Fe_2O_3 nanoparticles anchored firmly on the GE sheets and protected by PANI films was helpful to solve the poor cycling problems and offer a direct short pathway for charge/electrode diffusion. It exhibited an excellent cycling life, with a decrease in capacitance of only 8% after 5000 cycles and enhanced energy density of 107 Wh kg^{-1} at a power density of 351 W kg^{-1} and 17 Wh kg^{-1} even at a higher power density of 4407 W kg^{-1} [166].

Zhai groups have demonstrated the feasibility of supercapacitor material core with pseudocapacitive material shell such as CNT@PPy–MnO_2 [167], CNT@PEDOT–MnO_2 [168], and CNT@PANI–MnO_2 [169]. In CNT@PPy–MnO_2, multi-wall CNTs were well-dispersed and wrapped around using 18 wt% poly(4-styrenesulfonic acid) (PSS), which also provides attractive forces for pyrrole and metal ions upon negative charging. PPy–MnO_2 composite shell was subsequently prepared by adding pyrrole and $KMnO_4$. It showed $\sim$ 268 F g^{-1} specific capacitance much higher than CNT@MnO_2 ($\sim$ 170 F g^{-1}) and CNT@PPy ($\sim$ 160 F g^{-1}). It exhibited very stable cycle life (10% reduction after 5000 cycles); in contrast, a specific capacitance reduction of 61 and 45% was observed under the same test conditions for CNT@MnO_2 and CNT@PPy, respectively. Li et al. [170] demonstrate a facile, simple, and effective approach to synthesizing ultrafine (<10 nm in diameter) β-MnO_2/PPy nanorod composite powders for

high-performance supercapacitor electrodes. The proposed synthetic mechanism and the developed synthetic strategy provide design guidelines in synthesizing other energy storage materials toward ultrafine 1D nanostructure. Well-aligned CoO nanowire array grown on 3D nickel foam with PPy uniformly immobilized onto or firmly anchored to each nanowire surface to boost the pseudocapacitive performance with the elegant synergy between CoO and PPy shows the way to a high specific capacitance of 2223 F g^{-1}, good rate capability, and cycling stability (99.8% capacitance retention after 2000 cycles). Because the high electronic conductivity of PPy, and the short ion diffusion pathway in ordered mesoporous nanowires. The negative electrode has demonstrated high energy density ($\sim$43.5 Wh kg^{-1}), high power density ($\sim$5500 W kg^{-1} at 11.8 Wh kg^{-1}) and outstanding cyclability ($\sim$20,000 times). After charging for only $\sim$10 s, two such 4 cm^{-2} asymmetric supercapacitors connected in series exhibited efficiently power 5-mm diameter red, yellow, and green round LED indicators (lasting for 1 h for red LED) and drive a mini 130 rotation-motor robustly [146].

Hierarchical nanocomposite of vertical polyaniline (PANI) nanorods aligned on the surface of functional multi-walled carbon nanotubes (FMWNTs) by in situ polymerization of PANI on the surface of FMWNTs prepared nanocomposite possessed higher specific capacitance and better stability than each individual component as supercapacitor electrode materials due to the synergistic effect of both components, as well as to the special hierarchical structure, which not only increases the specific surface area of the nanocomposite but also facilitates the penetration of electrolyte ions [171]. PANI–MnO$_2$ nanocomposites prepared through 'interfacial syntheses' to use the interfacial region between an organic phase and an aqueous phase to synthesize the composite [172], which process was depicted in Fig. 9.5.
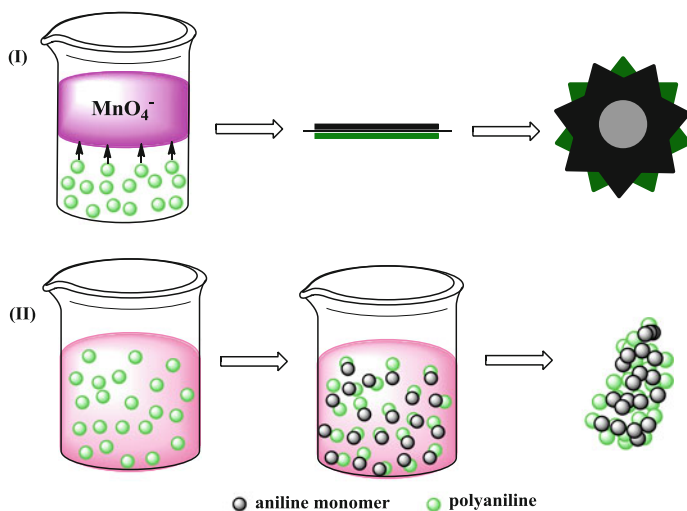
Fig. 9.5 Formation mechanisms of MnO$_2$–PANI composites: (*I*) interfacial synthesis and (*II*) chemical co-precipitation (Reproduced from Ref. [172] with kind permission of © 2012 Elsevier)

The organic phase was prepared by dissolving aniline monomers into inorganic ($CHCl_3$) solution, while the aqueous phase was obtained by dissolving potassium permanganate in distilled water. When the aqueous solution was added into the organic solution, an interface was formed immediately between the two phases and the reaction occurred. During the reaction, aniline was diffused from the organic solution to the interface and was chemically oxidized into polyaniline. At the same time, MnO_4^- was reduced to manganese oxide precipitate. Finally, the PANI–MnO_2 nanocomposite was formed and remained in the aqueous solution. It shows larger specific surface area (124 m^2 g^{-1}), more uniform pore-size distribution, and a higher specific capacitance of 262 F g^{-1} with better cycling stability. Other interesting PANI metal oxide nanocomposites include PANI–$MnWO_4$ nanocomposites, which were prepared in situ polymerization of aniline monomer in solution containing $MnWO_4$ nanoparticles [173]. The composite has shown good electrochemical property: With 50% of $MnWO_4$ loading, the PANI–$MnWO_4$ nanocomposite shows high specific capacitance of 475 F g^{-1}, which is much higher than that of the physical mixture of PANI and $MnWO_4$ (346 F g^{-1}).

9.3.3 Mechanical Methods

High energy ball milling is an industrially amenable technique as grinder and extra energy are used to squeeze the materials into extremely fine powder. It is suitable for batch and continuous operation, all degrees of hardness material, and open/closed circuit grinding. To make CO tolerant unsupported Pt–Ru-based catalysts for the oxidation of hydrogen in polymer electrolyte fuel cells. Nanocrystalline $Pt_{0.5}$–$Ru_{0.5}$ alloys obtained by ball milling, but their poor performances, are further processed by milling Pt, Ru, and Al in a 1:1:8 atomic ratios. After leaching Al, this catalyst [$Pt_{0.5}$–$Ru_{0.5}$ (Al_4)] displays a specific area of 38 m^2 g^{-1}. $Pt_{0.5}$–$Ru_{0.5}$ (Al_4) composite catalyst shows hydrogen oxidation performance and CO-tolerance equivalent to those of the commercial catalyst $Pt_{0.5}$–$Ru_{0.5}$ [174]. The hydrolysis properties for hydrogen generation from Mg metal chlorides composites were prepared by high energy ball milling in pure water. It is found that the Mg-10 wt% $FeCl_3$ composite ball-milled for 30 min has the best hydrolysis properties with an initial hydrogen generation rate of 1479.1 ml g^{-1} min^{-1} and a theoretical hydrogen production yield of 98% in 2 min [175].

The vast network of the PPy matrix is a suitable environment to cushion the volume change associated with Li_xSi alloying and dealloying reactions. The capacities of the composites were dependent on the amount of silicon added. A series of novel high capacity of Si/PPy composites was prepared by high-energy mechanical milling techniques [176]. Substantial shape change during cycling resulting in rapid capacity fading has so far limited the success of this material. Composites somehow remediating this detrimental effect have been studied, among them composites of silicon with PPy 10 wt% PPy nanowires introduced to Si particles prepared by high-energy mechanical milling for better reversibility and

cycle life than silicon, while the silicon/microparticles PPy composite shows no improvement because PPy NWs and microparticles PPy act as a matrix to hold the active silicon grains as they repeatedly alloy with lithium during the operation of LIBs [177].

Metal oxides are semiconductor, which cannot provide higher capacity. But mixing with polymers can produce a reversible capacity more than ten times that of plain MnO_2-based devices. They showed reversible capacities in the range 400–1000 mAh g^{-1} at 120 mA g^{-1} in 20th cycle [178]. Further, to enhance the long-term cyclability of Si anode by embedding SiNPs into a Li^+-conductive polymer (polyparaphenylene) (PPP) simply by ball milling the SiNPs with PPP as core–shell structure, in which nanoSi cores act as active Li-storage phase and the polymeric matrix as a strong buffer to accommodate the volume change, and protection barrier to prevent the direct contact of Si surface with electrolyte. Si/PPP composite exhibits a high capacity of 3184 mAh g^{-1} with 78% initial CE and 1670 mAh g^{-1} at 16 A g^{-1}, along with long-term cyclability with 60% capacity retention over 400 cycles [179]. More recently, high capacity VO_4 was synthesized by stoichiometric amounts of In_2O_3 and V_2O_5 in the ratio of 1:1 mixed under ball-milled for 18 h, which have surface area of 0.49–9.28 m^2 g^{-1} and capacity about 1200 mAh g^{-1} [180].

High electrical storage capacity of composite electrodes prepared from nanoscale activated carbon combined with PEDOT/PSS or multiple dopants such as ammonium persulfate (APS) and dimethyl sulfoxide (DMSO). They were fabricated by electropolymerization of the conducting polymers onto the nanoscale activated carbon backbone, in which the nanoscale activated carbon was produced by ball milling followed by chemical and thermal treatments. Activated carbon/PEDOT/PSS yielded capacitances of 640 F g^{-1} and 26 mF cm^{-2}. Further, use of multiple dopants in PEDOT improved the storage performance of the composite electrode well over that of PEDOT/PSS [181].

Polyaniline-$BaTiO_3$ and Nd-doped $BaTiO_3$ composites were prepared, and it is conductive enough to be a supercapacitive electrode. The composites were prepared by partial solution mixing. A novel technique called partial solution mixing method, which incorporates physical milling in a selected liquid medium, was successfully developed to prepare the composite electrode specimens. A new PANI-calcined barium titanate graphite system showed high capacitance of 189.2 Fg^{-1}, exploiting the pseudocapacitive and the double-layer features of both CBTG and PANI [182]. TiO_2 NWs were grown on carbon cloth substrate by a seed-assisted hydrothermal method, subsequently anodic deposition of PPy shell on the surface of TiO_2 NWs under 1 mA cm^{-2} for 20 min at 50 °C for formation of TiO_2@PPy core–shell nanowires (NWs) on carbon cloth. Fabricated device based on TiO_2@PPy core–shell NWs not only has excellent flexibility, but also exhibits remarkable electrochemical performance [183].

9.3.4 Blending Inorganic Nanoparticles into Polymer Matrix

Blending defined as a mixture of different substances or other things, i.e., inorganic nanoparticles mixed into the conducting polymers. The blends of PtNPs into PANI nanofibers route were presented in Scheme 9.6. PANI nanofibers of 60 nm diameter were synthesized by a scalable interfacial polymerization and then supported Pt electrocatalyst (Pt/PANINFs) and carbon black-supported Pt electrocatalyst (Pt/C) by reduction method. Prepared Pt/PANINFs composite catalyst shows a higher electrochemical active surface area and higher methanol oxidation reaction catalytic activity than the Pt/C. I_f/I_b ratio of Pt/PANINFs is 1.90, higher than that of the Pt/C catalyst (0.93), which reveals better tolerance of Pt/PANINFs [184]. PANI/C composite can serve as a support material for dispersing Pt and Pt-Ru particles in an electrocatalyst for methanol oxidation. The incorporation of PANI provides a suitable matrix for conventional carbon black particles and forms composite support materials with increased electrochemical accessible surface area and decreased charge-transfer resistance. Pt–PANI/C displays about a four times higher mass activity for methanol oxidation in comparison with Pt–PANI at a Pt loading of 80 μg cm^{-2} [185]. PANI-decorated Pt/C@PANI core–shell showed enhanced catalyst activity and durability compared with non-decorated Pt/C. Resulted the activity for the oxygen reduction reaction strongly depends on the thickness of the PANI shell and that the greatest enhancement in catalytic properties arised at 5-nm thickness, followed by 2.5, 0, and 14 nm. The high activity and stability of the

Scheme 9.6 Diagram of preparation of Pt/PANI NFs composite
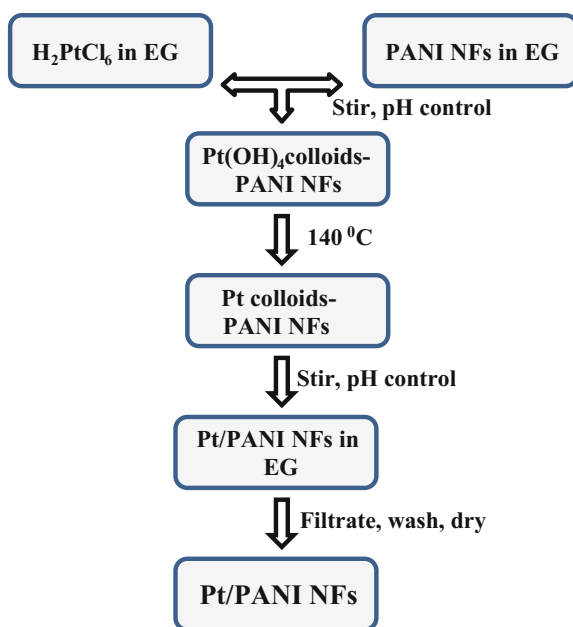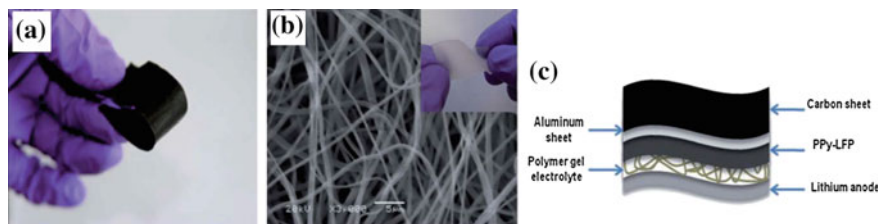
Fig. 9.6 Photographs **a** of a flexible PPy–LFP electrode, **b** SEM of electrospun P(VDF-HFP) matrix, and **c** scheme of the flexible battery. *Inset* of **b** Photograph of electrospun P(VDF-HFP) (Reproduced from Ref. [188] with kind permission of © 2012 Royal Society of Chemistry)

Pt/C@PANI catalyst were attributed to PANI-decorated core–shell structure induces both electron delocalization between the Pt d-orbitals and the PANI π-conjugated ligand and electron transfer from Pt to PANI and also protects the carbon support from direct exposure to the corrosive environment [186].

Just pressing the $LiMn_2O_4$ and PPy powder without using any binder as pellets anode material at potentials ranging between 4.3 and 3.2 V versus Li/Li^+, PPy works well as a conducting matrix for the redox reaction of $LiMn_2O_4 \rightleftharpoons Li_{1-x}Mn_2O_4 + xLi^+ + xe^-$. The PPy behaved also like a capacitor and contributed to the capacity density of the $LiMn_2O_4$/PPy composite [187]. Thin flexible polypyrrole–lithium iron phosphate (PPy–$LiFePO_4$) composite has been developed to enhance electrical conductivity of cathode [188]. The photograph of the PPY–LFP electrode is shown in Fig. 9.6, for flexible battery by the electrospun method. Deposition of PPy in a spherical-hollow crystalline V_2O_5 yielded a composite with slightly reduced capacity but increased cycling stability [189]. PPy coated on small particles of V_2O_5 evaluated as positive mass of a lithium-ion battery by Zhao et al. has shown improved cyclability [190]. Using pyridinesulfonic acid as an additive during preparation of a V_2O_5/PPy hybrid material has resulted in a capacity increase of 20% [165]. Differences between core/shell and host/guest nanocomposites of V_2O_5/PPy have been studied by Posudievsky et al. [191]. Thus, addition of a chemical oxidant and associated problems caused by excess of this oxidant in the reaction system and possibly the final product could be avoided. The observed capacity of this positive mass was 163 mA g^{-1}, close to the theoretical capacity of 170 mAh g^{-1} for $LiFePO_4$, with a superior high-rate performance attributed to the improved lithium-ion diffusivity of the composite material. The influence of the particle morphology of $LiFePO_4$ (donut-, dumbbell-shape, nanocrystalline) coated with PEDOT was studied by Dinh et al. [192]. Tannin sulfonic acid-doped PANI was prepared at 10 °C with two different ratios of aniline to sodium persulfate (oxidant) and the simultaneous incorporation of TiO_2, Al_2O_3, and ZnO nanopowders for good electronic properties and exploring their potential use in solar cell applications [193]. PEDOT has controllable electrical conductivity, but suffers from problems of volumetric swelling and shrinkage during the insertion and ejection of ions.

Sen et al. [194] prepared PEDOT–NiFe$_2$O$_4$ nanocomposites by chemical polymerization of EDOT monomer in solution containing NiFe$_2$O$_4$. The PEDOT-NiFe$_2$O$_4$ nanocomposite shows high specific capacitance (251 F g^{-1}) in comparison to NiFe$_2$O$_4$ (127 F g^{-1}) and PEDOT (156 F g^{-1}) where morphology of the pore structure was believed to play a significant role over the total surface area. PEDOT was also composited with MoO$_3$ by Murugan et al. [195] using chemical polymerization of EDOT monomer with FeCl$_3$ as oxidizing agent in MoO$_3$ suspension. The nanocomposite also has much higher specific capacitance (300 F g^{-1}) compared to that of pristine MoO$_3$ (40 mF g^{-1}). The improved electrochemical performance was attributed by the authors to the intercalation of electronically conducting PEDOT between MoO$_3$ layers and an increase in surface area. The electrical conductivity of intrinsic PPy is low, and doping of surfactants can enhance effectively the electrical conductivity of PPy. p-Toluenesulfonic acid (PTSA) was used as a dopant by Dong et al. [196] to prepare MnO$_2$–PPY/TSA nanocomposite for supercapacitor applications. TSA and pyrrole were dispersed ultrasonically in deionised water to form a homogeneous solution. With the addition of KMnO$_4$ oxidant, redox reactions occurred and MnO$_2$–PPY/TSA nanocomposite was produced. Nanocomposite electrode exhibited a higher specific capacitance of 376 F g^{-1} at 3 mA cm^{-2} and better cycling stability in 0.5 M Na$_2$SO$_4$ solution than the MnO$_2$–PPY. Another polymer-metal oxide composite that shows promising supercapacitive properties is MnO$_2$-poly(aniline-co-o-anisidine) [197], which has specific capacitance of the 262 F g^{-1} in 1 M Na$_2$SO$_4$ at a current density of 1 A g^{-1}.

9.3.5 *Nanostructured Polymer with Inorganic Particles*

Functional groups of polymer interact with inorganic salts and subsequent reduction or thermal (or other) treatment results in nanoparticles formation within the functional nanophase. The capping, reducing, stabilizing, or protective agents (polymers and surfactants) are play important during formation of nanoparticles. Incorporation of a PANI-phytic acid hydrogel into Si-based anodes via hydrogen bonding followed with cross-linking resulting in a well-connected three-dimensional network structure consisting of SiNPs conformally coated by the PANI. With this anode, demonstrate a cycle life of 5000 cycles with over 90% capacity retention at current density of 6.0 A g^{-1} [139]. LiMn$_2$O$_4$–PPy composite was studied for charge–discharge properties for 3 and 4 V (Scheme 9.7) [189, 198].

In order to improve the electrode performance, pyrrole dispersed in V$_2$O$_5$ forms hybrid composite by chemical polymerization method that can influence the acidic dopant [199]. LiFePO$_4$ exposed to hot air and regenerated with PPy as a reductant was studied. Excellent performance in particular at high rates was observed. This approach was further developed and optimized using EDOT as a monomer and its chemical oxidation by a slightly lithium-poor form of LiFePO$_4$ [200]. Fabricated high-performance Li-ion battery anodes by encapsulating SiNPs in a nanostructured
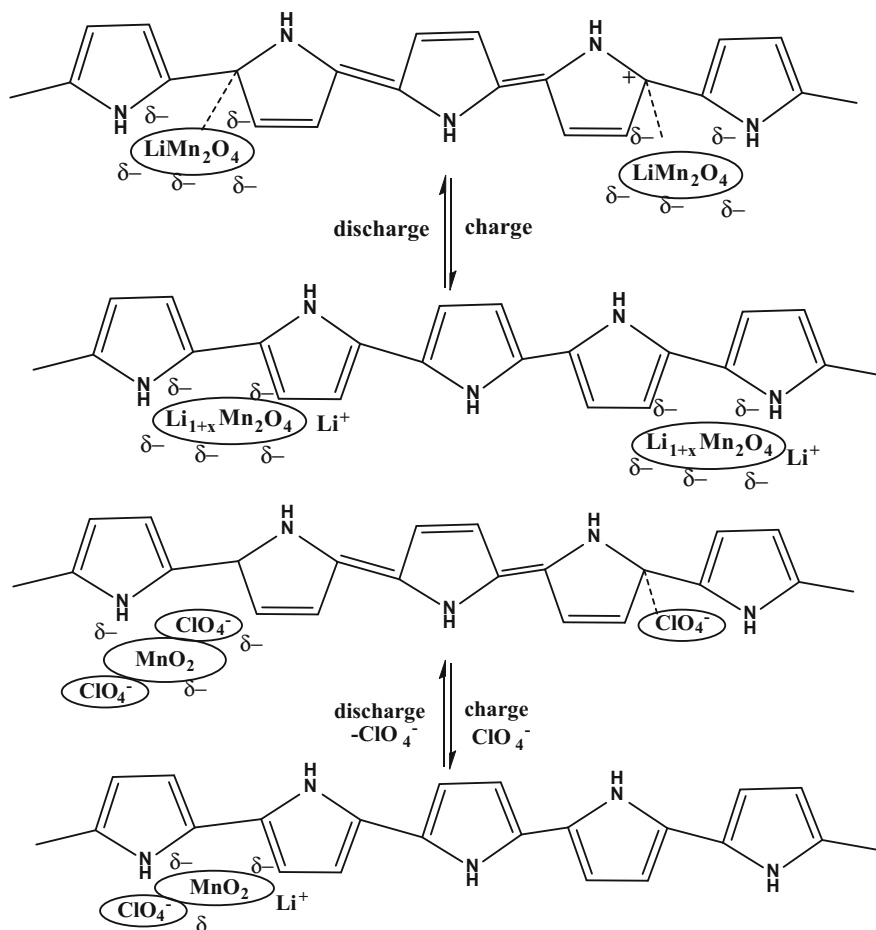
Scheme 9.7 Mechanism changes for the p-MnO_2/PPy and $LiMn_2O_4$/PPy during charge–discharge reactions

3D porous conductive polymer framework developed [201]. The hierarchical conductive hydrogel framework with carbon nanotubes is the electronic fortifier with high porosity and is prepared to accommodate the Si particles of SiNPs/PPy–CNT composite by in situ polymerization for improved cycling LIBs performance [9]. Chen et al. [202] synthesized a very high-performance PANI–MnO_2 nanocomposite using the hydroxylated MnO_2 nanoparticles which was surface modified with silane coupling agent (ND42). Electro-copolymerization of aniline and ND–MnO_2 nanoparticles was conducted on a carbon cloth in an electrolyte solution containing ND–MnO_2, aniline, H_2SO_4, and Na_3PO_3. The whole synthesis process is illustrated in Fig. 9.7.
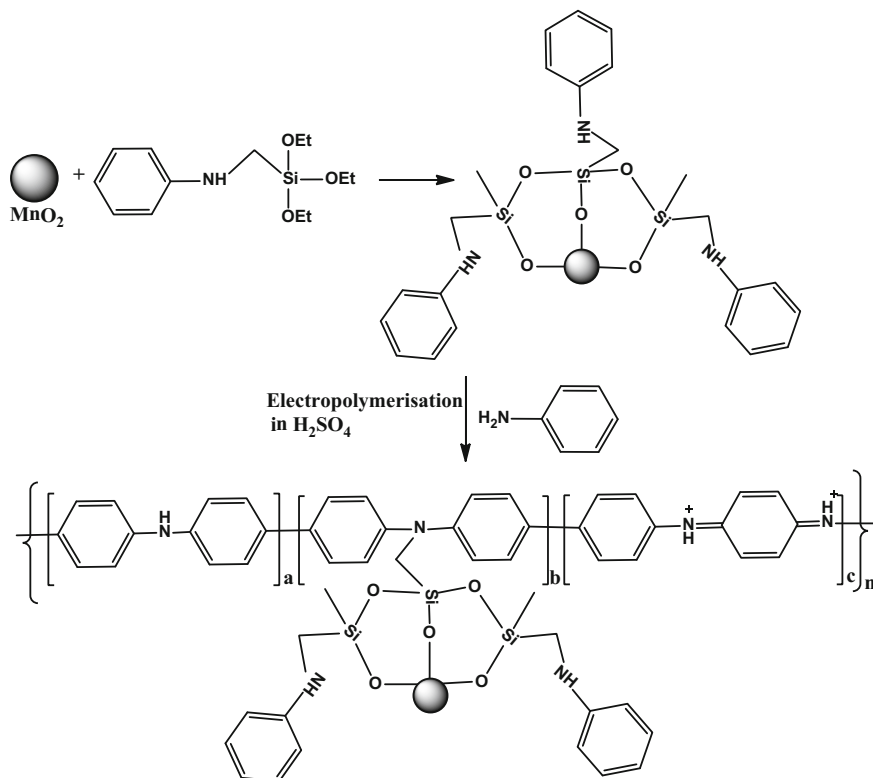
Fig. 9.7 Reaction pathway for the synthesis of PANI–ND–MnO$_2$ nanocomposite film (Reproduced from Ref. [202] with kind permission of © 2010 Elsevier)

Electro-copolymerization method was also used to prepare unmodified PANI–MnO$_2$ nanocomposite and pure PANI. PANI–ND–MnO$_2$ composite film has an average specific capacitance of ~ 80 F g^{-1} and a very stable coulombic efficiency of $\sim 98\%$ over 1000 cycles. It also exhibits high intrinsic electrical conductivity and good kinetic reversibility. The excellent properties were attributed by the improved interaction between MnO$_2$ and PANI and the increased effective surface area in PANI–ND–MnO$_2$ film, due to the surface modification of MnO$_2$ nanoparticles with the silane coupling reagent. Notably high specific capacitor was achieved with PANI–SnO$_2$ nanocomposites prepared by Hu et al. [203] using a chemical method in which SnO$_2$ nanoparticles and aniline were dispersed in sodium dodecylbenzenesulfonate solution, and then, ammonium persulfate was added to the above mixture to start polymerization. The PANI–SnO$_2$ nanocomposite, thus, prepared had a high specific capacitance of 305.3 F g^{-1} with a specific energy density of 42.4 Wh kg^{-1} and a coulombic efficiency of 96%. Sulfonic acid groups are then grafted on the carbonized PANF by ultrasonication in concentrated sulfuric acid to increase the surface hydrophilicity and Pt loading. The obtained sulfonated

carbonized PANF was found to own not just high conductivity but good hydrophilicity which can load more than 18% of Pt on the surface from a 25% H_2PtCl_6 (aq) and demonstrate better electrochemical activity in the cyclic voltaic and ORR testing. The surface area of the loaded Pt per unit support can be increased from 85.66 to 276.61 $cm^2 mg^{-1}$ after 24 h of sulfonation. The single-cell performance demonstrates an increasing power and maximum current density with degree of sulfonation for MEA made of the sulfonated carbonized PANF [204].

9.3.6 Sol–Gel

Sol–gel method is very attractive and instructive at process. They show an intense development accompanied by important practical applications of energy conversion and storage system and have significant advantages, for example, good crystallinity, homogeneous mixing at the atomic or molecular level, low synthesis temperature, short heating time, good stoichiometric control, uniform particle size and small diameter, and down to nanometer level [205]. The basic processing steps of this method are precursor, hydrolysis, reactive monomer, condensation, sol gelation, gel, and treatment. Controlled preparation of V_2O_5/PPy composite leads to favorable reversible electrochemical properties suggested by Ren et al. [206]. Further, V_2O_5/PPy nanocomposites for Li^+ ion transport had proposed [207, 208]. Hydrogel V_2O_5/PPy composite was proposed for systematic studies of spectral and structural characterization [209]. Electrochemical lithium intercalation properties of V_2O_5/PANI were studied [210, 211]. Park et al. deposited V_2O_5 on a layer of PANI [212]. $Li_4Ti_5O_{12}$ was prepared by sol–gel method, followed by PANI coating, which exhibits better rate capacability and cyclability [213]. Tethering carbon-coated LiFePO$_4$/PPy composite demonstrated enhancement of the rate capability of cathode composites [214]. The core/shell structures prepared from small crystals of V_2O_5 coated with PPy were inferior to host/guest structures synthesized from an aerogel of V_2O_5 with mechanochemical polymerization of pyrrole. Nanocomposites of PEDOT and V_2O_5 prepared with microwave assistance showed an increased capacity of 370 mAh g^{-1} [215].

9.3.7 Electrochemical and Chemical Deposition Methods

A thin film is a layer of material ranging from fractions of a nanometer (monolayer) to several micrometers in thickness. Electronic semiconductor devices and optical coatings are the main applications benefiting from thin-film construction. The polymer composite electrodes are mostly synthesized by deposition methods such as chemical or electrochemical ways. LiFePO$_4$ electrode is modified with PPy via monomer penetrated and coated in the inner pore, which would reduce the activity surface and further decrease undesirable reactions with the electrolyte, while the

lithium intercalation would not be inhibited. This strategy used to synthesize the PPy films [216]. Si/PPy core–shell nanofibers delivered by electropolymerized PPy nanofibers electrode followed by CVD of SiNPs are favorable for facile charge delivery and gathering, while the porosity of the electrode can efficiently cushion the volume expansion of Si (Fig. 9.8) [217]. PPy-doped $LiFePO_4$ cathodes were prepared by electrochemical deposition and showed poor electrochemical properties [218–220].

Huang et al. reported on porous NiO/polyaniline (PANI) film obtained by depositing the PANI layer on the surface of the NiO film, which showed 520 mAh g^{-1} at 1 C [221]. Porous NiO/PEDOT films are prepared by chemical bath and electrodeposition techniques, exhibit weaker polarization and better cycling performance [222]. Free-standing PPy/$LiFePO_4$ film electrodes were prepared using the same solution, but with the addition of $LiFePO_4$ powder. The cell with composite film had a higher discharge capacity beyond 50 cycles (80 mAh g^{-1}) than that of the cell with pure PPy (60 mAh g^{-1}) [223]. Wang et al. prepared electrochemically highly flexible, paper-like, free-standing PPy and PPy–$LiFePO_4$ composite film electrodes and observed that the cell with PPy–$LiFePO_4$ composite film had a higher discharge capacity beyond 50 cycles (80 mAh g^{-1}) than that of the cell with pure PPy (60 mAh g^{-1}) [224].

$LiFePO_4$ as a typical compound fraught with conductance problems was coated with carbon and embedded in PPy during electropolymerization of the latter. Improved specific capacity and rate behavior were reported with the capacitance attributed to the substitution of the inactive carbon matrix (and binder) by the redox-active PPy and the rate improvement to the vastly increased electronic conductance of the matrix. Carbon-coated particles of $LiFePO_4$ were tethered to PPy [213]. Substantial shape change during cycling resulting in rapid capacity fading has so far limited the success of this material. Composites somehow remediating this detrimental effect have been studied, among the composites of
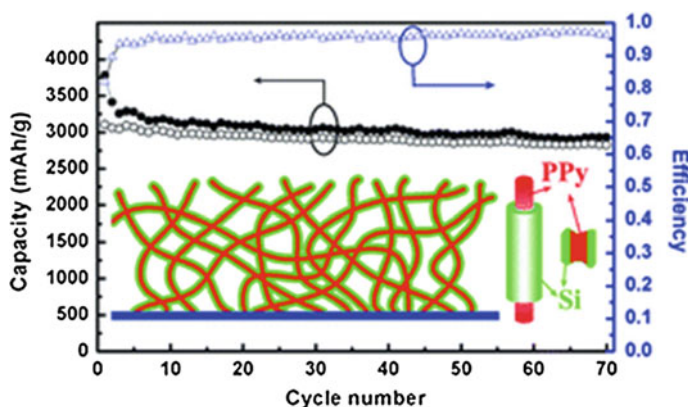
Fig. 9.8 Reaction pathway for the synthesis of PANI–ND–MnO_2 nanocomposite film (Reproduced from Ref. [217] with kind permission of © 2012 Royal Society of Chemistry)

silicon with PPy [177]. High capacity LIB anode SiNWs/PEDOT material formulated by electropolymerization method, which maintaining the mechanical integrity of the cycled Si material, along with preserving electrical connections between NWs that would otherwise have become electrically isolated during volume changes [225].

Electrochemically synthesized MnO_2 embedded PPy nanocomposite (MnO_2/PPy) thin-film electrodes on polished graphite substrates. Growing PPy polymer chains provide large surface area template that enables MnO_2 to form as nanoparticles embedded within polymer matrix. Co-deposition of MnO_2 and PPy has a complimentary action in which porous PPy matrix provides high active surface area for the MnO_2 nanoparticles, and, on the other hand, MnO_2 nanoparticles nucleated over polymer chains contribute to enhanced conductivity and stability of the nanocomposite material by interlinking the PPy polymer chains. MnO_2/PPy nanocomposite thin-film electrodes show significant improvement in the specific capacitance (~ 620 F g^{-1}) in comparison to its constituents MnO_2 (~ 225 F g^{-1}) and PPy (~ 250 F g^{-1}) [226].

The electrodeposition of platinum microparticles into PANI films on glassy carbon electrodes and their catalytic activity for the reduction of hydrogen and the oxidation of methanol was described by Kent [227]. Pulse galvanostatic method was used to synthesize nanofibular PANI followed and then modified by Pt microparticles, and at the same Pt loading, exhibits a considerably higher electrocatalytic activity on the methanol oxidation than that of the granular PANI electrode modified by Pt microparticles. When the value of Pt loading is over 0.2 mg cm^{-2}, the Pt/nanofibular PANI/SS electrode is greatly superior to the Pt/granular PANI/SS electrode in electrocatalytic activity [228].

Pt-Ru particle sizes of the 3–8 nm was electrodeposited onto PANI from distilled water solution containing ruthenium chloride and chloroplatinic acid by step-potential plating methods. From the loading content results as a function of plating time, the efficiency of loading was enhanced to N11 wt% with the increase of the plating time to 36 min. However, from the viewpoint of average particle sizes, the smallest nanoparticles of 3.1 nm were obtained by electrodeposition with 24 min plating time. H_2 adsorption/desorption study showed that Pt-Ru/PANI had the higher specific surface area for an electrochemical reaction. The enhanced methanol oxidation specific current (121 mA mg^{-1}) for polyaniline-supported Pt–Ru catalysts was attributed to the relatively higher electrical conductivity of the PANI or the increased electrochemical area, which could be related to small particle size and low degree of aggregation [229].

Electrodeposited platinum and polyaniline on graphitized carbon electrode were used for electrochemical oxidation of 1-propanol in alkaline medium [230]. Three-dimensional porous Pt films were prepared based on Pt electrodeposition on PANI-modified electrodes followed by selective dissolution of PANI with HNO_3. Electrochemical quartz crystal microbalance revealed that the PANI–H_2PtCl_6 interaction involves redox and coordination reactions, depending on the working potential. It can electrocatalyze the oxidation of H_2O_2 with a sensitivity of 414 mA cm^{-2} mM^{-1} and a detection limit of 9 nM [231]. Metallic particles were

dispersed in electrically conducting polymer films in order to achieve multi-electron transfer processes in a 3D matrix. Dispersions of Pt in PPy were formed by several electrochemical and chemical methods. Films were prepared in which Pt was deposited primarily at the polymer/solution interface, at the metal/polymer interface, or uniformly through the film. For the homogeneous film, the catalytic current is limited by the rate of O_2 permeation in the film [232].

The electrodeposition of polythiophene (PTh), polyaniline (PANI), and polypyrrole (PPy) films modified by dispersion of Pt or Pt + Pb and its employment in the electrocatalytic oxidation of HCOOH was studied. Under condition I of this Fig. 9.9, the polymeric electrode system is in the reduced state and the Pb atom was deposited on the surface of the Pt granules and on the polymeric matrix. The electroadsorption of HCOOH takes place on the Pt active sites, and the polymer eliminates anions through the undoping process. Under condition II, the following processes take place: (i) direct oxidation of HCOOH, (ii) partial oxidation of the polymer with subsequent anionic doping, and (iii) total oxidation of the Pb atoms [233].

Electrochemically growth the MnO_2 nanoflakes and polypyrrole (PPy) on carbon fiber for conductive wrapping, and hybrid structure have a high specific

Fig. 9.9 Schematic illustration of the behavior of Pt and Pb/PTh electrodes (Reproduced from Ref. [233] with kind permission of © 1998 Springer)
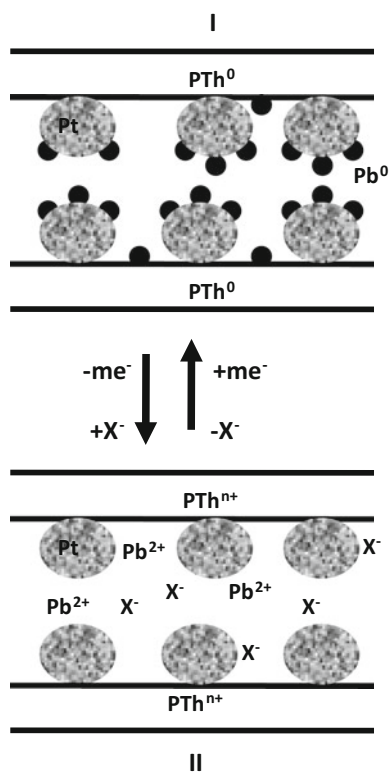
capacitance of 69.3 F cm^{-3} at a discharge current density of 0.1 A cm^{-3} and an energy density of 6.16 × 10^{-3} Wh cm^{-3} at a power density of 0.04 W cm^{-3}, the device can drive a commercial liquid crystal display (LCD) after being charged. The as-fabricated solid-state SC showed high mechanical flexibility, and the capacitance of the device had only a slight fluctuation of 0.24% when it was rolled up [234].

One-step electropolymerization of PANI/NiHCF/sCNT interconnected composite films was fabricated using cyclic voltammetry in the solution of sCNTs, NiSO$_4$, Na$_2$SO$_4$, K$_3$Fe(CN)$_6$, and aniline. Their formation mechanism is presented in Fig. 9.10. NiSO$_4$ and K$_3$Fe(CN)$_6$ concentrations can affect morphology of PANI/NiHCF/sCNTs composite film changed from the short nanotubes to
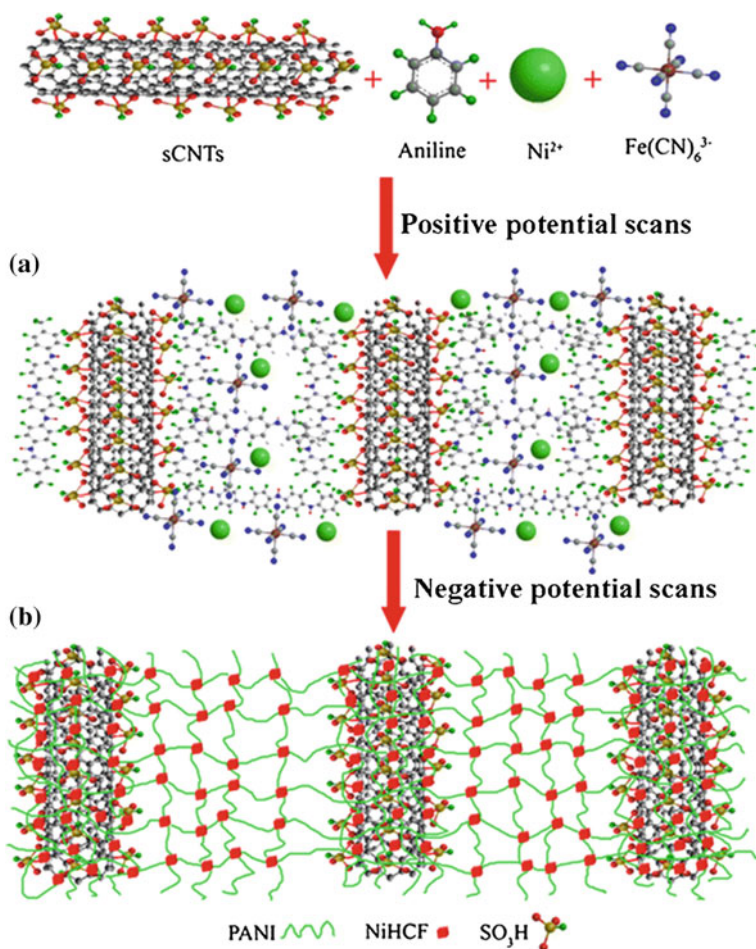
Fig. 9.10 Schematic illustration of the formation mechanism of PANI/NiHCF/sCNT composite films (Reproduced from Ref. [235] with kind permission of © 2015 Springer)

microparticle and coral-like structure as a result of the $\pi-\pi^*$ electron and hydrogen bonding interaction among sCNTs, NiHCF, and PANI. The specific capacitance of PANI/NiHCF/sCNTs composite film was 430.77 F g^{-1} with 0.04 mol L^{-1} NiSO$_4$ and 0.04 mol L^{-1} K$_3$Fe(CN)$_6$ due to self-doping effect of sCNT in composite films. The cycle stability of PANI/NiHCF/sCNTs composite films was enhanced with the increase of NiSO$_4$ and K$_3$Fe(CN)$_6$ in prepared solution [235].

9.3.8 Diversity Methods

[PEI-capped Pt NPs/(PEDOT/PSS)] was prepared by photoreduction and electrostatic LBL assembly qualified component for electrocatalysis. The stable and uniform multi-layer thin films of [PEI-capped Pt NPs/(PEDOT/PSS)] were found to be an active catalyst coating for the oxidation of methanol, and a 20 bilayer film proceeds with a stable level of catalyst activity for over 1000 oxidation cycles. [236]. Because of strong absorptive properties, PPY can be immobilized onto Au electrodes for the convenient studying of electrocatalytic. The obtained Pt-PPy nanocomposite-modified Au electrodes exhibit a strong elctrocatalytic activity toward O$_2$ reduction in acid solution. It can be concluded that the Pt-PPy composite may be developed for its application in fuel cells and oxygen sensors [237].

Recently, polypyrrole nanotube imidazolium moiety can be modified with $\sim$13.2 nm size of Pt–Au alloy nanoparticles hybrid was synthesized by covalently attached imidazolium moiety, which exhibited well-dispersed effect due to the mutual interaction between Au and Pt [238]. Highly porous PANI–Pt particle size (4 nm) composite reported that the methanol oxidation has better catalytic activity value of 109.5 mA mg^{-1} and it can contribute to the improvement of catalytic performance [239]. The preparation of Pt–Co bimetallic compounds were carried out on polypyrrole–multi-walled carbon nanotube composite by in situ polymerization method for DMFCs. The composite reached good CO-tolerance ability and great potential for DMFCs [240].

Zhou et al. [241] developed an electrocatalytic performance of methanol oxidation based on a novel modified composites of platinum-supported poly indole (Pt/Pin/GC) and poly(5-methoxy indole) (Pt/PMI/GC) in a electrodeposition method. The Pt/Pin/GC and Pt/PMI/GC catalysts were revealed higher catalytic activity and strong poisoning tolerance. Electrochemical impedance spectroscopy also used to measure the charge-transfer resistance for methanol oxidation. Methanol oxidation fuel cell based on Pt–Co-supported polyphosphazene modified with carbon nanotube was reported [242]. The composite fuel cell showed good distribution, small particle size, and high mass activity. PANI–PTSA composite modified with Pt on the electrode surface (Pt/PANI–PTSA). The catalyst was characterized by electrochemically, and it (Pt/PANI–PTSA) was used for methanol oxidation at the Pt electrode surface [243]. Treated polystyrene sphere (Pt/Ppy/PS) catalyst builds a profound impact in electrochemistry due to its remarkable electrochemical properties of methanol oxidation. The sphere type of Pt/Ppy/PS

electrode have big and small holes like catalysts exhibit particle size range around 2-200 nm [244].

The combination of sCPE/PAMT catalyst showed superior electrocatalytic properties than others [156]. Wang et al. [245] reported that a platinum microparticle interface on conducting polymer modified with nichrome matrix (Pt/PAn/Nc) catalyst by a simple and green approach method for methanol oxidation. The electrode observed anti-CO poisoning capacity, decreased the electrode cost and very simple. The polyethyleneimine-capped platinum nanoparticles (PEI–PtNPs) have been synthesized by photoreduction method. This catalyst (PEI–PtNPs) can be modified with conducting polymers of poly (3,4-ethylenedioxythiophene:poly(styrene sulfonate) [(PEDOT/PSS)–Na$^+$]. The catalyst [PEI-capped PtNPs/PEDOT/PSS] exhibits the best improvement of active catalyst for methanol oxidation [236]. The electrochemical preparation of Pt-supported polyindole (Pt/PIn) and poly(5-methoxy indole) (Pt/PMI) catalysts has been used for methanol oxidation. The resulted catalyst exhibits higher catalytic activity and stronger poisoning tolerance than Pt/polypyrrole/GC and Pt/GC. By applying electrochemical impedance spectroscopic (EIS) analysis, the charge-transfer resistances for methanol oxidation on Pt/Pin/GC and Pt/PMI/GC catalysts are smaller than the others [241]. Another approach has been the electropolymerization of aniline and its derivatives on pre-treated aluminum and platinum (Al/Pt) electrodes. The applied electrode potential was swept between 0.2 and 1.0 V versus SCE using 0.1 M H_2SO_4 and 0.1 M aniline. The Pt-supported polyaniline matrix enhanced the electrocatalytic activity toward methanol oxidation reactions [246]. Radiolysis and salient synthesis aspects were viable approaches in the preparation of conducting polymer (poly(diphenyl butadiene) (PDPB))-supported palladium nanoplate (PDPB/Pd) hybrid and are used in DMFCs. The composite was developed in a real passive DMFC and the enhancement of catalytic activity [247].

Electrochemical method used preparation of Pt-based catalysts with free-standing poly[poly(N-vinyl carbazole)] (PPVK) as support (Pt–M/PPVK, M=Pd, Au, and Ru) on a glassy carbon electrode (GCE). It is found that PPVK film as support effectively enhances the catalytic activity of Pt nanoparticles for methanol electro-oxidation in alkaline medium. The bimetallic Pt–M nanoparticles obtained potentiostatically on the PPVK film show the higher electrocatalytic activity than bare Pt/GCE and JM Pt/C [248]. PANI/Fe_2O_3 multi-channeled nanotube structure as aqueous rechargeable lithium-ion battery (ARLIB) anode is using PANI–Mo_3O_{10} nanowires as the template. The removal of MoO_x from the intercalated layered MoO_x/PANI structures results in a multi-channeled nanotube structure, and the subsequent hydrothermal growth of Fe_2O_3 nanoparticles on PANI surface can simultaneously re-dope PANI into a highly conductive form. The initial discharge and charge capacities of the PANI/Fe_2O_3 multi-channeled nanotube anode are 60.5 and 54.2 mAh g^{-1} at 150 mA g^{-1}, respectively. When fabricated as an ARLIB full cell with the PANI/Fe_2O_3 multi-channeled nanotube anode and a $LiMn_2O_4$ cathode, an initial discharge capacity of 50.5 mAh g^{-1} is obtained at the

current rate of 150 mA g^{-1}, with superior capacity retention of 73.3% after over 1000 charge/discharge cycles [249].

Iron species attached by physically or chemically on backbone of a PPy comprised with LiFePO$_4$ leads to stabilization of the charge/discharge characteristics and higher electrode capacities [104]. Se/PPy/graphene composites were synthesized by surfactant-free solution processes, which exhibit large discharge capacity of 678 Ah kg^{-1} at a current rate of C/120 used of Li–Se battery [250]. Layer-by-layer fashion was used for improving the characteristic properties of V$_2$O$_5$ and of PANI with a volumetric charge density of 264 mAh cm^{-3} [251]. PANI deposited by a self-assembly process onto carbon particles of LiFePO$_4$ found that capacity increases in particular at high rates [252]. PPy-covered NiO was used for remedying the inherent problems of volume change [253]. PPy can also be used to reduce charge-transfer resistance associated with the Li$^+$ ion intercalation/deintercalation reaction such as PPy/MoO$_3$, PPy/V$_2$O$_5$, PPy/LiCoO$_2$, and PPy/LiV$_3$O$_8$ [254–258]. Javier et al. found that theoretical value of LiFePO$_4$ is maintained using block copolymer of poly(3-hexylthiophene) and poly(ethylene oxide) [259]. A α-LiFeO$_2$–PPy nanocomposite was prepared by the chemical polymerization method as a cathode material for improving the reversible capacity and cycling stability (104 mAh g^{-1} at 0.1 C after 100 cycles) [260]. To prevent the contact of the nanoSi surface with electrolyte, SiNPs covered by Li$^+$-conductive polymer matrix, thus suppressing the continual rupturing-reformation of SEI film on the Si surfaces [261].

Han et al. found multi-functional nanostructure of PPy/Fe$_2$O$_3$/C as stable and high efficient anode [262]. Controlled Li$^+$ diffusion of anode material obtained from SnO$_2$/PPy nanocomposites [263, 264]. Significantly improving the conductivity of SiNPs by PPy prevents the cracking of the electrode during cycling [265]. Microemulsion polymerization method was used for SnO$_2$/PANI composite in anode material applications [266]. SnO$_2$-based composite coaxial nanocables carbon-related particles (MWCNT, graphene, SWNT) anchored on conducting polymers exhibited excellent stability and high reversible capacity [267–269]. TiO$_2$-based conducting polymer composites synthesized by hydrothermal with chemical polymerization methods developed for enabling fast discharge and charge with enhanced electrochemical performance [270–272].

Template utilized in synthesis of core–shell CuO/PPy composites led to improved stability, electric conductivity, and electrochemical performance [273]. Surface adsorption of PDDA on LiMn$_2$O$_4$ particles extends the lifetime of the LIB by arresting the Mn$^+$ dissolution, thus increasing battery stability [274]. Significantly improved the electrochemical performance of NiO/PPy composite was also studied [253]. Cation exchange technique was used for high-performance cathode material (PPy/VOx–NTs) [275]. Dissolution of metal oxide on LiNi$_{1/3}$Mn$_{1/3}$Co$_{1/3}$O$_2$/Li$_x$V$_2$O$_5$/PANI composite was studied [276]. Surface coating of PPy on LiFePO$_4$ particles was applied as improves the electron conductivity [277]. Mixed ion/electronic conductor of PPy with PAAMPSA was an additive in sulfur cathodes in Li–S batteries [278]. Nest-like PANI coated SiNPs was also proposed [279]. Reverse micelle approach of V$_2$O$_5$/PANI was analyzed, and the hybrid

material seems to be the stabilization of the capacity due to a probable homogeneous distribution of the induced stress during cycling [280]. Simple mixing of conductive binder (SPAn) and ramsdellite-MnO_2 used as cathodic material for LIPs [281]. Concomitant ion exchange and polymerization method used in MoO_3/PANI, which provided a moderate increase in cell capacity and improved the reversibility of the Li insertion reaction [282]. Organic–inorganic hybrid material formed by PANI/hexacyanoferrate (HCF) anion; the anchoring of the electroactive anion within the polymer caused its application as a functional material that harnesses the activity of the molecular species [283]. Pressurized method used for SnNPs/PANI synthesis and examined to anode properties [284].

Facile template-free approach to grow a well-aligned large-scale cone-shaped nanostructures of RuO_2/PPy was prepared for specific capacitance ~ 15.1 mF cm^{-2} (~ 302 F/g) at current density of 0.5 mA cm^{-2} with a potential range of—0.2–0.7 V. This material exhibited very high stability and promising supercapacitor performances [285]. Due to high cost of RuO_2, many research works based on MnO_2 with a variety of nanostructures were explored for the high specific capacitance and rate stability [286, 287]. But poor electrical conductivity is remaining the same as the other MO_x. For effective and promising supercapacitor applications, a range of MnO_2-based binary phase hybrids are demonstrated with CPs [145, 288].

Hou et al. [289] have demonstrated MnO_2/CNT/CP ternary nanostructures exhibiting high specific capacitance 427 F g^{-1} with high cycle stability. Zhou et al. [290] have claimed an impressive 2223 F g^{-1} for a composite with 3D CoO with PPy nanowire. In their work, the aqueous asymmetric supercapacitor device with a maximum potential window of 1.8 V was demonstrated with a very high energy density (~ 43.5 Wh/kg), high power density (~ 5500 W/kg at 11.8 Wh/kg), and outstanding cyclability. Reports also show that the core–shell or hybrid nanostructure composite has been potential for improved flexible supercapacitor applications. Recently, Li et al. [291] have demonstrated the core–shell CNT@PPy@MnO_2 ternary composite electrode for ES application. In their work, the synergistic effects from respective PPy and MnO_2, in addition of the porous conductive CNT framework, were attributed for the superior electrochemical performance of the hybrid electrode. In another work, Wang et al. have prepared MnO_2–PPy hybrid nanofilm directly on the CC for high-voltage symmetric ES application [292].

9.3.9 Challenges on Conducting Polymers/Inorganic Nanohybrid-based EES

From the above description, it can be obviously implicit that different inorganic particles composites with CPs can impel the future of CP-based inorganic hybrids, and flexible electrode engineering offers an significant way to optimize the CP-based high-performance flexible energy devices. Research studies also declare

that the composite formation can affect the overall electrochemical process, and the final electrochemical device performance and stability of the electroactive materials. Since past decades, clearly indicates that in the last five years how the CP-based energy devices materials improved from the binary to ternary compositions. Moreover, it is also found that, in the majority of the researches, CP-based composites were the best-performing flexible energy devices when directly fabricated on the flexible current collector.

But, it should be point out that, while the CP inorganic hybrids show very high specific capacitance, their device performances such as power density, energy density, and cycle stability are very far from the practical industrial applications. Also, most of the research works have mainly focused on the high performance of the energy device materials, but the optimization of the cell fabrication and their effect on device performance, such as power density, energy density, and stability, should be more focused near future. Thus, to research into the power density and energy density study of the complete battery or capacitor cell and more advance characterizations of the electrode material resistance should be focused carefully in this field as it would be very informative for real and commercial energy storage device applications. Lastly, it is needed to put some efforts on defining the industrial standards for the commercialization of EES. Even if, in the recent market, the carbon-based electrodes become commercially available; there is lacked of any industrial standards for EES at this moment. As a result, it is required to create some general industrial standards, such as performance and electrode structural and dimensional parameters, depending on the kinds of EES and its applications.

9.4   Conclusions

In spite of the huge amount of data produced during research laboratories across the globe, it is still not clear whether hybrid composites have the potential to revolutionize many aspects of our lives. This is mostly suitable for the electrochemical energy storage field, in which has reached rather high levels due to the continuous need for new materials that can meet the market's performance requirements. Conducting polymer-inorganic particle hybrids promises to increase substantially the energy density and power density of practical systems and allow the development of next-generation devices. Because of coupling the unique advantages of dissimilar storage materials to form hybrid composite electroactive materials is an important approach to control, develop, and optimize the structures and properties of electrode material for enhancing their performance for EES and the properties of hybrid composite electrodes depend not only upon the individual components used but also on the morphology and the interfacial characteristics. Therefore, hybrid electrode offers high energy storage, the possibility of long-term stability, and a less expensive, easy, and reproducible fabrication method, and as such they necessitate a renewed approach to their design and development. Additionally, it will push the development of useful and reliable EES devices. However, hybrid electrode-based

batteries have certain restriction such as uncertainty of safety, reducing capacity, poor rate capability, and conductivity. Also, need to understand the metal storage mechanisms of materials, the kinetic transport at the electrode/electrolyte interface, and the development of extrapolative theoretical tools for a better fundamental understanding of the relationships between composites and electrochemical properties.

Also, as hybrid electrode-based supercapacitors still have some dilemma. A synthesized hybrid composite electroactive material with precisely controlling their chemical composition ratio, micro/nanostructures, phases, surface area, and interfacial characteristics is still challenging. The property and behaviors of the hybrid composite electroactive materials can differ considerably depending on the preparation technique and process parameters; so, the ability to reproducibly synthesize materials with consistent properties is very important for their wide uses in supercapacitors. Aggregation and degradation can occur in the nanocomposite by relatively strong forces between them, and micro/nanostructure changes due to charging–discharging cycling and materials contaminations due to impurity introduced for original reactants or during synthesis processes etc. has to be resolved before their large-scale adoption by the industry. Further, the materials costs and their synthesis processes have to be reduced significantly. The future directions of electrode materials should focus on search new electrodes and designing structures and morphology for improving the power density, rate capability, service life, safety, and reduced cost. More sustainable and greener methods should be adopted to producing high power batteries, which will be limited the pollution and to secure a future for living system.

References

1. Choi HJ, Jung SM, Seo JM et al (2012) Graphene for energy conversion and storage in fuel cells and supercapacitors. Nano Energy 1(4):534–551
2. Padbury R, Zhang X (2011) Lithium-oxygen batteries-limiting factors that affect performance. J Power Sources 196(10):4436–4444
3. Gao X, Luo W, Zhong C et al (2014) Novel germanium/polypyrrole composite for high power lithium-ion batteries. Sci Rep 4:6095
4. Sengodu P, Deshmukh AD (2015) Conducting polymers and their inorganic composites for advanced Li-ion batteries: a review. RSC Adv 5(52):42109–42130
5. Prakash S, Chakrabarty T, Singh AK et al (2013) Polymer thin films embedded with metal nanoparticles for electrochemical biosensors applications. Biosens Bioelectron 41:43–53
6. Bruce PG, Scrosati B, Tarascon JM (2008) Nanomaterials for rechargeable lithium batteries. Angew Chem Int Ed 47(16):2930–2946
7. Arico AS, Bruce P, Scrosati B et al (2005) Nanostructured materials for advanced energy conversion and storage devices. Nat Mater 4(5):366–377
8. Liu N, Li W, Pasta M et al (2013) Nanomaterials for electrochemical energy storage. Front Phys 9(3):323–350
9. Liu B, Soares P, Checkles C et al (2013) Three-dimensional hierarchical ternary nanostructures for high-performance Li-ion battery anodes. Nano Lett 13(7):3414–3419

10. Prakash S, Rao CRK, Vijayan M (2008) New polyaniline (PAni)-polyelectrolyte (PDDMAC) composites: synthesis and applications. Electrochim Acta 53(18):5704–5710

11. Prakash S, Rao CRK, Vijayan M (2009) Polyaniline-polyelectrolyte-gold (0) ternary nanocomposites: synthesis and electrochemical properties. Electrochim Acta 54(24):5919–5927

12. Wei D, Cotton D, Ryhänen T (2012) All-solid-state textile batteries made from nano-emulsion conducting polymer inks for wearable electronics. Nanomaterials 2(3):268–274

13. Wallace GG, Campbell TE, Innis PC (2007) Putting function into fashion: organic conducting polymer fibres and textiles. Fibers Polym 8(2):135–142

14. Trohalaki S (2012) Energy focus: Li-ion batteries fabricated by spray painting. MRS Bull 37(10):883–884

15. Wu H, Zheng G, Liu N et al (2012) Engineering empty space between Si nanoparticles for lithium-ion battery anodes. Nano Lett 12(2):904–909

16. Bock K (2005) Polymer electronics systems-polytronics. Proc IEEE 93(8):1400–1406

17. Katz HE, Searson PC, Poehler TO (2010) Batteries and charge storage devices based on electronically conducting polymers. J Mater Res 25(08):1561–1574

18. Abdelhamid ME, O'Mullane AP, Snook GA (2015) Storing energy in plastics: a review on conducting polymers & their role in electrochemical energy storage. RSC Adv 5(15):11611–11626

19. Snook GA, Kao P, Best AS (2011) Conducting-polymer-based supercapacitor devices and electrodes. J Power Sources 196(1):1–12

20. Forrest SR (2004) The path to ubiquitous and low-cost organic electronic appliances on plastic. Nature 428(6986):911–918

21. Tsutsui T, Fujita K (2002) The shift from "hard" to "soft" electronics. Adv Mater 14(13–14):949–952

22. Ueda A, Nagao M, Inoue A et al (2013) Electrochemical performance of all-solid-state lithium batteries with Sn_4P_3 negative electrode. J Power Sources 244:597–600

23. Sun Q, Zhang XQ, Han F et al (2012) Controlled hydrothermal synthesis of 1D nanocarbons by surfactant-templated assembly for use as anodes for rechargeable lithium-ion batteries. J Mater Chem 22(33):17049–17054

24. Yin J, Cao H, Zhou Z et al (2012) SnS_2@ reduced graphene oxide nanocomposites as anode materials with high capacity for rechargeable lithium ion batteries. J Mater Chem 22(45):23963–23970

25. Otero TF, Cantero I (1999) Conducting polymers as positive electrodes in rechargeable lithium-ion batteries. J Power Sources 81:838–841

26. Kim JM, Park HS, Park JH et al (2014) Conducting polymer-skinned electroactive materials of lithium-ion batteries: ready for monocomponent electrodes without additional binders and conductive agents. ACS Appl Mater Interfaces 6(15):12789–12797

27. Shao L, Jeon JW, Lutkenhaus JL (2011) Polyaniline/vanadium pentoxide layer-by-layer electrodes for energy storage. Chem Mater 24(1):181–189

28. Huang YH, Goodenough JB (2008) High-rate $LiFePO_4$ lithium rechargeable battery promoted by electrochemically active polymers. Chem Mater 20(23):7237–7241

29. Liu G, Xun S, Vukmirovic N et al (2011) Polymers with tailored electronic structure for high capacity lithium battery electrodes. Adv Mater 23(40):4679–4683

30. Chou SL, Pan Y, Wang JZ et al (2014) Small things make a big difference: binder effects on the performance of Li and Na batteries. Phys Chem Chem Phys 16(38):20347–20359

31. Besenhard JO, Yang J, Winter M (1997) Will advanced lithium-alloy anodes have a chance in lithium-ion batteries? J Power Sources 68(1):87–90

32. Novák P, Müller K, Santhanam KSV et al (1997) Electrochemically active polymers for rechargeable batteries. Chem Rev 97(1):207–282

33. Chan CK, Peng H, Liu G et al (2008) High-performance lithium battery anodes using silicon nanowires. Nat Nanotechnol 3(1):31–35

34. McDowell MT, Lee SW, Wang C et al (2012) The effect of metallic coatings and crystallinity on the volume expansion of silicon during electrochemical lithiation/delithiation. Nano Energy 1(3):401–410

35. Scrosati B, Garche J (2010) Lithium batteries: status, prospects and future. J Power Sources 195(9):2419–2430

36. Pasquier DA, Plitz I, Menocal S et al (2003) A comparative study of Li-ion battery, supercapacitor and nonaqueous asymmetric hybrid devices for automotive applications. J Power Sources 115(1):171–178

37. Dubarry M, Liaw BY (2009) Identify capacity fading mechanism in a commercial LiFePO$_4$ cell. J Power Sources 194(1):541–549

38. Bittihn R, Ely G, Woeffler F et al (1987) Polypyrrole as an electrode material for secondary lithium cells. Makromol Chem Macromol Symp 8(1):51–59

39. Chen J, Wang J, Wang C et al (2006) Lithium-polymer battery based on polybithiophene as cathode material. J Power Sources 159(1):708–711

40. Kaneto K, Yoshino K, Inuishi Y (1983) Characteristics of polythiophene battery. Jpn J Appl Phys 22(9A):L567

41. Arbizzani C, Mastragostino M, Rossi M (2002) Preparation and electrochemical characterization of a polymer Li$_{1.03}$Mn$_{1.97}$O$_4$/PEDOT composite electrode. Electrochem Commun 4(7):545–549

42. Carlberg JC, Inganäs O (1997) Poly(3,4-ethylenedioxythiophene) as electrode material in electrochemical capacitors. J Electrochem Soc 144(4):L61–L64

43. Shown I, Ganguly A, Chen LC et al (2015) Conducting polymer-based flexible supercapacitor. Energy Sci Eng 3(1):2–26

44. Bredas JL, Street GB (1985) Polarons, bipolarons, and solitons in conducting polymers. Acc Chem Res 18(10):309–315

45. Vilela SO, Soto-Oviedo MA, Albers APF et al (2007) Polyaniline and mineral clay-based conductive composites. Mater Res 10(3):297–300

46. Naarmann H (2000) Polymers, electrically conducting. Ullmann's Encyclopedia of Industrial Chemistry apos, vol 29. p 295

47. Nalwa HS (2000) Hand book of nanostructured materials nanotechnology, vol 5. Academic Press, New York, p 501

48. Shirakawa H, Louis EJ, MacDiarmid AG et al (1977) Synthesis of electrically conducting organic polymers: halogen derivatives of polyacetylene, (CH)x. J Chem Soc Chem Commun 16:578–580

49. Bowley HJ, Gerrard DL, Maddams WF (1985) Resonance Raman spectroscopic studies on dehydrochlorinated stretched poly(vinyl chloride). Makromol Chem 188(4):899–906

50. Shirakawa H (2001) The discovery of polyacetylene film: the dawning of an era of conducting polymers (Nobel lecture). Angew Chem Int Ed 40(14):2574–2580

51. Ito T, Shirakawa H, Ikeda S (1974) Simultaneous polymerization and formation of polyacetylene film on the surface of concentrated soluble Ziegler-type catalyst solution. J Polym Sci Polm Chem 12(1):11–20

52. Dai LM (1999) Conjugated and fullerene-containing polymers for electronic and photonic applications: advanced syntheses and microlithographic fabrications. J Macromol Sci Rev Macromol Chem Phys 39:273–387

53. Baker GL (1988) In: Bowden MJ, Turner SR (eds) Electronic and photonic applications of polymers, vol 218. America Chemical Society, Washington, DC, pp 271–296

54. Armes SP (1996) Conducting polymer colloids. Curr Opin Colloid Interface Sci 1(2):214–220

55. de Meijere A (ed) (1999) Carbon rich compounds II, Macrocyclic Oligoacetylenes and other linearly conjugated systems. Springer, Berlin

56. Yoshino K, Hirohata M, Hidayat R et al (1997) Optical properties and electroluminescence characteristics of polyacetylene derivatives dependent on substituent and layer structure. Synth Met 91(1):283–287

57. Tamao K, Kodama S, Nakajima I et al (1982) Nickel-phosphine complex-catalyzed Grignard coupling-II: grignard coupling of heterocyclic compounds. Tetrahedron 38(22):3347–3354
58. Tour JM (1994) Soluble oligo-and polyphenylenes. Adv Mater 6(3):190–198
59. Bredas JL, Silbey R (1991) Conjugated polymers. Kluwer Academic, Dordrecht
60. Meier H, Lehmann M, Kolb U (2000) Stilbenoid dendrimers. Chem Eur J 6(13):2462–2469
61. Skotheim TA, Elsenbaumer RL, Reynolds JR (1998) Handbook of conducting polymers. Marcel Dekker, New York
62. Heinze J, Frontana-Uribe BA, Ludwigs S (2010) Electrochemistry of conducting polymers persistent models and new concepts. Chem Rev 110(8):4724–4771
63. Long YZ, Li MM, Gu C et al (2011) Recent advances in synthesis, physical properties and applications of conducting polymer nanotubes and nanofibers. Prog Polym Sci 36(10): 1415–1442
64. Huang J, Virji S, Weiller BH et al (2003) Polyaniline nanofibers: facile synthesis and chemical sensors. J Am Chem Soc 125(2):314–315
65. Huang J, Kaner RB (2004) A general chemical route to polyaniline nanofibers. J Am Chem Soc 126(3):851–855
66. Chiou NR, Epstein AJ (2005) Polyaniline nanofibers prepared by dilute polymerization. Adv Mater 17(13):1679–1683
67. Wan M (2008) A template-free method towards conducting polymer nanostructures. Adv Mater 20(15):2926–2932
68. Wan M, Huang J, Shen Y (1999) Microtubes of conducting polymers. Synth Met 101 (1):708–711
69. Huang J, Kaner RB (2004) Nanofiber formation in the chemical polymerization of aniline: a mechanistic study. Angew Chem Int Ed 43(43):5817–5821
70. Jang J, Yoon H (2003) Facile fabrication of polypyrrole nanotubes using reverse microemulsion polymerization. Chem Commun 6:720–721
71. Liu H, Hu XB, Wang JY et al (2002) Structure, conductivity, and thermopower of crystalline polyaniline synthesized by the ultrasonic irradiation polymerization method. Macromolecules 35(25):9414–9419
72. Pillalamarri SK, Blum FD, Tokuhiro AT et al (2005) Radiolytic synthesis of polyaniline nanofibers: a new templateless pathway. Chem Mater 17(2):227–229
73. Huang ZM, Zhang YZ, Kotaki M et al (2003) A review on polymer nanofibers by electrospinning and their applications in nanocomposites. Compos Sci Technol 63 (15):2223–2253
74. Norris ID, Shaker MM, Ko FK et al (2000) Electrostatic fabrication of ultrafine conducting fibers: polyaniline/polyethylene oxide blends. Synth Met 114(2):109–114
75. Huang C, Dong B, Lu N et al (2009) A strategy for patterning conducting polymers using nanoimprint lithography and isotropic plasma etching. Small 5(5):583–586
76. Thapa PS, Yu DJ, Wicksted JP et al (2009) Directional growth of polypyrrole and polythiophene wires. Appl Phys Lett 94(3):33104
77. Samitsu S, Shimomura T, Ito K et al (2005) Conductivity measurements of individual poly (3,4-ethylenedioxythiophene)/poly(styrenesulfonate) nanowires on nanoelectrodes using manipulation with an atomic force microscope. Appl Phys Lett 86(23):233103
78. Samitsu S, Takanishi Y, Yamamoto J (2009) Self-assembly and one-dimensional alignment of a conducting polymer nanofiber in a nematic liquid crystal. Macromolecules 42(13):4366–4368
79. Rissler J (2004) Effective conjugation length of π-conjugated systems. Chem Phys Lett 395(1):92–96
80. Heeger AJ (2001) Semiconducting and metallic polymers: the fourth generation of polymeric materials (Nobel lecture). Angew Chem Int Ed 40(14):2591–2611
81. Michinobu T (2011) Adapting semiconducting polymer doping techniques to create new types of click postfunctionalization. Chem Soc Rev 40(5):2306–2316
82. Wang G, Zhang L, Zhang J (2012) A review of electrode materials for electrochemical supercapacitors. Chem Soc Rev 41(2):797–828

83. Basescu N, Liu ZX, Moses D et al (1987) High electrical conductivity in doped polyacetylene. Nature 327(6121):403–405

84. Brédas JL, Beljonne D, Coropceanu V et al (2004) Charge-transfer and energy-transfer processes in π-conjugated oligomers and polymers: a molecular picture. Chem Rev 104(11):4971–5004

85. Mueller M, Fabretto M, Evans D et al (2012) Vacuum vapour phase polymerization of high conductivity PEDOT: role of PEG-PPG-PEG, the origin of water, and choice of oxidant. Polymer 53(11):2146–2151

86. Bruckenstein S, Brzezinska K, Hillman AR (2000) EQCM studies of polypyrrole films. 1. Exposure to aqueous sodium tosylate solutions under thermodynamically permselective conditions. Electrochim Acta 45(22):3801–3811

87. Cho SI, Lee SB (2008) Fast electrochemistry of conductive polymer nanotubes: synthesis, mechanism, and application. Acc Chem Res 41(6):699–707

88. Levi MD, Aurbach D (2008) A short review on the strategy towards development of π-conjugated polymers with highly reversible p- and n-doping. J Power Sources 180(2):902–908

89. Jeon JW, O'Neal J, Shao L et al (2013) Charge storage in polymer acid-doped polyaniline-based layer-by-layer electrodes. ACS Appl Mater Interfaces 5(20):10127–10136

90. Lee SW, Gallant BM, Byon HR et al (2011) Nanostructured carbon-based electrodes: bridging the gap between thin-film lithium-ion batteries and electrochemical capacitors. Energy Environ Sci 4(6):1972–1985

91. Kovacic P, Jones MB (1987) Dehydro coupling of aromatic nuclei by catalyst-oxidant systems: poly(p-phenylene). Chem Rev 87(2):357–379

92. Shi G, Xue G, Li C et al (1994) Uniaxial oriented poly(p-phenylene) fibrils and films. Macromolecules 27(13):3678–3679

93. Roth S, Bleier H (1987) Solitons in polyacetylene. Adv Phys 36(4):385–462

94. Lam JWY, Tang BZ (2005) Functional polyacetylenes. Acc Chem Res 38(9):745–754

95. Asato AE, Liu RSH, Rao VP et al (1996) Azulene-containing donor-acceptor compounds as second-order nonlinear chromophores. Tetrahedron Lett 37(4):419–422

96. Taoudi H, Bernede JC, Del Valle MA et al (2001) Influence of the electrochemical conditions on the properties of polymerized carbazole. J Mater Sci 36(3):631–634

97. Du Pasquier A, Laforgue A, Simon P et al (2002) A nonaqueous asymmetric hybrid $Li_4Ti_5O_{12}$/Poly(fluorophenylthiophene) energy storage device. J Electrochem Soc 149(3): A302–A306

98. Bhadra S, Khastgir D, Singha NK et al (2009) Progress in preparation, processing and applications of polyaniline. Prog Polym Sci 34(8):783–810

99. Cheung JH, Stockton WB, Rubner MF (1997) Molecular-level processing of conjugated polymers. 3. Layer-by-layer manipulation of polyaniline via electrostatic interactions. Macromolecules 30(9):2712–2716

100. Li D, Huang J, Kaner RB (2008) Polyaniline nanofibers: a unique polymer nanostructure for versatile applications. Acc Chem Res 42(1):135–145

101. Dumitrescu I, Unwin PR, Macpherson JV (2009) Electrochemistry at carbon nanotubes: perspective and issues. Chem Commun 45:6886–6901

102. Wei L, Yushin G (2012) Nanostructured activated carbons from natural precursors for electrical double layer capacitors. Nano Energy 1(4):552–565

103. Tran HD, Li D, Kaner RB (2009) One-dimensional conducting polymer nanostructures: bulk synthesis and applications. Adv Mater 21(14–15):1487–1499

104. Park KS, Schougaard SB, Goodenough JB (2007) Conducting-polymer/iron-redox-couple composite cathodes for lithium secondary batteries. Adv Mater 19(6):848–851

105. Su C, Ye Y, Xu L et al (2012) Synthesis and charge-discharge properties of a ferrocene-containing polytriphenylamine derivative as the cathode of a lithium ion battery. J Mater Chem 22(42):22658–22662

106. Aydın M, Esat B, Kılıç Ç et al (2011) A polythiophene derivative bearing TEMPO as a cathode material for rechargeable batteries. Eur Polym J 47(12):2283–2294

107. Zhou M, Qian J, Ai X et al (2011) Redox-active Fe (CN)$_6^{4-}$-doped conducting polymers with greatly enhanced capacity as cathode materials for Li-ion batteries. Adv Mater 23(42): 4913–4917

108. McCullough RD, Williams SP (1993) Toward tuning electrical and optical properties in conjugated polymers using side-chains: highly conductive head-to-tail, heteroatom functionalized polythiophenes. J Am Chem Soc 115(24):11608–11609

109. Wang CY, Ballantyne AM, Hall SB et al (2006) Functionalized polythiophene-coated textile: a new anode material for a flexible battery. J Power Sources 156(2):610–614

110. Liao Y, Strong V, Chian W et al (2012) Sulfonated polyaniline nanostructures synthesized via rapid initiated copolymerization with controllable morphology, size, and electrical properties. Macromolecules 45(3):1570–1579

111. Ghenaatian HR, Mousavi MF, Kazemi SH et al (2009) Electrochemical investigations of self-doped polyaniline nanofibers as a new electroactive material for high performance redox supercapacitor. Synth Met 159(17):1717–1722

112. Ghenaatian HR, Mousavi MF, Rahmanifar MS (2012) High performance hybrid supercapacitor based on two nanostructured conducting polymers: self-doped polyaniline and polypyrrole nanofibers. Electrochim Acta 78:212–222

113. Bian LJ, Luan F, Liu SS et al (2012) Self-doped polyaniline on functionalized carbon cloth as electroactive materials for supercapacitor. Electrochim Acta 64:17–22

114. Patel SN, Javier AE, Beers KM et al (2012) Morphology and thermodynamic properties of a copolymer with an electronically conducting block: poly(3-ethylhexylthiophene)-block-poly (ethylene oxide). Nano Lett 12(9):4901–4906

115. Patel SN, Javier AE, Stone GM et al (2012) Simultaneous conduction of electronic charge and lithium ions in block copolymers. ACS Nano 6(2):1589–1600

116. He D, Zeng C, Xu C et al (2011) Polyaniline-functionalized carbon nanotube supported platinum catalysts. Langmuir 27(9):5582–5588

117. Cindrella L, Kannan AM (2009) Membrane electrode assembly with doped polyaniline interlayer for proton exchange membrane fuel cells under low relative humidity conditions. J Power Sources 193(2):447–453

118. Michel M, Ettingshausen F, Scheiba F et al (2008) Using layer-by-layer assembly of polyaniline fibers in the fast preparation of high performance fuel cell nanostructured membrane electrodes. Phys Chem Chem Phys 10(25):3796–3801

119. Zhiani M, Rezaei B, Jalili J (2010) Methanol electro-oxidation on Pt/C modified by polyaniline nanofibers for DMFC applications. Int J Hydrog Energy 35(17):9298–9305

120. Wolz A, Zils S, Michel M et al (2010) Structured multilayered electrodes of proton/electron conducting polymer for polymer electrolyte membrane fuel cells assembled by spray coating. J Power Sources 195(24):8162–8167

121. Mentus S, Ćirić-Marjanović G, Trchová M et al (2009) Conducting carbonized polyaniline nanotubes. Nanotechnology 20(24):245601

122. Gavrilov N, Dašić-Tomić M, Pašti I et al (2011) Carbonized polyaniline nanotubes/nanosheets-supported Pt nanoparticles: synthesis, characterization and electrocatalysis. Mater Lett 65(6):962–965

123. Li ZF, Zhang H, Liu Q et al (2014) Novel pyrolyzed polyaniline-grafted silicon nanoparticles encapsulated in graphene sheets as Li-ion battery anodes. ACS Appl Mater Interfaces 6(8):5996–6002

124. Liu Z, Poyraz S, Liu Y et al (2012) Seeding approach to noble metal decorated conducting polymer nanofiber network. Nanoscale 4(1):106–109

125. Pringle JM, Lynam C, Wallace GG et al (2008) One-step synthesis of conducting polymer-noble metal nanoparticle composites using an ionic liquid. Adv Funct Mater 18(14):2031–2040

126. Feng X, Huang H, Ye Q et al (2007) Ag/polypyrrole core–shell nanostructures: interface polymerization, characterization, and modification by gold nanoparticles. J Phys Chem C 111(24):8463–8468

127. Muñoz-Rojas D, Oró-Solé J, Ayyad O et al (2011) Shaping hybrid nanostructures with polymer matrices: the formation mechanism of silver–polypyrrole core/shell nanostructures. J Mater Chem 21(7):2078–2086
128. Liu Z, Liu Y, Zhang L et al (2012) Controlled synthesis of transition metal/conducting polymer nanocomposites. Nanotechnology 23(33):335603
129. Qi Z (1998) Novel supported catalysts: platinum and platinum oxide nanoparticles dispersed on polypyrrole/polystyrenesulfonate particles. Chem Commun 1:15–16
130. Qi Z, Pickup PG (1998) High performance conducting polymer supported oxygen reduction catalysts. Chem Commun 21:2299–2300
131. Qi Z, Lefebvre MC, Pickup PG (1998) Electron and proton transport in gas diffusion electrodes containing electronically conductive proton-exchange polymers. J Electroanal Chem 459(1):9–14
132. Naveen MH, Gurudatt NG, Noh HB et al (2016) Dealloyed auni dendrite anchored on a functionalized conducting polymer for improved catalytic oxygen reduction and hydrogen peroxide sensing in living cells. Adv Funct Mater 26(10):1590–1601
133. Ban CM, Li Z, Wu ZC, Kirkham MJ, Chen L, Jung YS, Payzant EA, Yan YF, Whittingham MS, Dillon AC (2011) Adv Energy Mater 1:58–62
134. Lee JS, Tai Kim S, Cao R et al (2011) Metal-air batteries with high energy density: Li-air versus Zn-air. Adv Energy Mater 1(1):34–50
135. Mike JF, Lutkenhaus JL (2013) Recent advances in conjugated polymer energy storage. J Polym Sci Pol Phys 51(7):468–480
136. Song MK, Park S, Alamgir FM et al (2011) Nanostructured electrodes for lithium-ion and lithium-air batteries: the latest developments, challenges, and perspectives. Mater Sci Eng 72 (11):203–252
137. Leroux F, Goward G, Power WP et al (1997) Electrochemical Li insertion into conductive polymer/V$_2$O$_5$ nanocomposites. J Electrochem Soc 144(11):3886–3895
138. Huguenin F, Torresi RM, Buttry DA (2002) Lithium electroinsertion into an inorganic-organic hybrid material composed from V$_2$O$_5$ and polyaniline. J Electrochem Soc 149(5):A546–A553
139. Wu H, Yu G, Pan L et al (2013) Stable Li-ion battery anodes by in-situ polymerization of conducting hydrogel to conformally coat silicon nanoparticles. Nat Commun 4:1943
140. Chou SL, Gao XW, Wang JZ et al (2011) Tin/polypyrrole composite anode using sodium carboxymethyl cellulose binder for lithium-ion batteries. Dalton Trans 40(48):12801–12807
141. Sivakkumar SR, MacFarlane DR, Forsyth M et al (2007) Ionic liquid-based rechargeable lithium metal-polymer cells assembled with polyaniline/carbon nanotube composite cathode. J Electrochem Soc 154(9):A834–A838
142. Zhang D, Yin Y, Liu C et al (2015) Modified secondary lithium metal batteries with the polyaniline-carbon nanotube composite buffer layer. Chem Commun 51(2):322–325
143. Gómez-Romero P, Chojak M, Cuentas-Gallegos K et al (2003) Hybrid organic-inorganic nanocomposite materials for application in solid state electrochemical supercapacitors. Electrochem Commun 5(2):149–153
144. Sen P, De A, Chowdhury AD et al (2013) Conducting polymer based manganese dioxide nanocomposite as supercapacitor. Electrochim Acta 108:265–273
145. Liu R, Lee SB (2008) MnO$_2$/poly(3,4-ethylenedioxythiophene) coaxial nanowires by one-step coelectrodeposition for electrochemical energy storage. J Am Chem Soc 130 (10):2942–2943
146. Zhou C, Zhang Y, Li Y et al (2013) Construction of high-capacitance 3D CoO@ polypyrrole nanowire array electrode for aqueous asymmetric supercapacitor. Nano Lett 13(5):2078–2085
147. Meng F, Ding Y (2011) Sub-micrometer-thick all-solid-state supercapacitors with high power and energy densities. Adv Mater 23(35):4098–4102
148. Meng C, Liu C, Chen L et al (2010) Highly flexible and all-solid-state paperlike polymer supercapacitors. Nano Lett 10(10):4025–4031

149. Tsakova V, Winkels S, Schultze JW (2001) Crystallization kinetics of Pd in composite films of PEDT. J Electroanal Chem 500(1):574–583
150. Hepel M (1998) The electrocatalytic oxidation of methanol at finely dispersed platinum nanoparticles in polypyrrole films. J Electrochem Soc 145(1):124–134
151. Grzeszczuk M, Poks P (2000) The HER performance of colloidal Pt nanoparticles incorporated in polyaniline. Electrochim Acta 45(25):4171–4177
152. Choi JH, Park KW, Lee HK et al (2003) Nano-composite of PtRu alloy electrocatalyst and electronically conducting polymer for use as the anode in a direct methanol fuel cell. Electrochim Acta 48(19):2781–2789
153. Liu YC (2002) New pathway for the autopolymerization of pyrrole on the chlorine-and gold-containing complexes with nanostructures. Langmuir 18(24):9513–9518
154. Gautier JL, Restovic A, Poillerat G et al (1997) Physicochemical versus electrochemical properties of thin CuxMn$_{3-x}$O$_4$ spinel films. Eur J Solid State Inorg Chem 34(4):367–379
155. Cong HN, Guadarrama VG, Gautier JL et al (2002) NixCo$_{3-x}$O$_4$ mixed valence oxide nanoparticles/polypyrrole composite electrodes for oxygen reduction. J New Mat Electrochem Systems 5(1):35–40
156. Gao H, He JB, Wang Y et al (2012) Advantageous combination of solid carbon paste and a conducting polymer film as a support of platinum electrocatalyst for methanol fuel cell. J Power Sources 205:164–172
157. Xiao W, Chen JS, Lu Q et al (2010) Porous spheres assembled from polythiophene (PTh)-coated ultrathin MnO$_2$ nanosheets with enhanced lithium storage capabilities. J Phys Chem C 114(27):12048–12051
158. Yang L, Wang S, Mao J et al (2013) Hierarchical MoS$_2$/polyaniline nanowires with excellent electrochemical performance for lithium-ion batteries. Adv Mater 25(8):1180–1184
159. Wang Y, Wang Y, Hosono E et al (2008) The design of a LiFePO$_4$/carbon nanocomposite with a core–shell structure and its synthesis by an in situ polymerization restriction method. Angew Chem Int Ed 47(39):7461–7465
160. Ding Z, Yao B, Feng J et al (2013) Enhanced rate performance and cycling stability of a CoCO$_3$-polypyrrole composite for lithium ion battery anodes. J Mater Chem A 1(37):11200–11209
161. Yue L, Wang S, Zhao X et al (2012) Nano-silicon composites using poly (3,4-ethylenedioxythiophene):poly(styrenesulfonate) as elastic polymer matrix and carbon source for lithium-ion battery anode. J Mater Chem 22(3):1094–1099
162. Wang H, Zeng Y, Huang K et al (2007) Improvement of cycle performance of lithium ion cell LiMn$_2$O$_4$/LixV$_2$O$_5$ with aqueous solution electrolyte by polypyrrole coating on anode. Electrochim Acta 52(15):5102–5107
163. Wang YG, Wu W, Cheng L et al (2008) A polyaniline-intercalated layered manganese oxide nanocomposite prepared by an inorganic/organic interface reaction and its high electrochemical performance for Li storage. Adv Mater 20(11):2166–2170
164. Mai L, Xu X, Han C et al (2011) Rational synthesis of silver vanadium oxides/polyaniline triaxial nanowires with enhanced electrochemical property. Nano Lett 11(11):4992–4996
165. Boyano I, Bengoechea M, de Meatza I et al (2007) Improvement in the Ppy/V$_2$O$_5$ hybrid as a cathode material for Li ion batteries using PSA as an organic additive. J Power Sources 166(2):471–477
166. Xia X, Hao Q, Lei W et al (2012) Nanostructured ternary composites of graphene/Fe$_2$O$_3$/polyaniline for high-performance supercapacitors. J Mater Chem 22(33):16844–16850
167. Sharma RK, Karakoti A, Seal S et al (2010) Multiwall carbon nanotube-poly (4-styrenesulfonic acid) supported polypyrrole/manganese oxide nano-composites for high performance electrochemical electrodes. J Power Sources 195(4):1256–1262
168. Sharma RK, Zhai L (2009) Multiwall carbon nanotube supported poly (3,4-ethylenedioxythiophene)/manganese oxide nano-composite electrode for super-capacitors. Electrochim Acta 54(27):7148–7155

169. Li Q, Liu J, Zou J et al (2011) Synthesis and electrochemical performance of multi-walled carbon nanotube/polyaniline/MnO$_2$ ternary coaxial nanostructures for supercapacitors. J Power Sources 196(1):565–572

170. Zang J, Li X (2011) In situ synthesis of ultrafine β-MnO$_2$/polypyrrole nanorod composites for high-performance supercapacitors. J Mater Chem 21(29):10965–10969

171. Fan H, Wang H, Zhao N et al (2012) Hierarchical nanocomposite of polyaniline nanorods grown on the surface of carbon nanotubes for high-performance supercapacitor electrode. J Mater Chem 22(6):2774–2780

172. Wang JG, Yang Y, Huang ZH et al (2012) Interfacial synthesis of mesoporous MnO$_2$/ polyaniline hollow spheres and their application in electrochemical capacitors. J Power Sources 204:236–243

173. Saranya S, Selvan RK, Priyadharsini N (2012) Synthesis and characterization of polyaniline/MnWO$_4$ nanocomposites as electrodes for pseudocapacitors. Appl Surf Sci 258(11):4881–4887

174. Denis MC, Lalande G, Guay D et al (1999) High energy ball-milled Pt and Pt–Ru catalysts for polymer electrolyte fuel cells and their tolerance to CO. J Appl Electrochem 29(8): 951–960

175. Wang S, Sun LX, Xu F et al (2012) Hydrolysis reaction of ball-milled Mg-metal chlorides composite for hydrogen generation for fuel cells. Int J Hydrog Energy 37(8):6771–6775

176. Guo ZP, Wang JZ, Liu HK et al (2005) Study of silicon/polypyrrole composite as anode materials for Li-ion batteries. J Power Sources 146(1):448–451

177. Zhou X, Tang J, Yang J et al (2012) Effect of polypyrrole on improving electrochemical performance of silicon based anode materials. Electrochim Acta 70:296–303

178. Guo CX, Wang M, Chen T et al (2011) A hierarchically nanostructured composite of MnO$_2$/conjugated polymer/graphene for high-performance lithium ion batteries. Adv Energy Mater 1(5):736–741

179. Chen Y, Zeng S, Qian JF et al (2014) Li þ-conductive polymer-embedded nano-Si particles as anode. Material for advanced Li-ion batteries. Appl Mater Interfaces 6:3508–3512

180. Reddy MV, Wei Wen BL, Loh KP et al (2013) Energy storage studies on InVO$_4$ as high performance anode material for Li-ion batteries. ACS Appl Mater Interfaces 5(16): 7777–7785

181. Sonia TS, Mini PA, Nandhini R et al (2013) Composite supercapacitor electrodes made of activated carbon/PEDOT: PSS and activated carbon/doped PEDOT. Bull Mater Sci 36(4):547–551

182. Prabhu M (2012) M.Sc. dissertation to University of Cincinnati, p 106

183. Yu M, Zeng Y, Zhang C et al (2013) Titanium dioxide@ polypyrrole core–shell nanowires for all solid-state flexible supercapacitors. Nanoscale 5(22):10806–10810

184. Chen Z, Xu L, Li W et al (2006) Polyaniline nanofibre supported platinum nanoelectro-catalysts for direct methanol fuel cells. Nanotechnology 17(20):5254

185. Wu G, Li L, Li JH et al (2005) Polyaniline-carbon composite films as supports of Pt and PtRu particles for methanol electrooxidation. Carbon 43(12):2579–2587

186. Chen S, Wei Z, Qi XQ et al (2012) Nanostructured polyaniline-decorated Pt/C@ PANI core–shell catalyst with enhanced durability and activity. J Am Chem Soc 134(32):13252–13255

187. Kuwabata S, Masui S, Yoneyama H (1999) Charge-discharge properties of composites of LiMn$_2$O$_4$ and polypyrrole as positive electrode materials for 4 V class of rechargeable Li batteries. Electrochim Acta 44(25):4593–4600

188. Kim JK, Manuel J, Lee MH et al (2012) Towards flexible secondary lithium batteries: polypyrrole-LiFePO$_4$ thin electrodes with polymer electrolytes. J Mater Chem 22 (30):15045–15049

189. Wang Y, Heng LIU, Ding ZHU et al (2011) Preparation and electrochemical performance of hollow-spherical polypyrrole/V$_2$O$_5$ composite. Trans Nonferrous Met Soc China 21 (6):1303–1308

190. Zhao H, Yuan A, Liu B et al (2012) High cyclic performance of V_2O_5@PPy composite as cathode of recharged lithium batteries. J Appl Electrochem 42(3):139–144
191. Posudievsky OY, Kozarenko OA, Dyadyun VS et al (2011) Effect of host-guest versus core–shell structure on electrochemical characteristics of vanadium oxide/polypyrrole nanocomposites. Electrochim Acta 58:442–448
192. Dinh HC, Mho S, Yeo IH (2011) Electrochemical analysis of conductive polymer-coated $LiFePO_4$ nanocrystalline cathodes with controlled morphology. Electroanalysis 23(9): 2079–2086
193. Bairi VG, Warford BA, Bourdo SE et al (2012) Synthesis and characterization of tanninsulfonic acid doped polyaniline-metal oxide nanocomposites. J Appl Polym Sci 124 (4):3320–3328
194. Sen P, De A (2010) Electrochemical performances of poly(3,4-ethylenedioxythiophene)-$NiFe_2O_4$ nanocomposite as electrode for supercapacitor. Electrochim Acta 55(16): 4677–4684
195. Murugan AV, Viswanath AK, Gopinath CS et al (2006) Highly efficient organic-inorganic poly(3,4-ethylenedioxythiophene)-molybdenum trioxide nanocomposite electrodes for electrochemical supercapacitor. J Appl Phys 100(7):4319
196. Dong ZH, Wei YL, Shi W et al (2011) Characterisation of doped polypyrrole/manganese oxide nanocomposite for supercapacitor electrodes. Mater Chem Phys 131(1):529–534
197. Yang X, Wang G, Wang R et al (2010) A novel layered manganese oxide/poly (aniline-co-o-anisidine) nanocomposite and its application for electrochemical supercapacitor. Electrochim Acta 55(19):5414–5419
198. Gemeay AH, Nishiyama H, Kuwabata S et al (1995) Chemical preparation of manganese dioxide/polypyrrole composites and their use as cathode active materials for rechargeable lithium batteries. J Electrochem Soc 142(12):4190–4195
199. Boyano I, Bengoechea M, de Meatza I et al (2007) Influence of acids in the Ppy/V_2O_5 hybrid synthesis and performance as a cathode material. J Power Sources 174(2):1206–1211
200. Xia X, Wang Z, Chen L (2008) Regeneration and characterization of air-oxidized $LiFePO_4$. Electrochem Commun 10(10):1442–1444
201. Lepage D, Michot C, Liang G et al (2011) A soft chemistry approach to coating of $LiFePO_4$ with a conducting polymer. Angew Chem Int Ed 50(30):6884–6887
202. Chen L, Sun LJ, Luan F et al (2010) Synthesis and pseudocapacitive studies of composite films of polyaniline and manganese oxide nanoparticles. J Power Sources 195(11): 3742–3747
203. Hu ZA, Xie YL, Wang YX et al (2009) Polyaniline/SnO_2 nanocomposite for supercapacitor applications. Mater Chem Phy 114(2):990–995
204. Wu RH, Tsai MJ, Ho KS et al (2014) Sulfonated polyaniline nanofiber as Pt-catalyst conducting support for proton exchange membrane fuel cell. Polymer 55(8):2035–2043
205. Fu LJ, Liu H, Li C et al (2005) Electrode materials for lithium secondary batteries prepared by sol-gel methods. Prog Mater Sci 50(7):881–928
206. Ren X, Shi C, Zhang P et al (2012) An investigation of V_2O_5/polypyrrole composite cathode materials for lithium-ion batteries synthesized by sol-gel. Mater Sci Eng B 177(12):929–934
207. Huguenin F, Girotto EM, Torresi RM et al (2002) Transport properties of V_2O_5/polypyrrole nanocomposite prepared by a sol-gel alkoxide route. J Electroanal Chem 536(1):37–45
208. Huguenin F, Ticianelli EA, Torresi RM (2002) XANES study of polyaniline-V_2O_5 and sulfonated polyaniline-V_2O_5 nanocomposites. Electrochim Acta 47(19):3179–3186
209. Lira-Cantú M, Gómez-Romero P (1999) Synthesis and characterization of intercalate phases in the organic-inorganic polyaniline/V_2O_5 system. J Solid State Chem 147(2):601–608
210. Lira-Cantú M, Gómez-Romero P (1999) The organic-inorganic polyaniline/V_2O_5 system. Application as a high-capacity hybrid cathode for rechargeable lithium batteries. J Electrochem Soc 146(6):2029–2033
211. Kanatzidis MG, Wu CG, Marcy HO et al (1989) Conductive-polymer bronzes. Intercalated polyaniline in vanadium oxide xerogels. J Am Chem Soc 111(11):4139–4141

212. Park KI, Song HM, Kim Y et al (2010) Electrochemical preparation and characterization of V_2O_5/polyaniline composite film cathodes for Li battery. Electrochim Acta 55(27): 8023–8029

213. He ZQ, Xiong LZ, Shang C et al (2010) In situ polymerization preparation and characterization of $Li_4Ti_5O_{12}$-polyaniline anode material. Trans Nonferrous Met Soc China 20:s262–s266

214. Huang YH, Park KS, Goodenough JB (2006) Improving lithium batteries by tethering carbon-coated $LiFePO_4$ to polypyrrole. J Electrochem Soc 153(12):A2282–A2286

215. Murugan AV (2005) Electrochemical properties of microwave irradiated synthesis of poly (3,4-ethylenedioxythiophene)/V_2O_5 nanocomposites as cathode materials for rechargeable lithium batteries. Electrochim Acta 50(24):4627–4636

216. Gong Q, He YS, Yang Y et al (2012) Synthesis and electrochemical characterization of $LiFePO_4$/C-polypyrrole composite prepared by a simple chemical vapor deposition method. J Solid State Electrochem 16(4):1383–1388

217. Du Z, Zhang S, Liu Y et al (2012) Facile fabrication of reticular polypyrrole-silicon core–shell nanofibers for high performance lithium storage. J Mater Chem 22(23):11636–11641

218. Bates JB, Dudney NJ, Lubben DC et al (1995) Thin-film rechargeable lithium batteries. J Power Sources 54(1):58–62

219. Dudney NJ (2008) Thin film micro-batteries. J Electrochem Soc Interface 17(3):44

220. Song SW, Choi H, Park HY et al (2010) High rate-induced structural changes in thin-film lithium batteries on flexible substrate. J Power Sources 195(24):8275–8279

221. Huang XH, Tu JP, Xia XH et al (2008) Nickel foam-supported porous NiO/polyaniline film as anode for lithium ion batteries. Electrochem Commun 10(9):1288–1290

222. Huang XH, Tu JP, Xia XH et al (2010) Porous NiO/poly(3,4-ethylenedioxythiophene) films as anode materials for lithium ion batteries. J Power Sources 195(4):1207–1210

223. Wang JZ, Chou SL, Chen J et al (2008) Paper-like free-standing polypyrrole and polypyrrole–$LiFePO_4$ composite films for flexible and bendable rechargeable battery. Electrochem Commun 10(11):1781–1784

224. Wang GX, Yang L, Chen Y et al (2005) An investigation of polypyrrole-$LiFePO_4$ composite cathode materials for lithium-ion batteries. Electrochim Acta 50(24):4649–4654

225. Yao Y, Liu N, McDowell MT et al (2012) Improving the cycling stability of silicon nanowire anodes with conducting polymer coatings. Energy Environ Sci 5(7):7927–7930

226. Sharma RK, Rastogi AC, Desu SB (2008) Manganese oxide embedded polypyrrole nanocomposites for electrochemical supercapacitor. Electrochim Acta 53(26):7690–7695

227. Kost KM, Bartak DE, Kazee B et al (1988) Electrodeposition of platinum microparticles into polyaniline films with electrocatalytic applications. Anal Chem 60(21):2379–2384

228. Zhou HH, Jiao SQ, Chen JH et al (2004) Effects of conductive polyaniline (PANI) preparation and platinum electrodeposition on electroactivity of methanol oxidation. J Appl Electrochem 34(4):455–459

229. Kim S, Park SJ (2008) Electroactivity of Pt-Ru/polyaniline composite catalyst-electrodes prepared by electrochemical deposition methods. Solid State Ionics 178(37):1915–1921

230. Gawron EL, Křížek T, Kowalik MA et al (2015) Preparation of a carbon-platinum-polyaniline support for atomic metal deposition. J Electrochem Soc 162(7): H423–H427

231. Wang L, Chen C, Fu Y et al (2011) Electrodeposition of three-dimensional porous platinum film on removable polyaniline template for high-performance electroanalysis. Electroanalysis 23(7):1681–1690

232. Holdcroft S, Funt BL (1988) Preparation and electrocatalytic properties of conducting films of polypyrrole containing platinum microparticulates. J Electroanal Chem Interfacial Electrochem 240(1):89–103

233. Del Valle MA, Diaz FR, Bodini ME et al (1998) Polythiophene, polyaniline and polypyrrole electrodes modified by electrodeposition of Pt and Pt^+ Pb for formic acid electrooxidation. J Appl Electrochem 28(9):943–946

234. Tao J, Liu N, Ma W et al (2013) Solid-state high performance flexible supercapacitors based on polypyrrole–MnO_2–carbon fiber hybrid structure. Sci Rep 3:2286
235. Wang Y, Yang Y, Zhang X et al (2015) One-step electrodeposition of polyaniline/nickel hexacyanoferrate/sulfonated carbon nanotubes interconnected composite films for supercapacitor. J Solid State Electrochem 19(10):3157–3168
236. Knowles KR, Hanson CC, Fogel AL et al (2012) Layer-by-layer assembled multilayers of polyethylenimine-stabilized platinum nanoparticles and PEDOT: PSS as anodes for the methanol oxidation reaction. ACS Appl Mater Interfaces 4(7):3575–3583
237. Jiwei L, Jingxia Q, Miao Y et al (2008) Preparation and characterization of Pt–polypyrrole nanocomposite for electrochemical reduction of oxygen. J Mater Sci 43(18):6285–6288
238. Peng Y, Liu C, Pan C et al (2013) PPyNT–Im–PtAu alloy nanoparticle hybrids with tunable electroactivity and enhanced durability for methanol electrooxidation and oxygen reduction reaction. ACS Appl Matter Interfaces 5(7):2752–2760
239. Ruan D, Gao F, Gu Z (2014) Enhanced electrochemical properties of surface roughed Pt nanowire electrocatalyst for methanol oxidation. Electrochim Acta 147:225–231
240. Zhao H, Yang J, Li L et al (2009) Effect of over-oxidation treatment of Pt–Co/polypyrrole–carbon nanotube catalysts on methanol oxidation. Int J Hydrog Energy 34(9):3908–3914
241. Zhou W, Du Y, Ren F et al (2010) High efficient electrocatalytic oxidation of methanol on Pt/polyindoles composite catalysts. Int J Hydrog Energy 35(8):3270–3279
242. Qian J, Wei W, Huang X et al (2012) A study of different polyphosphazene-coated carbon nanotubes as a Pt-Co catalyst support for methanol oxidation fuel cell. J Power Sources 210:345–349
243. Gharibi H, Amani M, Pahlavanzadeh H et al (2013) Investigation of carbon monoxide tolerance of platinum nanoparticles in the presence of optimum ratio of doped polyaniline with para toluene sulfonic acid and their utilization in a real passive direct methanol fuel cell. Electrochim Acta 97:216–225
244. Xie F, Meng H, Shen PK (2008) Diffusion study in a novel three-dimensional electrode for direct methanol fuel cells. Electrochim Acta 53(15):5039–5044
245. Wang Z, Gao G, Zhu H et al (2009) Electrodeposition of platinum microparticle interface on conducting polymer film modified nichrome for electrocatalytic oxidation of methanol. Int J Hydrogen Energy 34(23):9334–9340
246. Habibi B, Pournaghi-Azar MH (2010) Methanol oxidation on the polymer coated and polymer-stabilized Pt nano-particles: a comparative study of permeability and catalyst particle distribution ability of the PANI and its derivatives. Int J Hydrog Energy 35 (17):9318–9328
247. Ghosh S, Teillout AL, Floresyona D et al (2015) Conducting polymer-supported palladium nanoplates for applications in direct alcohol oxidation. Int J Hydrog Energy 40(14):4951–4959
248. Jiang F, Ren F, Zhou W et al (2012) Free-standing poly[poly(N-vinyl carbazole)]-supported Pt-based catalysts with enhanced performance for methanol electro-oxidation in alkaline medium. Fuel 102:560–566
249. Wang Y, Wang Y, Tang J et al (2014) Aqueous Li-ion cells with superior cycling performance using multi-channeled polyaniline/Fe_2O_3 nanotube anodes. J Mater Chem A 2(47):20177–20181
250. Kundu D, Krumeich F, Nesper R (2013) Investigation of nano-fibrous selenium and its polypyrrole and graphene composite as cathode material for rechargeable Li-batteries. J Power Sources 236:112–117
251. Shao L, Jeon JW, Lutkenhaus JL (2012) Polyaniline/vanadium pentoxide layer-by-layer electrodes for energy storage. Chem Mater 24(1):181–189
252. Chen WM, Huang YH, Yuan LX (2011) Self-assembly $LiFePO_4$/polyaniline composite cathode materials with inorganic acids as dopants for lithium-ion batteries. J Electroanal Chem 660(1):108–113
253. Idris NH, Wang J, Chou S et al (2011) Effects of polypyrrole on the performance of nickel oxide anode materials for rechargeable lithium-ion batteries. J Mater Res 26(07):860–866

254. Wang GJ, Yang LC, Qu QT et al (2010) An aqueous rechargeable lithium battery based on doping and intercalation mechanisms. J Solid State Electrochem 14(5):865–869

255. Tang W, Liu L, Zhu Y et al (2012) An aqueous rechargeable lithium battery of excellent rate capability based on a nanocomposite of MoO_3 coated with PPy and $LiMn_2O_4$. Energy Environ Sci 5(5):6909–6913

256. Tang W, Gao X, Zhu Y et al (2012) A hybrid of V_2O_5 nanowires and MWCNTs coated with polypyrrole as an anode material for aqueous rechargeable lithium batteries with excellent cycling performance. J Mater Chem 22(38):20143–20145

257. Liu LL, Wang XJ, Zhu YS et al (2013) Polypyrrole–coated LiV_3O_8-nanocomposites with good electrochemical performance as anode material for aqueous rechargeable lithium batteries. J Power Sources 224:290–294

258. Tian F, Liu L, Yang Z et al (2011) Electrochemical characterization of a LiV_3O_8-polypyrrole composite as a cathode material for lithium ion batteries. Mater Chem Phys 127(1):151–155

259. Javier AE, Patel SN, Hallinan DT et al (2011) Simultaneous electronic and ionic conduction in a block copolymer: application in lithium battery electrodes. Angew Chem Int Ed 50(42):9848–9851

260. Zhang Z, Wang JZ, Chou SL et al (2013) Polypyrrole–coated α-$LiFeO_2$ nanocomposite with enhanced electrochemical properties for lithium-ion batteries. Electrochim Acta 108: 820–826

261. Chen Y, Zeng S, Qian JF et al (2014) Li þ-conductive polymer-embedded nano-Si particles as anode. Material for advanced Li-ion batteries. ACS Appl Mater Interfaces 6:3508–3512

262. Han F, Li D, Li WC et al (2013) Nanoengineered polypyrrole–coated Fe_2O_3@C multifunctional composites with an improved cycle stability as lithium-ion anodes. Adv Funct Mater 23(13):1692–1700

263. Cui L, Shen J, Cheng F et al (2011) SnO_2 nanoparticles@polypyrrole nanowires composite as anode materials for rechargeable lithium-ion batteries. J Power Sources 196(4): 2195–2201

264. Yuan L, Wang J, Chew SY et al (2007) Synthesis and characterization of SnO_2-polypyrrole composite for lithium-ion battery. J Power Sources 174(2):1183–1187

265. Chew SY, Guo ZP, Wang JZ et al (2007) Novel nano-silicon/polypyrrole composites for lithium storage. Electrochem Commun 9(5):941–946

266. He Z, Xiong L, Liu W et al (2008) Synthesis and electrochemical properties of SnO_2-polyaniline composite. J Cent South Univ Technol 15:214–217

267. Shao QG, Chen WM, Wang ZH et al (2011) SnO_2-based composite coaxial nanocables with multi-walled carbon nanotube and polypyrrole as anode materials for lithium-ion batteries. Electrochem Commun 13(12):1431–1434

268. Liang R, Cao H, Qian D et al (2011) Designed synthesis of SnO_2-polyaniline-reduced graphene oxide nanocomposites as an anode material for lithium-ion batteries. J Mater Chem 21(44):17654–17657

269. Zhao Y, Li J, Wang N et al (2012) Fully reversible conversion between SnO_2 and Sn in SWNTs@SnO_2@ PPy coaxial nanocable as high performance anode material for lithium ion batteries. J Phys Chem C 116(35):18612–18617

270. Lai C, Zhang HZ, Li GR et al (2011) Mesoporous polyaniline/TiO_2 microspheres with core–shell structure as anode materials for lithium ion battery. J Power Sources 196(10):4735–4740

271. Lai C, Li GR, Dou YY et al (2010) Mesoporous polyaniline or polypyrrole/anatase TiO_2 nanocomposite as anode materials for lithium-ion batteries. Electrochim Acta 55(15): 4567–4572

272. Zhang F, Cao H, Yue D et al (2012) Enhanced anode performances of polyaniline-Tio2-reduced graphene oxide nanocomposites for lithium ion batteries. Inorg Chem 51(17):9544–9551

273. Yin Z, Ding Y, Zheng Q et al (2012) CuO/polypyrrole core–shell nanocomposites as anode materials for lithium-ion batteries. Electrochem Commun 20:40–43

274. Vidu R, Stroeve P (2004) Improvement of the thermal stability of Li-ion batteries by polymer coating of $LiMn_2O_4$. Ind Eng Chem Res 43(13):3314–3324
275. Cui CJ, Wu GM, Yang HY et al (2010) A new high-performance cathode material for rechargeable lithium-ion batteries: polypyrrole/vanadium oxide nanotubes. Electrochim Acta 55(28):8870–8875
276. Wang H, Huang K, Zeng Y et al (2007) Stabilizing cyclability of an aqueous lithium-ion battery $LiNi_{1/3}Mn_{1/3}Co_{1/3}O_2/LixV_2O_5$ by polyaniline coating on the anode. Electrochem Solid-State Lett 10(9):A199–A203
277. Fedorková A, Nacher-Alejos A, Gómez-Romero P et al (2010) Structural and electrochemical studies of PPy/PEG–$LiFePO_4$ cathode material for Li-ion batteries. Electrochim Acta 55(3):943–947
278. Fu Y, Manthiram A (2012) Enhanced cyclability of lithium–sulfur batteries by a polymer acid-doped polypyrrole mixed ionic-electronic conductor. Chem Mate 24(15):3081–3087
279. Cai JJ, Zuo PJ, Cheng XQ et al (2010) Nano-silicon/polyaniline composite for lithium storage. Electrochem Commun 12(11):1572–1575
280. Ponzio EA, Benedetti TM, Torresi RM (2007) Electrochemical and morphological stabilization of V_2O_5 nanofibers by the addition of polyaniline. Electrochim Acta 52(13):4419–4427
281. Hwang KS, Lee CW, Yoon TH et al (1999) Fabrication and characteristics of a composite cathode of sulfonated polyaniline and Ramsdellite-MnO_2 for a new rechargeable lithium polymer battery. J Power Sources 79(2):225–230
282. Kerr TA, Wu H, Nazar LF (1996) Concurrent polymerization and insertion of aniline in molybdenum trioxide: formation and properties of a $[poly(aniline)]_{0.24}MoO_3$ nanocomposite. Chem Mater 8(8):2005–2015
283. Torres-Gómez G, Tejada-Rosales EM, Gómez-Romero P (2001) Integration of hexacyanoferrate as an active species in a molecular hybrid material. Transport properties and application of polyaniline/hexacyanoferrate as a cathode in rechargeable lithium batteries. Chem Mater 13(10):3693–3697
284. Zhang XW, Wang C, Appleby AJ et al (2002) Improvement in electrochemical properties of nano-tin-polyaniline lithium-ion composite anodes by control of electrode microstructure. J Power Sources 109(1):136–141
285. Zang J, Bao SJ, Li CM et al (2008) Well-aligned cone-shaped nanostructure of polypyrrole/RuO_2 and its electrochemical supercapacitor. J Phys Chem C 112(38):14843–14847
286. Sivakkumar SR, Ko JM, Kim DY et al (2007) Performance evaluation of CNT/polypyrrole/MnO_2 composite electrodes for electrochemical capacitors. Electrochim Acta 52(25):7377–7385
287. Zhang H, Cao G, Yang Y (2009) Carbon nanotube arrays and their composites for electrochemical capacitors and lithium-ion batteries. Energy Environ Sci 2(9):932–943
288. Sun LJ, Liu XX (2008) Electrodepositions and capacitive properties of hybrid films of polyaniline and manganese dioxide with fibrous morphologies. Eur Polymer J 44(1):219–224
289. Hou Y, Cheng Y, Hobson T et al (2010) Design and synthesis of hierarchical MnO_2 nanospheres/carbon nanotubes/conducting polymer ternary composite for high performance electrochemical electrodes. Nano Lett 10(7):2727–2733
290. Shahbazyan TV (2013) Theory of plasmon-enhanced metal photoluminescence. Nano Lett 13(1):194–198
291. Li P, Yang Y, Shi E et al (2014) Core–double–shell, carbon nanotube@ polypyrrole@ MnO_2 sponge as freestanding, compressible supercapacitor electrode. ACS Appl Mater Interfaces 6(7):5228–5234
292. Wang C, Zhan Y, Wu L et al (2014) High-voltage and high-rate symmetric supercapacitor based on MnO_2-polypyrrole hybrid nanofilm. Nanotechnology 25(30):305401

Chapter 10
Polymer-Derived Carbon/Inorganic Nanohybrids for Electrochemical Energy Storage and Conversion

Lichun Yang and Qingsheng Gao

Abstract Polymer-derived carbon/inorganic nanocomposites are developed as high-performed materials for electrochemical energy conversion and storage. Via the hybridization with carbon species, the enhanced conductivity, varied band structures, and promoted stability are responsible for the optimized thermodynamics and kinetics of electrochemical processes, resulting in the high capacity/activity and good durability. In this chapter, the general strategies to construct nanocomposites will be firstly introduced. And then, electrocatalytic hydrogen evolution reaction and lithium ion batteries are taken as the examples to illustrate the enhancement of inorganics by the integration with polymer-derived carbon. Their structure–activity relationship is focused in discussing the promising electrochemical performance. We seek to provide some rational design of key structures and properties for efficient electrode materials via the controlled derivation of polymer-derived carbon and their composites.

10.1 Introduction

As one of the most versatile materials, carbon has been applied in many fields, such as energy storage/conversion, sensing, catalysis, and environmental science, owing to its extraordinary properties, e.g., low density, high thermal and electrical conductivity, good chemical and electrochemical stability, and excellent mechanical strength [1]. Carbon is also frequently integrated with inorganic nanomaterials to form nanocomposites, showing the synergistically combined properties of carbon and inorganic phases. As a result, such carbon-based nanocomposites provide opportunities for developing novel function in energy field [1–3].

L. Yang
School of Materials Science and Engineering, South China University of Technology, 510640 Guangzhou, China

Q. Gao (✉)
Department of Chemistry, Jinan University, 510632 Guangzhou, China
e-mail: tqsgao@jnu.edu.cn

To fabricate a carbon/inorganic nanocomposite for a targeted application, the carbon source must be appropriately chosen [4]. On the one hand, the molecular structure of carbon source directly influences the architectures, morphology, and properties of the carbon phase. On the other hand, it also determines the processing routes, which make obvious effects on the interfacial interactions between carbon and inorganics, and thus the properties of nanocomposites. Common types of carbon sources, including small molecules, renewable compounds, and polymers, are effective to generate carbon/inorganic nanocomposites [5–7].

This chapter will focus on the polymers as carbon source, which are ideal to construct carbon/inorganic nanocomposites for energy storage and conversion. Remarkably, the utilization of polymers exhibits obvious merits in comparison with small organic molecules [6, 7]. Firstly, the good stability of polymers upon heating enables sufficient carbon source for carbonization, avoiding the inevitable loss of small organic molecules during heating. Secondly, the varied molecular structures (e.g., porous networks and linear chains) and the associated morphology of polymers make it easy to create the novel nanostructures of carbon/inorganics, which are of great importance for improving electrochemical performance. Thirdly, the adjustability and processability of polymers endow the resulting composites with well-controlled electronic properties and promoted application, due to the efficient doping (e.g., N, S, and P), the synergy on hetero-interfaces, etc.

The controlled integration with carbon can obviously boost the performance of inorganics for electrochemical energy storage and conversion, e.g., as the electrodes for Li^+ or Mg^{2+} ion batteries, and the electrocatalysts for water splitting (hydrogen and oxygen evolution) and its reversible reactions (hydrogen oxidation and oxygen reduction) [8–11]. Via the hybridization with carbon species, the enhanced conductivity, varied band structures, and promoted stability contribute to the optimized thermodynamics and kinetics, resulting in the superior capacity/activity with good cycleability [2, 10, 12]. Particularly, polymers, with tailored molecular structures, can facilitate the controlled evolution to functional and well-defined carbon species, further promoting the electrochemical applications of their nanocomposites.

In this decade, great efforts have been made to develop novel polymer-derived carbon/inorganic nanocomposites and exploit their applications as the key materials for energy storage and conversion [1, 4]. Regarding the rapidly booming attention in this cutting-edge area, it is necessary to highlight the new discoveries and achievements. Among various electrochemical devices and technologies for energy conversion and storage, the electrocatalytic hydrogen evolution reaction (HER) and lithium ion batteries (LIBs) can well represent the electrochemical behaviors depending on the surface and bulky properties of materials [13–18]. They will be discussed as the exampling systems for the polymer-derived carbon/inorganics. In this chapter, the general strategies to construct nanocomposites will be firstly introduced. And, the relevant materials and their promising performance in HER and LIBs are discussed to illustrate the importance of the controlled derivation from polymers and polymer-based composites. Their structure–activity relationship will be emphasized for understanding the promotion of polymer-derived carbon in electrochemistry.

10.2 General Synthesis

As one characteristic of polymer-derived carbon/inorganic nanocomposites, the combination of carbon and inorganics on nanoscale plays an important role in their electrochemical behaviors and applications [4, 12]. The different combination leads to the variation of their tailored interactions and synergic effects. There are three types for the combination, i.e., inorganic can be supported by carbon matrix, coated by carbon layers, and evenly integrated with carbon skeleton, as shown in Scheme 10.1. For example, porous carbon derived from polymers serves as versatile supports to load various nanosized inorganics (type I), offering large surface to construct a profitable micro-environment with good conductivity and highly exposed active surface [19]. Meanwhile, the coating of nanosized inorganics by carbon layers is conventional (type II).

As for LIBs, the carbon coating on electrode materials (e.g., Si, Sn, and Fe_2O_3) can effectively buffer the volume-variation of active components toward the satisfied cycleability and rate capacity [3, 11]. And recently, it is evidenced that the precise control over the thickness of carbon layers (a few layers of carbon) not only protects metal (e.g., Co and Fe) nanoparticles from corrosive H^+, but also serves as the catalytic centers for HER due to the electron perturbation by metal cores [20, 21]. In addition, carbon species can be evenly integrated with inorganics on nanoscale, in which carbon is the key skeleton to achieve various morphologies of their composites (type III). As highlighted by electrospinning, [22] polymers are firstly introduced as templates to form inorganic/polymer hybrid nanofibers, which are converted to the corresponding one-dimensional (1D) carbon/inorganics using polymer-derived carbon as skeleton.

The tailored synthesis emerges as the key issues in the development of such functional materials. Regarding the integration of inorganic nanostructures with polymer-derived carbon, the synthesis can be generally sorted as below (Scheme 10.2).
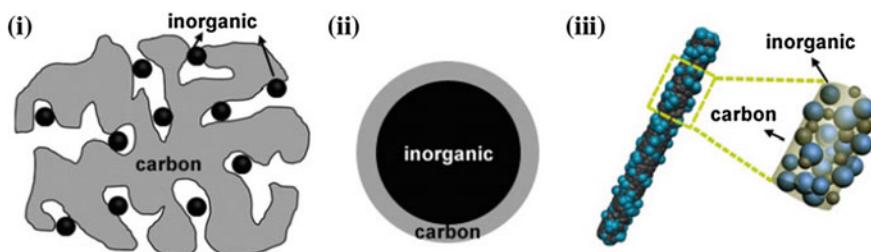
Scheme 10.1 Illustration for the integration between carbon and inorganics in polymer-derived carbon/inorganic nanocomposites
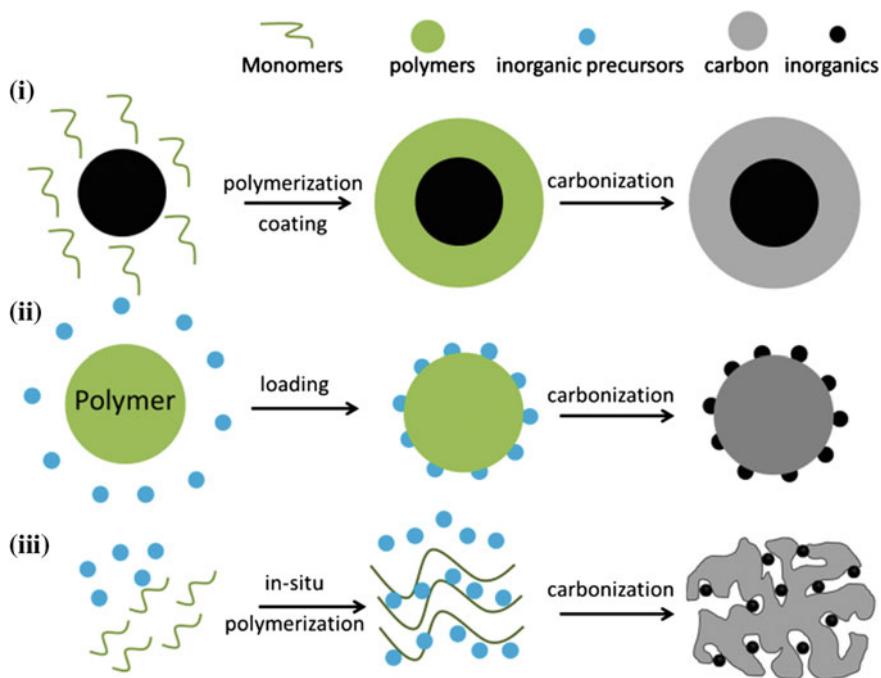
Scheme 10.2 Synthetic strategies for polymer-derived carbon/inorganic nanocomposites

10.2.1 Direct Coating Polymers on Inorganics Followed by Carbonization

Owing to the self-polymerization of monomers and the versatile adhesive properties, polymers can be directly coated onto numerous kinds of inorganic nanostructures with adjustable thickness (route I in Scheme 10.2). This leads to novel carbon/inorganic nanocomposites after carbonization under inert atmosphere. For example, Kong et al. reported the coating of polydopamine (PDA) on SnO_2 nanoparticles via the polymerization of dopamine (DOPA) in a basic solution [23]. After calcination at 700 °C under Ar flow, the carbon coated SnO_2 nanoparticles were finally obtained. Such carbon coating was demonstrated feasible to improve the electrical conductivity of inorganics for electrochemical applications, such as LIBs. Similarly, polymer-derived coating can be integrated with various inorganic nanostructures, e.g., micro/nanospheres, nanoparticles, nanocubes, nanowires, and nanorods [24–29].

10.2.2 Post-introduction of Inorganics Into Polymer-Derived Carbon Nanostructures

An alternative to direct polymer coating is to introduce inorganic precursors into/onto polymers or polymer-derived carbon hosts (route II in Scheme 10.2). The abilities of polymers to adsorb metal precursors, mainly the corresponding ions, enable the easy loading of inorganics, after which a carbonization is applied to convert polymers to carbon. In this regard, the structural evolution of inorganic components upon heating should be noticed. For example, when iron acetate (Fe $(CH_3COO)_2$) was introduced to PDA spheres, both Fe and Fe_3C generated from the carbonization of PDA, employing PDA as reductant and carbon source [30]. Another interesting route is that hollow/porous nanostructures of polymer-derived carbon could also provide nanoreactors for the synthesis of nanosized inorganics. For instance, MoS_2 nanosheets can be achieved in the nanocups of PDA-derived carbon [31].

10.2.3 In Situ Formation of Polymer-Derived Carbon/Inorganic Nanostructures

In order to achieve uniform polymer/inorganic hybrids, in situ polymerization accompanying with inorganic loading or generation is utilized, in which the strong interactions between as-formed polymer chains and inorganic components benefit the dispersion of inorganics in polymer matrix and even the derived carbon (route III in Scheme 10.2). Zhao et al. reported the in situ synthesis of H_2WO_4/PDA nanospheres, which can be further converted to WCN/C after carbonization [32]. During the polymerization of DOPA to PDA, the produced protons can further react with Na_2WO_4, resulting in the precipitate of H_2WO_4 in PDA matrix. Such uniform hybrids are good for the derivation to carbon loading tungsten carbonitride with controlled composition.

10.3 Electrocatalytic Hydrogen Evolution

To address the rapid growth of energy consumption and the associated environment issues, renewable and clean energy sources have attracted immense research interest on the global levels [33]. Hydrogen (H_2) is a promising alternative to traditional fossil fuel, as it can store energy from renewable sources (e.g., sunlight and wind) into the chemical bond via water electrolysis, which then can be released through

the reverse reaction in fuel cells on demand [34]. The electrochemical HER essentially depends on electrocatalysts, which must be stable and capable of reducing water rapidly at potentials close to its thermodynamic value ($2H^+ + 2e^- \rightarrow H_2$; $0-0.059 \times pH$, V vs. normal H_2 electrode at 298 K) [35].

Typically, the HER in both acidic and alkaline aqueous medias proceeds in two steps (Eqs. 10.1–10.6), where the * indicates the active-site, and H* a hydrogen atom bound to an active-site [18, 36]. The first one is an electrochemical reduction step (H^+ reduction, Volmer reaction) with a Tafel slope of 118 mV dec^{-1} (Eqs. 10.1 and 10.4); the second one (H_{ads} desorption) is either the ion and atom reactions (Heyrovsky-reaction) with a slope of 40 mV dec^{-1} (Eqs. 10.2 and 10.5) or the atom combination reaction (Tafel-reaction) with a slope of 30 mV dec^{-1} (Eqs. 10.3 and 10.6).

Acidic:

$$H_3O^+ (aq) + e^- + ^* \leftrightarrow H^* + H_2O\ (l) \tag{10.1}$$

$$H^* + H_3O^+ (aq) + e^- \leftrightarrow H_2(g) + H_2O\ (l) + ^* \tag{10.2}$$

$$H^* + H^* \leftrightarrow H_2(g) + 2^* \tag{10.3}$$

Alkaline:

$$H_2O\ (l) + e^- + ^* \leftrightarrow H^* + OH\ (aq) \tag{10.4}$$

$$H^* + H_2O\ (l) + e^- \leftrightarrow H_2(g) + OH\ (aq) + ^* \tag{10.5}$$

$$H^* + H^* \leftrightarrow H_2(g) + 2^* \tag{10.6}$$
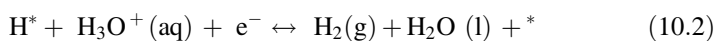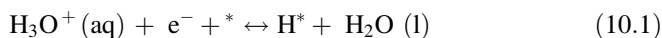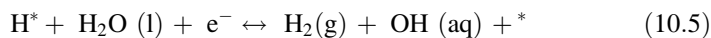
Obviously, the key parameter for the above reactions is the binding of the intermediate hydrogen to catalyst [36]. A catalyst surface possessing too weak hydrogen bonding strength cannot efficiently initiate the reaction, whereas a catalyst surface having too strong bonding strength would prohibit the releasing of adsorbed H (H_{ads}) (Scheme 10.3). For an ideal HER electrocatalyst, the hydrogen binding should be moderate to balance the two elementary steps for HER [37]. This is in line with the Sabatier principle which states that optimal catalytic activity can be achieved on a catalytic surface having intermediate bonding energies with reactive intermediates [38]. Norskov et al. calculated hydrogen adsorption free energy on different transition metals [39]. When the experimentally measured HER exchange current density was plotted as a function of the calculated free energy, an interesting volcano-shaped curve was obtained with the peak position close to that of platinum.

Although platinum (Pt) and its alloys show high efficiency, they are severely prohibited by high cost and low abundance. Therefore, the urgent issue in electrolytic systems is to explore efficient noble-metal-free catalysts that are cheap and earth-abundant [17]. Remarkable advances in electrocatalytic HER have been recently made regarding the use of transition metals and their carbides, nitrides, chalcogenides, and phosphides, which show the high HER activity due to their hydrogen binding close to that of Pt [16–18, 36]. They are remarkably featured by the good durability and economic cost. In the cases of above metal non-oxide electrocatalysts, the common shortages are their low conductivity and poor dispersion, the latter of which usually results from their harsh synthesis at high temperature. In this regards, the polymer-derived carbon matrix can effectively promote the conductivity and dispersion of active materials, improving the HER performance. Meanwhile, the strong interactions between carbon substrates and catalysts can also alter the electronic configuration on active-sites, which is very important for optimizing HER kinetics and activity.

To evaluate the efficacy of an electrocatalyst, there are many performance characteristics can be used, including its activity, stability, selectivity, and cost. Catalytic activity is almost always critical for HER, which can be determined by the varied overpotential (η) required to achieve the same current density (j) [40]. In solar water splitting, the potential for 10 mA cm^{-2} is a common figure of merit because this is the current density expected in a 12.3% efficient solar to hydrogen device, which is on the order of the efficiency that would be required for cost competitive photoelectrochemical water splitting [40]. Thus, the overpotential (η_{10}) required to achieve the j of -10 mA cm^{-2} is usually used to compare the total electrode activities. Meanwhile, Tafel plot is a useful metric to assess the HER performance of electrocatalysts and at the same time is an available indicator of the reaction mechanism [16, 41]. The small Tafel slope of electrocatalysts indicates a fast increase of hydrogen generation rate with the applied overpotential, corresponding to the promoted kinetics of HER. In the context, the activity of the metal non-oxides will be compared in terms of η_{10} and Tafel slope.

Scheme 10.3 Schematic illustration for the mechanism of electrocatalytic HER
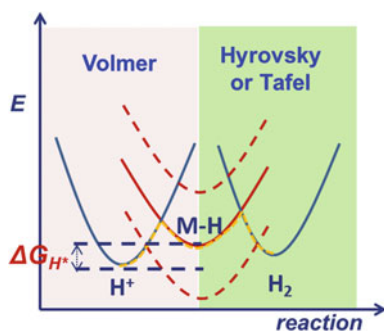
10.3.1 Polymer-Derived Carbon/Inorganics as Noble-Metal-Free Electrocatalysts

10.3.1.1 MoS$_2$-Based Nanocomposites

Inspired by nitrogenase enzymes, MoS$_2$ was discovered active for HER since 2005 [42]. And the most active-sites of MoS$_2$ were demonstrated to be the (010) and (100) planes exposing unsaturated Mo- and S-edges by Chorkendorff et al. [43], rather than the inert (002) basal plane (Fig. 10.1). Thus, increasing the number of exposed MoS$_2$ edges is crucial to improve the catalytic efficiency, which has been verified by engineering nanostructured MoS$_2$ to preferentially expose edge-sites in a highly ordered double-gyroidnanoporous network [44]. Meanwhile, it is important to note that MoS$_2$ electrocatalyst is prohibited by the extremely low conductivity between two adjacent van der Waals bonded S–Mo–S sheets [41]. Resistivity has been measured to be 2200 times larger through the basal planes than the 10^{-1} to 1 (Ω cm^{-1}) parallel to the planes (Scheme 10.4). To increase the conductivity between two adjacent S–Mo–S sheets, the construction of ultrathin MoS$_2$ nanosheets evenly integrated with conducting carbon should be taken into account.

Recently, Liu et al. demonstrated that the loading of MoS$_2$ into mesoporous carbon nanospheres (MCNs) was efficient to improve the HER activity in 0.5 M H$_2$SO$_4$, due to the enhanced conductivity by MCNs [45]. This strategy was further extended to load MoS$_2$ into the mesoporous graphene foam (MGF), which was prepared via the templating of silica nanosphere [46]. The as-obtained MGF had a high surface area of 819 m^2 g^{-1} and a pore size of $\sim$25 nm. This structure enabled the controlled growth of MoS$_2$ toward ultra-small nanoparticles ($\sim$2 nm), rather than typical nanosheets. The drastically reduced size of MoS$_2$ can massively increase the catalytic edge-sites in comparison with pure MoS$_2$ which was freely grown in solution. As expected, the MoS$_2$/MGF presented a high activity with a η_{10}
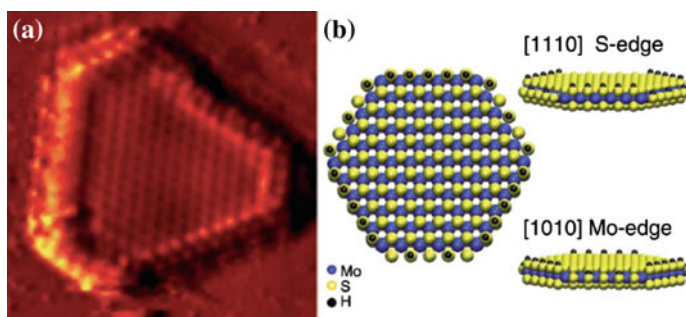
Fig. 10.1 a STM on MoS$_2$ nanoplatelets on Au [111], reproduced with permission.6 **b** A molecular model of a platelet exposing both Mo and S-edges from *top* and *side view* (Reproduced from Ref. [41] with kind permission of © 2012 Royal Society of Chemistry)
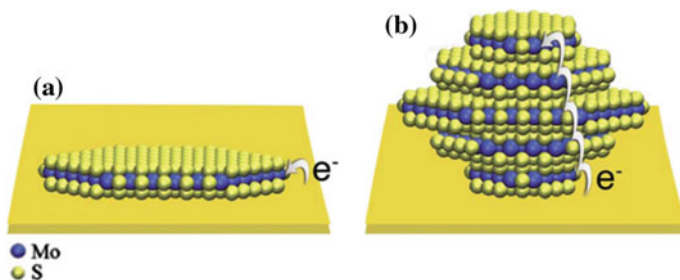
Scheme 10.4 Schematic of the difference in conductivity to the active-sites on nanoplatelets and nanoparticles (Reproduced from Ref. [41] with kind permission of © 2012 Royal Society of Chemistry)

of ~ 140 mV and a η_{100} of 200 mV in 0.5 H_2SO_4, which was superior to those of MoS_2/MCNs and MoS_2/graphene.

Lou et al. have synthesized a unique hybrid hollow structure by growing ultrathin MoS_2 nanosheets on N-doped carbon shells (denoted as C@MoS_2) [47]. As shown in Fig. 10.2, very uniform α-Fe_2O_3 nanocubes were used as templates to synthesize N-doped carbon nanoboxes, employing the smooth coating of polydopamine (PDA, thickness ~ 40 nm) as the efficient carbon source. After the removal of Fe_3O_4 by HCl, carbon nanoboxes were harvested, which further served as the support for the growth of ultrathin MoS_2. The hollow carbon nanoboxes were very uniform with an average size of about 580 nm, and the thickness of the MoS_2 shell was about 35 nm. The N-doped carbon shells can effectively prevent the aggregation of MoS_2 nanosheets, providing more active-sites for electrochemical HER. Meanwhile, the uniform hybridization of MoS_2 nanosheets with carbon can also improve the conductivity. As evaluated as electrocatalysts in 0.5 M H_2SO_4, the C@MoS_2 showed the low overpotentials of 165 and 200 mV to give current densities of 10 and 35 mA cm^{-2}, respectively.

Biomass-derived molecules, e.g., glucose and fructose are also feasible to construct the uniform nanocomposites of MoS_2/C. Their condensation to polysaccharide matrix during the hydrothermal preparation of MoS_2 provides a space-confined growth of MoS_2 nanosheets, leading to the ultrathin dimension with rich active-sites [48]. As for the hydrodesulfurization reactions in petrochemicals, a commonly accepted "rim-edge" model reveals that the rim-sites, referring to the edges of top and bottom S–Mo–S slabs, are more active for (de)hydrogenation than the edge-sites associated with the sandwiched S–Mo–S (Scheme 10.5a) [49].

Inspired by this innovation, Gao et al. introduced the space-confined growth by polysaccharides to fabricate ultrathin MoS_2 nanosheets, which further evolved to MoS_2/C after carbonization [48]. The polysaccharide matrix with abundant hydroxyl and glucosidic groups possessed the enhanced chemical interactions with Mo precursors, which would benefit the space-confined growth of MoS_2 toward ultrathin nanosheets (Scheme 10.5b). The as-obtained MoS_2/C nanospheres were uniform in size as a MoS_2 weight content of 14.8% is adopted (Fig. 10.3).
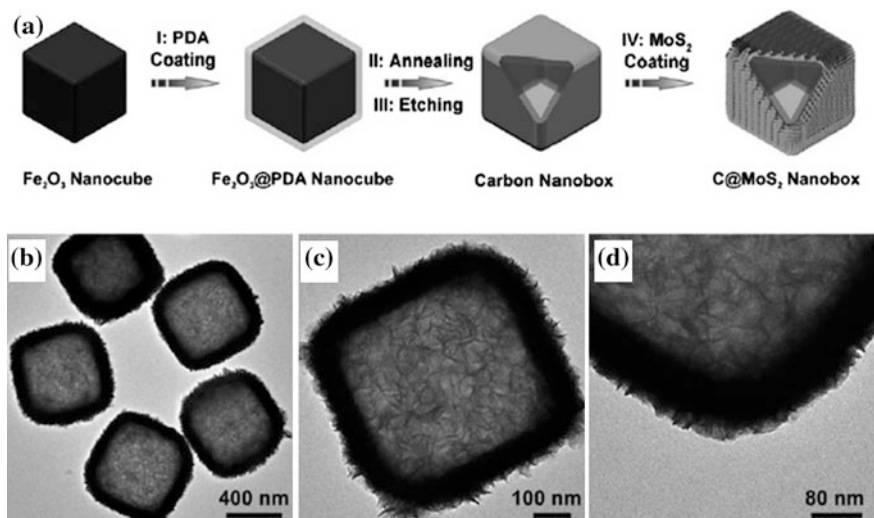
Fig. 10.2 a Illustration of the synthesis process of C@MoS$_2$ nanoboxes. **b–d** Images of C@MoS$_2$ nanoboxes (Reproduced from Ref. [47] with kind permission of © 2015 Wiley-VCH)
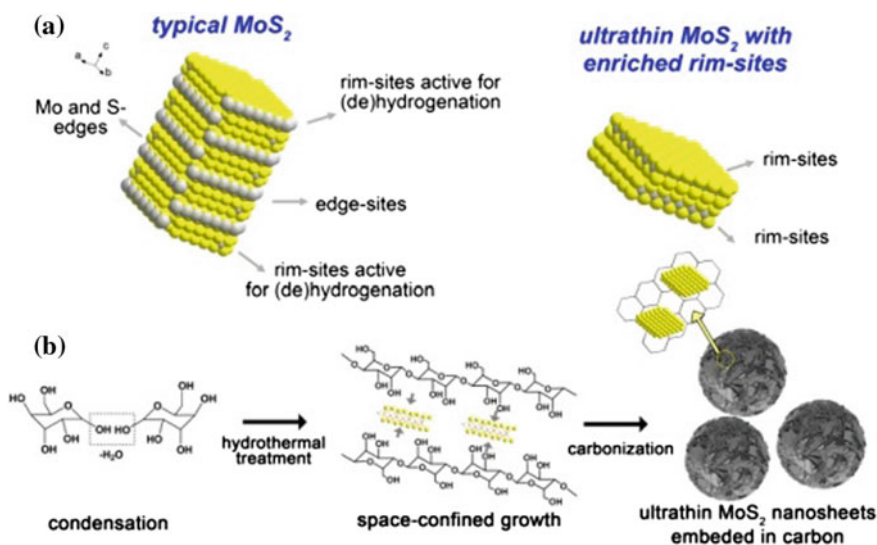
Scheme 10.5 Schematic illustration for **a** active-sites replying on the *different thickness* of MoS$_2$, and **b** fabrication of MoS$_2$/C employing in situ formed polysaccharides as a template to confine MoS$_2$ growth (Reproduced from Ref. [48] with kind permission of © 2015 Elsevier)

More importantly, the thickness of MoS$_2$ was about 2–4 nm, lower than that ($\sim$10 nm) received from the free generation under the same hydrothermal treatment. Such MoS$_2$/C exhibited an excellent activity for HER with a small onset

overpotential of ~ 80 mV and a high current density of 88 mA cm^{-2} at $\eta = 200$ mV. Both number and strength of active-sites were enhanced in MoS$_2$/C, which was reflected by their high C$_{dl}$ and TOF (Table 10.1), respectively. This work opened up new opportunities to construct hierarchical MoS$_2$/C nanostructures with reduced thickness and enriched active-sites via the biomass-derived polymers. The similar mechanism was also confirmed by the work conducted by Yang et al. [50], in which the low Tafel slope (40 mV dec^{-1}) of MoS$_2$/amorphous carbon indicates the striking kinetic metrics exceeding previous MoS$_2$.

Obviously, the polymer-derived carbon serves as versatile matrix in MoS$_2$/C, which enhances the control over the size and morphology of MoS$_2$, and improves the conductivity of nanocomposites. In this situation, polymers are only the carbon source toward supports. However, in some cases, polymers are also the key source for generating catalytic species.
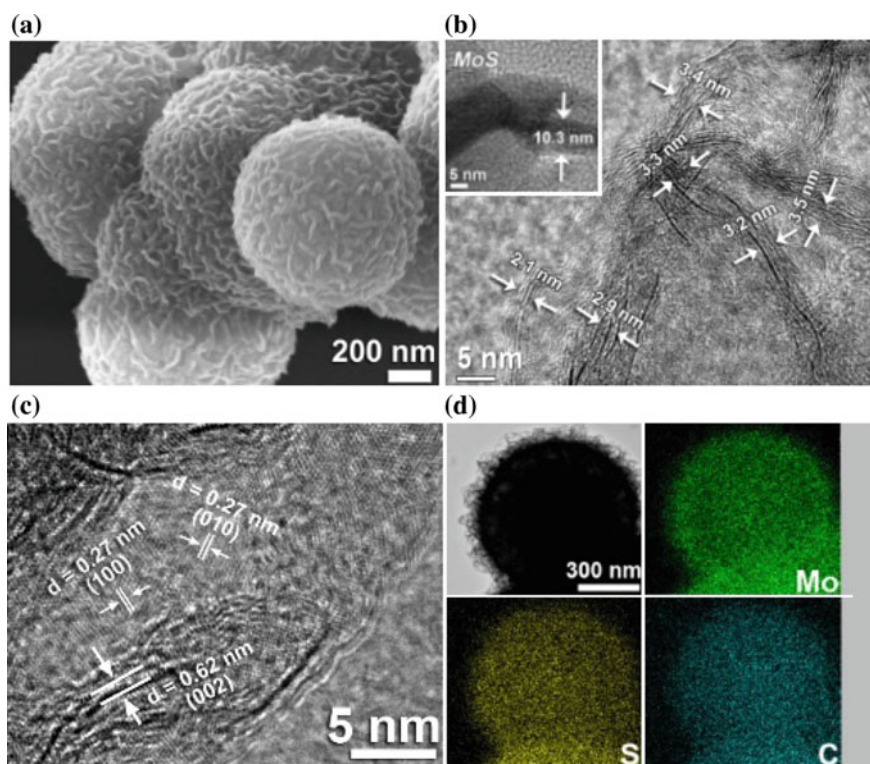
Fig. 10.3 **a** SEM and **b**, **c** HRTEM images of MoS$_2$/C-14.8. *Insets* of **b** are the TEM image of bare MoS$_2$, hydrothermally synthesized without glucose. **d** Elemental mapping of Mo, S and C detected on MoS$_2$/C-14.8 (Reproduced from Ref. [48] with kind permission of © 2015 Elsevier)

Table 10.1 HER parameters of various MoS_2 samples [48]

Catalysts[a]	Active-sites (mmol mol_{MoS2}^{-1})[b]	TOF (s^{-1})[c]	Tafel slope (mV dec^{-1})	Tafel region (mV)	j_0 (μA cm^{-2})[d]
MoS_2/C-14.8	67.4	13.1	60	80–120	131.8
MoS_2/C-19.7	43.7	2.9	72	100–150	63.1
MoS_2/C-29.0	29.0	2.1	77	130–180	25.8
Bare MoS_2	1.6	0.7	90	215–270	4.2

[a]All the parameters were measured under the same conditions, i.e., catalyst loading weight of 0.570 mg cm^{-2} on GCE in 0.5 M H_2SO_4 solution
[b]Data were calculated according the CV results
[c]TOFs were measured at $\eta = 200$ mV
[d]Exchange current densities were obtained from Tafel curves by using extrapolation methods

10.3.1.2 Carbide-Based Nanocomposites

Owing to the noble-metal-like electron properties around the Fermi level (E_F), transition metal carbides emerge as the promising noble-metal-free electrocatalysts for HER. In comparison with metal sulfides, the good electronic conductivity of carbides enables the high electrochemical performance [17, 18]. However, the high-temperature preparation required for metal carbides unfortunately results in the poor dispersity and the sintering of active-sites [51]. As expected, the polymer-derived carbon provides a feasible support to accommodate such challenge. More importantly, the polymer is reactive for the formation of active carbides, which would enhance the interactions between carbides and carbon and consequently promote the catalytic performance.

Presenting the varied electronic feature and catalytic property related to the tuneable phases and composition, molybdenum carbides have received special attentions [18]. Among them, β-Mo_2C has demonstrated the best performance [52]. Intense efforts have been made on Mo_2C nanostructures with enriched active-sites, which highlight the good activity on 1D nanostructures composed of well-defined Mo_2C nanoparticles [53–55]. The hierarchical surface in radial direction provides abundant sites for H_2 generation and bubble release; the axial dimension in micron facilitates charge transfer and avoids aggregation of active materials.

Recently, Lou et al. designed hierarchical β-Mo_2C nanotubes consisted by porous nanosheets via carburizing Mo-polydopamine nanotubes under a N_2 gas flow [56]. As shown in Fig. 10.4, Mo-polydopamine hybrid nanotubes constructed by 2D ultrathin nanosheets were first fabricated using MoO_4^{2-} as the Mo source, dopamine hydrochloride as coordination ligand, ammonia solution as the polymerization initiator, and MoO_3 nanorods as a reactive self-degraded template as well as additional Mo supply. The hierarchical β-Mo_2C nanotubes with a wall thickness of about 90 nm and a well-defined hollow interior could be clearly observed (Fig. 10.4). The highly porous texture was throughout the whole nanotubes, which were composed of ultrafine nanocrystallites (<3 nm) uniformly
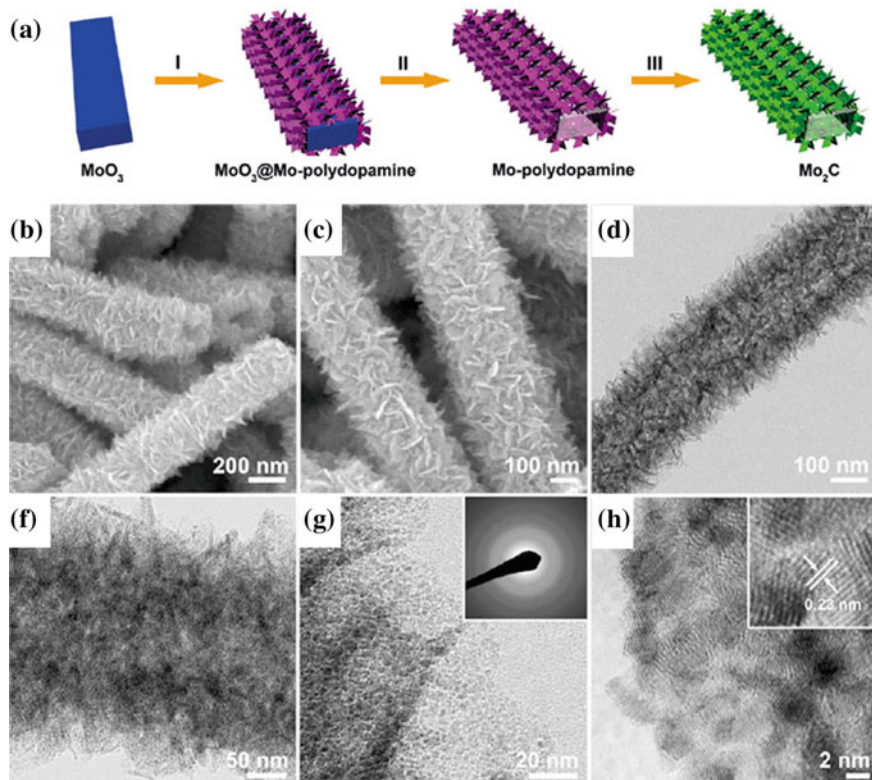
Fig. 10.4 a Schematic illustration for synthesis of β-Mo$_2$C nanotubes. **b, c** FESEM images, **d–g** TEM, and **h** HRTEM images of the hierarchical β-Mo$_2$C nanotubes (Reproduced from Ref. [56] with kind permission of © 2015 Wiley-VCH)

embedded in carbon matrix. Benefitting from the ultrafine primary nanocrystallites, the large exposed surface, the fast charge transfer, and the tubular structure, the as-prepared hierarchical β-Mo$_2$C nanotubes exhibited excellent electrocatalytic performance for HER (Fig. 10.5). They delivered a low η_{10} of 172 and 112 mV in 0.5 M H$_2$SO$_4$ and 0.1 M KOH, respectively.

Carbonization via polymer pyrolysis is feasible toward various porous metal-carbide electrocatalysts. Polymers, e.g., polydiaminopyridine and polyaniline, poly(m-aminobenzenesulfonic acid), have been proved efficient as the sources for metal carbides [57, 58]. However, to enhance the nanoporosity and large surface of catalysts, some assistant is required during the preparation. For example, Tan et al. reported the synthesis of cobalt and heteroatom (N and/or S) doped carbon through the pyrolysis of poly(m-aminobenzenesulfonic acid) using SiO$_2$ nanoparticles as the template [58]. The high Brunauer–Emmett–Teller (BET) surface area (725 m^2 g^{-1}) is helpful for exposing the catalytic sites to enhance electrocatalytic activity.
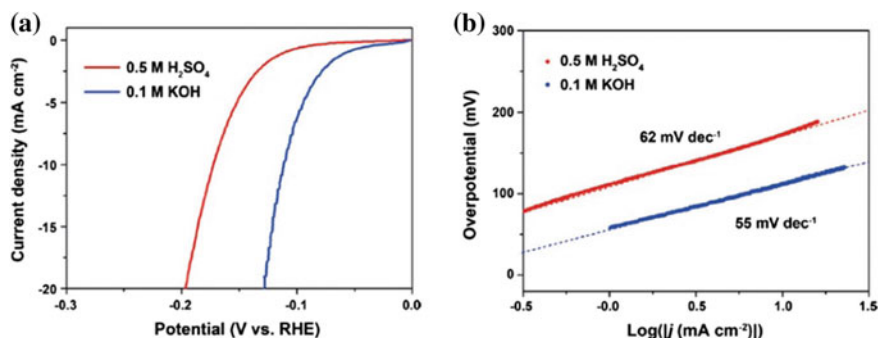
Fig. 10.5 Electrochemical evaluation of hierarchical β-Mo$_2$C nanotubes in 0.5 M H$_2$SO$_4$ (*red line*) and 0.1 m KOH (*blue line*). **a** Polarization curves on the GC electrode at 2 mVs^{-1} and **b** Tafel slopes (Reproduced from Ref. [56] with kind permission of © 2015 Wiley-VCH) (color figure online)

Nakanishi et al. synthesized tungsten carbonitride nanoparticles employing the in situ polymerized polydiaminopyridine (PDAP) as the precursor [32]. The pyrolysis in the presence of Fe species resulted in the highly active Fe-modified WCN/C nanospheres, in which the doping of N and Fe promoted the HER activity of WCN. Recently, they further develop molybdenum carbonitride (MoCN) nanomaterials by using in situ CO$_2$ emission strategy and the abundant amino group-based polydiaminopyridine precursors [57].

As depicted in Fig. 10.6a, the synthesis was divided into three synthetic steps. In step 1, hydrochloric acid was added to an aqueous solution of Na$_2$MoO$_4$ and diaminopyridine (DAP), forming a solid complex of DAP-2H$^+$/MoO$_4^{2-}$. In step 2, a solution of (NH$_4$)$_2$S$_2$O$_8$ and NaHCO$_3$ was further added to the above suspension to produce polydiaminopyridine (PDAP)-2H$^+$/MoO$_4^{2-}$. The NaHCO$_3$ was added for in situ CO$_2$-bubble emission in order to mechanically disrupt the solid-state monomer and/or polymer during polymerization and further create rich porosity in the final electrocatalysts after pyrolysis (800 °C, step 3). The final product was denoted as PDAP–MoCN–CO$_2$. The authors also synthesized two other MoCN materials as reference samples. The first (termed PDAP–MoCN) was prepared without adding NaHCO$_3$ during step 2, and the second (termed PANI–MoCN) was prepared using polyaniline (PANI), which has fewer amino groups than PDAP. The PDAP–MoCN–CO$_2$ was featured by the uniform distribution of particles, as compared with PDAP–MoCN and PANI–MoCN, which highlighted the importance of in situ CO$_2$ emission to improve the effective surface area of MoCN (107 m^2 g^{-1}). Moreover, the PDAP-based precursor significantly leads to the improved density of catalytic active-sites of carbonitrides, as evidenced by Fig. 10.6b. In the Mo 3d spectra, the peaks associated with the active species of Mo^{2+} and Mo^{3+} were dominant in PDAP–MoCN–CO$_2$ and PDAP–MoCN. This indicated that the higher capacity for N-coordinated MoO$_4^{2-}$ in the PDAP with abundant amino groups was beneficial for the exposure of active Mo species. Owing to the large surface area
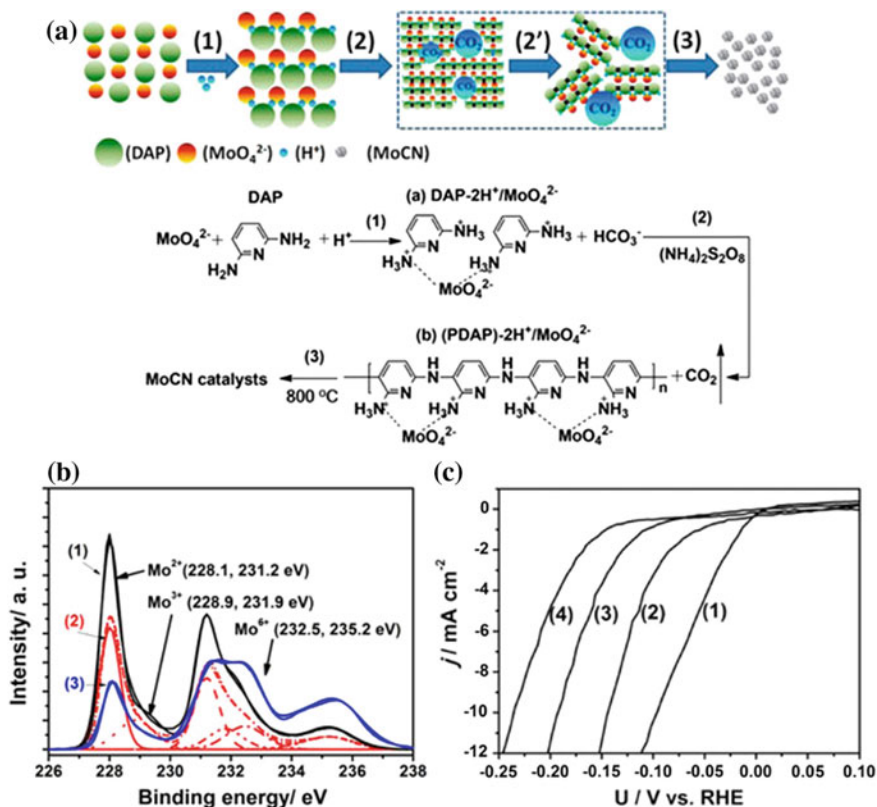
Fig. 10.6   a Schematic illustration of synthesis procedures of PDAP–MoCN–CO$_2$. **b** XPS Mo 3d spectra of (*1*) PDAP–MoCN–CO$_2$, (*2*) PDAPMoCN, and (*3*) PANI–MoCN materials. **c** HER polarization curves for (*1*) commercial Pt/C; (*2*) PDAP–MoCN–CO$_2$; (*3*) PDAP–MoCN; and (*4*) PANI–MoCN electrodes (Reproduced from Ref. [57] with kind permission of © 2015 American Chemical Society)

(107 m^2 g^{-1}) and high Mo^{2+} and Mo^{3+} surface ratios, PDAP–MoCN–CO$_2$ delivered the superior HER activity with a η_{10} of 140 mV and a Tafel slope of 46 mV dec^{-1} (Fig. 10.6c), outperforming that of PDAP–MoCN and PANI–MoCN.

The polymers as-formed during the formation of carbides served as in situ template to prohibit the aggregation of carbide, resulting in the ultrafine nanoparticles with rich active-sites. Meanwhile, the derived carbon coating on carbide surface would protect the active materials from corrosive acid or base electrolytes. N-rich molecules, e.g., cyanamide, dicyanamide, and melamine, can be polymerized to C$_3$N$_4$ and even CN$_x$ upon heating, which are the good matrix to load metal sources [59]. More importantly, the decomposition of C$_3$N$_4$ and even CN$_x$ at further evaluated temperature not only provides reactive source for carbide generation, but also results in intimate N-doped carbon on the well-defined carbides. And an

interesting electronic optimization on active-sites was recently evidenced due to strong interactions between carbide surface and ultrathin carbon coating [21].

Asefa et al. reported a facile, one-step synthetic route that leads to a novel electrocatalyst composed of ultra-small Mo_2C nanoparticles embedded within nitrogen-rich carbon (NC) nanolayers, employing dicyanamide as the carbon and nitrogen sources (Fig. 10.7) [60]. The crystalline carbons with 2–4 layers of carbon atoms were coated on the small Mo_2C with an average size 3.6 nm. The $Mo_2C@NC$ showed remarkable catalytic activity, great durability, and gives about 100% Faradaic yield toward HER over a wide pH range (pH 0–14). The optimal $Mo_2C@NC$ obtained after carbonization at 800 °C shows the low η_{10} of 124, 156, and 60 mV at pH 0, 7 and 14, respectively (Fig. 10.8). The authors further conducted theoretical calculations, which showed that the Mo_2C and N dopants in the material synergistically co-activate adjacent C atoms on the carbon nanolayers, creating superactive nonmetallic catalytic sites for HER.

Wang et al. further improved the above method to achieve ultrafine Mo_2C with an average size less than 3 nm, in which a heating-driven polymerization at 400 °C was employed to generate graphitic C_3N_4 [61]. This in situ formed polymer matrix can protect Mo_2C nanoparticles from aggregation during carbonization at high temperature. As a result, the η_{10} for HER in 0.5 M H_2SO_4 is as low as 78 mV, outperforming the most of ever-reported noble-metal-free electrocatalysts.

The polymers of carbon nitrides are also feasible to construct highly active bimetallic carbides electrocatalysts and even metal-modified carbides. For example, Zou et al. used dicyanamide as the carbon source to carbon-protected Co_6W_6C electrocatalysts, which were composed of bimetallic carbide nanoparticles (5–20 nm) embedded in carbon shells [62]. A low η_{10} of only 73 mV was observed for HER in 1.0 M KOH. Wang et al. introduced melamine as carbon and nitrogen sources to synthesize the Ni-encapsulated nitrogen-doped carbon vesicle material modified by molybdenum carbides [63]. Such nanocomposites had a hierarchically mesoporous structure and were proven to be a highly efficient nonprecious metal catalyst for HER in both acidic and basic electrolytes. Particularly, a low η_{10} of 68 mV was detected with 0.5 M H_2SO_4.

Biomass-derived polymers were used to fabricate active carbides on nanoscale, which were promising due to the low cost, high nature abundance, and good environmental-friendliness. Muckerman et al. proposed the synthesis of Mo_2C-Mo_2N/C from humble soybeans, which were high-protein biomass [64]. This catalyst, composed of a catalytic β-Mo_2C phase and an acid proof γ-Mo_2N phase, drove the HER with low overpotentials (η_{10} = 150–200 mV) and was highly durable in a corrosive acidic solution over a period exceeding 500 h. The author further extended the strategy to fabricate tungsten-based carbide-nitride electrocatalyst loading on reduced graphene oxide, which delivered a small η_{10} of 105 mV [65]. These findings prove that the high-protein biomass is a useful material for the generation of catalysts incorporating an abundant transition metal, thereby challenging the exclusivity of Pt catalysts in the hydrogen economy.
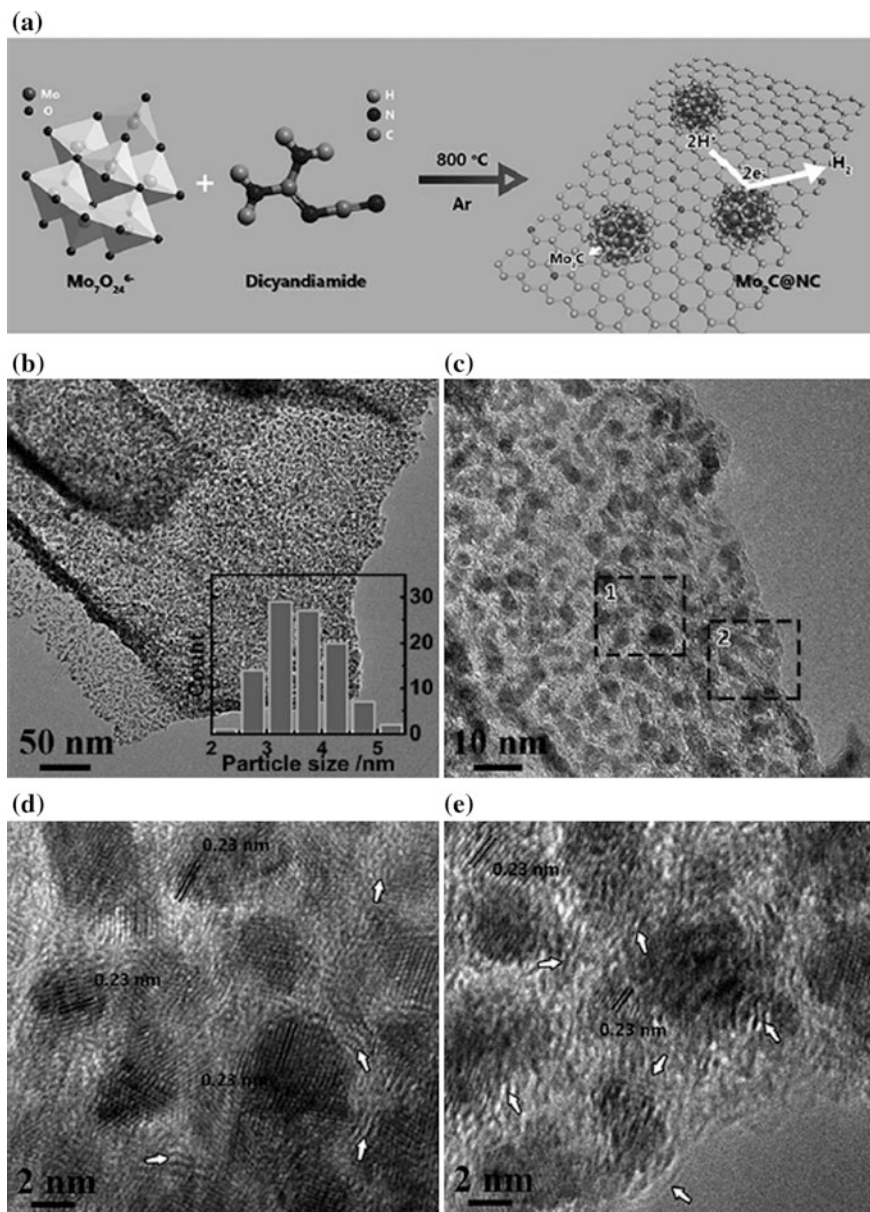
Fig. 10.7 a Illustration of the synthesis and the structure of Mo$_2$C@NC. **b, c** TEM images of Mo$_2$C@NC. *Inset* in **b** displays particle size distribution of the Mo$_2$C nanoparticles. **d, e** HRTEM images of the areas 1 and 2, respectively, in **c** (Reproduced from Ref. [60] with kind permission of © 2015 Wiley-VCH)
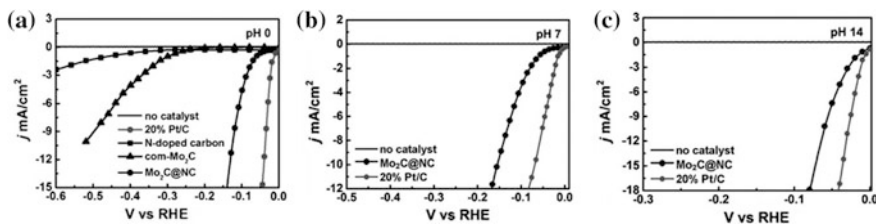
Fig. 10.8 Steady-state current density as a function of applied voltage during HER at pH **a** 0, **b** 7, and **c** 14 (Reproduced from Ref. [60] with kind permission of © 2015 Wiley-VCH)

10.3.1.3 Other Noble-Metal-Free Electrocatalysts

Metal phosphides are another kind of efficient noble-metal-free electrocatalysts for HER, such as phosphides of Ni, Co, Fe, Cu, Mo, and W [66]. They exhibit the most promising catalytic performance, which is close to that of commercially available Pt-based catalysts [67]. Constructing polymer-derived carbon/metal-phosphides nanocomposites would boost the activity owing to the enhanced conductivity and improved dispersity of active phosphides. Zhang et al. presented an efficient approach for preparing porous carbons embedded with Mo and Fe phosphides (MetP@PCs, Met = Mo, Fe, PCs = porous carbons) at a large scale through direct pyrolysis of cationic, phosphorous-based, porous polymer precursors loaded with metal-containing anions in a hydrogen atmosphere [68]. The successful formation of MoP@PC and FeP@PC was verified by XRD (Fig. 10.9). Uniform distributions of MoP and FeP were observed by SEM-EDX mapping (Fig. 10.9). The MetP@PC composites exhibit superior catalytic activity for HER under acidic conditions. In particular, MoP@PC with a low loading of 0.24 mg cm^{-2} affords a current density of up to -10 mA cm^{-2} at 51 mV and a very low Tafel slope of 45 mV dec^{-1} (Fig. 10.10). Meanwhile, Sun et al. proposed the one-step facile preparation of MoP nanosheets supported on carbon flake via a solid-state reaction using $(NH_4)_6Mo_7O_{24}\cdot4H_2O$, $NaH_2PO_4\cdot2H_2O$ and a biomass polymer, sodium alginate, as Mo, P and C sources, respectively [69]. When used as a novel HER electrocatalyst, such composites were active and durable in acidic and neutral electrolytes.

10.3.2 Some Particular Strategies Based on Polymer-Derivation to Fabricate Carbon/Inorganics Electrocatalysts

10.3.2.1 Electrospinning Followed by Controlled Pyrolysis

Electrospinning techniques have been studied for the fabrication of conductive polymer nanowires and a part of inorganic material nanowires [22]. This method
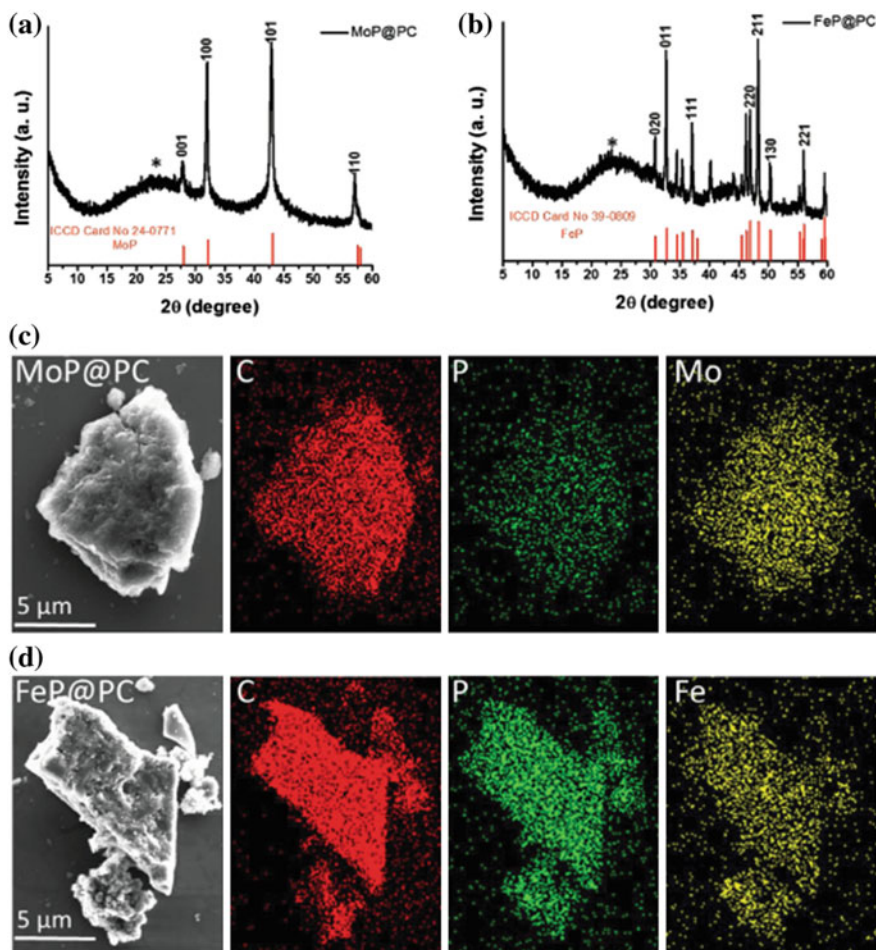
Fig. 10.9 **a**, **b** XRD patterns for MoP@PC (**a**) and FeP@PC (**b**); **c**, **d** SEM images and SEM elemental mappings of MoP@PC (**c**) and FeP@PC (**d**) (Reproduced from Ref. [68] with kind permission of © 2015 Wiley-VCH)

along with different post-treatments has been applied to synthesize some interesting surface multilevel structures (branched nanowires and necklace-like nanowires) and inner multilevel structures (core/shell nanowires and multichannel microtubes). Continuous nanofibers are easily obtained owing to the electrostatic repulsive force, driven by the electric field, during elongation of the viscous electrospinning solution. For noble-metal-free electrocatalysts, electrospinning provides a universal method to fabricate 1D nanostructures evenly integrated with conducting carbon, and more importantly to achieve a tailorable composition in a wide range, which is of great importance for the variation of electronic configuration and thus catalytic nature of materials.
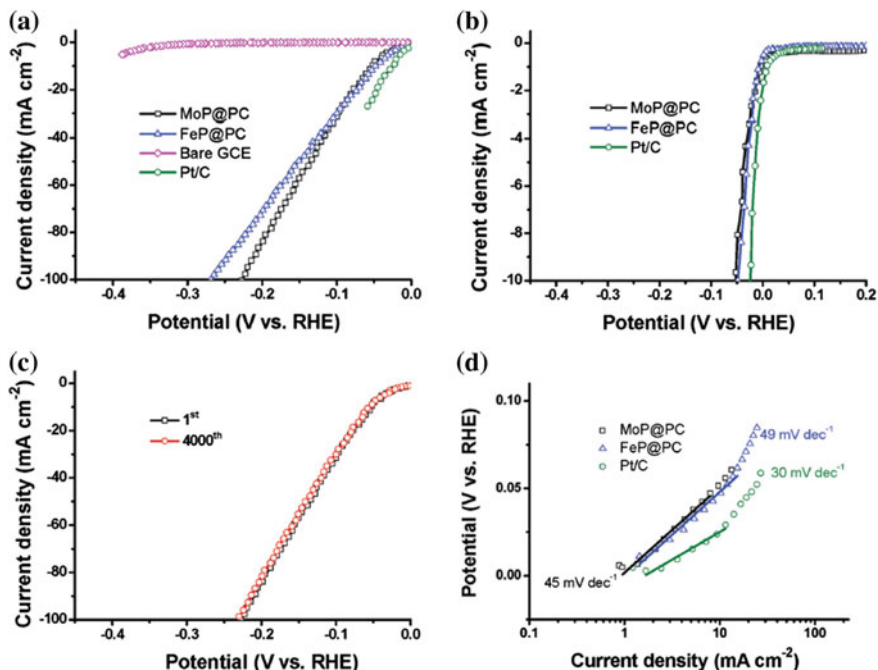
Fig. 10.10 **a**, **b** Polarization curves of bare glassy carbon electrode (GCE), MoP@PC, FeP@PC, and Pt/C. **c** Polarization curves of MoP@PC before and after 4000 cycles in 0.5 M H_2SO_4. **d** Tafel plots of MoP@PC, FeP@PC, and Pt/C (Reproduced from Ref. [68] with kind permission of © 2015 Wiley-VCH)

Recently, electrospinning followed by a pyrolysis was introduced to design the hierarchical nanofibers of metal sulfides and selenides, which were test as electrocatalysts for HER in acidic electrolytes. Du et al. conducted the synthesis of triangular WSe_2 and $W(Se_xS_{1-x})_2$ nanoflakes uniformly dispersed on electrospun carbon nanofiber via a chemical vapor deposition (CVD) system [70]. The morphology and structure of these products were systematically characterized, revealing that WSe_2 nanoflakes are configured in the 2H-phase with high crystallinity, and the $W(Se_xS_{1-x})_2$ nanoflakes are configured in the alloy form without any obvious phase separation. The hybrid catalysts were directly used as hydrogen evolution cathodes. The HER performances were optimized by the control on the cover density and thickness of the WSe_2 nanoflakes and the defective structure of the $W(Se_xS_{1-x})_2$ nanoflakes, which can be varied by the content of the initial W precursor and the appropriate substitution of selenium with sulfur.

Kim et al. reported a design via coaxial electrospinning [71]. The single-layered WS_2 nanoplates are uniformly anchored to hollow nitrogen-doped carbon nanofibers (WS_2@HNCNFs), fully exploiting the benefits of nanostructuring. The synthetic procedure of WS_2@HNCNFs was achieved via coaxial electrospinning of poly(styrene-acrylonitrile) (SAN) solution for the core and poly(acrylonitrile)

(PAN) solution for the sheath in which WS_2 precursor was homogeneously dispersed. Subsequently, a two-step thermal treatment was conducted in a 5% H_2/N_2. Single layer of WS_2 was visibly embedded in the nitrogen-doped carbon nanofibers (Fig. 10.11), which was further verified by XRD and Raman investigation. The WS_2@HNCNFs exhibited relatively low overpotential of 280 mV to reach -10 mA cm^{-2} as well as a small Tafel slope of 60 mV dec^{-1}.
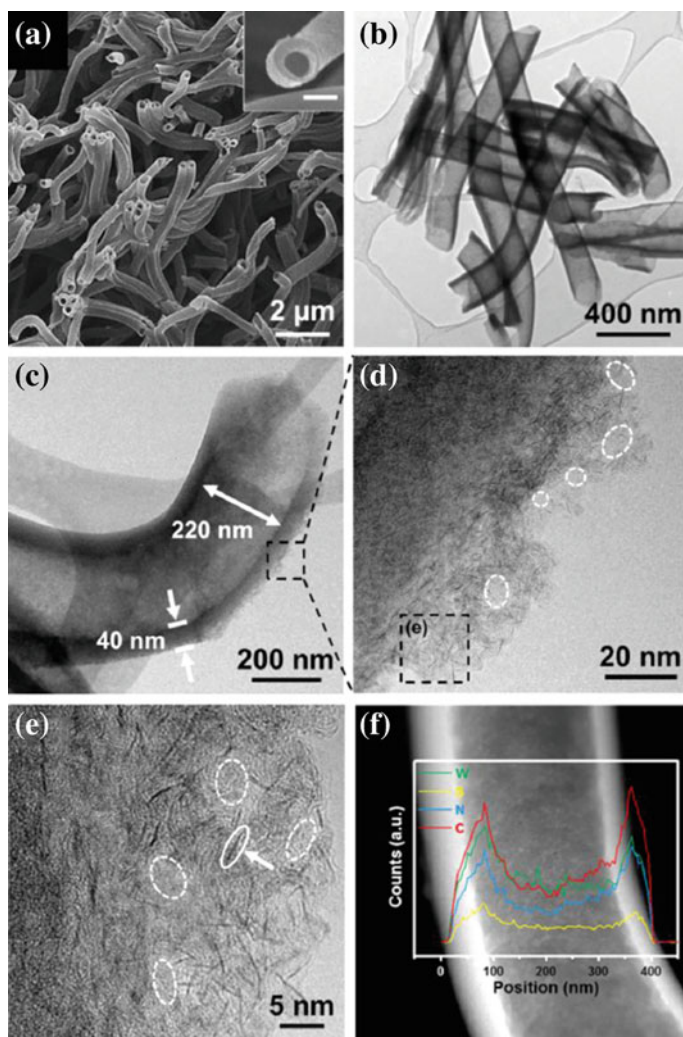
Fig. 10.11 **a** SEM image of WS_2@HNCNFs (*scale bar* in the *inset*: 200 nm), **b, c** TEM images and **d, e** HRTEM images of WS_2@HNCNFs. *Dashed white ellipses* indicate pores in the carbon matrix. A *white ellipse* with a *white* allow in **e** points at a WS_2 single layer. **f** STEM image of WS_2@HNCNFs on which EDS linescan profile of W, S, N, and C is superimposed (Reproduced from Ref. [71] with kind permission of © 2015 American Chemical Society)

Electrospinning was also introduced to design metal/carbon electrocatalysts. Liu et al. proposed the direct fabrication of Ni-decorated carbon nanofibers by calcining Ni^{2+}/poly(amic acid) (PAA), which was shaped into fibers via electrospinning [72]. Ni nanoparticles were uniformly distributed on the surface or partly embedded in the nanofibers. Such hierarchical Ni/C can catalyze the HER in basic electrolytes. Furthermore, it is facile to vary the compositions in the electrospinning solution, the polymer-based nanofibers and consequently the as-obtained inorganic/carbon nanostructures [22]. The tailored composition in inorganic/carbon facilitates the regulation on the surface structures and electronic configuration of electrocatalysts, which benefit the electrocatalytic kinetics and efficiency. For example, Xiong et al. developed novel nitrogen and phosphorus co-doped cobalt-based carbon nanofibers (Co–N–P–CNFs) by electrospinning [73]. Urea and triphenylphosphine were used as nitrogen and phosphorus sources, respectively. The characterization results showed that the large amounts of Co atoms embedded into the porous carbon nanofibers after the doping of N and P atoms. Meanwhile, Co–N–P–CNFs possessed abundant pyridinic-N and Co–N_x clusters as catalytic active-sites. Therefore, the optimal catalysts exhibited high durability of the ORR and HER electrocatalytic activity, and excellent methanol tolerance in both alkaline and acidic media.

Although electrospinning techniques have been demonstrated efficient for HER catalyst design, the further mechanism study and application are still ongoing. In particular, its application in design hetero-nanostructures is absent, which are featured by the rich interfaces on nanoscale and tunable electron structures. It is envisioned that the future work with a further controlled electrospinning would further boost the efficiency of noble-metal-free electrocatalysts.

10.3.2.2 Controlled Evolution from Designed Metal-Organic Frameworks (MOFs)

MOFs are highly porous materials which were first defined in late 1990s by Yaghi and Li [74]. MOFs are formed by linking organic and inorganic moieties through covalent coordination linkages. Other types of interactions such as H-bonding, π–π stacking, and van der Waals forces may also play a role in forming MOFs with three-dimensional (3D) structures. The MOFs are also called coordination polymers. These materials are extremely light (~ 0.13 g cm^{-3}) with very high surface areas (up to 10,000 m^2 g^{-1}), large pore volumes, and well-defined pore size [75]. And more importantly, the even integration of organic and inorganic species in atomic scale enables the versatile design of nanocomposites, as a new and important route toward polymer-derived inorganic/carbon electrocatalysts [76, 77].

Metal sulfides and phosphates can be synthesized via reacting MOFs with S and P sources, respectively, at a mild temperature (100–400 °C). The well-duplicated nanoporosity, large surface, and even hollow architecture significantly enable the good HER activity. For example, porous CoP concave polyhedrons have been synthesized by a facilely topological conversion strategy of low-temperature calcination using Co–MOF (ZIF-67) polyhedrons as the precursor [78]. The CoP

polyhedron showed a low η_{10} of 133 mV and a Tafel slope of 51 mV dec^{-1} in 0.5 M H_2SO_4. Zou et al. synthesized hollow Co-based bimetallic sulfide ($M_xCo_{3-x}S_4$, M = Zn, Ni, and Cu) polyhedra with superior HER activity and stability [79]. The homogenous MCo–MOFs were used as the precursor, which were transformed to hollow bimetallic sulfides by solvothermalsulfidation and thermal annealing. The analogous nanostructures of $Co_xFe_{1-x}P$ nanocubes, [80] CoP hollow polyhedrons, [81] and MoS_2 nanosheets [82] have been developed from the corresponding MOFs.

MOFs are feasible precursors for fabricating metal/carbon electrocatalysts via annealing under inert flow. Li et al. utilized the pyrolysis of Ni_2-(bdc)$_2$ted (bdc = 1,4-benzenedicarboxylic acid; ted = triethylene-diamine) in NH_3 to yield Ni nanoparticles with surface nitridation together with thin carbon coating layers [83]. The subtle surface modification significantly improved the catalytic performance for HER in basic electrolytes, in which a low overpotential of only 88 mV was achieved at a current density of 20 mA cm^{-2}. Yao et al. reported the synthesis of nickel–carbon electrocatalysts from Ni–MOFs by carbonization at 700 °C in N_2 atmosphere [84]. The Ni–C can be tuned by electrochemical methods to obtain atomically isolated Ni species anchored on graphitized carbon, consequently displaying high activity and durability for HER. Recently, Chen et al. developed a facile synthesis of an FeCo alloy encapsulated in highly nitrogen-doped graphene layers by one-step annealing of $Fe_3[Co(CN)_6]_2$ nanoparticles [85]. The sphere-like samples were composed of small encapsulated alloy particles (Fig. 10.12), which were coated with graphene layers (about five layers). The catalyst showed a low onset overpotential (88 mV) and an overpotential of only 262 mV at −10 mA cm^{-2} (Fig. 10.13). Besides, it exhibited an excellent long-term durability performance even after 10,000 cycles due to the protection of the graphene layers. The author further conducted the density functional theory calculations to reveal that N doping can provide adsorption sites for H^* and the appropriate increase of N will decrease ΔG_{H^*} for HER (Fig. 10.13d).

MOFs are the reasonable precursors toward well-defined metal-carbide nanostructures, in which the even integration of organic and inorganic species in atomic scale enables the quasi-homogeneous reactions for carbide generation. Lou et al. developed a MOF-assisted strategy for synthesizing porous molybdenum carbide octahedral nanoparticles (denoted as MoC_x nano-octahedrons) as efficient HER catalysts [86]. As shown in Fig. 10.14a, a unique MOFs-based compound was chosen as the precursor with a formula of $[Cu_2(BTC)_4/_3(H_2O)_2]_6[H_3PMo_{12}O_{40}]$ (NENU-5; BTC = benzene-1,3,5-tricarboxylate). After a direct pyrolysis at 800 °C under N_2 gas flow and a following etching by Fe^{3+}, MoC_x nano-octahedrons composed of small nanocrystallites were obtained. Each MoC_x nano-octahedron was composed of numerous small nanocrystallites (Fig. 10.14b–g). Benefiting from the porous and robust structure as well as ultrafine primary nanocrystallites, the MoC_x nano-octahedrons exhibited remarkable catalytic activity for HER in both acidic and basic conditions (Fig. 10.15). They displayed a low overpotential (η_{10} = 142 and 151 mV), a small Tafel slope (53 and 59 mV dec^{-1}), and a low onset overpotential (25 and 80 mV) in 0.5 M H_2SO_4 and 1.0 M KOH, respectively.
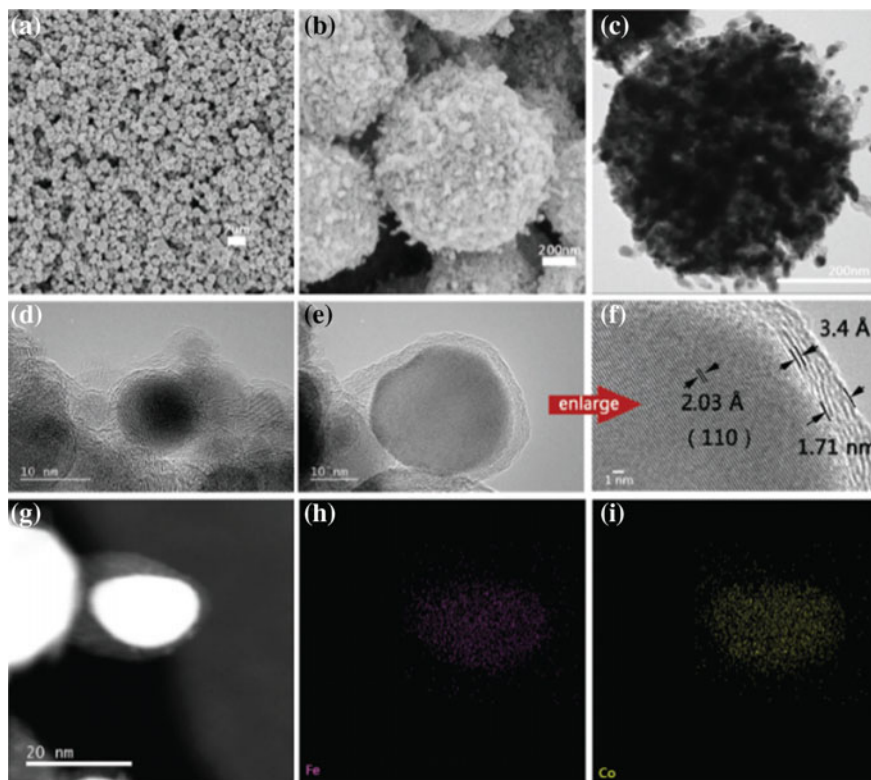
Fig. 10.12 **a–c** SEM and TEM images of FeCo@C obtained at 600 °C. **d**, **e** HRTEM images of the samples, **f** enlarged image of 1e where interplanar spacing of the alloy as well as the graphene shell was measured in the image, **g–i** STEM image of the single FeCo nanocrystal and the images of elemental mapping of Fe and Co (Reproduced from Ref. [85] with kind permission of © 2015 Royal Society of Chemistry)

However, MoC_x species are easily to oxidize on the surface even in ambient conditions; the above etching operation via oxidative Fe^{3+} should be avoided if possible. In addition, using Cu-MOFs as a template and carburizing the organic ligand with the supported POMs in the pores are not beneficial for real "atomic contact" between the Mo ions and organic ligands. Very recently, Tang et al. developed a "MOF-directed strategy" for synthesizing porous and uniformly nanostructured MoC via in situ carburization of Mo–MOF under inert atmosphere, [87] as shown in Fig. 10.16a. The as-obtained catalyst was denoted as nanoMoC@GS, meaning highly dispersed and nanosized MoC encapsulated in graphitized carbon shell. In the ordered porous architecture of the $Mo_3(BTC)_2$ precursor, the "atomic contact" between Mo ions and organic ligands enabled the formation of ultrafine MoC (~ 3 nm) which were encapsulated by fluffy and ultrathin graphitized carbon shell (ca. 1–3 layers, Fig. 10.16). Ultrafine MoC
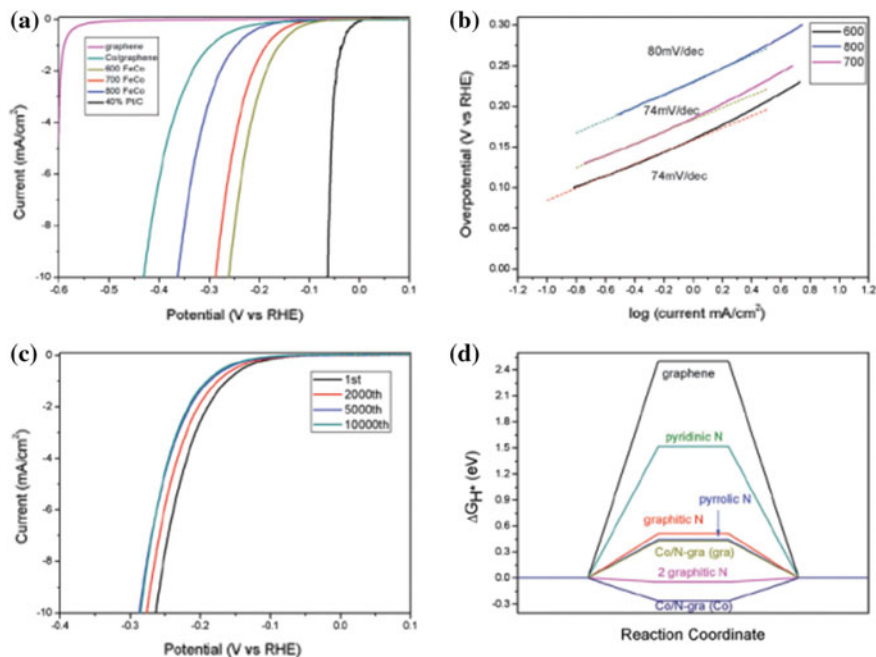
Fig. 10.13 **a** Polarization curves of samples versus RHE, **b** Tafel plots of FeCo@C obtained at varied temperature, **c** Polarization curves of FeCo@C-600 after 1st, 2000th, 5000th, and 10,000th cycles, **d** calculated ΔG_{H*} diagram of some models, the words in the brackets mean H* adsorbed on the graphene or Co_4 side (Reproduced from Ref. [85] with kind permission of © 2015 Royal Society of Chemistry)

nanoparticles (~ 3 nm) confined by 1–3 layered graphite shells significantly favored the efficient HER in acidic and basic media. A low overpotential ($\eta_{10} = 124$ and 77 mV), a small Tafel slope (43 and 50 mV dec^{-1}), and a high exchange current density ($j_0 = 0.015$ and 0.212 mA cm^{-2}) were achieved on nanoMoC@GS in 0.5 M H_2SO_4 and 1.0 M KOH, respectively.

As a good example, the 1D nanostructures of organic-inorganic hybrid MoO_x/amine were proved by Tang and Gao, as the versatile precursor toward well-defined MoC_x nanocatalyts [88–90]. As for such kind of coordination polymer, e.g., $Mo_3O_{10}(C_6H_5NH_3)_2\cdot2H_2O$ (aniliniumtrimolybdate), $Mo_3O_{10}(C_2H_4N_2H_6)$ (ethylenediaminetrimolybdate), and $Mo_3O_{10}(C_5H_5NH)_2\cdot H_2O$ (pyridiumtrimolybdate), the 1D growth originates from anisotropic molybdate anions $Mo_3O_{10}^{2-}$ [88]. More importantly, the hybrid nanostructures can provide the "sub-nanometer contact" between $Mo_3O_{10}^{2-}$ and protonated aniline and create a quasi-homogeneous carburization, which favors the formation of the nanoporous and 1D Mo_2C [89, 91]. In 2014, the high activity for HER was evidenced on the harvested nanoporous Mo_2C nanowires [53]. Very recently, Gao et al. made further efforts to boost the HER performance via the electron regulation on the active-site
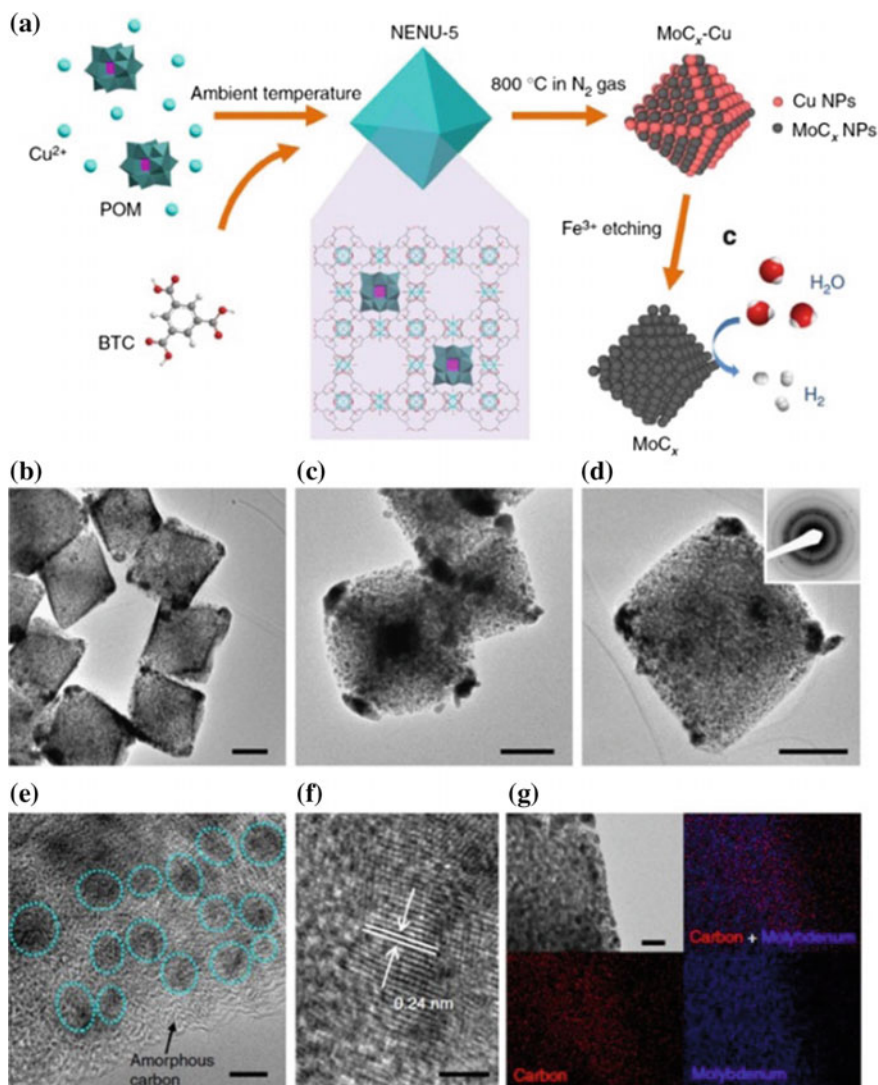
Fig. 10.14 a Schematic illustration of the synthesis procedure for porous MoC_x nano-octahedrons. Characterizations of MoC_x nano-octahedrons. **b–d** TEM images (*scale bar*, 200 nm; *inset* of c: SAED pattern), **e** magnified TEM image (*scale bar*, 5 nm), **f** HRTEM image (*scale bar*, 2 nm), and **g** elemental mapping (*red* carbon; *blue* molybdenum; *scale bar* 50 nm) of porous MoC_x nano-octahedrons (Reproduced from Ref. [86] with kind permission of © 2015 Macmillan Publishers Ltd) (color figure online)

of carbide surface [55, 92]. Although Mo_2C demonstrates the best HER performance among various MoC_x, e.g., α-MoC_{1-x}, η-MoC, γ-MoC, and β-Mo_2C, [52] the negative hydrogen binding energy (ΔG_{H^*}) on Mo_2C indicates a strong
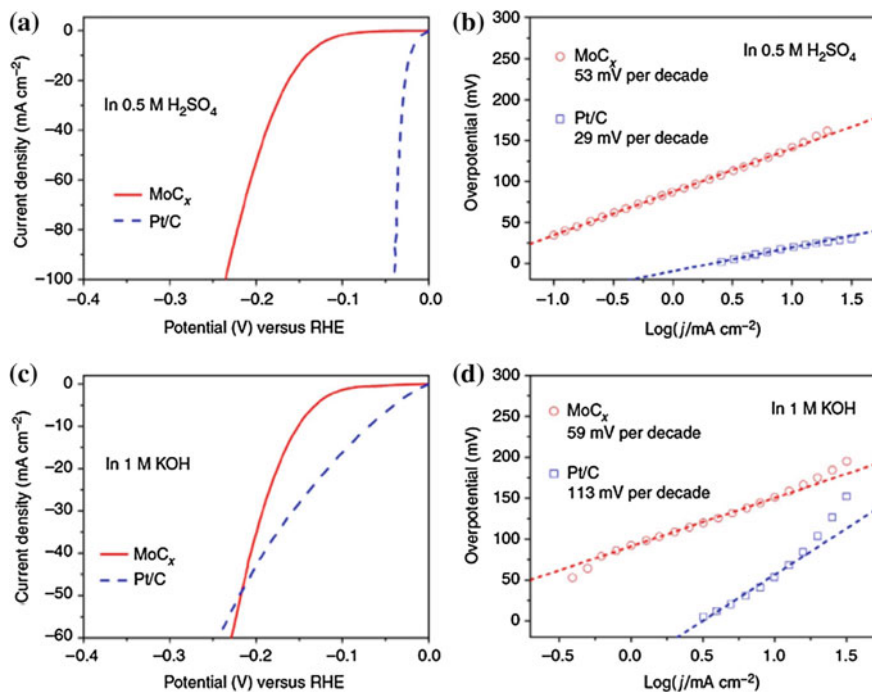
Fig. 10.15 HER performance of porous MoC_x nano-octahedrons: **a** polarization curve at 2 mV s^{-1} and **b** Tafel plots in 0.5 M H_2SO_4, **c** polarization curve at 2 mV s^{-1} and **d** Tafel plots in 1.0 M KOH (Reproduced from Ref. [86] with kind permission of © 2015 Macmillan Publishers Ltd)

adsorption of H on Mo_2C, [93] which benefits H^+ reduction (i.e., Volmer step) but restricts H_{ads} desorption (i.e., the Heyrovsky/Tafel step). An optimization on the electronic features is desired.

The electron density around the Mo active-sites mostly relies on the carbon in the lattice, which will be reduced with increasing C because of the electron transfer from Mo to C. For example, with a high C content, MoC usually presents weaker hydrogen binding in comparison with that on Mo_2C, and consequently a facilitated Heyrovsky/Tafel step, but a hindered Volmer reaction. Gao and Tang et al. reported MoC–Mo_2C heteronanowires (HNWs) as efficient HER electrocatalysts, [55] which were fabricated from MoO_x-aniline or MoO_x-p-methylaniline nanowires via controlled carbonization (Fig. 10.17). The HNWs denoted as MoC–Mo_2C-n (where n refers to the MoC weight percentage) were composed of defined nanoparticles and featured by rich nanoporosity, large surface area, and more importantly a tunable composition. The molar ratio of active Mo^{3+} and Mo^{2+} was tailored via this controlled carbonization (Fig. 10.17c), which would make obvious influence on the adsorption of H and thus the HER activity.
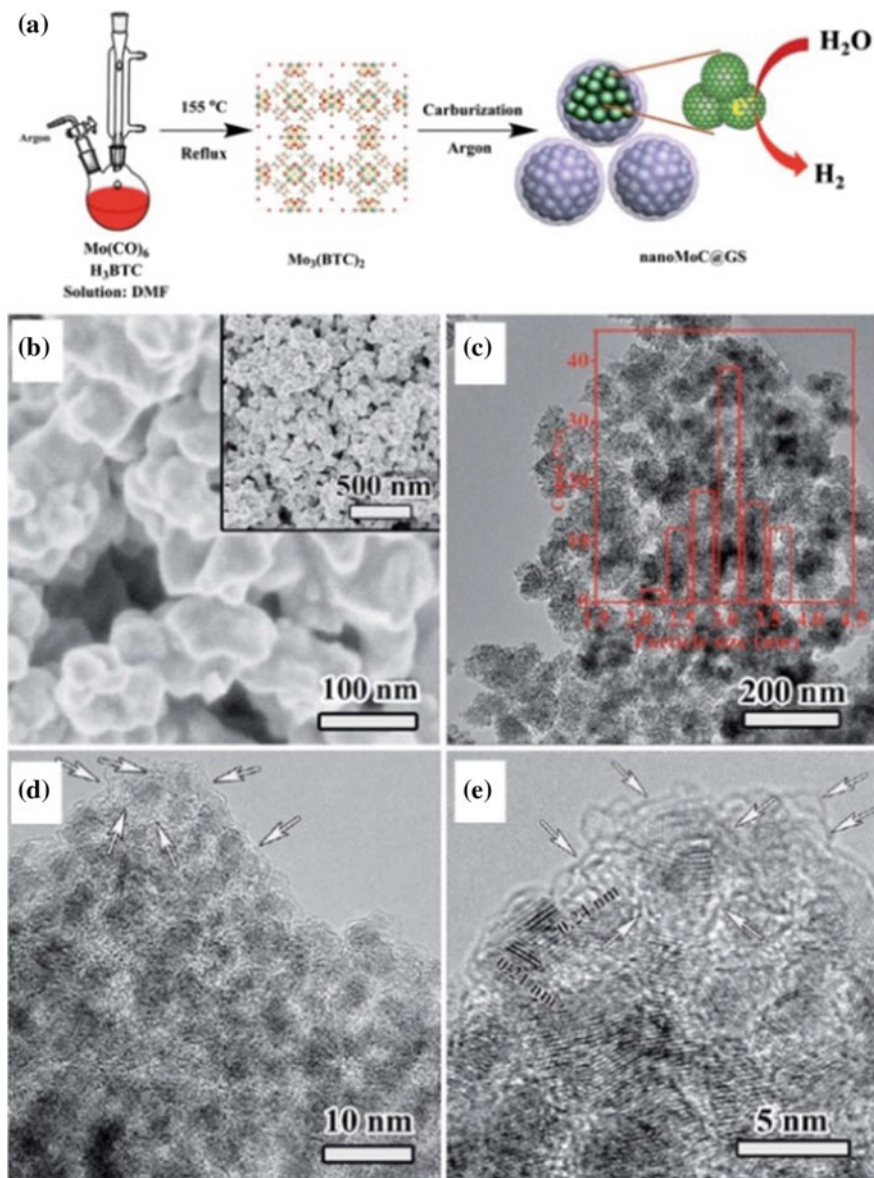
Fig. 10.16 **a** Procedure for synthesis of nanoMoC@GS. **b** SEM, **c**, **d** TEM and **e** HRTEM images of nanoMoC@GS obtained at 700 °C (Reproduced from Ref. [87] with kind permission of © 2016 Royal Society of Chemistry)

As expected, the optimal one consisting of 31.4 wt% MoC displayed a low η_{10} of 126, a small Tafel slope of 43 mV dec^{-1}, and a low onset overpotential of 38 mV in 0.5 M H$_2$SO$_4$, outperforming that of bare Mo$_2$C and MoC (Fig. 10.18).
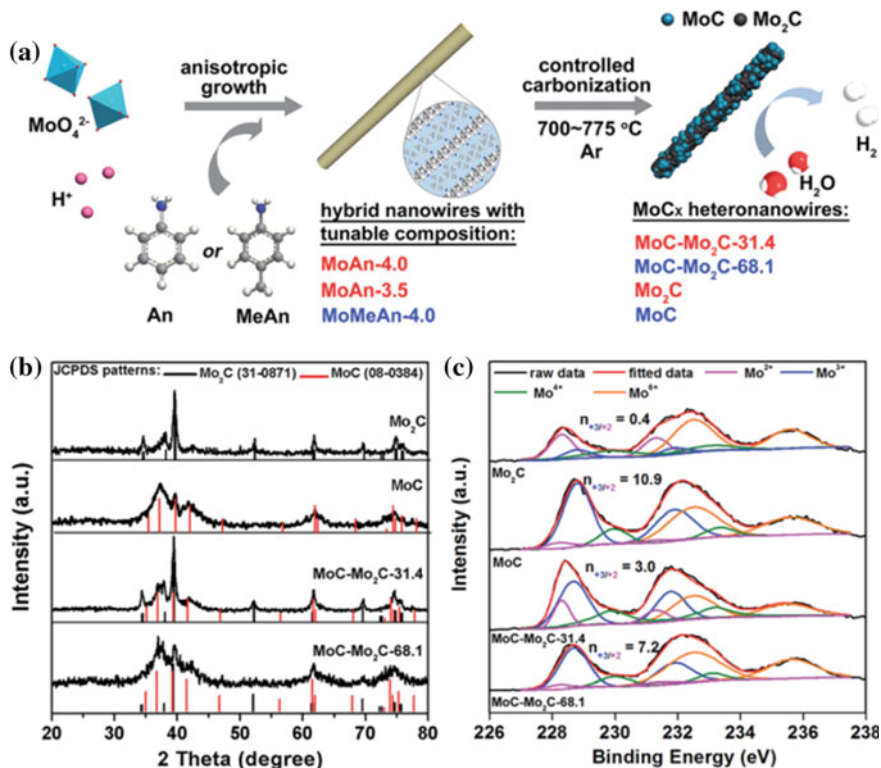
Fig. 10.17 **a** Illustration for the fabrication of MoC_x HNWs from MoO_x-amine NWs with tunable composition. **b** XRD patterns and **c** Mo 3d XPS profiles of the as-obtained MoC_x NWs (Reproduced from Ref. [55] with kind permission of © 2016 Royal Society of Chemistry)

This well indicated a synergy between nanosizedMoC and Mo_2C. Featured by the both of the current densities at $\eta = 0$ (j_0) and 150 mV (j_{150}), the HER activity of the heteronanowires was visibly dependent on the variation of the ratio of active Mo^{3+}/Mo^{2+} ($n_{3+/2+}$) on the surface (Fig. 10.19). The lower electron density around E_F in MoC–Mo_2C-31.4 than that of Mo_2C was further evidenced by the narrowed valance-band distribution. Regarding the strong hydrogen binding on Mo_2C and the consequently restricted H_{ads} desorption, the decreased electron density in the MoC–Mo_2C-31.4 HNWs would reduce the strength of Mo–H toward the promoted H_{ads} desorption and thus remarkably improve the HER activity (Fig. 10.19). With further improved $n_{3+/2+}$, the reduced activity and kinetics metrics were observed, because of weak hydrogen binding involving less electron donated by Mo. In addition, the MoC–Mo_2C-31.4 was also active for the HER in basic solution (1.0 M KOH), showing the best activity and kinetics in comparison with Mo_2C, MoC, MoC–Mo_2C-68.1, and MoC–Mo_2C-30 (mixed).

Furthermore, another strategy via the doping of late-transition metals (e.g., Co and Fe) was developed to optimize the electronic configuration of Mo_2C, which follows another mechanism that the rich electrons in dopants can effectively reduce the unoccupied d orbitals of Mo and transfer into Mo–H anti-bonding. As a result, the weakened Mo–H in turn favors H_{ads} desorption. Gao and Tang et al. developed a Co-doping into Mo_2C on the basis of Co-modified $Mo_3O_{10}(C_6H_5NH_3)_2 \cdot 2H_2O$ nanowires [92]. The successful Co-doping significantly increases the electronic density around E_F in Mo_2C, resulting in the weakened Mo–H toward optimized HER kinetics. As expected, the Co–Mo_2C nanowires presented a remarkably improved activity in comparison with parent Mo_2C. With an optimal Co-doping, Co–Mo_2C displays a low overpotential (η_{10} = 140 and 118 mV; η_{100} = 200 and 195 mV), a small Tafel slope (39 and 44 mV dec^{-1}), and a low onset overpotential (40 and 25 mV) in 0.5 m H_2SO_4 and 1.0 M KOH, respectively.

The above results have well attested the efficiency of MOFs-based materials for the development of high-performance noble-metal-free electrocatalysts. The rational evolutions on the basis of their rich nanoporosity, large surface, and tunable composition lead to the effective regulation on the architectures, surface structures, and electronic configuration, which are desired for the optimization of HER performance. It is envisioned that the future work with available and diverse MOFs would further boost the controlled generation and further applications in electrochemical HER.

It can be concluded for this part that the polymer-derivation provides a rational design of carbon/inorganic nanostructures as efficient electrocatalysts for electrochemical HER, e.g., metals and their non-oxides (sulfides, nitrides, carbides, and phosphates). They present the significance as noble-metal-free electrocatalysts, with the low-cost and high earth-abundance. The designed carbon-hybrid structures derived from polymers promote the conductivity and dispersity of active inorganics,
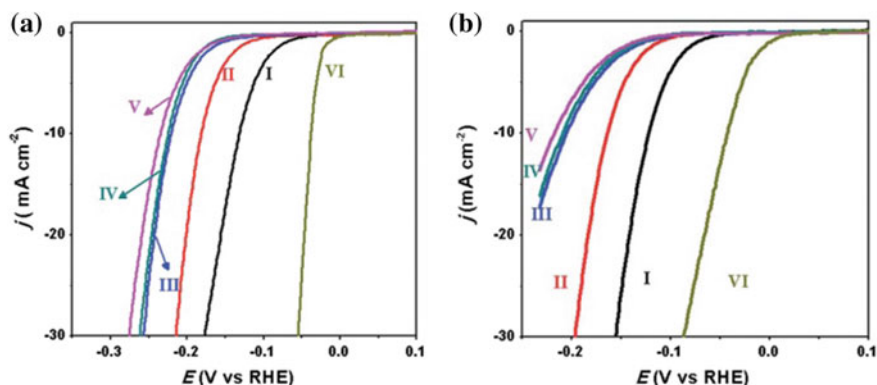
Fig. 10.18 Polarization curves for the HER on modified GCEs comprising (*I*) MoC–Mo_2C–31.4, (*II*) Mo_2C, (*III*) MoC–Mo_2C–68.1, (*IV*) MoC–Mo_2C–30 (mixed), (*V*) MoC, and (*VI*) commercial Pt/C in **a** 0.5 M H_2SO_4 and **b** 1.0 M KOH (Reproduced from Ref. [55] with kind permission of © 2016 Royal Society of Chemistry)

Fig. 10.19 a j_0 (obtained by extrapolating the Tafel curves to $\eta = 0$ mV) and j_{150} (current density at $\eta = 150$ mV) of the above MoC_x, which are associated with the ratio of surface Mo^{3+}/Mo^{2+} determined through XPS analysis. **b** Schematic illustration of the HER activity relying on the electron density of Mo in a series of MoC_x electrocatalysts (Reproduced from Ref. [55] with kind permission of © 2016 Royal Society of Chemistry)
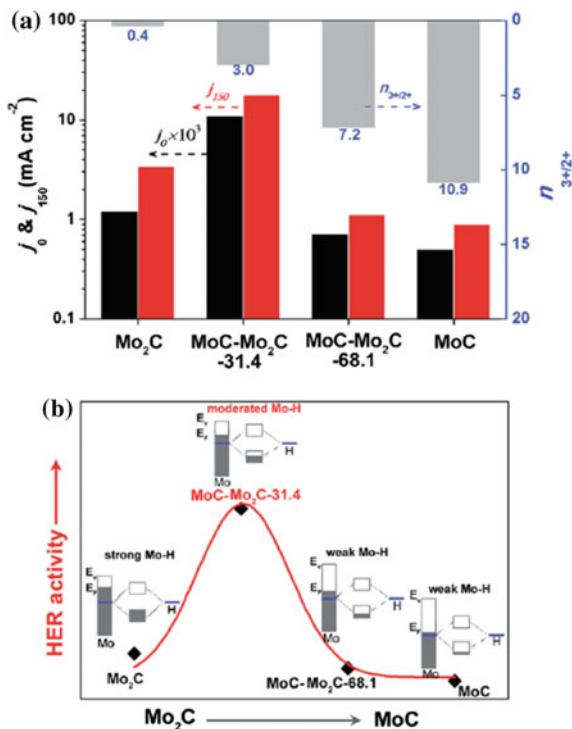
and more importantly enable the electron regulation on active-sites due to their rich interactions. The summary for their HER activity is listed in Table 10.2 and Table 10.3. It is worthy to mention that the use of Pt counter electrodes should be avoided in the test of noble-metal-free electrocatalysts. The possible oxidation of Pt and further re-deposition on cathode (HER electrode) would create a false impression on the activity of noble-metal-free materials [94]. In this regard, the reported results obtained with Pt counter electrode are not listed herein. In a common sense, carbides and phosphates-based nanocomposites displayed the high HER activity in both acidic and basic electrolytes, which points out a direction for the future research.

10.4 Lithium Ion Batteries

Since the introduction into the market in 1991, LIBs have been widely accepted by industry for portable electronic devices, owing to their advantages of high energy density, long lifespan, good environment compatibility, and low self-discharge compared with traditional lead-acid and Ni-based batteries [102, 103]. As a promising power source, the LIB is receiving more attention with the development
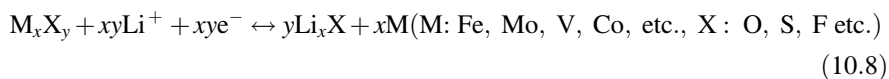
Table 10.2 Summary of HER performance of polymer-derived carbon/inorganic electrocatalysts in acid electrolytes

Catalysts	Electrolytes	Loading (mg cm^{-2})	j (mA cm^{-2})	η (mV)	Tafel slope (mV dec^{-1})	Ref.
MoS$_2$/mesoporous carbon nanospheres	0.5 M H$_2$SO$_4$	0.19	10	150	41	[45]
MoS$_2$/mesoporous graphene foam	0.5 M H$_2$SO$_4$	0.21	10	140	42	[46]
			100	200		
C@MoS$_2$	0.5 M H$_2$SO$_4$	0.50	10	165	55	[47]
			35	200		
MoS$_2$/C nanospheres with ultrathin MoS$_2$	0.5 M H$_2$SO$_4$	0.57	10	130	60	[48]
			88	200		
WSe$_2$/C nanofibers	0.5 M H$_2$SO$_4$	/	10	158	98	[70]
WS$_2$@hollow N-doped carbon nanofibers	0.5 M H$_2$SO$_4$	0.29	10	280	60	[71]
MoS$_2$ in nanoporous carbon	0.5 M H$_2$SO$_4$	0.29	10	240	51	[82]
Nanoporous Mo$_2$C nanowires	0.5 M H$_2$SO$_4$	0.21	10	130	53	[83]
			66	200		
Mo$_2$C/C nanotubes	0.5 M H$_2$SO$_4$	0.75	10	172	62	[56]
Co/N-, S-doped carbon	0.5 M H$_2$SO$_4$	0.3	10	180	66	[58]
MoCN nanoparticles	0.5 M H$_2$SO$_4$	0.4	10	140	46	[57]
Fe-WCN/C nanospheres	0.5 M H$_2$SO$_4$	0.4	10	220	47.1	[32]
Mo$_2$C@NC	0.5 M H$_2$SO$_4$	0.28	10	124	60	[95]
Mo$_2$C@C	0.5 M H$_2$SO$_4$	0.25	10	78	41	[61]
Mo$_2$C–Mo$_2$N/C	0.1 M HClO$_4$	2.8	10	∼150	/	[64]
WC$_x$–WN/C	0.1 M HClO$_4$	10	100	105	36	[65]
MoC$_x$ octahedrons	0.5 M H$_2$SO$_4$	0.8	10	142	53	[86]
			100	230		
nanoMoC@graphite sheets	0.5 M H$_2$SO$_4$	1.0	10	124	43	[87]
			146	200		
MoC–Mo$_2$C heteronanowires	0.5 M H$_2$SO$_4$	0.14	10	126	43	[55]
Co–Mo$_2$C nanowires	0.5 M H$_2$SO$_4$	0.14	10	140	39	[96]
			100	200		

<div align="right">(continued)</div>

Table 10.2 (continued)

Catalysts	Electrolytes	Loading (mg cm^{-2})	j (mA cm^{-2})	η (mV)	Tafel slope (mV dec^{-1})	Ref.
NiMoN$_x$/C	0.5 M H$_2$SO$_4$	0.25	2	170	36	[82]
MoN nanosheets	0.5 M H$_2$SO$_4$	0.28	10	∼200	90	[86]
MoP@porous carbon	0.5 M H$_2$SO$_4$	0.24	10	51	45	[68]
Co/N–P–C nanofibers	0.5 M H$_2$SO$_4$	0.23	10	248	56	[97]
CoP concave polyhedrons	0.5 M H$_2$SO$_4$	0.35	10	133	51	[78]
Co$_x$Fe$_{1-x}$P nanocubes	0.5 M H$_2$SO$_4$	0.35	10	72	52	[80]
CoP/C	0.5 M H$_2$SO$_4$	/	10	91	42	[98]
FeCo@NC	0.5 M H$_2$SO$_4$	0.29	10	262	74	[85]
Co–C–N nanofibers	0.5 M H$_2$SO$_4$	1.5	10	138	55	[99]
			100	212		

of newly emerging electronic devices, especially electronic and hybrid electronic vehicles. Accordingly, LIBs with even higher power density, higher energy density, and longer cycling life are in continuous demand. Electrode materials are significant for the high performance of LIBs. Here we will introduce the application of polymer-derived carbon/inorganic hybrids as electrode materials for LIBs.

10.4.1 Anode Materials

Graphite is a typical layered material which can reversibly store/release Li$^+$ in the interlayers. Due to the low potential of Li$^+$ intercalation and stable capacity delivery, graphite-based materials prevail as anodes for today's LIBs. However, the theoretical capacity of graphite is only 372 mAh g^{-1} (based on the intercalation mechanism: $6C + Li^+ + e^- \leftrightarrow LiC_6$), which is far from satisfactory to power electric vehicles. Driven by ever-increasing demand for higher energy density, various alternative anode materials have been investigated, which can be categorized into alloy/dealloy mechanism-based materials (e.g., Si, Ge, Sn) and conversion mechanism-based transition metal compounds such as oxides and sulfides (e.g., Fe$_2$O$_3$, Co$_3$O$_4$, MoO$_2$, MoS$_2$). These two kinds of materials reversibly store/release Li$^+$ through the following typical reactions.

Table 10.3 Summary of HER performance of polymer-derived carbon/inorganic electrocatalysts in basic electrolytes

Catalysts	Electrolytes	Loading (mg cm^{-2})	j (mA cm^{-2})	η (mV)	Tafel slope (mV dec^{-1})	Ref.
Mo$_2$C/C nanotubes	0.1 M KOH	0.75	10	112	55	[56]
Mo$_2$C@NC	1.0 M KOH	0.28	10	60	/	[100]
Mo$_2$C@C	1.0 M KOH	0.25	10	78	41	[61]
Carbon-protected Co$_6$W$_6$C	1.0 M KOH	0.28	10	73	25	[62]
Ni/C nanofibers	2.0 M KOH	/	3.1	200	105	[72]
Ni@N-C	1.0 M KOH	/	20	88	71	[83]
MoC$_x$ octahedrons	1.0 M KOH	0.8	10	151	59	[86]
			∼30	200		
MoC@graphite shell	1.0 M KOH	0.76	10	77	77	[87]
Co–Mo$_2$C nanowires	1.0 M KOH	0.14	10	118	44	[96]
			100	195		
MoC–Mo$_2$C heteronanowires	1.0 M KOH	0.14	10	120	42	[55]
MoS$_2$nanosheet arrays	1.0 M KOH	/	10	190	100	[82]
MoP	1.0 M KOH	0.86	10	130	48	[101]
Ni–Mo nanopowder	1.0 M KOH	1	10	∼80	/	[97]
Co@Co-oxo/hydoxo phosphate	1.0 M KOH	/	2	385	140	[98]
CoP NW arrays	1.0 M KOH	0.92	10	209	129	[99]

Alloy/dealloy mechanism:

$$M + x\text{Li}^+ + x\text{e}^- \leftrightarrow \text{Li}_x M (\text{M: Si, Ge, Sn, etc.}, x \leq 4.4) \qquad (10.7)$$

Conversion mechanism:

$$M_x X_y + xy\text{Li}^+ + xy\text{e}^- \leftrightarrow y\text{Li}_x X + x M (\text{M: Fe, Mo, V, Co, etc., X: O, S, F etc.})$$
$$(10.8)$$
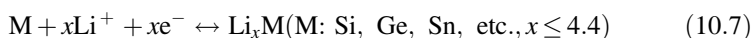
Through the alloy/dealloy and conversion mechanisms, these materials show much higher theoretical capacities (600–4400 mAh g^{-1}) than that of graphite. However, most of these materials are semiconductors; their relatively low conductivities hinder efficient utilizations of the active materials, resulting in poor rate capability. More importantly, these materials suffer from volume expansion in the discharge process and volume shrinkage in the charge process. As illustrated in Scheme 10.6 [104], severe volume change in the repeated cycles results in material pulverization (Scheme 10.6a) and electrode deformation (Scheme 10.6b), leading to loss of electrical contact and eventual capacity fading.

Another challenge is, during the discharge process, organic electrolyte decomposes on the interphase of the anode and electrolyte when the voltage is below 1 V versus Li/Li$^+$, forming a layer on the surface of the anode which is called "solid-electrolyte interphase" (SEI). This film is double-edged: Although it is electronically insulating, it prevents further contact of active materials with electrolyte, avoiding continuous decomposition of the electrolyte. Therefore, stable SEI is crucial for the long cycle life. However, due to the large volume changes in the discharge/charge process, SEI is easily broken. Freshly exposed surface of the active material induces further decomposition of the electrolyte (Scheme 10.6c). And the thickened SEI hinders charge transfer, therefore result in capacity decay.

Hybridizing anode active materials with carbon on nanoscale are an effective route to address these challenges. On one hand, nano engineering enhances the kinetics for Li$^+$ storage due to the shortened diffusion paths and relieves the strain
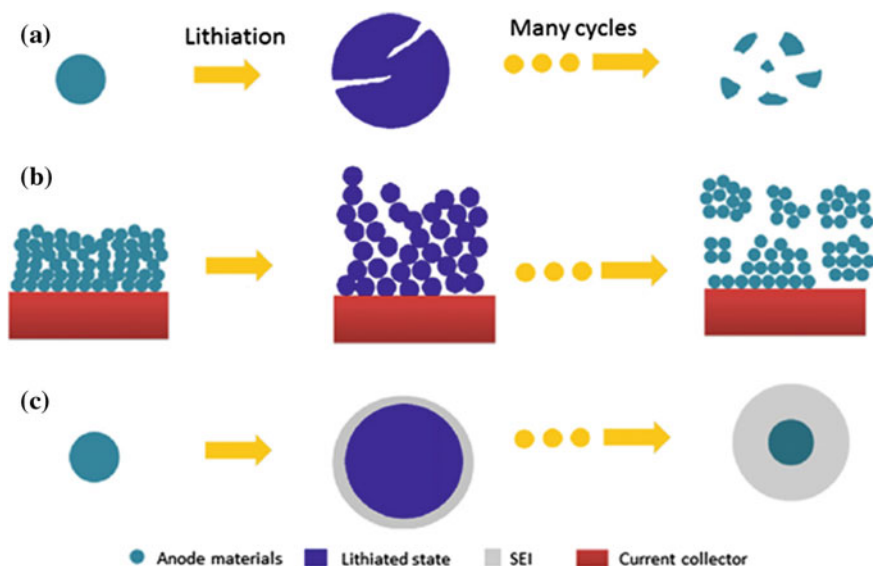
Scheme 10.6 Electrode failure mechanisms for alloy/dealloy and conversion reaction-based anode materials: **a** material pulverization, **b** electrode deformation, and **c** continuous SEI growth (Reproduced from Ref. [97] with kind permission of © 2012 Elsevier)

associated with the volume change during the discharge/charge process. On the other hand, hybridization with nanocarbon facilitates the charge transfer, avoids aggregation of active materials, and also buffers the volume changes. By constructing nanohybrids with carbon, the cycle performance and rate capability of the anode materials can be remarkably improved.

As discussed in the previous section, there are mainly three strategies to realize effective connection of anode nanomaterials with polymer-derived carbon: in situ formation of polymers on the surface of the nanomaterials followed by pyrolysis, post-introduction of anode nanomaterials into the polymer-derived carbon matrix, and one-pot construction of polymer/metal salts (or ions) followed by pyrolysis. With these strategies, polymer-derived carbon/inorganic nanohybrids with varied structure/morphologies can be successfully synthesized, which have been demonstrated to be promising anode candidates for LIBs.

Carbon coating is one of the most widely used coating techniques for anodes. The carbon coating layers not only significantly enhance the electronic conductivity of electrode materials,[5] but also lead to stabilized SEI films, which result in improved rate and cycling performance [105]. Compared with mechanical mixture of inorganics with carbonaceous materials (e.g., graphite, MCMB, and acetylene black) in solid states, dispersion of organics or their precursors in solutions of polymers followed by drying and carbonization offers comformal, uniform, and complete carbon coating. For example, block copolymer [106], polyvinylpyrrolidone (PVP) [107–109], polyvinyl chloride (PVC) [110, 111], polyvinylidene fluoride (PVDF) [112], and poly(cyclotriphosphazene-4,40-sulfonyldiphenol) (PZS) [113] were applied as carbon sources for the coating on MnO [106], MoO_2 [107], CuO [108] and Mn_3O_4 [109], and Si [110–113]. An improved method is to adopt in situ polymerization followed by pyrolysis under inert atmosphere, which can lead to more uniform and continuous carbon coating on the inorganic surface. Pyrrole monomers in situ polymerized on the surface of the sea urchin-like –FeOOH, after then, the generated polypyrrole coated –FeOOH was transformed to sea urchin-like Fe_3O_4@C nanocomposite after calcination (Fig. 10.20) [114]. This composite exhibit much improved capacity, cycle stability, and rate performance compared with the bare counterpart, as shown in Fig. 10.20b, c.

Hydrothermal carbonization of glucose has been proved to be a universal method for effective carbon coating on varied inorganics. Typically, the prepared nanostructured core materials are firstly suspended in a glucose solution. In the following hydrothermal process, the glucose molecules absorbed or attached through hydrogen bonding on the surface of the cores go through dehydration, polymerization to polysaccharides, and carbonization [115, 116]. The pre-coated products are annealed subsequently in the inert atmosphere to finally obtain the inorganic@carbon core-shell nanostructure. As an example, Si@SiO_x/C nanoparticles were prepared by the hydrothermal carbonization of glucose in the presence of Si nanoparticles and subsequent pyrolysis (Fig. 10.21) [117]. The carbon coating, in association with the vinylene carbonate (VC) additive for the electrolyte, leads to effective SEI structure that suppressed the pulverization of Si and continuous decomposition of electrolyte. As a result, this hybrid showed a significantly
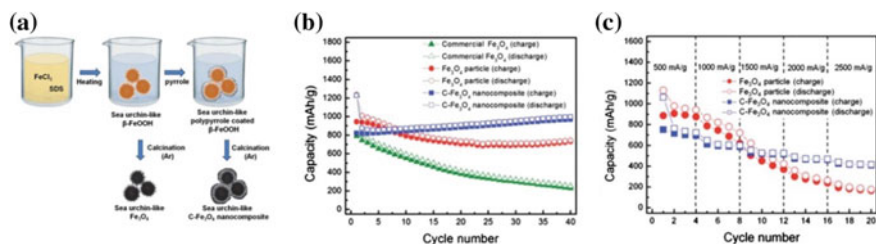
Fig. 10.20 **a** Schematic illustration of the synthetic procedure for a sea urchin-like porous C–Fe$_3$O$_4$ nanocomposite [114]. **b** Cycling performance of a sea urchin-like C–Fe$_3$O$_4$ nanocomposite, Fe$_3$O$_4$ particles without carbon shell and commercial Fe$_3$O$_4$ at a current density of 100 mA g^{-1}. **c** Rate performance of a sea urchin-like C–Fe$_3$O$_4$ nanocomposite and Fe$_3$O$_4$ particles without carbon shell. *Open symbols* indicate discharge cycles and *solid symbols* are charge cycles (Reproduced from Ref. [107] with kind permission of © 2012 Royal Society of Chemistry)

improved lithium-storage performance in terms of highly reversible capacity, excellent cycling performance, and high-rate capability (Fig. 10.21). It exhibited a reversible capacity of ~1100 mAh g^{-1} at a current density of 150 mA g^{-1} and retained above 600 mAh g^{-1} as the current densities increased to 1000 mA g^{-1} during the 200 cycles. MoO$_2$@C nanobelts can be prepared using MoO$_3$ nanobelts as precursor and glucose as carbon sources [118]. In the first hydrothermal process (Scheme 10.7), the polysaccharide coating on the surface of the nanobelts helps to maintain the morphology of the precursor during the transformation from MoO$_3$ to MoO$_2$. MoO$_2$@C nanobelts exhibit a reversible capacity of 518.5 mAh g^{-1} at a current density of 500 mA g^{-1}, retaining 82.3% of the initial capacity after 30 cycles. The hydrothermal carbonization of glucose is most widely applied to synthesis of various structured inorganics with carbon coating, e.g., Sn@C nanoparticles [119], SnO$_2$@C nanoparticles [120], SnO$_2$@C nanotubes [121], SnS$_2$@C nanoparticles [122], peapod-like Co$_3$O$_4$@C nanocomposite [123], Fe$_3$O$_4$@C nanospindles [124], Fe$_3$O$_4$@C microcapsules [125], Fe$_3$O$_4$@C hollow beads [126], porous NiO@C microspheres [127], and ZnO@Cnanorod array [128]. Following this line, the carbon coating derived from glucose can be further applied to inorganics which have been firstly loaded/supported on carbon nanotubes (CNTs), graphene, etc. For example, α–Fe$_2$O$_3$ hollow nanohorns were firstly grown on hierarchical CNT [129], SnO$_2$ nanoparticles were firstly distributed on graphene [130–132] or porous carbon [131] before the hydrothermal carbonization of glucose, which remarkably enhances the cycle stability compared with the pristine core materials.

Polymers with N-containing groups have recently drawn great attention as carbon sources, because N-doped carbon can be obtained during the carbonization process, which has been demonstrated the enhanced electronic conductivity and Li$^+$ storage capacity. Among various N-containing polymers, polydopamine with high concentrations of amine groups has strong binding affinity to inorganic materials and excellent coating capability. Accordingly, the conformal polydopamine-derived
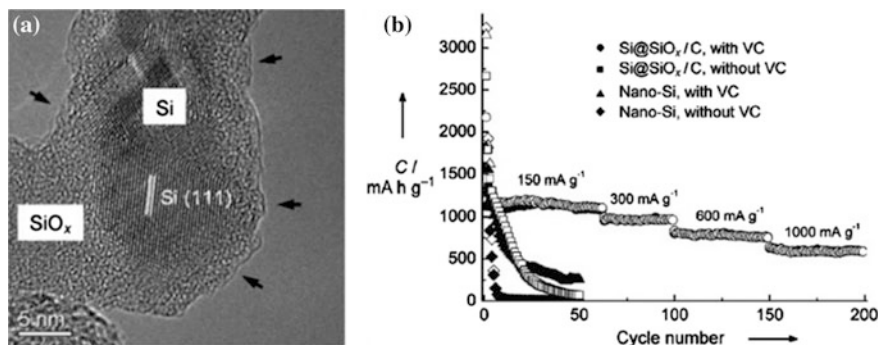
Fig. 10.21 a TEM images of the Si@SiO$_x$/C nanocomposite produced by hydrothermal carbonization and further carbonization at 750 °C under N$_2$. **b** Cycling and rate performances of pure Si nanoparticles and Si@SiO$_x$/C nanocomposite electrodes cycled in VC-free and VC-containing 1 m LiPF$_6$ in EC/DMC solutions (*solid symbols*: charge; *empty symbols*: discharge) (Reproduced from Ref. [110] with kind permission of © 2008 Wiley-VCH)
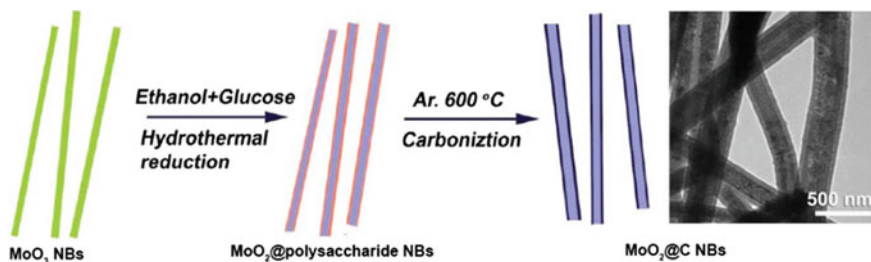
Scheme 10.7 Schematic illustration for the preparation of MoO$_2$@C nanobelts (Reproduced from Ref. [111] with kind permission of © 2012 Royal Society of Chemistry)

carbon with tailorable thickness is continuous and uniform. Due to the high percentage of nitrogen content in the precursor, the resulting carbon layer contains a moderate amount of N species, which can substantially improve the electrochemical performance. For example, polydopamine was applied as a precursor to prepare N-doped carbon coated Fe$_3$O$_4$ nanoparticles (denoted as Fe$_3$O$_4$@NC) [133]. As illustrated in Fig. 10.22a, dopamine monomers were firstly anchored on the surface of the rhombic-shaped α-Fe$_2$O$_3$ nanoparticles due to the strong binding affinity of catechol groups to Fe–OH of α-Fe$_2$O$_3$. Subsequently, the dopamine polymerized to form a conformal and continuous polymer layer. The core-shelled α-Fe$_2$O$_3$@polydopamine was lastly transformed to Fe$_3$O$_4$@NC nanocomposites by thermal annealing at 500 °C. In the obtained nanocomposites, the cores of Fe$_3$O$_4$ nanoparticles were encapsulated by continuous and uniform N-doped carbon layer of $\sim$10 nm (Fig. 10.22b) [133]. The composite exhibited remarkably high-specific capacity, high-rate capability, and excellent cycle performance. At a current density of 500 mA g^{-1}, it exhibited reversible capacity higher than 800 mA h g^{-1},

when the current density increased to mA g^{-1}, it still retained capacity of 595 mA h g^{-1} at a current of 1000 mA g^{-1}, and the capacity retention was 99% after 200 cycles even though the current density increases from 500 to 1000 mA g^{-1} after 100 cycles (Fig. 10.22c). Carbon coated SnO_2 nanoclusters were obtained using polydopamine as carbon source [23]. The continuous carbon coating of ~ 5 nm connected the SnO_2 nanoclusters, which enabled stable cycle performance. The SnO_2@C nanocomposite delivered a reversible capacity of about 700 mAh g^{-1} at a current density of 100 mA g^{-1}, realizing as high as 98% of the theoretical capacity of the hybrid. The capacity and stability were much improved compared with the pristine SnO_2 nanoparticles. Polydopamine-derived N-doped carbon coating also showed effective improvement of capacity and cycle stability for other anode materials, including $ZnFe_2O_4$ nanorods [134], MoS_2 hollow spheres [135], porous α-Fe_2O_3 nanospheres [136], and yolk-shell MnO spheres [137].

In conclusion, the polymer-derived carbon coating can provide rapid and continuous electronic transport, buffer the volume change, and prevent the direct contact between the nanomaterials with electrolyte, thus stabilizing the SEI film and avoiding capacity fading. By tuning the amount of monomers, the reaction time, temperature, etc., the carbon layer can be accordingly controlled to achieve the optimal thickness which ensures both elastic and good mechanical stability.

For most in situ formed polymerized-carbon coating on inorganic nanostructures, the contact between the carbon layers and active materials is fairly compact. To better accommodate large volume changes, void spaces were introduced between the active materials and the carbon coatings, turning core-shell structure into yolk-shell structure. This could efficiently enhance the capacity retention through buffering the local volume change during the lithium insertion–deinsertion processes, which is important to improve the cycling performance of the LIBs [138]. For example, Sn@C yolk-shell particles can be prepared as illustrated in Fig. 10.23a [139]. In the preparation procedure, SiO_2 submicroparticles were used as sacrificial template, after the coating with SnO_2, SiO_2 were etched to form SnO_2 hollow spheres. After coating with glucose-derived carbon, SnO_2@C hollow nanospheres were transformed to Sn@C nanocomposites with heat treatment in N_2. Sn@C nanocomposites presented a yolk-shell structure in which Sn nanoparticles were encapsulated in elastic hollow carbon spheres (Fig. 10.23b). The high Sn content and appropriate void space rendered the electrode advantageous features such as high-specific capacity (>800mAh g^{-1} in the initial 10 cycles, and >550 mAh g^{-1} even after 100 cycles), high-volume capacity, and good cycling performance (Fig. 10.23c).

Meanwhile, yolk-shell-structured Si@C nanocomposite can be prepared with the assistant of coating SiO_2 sacrificial layer. For example, Si nanoparticles were coated by SiO_2 before polydopamine coating, after the pyrolysis, SiO_2 layers were etched to make voids between the carbon layers (5–10 nm) and the Si nanoparticles (100 nm), forming a yolk-shell structure (Fig. 10.24a, b) [140]. The well-defined void space allows the Si particles to expand freely without breaking the outer carbon shell, therefore stabilizing the SEI on the shell surface. The yolk-shell-structured Si/C nanoparticles exhibited stable capacity of 1500 mAh g^{-1}
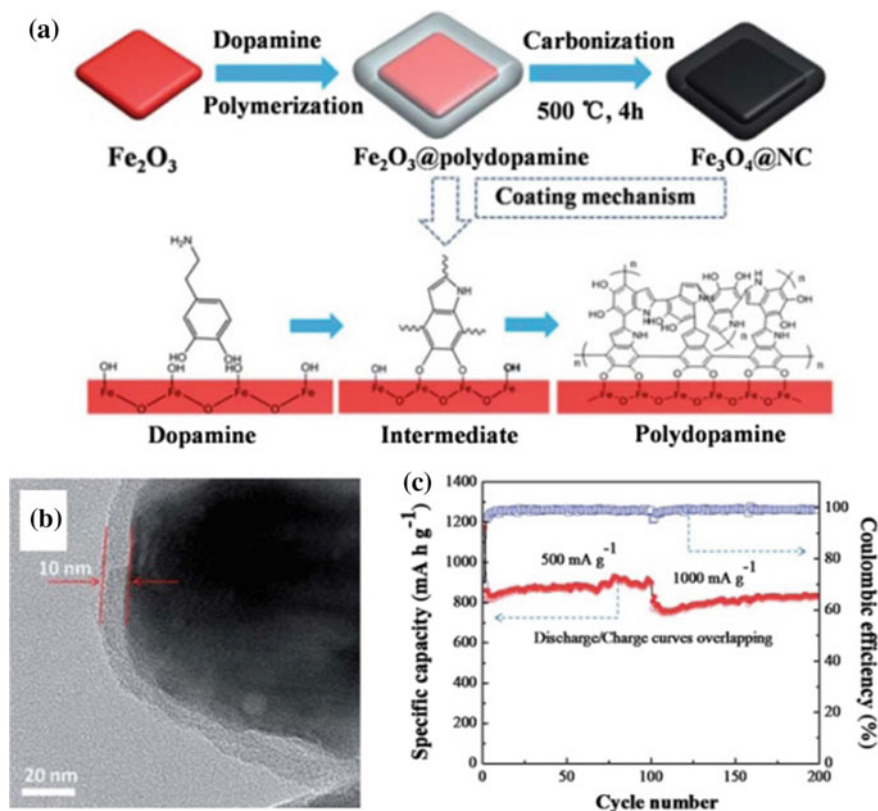
Fig. 10.22 **a** Schematic illustration of the fabrication of Fe_3O_4@NC composites and the coating mechanism of polydopamine on the surface of an iron oxide nanoparticle. **b** High-magnification image of a Fe_3O_4@NC composite. **c** Long-term cycling of Fe_3O_4@NC (Reproduced from Ref. [126] with kind permission of © 2013 Royal Society of Chemistry)

for 300 cycles and retain 74% of the capacity after 1000 cycles at a rate of 1C (4200 mA g^{-1}, Fig. 10.24c) [140]. In addition to dense SiO_2 layers, extra intro-duction of mesoporous SiO_2 template layers can result in mesoporous carbon shells derived from phenolic resin coating [141]. The obtained yolk-shell Si@mesoporous carbon yields long cycle life ($\sim$1000 mAh g^{-1} after 400 cycles) and excellent rate capability (62.3% capacity retained at a high current of 8.4 A g^{-1}). Analogously, resorcinol-formaldehyde, polyvinylidene fluoride, and polydopamine were also demonstrated as effective carbon precursors to construct various yolk-shell nanocomposites of Fe-, Sn- and Mn-based oxides, which showed the high Li$^+$ storage associated with the carbon coating [142–148].

Although nanostructure engineering has successfully extended the cycle life of anode materials with large volume change during the lithiation/delithiation process, it has also brought along fundamental challenges, including high surface area which
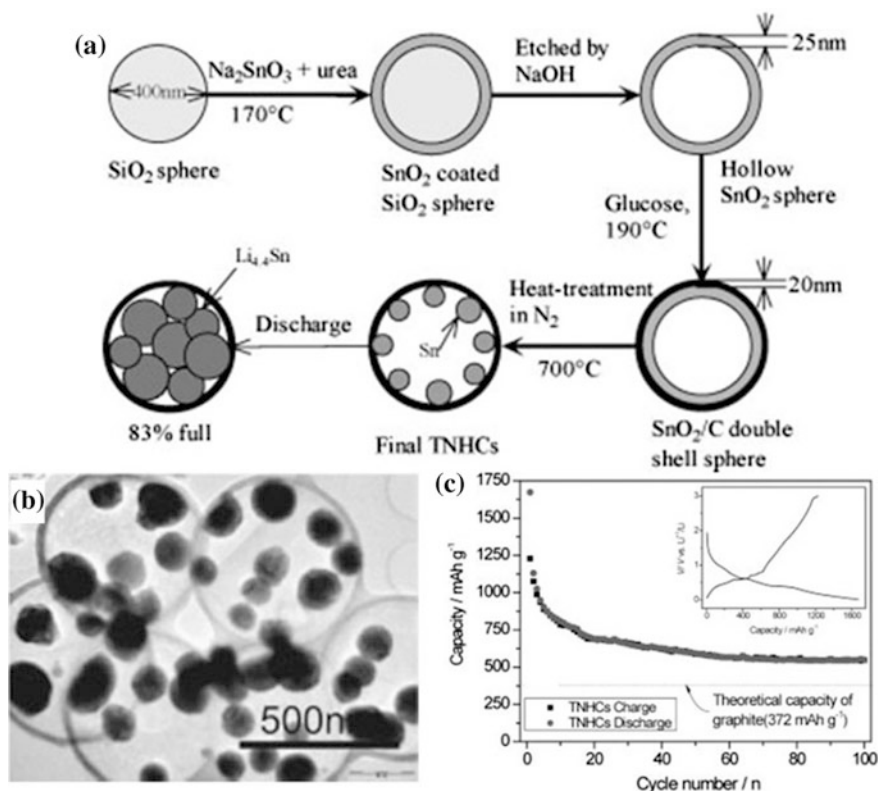
Fig. 10.23 **a** Synthetic scheme and **b** TEM image tin nanoparticles encapsulated elastic hollow carbon spheres (TNHCs). **c** The discharge/charge capacity profiles of TNHCs in 5 mV–3 V (vs. Li$^+$/Li) voltage window and C/5, the *inset* shows the first discharge/charge profiles of TNHCs cycled at a rate of C/5 (Reproduced from Ref. [132] with kind permission of © 2008 Wiley-VCH)

can increase side reactions with the electrolyte and low tap-density which leads to low volumetric capacity. These challenges stimulate the design of pomegranate structure, an advanced version of the yolk-shell [149]. In the preparation procedure as illustrated in Fig. 10.25a, Si@SiO$_2$ core-shell nanoparticles were assembled into secondary microbeads by a microemulsion approach before coating a layer of carbon derived from resorcinol-formaldehyde resin. And Si/C pomegranate structure could be obtained after the removal of the thickness tunable SiO$_2$ layers. The Si/C pomegranate anode retained a capacity of 1160 mAh g^{-1} after 1000 cycles at a rate of C/2 (2100 mA g^{-1}), with a retention of more than 97% (Fig. 10.25b). With a conventional slurry coating and calendaring process, electrodes prepared with the Si/C pomegranate exhibited a volumetric capacity in the range of 900–1270 mAh cm^{-3}, which is higher than the practical value for graphite anodes (600 mAh cm^{-3}). The pomegranate structure shows improvement compared with
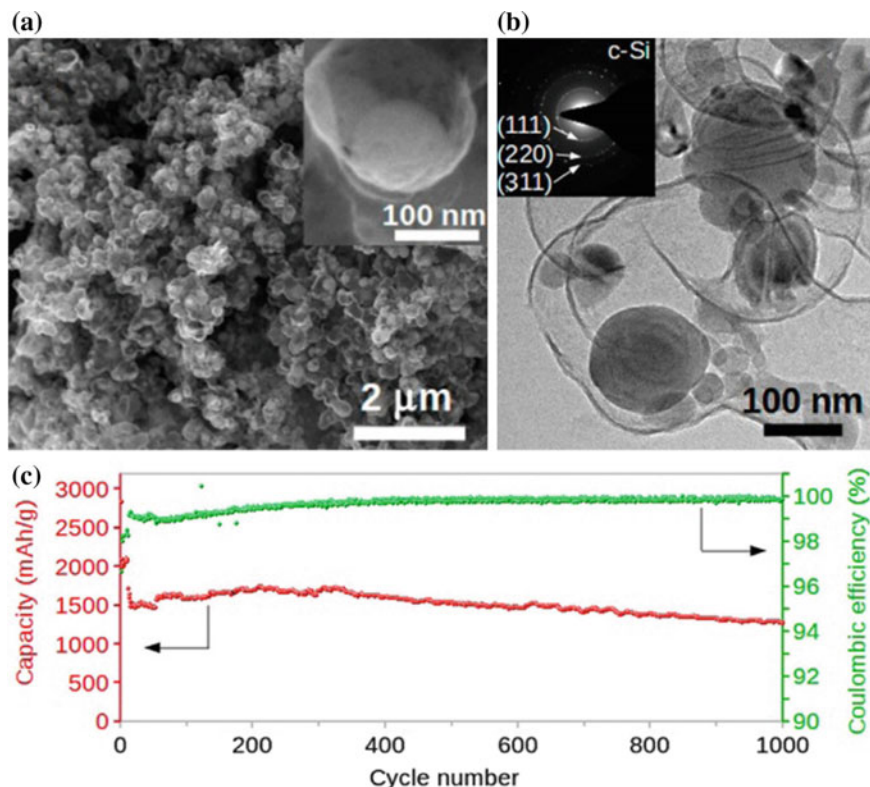
Fig. 10.24 a SEM and **b** TEM images of synthesized Si@void@C powder. **c** Delithiation capacity and coulombic efficiency of the first 1000 galvanostatic cycles between 0.01 and 1 V (alginate binder). The rate was C/10 for one cycle, then C/3 for 10 cycles, and 1 C for the later cycles (Reproduced from Ref. [133] with kind permission of © 2012 American Chemical Society)

the yolk-shell structure, in terms of areal mass loading, material tap-density, and electrical properties.

Besides core-shell and yolk-shell structure derived from polymer-carbon coating, another hybridization model is the loading of electrochemically active materials on/into polymer-derived carbon scaffold. Conductive carbon matrix provides fast ways for electron transfer which enables effective utilization of active materials, and at the same time acts as robust scaffolds which are very stable to accommodate the mechanical strain induced by the volume change during cycling.

One way to achieve the hybrid model of inorganic/C scaffold is post-introduction of inorganics or their precursors on/in polymers followed by pyrolysis. By dispersing SnO_2 nanoparticles into polymer solution in which triblock polymer (Pluronic F127) as soft template and resorcinol and formaldehyde as monomers for RF resin, framework of RF resin was obtained after polymerization with assistant of Pluronic F127. In the following heat treatment, RF resin was
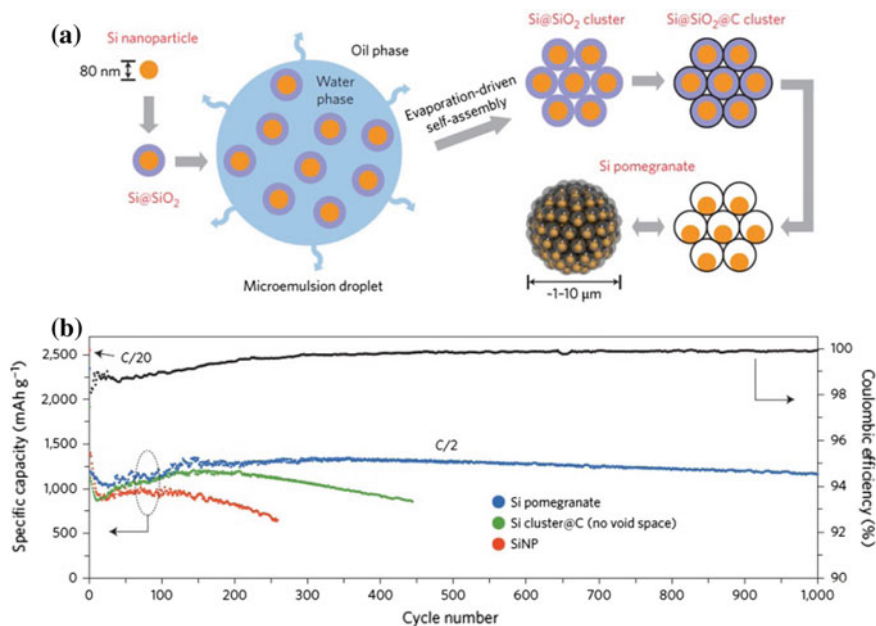
Fig. 10.25 a Schematic of the fabrication process for silicon pomegranates, **b** Reversible delithiation capacity for the first 1000 galvanostatic cycles of the silicon pomegranate and other structures tested under the same conditions (Reproduced from Ref. [143] with kind permission of © 2014 Macmillan Publishers Ltd)

carbonized while Pluronic F127 decomposed to form pores in the carbon, result in a sponge-like porous C/Sn composite. The mesoporous C/Sn anodes can deliver a capacity as high as 1300 mAh g^{-1} after 450 charge/discharge cycles and provide a capacity of 180 mAh g^{-1} even at 4000 mA g^{-1} charge/discharge current density.

And electrospinning is a most powerful and popular method way to evenly distribute nano inorganics or metal salt precursors in the polymers like polyaniline (PAN), poly(vinyl pyrrolidone) (PVP), poly(methyl methacrylate) (PMMA), and poly(vinyl acetate) (PVAc). Through tuning electrospinning and thermal treatment, 1D nanofibers with controllable phase (e.g., polymers, metals and ceramics), morphologies (e.g., porous, hollow and core-shell), and compositions (e.g., metal/metal oxides, carbon/metal or metal oxide composites) can be easily obtained [22].

Sn/C microtubes could be prepared by pyrolysis of coaxially electrospun nanofibers of tributyltin@polyacrylonitrile (TBT@PAN), as illustrated in Fig. 10.26a [150]. In such hybrids, Sn nanoparticles are well-confined inside the carbon microfibers with hollow channels (Fig. 10.26b), which offer adequate void space as "buffer zone" to accommodate the large volume change in the lithiation and delithiation processes, leading to improved cyclability of the Sn/C composite electrode. The composite displays a high reversible capacity of 737 mAh g^{-1} after

200 cycles at 250 mAh g^{-1} and retains 480 mAh g^{-1} when cycled at 2500 mAh g^{-1} (Fig. 10.26c). By introducing PMMA into PANI/DMF solution, porous carbon can be obtained, because PMMA decomposes into small molecular and evaporates during the carbonization of PANI, leaving voids in the carbon fiber. For example, by single-nozzle electrospinning of TBT-PMMA-PANI followed by high-temperature treatment, Sn nanoparticles encapsulated in porous multichannel carbon microtubes could be obtained and showed stable cycle performance [151]. Pores can be also obtained by etching of inorganics embed in the carbon nanofibers as mentioned in above yolk-shell structure.

For example, Si nanoparticles can be confined in porous carbon nanofibers using single-nozzle electrospinning of PAN/DMF suspension with Si@SiOx nanoparticles, high-temperature calcination and pore generation by etching of SiO$_x$ [152]. This Si/porous carbon-hybrid nanofibers showed 1104 mAh g^{-1} after 100 cycles at 0.5 A g^{-1} and maintained 485 mAh g^{-1} at 10 A g^{-1}. Other interesting structures like bubble-nanorod-structured Fe$_2$O$_3$/C composite nanofibers could be obtained with electrospun Fe(acac)$_3$/PAN composite fibers as precursors by using Kirkendall effect (Fig. 10.27) [153]. In the Fe$_2$O$_3$/C composite, hollow Fe$_2$O$_3$ nanospheres provided sufficient voids for volume expansion and carbon nanofiber matrix connecting the Fe$_2$O$_3$ nanospheres facilitates charge transfer. The special structure led to notable capacity retention and excellent rate capability.
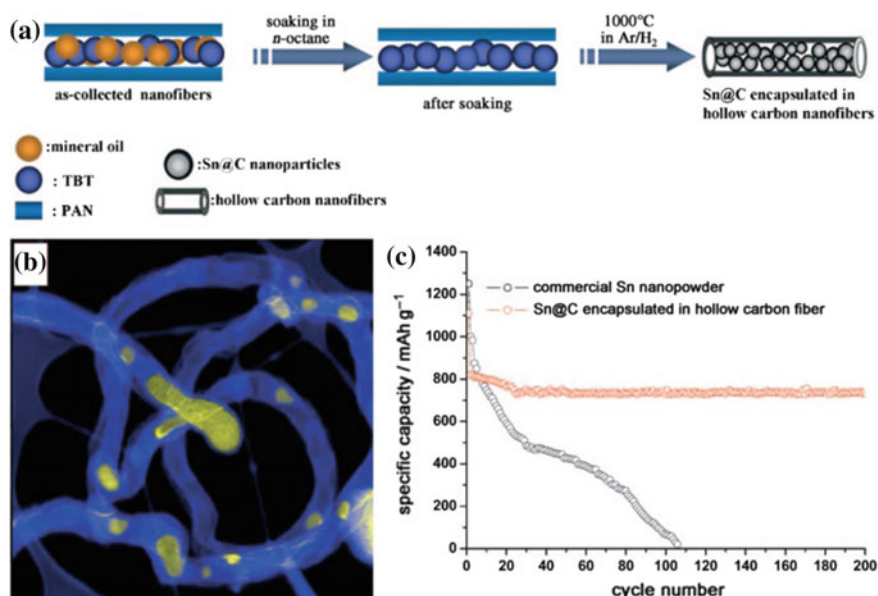
Fig. 10.26 **a** Schematic illustration of preparation of Sn@carbon nanoparticles encapsulated in hollow carbon nanofibers. **b** TEM image of Sn@C nanofibers. **c** Cycling performance of the commercial Sn nanopowder and the Sn@C nanofibers (Reproduced from Ref. [144] with kind permission of © 2009 Wiley-VCH)

The Fe_2O_3/C composite retained a discharge capacity of 812 mAh g^{-1} (84% of the second cycle) after 300 cycles at 1 A g^{-1} (Fig. 10.27).

And another way to achieve the hybrid model of inorganic/C scaffold is to directly grow inorganic nanostructures on/in the polymer-derived carbon matrix (e.g., carbon nanotubes, carbon nanofibers, porous carbon, etc.). For example, highly flexible, hollow, and end-opening carbon nanofibers could be derived from the self-assembly and carbonization of polypyrrole [154]. Through hydrothermal route, these nanofibers were homogenously coated by nanocrystalline SnO_2 (Scheme 10.8). As an anode material for LIBs, this composite showed a stable and high charge capacity (598.3 mA h g^{-1}) at a current density of 100 mA g^{-1} over 50 cycles with a low capacity fading of about 0.7% per cycle.
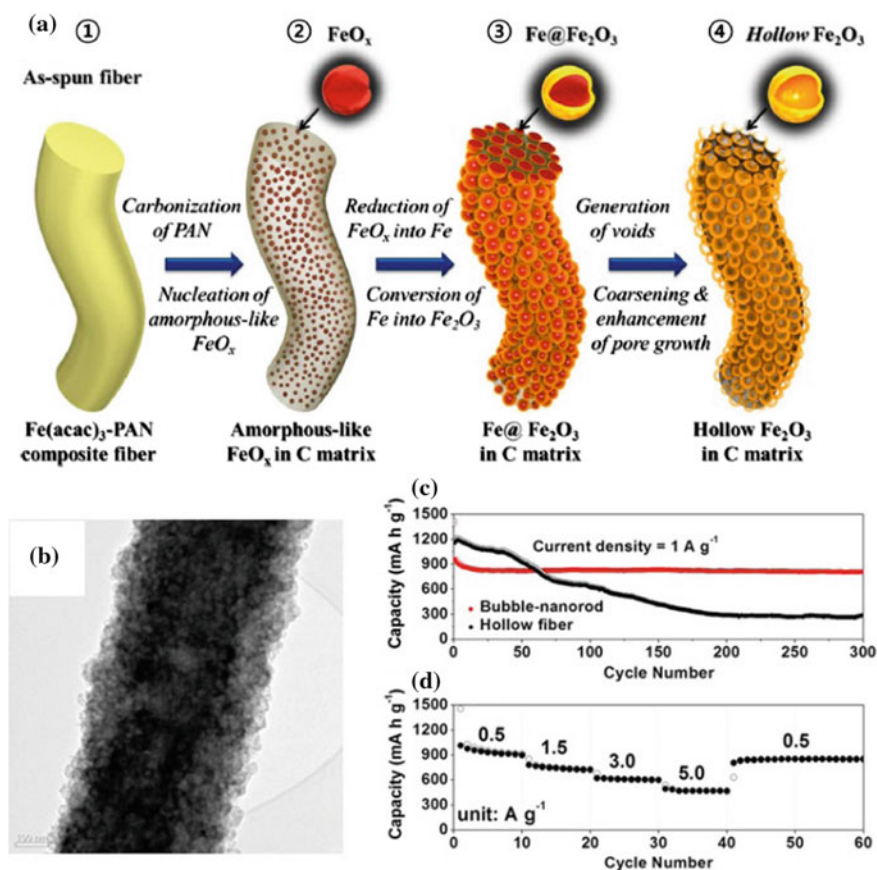
Fig. 10.27 a Schematic illustration of the formation mechanism of bubble-nanorod-structured Fe_2O_3–C composite nanofibers by Kirkendall-type diffusion. **b** TEM image and **c** cycling performance and rate performance of the bubble-nanorod-structured Fe_2O_3–C composite nanofibers (Reproduced from Ref. [147] with kind permission of © 2015 American Chemical Society)

Especially, carbons with open pores can provide additional benefits. On one hand, they allow more active materials to grow inside the pores, which well-confined the growth of nanomaterials, avoiding their agglomeration, and leading to favorable interactions between the two phases. On the other hand, the open pores can act as electrolyte container for high-rate charing/discharging and Li^+ reservoir for efficient Li^+ diffusion and storage. Ordered mesoporous carbon can be prepared through directly assembling mesoporous polymers based on soft templates of block copolymers or nanocasting monomers/polymers (sucrose, resorcinol-formaldehyde resin, PAN, etc.) into hard templates of ordered mesoporous silica or [153, 155, 156]. As the most well-known member of the mesoporous carbon family, CMK-3, a sucrose-derived replica of SBA-15, has a uniform pore diameter, large pore volume, interconnected porous structure, and high conductivity [157, 158]. These features enable a very high reversible capacity (up to 1100 mAh g^{-1}) and good cycle performance [159] and also make it a promising carbon matrix for enhancing the electrochemical performance of various electrode materials, e.g., NiO [160, 161], CoO [162, 163], α-Fe_2O_3 [164], Fe_3O_4 [165], FeF_3 [166], SnO_2 [167], CuO [168], and MoO_2 [169]. MoS_2 can be impregnated into CMK-3 by saturation with ammoniumtetrathiomolybdate (NH_4MoS_4) solution [170]. The as-obtained MoS_2@CMK-3 nanocomposite showed an improved cycling performance of 602 mA h g^{-1} at 250 mA g^{-1} after 100 cycles compared to the bulk MoS_2 and an excellent rate capability of 564 mA h g^{-1} at 2000 mA g^{-1} (Fig. 10.28). Hybrid nanostructure of MoS_2 nanosheets grown on CMK-3 can be obtained with hydrothermal method, as illustrated in Fig. 10.29 [171]. With the maintained mesoporous feature of CMK-3, this composite delivered a high discharge capacity of 934 mAh g^{-1} even after 150 cycles at a current density of 400 mA g^{-1}, with a coulombic efficiency close to 100% (Fig. 10.30).

Hybridization structure of inorganic/C scaffold can also be achieved by one-pot construction of polymer/metal ions (or salts) precursors followed by carbonization, which is more facile compared with the above two strategies. For example, by in situ polymerization of dopamine with zinc and iron species followed by carbonization, $ZnFe_2O_4$/C nanospheres could be synthesized [172]. The $ZnFe_2O_4$ nanoparticles (~ 8 nm) were well dispersed in the polydopamine-derived porous
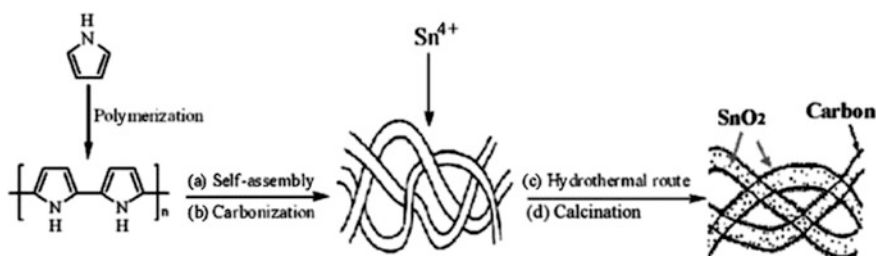

Scheme 10.8 Synthetic scheme for the SnO_2–C composites (Reproduced from Ref. [148] with kind permission of © 2011 Royal Society of Chemistry)

carbon matrix, which endowed the nanospheres with excellent rate capability and cycling stability. After high-rate cycling at 1, 2, and 5 A g^{-1} for 100, 200, and 200 cycles, the $ZnFe_2O_4$ nanospheres could still deliver very stable capacities of 606, 490, and 392 mA h g^{-1} and no obvious capacity fading was observed at each current density. Through complexation of dopamine and Mo^{VI} followed by hydrothermal treatment and post-annealing, sandwich-like structure of single-layer MoS_2/N-doped carbon nanocomposite could be successfully obtained (Fig. 10.31). The nanocomposite with a MoS_2 content of 76 wt% exhibited a stable capacity of 500 mA h g^{-1} for more than 800 cycles at 1.0 A g^{-1} [173]. Nevertheless, the complexation was restricted to certain species, and the composition determined by the coordination chemistry rather than the feed ratio is hard to control.

10.4.2 Cathode Materials

Basically, there are two kinds of cathode materials for LIBs, lithium transition metal oxides and phosphates [116]. Among diverse lithium transition metal oxides, layered $LiCoO_2$ and spinel-type $LiMn_2O_4$, as most promising and typical materials, have been attracting tremendous attention. $LiCoO_2$ has been successfully commercialized as a cathode material since the birth of the LIBs, owing to its merits such as high voltage (4.2 V vs. Li/Li^+), considerable reversible capacity (135 mAh g^{-1}), and easy production. By doping or substitution of Co atoms with elements such as Ni, Mn, and Fe in the lattice, the inherent electronic and Li^+ conductivity can be enhanced and the production cost can be reduced. And spinel-typed $LiMn_2O_4$, in which Mn can be partially substituted by Ni and Al, has long been studied as LIBs cathode materials because of their reliable safety and low cost. However, challenges of poor electronic and Li^+ conductivity, continuous dissolution of metal ions during discharge/charge cycles still remain for $LiCoO_2$ and $LiMn_2O_4$. As mentioned in the above section, carbon coating is regarded as a
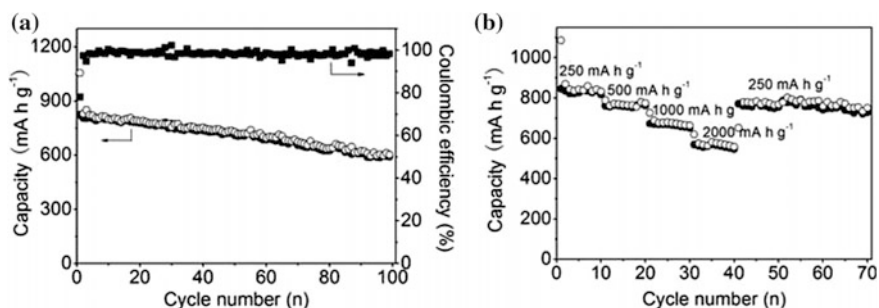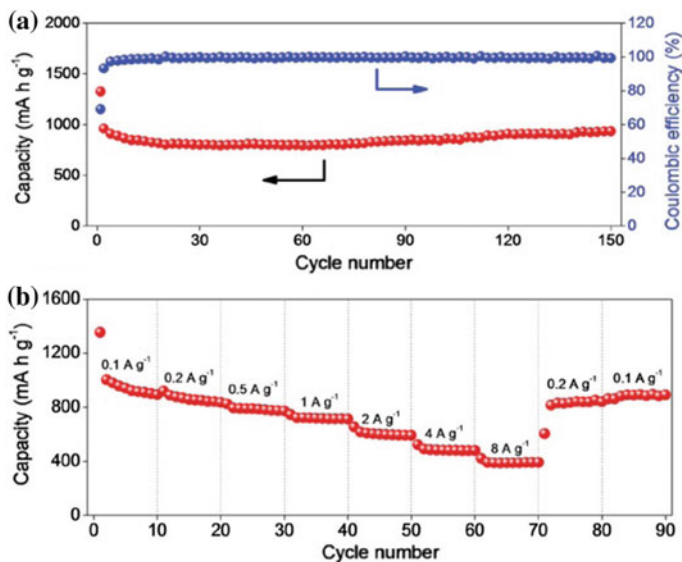

Fig. 10.28 **a** Cycling performance of MoS_2@CMK-3 electrode, and **b** rate capability of the MoS_2@CMK-3 electrode (Reproduced from Ref. [164] with kind permission of © 2012 Royal Society of Chemistry)
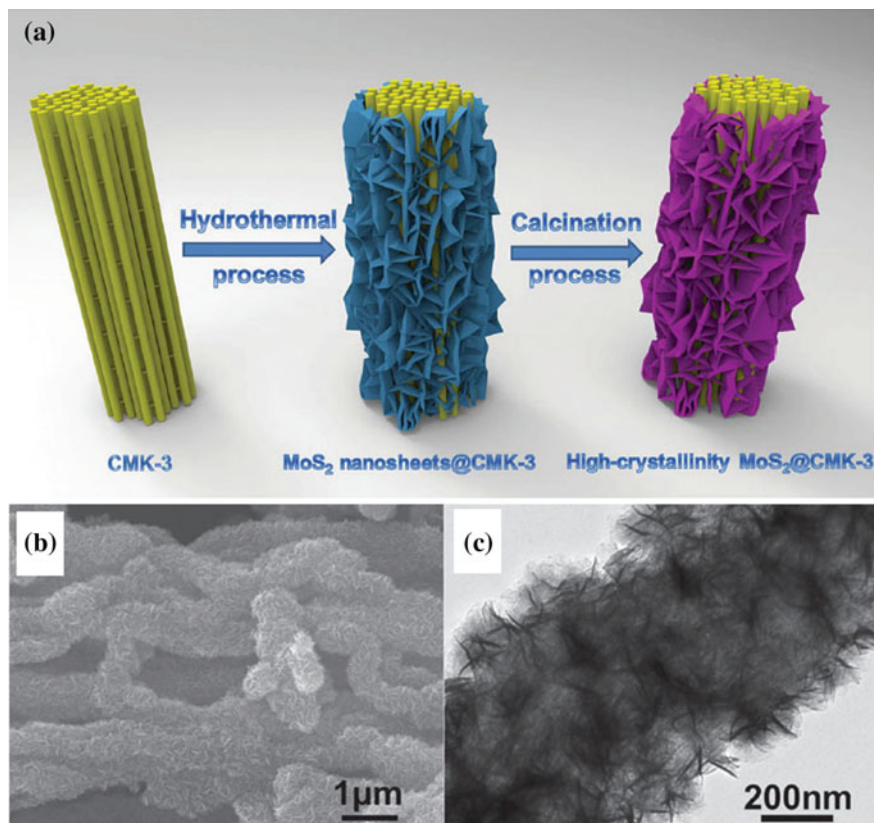
Fig. 10.29 **a** Schematic illustration of the formation of MoS$_2$@CMK-3 hybrid nanostructure.
b SEM and **c** TEM images of MoS$_2$ nanosheets on CMK-3 after the hydrothermal process
(Reproduced from Ref. [165] with kind permission of © 2014 Wiley-VCH)

general surface modification for anode materials, because it can enhance electronic
conductivity and isolate the active cores from outside environment. However,
polymer-derived carbon coating on the surface of LiCoO$_2$ and LiMn$_2$O$_4$ was less
reported, because the carbonization of polymer under inert atmosphere generates H$_2$
and CO, which may reduce the high-valence metal in these cathode materials.

The second class of cathode materials is phosphate. Since the proposal of
LiFeO$_4$ by Goodenough et al. in 1997, olivine-type LiMPO$_4$ (where M = Fe, Mn,
Co, or Ni) materials have been extensively studied as promising cathode materials.
Among them, LiFePO$_4$ is gaining significant attention because of its relatively low
cost, high theoretical capacity (170 mA h g^{-1}), environmental benignity, and safe
nature. However, its poor electronic ($\sim 10^{-9}$ S cm^{-1}) an ionic conductivity (10^{-14}
to 10^{-16} cm^2 s^{-1}) result in poor rate capability, which seriously hamper its practical
applications. Besides crystalline lattice optimization (doping transition metals or
polyanions) which can improve the inherently electronic and Li$^+$ conductivity,

Fig. 10.30 **a** Cycling performance together with Coulombic efficiency of MoS_2@CMK-3 at a current density of 400 mA g^{-1}. **b** Cycling performance of MoS_2@CMK-3 at different current densities(Reproduced from Ref. [165] with kind permission of © 2014 Wiley-VCH)
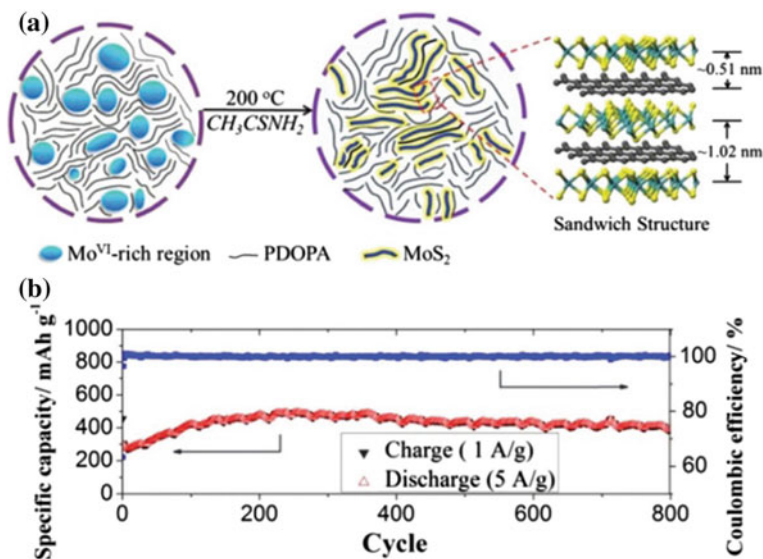
Fig. 10.31 **a** Schematics showing structural and morphological evolutions of MoS_2/C. **b** Cycling performance at a discharge rate of 5 A g^{-1} and a charge rate of 1 A g^{-1} of the MoS_2/C anode (Reproduced from Ref. [167] with kind permission of © 2014 Royal Society of Chemistry)

nanoengineering and hybridization with carbon are still two keys to solve the
kinetics problems as the same with anode materials. Nanostructures facilitate the
Li^+ diffusion in the cathode materials due to the reduced dimension, which, how-
ever, also brings along other problems. For example, due to the enlarged surface
area, more undesirable chemical reactions occur at the interface of the
electrode/electrolyte. The side reactions produce HF which attacks the surface of
$LiFePO_4$, leading to poor cycle performance [174]. Carbon coating is an effective
way to eliminate this problem. The carbon layer with good electric conductivity
prevents direct contact of electrode surface and electrolyte, therefore alleviating the
problems of low electronic conductivity as well as unfavorable side reactions.

Carbon coatings must also be either porous or very thin to allow easy penetration
of lithium ions [175]. Mechanically mixing the as-prepared powders with car-
bonaceous materials such as graphite, MCMB, and acetylene black can only obtain
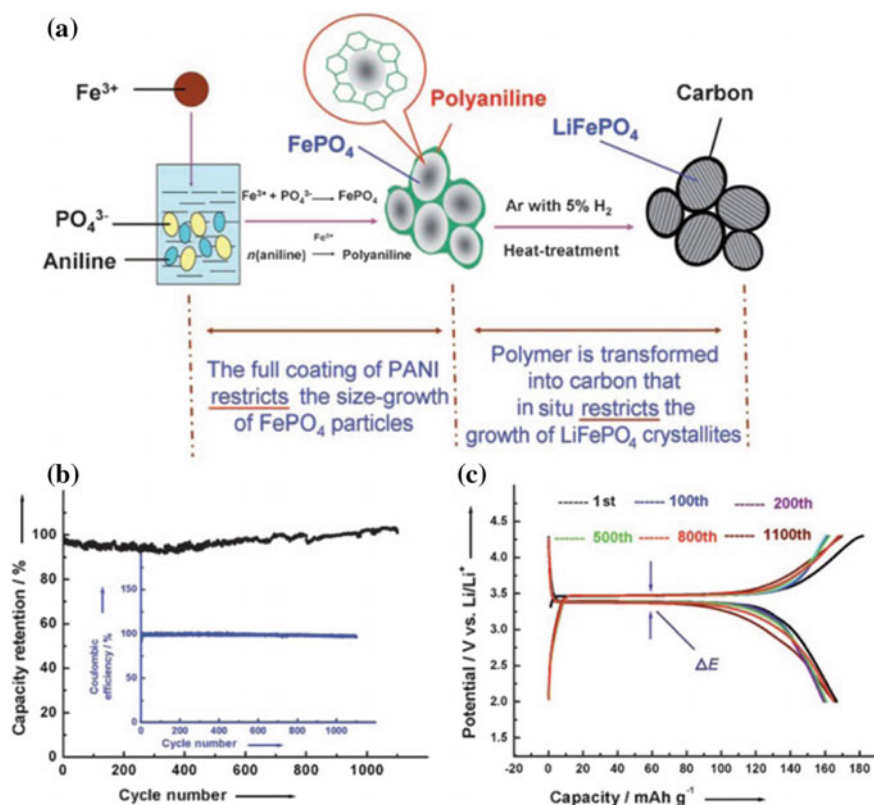

Fig. 10.32 a Preparation process for the LiFePO4/carbon composite including an in situ
polymerization reaction and two typical restriction processes. **b** cycling profile tested at a current
density of 0.1 Ag^{-1} between 2.0 and 4.3 V; **c** charge–discharge curves at different cycle number
(Reproduced from Ref. [170] with kind permission of © 2008 Wiley-VCH)

a rough-coating structure. Although these techniques significantly improve the electronic conductivity, the carbon coating is not uniform and the thickness is hard to control, uncoated areas remain weak sites for the attack of O_2 and electrolyte. Polymer coating followed by pyrolysis can offer more uniform, continuous, and complete carbon coating on the surface of $LiFeO_4$, because it is easier to obtain evenly distributed nanoparticles in solution than in solid phase, and monomers/polymers can be satisfactorily adhere to the surface of $LiFeO_4$ by coulombic forces or chemical adsorption/bonding. By control the concentration of monomers/polymers, the reaction time of polymerization, the thickness of the resultant carbon layer can be easily adjusted.

As a typical example, $LiFePO_4@C$ composite in which highly crystalline $LiFePO_4$ cores (20–40 nm) coated by a continuous semi-graphite carbon shell (1–2 nm) could be successfully obtained through in situ polymerization restriction method [176]. As shown in Fig. 10.32a, in the first step, aniline monomers were in situ polymerized on the surface of newly generated $FePO_4$ nanoparticles, forming a polyaniline shell which can effectively restrict the growth of $FePO_4$. And in the second step, polyaniline was transformed to carbon layer which in situ restricted the growth of $LiFePO_4$. The core-shell structured $LiFePO_4@C$ delivered a discharge capacity of 168 mAh g^{-1} at a current density of 0.1 A g^{-1} and maintained 95% of the capacity over 1100 cycles (Fig. 10.32b, c). $LiFePO_4@CNT$ core–shell nanowires could be obtained through using self-catalyzed pyrolysis of PMMA [174]. As shown in Scheme 10.9, PMMA coated on $LiFePO_4$ precursor nanowires was in situ
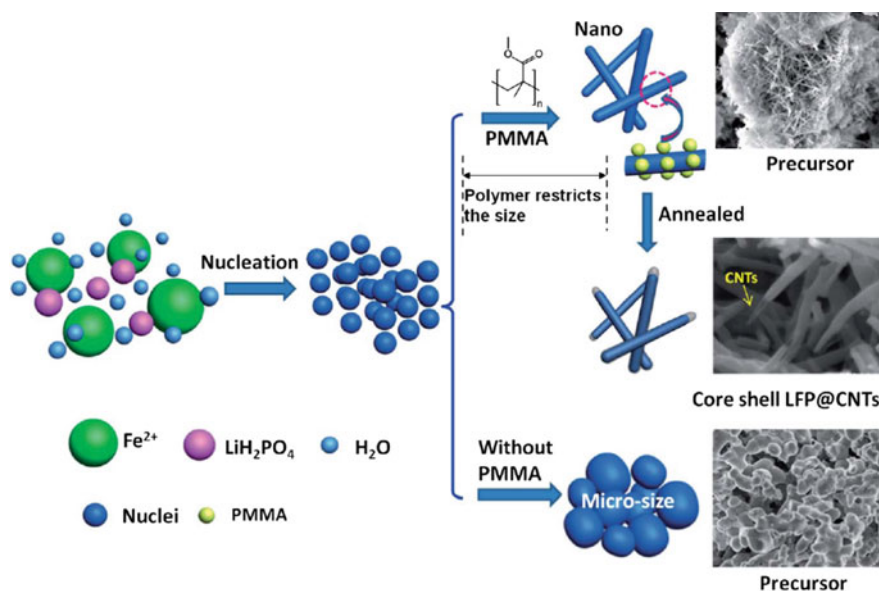

Scheme 10.9 Schematics to illustrate the synthetic procedure of the LFP@CNT nanocomposites (Reproduced from Ref. [168] with kind permission of © 2013 Royal Society of Chemistry)
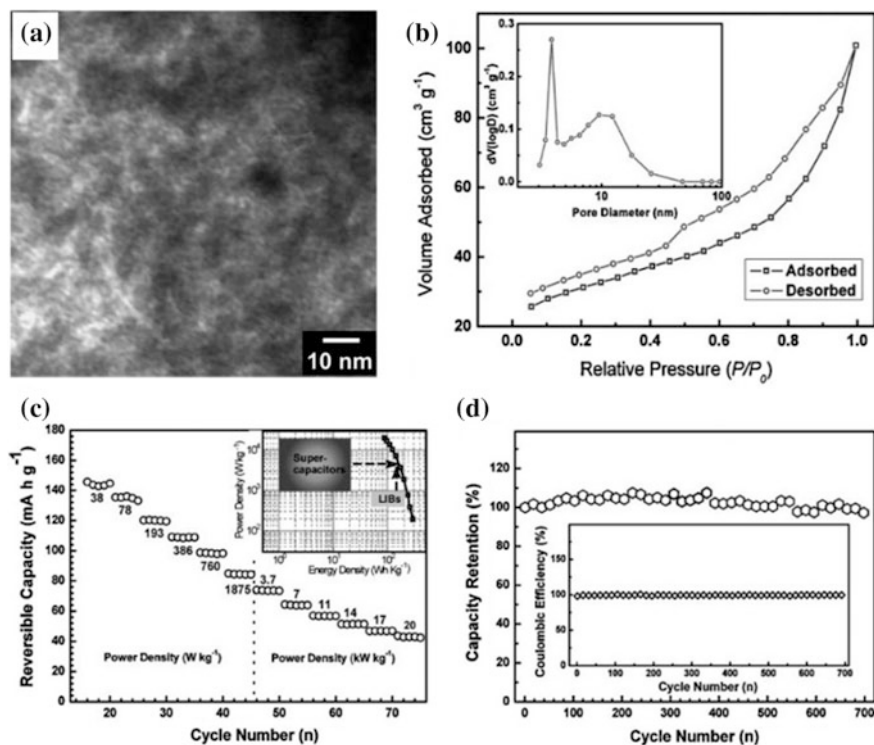
Fig. 10.33 a High-magnification TEM image and **b** Nitrogen adsorption/desorption isotherms of the LFP-NP@NPCM nanocomposite. **c** Rate performance at different power density; the *inset* shows the Ragone plots for the nanocomposite and commercially available supercapacitor electrodes. **d** Cycling performance of the LFP-NP@NPCM nanocomposite cycled at a rate of 1.5 C between 2.2 and 4.2 V (vs. Li$^+$/Li), the *inset* shows the corresponding Coulombic-efficiency profiles (Reproduced from Ref. [171] with kind permission of © 2009 Wiley-VCH)

catalyzed by Fe^{2+} to transform graphitized CNT, which in return restricts the growth of LiFePO$_4$ crystallite during the heat treatment. LiFePO$_4$@CNT nanowires delivered a capacity of 160 mA h g^{-1} at 17 mA g^{-1}, and 65 mA h g^{-1} at 8500 mA g^{-1} (50 C, 1.2 min for charging/discharge).

Porous carbons prepared from the pyrolysis of polymers and carbohydrates will form interconnected nanochannels and electronically conductive walls, which are characteristically good conducting networks for both Li$^+$ and electron. With Pluronic F127, a block copolymer, as a soft template for the nanoporous carbon matrix, the LiFePO$_4$@C nanocomposite with highly dispersed LiFePO$_4$ nanoparticles (60–100 nm) was obtained by two-step synthesis: sol–gel procedure and subsequent solid-state reaction (Fig. 10.33a, b) [177]. Owing to fast migration of Li$^+$ and e$^-$, this LiFePO$_4$@C nanocomposite showed high-rate capability and excellent cycling performance. At a high power density of up to 20 kW kg^{-1} (completing the discharge or charge process in about 16 s, corresponding to a rate
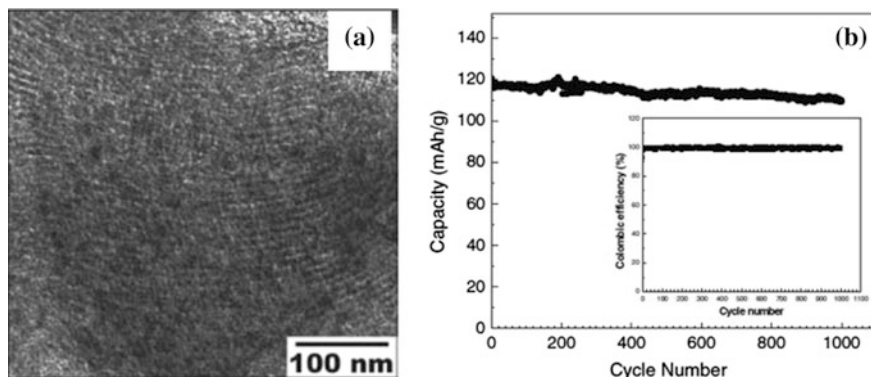
Fig. 10.34 a HRTEM images of mesoporous LiFePO$_4$/C nanocomposite, and **b** discharge capacity versus cycle number for the mesoporous nanocomposite electrode at the high rate of 10 C. The *inset* shows the high coulombic efficiency (Reproduced from Ref. [172] with kind permission of © 2010 Wiley-VCH)

of 230 C), it can maintain the discharge energy density of 87 Wh kg^{-1}. After 700 cycles at 1.5 C, it maintained 97% of the capacity (Fig. 10.33c, d). The performance of the LiFePO$_4$@C nanocomposite was similar to supercapacitors, but with higher energy density. LiFePO$_4$ embedded in ordered mesoporous carbon can be also prepared by nanocasting LiFePO$_4$ into a hard template, CMK-3 (Fig. 10.34) [178]. The mesoporous LiFePO$_4$/C composite can maintain ~ 110 mAh g^{-1}, 91% of the initial capacity after 1000 cycles at a rate of 10 C (completing the discharge or charge process in 6 min).

10.5 Conclusions

The recent advances on polymer-derived inorganic/carbon nanocomposites as efficient materials for electrochemical energy conversion and storage are highlighted in this chapter. Taking HER and LIBs as the good examples, the significant improvement of activity/capacity and durability associated with carbon integration from polymer-derivation has been demonstrated, which should be ascribed the optimized thermaldynamics and kinetics for electrochemical processes. In the case of HER, the hybridization of polymer-derived carbon contributes to the enhanced electronic conductivity, the varied electronic configuration, and the space-confinement for active catalysts. As for LIBs, the carbon-hybrid structures promote electronic and ionic conductivity and provide soft-matrix to accommodate the drastic volume variations during electrochemical processes, accomplishing the high capacity, good rate capacity, and long cycling life.

It should be pointed out that the design of polymer-derived inorganic/carbon electrode materials is still ongoing, and there are several important issues required

to be cleared. Firstly, the precise control on the electronic structure of inorganic/carbon nanocomposites should be taken into account as the keys to further enhance the electrochemical performance. The tailored electronic properties, such as Fermi level, d-band structure, and conductivity, are expected to optimize the surface activity of inorganics and utilize their synergy with carbon species. Secondly, the effective control over the combination between polymer-derived carbon and inorganic, and their nanostructures should be employed to design high-performance materials, in which the hierarchical nanostructures with uniform carbon–inorganic combination are demanded. Thirdly, the further mechanism underlying the efficient performance of such composites associated with the interactions of carbon and inorganic should be uncovered to open new opportunities in energy field. With rational design and delicate control in synthetic process, this unique class of nanocomposites may hold the key to overcome some bottlenecks of current materials in electrochemical energy conversion and storage.

References

1. Titirici M-M, White RJ, Brun N et al (2015) Sustainable carbon materials. Chem Soc Rev 44 (1):250–290
2. Jiang H, Lee PS, Li CZ (2013) 3D carbon based nanostructures for advanced supercapacitors. Energy Environ Sci 6(1):41–53
3. Meng H, Ma D, Yu X et al (2015) Tin-metal-carbon composite anode materials for lithium ion batteries. Prog Chem 27(8):1110–1122
4. Kong JH, Shahabadi SIS, Lu XH (2016) Integration of inorganic nanostructures with polydopamine-derived carbon: tunable morphologies and versatile applications. Nanoscale 8 (4):1770–1788
5. Rondeau-Gagne S, Morin J-F (2014) Preparation of carbon nanomaterials from molecular precursors. Chem Soc Rev 43(1):85–98
6. Liu R, Mahurin SM, Li C et al (2011) Dopamine as a carbon source: The controlled synthesis of hollow carbon spheres and yolk-structured carbon nanocomposites. Angew Chem Int Ed 50(30):6799–6802
7. Frank E, Steudle LM, Ingildeev D et al (2014) Carbon fibers: precursor systems, processing, structure, and properties. Angew Chem Int Ed 53(21):5262–5298
8. Ates M (2016) Graphene and its nanocomposites used as an active materials for supercapacitors. J Solid State Electrochem 20(6):1509–1526
9. Jung DS, Ko YN, Kang YC et al (2014) Recent progress in electrode materials produced by spray pyrolysis for next-generation lithium ion batteries. Adv Power Technol 25(1):18–31
10. Li Y, Wu JC, Chopra N (2015) Nano-carbon-based hybrids and heterostructures: progress in growth and application for lithium-ion batteries. J Mater Sci 50(24):7843–7865

11. Roy P, Srivastava SK (2015) Nanostructured anode materials for lithium ion batteries. J Mater Chem A 3(6):2454–2484
12. Wang HL, Dai HJ (2013) Strongly coupled inorganic-nano-carbon hybrid materials for energy storage. Chem Soc Rev 42(7):3088–3113
13. Etacheri V, Marom R, Elazari R et al (2011) Challenges in the development of advanced Li-ion batteries: a review. Energy Environ Sci 4(9):3243–3262
14. Goodenough JB, Kim Y (2010) Challenges for rechargeable li batteries. Chem Mater 22(3):587–603
15. Liu C, Li F, Ma LP et al (2010) Materials for energy storage. Adv Mater 22(8):28–62
16. Faber MS, Jin S (2014) Earth-abundant inorganic electrocatalysts and their nanostructures for energy conversion applications. Energy Environ Sci 7(11):3519–3542
17. McKone JR, Marinescu SC, Brunschwig BS et al (2014) Earth-abundant hydrogen evolution electrocatalysts. Chem Sci 5(3):865–878
18. Morales-Guio CG, Stern LA, Hu XL (2014) Nanostructured hydrotreating catalysts for electrochemical hydrogen evolution. Chem Soc Rev 43(18):6555–6569
19. Davis ME (2002) Ordered porous materials for emerging applications. Nature 417(6891):813–821
20. Deng J, Ren PJ, Deng DH et al (2015) Enhanced electron penetration through an ultrathin graphene layer for highly efficient catalysis of the hydrogen evolution reaction. Angew Chem Int Ed 54(7):2100–2104
21. Deng J, Ren PJ, Deng DH et al (2014) Highly active and durable non-precious-metal catalysts encapsulated in carbon nanotubes for hydrogen evolution reaction. Energy Environ Sci 7(6):1919–1923
22. Jung J-W, Lee C-L, Yu S et al (2016) Electrospun nanofibers as a platform for advanced secondary batteries: a comprehensive review. J Mater Chem A 4(3):703–750
23. Kong J, Yee WA, Yang L et al (2012) Highly electrically conductive layered carbon derived from polydopamine and its functions in SnO_2-based lithium ion battery anodes. Chem Commun 48(83):10316
24. Xie W, Li S, Wang S et al (2014) N-Doped amorphous carbon coated Fe_3O_4/SnO_2 coaxial nanofibers as a binder-free self-supported electrode for lithium ion batteries. ACS Appl Mater Interfaces 6(22):20334–20339
25. Li H, Shen L, Yin K et al (2013) Facile synthesis of N-doped carbon-coated $Li_4Ti_5O_{12}$ microspheres using polydopamine as a carbon source for high rate lithium ion batteries. J Mater Chem A 1(24):7270–7276
26. Yao X, Kong J, Zhao C et al (2014) Zinc ferrite nanorods coated with polydopamine-derived carbon for high-rate lithium ion batteries. Electrochim Acta 146:464–471
27. Tan L, Pan L, Cao C et al (2014) Nitrogen-doped carbon coated TiO_2 nanocomposites as anode material to improve cycle life for lithium-ion batteries. J Power Sources 253:193–200
28. Han F, Li W-C, Lei C et al (2014) Selective formation of carbon-coated, metastable amorphous $ZnSnO_3$ nanocubes containing mesopores for use as high-capacity lithium-ion battery. Small 10(13):2637–2644
29. Zhang C, Li H, Ping N et al (2014) Facile synthesis of nitrogen-doped carbon derived from polydopamine-coated $Li_3V_2(PO_4)_3$ as cathode material for lithium-ion batteries. RSC Adv 4(73):38791–38796
30. Ai K, Liu Y, Ruan C et al (2013) Sp^2 C-dominant N-doped carbon sub-micrometer spheres with a tunable size: A versatile platform for highly efficient oxygen-reduction catalysts. Adv Mater 25(7):998–1003
31. Kong J, Zhao C, Wei Y et al (2014) Nanocups-on-microtubes: a unique host towards high-performance lithium ion batteries. J Mater Chem A 2(36):15191–15199
32. Zhao Y, Kamiya K, Hashimoto K et al (2013) Hydrogen evolution by tungsten carbonitride nanoelectrocatalysts synthesized by the formation of a tungsten acid/polymer hybrid in situ. Angew Chem Int Ed 52(51):13638–13641
33. Dresselhaus MS, Thomas IL (2001) Alternative energy technologies. Nature 414(6861):332–337

34. Crabtree GW, Dresselhaus MS, Buchanan MV (2004) The hydrogen economy. Phys Today 57(12):39–44

35. Cook TR, Dogutan DK, Reece SY et al (2010) Solar energy supply and storage for the legacy and non legacy worlds. Chem Rev 110(11):6474–6502

36. Zeng M, Li YG (2015) Recent advances in heterogeneous electrocatalysts for the hydrogen evolution reaction. J Mater Chem A 3:14942–14962

37. Greeley J, Jaramillo TF, Bonde J et al (2006) Computational high-throughput screening of electrocatalytic materials for hydrogen evolution. Nat Mater 5(11):909–913

38. Parsons R (1911) Hydrogénations et déshydrogénations par catalyse. Ber Dtsch Chem Ges 44:1984–2001

39. Norskov JK, Bligaard T, Logadottir A et al (2005) Trends in the exchange current for hydrogen evolution. J Electrochem Soc 152(3):23–26

40. Benck JD, Hellstern TR, Kibsgaard J et al (2014) Catalyzing the hydrogen evolution reaction (HER) with molybdenum sulfide nanomaterials. ACS Catal 4(11):3957–3971

41. Laursen AB, Kegnæs S, Dahl S et al (2012) Molybdenum sulfides-efficient and viable materials for electro—and photoelectrocatalytic hydrogen evolution. Energy Environ Sci 5(2):5577–5591

42. Hinnemann B, Moses PG, Bonde J et al (2005) Biornimetic hydrogen evolution: MoS_2 nanoparticles as catalyst for hydrogen evolution. J Am Chem Soc 127(15):5308–5309

43. Jaramillo TF, Jorgensen KP, Bonde J et al (2007) Identification of active edge sites for electrochemical H-2 evolution from MoS_2 nanocatalysts. Science 317(5834):100–102

44. Kibsgaard J, Chen ZB, Reinecke BN et al (2012) Engineering the surface structure of MoS_2 to preferentially expose active edge sites for electrocatalysis. Nat Mater 11(11):963–969

45. Bian XJ, Zhu J, Liao L et al (2012) Nanocomposite of MoS_2 on ordered mesoporous carbon nanospheres: A highly active catalyst for electrochemical hydrogen evolution. Electrochem Commun 22:128–132

46. Liao L, Zhu J, Bian XJ et al (2013) MoS_2 formed on mesoporous graphene as a highly active catalyst for hydrogen evolution. Adv Funct Mater 23(42):5326–5333

47. Yu X-Y, Hu H, Wang Y et al (2015) Ultrathin MoS_2 nanosheets supported on N-doped carbon nanoboxes with enhanced lithium storage and electrocatalytic properties. Angew Chem Int Ed 54(25):7395–7398

48. Liu N, Yang LC, Wang SN et al (2015) Ultrathin MoS_2 nanosheets growing within an in-situ-formed template as efficient electrocatalysts for hydrogen evolution. J Power Sources 275:588–594

49. Daage M, Chianelli RR (1994) Structure-function relations in molybdenum sulfide catalysts: the "rim-edge" mode. J Catal 149(2):414–427

50. Yu P, Li Y, Zhao X et al (2014) Graphene-wrapped polyaniline nanowire arrays on nitrogen-doped carbon fabric as novel flexible hybrid electrode materials for high-performance supercapacitor. Langmuir 30(18):5306–5313

51. Zhong ZW, Liu N, Chen HY et al (2016) Molybdenum carbide supported by N-doped carbon: Controlled synthesis and application in electrocatalytic hydrogen evolution reaction. Mater Lett 176:101–105

52. Wan C, Regmi YN, Leonard BM (2014) Multiple Phases of molybdenum carbide as electrocatalysts for the hydrogen evolution reaction. Angew Chem Int Ed 53(25):6407–6410

53. Liao L, Wang S, Xiao J et al (2014) A nanoporous molybdenum carbide nanowire as an electrocatalyst for hydrogen evolution reaction. Energy Environ Sci 7(1):387–392

54. Graczyk-Zajac M, Reinold LM, Kaspar J et al (2015) New insights into understanding irreversible and reversible lithium storage within sioc and sicn ceramics. Nanomater 5(1): 233–245

55. Lin HL, Shi ZP, He SN et al (2016) Heteronanowires of MoC–Mo_2C as efficient electrocatalysts for hydrogen evolution reaction. Chem Sci 7:3399–3405

56. Ma FX, Wu HB, Xu CY et al (2015) Hierarchical b-Mo_2C nanotubes organized by ultrathin nanosheets as a highly efficient electrocatalyst for hydrogen production. Angew Chem Int Ed 54:15395–15399

57. Zhao Y, Kamiya K, Hashimoto K et al (2015) In situ CO_2-emission assisted synthesis of molybdenum carbonitride nanomaterial as hydrogen evolution electrocatalyst. J Am Chem Soc 137(1):110–113

58. Deng W, Jiang H, Chen C et al (2016) Co-, N-, and S-tridoped carbon derived from nitrogen- and sulfur-enriched polymer and cobalt salt for hydrogen evolution reaction. ACS Appl Mater Interfaces 8(21):13341–13347

59. Liu J, Wang HQ, Antonietti M (2016) Graphitic carbon nitride "reloaded": emerging applications beyond (photo)catalysis. Chem Soc Rev 45(8):2308–2326

60. Liu Y, Yu G, Li G-D et al (2015) Coupling Mo_2C with nitrogen-rich nanocarbon leads to efficient hydrogen-evolution electrocatalytic sites. Angew Chem Int Ed 54(37):10752–10757

61. Ma RG, Zhou Y, Chen YF et al (2015) Ultrafine molybdenum carbide nanoparticles composited with carbon as a highly active hydrogen-evolution electrocatalyst. Angew Chem Int Ed 54:14723–14727

62. Liu Y, Li G-D, Yuan L et al (2015) Carbon-protected bimetallic carbide nanoparticles for a highly efficient alkaline hydrogen evolution reaction. Nanoscale 7(7):3130–3136

63. Wang SP, Wang J, Zhu ML et al (2015) Molybdenum-carbide-modified nitrogen-doped carbon vesicle encapsulating nickel nanoparticles: a highly efficient, low-cost catalyst for hydrogen evolution reaction. J Am Chem Soc 137(50):15753–15759

64. Chen W-F, Iyer S, Iyer S et al (2013) Biomass-derived electrocatalytic composites for hydrogen evolution. Energy Environ Sci 6(6):1818

65. Meng FK, Hu EY, Zhang LH et al (2015) Biomass-derived high-performance tungsten-based electrocatalysts on graphene for hydrogen evolution. J Mater Chem A 3(36):18572–18577

66. Shi YM, Zhang B (2016) Recent advances in transition metal phosphide nanomaterials: synthesis and applications in hydrogen evolution reaction. Chem Soc Rev 45(6):1529–1541

67. Vesborg PCK, Seger B, Chorkendorff I (2015) Recent development in hydrogen evolution reaction catalysts and their practical implementation. J Phys Chem Lett 6(6):951–957

68. Han S, Feng Y, Zhang F et al (2015) Metal-Phosphide-Containing porous carbons derived from an ionic-polymer framework and applied as highly efficient electrochemical catalysts for water splitting. Adv Funct Mater 25(25):3899–3906

69. Cui W, Liu Q, Xing Z et al (2015) MoP nanosheets supported on biomass-derived carbon flake: One-step facile preparation and application as a novel high-active electrocatalyst toward hydrogen evolution reaction. Appl Catal B 164:144–150

70. Zou ML, Chen JD, Xiao LF et al (2015) WSe_2 and $W(Se_xS_{1-x})_2$ nanoflakes grown on carbon nanofibers for the electrocatalytic hydrogen evolution reaction. J Mater Chem A 3(35):18090–18097

71. Yu S, Kim J, Yoon KR et al (2015) Rational design of efficient electrocatalysts for hydrogen evolution reaction: single layers of ws_2 nanoplates anchored to hollow nitrogen-doped carbon nanofibers. ACS Appl Mater Interfaces 7(51):28116–28121

72. Ding Q, Liu M, Miao Y-E et al (2015) Electrospun nickel-decorated carbon nanofiber membranes as efficient electrocatalysts for hydrogen evolution reaction. Electrochim Acta 159:1–7

73. Wang Z, Zuo P, Fan L et al (2016) Facile electrospinning preparation of phosphorus and nitrogen dual-doped cobalt-based carbon nanofibers as bifunctional electrocatalyst. J Power Sources 311:68–80

74. Yaghi OM, Li H (1995) Hydrothermal synthesis of a metal-organic framework containing large rectangular channels. J Am Chem Soc 117(41):10401–10402

75. Furukawa H, Cordova KE, OKeeffe M et al (2013) The chemistry and applications of metal-organic frameworks. Science 341(6149):1230444

76. Sun J-K, Xu Q (2014) Functional materials derived from open framework templates/precursors: synthesis and applications. Energy Environ Sci 7(7):2071

77. Xia W, Mahmood A, Zou RQ et al (2015) Metal-organic frameworks and their derived nanostructures for electrochemical energy storage and conversion. Energy Environ Sci 8(7):1837–1866

78. Xu M, Han L, Han YJ et al (2015) Porous CoP concave polyhedron electrocatalysts synthesized from metal-organic frameworks with enhanced electrochemical properties for hydrogen evolution. J Mater Chem A 3(43):21471–21477

79. Huang Z-F, Song J, Li K et al (2016) Hollow cobalt-based bimetallic sulfide polyhedra for efficient all-ph-value electrochemical and photocatalytic hydrogen evolution. J Am Chem Soc 138(4):1359–1365

80. Hao J, Yang W, Zhang Z et al (2015) Metal–organic frameworks derived $Co_xFe_{1-x}P$ nanocubes for electrochemical hydrogen evolution. Nanoscale 7(25):11055–11062

81. Liu M, Li J (2016) Cobalt phosphide hollow polyhedron as efficient bifunctional electrocatalysts for the evolution reaction of hydrogen and oxygen. ACS Appl Mater Interfaces 8(3):2158–2165

82. Liu Y, Zhou X, Ding T et al (2015) 3D architecture constructed via the confined growth of MoS_2 nanosheets in nanoporous carbon derived from metal-organic frameworks for efficient hydrogen production. Nanoscale 7(43):18004–18009

83. Wang T, Zhou QY, Wang XJ et al (2015) MOF-derived surface modified Ni nanoparticles as an efficient catalyst for the hydrogen evolution reaction. J Mater Chem A 3(32):16435–16439

84. Fan LL, Liu PF, Yan XC et al (2016) Atomically isolated nickel species anchored on graphitized carbon for efficient hydrogen evolution electrocatalysis. Nat Commun 7:10667

85. Yang Y, Lun ZY, Xia GL et al (2015) Non-precious alloy encapsulated in nitrogen-doped graphene layers derived from MOFs as an active and durable hydrogen evolution reaction catalyst. Energy Environ Sci 8(12):3563–3571

86. Wu HB, Xia BY, Yu L et al (2015) Porous molybdenum carbide nano-octahedrons synthesized via confined carburization in metal-organic frameworks for efficient hydrogen production. Nat Commun 6:6512–6542

87. Shi ZP, Wang YX, Lin HL et al (2016) Porous nanoMoC@graphite shell derived from a MOFs-directed strategy: an efficient electrocatalyst for the hydrogen evolution reaction. J Mater Chem A 4(16):6006–6013

88. Gao QS, Wang SN, Fang HC et al (2012) One-dimensional growth of MoO_x-based organic-inorganic hybrid nanowires with tunable photochromic properties. J Mater Chem 22(11):4709–4715

89. Gao QS, Zhang CX, Xie SH et al (2009) Synthesis of nanoporous molybdenum carbide nanowires based on organic-inorganic hybrid nanocomposites with sub-nanometer periodic structures. Chem Mater 21(23):5560–5562

90. Gao QS, Zhang CX, Wang SN et al (2010) Preparation of supported Mo_2C-based catalysts from organic-inorganic hybrid precursor for hydrogen production from methanol decomposition. Chem Commun 46(35):6494–6496

91. Gao QS, Liu N, Wang SN et al (2014) Metal non-oxide nanostructures developed from organic-inorganic hybrids and their catalytic application. Nanoscale 6(23):14106–14120

92. Lin HL, Liu N, Shi ZP et al (2016) Cobalt-doping in molybdenum-carbide nanowires toward effi cient electrocatalytic hydrogen evolution. Adv Funct Mater 26:5590–5598

93. Michalsky R, Zhang YJ, Peterson AA (2014) Trends in the hydrogen evolution activity of metal carbide catalysts. ACS Catal 4(5):1274–1278

94. Dong GF, Fang M, Wang HT et al (2015) Insight into the electrochemical activation of carbon-based cathodes for hydrogen evolution reaction. J Mater Chem A 3:13080–13086

95. Lin H, Liu N, Shi Z, Guo Y et al (2016) Cobalt-Doping in molybdenum-carbide nanowires toward efficient electrocatalytic hydrogen evolution. Adv Funct Mater 26(31):5590–5598

96. Liu N, Yang L, Wang S (2015) Ultrathin MoS_2 nanosheets growing within an in-situ-formed template as efficient electrocatalysts for hydrogen evolution. J Power Sources 275:588–594

97. Yu X-Y, Hu H, Wang Y et al (2015) Ultrathin MoS_2 nanosheets supported on n-doped carbon nanoboxes with enhanced lithium storage and electrocatalytic properties. Angew Chem Int Ed 54(25):7395–7398

98. Zhao Y, Kamiya K, Hashimoto K et al (2015) In situ CO_2-emission assisted synthesis of molybdenum carbonitride nanomaterial as hydrogen evolution electrocatalyst. J Am Chem Soc 137(1):110–113

99. Zou M, Chen J, Xiao L et al (2015) WSe_2 and $W(Se_xS_{1−x})_2$ nanoflakes grown on carbon nanofibers for the electrocatalytic hydrogen evolution reaction. J Mater Chem A 3(35): 18090–18097

100. Ma F-X, Wu HB, Xia BY et al (2015) Hierarchical β-Mo_2C nanotubes organized by ultrathin nanosheets as a highly efficient electrocatalyst for hydrogen production. Angew Chem Int Ed 54(51):15395–15399

101. Lin H, Shi Z, He S (2016) Heteronanowires of MoC-Mo_2C as efficient electrocatalysts for hydrogen evolution reaction. Chem Sci 7(5):3399–3405

102. Tarascon JM, Armand M (2001) Issues and challenges facing rechargeable lithium batteries. Nature 414(6861):359–367

103. Zhao M-Q, Zhang Q, Huang J-Q et al (2012) Hierarchical nanocomposites derived from nanocarbons and layered double hydroxides—properties, synthesis, and applications. Adv Funct Mater 22(4):675–694

104. Wu H, Cui Y (2012) Designing nanostructured Si anodes for high energy lithium ion batteries. Nano Today 7(5):414–429

105. Guo YG, Hu JS, Wan LJ (2008) Nanostructured materials for electrochemical energy conversion and storage devices. Adv Mater 20(15):2878–2887

106. Sun B, Chen ZX, Kim HS et al (2011) MnO/C core-shell nanorods as high capacity anode materials for lithium-ion batteries. J Power Sources 196(6):3346–3349

107. Wang ZY, Chen JS, Zhu T et al (2010) One-pot synthesis of uniform carbon-coated MoO_2 nanospheres for high-rate reversible lithium storage. Chem Commun 46(37):6906–6908

108. Hong YJ, Kang YC (2014) Superior electrochemical performances of doubleshelled CuO yolk-shell powders formed from spherical copper nitrate-polyvinylpyrrolidone composite powders. RSC Adv 4(102):58231–58237

109. Wang CB, Yin LW, Xiang D et al (2012) Uniform carbon layer coated mn_3o_4 nanorod anodes with improved reversible capacity and cyclic stability for lithium ion batteries. ACS Appl Mater Interfaces 4(3):1636–1642

110. Si Q, Hanai K, Ichikawa T et al (2010) A high performance silicon/carbon composite anode with carbon nanofiber for lithium-ion batteries. J Power Sources 195(6):1720–1725

111. Yin YX, Xin S, Wan LJ et al (2011) Electrospray synthesis of silicon/carbon nanoporous microspheres as improved anode materials for lithium-ion batteries. J Phys Chem C 115(29): 14148–14154

112. Xu YH, Yin GP, Ma YL et al (2010) Nanosized core/shell silicon@carbon anode material for lithium ion batteries with polyvinylidene fluoride as carbon source. J Mater Chem 20(16):3216–3220

113. Gao PF, Fu JW, Yang J et al (2009) Microporous carbon coated silicon core/shell nanocomposite via in situ polymerization for advanced Li-ion battery anode material. Phys Chem Chem Phys 11(47):11101–11105

114. Lee JE, Yu SH, Lee DJ et al (2012) Facile and economical synthesis of hierarchical carbon-coated magnetite nanocomposite particles and their applications in lithium ion battery anodes. Energy Environ Sci 5(11):9528–9533

115. Titirici MM, Thomas A, Antonietti M (2007) Replication and coating of silica templates by hydrothermal carbonization. Adv Funct Mater 17(6):1010–1018

116. Qian HS, Yu SH, Luo LB et al (2006) Synthesis of uniform Te@Carbon-Rich composite nanocables with photoluminescence properties and carbonaceous nanofibers by the hydrothermal carbonization of glucose. Chem Mater 18(8):2102–2108

117. Hu YS, Demir-Cakan R, Titirici MM et al (2008) Superior storage performance of a Si@SiO_x/C nanocomposite as anode material for lithium-ion batteries. Angew Chem Int Ed 47(9):1645–1649

118. Yang L, Liu L, Zhu Y et al (2012) Preparation of carbon coated MoO_2 nanobelts and their high performance as anode materials for lithium ion batteries. J Mater Chem 22(26):13148

119. Noh M, Kwon Y, Lee H et al (2005) Amorphous carbon-coated tin anode material for lithium secondary battery. Chem Mater 17(8):1926–1929

120. Chen JS, Cheah YL, Chen YT et al (2009) SnO_2 Nanoparticles with controlled carbon nanocoating as high-capacity anode materials for lithium-ion batteries. J Phys Chem C 113(47):20504–20508

121. Wu P, Du N, Zhang H et al (2011) Carbon-coated SnO_2 nanotubes: template-engaged synthesis and their application in lithium-ion batteries. Nanoscale 3(2):746–750

122. Kim HS, Chung YH, Kang SH et al (2009) Electrochemical behavior of carbon-coated SnS_2 for use as the anode in lithium-ion batteries. Electrochim Acta 54(13):3606–3610

123. Wang Y, Zhang HJ, Lu L et al (2010) Designed functional systems from peapod-like Co@carbon to Co_3O_4@carbon nanocomposites. ACS Nano 4(8):4753–4761

124. Zhang WM, Wu XL, Hu JS et al (2008) Carbon Coated Fe_3O_4 Nanospindles as a superior anode material for lithium-ion batteries. Adv Funct Mater 18(24):3941–3946

125. Yuan SM, Li JX, Yang LT et al (2011) Preparation and lithium storage performances of mesoporous Fe_3O_4@C microcapsules. ACS Appl Mater Interfaces 3(3):705–709

126. Chen Y, Xia H, Lu L et al (2012) Synthesis of porous hollow Fe_3O_4 beads and their applications in lithium ion batteries. J Mater Chem 22(11):5006–5012

127. Huang XH, Tu JP, Zhang CQ et al (2007) Spherical NiO-C composite for anode material of lithium ion batteries. Electrochim Acta 52(12):4177–4181

128. Liu JP, Li YY, Ding RM et al (2009) Carbon/ZnO nanorod array electrode with significantly improved lithium storage capability. J Phys Chem C 113(13):5336–5339

129. Wang ZY, Luan DY, Madhavi S et al (2012) Assembling carbon-coated alpha-Fe_2O_3 hollow nanohorns on the CNT backbone for superior lithium storage capability. Energy Environ Sci 5(1):5252–5256

130. Zhang CF, Peng X, Guo ZP et al (2012) Carbon-coated SnO_2/graphene nanosheets as highly reversible anode materials for lithium ion batteries. Carbon 50(5):1897–1903

131. Li Y, Zhu SM, Liu QL et al (2012) Carbon-coated SnO_2@C with hierarchically porous structures and graphite layers inside for a high-performance lithium-ion battery. J Mater Chem 22(6):2766–2773

132. Wang DN, Yang JL, Li XF et al (2013) Layer by layer assembly of sandwiched graphene/SnO_2 nanorod/carbon nanostructures with ultrahigh lithium ion storage properties. Energy Environ Sci 6(10):2900–2906

133. Cheng L, Fei H, Duo L et al (2013) Dopamine as the coating agent and carbon precursor for the fabrication of N-doped carbon coated Fe_3O_4 composites as superior lithium ion anodes. Nanoscale 5(3):1168–1175

134. Yao XY, Kong JH, Zhao CY et al (2014) Zinc ferrite nanorods coated with polydopamine-derived carbon for high-rate lithium ion batteries. Electrochim Acta 146:464–471

135. Guo BJ, Yu K, Song HL et al (2016) Preparation of hollow microsphere@onion-like solid nanosphere MoS_2 coated by a carbon shell as a stable anode for optimized lithium storage. Nanoscale 8(1):420–430

136. Liang J, Xiao CH, Chen X et al (2016) Porous gamma-Fe_2O_3 spheres coated with N-doped carbon from polydopamine as Li-ion battery anode materials. Nanotechnology 27(21):215403

137. Wang SB, Xiao CL, Xing YL et al (2015) Formation of a stable carbon framework in a MnO yolk-shell sphere to achieve exceptional performance for a Li-ion battery anode. J Mater Chem A 3(30):15591–15597

138. Liu J, Qiao SZ, Chen JS et al (2011) Yolk/shell nanoparticles: new platforms for nanoreactors, drug delivery and lithium-ion batteries. Chem Commun 47(47):12578–12591

139. Zhang WM, Hu JS, Guo YG et al (2008) Tin-nanoparticles encapsulated in elastic hollow carbon spheres for high-performance anode material in lithium-ion batteries. Adv Mater 20(6):1160–1198

140. Liu N, Wu H, McDowell MT et al (2012) A yolk-shell design for stabilized and scalable li-ion battery alloy anodes. Nano Lett 12(6):3315–3321

141. Yang JP, Wang YX, Chou SL et al (2015) Yolk-shell silicon-mesoporous carbon anode with compact solid electrolyte interphase film for superior lithium-ion batteries. Nano Energy 18:133–142

142. Zhang JN, Wang KX, Xu Q et al (2015) Beyond yolk-shell nanoparticles: $Fe_3O_4@Fe_3C$ Core@shell nanoparticles as yolks and carbon nanospindles as shells for efficient lithium ion storage. ACS Nano 9(3):3369–3376

143. Li JP, Wu P, Ye Y et al (2014) Designed synthesis of $SnO_2@C$ yolk-shell spheres for high-performance lithium storage. Cryst Eng Comm 16(4):517–521

144. Wang JX, Li W, Wang F et al (2014) Controllable synthesis of $SnO_2@C$ yolk-shell nanospheres as a high-performance anode material for lithium ion batteries. Nanoscale 6(6): 3217–3222

145. Zhang HW, Zhou L, Noonan O et al (2014) Tailoring the void size of iron oxide@carbon yolk-shell structure for optimized lithium storage. Adv Funct Mater 24(27):4337–4342

146. Cai ZY, Xu L, Yan MY et al (2015) Manganese oxide/carbon yolk-shell nanorod anodes for high capacity lithium batteries. Nano Lett 15(1):738–744

147. Zhao Y, Feng ZX, Xu ZCJ (2015) Yolk-shell Fe_2O_3 circle dot C composites anchored on MWNTs with enhanced lithium and sodium storage. Nanoscale 7(21):9520–9525

148. Su LW, Xie J, Xu YW et al (2015) Preparation and lithium storage performance of yolk-shell Si@void@C nanocomposites. Phys Chem Chem Phys 17(27):17562–17565

149. Liu N, Lu Z, Zhao J et al (2014) A pomegranate-inspired nanoscale design for large-volume-change lithium battery anodes. Nat Nanotechnol 9(3):187–192

150. Yu Y, Gu L, Wang C et al (2009) Encapsulation of Sn@carbon nanoparticles in bamboo-like hollow carbon nanofibers as an anode material in lithium-based batteries. Angew Chem Int Ed 48(35):6485–6489

151. Yu Y, Gu L, Zhu C et al (2009) Tin nanoparticles encapsulated in porous multichannel carbon microtubes: preparation by single-nozzle electrospinning and application as anode material for high-performance Li-based batteries. J Am Chem Soc 131(44):15984–16012

152. Zhou XS, Wan LJ, Guo YG (2013) Electrospun silicon nanoparticle/porous carbon hybrid nanofibers for lithium-ion batteries. Small 9(16):2684–2688

153. Cho JS, Hong YJ, Kang YC (2015) Design and synthesis of bubble-nanorod-structured fe_2o_3 carbon nanofibers as advanced anode material for Li-Ion batteries. ACS Nano 9(4): 4026–4035

154. Hongyu M, Youlong X, Wei S et al (2011) Polymer-derived carbon nanofiber network supported SnO_2 nanocrystals: a superior lithium secondary battery material. J Mater Chem 21(48):19302–19309

155. Mi H, Xu Y, Shi W et al (2011) Polymer-derived carbon nanofiber network supported SnO_2 nanocrystals: a superior lithium secondary battery material. J Mater Chem 21(48):19302–19309

156. Stein A, Wang ZY, Fierke MA (2009) Functionalization of porous carbon materials with designed pore architecture. Adv Mater 21(3):265–293

157. Jun S, Joo SH, Ryoo R et al (2000) Synthesis of new, nanoporous carbon with hexagonally ordered mesostructure. J Am Chem Soc 122(43):10712–10713

158. Ji XL, Lee KT, Nazar LF (2009) A highly ordered nanostructured carbon-sulphur cathode for lithium-sulphur batteries. Nat Mater 8(6):500–506

159. Zhou HS, Zhu SM, Hibino M et al (2003) Lithium storage in ordered mesoporous carbon (CMK-3) with high reversible specific energy capacity and good cycling performance. Adv Mater 15(24):2107–2111

160. Cheng MY, Hwang BJ (2010) Mesoporous carbon-encapsulated NiO nanocomposite negative electrode materials for high-rate Li-ion battery. J Power Sources 195(15):4977–4983

161. Fan ZY, Liang J, Yu W et al (2015) Ultrathin NiO nanosheets anchored on a highly ordered nanostructured carbon as an enhanced anode material for lithium ion batteries. Nano Energy 16:152–162

162. Zhang HJ, Tao HH, Jiang Y et al (2010) Ordered CoO/CMK-3 nanocomposites as the anode materials for lithium-ion batteries. J Power Sources 195(9):2950–2955
163. Sun B, Liu H, Munroe P et al (2012) Nanocomposites of CoO and a mesoporous carbon (CMK-3) as a high performance cathode catalyst for lithium-oxygen batteries. Nano Res 5(7):460–469
164. Nagao M, Otani M, Tomita H et al (2011) New three-dimensional electrode structure for the lithium battery: Nano-sized gamma-Fe_2O_3 in a mesoporous carbon matrix. J Power Sources 196(10):4741–4746
165. Wu F, Huang R, Mu DB et al (2014) A novel composite with highly dispersed Fe_3O_4 nanocrystals on ordered mesoporous carbon as an anode for lithium ion batteries. J All Comp 585:783–789
166. Li BJ, Zhang NQ, Sun KN (2014) Confined iron fluoride@CMK-3 nanocomposite as an ultrahigh rate capability cathode for li-ion batteries. Small 10(10):2039–2046
167. Qiao H, Li J, Fu JP et al (2011) Sonochemical synthesis of ordered SnO_2/CMK-3 nanocomposites and their lithium storage properties. ACS Appl Mater Interfaces 3(9): 3704–3708
168. Yang M, Gao QM (2011) Copper oxide and ordered mesoporous carbon composite with high performance using as anode material for lithium-ion battery. Micro Meso Mater 143(1): 230–235
169. Chen AL, Li CX, Tang R et al (2013) MoO_2-ordered mesoporous carbon hybrids as anode materials with highly improved rate capability and reversible capacity for lithium-ion battery. Phys Chem Chem Phys 15(32):13601–13610
170. Zhou X, Wan L-J, Guo Y-G (2012) Facile synthesis of MoS_2@CMK-3 nanocomposite as an improved anode material for lithium-ion batteries. Nanoscale 4(19):5868–5871
171. Xu X, Fan Z, Yu X et al (2014) A nanosheets-on-channel architecture constructed from MoS_2 and CMK-3 for high-capacity and long-cycle-life lithium storage. Adv Energy Mater. doi:10.1002/aenm.201400902
172. Yao X, Zhao C, Kong J et al (2014) Dopamine-assisted one-pot synthesis of zinc ferrite-embedded porous carbon nanospheres for ultrafast and stable lithium ion batteries. Chem Commun 50(93):14597–14600
173. Zhao C, Kong J, Yang L et al (2014) The dopamine-MoVI complexation-assisted large-scale aqueous synthesis of a single-layer MoS_2/carbon sandwich structure for ultrafast, long-life lithium-ion batteries. Chem Commun 50(68):9672–9675
174. Yang J, Wang J, Tang Y et al (2013) In situ self-catalyzed formation of core-shell $LiFePO_4$@CNT nanowires for high rate performance lithium-ion batteries. J Mater Chem A 1(25):7306–7311
175. Wang J, Sun X (2012) Understanding and recent development of carbon coating on $LiFePO_4$ cathode materials for lithium-ion batteries. Energy Environ Sci 5(1):5163–5185
176. Wang Y, Wang Y, Hosono E et al (2008) The design of a $LiFePO_4$/carbon nanocomposite with a core-shell structure and its synthesis by an in situ polymerization restriction method. Angew Chem Int Ed 47(39):7461–7465
177. Wu X-L, Jiang L-Y, Cao F-F et al (2009) $LiFePO_4$ nanoparticles embedded in a nanoporous carbon matrix: superior cathode material for electrochemical energy-storage devices. Adv Mater 21(25–26):2710–2714
178. Wang G, Liu H, Liu J et al (2010) Mesoporous LiFePO4/C nanocomposite cathode materials for high power lithium ion batteries with superior performance. Adv Mater 22(44): 4944–4948

Chapter 11
Tailoring Performance of Polymer Electrolytes Through Formulation Design

Wei Wang, Dmitry Bedrov and Paschalis Alexandridis

Abstract The flammable organic solvent-based electrolytes used in lithium batteries impose serious safety concerns and temperature restrictions. A switch to solid polymer electrolytes can significantly increase chemical/mechanical stability, improve safety, reduce cost, and advance manufacturability, if only issues such as low conductivity and transference, limited operating temperature range, and insufficient mechanical strength can be overcome. To this end, significant research efforts have been directed to understand the mechanism of lithium ion motion in polymer matrices and to modify the chemistry, architecture, and morphology of the poly(ethylene oxide) polymer typically used in polymer electrolytes. Furthermore, the incorporation of nanoparticles into polymer electrolytes has created new opportunities for simultaneous improvement of conductivity and of mechanical properties. The performance of such composite polymer electrolytes can be modulated by the judicious surface chemical modification of the nanoparticles and/or by the addition of organic solvents or ionic liquids. The examples highlighted here point to the importance of formulation design for the improvement of the performance characteristics of multi-component systems such as polymer electrolytes.

W. Wang · P. Alexandridis (✉)
Department of Chemical and Biological Engineering, University at Buffalo,
The State University of New York (SUNY), Buffalo, NY 14260-4200, USA
e-mail: palexand@buffalo.edu

W. Wang
e-mail: wwang23@buffalo.edu

D. Bedrov
Department of Materials Science and Engineering, University of Utah,
Salt Lake City, UT 84112-0063, USA
e-mail: d.bedrov@utah.edu

11.1 Introduction

Polymer electrolytes are widely utilized in electrochemical devices such as lithium-ion batteries, fuel cells, and supercapacitors for energy storage and conversion [1–8]. In this chapter, we focus on different additives and their effects on polymer electrolyte performance for lithium-ion batteries. A battery is composed of two electrochemically active electrodes [9] separated by an ion-conductive, electronically insulating electrolyte medium [10]. Rechargeable batteries find widespread use because of their repeated charge and discharge capability [11].

The electrolyte is one of the critical components of the lithium-ion battery. It facilitates ion transport and blocks electron conduction between the two electrodes [12]. Desirable properties of electrolytes are: high ionic conductivity and cation mobility, low electronic conductivity, good mechanical strength, thermal and chemical stability, and interfacial contact with electrodes, and large electrochemical stability window [13, 14]. Organic solvent-based electrolytes and ionic liquid-based electrolytes are two classes of electrolytes that have been well studied but they exhibit several drawbacks [15]. Organic solvent-based electrolytes have problems that include intrinsically poor cycling efficiency and flammability [16]. For ionic liquid-based electrolytes, a challenge is their relatively high viscosity which limits the attainable ionic conductivity [17–19]. Polymer electrolytes [20, 21] have thus been considered with an aim to overcome such limitations. The archetype polymer electrolyte is based on poly(ethylene oxide) (PEO) with lithium salt dissolved in it [22]. However, the semi-crystalline structure of PEO presents inherent problems as a polymer matrix for Li^+: (1) not sufficiently high ionic conductivity, especially in ambient temperature; (2) insufficient mechanical strength; and (3) dendrite growth at the interface between electrode and electrolyte, which might cause internal short circuits [2].

In order to overcome these limitations of polymer electrolytes, several avenues have been explored. One promising line of investigation involves the introduction of nano-sized additives, as shown in Fig. 11.1 [23], in order to minimize the concentration of PEO crystalline domains without diminishing the PEO flexibility and mechanical stability over a wide temperature range [24, 25]. Inert oxide ceramics are the most common additives [26]. The effects of such additives have been analyzed in terms of Lewis acid–base interactions [24] between the surface groups of the fillers and active sites on the polymer chains.

Even though ternary systems incorporating nano-additives are promising, e.g., due to simultaneous improvement of conductivity and mechanical strength [24–27], composite polymer electrolytes (CPEs) are still away from desirable performance, e.g., room temperature conductivity higher than 10^{-3} S/cm [28]. For applications in electrochemical devices such as lithium-ion batteries [4, 12], research on CPEs is directed toward the formulation of modified ternary (polymer + lithium salt + nanoparticle) systems.

Different schemes have been reported for modifying each component in CPEs. Here, we focus on two avenues of modification: (1) surface chemical modification
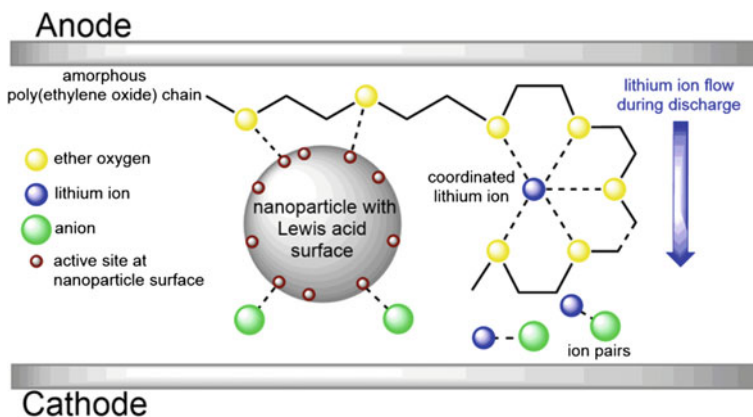
Fig. 11.1   Schematic of composite polymer electrolytes in the context of lithium-ion batteries

of nanoparticles, e.g., functionalization by oligomer groups or by ionic liquids; (2) physical modification via the addition of components such as organic solvents or ionic liquids. Section 11.2 discusses Li$^+$ transport mechanisms and factors that affect it in polymer-based electrolytes. Section 11.3 addresses the effect of nanoparticles on CPE properties and performance. Section 11.4 discusses nanoparticle chemical modification. Section 11.5 is concerned with the physical addition of a fourth component to CPEs. The purpose of Sects. 11.4 and 11.5 is to exemplify how different formulation modifications of CPEs have been designed and implemented, and to inspire ideas on novel CPE design for further CPE performance improvement.

11.2   Polymer-Based Electrolytes

First, we review key molecular mechanisms and phenomena influencing the motion of Li ions (and their counter-ions) in a polymer matrix, and we outline several major challenges that conventional polymer electrolytes are facing to become an efficient alternative to conventional organic solvent electrolytes. We use PEO-based polymer electrolytes to illustrate these issues as the overwhelming majority of polymer electrolytes investigated to date are PEO-based. In addition to a large number of experimental studies, PEO-based electrolytes have also been studied by molecular simulation [29–41], and therefore these systems provide good case studies to illustrate the full complexity of understanding and design of efficient polymer electrolytes.

11.2.1 Mechanism of Li⁺ Motion in PEO-Based Polymer Electrolytes

PEO is the quintessential polymer electrolyte owing largely to its effectiveness at dissolving lithium salts due to strong Li^+-ether oxygen binding. Quantum chemistry (QC) and molecular dynamics (MD) simulation studies [29, 42] of PEO have revealed that Li^+ cations are very strongly coordinated by an average of six ether oxygen atoms as shown in Fig. 11.2. Coordination of Li^+ usually involves a single PEO chain, with occasional coordination by two polymer chains.

The nature of ether--Li^+ interactions strongly affects the mechanism of Li^+ mobility in PEO-based solid polymer electrolytes (SPEs). This can be understood by comparing the mechanism of Li^+ diffusion in oligoethers with that in organic solvents. Li^+ motion in organic liquid electrolytes (typically carbonates) occurs by a combination of vehicular (with a solvent shell) and structural (exchange of solvent shell) diffusion [43]. In contrast, simulations reveal that Li^+ diffusion in pentaglyme + Li[bis[(trifluoromethyl) sulfonyl]imide] (TFSI) [43] salt occurs entirely by a vehicular mechanism, i.e., a pentaglyme/Li^+ complex diffuses long distances before Li^+ exchanges between complexing molecules. The residence time of Li^+ with a pentaglyme is around 50 ns, compared to $\sim$1 ns in carbonate, or 3–10 ns in ionic liquids [44]. While the lack of an efficient structural diffusion mechanism has relatively little influence on Li^+ motion in pentaglyme because of the fast center-of-mass diffusion of the low molecular weight (MW) solvent, the situation is different in higher molecular weight (MW) PEO. Because the center-of-mass diffusion of PEO is negligible, a Li^+ cation must change coordinating PEO chains, i.e., it will undergo "jumps" between PEO chains [45]. Compared with pentaglyme, Li^+ transport is considerably slower in the PEO-based SPE, while the diffusion of TFSI is reduced relatively little, indicative of the relative independence of anion motion from that of the polymer. This leads to a significantly lower transference number in the polymer electrolyte as a much greater fraction of charge is carried by the anion due to the very slow Li^+ motion. Furthermore, the PEO chain center-of-mass motion is considerably slower than that of the cation, intimating that the vehicular mechanism, which is so important in the oligoethers, does not contribute significantly to Li^+ motion in the SPE. Instead, Li^+ motion in the PEO-based electrolytes resembles diffusion along PEO chain contours with occasional inter-chain jumps on a time scale of $\sim$100 ns [41].

Fig. 11.2 Representative configurations of Li^+ coordination by PEO

● Li⁺   ● Ether oxygens   ● Carbons
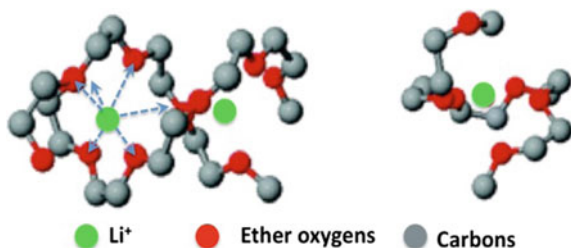
Simulation [29] and experimental studies [46, 47] of linear PEO-based electrolytes also showed strong dependence of the Li$^+$ and anion motion on salt concentration. While the anion motion remains much faster than that of Li$^+$ for all salt concentrations, the translational dynamics of both ions decrease dramatically with increasing salt concentration, suggesting strong coupling with local polymer relaxations. The slowing of polymer segmental dynamics with increasing salt content is due to the strong binding between ether oxygens and Li$^+$, which greatly restricts conformational motion. As a result, a maximum in PEO-based electrolyte conductivity is observed for Li:EO molar ratio $\sim$1:10 due to two counter-acting effects: Ionic conductivity increases with increasing salt concentration due to the increase in the number of charge carriers, while increasing salt concentration slows down polymer dynamics, thereby decreasing also the Li$^+$ transport [29, 48].

11.2.2 Influence of Polymer Architecture

Polyethers of comb-branch chain architecture have been investigated in efforts to develop polymer electrolytes that take advantage of the ability of oligoethers to coordinate Li$^+$ while, at the same time, preventing crystallinity due to use of short side chains, and allow for separate optimization of the backbone properties from those of the side chains [49]. The ideal comb-branch electrolyte might, for example, use a glassy backbone polymer, thereby leading to good mechanical properties, while Li$^+$ transport would be carried out by flexible ether (PEO) side chains (Fig. 11.3a). The use of relatively short side chains not only reduces/prevents PEO crystallinity, but may also facilitate the inter-chain hopping needed for large-scale Li$^+$ transport, due to sharing of Li$^+$ cations between side chains. Several polymer electrolytes formed from comb-branch polymer have been studied experimentally [50, 51] and in simulations [30], however, studies showed that the conductivity of the comb-branch electrolytes is very similar to that of the linear PEO electrolytes. Molecular simulations of the comb-branched systems revealed that Li$^+$ motion occurs primarily by hopping of the cation from one side chain to another [30]. However, a fraction of Li$^+$ cations are partially coordinated by the polyether backbone and, therefore, have very slow dynamics and do not contribute to conductivity. The slow dynamics of cations that are partially coordinated by the chain backbone can be correlated with conformational transitions of PEO segments: those that are closer to the backbone are significantly slower due to steric crowding. Hence, the Li$^+$ complexed by the slower segments exhibits the lowest mobility. Therefore, while the comb-branched PEO-based electrolytes investigated so far did not show improved Li$^+$ conductivity, they provided evidence of two promising trends: (1) the Li$^+$ that is not complexed by the backbone exhibits higher mobility than in the linear PEO electrolyte, indicating that the short side chains do promote inter-chain hopping, and (2) the Li$^+$ mobility, at least for those cations not complexed by the polymer backbone, is largely independent of the backbone motion.
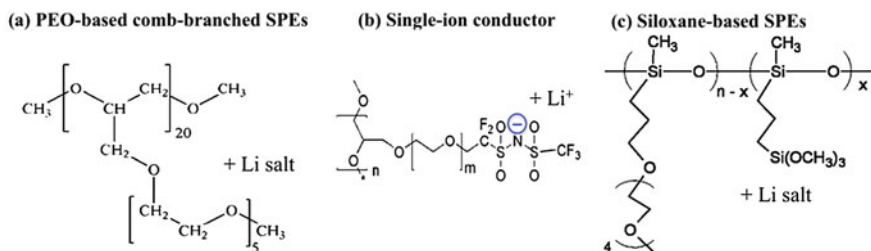
Fig. 11.3 Representative PEO-based polymer architectures considered for SPEs

One disadvantage of current PEO-based electrolytes is their low transference number due to relatively high anion mobility. Large-scale anion motion in comb-branch electrolyte can be eliminated by attaching the anions to the polymer (Fig. 11.3b), however, this has a deleterious effect on Li$^+$ mobility [52], because anions play an important role in the ability of Li$^+$ cations to undergo inter-chain jumps. While attaching the anion to the polymer has the advantage of improving transference number (all charge is carried by Li$^+$), further reducing the Li$^+$ mobility is a major disadvantage. Addition of a solvent/plasticizer [e.g., ethylene carbonate (EC)] to the single-ion conductor electrolytes showed dramatic improvement in ionic conductivity over the non-plasticized single-ion conductor. EC increases the rate of polymer conformational transitions, yet it is not directly involved in coordination and transport of Li$^+$ [53]. An experimental investigation [54] of a single-ion conductor made from blending PEO with a comb-branch polystyrene-based polyanion showed a low conductivity, but depending dramatically upon the polyanion structure. Such blending provides additional degrees of freedom in terms of composition and architecture design of polymer electrolyte [55].

Finally, there has been an interest in siloxane as a component for polymer electrolytes due to its conformational flexibility (and hence low glass transition temperature) and electrochemical stability. Because siloxane itself has limited ability to solvate Li$^+$, siloxane-based electrolytes contain ether groups for the purpose of solvating and transporting Li$^+$. Siloxane-ether oligomers [56–59] and comb-branch polymers with siloxane backbones and PEO side chains [60–63] (Fig. 11.3c) show indeed improved conductivity. However, these electrolytes do not exhibit adequate room temperature conductivity and mechanical stability for most applications.

11.2.3 Influence of Polymer Morphology

Microphase-separated copolymers consisting of PEO covalently linked to a different type polymer offer an attractive avenue to achieving both high ionic

conductivity and dimensional stability in polymer electrolytes [64]. Microphase-separated copolymers can also prevent the formation of semi-crystalline spherulites that reduce contact with electrodes [65]. It is important to note that added lithium salts modulate the degree of block segregation and can alter the resulting polymer organization and properties emanating from this [66, 67]. Copolymer electrolytes that provide nano-scale domains ion-rich and ion-lean can be advantageous [68]. The ion-rich domains play a primary role in ion transport and, to this end, the polymer segments localized there should be mobile, through appropriate polymer chemistry and architecture, or through heating and/or the introduction of plasticizers. The polymer segments of the ion-lean domains can be designed such that they contribute to the mechanical rigidity of the polymer electrolyte [69].

The conductivity of heterogeneous polymer electrolytes involves a pre-factor $f\,(\leq 1)$ that accounts for the tortuosity and connectivity of the conducting domains [68]. In the case of block copolymer electrolytes [69] with well-defined nano-scale morphologies [70], an ideal morphology factor, f_{ideal}, can be defined based on perfectly ordered lamellae, cylinders, etc. [68]. Experimentally determined f of heterogeneous polymer electrolytes relevant to Li-ion batteries is typically lower than f_{ideal} [67] indicating the importance of the resistance at grain boundaries, and associated with it, the importance of processing history [71, 72].

The effects of morphology on the ionic conductivities of polymer electrolytes are significant [69]. A polymer electrolyte membrane of a typical 100 μm thickness encompasses several micro-scale grains, each with well-defined nano-scale organization of the polymer, but each with different orientation. For intra-grain ion transport, the continuity and connectivity of the ion-conductive nano-scale domains are important, whereas for inter-grain ion transport, the connectivity of conducting channels across the boundary between adjacent grains is important. The mesoscopic and macroscopic orientation/alignment of nano-structured domains are outstanding issues in the field of microphase-separated polymers, but several methodologies have been found effective, such as thermal or solvent annealing, epitaxy, templating, stretching, shear alignment, application magnetic or electric fields, or combinations thereof [72–83].

While nano-scale polymer organization is driven by thermodynamics, meso-scale grain size and alignment are typically an outcome of processing, either deliberate or unintended consequence of sample preparation and testing [84]. An investigation of thermal history on the ionic conductivity of LiTFSI (lithium bis (trifluoromethanesulfonyl)imide, $LiN(SO_2CF_3)_2$)-doped PEO-PS (polystyrene) block copolymer electrolytes showed the conductivity of low MW samples to decrease after annealing, while the conductivity of high MW samples was unaffected. This was attributed to the development of well-defined nanostructure in the annealed samples [85]. A subsequent study on the dependence of ionic conductivity on the grain size of a lamellar PEO-PS block copolymer electrolyte showed well-formed lamellar grains to be less conducting than poorly defined, small grains [86]. Well-ordered solvent-cast films of polymerized ionic liquid block copolymers (single-ion conductors) exhibited up to an order of magnitude higher conductivity than poorly ordered melt-pressed films [87].

11.3   Composite Polymer Electrolytes

As nanoparticles are incorporated into a PEO + salt electrolyte to form a composite polymer electrolyte (CPE) [24, 25], the concentration of PEO crystalline domains can be reduced without harming the PEO chain flexibility. This is a main reason for the observed ionic conductivity enhancement in CPEs. Moreover, the cation transference number (t^+, fraction of the current carried by lithium ions) and the mechanical strength can be improved simultaneously over a wide temperature range. These effects of nanoparticles on polymer electrolytes are highlighted in this section.

11.3.1   Nanoparticle Effects on Conduction and Transference

The most critical requirement for the application of polymer electrolytes in lithium-ion batteries is the ionic conductivity. This is commonly described by the Vogel–Tamman–Fulcher (VTF) equation [25, 88, 89].

$$\sigma = AT^{-1/2} \exp[-E_a/(T - T_0)] \tag{11.1}$$

The conductivity variation with inverse temperature for the CPEs PEO (4×10^6 g/mol)–LiTf (lithium trifluoromethanesulfonate or lithium triflate, LiCF$_3$SO$_3$, EO: Li$^+$ = 9)–x wt% TiO$_2$ (x = 0, 5, 10, 15 and 20) is shown in Fig. 11.4. Only the 5 wt% sample behaves differently compared to the typical VTF behavior of other electrolytes. Specifically, the conductivity increases faster at temperatures $T > 80$ °C due to the increased mobility of ions via Lewis acid–base interaction. The sample with 10 wt% TiO$_2$ exhibited the optimal ionic conductivity among those studied. Further addition of nanoparticles (20 wt%) led to a drop in conductivity because of nanoparticle agglomeration that hindered ion transport [90].

In addition to their effect on ionic conductivity, nanoparticles also affect the transference number (t^+) of CPEs. t^+ directly describes the charge transport and thus the current of a specific ion [91]. Specifically, t^+ indicates the fraction of the current that is carried by the cation (Li$^+$) in the electrolytes. It is desirable to achieve a high t^+ value in order to enhance the electrode reaction kinetics and to eliminate the concentration gradients within the battery so that the internal voltage drop could be lowered and the output current increased [92]. t^+ is most commonly calculated by Eq. (11.2) [93, 94].

$$t^+ = \frac{\mu^+}{\mu^+ + \mu^-} = \frac{D^+}{D^+ + D^-} \tag{11.2}$$

Fig. 11.4 Variation of
conductivity with inverse
temperature on the heating
run for composite polymer
electrolytes incorporating
TiO_2 ceramic powder; PEO
(4×10^6 g/mol)–LiTf (EO:
$Li^+ = 9$)–x wt% TiO_2 ($x = 0$,
5, 10, 15 and 20)
(Reproduced from Ref. [90]
with kind permission of ©
2014 Elsevier)
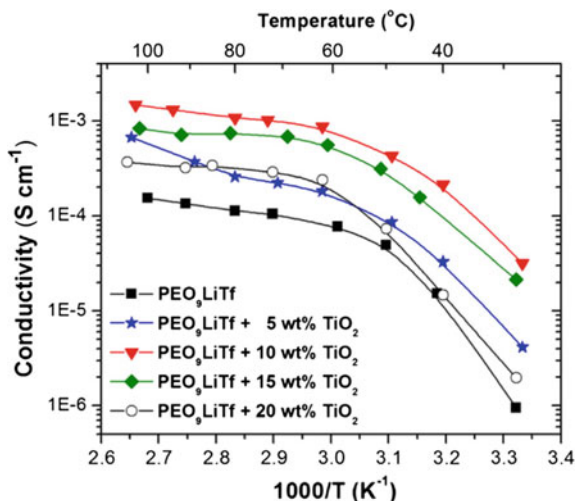
In Eq. (11.2), D^+ and D^- are the cation and anion self-diffusion coefficients; μ^+ and μ^- are the mobility [95, 96] of the cation and anion, respectively.

High lithium transference number (t_{Li}^+) at ambient temperature contributes to efficient battery performance [97, 98]. In view of the importance of t^+, the effect of additive surface functional sites on the transference number (t^+) is discussed here. For the system PEO–$LiCF_3SO_3$ (EO:Li^+ = 20)–10 wt% Al_2O_3 (basic, neutral, or acidic, d = 5.8 nm), the transference number t^+ increased in the sequence of updoped (t^+ = 0.46) < basic Al_2O_3 (t^+ = 0.48) < neutral Al_2O_3 (t^+ = 0.54) < acidic Al_2O_3 (t^+ = 0.63) [99]. As for an explanation, the hydrogens of acidic ceramic surfaces (Lewis acid) form hydrogen bonds with the lithium salt anions and the ether oxygens (Lewis base) [99], which promote salt dissociation and also decrease the PEO crystallinity [98, 99]. In this way, t^+ increased. As for the neutral and basic Al_2O_3, the number of Lewis acid sites decreased, leading to a weaker increase in t^+. This discussion would be more interesting if the number of acidic sites on the surface could be quantified in combination with oxygen vacancy analysis. The efficiency of acidic sites on the t^+ increase would thus be revealed.

We discuss above factors affecting the lithium transference number t^+. But how is t^+ related to conductivity? Conductivity and t_{Li}^+ results have been compared for CPEs, with the additive being ionically active or inert SiO_2 particles (active SiO_2 was mesoporous silica MCM-41 absorbing plasticizers of ethylene carbonate (EC)/ propylene carbonate; inert SiO_2 was mesoporous silica MCM-41 without plasticizers). For PEO (300,000 g/mol)–$LiClO_4$ (EO:Li^+ = 16)–SiO_2 (1000 m^2 g^{-1}), the conductivity initially increased upon addition of active SiO_2, attained a maximum value of about 2.4×10^{-5} S cm^{-1} at 10 wt% active SBA-15 (even though the free Li ion percentage was optimized at 5 wt%), followed by a mild decline with further loading of active SBA-15 [92]. In parallel, the transference number t^+ increased from 0.42 for the undoped sample, reached a maximum value of 0.54 at 10 wt%

active SBA-15, followed by a drastic decline with further loading of active SBA-15 (Fig. 11.5). As for the reasons, the –OH groups on the surface of SBA-15 compete with Li^+ (both as Lewis acid) to interact with ether oxygens and ClO_4^- (both as Lewis base) to promote Li^+ transport and thus enhance t^+. When the additive content exceeded 10 wt%, nanoparticle aggregation drastically impaired the Li^+ transference number.

In another study, mSBA-15 (silane-functionalized silica of SBA-15, 1000 m^2 g^{-1}) was added into PEO (300,000 g/mol)–LiClO$_4$ (EO:Li$^+$ = 16). The ionic conductivity (σ) and t^+ presented a similar increasing trend and achieved their peak values simultaneously at a level of 5 wt% doping. This mSBA-15 additive has been proposed to promote lithium salt dissociation and produce more free lithium ion, and to lower the activation for ion transport [100]. Following the peak values, σ decreased gradually and t^+ decreased steeper upon further nanoparticle addition.

11.3.2 Nanoparticle Effects on Mechanical Properties

Polymer electrolytes are promising to avoid drawbacks of the liquid-state electrolytes and help to expand the operating conditions, even in harsh conditions, e.g., high temperature. However, the mechanical strength of neat PEO is not satisfactory, especially at a high working temperature due to its low-melting temperature 66–75 °C. The binary systems of PEO with lithium salt do not exhibit an obvious improvement of mechanical strength despite the transient crosslinks [101] formed between lithium ions and ether oxygens. Thus, the mechanical properties of polymer electrolytes with nano-additives became of interest. In this section, we discuss how nanoparticles can improve CPE mechanical properties such as tensile strength, yield strength, elastic and viscous modulus.

Silane (KH550)-modified silica was added for simultaneous enhancement of the ionic conductivity and mechanical strength of PEO (MW = 300,000 g/mol)–


Fig. 11.5 Ionic conductivity σ and lithium transference number t^+ as a function of **a** active SBA-15 and **b** inert SBA-15 content for PEO (300,000 g/mol)–LiClO$_4$–SiO$_2$ (1000 m^2 g^{-1}) CPE at 25 °C. *Solid lines* correspond to the Y axis on the *left*. The *dashed line* corresponds to the Y axis on the *right* (Data from Wang et al. Ref. [92])
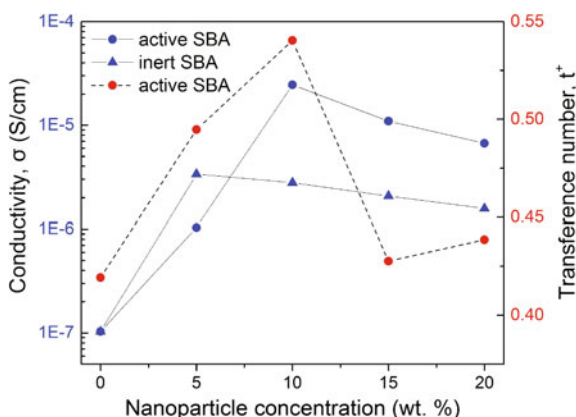
LiClO$_4$ (EO:Li$^+$ = 16) [102]. Less than 10 wt% nanoparticles caused the formation of an amorphous interface region around the nanoparticles and an increase in the polymer amorphous fraction [103], which led to an increase of the ionic conductivity as shown in Fig. 11.6. Further addition (>10 wt%) of nanoparticles led to agglomeration that impaired the ionic conductivity. In contrast, the CPE tensile strength kept increasing upon addition of nanoparticles to 15 wt% [102].

In another study, the tensile modulus and yield strength of PEO (300,000 g/mol)–LiClO$_4$–(mSBA-15: silane-functionalized mesoporous silica) increased with increasing mSBA-15 amount in the 0–15 wt% range [100]. This enhancement is due to the addition of ceramic fillers which acted as crosslinking media inside the polymer matrix by their surface interactions [104]. However, the enhancement was not always monotonic. For PEO (100,000 g/mol)–LiClO$_4$–(montmorillonite–CNT), the optimized tensile strength was achieved upon 5 wt% clay–CNT incorporation into the hybrid. The tensile strength increased by 160% compared to the PEO electrolyte [105]. This reinforcement has been ascribed to the large aspect ratio and surface roughness of the clay–CNT hybrid filler, which lead to strong interactions between nano-fillers and polymer [105]. The different surface roughness may also explain the difference in the optimal nano-additive amount for maximized tensile strength between these two systems. In combination with the knowledge that the maximum conductivity occurred at 10 wt% nano-additive [92, 106, 107], the incorporation of 10 wt% nano-additive appears to offer an optimal combination of improved mechanical properties as well as optimized ion conductivity. Very likely, a CPE composition involving around 10 wt% additive would also correspond to minimized T_g, T_m, and crystallinity. Of course, the surface conditions, e.g., roughness, functionalization, and possible surface defects of the nanoparticle additives may cause the final result to deviate.

Fig. 11.6 Ionic conductivity and tensile strength for PEO (MW = 300,000 g/mol)–LiClO$_4$ (EO:Li$^+$ = 16) with various contents of SiO$_2$ and KH550-modified SiO$_2$ (mSiO$_2$) at 30 °C. *Solid lines* correspond to the *Y* axis on the *left*. *Dashed lines* correspond to the *Y* axis on the *right* (Data from Fan et al. [102])
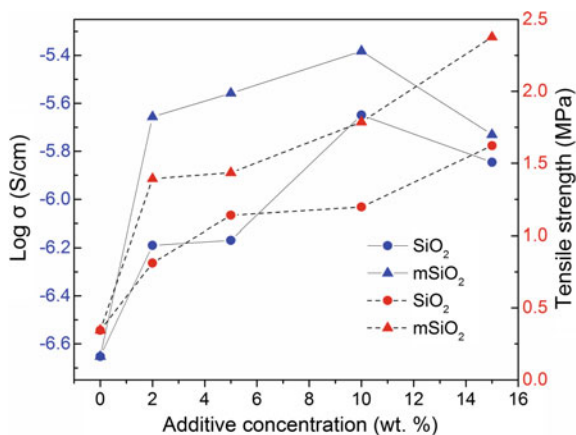
11.4   Ternary Polymer Electrolytes

With an aim to further improve the CPE performance, Sect. 11.3 discusses the silica
nanoparticle modification by plasticizers treatment or by silane compound to tune
the interactions between polymer, nanoparticles, and Li^+ ions (the notion of tuning
interactions also applies to the physical modification of CPEs that is discussed in
Sect. 11.4). The compatibility of nanoparticles with the polymer matrix can be
improved in this way. We discuss here pseudo-ternary systems consisting of
polymer, salt, and surface-modified nanoparticles. Typical methods of nanoparticle
chemical modification with polymers and ionic liquids are addressed in
Sects. 11.4.1 and 11.4.2, respectively.

11.4.1   Polymer-Functionalized Nanoparticles

In order to improve the compatibility of nanoparticles with the polymer matrix for a
better performance of CPEs, surface grafting of nanoparticles with oligomers (short
chain polymers) that share the same repeating unit as the polymer matrix has been
actively investigated. One example involves polyhedral oligomeric silsesquioxane
(POSS) nanoparticles functionalized by poly(ethylene glycol) (PEG) [108, 109],
and another example concerns silica functionalized by PEO [110]. POSS is an
organic–inorganic hybrid compound typically formed by inorganic cubic core
(siloxane cage) and outer organic groups (pendant arms), with a general formula of
$(RSiO_{1.5})_{n\,=\,6,\,8,\,or\,10}$ [111]. POSS are of interest for their broad applications [73,
83], inlcuding in connection to CPEs [112–115].

Different ways of POSS [116–118] application in combination with
ion-conductive polymers (e.g., PEO) for electrolytes in lithium-ion batteries have
been reported [73, 108, 109, 111–118]. In the first case, the outer organic groups of
POSS are ion-conductive PEO chains, and the organic–inorganic hybrid compound
(generally denoted as POSS–PEO) itself acts as an electrolyte with the grafted PEO
serving as conducting media. In this case, the POSS–PEO is the matrix. In the
second case, POSS–PEO can also be used as an additive for binary PEO + salt
polymer electrolytes; with the help of grafted PEO chains, compatibility with the
PEO matrix can be improved. A comparison of these two cases is presented next.

For the first case of POSS–R as matrix, POSS–PEO_8 ($n = 4$, where n denotes the
number of PEO-repeating units attached to POSS, while the subscript 8 of PEO
denotes octa-functionalization on POSS) and PEO 600 K were compared as ion
conduction medium upon addition of $LiClO_4$ at a fixed amount of EO:Li^+ = 12. As
shown in Fig. 11.7a, the POSS–PEO_8 ($n = 4$)-based electrolyte exhibited higher
conductivity than that of PEO (600 K)-based electrolyte over the whole temperature
range. In contrast, in Fig. 11.7b, PEO (600 K)–$LiClO_4$ (O/Li = 12:1) exhibited an
abrupt conductivity change [108] at the PEO-melting temperature of around 327 K.
At low temperatures ($T < T_m$), neat POSS–PEO_8 ($n = 4$, O/Li = 12:1) presented a
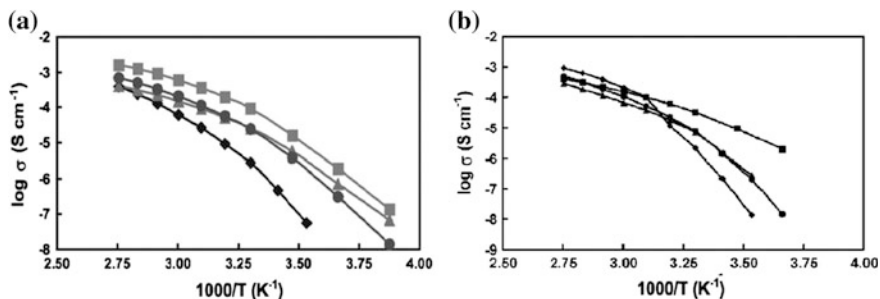
Fig. 11.7 **a** Conductivities of (i) POSS–PEO ($n = 3$)$_8$ (*filled triangle*); (ii) POSS–PEO ($n = <8>$)$_8$ (*filled circle*); (iii) PEGDME (MW = 500 g/mol) (*filled square*); and PEO (MW = 600 K) (*filled diamond*). All samples are prepared using LiClO$_4$ with O/Li = 8:1. Reproduced from Ref. [109] with kind permission of © 2006 The Electrochemical Society; **b** conductivity plots of (i) POSS–PEO$_8$ ($n = 4$) (*filled square*); (ii) PEO (MW = 600 K) (*filled diamond*); (iii) blend of 50 wt% POSS–PEO$_8$ ($n = 4$) with 50% PEO (600 K) (*filled triangle*); and (iv) blend of 60 wt% POSS–PEO($n = 4$)$_8$ with 40 wt% PEO (600 K) (*filled circle*); all samples are prepared using LiClO$_4$ with O/Li = 12:1 (Reproduced from Ref. [108] with kind permission of © 2007 American Chemical Society)

higher conductivity than that of PEO (600 K)–LiClO$_4$ (O/Li = 12:1) because of the low viscosity of POSS–PEO$_8$ and the crystallization of PEO. At high temperatures ($T > T_m$), it is the opposite case because of the inert SiO$_{1.5}$ core of POSS–PEO.

For the second case of POSS–R as additive, at low temperatures, the mixture of POSS–PEO$_8$ ($n = 4$) /PEO (600 K) exhibited a conductivity between that of POSS–PEO$_8$ ($n = 4$)- and PEO (600 K)-based electrolytes. This was attributed to the crystallinity decrease by addition of POSS–PEO$_8$ into PEO (600 K); at high temperatures, the mixture of POSS–PEO$_8$ ($n = 4$) /PEO (600 K) exhibited lower conductivity than PEO (600 K)–LiClO$_4$ (O/Li = 12:1) because of the presence of the inert SiO$_{1.5}$ core [108].

Fumed silica (FS) ($d = 12$ nm, surface area = 200 m^2/g) functionalized by non-polar alkyl moieties (FS-C$_8$) or by polar PEO oligomers with MW = 200 g/mol (FS-C3EG3ME) has been used in oligomer-based electrolytes with two different lithium salts, respectively: polyethylene glycol dimethyl ether (PEGDME, Mw = 250 g/mol)–LiN(CF$_3$SO$_3$)$_2$/LiCF$_3$SO$_3$ (Li:O = 1:20) [110]. The conductivity was not improved but rather dropped marginally with the addition of fumed silica at a doping amount of 10 and 20 wt%. FS-C3EG3ME even brought down the conductivity to a larger extent compared to FC-C8. High conductivities of over 10^{-3} S/cm at the 295–400 K temperature range were reported [110]. This high conductivity was attributed to the low molecular weight matrix of PEGDME with MW = 250 g/mol. In this case of low molecular weight oligomer electrolyte, the conductivity benefited from the liquid state of the matrix, while the addition of nanoparticles increased the viscosity to impair the ionic conductivity to some degree. This is opposite to the nanoparticle effect in SPEs to improve ion conduction. However, when it comes to a solid polymer matrix, it is possible that

FC-C3EG3ME would act more effectively to facilitate ion transport for its lithium ion coordination sites of EO units [114, 117]. Therefore, the incorporation of these differently grafted fumed silica into solid polymer electrolytes awaits to be investigated for comparison.

Other studies of polymer-functionalized nanoparticles include silica grafted with: [119] (1) homopolymer of poly(ethylene glycol) methyl ether methacrylate (PEGMA) of different molecular weight, or (2) poly(ethylene glycol) methyl ether methacrylate (PEGMA) copolymer, as additive for matrix of poly(ethylene glycol) dimethyl ether (PEGDME, Mw = 500 g/mol)–LiI/I_2 (EO:Li = 10:1). This system was reported to achieve room temperature conductivity 10^{-4} S/cm, but this result was around a threefold decrease from the undoped binary samples [119]. Thus, it can be concluded that the effectiveness of modified nanoparticle on properties of CPEs differs depending on the liquid or solid state of the polymer matrix, and it is not always the case that chemically functionalized nanoparticles can help improve the performance of the electrolytes. Similar work has been published, e.g., PEO-grafted silica was used in the matrix of PEO/sulfoisophthalate ionomers to improve the room temperature ionic conductivity by an order of magnitude [120].

11.4.2 Ionic Liquid-Modified Nanoparticles

In addition to PEO oligomer grafting on POSS surfaces, ionic liquids have also been introduced for nanoparticle chemical functionalization. The application of ionic liquids in polymer electrolytes has been motivated by their good chemical and electrochemical stability, low flammability, and negligible vapor pressure [18, 121–126]. Researchers then considered nanoparticles and ionic liquids chemically combined together as additives for CPEs. For example, studies have been reported on 1-methyl-3-[(triethoxysilyl)propyl]imidazolium chloride (TMICl) tethered to TiO_2 nanoparticles (20 nm in size) used in electrolytes for dye-sensitized solar cells (DSSC) [127], and on 1-undecyltrimethoxysilane-3-butyl imidazolium bis (trifluoromethylsulfonyl) imide tethered to ZrO_2 (average particle size 86 ± 2 nm) as hybrid electrolytes for lithium-ion batteries [128].

In a recent study, 1-methyl-3-propyl-imidazolium bromide ionic liquid attached on silica (MPIm-AS or AS-IL, size not given) was reported to improve the ionic conductivity of PEO (MW = 10^6 g/mol)/poly(ethylene imine) (PEI, MW = 1.2×10^5 g/mol)–LiClO$_4$ [129]. (PEO:PEI = 10:1, lithium salt, and nanoparticle amount not specified.) The novelties included: (1) physical mixing of PEI with PEO as polymer matrix, PEI itself providing alternative coordination sites to complex with lithium ions by its nitrogens on polymer chains; (2) blending with PEI makes the electrolyte formation easier due to its lower viscosity, and thus unnecessary to use plasticizers.

The impedance became much smaller upon the introduction of MPIm-AS, with the optimal content observed at 6 wt% and the corresponding conductivity at 9.1×10^{-5} S/cm as shown in Fig. 11.8 [129]. In contrast to the Sect. 11.3

Fig. 11.8 Ionic conductivity of poly(ethylene oxide) ($M_W = 10^6$ g/mol)/poly (ethylene imine) ($M_W = 1.2 \times 10^5$ g/mol)– $LiClO_4$ (PEO:PEI = 10:1) containing 0, 2, 4, 6, and 8 wt % of AS-IL at room temperature (Data from Kim et al. [129])
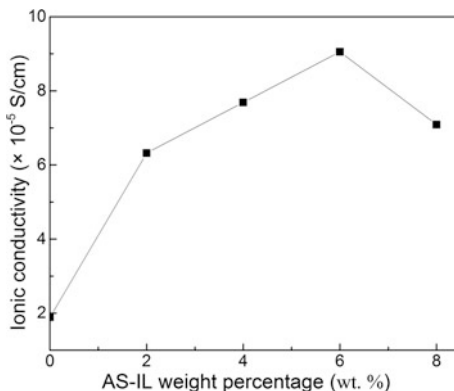
discussion of optimal doping at 10 wt%, [92, 106, 107], the optimal doping concentration of AS-IL is decreased in this case to 6 wt%. The difference may be due to the different composition of the polymer matrix. The different electron-donating ability of oxygen and nitrogen led to a different solvating ability for the lithium ions and interactions with AS-IL [129]. When the amount of AS-IL exceeded 6 wt%, particle aggregation hindered the ion transport and decreased the ionic conductivity.

Decreasing melting temperature T_m and heat of fusion ΔH_m values are reported in Table 11.1. It is worth noting that the optimal conductivity point, at 6 wt% MPIm-AS, is not the point of lowest PEO crystallinity. This was explained by a greater amount of additive that aggregated and impaired the ion transport within the matrix [129].

Another report of this type concerns 1-methylimidazole chloride (ImCl) ionic liquid-tethered TiO_2 (size not provided) as additives for plasticized polymer electrolytes: PEO (Mw = 10^6 g/mol) /PMMA (Mw = 1.2×10^5 g/mol)–$LiClO_4$– propylene carbonate–(3–12 wt%) IL-TiO_2 [130]. This study also followed the idea of "tuning the recipe" for CPEs by blending polymers as co-matrix, and also by the addition of plasticizer. The maximum conductivity was 1.05×10^{-4} S/cm at 9 wt% IL-TiO_2 [130]. Further addition of IL-TiO_2 led to conductivity drop due to immiscibility or aggregation of IL-TiO_2. For this type of IL-tethered nanoparticles, the topic of how the two counterparts, i.e., ionic liquid and nanoparticle, work in tandem with the CPEs remains of interest to this field.

To sum up Sect. 11.4, chemical modification of ternary CPEs is seeking to improve the compatibility of nanoparticles with the polymer matrix or to improve the "solubility" of the nano-additives in the polymer matrix. One common method is to graft functional groups onto the nanoparticle surface to interact with ether oxygens of the PEO matrix. Following the chemical modification of the nanoparticles, pre-existing Lewis acid–base interactions have been disturbed. The optimum doping (for optimal ionic conductivity) is no longer the typical 10 wt% for untreated nanoparticles [92, 106, 107]. For different studies, either the polymer matrix can accommodate more nanoparticles [108, 109] for a higher performance, or a smaller amount of nanoparticle doping [129] can function as well as the

Table 11.1 Melting point (T_m), melting enthalpy (ΔH) and crystallinity (χ_c) of for poly (ethylene oxide) (MW = 10^6 g/mol)/poly(ethylene imine) (MW = 1.2×10^5 g/mol)–LiClO$_4$ (PEO: PEI = 10:1) CPEs containing 0, 2, 4, 6 and 8 wt% AS-IL [129]

Content of AS-IL	T_m (°C)	ΔH_m (J/g)	χ_c (%)
a (0 wt%)	60.67	32.1	46.5
b (2 wt%)	55.23	31.7	45.8
c (4 wt%)	53.66	28.7	41.5
d (6 wt%)	51.89	27.8	40.2
e (8 wt%)	46.29	27.2	39.6

unmodified ternary CPEs. Moreover, in CPE studies with modified nanoparticles, the observation that "the sample with nanoparticle doping amount for lowest crystallinity point did not exhibit highest conductivity" [129] has not been thoroughly explained, even though the ion transport is believed to be facilitated in the amorphous state of the polymer matrix.

11.5 Quaternary Polymer Electrolytes

After the discussion in Sect. 11.4 concerning chemically modified nanoparticles in CPEs, we discuss here an alternative for CPE formulation, which is the physical addition of a fourth component in order to improve the performance. The advantages of this approach are the vast choice of co-additives and its ease of implementation (blending as opposed to organic/inorganic chemistry). We discuss here pseudo-quaternary systems consisting of polymer, salt, nanoparticles, and solvent. Two typical classes of the fourth CPE component are organic solvents as plasticizers and ionic liquids. These are highlighted in Sects. 11.5.1 and 11.5.2, respectively.

11.5.1 Organic Solvent Additives

Organic solvent-based electrolytes have been traditionally employed to obtain a high ionic conductivity such as 10^{-2} S/cm [16, 131, 132]. Organic solvents have also been added to polymer electrolytes to produce gel polymer electrolytes (GPE) [133–135]. Given the organic solvent contribution to a high conductivity, organic solvents have been employed as co-additives together with nanoparticles in CPEs. This is a popular approach due to a wide range of additive choices. Selected examples of such quaternary CPEs are discussed in this section.

Conductivity results of plasticized PEO–16 wt% LiCF$_3$SO$_3$–20 wt% EC incorporating 3–18 wt% of Al$_2$O$_3$ (d = 11.8 nm) [136] are shown in Fig. 11.9.

Fig. 11.9 Conductivity for PEO–LiCF$_3$SO$_3$–EC CPEs at different wt% Al$_2$O$_3$, and for PEO–LiCF$_3$SO$_3$–DBP CPEs as a function of MnO$_2$ content at room temperature (Data from Johan et al. [136, 137])
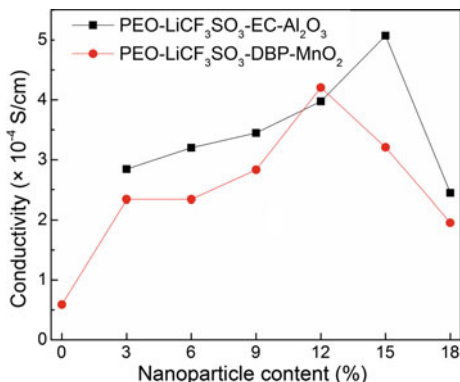
The addition of 15 wt% Al$_2$O$_3$ fillers maximized the ionic conductivity to 5.07×10^{-4} S/cm. For plasticized PEO (600,000 g/mol)–LiCF$_3$SO$_3$ (LiTf, Lithium triflate)–dibutyl phthalate (DBP) (20 wt%) incorporating MnO$_2$ ($d = 12$–15 nm), a maximum conductivity of 4.3×10^{-4} S/cm was achieved at 12 wt% MnO$_2$ [137]. Noticeably, the organic solvent-plasticized CPEs tend to accommodate more nanoparticles for optimized ionic conductivity.

The ionic conductivity of systems comprising PEO (4×10^6 g/mol)–LiCF$_3$SO$_3$ (EO:Li$^+$ = 9)–EC–Al$_2$O$_3$ (5.8 nm pore size, 150 mesh, neutral) is shown in Fig. 11.10 [138]. The observed conductivity enhancement originated from the structural modifications caused by the plasticizer and the nanoparticles. A sample consisting of PEO (4×10^6 g/mol)–LiCF$_3$SO$_3$ (EO:Li$^+$ = 9)–50 wt% EC–15 wt% Al$_2$O$_3$ (5.8 nm pore size, 150 mesh, neutral) exhibited the lowest T_g and T_m values together with the highest conductivity. However, in the case where EC was not added, the conductivity versus nanoparticle amount revealed that the highest conductivity occurred at 13 wt% Al$_2$O$_3$, which is lower than that at 15 wt% observed in the presence of EC. Compared to results from other ternary systems which usually present optimal conductivity at 10 wt% nanoparticle doping [92, 106, 107], the plasticized polymer electrolytes can accommodate higher amounts of nano-additives, with the assistance of organic solvent.

In parallel with the conductivity results, the thermal properties of polymer electrolytes incorporating co-additives reflect the conductivity trend to some extent, and thus can be employed to explain the conductivity changes. The T_g and T_m values for the binary PEO (4×10^6 g/mol)–LiCF$_3$SO$_3$ (Lithium triflate, LiTf, EO:Li$^+$ = 9) electrolytes were -44 and 58 °C, respectively [138]. Both T_g and T_m decreased with the addition of either Al$_2$O$_3$ filler or EC plasticizer. A quaternary system containing both nanoparticle and plasticizer further brought down both T_m and T_g as shown by samples 1–6 in Table 11.2 [138]. Follow-up work with TiO$_2$ (particle size not provided [90]) together with EC plasticizer added to the same binary system of PEO (4×10^6 g/mol)–Lithium triflate (LiTf) (EO:Li$^+$ = 9) exhibited a similar trend of T_m and T_g drop [90]. For samples 7–9 in Table 11.2, the activation energy (E_a) decreased from 120.6 to 78.8 kJ/mol with the addition of 10
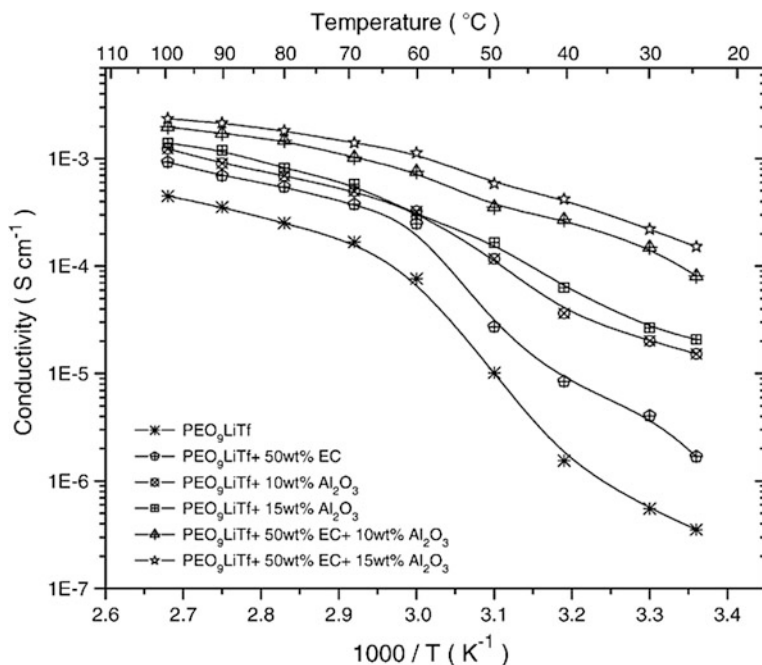
Fig. 11.10 Variation of the ionic conductivity with inverse temperature for the composite polymer electrolyte systems: PEO–LiTf, PEO–LiTf–50 wt% EC, PEO–LiTf–10 wt% Al_2O_3, PEO–LiTf–15 wt% Al_2O_3, PEO–LiTf–50 wt% EC–10 wt% Al_2O_3, PEO–LiTf–50 wt% EC–15 wt% Al_2O_3. EO:Li^+ = 9 for all samples (Reproduced from Ref. [138] with kind permission of © 2007 Elsevier)

wt% TiO_2, and further decreased to 57.5 kJ/mol with addition of both 10 wt% TiO_2 and 50 wt% EC at temperatures below 60 °C. This activation energy decrease suggested an improved mobility of ions within the polymer matrix, and hence increased conductivity. Whereas at temperatures above 60 °C, nearly equal E_a values were obtained for binary, ternary, and quaternary samples [138]. The conductivity increase could be explained by the improved ion mobility in the melted matrix above T_m, which overwhelmed the effect from added nanoparticles or plasticizer. For the plasticized CPE of PEO–LiTf (EO:Li^+ = 9)–50 wt% EC, addition of 15 wt% Al_2O_3 exhibited the lowest T_g and T_m (T_g decreased to −56 °C and T_m to 49 °C, respectively). The doping amount of 15 wt% differs from that reported to give optimal thermal property in ternary CPEs (without EC) at 10 wt% nanoparticles [92, 106, 107]. The difference originated from the plasticizing effect to accommodate more nanoparticles before aggregation would take place. As a result, the optimal content of nanoparticle doping increased from 10 to 15 wt%.

A similar trend was obtained for a system of the same components but with different formulation for optimal properties [136]. PEO (MW not provided)–16 wt% $LiCF_3SO_3$–20 wt% EC–15 wt% Al_2O_3 (d = 11.8 nm) gave the lowest T_g and T_m

Table 11.2 Crystallite melting temperatures (T_m), glass transition temperatures (T_g), and conductivity of different PEO (4×10^6 g/mol)–LiCF$_3$SO$_3$ (LiTf: Lithium triflate, EO:Li$^+$ = 9)–Al$_2$O$_3$/TiO$_2$ samples from [138] and [90]

Sample number	Polymer electrolyte	T_m (°C)	T_g (°C)	σ at 25 °C (Scm^{-1})
1	[a](PEO)$_9$LiTf	58	−44	3.5×10^{-7}
2	[a](PEO)$_9$LiTf–50 wt% EC[a]	57	−48	1.6×10^{-6}
3	[a](PEO)$_9$LiTf–10 wt% Al$_2$O$_3$	54	−49	1.5×10^{-5}
4	[a](PEO)$_9$LiTf–15 wt% Al$_2$O$_3$	51	−50	2.1×10^{-5}
5	[a](PEO)$_9$LiTf–50 wt% EC–10 wt% Al$_2$O$_3$	50	−53	8.2×10^{-5}
6	[a](PEO)$_9$LiTf–50 wt% EC–15 wt% Al$_2$O$_3$	49	−56	1.5×10^{-4}
7	[b](PEO)$_9$LiTf	64	−39	[c]1.4×10^{-6}
8	[b](PEO)$_9$LiTf–10 wt% TiO$_2$	60	−46	[c]4.9×10^{-5}
9	[b](PEO)$_9$LiTf–10 wt% TiO$_2$–50 wt% EC	50	−50	[c]1.6×10^{-4}

[a]Results from Pitawala's work [138]
[b]Results from Vignarooban's work [90]
[c]: σ at 30 °C

values, resulting from increased amorphous percentage and segmental flexibility caused by the EC plasticizer and the nano-filler [139–141]. However, the PEO (600,000 g/mol)–LiCF$_3$SO$_3$–dibutyl phthalate (DBP)–MnO$_2$ (12–15 nm) CPE exhibited a different change of T_g. As related to the polymer chain segmental movement, T_g increased marginally to −70 °C when MnO$_2$ was added to the plasticized system (T_g = −74 °C) and to the binary system (T_g = −71 °C).

From a comparison of these quaternary CPE systems with binary polymer + salt electrolytes and ternary CPE systems, we can see that for binary systems, T_g increased from neat PEO to binary PEO–Li$^+$ mixtures due to the transient crosslink formation between Li$^+$ and ether oxygens [98, 142, 143]. In ternary CPEs, nanoparticles tended to further decrease T_g, by different extent as different types of nanoparticles were used, while this is not always the case for quaternary systems. Organic solvent and nanoparticle co-additives make it more complicated to draw a general rule to predict property change upon additive incorporation. Further knowledge [144] on this promising direction would be desirable.

11.5.2 Ionic Liquid Additives

Ionic liquids have been extensively studied as additives for polymer electrolytes due to the unique properties of low-melting temperature and low vapor pressure [122, 145–147]. Reviews and research papers on ionic liquids as additives for polymer electrolytes have been published [148–151]. Here, we focus on physical co-doping of ionic liquids together with nanoparticles in CPEs.

Ternary systems of PEO–lithium bis (trifluoromethanesulfonyl) imide (LiTFSI, EO:Li$^+$ = 18)–10 wt%–nano-sized SiO$_2$ [152] and PEO–LiTFSI (EO:Li$^+$ = 18)–*N*-methyl-*N*-propylpiperidinium bis(trifluoromethanesulfonyl) imide (1.44 PP$_{13}$TFSI) have been reported [153]. In the discussion of quaternary systems of this subsection, nanoparticles and ionic liquids are doped together for the system of PEO (6 × 10^5 g/mol)–LiTFSI (EO:Li$^+$ = 18)–10 wt% SiO$_2$ (*d* = 50 nm)–PP$_{13}$TFSI (Li$^+$/PP$_{13}$$^+$ = 1:1.44) [154]. The conductivity exhibited an Arrhenius behavior as shown in Fig. 11.11. Conductivity enhancement in the melt state (*T* > *T*$_m$) by co-doping is not obvious, but at temperatures below the melting point (*T* < *T*$_m$), the enhancement is significant as explained by the activation energy decrease. From the Arrhenius plots of conductivity, with the addition to PEO$_{18}$LiTFSI of (1) nano-SiO$_2$, (2) PP$_{13}$TFSI, or (3) both nano-SiO$_2$ and PP$_{13}$TFSI, the activation energy (*E*$_a$) decreased from 115.3 kJ/mol for the binary PEO$_{18}$LiTFSI to (1) 105.0 kJ/mol, (2) 97.6 kJ/mol, and (3) 82.9 kJ/mol, respectively. The lower *E*$_a$ value implies a higher mobility of the lithium cations within the polymer matrix; the lowest *E*$_a$ and highest *σ* values were achieved by the co-doped sample at the low-temperature region. In contrast, in the high-temperature region, *E*$_a$ remained almost constant for all samples (35.1–37.2 kJ/mol) [154].

In closing Sect. 11.5, the physical modification of ternary CPEs can be summarized as "tuning the recipe" of binary polymer electrolytes (polymer + Li$^+$) by adding more ingredients to modulate interactions among nanoparticles, PEO (ether oxygens), and lithium ions within the system, and to affect properties such as crystallinity, glass transition temperature, and dielectric. The property changes favor an improvement of the ionic conductivity performance.

Fig. 11.11 Temperature dependence of the conductivity for PEO–LiTFSI, PEO–LiTFSI–SiO$_2$, PEO–LiTFSI–PP$_{13}$TFSI and PEO–LiTFSI–SiO$_2$–PP$_{13}$TFSI (EO:Li$^+$ = 18 for all samples) (Reproduced from Ref. [154] with kind permission of © 2011 Elsevier)
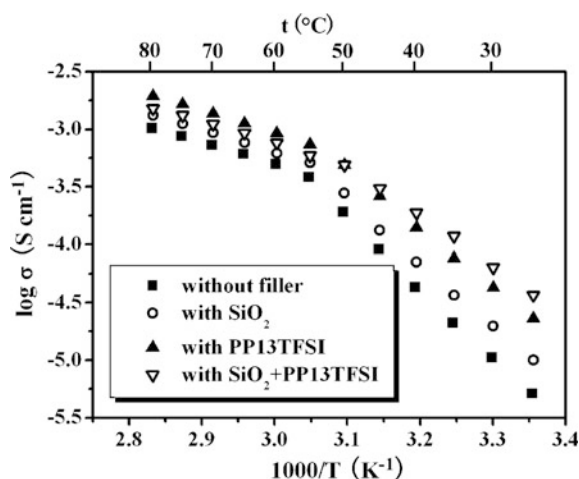
11.6   Summary and Outlook

Polymer electrolytes typically based on poly(ethylene oxide) and a lithium salt are being considered to improve the mechanical strength, thermal stability, and safety over traditional organic solvent-based electrolytes. The development of polymer electrolytes involves the simultaneous improvement of desirable properties for lithium-ion batteries.

For binary systems (polymer + lithium salt) [21], given the knowledge of Li$^+$ motion mechanism in PEO-based polymer electrolytes, controlling the polymer architecture and morphology are effective methods to improve the polymer electrolyte performance. However, it is difficult in binary polymer + salt systems to meet the performance required in practical applications. A breakthrough occurred when nano-additives were incorporated into binary systems for conductivity improvement [24–27]. This conductivity improvement can be explained by functions affected by nanoparticle: creating more amorphous domains, promoting lithium salt dissolution. Generally, samples with 5–12 wt% nanoparticle (depending on the type of additive and its surface, typically at 10 wt%) and molar ratio EO:Li$^+$ = 6–20 (typically at 8–10) yield the optimal ionic conductivity together with lowest degree of polymer crystallinity (χ_c), decreased glass transition temperature (T_g) and melting temperature (T_m), and improved mechanical strength [92, 103, 106, 155].

However, CPEs also suffer from possible nanoparticle agglomeration within the polymer matrix. This can limit the performance enhancement due to nanoparticles. The room temperature ionic conductivity, a critical performance indicator of ternary CPEs, remains below the desired level of 10^{-3} S/cm. In order to further improve the CPE performance, modified CPEs (PEO + salt +-modified nanoparticle and PEO + salt + nanoparticle + solvent) are being considered aiming to tune pre-existing interactions within polymer matrix.

Section 11.4 discusses nanoparticles that are chemically modified for an improved compatibility within CPEs. POSS–PEO$_8$ can be accommodated up to 30 wt% in high molecular weight polymer matrix due to the improved compatibility conferred by the PEO end groups. The conductivity improvement ranged from a few times in temperatures above T_m to almost two orders of magnitude in the low-temperature range. However, the conductivity dropped marginally when adding 10 and 20 wt% [110]. PEO–silica into PEGDME (200 g/mol) matrix due to the increased viscosity. Incorporation of PEO–silica in high molecular weight polymer electrolyte has not been reported yet; as for non-polymer modification of silica, the best conductivity that can be achieved in this case is a little higher than 10^{-5} S/cm at room temperature, which is less effective than that reported for the quaternary (polymer + salt + nanoparticle + solvent) polymer electrolytes discussed in Sect. 11.5.

Section 11.5 discusses the doping of CPEs with a fourth component in order to further modulate interactions. In the case of nanoparticle doping with an ionic liquid, the optimal room temperature conductivity can be in the range $10^{-4.5}$–10^{-4} S/cm. This approach did not always increase the conductivity over the whole temperature

range studied when compared to ternary systems of polymer + Li^+ + ionic liquid. In comparison, co-doping with nanoparticles and organic solvents for CPEs led to an obvious degree of crystallinity drop and marginal T_g and T_m decreases compared to ternary plasticized system (polymer + Li^+ + organic plasticizer). The conductivity enhancement is less than one order of magnitude (about 2–8 times) and presented an optimal conductivity a little lower than 10^{-4} S/cm at room temperature. It becomes apparent from the above that for quaternary polymer electrolytes, a level of 10^{-4} S/cm room temperature ionic conductivity is still difficult to achieve, and co-doping has shown limited contribution toward conductivity enhancement.

The research in CPEs is experiencing a bottleneck in that the highest ionic conductivity reported for solid-state CPEs just got close to 10^{-3} S/cm at room temperature [156–158], still not high enough to compete effectively with traditional organic solvent-based electrolytes. Future research in this field could fall into two broad directions. The first direction encompasses three-dimensional nano-scale ordered structure fabrication [105], such as ion tunnels [159] or ion paths [160], to facilitate ion conduction. Grafting side chains [161, 162] or a block of different chemistry [163–165] on the PEO polymer backbone can also be viewed as a nano-scale fabrication if further ordered structure can be obtained. The second direction is to adjust the CPE composition, with addition of certain other additives conferring special functions [90, 92, 137, 138, 166]. Sections 11.4 and 11.5 exemplify the current status of these two directions. The discussion in this chapter of various formulation strategies for electrolyte performance enhancement is intended to further stimulate the design of novel CPEs.

References

1. Scrosati B (1995) Battery technology-challenge of portable power. Nature 373(6515):557–558
2. Tarascon JM, Armand M (2001) Issues and challenges facing rechargeable lithium batteries. Nature 414(6861):359–367
3. Wakihara M (2001) Recent developments in lithium ion batteries. Mater Sci Eng, R 33 (4):109–134
4. Yoo HD, Markevich E, Salitra G et al (2014) On the challenge of developing advanced technologies for electrochemical energy storage and conversion. Mater Today 17(3):110–121
5. Winter M, Brodd RJ (2004) What are batteries, fuel cells, and supercapacitors. Chem Rev 104(10):4245–4269
6. Antunes RA, de Oliveira MCL, Ett G et al (2011) Carbon materials in composite bipolar plates for polymer electrolyte membrane fuel cells a review of the main challenges to improve electrical performance. J Power Sources 196(6):2945–2961
7. Frederick T, Wagner BL, Mathias MF (2010) Electrochemistry and the future of the automobile. J Phys Chem Lett 1:2204–2219

8. Simon P, Gogotsi Y (2008) Materials for electrochemical capacitors. Nat Mater 7(11):845–854

9. Nitta N, Wu F, Lee JT et al (2015) Li-ion battery materials: present and future. Mater Today 18(5):252–264

10. Palacin MR (2009) Recent advances in rechargeable battery materials: a chemist's perspective. Chem Soc Rev 38(9):2565–2575

11. Chen J, Cheng F (2009) Combination of lightweight elements and nanostructured materials for batteries. Acc Chem Res 42(6):713–723

12. Xu K (2014) Electrolytes and interphases in Li-ion batteries and beyond. Chem Rev 114(23):11503–11618

13. Scrosati B, Vincent CA (2000) Polymer electrolytes the key to lithium polymer batteries. MRS Bull 25(3):28–30

14. Kalhoff J, Eshetu GG, Bresser D et al (2015) Safer electrolytes for lithium-ion batteries: state of the art and perspectives. ChemSusChem 8(13):2154–2175

15. Cheng FY, Liang J, Tao ZL et al (2011) Functional materials for rechargeable batteries. Adv Mater 23(15):1695–1715

16. Xu K (2004) Nonaqueous liquid electrolytes for lithium-based rechargeable batteries. Chem Rev 104(10):4303–4417

17. Quartarone E, Mustarelli P (2011) Electrolytes for solid-state lithium rechargeable batteries: recent advances and perspectives. Chem Soc Rev 40(5):2525–2540

18. He Z, Alexandridis P (2017) Ionic liquid and nanoparticle hybrid systems: emerging applications. Adv Colloid Interface Sci. doi:10.1016/j.cis.2016.08.004

19. He ZQ, Alexandridis P (2015) Nanoparticles in ionic liquids: interactions and organization. Phys Chem Chem Phys 17(28):18238–18261

20. Berthier C, Gorecki W, Minier M et al (1983) Microscopic investigation of ionic-conductivity in alkali-metal salts poly(ethylene oxide) adducts. Solid State Ionics 11(1):91–95

21. Armand MB (1986) Polymer electrolytes. Annu Rev Mater Sci 16:245–261

22. Fenton DE, Parker JM, Wright PV (1973) Complexes of alkali-metal ions with poly(ethylene oxide). Polymer 14(11):589

23. Wang W, Alexandridis P (2016) Composite polymer electrolytes: nanoparticles affect polymers structure and properties. Polymers 8(11):387

24. Florjanczyk Z, Marcinek M, Wieczorek W et al (2004) Review of PEO based composite polymer electrolytes. Pol J Chem 78(9):1279–1304

25. Quartarone E, Mustarelli P, Magistris A (1998) PEO-based composite polymer electrolytes. Solid State Ionics 110(1–2):1–14

26. Jung S (2009) Fillers for solid-state polymer electrolytes. Bull Korean Chem Soc 30(10):2355–2361

27. Stephan AM, Nahm KS (2006) Review on composite polymer electrolytes for lithium batteries. Polymer 47(16):5952–5964

28. Baldwin RS, Bennett WR (2007) The NASA "PERS" program: solid polymer electrolyte development for advanced lithium-based batteries

29. Borodin O, Smith GD (2006) Mechanism of ion transport in amorphous poly(ethylene oxide)/LiTFSI from molecular dynamics simulations. Macromolecles 39(4):1620–1629

30. Borodin O, Smith GD (2007) Molecular dynamics simulations of comb-branched poly(epoxide ether)-based polymer electrolytes. Macromolecles 40(4):1252–1258

31. Borodin O, Smith GD, Bandyopadhyaya R et al (2004) Molecular dynamics study of nanocomposite polymer electrolyte based on poly(ethylene oxide)/LiBF$_4$. Modell Simul Mater Sci En 12(3):S73–S89

32. Brandell D, Priimägi P, Kasemägi H et al (2011) Branched polyethylene/poly(ethylene oxide) as a host matrix for Li-ion battery electrolytes a molecular dynamics study. Electrochim Acta 57:228–236

33. Ferreira B, Mullerplathe F, Bernardes A et al (2002) A comparison of Li$^+$ transport in dimethoxyethane, poly(ethylene oxide) and poly(tetramethylene oxide) by molecular dynamics simulations. Solid State Ionics 147(3–4):361–366

34. Hektor A, Klintenberg MK, Aabloo A et al (2002) Molecular dynamics simulation of the effect of a side chain on the dynamics of the amorphous LiPF$_6$–PEO system. J Mater Chem 13(2):214–218

35. Karo J, Brandell D (2009) A molecular dynamics study of the influence of side-chain length and spacing on lithium mobility in non-crystalline LiPF$_6$·PEO$_x$; x = 10 and 30. Solid State Ionics 180(23–25):1272–1284

36. Maitra A, Heuer A (2007) Understanding segmental dynamics in polymer electrolytes: a computer study. Macromol Chem Phys 208(19–20):2215–2221

37. Müller-Plathe F, van Gunsteren WF (1995) Computer simulation of a polymer electrolyte: lithium iodide in amorphous poly(ethylene oxide). J Chem Phys 103(11):4745–4756

38. Siqueira LJA, Ribeiro MCC (2005) Molecular dynamics simulation of the polymer electrolyte poly(ethylene oxide)/LiClO$_4$ structural properties. J Chem Phys 122(19):194911

39. Siqueira LJA, Ribeiro MCC (2006) Molecular dynamics simulation of the polymer electrolyte poly(ethylene oxide)/LiClO$_4$ II dynamical properties. J Chem Phys 125 (21):214903

40. Snyder J (2002) Polymer electrolytes and polyelectrolytes: Monte Carlo simulations of thermal effects on conduction. Solid State Ionics 147(3–4):249–257

41. Diddens D, Heuer A, Borodin O (2010) Understanding the lithium transport within a rouse-based model for a PEO/LiTFSI polymer electrolyte. Macromolecules 43(4):2028–2036

42. Sutjianto A, Curtiss LA (1998) Li$^+$-diglyme complexes: barriers to lithium cation migration. J Phys Chem A 102(6):968–974

43. Borodin O, Smith GD (2007) Li$^+$ transport mechanism in oligo(ethylene oxide)s compared to carbonates. J Solution Chem 36(6):803–813

44. Li Z, Smith GD, Bedrov D (2012) Li$^+$ Solvation and transport properties in ionic liquid/lithium salt mixtures: a molecular dynamics simulation study. J Phys Chem B 116 (42):12801–12809

45. Borodin O, Smith GD (2006) Development of many-body polarizable force fields for Li-battery applications. J Phys Chem B 110(12):6293–6299

46. Hayamizu K, Akiba E, Bando T et al (2002) H-1, Li-7, and F-19 nuclear magnetic resonance and ionic conductivity studies for liquid electrolytes composed of glymes and polyethyneg-lycol dimethyl ethers of CH$_3$O(CH$_2$CH$_2$O)$_n$CH$_3$ (n = 3–50) doped with LiN(SO$_2$CF$_3$)$_2$. J Chem Phys 117(12):5929–5939

47. Edman L, Ferry A, Orädd G (2002) Analysis of diffusion in a solid polymer electrolyte in the context of a phase-separated system. Phys Rev E 65(4):042803

48. Lascaud S (1994) Phase diagrams and conductivity behavior of poly(ethylene oxide)-molten salt rubbery electrolytes. Macromol 27(25):7469–7477

49. Voege A, Deimede V, Paloukis F et al (2014) Synthesis and properties of aromatic polyethers containing poly(ethylene oxide) side chains as polymer electrolytes for lithium ion batteries. Mater Chem Phys 148(1–2):57–66

50. Buriez O, Han YB, Hou J et al (2000) Performance limitations of polymer electrolytes based on ethylene oxide polymers. J Power Sources 89(2):149–155

51. Kerr JB, Sloop SE, Liu G et al (2002) From molecular models to system analysis for lithium battery electrolytes. J Power Sources 110(2):389–400

52. Smith GD, Borodin O (2012) Lithium battery electrolyte stability and performance from molecular modeling and simulations. In: Batteries for sustainability. Springer Science Business Media, New York, pp 195–237

53. Wu H, Wick CD (2010) Computational investigation on the role of plasticizers on ion conductivity in poly(ethylene oxide) LiTFSI electrolytes. Macromolecules 43(7):3502–3510

54. Meziane R, Bonnet JP, Courty M et al (2011) Single-ion polymer electrolytes based on a delocalized polyanion for lithium batteries. Electrochim Acta 57:14–19

55. Inceoglu S, Rojas AA, Devaux D et al (2014) Morphology-conductivity relationship of single-ion-conducting block copolymer electrolytes for lithium batteries. ACS Macro Letters 3(6):510–514
56. Amine K, Wang Q, Vissers DR et al (2006) Novel silane compounds as electrolyte solvents for Li-ion batteries. Electrochem Commun 8(3):429–433
57. Nakahara H, Tanaka M, Yoon S-Y et al (2006) Electrochemical and thermal stability of a siloxane-based electrolyte on a lithium transition metal oxide cathode. J Power Sources 160 (1):645–650
58. Zhang Z, Dong J, West R et al (2010) Oligo(ethylene glycol)-functionalized disiloxanes as electrolytes for lithium-ion batteries. J Power Sources 195(18):6062–6068
59. Rossi NAA, West R (2009) Silicon-containing liquid polymer electrolytes for application in lithium ion batteries. Polym Int 58(3):267–272
60. Karatas Y, Kaskhedikar N, Burjanadze M et al (2006) Synthesis of cross-linked comb polysiloxane for polymer electrolyte membranes. Macromol Chem Phys 207(4):419–425
61. Kunze M, Karatas Y, Wiemhöfer H-D et al (2010) Activation of transport and local dynamics in polysiloxane-based salt-in-polymer electrolytes: a multinuclear NMR study. Phys Chem Chem Phys 12(25):6844–6851
62. Zhang Z, Jin J, Bautista F et al (2004) Ion conductive characteristics of cross-linked network polysiloxane-based solid polymer electrolytes. Solid State Ionics 170(3–4):233–238
63. Zhang Z, Lyons LJ, West R et al (2007) Synthesis and ionic conductivity of mixed substituted polysiloxanes with oligoethyleneoxy and cyclic carbonate substituents. Silicon Chem 3(5):259–266
64. Ruzette AVG, Soo PP, Sadoway DR et al (2001) Melt-formable block copolymer electrolytes for lithium rechargeable batteries. J Electrochem Soc 148(6):A537–A543
65. Chen J, Frisbie CD, Bates FS (2009) Lithium perchlorate-doped poly(styrene-b-ethylene oxide-b-styrene) lamellae-forming triblock copolymer as high capacitance, smooth, thin film dielectric. J Phys Chem C 113(10):3903–3908
66. Gomez ED, Panday A, Feng EH et al (2009) Effect of ion distribution on conductivity of block copolymer electrolytes. Nano Lett 9(3):1212–1216
67. Young WS, Epps TH (2009) Salt doping in peo-containing block copolymers: counterion and concentration effects. Macromolecules 42(7):2672–2678
68. Hallinan DT, Balsara NP (2013) Polymer electrolytes. Annu Rev Mater Res 43(1):503–525
69. Young WS, Kuan WF, Epps TH (2014) Block copolymer electrolytes for rechargeable lithium batteries. J Polym Sci Pol Phys 52(1):1–16
70. Spontak RJ, Alexandridis P (1999) Advances in self-ordering macromolecules and nanostructure design. Curr Opin Colloid Interface Sci 4(2):140–146
71. Schmidt G, Richtering W, Lindner P et al (1998) Shear orientation of a hexagonal lyotropic triblock copolymer phase as probed by flow birefringence and small-angle light and neutron scattering. Macromolecules 31(7):2293–2298
72. Zipfel J, Berghausen J, Schmidt G et al (2002) Influence of shear on solvated amphiphilic block copolymers with lamellar morphology. Macromolecules 35(10):4064–4074
73. Ayandele E, Sarkar B, Alexandridis P (2012) Polyhedral oligomeric silsesquioxane (POSS)-containing polymer nanocomposites. Nanomaterials 2(4):445–475
74. Edwards EW, Stoykovich MP, Müller M et al (2005) Mechanism and kinetics of ordering in diblock copolymer thin films on chemically nanopatterned substrates. J Polym Sci Pol Phys 43(23):3444–3459
75. Golodnitsky D, Peled E (2000) Stretching-induced conductivity enhancement of LiI(PEO)-polymer electrolyte. Electrochim Acta 45(8–9):1431–1436
76. Hu H, Gopinadhan M, Osuji CO (2014) Directed self-assembly of block copolymers: a tutorial review of strategies for enabling nanotechnology with soft matter. Soft Matter 10(22):3867
77. Kim JK, Lee JI, Lee DH (2008) Self-assembled block copolymers: bulk to thin film. Macromol Res 16(4):267–292

78. Kovarsky R, Golodnitsky D, Peled E et al (2011) Conductivity enhancement induced by casting of polymer electrolytes under a magnetic field. Electrochim Acta 57:27–35

79. Majewski PW, Gopinadhan M, Jang W-S et al (2010) Anisotropic ionic conductivity in block copolymer membranes by magnetic field alignment. J Am Chem Soc 132(49):17516–17522

80. Marencic AP, Register RA (2010) Controlling order in block copolymer thin films for nanopatterning applications. Annu Rev Chem Biomol Eng 1(1):277–297

81. Tong Q, Sibener SJ (2014) Electric-field-induced control and switching of block copolymer domain orientations in nanoconfined channel architectures. J Phys Chem C 118(25):13752–13756

82. Li J, Kamata K, Komura M et al (2007) Anisotropic ion conductivity in liquid crystalline diblock copolymer membranes with perpendicularly oriented PEO cylindrical domains. Macromol 40(23):8125–8128

83. Sarkar B, Alexandridis P (2015) Block copolymer-nanoparticle composites: structure, functional properties, and processing. Prog Polym Sci 40:33–62

84. Young WS, Epps TH (2012) Ionic conductivities of block copolymer electrolytes with various conducting pathways: sample preparation and processing considerations. Macromol 45(11):4689–4697

85. Mullin SA, Teran AA, Yuan R et al (2013) Effect of thermal history on the ionic conductivity of block copolymer electrolytes. J Polym Sci Pol Phys 51(12):927–934

86. Chintapalli M, Chen XC, Thelen JL et al (2014) Effect of grain size on the ionic conductivity of a block copolymer electrolyte. Macromol 47(15):5424–5431

87. Weber RL, Ye Y, Schmitt AL et al (2011) Effect of nanoscale morphology on the conductivity of polymerized ionic liquid block copolymers. Macromolecules 44(14):5727–5735

88. Williams ML, Landel RF, Ferry JD (1955) The temperature dependence of relaxation mechanisms in amorphous polymers and other glass-forming liquids. J Am Chem Soc 77:3701–3707

89. Rietman EA, Kaplan ML, Cava RJ (1985) Lithium ion-poly (ethylene-oxide) complexes. 1. Effect of anion on conductivity. Solid State Ionics 17(1):67–73

90. Vignarooban K, Dissanayake MAKL, Albinsson I et al (2014) Effect of TiO_2 nano-filler and ec plasticizer on electrical and thermal properties of poly(ethylene oxide) (PEO) based solid polymer electrolytes. Solid State Ionics 266:25–28

91. Zugmann S, Gores H (2014) Transference numbers of ions in electrolytes. In: Kreysa G, Ota K-I, Savinell R (eds) Encyclopedia of applied electrochemistry. Springer, New York, pp 2086–2091

92. Wang XL, Mei A, Li M et al (2007) Polymer composite electrolytes containing ionically active mesoporous SiO_2 particles. J Appl Phys 102(5):054907

93. Gorecki W, Andreani R, Berthier C et al (1986) NMR, DSC, and conductivity study of a poly(ethylene oxide) complex electrolyte: $PEO(LiClO_4)_x$. Solid State Ionics 18–9:295–299

94. McLin MG, Angell CA (1996) Probe ion diffusivity measurements in salt-in-polymer electrolytes: stokes radii and the transport number problem. J Phys Chem 100(4):1181–1188

95. Abbrent S, Greenbaum S (2013) Recent progress in NMR spectroscopy of polymer electrolytes for lithium batteries. Curr Opin Colloid Interface Sci 18(3):228–244

96. Volkov VI, Marinin AA (2013) NMR methods for studying ion and molecular transport in polymer electrolytes. Russ Chem Rev 82(3):248–272

97. Golodnitsky D, Ardel G, Peled E (2002) Ion-transport phenomena in concentrated PEO-based composite polymer electrolytes. Solid State Ionics 147(1–2):141–155

98. Ciosek M, Sannier L, Siekierski M et al (2007) Ion transport phenomena in polymeric electrolytes. Electrochim Acta 53(4):1409–1416

99. Croce F, Persi L, Scrosati B et al (2001) Role of the ceramic fillers in enhancing the transport properties of composite polymer electrolytes. Electrochim Acta 46(16):2457–2461

100. Wang XL, Mei A, Li M et al (2006) Effect of silane-functionalized mesoporous silica SBA-15 on performance of PEO-based composite polymer electrolytes. Solid State Ionics 177(15–16):1287–1291
101. Bandara LRAK, Dissanayake MAKL, Furlani M et al (2000) Broad band dielectric behavior of plasticized PEO-based solid polymer electrolytes. Ionics 6(3–4):239–247
102. Fan L (2003) Effect of modified SiO_2 on the properties of PEO-based polymer electrolytes. Solid State Ionics 164(1–2):81–86
103. Croce F, Appetecchi GB, Persi L et al (1998) Nanocomposite polymer electrolytes for lithium batteries. Nature 394(6692):456–458
104. Appetecchi GB, Carewska M, Alessandrini F et al (2000) Characterization of PEO-based composite cathodes morphological thermal, mechanical, and electrical properties. J Electrochem Soc 147(2):451–459
105. Tang CY, Hackenberg K, Fu Q et al (2012) High ion conducting polymer nanocomposite electrolytes using hybrid nanofillers. Nano Lett 12(3):1152–1156
106. Karmakar A, Ghosh A (2011) Poly ethylene oxide (PEO)-LiI polymer electrolytes embedded with CdO nanoparticles. J Nanopart Res 13(7):2989–2996
107. Fan LZ, Dang ZM, Wei GD et al (2003) Effect of nanosized ZnO on the electrical properties of $(PEO)_{16}$-$LiClO_4$ electrolytes. Mater Sci Eng, B 99(1–3):340–343
108. Zhang HJ, Kulkarni S, Wunder SL (2007) Blends of POSS-PEO(n = 4)$_8$ and high molecular weight poly(ethylene oxide) as solid polymer electrolytes for lithium batteries. J Phys Chem B 111(14):3583–3590
109. Zhang HJ, Kulkarni S, Wunder SL (2006) Polyethylene glycol functionalized polyoctahedral silsesquioxanes as electrolytes for lithium batteries. J Electrochem Soc 153(2):A239–A248
110. Fan J, Raghavan SR, Yu XY et al (1998) Composite polymer electrolytes using surface-modified fumed silicas: conductivity and rheology. Solid State Ionics 111(1–2):117–123
111. Cordes DB, Lickiss PD, Rataboul F (2010) Recent developments in the chemistry of cubic polyhedral oligosilsesquioxanes. Chem Rev 110(4):2081–2173
112. Jung G-Y, Choi JH, Lee JK (2015) Thermal behavior and ion conductivity of polyethylene oxide/polyhedral oligomeric silsesquioxane nanocomposite electrolytes. Adv Polym Technol 34(3):21–49
113. Kim D-G, Shim J, Lee JH et al (2013) Preparation of solid-state composite electrolytes based on organic/inorganic hybrid star-shaped polymer and PEG-functionalized POSS for all-solid-state lithium battery applications. Polymer 54(21):5812–5820
114. Polu AR, Rhee H-W (2015) Nanocomposite solid polymer electrolytes based on poly (ethylene oxide)/POSS-PEG (n = 13.3) hybrid nanoparticles for lithium ion batteries. J Ind Eng Chem 31:323–329
115. Polu AR, Rhee H-W (2015) Effect of organic–inorganic hybrid nanoparticles (POSS–PEG (n = 4)) on thermal, mechanical, and electrical properties of PEO-based solid polymer electrolytes. Adv Polym Technol 00:21–58
116. Chinnam PR, Wunder SL (2013) Self-assembled Janus-like multi-ionic lithium salts form nano-structured solid polymer electrolytes with high ionic conductivity and Li^+ ion transference number. J Mater Chem A 1(5):1731–1739
117. Chinnam PR, Wunder SL (2011) Polyoctahedral silsesquioxane-nanoparticle electrolytes for lithium batteries: POSS-lithium salts and POSS-PEGs. Chem Mater 23(23):5111–5121
118. Chinnam PR, Zhang HJ, Wunder SL (2015) Blends of pegylated polyoctahedralsilsesquioxanes (POSS-PEG) and methyl cellulose as solid polymer electrolytes for lithium batteries. Electrochim Acta 170:191–201
119. Jia Z, Yuan W, Zhao H et al (2014) Composite electrolytes comprised of poly(ethylene oxide) and silica nanoparticles with grafted poly(ethylene oxide)-containing polymers. RSC Adv 4(77):41087–41098
120. O'Reilly MV, Winey KI (2015) Silica nanoparticles densely grafted with PEO for ionomer plasticization. RSC Adv 5(25):19570–19580

121. Wetjen M, Navarra MA, Panero S et al (2013) Composite poly(ethylene oxide) electrolytes plasticized by N-Alkyl-N-butylpyrrolidinium bis(trifluoromethanesulfonyl)imide for lithium batteries. ChemSusChem 6(6):1037–1043

122. Park MJ, Choi I, Hong J et al (2013) Polymer electrolytes integrated with ionic liquids for future electrochemical devices. J Appl Polym Sci 129(5):2363–2376

123. Ketabi S, Lian K (2013) Effect of SiO_2 on conductivity and structural properties of PEO-$EMIHSO_4$ polymer electrolyte and enabled solid electrochemical capacitors. Electrochim Acta 103:174–178

124. Chaurasia SK, Singh RK, Chandra S (2013) Ion-polymer complexation and ion-pair formation in a polymer electrolyte PEO:$LiPF_6$ containing an ionic liquid having same anion: a Raman study. Vib Spectrosc 68:190–195

125. Zhang SP, Lee KH, Sun JR et al (2011) Viscoelastic properties, ionic conductivity, and materials design considerations for poly(styrene-b-ethylene oxide-b-styrene)-based ion gel electrolytes. Macromol 44(22):8981–8989

126. Mecerreyes D (2011) Polymeric ionic liquids: broadening the properties and applications of polyelectrolytes. Prog Polym Sci 36(12):1629–1648

127. Chen XJ, Li Q, Zhao J et al (2012) Ionic liquid-tethered nanoparticle/poly(ionic liquid) electrolytes for quasi-solid-state dye-sensitized solar cells. J Power Sources 207:216–221

128. Moganty SS, Jayaprakash N, Nugent JL et al (2010) Ionic-liquid-tethered nanoparticles: hybrid electrolytes. Angew Chem Int Ed 49(48):9158–9161

129. Kim J, Park DW, Park SJ et al (2013) Ion conducting properties of poly(ethylene oxide)-based electrolytes incorporating amorphous silica attached with imidazolium salts. Res Chem Intermed 39(3):1409–1416

130. Lee L, Kim I-J, Yang S et al (2014) Filler effect of ionic liquid attached titanium oxide on conducting property of poly(ethylene oxide)/poly(methyl methacrylate) composite electrolytes. Am J Nanosci Nanotechnol 14(10):8010–8013

131. Beck F, Ruetschi P (2000) Rechargeable batteries with aqueous electrolytes. Electrochim Acta 45(15–16):2467–2482

132. Zhang SS (2007) A review on the separators of liquid electrolyte Li-ion batteries. J Power Sources 164(1):351–364

133. Croce F, Gerace F, Dautzemberg G et al (1994) Synthesis and characterization of highly conducting gel electrolytes. Electrochim Acta 39(14):2187–2194

134. Song JY (1999) Review of gel-type polymer electrolytes for lithium-ion batteries. J Power Sources 77(2):183–197

135. Soni SS, Fadadu KB, Gibaud A (2012) Ionic conductivity through thermoresponsive polymer gel: ordering matters. Langmuir 28(1):751–756

136. Johan MR, Shy OH, Ibrahim S et al (2011) Effects of Al_2O_3 nanofiller and ec plasticizer on the ionic conductivity enhancement of solid PEO-$LiCF_3SO_3$ solid polymer electrolyte. Solid State Ionics 196(1):41–47

137. Johan MR, Ting LM (2011) Structural, thermal and electrical properties of nano manganese-composite polymer electrolytes. Int J Electrochem Sci 6(10):4737–4748

138. Pitawala H, Dissanayake M, Seneviratne VA (2007) Combined effect of Al_2O_3 nano-fillers and EC plasticizer on ionic conductivity enhancement in the solid polymer electrolyte $(PEO)_9LiTF$. Solid State Ionics 178(13–14):885–888

139. Leo CJ, Rao GVS, Chowdari BVR (2002) Studies on plasticized PEO-Lithium Triflate-Ceramic filler composite electrolyte system. Solid State Ionics 148(1–2):159–171

140. Wang YJ, Pan Y, Wang L et al (2005) Conductivity studies of plasticized PEO-Lithium Chlorate-FIC filler composite polymer electrolytes. Mater Lett 59(24–25):3021–3026

141. Xi JY, Qiu XP, Ma XM et al (2005) Composite polymer electrolyte doped with mesoporous silica SBA-15 for lithium polymer battery. Solid State Ionics 176(13–14):1249–1260

142. Bruce PG, Vincent CA (1993) Polymer electrolytes. J Chem Soc Faraday T 89(17):3187–3203

143. Karan NK, Pradhan DK, Thomas R et al (2008) Solid polymer electrolytes based on polyethylene oxide and lithium trifluoro-methane sulfonate (PEO-LiCF$_3$SO$_3$): ionic conductivity and dielectric relaxation. Solid State Ionics 179(19–20):689–696

144. Mejia A, Garcia N, Guzman J et al (2014) Thermoplastic and solid-like electrolytes with liquid-like ionic conductivity based on poly(ethylene oxide) nanocomposites. Solid State Ionics 261:74–80

145. Shin JH, Henderson WA, Passerini S (2003) Ionic liquids to the rescue overcoming the ionic conductivity limitations of polymer electrolytes. Electrochem Commun 5(12):1016–1020

146. Shin JH, Henderson WA, Passerini S (2005) PEO-based polymer electrolytes with ionic liquids and their use in lithium Metal-Polymer electrolyte batteries. J Electrochem Soc 152 (5):A978–A983

147. Choi J, Cheruvally G, Kim Y et al (2007) Poly(ethylene oxide)-based polymer electrolyte incorporating room-temperature ionic liquid for lithium batteries. Solid State Ionics 178(19–20):1235–1241

148. Zhang RS, Chen YF, Montazami R (2015) Ionic liquid-doped gel polymer electrolyte for flexible lithium-ion polymer batteries. Mater 8(5):2735–2748

149. Zain NF, Zainal N, Mohamed NS (2015) The influences of ionic liquid to the properties of poly(ethylmethacrylate) based electrolyte. Phys Scripta 90(1):015702

150. Shalu, Singh VK, Singh RK (2015) Development of ion conducting polymer gel electrolyte membranes based on polymer PVdF-HFP, BMIMTFSI ionic liquid and the Li-salt with improved electrical, thermal and structural properties. J Mater Chem C 3(28):7305–7318

151. Shalu, Chaurasia SK, Singh RK et al (2015) Electrical, mechanical, structural, and thermal behaviors of polymeric gel electrolyte membranes of poly(vinylidene fluoride-co-hexafluoropropylene) with the ionic liquid 1-buty l-3-methylimidazolium tetrafluoroborate plus lithium tetrafluoroborate. J Appl Polym Sci 132(7):41456

152. Liu S, Imanishi N, Zhang T et al (2010) Effect of nano-silica filler in polymer electrolyte on Li dendrite formation in Li/Poly(ethylene oxide)-Li(CF$_3$SO$_2$)$_2$N/Li. J Power Sources 195 (19):6847–6853

153. Liu S, Imanishi N, Zhang T et al (2010) Lithium dendrite formation in Li/poly(ethylene oxide)-Lithium bis(trifluoromethanesulfonyl)imide and N-methyl-N-propylpiperidinium bis(trifluoromethanesulfonyl)imide/Li Cells. J Electrochem Soc 157(10):1092–1098

154. Liu S, Wang H, Imanishi N et al (2011) Effect of co-doping nano-silica filler and N-methyl-N-propylpiperidinium bis(trifluoromethanesulfonyl)imide into polymer electrolyte on Li dendrite formation in Li/Poly(ethylene oxide)-Li(CF$_3$SO$_2$)$_2$N/Li. J Power Sources 196 (18):7681–7686

155. Aihara Y, Appetecchi GB, Scrosati B et al (2002) Investigation of the ionic conduction mechanism of composite poly(ethyleneoxide) PEO-based polymer gel electrolytes including nano-size SiO$_2$. Phys Chem Chem Phys 4(14):3443–3447

156. Qi DJ, Ru HQ, Bi XG et al (2012) A novel PEO-based composite polymer electrolyte with NaAlOSiO molecular sieves powders. Ionics 18(3):267–273

157. Angulakshmi N, Kumar RS, Kulandainathan MA et al (2014) Composite polymer electrolytes encompassing metal organic frame works: a new strategy for all-solid-state lithium batteries. J Phys Chem C 118(42):24240–24247

158. Kumar RS, Raja M, Kulandainathan MA et al (2014) Metal organic framework-laden composite polymer electrolytes for efficient and durable all-solid-state-lithium batteries. RSC Adv 4(50):26171–26175

159. Gadjourova Z, Andreev YG, Tunstall DP et al (2001) Ionic conductivity in crystalline polymer electrolytes. Nature 412(6846):520–523

160. Wang Y, Li B, Ji J et al (2014) Controlled Li$^+$ conduction pathway to achieve enhanced ionic conductivity in polymer electrolytes. J Power Sources 247:452–459
161. Li H, Zhang H, Liang ZY et al (2014) Preparation and properties of poly (vinylidene fluoride)/poly(dimethylsiloxane) graft (poly(propylene oxide)-block-poly(ethylene oxide)) blend porous separators and corresponding electrolytes. Electrochim Acta 116:413–420
162. Jankowsky S, Hiller MM, Wiemhoefer HD (2014) Preparation and electrochemical performance of polyphosphazene based salt-in-polymer electrolyte membranes for lithium ion batteries. J Power Sources 253:256–262
163. Kwon S-J, Kim D-G, Shim J et al (2014) Preparation of organic/inorganic hybrid semi-interpenetrating network polymer electrolytes based on poly(ethylene oxide-co-ethylene carbonate) for all-solid-state lithium batteries at elevated temperatures. Polymer 55(12):2799–2808
164. Kuo P-L, Wu C-A, Lu C-Y et al (2014) High performance of transferring lithium ion for polyacrylonitrile-interpenetrating crosslinked polyoxyethylene network as gel polymer electrolyte. ACS Appl Mater Interface 6(5):3156–3162
165. Huang J, Wang RY, Tong ZZ et al (2014) Influence of ionic species on the microphase separation behavior of PCL-b-PEO/Salt hybrids. Macromol 47(23):8359–8367
166. Bodratti AM, Sarkar B, Alexandridis P (2017) Adsorption of poly(ethylene oxide)-containing amphiphilic polymers on solid–liquid interfaces: fundamentals and applications. Adv Colloid Interfac. doi:10.1016/j.cis.2016.09.003

Chapter 12
Polymer Nanocomposites Dielectrics for Energy Applications

Yang Shen, Xin Zhang, Yuanhua Lin and Ce-Wen Nan

Abstract Dielectric capacitors have been the major enabler for many applications in advanced electronic and electrical power systems due to their capability of ultrafast charging–discharging and ultrahigh power density. The low energy density of polymer dielectrics used in these capacitors could not meet the ever increasing demands for compact, reliable, and efficient electrical power systems. Polymer nanocomposites, in which high dielectric constant (k) nanofillers are incorporated in polymer matrix, have been actively pursued. In this chapter, we begin with two theoretical considerations for concomitantly increasing the dielectric permittivity and breakdown strength of nanocomposites, i.e., the critical interfacial polarization and distribution of local electric field. In the framework of these considerations, recent progresses based on two approaches, e.g., core–shell structured polymer nanocomposites and dielectric anisotropy, toward polymer nanocomposites of high energy density are reviewed. Novel composite design paradigm, such as nanocomposites with hierarchical interfaces and topological-structure modulated nanocomposites, for concomitant enhancement of dielectric permittivity and breakdown strength is also reviewed. In addition to energy density, thermal stability of nanocomposites is another critical parameter that dominates the reliability of nanocomposites at high temperatures. The advantages and promises of nanocomposite approach in raising the energy storage performance at temperatures are also considered.

12.1 Introduction

High power and high energy capacitor is one of the major enabling technologies for the development of commercial, consumer, and military systems with ever increasing demands for compact, reliable, and efficient electrical power systems [1].

Y. Shen (✉) · X. Zhang · Y. Lin · C.-W. Nan
School of Materials Science and Engineering,
Tsinghua University, Beijing 100084, China
e-mail: shyang_mse@tsinghua.edu.cn

The electrostatic capacitors offer the highest power density, lowest loss, and highest operating voltage compared to other types of capacitors such as electrolytic capacitors and supercapacitors. Examples of their important applications include high frequency inverters, IGBT snubbers, power factor correction, and pulsed power generation. However, the low energy density of these capacitors (<2 J/cm^3) leads to large capacitor volume and weight. For instance, DC bus capacitors in the power inverters of electrical vehicles can occupy $\sim 35\%$ of the inverter volume and $\sim 23\%$ of the converter weight [2]. Therefore, it is imperative to develop novel technologies that can significantly increase the energy density of the electrostatic capacitors.

An electrostatic capacitor consists of dielectric layers placed between metallic electrodes. According to thermodynamic relationships for dielectrics, when an electric field (E) is applied on the dielectric and induces an electric displacement D [3], the change of energy (U) is:

$$U = \int E dD = \int E d(\varepsilon_0 K \cdot E) \left(K = \frac{D}{E \varepsilon_0} \right) \qquad (12.1)$$

Here, $\varepsilon_0 = 8.85 \times 10^{-12}$ F/m is the vacuum permittivity and K is defined as the dielectric constant. As the electric field is increased (decreased), electrical energy is stored in (discharged from) the dielectric. The electric displacement is related to the polarization P by $D = P + \varepsilon_0 E$, hence high polarization leads to high displacement. For linear dielectrics where K is independent of E, Eq. (12.1) can be simplified into:

$$U = \frac{1}{2} \varepsilon_0 K E^2 = \frac{1}{2} DE \qquad (12.2)$$

For capacitors with large capacitance and high energy, polymers are generally preferred over inorganic materials as the dielectric. Large area, high quality polymer films can be produced using low cost, high throughput manufacturing methods. Moreover, the unique "self-healing" behavior in polymers ensures that a local dielectric breakdown on a large area capacitor film will lead to open circuit instead of short circuit at the spot of breakdown, thus avoiding the catastrophic failure of the entire system [4].

Currently, one of the most commonly used polymer capacitor film is the biaxially oriented polypropylene (BOPP) film. Polypropylene (PP) is a nonpolar semicrystalline polymer with the outstanding characteristics of high breakdown strength (>700 V/m), low dielectric loss ($<0.02\%$), nearly temperature- and frequency-independent dielectric constant, good mechanical strength, and reliable self-healing capability [5].

The major drawback of PP is its low dielectric constant ($K = 2.2$), resulting in an "intrinsic" energy density of about 6 J/m3 (at 800 MV/m). The energy density of packaged capacitors is significantly lower because of the derating of electric field needed to ensure reliable long-term operation, and the volume occupied by packaging materials. In spite of significant effort, it is proven very difficult to improve the

energy density of BOPP film capacitors beyond 2 J/cm^3 for long operation lifetime. In order to increase the energy density of electrostatic capacitors, novel polymer dielectric with dramatically improved energy density than PP is critically needed.

In parallel to the development of high energy density polymers, tremendous efforts have also been made in preparing polymer composites filled with inorganic nanoparticles, especially 0–3 composites, in which particles (zero dimension, usually ceramic particles of high dielectric constants) are embedded in three-dimensionally connected polymer matrix [6]. The major drawback of polymers dielectrics is their low dielectric permittivity, hence small electrical displacement (D), which results in low energy density albeit the ultrahigh breakdown strength. The rationale of these 0–3 composites thus lies in their potential of combining the high breakdown strength and low dielectric loss of the polymer with ceramic fillers of high dielectric constant, representing a promising approach to realize high energy density.

The benefits of this approach are twofold: (i) The enormous interfaces inside the 0–3 polymer composites could promote interfacial exchange coupling through a dipolar interface layer and lead to enhanced polarization and polarizability in polymer matrix close to the interface [7]. (ii) Given the nanometer size of the ceramic particles, it is possible to reduce the thickness of the polymer matrix film to nanoscale and hence further enhance its already high breakdown strength by avoiding avalanche effects. Straightforward at first sight, this strategy is highly complicated by a number of factors, such as the filler/matrix interfaces and the anisotropy of fillers, that may to a large extend determine the dielectric behavior of the 0–3 composites. Moreover, a highly inhomogeneous electric field is induced by the nanoparticles of high dielectric constants, which gives rise to local hot spots of increased electric field concentration and reduces the effective breakdown strength of the composites. It is quite challenging to balance the seemingly contradictory criteria of enhancing dielectric constants while maintaining high dielectric strength.

12.2 Interface and Interfacial Polarization: The Theoretical Considerations

In the 0–3 composites dielectrics, the interface between the ceramic nanoparticles and polymer matrix is defined as the range over which the permittivity changes from the value for ceramic nanoparticles to that for polymer matrix [8]. Interface is considered to have finite thickness. Consider a system consisting of a spherical nanoparticle with the diameter d and an interface with thickness t inside the diameter of the nanoparticle, the fraction f of the interfacial volume is expressed as: [9].

$$f = 3\frac{2t}{d}\left[1 - \left(\frac{2t}{d}\right) + \frac{1}{3}\left(\frac{2t}{d}\right)^2\right] (2t/d < 1) \qquad (12.3)$$

As suggested by Eq. (12.3), decrease of the ratio t/d of the interface thickness to the diameter of nanoparticles leads to dramatic increase of the volume fraction of the interface. For instance, for a nanoparticle of 10 nm in diameter with interface of 1.0 nm in thickness, the interfacial volume fraction exceeds 50%. The dielectric property of the interfacial region differs from either the polymer matrix or the nanoparticle. Given their high-volume fraction in the composites, interfaces are the dominant feature of dielectrics at the nanometric scale [8].

Two characteristics of interface are critical in describing their dielectric responses, i.e., how they are chemically formed and how the charges are distributed across the interfacial regions. To describe the formation of interfaces, a multilayer core model is proposed by Tanaka et al. [10] for a spherical inorganic filler particle embedded in a polymer matrix, as shown in Fig. 12.1. As seen, the first layer is the bonded layer with a thickness of ∼1 nm, which corresponds to the transition layer tightly bonded, by ionic, covalent or hydrogen bonds, or van der Waals force, to both nanoparticles and polymer. The second layer (a bound layer) is an interfacial region consisting of a layer of polymer chains strongly bound and/or interacted to the bonded layer and the surface of the nanoparticles. Its thickness is in the range of 2–9 nm. The third layer is a region loosely coupling and interacting to the second layer, in which the chain conformation, chain mobility, and even free value or crystallinity differ from the polymer matrix. In addition to the chemical bonds, the morphology of the interface layers is also strongly affected by the charge
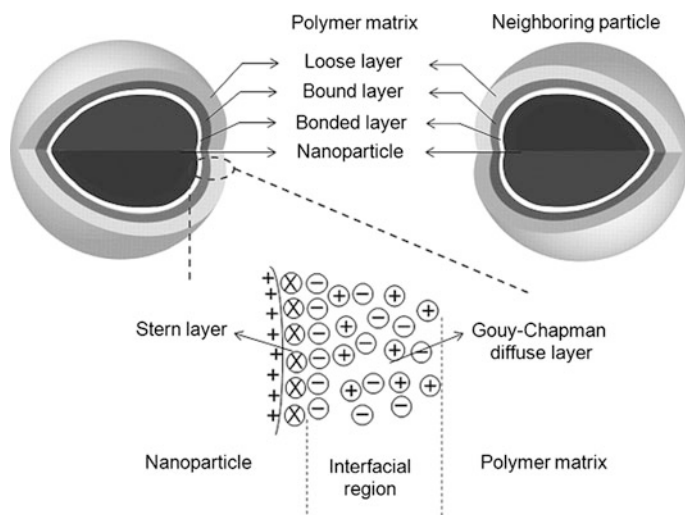
Fig. 12.1 Multicore model for interfaces between inorganic nanoparticles and polymer matrix in a polymer nanocomposite. It consists of a bonded layer, a bound layer, and a loose layer. As the nanoparticle is positively charged, a diffuse electrical double layer would form in the interfacial region and overlap the three layers above (Reproduced from Ref. [6] with kind permission of © 2014 Wiley-VCH)

distribution across the interfacial regions. Within these regions, Coulombic forces (long range), van der Waals forces (moderate range), or electrostatic forces (short range) are involved and may significantly alter the interface layers.

When subjected to electric field, interfaces in polymer composite could be charged. The charged interface is generally described in terms of three charged layers that invariably form and determine the dielectric characteristics of the interface, as shown in Fig. 12.1. On the nanoparticle side, a double layer associated with surface states is induced by immobile charged impurities, trapped carriers, and mobile electrons and holes in the nanoparticle. After the nanoparticle becomes effectively charged, the surrounding polymer responds by establishing a screening countercharge confronting the charge on the nanoparticles. Two mechanisms are involved in this reorganization process [11]. The first is concerned with the polymer polarization involving both electronic polarization (dipole motion) and the orientation of permanent dipoles (molecular motion).

The second screening action occurs when mobile ions are present in the polymer. The mobile ions will migrate to establish a diffuse electrical double layer (the so-called Stern–Helmholtz double layer) around the nanoparticles. This layer is of molecular thickness and may have a high charge density. The nanoparticle side of Stern–Helmholtz double layer is consisted of adsorbed ions or dipoles, while the polymer side of this layer [also called the outer Helmholtz plane (OHP)] is determined by the nearest approach of ions. Further extending beyond OHP into polymer is the so-called Gouy–Chapman diffusion layer. In this region, the mobile charges are distributed in such a way that the countercharge carriers with the opposite polarity are diffused outward from the OHP to the Debye shielding length, decaying exponentially with distance according to the Born approximation. The thickness of the Gouy–Chapman diffusion layer is significantly influenced by the electric conductivity of polymer. In highly conductive polymer, the layer shrinks into OHP; while in weakly conductive polymer, the thickness of this layer could be over 10 nm. Filled with mobile charge, the Gouy–Chapman diffusion layer has a significant role in influencing the dispersion of nanoparticles in polymer matrix. More importantly, this layer is the dominant feature that determines the dielectric response of polymer composite dielectrics. Within the electrical double layers, the charge density (ρ_i) is closely related to the electric potential (φ) as: [11].

$$\rho_i(r) = \rho_i(\infty)e^{-z_i e\varphi(r)/kT} \tag{12.4}$$

As indicated by Eq. (12.4), the charge density in the double layer is very sensitive to the electric potential and therefore to the electric field. At the surface of the nanoparticle, i.e., $r = 0$, the charge density in the double layer ($\rho_i(0)$) is then related to the surface conductivity of the nanoparticle (σ) as: [11].

$$\sum_i \rho_i(0) = \sum_i \rho_i(\infty) + \sigma^2/2\varepsilon kT \tag{12.5}$$

As suggested by Eq. (12.5), higher surface conductivity at the surface of nanoparticles may induce higher charge density in the electrical double layer in the surrounding polymer matrix. The charges within the interfaces often take on an active role when subjected to an impressed electric field. To study the effect of surface conductivity of nanoparticle on the apparent dielectric behavior of a composite system O'Konski [12] considered the random suspension of spherical particles with surface conductivity σ_s in a dielectric medium. At low frequencies or high σ_s, the charges in the interfaces are efficiently transferred by the applied electric field and induce polarization at opposite ends of the nanoparticle. This polarization creates a large dipole over the nanoparticle and may give rise to greatly enhanced effective dielectric permittivity of the composite, exceeding the dielectric permittivity of the nanoparticle.

Chew and Sen [13] made further improvement to this model by considering the countercharge effects in the double layers. At low frequencies, charge could be efficiently transferred into the surround matrix and form a neutral cloud of charge. At low frequencies, the diffusion cloud is large and out of phase of the applied electric field, which results in an out of phase dipole moment. As the frequency increases, the diffusion cloud lessens and with it the out of phase dipole moment. This model gives plausible explanations for the frequency dependence of dielectric behavior of many composite systems, where significant dielectric loss is usually observed at low frequencies and is attributed to the large out-of-phase dipole moment caused by surface charge polarization.

Given their complex nature, interfaces in polymer composites are usually considered as an interphase between polymer and nanoparticle fillers, which exhibit finite thickness and specified dielectric permittivity. Very recently, Lopez-Pamies et al. [9] constructed an analytical solution for the macroscopically homogenized dielectric response of particulate composites comprising a random distribution of particles bonded to a matrix material through interphases of finite size that contain space charges. In this approach, the charge density of the interphase is related to the electric potential (φ) in a more concise form as: [14]

$$\rho_i(r) = q_i \frac{-\varphi(r)}{R_p |r|},\tag{12.6}$$

where R_p denotes the radius of the nanoparticle and q_i is a measure of charge content in the interphase (of units F/m). By solving Gauss equations, the effective permittivity of the polymer composite (κ^*) can be written explicitly as: [14].

$$\kappa^* = \kappa_1 + \frac{3\kappa_1(f_2+f_3)[f_2(\kappa_2-\kappa_1)(2\kappa_2+\kappa_3)+3f_3\kappa_2(\kappa_3-\kappa_1)]}{\kappa_3[\kappa_2(1-f_2-f_3)(f_2+3f_3)+f_2\kappa_1(f_2+f_3+2)]+\kappa_2[\kappa_1(f_2+f_3+2)(2f_2+3f_3)-2f_2\kappa_2(f_2+f_3-1)]}$$
$$+ \frac{3\kappa_1 f_3(f_2+f_3)\left[\left(\frac{f_2}{f_3}+1\right)^{4/3}(2\kappa_2+\kappa_3)+4\left(\frac{f_2}{f_3}+1\right)^{1/3}(\kappa_2-\kappa_3)+3(\kappa_3-\kappa_2)\right]q_i}{4\kappa_3[\kappa_2(1-f_2-f_3)(f_2+3f_3)+f_2\kappa_1(f_2+f_3+2)]+4\kappa_2[\kappa_1(f_2+f_3+2)(2f_2+3f_3)-2f_2\kappa_2(f_2+f_3-1)]}$$
$$\tag{12.7}$$

Two remarks could be observed from Eq. (12.7): (i) In the absence of interphases ($f_2 = 0$ and $q_i = 0$), Eq. (12.7) reduces to the famous Maxwell–Garnett formula; (ii) the macroscopic permittivity is linearly related to q_i, a measure of the amount of charges in the interphases. Large positive values of q_i, which imply that the interphasial charges form an overall dipole that is aligned with the applied electric field, lead to a great enhancement of the macroscopic permittivity. While this model is able to describe and explain the extreme enhancement in dielectric response of polymer composites, its basic assumption is that the electric field remains unaltered outside the core–shell type nanoparticles, which obviously is not the case in real polymer composites.

In fact, in polymer composite, the local electric field close to the nanoparticle fillers could be significantly altered, giving rise to electric field fluctuation throughout the polymer composites. Take polymer composites filled with ferroelectric ceramic particles as an example. To enhance dielectric constants of polymer composites, ferroelectric ceramic nanoparticles, such as $BaTiO_3$ and $PbTiO_3$, are employed due to their high dielectric constants. When these nanoparticles are introduced, the ferroelectric domains inside the nanoparticles are encouraged to grow in the field direction, giving rise to increased polarization hence higher charge density at the surface of the nanoparticles. This polarization is then countered by charge (mobile ions or dipoles induced by the polar groups in polymer chain) in the polymer matrix. Within the double layer, the lateral movement of charge around the interfaces could reinforce this process. The outcome is the significantly enhanced electrical fields in the double layers, which is higher than the field in either the nanoparticles or the polymer matrix. Thus, the interfaces are seen to be sites of enhanced electric fields and the seats of polarization and conduction phenomena, which can dominate the behavior of polymer composite dielectrics [10]. The implication of enhanced electric field in the interface is that these hot spots in local electric field could be the weak point under high electric field, resulting dielectric breakdown of polymer composites at electric field much lower than the breakdown strength of polymer. This is especially so at high volume fraction of nanoparticles in the polymer composites where overlap of the interfacial double layers will give rise to percolated path for charge transfer and even further reduce the breakdown strength of the polymer composites [11].

The reduction in breakdown strength is a serious drawback of nanocomposite approach due to the quadratical scale of electric energy density with electric field. It is of critical importance to balance the dielectric constants and breakdown strength in polymer composites. To this end, theoretical studies have recently been performed to deepen the understanding of the trade-offs in polymer composites and, more importantly, to provide guidelines to the design of high-energy-density polymer composites. In modeling within the frame work of self-consistent effective media theory [15], interfaces in polymer composites are considered as interfacial phase with finite thickness, which is between the nanoparticles and polymer matrix and can be viewed as a core–shell type structure with the nanoparticle. The dielectric nanocomposite could then be considered as a three-phase material, consisting of a polymer matrix (phase 1), an interfacial phase (phase 2) of finite

thickness l, and nanoparticle fillers (phase 3). For this three-phase composite, the effective permittivity κ^* can be expressed as:

$$\kappa^* = \kappa_1 + f_2(\kappa_2 - \kappa_1)a_2 + f_3(\kappa_3 - \kappa_1)a_3 \qquad (12.8)$$

where f_r and a_r are the volume fraction and electric field concentration factor for corresponding phase r, respectively. The average electric field in phase r is then related to the electric field applied at the boundary (E_0) as:

$$\langle E_r \rangle = a_r E_0 \qquad (12.9)$$

The effective medium approximation provides a reasonable estimate of a_r as:

$$a_r = 1 - s\left[(\kappa_r - \kappa^*)^{-1}\kappa^* + s\right]^{-1}, \quad r = 2, 3 \qquad (12.10)$$

where s is the depolarization factor and is 1/3 for spherical particles. The field concentration factor for the polymer matrix can then be determined from the normalization condition as $\sum_{r=1}^{3} f_r a_r = 1$. By taking into account the statistical fluctuation of the average field throughout of the polymer composites, the apparent breakdown strength of polymer composites (E_b) could be predicted more accurately as:

$$E_0\left(a_1 + \sqrt{\frac{1}{f_1}\frac{\partial \kappa^*}{\partial \kappa_1} - a_1^2}\right) \geq E_b \qquad (12.11)$$

The implication of these modeling results is that measurements should be taken to mitigate electric field concentration in order not to cause serious reduction of the dielectric breakdown strength of polymer composites.

12.3 Modulation of the Filler/Polymer Interface: Surface Modification of Nanoparticles and Beyond

The most common approach of modulating the filler/polymer interface is surface modification of nanoparticles. Surfactants such as phosphate esters or oligomers are usually employed [16], which could improve the compatibility between the nanoparticles and polymer matrix and facilitate the homogeneous dispersion of nanoparticles in the matrix. In order to form robust interface layers on the surface of nanoparticles and suppress the dielectric loss, covalent bonding between the surface modifiers and nanoparticles are highly desirable. To this end, a number of ligands have been explored as coupling agent between the nanoparticles and polymer

matrix. Kim et al. [17, 18] demonstrated that phosphonic acid is capable of forming covalent bonding with $BaTiO_3$ nanoparticle through coordination of metal ions on the surface or condensation with surface hydroxyl groups. These surface modifiers tightly bind to the $BaTiO_3$ nanoparticle could then effectively decrease the aggregation of $BaTiO_3$ nanoparticles in the polymer matrix. Rational selection of phosphonic acid with different functional groups could effectively improve the compatibility between the $BaTiO_3$ nanoparticle and different polymers.

For instance, {2-[2-(2-methoxyethoxy)ethoxy]ethyl} phosphonic acid (PEGPA) has a tri(ethylene glycol) chain to compatibilize $BaTiO_3$ nanoparticles with polar, hydrophilic resins and solvents. Pentafluorobenzyl phosphonic acid (PFBPA) features a fluorinated aryl group to afford good compatibility with fluoroelastomers and common organic solvents. Enhanced dielectric permittivity ($\sim$37), reasonably low dielectric loss (<0.07) and hence increased energy density ($\sim$6.1 J/cm3) are achieved in these composites filled with phosphonic acid-modified $BaTiO_3$ nanoparticles. Covalent bonding between the nanoparticles and polymer matrix could also be induced by hydroxyl groups which could be achieved either by the introduction of hydroxyl groups on the nanoparticle surface or by the employment of surfactants containing hydroxyl groups. For instance, hydrogen peroxide has been used to treat the $BaTiO_3$ nanoparticles [19] or $Ba_{0.6}Sr_{0.4}TiO_3$ nanofibers [20] in order to anchor hydroxyl groups on the surface of the nanofillers. Upon mixing of these surface hydroxylated nanoparticles with polymer matrix, hydrogen bonds could be formed between the electrophilic atoms on the polymer chains and the –OH groups.

Dopamine, a bio-inspired building block for surface coatings, has recently received considerable attention for their capability of forming robust and dense surface layers on a variety of substances [21]. Simultaneously with aromatic and amido groups, dopamine is an ideal compatibilizer between the inorganic nanoparticles and polymer matrix. Song et al. [22, 23] treated $BaTiO_3$ nanoparticles and nanofibers with dopamine in aqueous solutions, and a layer of $\sim$5 nm in thickness is formed on the surface of the nanoparticles. The layer is of high structural integrity and tightly bonded to the nanoparticle surface through BT–O–C bonds, as verified by XPS analysis and the microstructural images. The dense layer formed by dopamine not only affords homogeneous dispersion of nanoparticles but also suppresses the remnant polarization usually associated with surface charges in the loose interface between nanoparticles and polymer. The synergistic effects of these features give rise to an enhancement of over 200% in dielectric breakdown strength for the resultant polymer composites. As a result, the extractable energy density is enhanced up to 5.4 J/cm^3, which is an enhancement of over twofold as compared with pure PVDF.

One other strategy of modulating the filler/polymer interface is to graft the host polymer chains directly to the nanoparticles without the use of small molecular surface modifiers. For this purpose, in situ polymerization on the surface of the nanoparticles is most commonly adopted approach. A series of core–shell structure BaTiO3/polymer composites have been successfully prepared by Huang et al. In these composites, nonpolar poly(methyl methacrylate) (PMMA) [24] or polar poly

(1*H*,1*H*,2*H*,2*H*-heptadecafluorodecyl acrylate) (PHFDA) [25] is synthesized by grafting the corresponding monomers to the surface of BaTiO$_3$ nanoparticles. The subsequent atom transfer radical polymerization (ATRP) or surface-initiated reversible addition–fragmentation chain transfer polymerization (RAFTP) yields dense polymer surface layer on BaTiO$_3$ nanoparticles. Besides the increased the dielectric permittivity induced by the BaTiO$_3$ nanoparticles, the most attractive feature of these composites is their ultralow dielectric loss. In the polymer composites filled with PHFDA-coated BaTiO$_3$ nanoparticles, the dielectric loss is only 0.02 (@100 Hz), which is even lower than that of the PVDF-HFP matrix (0.06), even the volume fraction of BaTiO$_3$ nanoparticles is as high as 50 vol%.

In addition to the in situ approach to bind polymer chains to the surface of nanoparticles, Li et al. [26] proposed and demonstrated that polymer chains could also be covalently bonded to the surface of nanoparticles via chain end functionalization. In this approach, phosphonic acid end groups are attached to the chain of poly(vinylidene fluoride-chlorotrifluoroethylene) P(VDF-CTFE). The reactive terminal groups then direct couple with ZrO$_2$ nanoparticles through the Zr–OH condensation. The covalent-bonded nanocomposite affords an energy density as large as 11.2 J/cm^3 with a considerably high dielectric strength of 270 MV/m, which is comparable to that of the pure polymer matrix.

It is worth noting that these aforementioned approaches have only addressed one challenge in the modulation of filler/polymer interface, i.e., how to improve the compatibility between the nanoparticles and polymer matrix and guarantee homogeneous dispersion. It still remains untouched as how to manipulate the interfacial polarization by modulating the charge distribution inside the interface/interfacial regions, or to mitigate the electrical field concentration caused by the abrupt dielectric permittivity gradient across the filler/polymer interface, which is of utmost significance for the polymer composite dielectrics. In answer to these challenges, attempts to control the charge distribution across the interface have been made by Jung et al. [27]. In a polystyrene (PS) nanocomposite comprising core–shell BaTiO$_3$ nanoparticles with diblock copolymer shielding layers, polystyrene-block-poly (styrene-co-vinylbenzylchloride) (PS-b-PSVBC) self-assembled and formed a dense shell layer on the BaTiO$_3$ nanoparticles via a two-step process. Within the shell layer, nonpolar polystyrene blocks of the diblock copolymers form the outer layer with the polar ammonium-containing blocks preferentially residing in the inner layer and bonding closely with BaTiO$_3$ nanoparticles. As a result of the special conformation of PS-b-PSVBC shell layer, the surface of BaTiO$_3$ nanoparticles can be largely charged with ammonium groups in the inner layer, which contributes to a high polarization level in the composites. Plus, this charge-rich layer is directly buried and shielded by the 3–5 nm thick insulating outer layer so as to minimize the development of the breakdown path and leakage current. The high charge density in interface gives rise to much enhanced interfacial polarization hence high dielectric permittivity of the corresponding polymer composites ($\sim$44 at 10 kHz).

Notably, this high dielectric permittivity is obtained by using polystyrene host of low dielectric permittivity ($\varepsilon_r \sim$ 2.5–2.6), while the reported highest results have

mostly been obtained by introducing high dielectric ferroelectric polymers such as PVDF or its copolymers ($\varepsilon_r > 10$). In the meantime, thanks to the insulating layers, large dielectric breakdown strength (up to 222 kV/mm) is also achieved at high permittivity, giving rise to a high calculated energy density of 9.7 J/cm^3. Recently, the role of charge density in the interface is further explored by Siddabattuni et al. [28] more systematically. Five different monolayers of electron-rich or electron-poor organophosphate coupling groups were self-assembled to the surface of TiO$_2$ or BaTiO$_3$ nanoparticles to affect the filler/polymer interface. The nanoparticles were then dispersed into epoxy to form composite films and the role of modulated interface in dielectric behavior of composite behavior was investigated. It is found that the surface of TiO$_2$ nanoparticles is best modified with electropositive aromatic organophosphate ligands that contain an electron-withdrawing functional groups such as nitro, which showed improved leakage current (<5 pA/cm^2 at 100 V), low dielectric loss, and enhanced dielectric breakdown strength compared to electron-donating functional group modified TiO$_2$ composites. These results support the hypothesis that the electronic structure of the filler ligand can indeed control the dielectric properties of the composites. Electropositive ligands may be useful for particle surface modification to minimize leakage current and dielectric loss and provide for higher dielectric breakdown strength, hence higher energy storage density of the polymer composites.

The implication of these results is that decoupled modulation of dielectric permittivity and dielectric breakdown strength may indeed be realized by careful tuning of charge density in the bonded layer while maintaining the low electrical conductivity of the bound layer. A true realization of Tanaka's multicore model is thus highly desirable. To this end, the most encouraging progresses have recently been made by Lanagan et al. [29–31]. Instead of polymer chains or small molecular surfactants, a thin layer of Al$_2$O$_3$ with dielectric permittivity of ~ 10 is deposited on a variety of metal oxide nanoparticles including BaTiO$_3$, ZrO$_2$, MgO, SrTiO$_3$, and Ba$_{0.5}$Sr$_{0.5}$TiO$_3$ [32]. To introduce the Al$_2$O$_3$ layer, methylaluminoxane (MAO) is firstly grafted to the surface of metal oxide nanoparticles. Upon exposure of these precursors to oxygen and moisture, the pyrolysis of MAO yields a dense layer of Al$_2$O$_3$ on the surface of metal oxide nanoparticles, as schematically shown in Fig. 12.2. These core–shell nanoparticles subsequently served as support and metallocene cocatalyst for the following in situ isotactic-propylene polymerization.
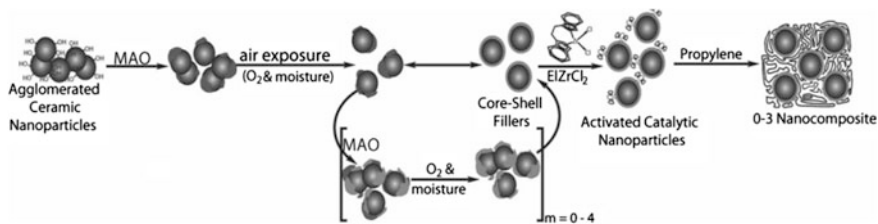
Fig. 12.2 Synthetic route to 0–3 ceramic-polypropylene nanocomposites (Reproduced from Ref. [32] with kind permission of © 2012 Wiley-VCH)

The significance of this composite system lies in two aspects: (i) It is the first systematically testable realizations of Tanaka's multicore model, where the bonded layer (nanoparticle) and the bound layer (Al_2O_3 layer) are modulated with their effects on the dielectric behavior of polymer composites investigated while the polymer matrix being held constant. (ii) The resulting nanocomposites have nanoparticle permittivities ranging from 6 to 2000 with varied thickness (2–10 nm) Al_2O_3 shells ($\varepsilon_r \sim 10$), and isotactic-polypropylene ($\varepsilon_r \sim 2$) as the matrix. With the presence of Al_2O_3 buffer layer of moderate dielectric permittivity, electric field concentration caused by the large contrast of the dielectric permittivity between the nanoparticle and polymer matrix could thus be mitigated by the dielectric permittivity gradient. Proper adjustment of materials parameters yields recoverable energy storage capacities as high as 2.05 J/cm^3, and total energy storage capacities as high as 15.6 J/cm^3 at voltages close to breakdown. Also of significance is the finding that the loss in these materials is largely proportional to the particle interfacial area within the sample, regardless of the constituent nanoparticle material, is dependent on the Al_2O_3 layer thickness [32].

Besides, introducing buffer layer of moderate dielectric permittivity in between the nanoparticles and polymer matrix, the approach of balancing dielectric permittivity by rational selection of filler and polymer matrix with comparable permittivity values has also been adopted to mitigate the electric field concentration induced by the large contrast of dielectric permittivity. Wang et al. [33] prepared a nanocomposites comprised of P(VDF-TrFE-CTFE) ($\varepsilon_r \sim 42$) and TiO_2 nanoparticles ($\varepsilon_r \sim 47$). Due to the close dielectric permittivities of the two constituents, very minor enhancement of dielectric permittivity is observed in these nanocomposites. Yet, the large interfacial area between the TiO_2 nanoparticles and the polymer significantly promotes the interfacial polarization and leads to substantial improvement in electric displacement and thus high energy density at high electric field (6.9 J/cm^3 at 200 kV/m). More importantly, the balanced dielectric permittivity gives rise to a maximum dielectric breakdown strength of 230 kV/m, which is considerably larger than that of conventional dielectric polymer nanocomposites (below 100 MV/m).

12.4   The Implications of Dielectric Anisotropy

Equally important as the filler/polymer interface is the dielectric anisotropy in determining the dielectric and energy storage performance of nanocomposites. The properties of the composites not only depend on the properties of respective constituent materials (i.e., matrix and inclusions), but also sensitively depend on the filler microstructures (i.e., size, shape, and spatial arrangement) embedded in the matrix. For polymer composites, dielectric anisotropy could be induced either by the introduction of anisotropic nanoparticles, such as nanofibers (1D) or nanosheets (2D) of large aspect ratio, or by the alignment of spherical nanoparticles into chains [34]. Much enhanced dielectric permittivity, hence higher electrical polarization,

could be obtained when the orientation or alignment of nanoparticles is in line with the external electric field. The dielectric anisotropy is usually associated with the large aspect ratio of anisotropic nanoparticles [35]. Along the longitudinal direction of the large-aspect-ratio nanoparticles, the depolarization factor is smaller, as compared with transverse directions, which allows the electric field to penetrate into the fillers and propagate through the chains, leading to a high composite dielectric permittivity. For instance, the alignment of lead zirconium titanate (PZT) nanowires was induced via uniaxial strain assembly in a thermoplastic polymer matrix. In these highly oriented polymer nanocomposites, the dielectric permittivity was enhanced by over threefold, as compared with randomly filled polymer nanocomposites, when the PZT nanowires were aligned with the external electric field [36].

The implications of dielectric anisotropy on the energy storage performance of polymer nanocomposites are twofold: (i) The enhanced dielectric permittivity, hence higher electrical polarization, along the direction in which the nanoparticles are oriented or aligned in line with the external electric field is highly desirable for higher energy density of polymer nanocomposites; (ii) the filler particle microstructural arrangements that provide higher composite dielectric permittivity also suffer from higher local electric field concentration in the polymer matrix, which would decrease dielectric breakdown strength of the composites. Phase field modeling [37, 38] indicates that electric field concentration is severely intensified in the matrix regions between spherical nanoparticles, in particular, when aligned into chains along the externally applied electric field direction. As for polymer nanocomposites filled with nanofibers or nanosheets, hot spot of local electric field is mostly found at the tip of these large-aspect-ratio nanoparticles. Dielectric breakdown process could thus be initiated from these hot spots of local electric field at an external electric field still far below the intrinsic dielectric breakdown strength of the polymer matrix. It is worth noting that same modeling also indicates that the susceptibility of the polymer composite could be lowered by the orientation of the large-aspect-ratio nanoparticles in the in-plane directions when the electric field is applied out of plane, leading to a lower concentration of the electric field in the polymer matrix and strong anisotropy in dielectric breakdown strength [39].

In fact, the orientation of large-aspect-ratio nanoparticles perpendicular to the external electric field could even enhance the dielectric breakdown strength of polymer nanocomposites. The enhanced breakdown strength could be explained by the electrical breakdown process. Electrical breakdown usually happens as a result of the progress of electrical treeing throughout the material. Partially oriented nanofibers in the nanocomposites are capable of restraining the growth of electrical treeing by providing tortuous paths for treeing, as well as more scattering centers for the hot electrons. The nanofibers partially oriented in the direction perpendicular to the applied electric field also provide more ordered trapping or scattering centers for the injected charges, hindering the traverse of the injected charges to the opposite electrode. Plus, a higher resistance to filamentary thermal and electromechanical breakdown events is also obtained as a result of the orientation of the

nanofibers. Enhanced mechanical properties are also expected in the nanocomposite filled with fibers. The local thermal and electric stresses are spread over a larger material volume, leading to improved breakdown strength.

Given the quadratic dependence of electrostatic energy density on dielectric breakdown strength versus linear dependence on dielectric permittivity, maximization of energy density prioritizes optimization of composite breakdown strength rather than effective dielectric permittivity, which then rationalize the employment of ceramic nanofibers as dielectric fillers for higher energy density of polymer nanocomposites. A variety of ceramic nanofibers have recently been explored for their energy storage performance in polymer nanocomposites, including $BaTiO_3$, $Ba_xSr_{1-x}TiO_3$, PZT. The rational selection of ceramic nanofibers initially lies in their different intrinsic polarization behavior. In order to obtain the high extractable energy density, the remnant polarization needs to be as small as possible so that more electrical energy stored could be released in the discharging process instead of being stored in the form of remnant polarization of the ceramic nanofibers or space charge polarization at the filler/polymer interface. Paraelectric ceramic nanofibers with small remnant polarization, such as $Ba_xSr_{1-x}TiO_3$ ($x < 0.7$), are thus considered superior than their ferroelectric counterparts, i.e., $BaTiO_3$ or PZT, in enhancing the extractable energy density of polymer nanocomposites.

However, as been elaborated in the previous section, the dominant interfacial polarization at the filler/polymer interface may well overwhelm the intrinsic polarization behavior of these ceramic nanofibers, leading to very minor differences in the polarization behavior of the corresponding polymer nanocomposites. In a direct comparison, the electrospun $Ba_{0.6}Sr_{0.4}TiO_3$ [40] and $BaTiO_3$ nanofibers [22] were surface modified with dopamine and composed with PVDF to form polymer nanocomposites. At 11 vol% of nanofibers, the remnant polarization mildly decreased from 1.5 $\mu C/cm^2$ for $BaTiO_3$ to ~ 0.5 $\mu C/cm^2$ for $Ba_{0.6}Sr_{0.4}TiO_3$ in the polymer nanocomposites. However, in a very similar PVDF-based composite where the $Ba_{0.6}Sr_{0.4}TiO_3$ nanofibers were treated with H_2O_2, Zhai et al. [20] reported a higher remnant polarization of ~ 2.0 $\mu C/cm^2$ at much lower volume fraction of 2.5 vol%. The substantial difference in the remnant polarizations observed is indicative of the overwhelming role of interfacial polarization in the electrical polarization behavior of polymer nanocomposites. Also, the effects of polymer matrix should not be overlooked. Hu et al. [41] introduced the dopamine-modified $Ba_{0.6}Sr_{0.4}TiO_3$ nanofibers into PVDF-TrFE of higher dielectric permittivity. In the resultant polymer nanocomposites, the lowest remnant polarization observed is >4.0 $\mu C/cm^2$, which is mainly attributed to the high remnant polarization of PVDF-TrFE matrix.

Compared with 1-D nanofibers, very few types of 2-D nanosheets have been explored for their energy storage performance in polymer nanocomposites, due largely to the limited availability of nanosheets. Nanofibers could be synthesized through a number of methods, such as electrospinning, hydrothermal treatments, or substrate-mediated electrochemical deposition while long-time exfoliation processes are needed for the preparation of nanosheets. So far, the most commonly

used 2-D nanosheet is montmorillonite (MMT), a layered silicate which is naturally abundant and commercially available. The rationale of using MMT lies in their ability to provide more ordered trapping centers and more efficient scattering for the injected charge, thus obstructing its ability to traverse the sample to the opposite electrode. Plus, increased path tortuosity in the electrical treeing process during breakdown is also favorable for enhanced dielectric breakdown strength. Indeed, Tomer et al. [42] found that highly oriented oMMT has a measurable positive effect on the breakdown strength of the polymer nanocomposites. The dielectric breakdown strength was enhanced 370 kV/mm in the nanocomposites containing oriented oMMT, an enhancement of >20% over the unfilled PE matrix (300 kV/mm), even the loading of oMMT is only 6 wt%.

More importantly, markedly lower dielectric losses were observed in the nanocomposites containing oriented oMMT as compared with its random counterparts. It is worth noting that insufficient control of the hierarchal morphology of the blend, especially at intermediate or high loading of MMT where polymer-deficient structural defects could form, usually results in a precipitous decline in dielectric breakdown strength of polymer nanocomposites. The benefits of increased path tortuosity are compromised by the polymer-deficient structural defects at high loading of MMT. The extent to which these nanosheet concepts can be exploited to create an extreme density of barriers has not been explored by Fillery et al. [43]. In a model system composed of organically modified montmorillonite (oMMT) and polyvinyl butyral (PVB), the high degree of compatibility in solution allows control of nanocomposite morphology and filler orientation across the entire range of volume fractions from pure polymer to pure oMMT. A facile spray processing technique ensures the generation of large area, free-standing, nanolaminate films. These large uniform films enable a statistically relevant assessment of failure, demonstrating that dielectric breakdown strength of the nanolaminates can increase 2.5 times relative to the unfilled polymer at a rather high volume fraction of 25 vol% inorganic (70 wt% oMMT). This implies that an idealized morphology of polymer nanocomposites to retard the breakdown cascade perpendicular to the electrodes will occur at intermediate volume fractions and resemble a discotic nematic phase where highly aligned, high-aspect-ratio nanometer thick plates are uniformly surrounded by nanoscopic regions of polymer.

On the other side of the composite spectrum, the role of polymer matrix in the energy storage performance should not be overlooked. In pure PVDF films, Li et al. [44] demonstrated that thermal quenching of PVDF films (from 200 °C into ice water) induces phase transformation from the polar β-phase to the nonpolar γ-phase, which could withstand a high electric field of ~ 500 kV/mm and avoid the early polarization saturation in β-phase. The highest polarization obtained is ~ 9 $\mu C/cm^2$, very close to the theoretical irreversible saturate polarization of PVDF. Careful attentions have thus to be paid in the processing of polymer matrix with an aim to modulate their crystalline phase, degree of crosslinking, and, most importantly, to decrease the structural imperfections in the polymer matrix. Along

this line, Tang et al. [45] recently took a concerted approach toward ultrahigh energy density of polymer nanocomposites. Paraelectric $Ba_{0.2}Sr_{0.8}TiO_3$ nanowires of large aspect ratio were synthesized through hydrothermal method. The following surface treatments to the $Ba_{0.2}Sr_{0.8}TiO_3$ nanowires with ethylenediamine improved their compatibility with PVDF matrix. Most critically, the resultant polymer nanocomposites were thermally quenched from 200 °C into ice water, which could not only induce γ-phase of PVDF but also help eliminate pores or voids formed during the casting process of the composite films. As shown in Fig. 12.3, through these combined efforts, the nanocomposites are shown to have an ultrahigh energy density of 14.86 J/cm^3 at 450 kV/mm and provide microsecond discharge time quicker than commercial BOPP capacitors.

In addition to thermal treatment, the interplay between introduced nanoparticles and the crystallization of polymer matrix may also be capitalized as an efficient approach to modulate the crystalline phase of polymer matrix. Tomer et al. [46] explored a promising route to improve the energy storage performance of PVDF, through a synergy of HFP comonomers and of kaolinite clay nanofillers. This study shows that the addition of these high-aspect-ratio fillers to poly(vinylidene fluoride-hexafluoropropylene) [P(VDF-HFP)] copolymers does not increase the polar phase and, consequently, these composites exhibit markedly enhanced dielectric properties at high electric fields. With 5 wt% of kaolinite clay nanofillers added, the dielectric breakdown strength of the corresponding polymer nanocomposites was increased up to ∼780 kV/mm, an enhancement of >50% over that of the unfilled PVDF-HFP films. The highest electrical energy density achieved is ∼19 J/cm^3.
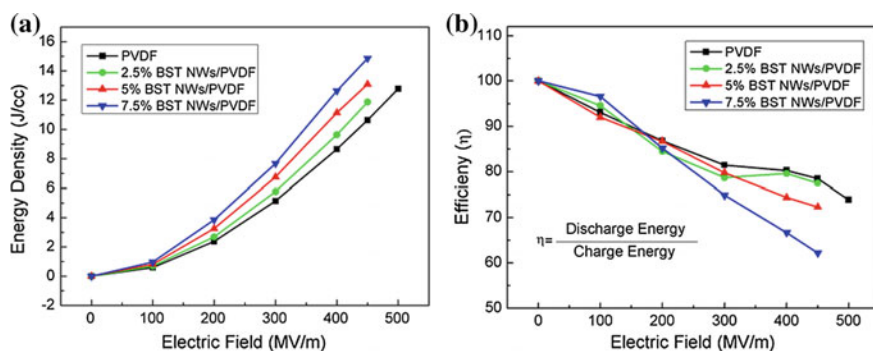
Fig. 12.3 Energy storage performance of the BST/PVDF nanocomposite capacitor: **a** energy density of the nanocomposite with different volume fraction as a function of the electric field calculated from D–E loops; **b** efficiencies of the nanocomposites with different volume fraction as a function of the electric field (Reproduced from Ref. [45] with kind permission of © 2013 American Chemical Society)

12.5   Concomitant Enhancement of Dielectric Permittivity and Breakdown Strength

Until this point, the high energy density is mainly obtained through enhancing the dielectric breakdown strength of polymer nanocomposites. After years of intensive study, the dielectric breakdown strength of polymer nanocomposites has been substantially increased rather close to, if not beyond, the intrinsic dielectric breakdown strength of the corresponding polymer matrix, leaving limited room for further improvement. Plus, it is also of interest to achieve high energy density at comparatively low electric field. For these reasons, novel approaches have recently been proposed for the concurrent enhancement of the dielectric permittivity, hence electrical polarization, and dielectric breakdown strength of polymer nanocomposites. The bottom line is to enhance electrical polarization without causing decreased dielectric breakdown strength.

To this end, Polizos et al. [47] prepared inorganic nanofillers consisted of well-dispersed $BaTiO_3$ spherical nanoparticles that are surrounded by attached layered MMT nanoplatelets, with the latter having the ability to react with the epoxy matrix. Through covalent bonding between $BaTiO_3$ nanoparticles and the high-aspect-ratio oMMT fillers, detrimental effects in the performance of the epoxy composites under high electric fields, when adding high-permittivity $BaTiO_3$ nanoparticles, are significantly reduced in the systems. With the presence of $BaTiO_3$ nanoparticles, the maximum electrical polarization increased by >40% over the nanocomposites solely filled with oMMT. Also, the slope of the P-E loop for the 5 wt% BT/oMMT indicates a higher permittivity at high E-fields without increasing the high-field losses, compared to all other systems. Most recently, Li et al. [48] took a very similar approach in which two-dimensional (2-D) hexagonal boron nitride nanosheets (BNNSs) was used to improve dielectric breakdown strength and $BaTiO_3$ nanoparticles was used to induce higher electrical polarization of the polymer nanocomposites. Ferroelectric poly (vinylidene fluoride-co-chlorotrifluoroethylene), P(VDF-CTFE), was chosen as the matrix because of its highest intrinsic energy density among the known polymers. Notably, a 20% increase in dielectric permittivity along with a 43% improvement in dielectric breakdown strength relative to the pristine matrix is found at a composition of 12 wt% BNNSs and 15 wt% $BaTiO_3$. As a result, an unprecedented high energy density of 21.2 J/cm^3 was obtained at an electrical field of 532 kV/mm. The addition of these nanoparticles also hindered the partial conversion of nonpolar α-phase in PVDF to the polar β-phase, giving rise to a high charge–discharge efficiency of 82% even at the highest electrical field. It is worth noting that in these approaches, the nanoparticles of high dielectric permittivity are randomly mixed with the large-aspect-ratio nanofillers to form the 0–3 composite, although some type of hierarchical structure formed by the two fillers may be occasionally found.

Recently, Hu et al. [49] proposed that by expanding the traditional 0–3 nanocomposite approach to a multilayered structure, one may achieve both enhanced electrical displacement as well as a higher breakdown field than that of

the polymer matrix. Such a topological-structure nanocomposite combines synergistically the complementary properties of the constituent layers. In a three-layer demo nanocomposite, $BaTiO_3$ nanoparticles were introduced in the outer composite layers to induce high electrical polarization, while $BaTiO_3$ nanofibers were used in the central composite layer for improving the breakdown strength. In this configuration, the outer composite layers filled with large amount of $BaTiO_3$ nanoparticles can be polarized up to higher electric field, hence enhancing the electric displacement. As shown in Fig. 12.4, simultaneously, enhanced electric displacement and breakdown strength were achieved, as highlighted in the shaded area. Particularly, with 10 vol% of $BaTiO_3$ nanoparticles in the outer layers, the maximum electric displacement was increased from ~ 5.2 $\mu C/cm^2$ for 0 vol% to 6.0 $\mu C/cm^2$ for 2 vol% of $BaTiO_3$ nanofibers, an enhancement of $\sim 16\%$. Concomitantly, the breakdown strength was also enhanced by 67%, i.e., from ~ 228 kV/mm for 0 vol% to ~ 382 kV/mm for 2 vol% of $BaTiO_3$ nanofibers. By careful tuning of the relative thickness of the constituent layers, a maximum discharged energy density of 9.7 J/cm^3 was achieved.
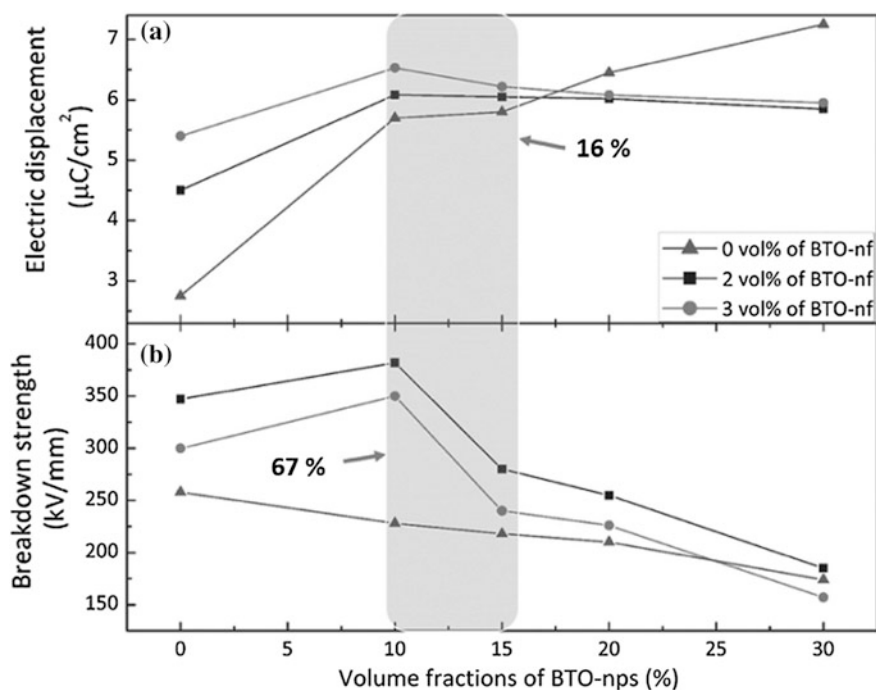
Fig. 12.4 Variation of **a** maximal electric displacement and **b** breakdown strength of the multilayer composites with the volume fractions of BTO-np in the outer layers and BTO-nf in the central layers (2 vol%: *square*; 3 vol%: *solid circle*). Also, superimposed are the data for the composites filled solely with BTO-np (denoted as 0 vol%: *up-triangle*) (Reproduced from Ref. [49] with kind permission of © 2014 Wiley-VCH)

The dual-filler approach still requires a large amount of fillers to be incorporated in polymer matrix, which imposes much challenge on the preparation of defect-free nanocomposite and may compromise the reliability of composite dielectrics at high voltage. To address this issue, Shen et al. [50, 51] recently proposed and demonstrated that composite nanofibers with hierarchical interfaces inside the nanofibers are capable of inducing much enhanced electrical polarization at a rather low-volume fraction. Moreover, the orientation of these large-aspect-ratio nanofibers in the directions perpendicular to the external electric field gives rise to improved breakdown strength. In a demo system, TiO_2 nanofibers embedded with $BaTiO_3$ nanoparticles (BTO@TO_nfs) were prepared by a modified electrospinning process. The hierarchical interfaces inside the BTO@TO_nfs are highlighted in Fig. 12.5.
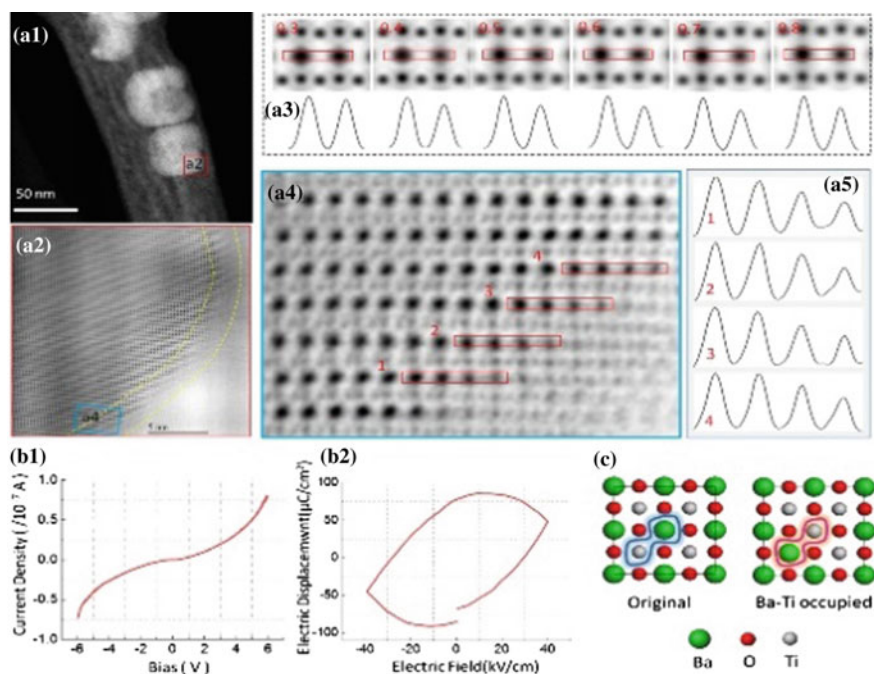
Fig. 12.5 a1 The low-magnification HAADF image of $BaTiO_3$ particles coated by a TiO_2 nanofiber; atomic resolution ABF images indicated by *colored frames* in **a1** are presented in **a2**, where the surface regions have been outlined by *yellow dotted lines*; **a3** is simulated ABF images and *line* profiles of inversed intensities with varied Ti^{4+} content at the Ba^{2+} sites, indicated by numbers at the *upper left* of each image, in each *line* profile, the *left peak* corresponds to the non-substituted Ba^{2+} ions and the *right peak* corresponds to the Ti^{4+}-substituted Ba^{2+} ions; **a4** *line* profiles of experimental inversed intensities near the interface (which is the inserted image in **a3**), the *peaks* correspond to the locations of the Ba^{2+} ions doped with Ti ions. **b1** the I–V curve and **b2** the D–E loop of BTO@TO_nfs; **c** the structure model for the DFT calculation (Reproduced from Ref. [50] with kind permission of © 2016 Wiley-VCH) (color figure online)

Simulations of the angular bright-field (ABF) images suggest that there is mutual occupation of Ba^{2+}–Ti^{4+} within the interfacial regions between TiO_2 and $BaTiO_3$. On the atomic scale, results of first-principle calculation based on density–function theory (DFT) further indicate that the mutual occupation of Ba^{2+}–Ti^{4+} within the unit cell of $BaTiO_3$ leads to substantially increased electrical polarization of the interfacial regions. On the mesoscopic scale, phase field simulations reveal that the percolation of the TiO_2/$BaTiO_3$ interfaces inside the BTO@TO_nfs could significantly change the electrical polarization behavior of the nanofibers from being insulting to being more semiconductive like [52]. These BTO@TO_nfs are then fused with poly (vinylidene fluoride-hexafluoropropylene) [P(VDF-HFP)] by a solution-casting method. The following annealing and thermal-quenching treatments give rise to nanocomposites films of high structural integrity and flexibility. In these P(VDF-HFP)-based nanocomposites, the dielectric permittivity is substantially enhanced up to 35 with a small loading of 7 vol% of BTO@TO_nfs. More importantly, thanks to the high structural integrity and partial orientation of BTO@TO_nfs, the nanocomposites loaded with 3 vol% of BTO@TO_nfs still exhibit a rather high breakdown strength of ~ 800 kV/mm. The synergistic effects of these favorable features give rise to an ultrahigh energy density of ~ 31 J/cm^3 at ~ 800 kV/mm, which is even comparable to electrochemical supercapacitors. Plus, the nanocomposite also bears high discharge efficiency of >70% even at this very high electric field of ~ 800 kV/mm, as compared to BOPP with a low discharge efficiency of <40% at a much lower electric field <700 kV/mm.

12.6 Considerations Beyond Energy Density: Thermal Stability

The ever increasing demands for miniaturization and functionality of electrical and electronic devices also impose higher challenges for the thermal stability of dielectric materials, especially in the scenarios where capacitors are subjected to both high temperature and high voltage. For example, to accommodate BOPP film capacitors in the power inverters of hybrid and electric vehicles, which are used to control and convert direct current from batteries into the alternating current required to power the motor, cooling systems have to be employed to decrease the environmental temperature from about 140 °C to about 70 °C. This brings extra weight, volume, and energy consumption to the integrated power system and reduces its reliability and efficiency. When subjected to high voltage, even the most robust engineering polymers (Tg), such as poly(ether ether ketone) (PEEK) or polycarbonate which exhibits high glass-transition temperatures and is theoretically capable of withstanding a high temperature up to 300 °C, fail at rather low temperature (<150 °C), exhibiting significantly increased dielectric loss and dramatically decreased discharge efficiency. With low intrinsic thermal conductivity (usually 0.1–0.5 Wm/K), pure polymers are susceptible to thermal runaways. When the joule heat generated by the much increased high-field

electrical conduction is accumulated from inside the polymer, local temperature is substantially raised well above T_g, resulting in drastically decreased Young's modulus and breakdown strength.

Wang et al. [53, 54] recently demonstrated that incorporation of hexagonal boron nitride (h-BN) nanosheets in divinyltetramethyldisiloxane-bis(benzocyclobutene) (BCB) polymer matrix dramatically improve the thermal stability of nanocomposites at high electric field. The BN-filled nanocomposites exhibit high breakdown strength of 403 kV/mm at a record high temperature of 250 °C. When composed with polymer matrix, h-BN sheets of high intrinsic thermal conductivity ($\sim$300 Wm/K) form network throughout polymer matrix, which raises thermal conductivity from $\sim$0.1 Wm/K for BCB to $\sim$1.8 Wm/K for h-BN-filled nanocomposites. A finite element simulation on the steady-state internal temperature distribution indicates that, with the accelerated heat conduction from inside h-BN-filled nanocomposites, the highest temperature inside c-BCB/BNNS is only 204 °C at 200 kV/mm with an ambient temperature of 200 °C. At the same operating conditions, the PEI-, FPE-, and Kapton-based film capacitors are all overheated. Moreover, the h-BN networks also render nanocomposites with robust mechanical properties, making them less susceptible to electromechanical failure at high electric field.

12.7   Conclusions

In summary, years of intensive research has led to rather high energy density of 0–3 polymer nanocomposites, i.e., $\sim$20 J/cm^3 which is comparable with the electrochemical capacitors. More importantly, it is now commonly accepted that it takes concerted efforts toward high energy density of nanocomposites. The design of polymer nanocomposites requires the rational selection of nanoparticles and polymer matrix that takes into account their interplay and the subsequent effects on the dispersion of nanoparticles and crystallization of polymer matrix, the interface engineering that not only promotes homogeneous dispersion of nanoparticles but also modulates the critical interfacial polarization. As the dielectric media subjected to rather high electrical field, these polymer nanocomposites are also hypersensitive to any structural defects that have detrimental effects on the dielectric breakdown strength of nanocomposites and compromise the energy storage performance of polymer nanocomposites or even counteract any benefits one may obtain through rational design of nanocomposite microstructure. Careful control of processing conditions is thus equally, if not more, important as the rational design of polymer nanocomposites. Novel strategies for mass production of polymer nanocomposites films are also highly desirable for the application of nanocomposite dielectrics. The current melt-casting and stretching technique could not be readily applied to the fabrication of polymer nanocomposite films, due to the fact that the incorporated

nanofillers as well as the structural imperfections introduced, may act as hot spot for local stress concentration and result in cracks during the stretching process. Hot-pressing techniques could eliminate the pores or voids in composites and may hold the promise for roll-to-roll fabrication of nanocomposite films.

References

1. Chu B, Zhou X, Ren K et al (2006) A dielectric polymer with high electric energy density and fast discharge speed. Science 313(5785):334–336
2. Cao Y, Irwin PC, Younsi K (2004) The future of nanodielectrics in the electrical power industry. IEEE Trans Dielectr Electr Insul 11(5):797–807
3. Jackson JD (1999) Classical electrodynamics. Wiley, New York
4. Reed CW, Cichanowski SW (1994) The fundamentals of aging in HV polymer-film capacitors. IEEE Trans Dielectr Electr Insul 1(5):904–922
5. Rabuffi M, Picci G (2002) Status quo and future prospects for metallized polypropylene energy storage capacitors. IEEE Trans Plasma Sci 30(5):1939–1942
6. Dang ZM, Yuan JK, Yao SH et al (2013) Flexible nanodielectric materials with high permittivity for power energy storage. Adv Mater 25:6335–6365
7. Li JY (2003) Exchange coupling in P(VDF-TrFE) copolymer based all-organic composites with giant electrostriction. Phys Rev Lett 90:2176–2201
8. Lewis TJ (2005) Interfaces nanometric dielectrics. J Phys D Appl Phys 38:202–212
9. Hanemann T, Vinga Szabo D (2010) Polymer-nanoparticle composites from synthesis to modern applications. Materials 3:3468–3517
10. Tanaka T, Kozako M, Fuse N et al (2005) Proposal of a multi-core model for polymer nanocomposite dielectrics. IEEE Trans Dielectr Electr Insul 12:669–681
11. Lewis TJ (2004) Interfaces are the dominant feature of dielectrics at the nanometric level. IEEE Trans Dielectr Electr Insul 11:739–753
12. O'Konski CT (1960) Electrical properties of macromolecules V theory of ionic polarisation in polyelectrolytes. J Phys Chem 64:605–619
13. Chew CW, Sen PN (1982) Dielectric enhancement due to electrochemical double layer: thin double layer approximation. J Chem Phys 77:4683–4693
14. Lopez-Pamies O, Goudarzi T, Meddeb AB et al (2014) Extreme enhancement and reduction of the dielectric response of polymer nanoparticulate composites via interphasial charges. Appl Phys Lett 104:2429–2504
15. Li JY, Ducharme S (2007) Electric energy density of dielectric nanocomposites. Appl Phys Lett 90:1329–1401
16. Rao Y, Wong CP (2004) Material characterization of a high-dielectric-constant polymer-ceramic composite for embedded capacitor for RF applications. J Appl Polym Sci 92:2228–2231
17. Kim P, Jones SC, Hotchkiss PJ et al (2007) Phosphonic acid-modified barium titanate polymer nanocomposites with high permittivity and dielectric strength. Adv Mater 19:1001–1005
18. Kim P, Doss M, Tillotson JP et al (2009) High energy density nanocomposites based on surface-modified $BaTiO_3$ and a ferroelectric polymer. ACS Nano 3:2581–2592
19. Zhou T, Zha JW, Cui RY et al (2011) Improving dielectric properties of $BaTiO_3$/ferroelectric polymer composites by employing surface hydroxylated $BaTiO_3$ nanoparticles. ACS Appl Mater Interfaces 3:2184–2188
20. Liu SH, Zhai JW, Wang JW et al (2014) Enhanced energy storage density in poly(vinylidene fluoride) nanocomposites by a small loading of suface-hydroxylated $Ba_{0.6}Sr_{0.4}TiO_3$ nanofibers. ACS Appl Mater Interfaces 6:1533–1540

21. Lee HS, Dellatore SM, Miller WM et al (2007) Mussel-inspired surface chemistry for multifunctional coatings. Science 318:426–430
22. Song Y, Shen Y, Liu HY et al (2012) Improving the dielectric constants and breakdown strength of polymer composites: effects of the shape of the $BaTiO_3$ nanoinclusions, surface modification and polymer matrix. J Mater Chem 22:16491–16498
23. Song Y, Shen Y, Liu H et al (2011) Enhanced dielectric and ferroelectric properties induced by dopamine-modified $BaTiO_3$ nanofibers in flexible poly(vinylidene fluoride-trifluoroethylene) nanocomposites. J Mater Chem 22:8063–8068
24. Xie L, Huang XY, Wu C et al (2011) Core–shell structured poly(methyl methacrylate)/$BaTiO_3$ nanocomposites prepared by in situ atom transfer radical polymerization: a route to high dielectric constant materials with the inherent low loss of the base polymer. J Mater Chem 21:5897–5906
25. Yang K, Huang XY, Huang YH et al (2013) Fluoro-polymer@$BaTiO_3$ hybrid nanoparticles prepared via RAFT polymerization: toward ferroelectric polymer nanocomposites with high dielectric constant and low dielectric loss for energy storage application. Chem Mater 25:2327–2338
26. Li JJ, Khanchaitit P, Han K et al (2010) New route toward high-energy-density nanocomposites based on chain-end functionalized ferroelectric polymers. Chem Mater 22:5350–5357
27. Jung HM, Kang JH, Yang SY et al (2010) Barium titanate nanoparticles with diblock copolymer shielding layers for high-energy density nanocomposites. Chem Mater 22:450–456
28. Siddabattuni S, Schuman TP, Dogan F (2013) Dielectric properties of polymer–particle nanocomposites influenced by electronic nature of filler surfaces. ACS Appl Mater Interfaces 5:1917–1927
29. Li Z, Fredin LA, Tewari P et al (2010) In-situ catalytic encapsulation of core–shell nanoparticles having variable shell thickness: dielectric and energy storage properties of high-permittivity metal oxide nanocomposites. Chem Mater 22:5154–5164
30. Guo N, DiBenedetto SA, Tewari P et al (2010) Nanoparticle, size, shape, and interfacial effects on leakage current density, permittivity, and breakdown strength of metal oxide-polyolefin nanocomposites: experiment and theory. Chem Mater 22:1567–1578
31. Fredin LA, Li Z, Ratner MA et al (2013) Substantial recoverable energy storage in percolative metallic aluminum-polypropylene nanocomposites. Adv Funct Mater 23:2650–2669
32. Fredin LA, Li Z, Ratner MA et al (2012) Enhanced energy storage and suppressed dielectric loss in oxide core–shell–polyolefin nanocomposites by moderating internal surface area and increasing shell thickness. Adv Mater 24:5946–5953
33. Li JJ, Seok SI, Chu BJ et al (2009) Nanocomposites of ferroelectric polymers with TiO_2 nanoparticles exhibiting significantly enhanced electrical energy density. Adv Mater 21:217–221
34. Tomer V, Randall CA, Polizos G et al (2008) High- and low-field dielectric characteristics of dielectrophoretically aligned ceramic/polymer nanocomposites. J Appl Phys 103:34–115
35. Nan C-W (1993) Physics of inhomogeneous inorganic materials. Prog Mater Sci 37:1–116
36. Tang HX, Lin YR, Sodano HA (2012) Enhanced energy storage in nanocomposite capacitors through aligned PZT nanowires by uniaxial strain assembly. Adv Energy Mater 2:469–476
37. Wang YU, Tan DQ (2011) Computational study of filler microstructure and effective property relations in dielectric composites. J Appl Phys 110:1041–1102
38. Wang YU, Tan DQ, Krahn J (2011) Computational study of dielectric composites with core–shell filler particles. J Appl Phys 110:1044–1103
39. Tomer V, Randall CA (2008) High field dielectric properties of anisotropic polymer-ceramic composites. J Appl Phys 104:1074–1106
40. Song Y, Shen Y, Hu PH et al (2012) Significant enhancement in energy density of polymer composites induced by dopamine-modified $Ba_{0.6}Sr_{0.4}TiO_3$ nanofibers. Appl Phys Lett 101:1529–1604

41. Hu PH, Song Y, Liu HY et al (2013) Largely enhanced energy density inflexible P (VDF-TrFE) nanocomposites by surface-modified electrospun BaSrTiO$_3$ fibers. J Mater Chem A 1:1688–1693
42. Tomer V, Polizos G, Randall CA et al (2011) Polyethylene nanocomposite dielectrics: Implications of nanofiller orientation on high field properties and energy storage. J Appl Phys 109:1074–1113
43. Fillery SP, Koerner H, Drummy L et al (2012) Nanolaminates: increasing dielectric breakdown strength of composites. ACS Appl Mater Interfaces 4:1388–1396
44. Li WJ, Meng QJ, Zheng YS et al (2010) Electric energy storage properties of poly(vinylidene fluoride). Appl Phys Lett 96:192905
45. Tang HX, Sodano HA (2013) Ultra high energy density nanocomposite capacitors with fast discharge using Ba$_{0.2}$Sr$_{0.8}$TiO$_3$ nanowires. Nano Lett 13:1373–1379
46. Tomer V, Manias E, Randall CA et al (2011) High field properties and energy storage in nanocomposite dielectrics of poly(vinylidene fluoride-hexafluoropropylene). J Appl Phys 110:1044–1107
47. Polizos G, Tomer V, Manias E et al (2010) Epoxy-based nanocomposites for electrical energy storage II: nanocomposites with nanofillers of reactive montmorillonite covalently-bonded with barium titanate. J Appl Phys 108:1074–1117
48. Li Q, Han K, Gadinski MR et al (2014) High energy and power density capacitors from solution-processed ternary ferroelectric polymer nanocomposites. Adv Mater 26(36): 6244–6249
49. Hu PH, Shen Y, Guan YH et al (2014) Topological-structure modulated polymer nanocomposites exhibiting highly enhanced dielectric strength and energy density. Adv Funct Mater 24:3172–3178
50. Zhang X, Shen Y, Xu B et al (2016) Giant energy density and improved discharge efficiency of solution-processed polymer nanocomposites for dielectric energy storage. Adv Mater 28:2055–2062
51. Zhang X, Shen Y, Zhang QH et al (2015) Ultrahigh energy density of polymer nanocomposites containing TiO$_2$@BaTiO$_3$ nanofibers by atomic scale interface-engineering. Adv Mater 27:819–825
52. Zhang X, Chen W, Wang J, Shen Y, Gu L, Lin Y, Nan C-W (2014) Hierarchical interfaces induce high dielectric permittivity in nanocomposites containing TiO @BaTiO nanofibers. Nanoscale 6(12):6701–6709
53. Li Q, Chen L, Gadinski MR, Zhang S, Zhang G, Li H, Haque A, Chen L-Q, Jackson T, Wang Q (2015) Flexible high-temperature dielectric materials from polymer nanocomposites. Nature 523(7562):576–579
54. Li Q, Zhang G, Liu F, Han K, Gadinski MR, Xiong C, Wang Q (2015) Solution-processed ferroelectric terpolymer nanocomposites with high breakdown strength and energy density utilizing boron nitride nanosheets. Energ Environ Sci 8(3):922–931

Part III
Nanostructured Materials for Energy Conversion

Chapter 13
Flexible Piezoelectric and Pyroelectric Polymers and Nanocomposites for Energy Harvesting Applications

Chaoying Wan and Christopher Rhys Bowen

Abstract Ferroelectric polymers are promising functional materials for energy harvesting applications, given their low stiffness, high flexibility, toughness, ease of modification to tailor properties, processability and low density. This chapter provides detailed description of the molecular structure, polymorphs and properties of ferroelectric vinylidene fluoride (VDF)-based fluoropolymers and related nanocomposites. The nature of the ferroelectric crystalline phase plays a key role in the piezo- and pyroelectric properties of the polymer, various methods to increase the content of the polar ferroelectric polymorphs in the polymers are discussed, such as copolymerization, addition of nanoparticles, nanoconfinement, electrospinning, and post-treatment.

13.1 Piezo- and Pyroelectric Polymers

Electroactive polymers have a number of obvious advantages over ferroelectric and piezoelectric ceramics in specific applications in terms of their ease of processing at low temperatures, low density, low mechanical stiffness, flexibility and mechanical robustness/toughness, such as high strains to failure. These materials have found diverse applications in smart and multifunctional systems such as transducers, sensors, actuators, energy harvesting and storage devices, in the forms of fibres, foams, thin films, textiles and coatings. Ferroelectric polymers that contain net molecular dipole moments of their macromolecular structures are of interest as materials for energy harvesting and storage applications as a result of their high

C. Wan (✉)
Warwick Manufacturing Group, International Institute for Nanocomposites
Manufacturing (IINM), University of Warwick, Coventry CV4 7AL, UK
e-mail: chaoying.wan@warwick.ac.uk

C.R. Bowen (✉)
Department of Mechanical Engineering, Materials and Structures Centre,
University of Bath, Bath BA2 7AY, UK
e-mail: c.r.bowen@bath.ac.uk

537

levels of polarization. The molecular dipoles in these materials are spontaneously polarized, and they can be oriented by the application of an electric field, temperature variation, mechanical stretching, magnetic field and by interactions with nanoparticles [1]; thereby leading to a piezo- and pyroelectric response of the polymer. Polarized and electroactive polymers of interest include vinylidene fluoride (VDF)-based fluoropolymers, odd-numbered nylon, poly-L-lactide, polyurethane and liquid crystal elastomers. The electroactive performance of these materials is highly dependent on their macromolecular structures, i.e., the crystalline structure, chain conformation, dipole orientation in the crystalline regions towards the direction of the applied electrical poling field [1, 2], processing conditions and post-treatment methods that are applied.

Compared to ferroelectric ceramics, electroactive polymers often have a lower permittivity and lower piezoelectric coefficients. As a result, significant effort has been undertaken to enhance the dielectric properties and piezoelectric coefficients of the polymers, and the approaches employed include modifying the molecular structure, forming composites, controlling processing conditions and posttreatment methods; this includes mechanical stretching and electrical poling. In this chapter, we will discuss the latest research progress in strategies to enhance the piezo- and pyroelectric properties of electroactive polymers, in particular poly vinylidene fluoride (PVDF) and its copolymers with a particular emphasis on energy harvesting applications. For energy harvesting or scavenging applications, a variety of properties is of interest such as the relative permittivity (dielectric constant), d_{ij} piezoelectric coefficients (such as the d_{33} and d_{31} coefficients) to determine the charge generated due to an applied mechanical load and the pyroelectric coefficient (p) to determine the charge generated due to a temperature fluctuation. To achieve a piezoelectric and pyroelectric response, there is also a need to readily polarize the material, therefore the remanent polarization (P_r) and coercive field (E_c) are also of interest. The ability to tailor these properties for potential harvesting applications will be described in this chapter.

13.1.1 Polyvinylidene Fluoride (PVDF) and Polymorphs

PVDF is a thermoplastic semicrystalline polymer and is one of the most important ferroelectric polymers due to its unique molecular structure and crystalline forms. The PVDF homopolymer contains 59.4 wt% fluorine and 3 wt% hydrogen [1], and the presence of fluorine atoms with large van der Waals radius (1.35 Å, vs. hydrogen 1.2 Å) and electronegativity in the polymer chains [$-CH_2-CF_2-$] induces a dipole moment perpendicular to the chain in each monomer unit [2, 3]. PVDF has approximately 50% crystallinity and exhibits five different polymorphs: α (phase II), β (phase I), γ (phase III), δ and ε, which are related to the molecular chain conformations; Fig. 13.1 shows the α, β and γ phases [4]. The α-crystal phase is hexagonal, with aligned polymer chains antiparallel to each other, in the conformation of trans-gauche-trans-gauche′ (TGTG′) [4]. The β-crystal is orthorhombic

Fig. 13.1 Three α, β and γ primary polymorphic crystalline phases of PVDF (Reproduced from Ref. [4] with kind permission of © 2009 American Chemical Society)
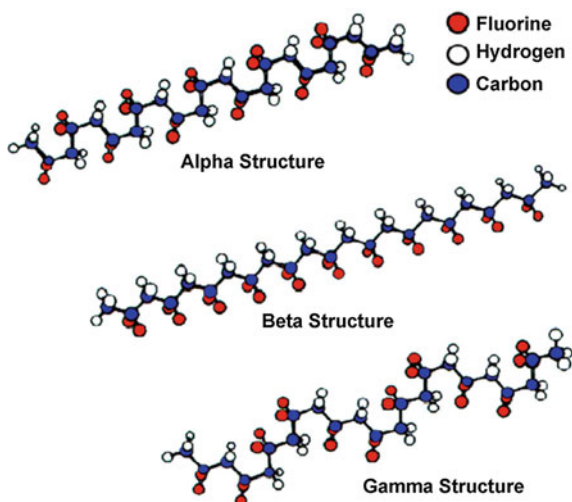
and has an all-trans planar zigzag conformation with their dipoles parallel to the *b*-axis, which contribute to the highest dipolar moment per unit cell (8×10^{-30} C m) [5]. The phase transition from the ferroelectric β-phase to paraelectric α-phase is defined as Curie transition or Curie temperature (T_c), which is highly dependent on the polymer chain structure, processing condition and posttreatment. A higher β-phase content in PVDF, therefore, leads to higher piezo-, pyro- and ferroelectric properties [1, 2, 6].

A variety of methods has been developed to increase the fraction of the ferroelectric β-phase content in PVDF, including copolymerization with a second monomer, blending with other polymers, forming composites with nucleating agents or nanofillers, tailoring processing conditions, mechanical stretching and electrical poling. The nonpolar α-phase of PVDF is kinetically favourable and can readily form on crystallization from the melt at moderate or high levels of supercooling [7] (<160 °C), or from solution crystallization of a xylene/acetone mixture, monochlorobenzene or dimethylformamide (DMF) solutions [8]. The polar β-phase is the most thermodynamically stable form and can only be induced to form under special conditions. These include (i) melt crystallization at high pressures [9] or at very high cooling rates [7, 10], (ii) solution casting from highly polar solutions, such as hexamethyl phosphoramide [11], (iii) vapour deposition of oligomeric PVDF [12, 13] or (iv) by blending with negatively charged nanoparticles. The α-phase can transform to the β-phase by mechanical stretching and electrically poling at electric fields as high as 100 kV mm^{-1} under elevated temperature of 80–165 °C [1]. From first-principles simulations and a generalized solid-state nudged elastic band method [14], it has been suggested that the electric field induces the α-phase to transform to the polar δ-phase and then to the β-phase. This is shown in Fig. 13.2 where the α-phase forms from the melt and progressively transforms to the β-phase at high electric fields; the impact of cold drawing and annealing at high
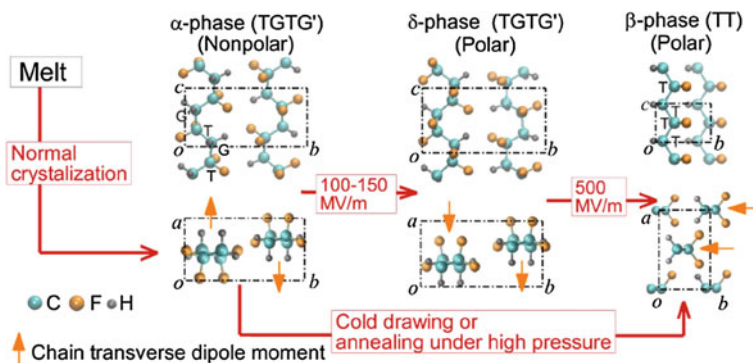
Fig. 13.2 Electric field-induced phase transitions of PVDF. The unit cells are shown as viewed from the *ab* and *bc* planes. The transverse dipole moment of each polymer chain is shown using the *orange arrow* that points from the negatively charged fluorine atoms to the positively charged hydrogen atoms (Reproduced from Ref. [15] with kind permission of © 2016 AIP) (Color figure online)

temperature to form the β-phase is also shown [15]. By stretching blown films of PVDF biaxially or uniaxially [16], the highest content of highly oriented β-phase, 86.5%, was achieved during drawing at 87 °C, with a drawing rate of 50 mm min^{-1} for a stretch ratio of 6.5. At this level of stretch ratio, a maximum stress piezo-electric d_{33} coefficient (charge per unit force) of 33 pC N^{-1} was obtained. Other studies have shown that the β-phase is more favourably formed in the temperature range of 70–100 °C and at a stretch ratio of approximately 3–5 [17]. Higher stretching temperatures reduce the efficiency of the phase conversion, and conversion to the β-phase only takes place for stretch ratios above 5. It has also been shown that annealing of the PVDF film at 90 °C transforms the γ-phase to the β-phase, and this is reflected as a decreased local relative permittivity [18].

In recent years, nanofabrication technologies, such as electrospinning, nanoimprint lithography [19] and the horizontal Langmuir–Schaefer technique [20] have attracted significant attention in producing nonvolatile memory and flexible piezoelectric sensors. In particular, electrospinning has the potential to produce a high β-polymorph content in PVDF via a one-step process that avoids additional processing stages such as mechanical stretching or electrical poling; details of this process will be described later in this chapter. In the following sections, the latest research progress on the effects of copolymerization, processing condition, post-treatment, addition of nanoparticles and electrospinning on the piezo- and pyro-electric properties of PVDF is discussed.

13.1.2 Copolymerization and Phase Transition

Copolymerization is an effective method to tune the polymorph structure and phase transition behaviour of PVDF. The co-monomer type and composition ratios
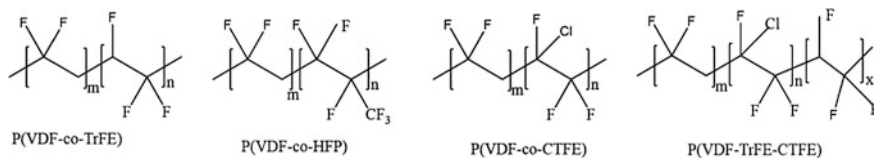
Fig. 13.3 Molecular structures of **a** P(VDF-co-TrFE), **b** P(VDF-co-HFP), **c** P(VDF-co-CTFE) and **d** P(VDF-TrFE-CTFE)

determine the crystalline structures and degree of crystallinity which directly affect the ferro-, piezo- and pyroelectric properties of the copolymers. A variety of VDF copolymers and terpolymers has been synthesized by incorporation of tri-fluoroethylene (TrFE), chlorotrifluoroethylene (CTFE) or hexafluoropropylene (HEP) co-monomer. The molecular structures of these commonly studied PVDF copolymers are shown in Fig. 13.3.

The introduction of a bulky co-monomer to PVDF chains generally facilitates the formation of the ferroelectric β-phase due to a steric hindrance effect [21]. For example, in P(VDF-co-TrFE), Fig. 13.3a, the introduction of a third fluoride atom in the TrFE [–CHF–CF$_2$–] co-monomer unit forces the polymer chains to align in an extended planar zigzag all-trans conformation below the Curie temperature, when the TrFE content is over 11 mol% [22]. When the TrFE is above 20 mol%, the formation of β-phase is independent of the processing conditions and electric poling [23]. For P(VDF-co-HFP), see Fig. 13.3b, the presence of bulky CF$_3$ in the PVDF chains provides more space to allow the dipoles to reorient. With a HFP content of 5 mol%, the highest value of remanent polarization ($P_r \sim 80$ m Cm^{-2}) was achieved for solvent-cast films, resulting in a higher piezoelectric coefficient d_{31} of 30 pC N^{-1} as compared to those of PVDF homopolymers [24]. In the case of P(VDF-co-CTFE) copolymer, Fig. 13.3c, with a CTFE content lower than 16 mol % [4], the piezoelectric constant d_{33} was as high as 140 pC N^{-1} [25]. Therefore, the advantages of PVDF copolymers over PVDF are that the β-crystalline phase is always present regardless of the processing method, which can be attributed to the steric hindrance of the co-monomer that expands the interchain distance and reduces the activation energy for the α-β phase transition [2, 26]. Further annealing, mechanical stretching or electrical poling process can increase the crystallinity and align the CF$_2$ dipoles, which leads to higher piezo- and pyroelectricity than PVDF homopolymers. On introducing a chloro-containing third monomer termonomer, such as chlorotrifluoroethylene (CTFE) to P(VDF-co-TrFE) copolymers, as in Fig. 13.3d, with over 20 mol% of TrFE, some of the ferroelectric β-phase trans-forms to the γ-phase when the termonomer units reach 7 mol% [27]. As a result of the mixed ferroelectric and paraelectric phase, the T_c was reduced to almost ambient temperature; these terpolymers exhibit a high dielectric constant (>70), slim polarization hysteresis and ferroelectric relaxor behaviour making it of interest for energy storage applications.

13.1.3 Processing Conditions and Influence on Curie Temperature

The effects of processing conditions, annealing, mechanical drawing, electrical poling, pressure [28], thermal history and addition of inorganic particles on the generation and orientation of the β-phase are now discussed. As discussed, the paraelectric α-crystal phase is generally formed in PVDF upon cooling from the melt or from solution-cast films, see Fig. 13.2. A mixture of α-, β- or γ-phase crystals is generally observed in PVDF copolymers when crystallized from the melt or solution under different conditions. The conversion of the ferroelecric β-crystalline phase to the paraelctric α-crystalline phase takes place thermally when the material is heated above the Curie temperature (T_c), which accordingly defines the upper use temperature of the copolymers for piezoelectric and pyroelectric applications such as energy harvesting. The T_c of β-PVDF is approximately 170 °C [29] and the introduction of a co-monomer to the polymer chains can restrict the degree of crystal growth down to nanosized crystalline domains [15, 27], which accordingly increases the interchain distance and dipolar mobility and leads to a decreased T_c. For example, a T_c = 105 °C was measured for a copolymer with a 70/30 composition ratio [30]. The T_c of PVDF copolymers relies on the chemical compositions of the copolymers and is highly dependent on the polymer annealing conditions. Generally, a higher annealing or crystallization temperature and/or longer annealing time above T_c yields lamellar thickening and better crystalline packing, less defects and higher crystallinity of the paraelectric phase. These factors result in an increase of the T_m and decrease the T_c [31]. When annealing the polymer in the β-phase state, an increase in the T_c is expected.

As an example of the influence of such processing conditions, for a solution-cast P(VDF-co-TrFE) (81/19) copolymer, annealing at 120 °C (close to the T_c) for 16 h increased the T_c to 128 °C but no change of T_m was observed. In contrast, the T_c increased to 125 °C and T_m increased to 151 °C after annealing at 140 °C for 16 h [22]. The changes of T_c were associated with changes in the Gibbs free energies in the orthorhombic β-phase and hexagonal α-phase during annealing. Annealing of the material below its T_c favours the removal of gauche defects in the ferroelectric phase, which can increase the degree of crystallinity and β-phase concentration. Annealing above the T_c facilitates the transformation of more paraelectric phase into the β-phase. The β-phase concentration in the as-cast film was determined to be approximately 75%, and it increased to 93% after annealing at 130 °C for 2 h; see Fig. 13.4. The increase in β-phase concentration correspondingly increased the d_{33} piezoelectric coefficient from an original value of 13–18 pC N^{-1} after 4 h of annealing, see Fig. 13.4a, with a threefold increase in elastic modulus and tenfold reduction of oxygen permeability [22].

The annealing treatment that is applied critically affects both T_c and T_m. Copolymers with 50–80% VDF show a T_c in the range of 70–140 °C [32], which is absent in pure PVDF. In the temperature range between T_c and T_m, the polymer chains move more freely to reorganize into a higher degree of crystallinity.
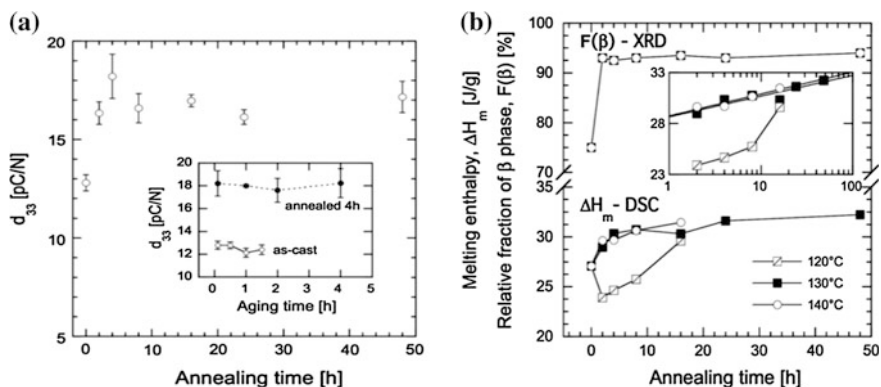
Fig. 13.4 **a** Piezoelectric d_{33} coefficient of solvent-cast P(VDF-co-TrFE) films as a function of annealing time at 130 °C. The *inset* shows the d_{33} coefficient of the copolymer, as-cast (*open symbols*) and annealed 4 h at 130 °C (*black symbols*), during ageing at room temperature. **b** Melting enthalpy of solvent-cast P(VDF-co-TrFE) films as a function of annealing time at 120, 130 and 140 °C, and relative fraction of crystalline β-phase as a function of annealing time at 130 °C. The *inset* shows ΔH_m versus annealing time in logarithmic scale (Reproduced from Ref. [22] with kind permission of © 2014 Wiley-VCH)

Generally, annealing at temperature above T_m but below T_m can increase the degree of crystallinity and decreases T_c [32, 33]. Solution-cast P(VDF-co-TrFE) (72/28) thin films were annealed at 120 °C for 3 h (above T_c, but below T_m) led to a preferential chain orientation that was aligned parallel to the substrate surface with higher degree of crystallinity, and dipole alignment upon electrical poling. These factors lead to a large permanent polarization in the thin films, a remanent polarization (P_r) = 7.8 μC cm^{-2}, and coercive field (E_c) of 0.75 MV cm^{-1} for a 100-nm-thick film [31]. Therefore, to achieve high piezoelectric coefficients, it is essential to control the annealing procedures through the Curie transition temperature [32].

13.1.4 Dielectric Displacement (D)–Field (E) Properties

The ferroelectric behaviour of PVDF-based materials has been investigated as a function of temperature and poling frequency, see Fig. 13.5 [34]. For a uniaxial-stretched P(VDF-co-TrFE) (50/50) film, paraelectric behaviour was obtained due to the nucleation of electric field-induced ferroelectric nanodomains inside the paraelectric phase matrix when it was poled at a high poling frequency (e.g., 1000 Hz) and 100 °C (above the T_c of 64 °C). These ferroelectric nanodomains were highly reversible and could be rapidly depolarized on removal of the poling field, see Fig. 13.5c. At an intermediate poling frequency (10 Hz) and 100 °C, an 'antiferroelectric-like' behaviour was observed, which could be attributed to the competition between depolarization and polarization fields upon reverse
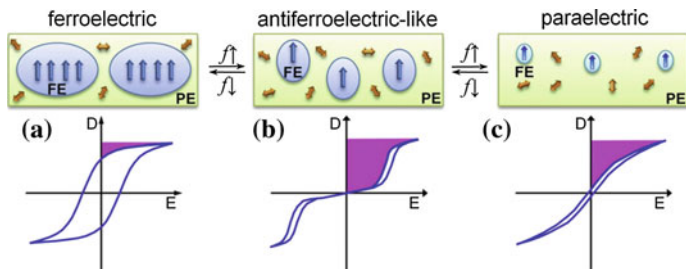
Fig. 13.5 Schematic illustration dielectric displacement (D)–electric field (E) loops and domain structure of **a** normal ferroelectric, **b** antiferroelectric-like and **c** paraelectric behaviours of the high-temperature PE phase in P(VDF-co-TrFE) under different poling frequencies (f) (Reproduced from Ref. [34] with kind permission of © 2012 Elsevier)

poling, see Fig. 13.5b. Finally, at a low poling frequency (e.g., 1 Hz) and 100 °C, a normal ferroelectric behaviour with more rectangular hysteresis loops was observed since the small, reversible ferroelectric domains had time to grow into large irreversible ones, see Fig. 13.5a. For energy harvesting applications, the ability to pole the material and achieve a high remanent polarization (P_r) which is modulated with stress or temperature is of interest for piezo- or pyroelectric harvesting, as in Fig. 13.5a. For energy storage applications, an antiferroelectric-like (Fig. 13.5b) or paraelectric (Fig. 13.5c) behaviour is more desirable due to the ability to store and recover energy, as given by the larger areas in the dielectric displacement (D)– electric field (E); these are indicated by the purple areas in Fig. 13.5.

A β-phase fraction ($F_{(\beta)}$) of 0.74 and an overall crystallinity of 42.6% was achieved for melt-quenched stretched PVDF films [35]. A higher $F_{(\beta)}$ of 82% and a $d_{33} = 21$ pC N^{-1} was obtained by stretching PVDF films that were solution-cast from N,N-dimethylacetamide (DMAc) solutions [36]. It is reported that an overall crystallinity of 52–60% with $F_{(\beta)} = 0.53$ for PVDF films that were prepared by spin coating from an acetone/DMF solution and subsequently stretched uniaxially [37]. The pyroelectricity of a ferroelectric VDF-oligomer [$CF_3(CH_2CF_2)_{17}I$]-evaporated film was investigated utilizing a low-frequency sinusoidal heat source [13]. The pyroelectric coefficient (p) of the 600-nm-thick VDF oligomer film was estimated to be −68 μC m^{-2} K at 37 °C whose value is larger than those reported for ferroelectric polymers. The VDF oligomer is, therefore, a promising material for application in pyroelectric thin film infrared detectors and pyroelectric harvesting applications.

A simple two-step annealing scheme [38] was applied for the fabrication of stable nonvolatile PVDF thin film memory devices. This consisted of the crystallization of ferroelectric γ-phase during the first step and enhancement of the PVDF film dense morphology during the second step. The PVDF films also exhibit a coercive field of 113 MV m^{-1} and a ferroelectric polarization of 5.4 μC cm^{-2}.

Nanoconfinement also facilitates polar β-phase formation. PVDF nanowires can be crystallized into the β-phase due to nanoporous confinement (200 nm channel), with well-aligned polymer chains and crystallites arranged perpendicularly to the

channel walls. PVDF-templated nanowires show a remanent polarization higher than the saturation one (P_r = 19 μC cm^{-2} vs. P_s = 9 μC cm^{-2}) [39]. This is attributed to the combination of the polarization of the ferroelectric polymer with the charge derived from the superposition of leakage current to the displacement current.

In contrast, thin films of PVDF without any poling stage did not show any ferroelectric behaviour. P(VDF-co-TrFE)(70/30)-templated nanowires exhibit a remanent polarization of 7.4 μC cm^{-2} and a saturation polarization of 9.6 μC cm^{-2}, values that are similar with respect to the as-prepared P(VDF-co-TrFE) thin film saturation polarization (P_s), remanent polarization (P_r) and coercive field (E_c). Maximum d_{33} values of −8.2 and −6.5 pm V^{-1} were obtained for the P(VDF-co-TrFE) and PVDF nanowires. Non-poled P(VDF-co-TrFE) thin films exhibited a d_{33} of −15 pC N^{-1} in comparison with the poled films and bulk materials of both P(VDF-co-TrFE) and PVDF were in the range of −20 and −30 pC N^{-1} [39].

For a P(VDF-co-TrFE) copolymer with a composition ratio of 72.2/27.8 mol% [30], the polymer chain length affects the conformations. It was found that a short polymer chain length corresponds to a higher crystal size and leads to a higher β-phase content; the d_{33} piezoelectric coefficient was enhanced by decreasing the molecular weight (M_w) of the copolymer. A maximum d_{33} value of −50 pC N^{-1} was achieved for the composition 72.2/27.8 mol% with a molecular weight of 470 kg mol^{-1}.

Interestingly, the pyroelectric properties were enhanced for the lowest polymer crystalline grain size studied. A pyroelectric coefficient of 37.8 μC m^{-2} K was obtained with the composition 71/29 mol% with a molecular weight of 505 kg mol^{-1}. These differences may be related to how the polarization changes with either stress (influencing the piezoelectric coefficient) or temperature (influencing the pyroelectric coefficient).

PVDF films were produced by varying the quenching temperature [40]. Nearly, 100% of β-phase crystals formed at −20 °C, and the β-phase was self-aligned and polarized, with a high d_{33} piezoelectric coefficient of up to −49.6 pm V^{-1} (or pC N^{-1}). The self-polarized β-phase and high piezoelectric coefficient of the PVDF films make them suitable for energy harvesting applications, such as vibration harvesting.

In addition to tailoring the processing conditions and heat treatment conditions, a recent approach to tailor the piezoelectric and pyroelectric properties is to form nanocomposites, and this will be now discussed.

13.2   PVDF Nanocomposites

Polymer-based nanocomposites have attracted intensive interest as high-energy density capacitors with high energy density (U_e), since heterogeneous materials make it possible to combine the high relative permittivity and electrical properties

of nanofillers, such as ferroelectrics, with the high breakdown strength, low dielectric loss and lightweight of polymers. Generally, PVDF and its copolymers only present α-phase ($\sim$0.4%) [41] or a small amount of β-phase when cooled from the melt; as shown in Fig. 13.2. Research has demonstrated that nanoparticles with a negatively charged surface can interact with the positively charged –CH_2 groups, and induces the formation of the more polar β-phase, with fractions up to 100% [42–44], and a high d_{33} piezoelectric coefficient of $\sim$33 pC N^{-1} [45]. The dipole-surface charge interaction model has been found in various PVDF-based composites systems, with additives such as clay, barium titanate ($BaTiO_3$) [46], lead zirconium titanate (PZT) [47], SiO_2 [48] ionic liquids, carbon materials (carbon nanotube, graphene, carbon fibres), metal nanoparticles (nanoparticles of Pd, [49] Ag [50], Pt [51]), metal salts (CuO [52], ZrO_2 [53] TiO_2, Fe_3O_4 [54, 55] $BaFe_{12}O_{19}$ [56], Cerium(III)-N,N-dimethylformamide-bisulphate [Ce(DMF) $(HSO_4)_3$] complex [57]) and conducting polymers. The effect of nanoparticle additions on the structure and piezoelectric properties of PVDF polymers generally depends on their nucleating efficiency, supercooling effect as well as interfacial interactions. Specifically, the nucleating effect of the nanoparticle additions strongly depends on the particle size [46, 52] shape [58], surface chemistry [52], concentration [47], dispersion, interfacial interaction and processing conditions.

For metal and metal salt-filled PVDF composites, it has been shown that 5 wt% of copper can induce the formation of up to 90% of β-phase due to the high interfacial area between the well-dispersed nanoparticle surface and the polymer [52]. Cerium(III)/yttrium(III) nitrate hexahydrate salts (1–30 wt%) [59] induced the formation of β-phase due to the strong ion–dipole interaction through the formation of hydrogen bonds between the water molecules of the salts and the –CF_2 dipoles of the polymer chains, which enhanced the nucleation of polar β-phase to achieve a large permittivity in PVDF films. The Fe_2O_3–Co_3O_4 nanoparticles that formed in situ in the PVDF matrix led to the formation of more β-phase and a higher permittivity in thin films [55]. A 15 mass% SiO_2-loaded PVDF film showed the highest permittivity, which was attributed to the smaller size of SiO_2 nanoparticles and the homogeneous and discrete dispersion of SiO_2 nanoparticles in the PVDF matrix [48]. Furthermore, by adding mesoporous SiO_2 nanorods to a PVDF-co-HFP matrix, the SiO_2 nanorods with its anisotropic rod shape and ordered mesopores doubled the amount of the –OH groups present and increased the intermolecular interactions and enhanced the β-phase content and piezo-/ferroelectric properties of PVDF-co-HFP [60]. $BaTiO_3$ hollow nanospheres [58] with particle sizes of $\approx$20 nm and BET surface area of 297 m^2 g^{-1} were surface treated to enhance their compatibility with PVDF. Both the large specific surface areas and increased surface functionality of the hollow spheres increased the β-phase content and degree of crystallinity at 16 wt% of filler content. The changes in crystallinity lead to a higher relative permittivity ($\varepsilon' \approx 109.6$) and energy density for energy storage ($U_e \approx 21.7$ J cm^{-3}) with a high breakdown strength ($E_b = 3.81 \times 10^3$ kV cm^{-1}) compared to pristine PVDF ($\varepsilon' \approx 11.6$ and $U_e \approx 2.16$ J cm^{-3} at 3.98×10^3 kV cm^{-1}); thereby indicating the benefits of nanoparticle-filled composites. In this way, the nucleation of the ferroelectric β-phase in PVDF was influenced by the geometry

of the fillers through the interface interactions between the local electric field of the filler and PVDF dipoles, such as ion–dipole and dipole–dipole interactions.

Superior ferro- and piezo-electret properties in a self-poled [51], porous hybrid ferroelectretic polymer nanocomposite film were introduced by in situ generation of platinum (Pt) nanoparticles embedded in a P(VDF-co-HFP) matrix. The cooperative functionality between the self-polarized β-phase and the micropores as charge trapping sites to form an electret was achieved using a simple solvent evaporation method. As a consequence, the resulting films exhibited a superior electrical square-shaped hysteresis loop with a large remanent polarization ($P_r \approx 61.7$ μC cm^{-2}), piezoelectric charge coefficient ($d_{33} \sim -686$ pC N^{-1}) and ultrahigh dielectric properties ($\varepsilon' = 2678$, tan$\delta = 0.79$ at 1 kHz). A new type of 'ferroelectretic' nanogenerator (FTNG) was fabricated using a flexible hybrid nanocomposite film that converted the applied mechanical energy into electrical energy with a compressive stress (e.g., by actuating with a human finger). An 18 V open-circuit output voltage with an expected 17.7 μA short-circuit current was generated from the FTNG with a 4 MPa of normal stress amplitude. The high piezoelectric energy conversion efficiency ($\eta_{piezo} \approx 0.2$ %) of the FTNG indicated that the hybrid polymer nanocomposite film was well suited for piezoelectric-based energy harvesters.

13.2.1 Nanoclay-Based Composites

Organoclays have been shown to promote the formation of β-phase of PVDF, while unmodified clay shows no, or little, influence. The solution-casting method [61] can facilitate the dispersion and strengthen the interaction between organoclay with PVDF as compared to melt processing. The effects of nanoclay inclusion on the crystallization behaviour of PVDF depend on the dispersion, exfoliation and interfacial interactions of nanoclay in the PVDF matrix. Ammonium clay shows the best dispersion and phosphonium clay is more efficient in forming the β-phase [41], the highest β-phase fractions, up to $\sim 99\%$, were obtained at 5 wt% of octade-cyltriphenylphosphonium bromide modified clay (28.2 wt% organic content). In comparison, the addition of 5 wt% of unmodified clay leads to only $\sim 23\%$ of β-phase content in the composites. The presence of nanoclay can also act as a nucleating agent and enhance the melting and crystallization temperature of PVDF by 10 and 13 °C, respectively; the relative permittivity of PVDF at 1 Hz was increased from 8 to 13.3 with 5 wt% of unmodified clay addition, while it reached 16.3 with 5 wt% of organoclay [41]. By tuning the surface charge and dispersion of clay in PVDF, the energy density (U_e) of PVDF/clay nanocomposites was increased from 5.34 to 5.91 J cm^{-3} at 1 wt% clay content and the highest energy density could reach 10.2 J cm^{-3}, as compared to the pristine PVDF film [62].

Organically modified clay generally has a good dispersion behaviour and a strong interfacial interaction with PVDF. Exfoliated organoclay nanosheets promote and stabilize the epitaxial growth of the β-phase of PVDF [63, 64] mainly by

the stronger interfacial interactions rather than heterogeneous nucleating effects or a supercooling effect [63]. While the majority of work has been for energy storage applications, the high β-phase content may lead to energy harvesting applications.

13.2.2 Carbon Nanotube-Based Composites

Single-walled carbon nanotubes (SWCNTs) and multi-walled carbon nanotubes (MWCNTs) have been used to modify PVDF and its copolymers. With a solution-mixing method using dimethylacetamide (DMAc) as the solvent [65], pristine MWCNT (diameter of 10–50 nm, length of 4–10 μm) can induce the formation of both the α- and β-phase in PVDF under a sonication treatment, while no β-phase was formed in mechanical mixtures. For SWCNT-filled P (VDF-co-TrFE) composites prepared by solution casting followed by annealing at 70 °C for 38 h [66], the pyroelectric coefficients of the composites were higher than that of the pure P(VDF-co-TrFE) copolymer at room temperature. As a function of temperature, the increase in the pyroelectric coefficients of the composites is more gradual than that of the copolymer, see Fig. 13.6a. This may be due to the interfacial interactions between the SWCNTs and the polymer chains that hinder the mobility of the dipoles at higher temperatures and limit the overall contribution to pyroelectricity. The measured d_{31} values were 25 pC N^{-1}, which is higher than the 20 pC N^{-1} for the pure PVDF-TrFE film with no additions, see Fig. 13.6b.

One of the benefits of the inclusion of nanoparticles into the PVDF is that the crystalline structures of PVDF can be tuned using surface modified particles through melt processing, without an additional need for an annealing or poling treatment. The nucleating efficiency of three types of surface functionalized MWCNTs in β-crystals of PVDF was compared [67]. The contents of the
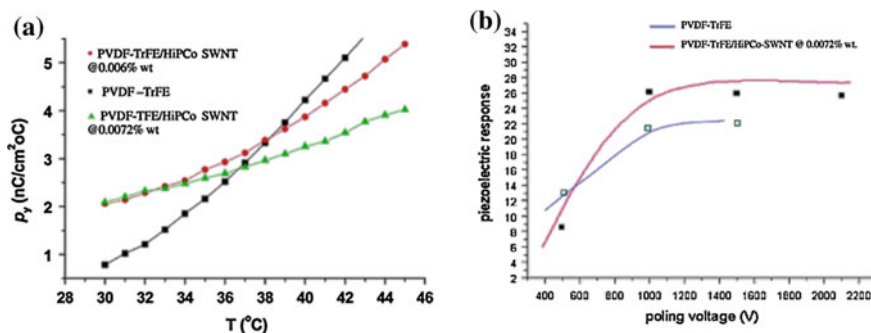
Fig. 13.6 **a** Pyroelectric coefficient for P(VDF-co-TrFE) and its composites containing SWCNTs of approximately 0.01 wt%; **b** piezoelectric response of composites at 0.0072 wt% as compared to the pure copolymer (Reproduced from Ref. [66] with kind permission of © 2004 American Chemical Society)

functional groups on the MWCNTs surface were carboxyl (–COOH ∼3 at.%), amino (–NH$_2$ ∼0.5 at.%) and hydroxyl (–OH ∼1.2 at.%). The work revealed that the amino group functionalized MWCNTs had the highest percentage of β-phase (17.4%) in PVDF [67], followed by those with hydroxyl groups (11.6%) and unmodified MWCNTs (9.4%). The nanocomposites containing carboxyl functionalized MWCNTs had the lowest amount of β-phase (4.7%). It is believed that the combined effects of the dispersion of MWCNTs and the interfacial interactions account for the formation of the β-phase in PVDF; see Fig. 13.7. When NH$_2$-MWCNTs and COOH-MWCNTs were melt blended with PVDF/PMMA blends [68], only the NH$_2$-MWCNTs (1 wt%) favoured the formation of β-crystals, where both the neat blends and COOH-MWCNTs-filled composites show only β-phase after melt mixing. This observation was ascribed to the preferable location of the NH$_2$-MWNTs in the amorphous phases of PVDF and in the interlamellar regions of PVDF/PMMA (70/30).

Therefore, the effects of CNT on the nucleation of β-phase of PVDF are mainly dependent on the surface charge–dipole interactions (surface chemistry), the particle size and concentration, as well as processing conditions (solvent, temperature, annealing, shearing, posttreatment).
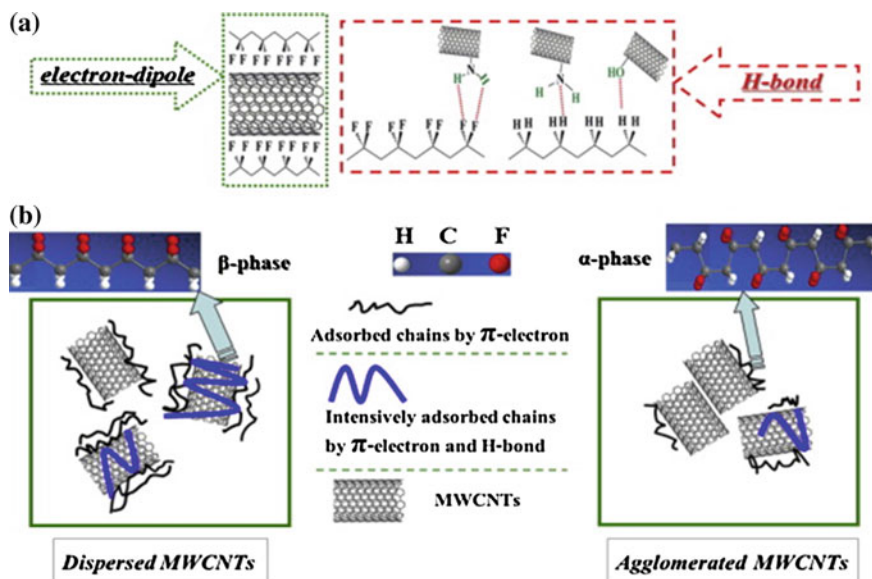
Fig. 13.7 Schematic of the role of CNTs on the formation of the β-phase in PVDF: **a** the chemical bonding between functionalized CNTs and PVDF chains; **b** the adsorbed chains of PVDF on the surface of CNTs influenced by the dispersion of CNTs (Reproduced from Ref. [67] with kind permission of © 2014 Elsevier)

13.2.3 Graphene in PVDF

Graphene and its derivatives are effective nanoparticles for modification of PVDF and its copolymers [69]. The oxygen functional groups on the surface of graphene oxide (GO) or reduced graphene oxide (RGO) can interact with the $-CF_2$ in PVDF via electrostatic interaction and/or hydrogen bonding, thereby benefiting the nucleation of ferroelectric γ- or β-phase [70]. With a solvent-casting route, approximately 80% of the polar ferroelectric β-phase was formed in PVDF/RGO films and this led to an enhanced permittivity and electric polarization [71]. In comparison, a combination of zinc oxide (ZnO), magnetic iron oxide (Fe_3O_4) nanoparticles and RGO reduced the amount of β-phase ($\sim 50\%$) present in the films [71]. The Fe_3O_4 loaded-PVDF composite films exhibit reduced values of both permittivity and electric polarization. A weak magneto-dielectric behaviour was observed in Fe_3O_4-loaded PVDF nanocomposite films at room temperature with a coupling constant $\sim 0.04\%$. However, with a Fe-doped RGO, a 99% of polar γ-phase was formed in PVDF [72], which is ascribed to electrostatic interactions among the $-CH_2$ and $-CF_2$ dipoles of PVDF and the delocalized π-electrons and remaining oxygen functionalities of Fe-doped RGO via ion–dipole and/or hydrogen bonding interactions. For energy harvesting applications, the nanocomposite films generated an open-circuit output voltage of 5.1 V and a short-circuit current up to 0.254 μA on loading with a human finger, thereby acting as a self-poled piezo-electric energy harvester. In addition, the nanocomposite exhibited a higher electrical energy density of ≈ 0.84 J cm^{-3} at an electric field of 537 kV cm^{-1}, which indicates that it is appropriate for energy storage capabilities.

To evaluate the effects of surface functionalization of graphene on the formation of β-phase [73], a thermally reduced exfoliated graphene (EG) with various oxygen-containing functional groups was studied, including fluorination-EG, ozone-EG and PMMA-g-EG. The solution-mixed composites with 0.5 wt% of functionalized EG were characterized by Fourier transform infrared spectroscopy and X-ray diffraction. The β-phase content of PVDF is PMMA-g-EG > ozone-EG > fluorination-EG > EG and was directly related to its specific interaction between the C=O group of PMMA and the CF_2 group of PVDF. In the frequency range of 10^2–10^7 Hz, the relative permittivity of the PVDF composites showed an increase owing to a variation of the carbonyl group (C=O) content. Among all the composites studied, the PVDF/PMMA-g-EG composite has the highest relative permittivity ($\varepsilon' = 18$) and dielectric loss.

An enhanced piezoelectric energy harvesting performance was observed in bilayer films of poled P(VDF-co-TrFE) and GO [74]. The bilayer film exhibited a voltage output of 4 V and power output of 4.41 μW cm^{-2} compared to poled P (VDF-co-TrFE) films alone (voltage output of 1.9 V and power output of 1.77 μW cm^{-2}). The enhanced voltage and power output in the presence of GO film was due to the combined effect of electrostatic contribution from the GO, residual tensile stress, enhanced Young's modulus of the bilayer films and the

presence of space charge at the interface of the P(VDF-co-TrFE) and GO films, arising from the uncompensated polarization of P(VDF-co-TrFE).

## 13.2.4   Electrospinning of PVDF Nanocomposites

Electrospinning has demonstrated many advantages for producing ferroelectric polymeric materials, such as ease of setup, scalability, generation of continuous nanofibres and membranes with high-specific surface area and high porosity. The electrospinning parameters, such as applied voltage and electrode-to-collector distance, solvent polarity, polymer molecular weight and concentration and additives have considerable effects on the fibre morphology and properties. Electrospinning favours the formation of β-phase formation or induces α- to β-phase transformation due to its unique in situ electrical poling and mechanical stretching effects. The β-phase content in polymeric fibres is highly dependent on the solvent type, additives and electrospinning parameters.

For example, when electrospinning PVDF from DMF solution, a β-phase fraction $F_{(\beta)}$ of 0.75 and an overall crystallinity in the range of 49–58% can be produced. By adjusting the electrospinning conditions to narrow down the fibre diameters or increase voltage, more β-phase could be obtained, which is ascribed to the increased elongation and a larger electric field that act as an increased poling field on the polymer jet [75]. When electrospinning PVDF from *N*-methyl-2-pyrrolidinone (NMP)/acetone (5/5 v/v) mixed solution at 16 wt% concentration, PVDF nanofibres with a $F_{(\beta)}$ larger than 95% was collected from a rotating drum at 800 rpm [76]. When electrospinning 20 wt% PVDF from DMF/acetone (6/4 v/v) solution [77] in the presence of 3 wt% of tetrabutylammonium chloride (TBAC) additive, almost pure β-phase fibres were produced. The TBAC salts are believed to facilitate the degree of hydrogen bonding between the contained water molecules and the fluorine atoms of PVDF and hence induce more trans-conformation. In contrast, only the α- and γ-phase was detected in the spin-coated samples from the same solutions. It is believed that the TBAC additive induced local conformational changes, and electrospinning promotes interchain interactions. A higher fraction of β-phase can lead to higher d_{33} piezoelectric coefficients [6], and therefore a higher voltage or charge output in energy harvesting applications, however, the piezoelectric performance of PVDF fibres is also affected by the total dipole moment, i.e., the orientation of dipoles which is closely related to the poling effect.

Given the high-applied electrostatic fields and polymer jet characteristics of the electrospinning process, it is believed that electrospinning can not only facilitate more piezoelectric phase formation but also induce dipole orientation in the polymer fibres. A number of studies have reported flexible, high-output piezoelectric

nanogenerators based on PVDF fibres using near-field electrospinning (NFES) or conventional far-field electrospinning (FFES) processes [78–80]. However, the effects of the electrospinning process on the dipolar orientation of the polymer fibres are still not fully understood and conflicting results have been reported [79, 80]. Using a rotating drum or disc as a fibre collector is believed to exert additional mechanical stretching and promotes the formation and alignment of the c-axis of the β-phase crystallites along the fibre axis [77]. One study [81] reported that rotation of the collecting drum has an important role in the enhancement of β-phase formation, and degree of the orientation of the fibres in the electrospun mats controls the ferroelecric properties. However, another study found that the degree of orientation and the polymorphism behaviour of the fibres did not vary significantly with either the rotating disc speed or the size of the spinneret used [77, 82]. This implies that the formation of the β-phase is likely to be caused by the columbic force imposed by the electric field rather than the mechanical and shear force exerted by the rotation disc collector and spinnerets.

To seek evidence of dipole orientation during electrospinning process, Sun et al. [76] compared electrospun PVDF nanofibres with fibres made by a force-spinning process (mechanical stretching without electrostatic force), in which the nanofibres were produced by an electrostatic force and by centrifugal force. It is found that both fibrous mats showed aligned PVDF fibres with high $F_{(\beta)} > 95\%$. However, the force-spun PVDF fibres did not show piezoelectricity although it has a high β-phase, which is because the mechanical force may only induce the phase transformation but fails to align the ferroelectric dipoles. In comparison, the FFES process can create an electric poling field (~ 1 kV cm^{-1}) on the polymer jet, thus inducing polarization of the crystallites with a preferential orientation along the fibres; see Fig. 13.8.
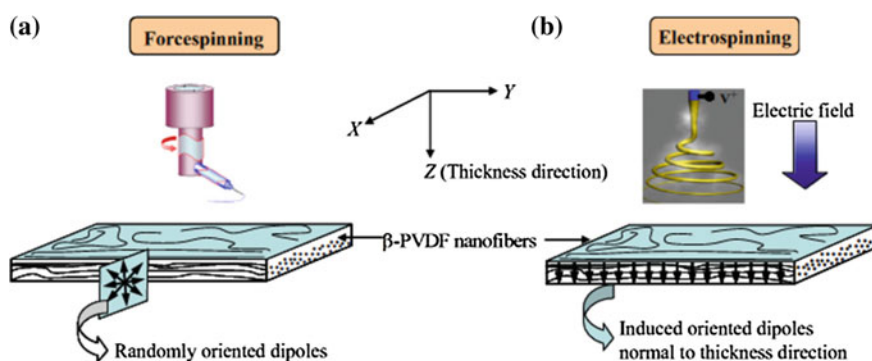
Fig. 13.8 Representation of dipole arrangement in the fibre mats produced by force-spinning (**a**) and electrospinning (**b**) (Reproduced from Ref. [76] with kind permission of © 2015 Springer)

13.3 Conclusions

Ferroelectric polymers are promising functional materials for energy harvesting applications as a result of their mechanical flexibility, high strains to failure, toughness, ease of modification to tailor properties, low temperature processing and low density. This chapter has provided of detailed description of the molecular structure, polymorphs and properties of ferroelectric vinylidene fluoride (VDF)-based fluoropolymers and related nanocomposites. The ferroelectric crystalline phase plays a key role in the piezo- and pyroelectric properties of the polymers, and various methods have been described to increase the content of the polar ferroelectric polymorphs in the polymers. Methods employed include copolymerization, addition of nanoparticles, nanoconfinement, electrospinning and posttreatments. The ability to tailor the structure and phase composition of these ferroelectric polymers provides opportunities to tune their properties for high-performance flexible ferroelectrics for energy harvesting and energy storage applications.

References

1. Nalwa HS (1995) Ferroelectric polymers: chemistry physics, and applications. CRC Press, Boca Raton
2. Martins P, Lopes AC, Lanceros-Mendez S (2014) Electroactive phases of poly(vinylidene fluoride) determination, processing and applications. Prog Polym Sci 39(4):683–706
3. Cui Z, Hassankiadeh NT, Zhuang Y et al (2015) Crystalline polymorphism in poly (vinylidenefluoride) membranes. Prog Polym Sci 51:94–126
4. Ameduri B (2009) From vinylidene fluoride (VDF) to the applications of VDF-containing polymers and copolymers: recent developments and future trends. Chem Rev 109(12):6632–6686
5. Lovinger AJ (1981) Conformational defects and associated molecular motions in crystalline poly(vinylidene fluoride). J Appl Phys 52(10):5934–5938
6. Gomes J, Nunes JS, Sencadas V et al (2010) Influence of the phase content and degree of crystallinity on the piezo- and ferroelectric properties of poly(vinylidene fluoride). Smart Mater Struct 19(6):1065–1110
7. Yamada E, Nishioka A, Suzuki H et al (2009) Effect of blended montomollironite on crystallization of poly(vinylidene fluoride). Polym J 41(5):383–388
8. Gregorio JR, Cestari M (1994) Effect of crystallization temperature on the crystalline phase content and morphology of poly(vinylidene fluoride). J Polym Sci Pol Phys 32(5):859–870
9. Li Y, Tang S, Pan M-W et al (2015) Polymorphic extended-chain and folded-chain crystals in poly(vinylidene fluoride) achieved by combination of high pressure and ion-dipole interaction. Macromolecules 48(23):8565–8573
10. Song D, Yang D, Feng Z (2006) Formation of β-phase microcrystals from the melt of PVF2-PMMA blends induced by quenching. J Mater Sci 25(1):57–64

11. Tao M, Liu F, Ma B et al (2013) Effect of solvent power on PVDF membrane polymorphism during phase inversion. Desalination 316:137–145

12. Ramasundaram S, Yoon S, Kim KJ et al (2009) Crystalline structure and ferroelectric response of poly(vinylidene fluoride)/organically modified silicate thin films prepared by heat controlled spin coating. Macromol Chem Phys 210(11):951–960

13. Kei N, Kenji I, Toshihisa H et al (2003) Pyroelectricity of ferroelectric vinylidene fluoride-oligomer-evaporated thin films. Jpn J Appl Phys 42(11A):13–34

14. Kim WJ, Han MH, Shin Y-H et al (2016) First-Principles study of the α-β phase transition of ferroelectric poly(vinylidene difluoride): observation of multiple transition pathways. J Phys Chem B 120(12):3240–3249

15. Yu Y-J, McGaughey AJH (2016) Energy barriers for dipole moment flipping in PVDF-related ferroelectric polymers. J Chem Phys 144(1):014901

16. Mohammadi B, Yousefi AA, Bellah SM (2007) Effect of tensile strain rate and elongation on crystalline structure and piezoelectric properties of PVDF thin films. Polym Test 26(1):42–50

17. Hsu T-C, Geil PH (1989) Deformation and transformation mechanisms of poly(vinylidene fluoride) (PVF$_2$). J Mater Sci 24(4):1219–1232

18. Hess CM, Rudolph AR, Reid PJ (2015) Imaging the effects of annealing on the polymorphic phases of poly(vinylidene fluoride). J Phys Chem 119(10):4127–4132

19. Shklovsky J, Engel L, Sverdlov Y et al (2012) Nano-imprinting lithography of P (VDF-TrFE-CFE) for flexible freestanding MEMS devices. Microelectron Eng 100:41–46

20. Maji S, Sarkar PK, Aggarwal L et al (2015) Self-oriented [small beta]-crystalline phase in the polyvinylidene fluoride ferroelectric and piezo-sensitive ultrathin Langmuir–Schaefer film. Phys Chem Chem Phys 17(12):8159–8165

21. Chen Y, Chen X, Zhou D et al (2016) Low-temperature crystallization of P(VDF-TrFE-CFE) studied by Flash DSC. Polymer 84:319–327

22. Oliveira F, Leterrier Y, Månson J-A et al (2014) Process influences on the structure, piezoelectric, and gas-barrier properties of PVDF-TrFE copolymer. J Polym Sci Pol Phys 52 (7):496–506

23. Hu Z, Tian M, Nysten B et al (2009) Regular arrays of highly ordered ferroelectric polymer nanostructures for non-volatile low-voltage memories. Nat Mater 8(1):62–67

24. Cao J-H, Zhu B-K, Ji G-L et al (2005) Preparation and characterization of PVDF-HFP microporous flat membranes by supercritical CO_2 induced phase separation. J Membr Sci 266 (1–2):102–109

25. Li Z, Wang Y, Cheng Z-Y (2006) Electromechanical properties of poly(vinylidene-fluoride-chlorotrifluoroethylene) copolymer. Appl Phys Lett 88(6):862–904

26. Furukawa T (1989) Ferroelectric properties of vinylidene fluoride copolymers. Phase Transit A Multi J 18(3–4):143–211

27. Chung TC, Petchsuk A (2002) Synthesis and properties of ferroelectric fluoroterpolymers with curie transition at ambient temperature. Macromollecule 35(20):7678–7684

28. Hattori T, Hikosaka M, Ohigashi H (1996) The crystallization behaviour and phase diagram of extended-chain crystals of poly(vinylidene fluoride) under high pressure. Polymer 37 (1):85–91

29. Teyssedre G, Bernes A, Lacabanne C (1995) Cooperative movements associated with the Curie transition in P(VDF-TrFE) copolymers. J Polym Sci Pol Phys 33(6):879–890

30. Aliane A, Benwadih M, Bouthinon B et al (2015) Impact of crystallization on ferro-, piezo- and pyro-electric characteristics in thin film P(VDF-TrFE). Org Electron 25:92–98

31. Lee JS, Prabu AA, Kim KJ (2010) Annealing effect upon chain orientation, crystalline morphology, and polarizability of ultra-thin P(VDF-TrFE) film for nonvolatile polymer memory device. Polymer 51(26):6319–6333

32. Bourgaux-Leonard C, Legrand JF, Renault A et al (1991) Annealing effects in ferroelectric poly(vinylidene fluoride-trifluoroethylene) copolymers: real-time studies using synchrotron radiation. Polymer 32(4):597–604

33. Green JS, Farmer BL, Rabolt JF (1986) Effect of thermal and solution history on the Curie point of VF2-TrFE random copolymers. J Appl Phys 60(8):2690–2693

34. Su R, Tseng J-K, Lu M-S et al (2012) Ferroelectric behavior in the high temperature paraelectric phase in a poly(vinylidene fluoride-co-trifluoroethylene) random copolymer. Polymer 53(3):728–739
35. Salimi A, Yousefi AA (2003) Analysis method: FTIR studies of β-phase crystal formation in stretched PVDF films. Polym Test 22(6):699–704
36. Salimi A, Yousefi AA (2004) Conformational changes and phase transformation mechanisms in PVDF solution-cast films. J Polym Sci Pol Phys 42(18):3487–3495
37. Benz M, Euler WB (2003) Determination of the crystalline phases of poly(vinylidene fluoride) under different preparation conditions using differential scanning calorimetry and infrared spectroscopy. J Appl Polym Sci 89(4):1093–1100
38. Park JH, Kurra N, AlMadhoun MN et al (2015) A two-step annealing process for enhancing the ferroelectric properties of poly(vinylidene fluoride) (PVDF) devices. J Mater Chem C 3 (10):2366–2370
39. Cauda V, Stassi S, Bejtka K et al (2013) Nanoconfinement: an effective way to enhance PVDF piezoelectric properties. ACS Appl Mater Interfaces 5(13):6430–6437
40. Soin N, Boyer D, Prashanthi K et al (2015) Exclusive self-aligned [small beta]-phase PVDF films with abnormal piezoelectric coefficient prepared via phase inversion. Chem Commun 51 (39):8257–8260
41. Patro TU, Mhalgi MV, Khakhar DV et al (2008) Studies on poly(vinylidene fluoride)-clay nanocomposites: effect of different clay modifiers. Polymer 49(16):3486–3499
42. Martins P, Costa CM, Ferreira JCC et al (2012) Correlation between crystallization kinetics and electroactive polymer phase nucleation in ferrite/poly(vinylidene fluoride) magnetoelectric nanocomposites. J Phys Chem B 116(2):794–801
43. Zhang Q, Xia W, Zhu Z et al (2013) Crystal phase of poly(vinylidene fluoride-co-trifluoroethylene) synthesized via hydrogenation of poly(vinylidene fluoride-co-chlorotrifluoroethylene). J Appl Polym Sci 127(4):3002–3008
44. Wu Y, Hsu SL, Honeker C et al (2012) The role of surface charge of nucleation agents on the crystallization behavior of poly(vinylidene fluoride). J Phys Chem B 116(24):7379–7388
45. Martins P, Caparros C, Gonçalves R et al (2012) Role of nanoparticle surface charge on the nucleation of the electroactive β-poly(vinylidene fluoride) nanocomposites for sensor and actuator applications. J Phys Chem C 116(29):15790–15794
46. Mofokeng TG, Luyt AS, Pavlović VP et al (2014) Ferroelectric nanocomposites of polyvinylidene fluoride/polymethyl methacrylate blend and BaTiO$_3$ particles: Fabrication of β-crystal polymorph rich matrix through mechanical activation of the filler. J Appl Phys 115 (8):1084–1109
47. Tiwari V, Srivastava G (2015) Structural, dielectric and piezoelectric properties of 0–3 PZT/PVDF composites. Ceram Int 41(6):8008–8013
48. Kar E, Bose N, Das S et al (2015) Enhancement of electroactive [small beta] phase crystallization and dielectric constant of PVDF by incorporating GeO$_2$ and SiO$_2$ nanoparticles. Phys Chem Chem Phys 17(35):22784–22798
49. Mandal D, Kim KJ, Lee JS (2012) Simple synthesis of palladium nanoparticles, β-phase formation, and the control of chain and dipole orientations in palladium-doped poly (vinylidene fluoride) thin films. Langmuir 28(28):10310–10317
50. Lopes AC, Carabineiro SAC, Pereira MFR et al (2013) Nanoparticle size and concentration dependence of the electroactive phase content and electrical and optical properties of Ag/poly (vinylidene fluoride) composites. Chem Phys Chem 14(9):1926–1933
51. Ghosh SK, Sinha TK, Mahanty B et al (2015) Self-poled efficient flexible "ferroelectretic" nanogenerator: a new class of piezoelectric energy harvester. Energy Technol 3(12):1190–1197
52. Dutta B, Kar E, Bose N et al (2015) Significant enhancement of the electroactive [small beta]-phase of PVDF by incorporating hydrothermally synthesized copper oxide nanoparticles. RSC Adv 5(127):105422–105434

53. Li J, Khanchaitit P, Han K et al (2010) New route toward high-energy-density nanocomposites based on chain-end functionalized ferroelectric polymers. Chem Mater 22(18):5350–5357
54. Jayakumar OD, Mandal BP, Majeed J et al (2013) Inorganic-organic multiferroic hybrid films of Fe_3O_4 and PVDF with significant magneto-dielectric coupling. J Mater Chem C 1 (23):3710–3715
55. Thakur P, Kool A, Bagchi B et al (2015) Effect of in situ synthesized Fe_2O_3 and Co_3O_4 nanoparticles on electroactive [small beta] phase crystallization and dielectric properties of poly(vinylidene fluoride) thin films. Phys Chem Chem Phys 17(2):1368–1378
56. Anithakumari P, Mandal BP, Abdelhamid E et al (2016) Enhancement of dielectric, ferroelectric and magneto-dielectric properties in PVDF-BaFe12O19 composites: a step towards miniaturized electronic devices. RSC Adv 6(19):16073–16080
57. Garain S, Sinha TK, Adhikary P et al (2015) Self-Poled transparent and flexible UV light-emitting cerium complex-PVDF composite: a high-performance nanogenerator. ACS Appl Mater Interface 7(2):1298–1307
58. Cho S, Lee JS, Jang J (2015) Enhanced crystallinity, dielectric, and energy harvesting performances of surface-treated barium titanate hollow nanospheres/PVDF nanocomposites. Adv Mater Interfaces 2(10)
59. Thakur P, Kool A, Bagchi B et al (2015) The role of cerium (iii)/yttrium (iii) nitrate hexahydrate salts on electroactive [small beta] phase nucleation and dielectric properties of poly(vinylidene fluoride) thin films. RSC Adv 5(36):28487–28496
60. Yuan D, Li Z, Thitsartarn W et al (2015) [small beta] Phase PVDF-hfp induced by mesoporous SiO_2 nanorods: synthesis and formation mechanism. J Mater Chem C 3 (15):3708–3713
61. Dillon DR, Tenneti KK, Li CY et al (2006) On the structure and morphology of polyvinylidene fluoride-nanoclay nanocomposites. Polymer 47(5):1678–1688
62. Wang Y, Li J, Deng Y (2015) Enhanced ferroelectricity and energy storage in poly(vinylidene fluoride)-clay nanocomposite films via nanofiller surface charge modulation. RSC Adv 5 (104):85884–85888
63. Ramasundaram S, Yoon S, Kim KJ et al (2008) Preferential formation of electroactive crystalline phases in poly(vinylidene fluoride)/organically modified silicate nanocomposites. J Polym Sci Pol Phys 46(20):2173–2187
64. Tiwari VK, Kulriya PK, Avasthi DK et al (2009) Radiation-resistant behavior of poly (vinylidene fluoride)/layered silicate nanocomposites. ACS Appl Mater Interfaces 1(2):311–318
65. Yu S, Zheng W, Yu W et al (2009) Formation mechanism of β-phase in PVDF/CNT composite prepared by the sonication method. Macromolecules 42(22):8870–8874
66. Levi N, Czerw R, Xing S et al (2004) Properties of polyvinylidene difluoride–carbon nanotube blends. Nano Lett 4(7):1267–1271
67. Ke K, Pötschke P, Jehnichen D et al (2014) Achieving β-phase poly(vinylidene fluoride) from melt cooling: effect of surface functionalized carbon nanotubes. Polymer 55(2):611–619
68. Sharma M, Sharma K, Bose S (2013) Segmental relaxations and crystallization-induced phase separation in pvdf/pmma blends in the presence of surface-functionalized multiwall carbon nanotubes. J Phys Chem B 117(28):8589–8602
69. Sadasivuni KK, Kafy A, Zhai L et al (2015) Multi functional and smart graphene filled polymers as piezoelectrics and actuators. Graphene-based polymer nanocomposites in electronics. Springer International Publishing, New York, pp 67–90
70. El Achaby M, Arrakhiz FZ, Vaudreuil S et al (2012) Piezoelectric β-polymorph formation and properties enhancement in graphene oxide-PVDF nanocomposite films. Appl Surf Sci 258 (19):7668–7677
71. Abdelhamid E, Jayakumar OD, Katari V et al (2016) Multiferroic PVDF-Fe3O4 hybrid films with reduced graphene oxide and ZnO nanofillers. RSC Adv 6(24):20089–20094

72. Karan SK, Mandal D, Khatua BB (2015) Self-powered flexible Fe-doped RGO/PVDF nanocomposite: an excellent material for a piezoelectric energy harvester. Nanoscale 7 (24):10655–10666
73. Wang S, Liu L, Zeng Y et al (2015) Improving dielectric properties of poly(vinylidene fluoride) composites: effects of surface functionalization of exfoliated graphene. J Adhes Sci Technol 29(7):678–690
74. Bhavanasi V, Kumar V, Parida K et al (2016) Enhanced piezoelectric energy harvesting performance of flexible PVDF-trfe bilayer films with graphene oxide. ACS Appl Mater Interfaces 8(1):521–529
75. Andrew JS, Clarke DR (2008) Effect of electrospinning on the ferroelectric phase content of polyvinylidene difluoride fibers. Langmuir 24(3):670–672
76. Lei T, Yu L, Zheng G et al (2015) Electrospinning-induced preferred dipole orientation in PVDF fibers. J Mater Sci 50(12):4342–4347
77. Yee WA, Kotaki M, Liu Y et al (2007) Morphology, polymorphism behavior and molecular orientation of electrospun poly(vinylidene fluoride) fibers. Polymer 48(2):512–521
78. Chang C, Tran VH, Wang J et al (2010) Direct-write piezoelectric polymeric nanogenerator with high energy conversion efficiency. Nano Lett 10(2):726–731
79. Liu ZH, Pan CT, Lin LW et al (2014) Direct-write PVDF nonwoven fiber fabric energy harvesters via the hollow cylindrical near-field electrospinning process. Smart Mater Struct 23(2)
80. Hansen BJ, Liu Y, Yang R et al (2010) Hybrid nanogenerator for concurrently harvesting biomechanical and biochemical energy. ACS Nano 4(7):3647–3652
81. Fang J, Wang X, Lin T (2011) Electrical power generator from randomly oriented electrospun poly(vinylidene fluoride) nanofibre membranes. J Mater Chem 21(30):11088–11091
82. Abolhasani MM, Azimi S, Fashandi H (2015) Enhanced ferroelectric properties of electrospun poly(vinylidene fluoride) nanofibers by adjusting processing parameters. RSC Adv 5(75):61277–61283

Chapter 14
Nanostructured Polymers and Polymer/Inorganic Nanocomposites for Thermoelectric Applications

Zongqiong Lin and Qichun Zhang

Abstract Thermoelectric generators (TEGs) are being considered as one of the most promising green technology to convert the waste energy into useful electricity. Conjugated polymers and their nanostructures possess high electrical conductivity, low thermal conductivity, and reasonable Seebeck coefficient, which can meet the requirements for high-efficiency TEGs. This chapter focuses on recent progress in the development of nanostructured polymers and polymer/inorganic nanocomposites with multi-dimensional nanostructures (0D, 1D to 2D) for thermoelectric applications. The challenges and perspectives in the emerging field of nanostructured polymers are also involved.

14.1 Introduction

As a green technology to harvest waste energy, thermoelectric generators (TEGs), which are able to produce an electrical current or electrical power from a temperature gradient ΔT [1], have evoked a lot of researchers' interests. They possess a series of charming advantages such as high reliability, portable weight, no maintenance required, and friendly to environment [2]. The working principle of thermoelectricity is associated with two fundamental effects (Fig. 14.1), including: (1) the Seebeck

Z. Lin · Q. Zhang
School of Materials Science and Engineering, Nanyang Technological University, Singapore 639798, Singapore

Q. Zhang (✉)
Division of Chemistry and Biological Chemistry, School of Physical and Mathematical Sciences, Nanyang Technological University, Singapore 637371, Singapore
e-mail: qczhang@ntu.edu.sg

Z. Lin
Key Laboratory of Flexible Electronics (KLOFE) and Institute of Advanced Materials (IAM), Jiangsu National Synergetic Innovation Center for Advanced Materials (SICAM), Nanjing Tech University (NanjingTech), 30 South Puzhu Road, 211816 Nanjing, China
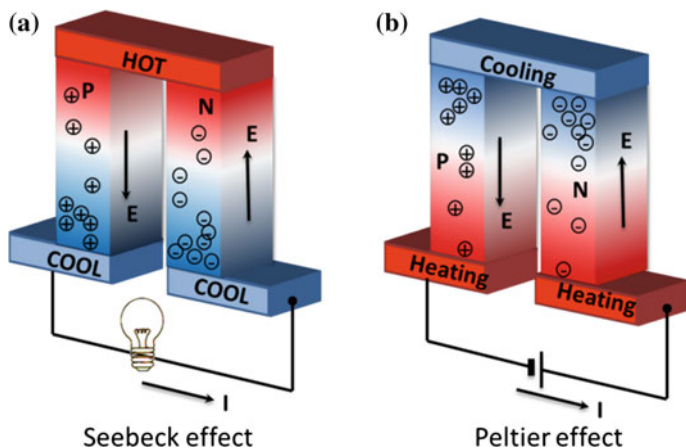
Fig. 14.1 Thermoelectric heat engines. **a** When current is run across a thermoelectric junction, it heats or cools through the Peltier effect, depending on the direction of the current flow. **b** When heat flows across the junction, electrical current is generated through the Seebeck effect

effect, also referred to as the thermopower, in which an electrical potential is produced within a single conductor that is subjected to a temperature gradient; and (2) the Peltier effect, in which a temperature difference is created at the junction of two dissimilar conductors when an electric current crosses. TEGs are typically an assembly of both n- and p-type semiconductors which may simplistically be described as electron rich (donor) and electron poor (acceptor), respectively. Thermoelectric efficiency is measured by the dimensionless figure of merit, $ZT = (S^2\sigma/\kappa) * T$, where S is the Seebeck coefficient, σ is the electrical conductivity, κ is the thermal conductivity, and T is the absolute temperature.

Generally, $\sim 50\%$ of the waste heat is stored in large-volume warm fluids ($T < 250\ °C$). However, rare-efficient TE materials have been found at room temperature (typically as a p-type Bi_2Te_3/Sb_2Te_3 superlattice with ZT = 2.4) [3]. Most of inorganic materials with high thermoelectric efficiency are working at high temperature (>500 K), e.g., the most efficient skutterudite material (Ce-filled skutterudites, $CeFe_{3.5}Co_{0.5}Sb_{12}$) with $ZT = 1.4$ at $T = 900$ K [4], the most efficient SnSe with $ZT = 2.6 \pm 0.3$ at 923 K [5], and the most efficient lead chalcogenide with $ZT = 0.8–1$ at ~ 650 K (PbTe for example) [6]. In contrast, organic/polymer semiconductors are superior over their inorganic counterparts in low temperature waste heat harvesting, and leading to a bright future in TEGs. Nanostructuring strategy of bulk materials has led to significant improvements in ZT because engineered nano-scale interfaces could introduce many possibilities for both phonon scattering and the energy-dependent scattering of electrical carriers [7]. Both theoretical calculations and experiments have already demonstrated that low-dimensional TE materials can efficiently enhance ZT values, due to the

quantum size effect and the enhanced interface scattering of phonons [8]. Thus, solution-processed inorganic nanoparticles have been previously suggested for these applications to reduce the costs of devices' fabrication. However, their low electrical conductivities have resulted in a very low power factor $\sim 0.5~\mu\text{W m}^{-1}~\text{K}^{-2}$ at 300 K, which makes their application impractical [9]. Similarly, although thermally evaporated organic thin films show low thermal conductivities and intriguing Seebeck coefficient, their low electrical conductivities have set up a limitation [10]. In contrast, solution-processed polymers with heavily doping can have sufficiently high electrical conductivities, however their thermopowers are relatively lower. Thus, polymer–inorganic thermoelectric nanocomposites have become a hot research topic because they might possess one of the most particularly attractive features, namely, the synergetic combination of the easy processability of conjugated polymers and the excellent thermoelectric performance of inorganic semiconductors. As alternative, many researchers have paid their attentions to the conductive polymer–carbon-based nanocomposites (carbon sources are carbon nanotubes [11] and graphenes [12]). Their research has demonstrated that the as-prepared composites have the enhanced TE properties [13]. In this chapter, we only highlight the recent progresses on the preparation, modification, and optimization of nanostructured polymer and their composites with inorganic materials for TEGs.

14.2 Polymer-Based TE Materials

Compared to inorganic materials, organic materials have the noteworthy advantages such as mechanical flexibility, low-cost synthesis, and solution processability. The excellent thermoelectric material should have high electroconductivity, a significant Seebeck coefficient in order to ensure efficient thermoelectric power generation, and lower thermal conductivity. Organic thermoelectric materials based on conductive polymers have already shown high electrical conductivity (σ, up to $10^4~\text{S cm}^{-1}$, depends on the doping level) [14], low κ (in range of 0.1–1.0 W m^{-1} K^{-1}) [15] and reasonable S ($10 \sim 1 \times 10^3$ mV K^{-1}) [16], which can meet the requirements for high efficiency of energy conversion TEGs. The progresses of conductive polymers for potential applications in TEGs, including polyanilines (PANI), polythiophenes (PT), PEODT:poly(styrenesulfonate) (PSS), polyacetylene (PA), polypyrrole (PPY), poly(2,7-carbazole), and their derivatives (Fig. 14.2), have been well summarized by several recent review articles or book chapters [13c, 17]. Since three variable factors (S, σ and κ) are somewhat interdependent, it makes the optimization of ZT more challenging and more difficult [13c, 14b, c, 18]. One of the key strategies to optimize ZT in inorganic conductors is to reduce their thermal conductivity via the introduction of nanostructures acting as phonon-scattering centers. Therefore, the nano-engineering strategy in conductive polymer particles [19],
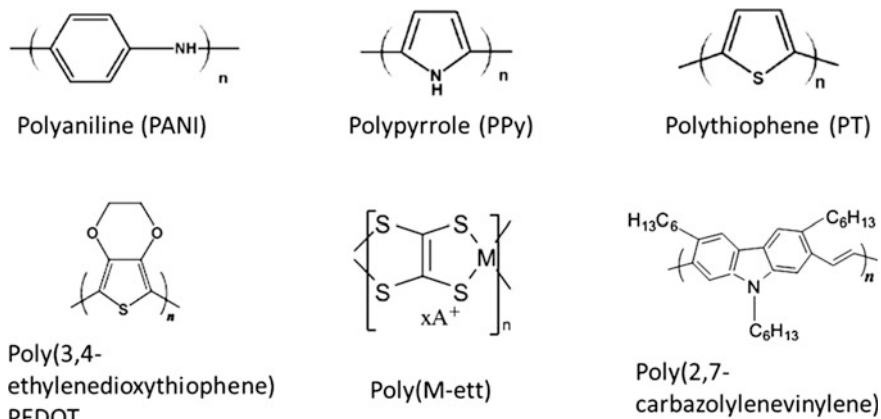
Fig. 14.2 Chemical structures of typical organic conducting thermoelectric polymers

especially 1D nanostructures, have also been proposed to approach a higher ZT, due to their excellent physical properties rising from the size, surface quantum effects [20], and enhanced interface scattering of phonons [18, 21].

14.3 0D Nanostructures of Polymer-Inorganic Nanocomposites

Composite materials consisting of inorganic nanostructures and polymers may have better TE properties than pure polymers because the composite materials could embrace the properties of both polymer and inorganic nanostructures to enhance the performance through a synergistic effect. Pinter et al. [22] prepared Ag–poly (3-octylthiophene) nanocomposites that exhibit an extremely large Seebeck coefficient (1283 μV K^{-1}). Since Ca$_3$Co$_4$O$_9$ single crystals show a high S up to 130 μV K^{-1} and good chemical stability at room temperature [23], Liu et al. [24] successfully fabricated free-standing PEDOT:PSS/Ca$_3$Co$_4$O$_9$ composite films by mechanically blending Ca$_3$Co$_4$O$_9$ powder with PEDOT:PSS, but rather poor in performance. Note that the σ of the as-fabricate composite film dramatically decreases to 75 S cm^{-1}, when further increasing the content of Ca$_3$Co$_4$O$_9$. However, the S only takes 24.8% improvement. The power factor of the composite film decreases with Ca$_3$Co$_4$O$_9$ content, mainly due to the decline of electrical conductivity and the limited improvement of the S. Ag$_2$Te–PANI core–shell nanostructures were prepared by Cai et al. [25] through a one-pot interfacial synthesis method, with about 80–100 nm in size, and $\sim$10 nm Ag$_2$Te nanoparticles as the core of composites. The σ of the as-obtained Ag$_2$Te–PANI composite is measured as 0.043 S cm^{-1}, accompanied by a higher S (251 μV K^{-1}) and lower κ as 0.387 W m^{-1} K^{-1}.

Lead telluride (PbTe) is a narrow band gap (E_g = 0.32 eV) semiconductor, which has been reported to show superior TE properties [26]. Cai et al. [27] synthesized a PANi/PbTe core–shell nanostructure and PbTe/PANi/PbTe three-layer sphere-like morphology by interfacial polymerization. The S of the composite can reach 578 μV K^{-1} with temperature increases to 373 K, but σ (2.2 S m^{-1}) is still very poor, which leads to a low power factor in these PbTe–PANI composites.

Bi_2Te_3-based alloy has been reported as the best TE material system at room temperature and has attracted a great research interesting [3]. Zhao et al. [28] prepared $Bi_{0.5}Sb_{1.5}Te_3$–PANI composite by mixing $Bi_{0.5}Sb_{1.5}Te_3$ powder and PANI powder and then pressing them into pellets. But the power factors of the hybrid materials decrease significantly with the increase of the polymer content due to mainly the decline of electric conductivities. The Bi_2Te_3 nanoparticles and PANI in emeraldine form are physically mixed with camphorsulfonic acid in m-cresol, which results in $\sim$50 times higher power factor (as 51 μW m^{-1} K^{-2}) than the polyaniline film reported by Toshima et al. [29]. The physically mixed hybrid film displays much higher power factor and S in comparison with those by solution mixture, which is attributed to the different morphology and dispersibility of nanoparticles between these two methods. However, Song et al. [30] prepared Bi_2Te_3/PEDOT:PSS TE composite films by a physical mixing method with different contents of the Bi_2Te_3 particle, and the optimized power factor of the composite film is only 9.9 μW m^{-1} K^{-2} (10 wt% Bi_2Te_3). The low power factor is assigned to the micrometer size of Bi_2Te_3 particles (325 mesh), which cannot be homogeneously dispersed in the PEDOT:PSS matrix.

Katz et al. [31] incorporated both ball-milled n- and p-type Bi_2Te_3 powders with commercialized highly conductive PEDOT:PSS (named as CLEVIOS P, PH500 and PH1000). The σ of all three PEDOT grades increases significantly when the dimethyl sulfoxide (DMSO) is added from 1 to 5 wt%, and then starts to decrease. PH1000 products show both S and power factor superior to other products at all the DMSO contents. The best power factor is obtained as 47 μW m^{-1} K^{-2} in CLEVIOS PH1000 (4–5 wt%). Two representative SEM pictures are shown in Fig. 14.3a. On the cross section of the fracture surface, PEDOT:PSS coats on the surface of Bi_2Te_3 Âµm size particles, which also is covered by a PEDOT:PSS thin layer. From the top view picture, the rough surface of samples revealed that Bi_2Te_3 particles are not uniformly dispersed. Figure 14.3c, d show the TE properties of the mixture of CLEVIOS PH1000 and n/p-type Bi_2Te_3 ball-milled powders. Bi_2Te_3 powders have a size distribution from submicrometer to several micrometers. The σ increased and S decreased with the incensement of PEDOT volume ratio. The power factor of the mixture using PH1000 is generally better than other products due to the best power factor associated with PH1000 (Fig. 14.3c). The highest power factors reaches 131 μW m^{-1} K^{-2} for 10 vol% of PEDOT. The estimated ZT for the three samples should be more than 0.08 (10%), 0.06 (17%), and 0.07 (23%).
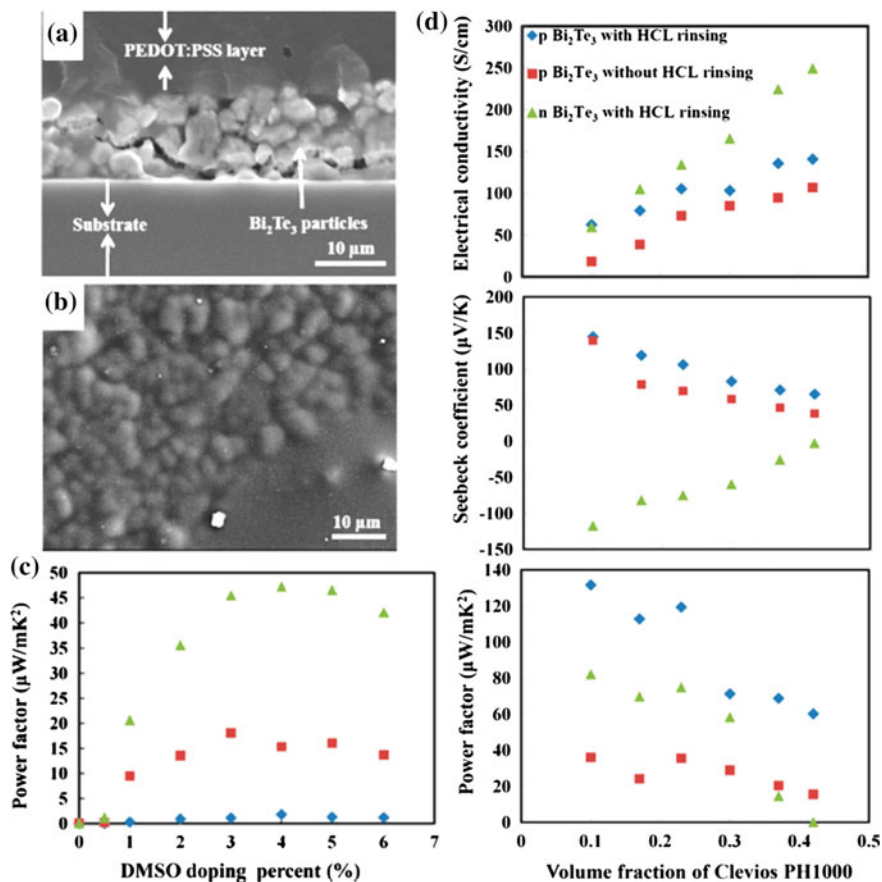
Fig. 14.3 a Cross section SEM picture of the PH1000 mixed with Bi_2Te_3 ball-milled particles (30% volume ratio of PEDOT:PSS). **b** Top view of the sample. **c** Power factor of CLEVIOS P (*blue*), PH500 (*red*), and PH1000 (*green*) mixed with Bi_2Te_3 particles. **d** σ, S, and power factor of CLEVIOS PH1000 mixed with Bi_2Te_3 particles. Reproduced from Ref. [31] with kind permission of © 2010 American Chemical Society (color figure online)

14.4 1D Nanostructure of Polymer-Inorganic Composites

Tellurium (Te) possesses a high thermopower larger than 500 μV K^{-1} in bulky form with oxide impurities [32] of its nanocrystal, which can be synthesized in water in the presence of surfactant toward a solution processing of eco-friendly TE generator. Segalman et al. [33] reported aqueous-processed nanocrystal films composing of Te nanorods functionalized with PEDOT:PSS, and the as-prepared nanocomposite has a high TE performance ($ZT \sim 0.1$). The Te nanorods are synthesized in situ with water-soluble PEDOT:PSS (Fig. 14.4a), which can be drop-cast to form a continuous film as shown in Fig. 14.4b. The introduction of

PEDOT:PSS onto the surface of nanorods is to purposely increase the electrical conductivity with the decreased thermal conductivity of the whole film. Te/PEDOT:PSS nanocomposite film exhibits higher σ (19.3 S cm^{-1}) than both that of PEDOT:PSS and unmodified Te nanorods, which is ascribed to that PEDOT:PSS can prevent the oxidation of Te nanorods and improve the interparticle contact. Higher S (163 µV K^{-1}, approximately an order of magnitude than the bulk polymer) indicates that hole transport does not occur strictly through the PEDOT:PSS. Interestingly, the value of κ for the nanocomposite is in range of 0.22–0.30 Wm^{-1} K^{-1}, which is approximately the same as that of PEDOT:PSS. The possible reasons are attributed to the porosity of the films, different vibrational states between the two components, and the inhibition of heat-carrying phonons transport in such a small diameter of nanorods. Furthermore, it is found that the σ, S, and power factor in the composite films are the function of the mass fraction of Te [34]. Figure 14.4c shows the AFM images of the morphology of composite
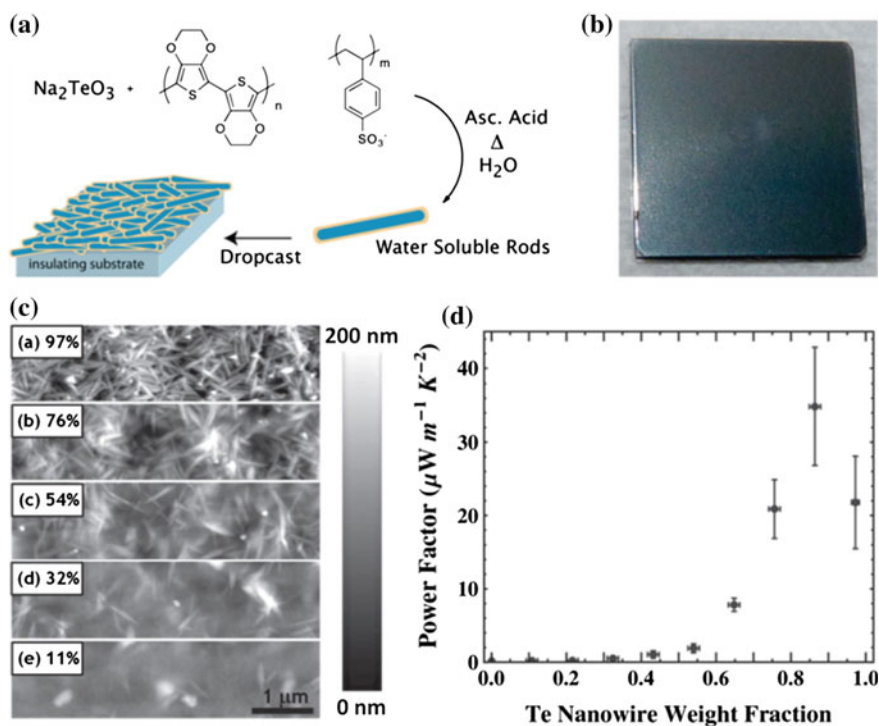
Fig. 14.4 a Synthesis of PEDOT:PSS passivated Te nanorods, followed by formation of smooth nanocomposite films during solution casting. b Picture of a typical drop-cast composite film on a 1 cm^2 quartz substrate, illustrating excellent film uniformity. Reproduced from Ref. [33]. Copyright 2010 American Chemical Society. c Atomic force microscopy images of microns thick Te nanowire polymer composite films with Te nanowire mass fractions and RMS roughness of a 97%, 22.2 nm, b 76%, 8.8 nm, c 54%, 12.8 nm, d 32%, 10.8 nm, and e 11%, 7.3 nm (reproduced from Ref. [34] with kind permission of © 2013 Wiley-VCH)

films in microns thickness and with different roughness in various Te fractions. The σ of the films exhibits a peak at 76 wt% Te (~ 12 S cm^{-1}), which indicates that the control over the interfacial volume in polymer/nanocrystal composites could be a novel route for optimizing carrier transport in nanocomposites. The S increases monotonically with increasing Te and can be well consisted with the two-component series-connected fitting using a brick–wall interface model, which has been used to fit data from the conductor–insulator, and composite solid electrolyte [35]. The κ also is determined by the function of the mass fraction of Te. At the extreme ratio (>80 wt% Te), there is not enough remaining polymers to make a fully dense matrix between particles to further suppress the thermal conductivity. These two studies highlight the importance of nano-scale interfaces in polymer/nanocrystal thermoelectric composites, and provide a general route for the enhancement of carrier transport in hybrid materials and devices.

Wang et al. [36] further studied a patterned single microribbons of the Te nanowire/PEDOT:PSS composite through a standard lift-off process. The temperature-dependent transport behavior and the long-term stability are explored to get a deeper insight of the transport phenomena. Electrical current will pass through regions of polymer, Te nanowire, or the interface of Te nanowire/PEDOT: PSS, according to their fitting of σ versus $T^{-1/4}$ plot. With a band-like conduction in Te nanowires as well as hopping sites in the PEDOT:PSS, the conduction at the Te/PEDOT:PSS interface may better be described by a Poole-Frenkel type process [37]. It is found that the Te nanowires are slowly oxidized over time and a decrease in σ is seen after three weeks, but this is offset by an increase in S.

Layered semiconductor bismuth trisulfide (Bi_2S_3) is a promising TE material with a band gap of 1.3 eV [38]. Cai et al. [39] developed a facile route (one-pot self-assembly method) to prepare Bi_2S_3 nanotubes and PEDOT composite. When the content of Bi_2S_3 increases (up to 36.1 wt%), the electrical conductivity of the composite powder after cold pressing increases, whereas the S firstly increases then decreases, and the power factor monotonically increases. The sample with 36.1 wt% Bi_2S_3 had a highest power factor (2.3 W m^{-1} K^{-2}), which is about five times larger than that of the pure PEDOT.

Wang et al. [40] successfully developed a facile route to fabricate PbTe-modified PEDOT nanotubes and achieved extremely large Seebeck coefficient values. For the synthesis of PEDOT nanotubes, a facile interfacial polymerization [41] is developed at room temperature and the chemical oxidation occurs at the interface of n-hexane/acetonitrile. The diameter of the as-prepared pure PEDOT nanotubes is ~ 50 nm, and the length of the nanotubes ranges from 0.5 to 1.5 μm. Whereas the PbTe-doped nanotubes can give out a length more than 4 μm and ~ 40 nm in diameter, where the size of the as-coated PbTe nanoparticles is between 20 and 50 nm as shown in Fig. 14.5a and a′. The reason for the formation of longer and thinner PbTe-doped PEDOT nanowire may be that PbTe nanoparticles act as a solid stabilizer and assist to form solid-stabilized emulsion nanoparticles, which have much finer droplets of the mixture than that made by simply agitation. The σ and S of the powder pallets after cold pressing are plotted as a function of PbTe content (Fig. 14.5b) at room temperature. N-type conduction and an extremely large S value
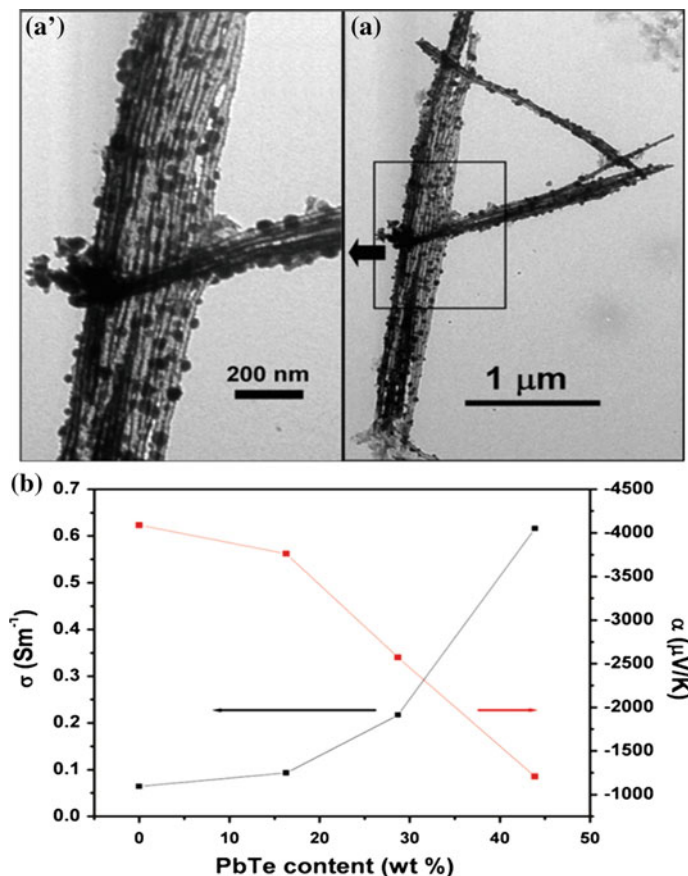
Fig. 14.5 Typical TEM images for PbTe-doped PEDOT nanotubes **a** and **a′** high-magnification image of the marked zone in **a**, **b**, σ, S of PEDOT nanotubes composite pellets with different PbTe content (reproduced from Ref. [40] with kind permission of © 2011 American Chemical Society)

($-4088\ \mu V\ K^{-1}$) are obtained in the pure-dedoped PEDOT, but low electrical conductivity ($6.4 \times 10^{-4}\ S\ cm^{-1}$) is observed. The absolute Seebeck value decreases to $1205\ \mu V\ K^{-1}$ (the sample with 43.9 wt% PbTe) with the increase PbTe content, and the calculated power factor increases from $1.07\ \mu W\ m^{-1}\ K^{-2}$ (pure PEDOT) to $1.44\ \mu W\ m^{-1}\ K^{-2}$ (28.7 wt% PbTe sample).

Ternary hybrid strategy is employed for further optimizing the carrier transport at the interface of Te/PEDOT:PSS composites. The carrier-filtering process is utilized to modify the energy dependence of carrier scattering [42], which can selectively scatter low-energy charge carriers and cause an asymmetry in the distribution of mobile charge carriers around the energy level of the potential barrier. Urban et al. [43] demonstrated the controlled patterning through varying the

amounts of Te-Cooper alloy subphases within nanowire to introduce energy-dependent carrier-scattering mechanisms and characterize the resulting change in thermoelectric and electronic properties. They reported the synthesis of $Cu_{1.75}Te$ alloy subphases with precise conversion within PEDOT:PSS-Te nanowires (NWs) in aqueous solution with aspect ratios of 36 ± 4.0. After growth of the PEDOT:PSS-Te NWs, aliquots of aqueous copper ions with different amounts of copper loading are injected to produce various nanowires (Fig. 14.6a). Unlike the
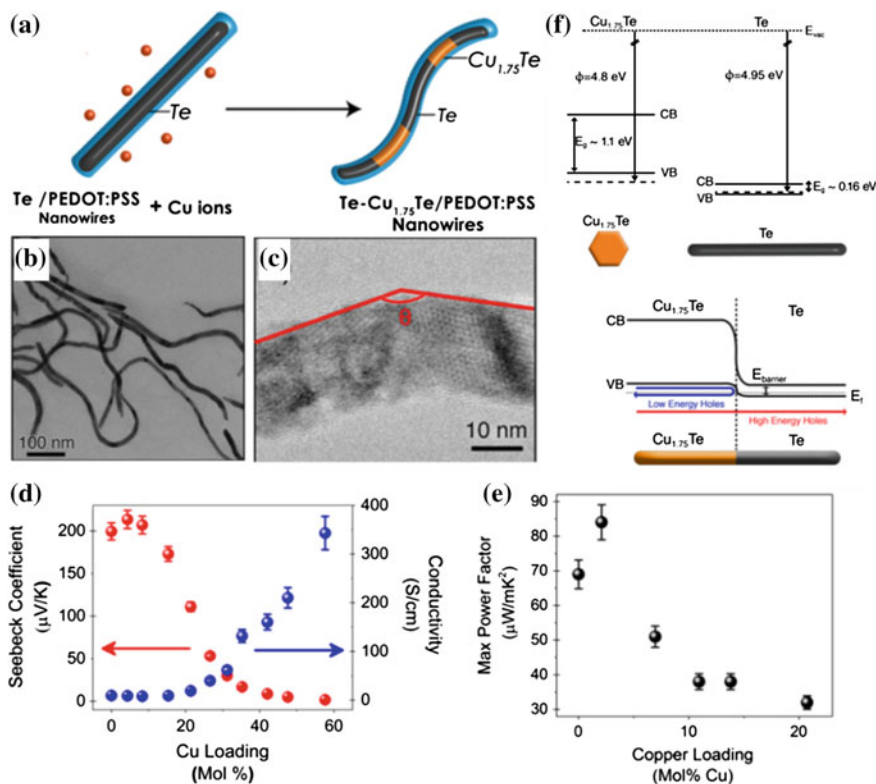
Fig. 14.6 TEM images of nanowires with alloy subphases. **a** Cartoon depiction of Cu incorporation and nucleation of alloy phases within PEDOT:PSS-Te NWs. **b** PEDOT:PSS-Te (Cu_x) NWs exhibit morphological transition to bent wires. **c** PEDOT:PSS-Te(Cu_x) NWs appear polycrystalline, and grain boundaries are observed at angled portions of "bent" wires. The interface between two crystal domains results in angles (θ) ranging from 100 to 160°, which defines the curvature of the "bent" wires. **d** Nonmonotonic trends in both S and σ suggest the energy dependence of carrier scattering has been modified by growth of semimetal–alloy nanointerfaces. **e** Up to 22% improvement in the power factor of the system is realized upon initial subphase growth. Note that power factors are reported after optimization of PEDOT:PSS content, whereas the S and σ are reported before this optimization. **f** Band structure of Te and $Cu_{1.75}Te$ before contact. Equilibrium band alignment in Te–$Cu_{1.75}Te$ nanocomposites. Bending of the valence bands at the interface introduces an energetic barrier that preferentially scatters low energy holes (reproduced from Ref. [43] with kind permission of © 2016 American Chemical Society)

rigid rods for the as-prepared PEDOT:PSS-Te NWs, PEDOT:PSS-Te(Cu$_x$) NWs suffers a morphological transition from a straight and rigid wires to the curved rods due to the growth of alloy subphases (Fig. 14.6b). The growth of this new crystalline phase happens at an angle of θ versus the original Te nanowire (Fig. 14.6c) as shown in HR-TEM, which leads to the wire to kink. From this detail, it was concluded that the structurally mismatched interfaces at grain boundaries would cause kinks rather than an increase in mechanical flexibility. Note that, at low copper loadings, an increase in the S is observed, which is well consisted with a modest drop in σ (Fig. 14.6d). A 22% increase in the maximum power factor of the system, up to 84 μW m^{-1} K^{-2}, is realized (Fig. 14.6e).

The enhancement of the S (up to 220 μV K^{-1}) is observed in the alloyed nanowire representing a 16% increase over the unalloyed hybrid, which is much higher than expected. The reason might be ascribed to a mismatch in available energetic states caused by the estimated 150–300 meV gap in work functions when carriers traveling the length of a nanowire must hop from the Te phase into an alloy subphase. "Hot" carriers may have sufficient energy to overcome the semimetal–alloy interface mismatch and hop across the Cu$_{1.75}$Te barriers, but low-energy "cold" carriers are scattered. In the future, other metal–Te alloy phases are expected to systematically probe the effect of energetic and structural matching across interfaces on carrier scattering and dynamics. Kim et al. [44] designed a ternary hybrid paper composed of reduced graphene oxide, PEDOT:PSS, and Te nanowires to enhance the TE performance, as well as to improve the flexibility and mechanical and chemical durability. The ternary hybrid shows a power factor of 143 μW m^{-1} K^{-1} at 300 K, which is one to two orders of magnitude higher than those of single- or binary-component materials. The reason is also proposed as that the two heterojunctions that induce double-carrier filtering significantly increase the electrical conductivity without a major decrease in the thermopower.

14.5 2D Nanostructure of Polymer-Inorganic Composites

Wang et al. [45] proposed a directly mechanical blending of Bi$_2$Te$_3$/PANI nanocomposite, where Bi$_2$Te$_3$ flakes and rice-like PANI particles was synthesized using hydrothermal and chemical oxidation routes, respectively. However, this method only obtains a poor power factor (5.02 μW m^{-1} K^{-2}). Beside Bi$_2$Te$_3$-based alloy, Bi$_{0.5}$Sb$_{1.5}$Te$_3$ nanosheet (BST)/PEDOT:PSS composite was also investigated to show a higher power factor value ($ZT \sim 0.05$ at room temperature) [46]. The process for the preparation of BST NS/PEDOT:PSS films is illustrated in Fig. 14.7a, as the hydrothermal synthesis, Li$^+$ intercalation and exfoliation route [47], and then spin-coating or drop-casting of nanosheets. The as-prepared BST nanosheets possess a hexagon shape with the edge length ranges from ~ 125 to 800 nm (Fig. 14.7b). Figure 14.7c shows a hexagonal electron diffraction pattern of a BST nanosheet, indicating the single crystalline nature of the BST nanosheets. The growth direction of the BST NSs is along the basal plane of the Bi$_2$Te$_3$ crystal
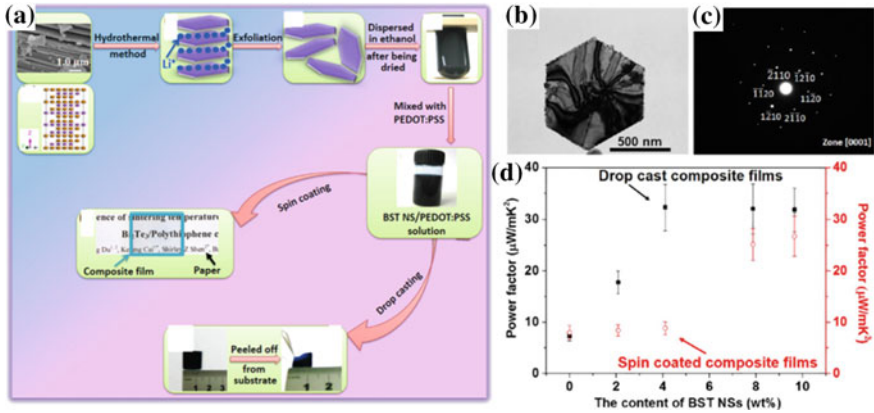
Fig. 14.7 a Illustration of the process for preparation of BST NS/PEDOT:PSS films. TEM images of the P-type BST NSs **b** and **c** the corresponding selected area electron diffraction pattern. **d** Power factor calculated for the drop-cast and the spin-coated films as a function of the BST NS content in the composite films (reproduced from Ref. [46] with kind permission of © 2014 American Chemical Society)

structure [48]. The drop-cast composite film has the highest electrical conductivity (1295.2 S cm^{-1}) if the BST NS content was 4.10 wt%. The S increases for both spin-coating and drop-casting composite films. The spin-coated composite films show an obviously higher S comparing with that of drop-casting film, which is ascribed to the strong carrier scattering and quantum-confinement effect of such a thin film in nano-scale. Figure 14.7d shows the power factor of both composite films. The power factor for the spin-coated films increases dramatically with the increasing content of BST nanosheets, due to the considerably rising S. The highest power factor value (32.26 μW m^{-1} K^{-2}) is obtained on the drop-cast composite film containing 4.10 wt% BST nanosheets. The ZT value is estimated as $\sim$0.05 at room temperature for the drop-cast 4.10 wt% BST nanosheets/PEDOT:PSS composite film (if $\kappa = 0.2$ W m^{-1} K^{-1}), which is much higher than that of the spin-coated film ($\sim$0.01 at RT). The manufacturing processing for the composite films has a significant effect on TE properties.

As one of the most attractive 2D semiconductive materials, MoS$_2$ has gained considerable attention as a potential TE material, due to its low thermal conductivity (0.1–1 W m^{-1} K^{-1}) [49] and large in-plane mobility (200–500 cm V^{-1} s^{-1}) [50]. A very large TE power factor (2.8 $\times$ 10^4 mW m^{-1} K^{-2}) and a large ZT ($\sim$3.4) have been achieved using Boltzmann transport theory and first principle calculations for single-layer MoS$_2$ and MoS$_2$ nanoribbons, respectively [51]. In early 1953, Manseld et al. [52] obtained a remarkable S of −600 mV K^{-1} for bulk MoS$_2$ crystal. Recent reports of the TE performance of MoS$_2$ (prepared by chemical vapor deposition (CVD) in a single-layer transistor device could reach a high S as $\sim$30 mV K^{-1}, but rather poor in power factor because the poor electrical

conductivity of MoS$_2$ (10^{-9} to 10^{-7} S cm^{-1}) limits its TE performance. The first TE demonstration of MoS$_2$/polymer nanocomposite can be traced back to 1993.

Kanatzidis et al. [53] reported the encapsulation of PANI in MoS$_2$ as a nano-composite, and observed a highly σ (0.4 S cm^{-1}) as well as $\sim$10 μV K^{-1} in S. Later on, Xu et al. [54] fabricated a flexible PEDOT:PSS/MoS$_2$ (PM) thin film via direct vacuum filtration with pristine PEDOT:PSS and exfoliated MoS$_2$ nanosheets in different organic solvents. A mass of 0.5 g of MoS$_2$ powder is added into 100 mL N,N-Dimethylformamide (DMF) or N-methyl-2-pyrrolidone (NMP) (Step A in Fig. 14.8). Chemical exfoliation with n-butyllithium is also
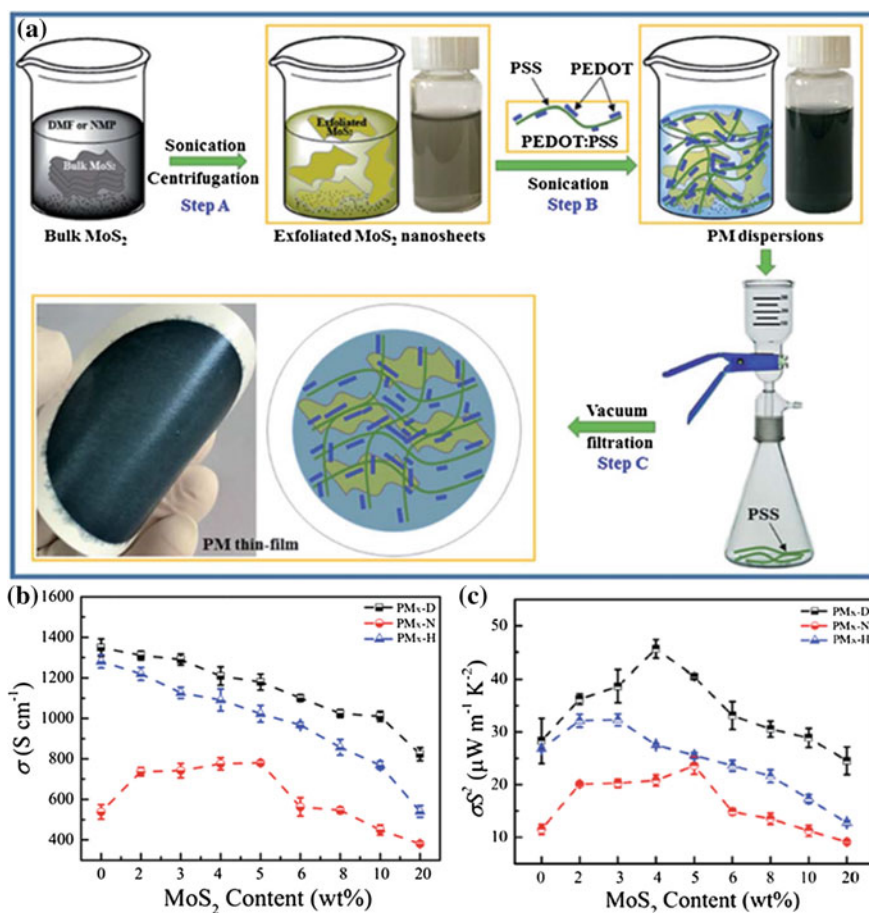
Fig. 14.8 a Schematic illustration of the preparation of the flexible PM thin films. **b** Electrical conductivity of PM thin films with different contents of exfoliated MoS$_2$ nanosheets in DMF (PM$_x$–D), NMP (PM$_x$–N), and H$_2$O (PM$_x$–H). **c** Power factor of PM thin films with different contents of exfoliated MoS$_2$ nanosheets in DMF, NMP, and H$_2$O (reproduced from Ref. [54] with kind permission of © 2016 Royal Society of Chemistry)

introduced to obtain MoS_2 nanosheets. After sonication and centrifugation, MoS_2 nanosheet dispersions in DMF, NMP, or water have been mixed with aqueous PEDOT:PSS solution (Step B), and denoted as PM_x–D, PM_x–N, and PM_x–H, respectively (x is the mass percentage of MoS_2 in the dried PM thin film). The well-dispersed mixture in water is vacuum filtrated (Step C) through a polyvinylidene fluoride (PVDF) membrane (pore size: 0.22 μm) to form uniform films. The average electrical conductivity values for MoS_2/PEDOT:PSS thin films diluted with DMF, NMP, and ethanol are 1349, 528, and 1250 S cm^{-1}, respectively (10^4-fold higher than that of pristine PEDOT:PSS), which is due to the washout of PSS chains. The PM-composite thin films decreases by 30–50% with the increased MoS_2 nanosheet content from 0 to 20 wt%, but still $\sim 10^3$ times higher than that of pristine PEDOT:PSS. The σ is found to decrease with the decreasing temperature. The S of PM thin films increase with the amount of MoS_2 nanosheets and reached the maximum values at 3–5 wt% MoS_2 nanosheets. Note that the PM_4–D thin film shows a higher S value (19.5 μV K^{-1}) than that of PM–N and PM-H. The enhancement of S in PM thin films is possibly resulted from the high carrier mobility of MoS_2 nanosheets and the well connection between PEDOT and MoS_2 nanosheets. The power factor of PM thin films exhibit maximum values at 3–5 wt% MoS_2. Also, the PM-D thin films generally show a higher power factor than that of PM–N and PM–H due to their higher σ and S. An optimized power factor of 45.6 μW m^{-1} K^{-2} presents at 4 wt% MoS_2 nanosheets for PM4–D thin films, which is about much larger than that of the PEDOT thin film (28.3 μW m^{-1} K^{-2}) and higher than those of the previous reported PEDOT:PSS-based composites. The ZT value of the PM4-D thin film is calculated to be 0.04 at room temperature.

14.6 Summary and Perspective

TE properties of polymer matrix or polymer/inorganic nansomposites still have a lot of room to be enhanced through doping or dedoping processes. Generally, the σ, κ, and S of conducting polymers and inorganic TE nanostructure/polymer nanocomposites are interdependent. Thus, it becomes more difficult to increase the σ and S simultaneously in inorganic nanostructure/conductive polymer nanocomposites without affecting thermal conductivity. However, improving backbone ordering of polymer chains and increasing charge carrier mobility in nanostructures should increase σ and S simultaneously.

Moreover, the present techniques for the preparation of inorganic nanostructure/polymer nanocomposites such as physical mixing, solution mixing, and in situ oxidative polymerization still remain challenging in dispersing inorganic TE nanostructures into polymer matrix. Obviously, poor wettability between polymer and inorganic TE nanostructures as well as easy oxidation of inorganic TE nanostructures during the processing has prevented inorganic TE nanostructures from effective dispersion in a polymer matrix. In situ synthesis technique of

nanoparticles in polymer solution (or nano-suspensions) might avoid the oxidation of the nanostructures and constructed the nanoheterojunction directly.

More importantly, the so-called carrier-filtering effect has recently become an attractive approach for ternary hybrid system because this effect can significantly increase the electrical conductivity without a major decrease in the thermopower (or Seebeck). Therefore, the engineering of interfaces at the heterojunctions is critical for matching energy levels, through tuning the electric structure of conjugated polymers.

Lastly, the diversity of nanostructures beyond nanoparticles and nanowires for the inorganic/polymer hybrid system is also promising for the high-performance TEGs, due to the enhancement interface scattering of phonons, especially the novel inorganic 2D semiconductor and various morphologies in higher dimensionality with complex structures and nanoporosity. For the organic counterpart, the low density and highly porosity of metal organic framework (MOF) and covalent organic frameworks (COF) with high conductivity would provide extremely small thermal conductivity and could act as novel candidates for enhancing TE properties.

References

1. a) Jaworski CM, Yang J, Mack S et al (2010) Observation of the spin-Seebeck effect in a ferromagnetic semiconductor. Nat Mater 9:898–903; b) Uchida K, Takahashi S, Harii K et al (2008) Observation of the spin Seebeck effect. Nature 455:778–781; c) Geballe TH, Hull GW (1955) Seebeck effect in silicon. Phys Rev 98(4):940; d) Geballe TH, Hull GW (1954) Seebeck effect in germanium. Phys Rev 94(5):1134
2. a) Yang J, Caillat T (2006) Thermoelectric materials for space and automotive power generation. MRS Bull 31(03):224–229; b) Xie J, Zhao C, Lin Z et al (2016) Nanostructured conjugated polymers for energy-related applications beyond solar cells. Chem Asian J 11(10): 1489–1511
3. a) Venkatasubramanian R, Siivola E, Colpitts T et al (2001) Thin-film thermoelectric devices with high room-temperature figures of merit. Nature 413(6856):597–602; b) Sootsman JR, Chung DY, Kanatzidis MG (2009) New and old concepts in thermoelectric materials. Angew Chem Int Ed 48(46):8616–8639
4. a) Bubnova O, Crispin X (2012) Towards polymer-based organic thermoelectric generators. Energy Environ Sci 5(11):9345–9362; b) Zhou C, Morelli D, Zhou X et al (2011) Thermoelectric properties of P-type Yb-filled skutterudite $Yb_x Fe_y Co_{4-y} Sb_{12}$. Intermetallics 19(10):1390–1393
5. a) Wu D, Zhao LD, Hao S et al (2014) Origin of the high performance in GeTe-based thermoelectric materials upon Bi_2Te_3 doping. J Am Chem Soc 136(32):11412–11419; b) Zhao LD, Zhang X, Wu H et al (2016) Enhanced thermoelectric properties in the counter-doped SnTe system with strained endotaxial SrTe. J Am Chem Soc 138(7): 2366–2373
6. a) Dughaish ZH (2002) Lead telluride as a thermoelectric material for thermoelectric power generation. Phys B Condens Matter 322(1):205–223; b) Zhao LD, Hao S, Lo SH et al (2013) High thermoelectric performance via hierarchical compositionally alloyed nanostructures. J Am Chem Soc 135(19):7364–7370; c) Yim WM, Rosi FD (1972) Compound tellurides and their alloys for peltier cooling—A review. Solid State Electron 15(10):1121–1140

7. a) Boukai AI, Bunimovich Y, TahirKheli J et al (2008) Silicon nanowires as efficient thermoelectric materials. Nature 451(7175):168–171; b) Hicks LD, Dresselhaus MS (1993) Effect of quantum-well structures on the thermoelectric figure of merit. Phys Rev B 47 (19):12727–12731; c) Hicks LD, Harman TC, Sun X et al (1996) Experimental study of the effect of quantum-well structures on the thermoelectric figure of merit. Phys Rev B 53 (16):10493–10496; d) Hochbaum AI, Chen R, Delgado RD et al (2008) Enhanced thermoelectric performance of rough silicon nanowires. Nature 451(7175):163–167

8. Harman TC, Taylor PJ, Walsh MP et al (2002) Quantum dot superlattice thermoelectric materials and devices. Science 297(5590):2229–2232

9. Wang RY, Feser JP, Lee JS et al (2008) Enhanced thermopower in PbSe nanocrystal quantum dot superlattices. Nano Lett 8(8):2283–2288

10. Harada K, Sumino M, Adachi C et al (2010) Improved thermoelectric performance of organic thin-film elements utilizing a bilayer structure of pentacene and 2,3,5,6-tetrafluoro-7,7,8,8-tetracyanoquinodimethane (F_4-TCNQ). Appl Phys Lett 96(25):253–304

11. a) Hong C T, Lee W, Kang Y H et al (2015) Effective doping by spin-coating and enhanced thermoelectric power factors in SWCNT/P_3HT hybrid films. J Mater Chem A 3(23):12314–12319; b) Bounioux C, DíazChao P, CampoyQuiles M et al (2013) Thermoelectric composites of poly (3-hexylthiophene) and carbon nanotubes with a large power factor. Energy Environ Sci 6(3):918–925; c) Meng C, Liu C, Fan S (2010) A promising approach to enhanced thermoelectric properties using carbon nanotube networks. Adv mater 22(4):535–539

12. a) Balandin AA (2011) Thermal properties of graphene and nanostructured carbon materials. Nat Mater 10(8):569–581; b) Zhang K, Zhang Y, Wang S (2013) Enhancing thermoelectric properties of organic composites through hierarchical nanostructures. Sci Rep 3:3448

13. a) Liu H, Wang J, Hu X et al (2002) Structure and electronic transport properties of polyaniline/NaFe 4P composite. Chem Phys Lett 352(3):185–190; b) Yao Q, Chen L, Qu S (2015) Conducting polymer-based nanocomposites for thermoelectric applications fundamentals of conjugated polymer blends, copolymers and composites: synthesis, properties and applications, pp 339–378; c) He M, Qiu F, Lin Z (2013) Towards high-performance polymer-based thermoelectric materials. Energy Environ Sci 6(5):1352–1361; d) Du Y, Shen S Z, Cai K et al (2012) Research progress on polymer–inorganic thermoelectric nanocomposite materials. Prog Polym Sci 37(6):820–841

14. a) Sun J, Yeh ML, Jung BJ et al (2010) Simultaneous increase in seebeck coefficient and conductivity in a doped poly(alkylthiophene) blend with defined density of states. Macromolecules 43(6):2897–2903; b) Zhang Q, Sun Y, Xu W et al (2014) What to expect from conducting polymers on the playground of thermoelectricity: lessons learned from four high-mobility polymeric semiconductors. Macromolecules 47(2):609–615; c) Poehler TO, Katz HE (2012) Prospects for polymer-based thermoelectrics: state of the art and theoretical analysis. Energy Environ Sci 5(8):8110–8115; d) Park T, Park C, Kim B et al (2013) Flexible PEDOT electrodes with large thermoelectric power factors to generate electricity by the touch of fingertips. Energy Environ Sci 6(3):788–792

15. a) Moses D, Denenstein A (1984) Experimental determination of the thermal conductivity of a conducting polymer: Pure and heavily doped polyacetylene. Phys Rev B 30(4): 2090–2097; b) Costa ACR, Siqueira AF (1996) Exact optimum design of segmented thermoelectric generators. J Appl Phys 80:5579–5582

16. a) Yang J, Yip HL, Jen AKY (2013) Rational design of advanced thermoelectric materials. Adv Energy Mater 3(5):549–565; b) Bubnova O, Crispin X (2012) Towards polymer-based organic thermoelectric generators. Energy Environ Sci 5(11):9345–9362

17. a) Yue R, Xu J (2012) Poly(3,4-ethylenedioxythiophene) as promising organic thermoelectric materials a mini review. Synth Met 162(11):912–917; b) Zhang Q, Sun Y, Xu W et al (2014) Organic thermoelectric materials Emerging green energy materials converting heat to electricity directly and efficiently. Adv Mater 26(40):6829–6851

18. Bubnova O, Khan ZU, Wang H et al (2014) Semi-metallic polymers. Nat Mater 13(2):190–194

19. a) Wu J, Zhang Q (2015) Thermoelectric polymers. Encycl Polym Nanomater 2510–2516; b) Xie J, Zhang Q (2016) Recent progress in rechargeable lithium batteries with organic

materials as promising electrodes. J Mater Chem A 4(19):7091–7106; c) Wu J, Sun Y, Pei WB et al (2014) Polypyrrole nanotube film for flexible thermoelectric application. Synthetic Metals 196:173–177; d) Wu J, Sun Y, Xu W et al (2014) Investigating thermoelectric properties of doped polyaniline nanowires. Synth Metals 189:177–182

20. a) Wu J, Sun Y, Xu W et al (2014) Investigating thermoelectric properties of doped polyaniline nanowires. Synth Metals 189:177–182; b) Cademartiri L, Ozin GA (2009) Ultrathin nanowires a materials chemistry perspective. Adv Mater 21(9):1013–1020

21. a) Dresselhaus MS, Chen G, Tang MY et al (2004) New directions for low-dimensional thermoelectric materials. Adv Mater 19(8):1043–1053; b) Hsu KF, Loo S, Guo F et al (2004) Cubic agb msbte bulk thermoelectric materials with high figure of merit. Science 303 (5659):818–821

22. Pintér E, Fekete ZA, Berkesi O et al (2007) Characterization of poly (3-octylthiophene)/silver nanocomposites prepared by solution doping. J Phys Chem C 111(32):11872–11878

23. Liu Y, Lin Y, Shi Z et al (2005) Preparation of $Ca_3Co_4O_9$ and improvement of its thermoelectric properties by spark plasma sintering. J Am Cer Soc 88(5):1337–1340

24. Liu C, Jiang F, Huang M et al (2011) Free-standing PEDOT-PSS/$Ca_3Co_4O_9$ composite films as novel thermoelectric materials. J Electron Mater 40(5):948–952

25. Wang YY, Cai KF, Yin JL et al (2012) One-pot fabrication and thermoelectric properties of Ag Te–polyaniline core–shell nanostructures. Mater Chem Phys 133(2):808–812

26. Heremans JP, Jovovic V, Toberer ES et al (2008) Enhancement of thermoelectric efficiency in PbTe by distortion of the electronic density of states. Science 321(5888):554–557

27. Wang YY, Cai KF, Yin JL et al (2010) Research progress on polymer-inorganic thermoelectric nanocomposite materials. J Nanopart Res 13:533–539

28. Zhao XB, Hu SH, Zhao MJ et al (2002) Thermoelectric properties of polyaniline hybrids prepared by mechanical blending. Mater Lett 52(3):147–149

29. Toshima N, Imai M, Ichikawa S (2010) Organic–inorganic nanohybrids as novel thermo-electric materials: hybrids of polyaniline and bismuth (III) telluride nanoparticles. J Elect Mater 40(5):898–902

30. Song H, Liu C, Zhu H et al (2013) Improved thermoelectric performance of free-standing PEDOT: PSS/Bi_2Te_3 films with low thermal conductivity. J Elect Mater 42(6):1268–1274

31. Zhang B, Sun J, Katz HE et al (2010) Promising thermoelectric properties of commercial PEDOT: PSS materials and their Bi2Te3 powder composites. ACS Appl Mater Interfaces 2 (11):3170–3178

32. Horne RA (1959) Estrogen resistance caused by a mutation in the estrogen-receptor gene in a man. J Appl Phys 30:393–397

33. See KC, Feser JP, Chen CE et al (2010) Water-processable polymer–nanocrystal hybrids for thermoelectrics. Nano Lett 10(11):4664–4667

34. Coates NE, Yee SK, McCulloch B et al (2013) Effect of interfacial properties on polymer–nanocrystal thermoelectric transport. Adv Mater 25(11):1629–1633

35. Uvarov NF (2000) Grundlagen der strahlentherapeutischen methoden[m]/allgemeine strahlen-therapeutische methodik/methods and procedures of radiation therapy. Solid State Ion 136–137:1267–1272

36. Ma S, Anderson K, Guo LA et al (2014) Fast conductance switching in single-crystal organic nanoneedles prepared from an interfacial polymerization-crystallization of 3,4-ethylenedioxythiophene. Appl Phys Lett 105:905–922

37. Stallinga P (2011) Electronic transport in organic materials: comparison of band theory with percolation/(variable range) hopping theory. Adv Mater 23(30):3356–3362

38. Chen B, Uher C, Iordanidis L et al (1997) Transport properties of Bi_2S_3 and the ternary bismuth sulfides $KBi_{6,33}S_{10}$ and $K_2Bi_8S_{13}$. Chem Mater 9(7):1655–1658

39. Wang YY, Cai KF, Yao X (2012) Adsorptive remediation of environmental pollutants using novel graphene-based nano materials. J Nanopart Res 14:1–7

40. Wang Y, Cai K, Yao X (2011) Facile fabrication and thermoelectric properties of Pb_2Te_3-modified poly(3,4-ethylenedioxythiophene) nanotubes. ACS Appl Mater Interfaces 3 (4):1163–1166

41. a) Cho B, Park KS, Baek J et al (2014) Single-crystal poly(3, 4-ethylenedioxythiophene) nanowires with ultrahigh conductivity. Nano Lett 14(6):3321–3327; b) Huang J, Virji S, Weiller BH et al (2003) Polyaniline nanofibers: facile synthesis and chemical sensors. J Am Chem Soc 125(2):314–315; c) Su K, Nuraje N, Zhang L et al (2007) Fast conductance switching in single-crystal organic nanoneedles prepared from an interfacial polymerization crystallization of 3, 4-ethylenedioxythiophene. Adv Mater 19(5):669–672

42. Vineis CJ, Shakouri A, Majumdar A et al (2010) Nanostructured thermoelectrics: big efficiency gains from small features. Adv Mater 22(36):3970–3980

43. Zaia EW, Sahu A, Zhou P et al (2016) Carrier scattering at alloy nanointerfaces enhances power factor in PEDOT:PSS hybrid thermoelectrics. Nano Lett 16(5):3352–3359

44. Choi J, Lee JY, Lee SS et al (2016) Engineering carrier scattering at the interfaces in polyaniline based nanocomposites for high thermoelectric performances. Adv Energy Mater 150(2):181–189

45. Li Y, Zhao Q, Wang Y et al (2011) Synthesis and characterization of Bi_2Te_3/polyaniline composites. Mater Sci Semicond Process 14(3):219–222

46. Du Y, Cai KF, Chen S et al (2014) Facile preparation and thermoelectric properties of Bi2Te3 based alloy nanosheet/PEDOT:PSS composite films. ACS Appl Mater Interfaces 6(8):5735–5743

47. Ren L, Qi X, Liu Y et al (2012) Large-scale production of ultrathin topological insulator bismuth telluride nanosheets by a hydrothermal intercalation and exfoliation route. J Mater Chem 22(11):4921–4926

48. Mehta RJ, Zhang Y, Karthik C et al (2012) A new class of doped nanobulk high-figure-of-merit thermoelectrics by scalable bottom-up assembly. Nat Mater 11(3):233–240

49. Huang W, Luo X, Gan CK et al (2014) Theoretical study of thermoelectric properties of few-layer MoS_2 and WSe_2. Phys Chem Chem Phys 16(22):10866–10874

50. Radisavljevic B, RadenovicA Brivio J et al (2011) High-quality BN WSe_2 BN heterostructure and its quantum oscillations. Nat Nanotechnol 6:147–150

51. a) Liu X, Zhang G, Pei QX et al (2013) Phonon thermal conductivity of monolayer MoS_2 sheet and nanoribbons. Appl Phys Lett 103(13):113–133; b) Babaei H, Khodadadi JM, Sinha S (2014) Large theoretical thermoelectric power factor of suspended single-layer MoS_2. Appl Phys Lett 105(19):193901

52. Mansfield R, Salam SA (1953) Electronic and thermoelectric properties of few-layer transition metal dichalcogenides. Proc Phys Soc 66:377

53. Kanatzidis MG, Bissessur R, DeGroot DC et al (1993) New intercalation compounds of conjugated polymers. Encapsulation of polyaniline in molybdenum disulfide. Chem Mater 5(5):595–596

54. Jiang F, Xiong J, Zhou W et al (2016) Use of organic solvent-assisted exfoliated MoS_2 for optimizing the thermoelectric performance of flexible PEDOT:PSS thin films. J Mater Chem A 4(14):5265–5273

Chapter 15
Polymer-Inorganic Nanocomposites for Polymer Electrolyte Membrane Fuel Cells

Kingshuk Dutta

Abstract Polymer/inorganic nanocomposites represent a unique class of amorphous, flexible, and isotropic materials for applications in high, intermediate, and low temperature polymer electrolyte membrane fuel cells (PEMFCs). Nanocomposite polymer electrolyte membranes in PEMFCs constitute of either a polymer matrix continuous phase with dispersed inorganic proton conducting particles or a proton conducting polymer matrix continuous phase with dispersed inorganic particles. Therefore, these nanocomposites are basically composites of polymer having nanoscale building blocks of inorganic particles. These remarkable hybrid materials possess combined advantages of both the inorganic and the polymer phases, often with synergistic outcomes. In essence, materials of hybrid nature possessing nanosized interfaces between the dispersed inorganic and the continuous polymer domains present remarkable opportunities to produce unique material properties. Accordingly, significant thermal and ionic conductivities, thermal stability, flexibility, corrosion resistance, mechanical strength, dielectricity, ductility, optical density, and processability are some important and attractive attributes of these nanocomposite materials. In addition, these properties can be controlled easily by varying the composition, synthetic procedure, bonding between the polymer and the inorganic particles, and the size of the nanophases. This chapter will deal with the use of polymer/inorganic nanocomposite materials in various categories of PEMFCs, namely hydrogen, direct methanol, and microbial fuel cells. The advantages obtained upon utilizing these hybrid nanocomposite materials over that of the state-of-the-art materials will be highlighted in details. In addition, possible future directions will be provided regarding possibilities of fabricating and utilizing new and prospective hybrid materials for these applications.

K. Dutta (✉)
Department of Chemical Engineering, Indian Institute of Technology,
Kharagpur 721302, India
e-mail: kingshukdutta.pst@gmail.com

15.1 Introduction

Fuel cells represent a class of alternative energy harnessing and storing devices which are essential in today's world, considering the extremely high energy demand and consumption by human population and equally threatening scarcity of conventional fossil fuel-based energy reserves. Within the category of fuel cell devices, polymer electrolyte membrane (PEM)-based fuel cells (PEMFCs) are one of the most important types. These are fuel cells containing solid polymer membranes functioning as electrolytes/ion-exchangers. PEMFCs can be further sub-categorized based on the type of fuels used: (a) hydrogen fuel cells using hydrogen as a fuel, (b) microbial fuel cells (MFCs) using organic matter present in wastewater and sludge as a fuel, and (c) direct methanol fuel cells (DMFCs) using methanol as a fuel [1–5].

A PEM in a fuel cell is responsible for performing three basic functions: (a) selective transport of protons from the anode to the cathode side of the cell, (b) prevent passage of generated electrical charges in the anode to the cathode, and (c) prevent mixing of the contents of the anode chamber with that of the cathode chamber. Over the years, PEMFCs have witnessed employment of a wide variety of polymeric membrane materials as electrolytes. These include primarily of commercially available membranes, such as Nafion®, Dow XUS®, Aciplex-S®, and other laboratory-based membranes composed of blends, composites, copolymers, and interpenetrating networks of pure and/or sulfonated polymers poly(ether ether ketone) (PEEK), poly(vinylidene fluoride) (PVdF) and its copolymer (PVdF-*co*-HFP), polystyrene, polybenzimidazole (PBI), polyaniline (PAni), etc. [3, 6–12]. Membranes constituting these laboratory-based membrane materials in conjunction with commercial membrane materials, majorly Nafion, have dominated the field of PEM research so far [13–16].

However, irrespective of such a huge thrust in PEM research for over two and a half decades, the underlying problems associated with PEMFCs have remained largely unsolved in totality [17–19]. PEM materials which potentially solve one problem often lead to aggravation of other associated problems. This has, in turn, critically hampered the widespread commercialization of fuel cell device as a power source in stationary and portable applications. In this regard, the new generation of hybrid membranes, composed of polymer/inorganic hybrid materials, has shown extreme potential in solving the lingering drawbacks of fuel cell devices. These polymer/inorganic hybrid nanocomposites are amorphous, flexible, and isotropic materials, which have recently found prospective use in PEMs of PEMFCs. Morphologically, these nanocomposite PEMs constitute of either a polymer matrix continuous phase with dispersed inorganic proton conducting particles or a proton conducting polymer matrix continuous phase with dispersed inorganic particles. Therefore, in essence, these nanocomposites are basically composites of polymer having nanoscale building blocks of inorganic particles. Metal/ceramic oxides are commonly employed as the inorganic particles. These unique hybrid materials exhibit combined advantages, often synergistic, obtained from both the inorganic

and the polymer phases. Significant thermal and ionic conductivities, thermal stability, flexibility, corrosion resistance, mechanical strength, dielectricity, ductility, optical density, and processability are some critical and attractive attributes of these nanocomposite materials.

In addition, these properties can be controlled easily by varying the composition, synthetic procedure, bonding between the polymer and the inorganic particles, and the size of the nanophases. This chapter will present the application of polymer/inorganic nanocomposite materials in high, medium, and low temperature PEMFCs. The associated advantages that have been realized upon utilizing these hybrid nanocomposite materials, over that of the state-of-the-art materials, will be discussed in details. In addition, possible future perspectives will be analyzed regarding possibilities of fabricating and utilizing new and prospective hybrid materials toward application in PEMFCs.

15.2   Polymer-Inorganic Nanocomposites as Polymer Electrolyte Membranes in Hydrogen Fuel Cells

A hydrogen fuel cell is an electrochemical device responsible for chemical to electrical energy conversion via combination of hydrogen as a fuel (anode reactant or anolyte) and oxygen or air as an oxidant (cathode reactant or catholyte). In general, the anode and the cathode reactions take place in presence of platinum (Pt) as both the anode and the cathode catalysts. A schematic illustration of a hydrogen fuel cell has been presented in Fig. 15.1. Although a lot of components and associated advantages/disadvantages are involved with a fuel cell system, this chapter will deal only with the employed PEM component and its detailing.

Fig. 15.1 A schematic illustration of a hydrogen fuel cell (reproduced from Ref. [1] with kind permission of © 2016 Elsevier)
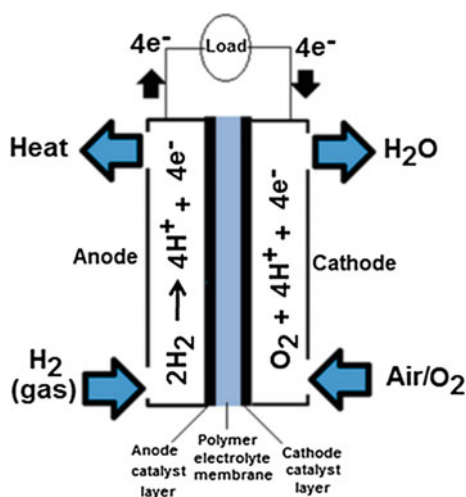
Commercial Nafion® membranes of DuPont represent the state-of-the-art PEMs involved in the fabrication of hydrogen fuel cell systems. It presents several advantages, including high proton conductivity (under fully hydrated condition), excellent electrochemical and chemical stabilities, and structural integrity at moderate temperatures of up to 90 °C.

However, Nafion membranes suffer from extreme high cost, which eventually increases the overall cost of the fuel cell device, thus, hindering its widespread commercialization. In addition, at high temperatures (>90–100 °C), Nafion membranes loses their chemical and mechanical stability, as well as, their moisture retention capacity, leading to a decrease in its proton conductivity. Moreover, Nafion, consisting of pendant sulfonic acid ($-SO_3H$) groups, also exhibit loss of these groups via hydrolysis at temperatures >100 °C. In order to overcome these critical problems various alternative membranes have been designed and fabricated [17, 20]. However, this chapter will only focus on PEMs based on polymer/inorganic composite materials.

Mixed membranes composed of Nafion and silicon oxide have been fabricated by incorporation of silicon oxide within Nafion membranes [21]. The incorporated oxide particles were concentrated within the middle of the membrane, so that the membrane surfaces remain similar to that of the pristine Nafion-117 membrane. This was done in order to maintain the nature of the membrane-electrode interface same as that using the pristine Nafion-117 membrane, while varying the bulk membrane properties such as proton conductivity. At a temperature of 80 °C, this hybrid membrane exhibited a higher conductivity of 9.9×10^{-2} S cm^{-1} compared to pristine the Nafion-117 membrane (i.e., 7.4×10^{-2} S cm^{-1}), although its room temperature (25 °C) conductivity (i.e., 4.4×10^{-2} S cm^{-1}) was lower than that exhibited by the pristine Nafion-117 membrane (i.e., 8.7×10^{-2} S cm^{-1}). A series of recast Nafion-inorganic composite membranes have been fabricated, employing tungsten oxide (WO_3), titanium dioxide (TiO_2), silicon dioxide (SiO_2), or SiO_2/phosphotungstic acid (PWA) as the inorganic constituent(s) [22]. The inorganic content was maintained at 10 wt%. Scanning electron microscope (SEM) images of these composite membranes have been presented in Fig. 15.2. The PEMFC performance at high temperature (>100 °C) using the modified membranes Nafion/SiO$_2$, Nafion/WO$_3$, and Nafion/SiO$_2$/PWA revealed that their proton conducting abilities were comparable to that of Nafion-115 membrane at a relative humidity of 100%; however, their conductivities were found to be superior than the pristine Nafion-115 membrane at lower relative humidity values. For example, under an operation condition of 70% relative humidity and 110 °C temperature, the Nafion/SiO$_2$/PWA hybrid membrane exhibited the best proton conductivity (i.e., 2.67×10^{-2} S cm^{-1}) followed by the Nafion/SiO$_2$ (i.e., 1.07×10^{-2} S cm^{-1}), the Nafion/WO$_3$ (i.e., 1.01×10^{-2} S cm^{-1}), the Nafion/TiO$_2$ (i.e., 8.93×10^{-3} S cm^{-1}) and the pristine Nafion-115 (i.e., 8.13×10^{-3} S cm^{-1}) membranes. Again, under this particular operating condition, the PEMFC current density values exhibited by the tested membranes at 0.4 V potential were Nafion/SiO$_2$/PWA (i.e., 540 mA cm^{-2}) > Nafion/SiO$_2$ (i.e., 320 mA cm^{-2}) > Nafion/WO$_3$ (i.e., 230 mA cm^{-2}) > Nafion/TiO$_2$ (i.e., 150 mA cm^{-2}) > pristine Nafion 115 (i.e., 95 mA cm^{-2}).
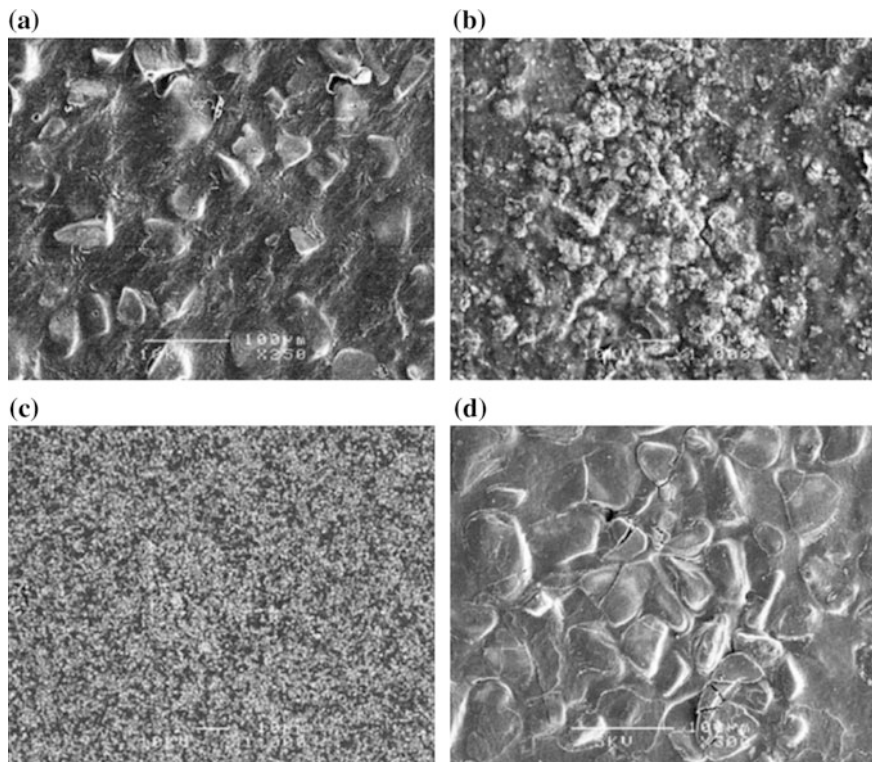
Fig. 15.2 Scanning electron micrographs of composite membranes: **a** recast Nafion/SiO$_2$, **b** recast Nafion/TiO$_2$, **c** recast Nafion/WO$_3$, and **d** recast Nafion/SiO$_2$/PWA (reproduced from Ref. [22] with kind permission of © 2006 Elsevier)

In order to improve on the proton conductive and water retention capacity under conditions of higher temperature (i.e., 90 and 120 °C) and low relative humidity (i.e., 40%), nanocomposite PEMs comprising of recast Nafion/MO$_2$ (where, M represents Si, Zr, or Ti) have been fabricated [23]. These sol–gel nanocomposite membranes demonstrated enhanced water uptake capacities compared to the pristine Nafion-112 membrane at 90 and 120 °C temperatures. However, at these temperatures and 40% relative humidity, only the Nafion/zirconium oxide (ZrO$_2$) nanocomposite membrane exhibited higher proton conducting ability (by 10%) over that of the pristine Nafion-112 membrane. This particular enhancement was due to the fact that Nafion/ZrO$_2$ sol–gel nanocomposite membrane produced increased acidity as represented by a decreased equivalent weight of this membrane over that of Nafion/TiO$_2$ and Nafion/SiO$_2$ sol–gel nanocomposite membranes. Recast Nafion/ZrO$_2$-SiO$_2$ composite membranes were fabricated by varying the ratio of incorporated Zr to Si [24]. The total inorganic content was maintained at 10 wt%. These composite membranes exhibited higher water uptake capacities, compared to the pristine Nafion-112, recast Nafion/ZrO$_2$ and recast Nafion/SiO$_2$ membranes,

when measured at 80 °C temperature. At this temperature, increase in the ZrO_2 content of the membrane was found to result in increasing proton conducting ability.

However, a reverse trend in proton conducting ability of the membranes was noted at 120 °C. Composite membranes constituting of a Zr to Si ratio of 0.5 was reported to produce the best cell performance (i.e., an output power density of 610 mW cm^{-2} at an applied voltage of 0.6), when tested at 120 °C temperature, 50% relative humidity and 2 atm. pressure. Nafion/ZrO_2 composite membranes exhibited increased water uptake capacity with increasing ZrO_2 content of the membrane [25]. At 10 wt% incorporated ZrO_2, the composite membrane exhibited 387 mW cm^{-2} and 604 mW cm^{-2} power density values, when tested at an applied voltage of 0.6, under conditions of 85% relative humidity, 130 °C temperature and 100% relative humidity, 110 °C temperature, respectively. ZrO_2 incorporation was found to render little effect on the structure and crystallinity of recast Nafion membranes [26]. Recast Nafion/ZrO_2 nanocomposite membranes demonstrated increased water retention capability over the pristine membrane at 100 °C, under conditions of medium to high relative humidity.

A zirconium phosphate-modified sulfonated poly(fluorinated arylene ether)s composite membrane demonstrated better cell performance at an operating temperature range of 100–140 °C, compared to the unmodified membrane [27]. Moreover, this composite membrane exhibited significant stability at 120 °C cell operating temperature; whereas the unmodified membrane suffered from irreversible degradation during operation. It produced current density values of 760 and 460 mA cm^{-2} at cell operating temperatures of 120 and 130 °C, respectively, at 0.6 V applied voltage. This was higher compared to the corresponding values obtained for Nafion membrane, i.e., 620 and 260 mA cm^{-2} at 120 and 130 °C, respectively, at 0.6 V. A Nafion-115/zirconium phosphate (23 wt%) composite membrane exhibited a current density of ∼1000 mA cm^{-2} at 0.45 V, 130 °C and 3 bar, in comparison with the exhibition of only 250 mA cm^{-2} by pristine Nafion-115 under identical operating conditions [28]. Similarly, a recast Nafion/zirconium phosphate composite membrane produced ∼1500 mA cm^{-2} under similar operating conditions.

In addition, these composite membranes showed stability during operation at 130 °C, while pristine Nafion membranes suffered from irreversible degradation. This performance improvement of the composite membranes over the pristine membranes was attributed to the interrelationship between structure and proton conductivity of the membranes [29]. Uniform distribution of the incorporated Zr and P particles within the composite membranes, as compared to the pristine Nafion-115 membrane, was realized from electron microprobe elemental analysis, as presented in the cross-sectional micrographs in Fig. 15.3 [28]. Incorporation of zirconium phosphate within Nafion-115 membrane results in formation of rigid scaffold within the membrane structure, which facilitates uptake of water by the composite membrane [30]. This, in turn, gets reflected in the improved ion-exchange capacity, proton conductivity and ultimate fuel cell performance of the composite membrane.

Inorganic silica particles have been extensively used in fabrication of polymer/inorganic nanocomposite PEMs for hydrogen fuel cells [31]. These
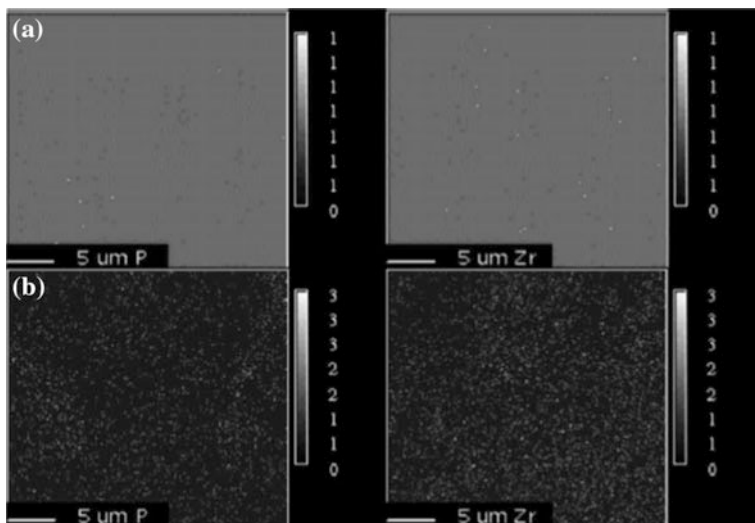
Fig. 15.3 Cross-sectional micrographs representing the electron microprobe elemental analysis of phosphorus (*left*) and zirconium (*right*) in **a** pristine Nafion-115 and **b** Nafion-115/zirconium phosphate (23 wt%) composite membranes (reproduced from Ref. [28] with kind permission of © 2002 Elsevier)

particles enjoy wide availability, low cost, and high thermal stability and hydrophilicity. Nafion/SiO_2 composite membranes were found to perform satisfactorily at and above 130 °C temperature, in comparison with pristine recast Nafion and pristine Nafion-115 membranes. These pristine membranes undergo irreversible thermal degradation beyond 100 °C temperature [32]. A hybrid Nafion/SiO_2 composite membrane was found to produce enhanced proton conductivity over pristine Nafion-112 and pristine recast Nafion membranes at 95 °C [33]. The hybrid membrane also enjoyed higher ion-exchange capacity over the pristine membranes. At a cell operating temperature of 120 °C and low relative humidity, this hybrid membrane demonstrated an improvement in current density over that of pristine Nafion membrane of ~ 60 mA cm^{-2} at 0.7 V, along with a 16% enhancement in power density. Sulfonated phenethylsilica incorporated within Nafion membrane proved to be a potential bifunctional additive, with enhanced proton conduction ability and water uptake [34]. The ion-exchange capacity and the water uptake ability were found to increase with increasing amount of added silica. Under conditions of 100% relative humidity and 80 °C temperature, the composite membrane containing 2.5–5 wt% incorporated silica demonstrated a 2.7–5.8 times increment in proton conductivity over that of pristine Nafion-117 membrane.

A nanocomposite silicon membrane, consisting of a porous and hydrophilic SiO_2 layer to reduce the pore size, exhibited a higher proton conducting ability by 2–3 orders of magnitude over that of Nafion-117 membrane at low humidification conditions, as well as, an improved power density by one order of magnitude [35].
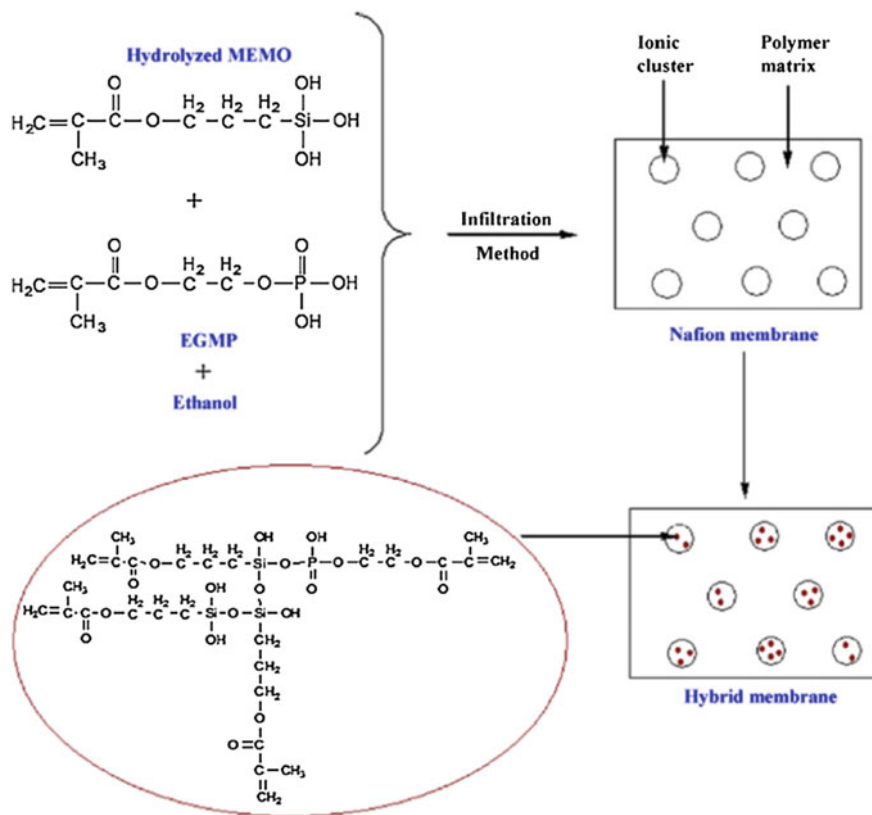
Fig. 15.4 Schematic representation of in situ modification of Nafion membrane using phosphosilicate by infiltration method (reproduced from Ref. [36] with kind permission of © 2009 Elsevier)

Nafion-117 membrane was modified in situ by phosphosilicate particles via infiltration (Fig. 15.4) [36]. This Nafion/phosphosilicate composite membrane was found to produce a higher stability and proton conducting ability under anhydrous conditions and >100 °C temperature, compared to pristine Nafion-117 membrane. This proton conduction and water uptake of the hybrid membrane got increased with increasing phosphate content of the membrane. A water uptake capacity of 10.5% was produced by the hybrid membrane as compared to the value of only 4.5% exhibited by pristine Nafion-117 membrane. However, at <100 °C temperature, the proton conductivity of the composite membrane was observed to be lower than pristine Nafion-117 membrane owing to restrictions imposed upon proton mobility and blocking of proton conduction path by reduced free volume and disruptions of hydrophilic domain arrangement.

An organic polymer membrane, incorporated with SiO_2 particles, exhibited improved water uptake, thermal stability, and fuel cell performance at temperatures

>100 °C, compared to the pristine membrane [37]. The presence of SiOH group within the composite membrane structure was found to be responsible toward exhibition of high water uptake and significant proton conductivity at high temperatures. Poly(ethylene oxide)/SiO_2 composite membranes have also been fabricated by sol–gel method for potential application in high temperature PEMFCs [38, 39]. A Nafion/SiO_2/PWA composite membrane, prepared by sol–gel method, exhibited a current density of 82 mA cm^{-2} at an applied voltage of 0.6 [40]. Following a similar synthetic approach, a fabricated Nafion/SiO_2 membrane demonstrated a better performance compared to pristine Nafion-1135 membrane by ∼5 times at a relative humidity of 18% [41].

Presence of a homogeneous and even distribution of siloxane inside the polymeric matrix was also noted. A self-assembled Nafion/SiO_2 composite membrane was found to possess higher durability and retention of water compared to a sol–gel prepared Nafion/SiO_2 nanocomposite membrane [42]. This self-assembled membrane exhibited a proton conduction ability of 9×10^{-2} S cm^{-1}, which is comparable to that obtained for a commercial Nafion-112 membrane. A PBI/SiO_2 (10 wt%) membrane, doped with phosphoric acid, demonstrated a twofold higher storage modulus, as well as, a higher proton conduction (i.e., 3.8×10^{-2} S cm^{-1}) at a temperature of 140 °C and a relative humidity of 1%, compared to the membrane devoid of incorporated SiO_2 (i.e., 1.52×10^{-3} S cm^{-1}) [43]. A PBI/SiO_2-PBI (10 wt%) nanocomposite membrane, synthesized by an ozone-mediated technique, exhibited a 25% greater proton conduction (i.e., 5×10^{-2} S cm^{-1} at 160 °C) that the unmodified PBI membrane and a higher maximum power density (i.e., 650 mW cm^{-2}) than the unmodified PBI membrane (i.e., 530 mW cm^{-2}) [44].

A hybrid organic/inorganic membrane, containing polysilsesquioxanes bridges, fabricated by sol–gel method and doped with PWA (Fig. 15.5), demonstrated proton conducting ability of greater than 10^{-2} S cm^{-1} at temperatures as high as 160 °C [45]. In addition, at a low relative humidity of 20%, the proton conduction of this membrane was found to be higher than 2×10^{-3} S cm^{-1} at 120 °C, thereby indicating a negligible dependence of conductivity on relative humidity at >100 °C. A Nafion/$[(ZrO_2).(SiO_2)_{0.67}]_x$ (where, $x = 0$–1.79) nanocomposite membranes were fabricated as PEMs for high temperature PEMFCs [46]. Nanocomposite membrane, with $x = 0.313$ and 0.534, produced conductivities of 4.3×10^{-2} and 3.5×10^{-2} S cm^{-1} at 135 and 115 °C, respectively. A recast Nafion/TiO_2 (3 wt%) composite membrane demonstrated higher maximum power densities of 256 and 514 mW cm^{-2} at 130 and 110 °C temperatures, respectively, at 0.56 applied voltage; while pristine Nafion-115 membrane got decomposed at 130 °C [47]. This hybrid membrane also exhibited higher water uptake, ion-exchange capacity, and proton conductivity compared to the pristine Nafion-115 and the pristine recast Nafion membranes. Other Nafion/TiO_2 membranes have also been fabricated with good mechanical and electrical properties, and cell performances [48, 49]. Recast perfluorosulfonic acid (PFSA)/WO_3 composite membranes, having varied WO_3-content, were synthesized and their performances were compared to the commercial Nafion-112 membrane [50]. These composite membranes exhibited higher water uptake and proton conducting abilities compared to the commercial membrane.
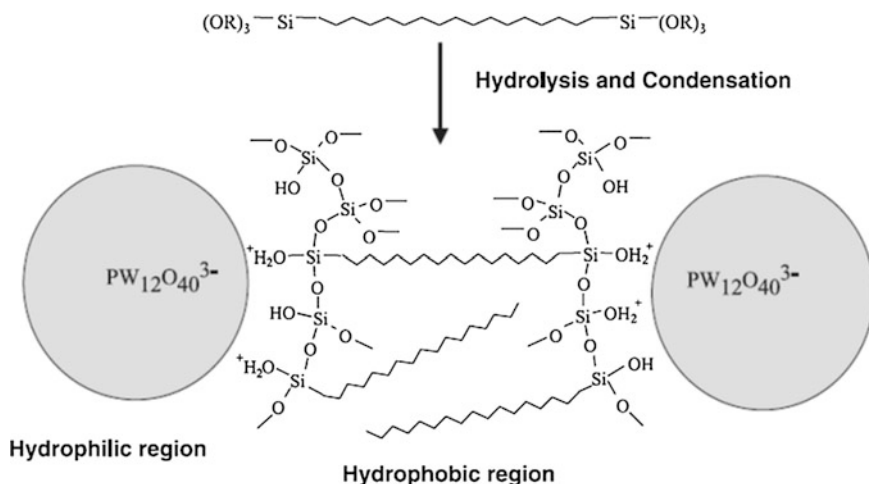
Fig. 15.5 A schematic of the molecular organic/inorganic interface. The monomers are crosslinked by catalytic reaction of PWA to the hybrid macromolecules (reproduced from Ref. [45] with kind permission of © 2003 Elsevier)

Incorporation of 15 wt% of WO_3 within recast PFSA membrane resulted in exhibition of highest current and power density values over all the membranes studied. A sulfonated PEEK (SPEEK)/zeolite beta composite membrane, at an inorganic loading of 10 wt% and a constituent ratio of SiO_2/alumina (Al_2O_3) = 50/50, exhibited the highest proton conductivity [51]. This conductivity value was higher than that obtained for pristine SPEEK membrane.

The above reports, highlights, and discussions summarize the important works reported so far regarding research and development in the field of polymer/inorganic PEMs for hydrogen fuel cells. Table 15.1 lists a compilation of the results obtained using different polymer/inorganic nanocomposite membranes in hydrogen fuel cells. For further reading, the readers are referred to other major literary works listed in the reference section of this chapter [17, 20, 52, 53].

15.3 Polymer-Inorganic Nanocomposites as Polymer Electrolyte Membranes in Microbial Fuel Cells

An MFC is an electrochemical device responsible for chemical to electrical energy conversion via combination of organic matter present in wastewater as a fuel (anode reactant or anolyte) and oxygen or air as an oxidant (cathode reactant or catholyte). In general, the anode and the cathode reactions take place in presence of microorganisms as both the anode catalyst and platinum as the cathode catalyst. A schematic

Table 15.1 A compilation of the results obtained using different polymer/inorganic nanocomposite membranes in hydrogen fuel cells

Membrane material	Cell type	Water uptake (%) at r.t. or 25 °C	IEC at r.t. (meq g⁻¹)	Proton conductivity (S cm⁻¹)	Maximum power density (mW cm⁻²)	Refs.
Nafion-115	H$_2$/O$_2$ single cell	26	–	8.13×10^{-3} at 110 °C and 70% relative humidity	38 at 0.4 V, 110 °C and 70% relative humidity	[22]
Recast Nafion/TiO$_2$	H$_2$/O$_2$ single cell	34	–	8.93×10^{-3} at 110 °C and 70% relative humidity	60 at 0.4 V, 110 °C and 70% relative humidity	[22]
Recast Nafion/SiO$_2$	H$_2$/O$_2$ single cell	34	–	1.07×10^{-2} at 110 °C and 70% relative humidity	128 at 0.4 V, 110 °C and 70% relative humidity	[22]
Recast Nafion/WO$_3$	H$_2$/O$_2$ single cell	37	–	1.01×10^{-2} at 110 °C and 70% relative humidity	92 at 0.4 V, 110 °C and 70% relative humidity	[22]
Recast Nafion/SiO$_2$/PWA	H$_2$/O$_2$ single cell	38	–	2.67×10^{-2} at 110 °C and 70% relative humidity	216 at 0.4 V, 110 °C and 70% relative humidity	[22]
Nafion-112	H$_2$/air single cell	35.7	0.91	2.12×10^{-2} and 1.75×10^{-2} at 80 and 120 °C, respectively (at 50% relative humidity)	~490 at 0.6 V, 120 °C and 50% relative humidity	[24]
Recast Nafion	H$_2$/air single cell	36.2	0.91	2.12×10^{-2} and 1.81×10^{-2} at 80 and 120 °C, respectively (at 50% relative humidity)	~490 at 0.6 V, 120 °C and 50% relative humidity	[24]
Recast Nafion/ZrO$_2$	H$_2$/air single cell	37.5	0.93	2.81×10^{-2} and 2.3×10^{-2} at 80 and 120 °C, respectively (at 50% relative humidity)	~520 at 0.6 V, 120 °C and 50% relative humidity	[24]

(continued)

Table 15.1 (continued)

Membrane material	Cell type	Water uptake (%) at r.t. or 25 °C	IEC at r.t. (meq g^{-1})	Proton conductivity (S cm^{-1})	Maximum power density (mW cm^{-2})	Refs.
Recast Nafion/SiO$_2$	H$_2$/air single cell	39.2	0.90	2.12×10^{-2} and 2.2×10^{-2} at 80 and 120 °C, respectively (at 50% relative humidity)	~520 at 0.6 V, 120 °C and 50% relative humidity	[24]
Recast Nafion/ZrO$_2$–SiO$_2$ (Zr:Si = 0.5)	H$_2$/air single cell	39.5	0.91	2.59×10^{-2} and 2.89×10^{-2} at 80 and 120 °C, respectively (at 50% relative humidity)	610 at 0.6 V, 120 °C and 50% relative humidity	[24]
Membrane fabricated from 5% (w/w) alcoholic Nafion solution	H$_2$/air single cell	20	0.89	–	480 at 0.6 V, 110 °C and 100% relative humidity	[25]
Nafion/ZrO$_2$ (90:10 w/w)	H$_2$/air single cell	24	0.85	–	604 and 387 at 110 °C, 100% relative humidity and 130 °C, 85% relative humidity, respectively (at 0.6 V)	[25]
Nafion-115	H$_2$/O$_2$ single cell	26.4	–	1.73×10^{-2} at room temperature	372 at 0.6 V, 120 °C and 3 atm.	[27]
Sulfonated poly (fluorinated arylene ether)s	H$_2$/O$_2$ single cell	130.0	–	2.54×10^{-3} at room temperature	516 at 0.6 V, 100 °C and 3 atm.	[27]
Zirconium phosphate-modified sulfonated poly (fluorinated arylene ether)s	H$_2$/O$_2$ single cell	85.6	–	1.63×10^{-2} at room temperature	456 at 0.6 V, 120 °C and 3 atm.	[27]

Table 15.1 (continued)

Membrane material	Cell type	Water uptake (%) at r.t. or 25 °C	IEC at r.t. (meq g⁻¹)	Proton conductivity (S cm^{-1})	Maximum power density (mW cm^{-2})	Refs.
Nafion-115	H$_2$/O$_2$ single cell	–	–	–	112.5 at 0.45 V, 130 °C and 3 bar	[28]
Nafion-115/zirconium phosphate (23 wt%)	H$_2$/O$_2$ single cell	–	–	–	~450 at 0.45 V, 130 °C and 3 bar	[28]
Recast Nafion/zirconium phosphate (36 wt%)	H$_2$/O$_2$ single cell	–	–	–	~675 at 0.45 V, 130 °C and 3 bar	[28]
Nafion-115	H$_2$/air single cell	27	0.91	1×10^{-1} to 1.6×10^{-1} at 80 °C, 85% relative humidity and 130 °C, 100% relative humidity, respectively	420 at 90 °C and 0.5 V, at 130 °C the membrane got damaged	[47]
Recast Nafion	H$_2$/air single cell	20	0.89	1.2×10^{-1} to 1.4×10^{-1} at 80 °C, 85% relative humidity and 130 °C, 100% relative humidity, respectively	–	[47]
Recast Nafion/TiO$_2$ (3 wt%)	H$_2$/air single cell	29	0.93	1.5×10^{-1} to 1.8×10^{-1} at 80 °C, 85% relative humidity and 130 °C, 100% relative humidity, respectively	680 and 254 at 90 °C and 130 °C, respectively, at 0.5 V	[47]

Unavailable or unclear values have been presented as '–'
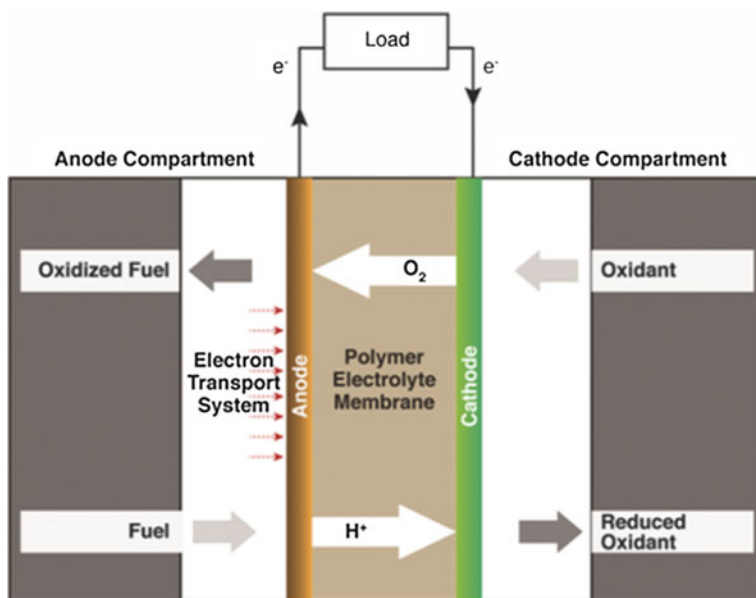
Fig. 15.6 A schematic illustration of a microbial fuel cell (reproduced from Ref. [5] with kind permission of © 2014 Taylor & Francis)

illustration of an MFC has been presented in Fig. 15.6. An MFC can be seen as a dual-utility device which can effectively generate electrical energy from wastewater, cleaning and purifying the wastewater in the process. It can also serve in production of biohydrogen and can also act as a biosensor [5]. However, as of now, the electrical energy generated by an MFC is too low for commercial production. Similar to hydrogen fuel cells, MFCs have also witnessed the utilization of commercial Nafion membranes in majority of PEMs. However, these commercial Nafion membranes suffered from certain drawbacks, such as (a) extreme high cost; (b) allowance of passage of positive ions other than protons, resulting in accumulation of these ions in the cathode chamber and a reduction in the rate of cathode reaction [54]; and (c) formation of biofilm on the membrane surface, leading to reduced transport potential [55]. Therefore, in order to overcome these critical problems, various alternative membranes have been designed and fabricated [56–58]. However, this chapter will only focus on PEMs based on polymer/inorganic composite materials.

Polymer/inorganic nanocomposite membranes enjoy lower cost, easier transport of protons and higher resistance against biofouling in comparison with other PEMs. A novel poly(ether sulfone) (PES)/ferrosoferric oxide (Fe_3O_4) (15 wt%) nanocomposite membrane exhibited a highest voltage production of 0.656 (among all the membranes studied), which was found to remain stable over 72 h operation [59]. This nanocomposite membrane demonstrated higher current and power

densities of 148 and 20 mW m^{-2}, respectively, compared to the corresponding values of 112 and 15.4 mW m^{-2} obtained for a commercial Nafion-117 membrane.

In this work, *Saccharomyces cerevisiae* and low-concentration neutral red were used as the biocatalyst and the anode chamber electron shuttle, respectively. A SPEEK/Fe$_3$O$_4$ (7.5 wt%) nanocomposite membrane demonstrated high selectivity in transfer of protons over other available cationic species and low extent of crossover of oxygen [60]. This, in turn, resulted in the membrane exhibiting a higher maximum power density (i.e., 104 mW m^{-2}) compared to that obtained for a commercial Nafion-117 membrane (i.e., 47 mW m^{-2}). SEM images (Fig. 15.7) of the nanocomposite membranes synthesized using different loadings of Fe$_3$O$_4$ particles show that these inorganic particles were largely present on the surface of the SPEEK membrane, with uniform distribution. *Escherichia coli* and Pt/C were utilized as the anode biocatalyst and the air-cathode catalyst, respectively.

Nano-Al$_2$O$_3$-incorporated sulfonated PVdF-*co*-HFP (SPVdF-*co*-HFP)/Nafion nanocomposite membranes were fabricated for potential application as PEMs in MFCs [61]. The nanocomposite membrane containing 5 wt% of incorporated nano-Al$_2$O$_3$ produced higher proton conducting and water uptake abilities compared to the pristine SPVdF-*co*-HFP and the commercial Nafion-115 membrane. Moreover, this particular membrane also demonstrated current and maximum power density values of 1900 ± 95 mA m^{-2} and 541.52 ± 27 mW m^{-2},
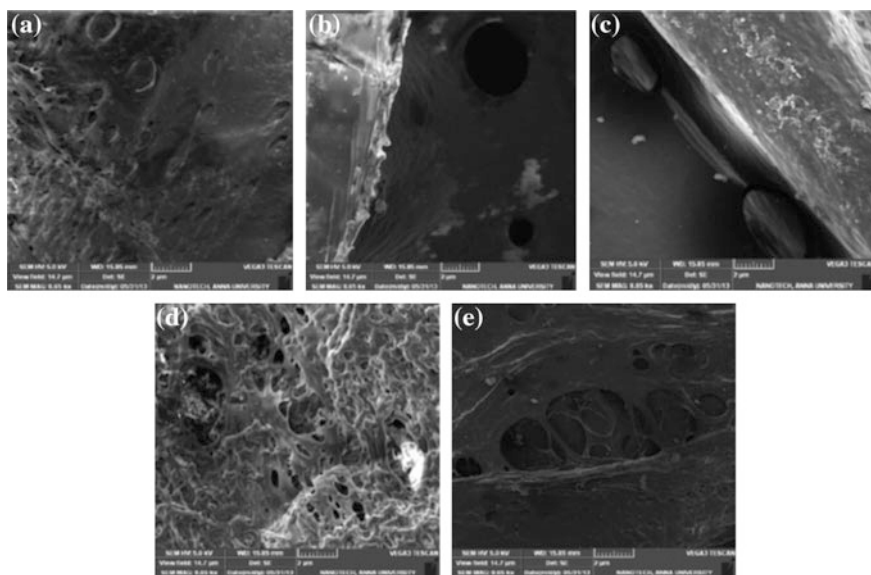
Fig. 15.7 Scanning electron micrographs of **a** pristine SPEEK, **b** SPEEK/Fe$_3$O$_4$ (2.5 wt%), **c** SPEEK/Fe$_3$O$_4$ (5 wt%), **d** SPEEK/Fe$_3$O$_4$ (7.5 wt%), and **e** SPEEK/Fe$_3$O$_4$ (10 wt%); *Darker portions* localized hydrophilic ion clusters, *lighter portions* hydrophobic moieties (reproduced from Ref. [60] with kind permission of © 2014 Elsevier)

respectively. This output power density was higher that the values obtained for the
pristine SPVdF-*co*-HFP and the commercial Nafion-115 membranes by $\sim$48 and
$\sim$11%, respectively. Mixed *firmicutes* was employed as a biocatalyst in this work.

15.4   Polymer-Inorganic Nanocomposites as Polymer
Electrolyte Membranes in Direct Methanol Fuel Cells

A DMFC is an electrochemical device responsible for chemical to electrical energy
conversion via combination of methanol as a fuel (anode reactant or anolyte) and
oxygen or air as an oxidant (cathode reactant or catholyte). In general, the anode
and the cathode reactions take place in presence of Pt-Ru as the anode catalyst and
Pt as the cathode catalyst [62, 63]. A schematic illustration of a DMFC has been
presented in Fig. 15.8. Like, the other two fuel cell systems discussed above,
DMFCs have also witnessed the application of commercial Nafion membranes as
the state-of-the-art PEMs. In DMFCs, Nafion membranes offer several positive
attributes, including high conduction of protons (under fully hydrated condition),
excellent electrochemical and chemical stabilities, and structural integrity at mod-
erate temperatures of up to 80 °C. However, as mentioned above, these Nafion
membranes are extremely costly; thus, contributing to an overall increase in the cost
of the DMFC device, which hinders its widespread application and commercial-
ization. In addition, in a DMFC, Nafion membranes suffer from high permeability
of methanol from the anode chamber to the cathode chamber [64]; thus, leading to
generation of high cross-potential and sluggish cathode reaction kinetics [65].
Moreover, at high temperatures (>80–90 °C), Nafion membranes face loss of
moisture retention capacity and chemical and mechanical stability, leading to a
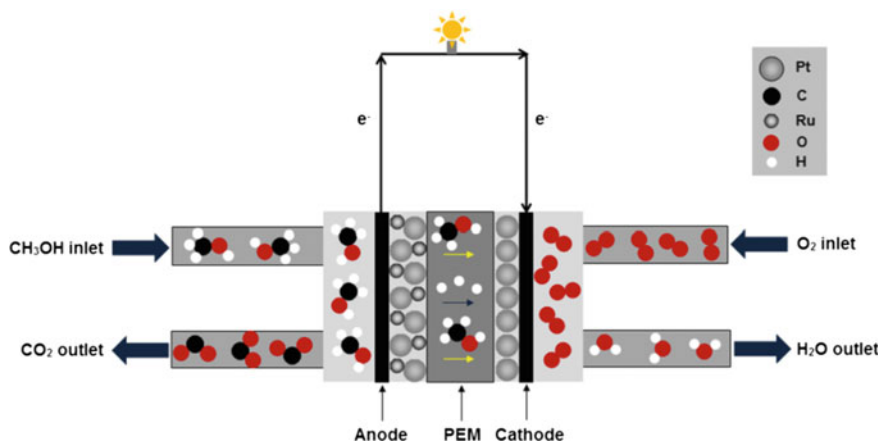
Fig. 15.8 A schematic illustration of a direct methanol fuel cell (reproduced from Ref. [8] with
kind permission of © 2014 Taylor & Francis)

decrease in its proton conductivity. Furthermore, Nafion suffers from loss of pendant –SO$_3$H groups owing to hydrolysis at temperatures >100 °C. These critical drawbacks of commercial Nafion membranes have demanded designing, synthesis and fabrication of alternative membranes for application as PEMs in DMFCs [66–68]. This chapter will review the development of PEMs fabricated from polymer/inorganic composite materials.

Nanocomposite membranes composed of PVdF-*co*-HFP, Nafion, and aluminum oxy hydroxide (AlO[OH]$_n$) were synthesized and evaluated for use as PEMs in DMFCs [69]. The membrane consisting of 51 wt% of PVdF-*co*-HFP, 41 wt% of Nafion and 8 wt% of AlO[OH]$_n$ produced the best results among the prepared membranes (with varying constituent loading) in terms water uptake (i.e., 33.8%), methanol uptake (i.e., 17.27%) and proton conductivity (i.e., 1×10^{-3} S cm^{-1}). However, in terms of methanol permeability, the PEM composed of 90 wt% of PVdF-*co*-HFP and 10 wt% of AlO[OH]$_n$ exhibited the best result (i.e., 6.2×10^{-8} cm^2 min^{-1}) in comparison with commercial Nafion-117 membrane (i.e., 2.32×10^{-5} cm^2 min^{-1}) and the PVdF-*co*-HFP (51 wt%)/Nafion (41 wt%)/AlO[OH]$_n$ (8 wt%) membrane (i.e., 9.8×10^{-7} cm^2 min^{-1}). Incorporation of the inorganic component was also found to increase the thermal stability of the PEMs. Presence of ceramic oxides within polymer-based membranes has been observed to improve the high temperature performance of DMFCs. The oxygen atoms present in these oxides, along with their high surface area, play a major role in enhancing the electrochemical properties of the composite PEMs. Nano-alumina, as an inorganic constituent, has been utilized in blends of SPVdF-*co*-HFP/Nafion for fabrication of PEMs for DMFCs [70]. This nanocomposite membrane, containing 5 wt% of incorporated nano-alumina, demonstrated current density values of 270 and 285 mA cm^{-2} at 110 and 90 °C, respectively, at an applied potential of 0.2 V. This particular membrane also exhibited an optimum power density value of 57 mW cm^{-2} at 0.2 V and 90–110 °C cell temperature, compared to the corresponding values of 28 mW cm^{-2} obtained for the commercial Nafion-117 membrane and 32 mW cm^{-2} obtained for the SPVdF-*co*-HFP/Nafion blend membrane. Therefore, the nanocomposite membrane was significantly successful in preventing the loss of moisture retention capacity of Nafion at high temperatures.

A recast Nafion/TiO$_2$ nanocomposite membrane demonstrated a current density of >800 mA cm^{-2} and a maximum power density of 350 mW cm^{-2} at 0.4 V applied potential, 145 °C cell temperature, 2 M methanol feed at the anode and oxygen feed at the cathode [71]. TiO$_2$, calcined as 500 °C, was found to produce the best results [71, 72]. Tin oxide (SnO$_2$) has also been utilized as the inorganic component in polymer/inorganic nanocomposite membranes [73]. Presence of 9 wt% of SnO$_2$ in poly(styrene sulfonic acid)-grafted PVdF-*co*-HFP/SnO$_2$ nanocomposite membrane was found to exhibit an IEC of 0.9 meq g^{-1}, a water uptake of $\sim$50%, a methanol uptake of $\sim$23% (2 M methanol), a proton conductivity of $\sim$9.9 $\times$ 10^{-2} S cm^{-1} and a methanol permeability of $\sim$8$\times$10^{-7} cm^2 s^{-1}, in comparison with the corresponding values of 1.55 meq g^{-1}, $\sim$58, $\sim$29% (2 M methanol), $\sim$1.32 $\times$ 10^{-1} S cm^{-1} and $\sim$2.3 $\times$ 10^{-6} cm^2 s^{-1}, respectively, obtained for the pristine PVdF-*co*-HFP membrane. This particular nanocomposite

membrane demonstrated the highest efficiency among all other nanocomposite membranes fabricated. The proton conductivities of the different composite membranes were observed to increase with increasing relative humidity and temperature. In addition, this 9 wt% SnO_2-containing nanocomposite membrane demonstrated a superior current density of ~ 240 mA cm^{-2} and a corresponding maximum power density of ~ 110 mW cm^{-2} at 0.4 V, 60 °C cell temperature, 2 M methanol feed at the anode and non-humidified air feed at the cathode; as compared to the corresponding values of ~ 170 mA cm^{-2} and ~ 81 mW cm^{-2}, respectively, obtained for the pristine membrane. Similarly, a nanocomposite PEM, constituting of SPEEK and 50 wt% $SnO_2.nH_2O$, demonstrated significant proton conductivity and stability, as well as, low methanol permeability toward exhibition of good DMFC performance at 100 °C [74].

Methanol crossover through the PEM is one of the most critical drawbacks of a DMFC system, since this leads to generation of high cross-potential and sluggish cathode reaction kinetics. An approach to circumvent this serious problem is to directly deposit transition metal nanoparticles onto the PEM surface. Uniform distribution of these deposited nanoparticles leads to blocking of pores/methanol transport channels present within the PEM; thus, resulting in suppression of methanol crossover. Pt, Pd, and Au nanoparticles have found use in this respect and have exhibited promising results [75–79].

A nanocomposite membrane composed of recast Nafion and acid-functionalized zeolite beta (5 wt%) exhibited 40% reduced methanol permeability compared to commercial Nafion-115 membrane, while maintaining comparable proton conductivity with the commercial membrane [80]. Schematic illustrations of the nanocomposite membrane and its transport potential have been presented in Fig. 15.9. This figure clearly demonstrates the ability of the nanocomposite membrane to restrict flow of methanol across the membrane while allowing smaller size protons to pass through. During DMFC operation, using 1 M methanol as the
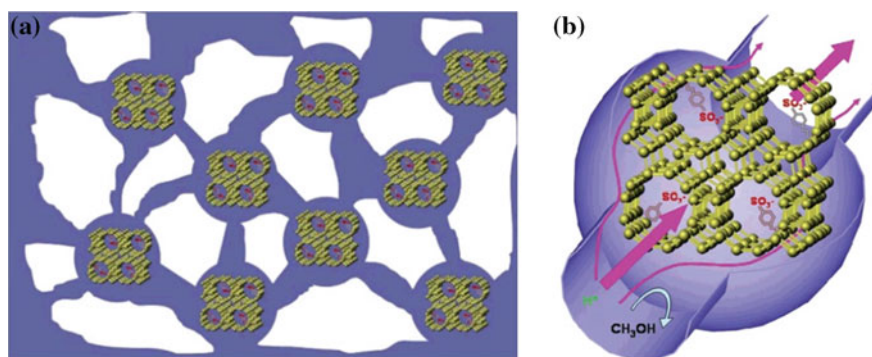

Fig. 15.9 Schematic illustrations of the Nafion/acid-functionalized zeolite beta nanocomposite membrane and its transport potential; **a** *White portions* hydrophobic sections present within Nafion and *colored portions* hydrophilic sections present within Nafion; **b** transport of methanol and proton in the nanocomposite membrane (reproduced from Ref. [80] with kind permission of © 2006 American Chemical Society)

feed and 70 °C cell temperature, this nancomposite membrane demonstrated a 21% higher maximum power density and a 3% higher open circuit voltage (OCV) over that of the commercial Nafion-115 membrane. However, when the feed methanol concentration was increased to 5 M, the nanocomposite membrane exhibited a 93% higher maximum power density and a 14% higher OCV over that of the commercial membrane. Similarly, recast Nafion/montmorillonite, recast Nafion/Aerosil®, SPEEK/laponite and SPEEK/montmorillonite nanocomposite membranes have been fabricated and utilized as PEMs for normal and high temperature DMFC operations [81–85]. These membranes exhibited significantly high proton conductivity, much reduced methanol permeability and enhanced membrane selectivity compared to state-of-the-art Nafion membranes.

DMFC operation under conditions of high temperature and low humidity demands tailor-made acid-base characteristics of the surface of the inorganic nanoparticles [86]. The number of acidic functional groups present on the surface of the nanocomposite membranes, as well as, the strength of these acidic functionalities determine the capacity of these membranes toward absorption and retention of water, via electrostatic interaction, for proper functioning of the membranes under conditions of low humidity present during high temperature (>140 °C) DMFC operation. This phenomenon, in turn, directly affects the proton conducting abilities of the membranes [87, 88], via both Grotthus and vehicular mechanism of proton transport (Fig. 15.10) [8, 66].

ZrO_2, SiO_2, calcium oxide (CaO), zirconium phosphate, and titanium phosphate nanoparticles have also found utilization toward fabrication of as PEMs in DMFCs. For example, a CaO-containing chitosan/poly(vinyl alcohol) (PVA) nanocomposite membrane was found to exhibit lower methanol permeability compared to commercial Nafion-115 membrane [89]. Again, SPEEK/ZrO_2 nanocomposite membranes demonstrated large reduction in methanol, water, nitrogen, oxygen, and carbon dioxide permeabilities compared to the pristine SPEEK membrane [90]. This reduced permeabilities of the different species present within the cell was a result of uniform distribution of the ZrO_2 nanoparticles (of $\sim$100 nm diameter) on the base SPEEK membrane, pore-blocking of the SPEEK membrane by the deposited ZrO_2 particles, and strong adhesion between the polymer matrix and the deposited inorganic phase (Fig. 15.11).

Like hydrogen fuel cells, DMFCs have also witnessed involvements of SiO_2 and SiO_2-based inorganic nanoparticles toward fabrication of PEMs. For instance, PVA/sulfosuccinic acid/SiO_2 nanocomposite membranes have been designed in order to reduce the methanol permeation ability of the PEMs [91]. These hybrid PEMs demonstrated a methanol permeation range of 10^{-7}–10^{-8} cm^2 s^{-1} and a proton conduction range of 10^{-2}–10^{-3} S cm^{-1}. These two PEM properties were found to be reliant on the content of the sulfosuccinic acid within the hybrid membrane, which in this case plays the role of providing hydrophilic –SO_3H functionalities and as a crosslinker. Again, a Nafion/SiO_2/PWA nanocomposite membrane demonstrated a higher maximum power density at 145 °C, i.e., 400 mW cm^{-2} using oxygen catholyte and 250 mW cm^{-2} using air catholyte, compared to Nafion/SiO_2 and Nafion/SiO_2/silicotungstic acid nanocomposite
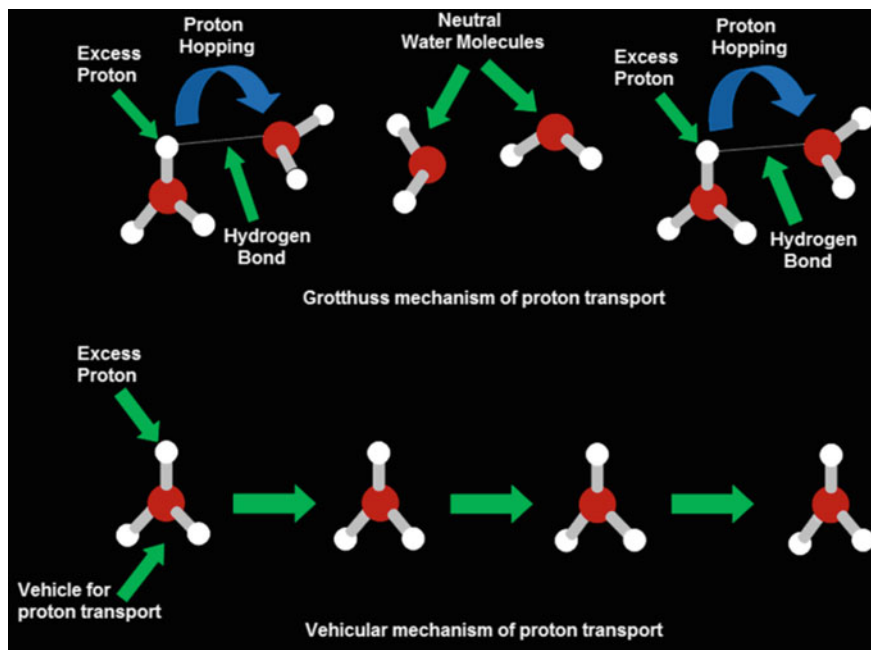
Fig. 15.10 Grotthus and vehicular mechanism of proton transport through a PEM. In the Grotthus mechanism, transfer and transport of excess protons occur along the hydrogen bonds via neutral water molecules; while in the vehicular mechanism, transport of excess protons occur with the aid of moving vehicles such as water, hydroxonium, and other complex ions (reproduced from Ref. [8] with kind permission of © 2014 Taylor & Francis)

Fig. 15.11 Scanning electron micrograph demonstrating the fine dispersion of deposited ZrO_2 particles in the SPEEK/ZrO_2 (5 wt%) composite membrane (reproduced from Ref. [90] with kind permission of © 2005 Elsevier)
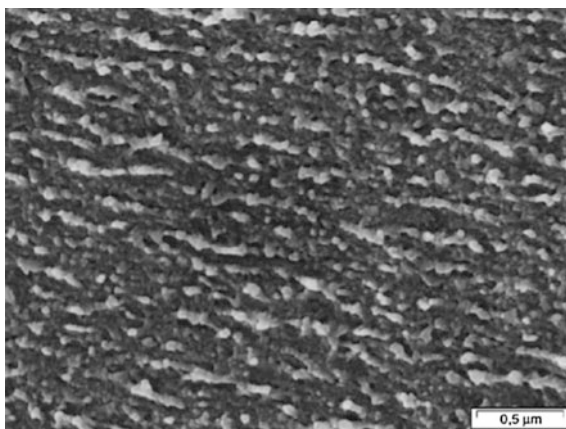
membranes [92]. This better DMFC performance induced by the presence of PWA within the PEM was attributed to its ability of higher water retention and the resulting higher proton conductivity. Similarly, Nafion/PAni/SiO_2 nanocomposite

membranes exhibited reduced methanol crossover compared to commercial Nafion-117 membrane [93].

In essence, an increase in silica content of a membrane leads to increase in its oxidative stability and membrane selectivity, and decrease in its methanol permeability, methanol uptake, proton conductivity, and water uptake [94–96]. Again, incorporation of mesoporous titanium phosphate, mesoporous zirconium phosphate or SiO_2 nanoparticles within Nafion membranes has been reported to produce enhanced water uptake, reduced methanol permeability and similar proton conductivity compared to the commercial Nafion-117 membrane [97]. The DMFC performances obtained with these nanocomposite membranes have been presented in Fig. 15.12. Other silica-based hybrid polymer/inorganic nanocomposite membranes, such as Nafion/imidazole-functionalized nanosilica and sulfonated poly (arylene ether ketone) (SPAEK)/3-glycidoxypropyl-trimethoxysilane (GPTMS)/ 3-mercaptopropyl-trimethoxysilane (MPTMS), have produced similar results as discussed above [98, 99].

The above reports, highlights, and discussions summarize the important works reported so far regarding research and development in the field of polymer/ inorganic PEMs for DMFCs. Table 15.2 lists a compilation of the results obtained using different polymer/inorganic nanocomposite membranes in DMFCs. For further reading, the readers are referred to other major literary works listed in the reference section of this chapter [17, 20, 52, 53].
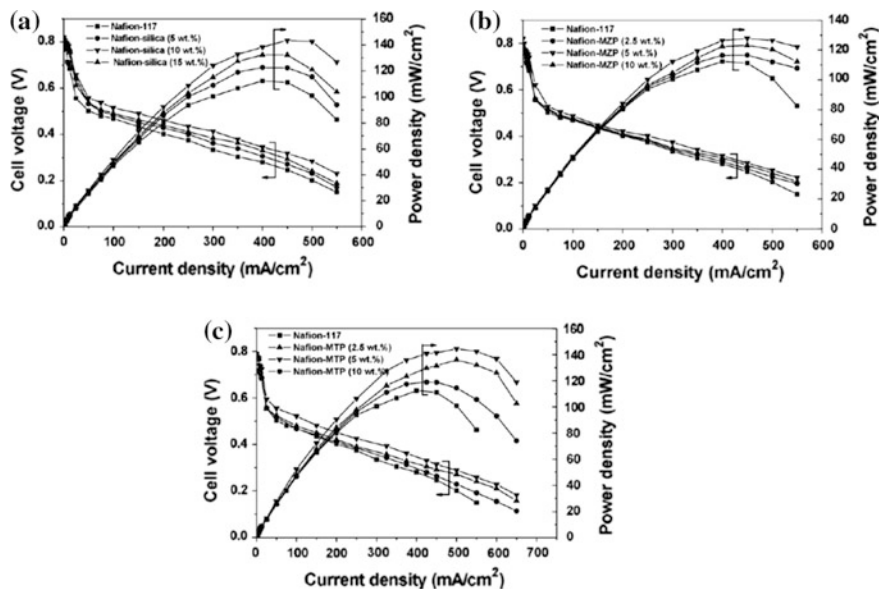
Fig. 15.12 DMFC performances obtained with **a** Nafion/SiO_2, **b** Nafion/mesoporous zirconium phosphate and **c** Nafion/mesoporous titanium phosphate nanocomposite membranes, in comparison with the commercial Nafion-117 membrane, at 70 °C (*anolyte* 2 M aqueous methanol at a flow rate of 2 sccm, *catholyte* oxygen at a flow rate of 200 sccm) (reproduced from Ref. [97] with kind permission of © 2009 Elsevier)

Table 15.2 A compilation of the results obtained using different polymer/inorganic nanocomposite membranes in direct methanol fuel cells

Membrane materials	Cell type	Water uptake (%)	IEC (meq g^{-1})	Proton conductivity (S cm^{-1})	Methanol permeability (cm^{2}s^{-1})	Membrane selectivity (S cm^{-3})	Maximum power density (mW cm^{-2})	Refs.
PVdF-*co*-HFP (51 wt%)/Nafion (41 wt%)/AlO[OH]$_n$ (8 wt%)	–	33.8 at room temperature	–	1×10^{-3} at room temperature	1.6×10^{-8} at room temperature	6.25×10^4 at room temperature	–	[69]
PVdF-*co*-HFP (90 wt%)/AlO[OH]$_n$ (10 wt%)	–	25.3 at room temperature	–	8×10^{-5} at room temperature	1×10^{-9} at room temperature	8×10^4 at room temperature	–	[69]
Nafion-117	Methanol/non-humidified air single cell	16.2 at 20 °C	0.81 at 20 °C	3.02×10^{-2} at 20 °C	1.22×10^{-6} at 20 °C	2.47×10^4 at 20 °C	39 at 60 °C, 28 at 90 °C and 11 at 110 °C, at 0.2 V	[70]
SPVdF-*co*-HFP/Nafion	Methanol/non-humidified air single cell	~18.5 at 20 °C	0.73 at 20 °C	2.32×10^{-2} at 20 °C	6.21×10^{-7} at 20 °C	3.79×10^4 at 20 °C	49 at 60 °C, 32 at 90 °C and 15 at 110 °C, at 0.2 V	[70]
SPVdF-*co*-HFP/Nafion/nano-Al$_2$O$_3$ (5 wt%)	Methanol/non-humidified air single cell	34.8 at 20 °C	0.68 at 20 °C	3.57×10^{-2} at 20 °C	6.41×10^{-7} at 20 °C	5.56×10^4 at 20 °C	35 at 60 °C, 57 at 90 °C and 54 at 110 °C, at 0.2 V	[70]
Nafion/TiO$_2$	Methanol/O$_2$ single cell	–	–	–	–	–	350 at 0.4 V applied potential, 145 °C and 2 M methanol feed	[71]
PVdF-*co*-HFP/SnO$_2$ (9 wt%)	Methanol/non-humidified air single cell	~50 at room temperature	0.90 at room temperature	~9.9×10^{-2} at 100 °C and 100% relative humidity	~8×10^{-7} at 30 °C	–	~110 at 0.4 V applied potential, 60 °C and 2 M methanol feed	[73]
PVdF-*co*-HFP	Methanol/non-humidified air single cell	~58 at room temperature	1.55 at room temperature	~1.32×10^{-1} at 100 °C and 100% relative humidity	~2.3×10^{-6} at 30 °C	–	~81 at 0.4 V applied potential, 60 °C and 2 M methanol feed	[73]

(continued)

Table 15.2 (continued)

Membrane materials	Cell type	Water uptake (%)	IEC (meq g⁻¹)	Proton conductivity (S cm⁻¹)	Methanol permeability (cm²s⁻¹)	Membrane selectivity (S cm⁻³)	Maximum power density (mW cm⁻²)	Refs.
Nafion-115	Methanol/O$_2$ single cell			9.1×10^{-2} at room temperature	2.36×10^{-6} at room temperature	3.86×10^{4} at room temperature	81 and 62 at 1 M and 5 M methanol feed concentration, respectively, at 70 °C	[80]
Nafion/acid-functionalized zeolite beta	Methanol/O$_2$ single cell			8.8×10^{-2} at room temperature	1.40×10^{-6} at room temperature	6.29×10^{4} at room temperature	98 and 120 at 1 M and 5 M methanol feed concentration, respectively, at 70 °C	[80]
Recast Nafion	–	32 at room temperature	0.89 at room temperature	$\sim 8.6 \times 10^{-2}$ at room temperature	$\sim 2.27 \times 10^{-6}$ at room temperature	$\sim 3.8 \times 10^{4}$ at room temperature	–	[98]
Nafion/nanosilica (2 wt%)	–	30 at room temperature	0.88 at room temperature	$\sim 8.55 \times 10^{-2}$ at room temperature	$\sim 1.51 \times 10^{-6}$ at room temperature	$\sim 5.7 \times 10^{4}$ at room temperature	–	[98]
Nafion/imidazole-functionalized nanosilica (2 wt%)	–	29 at room temperature	0.90 at room temperature	$\sim 8.95 \times 10^{-2}$ at room temperature	$\sim 9.3 \times 10^{-7}$ at room temperature	$\sim 9.6 \times 10^{4}$ at room temperature	–	[98]
Nafion-117	–	18.3 ± 3 at 25 °C	0.92 at 25 °C	7.6×10^{-2} at 25 °C	1.01×10^{-6} at 25 °C	7.56×10^{4} at 25 °C	–	[99]
SPAEK	–	51.3 ± 0.6 at 25 °C	1.6 at 25 °C	5×10^{-2} at 25 °C	6.65×10^{-7} at 25 °C	7.52×10^{4} at 25 °C	–	[99]
SPAEK (95 wt%)/GPTMS (1.25 wt%)/MPTMS (3.75 wt%)	–	52.8 ± 0.6 at 25 °C	2.0 at 25 °C	6.3×10^{-2} at 25 °C	3.64×10^{-7} at 25 °C	1.73×10^{5} at 25 °C	–	[99]

Unavailable or unclear values have been presented as '–'

15.5 Conclusions and Future Perspectives

The overall development that has taken place over the years, especially in the last decade, in the field of polymer/inorganic nanocomposite PEMs for PEMFCs has been reviewed in this chapter. Evidence of enormous research and developmental activities toward designing, synthesizing, and fabrication of polymer/inorganic nanocomposite PEMs has been witnessed. These hybrid nanocomposite membranes have been tested and applied with the objective of replacing conventional commercial PEMs, such as Nafion membranes, and other PEMs, which are fabricated either from a single polymer or via formation of blends, grafts, coats, laminates, and interpenetrating networks involving two or more polymers. Applications of these polymer/inorganic hybrid nanocomposite PEMs in three most important PEMFCs, namely hydrogen fuel cells, MFCs and DMFCs, have been highlighted and discussed, and the results obtained from these applications have been presented categorically and systematically in the representative figures and the tables.

Conventional PEM materials suffer from certain critical drawbacks that have been discussed under the respective sections of this chapter. The most important aspects in this regard are the inabilities of the conventional PEMs to (a) perform under conditions of high temperature and low humidity in both hydrogen fuel cells and DMFCs, (b) resist flow of cations other than protons in MFCs, (c) resist formation of surface biofilms and material degradation by microorganisms in MFCs, (d) resist methanol crossover in DMFCs, and (e) maintain a high proton conductivity while reducing methanol permeability in DMFCs. Moreover, the cost consideration of the high-cost commercial PEMs are also important, since a high material cost leads to an increase in the overall cost of the device operation and energy generation. These drawbacks have led to the concept of incorporation of low cost inorganic fillers within PEM matrices, since these inorganic nanomaterials possess (a) nanodimensions of <100 nm enabling them to fit within the pores present in the membrane matrix, thus hindering the flow of liquids and gases through the membrane pores; (b) selective transfer of small-sized protons, thus restricting the passage of other large-sized cations through the membrane pores; (c) high surface area enabling them to uniformly disperse and distribute over the entire PEM matrices; and (d) acidic functionalities, which enhances the capacity of the PEMs toward absorption and retention of water, via electrostatic interaction, for proper functioning under conditions of low humidity present during high temperature DMFC operation, as well as, allowing high rate and amount of proton transport while restricting the flow of fuel, gases and other cations.

Future research in this area shall witness greater involvements of high performance materials, such as aromatic conjugated polymers, graphenes, and carbon nanotubes, as co-components in conjunction with the already established base polymer matrix and dispersed inorganic domains systems. These high performance materials, as evident from literature, have found extensive use in a wide variety of applications, including the fabrication of PEMs for PEMFCs. Therefore, their proper and judicious utilization shall render positive attributes to this area of

research. Another approach, which is also an established technique, is to directly deposit inorganic catalyst nanoparticles onto the surface of the PEMs. This will ensure intimate contact between the catalyst layer and the electrolyte, which is essential to minimize the internal resistance of the cell. Moreover, these deposited catalyst nanoparticles will also serve the purpose of blocking the available pores present within the base polymer matrix, thus ensuring restricted flow of undesired species and selective flow of protons. Lastly, synthesis of potential matrix polymer materials and dispersed inorganic nanoparticles with tailor-made properties, which shall ensure better interaction between these two phases, should be designed and performed. The resulting PEMs, with intimately bonded phases, shall inherently possess controlled pore size and pore distribution to restrict flow of unwanted substances, ability to withstand high temperature and low humidity conditions, and long-term stability under practical cell operating environments.

References

1. Kundu PP, Dutta K (2016) Hydrogen fuel cells for portable applications. In: Ball M, Basile A, Veziroglu TN (eds) Compendium of hydrogen energy, 4th edn. Woodhead Publishing, Elsevier, pp 111–131
2. Das S, Dutta K, Kundu PP (2015) Nickel nanocatalysts supported on sulfonated polyaniline: potential toward methanol oxidation and as anode materials for DMFCs. J Mater Chem A 3:11349–11357
3. Das S, Dutta K, Kundu PP et al (2016) Ulfonated polypyrrole matrix induced enhanced efficiency of Ni nanocatalyst for application as an anode material for DMFCs. Mater Chem Phys 176:143–151
4. Nandy A, Kumar V, Mondal S (2015) Performance evaluation of microbial fuel cells: effect of carrying electrode configuration and presence of a membrane electrode assembly. New Biotechnol 32:272–281
5. Dutta K, Kundu PP (2014) A review on aromatic conducting polymers-based catalyst supporting matrices for application in microbial fuel cells. Polym Rev 54:401–435
6. Inan TY, Doğan H, Unveren EE et al (2010) Sulfonated PEEK and fluorinated polymer based blends for fuel cell applications: investigation of the effect of type and molecular weight of the fluorinated polymers on the membrane's properties. Int J Hydrog Energy 35:12038–12053
7. Zhang H, Li X, Zhao C (2008) Composite membranes based on highly sulfonated PEEK and PBI: morphology characteristics and performance. J Membr Sci 308:66–74
8. Dutta K, Kumar P, Das S (2014) Utilization of conducting polymers in fabricating polymer electrolyte membranes for application in direct methanol fuel cells. Polym Rev 54:1–32
9. Dutta K, Das S, Kundu PP (2016) Highly methanol resistant and selective ternary blend membrane composed of sulfonated PVDF-co-HFP, sulfonated polyaniline and nafion. J Appl Polym Sci 133:1–10
10. Dutta K, Das S, Kundu PP (2016) Effect of the presence of partially sulfonated polyaniline on the proton and methanol transport behavior of partially sulfonated PVdF membrane. Polym J 48:301–309
11. Kumar P, Dutta K, Das S et al (2014) Membrane prepared by incorporation of crosslinked sulfonated polystyrene in the blend of PVDF-*co*-HFP/Nafion: a preliminary evaluation for application in DMFC. Appl Energy 123:66–74

12. Dutta K, Das S, Kundu PP (2014) Low methanol permeable and highly selective membranes composed of pure and/or partially sulfonated PVDF-*co*-HFP and polyaniline. J Membr Sci 468:42–51

13. Cho K-Y, Eom J-Y, Jung H-Y et al (2004) Characteristics of PVdF copolymer/Nafion blend membrane for direct methanol fuel cell (DMFC). Electrochim Acta 50:583–588

14. Yang J, Shen PK, Varcoe J et al (2009) Nafion/polyaniline composite membranes specifically designed to allow proton exchange membrane fuel cells operation at low humidity. J Power Sources 189:1016–1019

15. Dutta K, Das S, Kundu PP (2015) Partially sulfonated polyaniline induced high ion-exchange capacity and selectivity of Nafion membrane for application in direct methanol fuel cells. J Membr Sci 473:94–101

16. Das S, Dutta K, Hazra S et al (2015) Partially sulfonated poly(vinylidene fluoride) induced enhancements of properties and DMFC performance of Nafion electrolyte membrane. Fuel Cells 15:505–515

17. Peighambardoust SJ, Rowshanzamir S, Amjadi M et al (2010) Review of the proton exchange membranes for fuel cell applications. Int J Hydrog Energy 35:9349–9384

18. Kumar P, Dutta K, Das S et al (2014) An overview of unsolved deficiencies of direct methanol fuel cell technology: factors and parameters affecting its widespread use. Int J Energy Res 38:1367–1390

19. Rinaldi A, Mecheri B, Garavaglia V et al (2008) Traversa, engineering materials and biology to boost performance of microbial fuel cells: a critical review. Energy Environ Sci 1:417–429

20. Zhang H, Shen PK (2012) Recent development of polymer electrolyte membranes for fuel cells. Chem Rev 112:2780–2832

21. Baradie B, Dodelet JP, Guay D (2000) Hybrid Nafion®-inorganic membrane with potential applications for polymer electrolyte fuel cells. J Electroanal Chem 489:101–105

22. Shao ZG, Xu H, Li M et al (2006) Hybrid Nafion-inorganic oxides membrane doped with heteropolyacids for high temperature operation of proton exchange membrane fuel cell. Solid State Ionics 177:779–785

23. Jalani NH, Dunn K, Datta R et al (2005) Synthesis and characterization of Nafion-MO$_2$ (M = Zr, Si, Ti) nanocomposite membranes for higher temperature PEM fuel cells. Electrochim Acta 51:553–560

24. Park KT, Jung UH, Choi DW et al (2008) ZrO$_2$-SiO$_2$/Nafion composite membrane for polymer electrolyte membrane fuel cells operation at high temperature and low humidity. J Power Sour 177:247–253

25. SaccàA Gatto I, Carbone A et al (2006) ZrO$_2$-Nafion composite membranes for polymer electrolyte fuel cells (PEFCs) at intermediate temperature. J Power Sour 163:47–51

26. Pan J, Zhang H, Chen W et al (2010) Nafion-zirconia nanocomposite membranes formed via in situ sol–gel process. Int J Hydrog Energy 35:352796–352801

27. Woo MH, Kwon O, Choi SH et al (2006) Zirconium phosphate sulfonated poly (fluorinated arylene ether)s composite membranes for PEMFCs at 100–140 °C. Electrochim Acta 51:6051–6059

28. Costamagna P, Yang C, Bocarsly AB et al (2002) Nafion® 115/zirconium phosphate composite membranes for operation of PEMFCs above 100 °C. Electrochim Acta 47: 1023–1033

29. Damay F, Klein LC (2003) Transport properties of Nafion™ composite membranes for proton-exchange membranes fuel cells. Solid State Ionics 162–163:261–267

30. Yang C, Srinivasan S, Bocarsly AB et al (2004) A comparison of physical properties and fuel cell performance of Nafion and zirconium phosphate/Nafion composite membranes. J Membr Sci 237:145–161

31. Mishra AK, Bose S, Kuila T (2012) Silicate-based polymer-nanocomposite membranes for polymer electrolyte membrane fuel cells. Prog Polym Sci 37:842–869

32. Adjemian KT, Lee SJ, Srinivasan S (2002) Silicon oxide Nafion composite membranes for proton-exchange membrane fuel cell operation at 80–140 °C. J Electrochem Soc 149: A256–A261

33. Pereira F, ValléK Belleville P et al (2008) Advanced mesostructured hybrid silica-nafion membranes for high-performance PEM fuel cell. Chem Mater 20:1710–1718
34. Wang H, Holmberg BA, Huang L et al (2002) Nafion-bifunctional silica composite proton conductive membranes. J Mater Chem 12:834–837
35. Moghaddam S, Pengwang E, Jiang Y-B et al (2010) An inorganic-organic proton exchange membrane for fuel cells with a controlled nanoscale pore structure. Nat Nano Technol 5:230–236
36. Kannan AG, Choudhury NR, Dutta NK (2009) In situ modification of Nafion membranes with phospho-silicate for improved water retention and proton conduction. J Membr Sci 333:50–58
37. Kim YM, Choi SH, Lee HC et al (2004) Organic-inorganic composite membranes as addition of SiO_2 for high temperature-operation in polymer electrolyte membrane fuel cells (PEMFCs). Electrochim Acta 49:4787–4796
38. Qi L, Dong SJ (2007) Organic/inorganic nanocomposite polymer electrolyte. Chin Chem Lett 18:185–188
39. Honma N, Hirakawa S, Yamada K et al (1999) Synthesis of organic/inorganic nanocomposites protonic conducting membrane through sol–gel processes. Solid State Ionics 118:29–36
40. Mahreni A, Mohamad AB, Kadhum AAH et al (2009) Nafion®/silicon oxide/phosphotungstic acid nanocomposite membrane with enhanced proton conductivity. J Membr Sci 327:32–40
41. Sahu AK, Selvarani G, Pitchumani S et al (2007) A sol–gel modified alternative Nafion-silica composite membrane for polymer electrolyte fuel cells. J Electrochem Soc 154:B123–B132
42. Tang HL, Pan M (2008) Synthesis and characterization of a self-assembled Nafion/silica nanocomposite membrane for polymer electrolyte membrane fuel cells. J Phys Chem C 112:11556–11568
43. Linlin M, Mishra AK, Kim NH et al (2012) Poly(2,5-benzimidazole)-silica nanocomposite membranes for high temperature proton exchange membrane fuel cell. J Membr Sci 411–412:91–98
44. Suryani S, Chang YN, Lai JY et al (2012) Polybenzimidazole (PBI)-functionalized silica nanoparticles modified PBI nanocomposite membranes for proton exchange membranes fuel cells. J Membr Sci 403–404:1–7
45. Honma E, Nakajima H, Nishikawa O (2003) Organic/inorganic nano-composites for high temperature proton conducting polymer electrolytes. Solid State Ionics 162–163:237–245
46. Noto VD, Piga M, Piga L et al (2008) New inorganic-organic proton conducting membranes based on Nafion and [(ZrO2).(SiO2)0.67] nanoparticles: synthesis vibrational studies and conductivity. J Power Sources 178:561–574
47. SaccàA Carbone A, Passalacqua E (2005) Nafion-TiO_2 hybrid membranes for medium temperature polymer electrolyte fuel cells (PEFCs). J Power Sour 152:16–21
48. Satterfield MB, Majsztrik PW, Ota H et al (2006) Mechanical properties of nafion and titania/nafion composite membranes for polymer electrolyte membrane fuel cells. J Polym Sci Pol Phys 44:2327–2345
49. Tian JH, Gao PF, Zhu ZY (2008) Preparation and performance evaluation of a Nafion-TiO_2 composite membrane for PEMFCs. Int J Hydrog Energy 33:5686–5690
50. Yang J, Li Y, Huang Y (2008) Dynamic conducting effect of WO_3/PFSA membranes on the performance of proton exchange membrane fuel cells. J Power Sour 177:56–60
51. Şengül E, Erdener H, Akay RG (2009) Effects of sulfonated polyether-etherketone (SPEEK) and composite membranes on the proton exchange membrane fuel cell (PEMFC) performance. Int J Hydrog Energy 34:4645–4652
52. Nagarale RK, Shin W, Singh PK (2010) Progress in ionic organic-inorganic composite membranes for fuel cell applications. Polym Chem 1:388–408
53. Robert C, ValléK Pereira F et al (2011) Design and properties of functional hybrid organic-inorganic membranes for fuel cells. Chem Soc Rev 40:961–1005
54. Rozendal RA, Hamelers HVM, Buisman CJN (2006) Effects of membrane cation transport on pH and microbial fuel cell performance. Environ Sci Technol 40:5206–5211

55. Choi MJ, Chae KJ, Ajayi FF (2011) Effects of biofouling on ion transport through cation exchange membranes and microbial fuel cell performance. Bioresour Technol 102:298–303
56. Dhar BR, Lee HS (2013) Membranes for bioelectrochemical systems: challenges and research advances. Environ Technol 34:1751–1764
57. Rahimnejad M, Bakeri G, Ghasemi M (2014) A review on the role of proton exchange membrane on the performance of microbial fuel cell. Polym Adv Technol 25:1426–1432
58. Leong JX, Daud WRW, Ghasemi M (2013) Ion exchange membranes as separators in microbial fuel cells for bioenergy conversion: a comprehensive review. Renew Sustain Energy Rev 28:575–587
59. Rahimnejad M, Ghasemi M, Najafpour GD (2012) Characterization and application studies of self-made Fe_3O_4/PES nanocomposite membranes in microbial fuel cell. Electrochim Acta 85:700–706
60. Prabhu NV, Sangeetha D (2014) Characterization and performance study of sulfonated poly ether ether ketone/Fe_3O_4 nano composite membrane as electrolyte for microbial fuel cell. Chem Eng J 243:564–571
61. Kumar V, Kumar P, Nandy A (2016) A nanocomposite membrane composed of incorporated nano-alumina within sulfonated PVDF-co-HFP/Nafion blend as separating barrier in a single chambered microbial fuel cell. RSC Adv 6:23571–23580
62. DasS Dutta K, Shul YG et al (2015) Progress in developments of inorganic nanocatalysts for application in direct methanol fuel cells. Solid State Mater Sci 40:316–357
63. Dutta K, Das S, Rana D et al (2015) Enhancements of catalyst distribution and functioning upon utilization of conducting polymers as supporting matrices in DMFCs. Polym Rev 55:551–556
64. Dutta K, Kundu PP, Kundu A (2014) Fuel cells-exploratory fuel cells micro-fuel cells. In: Reedijk J (ed) Reference module in chemistry, molecular sciences and chemical engineering. Elsevier, London
65. Kumar P, Dutta K, Kundu PP (2014) Enhanced performance of direct methanol fuel cells: a study on the combined effect of various supporting electrolytes, flow channel designs and operating temperatures. Int J Energy Res 38:41–50
66. Dutta K, Das S, Kundu PP (2015) Synthesis, preparation and performance of blends and composites of π-conjugated polymers and their copolymers in DMFCs. Polym Rev 55:630–677
67. Das S, Kumar P, Dutta K et al (2014) Partial sulfonation of PVDF-co-HFP: a preliminary study and characterization for application in direct methanol fuel cell. Appl Energy 113:169–177
68. Dutta K, Das S, Kumar P et al (2014) Polymer electrolyte membrane with high selectivity ratio for direct methanol fuel cells: a preliminary study based on blends of partially sulfonated polymers polyaniline and PVDF-co-HFP. Appl Energy 118:183–191
69. Kumar GG, Lee DN, Kim P et al (2008) Characterization of PVDF-HFP/Nafion/Al[OH]$_n$ composite membranes for direct methanol fuel cell (DMFC). Eur Polym J 44:2225–2230
70. Kumar P, Singh AD, Kumar V et al (2015) Incorporation of nano-Al_2O_3 within the blend of sulfonated-PVDF-co-HFP and Nafion for high temperature application in DMFCs. RSC Adv 5:63465–63472
71. Baglio V, Aricò AS, Blasi AD et al (2005) Nafion-TiO_2 composite DMFC membranes: physico-chemical properties of the filler versus electrochemical performance. Electrochim Acta 50:1241–1246
72. Licoccia S, Traversa E (2006) Increasing the operation temperature of polymer electrolyte membranes for fuel cells: from nanocomposites to hybrids. J Power Sour 159:12–20
73. Kumar GG, Shin J, Nho YC et al (2010) Irradiated PVDF-HFP-tin oxide composite membranes for the applications of direct methanol fuel cells. J Membr Sci 350:92–100
74. Mecheri B, Epifanio AD, Traversa E et al (2008) Sulfonated polyether ether ketone and hydrated tin oxide proton conducting composites for direct methanol fuel cell applications. J Power Sour 178:554–560

75. Mu S, Tang H, Wan Z et al (2005) Au nanoparticles self-assembled onto nafion membranes for use as methanol-blocking barriers. Electrochem Commun 7:1143–1147
76. Liang ZX, Shi JY, Liao SJ et al (2010) Noble metal nanowires incorporated Nafion membranes for reduction of methanol crossover in direct methanol fuel cells. Int J Hydrog Energy 35:9182–9185
77. Tang H, Pan M, Jiang S et al (2005) Self-assembling multi-layer Pd nanoparticles onto Nafion^{TM} membrane to reduce methanol crossover. Colloids Surf A 262:65–70
78. Park HS, Kim YJ, Choi YS et al (2008) Surface chemistry and physical properties of nafion/polypyrrole/Pt composite membrane prepared by chemical in situ polymerization for DMFC. J Power Sour 178:610–619
79. Tian AH, Kim JY, Shi JY et al (2009) Surface-modified nafion membrane by trioctylphosphine-stabilized palladium nanoparticles for DMFC applications. J Phys Chem Solids 70:1207–1212
80. Chen Z, Holmberg B, Li W et al (2006) Nafion/zeolite nanocomposite membrane by in situ crystallization for a direct methanol fuel cell. Chem Mater 18:5669–5675
81. Jung DH, Cho SY, Peck DH et al (2003) Preparation and performance of a Nafion/montmorillonite nanocomposite membrane for direct methanol fuel cell. J Power Sour 118:205–211
82. Dimitrova P, Friedrich KA, Stimming U (2002) Modified nafion-based membranes for use in direct methanol fuel cells. Solid State Ionics 150:115–122
83. Dimitrova P, Friedrich KA, Vogt B et al (2002) Transport properties of ionomer composite membranes for direct methanol fuel cells. J Electroanal Chem 532:75–83
84. Chang JH, Park JH, Park GG et al (2003) Proton-conducting composite membranes derived from sulfonated hydrocarbon and inorganic materials. J Power Sour 124:18–25
85. Jaafar J, Ismail AF, Matsuura T (2012) Effect of dispersion state of cloisite15A on the performance of SPEEK/Cloisite15A nanocomposite membrane for DMFC application. J Appl Polym Sci 124:969–977
86. Aricò AS, Baglio V, Blasi AD et al (2004) Surface properties of inorganic fillers for application in composite membranes-direct methanol fuel cells. J Power Sour 128:113–118
87. Aricò AS, Baglio V, Blasi AD (2003) FTIR spectroscopic investigation of inorganic fillers for composite DMFC membranes. Electrochem Commun 5:862–866
88. Aricò AS, Baglio V, Blasi AD (2003) Influence of the acid-base characteristics of inorganic fillers on the high temperature performance of composite membranes in direct methanol fuel cells. Solid State Ionics 161:251–265
89. Mat NC, Liong A (2009) Chitosan-poly (vinyl alcohol) and calcium oxide composite membrane for direct methanol fuel cell applications. Eng Lett 17:14–17
90. Silva VS, Ruffmann B, Silva H et al (2005) Proton electrolyte membrane properties and direct methanol fuel cell performance I characterization of hybrid sulfonated poly(ether ether ketone)/zirconium oxide membranes. J Power Sour 140:34–40
91. Kim DS, Park HB, Rhim JW (2004) Preparation and characterization of crosslinked PVA/SiO$_2$ hybrid membranes containing sulfonic acid groups for direct methanol fuel cell applications. J Membr Sci 240:37–48
92. Staiti P, Aricò AS, Baglio V et al (2001) Hybrid nafion-silica membranes doped with heteropolyacids for application in direct methanol fuel cells. Solid State Ionics 145:101–107
93. Chen CY, Garnica JI, Rodriguez MC, Duke MC et al (2007) Nafion/polyaniline/silica composite membranes for direct methanol fuel cell application. J Power Sour 166:324–330
94. Fu RQ, Woo JJ, Seo SJ et al (2008) Covalent organic/inorganic hybrid proton-conductive membrane with semi-interpenetrating polymer network: preparation and characterizations. J Power Sour 179:458–466
95. Zhang Y, Cai W, Si F et al (2012) A modified Nafion membrane with extremely low methanol permeability *via* surface coating of sulfonated organic silica. Chem Commun 48:2870–2872
96. Xiong Y, Liu QL, Zhu AM et al (2009) Performance of organic-inorganic hybrid anion-exchange membranes for alkaline direct methanol fuel cells. J Power Sour 186:328–333

97. Sahu AK, Bhat SD, Pitchumani S et al (2009) Novel organic-inorganic composite polymer-electrolyte membranes for DMFCs. J Membr Sci 345:305–314
98. Tohidian M, Ghaffarian SR, Nouri M et al (2015) Polyelectrolyte nanocomposite membranes using imidazole-functionalized nanosilica for fuel cell applications. J Macromol Sci Phys 54:17–31
99. Lin H, Zhao C, Jiang Y et al (2011) Novel hybrid polymer electrolyte membranes with high proton conductivity prepared by a silane-crosslinking technique for direct methanol fuel cells. J Power Sour 196:1744–1749

Chapter 16
Effects of Polymer-Packing Orientation on the Performances of Thin Film Transistors and Photovoltaic Cells

Yang Wang and Tsuyoshi Michinobu

Abstract Controlling the solid-state orientation of semiconducting polymers has been a challenging topic in order to achieve high mobilities in organic field-effect transistors and good power conversion efficiencies in organic photovoltaics. In this chapter, we focus on how the orientation of semiconducting polymer backbones is influenced by the chemical structures, such as backbone regularity, polymer main chain geometry, backbone coplanarity, molecular weight, heteroatoms, and side chains. A detailed analysis of the polymer thin films has been conducted by various techniques, especially including two-dimensional grazing incidence X-ray diffraction measurements, and there is now a clear correlation between the polymer orientation and electronic device performances.

16.1 Introduction

Conjugated polymers are promising semiconducting materials for the next-generation electronic devices. Compared to their inorganic counterparts that need complicated processing methods under harsh conditions, organic/polymeric semiconductors can be simply and cost-effectively implemented into flexible displays, electronic papers, and large-area solar cells by printing technologies due to their versatile chemical synthesis, solution processability, film uniformity, thermal stability, and mechanical flexibility [1]. Since the first report of polycyclic aromatic compounds with high conductivities in 1950s [2], remarkable progress has been achieved during the past few decades in organic electronic devices, such as organic light-emitting diodes (OLEDs) [3], organic field-effect transistors (OFETs) [4], organic photovoltaics (OPVs) [5], and most recently, bio-sensors [6].

Conjugated polymers, as the core component of organic electronics, have a significant impact on the overall device performances. Besides the optical and

Y. Wang · T. Michinobu (✉)
Department of Organic and Polymeric Materials, Tokyo Institute of Technology,
2-12-1 Ookayama, Meguro-Ku, Tokyo 152-8552, Japan
e-mail: michinobu.t.aa@m.titech.ac.jp

electronic properties of the conjugated polymers, the molecular ordering and orientation in the crystalline domains have a significant impact on the charge transfer and transport properties [7]. Thus, controlling the mesoscale and/or nanoscale ordering of conjugated polymers with the desired orientation is essential for high-performance organic electronics. Due to the internal factors (such as the wide polydispersity indices of polymers and complicated inter-/intramolecular interactions) and external factors (such as organic solvents, wet processes, and substrate characteristics), it is a scientific challenge to control the polymer ordering with the desired alignment motif in the solid state. Therefore, intensive studies have been carried out in this field [8]. So far, a high number of research studies have demonstrated that there are mainly two types of stacking models, namely face-on and edge-on molecular packing orientations, which are applied to different kinds of device configurations because of the different charge transport directions [9]. For example, the edge-on orientation is favorable for the in-plane charge carrier transport, leading to high-performance OFETs, whereas the face-on orientation has led to much higher power conversion efficiencies in polymer solar cells due to its benefit regarding facile out-of-plane charge transport.

Generally speaking, there are two ways to tune the molecular ordering and orientations. The first way is the rational chemical design and synthesis by the polymer self-assembly ability. The second way is film processing techniques which force the polymer chains to orient in long-range orders, such as solution shearing [10], mechanical stretching and rubbing [11], drop-casting onto inclined substrates [12], off-center spin-coating [13], directional epitaxial crystallization [14], and epitaxial polymer crystal growth methods [15]. Considering our group's research specialty, in this chapter, we focus on how the orientations of the semiconducting polymer backbones are tuned by the rational molecular design and the corresponding implications of the backbone orientation for the performance of organic electronic devices, such as OFETs (Sect. 16.2) and OPVs (Sect. 16.3) based on our and other research group studies.

16.2 Molecular Design Strategies: Tuning the Polymer-Packing Orientations for High-performance OFETs

16.2.1 Introduction

One of the most important parameters of OFETs is their charge carrier mobility. The traveling speed of the injected carriers through the π-orbital overlap of the molecules determines the performance of the OFETs. Therefore, it is crucial to control the polymer-packing ordering with a favorable orientation for the realization of high-performance OFETs [16]. Rational design and careful organic synthesis is a common approach to adjust the self-assembly characteristics and realize

polymer-packing ordering with suitable chemical structures. Up to now, all the design strategies can be mainly divided into two categories: i.e., the first strategy is the rational design of the polymer main chains, including the backbone regularity, backbone geometry, and backbone coplanarity, and the second strategy is the side-chain engineering.

16.2.2 Rational Polymer Main Chain Design Strategies

16.2.2.1 Effects of Backbone Regularity and Geometry

Regioregular poly(3-hexylthiophene) (rrP3HT, Fig. 16.1) [17], synthesized by the head-to-tail regio-controlled polymerization of the monomer unit, achieves a coplanar backbone, resulting in highly crystalline lamellar and π–π stacking structures. While the spin-coated P3HT samples with a lower regioregularity (81%) exhibited a face-on orientation, the P3HT with a higher regioregularity (>91%) demonstrated an edge-on orientation. Therefore, high charge carrier mobilities up to 0.1 cm^2 V^{-1} s^{-1} have been achieved in the highly regioregular P3HT [18]. On the other hand, the regiosymmetric polythiophene, namely the repeat unit, which consists of thiophene spacer(s) sandwiched between two alkylthiophenes in a "head-to-head" fashion, such as poly(3,3′′′-didodecylquaterthiophene) (PQT-12, Fig. 16.1), is another important example of this class [19]. The major merit of this molecular design is that a free space can be generated by the unsubstituted thiophenes, allowing the interdigitation of side alkyl chains between adjacent polymer backbones, which result in well-ordered lamellae [20]. Together with linear alkyl side chains, which can interact with each other through van der Waals forces, this highly ordered structure is believed to be the origin of the edge-on orientation.

Furthermore, the incorporation and extension of thiophene-based fused aromatic rings (heteroarenes) into the regiosymmetric system can afford higher mobilities due to the enhanced coplanarity, and thus stronger π–π stacking interactions of the polymer backbones, as represented by the poly(2,5-bis(3-alkylthiophen-2-yl)thieno [3,2-b]thiophene)s (pBTTTs, Fig. 16.1) [21]. pBTTTs have been reported to demonstrate the mobility of ∼1 cm^2 V^{-1} s^{-1} with strong π-stacking and a narrow π–π distance of 3.7 Å [22]. Going a step further, a more sophisticated polymer design strategy, the so-called donor–acceptor or push–pull motif, has been developed. Due to their strong intra- and intermolecular interactions between the donor and acceptor units, such polymers not only self-assemble into ordered structures, but also enhance the π-stacking of the polymer chains.

More recently, even higher charge carrier mobilities have been achieved via the rational design and control of the regularity of the donor and acceptor units [23]. For example, Perez et al. reported regioirregular (RI) and regioregular (RR) donor–acceptor conjugated copolymers based on cyclopenta[2,1-b:3,4-b′]dithiophene (CDT) and pyridal [2,1,3] thiadiazole (PT) (see Figs. 16.1 and 16.2) [24]. Compared to its RI counterpart, the RR polymer exhibits a two order of magnitude
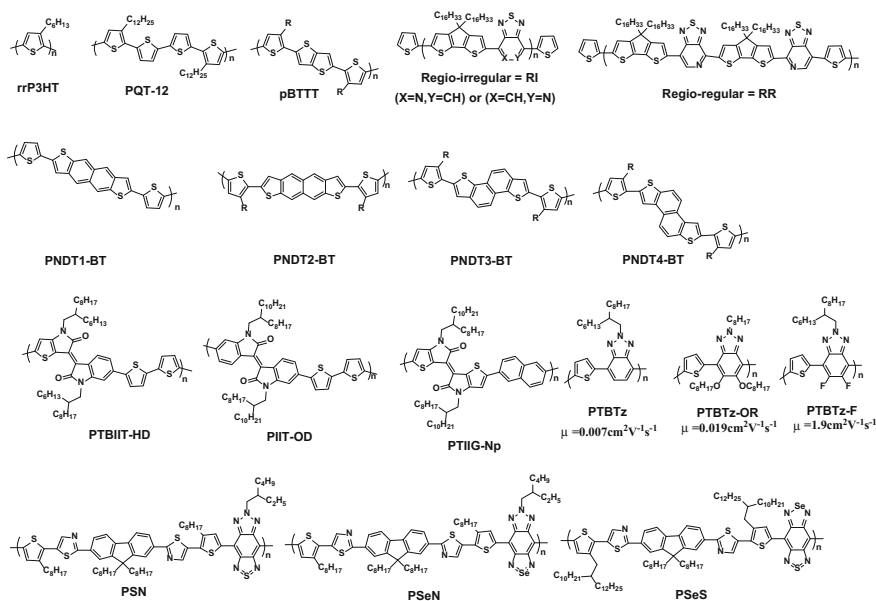
Fig. 16.1 Representative cases of backbone engineering leading to high-mobility polymers

higher hole mobility. Based on the grazing incidence X-ray diffraction (GIXD) measurements (see Fig. 16.2), the RI polymer adopts the edge-on orientation throughout the film. However, in the RR film, the crystallites adopt a mixed edge-on and face-on texture in the bulk and a slight preponderance of edge-on at the surface, which can afford higher charge transport properties utilizing 3D conduction channels. All the above examples demonstrate that controlling the backbone regularity is an important design criterion to develop high-performance polymer OFETs.

Besides control of the backbone regularity, we should also pay attention to the backbone geometry because it also has a prominent effect on the transistor performances as demonstrated in an earlier study by Rieger et al. using various benzodithiophene isomers [25]. Inspired by this study, Osaka et al. reported a series of semiconducting polymers by incorporating different isomeric naphthodithiophene (NDT) (namely, PNDT1-BT, PNDT2-BT, PNDT3-BT, and PNDT4-BT, see Fig. 16.1). The highest mobility of 0.8 cm^2 V^{-1} s^{-1} has been achieved for the NDT3-based polymer. The trend in the hole mobility is in the order of PNDT3-BT > PNDT4-BT > PNDT1-BT > PNDT2-BT. Based on GIXD studies (see Fig. 16.3a, b), PNDT3-BT exhibits the most highly ordered lamellar structure with the edge-on orientation, and PNDT4-BT has a similar but less ordered structure, whereas the PNDT1-BT has a very weak π-stacking order, and no orientation preference has been observed for the PNDT2-BT. Therefore, one has to consider that the above result originated from the polymer backbone geometry.
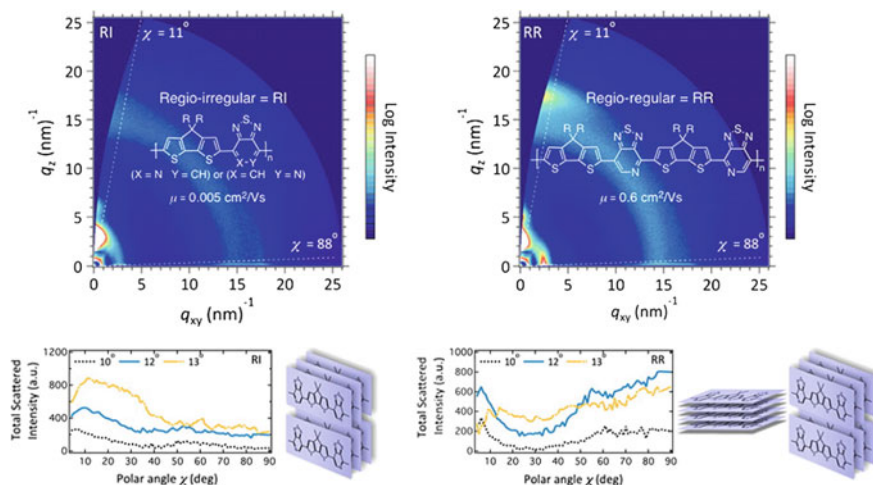
Fig. 16.2 GIXD patterns of regioirregular (RI) and regioregular (RR) donor–acceptor polymers (Reproduced from Ref. [47] with kind permission of © 2014 American Chemical Society)
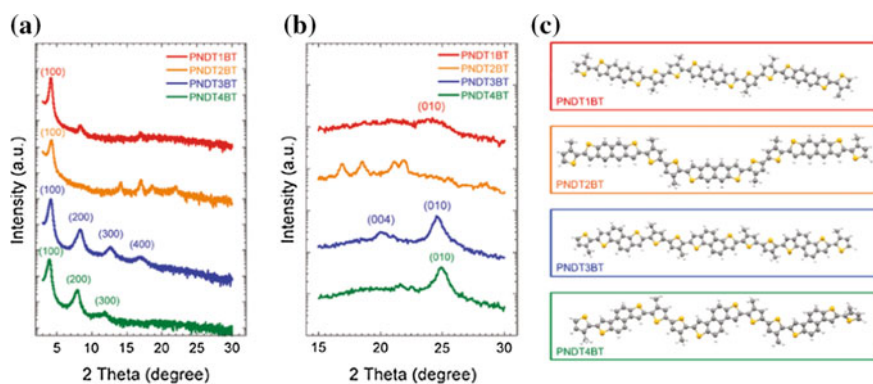
Fig. 16.3 **a** Out-of-plane and **b** in-plane GIXD patterns of PNDTmBT ($m = 1$–4) in the annealed thin films; **c** optimized backbone structures of the polymers (Reproduced from Ref. [26] with kind permission of © 2011 American Chemical Society)

Although the NDT1- and NDT2-monomers appear to have a linear shape, their polymers form a zigzag-shaped backbone which is not favorable for molecular packings. In contrast, PNDT3-BT and PNDT4-BT form a pseudo-straight backbone, which can effectively pack into a highly ordered structure (see Fig. 16.3c) [26]. As a consequence, the mobility trend in the above study is completely consistent with the ordering and extent of the edge-on orientation of the molecules determined by the polymer backbone geometry.

16.2.2.2 Effects of Polymer Backbone Coplanarity

The isoindigo (II)-based polymers have attracted much attention in the field of polymer OFETs due to the high mobility and good air stability. It is notable that by simply coupling with bithiophene, the isoindigo-based polymers are able to achieve mobilities as high as 0.8 cm^2 V^{-1} s^{-1} as reported by Pei et al. [27]. However, the steric effects of the phenyl protons induce a torsional strain between the isoindigo and adjacent π-systems, resulting in the nonplanar polymer main chains [28]. Therefore, Chen et al. proposed a method of replacing the phenyl rings in the isoindigo unit with thiophenes to enhance the polymer backbone planarity [29]. As a result, the corresponding polymers displayed a range of backbone coplanarities. The polymers with a greater thienyl substitution displayed greater backbone coplanarities, lower mobilities, but higher solar cell efficiencies, as represented by PTBIIT-HD (see Fig. 16.1).

However, PII2T-OD (see Fig. 16.1) provided the highest hole mobility of 0.93 cm^2 V^{-1} s^{-1} despite having a low degree of backbone coplanarity. From this study based on the isoindigo polymers, it seems that the planar polymers with a high solubility were able to form a face-on orientation, while the nonplanar polymers favored packings with an edge-on orientation. Very recently, Kim et al. reported that poly(thienoisoindigo-*alt*-naphthalene) (PTIIG-Np, see Fig. 16.1) can achieve a hole mobility of 14.4 cm^2 V^{-1} s^{-1} with a high k gate dielectric poly (vinylidenefluoride-trifluoroethylene) (P(VDF-TrFE)) [30]. It was determined that PTIIG-Np forms a well-ordered lamellar packing microstructure with the bimodal distribution of both edge-on and face-on crystallites (see Fig. 16.4). The most important discovery is that PTIIG-Np exhibits a stronger preference for the edge-on orientation near the top surface of the polymer film. Therefore, the highest mobility (14.4 cm^2 V^{-1} s^{-1}) has been obtained via a top-gate/bottom-contact (TG-BC) device architecture because the edge-on orientation is favorable for the in-plane charge transport. In sharp contrast, only 0.01 cm^2 V^{-1} s^{-1} has been obtained in the PTIIG-Np-based bottom-gate and top-contact devices.

Besides the replacement of the benzene-fused rings with thiophene-fused ring structures, the noncovalent interaction via heteroatom substitution is another important method of tuning the polymer backbone coplanarity. For example, Yum et al. have reported a series of donor–acceptor (D–A) polymers based on benzo-triazole with different substitutions [31]. Surprisingly, when fluorine atoms are introduced to the benzotriazole unit, the fluorinated polymer, PTBTz-F (see Fig. 16.1), shows a highly ordered structure with a preferred edge-on orientation due to the intra- and intermolecular F···S, F···H–C, C–F···πF attractive interactions. With these ordered polymer-packing structures, PTBTz-F has achieved a remarkably enhanced hole mobility as high as 1.9 cm^2 V^{-1} s^{-1}, dramatically outperforming the unsubstituted one (PTBTz) which only shows a mobility of 0.007 cm^2 V^{-1} s^{-1}. In addition, our group has recently reported a series of benzobisthiadiazoles and their related heterocycle-based polymers (see Fig. 16.1) [32]. During the course of the GIXD study, it was found that the polymer orientation significantly changes from edge-on dominant to face-on dominant packing
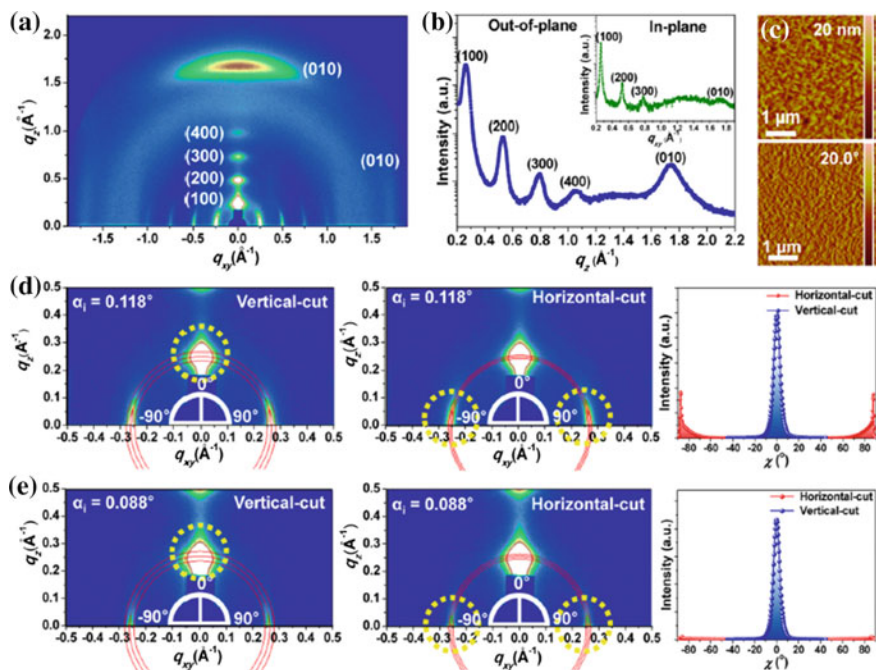
Fig. 16.4 GIXD profiles and AFM images of solution-processed PTIIG-Np films annealed at 310 °C. 2D-GIXD images (**a**) and 1D out-of-plane GIXD profile (**b**) of the thin films. **c** AFM height (*top*) and phase (*bottom*) images. **d**, **e** The local GIXD data ranged from −0.5 to 0.5 Å^{-1} in q_{xy} and from 0 to 0.5 Å^{-1} in q_z and the corresponding intensity-corrected pole figures of the (100) reflection (Reproduced from Ref. [30] with kind permission of © 2014 American Chemical Society)

orientations on a Si substrate by simply substituting the heteroatoms of the benzobisthiadiazole acceptor. For example, the substitution of sulfur by the selenium atom can lead to a face-on orientation texture, while replacing the sulfur with the nitrogen atom can result in a molecular packing ordering with more preference for the edge-on orientation (see Fig. 16.5). There is a clear correlation between the polymer orientation and electronic device performances for the polymers with a greater molecular population of edge-on orientations that tend to show higher mobilities.

16.2.3 Side Chain Engineering

In general, the high solubilities of conjugated polymers in common organic solvents (such as tetrahydrofuran, chloroform, toluene, chlorobenzene, and 1,2-dichlorobenzene) typically originate from the attached flexible side chains on the rigid conjugated backbones. The importance of side chains in dictating the
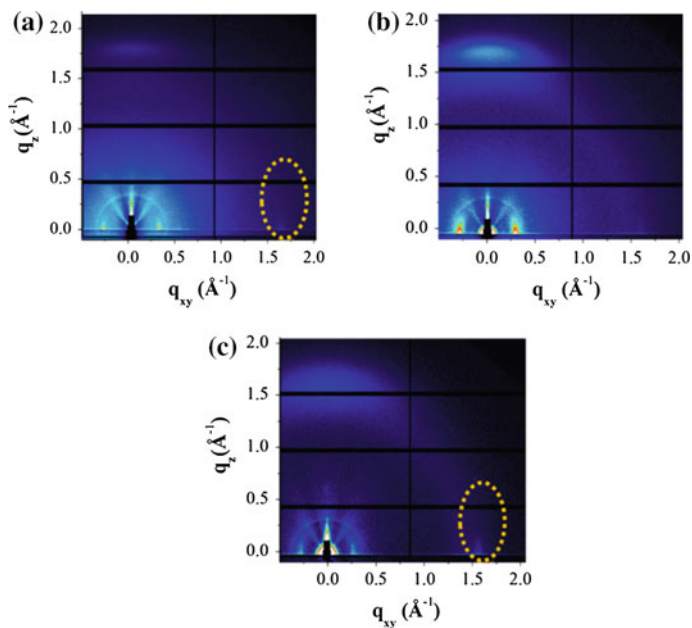
Fig. 16.5 2D-GIXD patterns of the thin films of **a** PSN, **b** PSeN, and **c** PSeS after the treatment of the optimized annealing conditions (Reproduced from Ref. [32] with kind permission of © 2015 American Chemical Society)

performance of organic electronics is underestimated in the past because they are insulating and bulky that hinder the efficient intermolecular charge transport. However, selecting the suitable side chains is as important as synthesizing the conjugated backbones as proposed by Bao et al. [33]. The selection of the solubilizing groups is like the art of trade-off, as they not only affect the solubility, but also tune the molecular packing, orientation, thin film morphology, and hence the device performances [34]. Currently, enormous flexible chains, namely alkyl, organic–inorganic hybrid, oligoether, and fluoroalkyl, have appeared as the side chains of the conjugated polymers. However, the full summary of the functionality of these side chains is not an objective of this chapter. For the sake of simplicity, we focus on the effects of using hybrid siloxane chains and branched alkyl chains.

First, using isoindigo-based polymers as a model system, we would like to illustrate how the hybrid siloxane chains could lead to high-performance OFETs. As shown in Fig. 16.6, Pei and his coworkers, for the first time, reported an isoindigo-based polymer (IIDDT) with the hole mobility of around 0.79 cm^2 V^{-1} s^{-1} [27]. However, the branching point of these alkyl chains was close to the conjugated backbone, which was thought to disrupt the intermolecular π–π interactions between the conjugated backbones. With newly designed siloxane
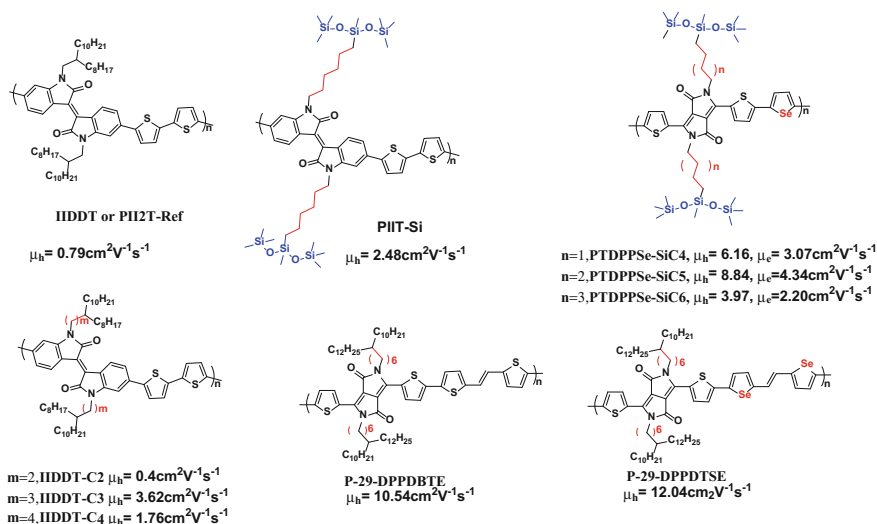
Fig. 16.6 Representative cases of side chain engineering leading to high-performance conjugated polymers for OFETs

hybrid chains (PIIT-Si, see Fig. 16.6), the π–π stacking distance was shortened from 3.75 to 3.58 Å because moving the branched site away from the polymer main chain led to the realization of close packings of the conjugated backbones, as reported by Bao et al. [35]. Therefore, the hole mobility as high as 2.48 cm^2 V^{-1} s^{-1} has been achieved.

The most interesting phenomenon is that the molecular orientation changed from edge-on to dual texture by replacing the branched alkyl chain with the siloxane hybrid chain (see Fig. 16.7). The reflection corresponding to the π–π stacking was the strongest along the out-of-plane q_z axis. It is well known that the charge transport in the OFETs primarily occurs in-plane, and holes and electrons particularly move along the π-stacking direction of the conjugated polymers. However, when a carrier encounters a grain boundary, it should move around such a boundary in the direction normal to the substrate plane in order to achieve a more efficient charge transport. Therefore, Bao and her coworkers proposed 3D conduction channels. For example, charges in a PII2T-Si film can move more effectively as compared to PII2T-Ref due to the presence of both parallel and perpendicular orientations of the π-stacking planes.

Inspired by Bao's work, Yang and Oh et al. employed the siloxane hybrid side chains in the DPP-based polymers (PTDPPSe-SiC6, see Fig. 16.6), generating an ambipolar OFET with the high hole mobility of 3.97 cm^2 V^{-1} s^{-1} and electron mobility of 2.20 cm^2 V^{-1} s^{-1} [36]. Furthermore, after tuning the spacers between the siloxane and backbone, a record ambipolar characteristic with the hole mobility

Fig. 16.7 GIXD images of PII2T-Ref (**a**) and PII2T-Si (**b**) (Reproduced from Ref. [35] with kind permission of © 2011 American Chemical Society)
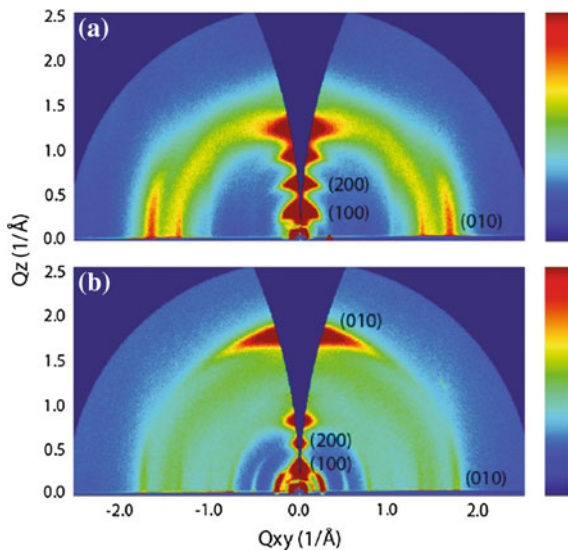
of 8.84 cm^2 V^{-1} s^{-1} and electron mobility of 4.34 cm^2 V^{-1} s^{-1} has been achieved (PTDPPSe-SiC5, see Fig. 16.6) [37]. However, the siloxane chains are not stable and persistent under certain conditions [38], hence limiting the application of this useful hybrid chain. Subsequently, alkyl chains with a farther branching point, namely the branching site from the 2-position to the 3-, 4-, and 5-positions, have been designed by Pei and his coworkers (namely, IIDDT-C2, IIDDT-C3, IIDDT-C4, see Fig. 16.6) [39]. It was observed that the π–π stacking distances of the polymers do not decrease beyond the 3-position. A polymer with 4-decyltetradecyl chains achieved the hole mobility as high as 3.62 cm^2 V^{-1} s^{-1}. This may arise from strong polymer backbone interactions as well as a conformational change in the stacking of the polymer backbone induced by the branching of the alkyl chains.

Soon afterward, Kim and his coworkers, inspired by this farther branched alkyl chain engineering, have tried to adjust the branching position of the two DPP-polymers, thus resulting in P-29-DPPDBTE and P-29-DPPDTSE (see Fig. 16.6) [40]. The OFETs based on these polymers demonstrated very high hole mobilities up to 5 cm^2 V^{-1} s^{-1} even without any optimization. By optimizing the device geometry and thermal annealing treatments, the maximum hole mobility as high as 12 cm^2 V^{-1} s^{-1} was achieved. From the XRD measurements (see Fig. 16.8), it was found that moving the branching position of the side chain away from the backbone can give rise to a better ordered edge-on orientation with the exceptionally short π–π stacking distance of 3.58 Å. All these examples indicate the power of side chain engineering for tuning the polymer packing orientation and charge carrier mobility.
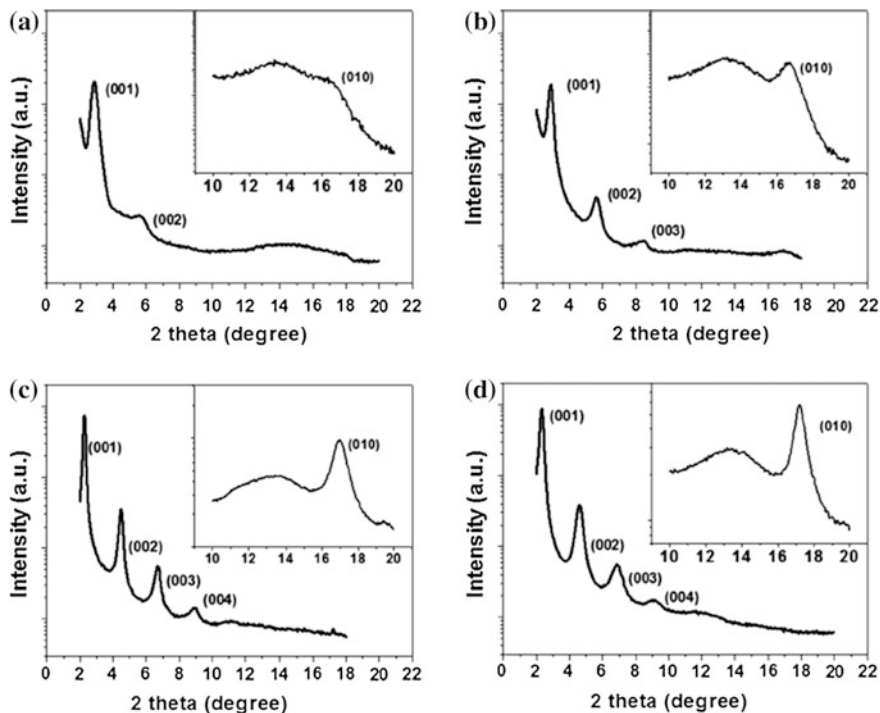
Fig. 16.8 Out-of-plane and in-plane XRD patterns: **a**, **b** polymers with normal alkyl chains and **c** P-29-DPPDBTE and **d** P-29-DPPDTSE with farther branched alkyl chains (Reproduced from Ref. [40] with kind permission of © 2013 American Chemical Society)

16.3   Molecular Design Strategies: Tuning the Polymer-Packing Orientation for High-performance OPVs

16.3.1   Introduction

Organic photovoltaics (OPV) have attracted significant interests from both the industrial and academic communities over the past two decades due to their advantages, such as low cost, solution processability, and mechanical flexibility [41]. Most recently, single-junction bulk-heterojunction (BHJ) polymer solar cells (PSCs) with record high-power conversion efficiencies (PCEs) up to 11.7% have been reported, indicating the bright future for the full-scale commercialization of the OPV [42]. Molecular engineering of conjugated polymers has become one of the main driving forces to spur the advancement of the PCEs [43]. Besides the polymers' absorption bands and highest occupied molecular orbital (HOMO) and lowest unoccupied molecular orbital (LUMO) levels, the photovoltaic properties of the PSCs mostly depend on the ordering structures of the polymers,

i.e., crystallinity and backbone orientation [44], which have a significant impact on the exciton diffusion, charge separation, and charge transport properties. On the one hand, the crystallinity of the polymers, which is usually explained by the strength of the π–π stacking, can be enhanced by the introduction of rigid and fused heteroaromatic π-cores into the polymer main chain [45]. On the other hand, although we have the knowledge that the face-on orientation facilitates the vertical charge transport and thus enhances the OPV performance, to direct the polymer backbone from the edge-on (or no direction) to face-on orientation is still very challenging. Thus, in this section, we focus on various molecular design strategies for tuning the polymer orientation for highly efficient OPVs.

16.3.2 Effects of Molecular Weights

For a variety of D–A polymers, it has been reported that there is a correlation between the number-average molecular weight (M_n) of the polymer and its photovoltaic performance [46]. For the same polymer, modest differences in the M_n sometimes lead to significant batch-to-batch performance variations [47]. Although authors usually do not clearly state the results of the M_n optimizations, it is generally the case that polymers having a higher molecular weight outperform those of a lower molecular weight when used in OPV devices. Such an effect of the molecular weights on the OPV performance was first observed in the benchmark combination based on the poly(3-hexylthiophene): [6,6]-phenyl-C61-butyric acid methyl ester (P3HT:PCBM) system by Brabec et al. [48] and Heeger et al. [49]. Later, similar effects were also found in narrow band gap polymers by Bazan et al. [50] and others [51].

The device performance enhancement as the M_n increases is primarily attributed to the increased charge carrier mobility and the formation of a more optimal BHJ morphology [52]. However, some studies have suggested that the increased molecular weights facilitate the face-on orientation of the polymers, thus enhancing the charge transport property and short-circuit current (J_{sc}). For example, Osaka and his coworkers first reported the observation of drastic changes in the polymer packing textures by increasing the molecular weight of PTzBT-14HD (see Fig. 16.9) [53].

The GIXD measurements revealed that PTzBT-14HD with a low M_n of 13 kDa does not have preferential orientations (Fig. 16.10a–d). Intriguingly, when the molecular weight increased, the lamellar diffractions tended to preferentially appear on the q_z axis as arcs for the polymer with $M_n = 20$ kDa and as oval spots for the polymer of $M_n = 33$ kDa. Meanwhile, a strong π–π stacking diffraction converged on the q_{xy} axis, indicating the strong tendency of the edge-on orientation for high M_n polymers. In the case of the BHJ films (Fig. 16.10e–f), the sample with the M_n of 13 kDa showed a very weak π–π stacking crystallinity and no preferential orientation. With the higher molecular weights, the polymers unexpectedly showed a strong tendency for the face-on orientation, which was in sharp contrast to the

Fig. 16.9 Representative high-performance photovoltaic polymers

results observed for the polymer-only films. As the polymers adopted a greater face-on orientation, the charge transport properties were significantly improved, as evidenced by the J_{sc} increasing from 6.1 with M_n = 13 kDa to 10.6 mA cm^{-2} with M_n = 33 kDa. In a later study, a similar result was reported by You and his coworkers based on their medium band gap polymer, PBnDT-FTAZ [54]. The lowest molecular weight polymer (10 kDa) showed no preferential orientation of "face-on" or "edge-on" with respect to the substrate. However, as the molecular weight increased, the diffraction intensity of the (010) π–π stacking peak, ascribed to the out-of-plane rather than to the in-plane direction, became stronger (see Fig. 16.11). This result implies that the conjugated backbone adopts a greater "face-on" orientation as the molecular weight increases.

It should be noted that although we have claimed that the molecular weight effects on the OPV properties originated from the change in the polymer packing orientation, each conjugated polymer undergoes a different degree of such effects, and accordingly, it is hard to quantify them. For example, some groups have qualitatively discussed that the crystalline region of polymers in the BHJ blends can be the principal factor that determines the performance [55].

16.3.2.1 Effects of Halogenation

The halogenation of molecules is a simple but effective method of finely tuning the frontier energy levels and other physiochemical properties [56]. As the most electrophilic atom of the halogens, fluorine and its substituents have been extensively studied not only in organic semiconductors but also in other research fields, such as medicinal chemistry [57], in vivo bioorthogonal chemistry [58], and food chemistry [59]. In the research field of organic semiconductors, fluorinated materials generally show better device performances because of their deeper HOMO

Fig. 16.10 2D GIXD images of the PTzBT-14HD thin films (*left column*, **a–d**) and PTzBT-14HD/PC$_{61}$BM BHJ films (*right column*, **e–h**) with different molecular weights (Reproduced from Ref. [53] with kind permission of © 2012 Wiley-VCH)

levels, more planar backbones, and internal dipoles higher than their unsubstituted counterparts [60]. Recent studies have also demonstrated that adding fluorine substituents to the conjugated polymer backbone can lead to a more face-on packing orientation, which contributes to the suppressed charge recombination and thus increasing the short-circuit current (J_{sc}) and fill factor (FF) of related solar cells.

For example, You and his coworkers have shown that through F substitution, the polymer packing orientation can be manipulated at the donor–acceptor

Fig. 16.11 GIXD out-of-plane and in-plane 20° sector averages along with circular averaged data of the five blended films (Reproduced from Ref. [54] with kind permission of © 2014 Wiley-VCH)
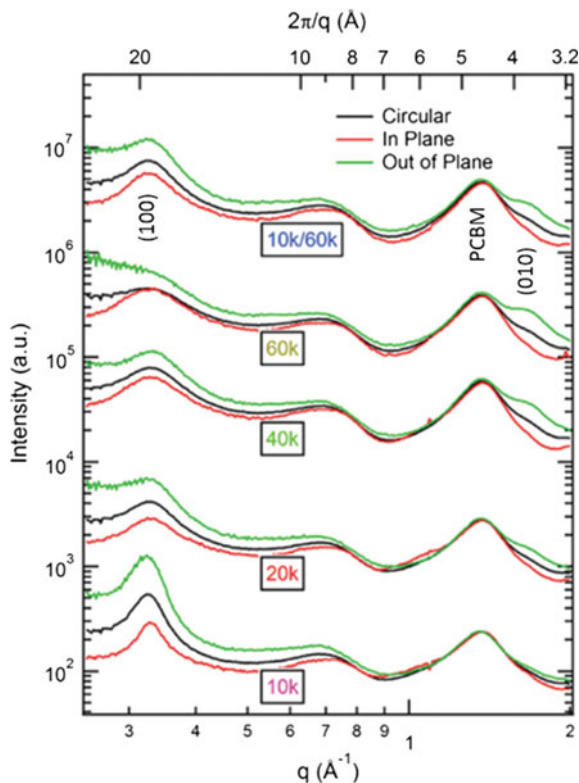
heterojunction interfaces, which can be observed for three different polymers (PNDT-DTBT, PBnDT-DTBT, and PBnDT-TAZ, see Fig. 16.9) [61]. By using resonant soft X-ray scattering (SoXS), they have characterized the degree of molecular orientation (DMO) as well as an order parameter that describes the face-on (+1) or edge-on (−1) orientations relative to the heterojunction interfaces. In all three polymer blend systems, the device performances were improved when the fluorine derivatives were employed. The DMO of the blended films with the fluorinated derivatives was positive, indicating a face-on orientation. On the other hand, the DMO was slightly negative for the low-efficiency devices based on the polymers without F substitutions, indicating an edge-on orientation (see Fig. 16.12).

Subsequently, You and his coworkers also designed and synthesized a series of polymers with the same backbone but varied amounts of fluorine substitution (PBnDT-$(1 - x)$ HTAZ-(x) FTAZ, $x = 0$ (F00), $x = 0.25$ (F25), $x = 0.50$ (F50), $x = 0.75$ (F75), and $x = 1$ (F100), see Fig. 16.9) [62]. Their results clearly indicated that the increased fluorination on the conjugated backbone, more specifically, on the acceptor moiety of the "donor–acceptor (D–A)" copolymers, benefits the hole carrier mobility with a strikingly monotonic correlation (Fig. 16.13). Because similar
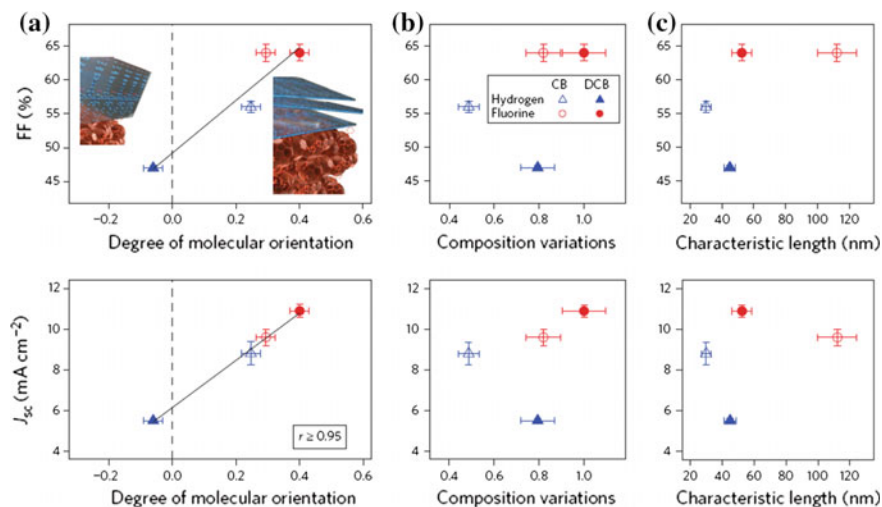
Fig. 16.12 Device performance strongly correlates with DMO. **a–c**, FF (*top*) and J_{sc} (*bottom*) as a function of DMO (**a**), average composition variations (**b**) and median characteristic length of morphology (**c**) for devices based on PNDT-DTBT polymers that are either fluorinated or hydrogen-based controls (Reproduced from Ref. [61] with kind permission of © 2014 Macmillan Publishers Ltd)

morphologies, probed by SoXS, have been observed for all five BHJ blends, the increased hole mobility with additional fluorination was likely due to the improved interchain transport, supported by the improved (010) π–π stacking and face-on orientation observed by GIXD (Fig. 16.14).

However, introducing an F atom into the polymer backbone does not always enhance the PCE. A recent study, reported by Pei et al., has shown that because of the strong crystallization tendency of the fluorinated polymers (F-IIDT, see Fig. 16.9), very large crystal domains are formed within the blended films [63]. This impeded the efficient polymer–fullerene miscibility and the formation of interpenetrated networks, thus resulting in an insufficient charge separation and low short-current density of F-IIDT-based devices. Instead, they have proposed that the introduction of chlorine into the polymer backbone (Cl-IIDT, see Fig. 16.9) may improve the PCE. The incorporation of large-size chlorine atoms not only provides the HOMO levels similar to the fluorinated ones, but also induces a slight torsion on the backbone and mitigates the strong intermolecular interactions between the isoindigo-based polymers. As shown in Fig. 16.15, the intensity distribution of the lamellar diffraction peaks (h00) of the F-IIDT/PC$_{71}$BM blend depicted a ring with a uniform intensity, indicating no directionality for the molecular packing of F-IIDT. In contrast, for Cl-IIDT/PC$_{71}$BM, the (100) diffraction peaks contained arcs of the intensity along the q_z and q_{xy} directions. The π–π stacking diffraction peaks also appeared without directionality in the case of the F-IIDT blended films, while the Cl-IIDT blended films displayed such peaks along the q_z direction. All these results
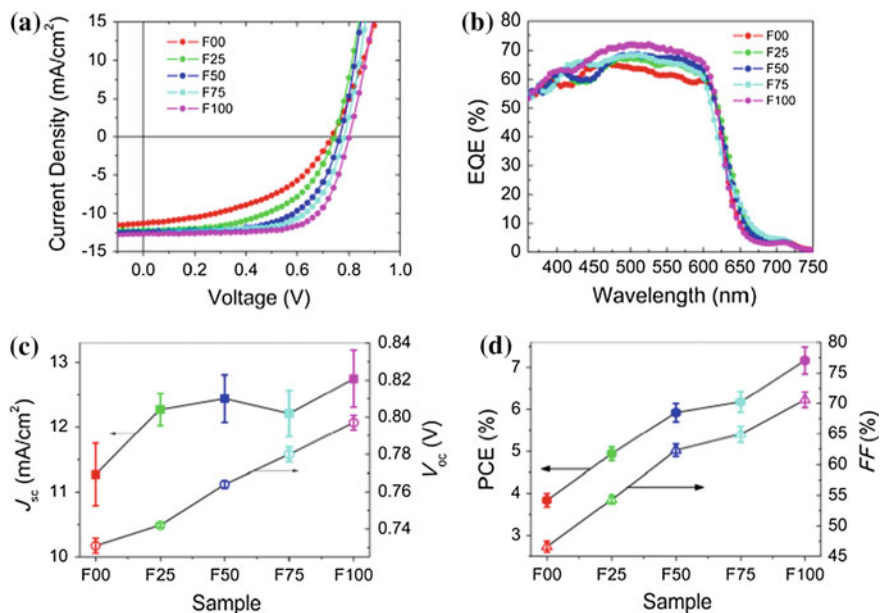
Fig. 16.13 a *J–V* curves for the BHJ devices of ~350 nm thick films based on all five copolymers under 1 sun, AM 1.5G condition. **b** *EQE* for the same devices in (**a**). **c** Changes in J_{sc} and V_{oc} with the increasing amount of F substitution. **d** The increase in the fill factor tracks the increase in the overall device efficiency (PCE) as more F substituents are incorporated into the copolymers (Reproduced from Ref. [62] with kind permission of © 2014 American Chemical Society)

suggest that the packing direction of the polymer backbone is isotropic without any preferred crystallographic orientations in the case of the F-IIDT blended films, while Cl-IIDT prefers the face-on packing in the blended films. Therefore, Cl-TTDT with the stronger face-on orientation and smaller crystal domain significantly outperformed F-IIDT in OPV devices (Fig. 16.15).

16.3.3 Side Chain Engineering

One of the keys of producing efficient photovoltaic polymers is the introduction of side chains with the appropriate length, topology, and distribution [64], which can determine the crystallinity and orientation of the polymers in the solid film state. Osaka et al. demonstrated that the polymer orientation substantially changed upon the simple introduction of linear alkyl groups at the donor unit [65]. It was observed that when a linear dodecyl ($–C_{12}H_{25}$) chain is attached at the 5- and 10-positions of the naphtho[1,2-b:5,6-b′]dithiophene (NDT3) unit of PNNT-12HD (see Fig. 16.9), the ordered structure mostly changes without any alterations in the energy levels,
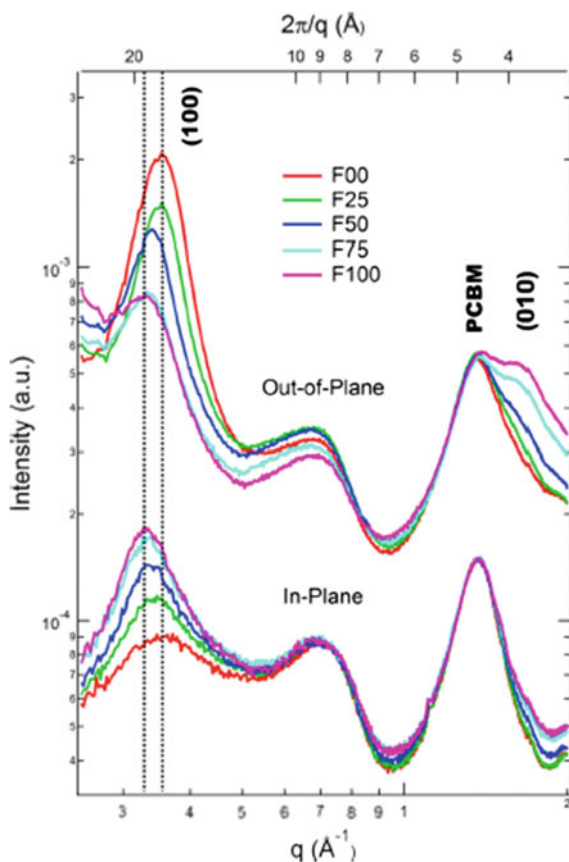
Fig. 16.14 GIXD data of the blended films. π–π Stacking intensity, face-on crystallite orientation with respect to the substrate, and lamellar distance increase with higher fluorine contents (Reproduced from Ref. [62] with kind permission of © 2014 American Chemical Society)
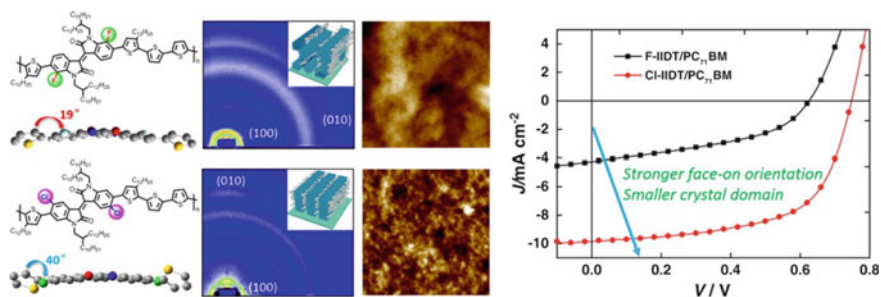
Fig. 16.15 GIXD patterns of F-IIDT/PC_{71}BM blended film and Cl-IIDT/PC_{71}BM blended film together with the corresponding OPV properties (Reproduced from Ref. [63] with kind permission of © 2015 American Chemical Society)
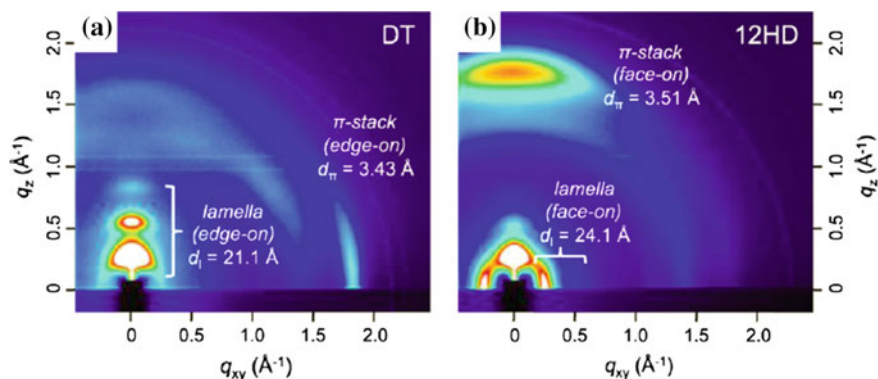
Fig. 16.16 2D-GIXD images of as-spun thin films of **a** PNNT-DT and **b** PNNT-12HD (Reproduced from Ref. [65] with kind permission of © 2013 American Chemical Society)

resulting in high PCEs above 8%. As shown in Fig. 16.16a, the original polymer (PNNT-DT) was oriented in an edge-on manner, as the diffractions corresponding to the lamellar structure and the π–π stacking predominantly appeared along the q_z axis and the q_{xy} axis, respectively. However, in sharp contrast to this polymer, PNNT-12HD preferentially adopted the face-on orientation as the π–π stacking diffraction appeared along the q_z axis (Fig. 16.16b). After blending with $PC_{61}BM$, the positions and distances of both lamellar structures and π–π stacking were not changed, indicating the preservation of the polymer packing structures. The face-on orientation and the crystalline π–π stacking of PNNT-12HD are consistent with the low in-plane mobility and the high out-of-plane mobility compared to PNNT-DT, and this should be the cause of the significantly enhanced FF of the solar cells in particular when the thicker active layers are fabricated. In conventional PSCs, the optimized thickness is thought to be 80–120 nm, because as the thickness increases, the FF significantly decreases. However, in the case of PNNT-DT with highly crystalline face-on packing structures, FF was still 0.64 when the thickness reached 300 nm. Since thick films can harvest more solar photons, a higher J_{sc} is expected. Therefore, PSCs based on PNNT-HD achieved the high PCE of 8.2% at the thickness of 300 nm, while PSCs based on PNNT-DT achieved the highest efficiency of 5.5% at the optimized thickness of 170 nm.

Soon afterward, Osaka et al. demonstrated that the backbone orientation in the thiophene–thiazolothiazole (TzTz) copolymer system (see Fig. 16.17) could be modified by tuning the alkyl side chain composition. Their hypothesis about the reason why the previously studied PTzBT-14HD forms the edge-on orientation in the polymer-only film is that the tetradecyl linear alkyl chain (C14) is longer than the trunk part of the branched 2-hexyldecyl (HD) chain, and thus, the character of the linear alkyl chain, which often directs the backbone to the edge-on orientation, becomes stronger [66]. Consequently, they propose two design strategies of the alkyl side chains to form the face-on orientation: i.e., (1) shortening the linear or
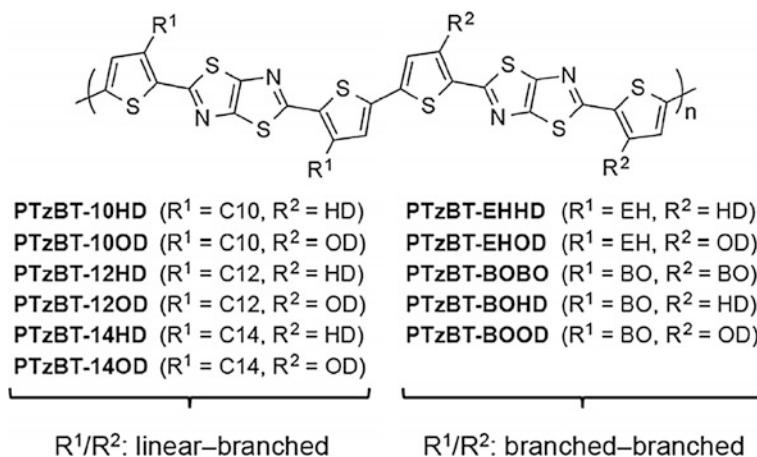
Fig. 16.17 Chemical structures of thiophene–thiazolothiazole copolymers (PTzBTs) with various alkyl side chains (Reproduced from Ref. [67] with kind permission of © 2014 Wiley-VCH)

elongating the branched alkyl chain and (2) replacing the linear alkyl chain with a branched chain [67].

For quantification, the intensity ratio of the out-of-plane (q_z axis) to in-plane (q_{xy} axis) lamellar peaks (I_{op}/I_{ip}) was calculated, which can be considered as the edge-on to face-on crystallite ratio. The I_{op}/I_{ip} was 30.1 for PTzBT-14HD, which is the highest value among these polymers and also indicates the highest degree of edge-on orientation. When the linear side chain (R1) was changed to shorter chains, such as dodecyl (C12) and decyl (C10) (PTzBT-12HD and PTzBT-10HD) in which the length difference between the R1 and R2 chains was negligible, the face-on crystallite was observed (see Fig. 16.18b upper middle and left; the lamellar and π-stacking diffractions appeared on the q_{xy} and q_z axis, respectively).

Similar changes were observed in the case of a longer branched side chain, R2 = octyldodecyl (OD) (Fig. 16.18b, bottom right). By shortening the linear side chain (PTzBT-12OD and PTzBT-10OD), the face-on orientations again became more dominant (Fig. 16.18b, bottom middle and left), in which the I_{op}/I_{ip} was 0.6 and 0.5, respectively. These results clearly demonstrated that by shortening the linear or elongating the branched alkyl chain, the PTzBT polymers are able to form the face-on orientation. When the linear side chain (R1) was substituted with the branched 2-ethylhexyl (EH) or 2-butyloctyl (BO) side chains (PTzBT-EHHD or PTzBT-BOHD), the polymers also stacked in a face-on configuration (Fig. 16.18c, upper left and middle).

In particular, in PTzBT-BOHD, in which the length difference between R1 and R2 was smaller as compared to PTzBT-EHHD, the π–π stacking diffraction on the q_z axis was more dominant, indicating that PTzBT-BOHD was more preferentially face-on oriented. When both R1 and R2 changed to BO, the polymer (PTzBT-BOBO) exhibited the strongest π–π stacking diffraction on the q_z axis,
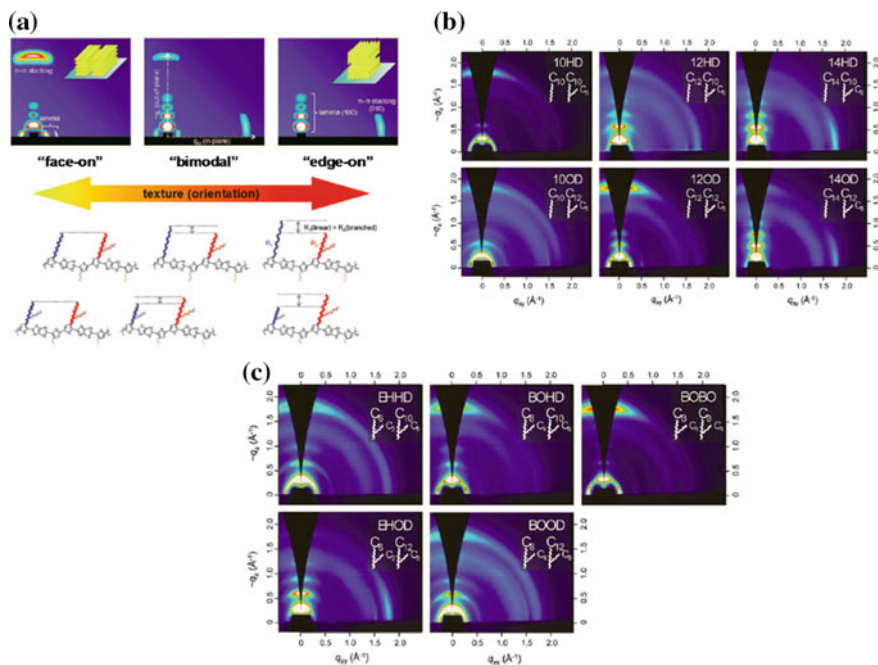
Fig. 16.18 **a** Schematic illustrations of the textures for the edge-on and face-on orientation and the mixture of the edge-on and face-on (bimodal orientation); **b** 2D-GIXD patterns of polymer-only films for PTzBTs with the linear and branched side chains **c** and with all branched side chains (Reproduced from Ref. [67] with kind permission of © 2014 Wiley-VCH)

indicating the highest degree of face-on orientation among the five polymers with branched R1-branched R2 chains (Fig. 16.18c, upper right). Furthermore, when compared to the linear-branched chain system, one could easily obtain the polymers with face-on dominant textures in the branched-branched chain system, as shown in Fig. 16.18c (among the five polymers with branched R1-branched R2 chains, only PTzBT-EHOD showed the edge-on orientation). In addition, it was also found that the length difference between R1 and R2 seems to play an important role in determining the backbone orientation. When the difference is greater, the polymers tend to form an edge-on orientation, and when the difference is smaller, the polymers tend to form a well-ordered face-on orientation.

16.4   Conclusions

In this chapter, we have highlighted how the molecular structure modifications direct the polymer packing orientations and affect the corresponding device performances. Although the backbone orientation is governed by many factors,

we believe that the degree of intermolecular interactions is the most important factor for the stacking orientation. That is to say, polymers with strong intermolecular interactions tend to form edge-on orientations, whereas polymers with weak intermolecular interactions tend to form face-on orientations. It becomes the paradigm that polymers should adopt the edge-on orientation for high-mobility OFETs and the face-on orientation for high-efficiency OPVs. However, it should be noted that in reality, the device performance is not always determined by the backbone orientation, especially in the case of OPVs in which polymers with a higher face-on population do not always show high efficiencies. This is because the efficiency is also affected by the BHJ film morphology which also affects the charge carrier transport. Although remarkable achievements have been produced in this field, it is still a scientific challenge to easily control or change the polymer orientation within the thin films of organic devices. We hope that this chapter will help researchers, especially the synthetic chemists, efficiently develop high-performance semiconducting polymers for specific purposes.

References

1. (a) Yan H, Chen Z, Zheng Y et al (2009) A high-mobility electron-transporting polymer for printed transistors. Nature 457(7230):679–686; (b) Arias AC, MacKenzie JD, McCulloch I et al (2010) Materials and applications for large area electronics solution-based approaches. Chem Rev 110(1):3–24; (c) Wang C, Dong H, Hu W et al (2011) Semiconducting π-conjugated systems in field-effect transistors: a material odyssey of organic electronics. Chem Rev 112(4):2208–2267; (d) Sirringhaus H (2014) Approaching disorder-free transport in high-mobility conjugated polymers. Adv Mater 26:1319–1331
2. https://en.wikipedia.org/wiki/Organic_semiconductor
3. (a) Huang J, Li G, Wu E et al (2006) Achieving high-efficiency polymer white-light-emitting devices. Adv Mater 18:114–117; (b) Huang J, Watanabe T, Ueno K et al (2007) Highly efficient red-emission polymer phosphorescent light-emitting diodes based on two novel tris (1-phenylisoquinolinato-2n) iridium (iii) derivatives. Adv Mater 19(5):739–743
4. (a) Briseno AL, Mannsfeld SCB, Ling MM et al (2006) Patterning organic single-crystal transistor arrays. Nature 444(7121):913–917; (b) Briseno AL, Tseng RJ, Ling, MM et al (2006) High-performance organic single-crystal transistors on flexible substrates. Adv Mater 18:2320–2324; (c) Mei J, Diao Y, Appleton AL et al (2013) Integrated materials design of organic semiconductors for field-effect transistors. J Am Chem Soc 135(18):6724–6746; (d) Holliday S, Donaghey JE, McCulloch I (2013) Advances in charge carrier mobilities of semiconducting polymers used in organic transistors. Chem Mater 26(1):647–663; (e) Wang Y, Kadoya T, Wang L et al (2015) Benzobisthiadiazole-based conjugated donor–acceptor polymers for organic thin film transistors: effects of π -conjugated bridges on ambipolar transport. J Mater Chem C 3(6):1196–1207
5. (a) Li G, Shrotriya V, Huang J et al (2005) High-efficiency solution processable polymer photovoltaic cells by self-organization of polymer blends. Nat Mater 4(11):864–868; (b) Chen HY, Lo MKF, Yang G et al (2008) Nanoparticle-assisted high photoconductive gain in composites of polymer and fullerene. Nat Nanotechnol 3(9):543–547; (c) Hou J, Park MH, Zhang S et al (2008) Bandgap and molecular energy level control of conjugated polymer photovoltaic materials based on benzo [1,2-b 4,5-b′] dithiophene. Macromolcules 41(16): 6012–6018; (d) Hou J, Chen HY, Zhang S et al (2008) Synthesis, characterization, and photovoltaic properties of a low band gap polymer based on silole-containing polythiophenes

and 2,1,3-benzothiadiazole. J Am Chem Soc 130(48):16144–16145; (e) Chen HY, Hou J, Zhang S et al (2009) Polymer solar cells with enhanced open-circuit voltage and efficiency. Nat Photon 3(11):649–653; (f) Chu TY, Lu J, Beaupré S, et al (2011) Bulk heterojunction solar cells using thieno [3,4-c] pyrrole-4,6-dione and dithieno [3,2-b 2′,3′-d] silole copolymer with a power conversion efficiency of 7.3%. J Am Chem Soc 133(12):4250–4253; (g) Wang Y, Liu Y, Chen S et al (2013) Significant enhancement of polymer solar cell performance via side-chain engineering and simple solvent treatment. Chem Mater 25 (15):3196–3204; (h) Wang Y, Yang F, Liu Y et al (2013) New alkylfuranyl-substituted benzo [1,2-b 4,5-b′] dithiophene-based donor–acceptor polymers for highly efficient solar cells. Macromolcules 46(4):1368–1375; (i) Liu Q, Liu Y, Wang Y et al (2013) Anthradithiophene-benzothiadiazole-based small molecule donors for organic solar cells. New J Chem 37 (11):3627–3633; (j) Kim G, Kang SJ, Dutta GK et al (2014) A thienoisoindigo-naphthalene polymer with ultrahigh mobility of 14.4 cm^2/V s that substantially exceeds benchmark values for amorphous silicon semiconductors. J Am Chem Soc 136(26):9477–9483; (k) Liu Y, Wang Y, Ai L et al (2015) Perylenebisimide regioisomers effect of substituent position on their spectroscopic, electrochemical, and photovoltaic properties. Dyes Pigm 121:363–371; (l) Wang Y, Klein MFG, Hiyoshi J et al (2015) Bulk-Heterojunction organic solar cells based on benzobisthiadiazole semiconducting polymers. J Photopolym Sci Technol 28(3):385–391; (m) Yang YM, Chen W, Dou L et al (2015) High-performance multiple-donor bulk heterojunction solar cells. Nat Photon 9(3):190–198

6. (a) Tee BCK, Chortos A, Berndt A et al (2015) A skin-inspired organic digital mechanoreceptor. Science 350(6258):313–316; (b) Yokota T, Inoue Y, Terakawa Y et al (2015) Ultraflexible, large-area, physiological temperature sensors for multipoint measurements. Proc Natl Acad Sci USA 112: 14533–14538

7. (a) Torrent MM, Rovira C (2011) Role of molecular order and solid-state structure in organic field-effect transistors. Chem Rev 111(8):4833–4856; (b) Kim FS, Ren GQ, Jenekhe SA (2011) One-dimensional nanostructures of π -conjugated molecular systems: assembly, properties, and applications from photovoltaics, sensors, and nanophotonics to nanoelectronics. Chem Mater 23(3):682–732

8. (a) Sirringhaus H, Bird M, Zhao N (2010) Charge transport physics of conjugated polymer field-effect transistors. Adv Mater 22(34):3893–3898; (b) Dong HL, Hu WP (2011) Doped ceria based solid oxide fuel cell electrolytes and their sintering aspects. Prog Chem 23:104–121

9. Salleo A (2007) Charge transport in polymeric transistors. Mater Today 10(3):38–45

10. Giri G, Verploegen E, Mannsfeld SCB et al (2011) Tuning charge transport in solution-sheared organic semiconductors using lattice strain. Nature 480(7378):504–508

11. (a) Tremel K, Fischer FSU, Kayunkid N et al (2014) Charge transport anisotropy in highly oriented thin films of the acceptor polymer (NDI2OD-T2). Adv Energy Mater 4(10): 1301659; (b) O'Connor BT, Reid OG, Zhang X et al (2014) Morphological origin of charge transport anisotropy in aligned polythiophene thin films. Adv Funct Mater 24(22):3422–3431

12. Rivnay J, Jimison LH, Northrup JE et al (2009) Large modulation of carrier transport by grain-boundary molecular packing and microstructure in organic thin films. Nat Mater 8 (12):952–958

13. Yuan Y, Giri G, Ayzner AL et al (2014) Ultra-high mobility transparent organic thin film transistors grown by an off-centre spin-coating method. Nat Commun 3005

14. (a) Jimison LH, Toney MF, McCulloch I et al (2009) Charge-transport anisotropy due to grain boundaries in directionally crystallized thin films of regioregular poly(3-hexylthiophene). Adv Mater 21:1568; (b) Brinkmann M, Gonthier E, Bogen S et al (2012) Segregated versus mixed interchain stacking in highly oriented films of naphthalene diimide bithiophene copolymers. ACS Nano 6(11):10319–10326

15. (a) Müller C, Aghamohammadi M, Himmelberger S et al (2013) One-Step macroscopic alignment of conjugated polymer systems by epitaxial crystallization during spin-coating. Adv Funct Mater 23(19):2368–2377; (b) Park KS, Salunkhe SM, Lim I et al (2013) High-performance air-stable single-crystal organic nanowires based on a new indolocarbazole derivative for field-effect transistors. Adv Mater 25(24):3351–3356; (c) Kim JY, Yang DS,

Shin J et al (2015) High-performing thin-film transistors in large spherulites of conjugated polymer formed by epitaxial growth on removable organic crystalline templates. ACS Appl Mater Interfaces 7(24):13431–13439

16. Sirringhaus H, Brown PJ, Friend RH et al (1999) Two-dimensional charge transport in self-organized high-mobility conjugated polymers. Nature 401(6754):685–688

17. (a) McCullough RD, Lowe RD (1992) Molecular engineering of π-conjugated polymers. Radical polymerisation polyelectrolytes. J Chem Soc 70:2–14; (b) Chen TA, Rieke RD (1992) The first regioregular head-to-tail poly (3-hexylthiophene-2,5-diyl) and a regiorandom isopolymer: nickel versus palladium catalysis of 2(5)-bromo-5(2)-(bromozincio)-3-hexylthiophene polymerization. J Am Chem Soc 114(25):10087–10088; (c) McCullough RD (1998) The chemistry of conducting polythiophenes. Adv Mater 10(2):93–116

18. Osaka I, McCullough RD (2008) Advances in molecular design and synthesis of regioregular polythiophenes. Acc Chem Res 41(9):1202–1214

19. Ong BS, Wu Y, Liu P et al (2004) High-performance semiconducting polythiophenes for organic thin-film transistors. J Am Chem Soc 126(11):3378–3379

20. Kline RJ, Delongchamp DM, Fischer DA et al (2007) Critical role of side-chain attachment density on the order and device performance of polythiophenes. Macromolecules 40 (22):7960–7965

21. (a) McCulloch M, Heeney M, Bailey C et al (2006) Local charge trapping in conjugated polymers resolved by scanning Kelvin probe microscopy. Nature Mater 5:328–342; (b) McCulloch I, Heeney M, Chabinyc ML et al (2009) Semiconducting thienothiophene copolymers: design, synthesis, morphology, and performance in thin-film organic transistors. Adv Mater 21(10–11):1091–1109

22. (a) Chabinyc ML, Toney MF, Kline RJ et al (2007) X-ray scattering study of thin films of poly (2,5-bis (3-alkylthiophen-2-yl) thieno [3,2-b] thiophene). J Am Chem Soc 129 (11):3226–3237; (b) Hamadani BH, Gundlach DJ, McCulloch I et al (2007) Undoped polythiophene field-effect transistors with mobility of 1 cm^2. App Phys Lett 91(24):3512.; (c) Umeda T, Kumaki D, Tokito S (2009) Surface-energy-dependent field-effect mobilities up to 1 cm^2/V for polymer thin-film transistor. J App Phys 105(2): 516–529

23. (a) Ying L, Hsu BB, Zhan H et al (2011) Regioregular pyridal [2,1,3] thiadiazole π-conjugated copolymers. J Am Chem Soc 133(46):18538–18541; (b) Zhang X, Richter LJ, DeLongchamp DM, et al (2011) Molecular packing of high-mobility diketo pyrrolo-pyrrole polymer semiconductors with branched alkyl side chains. J Am Chem Soc 133(38):15073–15084; (c) Biniek L, Schroeder BC, Nielsen CB et al (2012) Recent advances in high mobility donor–acceptor semiconducting polymers. J Mater Chem 22(30):14803–14813

24. Perez LA, Zalar P, Ying L et al (2014) Effect of backbone regioregularity on the structure and orientation of a donor–acceptor semiconducting copolymer. Macromolecules 47(4):1403–1410

25. Rieger R, Beckmann D, Mavrinskiy A et al (2010) Backbone curvature in polythiophenes. Chem Mater 22:5314–5318

26. Osaka I, Abe T, Shinamura S et al (2011) Impact of isomeric structures on transistor performances in naphthodithiophene semiconducting polymers. J Am Chem Soc 133 (17):6852–6860

27. Lei T, Cao Y, Fan Y et al (2011) High-performance air-stable organic field-effect transistors isoindigo-based conjugated polymers. J Am Chem Soc 133(16):6099–6101

28. Ma Z, Wang E, Jarvid ME et al (2012) Imide/amide based π-conjugated polymers for organic electronics. J Mater Chem 22:2306–2318

29. Chen MS, Niskala JR, Unruh DA et al (2013) Control of polymer-packing orientation in thin films through synthetic tailoring of backbone coplanarity. Chem Mater 25(20):4088–4096

30. Kim G, Kang SJ, Dutta GK et al (2014) A thienoisoindigo-naphthalene polymer with ultrahigh mobility of 14.4 cm^2/V s that substantially exceeds benchmark values for amorphous silicon semiconductors. J Am Chem Soc 136(26):9477–9483

31. Yum S, An TK, Wang X et al (2014) Benzotriazole-containing planar conjugated polymers with noncovalent conformational locks for thermally stable and efficient polymer field-effect transistors. Chem Mater 26(6):2147–2154

32. Wang Y, Masunaga H, Hikima T et al (2015) New semiconducting polymers based on benzobisthiadiazole analogues tuning of charge polarity in thin film transistors via heteroatom substitution. Macromolecules 48(12):4012–4023

33. Mei J, Bao Z (2013) Side chain engineering in solution-processable conjugated polymers. Chem Mater 26(1):604–615

34. (a) Tao HN, Cho DM, Park I et al (2011)Ultrahigh mobility in polymer field-effect transistors by design. J Am Chem Soc 133(8):2605–2612; (b) Piliego C, Holcombe TW, Douglas JD et al (2010) Synthetic control of structural order in N-alkylthieno [3,4-c] pyrrole-4,6-dione-based polymers for efficient solar cells. J Am Chem Soc 132(22):7595–7597

35. Mei J, Kim DH, Ayzner AL et al (2011) Siloxane-terminated solubilizing side chains: bringing conjugated polymer backbones closer and boosting hole mobilities in thin-film transistors. J Am Chem Soc 133(50):20130–20133

36. Lee J, Han AR, Kim J et al (2012) Solution-processable ambipolar diketopyrrolopyrrole-selenophene polymer with unprecedentedly high hole and electron mobilities. J Am Chem Soc 134(51):20713–20721

37. Lee J, Han AR, Yu H et al (2013) Boosting the ambipolar performance of solution-processable polymer semiconductors via hybrid side-chain engineering. J Am Chem Soc 135(25):9540–9547

38. Kocieński PJ, Protecting Groups, 3rd Ed., (Georg Thieme Verlag, New York 2005)

39. Lei T, Dou JH, Pei J (2012) Design of high-mobility diketopyrrolopyrrole-based π-conjugated copolymers for organic thin-film transistors. Adv Mater 24:6457–6482

40. Kang IL, Yun HJ, Chung DS et al (2013) Record high hole mobility in polymer semiconductors via side-chain engineering. J Am Chem Soc 135(40):14896–14899

41. (a) Li G, Zhu R, Yang Y (2012) Polymer solar cells. Nat Photon 6:153–161; (b) Ouyang X, Peng R, Ai L et al (2015) Efficient polymer solar cells employing a non-conjugated small-molecule electrolyte. Nat Photon 9(8):520–524

42. Zhao J, Li Y, Yang G et al (2016) Efficient organic solar cells processed from hydrocarbon solvents. Nat Energy 1:15027–15040

43. Zhang M, Guo X, Zhang S et al (2014) Synergistic effect of fluorination on molecular energy level modulation in highly efficient photovoltaic polymers. Adv Mater 26(7):1118–1123

44. (a) Li G, Shrotriya V, Huang J et al (2005) High-efficiency solution processable polymer photovoltaic cells by self-organization of polymer blends. Nat Mater 4(11):864–868; (b) Kim Y, Cook S, Tuladhar SM et al (2006) A strong regioregularity effect in self-organizing conjugated polymer films and high-efficiency polythiophene: fullerene solar cells. Nat Mater 5(3):197–203

45. (a) Blouin N, Michaud A, Gendron D et al (2008) Toward a rational design of poly (2,7-carbazole) derivatives for solar cells. J Am Chem Soc 130(2):732–742; (b) Liang Y, Wu Y, Feng D et al (2008) Development of new semiconducting polymers for high performance solar cells. J Am Chem Soc 131(1):56–57; (c) Wang M, Hu X, Liu P et al (2011) Donor-acceptor conjugated polymer based on naphtho[1,2-c:5,6-c]bis[1,2,5]thiadiazole for high-performance polymer solar cells. J Am Chem Soc 133(25):9638–9641

46. (a) Schilinsky P, Asawapirom U, Scherf U et al (2005) Polymer-fullerene bulk-heterojunction solar cells. Chem Mater 17:175–182 (b) Koppe M, Brabec CJ, Heiml S et al (2009) Influence of molecular weight distribution on the gelation of P_3HT and its impact on the photovoltaic performance. Macromolecules 42(13):4661–4666; (c) Bijleveld JC, Zoombelt AP, Mathijssen SGJ et al (2009) Small band gap copolymers based on furan and diketopyrrolopyrrole for field-effect transistors and photovoltaic cells. J Am Chem Soc 31:16616–16634; (d) Müller C, Wang E, Andersson LM et al (2010) Influence of molecular weight on the performance of organic solar cells based on a fluorene derivative. Adv Funct Mater 20(13):2124–2131

47. (a) Piliego C, Holcombe TW, Douglas JD et al (2010) Synthetic control of structural order in *N*-alkylthieno [3, 4-c] pyrrole-4, 6-dione-based polymers for efficient solar cells. J Am Chem Soc 132(22):7595–7597; (b) Zhang Y, Hau SK, Yip HL et al (2010) Efficient polymer solar cells based on the copolymers of benzodithiophene and thienopyrroledione. Chem Mater 22 (9):2696–2698; (c) Zou Y, Najari A, Berrouard P et al (2010) A thieno [3,4-c] pyrrole-4, 6-dione-based copolymer for efficient solar cells. J Am Chem Soc 132(15):5330–5331; (d) Cabanetos C, Labban A, Bartelt JA et al (2013) Linear side chains in benzo [1,2-b 4,5-b′] dithiophene-thieno [3,4-c] pyrrole-4, 6-dione polymers direct self-assembly and solar cell performance. J Am Chem Soc 135(12):4656–4659

48. Schilinsky P, Asawapirom U, Scherf U et al (2015) Polymer–fullerene bulk-heterojunction solar cells. Chem Mater 17:175–182

49. Ma W, Kim JY, Lee K et al (2007) Effect of the molecular weight of poly (3-hexylthiophene) on the morphology and performance of polymer bulk heterojunction solar cells. Macromol Rapid Comm 28(17):1776–1780

50. Coffin RC, Peet J, Rogers J et al (2009) Streamlined microwave-assisted preparation of narrow-bandgap conjugated polymers for high-performance bulk heterojunction solar cells. Nat Chem 1(8):657–661

51. Zhou HX, Yang LQ (2010) Fast conductance switching in single-crystal organic nanoneedles prepared from an interfacial polymerization-crystallization of 3,4-ethylenedioxythiophene. Macromolecules 43:811–832

52. (a) Chu TY, Lu J, Beaupré S et al (2012) Effects of the molecular weight and the side-chain length on the photovoltaic performance of dithienosilole/thienopyrrolodione copolymers. Adv Funct Mater 22:2345–2351; (b) Liu C, Wang K, Hu X et al (2013) Molecular weight effect on the efficiency of polymer solar cells. ACS Appl Mater Interfaces 5(22):12163–12167; (c) Hendriks KH, Heintges GHL, Gevaerts VS et al (2013) High-molecular-weight regular alternating diketopyrrolopyrrole-based terpolymers for efficient organic solar cells. Angew Chem Int Ed 52:8341–8344

53. Osaka I, Saito M, Mori H et al (2012) Drastic change of molecular orientation in a thiazolothiazole copolymer by molecular-weight control and blending with PC61BM leads to high efficiencies in solar cells. Adv Mater 24(3):425–430

54. Li W, Yang L, Tumbleston JR et al (2014) Controlling molecular weight of a high efficiency donor–acceptor conjugated polymer and understanding its significant impact on photovoltaic properties. Adv Mater 26(26):4456–4462

55. Tong M, Cho S, Rogers JT et al (2010) Higher molecular weight leads to improved photoresponsivity, charge transport and interfacial ordering in a narrow bandgap semiconducting polymer. Adv Funct Mater 20(22):3959–3965

56. Tang ML, Bao Z (2010) Halogenated materials as organic semiconductors. Chem Mater 23 (3):446–455

57. Li J, Zhang X, Jin H et al (2015) Synthesis of fluorine-containing phosphodiesterase 10A (PDE10A) inhibitors and the in vivo evaluation of F-18 labeled PDE10A PET tracers in rodent and nonhuman primate. Int J Med Chem 58(21):8584–8600

58. Keinänen XG, Li NK, Lumen Chenna D et al (2016) A new highly reactive and low lipophilicity fluorine-18 labeled tetrazine derivative for pretargeted PET imaging. ACS Med Chem Lett 7(1):62–66

59. Jian W, He D, Xi P et al (2015) Synthesis and biological evaluation of novel fluorine-containing stilbene derivatives as fungicidal agents against phytopathogenic fungi. J Agric Food Chem 63(45):9963–9969

60. (a) Bronstein H, Frost JM, Hadipour A et al (2013) Effect of fluorination on the properties of a donor–acceptor copolymer for use in photovoltaic cells and transistors. Chem Mater 25 (3):277–285; (b) Yang Y, Wu R, Wang X et al (2014) Isoindigo fluorination to enhance photovoltaic performance of donor–acceptor conjugated copolymers. Chem Commun 50(4): 439–441

61. Tumbleston JR, Collins BA, Yang L et al (2014) The influence of molecular orientation on organic bulk heterojunction solar cells. Nat Photon 8:385–391

62. Li W, Albrecht S, Yang L et al (2014) Mobility-controlled performance of thick solar cells based on fluorinated copolymers. J Am Chem Soc 136(44):15566–15576
63. Zheng YQ, Wang Z, Dou JH et al (2015) Effect of halogenation in isoindigo-based polymers on the phase separation and molecular orientation of bulk heterojunction solar cells. Macromocules 48(16):5570–5577
64. Szarko JM, Guo J, Liang Y et al (2010) When function follows form: effects of donor copolymer side chains on film morphology and BHJ solar cell performance. Adv Mater 22(48):5468–5472
65. Osaka I, Kakara T, Takemura N et al (2013) Naphthodithiophene-naphthobisthiadiazole copolymers for solar cells: alkylation drives the polymer backbone flat and promotes efficiency. J Am Chem Soc 135(24):8834–8837
66. Osaka I, Zhang R, Sauvé G et al (2009) High-lamellar ordering and amorphous-like π-network in short-chain thiazolothiazole-thiophene copolymers lead to high mobilities. J Am Chem Soc 131(7):2521–2529
67. Osaka I, Saito M, Koganezawa T et al (2014) Thiophene-thiazolothiazole copolymers: significant impact of side chain composition on backbone orientation and solar cell performances. Adv Mater 26(2):331–338

Chapter 17
Design and Control of Nanostructures and Interfaces for Excitonic Solar Cells

Jianjun Tian, Shixun Wang and Guozhong Cao

Abstract Excitonic solar cells (ESCs) including dye-sensitized solar cells, quantum dot-sensitized solar cells, perovskites solar cells, and inverted organic photovoltaics are built upon metal oxide semiconductors (MOSs), which have attracted considerable attention recently and showed a promising development for the next generation solar cells. The development of nanotechnology has created various MOS nanostructures to open up new perspectives for their exploitation, significantly improving the performances of ESCs. One of the outstanding advantages is that the nanostructured mesoporous MOSs offer large specific surface area for loading a large number of active materials (dyes, quantum dots, or perovskites) so as to capture a sufficient fraction of photons as well as to facilitate efficient charge transfer. This review focuses on the recent work on the design, fabrication, and surface modification of nanostructured MOSs to improve the performance of ESCs. The key issues for the improvement of efficiency, such as enhancing light harvesting and reducing surface charge recombination, are discussed in this paper.

17.1 Introduction

As a cost-effective alternative to silicon-based photovoltaics, excitonic solar cells (ESCs) including dye-sensitized solar cells (DSCs), quantum dot-sensitized solar cells (QDSCs), perovskites solar cells (PSCs), and inverted polymer solar cells or inverted

J. Tian (✉) · S. Wang
Institute of Advanced Materials and Technology, University of Science
and Technology Beijing, Beijing 100083, China
e-mail: tianjianjun@mater.ustb.edu.cn

S. Wang
e-mail: shixunwang@163.com

G. Cao (✉)
Department of Materials Science and Engineering, University of Washington,
Seattle, WA 98195-2120, USA
e-mail: gzcao@u.washington.edu

organic photovoltaics (OPVs), based upon nanostructured MOSs have attracted considerable attention recently and showed a promising development for the next generation solar cells [1–7]. MOS plays a very important role in ESCs either as electron transporting layer while blocking hole transport (known as cathode buffer layer) or as hole transporting layer while blocking the electron transport (anode buffer layer) [8]. As early as 1991, MOS TiO_2 with porous nanostructure was successfully used in DSCs to get high power conversion efficiency (PCE) of greater than 7%, which was a significant breakthrough for the next generation solar cells with low cost [6]. DSC is a category of photovoltaic device based on a photoelectrochemical system in which a porous MOS film with dye molecules adsorbed on the surface serving as the working electrode for light harvesting and the generation of photoexcited electrons [9]. Many efforts have been focused on improving light absorption of sensitizers [10–13].

In 2014, a recorded PCE of 13% of DSC has been obtained by using a molecularly engineered porphyrin dye coded SM315 and the cobalt (II/III) redox electrolyte [14]. In comparison with c-Si solar cells, PCE of DSCs still is much low. One of the effective approaches is to develop new sensitizers for absorbing photons in the full sunlight spectra. Narrow-bandgap semiconductor quantum dots (QDs) with wide light absorption region, such as CdS [15, 16], CdSe [7, 17], PbS [18], and InAs [19] have been investigated as photo-sensitizers instead of organic dyes to form QDSCs that have attracted a lot of attention particularly due to: (1) adjustable bandgap through design and control the size of QD, (2) good chemical stability, (3) much efficient light absorption (a high extinction coefficient), and (4) multiple exciton generation (MEG) promising a power conversion efficiency theoretically up to 40% in a single junction solar cell [20–22]. Practically, efficiencies in the range of 6% for CdSe [23, 24] and 8% for CdSeTe [25–27] QDSCs have already been achieved; the PCE of QDSCs remains lower than that of DSCs, due likely to large surface charge recombination, attributable to the surface imperfection of QDs and the less ideal contact between QDs and MOS scaffold [28].

In 2009, Miyasaka group reported the solar cells with DSC structure using organic-inorganic hybrid perovskite $CH_3NH_3PbBr_3$ and $CH_3NH_3PbI_3$ as visible-light sensitizers instead of organic dyes [29]. This attempt led to PCE of 3.8%. Although, the PCE was low, the attempt provided a new approach for the next generation solar cells [30]. In 2011, Park's group reported a 6.5% efficient $CH_3NH_3PbI_3$ PSC [31], though this work did not attract much attention due to the liquid electrolyte used in the devices. In 2012, an all solid ESC using perovskite with a PCE greater than 10% was obtained by Snaith's group, which had attracted worldwide attention [32]. In 2015, PSCs based on the MOS TiO_2 assembled with $CH_3NH_3PbX_3$ achieved PCE of greater than 20% [33].

In recent years, OPVs have attracted extensive investigation as one of ESCs, mainly due to their inherent advantages of being low cost, and compatible with flexible substrate and solution-based roll-to-roll processing technique [1–5, 34]. Compared with the organic photovoltaics with a traditional structure, which typically have a configuration ITO/PEDOT/P3HT:PCBM/MOS/Al, inverted OPVs with the configuration ITO/MOS/PCBM:P3HT/PEDOT/Ag avoid the contact of ITO with PEDOT (which degrades the conductivity of ITO glass) and allow the use

of high-work-function metal (e.g., Ag) as top electrode and can therefore significantly enhance the stability of polymer solar cells [8].

Among various MOSs, TiO_2, ZnO, and SnO_2 have been studied widely in ESCs, due to their matching band structure, excellent physical properties, and high electronic mobility [35–40]. Table 17.1 [41] shows structural and electronic characteristics of TiO_2, ZnO, and SnO_2 [42]. It can be seen that TiO_2, ZnO, and SnO_2 have similar band structure and physical properties. In the past decades, more and more efforts have been focused on the application of TiO_2, ZnO, and SnO_2 in ESCs. For example, Fig. 17.1 displays the evolution of the number of publications for 'dye-sensitized solar cell.' In addition to research works, many excellent reviews and perspective articles have covered the fundamentals and technical approaches for the design, fabrication, and characterization of MOSs for ESCs [36, 39, 43–49]. In this review, we would focus mainly on the recent work on the MOS structure and their interface for improving the efficiency of ESCs, such as enhancing light harvesting and reducing surface charge recombination.

As to the evaluation method, current density–voltage (I–V) measurement is frequently used in the investigation of the performance of solar cells. We can get four vital parameters obtained from I–V measurements as follows: the open-circuit voltage (V_{oc}), the short-circuit current density (J_{sc}), fill factor (FF), and the PCE. PCE is defined as the output power divide by the input power, as Eq. (17.1) shows:

$$\eta = \frac{P_{max}}{P_{inc}} = \frac{I_{max} \times V_{max}}{P_{inc}} = \frac{I_{sc} \times V_{oc} \times FF}{P_{inc}}, \qquad (17.1)$$

where the η is PCE and P_{inc} represents the input power of irradiated light (usually 100 mW cm^{-2}). FF varies from zero to one in the actual courses of solar cell due to recombination between electrons and holes and corrosion of sensitizers. There are many factors that directly determine the value of FF such as the charge-transfer resistance (R_{ct}), series resistance (R_s), and Warburg impedance (Z_w).

17.2   Dye-sensitized Solar Cells (DSCs)

DSCs are in essence a photoelectrochemical system as shown in Fig. 17.2 [50]. Nanostructured MOS films are the framework of DSC photoanodes, which serve dual functions as the support for sensitizer loading and transporter of photoexcited electrons from sensitizer to external circuit [44]. Usually, a layer of MOS with the thickness 10–20 μm is prepared on a glass substrate coated with a transparent conductive film. The other electrode, the so-called counter electrode, is a glass or silicon substrate coated with a platinum film. As a conductive medium, the liquid electrolyte with I^-/I_3^- redox couples is filled in the gaps of MOS and the space between the photoanode and counter electrode. The work process of DSC is [50] as follows: The light irradiating from the photoanode side is captured by the dye molecules that are adsorbed on the oxide, leading to the generation of photoexcited

Table 17.1 Structural and electronic characteristics of TiO$_2$, ZnO and SnO$_2$ [42]

MOSs	Crystal structure	Bandgap (eV)	Conduction band minimum (eV)	Electron effective mass	Static dielectric constant	Electron Mobility (9 cm^2 V^{-1} s^{-1})	Electron diffusion coefficient (nanoporous film) (cm^2 s^{-1})
TiO$_2$	Rutile, Anatase	3.0–3.2	−4.41	9	86, 170	0.1–4	4.3×10^{-4}
ZnO	Wurtzite	3.2–3.4	−4.36	0.26	9.26, 8.2	130–200	1.1×10^{-4}
SnO$_2$	Rutile	3.6–3.8	−4.88	0.275	14, 9	200–250	7.3×10^{-5}

Fig. 17.1 Evolution of the number of publications for 'dye-sensitized solar cell' with 'TiO$_2$', 'ZnO', and 'SnO$_2$', respectively. *Source* ISI Web of Science, Thomson Reuters (Reproduced from Ref. [41] with kind permission of © 2016 Elsevier)
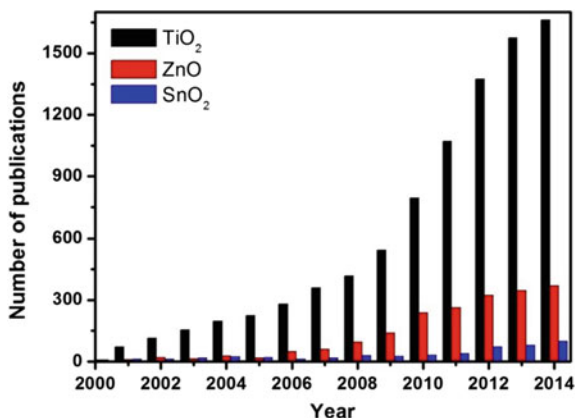
electrons in the dye molecules; the photogenerated electrons then transfer into the oxide, diffuse in the oxide, and are finally collected by the transparent conductive film on the glass substrate, which is connected to external circuit; the photooxidized dye molecules are reduced by electrons provided by I^-/I_3^- redox couples in the electrolyte. Those photogenerated electrons at the photoanode travel through the external circuit, reach the platinum-coated counter electrode, and finally, gain access to the electrolyte, reducing I^-/I_3^- redox couples and enabling the electrolyte to be regenerated.

In DSCs, the structure of photoanodes has important effect on the light harvesting and photoexcited electrons transport. Not only does the nanostructured MOS offer large surface area to adsorb a large number of dyes for light harvesting, but also collects the electrons from dyes and transfers them to electrodes. MOS nanoparticles film is first used in DSCs due to its large surface area for loading dyes. But it is not an ideal structure in regard to the electron transport [53, 54]. The first non-ideality results from the lack of a macroscopic electrostatic potential gradient in the film due to the fact that the film is permeated with a concentrated electrolyte [53]. The mesoporous films are very much different compared to their compact analogues because (i) the inherent conductivity of the film is very low, (ii) the small size of the individual colloidal particles does not support a built-in electrical field, and (iii) the oxide particles and the electrolyte-containing pores form interpenetrating networks whose phase boundaries produce a junction of huge contact area [55]. Therefore, the electron transport in the nanoparticle film is dominated by a process of diffusion instead of drift. The drift is a common way in p–n junction solar cells for carrier separation in the presence of an electric field. The second non-ideality comes from the fact that the electron transport in a nanoparticle film undergoes a trapping and detrapping process as shown in Fig. 17.3 [41] Numerous grain boundaries, interface defects, and connections existing in the nanoparticle film also increase the surface charge recombination, and retard effective charge injection and charge transport, which result in a loss of PCE. So many efforts have been made on the synthesis of a variety of nanostructured MOS
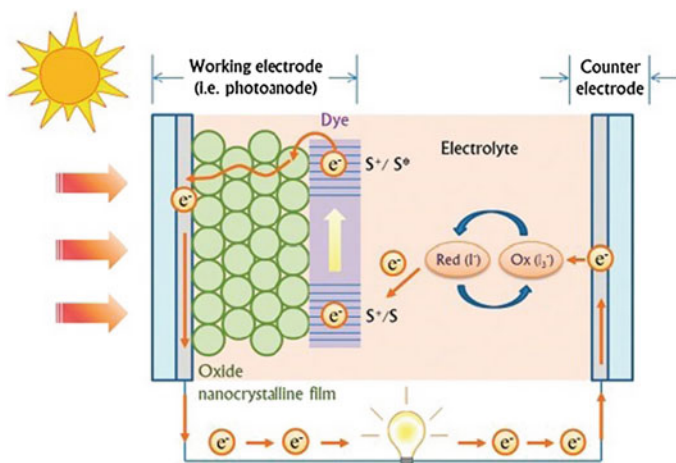
Fig. 17.2 Structure and operating mechanism of a DSC (Reproduced from Ref. [66] with kind permission of © 2010 Royal Society of Chemistry)
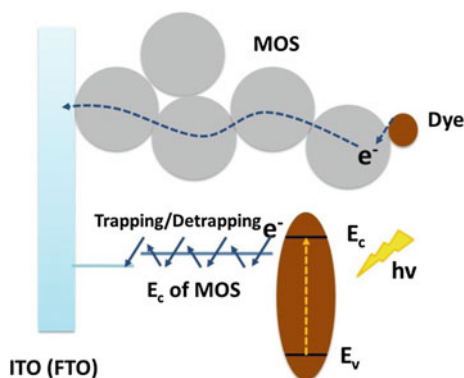
Fig. 17.3 Schematic illustrations of electron transport in a nanoparticle film suffering a trapping/detrapping process (Reproduced from Ref. [41] with kind permission of © 2016 Elsevier)

photoanodes in the forms of wires, tubes, spheres, rods, sheets, belts, flowers, and trees for the efficient DSC devices [56–63].

To increase the electron mobility and reduce the grain boundaries and interfaces, one-dimensional (1D) nanostructures, such as nanotube arrays and single-crystalline nanowire arrays, have been studied as photoanodes for DSCs [56]. However, DSCs based on 1D structures have not reached high conversion efficiency as expected due to the much small surface area for dye adsorption [64]. The 3D hierarchical nanostructures can offer larger surface areas for dye adsorption while simultaneously enhancing light scattering for efficient photon harvesting, and thereby, improving PCE [60, 64–66]. The aggregate structure consisting of primary

nanocrystallites can provide both large specific surface area and light scattering effect so as to enhance the performance of DSCs [9, 53, 66–70]. In addition, the diffusion of electrolyte in the aggregate structure is faster than that in nanoparticle film, which boosts the charge transport. Our previous works [9, 53, 67, 69, 71–73] showed that the photoanodes with the hierarchical aggregates structure are promising for the highly efficiency DSCs. Our recent works have been continuing to improve the fabrication and design of the hierarchical structure of MOSs for increasing the PCE of DSCs.

17.2.1   TiO$_2$ Hierarchical Structures for DSCs

In the last few decades, many methods have been used to synthesize TiO$_2$ nanostructures, such as sol–gel processing [74], hydrothermal [75], solvothermal [76], and template growth [77] approaches. The hydrothermal and solvothermal methods have been frequently used for the reason that they are readily capable of obtaining the desired size and structure of TiO$_2$ nanocrystals by controlling the temperature and duration of the reaction, and the type and concentration of the reactants, as well as the solvent and additives used. However, defects in the resultant nanocrystals like complex and time-consuming process have been pointed out in the hydrothermal and solvothermal methods. The high cost and low productivity of the hydrothermal and solvothermal methods are also considered as a big hindrance for their applications in DSCs. There is a growing need to develop a fast and high productivity synthesis method to obtain TiO$_2$ nanocrystals for the application in DSCs.

Compared with hydrothermal and solvothermal methods, the microwave assisted synthesis offers rapid processing speed, homogeneous heating, and simple control of processing conditions, and thus has attracted much attention in the last few years [78]. Recently, microwave assisted synthesis was employed to fabricate hierarchically structured TiO$_2$ nanocrystallite aggregates, which are shown in Fig. 17.4 [79]. Hierarchically structured TiO$_2$ nanocrystallite aggregates with a size of ∼500 nm in diameter consisted of ∼10 nm nanocrystallites were synthesized by microwave assisted method at 150 °C in a short time (∼10 min) using ethanol and TiCl$_4$ as the solvent and titanium precursor, respectively. The rapid heating rate and superheating/"hot spots" of the reaction system under microwave irradiation resulted in huge supersaturation leading to a high density of nuclei instantly so as to form a great deal of uniformly sized small particles/nanocrystals, which were subsequently assembled to uniformly sized aggregates. The TiO$_2$ aggregates showed much better light scattering property, larger specific surface area, and higher dye-loading than those of the commercial P25 TiO$_2$ nanoparticles. In comparison with P25, the short current density (J_{sc}) and dye-loading of DSC based on the as-synthesized TiO$_2$ aggregates increased by 33 and 62%, respectively. As a result, the PCE of the DSC was up to 7.64%.
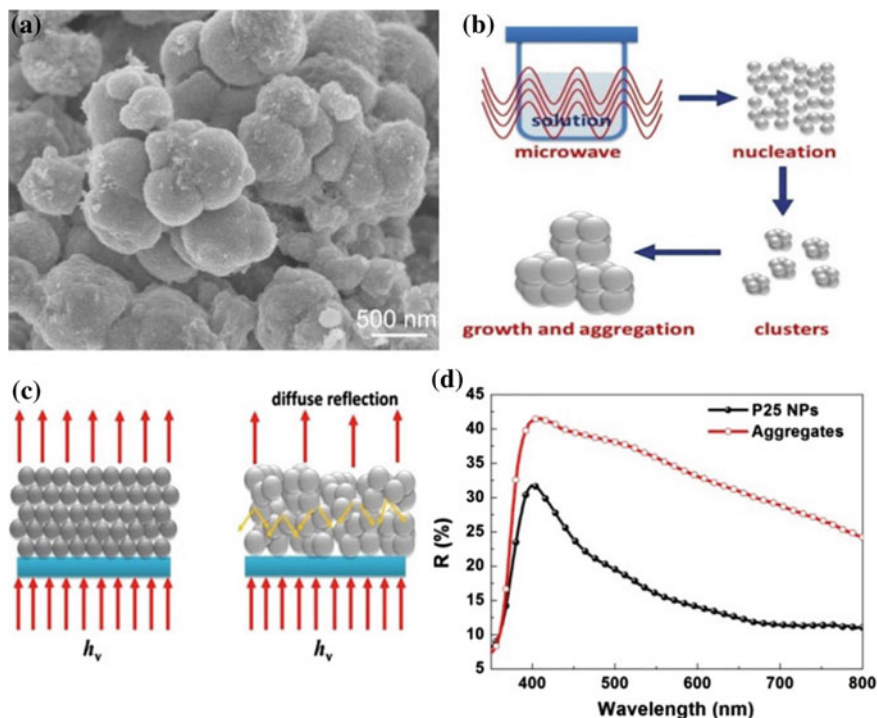
Fig. 17.4 a SEM images of as-synthesized TiO$_2$ aggregates, **b** schematic illustration of TiO$_2$ aggregates formation process, **c** schematic illustration of the effect of the aggregates for the light scattering and **d** diffuse reflection spectra curves of P25 nanoparticles TiO$_2$ film and TiO$_2$ aggregates film. Reprinted from reference (Reproduced from Ref. [79] with kind permission of © 2010 Royal Society of Chemistry)

It was also found that the electron diffusion in the TiO$_2$ aggregate network was enhanced through the addition of TiO$_2$ nanoparticles with preferential filling at the necks between adjacent TiO$_2$ aggregates, which resulted in strengthening the connections, while retaining the porous structure of the TiO$_2$ network as shown in.

Figure 17.5 [80] The fortified necks were found to reduce the transport resistance (R_t) by allowing facile transfer of electrons from one aggregate to another, while the scattering effect of the TiO$_2$ aggregate network got weakened with adding the TiO$_2$ nanoparticles as a result of reduction of the light scattering centers such as the necks and gaps between the aggregates. However, due to the increase in surface area as the TiO$_2$ nanoparticles were added, the diminished light scattering effect of the aggregate network was compensated and even the highest performance was achieved when the 10% TiO$_2$ nanoparticle was added into the TiO$_2$ aggregate film, suggesting that widening necks between submicrometer-sized light scatters such as an aggregate would be a good strategy in achieving further improvement of PCE of dye-sensitized solar cells through the improved charge transport property.
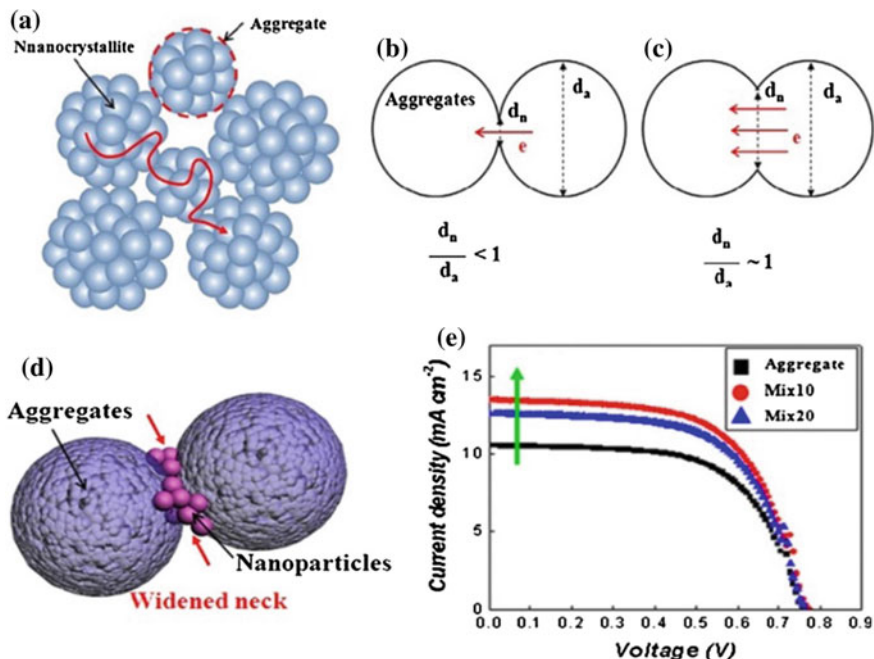
Fig. 17.5 Schematics illustrating **a** electron diffusion in aggregates and through necks between aggregates, **b** low possibility of electron transfer from one aggregate to adjacent one due to poor neck, **c** high possibility of electron transfer as a result of widened neck compared to the diameter of the aggregate, **d** the widened neck between two aggregates achieved by filling with the added nanoparticles and **e** *J–V* curves of the DSCs with the photoanodes composed of TiO_2 aggregate and mixture of the aggregates and nanoparticles (Mix10 and Mix20) (Reproduced from Ref. [80] with kind permission of © 2015 Elsevier)

However, dye molecules and electrolyte are difficult to penetrate into the interior pores of the aggregates, which is not helpful for the improvement of enhanced photon capture and efficient transport of the photoexcited electron. The inverted aggregate hierarchical structure would have both high dye adsorption and strong light scattering. Our recent work reported a strategy for the synthesis of hierarchically structured three-dimensionally ordered macroporous (HS-3DOM) TiO_2 with controlled macropore sizes (ca. 85–155 nm) by using well-arrayed polymethyl methacrylate with different diameters as well as two kinds of photoanode films based on hierarchically structured porous TiO_2 filled with nanoparticles have been demonstrated as shown in Fig. 17.6 [81]. DSCs based on a special TiO_2 photoanode with a macropore size of 105 nm exhibited a current density of 20.6 mA/cm^2 and a high PCE of 9.7%. The hierarchically structured porous TiO_2 layer has much large surface area to load dyes and high-diffused reflectance and scattering to harvest photons, which is the main reason for high photogenerated current density. The results showed the electron lifetime was prolonged and charge recombination was reduced. This may be due to the special geometry architecture of
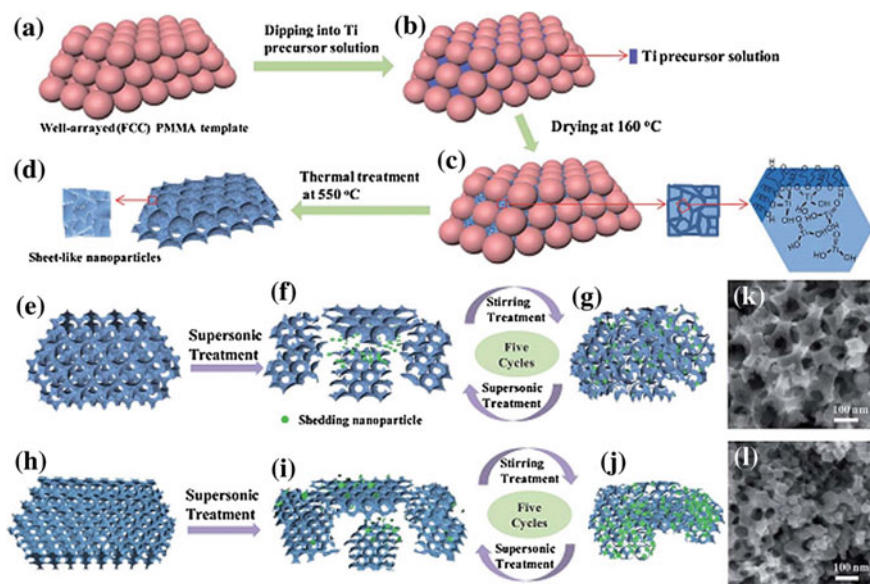
Fig. 17.6 Schematic illustration of the paste formation process based on **a** Ti-155, Ti-115, and **b** Ti-105 samples and the ones based on **c** Ti-85 sample, as well as HR-SEM pictures of photoanode films based on **e** Ti-105 and **h** Ti-85 samples. Schematic diagram of **d** HS-3DOM TiO$_2$, **f** and **i** shedding 3DOM architectures of TiO$_2$ after supersonic treatment, **g** and **j** agglomerate 3DOM architectures of TiO$_2$ after stirring treatment. Reprinted from reference (Reproduced from Ref. [81] with kind permission of © 2010 Royal Society of Chemistry)

the photoelectrodes. Therefore, this high PCE is ascribed to the special morphology of the TiO$_2$ photoanode with high dye adsorption due to its ordered and open structures, and also its light scattering and charge-collection efficiency.

17.2.2 ZnO Hierarchical Structures for DSCs

ZnO is known to have band structure and physical properties similar to that of TiO$_2$, but a higher electron mobility than that of TiO$_2$ [9, 67, 69]. In addition, ZnO with a hexagonal crystal structure possesses facets with different surface energy and, thus, can easily form anisotropic structures, such as nanorods, nanowires, and nanoflowers, which enables it to exhibit unique electronic and optical properties [73, 82]. ZnO nanostructured photoelectrodes for DSCs have been investigated over the last several years [63, 64, 83, 84]. For ZnO-based DSCs, the ZnO films with hierarchical structure have exhibited much better performance in DSCs than that of nanoparticles and 1D structure, due to the larger specific surface area for dye adsorption, effective light scattering within the photoanode, and more pores for the penetration of electrolyte into the photoanode films [66]. As early as 2008, we had prepared ZnO aggregates spheres made up of nanocrystallites for DSCs [69]. With
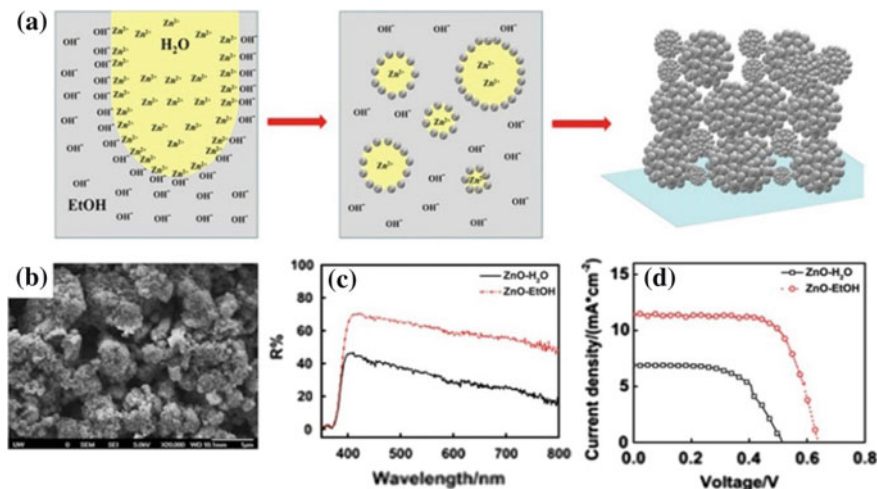
Fig. 17.7 a Schematic diagram of ZnO formation process using interface precipitation, **b** SEM image of ZnO aggregates, **c** diffuse reflectance of ZnO film prepared by different precipitation process, and **d** *J–V* curves of DSCs based on the different ZnO photoanodes (Reproduced from Ref. [66] with kind permission of © 2012 Elsevier Ltd.)

increased dye adsorption and improved light-scattering capabilities by the primary nanoparticles and secondary colloids, 5.4% of PCE was obtained, which is one of the highest PCE of ZnO-based DSCs at that time. Recently, we develop a novel interface precipitation method to synthesize hierarchically structured ZnO nanocrystallite aggregates as shown in Fig. 17.7 [66].

The conventional homogeneous precipitation process in aqueous solution is an efficient way to synthesize ZnO nanoparticles at low temperature. In this process, ethanol and water were used as solvents to first separately dissolve NaOH and zinc acetate dihydrate under stirring, respectively. The reaction occurred in the interface of the different solvents with a slow rate, which was easier to form a porous hierarchical structure. In comparison with ZnO nanoparticles synthesized by conventional homogeneous precipitation method, such hierarchical structure has larger specific surface area, more efficient dye-loading and effective light scattering within the photoelectrode; all result in an increased photocurrent. Furthermore, electrochemical impedance spectroscopy study revealed that reduced charge recombination in ZnO nanocrystallite aggregates resulted in enhanced Voc. As a result, a PCE of 5.07% with commercially available dye N719 had been obtained without applying anti-reflection coating and chemical treatment, which was more than 200% of the PCE achieved in ZnO nanoparticles synthesized by homogeneous precipitation method in aqueous solution.

Porous ZnO aggregates of nanocrystallites were thought to be helpful to retain their high surface area. However, their PCEs are still lower than that of TiO_2-based DSCs, due likely to the poor chemical stability for dye solution and lots of surface

defects for high charge recombination. A lot of research results showed that the charge recombination could be reduced by applying a core-shell configuration [85, 86]. Such a core-shell configuration is expected to suppress the charge recombination by forming an energy barrier to prevent the electrons in the conduction band of the semiconductor from transferring to the oxidized dyes and ions in the electrolyte, leading to increased open-circuit voltage and short current density [85–87]. It was also reported [83] that the shell (TiO_2) has a more negative conduction band edge than that of the core oxide (ZnO) or it creates a dipole at the core—shell interface that shifts the band edge of the core upward in energy, which suppresses recombination and increases the open voltage and fill factor. Many novel core/shell structures, for example, ZnO/TiO_2, ZnO/Al_2O_3, ZnO/ZrO_2, and ZnO/MgO photoelectrodes, have been used in DSCs for this purpose [83, 85–88]. In an earlier study, atomic layer deposition (ALD) method was utilized to deposit ultrathin TiO_2 layer on the porous structure of ZnO aggregates, and the resultant devices demonstrated much enhanced PCE of ZnO DSC with photoelectrodes made of submicrometer-sized aggregates of ZnO nanocrystallites as shown in Fig. 17.8 [86]. The ZnO core/TiO_2 shell structure increases the open-circuit voltage, without impairing the photocurrent density, and results in an increased PCE from 5.2 to 6.3%.

ALD is rather time-consuming and not cost effective [89]. Recently, a facile solution method was applied to modify the surface of ZnO aggregate photoanodes for DSCs as shown in Fig. 17.9 [90]. During the modification process, the surface of the ZnO will be dissolved through a chemical reaction in an aqueous solution of $(NH_4)_2TiF_6$ and H_3BO_3, while the deposition of TiO_2 nanocrystallites takes place sequentially and concurrently. This method can be considered as an in situ alternative deposition method. As the chemical reaction on the surface of photoanode material is always easy to take place at an area with high surface energy, so TiO_2 is more likely to deposit on the defect region of ZnO surface, which reduces the surface defects while further increases the surface stability [90]. The IPCE of the TiO_2-modified film with a 3 min treatment exhibits a highest maximum to 60%, whereas the film with a 20 min treatment shows a lowest maximum as shown in Fig. 17.9c. The trend observed with IPCE matches with that of the J_{sc}, and the integrated current from the spectra correlates closely with the photovoltaic data. Figure 17.9d displays the whole process of the photon-electric conversion in solar cells. Initially, the photons are captured by the dyes to realize the harvesting of

Fig. 17.8 Schematics illustrating ALD TiO_2 thin layer on the surface of ZnO nanocrystallites, *inset* shows SEM image ZnO aggregate coated by TiO_2 thin layer (Reproduced from Ref. [86] with kind permission of © 2010 Wiley-VCH)
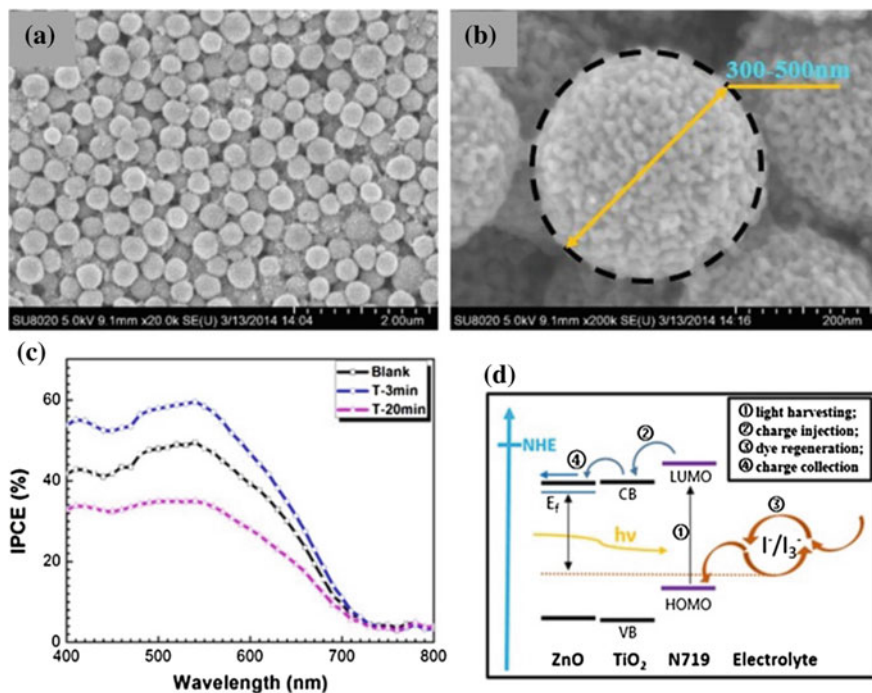
Fig. 17.9 **a**, **b** SEM images of submicrometer-sized aggregates of ZnO nanocrystallites in different magnifications, **c** incident photon-to-current conversion efficiency (IPCE) spectra of ZnO-based DSCs with different solution treatment times; **d** photoelectric conversion process in solar cells (Reproduced from Ref. [90] with kind permission of © 2014 Elsevier)

light. Then, the electrons generated by dye will inject into photoanode. The energy difference between the lowest unoccupied molecular orbital (LUMO) of the dye and the conduction band of TiO_2 provides driving force for charge injection. Therefore, the surface modification process introduces a thin layer of TiO_2 nanoparticles on the surface of ZnO aggregates can reduce the charge recombination and increase the charge collection, at the same time, open the inner pores through in situ selective etching of ZnO at pore apertures. As a result, the PCE of DSC was increased from 4.81 to 6.27%, after surface modification of ZnO aggregates.

17.2.3 SnO₂ Hierarchical Structures for DSCs

SnO_2 is an important n-type wide-bandgap semiconductor with wide applications in transparent conductive films, gas sensors, lithium-ion batteries, and solar cells [38, 91–95]. SnO_2 as a possible alternative of TiO_2 photoanode in DSCs with various

morphologies, such as nanoparticles [96, 97], nanofibers [98], nanowires [99], nanotubes [100], and hollow nanospheres [101–105], has been successfully synthesized and characterized. For example, Cheng et al. [106] reported the synthesis of single-crystalline SnO_2 nanorods with small size (15–20 nm in length and 2.5–5 nm in diameter) by hydrothermal treatment of $TiCl_4$. Wu et al. [107] prepared 3D hierarchical SnO_2 nanostructures composed of 2D nanosheets. TiO_2-coated multi-layered SnO_2 hollow microspheres had achieved 5.65% of PCE [108]. Among various techniques used for SnO_2 synthesis, hydrothermal growth is one of the most common methods, which can form desired size and morphology by manipulating reactant ratio and reaction parameters [109].

Our recent work reported a microwave assisted synthesis of assembled SnO_2 nanosheets and their characterization and application as photoanodes in DSCs as shown in Fig. 17.10 [110]. The assembled SnO_2 nanosheets photoanode, with large specific surface area, effective light scattering, and an easy path for electron transport with long lifetime, demonstrated appreciably increased short-circuit photocurrent density, reduced charge recombination, and consequently high PCE. However, the limitations of SnO_2-based DSCs are the relatively weak adsorption of
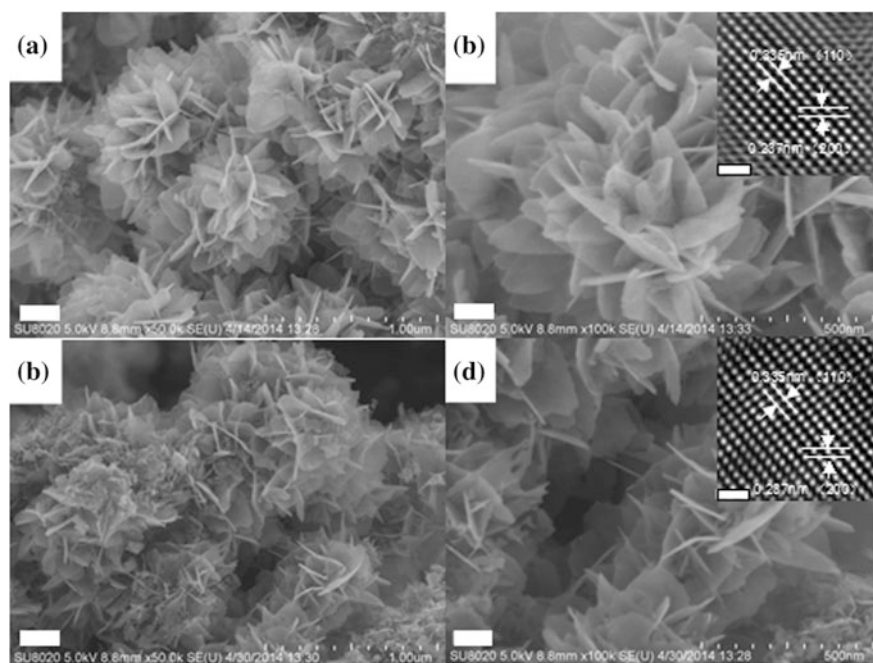
Fig. 17.10 SEM images of **a**, **b** SnO_2 (hydrothermal) nanostructure and HRTEM images, *inset*, SEM images of **c**, **d** SnO_2 (microwave) nanostructure, and HRTEM images, *inset*. The scale bars in SEM images of **a** and **c** represent 200 nm. The *scale bars* in SEM images of **b** and **d** represent 100 nm. The *scale bars* in HRTEM figures represent 1 nm (Reproduced from Ref. [110] with kind permission of © 2010 American Chemical Society)
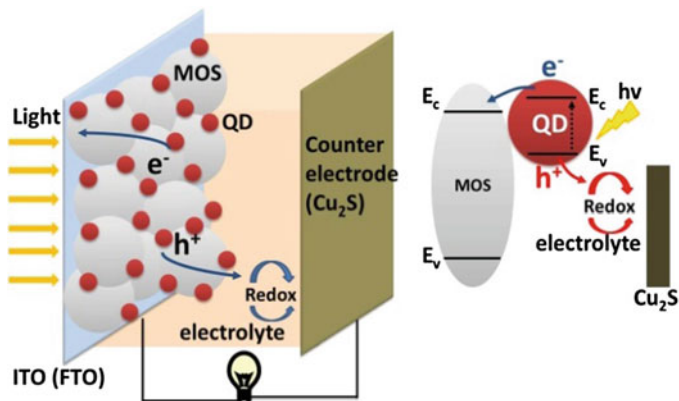
Fig. 17.11 Schematic illustration of the structure of QDSC and photoinduced charge-transfer processes (Reproduced from Ref. [54] with kind permission of © 2015 American Chemical Society)

the dyes with acidic anchoring groups, and the recombination of conduction band electrons with the oxidized dye [38]. In future, a lot of efforts should be focused on the surface and electronic modification of hierarchical SnO_2 photoanodes to improve the PCE of DSCs.

17.3 Quantum Dot-sensitized Solar Cells (QDSCs)

QDSCs can be regarded as a derivative of DSCs which use narrow-bandgap semiconductor quantum dots (QDs) photosensitizer instead of organic dyes in DSCs. Figure 17.11 shows the QDSC structure consists of a MOS photoanode, QDs (sensitizer), polysulfide electrolyte, and counter electrode [54]. When the photons are harvested by QDs, the electron–hole pairs will be excited and then are rapidly separated into electrons and holes at interface between the MOS and QDs. The electrons are transferred by MOS at the same time; the holes are released by redox couples in the liquid electrolyte [22, 110]. The principles for choosing QDs and MOS photoanodes to construct QDSs are as follows: (1) narrow and direct bandgap QDs are preferred due to their high optical absorption, (2) MOS and QDs should have perfect matching in energy levels so that charges transport efficiently in the solar cells [70].

Table 17.2 shows the energy band parameters of QDs, which are usually chosen to fabricate QDSCs. Similar to DSCs, we can know that nanostructured MOS plays a key role in designing QDSCs. The difference between them is that the size of QDs is much larger than that of organic dye. The distribution and adsorbing capacities of QDs in MOS substrate are important issues for the performance of QDSCs. In this section, we will introduce and discuss our recent works on the fabrication of QDs,

Table 17.2 Energy band parameters of some most commonly used QDs for QDSCs [51, 52]

Semiconductors	Bandgap (eV)	Conduction band minimum (eV)	Valence band maximum (eV)
Ag_2S	0.92	−4.5	−5.42
CdS	2.40	−3.98	−6.38
CdSe	1.74	−4.10	−5.84
$CuInS_2$	1.50	−4.06	−5.56
Cu_2S	1.10	−4.44	−5.54
PbS	0.37	−4.74	−5.11
PbSe	0.27	−4.93	−5.20
Sb_2S_3	1.72	−4.72	−6.44
SnS_2	2.10	−4.44	−6.54
SnS	1.01	−4.66	−5.67

design and surface modification of TiO_2 and ZnO MOSs to improve the performance of QDSCs.

17.3.1 Fabrication of QDs for QDSCs

QDs are usually deposited onto mesoporous MOS films to form QDSCs electrodes via two approaches: (a) adsorption of pre-synthesized quantum dots, and (b) in situ growth directly from the precursor solutions. The introduction of rapid injection of precursors into the reaction solvent at a certain temperature, called hot-injection synthesis, has been used to prepare colloid QDs since 1993 [111, 112]. This method has attracted much attention for QDSCs due to the advantages in using pre-synthesized monodispersed QDs of high crystallinity, with expectation to obtain overall control over the QD size, size distribution, and surface passivation. Recent years have witnessed the development of the post-synthesis assembly to fabricate high efficiency QDSCs, which generally involves three approaches: direct adsorption, electrophoretic deposition, and linker-assisted deposition [113]. By exploiting this approach, $CdSe_xTe_{1-x}$ QDSCs with greater than 8% of PCE were obtained in 2015 [27]. In situ growth of QDs within the mesoporous MOS scaffolds, including chemical bath deposition (CBD) [114] and successive ionic layer absorption and reaction (SILAR) [21, 115], has shown highly photoelectric conversion efficiency when being adopted to assemble QDSCs [116]. The CBD is a relatively simple method to deposit QDs and nanoparticle films, which possesses many advantages, such as stable yields, robust adherence, uniform and good reproducibility. The growth of QDs strongly depends on the growth conditions, such as the duration of deposition, composition, and temperature of the solution, and characteristics of the mesoporous films. The SILAR method is based on successive reactions on the surface oxides. Each reaction is followed by rinsing, which enables a heterogeneous reaction between the solid phase and the solvated ions in
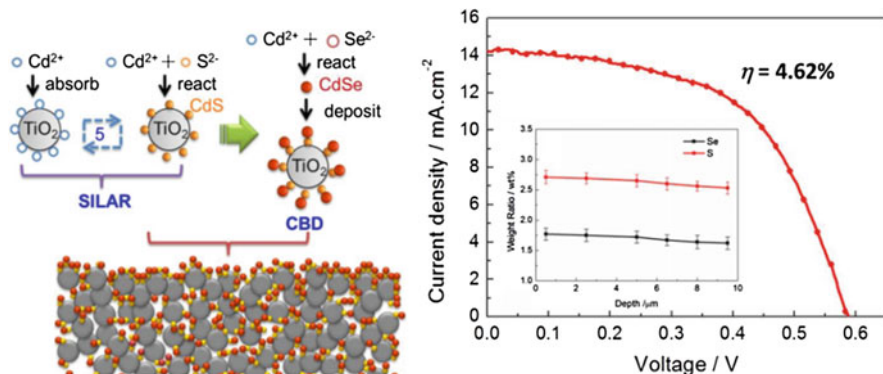
Fig. 17.12 Sketch of the formation of CdS/CdSe QDs on the mesoporous TiO$_2$ film and *J–V* curve of QDSCs (Reproduced from Ref. [22] with kind permission of © 2012 American Chemical Society)

the solution. So a thin film can be grown layer by layer. In situ growth method is regarded as a convenient, reproducible, and cost-effective way to QDSCs. In addition, QDs can be adsorbed on the surface of MOS, which is helpful for injecting and transfer of photoexcited electron. We deposited CdS and CdSe QDs onto the mesoporous TiO$_2$ film using SILAR and CBD, respectively, to form CdS/CdSe co-sensitized QD [22]. Figure 17.12 shows the schematic illustration of the formation process of CdS/CdSe QDs co-sensitized solar cells. The PCE of QDSC was up to 4.62%.

Recently, the method of using doping metal ions into QDs is thought an effective way to improve the performance of QDSCs. Some results, such as Hg^{2+} into PbS [117], Mn^{2+} into CdS [118], and Mn^{2+} into CdSe [23], showed the increase of photoelectric properties of the solar cells. By using doping Mn^{2+} into CdSe, we have successfully prepared a high efficiency of 6.33% Cd$_{0.8}$Mn$_{0.2}$Se quantum dot solar cell using CBD method as shown in Fig. 17.13 [23]. The Mn^{2+} ions doped into QDs can increase the light harvesting to produce more excitons. In addition, Mn^{2+} dopant also raises the conduction band of CdSe, accelerates the electron injection kinetics, and reduces the charge recombination to improve the charge transfer and collection. The increase of the efficiencies of light harvesting, charge transfer, and charge collection results in the improvement of the quantum efficiency of the solar cells.

Inserting a layer of non-sensitized QDs on the surface of MOS photoanodes not only helps to grow the subsequent sensitized QDs, but also suppresses the back charge recombination between the electrons in oxide and the holes in electrolyte. Recently, we prepared a multi-layered semiconductor (ZnSe/CdS/CdSe) QDs on the surface of TiO$_2$ mesoporous films as shown in Fig. 17.14 [119]. The multi-layered QDs-sensitized solar cells showed a larger short-circuit currents and higher efficiency than those of single-layered QDs-sensitized solar cells due to a complementary effect in light harvesting. Figure 17.14b shows the recombination
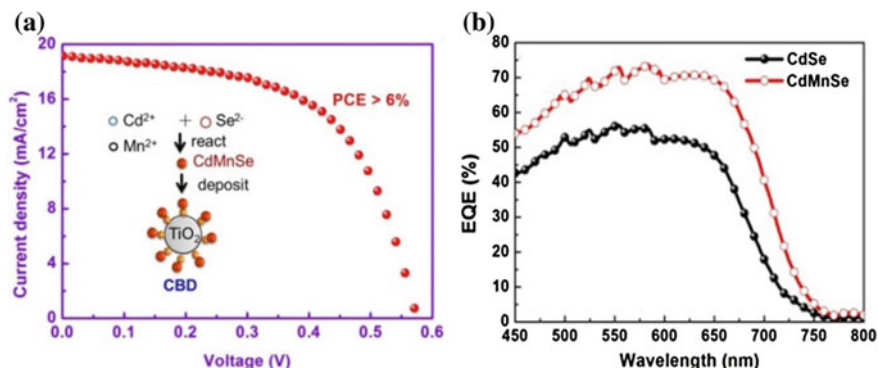
Fig. 17.13 **a** *J–V* curve of CdMnSe QDSC, *inset* is the CBD process of CdMnSe QD; **b** external quantum efficiency (EQE) spectra curves of QDSCs (Reproduced from Ref. [23] with kind permission of © 2014 Royal Society of Chemistry)
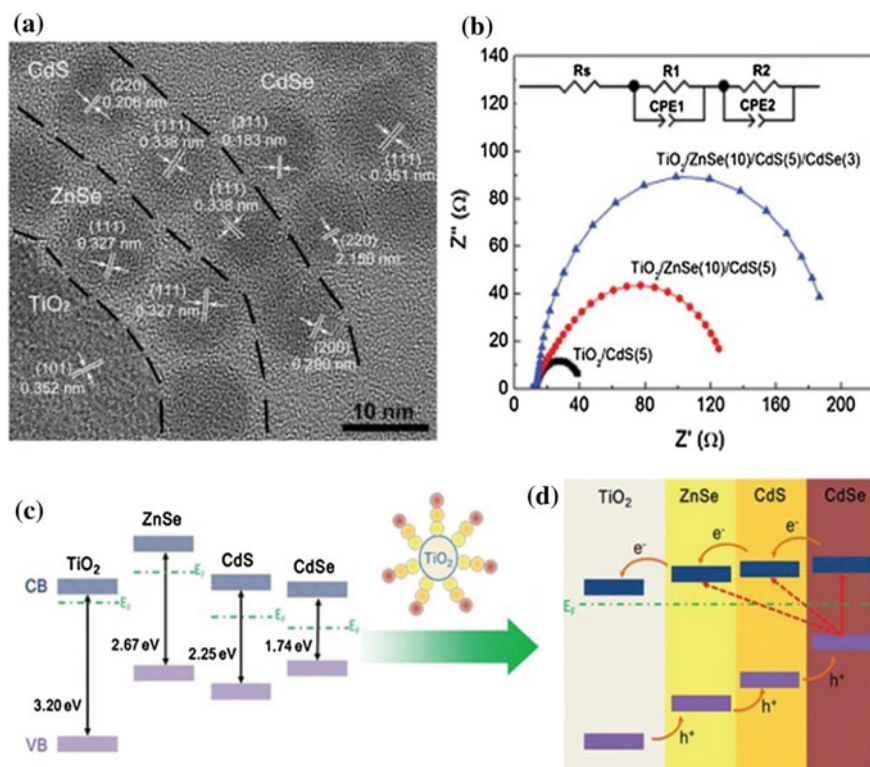
Fig. 17.14 **a** HRTEM image showing the arrangement of ZnSe/CdS/CdSe QDs around a TiO$_2$ crystallite and **b** Nyquist curves of the different layered QD-sensitized solar cell measured in the dark at −0.6 V bias. **c** relative band positions of TiO$_2$, ZnSe, CdS, and CdSe in bulk and **d** ideal stepwise structure of band edges for the efficient transport of excited electrons and holes in a TiO$_2$/ZnSe/CdS/CdSe photoelectrode (Reproduced from Ref. [120] with kind permission of © 2014 American Chemical Society)

resistance is also increased by a seeding layer of ZnSe, which leads the reduction of the charge recombination and the prolonging of the electron lifetime. The possible reason is that the cascade structure of multi-layered semiconductor is advantageous to the electron injection and hole recovery of QDs. The band edges and relative Fermi levels positions of TiO_2, ZnSe, CdS, and CdSe in the bulk are schematically shown in Fig. 17.14c. When TiO_2, ZnSe, CdS, and CdSe are connected together, the difference in energy levels induces electron flow from the higher level (ZnSe) to the other lower levels. Therefore, the Fermi level of ZnSe would shift down with respect to the location of Fermi level in TiO_2, and the conduction band edges of CdS and CdSe are elevated. Such electron transfer is known as the Fermi level alignment. The photoexcited electrons would transfer from the higher conduction band to the lower band with the help of a driving force. Therefore, the resulting conduction band edges for the ZnSe/CdS/CdSe device are inferred to have a stepwise structure, as shown in Fig. 17.14d. The layer of ZnSe also acts as a blocking layer to shield the TiO_2 core from the outer CdS/CdSe QDs and electrolyte and provides a physical separation of the injected electrons in TiO_2 from the positively charged QDs and the electrolyte, thus retarding the interfacial recombination to obtain a high efficiency. As a result, the PCE was increase from 2.26% for QDSC without ZnSe to 4.94% for QDSC with multi-layered QDs. So researchers may concentrate on designing more multi-layered QDs for QDSCs.

17.3.2 TiO$_2$ Hierarchical Structures for QDSCs

The TiO_2 aggregates film shows a better light-scattering property to extend the light pathway for light harvesting, which has been used in DSCs in our previous works. Different from dye, QD is difficult to enter into the interior of the aggregates film due to their large size, which results in the low loading of QDs and poor performance of QDSCs. In order to dissolve this problem, we proposed a two-step fabrication method of TiO_2 aggregates to increase the porosity of the aggregates [120]. The aggregate made of the mesoporous TiO_2 beads has been prepared through a combined precipitation and solvothermal process. Figure 17.15a–d shows SEM image of the mesoporous TiO_2 beads aggregates. The aggregates were first synthesized using precipitation and solvothermal process. And then, an optimal amount of ammonia was adopted to etch TiO_2 spheres and achieve the desired porosity of the beads for QDs adsorption. The ammonia etches the precursor aggregate beads to open the pore size of the aggregates. From Fig. 17.15g, the absorbance of the films increases with increase of the additional ammonia, which followed the trend of increased pore size and pore volume but a decreased specific surface area. The properties of QDSCs are almost in accordance with the light absorbance of the aggregates (Fig. 17.15h). As a result, a PCE of the solar cell up to 4.05% has been achieved for a CdS/CdSe QDSC.
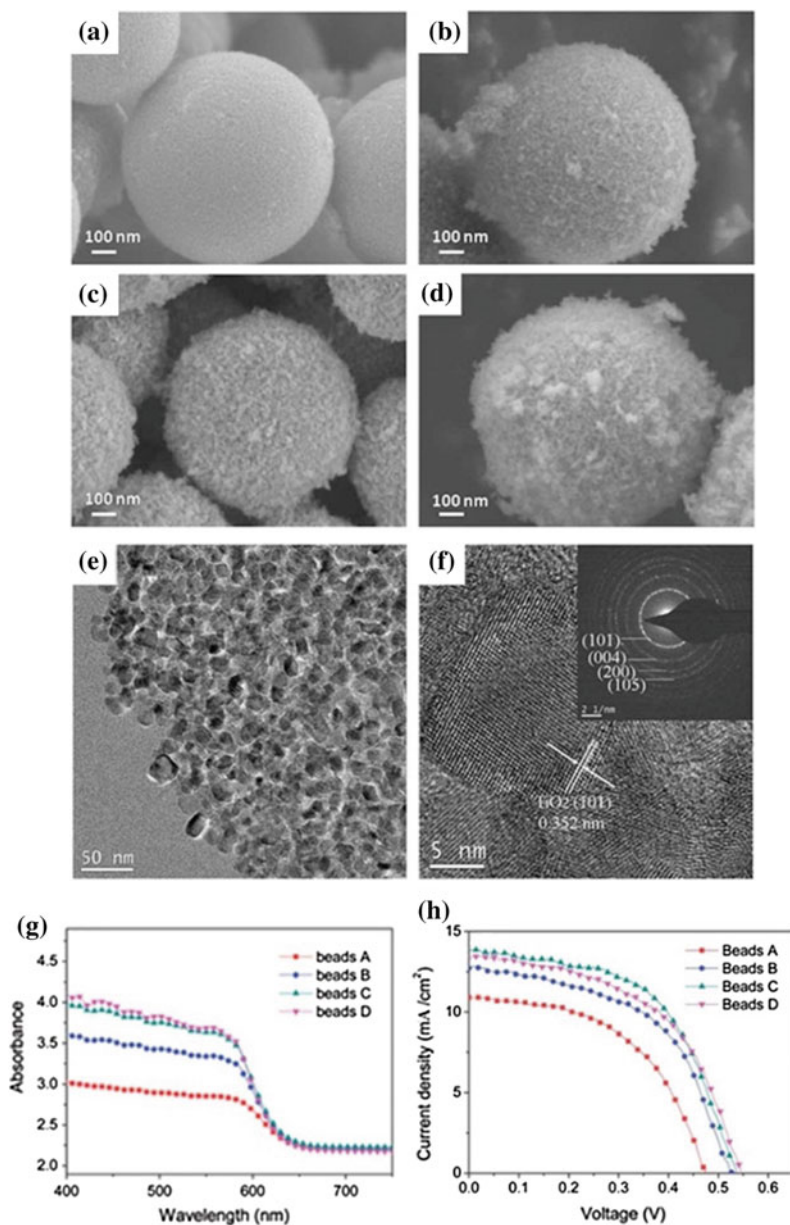
Fig. 17.15 SEM image of TiO$_2$ beads aggregates **a** 0 mL, **b** 0.5 mL, **c** 1 mL and **d** 2 mL ammonia solution; **e** TEM and **f** HRTEM images of the ultramicrotomed sample of the calcined mesoporous TiO$_2$ beads without ammonia treatment during the solvothermal process. The *inset* of **f** shows the SAED pattern of TiO$_2$ beads. **g** UV–Vis spectra of CdS/CdSe QDs co-sensitized TiO$_2$ beads aggregates films, and **h** *J–V* curves for CdS/CdSe QDs co-sensitized solar cells using the photoanodes prepared by TiO$_2$ beads aggregates. The beads prepared with the addition of 0, 0.5, 1 and 2 mL ammonia to a mixture of 12 mL ethanol and 6 mL deionized water during the solvothermal treatment are denoted as beads *A*, *B*, *C* and *D*, respectively (Reproduced from Ref. [121] with kind permission of © 2014 Royal Society of Chemistry)

17.3.3 Nanostructured ZnO for QDSCs

17.3.3.1 1D Nanostructured ZnO for QDSC

It was demonstrated [22] that QDs experienced difficulty penetrating into the inner pores of the nanoparticles films, leading to several issues: (1) the direct exposure of MOS film in electrolyte resulting in a serious degree of recombination between the electrons in the MOS and holes in the electrolyte; (2) less QD loading in the films. Open structures, such as 1D structure of nanorods, nanowires, and nanotubes, can facilitate the distribution of QDs from the surface to the interior of the films and enhance the QD loading. In addition, 1D-structured MOS has a higher electron mobility than that of the nanoparticles. For ZnO nanowires, the electron diffusion coefficients (D_n) are 0.05–0.5 cm^2 s^{-1}, which are several hundred times larger than those of nanoparticle films. The electron diffusion coefficient determines the electron diffusion length as Eq. (17.2) [53, 54]:

$$L_n = \sqrt{D_n \tau_n}, \tag{17.2}$$

where L_n is the electron diffusion length, D_n is the electron diffusion coefficient, and τ_n is the electron lifetime. A longer diffusion length is typically associated with the higher charge-collection efficiency. For QDSCs, such open structures of 1D MOS can also facilitate the permeation of QDs from the surface to the interior of the films. 1D nanostructure offers a straightforward path for the electrons and shortens their transport time inside MOS, and then reduces the charge recombination probability. So the 1D nanostructure array is considered the most promising candidate materials for QDSCs owing to its effective electron transport, which helps to collect photogenerated electrons [121].

However, QDSCs based on 1D structure have not reached a high conversion efficiency as expected due to the limited surface area for QDs adsorption. Introducing a surface profile modification for 1D MOS can be thought as an effective way to increase QD loading. Recently, we designed a facile surface modification process for ZnO nanowire arrays as shown in Fig. 17.16 [122]. The ZnO nanowire arrays were fabricated by growing on seeded indium-doped tin oxide (ITO) substrate without using a template or high temperature conditions. After surface modification, the edges of the ZnO nanowires become 'rough,' which helps to harvest QDs as shown in Fig. 17.16d. The surface modification method not only formed a barrier layer on the surface of the ZnO nanowire, which suppresses charge recombination by preventing the electrons in the ZnO conduction band from transferring to the oxidized ions in the electrolyte, but also modified the surface characteristics of the ZnO nanowire so as to harvest a greater number of QDs and increase the short current density of the QDSC. PCE of QDSC was increased from 1.54 to 3.14% by surface modification.
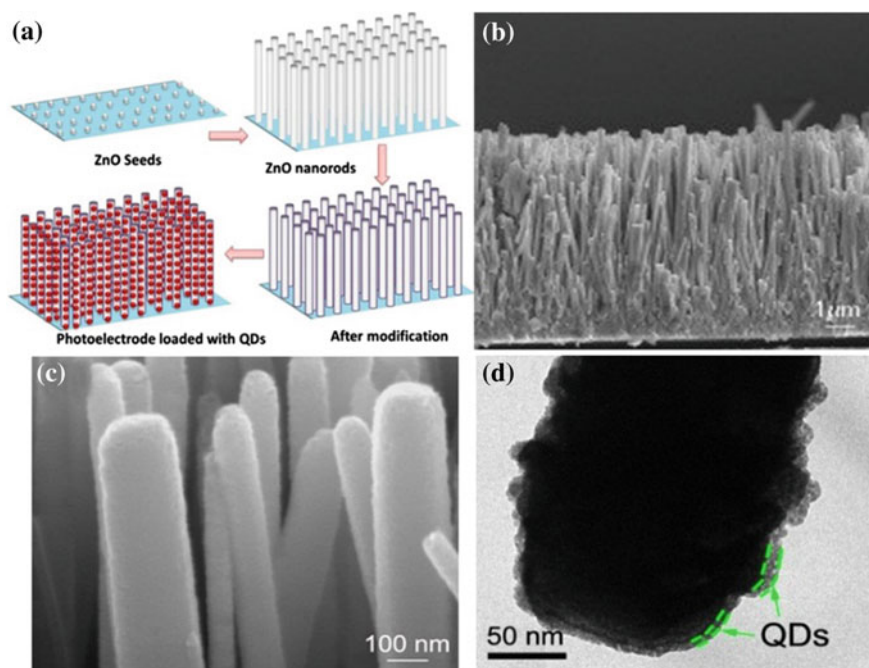
Fig. 17.16 **a** Schematic illustration of the fabrication process of ZnO NR array photoelectrode for QDSC, **b** SEM images of ZnO NR array, **c** SEM image of modified ZnO nanorod array, **d** TEM image of ZnO nanorod coated by QDs (Reproduced from Ref. [122] with kind permission of © 2013 Royal Society of Chemistry)

17.3.3.2 Hierarchical Nanostructured ZnO for QDSCs

It is well-known that the surface area of photoanodes is a key factor for the loading of QDs. For 1D-nanostructured MOS, a fundamental drawback is the insufficient internal surface area owing to a low roughness factor or the considerable free space between adjacent 1D nanostructures [122]. Hierarchical branched nanostructures are derived from 1D nanostructures, however, with a consideration to enlarge the surface area through using extended 'branches' [53], which mainly include branched and dendritic nanowires or nanorods. Our recent work reported a ZnO nanorods branched by nanosheets for QDSCs as shown Fig. 17.17 [123]. The thin ZnO nanosheets were slowly assembled on the surface of nanorods to form a hierarchically branched photoanode for constructing CdS/CdSe QDSCs. This branched structure had two advantages in improving the PCE of the solar cells: (a) it increased surface area and modified surface profile of the ZnO nanosheets to aid in harvesting more quantum dots (as shown Fig. 17.17g), which leads to a high short current density J_{sc}; (b) it facilitated the transportation of the electrons in this compact structure to reduce the charge recombination, which led to the enhancement of V_{oc} and FF. As a result, the QDSC assembled with the hierarchical

photoanode exhibited a high PCE of 3.28%, which is twice more than that of NRs photoelectrode (1.37%).

Although ZnO hierarchical aggregates show good light scattering for QDSC, its PCE is much lower than that of nanoparticles. In order to utilize the light scattering of the aggregates, a bilayer structure was constructed by ZnO nanoparticles film and ZnO nanosheets aggregates scattering layer as shown in Fig. 17.18 [124]. The growth orientations of ZnO crystals were controlled to form nanosheets, which attached together and assembled into aggregates due to the high surface energy of the nanosheets. The aggregates were used as a top layer to effectively increase the light diffuse reflection and harvesting to enhance photogenerated current (as shown Fig. 17.18c). In comparison with ZnO single nanoparticles film, the J_{sc} of QDSC assembled by ZnO bilayer structure is increased from 10.3 to 17.0 mA/cm^2, which represents an enhancement of 55%. Such structured QDSC exhibited a high PCE of 5.08%.

17.3.3.3   Surface Modification of ZnO for QDSCs

Nanostructured ZnO faces two questions: (1) instability in the electrolyte; (2) a large number of surface defects. For ZnO-based QDSCs, the surface charge recombination is limit factor for improving the performance of the devices. The processes of charge recombination in QDSCs are somewhat different to DSCs, which can be simplified as shown in Fig. 17.19. There are seven pathways of recombination in QDSCs [54]: ① recombination of electrons in the QD conduction band and holes in the QD valence band; ② recombination of electrons with the electron acceptors in the electrolyte; ③ trapping of the exited electrons at the surface states of QDs; ④ trapping of the free electrons at the a surface states of QDs; ⑤ back electron injection from ZnO to QDs; ⑥ trapping of the free electrons at the interface states of ZnO particles; and ⑦ back electron injection from ZnO to the electrolyte. The electron quenching (①), recombining with the electrolyte (②), trapping (③ and ④) strongly depend on the surface quality of QDs. The pathways ⑤, ⑥, and ⑦ relate directly to the interfaces state of ZnO. Therefore, a lot of interfaces in the nanostructured ZnO provide easy pathways for charge recombination. The state of adjacent surface between QDs and ZnO also propels the free electron trapping. The introduction of surface modification for ZnO is believed to be an effective approach for decreasing the charge recombination and improving the transports of the electrons or holes [46]. For example, the surface modification for ZnO can increase the interfacial resistance and decrease the surface defects, which results in the recombination reduction through the mechanisms ④, ⑤, ⑥, and ⑦. In addition, the surface modification can also change the surface energy of ZnO for loading more QDs [124].

However, the introduction of shell layer on the ZnO surface will reduce the porosity of the ZnO film, which could result in the decrease of the loading of QDs.
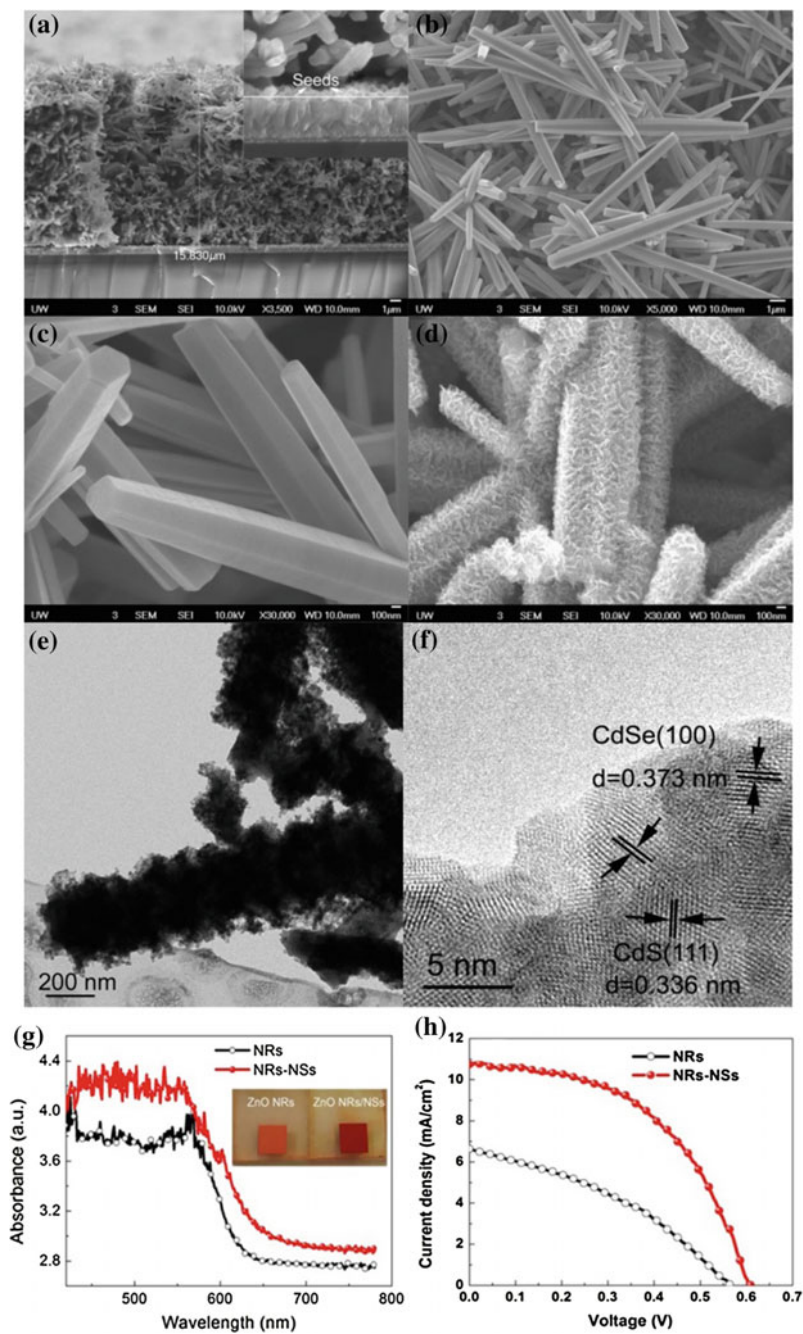
◄**Fig. 17.17** **a** SEM images of the cross section of the ZnO nanorods film, *inset* shows the cross section of the seed layer and nanorods film; **b**, **c** SEM images of ZnO nanorods, **d** SEM images of ZnO nanorods–nanosheets branched structure, **e** TEM and **f** HRTEM images of the branched ZnO loaded with QDs, **g** optical absorbance spectra of the ZnO photoelectrodes loaded with QDs, and **h** J–V curves of QDSCs assembled with different photoelectrodes under simulated AM 1.5, 100 mW/cm^2 sunlight (Reproduced from Ref. [123] with kind permission of © 2014 American Chemical Society)
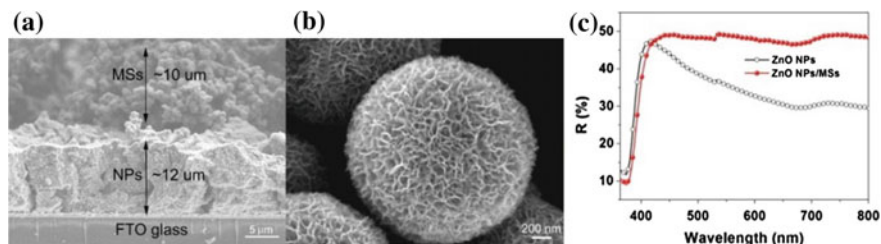
Fig. 17.18 **a** SEM image of the bilayer structure composed of ZnO NPs film and NSs aggregates layer, **b** SEM image of the ZnO NSs aggregate, and **c** diffuse reflection spectra curves of ZnO films (Reproduced from Ref. [124] with kind permission of © 2014 American Chemical Society)
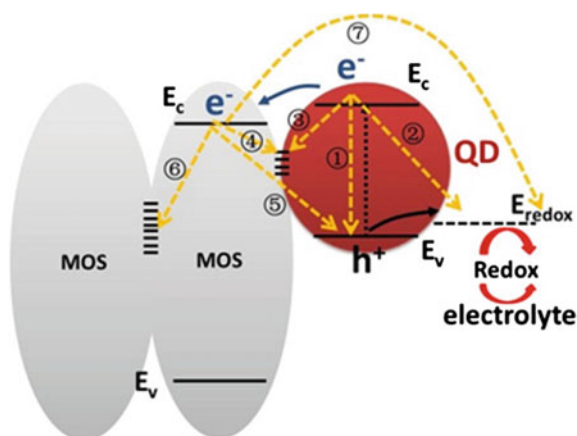
Fig. 17.19 Schematic illustrations of charge recombination processes in QDSCs (Reproduced from Ref. [54] with kind permission of © 2015 American Chemical Society)

Recently, we develop a facile chemical passivation strategy for ZnO mesoporous photoelectrode, which not only enlarged the apertures in the ZnO mesoporous photoelectrode to harvest more QDs, but also introduced a thin TiO$_2$ nanoparticle layer on the surface of ZnO to decrease the surface charge recombination [125]. The process can be expressed via the following equations [125, 126]:

$$\text{TiF}_6^{2-} + 2\text{H}_2\text{O} \leftrightarrow \text{TiO}_2 + 6\text{F}^- + 4\text{H}^+ \tag{17.3}$$

$$\text{H}_3\text{BO}_3 + 4\text{H}^+ + 4\text{F}^- \leftrightarrow \text{BF}_4^- + \text{H}_3\text{O}^+ + 2\text{H}_2\text{O} \tag{17.4}$$

$$\text{ZnO} + 2\text{H}_3\text{O}^+ \rightarrow \text{Zn}^{2+} + 3\text{H}_2\text{O} \tag{17.5}$$
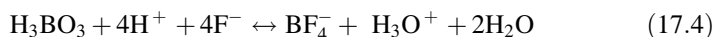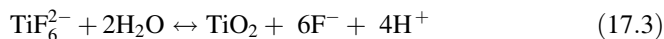
The reaction (17.3) and (17.4) can be shifted to the right by reaction (17.5), which indicates the dissolution of ZnO can boost the hydrolyzation of TiF_6^{2-}. Figure 17.20a shows the variation of pore size, porosity, and surface area of the film during the passivation process. ZnO is dissolved by reacting with H_3O^+ so as to open the apertures and pores, at the same time, TiO_2 particles are deposited on the fresh surface and combine with the newly broken chemical bonds to form a passivation layer. Figure 17.20b illustrates the recombination pathways of QDSCs. The passivation layer can increase the interfacial resistance and lead to recombination reduction through decreasing the back electron injection from photoanode to electrolyte. According to the results of electrochemical impedance spectroscopy (EIS) and light absorbance as shown in Fig. 17.20c–e, both QDs loading and electron lifetime have been improved by the surface modification. The PCE of QDSC is also increased from 2.38 to 4.68%, almost doubled the PCE.
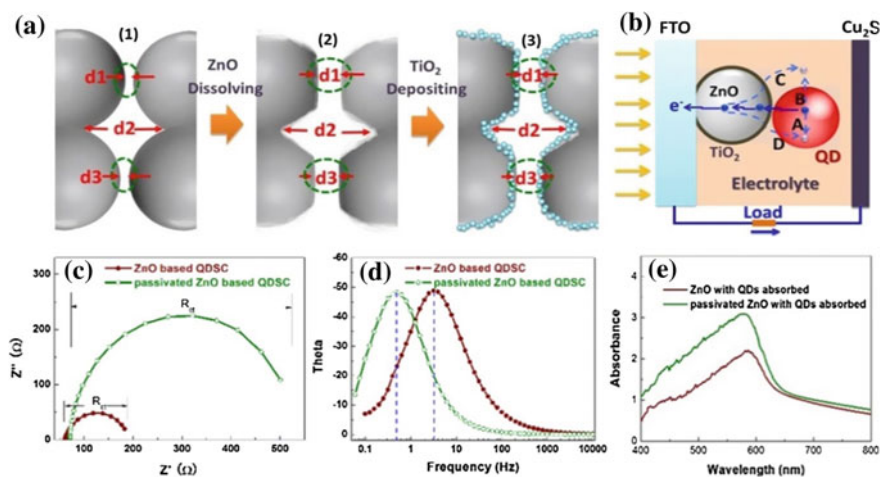
Fig. 17.20 **a** Passivation process of the ZnO mesoporous film, **b** surface charge recombination pathways of the QDSC, **c** Nyquist plots curves, and **d** bode plot curves of the QDSCs under forward bias (−0.6 V) and dark condition, and **e** UV–Vis spectra curves of the ZnO films loaded with QDs (Reproduced from Ref. [122] with kind permission of © 2013 Royal Society of Chemistry)

17.4 Perovskite Solar Cells (PSCs)

Organic-inorganic hybrid perovskite is a star material for the solar cells. In 2012, there are only several articles of PSCs. But the number of the publications of PSCs is more than 600 in the half year of 2015. In fact, the hybrid perovskites $[(C_4H_9NH_3)_2PbI_4, CH_3NH_3PbI_3, CH_3NH_3SnI_3,$ etc.] had been synthesized several decades ago, which were widely used in organic light-emitting diodes due to high electrical mobility and good optical properties [127]. The bandgap of the perovskite $CH_3NH_3PbI_3$ is 1.5 eV, which is very close to the Shockley–Queisser limit optimal bandgap (1.34 eV) for solar cells [128]. So the perovskite $CH_3NH_3PbI_3$ is an excellent potential light absorber material for the solar cell. There are two structures of PSCs: perovskite-sensitized solar cell and planar heterojunction perovskite solar cell as shown in Fig. 17.21 [129]. Perovskites were first employed as 'sensitizers' on mesoporous TiO_2 and their function in the solar cell was assumed to be analogous to the dye in DSCs (as shown in Fig. 17.21a) [29, 130]. In this case, the working principle is expected to be similar to DSCs. However, the working mechanism is different from DSCs, because of charge transport and charge accumulation properties in the perovskite [30]. So the structure of the solar cell can be evolved into a simple planar heterojunction architecture, where a solid intrinsic perovskite layer is sandwiched between p- and n-type selective contacts (as shown in Fig. 17.21b) [129].

The perovskites are usually deposited on a substrate by low-temperature solution process, including one-step and two-step coating methods. Perovskite forms either by spin-coating a mixed CH_3NH_3I and PbI_2 solution (one-step coating) or by spin-coating CH_3NH_3I after coating with PbI_2 (two-step coating). However, the two methods face a problem that is a poor stability of PCE, even under the same
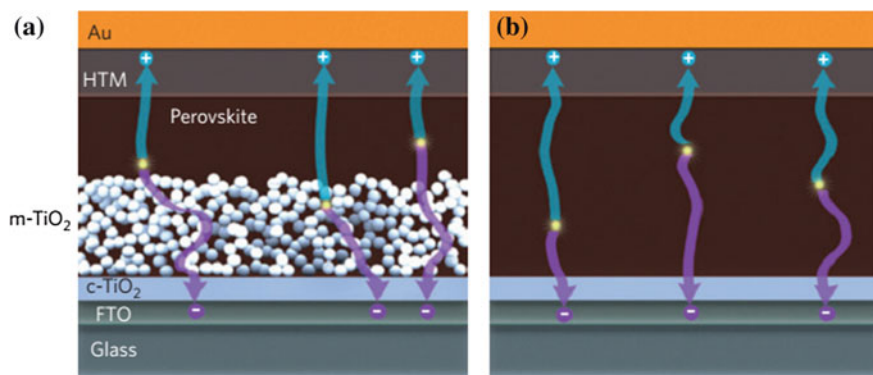
Fig. 17.21 Illustration of the charge generation processes in a 'perovskite-sensitized' solar cell (**a**) and a planar heterojunction perovskite solar cell (**b**). m-TiO_2 and c-TiO_2 denote mesoporous and compact TiO_2 layers, respectively, HTM (hole transport material) is the hole transporter material, and FTO (F-doped tin oxide) is the transparent conducting oxide (Reproduced from Ref. [129] with kind permission of © 2015 Nature Publishing Group)

fabrication process parameters [129, 131]. One important reason should be attributed to the inhomogeneous perovskite film that fabricated by those methods. Controlling the morphology of perovskite crystallites has been regarded as an essential condition to guarantee reproducibility for high performance PSC [132–135]. Recently, a dynamic growth process was used to fabricate perovskite crystallites. As shown in Fig. 17.22a, b, the coverage rate of perovskites by this method is more than that of perovskites prepared by usual solution process. So the bareness of mesoporous TiO_2 layer is significantly avoided [136]. Due to high quality perovskite capping layer, the PCE of the solar cell is increased from 11 to 13%.

From the structure of PSCs, the compact MOS layer (such as c-TiO_2 as shown in Fig. 17.21a) that plays an important role in charge transfer, which reduces the energy barrier between FTO and perovskites to increase the charge collection. As n-type semiconductor, the compact layer can transport the electrons and prevent the transfer of the holes. So it reduces the charge recombination at the interface of FTO and perovskite. Recently, some methods, such as ALD, magnetron sputtering, thermal spraying, and sol–gel, have been used in the fabrication of the compact MOS layer [30, 48, 49, 130]. Among these methods, the sol–gel method is one of
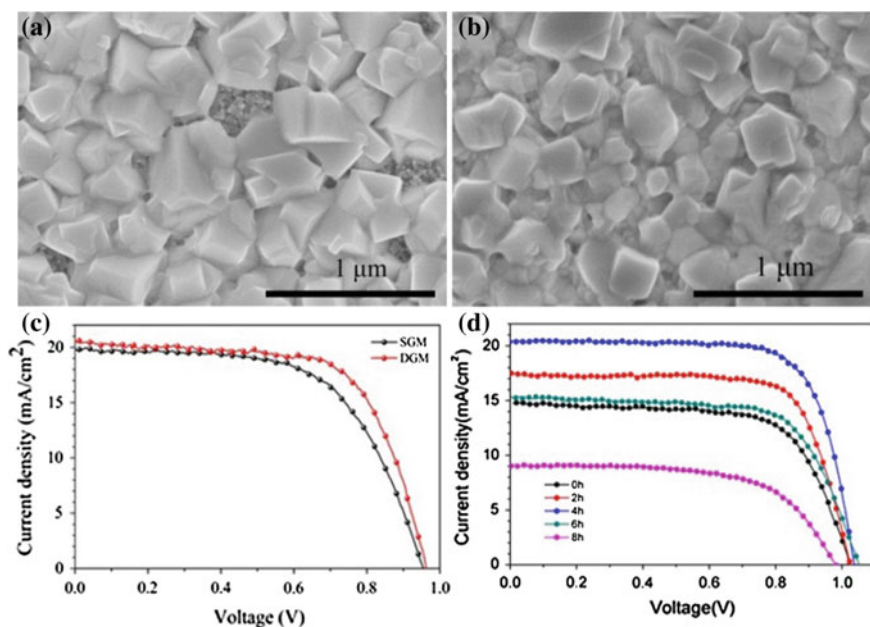
Fig. 17.22 SEM images of perovskites prepared by **a** static growth process, **b** dynamic growth process, **c** J–V curves of PSCs and **d** PSCs assembled TiO_2 compact layers prepared by sol–gel using different aging time (Reproduced from Ref. [136] with kind permission of © 2016 American Chemical Society)

the most widely used methods due to flexible adjustability and low cost without complex equipment. For sol–gel process, the aging time and temperature are two key factors for the compact layer. In our recent work, the PCS with greater than 15% of PCE was obtained by controlling the sol–gel aging of TiO_2 compact layer as shown in Fig. 17.22d [136]. It was found that the sol–gel aging time is 4 h under room temperature, PCS shows the best performance: the highest and average values of PCEs are 15.6 and 14.01%, respectively [137].

Most recently, scanning Kelvin probe force microscopy (SKPM) and photo-conductive atomic force microscopy (pcAFM) were used in the investigation of the variation of the surface potential, photogenerated voltage, and photocurrent networks of the PSCs with different film topography [137]. Three perovskite $CH_3NH_3PbI_3$ films with different morphologies and crystallite sizes as well as the corresponding complete PSC devices based on those three films were prepared as shown in Fig. 17.23 [137]. It has been found that the defect regions on the capping layer showed little photovoltaic response while exhibited good conductivity, which can form small current paths for the photo-charge recombination. Accordingly, even though the P52 film with largest grain size shows most significant photo-voltaic response in the KPFM measurement, the V_{oc} of P52-based PSCs was suppressed due to the existence of defect regions. Meanwhile, the insufficient exciton generation in the grain boundary region was also observed by the pcAFM measurement. Hence, P15 film with the smallest grain size can eliminate the defect region, while it can also reduce the I_{sc} due to the increase of the grain boundary region.

17.5   Inverted Organic Photovoltaic (OPVs)

Figure 17.24a shows a schematic of an inverted OPV with a stacked structure of a transparent electrode (e.g., ITO, FTO, and AZO), an interfacial layer named as cathode buffer layer (CBL), a BHJ active layer, an anode buffer layer (ABL) usually made of PEDOT:PSS, and a metal electrode with high-work-function such as Ag and Au [8]. The structure of conventional PSCs is also schematically presented in Fig. 17.24b for comparison. In the inverted device architecture, the contact between the ITO and PEDOT:PSS is avoided, and meanwhile Al for top electrode adopted in conventional PSCs is replaced with an air stable high-work-function metal, such as Au or Ag [137, 138]. As a result, the inverted PSCs exhibit greatly improved ambient stability as compared to the PSCs with a conventional structure, over-coming one big hurdle for possible widespread application of PSCs [139–144]. The MOS used in the inverted OPVs deposited on ITO glass substrate serves as a CBL and is a critically important component. Its composition, morphology, structure, and crystallinity can largely affect the solar cell performance.
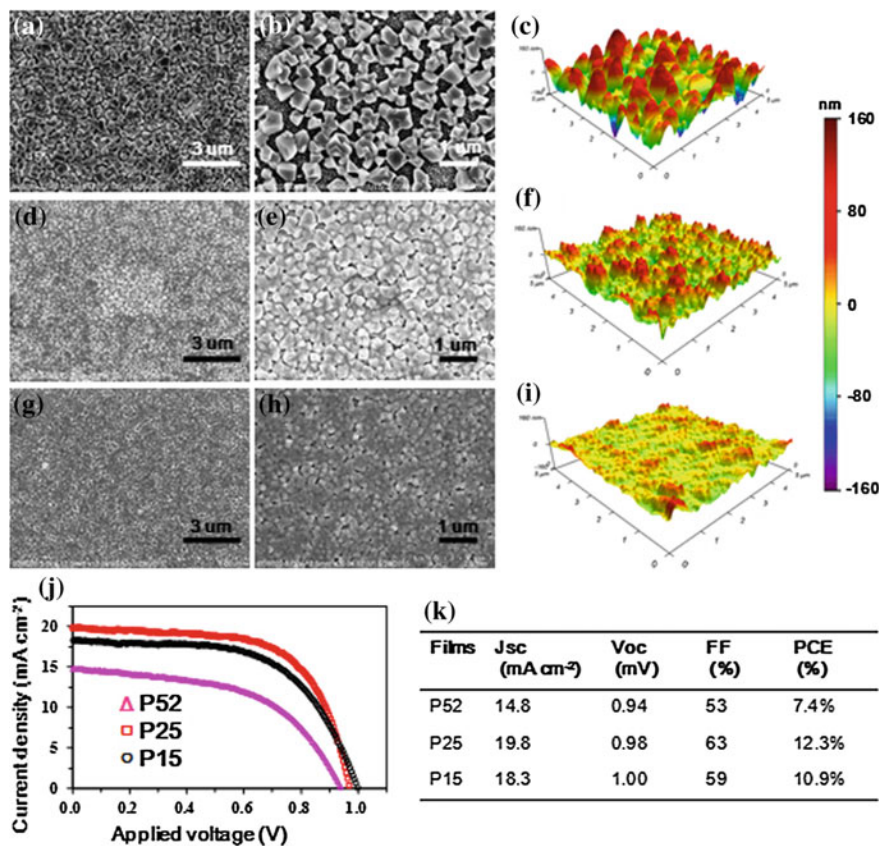
Fig. 17.23 Three of perovskite-based films with different roughness and coverage rate have been studied in this experiment. The low (**a**, **d**, **g**) and large (**b**, **e**, **h**) magnified SEM images of the film surfaces and their corresponding three-dimensional SPM images (**c**, **f**, **i**). The roughness was 52, 25, and 15 nm for **a–c**, **d–f**, and **g–h** films, respectively. For clarification, they are noted as P52, P25, and P15. **j** I–V curves measured for the perovskite solar cells employing these P52, P25, and P15 films from 0 to 1 V bias voltage with 200 ms speed rate under AM 1.5 G one sun (100 mW/cm^2). **i** Photovoltaic parameters obtained from I–V curves (Reproduced from Ref. [137] with kind permission of © 2016 Wiley-VCH)

17.5.1 Nanostructured TiO$_2$ CBLs for OPVs

17.5.1.1 TiO$_2$ Mesoporous Film

Besides facilitating the PCBM to form a continuous layer, CBL may play a role in enhancing the solar cell performance. We [145] found that, in the case of a TiO$_2$ mesoporous oxide film with the pore size of $\sim$10–20 nm as cathode buffer layer, the PCE of the OPV could reach a value as high as 3.4%, while they were 1.7 and 1.9% when using a macroporous film with the size of 2–50 nm and a dense film,
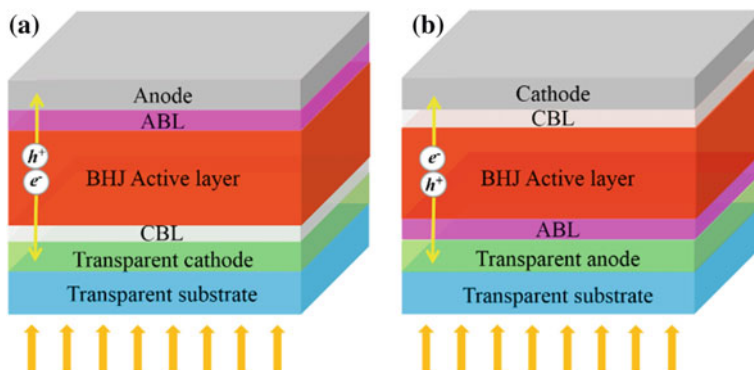
Fig. 17.24 Schematic illustration of device structures of **a** inverted and **b** conventional OPVs with bulk heterojunction active layer (Reproduced from Ref. [8] with kind permission of © 2015 Royal Society of Chemistry)

respectively. Figure 17.25 shows SEM images of dense, mesoporous, and macroporous TiO_2 CBLs [146]. When the conduction band bottom of the oxide such as TiO_2 is lower than the LUMO level of PCBM and meanwhile the film thickness is not much larger than the electron diffusion length, the electron can transport within the oxide film efficiently, and the transport is much more efficient than within a polymer such as PCBM. When the CBL has a suitable structure, for example, in this work it is a mesoporous film, the polymers can penetrate into the mesoporous film, leading to the formation a much large interface between the polymers and the oxide. This makes the electrons in the PCBM have a significantly increased probability to transport into the oxide before they get trapped during transport within the PCBM. Since the electron transport in an oxide is much more efficient than in a polymer, the use of nanostructure which stretches into the polymers to extract electrons can largely enhance the electron collection efficiency, resulting in the high efficiency. However, in the case of preparing macroporous film via spin-coating a sol precursor of TiO_2 and PVP solution with different stirring time (60 and 30 min), the nanocrystallites aggregate to larger agglomerate than that of the mesoporous film, and the electron transport in the oxide becomes less efficient due to the size of aggregates which are larger than the diffusion length of electrons within the corresponding oxide. Consequently, the macroporous film achieved a PCE of 1.7%, much lower than the 3.4% efficiency achieved by using a mesoporous film. This work illustrates that there is a trade-off between the nanostructure forming a large interface with the polymers to improve electron collection and it hindering electron transport in case of its size much larger than the electron diffusion length.
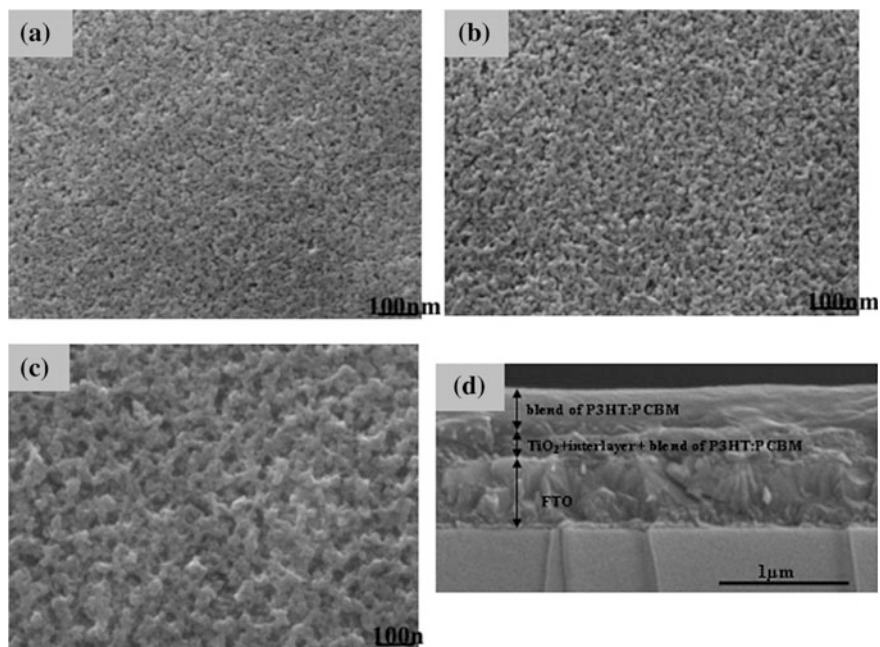
Fig. 17.25 Top-view SEM images of **a** dense TiO_2, **b** mesoporousTiO_2, and **c** macroporousTiO_2 films, respectively; **d** the cross section SEM of an OPV using a porous TiO_2 films (Reproduced from Ref. [146] with kind permission of © 2014 Elsevier)

17.5.1.2 TiO$_2$ Nanorod Array

Nanostructured TiO_2 for the enhancement of electron collection in OPVs has also demonstrated in another work with regard to the use of TiO_2 nanorod array grown on a FTO glass substrate through a hydrothermal method as shown Fig. 17.26 [147]. By controlling the time for hydrothermal growth, the length of nanorods (i.e., the height of the nanorod array) could be adjusted. When the nanorod arrays were used as the CBL in OPVs, it was observed that the solar cell efficiency could be much affected by the length of nanorods. For the nanorods ~ 150 nm in length, the solar cell reached a high PCE of $\sim 3.21\%$, which was apparently higher than the efficiency of $\sim 2.70\%$ when using the nanorods with a length of ~ 500 nm, and was also higher than the efficiency of 2.79% when using a very thin TiO_2 dense film. The high efficiency obtained for the solar cell using the nanorods with a relatively small length was explained that, similar to the mechanism in the case of mesoporous film mentioned above, the nanorods stretching into the polymers resulted in a large oxide/polymer interface and could thus improve the electron transport and collection.

However, when the nanorods were as long as 500 nm (which is much larger than the electron diffusion length in TiO_2), although the TiO_2 nanorods were single
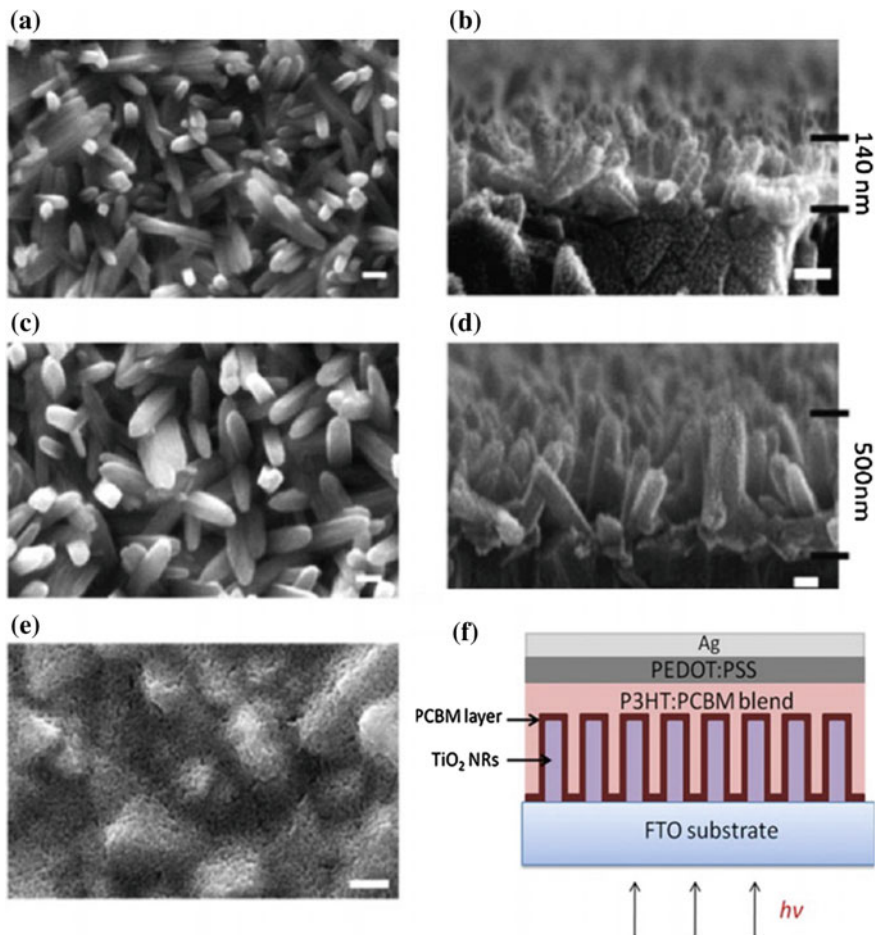
Fig. 17.26 The top-view and cross section SEM images of TiO$_2$ nanorods with length of 140 nm (**a**, **b**), and nanorod with length of 500 nm (**c**, **d**). **e** SEM image of TiO$_2$ dense film. The *scale bars* are all 100 nm. **f** schematic of the OPV based on TiO$_2$ nanorods array CBL (Reproduced from Ref. [147] with kind permission of © 2012 Springer)

crystalline, the electron transport through the entire nanorods became somewhat difficult, leading to electron traps to a large extent and thus giving rise to a smaller photocurrent density than in the case of short nanorods (9.05 mA/cm^2 for 500 nm and 10.06 mA/cm^2 for 150 nm). This eventually yielded a low PCE. It had also been observed that the solar cell with the long nanorods presented a fill factor (FF), 51.3%, lower than the fill factor of 53.6% for short nanorods and 53.8% for dense film. This can be explained that, in the case of too long nanorods, the polymers are hard to penetrate into the entire nanorod array so that the bottom area of the nanorod

array is not fully covered by the polymers, resulting in an increase in the series resistance of the solar cell.

17.5.2 Nanostructured ZnO CBLs for OPVs

17.5.2.1 ZnO Dense Layer

ZnO has drawn much attention in serve as the buffer layer because it has good transparency across the whole visible spectral range, relatively high electron mobility, and environmental stability [8, 148]. Recently, we compared the efficiencies of OPVs constructed with ZnO dense CBL having different thickness and roughness achieved by changing the concentration of the ZnO sol used for the fabrication of cathode buffer layer [148]. It was revealed that, when the thickness of ZnO film varied from 20 to 65 nm, the PCE basically remained the same, around 3.1%. In other words, the solar cell efficiency is not sensitive to the thickness of the CBL. This makes sense considering that the film thicknesses in 20–65 nm are comparable to the electron diffusion length in ZnO and, therefore, the electron transport within the CBL is not affected perceptibly by varying the film thickness. However, it was found that the solar cell efficiency could be significantly affected by the roughness of the cathode buffer layer; a smaller roughness gave rise to higher power conversion efficiency, which increased from 1.82 to 3.30% when the roughness (as shown in Fig. 17.27 measured with AFM) decreased from 4.25 to 2.86 nm. It was explained that the ZnO cathode buffer layer with small roughness could lead to a good contact with the polymer, which benefited the electron transport at the polymer/ZnO interface and meanwhile gave rise to the solar cell with low series resistance; in the case of large roughness, there likely formed some voids at the polymer/ZnO interface, which hindered the electron transport and increased the series resistance of the solar cell. Such a speculated mechanism was in line with the experimental observation that higher photocurrent density and larger fill factor were obtained in the case of smaller roughness.

17.5.2.2 SrTiO₃:ZnO Composite Layer

Compared with ZnO, $SrTiO_3$ has a higher dielectric constant ($\sim 10^4$), similar bandgap structure, but lower electron mobility. It was hypothesized that the material with larger dielectric constant and spontaneous polarization, such as $SrTiO_3$, may create an internal electric field while PSCs operation. Such a high dielectric constant material would favor the effective charge transfer in OPVs. $SrTiO_3$:ZnO CBL was used in OPVs as shown in Fig. 17.28a, b [148]. The fabrication of $SrTiO_3$:ZnO CBL was achieved by mixing a sol of $SrTiO_3$ and a sol of ZnO in certain molar ratios and then spin-coating on a ITO glass substrate followed by a heat treatment at 350 °C to enable the formation of $SrTiO_3$:ZnO composite. The ratios of $SrTiO_3$ to
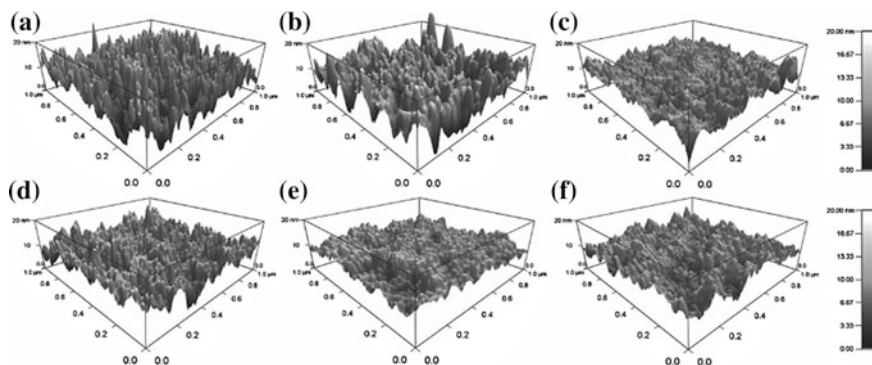
Fig. 17.27 3D AFM images of the ZnO buffer layers of devices (**a**–**f**), which were deposited by spin-coating 0.02, 0.05, 0.1, 0.3, 0.6, and 1 M sol one time (Reprinted from reference [148] with kind permission of © 2012 Wiley-VCH)

ZnO changed from 5:95, 10:90, 15:85, and 20:80 to 25:75. It was revealed that the solar cell efficiency increased from 3.58% for pure ZnO to 4.10% for the ratio of $SrTiO_3$:ZnO being 10:90; a further increase of the $SrTiO_3$:ZnO ratio, however, led to a decrease in the efficiency, which dropped to 2.38% when the ratio was 25:75 as shown in Fig. 17.28c. The increase in the solar cell efficiency was found to result from an increase in the FF of the solar cell while the open-circuit voltage and short-circuit photocurrent density did not show an apparent change. The increase in the FF likely suggests that the contact between the polymers and the CBL is improved in view of the addition of suitable amount of $SrTiO_3$ to ZnO, which changes the surface status of ZnO (possibly due to local spontaneous polarization of the $SrTiO_3$) and results in the interface between the polymers and cathode buffer layer with a relatively low energy barrier; a low energy barrier is beneficial to the electron transport over the polymer/CBL interface especially when the kinetic energy of electrons is small, corresponding to the high voltage range (adjacent to open-circuit voltage) during the *I–V* measurement. The allowing of the electrons with small kinetic energy to transport through the polymer/CBL interface straightforwardly leads to an increase in the FF.

17.5.2.3 Ta_2O_5:ZnO Composite Layer

Similar to $SrTiO_3$, Ta_2O_5 is also known for its high dielectric constant and index of refraction, which is helpful for the effective charge transfer in OPVs. Ta_2O_5:ZnO is another composite studied for CBL of OPVs [149]. The results are very similar to what are obtained for $SrTiO_3$:ZnO as shown in Table 17.3. It was observed that the PCE of OPV increased gradually when the percentage of Ta_2O_5 in the composite increased from 0 to 18% (in molar), and when the percentage is higher than 18%, the efficiency dropped quickly. For pure ZnO (i.e., 0% Ta_2O_5), the PCE was 3.70%.
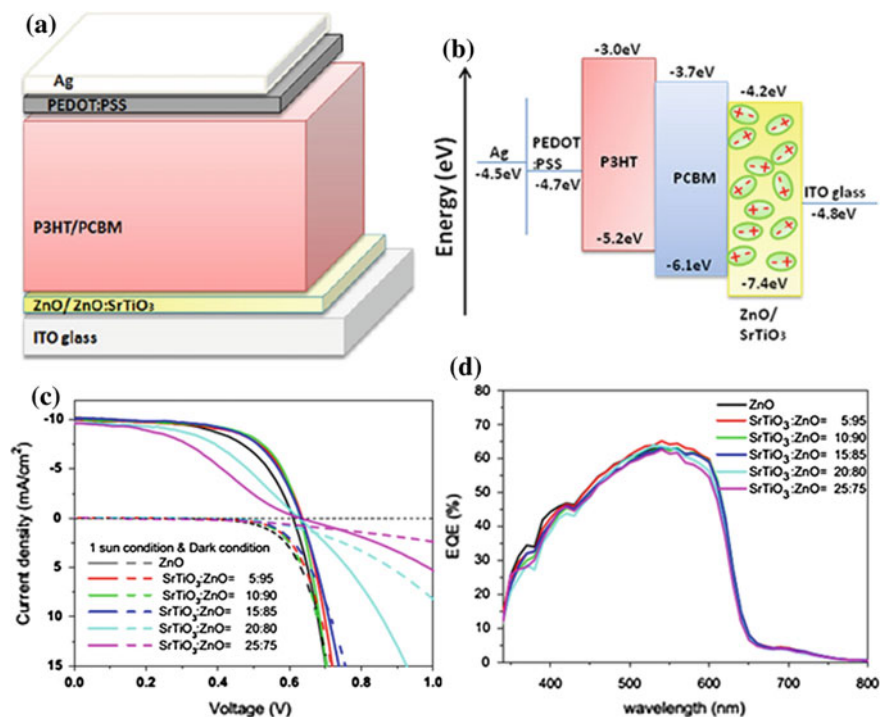
Fig. 17.28 a, **b** OPVs and the corresponding energy level diagram of the components of the devices, **c** I–V curve at 1 sun and dark condition with various SrTiO$_3$:ZnO films as the cathodic buffer layer and **d** IPCE results of various SrTiO$_3$:ZnO films as CBLs (Reprinted from reference [149]. with kind permission of © 2014 Elsevier)

Table 17.3 Properties of OPVs with various Ta$_2$O$_5$:ZnO CBLs (Reproduced from Ref. [150] with kind permission of © 2014 Royal Society of Chemistry)

Ta$_2$O$_5$ (%)	V_{oc} (V)	J_{sc} (mA cm^{-2})	FF	PCE (%)	R_{sh} (kΩ cm^2)	R_s (kΩ cm^2)
0	0.636	9.49	0.613	3.70	0.67	8.72
6	0.637	9.75	0.649	4.03	1	7.58
12	0.634	9.73	0.661	4.08	5	7.20
18	0.637	9.64	0.670	4.12	3.3	7.28
24	0.631	9.75	0.616	3.79	1.67	10.07
30	0.563	8.61	0.260	1.26	0.2	243.9
100	0.564	0.04	0.374	0.0009	11	125,000

The maximum efficiency corresponding to 18% Ta$_2$O$_5$ was 4.12%. When the Ta$_2$O$_5$ was 30%, the efficiency was as low as 1.26%. When the CBL only consisted of Ta$_2$O$_5$, the solar cell efficiency was nearly close to zero. Same as the case of SrTiO$_3$:ZnO, when the content of Ta$_2$O$_5$ increased from 0 to 18%, the increase in
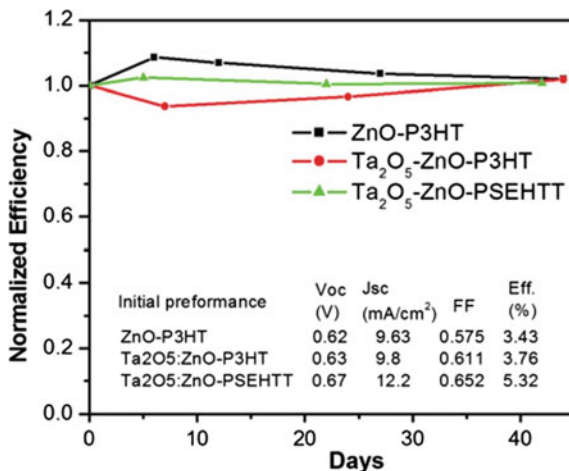
PCE mainly resulted from an increase in FF, from 0.61 for pure ZnO to 0.67 for 18% Ta_2O_5, while the solar cell's open-circuit voltage and short-circuit current density did not show an apparent change. When the content of Ta_2O_5 exceeded 18%, it was found that the electron mobility of the $SrTiO_3$:ZnO films decreased greatly with increasing the amount of Ta_2O_5 in the composite, and as a result, the series resistance of the solar cell increased significantly, which were 7.28 Ω cm^2 for 18% Ta_2O_5, 10.07 Ω cm^2 for 24% Ta_2O_5, and 243.9 Ω cm^2 for 30% Ta_2O_5. The mechanism of Ta_2O_5:ZnO composite CBL enhancing the solar cell efficiency is same as what was depicted above for $SrTiO_3$:ZnO. The addition of Ta_2O_5 to ZnO gives the cathode buffer layer with a surface status different from that of ZnO film. When the amount of Ta_2O_5 is suitable, it seems that the use of Ta_2O_5:ZnO composite can improve the contact between the polymers and the cathode buffer layer, so as to enable the formation of an interface with low energy barrier, which benefits the solar cell with increasing its fill factor. However, when the composite contains too much Ta_2O_5, for example, over 18% as revealed by this work, a dramatic decrease in the electron mobility will largely increase the series resistance of the solar cell and result in a low efficiency. So the study of the use of composites for CBL of OPVs delivers new understanding to the criteria for choosing material for the CBL.

As it was mentioned in the beginning of Sect. 17.5, one of the biggest attraction of inverted OPVs is its excellent ambient stability in comparison with the conventional OPVs. The PCE of the unencapsulated inverted organic photovoltaics was periodically measured for 42 days to monitor their long-term stability in air (Fig. 17.29). All devices retained around 100% of the magnitude of their original power conversion efficiency after being exposed to ambient conditions for 42 days. This explicitly demonstrates the superior air stability of inverted organic photovoltaics.

17.6 Concluding Remarks

As the essential component, MOSs, such as TiO_2, ZnO, and SnO_2, have been widely used in the ESCs including DSCs, QDSCs, PSCs, and OPVs. With the development of nanotechnology, a big breakthrough in ESCs will be made due to the novel nanoarchitectures of MOSs. For example, hierarchical nanostructured MOSs not only offer large specific surface area for loading a large number of active materials (dyes, quantum dots, or perovskites), but also have strong light scattering to capture a sufficient fraction of photons. This review summarized the recent works on the structure design, fabrication, and surface modification of MOSs to enhance PCE of ESCs. In addition to the design and fabrication of the nanostructured MOSs, it was also found that the poor chemical stability and lots of surface defects of nanostructured MOSs caused much high surface charge recombination of the solar cells, which resulted in the decrease of PCE. So the rational design and engineering surface and interface chemistry would favor charge transfer and at the same time prevent or minimize the charge recombination of the solar cells.

References

1. Li G, Shrotriya V, Huang J et al (2005) High-efficiency solution processable polymer photovoltaic cells by self-organization of polymer blends. Nat Mater 4(11):864–868
2. Hau SK, Yip H-L, Jen AKY (2010) A review on the development of the inverted polymer solar cell architecture. Polym Rev 50(4):474–510
3. Po R, Carbonera C, Bernardi A (2011) The role of buffer layers in polymer solar cells. Energy Environ Sci 4(2):285–310
4. Li G, Zhu R, Yang Y (2012) Polymer solar cells. Nat Photonics 6(3):153–161
5. He F, Yu L (2011) How far can polymer solar cells go in need of a synergistic approach. J Phys Chem Lett 2(24):3102–3113
6. Oregan B, Gratzel M (1991) A low-cost, high-efficiency solar-cell based on dye-sensitized colloidal TiO_2 films. Nature 353(6346):737–740
7. Robel I, Subramanian V, Kuno M et al (2006) Quantum dot solar cells harvesting light energy with CdSe nanocrystals molecularly linked to mesoscopic TiO_2 films. J Am Chem Soc 128(7):2385–2393
8. Liang Z, Zhang Q, Jiang L et al (2015) ZnO Cathode buffer layers for inverted polymer solar cells. Energy Environ Sci 8(12):3442–3476
9. Zhang QF, Cao GZ (2011) Hierarchically structured photoelectrodes for dye-sensitized solar cells. J Mater Chem 21(19):6769–6774
10. Bessho T, Yoneda E, Yum JH et al (2009) New paradigm in molecular engineering of sensitizers for solar cell applications. J Am Chem Soc 131(16):5930–5934
11. Bomben PG, Robson KCD, Sedach PA et al (2009) On the viability of cyclometalated Ru(II) complexes for light-harvesting applications. Inorg Chem 48(20):9631–9643
12. Johansson PG, Rowley JG, Taheri A et al (2011) Long-wavelength sensitization of TiO_2 by ruthenium diimine compounds with low-lying pi orbitals. Langmuir 27(23):14522–14531
13. Zhao HC, Harney JP, Huang YT et al (2012) Evaluation of a ruthenium oxyquinolate architecture for dye-sensitized solar cells. Inorg Chem 51(1):1–3

14. Mathew S, Yella A, Gao P et al (2014) Dye-sensitized solar cells with 13% efficiency achieved through the molecular engineering of porphyrin sensitizers. Nat Chem 6(3):242–247

15. Kim J, Choi H, Nahm C et al (2011) The effect of a blocking layer on the photovoltaic performance in CdS quantum-dot-sensitized solar cells. J Power Sources 196(23):10526–10531

16. Panigrahi S, Basak D (2011) Morphology driven ultraviolet photosensitivity in ZnO-CdS composite. J Colloid Interface Sci 364(1):10–17

17. Shen Q, Kobayashi J, Diguna L et al (2008) Effect of ZnS coating on the photovoltaic properties of CdSe quantum dot-sensitized solar cells. J Appl Phys 103(8):522–530

18. Plass R, Pelet S, Krueger J et al (2002) Quantum dot sensitization of organic-inorganic hybrid solar cells. J Phys Chem B 106(31):7578–7580

19. Yu P, Zhu K, Norman AG et al (2006) Nanocrystalline TiO_2 solar cells sensitized with InAs quantum dots. J Phys Chem B 110(50):25451–25454

20. Zhu G, Pan L, Xu T et al (2011) CdS/CdSe cosensitized TiO_2 photoanode for quantum-dot-sensitized solar cells by a microwave-assisted chemical bath deposition method. ACS Appl Mater Interfaces 3(8):3146–3151

21. Lee YL, Lo YS (2009) Highly efficient quantum-dot-sensitized solar cell based on co-sensitization of CdS/CdSe. Adv Funct Mater 19(4):604–609

22. Tian JJ, Gao R, Zhang QF et al (2012) Enhanced performance of CdS/CdSe quantum dot cosensitized solar cells via homogeneous distribution of quantum dots in TiO_2 film. J Phys Chem C 116(35):18655–18662

23. Tian J, Lv L, Fei C et al (2014) A highly efficient (>6%) $Cd_{1-x}Mn_xSe$ quantum dot sensitized solar cell. J Mater Chem A 2(46):19653–19659

24. Kamat PV, Christians JA, Radich JG (2014) Quantum Dot Solar Cells: Hole transfer as a limiting factor in boosting the photoconversion efficiency. Langmuir 30(20):5716–5725

25. Pan Z, Zhao K, Wang J et al (2013) Near infrared absorption of $CdSe_xTe_{1-x}$ alloyed quantum dot sensitized solar cells with more than 6% efficiency and high stability. ACS Nano 7(6):5215–5222

26. Wang J, Mora-Sero I, Pan Z et al (2013) Core/shell colloidal quantum dot exciplex states for the development of highly efficient quantum-dot-sensitized solar cells. J Am Chem Soc 135(42):15913–15922

27. Zhao K, Pan Z, Mora-Sero I et al (2015) Boosting power conversion efficiencies of quantum-dot-sensitized solar cells beyond 8% by recombination control. J Am Chem Soc 137(16):5602–5609

28. Hines DA, Kamat PV (2014) Recent advances in quantum dot surface chemistry. ACS Appl Mater Interface 6(5):3041–3057

29. Kojima A, Teshima K, Shirai Y et al (2009) Organometal halide perovskites as visible-light sensitizers for photovoltaic cells. J Am Chem Soc 131(17):6050–6051

30. Jung HS, Park NG (2015) Perovskite solar cells: from materials to devices. Small 11(1):10–25

31. Im J-H, Lee C-R, Lee J-W (2011) 6.5% Efficient perovskite quantum-dot-sensitized solar cell. Nanoscale 3(10):4088–4093

32. Lee MM, Teuscher J, Miyasaka T et al (2012) Efficient hybrid solar cells based on meso-superstructured organometal halide perovskites. Science 338(6107):643–647

33. Yang WS, Noh JH, Jeon NJ et al (2015) High-performance photovoltaic perovskite layers fabricated through intramolecular exchange. Science 348(6240):1234–1237

34. Cheng YJ, Yang SH, Hsu CS (2009) Synthesis of conjugated polymers for organic solar cell applications. Chem Rev 109(11):5868–5923

35. Ramasamy K, Malik MA, Revaprasadu N et al (2013) Routes to nanostructured inorganic materials with potential for solar energy applications. Chem Mater 25(18):3551–3569

36. Nozik AJ (2010) Nanoscience and nanostructures for photovoltaics and solar fuels. Nano Lett 10(8):2735–2741

37. Koziej D, Lauria A, Niederberger M (2013) 25th Anniversary article: metal oxide particles in materials science: addressing all length scales. Adv Mater 26(2):235–257
38. Wang H, Rogach AL (2013) Hierarchical SnO_2 nanostructures: recent advances in design, synthesis, and applications. Chem Mater 26(1):123–133
39. Bai Y, Mora-Sero I, De Angelis F et al (2014) Titanium dioxide nanomaterials for photovoltaic applications. Chem Rev 114(19):10095–10130
40. Chen Z, Pan D, Li Z et al (2014) Recent advances in tin dioxide materials: some developments in thin films, nanowires, and nanorods. Chem Rev 114(15):7442–7486
41. Tian J, Cao G (2016) Design fabrication and modification of metal oxide semiconductor for improving conversion efficiency of excitonic solar cells. Coord Chem Rev 320–321:193–215
42. Xu J, Chen ZH, Zapien JA (2014) Surface engineering of ZnO nanostructures for semiconductor-sensitized solar cells. Adv Mater 26(31):5337–5367
43. Hagfeldt A, Boschloo G, Sun L et al (2010) Dye-sensitized solar cells. Chem Rev 110 (11):6595–6663
44. Ye M, Wen X, Wang M et al (2014) Recent advances in dye-sensitized solar cells: from photoanodes, sensitizers and electrolytes to counter electrodes. Mater Today 18(3):155–162
45. Concina I, Vomiero A (2014) Metal oxide semiconductors for dye and quantum-dot-sensitized solar cells. Small 11(15):1744–1774
46. Mora-Sero I, Gimenez S, Fabregat-Santiago F et al (2009) Recombination in quantum dot sensitized solar cells. Acc Chem Res 42(11):1848–1857
47. Zhang S, Yang X, Numata Y (2013) Highly efficient dye-sensitized solar cells: progress and future challenges. Energy Environ Sci 6(5):1443
48. Sum TC, Mathews N (2014) Advancements in perovskite solar cells: photophysics behind the photovoltaics. Energy Environ Sci 7(8):2518–2534
49. Boix PP, Nonomura K, Mathews N et al (2014) Current progress and future perspectives for organic/inorganic perovskite solar cells. Mater Today 17(1):16–23
50. Zhang Q, Myers D, Lan J et al (2012) Applications of light scattering in dye-sensitized solar cells. Phys Chem Chem Phys 14(43):14982–14998
51. Kamat PV (2008) Quantum dot solar cells. Semiconductor nanocrystals as light harvesters. J Phyl Chem C 112(48):18737–18753
52. Xu Y, Schoonen MAA (2000) The absolute energy positions of conduction and valence bands of selected semiconducting minerals. Am Mineral 85(3–4):543–556
53. Zhang QF, Cao GZ (2011) Nanostructured photoelectrodes for dye-sensitized solar cells. Nano Today 6(1):91–109
54. Tian J, Cao G (2015) Control of nanostructures and interfaces of metal oxide semiconductors for quantum-dots-sensitized solar cells. J Phys Chem Lett 6(10):1859–1869
55. Hagfeldt A, Gratzel M (2000) Molecular photovoltaics. Acc Chem Res 33(5):269–277
56. Feng X, Zhu K, Frank AJ et al (2012) Rapid charge transport in dye-sensitized solar cells made from vertically aligned single-crystal rutile TiO_2 nanowires. Angew Chem Int Ed 51(11):2727–2730
57. Kim YJ, Lee MH, Kim HJ et al (2009) Formation of highly efficient dye-sensitized solar cells by hierarchical pore generation with nanoporous TiO_2 spheres. Adv Mater 21(36):3668–3673
58. Wang J, Lin Z (2008) Freestanding TiO_2 nanotube arrays with ultrahigh aspect ratio via electrochemical anodization. Chem Mater 20(4):1257–1261
59. Ye MD, Xin XK, Lin CJ et al (2011) High efficiency dye-sensitized solar cells based on hierarchically structured nanotubes. Nano Lett 11(8):3214–3220
60. Lin J, Heo YU, Nattestad A et al (2014) 3D Hierarchical rutile TiO_2 and metal-free organic sensitizer producing dye-sensitized solar cells 8.6% conversion efficiency. Sci Rep 4:57–69
61. Bai Y, Yu H, Li Z et al (2012) In situ growth of a ZnO nanowire network within a TiO_2 nanoparticle film for enhanced dye-sensitized solar cell performance. Adv Mater 24(43):5850–5856

62. Dong Z, Ren H, Hessel CM et al (2013) Quintuple-shelled SnO_2 hollow microspheres with superior light scattering for high-performance dye-sensitized solar cells. Adv Mater 26(6):905–909
63. Shi Y, Wang K, Du Y et al (2013) Solid-state synthesis of ZnO nanostructures for quasi-solid dye-sensitized solar cells with high efficiencies up to 6.46%. Adv Mater 25(32):4413–4419
64. Gao R, Tian J, Liang Z et al (2013) Nanorod-nanosheet hierarchically structured ZnO crystals on zinc foil as flexible photoanodes for dye-sensitized solar cells. Nanoscale 5(5):1894–1901
65. Wang W, Zhang H, Wang R et al (2014) Design of a TiO_2 nanosheet/nanoparticle gradient film photoanode and its improved performance for dye-sensitized solar cells. Nanoscale 6(4):2390–2396
66. Gao R, Liang Z, Tian J et al (2013) ZnO nanocrystallite aggregates synthesized through interface precipitation for dye-sensitized solar cells. Nano Energy 2(1):40–48
67. Chou TP, Zhang QF, Fryxell GE (2007) Hierarchically structured ZnO film for dye-sensitized solar cells with enhanced energy conversion efficiency. Adv Mater 19(18):2588–2592
68. Xi J, Zhang Q, Park K et al (2011) Enhanced power conversion efficiency in dye-sensitized solar cells with TiO_2 aggregates/nanocrystallites mixed photoelectrodes. Electrochim Acta 56(5):1960–1966
69. Zhang QF, Chou TR, Russo B et al (2008) Aggregation of ZnO nanocrystallites for high conversion efficiency in dye-sensitized solar cells. Angew Chem Int Ed 47(13):2402–2406
70. Zhang Q, Uchaker E, Candelaria SL et al (2013) Nanomaterials for energy conversion and storage. Chem Soc Rev 42(7):3127–3171
71. Zhang Q, Chou TP, Russo B (2008) Polydisperse aggregates of ZnO nanocrystallites: a method for energy-conversion-efficiency enhancement in dye-sensitized solar cells. Adv Funct Mater 18(11):1654–1660
72. Zhang Q, Park K, Xi J et al (2011) Recent progress in dye-sensitized solar cells using nanocrystallite aggregates. Adv Energy Mater 1(6):988–1001
73. Zhang QF, Dandeneau CS, Zhou XY et al (2009) ZnO nanostructures for dye-sensitized solar cells. Adv Mater 21(41):4087–4108
74. Alam MJ, Cameron DC (2002) Preparation and characterization of TiO_2 thin films by sol–gel method J Sol–gel. Sci Technol 25(2):137–145
75. K-i Katsumata, Ohno Y, Tomita K et al (2012) Synthesis of amphiphilic brookite nanoparticles with high photocatalytic performance for wide range of application. ACS Appl Mater Inter 4(9):4846–4852
76. Dinh C-T, Nguyen T-D, Kleitz F et al (2009) Shape-controlled synthesis of highly crystalline titania nanocrystals. ACS Nano 3(11):3737–3743
77. Gordon TR, Cargnello M, Paik T et al (2012) Nonaqueous synthesis of TiO_2 nanocrystals using TiF_4 to engineer morphology, oxygen vacancy concentration, and photocatalytic activity. J Am Chem Soc 134(15):6751–6761
78. Bilecka I, Niederberger M (2010) Microwave chemistry for inorganic nanomaterials synthesis. Nanoscale 2(8):1358–1374
79. Wang X, Tian J, Fei C et al (2014) Rapid construction of TiO_2 aggregates using microwave assisted synthesis and its application for dye-sensitized solar cells. RSC Adv 5(12):8622–8629
80. Park K, Zhang Q, Xi J et al (2015) Enhanced charge transport properties by strengthened necks between TiO_2 aggregates for dye sensitized solar cells. Thin Solid Films 588:19–25
81. Zhao Z, Liu G, Li B, Guo L et al (2015) Dye-sensitized solar cells based on hierarchically structured porous TiO_2 filled with nanoparticles. J Mater Chem A 3(21):11320–11329
82. Zhang QF, Yodyingyong S, Xi JT et al (2012) Oxide nanowires for solar cell applications. Nanoscale 4(5):1436–1445
83. Law M, Greene LE, Radenovic A et al (2006) $ZnO–Al_2O_3$ and $ZnO–TiO_2$ core-shell nanowire dye-sensitized solar cells. J Phys Chem B 110(45):22652–22663

84. Zhu S, Shan L, Chen X, He L, Chen J et al (2013) Hierarchical ZnO architectures consisting of nanorods and nanosheets prepared via a solution route for photovoltaic enhancement in dye-sensitized solar cells. RSC Adv 3(9):2910

85. Park K, Zhang QF, Garcia BB et al (2011) Effect of annealing temperature on TiO_2-ZnO core-shell aggregate photoelectrodes of dye-sensitized solar cells. J Phys Chem C 115(11):4927–4934

86. Park K, Zhang QF, Garcia BB et al (2010) Effect of an ultrathin TiO_2 layer coated on submicrometer-sized ZnO nanocrystallite aggregates by atomic layer deposition on the performance of dye-sensitized solar cells. Adv Mater 22(21):2329–2332

87. Wang ML, Huang CG, Cao YG et al (2009) Dye-sensitized solar cells based on nanoparticle-decorated ZnO/TiO_2 core/shell nanorod arrays. J Phys Appl Phys 42(15):155104

88. Plank NOV, Howard I, Rao A et al (2009) Efficient ZnO nanowire solid-state dye-sensitized solar cells using organic dyes and core-shell nanostructures. J Phys Chem C 113(43):18515–18522

89. Peng Q, Lewis JS, Hoertz PG et al (2012) Atomic layer deposition for electrochemical energy generation and storage systems. J Vac Sci Technol A 30(1):010803

90. Fei C, Tian J, Wang Y et al (2014) Improved charge generation and collection in dye-sensitized solar cells with modified photoanode surface. Nano Energy 10:353–362

91. Kato M, Ono H, Ichimura M et al (2011) Observation of defects that reduce schottky barrier height in 4H-SiC schottky contacts using electrochemical deposition of ZnO. Jpn J Appl Phys 50(3):036603

92. Zhang M, Wang T, Cao G (2015) Promises and challenges of tin-based compounds as anode materials for lithium-ion batteries. Int Mater Rev 60(6):330–352

93. Zhang L, Zhao K, Xu W et al (2015) Integrated SnO_2 nanorod array with polypyrrole coverage for high-rate and long-life lithium batteries. Phys Chem Chem Phys 17(12):7619–7623

94. Xu W, Zhao K, Niu C et al (2014) Heterogeneous branched core-shell SnO_2-PANI nanorod arrays with mechanical integrity and three dimentional electron transport for lithium batteries. Nano Energy 8:196–204

95. Mai L-Q, Yang F, Zhao Y-L et al (2011) Hierarchical $MnMoO_4$/$CoMoO_4$ heterostructured nanowires with enhanced supercapacitor performance. Nat Commun 2:381

96. Zhao Y, Xu L, Mai L et al (2012) Hierarchical mesoporous perovskite $La_{0.5}Sr_{0.5}CoO_{2.91}$ nanowires with ultrahigh capacity for Li-air batteries. Proc Natl Acad Sci USA 109 (48):19569–19574

97. Chen W, Qiu Y, Yang S (2010) A new ZnO nanotetrapods/SnO_2 nanoparticles composite photoanode for high efficiency flexible dye-sensitized solar cells. Phys Chem Chem Phys 12 (32):9494–9501

98. Chen W, Qiu YC, Zhong YC et al (2010) High-efficiency dye-sensitized solar cells based on the composite photoanocles of SnO_2 nanoparticles/ZnO nanotetrapods. J Phys Chem A 114 (9):3127–3138

99. Li NC, Martin CR, Scrosati B (2000) A high-rate, high-capacity, nanostructured tin oxide electrode. Electrochem Solid-State Lett 3(7):316–318

100. Kim DW, Hwang IS, Kwon SJ et al (2007) Highly conductive coaxial SnO_2–In_2O_3 heterostructured nanowires for li ion battery electrodes. Nano Lett 7(10):3041–3045

101. Park MS, Kang YM, Wang GX et al (2008) The effect of morphological modification on the electrochemical properties of SnO_2 nanomaterials. Adv Funct Mater 18(3):455–461

102. Han SJ, Jang BC, Kim T, Oh SM, Hyeon T (2005) Simple synthesis of hollow tin dioxide microspheres and their application to lithium-ion battery anodes. Adv Funct Mater 15(11):1845–1850

103. Zhao QR, Xie Y, Dong T et al (2007) Oxidation-crystallization process of colloids: an effective approach for the morphology controllable synthesis of SnO_2 hollow spheres and rod bundles. J Phys Chem C 111(31):11598–11603

104. Lou XW, Wang Y, Yuan CL (2006) Template-free synthesis of SnO$_2$ hollow nanostructures with high lithium storage capacity. Adv Mater 18(17):2325–2329
105. Yang HX, Qian JF, Chen ZX et al (2007) Multilayered nanocrystalline SnO$_2$ hollow microspheres synthesized by chemically induced self-assembly in the hydrothermal environment. J Phys Chem C 111(38):14067–14071
106. Cheng B, Russell JM, Shi WS et al (2004) Large-scale, solution-phase growth of single-crystalline SnO$_2$ nanorods. J Am Chem Soc 126(19):5972–5973
107. Wu HB, Chen JS, Lou XW et al (2011) Synthesis of SnO$_2$ hierarchical structures assembled from nanosheets and their lithium storage properties. J Phys Chem C 115(50):24605–24610
108. Qian JF, Liu P, Xiao Y et al (2009) TiO$_2$-coated multilayered SnO$_2$ hollow microspheres for dye-sensitized solar cells. Adv Mater 21(36):3663–3667
109. Hossain A, Yang GW, Parameswaran M et al (2010) Mesoporous SnO$_2$ spheres synthesized by electrochemical anodization and their application in cdse-sensitized solar cells. J Phys Chem C 114(49):21878–21884
110. Wang Y, Tian J, Fei C et al (2014) Microwave-assisted synthesis of SnO$_2$ nanosheets photoanodes for dye-sensitized solar cells. J Phyl Chem C 118(45):25931–25938
111. Kim SH, Markovich G, Rezvani S et al (1999) Tunnel diodes fabricated from CdSe nanocrystal monolayers. Appl Phys Lett 74(2):317–319
112. Murray CB, Norris DJ, Bawendi MG (1993) Synthesis and characterization of nearly monodisperse CdE (E = sulfur, selenium, tellurium) semiconductor nanocrystallites. J Am Chem Soc 115(19):8706–8715
113. Pan ZX, Zhang H, Cheng K (2012) Highly efficient inverted type-I CdS/CdSe core/shell structure QD-sensitized solar cells. ACS Nano 6(5):3982–3991
114. Li W, Zhong X (2015) Capping ligand-induced self-assembly for quantum dot sensitized solar cells. J Phys Chem Lett 6(5):796–806
115. Huang X, Huang S, Zhang Q et al (2011) A flexible photoelectrode for CdS/CdSe quantum dot-sensitized solar cells (QDSSCs). Chem Commun 47(9):2664–2666
116. Yang Z, Zhang QF, Xi JT et al (2012) CdS/CdSe Co-sensitized solar cell prepared by jointly using successive ion layer absorption and reaction method and chemical bath deposition process. Sci Adv Mater 4(10):1013–1017
117. Etgar L (2013) Semiconductor nanocrystals as light harvesters in solar cells. Materials 6(2):445–459
118. Lee J-W, Son D-Y, Ahn TK et al (2013) Quantum-dot-sensitized solar cell with unprecedentedly high photocurrent. Sci Rep 3:1050
119. Santra PK, Kamat PV (2012) Mn-doped quantum dot sensitized solar cells: a strategy to boost efficiency over 5%. J Am Chem Soc 134(5):2508–2511
120. Yang L, Zhou R, Lan J (2014) Efficient band alignment for Zn$_x$Cd$_{1-x}$Se QD-sensitized TiO$_2$ solar cells. J Mater Chem A 10:3669–3676
121. Zhou R, Zhang Q, Uchaker E et al (2014) Mesoporous TiO$_2$ beads for high efficiency CdS/CdSe quantum dot co-sensitized solar cells. J Mater Chem A 2(8):2517–2525
122. Tian J, Zhang Q, Uchaker E et al (2013) Constructing ZnO nanorod array photoelectrodes for highly efficient quantum dot sensitized solar cells. J Mater Chem A 1(23):6770–6775
123. Tian J, Uchaker E, Zhang Q et al (2014) Hierarchically structured ZnO nanorods-nanosheets for improved quantum-dot-sensitized solar cells. ACS Appl Mater Interfaces 6(6):4466–4472
124. Tian J, Lv L, Wang X et al (2014) Microsphere light-scattering layer assembled by ZnO nanosheets for the construction of high efficiency (5%) quantum dots sensitized solar cells. J Phys Chem C 118(30):16611–16617
125. Tian JJ, Zhang QF, Zhang LL (2013) ZnO/TiO$_2$ nanocable structured photoelectrodes for CdS/CdSe quantum dot co-sensitized solar cells. Nanoscale 5:936–943
126. Tian J, Zhang Q, Uchaker E (2013) Architectured ZnO photoelectrode for high efficiency quantum dot sensitized solar cells. Energy Environ Sci 6(12):35–42

127. Yodyingyong S, Zhou XY, Zhang QF (2010) Enhanced photovoltaic performance of nanostructured hybrid solar cell using highly oriented TiO_2 nanotubes. J Phys Chem C 114 (49):21851–21855
128. Mitzi DB (2004) Solution-processed inorganic semiconductors. J Mater Chem 14(15):2355
129. Stranks SD, Snaith HJ (2015) Metal-halide perovskites for photovoltaic and light-emitting devices. Nat Nanotechnol 10(5):391–402
130. Shockley W, Queisser HJ (1961) Detailed balance limit of efficiency of P-N junction solar cells. J Appl Phys 32(3):510
131. Jeon NJ, Noh JH, Kim YC et al (2014) Solvent engineering for high-performance inorganic-organic hybrid perovskite solar cells. Nat Mater 13(9):897–903
132. Christians JA, Manser JS, Kamat PV (2015) Best practices in perovskite solar cell efficiency measurements. avoiding the error of making bad cells look good. J Phys Chem Lett 6(5):852–857
133. Eperon GE, Burlakov VM, Docampo P et al (2014) Morphological control for high performance, solution-processed planar heterojunction perovskite solar cells. Adv Funct Mater 24(1):151–157
134. Chen C, Ye M, Lv M et al (2014) Ultralong Rutile TiO_2 nanorod arrays with large surface area for CdS/CdSe quantum dot-sensitized solar cells. Electrochem Acta 121:175–182
135. Xiao Z, Dong Q, Bi C, Shao Y et al (2014) Solvent annealing of perovskite-induced crystal growth for photovoltaic-device efficiency enhancement. Adv Mater 26(37):6503–6509
136. Li B, Guo L, Fei C et al (2015) Dynamic growth of compact $CH_3NH_3PbI_3$ capping layer for perovskite solar cell. ACS Appl Mater Interfaces 8(7):4680–4690
137. Zhao Z, Chen X, Cao G (2015) Probing the photovoltage and photocurrent in perovskite solar cells with nanoscale resolution. Adv Funct Mater 26(18):3048–3058
138. White MS, Olson DC, Shaheen SE et al (2006) Inverted bulk-heterojunction organic photovoltaic device using a solution-derived ZnO underlayer. Appl Phys Lett 89(14):143517
139. Zhang F, Xu X, Tang W et al (2011) Recent development of the inverted configuration organic solar cells. Sol Energ Mater Sol C 95(7):1785–1799
140. Hau SK, Yip H-L, Baek NS et al (2008) Air-stable inverted flexible polymer solar cells using zinc oxide nanoparticles as an electron selective layer. Appl Phys Lett 92(25):253301–253303
141. Yang T, Cai W, Qin D et al (2010) Solution-processed zinc oxide thin film as a buffer layer for polymer solar cells with an inverted device structure. J Phys Chem C 114(14):6849–6853
142. Li C-Y, Wen T-C, Lee T-H et al (2009) An inverted polymer photovoltaic cell with increased air stability obtained by employing novel hole/electron collecting layers. J Mater Chem 19(11):1643–1647
143. Huang J-H, Wei H-Y, Huang K-C et al (2010) Using a low temperature crystallization process to prepare anatase TiO_2 buffer layers for air-stable inverted polymer solar cells. Energy Environ Sci 3(5):654–658
144. Yip H-L, Jen AKY (2012) Recent advances in solution-processed interfacial materials for efficient and stable polymer solar cells. Energy Environ Sci 5(3):5994–6011
145. Yin Z, Zheng Q, Chen S-C et al (2013) Interface control of semiconducting metal oxide layers for efficient and stable inverted polymer solar cells with open-circuit voltages over 1.0 volt. ACS Appl Mater Interfaces 5(18):9015–9025
146. Wiranwetchayan O, Zhang Q, Zhou X et al (2012) Impact of the morphology of TiO_2 films as cathode buffer layer on the efficiency of inverted-structure polymer solar cells. Chalcogenide Lett 9(4):157–163
147. Xi J, Wiranwetchayan O, Zhang Q et al (2012) Growth of single-crystalline rutile TiO_2 nanorods on fluorine-doped tin oxide glass for organic-inorganic hybrid solar cells. J Mater Sci: Mater Electron 23(9):1657–1663

148. Liang Z, Zhang Q, Wiranwetchayan O et al (2012) Effects of the morphology of a ZnO buffer layer on the photovoltaic performance of inverted polymer solls. Adv Funct Mater 22 (10):2194–2201
149. Lan J-L, Liang Z, Yang Y-H et al (2014) The effect of SrTiO$_3$:ZnO as cathodic buffer layer for inverted polymer solar cells. Nano Energy 4:140–149
150. Lan J-L, Cherng S-J, Yang Y-H et al (2014) The effects of Ta$_2$O$_5$–ZnO films as cathodic buffer layers in inverted polymer solar cells. J Mater Chem A 2(24):9361–9370

Chapter 18
Nanostructured Porous Polymers for Metal-Free Photocatalysis

Wei Huang, Run Li, Beatriz Chiyin Ma and Kai A.I. Zhang

Abstract The direct utilization of sunlight, especially the visible light part of solar spectrum as a clean and abundant energy source to activate organic reactions is a great challenge in organic chemistry and materials science. Beside the well-developed metal-based photocatalysts such as inorganic semiconductors or transition metal complexes, pure organic photocatalytic systems have gained much attention currently. Among metal-free photocatalysts, nanostructured and highly porous conjugated polymers are of particular interest due to their flexible tunability of optical and electronic properties. In this chapter, an overview on the development of this new class of functional materials is given. Various structural design methods such as donor–acceptor combination on the molecular level, band positions modification, and *p/n* character variation are shown, and porosity, morphology control and their impact on the photocatalytic efficiency are also described.

18.1 Introduction

Sunlight has been regarded as a clean and abundant energy source. The direct utilization of sunlight, especially the visible light part of solar spectrum as the activation energy for organic transformation reactions has attracted much attention in the field of organic chemistry and materials science [1]. Tremendous effort has been paid for the development of visible light photocatalytic systems. Beside the well-developed metal-based photocatalysts such as inorganic semiconductors or transition metal complexes, organic photocatalytic systems have gained much attention currently. Among those, binary carbon nitrides, a state-of-art example, have been recently wildly employed as metal-free photocatalysts due to their promising electronic and optical properties. Another emerging class of metal-free photocatalysts, conjugated polymer-based nanostructured and highly porous materials, is of particular interest due to the ease tunability of their semiconductor

W. Huang · R. Li · B.C. Ma · K.A.I. Zhang (✉)
Max Planck Institute for Polymer Research, Ackermannweg 10, 55128 Mainz, Germany
e-mail: kai.zhang@mpip-mainz.mpg.de

properties via donor–acceptor combination on the molecular level, and the ability of modifying the band gap, band positions, and p/n characters. In this chapter, a general overview on this new class of functional materials for applications in metal-free photocatalysis is given and the impact of important properties such as porosity, morphology, and band structures on the photocatalytic efficiency is also described.

18.2 Conjugated Microporous Polymers (CMPs) for Visible Light Photocatalysis

Conjugated microporous polymers (CMPs) are a subclass of porous organic materials with an amorphous three-dimensional conjugated network combined with permanent microporosity [2–5]. Recently, CMPs have been employed as promising photocatalysts for a vast number of organic reactions, taking advantage of their broad absorption in the visible range and highly tunable energy band positions.

18.2.1 Singlet Oxygen Generation

Singlet oxygen ($^1O_2$), a reactive oxygen species, has been applied in a wide spectrum of applications including wastewater purification, photodynamic therapy, and selective oxidation of organic compounds due to its high reactivity and oxidative ability [6–8]. In 2013, Vilela and coworkers reported the first example of photocatalytic application of CMPs as photosensitizer for $^1O_2$ generation under visible light irradiation [9]. A string electron-withdrawing unit, benzothiadiazole was introduced into the polymer backbone combined with 1,3,5-triethynylbenzene as a weak electron donor and cross-linker via Sonogashira–Hagihara cross-coupling reaction (Fig. 18.1). The authors introduced a template method using silica nanoparticles (SiO_2NPs) to modify the surface area of the polymer networks. They found out that the photocatalytic activity of the polymers depended strongly on their surface area, and the polymer with highest surface area of 660 m^2/g could oxidize α-terpinene with a conversion of 96% upon irradiation at 420 nm, with a singlet oxygen generation quantum yield of 0.06.

Han and coworkers presented a series of metallophthalocyanine-based CMPs (MPc-CMPs) as photosensitizer for the generation of $^1O_2$ [10]. The CMPs were synthesized by Schiff base chemistry between tetraaminometallophthalocyanime ($MPc(NH_2)_4$) and terephthalaldehyde under solvothermal conditions (Fig. 18.2). The CMPs exhibited high efficiency for $^1O_2$ generation upon irradiation in long wavelength range at 700 nm.
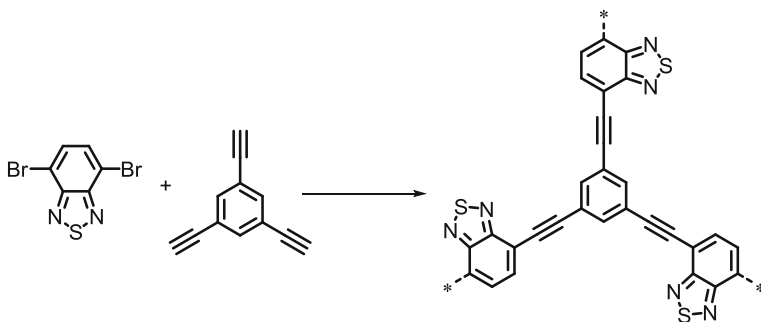
Fig. 18.1 Schematic representation of the synthesis of a benzothiadiazole-based CMP

M = Co, Ni, Cu, Zn
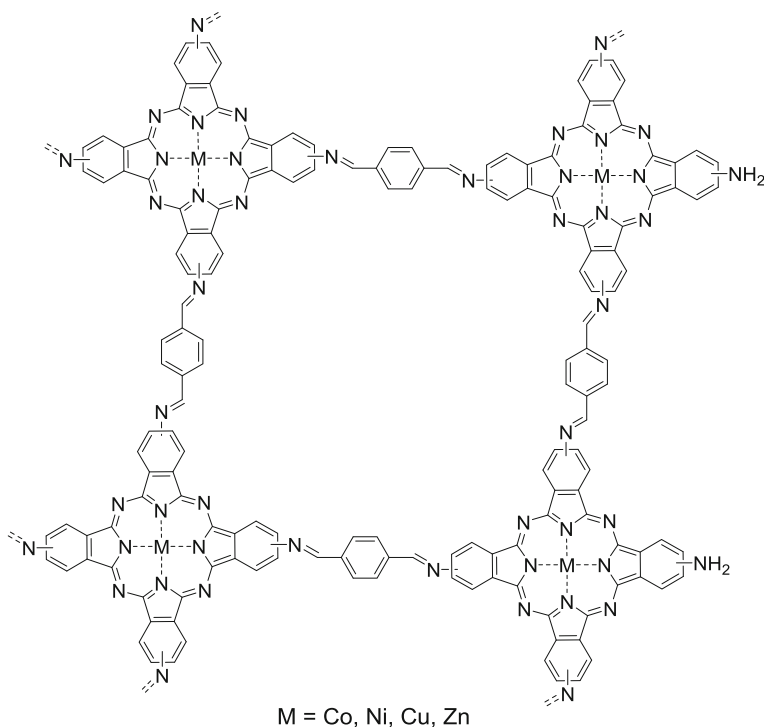
Fig. 18.2 Representative of the MPc-CMPs

18.2.2 Organic Transformation Reactions

Recently, CMPs have recently emerged as an efficient and stable platform for heterogeneous visible-light-promoted chemical transformations owing to their semiconductor-range band gaps and excellent absorption of visible light. The
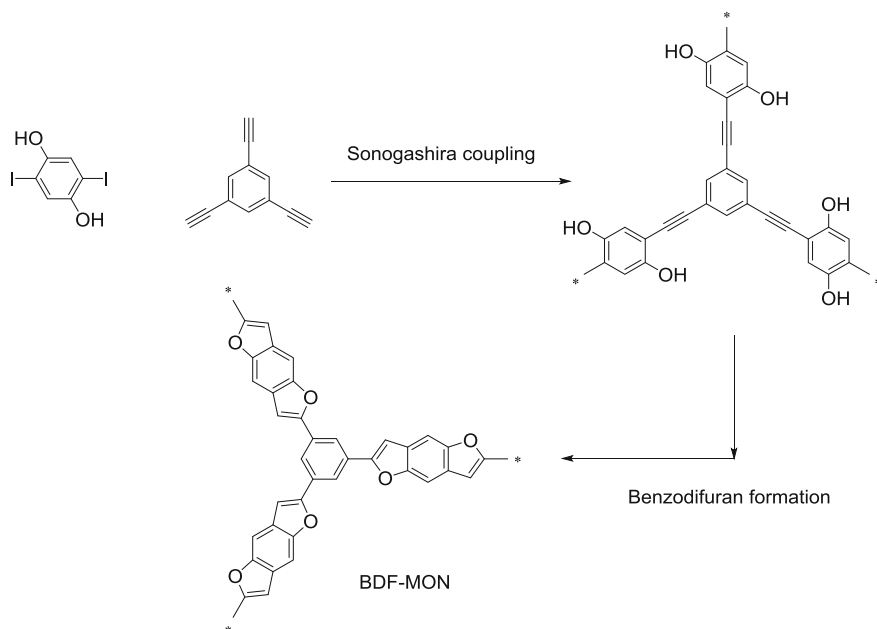
Fig. 18.3 Synthesis of microporous organic networks containing benzodifuran moieties

incorporation of designed photoactive units into the polymer network backbone is a promising strategy to obtain polymer-based organic materials with photocatalytic activity. As displayed in Fig. 18.3, Son et al. reported a tandem synthetic strategy for the preparation of microporous organic networks containing benzodifuran moieties (BDF-MON) [11]. The corresponding polymers networks showed promising photocatalytic activities in the oxidation conversion of primary amine into imines under visible light irradiation.

Rose Bengal is an effective molecular organic photocatalyst and has been used in the field of homogeneous photocatalysis due to its low cost and low toxicity [12]. Jiang et al. [13] have recently reported on CMP networks by incorporating the photoactive Rose Bengal unit into the polymer skeletons via Sonogashira–Hagihara cross-coupling reaction (Fig. 18.4). The polymers were used for aza-Henry reaction at room temperature under visible light irradiation.

For the light-induced photoredox reactions, one of the main factors of the catalyst is the photo-generated valance band (VB) and conduction band (CB) positions, which represent the crucial oxidative and reductive potentials of the catalyst. Zhang and coworkers showed recently a structural design principle of a series of conjugated microporous polymer networks to allow the fine alignment of the valence and conduction band levels for enhanced catalytic activity [14]. As shown in Fig. 18.5, via merely altering the substitution positions on the centered phenyl unit, which functions as the 3D center of a series of poly(benzooxadiazole) networks, the resulted VB and CB positions of the polymers can be optimally
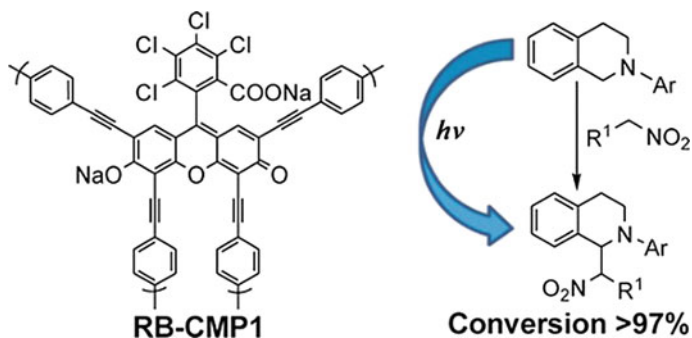
Fig. 18.4 Molecular structure of RB-CMP1 and its application for photocatalytic aza-Henry reactions (reproduced from Ref. [13] with kind permission of © 2013 American Chemical Society)
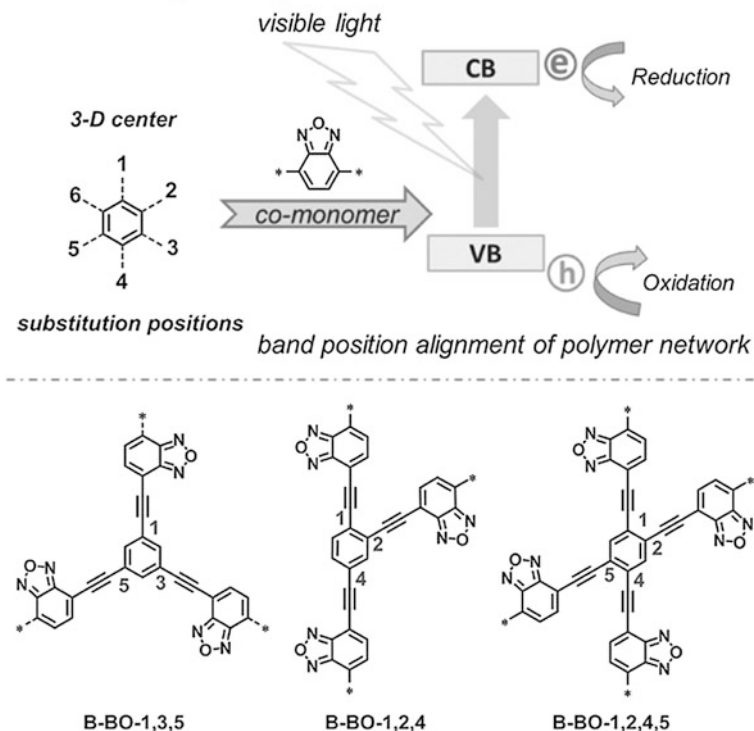
Fig. 18.5 Structural design principle of valence and conduction band position modification of conjugated microporous poly(benzooxadiazole) networks by altering the substitution position on the 3D center (reproduced from Ref. [14] with kind permission of © 2015 Wiley-VCH)
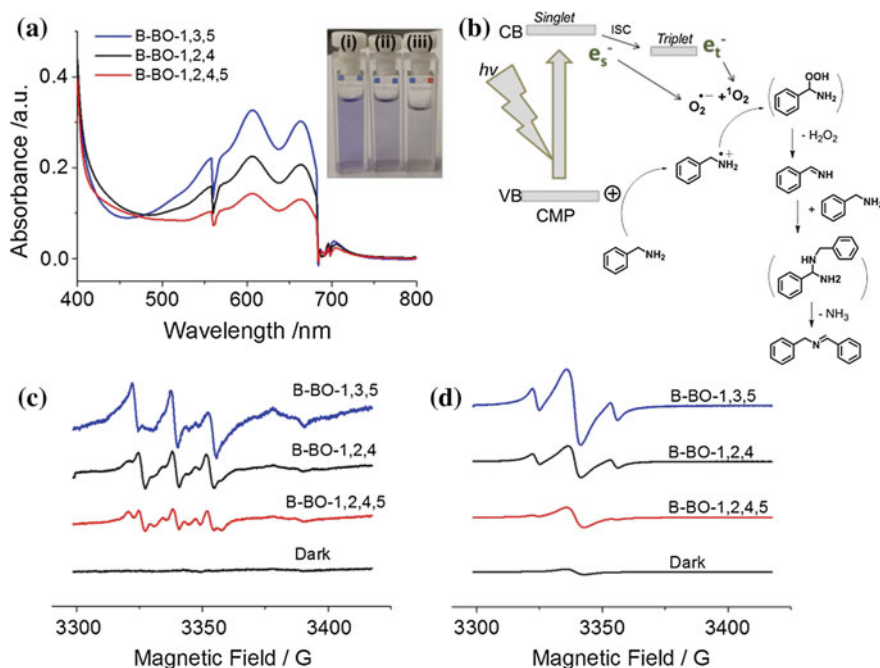
Fig. 18.6 a UV/Vis spectra and photograph of the cationic radical of TMPD (100 mM in 3 mL CH$_3$CN) after photo-inducted oxidation by CMPs (2 mg/mL) in after 1 h under *blue* LED in air. *Inset* (i) B–BO–1,3,5; (ii) B–BO–1,2,4; (iii) B–BO–1,2,4,5; **b** Proposed reaction mechanism of the photocatalytic oxidative coupling of benzylamine. *ISC* intersystem crossing. **c** ESR spectra of DMPO–O$_2^-$, and **d** TEMPO–^{1}O$_2$ adducts for different CMPs under light and in dark (reproduced from Ref. [14] with kind permission of © 2015 Wiley-VCH)

aligned without changing the electron donor and acceptor moieties in the polymer network backbone. It was shown that the photocatalyst designed with the 1,3,5-substitution positions of the centered phenyl ring demonstrated the superior photocatalytic activity in the oxidative coupling of benzyl amines (Fig. 18.6). The superior photo-oxidative activity of B-BO-1,3,5 compared to B-BO-1,2,4 and B-BO-1,2,4,5 results from the highest oxidation potential of 1.55 V and reduction potential of −1.19 V of B–BO–1,3,5. The authors also demonstrated that during the catalytic reaction, both reactive oxygen species (O$_2^-$ and ^{1}O$_2$) could be generated, indicating the existence of photo-generated electrons from both singlet and triplet states (Fig. 18.6).

By keeping the same geometric structure of the polymer network, Zhang and coworkers also demonstrated that the chemical composition inside the polymer backbone also had a considerable impact on the photocatalytic efficiency [15]. In their report, a series of poly(benzochalcogenadiazole)s were synthesized and applied for the photocatalytic oxidation of amines (Fig. 18.7). It was found that the benzothiadiazole-based polymer exhibited the highest catalytic activity.
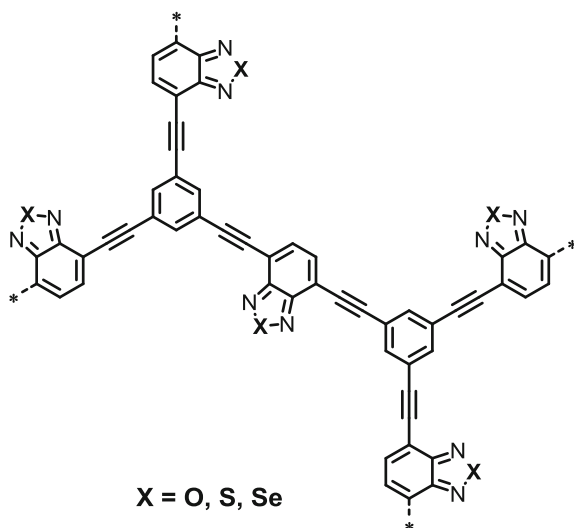
Fig. 18.7 Representative structures of the designed conjugated porous poly(benzochalcogenadiazole)s
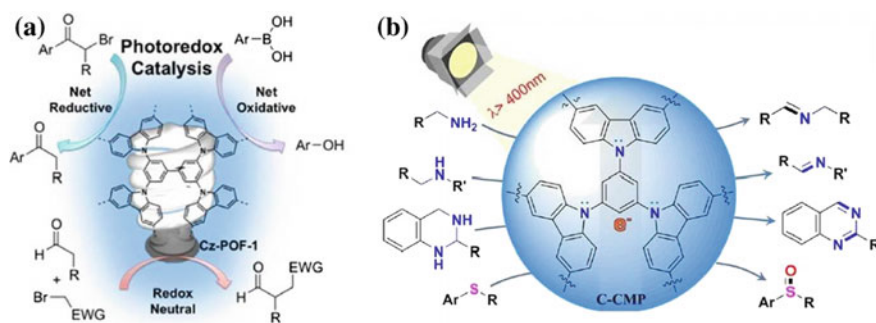
Fig. 18.8 Chemical composition of carbazolic-based CMPs and their application as visible light photocatalyst for **a** a series of photoredox reactions and **b** photocatalytic oxidation of organic compounds (reproduced from Ref. [16, 17] with kind permission of © 2015, 2016 American Chemical Society)

Very recently, Zhang and Loh prepared a series of carbazolic-based CMPs for photocatalytic applications [16, 17]. The chemical compositions are shown in Fig. 18.8. Unlike the convenient CMPs prepared via palladium (Pd)-catalyzed cross-coupling reaction, these carbazolic-based CMPs can be easily synthesized by $FeCl_3$-induced oxidative polymerization of the carbazolic monomers and usually exhibit extremely high-BET surface area (up to 2065 m^2/g). These carbazolic-based CMPs show highly efficient photocatalytic efficiency toward a broad range of organic reaction, including dehalogenation of phenacyl bromide derivatives, α-alkylation of aldehydes, hydroxylation of arylboronic acids, oxidative coupling of

primary amines, aerobic dehydrogenation of non-active secondary amines, and selective oxidation of sulfides.

Covalent triazine frameworks (CTFs), a type of nitrogen-rich porous polymer, have been intensely studied in various application fields in the past decade such as energy storage, catalysis, and gas absorption/separation, due to their extraordinary chemical stability and high porosity [18–21]. However, the optical property of the CTFs has been largely ignored. To date, the utilization of CTFs as catalyst for photocatalytic organic transformation is rarely reported. Very recently, Zhang and coworkers reported nanoporous CTF-based materials as a metal-free photocatalyst for photocatalytic reduction of 4-nitropheno (4-NP) to 4-aminepheno (4-AP) [22]. The photoactive CTFs were synthesized based on trimerization reaction of aromatic nitrile units catalyzed by trifluoromethanesulfonic acid (TfOH) vapor in a solid state with silica nanoparticle as templates (Fig. 18.9).

In addition to the pure organic photocatalytic systems, a hybrid material of Pd nanoparticles deposited on CMP network was recently developed for visible-light-promoted Suzuki cross-coupling reactions [23], via the formation of a hybrid heterojunction, i.e., a metal–semiconductor contact between Pd nanoparticles and CMP, resulting in a positively charged region on the CMP and a negatively charged site on the Pd nanoparticles at the interface due to the Schottky effect [24–27]. As shown in Fig. 18.10, a conjugated microporous poly(benzoxadiazole) network ($B–BO_3$) was chosen as the semiconductive polymer support, on which Pd NPs with sizes between 5 and 10 nm were subsequently immobilized. The coupling reactions of aryl halides with arylboronic acid yielded excellent conversions up to 98% under visible light irradiation at room temperature (Fig. 18.11).
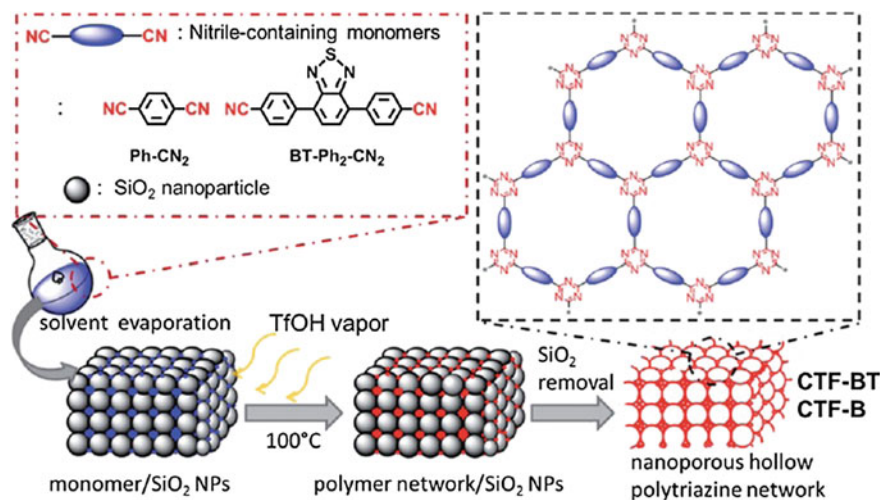
Fig. 18.9 Schematic of solid–vapor synthesis and idealized structures of the nanoporous hollow polytriazine networks (reproduced from Ref. [22] with kind permission of © 2016 Royal Society of Chemistry)
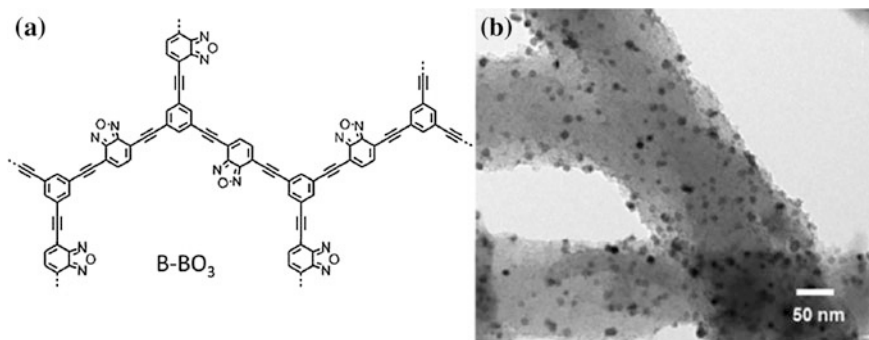
Fig. 18.10 **a** Polymer backbone structure of B–BO$_3$. **b** TEM image of B–BO$_3$ immobilized with Pd NPs with sizes between 5 and 10 nm (reproduced from Ref. [23] with kind permission of © 2015 American Chemical Society)



R= H, F, NO$_2$, OH, COCH$_3$
X= I, Br

Yield up to 98%
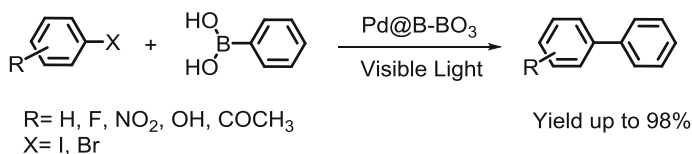
Fig. 18.11 Photocatalytic Suzuki cross-coupling reaction using a conjugated microporous polymer network with immobilized with Pd nanoparticles

18.2.3 Photocatalytic Water Splitting

Solar-driven hydrogen generation through a photocatalytic process has been attracting strong research attentions as one of the most promising strategies to obtain sustainable energy resources [28]. A vast number of studies have focused on inorganic semiconductors as photocatalysts for hydrogen production from water using ultraviolet (UV) or visible light. In the past decade, the use of organic semiconductor as metal-free photocatalysts for visible-light-induced hydrogen production from water has attracted increasing interest because of their vast synthetic diversities for modifying the electronic and structural properties of the photocatalysts [29, 30]. Cooper et al. currently prepared a series of amorphous, microporous organic polymers with exquisite synthetic control over the optical gap in the range 1.94–2.95 eV by varying monomer composition with the best hydrogen evolution rate of 18.4 µmol h^{-1} (Fig.18.12) [31]. Interestingly, the polymers do not require the deposition of an additional metal cocatalyst.

Wang et al. [32] recently reported on a series of conjugated polybenzothiadiazole polymers for hydrogen production using visible light. By alternating the substitution position of the electron-withdrawing benzothiadizole unit on the phenyl unit as a comonomer, various polymers with either one- or three-dimensional
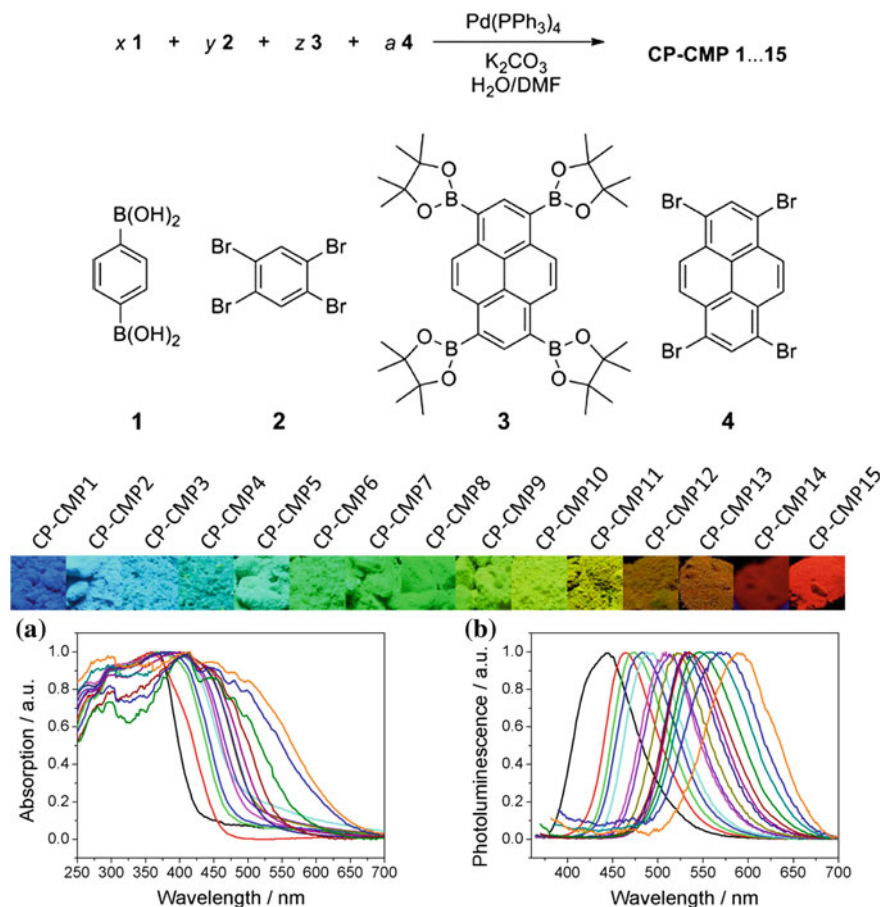
Fig. 18.12 (*Top*) Synthesis of conjugated copolymer photocatalysts (CP-CMP1-15) via Suzuki–Miyaura cross-coupling reaction. (*bottom*) Optical properties of the polymers with **a** UV/Vis absorption and **b** photoluminescence spectra of the polymers (reproduced from Ref. [31] with kind permission of © 2015 American Chemical Society)

structures were synthesized and the effect of the molecular structure on their catalytic activity was investigated (Fig. 18.13). Significantly, the linear conjugated polymers exhibited superior photocatalytic activity, compared to its three-dimensional polymer network counterparts in H_2 evolution from water with a hydrogen evolution rate (HER) of 116 μm mol h^{-1} (Fig. 18.14). The authors proposed that the main reason for the superior efficiency of the linear polymers was likely the high efficiency of its light-induced charge-transfer, charge-separation, and electron-transfer ability.

Yu et al. presented noble porous conjugated polymers, which were synthesized with different light-harvesting chromophores and transition metal-binding bipyridyl
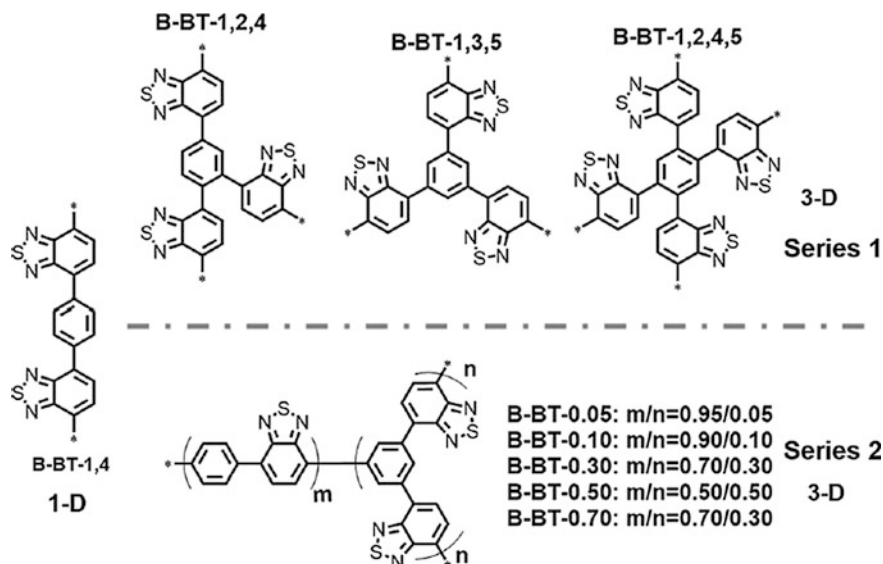
Fig. 18.13 Structures of two series of polybenzothiadiazoles with different molecular designs (reproduced from Ref. [32] with kind permission of © 2016 Wiley-VCH)
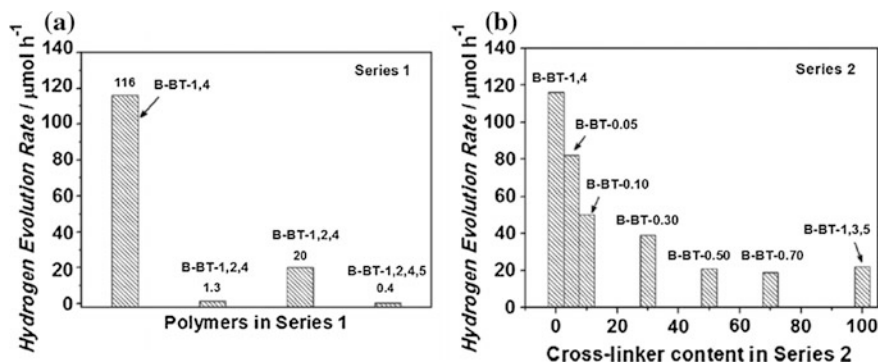
Fig. 18.14 H$_2$ evolution rates using polymers in Series 1 (**a**) and Series 2 (**b**) (reproduced from Ref. [32] with kind permission of © 2016 Wiley-VCH)

(bpy) sites (Fig. 18.15) [33]. Their results showed that the incorporation of bpy units can greatly increase the photocatalytic activity of hydrogen generation due to the improved light absorption, better wettability, local ordering structure, and the improved charge-separation process. The authors found that the hydrogen generation rate of photocatalyst increased rapidly as the residual metal content increases from 0.04 to 0.46% and becomes saturated at higher Pd content.
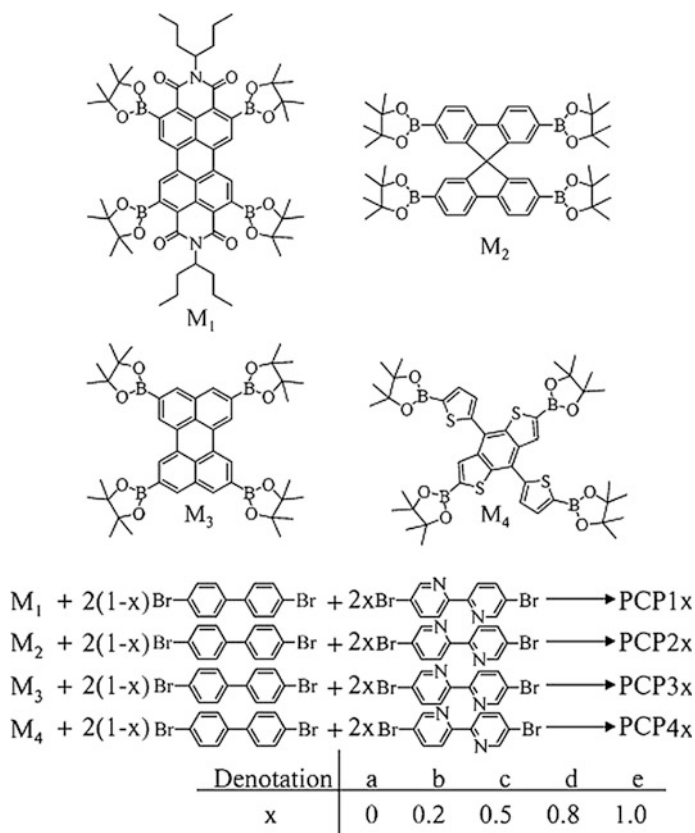
Fig. 18.15 Structures of monomers and synthesis of PCP photocatalysts by Suzuki polycondensation (reproduced from Ref. [33] with kind permission of © 2016 American Chemical Society)

18.3 Water-Compatible Conjugated Microporous Polymers for Visible Light-Driven Photocatalysis in Aqueous Medium

Most of the CMPs are insoluble networks, which limit the range of processing options. Regarding the development of more sustainable reaction media for organic reactions, much effort has been devoted to the use of "green" solvents, in particular water, as a cheap and environment-friendly alternative for chemical transformations instead of hazardous halogenated solvents [34, 35]. So far, only few research reports have been described as steps toward the synthesis of water-soluble CMPs for photocatalytic reactions. Modifications of pristine CMPs [36, 37] and emulsion techniques for formation of nanoparticulate CMPs [38, 39] have been employed as strategies to enhance the water compatibility of the polymer networks. A post-modification method of alkyne-bearing conjugated microporous
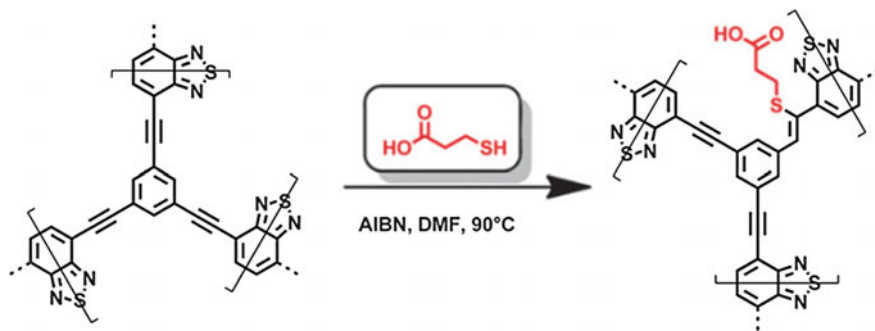
Fig. 18.16 Schematic representation of post-modification of CMP via thiol-yne chemistry (reproduced from Ref. [36] with kind permission of © 2013 Royal Society of Chemistry)

polybenzothiadiazoles via a thiol-yne chemistry (Fig. 18.16) was reported to generate *singlet* oxygen for the conversion of furoic acid to 5-hydroxy-2(5H)-furanone in water [36].

Another modification strategy based on a simple protonation method (Fig. 18.17) showed that stable water-compatible conjugated microporous polyazulenes were able to photoreduce Cr^{VI} to Cr^{III} in aqueous medium [37].

A recent report by Zhang and coworkers showed that CMP nanoparticles (CMP NPs) with a variety of shapes could be obtained via Suzuki–Miyaura and Sonogashira–Hagihara coupling in miniemulsion (Table 18.1, Fig. 18.18). The stable CMP NPs were employed in the reductive activation of molecular oxygen for the photodegradation of organic dyes and also showed the ability for the photooxidation of *N,N,N',N'*-tetramethyl-p-phenylenediamine in water under visible light irradiation [39]. The authors also pointed out that by using the CMP NPs in water, different reactive species such as superoxide ($•O_2^-$), *singlet* oxygen ($^1O_2$), •OH, and h^+ could be generated under visible light irradiation.

18.4   Macroporous Conjugated Polymers for Visible Light Photocatalysis

Polymerized high internal phase emulsion (polyHIPE) was a relatively novel method for the synthesis of conjugated macroporous polymers containing large-scale porosity in micrometer scale. In the past, the class of macroporous polymer-based materials has been used in a large range of applications such as tissue-engineering scaffolds [40], enzyme immobilization [41, 42], gas storage [43], and separation media [44]. The first examples of fully conjugated polyHIPEs were reported by Vilela and coworkers (Fig. 18.19) [45]. The authors showed that with the increase of benzothiadiazole moiety inside the polymer backbone, the
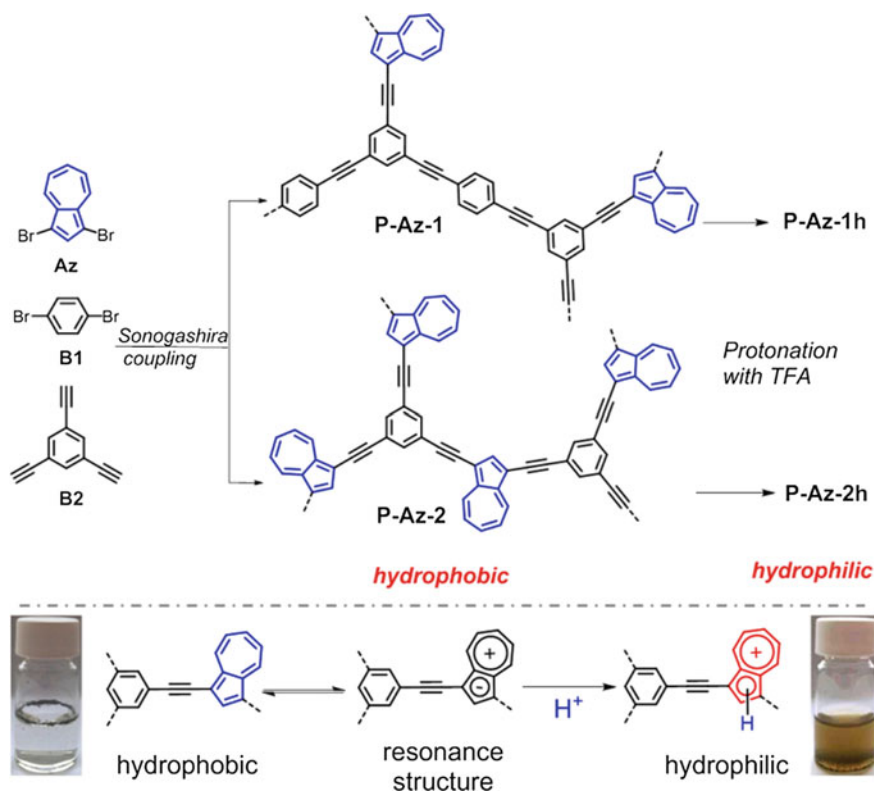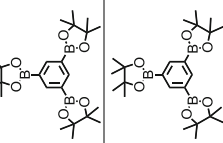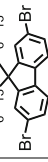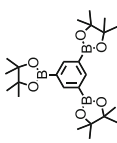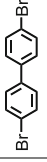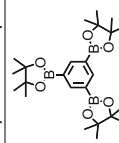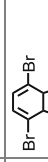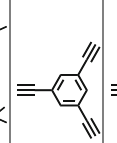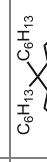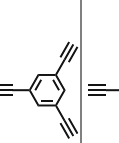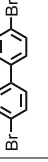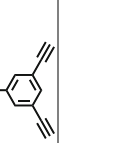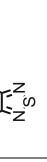
Fig. 18.17 Synthetic pathway and modification method for hydrophilic, conjugated microporous poly-azulene networks (reproduced from Ref. [37] with kind permission of © 2016 Wiley-VCH)

generation rate of singlet oxygen increased. In addition, a flow photoreactor was also designed for continuous and efficient singlet oxygen production.

Zhang and coworkers demonstrated a nanopore-engineering method of fully conjugated polyHIPEs in order to introduce micropores into the macorporous polymer networks [46]. By using cleavable *tert*-butyl carboxylate group as building unit for the polymer, extra nano-sized pores could be created by removing the *tert*-butyl carboxylate functional group, gaining a surface area increase by maximal eight times (Fig. 18.20). The photocatalytic oxidation of sulfides was carried out to demonstrate the photocatalytic efficiency in a continuous flow setup system. It was shown that mono-oxidized product of the thioethers could be obtained with yields of >99% and selectivity of >99% in best cases.

Two other examples of conjugated polyHIPEs were reported recently by Zhang et al. [47, 48]. The polyHIPE containing the strong electron-withdrawing benzo-bisthiadiazole (BBT) demonstrated a high photocatalytic efficiency in the dehalo-genation reaction of a-bromoacetophenones under the irradiation of 23 W household bulb [47]. Another conjugated polyHIPE containing benzoxadiazole

Table 18.1 Various monomers used for the different CMP NPs and their physical properties (reproduced from Ref. [39] with kind permission of © 2015 Royal Society of Chemistry)

| CMP NPs	Cross-linker (A₃-type)	Comonomer (B₂-type)	Shape	Surface area (m² g⁻¹)	Pore volume (cm³ g⁻¹)	Pore diameter (nm)	Band gap/opt. (eV)
B–FL₃–a			Spherical	18	0.058	7.5	3.04
B–BPh₃–a			Irregular shape	281	0.264	1.5	2.52
B–BT₃–a			Rod-shape	93	0.220	1.5	1.96
B–FL₃–b			Spherical	48	0.067	3.8	2.64
B–BPh₃–b			Spherical	512	0.382	1.4	2.36
B–BT₃–b			Ring-shape	200	0.560	1.4	1.76
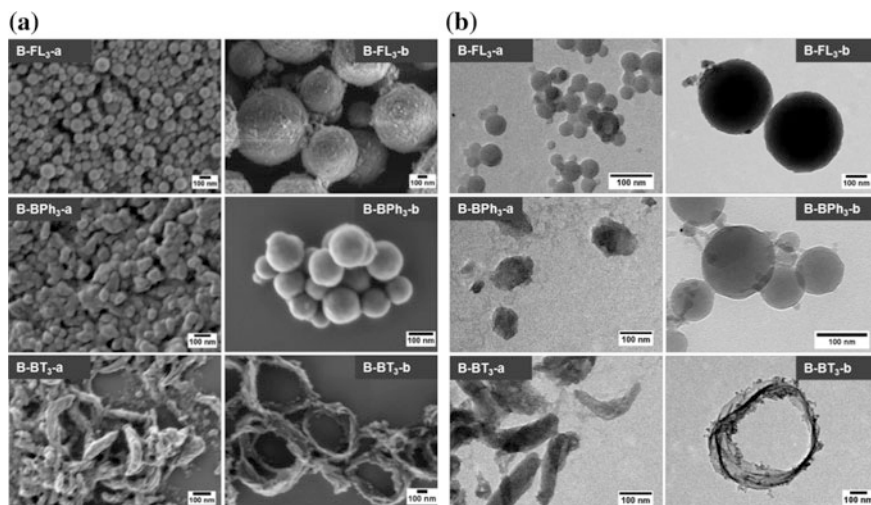
Fig. 18.18 a SEM and **b** TEM images of the CMP NPs with different shapes (reproduced from Ref. [39] with kind permission of © 2015 Royal Society of Chemistry)
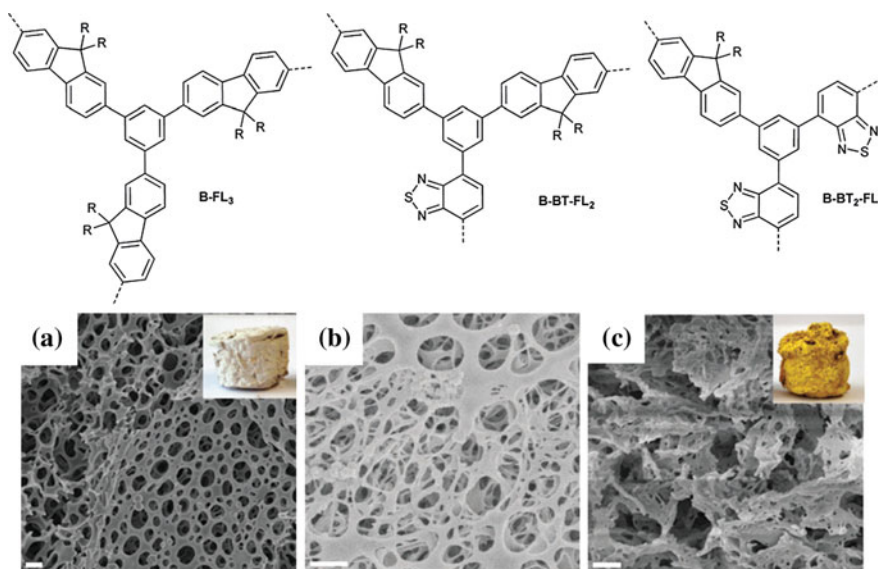
Fig. 18.19 Chemical structures and morphology of the conjugated polyHIPEs (reproduced from Ref. [45] with kind permission of © 2013 Royal Society of Chemistry)
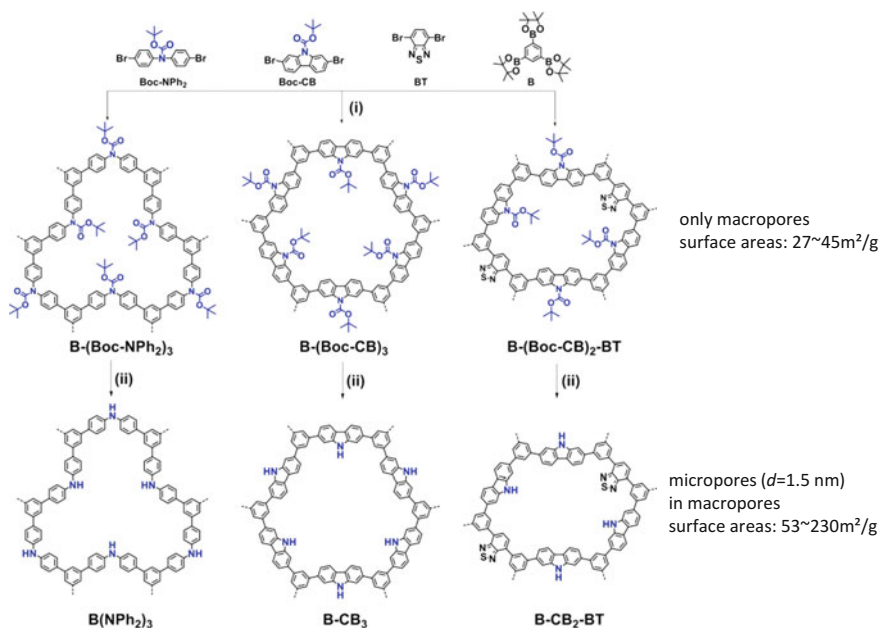
Fig. 18.20 Idealized structures and surface area control via nanopore engineering of macroporous polymer networks (reproduced from Ref. [46] with kind permission of © 2014 Royal Society of Chemistry)

(BO) as photoactive moiety showed a high activity for visible-light-activated radical polymerization of methyl methacrylate (MMA) [48].

18.5 Non-conjugated Nanoporous Polymer Containing Organic Semiconductor Moieties

Besides the fully conjugated polymer networks, non-conjugated nanoporous polymers have also been developed as visible-light-active photocatalysts. To achieve a high catalytic efficiency, highly photoactive units such as benzothiadiazole [49], boron-dipyrromethene [50], and thioxanthone [51] were introduced into cross-linked polymer networks for the design of photocatalysts. The cross-linking of the photoactive units could be realized in various methods, for example, Friedel–Crafts alkylation reaction [49], "click" reaction [50] and anion polymerization [52].

Various organic reactions driven by active oxygen species such as oxygenation of sulfides [50] and olefinic compounds [53] and degradation of organic pollutions [54] were reported. Jing et al. prepared cross-linked porous polymers by introducing the Boron-dipyrromethene (BODIPY) unit into a polystyrene matrix, which demonstrated a high catalytic efficiency for the oxidation of organic sulfides [50].

Yagci et al. [51] reported the photo-generated radical initiator could be used for the polymerization of MMA with both conjugated polymer and non-conjugated polymer containing thioxanthone unit. A recent report of Vilela et al. [54] demonstrated that a benzothiadiazole-containing polyamide polymer could efficiently photo-generated singlet oxygen and therefore degrade organic contaminants such as bisphenol A and cimetidine. Zhang and coworkers reported a series of microporous polymers containing 4,7-diphenyl-2,1,3-benzothiadiazole as photoactive moiety via Friedel–Crafts alkylation reaction [49]. The polymers were employed for highly selective bromination reaction of electron-rich aromatic compounds with conversion up to 99% and selectivity up to 99% in best cases.

18.6 Conclusions

In summary, in this chapter, an overview on the preparation and application of nanostructured and highly porous polymers containing conjugated organic semiconductor units in visible-light-promoted and metal-free photocatalysis is given. Due to the ease on tunability of their semiconductor properties via donor–acceptor combination on the molecular level, and the ability for modifying the band gap, band positions, and *p/n* characters, this new class of materials demonstrated a promising perspective in light-promoted organic synthesis. Important properties such as porosity, morphology, and band structures should be considered for the design of the polymer-based materials in order to achieve high photocatalytic efficiency. There is a high potential for further optimization and molecular design possibilities. Nevertheless, we believe that the nanostructured, highly porous polymers could offer a high potential for chemical reactions under sustainable and environmentally friendly conditions.

References

1. Narayanam JM, Stephenson CR (2011) Visible light photoredox catalysis: applications in organic synthesis. Chem Soc Rev 40(1):102–113
2. Cooper AI (2009) Conjugated microporous polymers. Adv Mater 21(12):1291–1295
3. Xu Y, Jin S, Xu H et al (2013) Conjugated microporous polymers: design, synthesis and application. Chem Soc Rev 42(20):8012–8031
4. Jiang JX, Su F, Trewin A et al (2007) Conjugated microporous poly(aryleneethynylene) networks. Angew Chem Int Ed 46(45):8574–8578
5. Vilela F, Zhang K, Antonietti M (2012) Conjugated porous polymers for energy applications. Energy Environ Sci 5(7):7819–7832
6. Ogilby PR (2010) Singlet oxygen: there is indeed something new under the sun. Chem Soc Rev 39(8):3181–3209
7. Lovell JF, Liu TW, Chen J et al (2010) Activatable photosensitizers for imaging and therapy. Chem Rev 110(5):2839–2857

8. DeRosa MC, Crutchley RJ (2002) Photosensitized singlet oxygen and its applications. Chem Rev 233:351–371

9. Zhang K, Kopetzki D, Seeberger P H et al (2013) Surface area control and photocatalytic activity of conjugated microporous poly (benzothiadiazole) networks. Angewandte Chemie, 125(5):1472-1476.

10. Ding X, Han BH (2015) Metallophthalocyanine-based conjugated microporous polymers as highly efficient photosensitizers for singlet oxygen generation. Angew Chem Int Ed 54 (22):6536–6539

11. Kang N, Park JH, Ko KC et al (2013) Tandem synthesis of photoactive benzodifuran moieties in the formation of microporous organic networks. Angew Chem Int Ed 52(24):6228–6232

12. Ravelli D, Fagnoni M, Albini A (2013) Photoorganocatalysis. What for? Chem Soc Rev 42 (1):97–113

13. Jiang J-X, Li Y, Wu X et al (2013) Conjugated microporous polymers with rose bengal dye for highly efficient heterogeneous organo-photocatalysis. Macromolecules 46(22):8779–8783

14. Wang Z J, Ghasimi S, Landfester K et al (2015) Molecular structural design of conjugated microporous poly (benzooxadiazole) networks for enhanced photocatalytic activity with visible light. Advanced Materials 27(40):6265–6270.

15. Wang ZJ, Garth K, Ghasimi S et al (2015) Conjugated microporous poly (benzochalcogenadiazole) for photocatalytic oxidative coupling of amines under visible light. Chem Sus Chem 8(20):3459–3464

16. Luo J, Zhang X, Zhang J (2015) Carbazolic porous organic framework as an efficient, metal-free visible-light photocatalyst for organic synthesis. ACS Catal 5(4):2250–2254

17. Su C, Tandiana R, Tian B et al (2016) Visible-light photocatalysis of aerobic oxidation reactions using carbazolic conjugated microporous polymers. ACS Catal 6(6):3594–3599

18. Kuhn P, Antonietti M, Thomas A (2008) Porous, covalent triazine-based frameworks prepared by ionothermal synthesis. Angew Chem Int Ed 47(18):3450–3453

19. Sakaushi K, Hosono E, Nickerl G et al (2013) Aromatic porous-honeycomb electrodes for a sodium-organic energy storage device. Nat Commun 4:1485

20. Palkovits R, Antonietti M, Kuhn P et al (2009) Solid catalysts for the selective low-temperature oxidation of methane to methanol. Angew Chem Int Ed 48(37):6909–6912

21. Bhunia A, Boldog I, Möller A et al (2013) Highly stable nanoporous covalent triazine-based frameworks with an adamantane core for carbon dioxide sorption and separation. J Mater Chem A 1(47):14990–14999

22. Huang W, Wang ZJ, Ma BC et al (2016) Hollow nanoporous covalent triazine frameworks via acid vapor-assisted solid phase synthesis for enhanced visible light photoactivity. J Mater Chem A 4:7555–7559

23. Wang ZJ, Ghasimi S, Landfester K et al (2015) Photocatalytic suzuki coupling reaction using conjugated microporous polymer with immobilized palladium nanoparticles under visible light. Chem Mater 27(6):1921–1924

24. Rikken GLJA, Braun D, Staring EGJ et al (1994) Schottky effect at a metal-polymer interface. Appl Phys Lett 65(2):219–221

25. Subramanian V, Wolf E, Kamat PV (2001) Semiconductor-metal composite nanostructures. To what extent do metal nanoparticles improve the photocatalytic activity of TiO_2 films. J Phys Chem B 105(46):11439–11446

26. Li XH, Baar M, Blechert S et al (2013) Facilitating room-temperature Suzuki coupling reaction with light: Mott-Schottky photocatalyst for C–C-coupling. Sci Rep 3

27. Li X-H, Antonietti M (2013) Metal nanoparticles at mesoporous N-doped carbons and carbon nitrides: functional Mott-Schottky heterojunctions for catalysis. Chem Soc Rev 42(16):6593–6604

28. Chen X, Shen S, Guo L et al (2010) Semiconductor-based photocatalytic hydrogen generation. Chem Rev 110(11):6503–6570

29. Wang X, Maeda K, Chen X et al (2009) Polymer semiconductors for artificial photosynthesis: hydrogen evolution by mesoporous graphitic carbon nitride with visible light. J Am Chem Soc 131(5):1680–1681

30. Zhang J, Zhang G, Chen X et al (2012) Co-monomer control of carbon nitride semiconductors to optimize hydrogen evolution with visible light. Angew Chem Int Ed 124(13):3237–3241

31. Sprick RS, Jiang J-X, Bonillo B et al (2015) Tunable organic photocatalysts for visible-light-driven hydrogen evolution. J Am Chem Soc 137(9):3265–3270

32. Yang C, Ma BC, Zhang L et al (2016) Molecular engineering of conjugated polybenzothiadiazoles for enhanced hydrogen production by photosynthesis. Angew Chem Int Ed 55:9202–9206

33. Li L, Cai Z, Wu Q et al (2016) Rational design of porous conjugated polymers and roles of residual palladium for photocatalytic hydrogen production. J Am Chem Soc 138(24):7681–7686

34. Cheng G, Hasell T, Trewin A et al (2012) Soluble conjugated microporous polymers. Angew Chem Int Ed 51(51):12727–12731

35. Deng S, Zhi J, Zhang X et al (2014) Size-controlled synthesis of conjugated polymer nanoparticles in confined nanoreactors. Angew Chem Int Ed 53(51):14144–14148

36. Urakami H, Zhang K, Vilela F (2013) Modification of conjugated microporous poly-benzothiadiazole for photosensitized singlet oxygen generation in water. Chem Commun 49(23):2353–2355

37. Ghasimi S, Landfester K, Zhang KAI (2016) Water compatible conjugated microporous polyazulene networks as visible-light photocatalysts in aqueous medium. Chem Cat Chem 8(4):694–698

38. Zhang P, Weng ZH, Guo J et al (2011) Solution-dispersible, colloidal, conjugated porous polymer networks with entrapped palladium nanocrystals for heterogeneous catalysis of the suzuki-miyaura coupling reaction. Chem Mater 23(23):5243–5249

39. Ma BC, Ghasimi S, Landfester K et al (2015) Conjugated microporous polymer nanoparticles with enhanced dispersibility and water compatibility for photocatalytic applications. J Mater Chem A 3(31):16064–16071

40. Bokhari M, Carnachan RJ, Cameron NR et al (2007) Novel cell culture device enabling three-dimensional cell growth and improved cell function. Biochem Biophys Res Commun 354(4):1095–1100

41. Dizge N, Keskinler B, Tanriseven A (2008) Covalent attachment of microbial lipase onto microporous styrene-divinylbenzene copolymer by means of polyglutaraldehyde. Colloid Surface B 66(1):34–38

42. Pierre SJ, Thies JC, Dureault A et al (2006) Covalent enzyme immobilization onto photopolymerized highly porous monoliths. Adv Mater 18(14):1822–1826

43. Su F, Bray CL, Tan B et al (2008) Rapid and reversible hydrogen storage in clathrate hydrates using emulsion-templated polymers. Adv Mater 20(14):2663–2666

44. Mert EH, Yıldırım H, Üzümcü AT et al (2013) Synthesis and characterization of magnetic polyHIPEs with humic acid surface modified magnetic iron oxide nanoparticles. React Funct Polym 73(1):175–181

45. Zhang K, Vobecka Z, Tauer K et al (2013) Conjugated polyHIPEs as highly efficient and reusable heterogeneous photosensitizers. Chem Commun 49(95):11158–11160

46. Wang ZJ, Ghasimi S, Landfester K et al (2014) Highly porous conjugated polymers for selective oxidation of organic sulfides under visible light. Chem Commun 50(60):8177–8180

47. Wang ZJ, Ghasimi S, Landfester K et al (2014) A conjugated porous poly-benzobisthiadiazole network for a visible light-driven photoredox reaction. J Mater Chem A 2(44):18720–18724

48. Wang ZJ, Landfester K, Zhang KAI (2014) Hierarchically porous [small pi]-conjugated polyHIPE as a heterogeneous photoinitiator for free radical polymerization under visible light. Polym Chem 5(11):3559–3562

49. Li R, Wang ZJ, Wang L et al (2016) Photocatalytic selective bromination of electron-rich aromatic compounds using microporous organic polymers with visible light. ACS Catal l6(2):1113–1121

50. Li W, Zhang W, Dong X et al (2012) Porous heterogeneous organic photocatalyst prepared by HIPE polymerization for oxidation of sulfides under visible light. J Mater Chem 22 (34):17445–17448
51. Dadashi-Silab S, Bildirir H, Dawson R et al (2014) Microporous thioxanthone polymers as heterogeneous photoinitiators for visible light induced free radical and cationic polymerizations. Macromolecules 47(14):4607–4614
52. Pastor-Pérez L, Barriau E, Frey H et al (2008) Photocatalysis within hyperbranched polyethers with a benzophenone core. J Org Chem 73(12):4680–4683
53. Chavan SA, Maes W, Gevers LEM et al (2005) Porphyrin functionalized dendrimers: synthesis and application as recyclable photocatalysts in a nanofiltration membrane reactor. Chem Eur J 11(22):6754–6762
54. Shen J, Steinbach R, Tobin JM et al (2016) Photoactive and metal-free polyamide-based polymers for water and wastewater treatment under visible light irradiation. Appl Catal B 193:226–233